

Bo Huang  
Yufeng Yao  
*Editors*

# Proceedings of the 5th International Conference on Electrical Engineering and Automatic Control

# Lecture Notes in Electrical Engineering

Volume 367

## Board of Series editors

Leopoldo Angrisani, Napoli, Italy  
Marco Arteaga, Coyoacán, México  
Samarjit Chakraborty, München, Germany  
Jiming Chen, Hangzhou, P.R. China  
Tan Kay Chen, Singapore, Singapore  
Rüdiger Dillmann, Karlsruhe, Germany  
Haibin Duan, Beijing, China  
Gianluigi Ferrari, Parma, Italy  
Manuel Ferre, Madrid, Spain  
Sandra Hirche, München, Germany  
Faryar Jabbari, Irvine, USA  
Janusz Kacprzyk, Warsaw, Poland  
Alaa Khamis, New Cairo City, Egypt  
Torsten Kroeger, Stanford, USA  
Tan Cher Ming, Singapore, Singapore  
Wolfgang Minker, Ulm, Germany  
Pradeep Misra, Dayton, USA  
Sebastian Möller, Berlin, Germany  
Subhas Mukhopadhyay, Palmerston, New Zealand  
Cun-Zheng Ning, Tempe, USA  
Toyoaki Nishida, Sakyo-ku, Japan  
Bijaya Ketan Panigrahi, New Delhi, India  
Federica Pascucci, Roma, Italy  
Tariq Samad, Minneapolis, USA  
Gan Woon Seng, Nanyang Avenue, Singapore  
Germano Veiga, Porto, Portugal  
Haitao Wu, Beijing, China  
Junjie James Zhang, Charlotte, USA

### *About this Series*

“Lecture Notes in Electrical Engineering (LNEE)” is a book series which reports the latest research and developments in Electrical Engineering, namely:

- Communication, Networks, and Information Theory
- Computer Engineering
- Signal, Image, Speech and Information Processing
- Circuits and Systems
- Bioengineering

LNEE publishes authored monographs and contributed volumes which present cutting edge research information as well as new perspectives on classical fields, while maintaining Springer’s high standards of academic excellence. Also considered for publication are lecture materials, proceedings, and other related materials of exceptionally high quality and interest. The subject matter should be original and timely, reporting the latest research and developments in all areas of electrical engineering.

The audience for the books in LNEE consists of advanced level students, researchers, and industry professionals working at the forefront of their fields. Much like Springer’s other Lecture Notes series, LNEE will be distributed through Springer’s print and electronic publishing channels.

More information about this series at <http://www.springer.com/series/7818>

Bo Huang · Yufeng Yao  
Editors

# Proceedings of the 5th International Conference on Electrical Engineering and Automatic Control

 Springer

*Editors*

Bo Huang  
Robotics Institute  
Harbin Institute of Technology  
Weihai  
China

Yufeng Yao  
Robotics Institute  
Harbin Institute of Technology  
Weihai  
China

ISSN 1876-1100                      ISSN 1876-1119 (electronic)  
Lecture Notes in Electrical Engineering  
ISBN 978-3-662-48766-2              ISBN 978-3-662-48768-6 (eBook)  
DOI 10.1007/978-3-662-48768-6

Library of Congress Control Number: 2016936432

© Springer-Verlag Berlin Heidelberg 2016

This work is subject to copyright. All rights are reserved by the Publisher, whether the whole or part of the material is concerned, specifically the rights of translation, reprinting, reuse of illustrations, recitation, broadcasting, reproduction on microfilms or in any other physical way, and transmission or information storage and retrieval, electronic adaptation, computer software, or by similar or dissimilar methodology now known or hereafter developed.

The use of general descriptive names, registered names, trademarks, service marks, etc. in this publication does not imply, even in the absence of a specific statement, that such names are exempt from the relevant protective laws and regulations and therefore free for general use.

The publisher, the authors and the editors are safe to assume that the advice and information in this book are believed to be true and accurate at the date of publication. Neither the publisher nor the authors or the editors give a warranty, express or implied, with respect to the material contained herein or for any errors or omissions that may have been made.

Printed on acid-free paper

This Springer imprint is published by Springer Nature  
The registered company is Springer-Verlag GmbH Berlin Heidelberg

# Contents

<b>Individual Pitch Control Based on Radial Basis Function Neural Network</b> . . . . .	1
Bing Han, Lawu Zhou, Zhiwen Zhang, Meng Tian and Ningfeng Deng	
<b>Study on the Distribution Automation System Terminal Automatic Test Method</b> . . . . .	9
Peng Li, Yimin Qian and Wei Li	
<b>Identification for Acoustic Emission Signal of Crack Based on EMD Approximate Entropy and SVM</b> . . . . .	19
Zhen-hua Zeng, Shou-ming Zhang and Li Si	
<b>Capacitors Optimization of Novel Series-Connected Capacitor-Run Three-Phase Induction Motor Fed by Single-Phase Supply</b> . . . . .	27
Hui Zhong, Xiuhe Wang and Dongwei Qiao	
<b>Distributed Cooperative Secondary Control of Microgrids with Bounded Control Input</b> . . . . .	35
Xinsheng Wang and Tianyi Xiong	
<b>Distributed Robust Control of Uncertain Multi-agent Systems with Directed Networks</b> . . . . .	45
Wei Liu, Qingpo Wu and Shaolei Zhou	
<b>Resonant Analysis and Depression in Multi-inverter Grid-Connection System</b> . . . . .	55
Jian Wu, Caihong Zhang, Rui Wang and Dianguo Xu	
<b>The Application of Power Electronic Switch in the Regulated Capacity Transformer</b> . . . . .	63
Hongxing Chen, Zhizhen Liu, Tong Hei, Xiaodong Qu and Guozheng Qi	
<b>DC Fault Analysis and Protection Design in Shunt Modular Multilevel-Based MTDC System</b> . . . . .	71
Jian Wu, Yue Qi, Yanfei You and Dianguo Xu	

<b>The Simulation of Zero-Sequence Blocking Transformer (ZSBT) . . . .</b>	81
Kai Xu, Zhi-zhen Liu, Xiao-dong Qu and Guo-zheng Qi	
<b>Design and Simulation of a Vivaldi Antenna Fed by Coplanar Waveguide . . . . .</b>	89
Lizhong Song, Weiwei Yin and Jia Li	
<b>The PID Parameters Optimization Method Based on GA for NC Power Supply . . . . .</b>	97
Chenjia Wei, Zehao Liu, Peizheng Li, Jianfei Chen and Sheng Zhang	
<b>Different Feature Combination Rules in CNNs for Face Detection . . . . .</b>	105
Qingyang Xu and Li Zhang	
<b>The Contact Behavior Analysis Between Microcomponents on a Low-Frequency Reciprocating-Fretting Ball-on-Flat Tribometer . . . . .</b>	111
Zhongnan Wang, Wuyi Wang, Guangyu Zhang and Hejuan Chen	
<b>Single-Phase AC Voltage Control Circuit for Flow-Induced Acoustic-Vibration Piezoelectric Generator . . . . .</b>	127
Bo Chen, Jiacun Sun, Hejuan Chen, Jian Yang and Wei Qu	
<b>Medium and Long-Term Electric Power Planning Load Forecasting Based on Variable Weights Gray Model . . . . .</b>	137
Da Song and Xiaobo Liu	
<b>Combination and Optimization Load Forecasting Based on Credibility . . . . .</b>	145
Jia-liang Chen, Shu-bo Hu, Wei Zhou, Lin Zhao, Jian-ming Yu, Guo-hui Shen and Jing-jie Sun	
<b>Actuated Signal Control System for Pedestrian Street Crosswalk at Midblock Crossings . . . . .</b>	153
Longjian Wang, Yonggang Wang and Mengyang Xin	
<b>Study of a Unidirectional Hybrid Three-Phase Voltage Source Rectifier . . . . .</b>	163
She Dongjin, Wang Jiuhe and Zhai Dandan	
<b>The Heading Control of POD-Driven Ship Using Adaptive Integrator Backstepping . . . . .</b>	173
Yacong Zhao, Haibin Huang and Yufei Zhuang	
<b>Dynamic Modeling of RR-RRR Spherical Parallel Manipulator for Vector Thruster . . . . .</b>	181
Han Xu, Yuan Chen and Jun Gao	

**Synchronous Generator-Based Design of Damping Emulation Controller for DFIG** . . . . . 189  
 Zhang Yan, Yang Chunhua and Sun Hui

**Study on Control Strategy of Harmonic Suppression in a Wide Power Range Based on V2G Bidirectional Onboard Charger** . . . . . 197  
 Fuhong Xie, Weifeng Gao, Xiaofei Liu and Shumei Cui

**Snow Removal of Video Image Based on FPGA** . . . . . 207  
 H.H. Li, S. Liu and Y. Piao

**A New Concept: Azimuth Dilution of Precision for Monocular Observational Tracking System** . . . . . 217  
 Bing Liu, Dong Wang, Zhen Shen, Taihe Yi and Dongyun Yi

**Study on Self-adaptive Packet Scheduling Algorithm of TD-LTE System’s Downward Frequency Domain** . . . . . 225  
 Jia-liang Ling, Jian-zhong Cao and Tian-fa Liao

**The Research and Simulation of Three-Level NPC Inverter** . . . . . 233  
 Yuan Deng and Guangyao Jin

**Research and Application of 350 MW Unit Water Wall Crack Failure** . . . . . 241  
 Rui Zhang and Chunying Wu

**Optimal Design of a Linear Induction Motor for Traction Application** . . . . . 251  
 J. Gong, F. Gillon and H. Zhong

**Simulation on the Boost-Buck Current Compensation Device of PV Grid Connection and Active Power Filter All-in-One Machine** . . . . . 259  
 Tian-fa Liao, Zhao-quan Cai, Jia-xiang Xue and Hong-wei Zhang

**An Improved DV-Hop Node Localization Algorithm Combined with RSSI Ranging Technology** . . . . . 269  
 Hongyu Shi and Ling Peng

**Processing to the Commutation Failure in Multi-infeed Direct Current System** . . . . . 277  
 Xuan Wang, Hui Yan, Yuhong Wang, Junfeng Gui, Mingchao Xia, Xiaogang Hu and Pingzhu Liu

**Research on Friction and Thermal Load Performance of Hydro-viscous Clutch** . . . . . 285  
 Li-gang Ma, Chang-le Xiang, Ming-gang Du and Liu-yang Guo

**A Comprehensive Evaluation Model for Switchgear Based on the Normal Cloud Model and D–S Evidence Theory** . . . . . 295  
 Y. Jia, D. Liu and H. Sui



<b>Target Tracking Based on Audio and Video Information Fusion. . . . .</b>	305
H. Wang	
<b>Experimental Research on Fatigue Damage of Composite Solid Propellant with Constant Constrain. . . . .</b>	315
Jinfei Li, Weidong Huang, Kai Qu, Wenshuang Wang and Ming Yang	
<b>Impacts and Analysis of Electric Vehicles and Photovoltaic Integration into Power Systems . . . . .</b>	323
Cheng Gong, Zhongjun Chi, Baoqun Zhang, Longfei Ma, Rui Shi and Ran Jiao	
<b>A Wireless Multipoint Parameter Monitoring System for Greenhouse Environment . . . . .</b>	333
Xiaoqing Zhang and Yudong Jia	
<b>A Survey of Fault Location for Distribution Systems . . . . .</b>	343
Yongjun Liu, Min Liu, Cheng Lin and Kefeng Ou-yang	
<b>Numerical Simulation of Flow Field of a Centrifugal Compressor with a High Pressure Ratio . . . . .</b>	349
Zhipeng Xu, Wei Shen, Yong Zhang and Longbo Gao	
<b>Render Synthetic Objects with Background Image According to Image-Based Lighting . . . . .</b>	357
Binling Luo, Shuting Cai, Shaojia Wen and Daolin Hu	
<b>Reliability Evaluation of Distribution Systems Incorporating Distributed Generators Using Monte Carlo Simulation . . . . .</b>	367
Zhenpeng Wu and Aoying Ji	
<b>Circular Synthetic Aperture Sonar Imaging Using Isometric Angle Characteristic . . . . .</b>	375
Guo-hui Di, Jun Wang and Fu-lin Su	
<b>Analysis of the Choice of a Serial Reactor in a Parallel Capacitor Device . . . . .</b>	385
Xianzhong Long, Xiaobo Liu and Da Song	
<b>Decision Fusion Moving Target Detection of Radar Video Based on D-S Evidence Theory . . . . .</b>	393
Xiaohan Yu, Wei Zhou, Jian Guan and Wenchao Hu	
<b>Effect of Co-doping on the Electronic Structure and Absorption Spectrum of Wurtzite ZnO Under Pressure . . . . .</b>	403
Jing Leng, De-jun Wang, Zheng-hao Sun, Wei-jie Liu and Run-ru Liu	
<b>Fitting Formula of Sheath Currents and Arrangement Optimization of Cables . . . . .</b>	411
Yong-zhi Wang, Wei Cao, Hai-sheng Liang and Fan Li	

**Analysis and Simulation of Electric Vehicle Power Battery . . . . .** 421  
 Longfei Ma, Baoqun Zhang, Cheng Gong, Ran Jiao, Rui Shi  
 and Zhongjun Chi

**Vibration Suppression of a 3-DOF Parallel Manipulator Based  
 on Single-Mode Input Shaping Combined with PD. . . . .** 429  
 Bing Li and Yulan Wei

**Hybrid Dual-Loop Control for a Three-Phase PWM Rectifier. . . . .** 439  
 Jing Cao, Chaonan Tong and Hongtao Li

**A Voltage Regulating Electronic Transformer with High Power  
 Factor and Wide Working Voltage . . . . .** 447  
 Hui Su, Yonggao Jin and Xiaodong Qu

**The Quantitative Assessment Study on the ‘First-Class’ of the Key  
 Indices of Grid Evaluation . . . . .** 457  
 Zheng Wu, Ming Zeng, Junhui Huang, Jan Tan, Jun Han, Wenqi Gu  
 and Han Xu

**A Novel Polarimetric Marine Radar . . . . .** 465  
 Tao Jin, Huihui Xian, Xuebin Wang and Xiaohui Qi

**Monitoring of the Performance of Excitation System Based on  
 Measured PMU Data . . . . .** 473  
 Sai Wang, Xueping Gu, Wei Tang, Zhen Li and Yuanchao Huang

**Comprehensive Evaluation on the Primary Frequency Regulation  
 Performance of Generator Units Based on Data from a Wide Area  
 Measurement System . . . . .** 483  
 Yan Zhang, Xuan Pan, Xinqiao Fan, Sai Wang, Zhen Li  
 and Yuanchao Huang

**A Novel PQ Control Strategy of Microgrid with Single-Phase  
 Connected to Grid . . . . .** 493  
 Baoqun Zhang, Longfei Ma, Cheng Gong, Ran Jiao, Rui Shi  
 and Zhongjun Chi

**Assessment of Civilian Demand Response Behavior Supporting  
 Wind Power Digestion . . . . .** 503  
 Ran Jiao, Baoqun Zhang, Cheng Gong, Longfei Ma, Rui Shi,  
 Zhongjun Chi, Bing Yang and Huizhen Liu

**Research on CO<sub>2</sub> Laser Frequency Stabilization by Adjusting  
 Grating Angle. . . . .** 513  
 Yanchao Zhang, Zhaoshuo Tian, Guang Dai, Chunlei Jin and Zhenghe Sun

**Study on Shipborne Video Electro-optical Tracking System  
 Based on FPGA . . . . .** 521  
 Zongjie Bi, Zhaoshuo Tian, Tao Luo and Shiyou Fu

<b>A Timing Synchronization Method with Peak Plateau for OFDM Systems</b> . . . . .	531
Yanping Li	
<b>GRNN Model for Fault Diagnosis of Unmanned Helicopter Rotor's Unbalance</b> . . . . .	539
Xi-hua Xie, Lei Xu, Liang Zhou and Yao Tan	
<b>A Double-Stage Strategy Based on DNA Computing to Search the Optimal Section of Active Splitting</b> . . . . .	549
Xiaoli Ye, Fei Tang, Jian Yang, Junru Xu, Yongle Zheng and Qiang Zhao	
<b>The Design and Realization of Motion Controller for Truss Robot</b> . . .	559
Peng Zheng, Wusheng Chou and Huaidong Zhou	
<b>Dynamic Characteristics of Wind Turbine Gearbox with the Chipping Fault</b> . . . . .	567
Xin Wang, Yuxiu Xu and Taotao Li	
<b>Demonstration for Low Cost Wireless Smart Sensor Networks Based on ARM for Structural Health Monitoring</b> . . . . .	575
Jian Xu, Wenhao Wan, Yuying Wu and Zhaoyu Sun	
<b>Risk Study on Long-Distance Oil and Gas Pipelines Engineering</b> . . . .	583
Shujiao Tong, Zongzhi Wu, Rujun Wang and Yingquan Duo	
<b>Optimization Method Based on Selection Strategy of Initial Point and Six Sigma Robust Design</b> . . . . .	591
Aimin Ji, Mengni Zhang, Pin Lv and Xu Yin	
<b>Dynamic Flux and Torque Estimation of Single-Phase Induction Motors Based on the Vector Control Theory of Motors</b> . . . . .	601
Dandan Sun and Ding Wang	
<b>Performance Evaluation of Ballistic Missile Detection for the Skywave OTHR Based on the Preliminary and the Weighted Indexes</b> . . . . .	609
Shihua Liu, Defang Li and Bing Hu	
<b>Personnel Surface Electric Field Research of Live Working on Insulation Bucket Arm Car of 500-kV Transmission Lines</b> . . . . .	617
Bing-ling Zhou and Dong-ze Xu	
<b>Failure Mode Analysis on Machining Center Based on Possibility Theory</b> . . . . .	627
Hongzhou Li, Fei Chen, Zhaojun Yang, Liding Wang and Yingnan Kan	
<b>Microstructure and Tensile Properties of Squeeze Cast AZ91D Magnesium Alloy</b> . . . . .	637
Xizi Xiao, Yun Chen and Juan Du	

**Research and Design of Merging Unit of Electronic Transducer . . . . .** 647  
 Zheng Qiao, Bujuan Li, Yikang Zu and Yanqin Sun

**Overall Iteration Design of a New Concept Wing Disk  
 Solar-Powered Aircraft . . . . .** 655  
 Hong Da and Zhu Jihong

**Research on an Automation Network for CSP Product Line . . . . .** 665  
 Tongbin Li, Bin Wang, Ning Zheng and Xin Kang

**An Improved BBO Algorithm and Its Application in PID  
 Optimization of CFB Bed Temperature System . . . . .** 675  
 Hong Xue and Han Pu

**Study on Joint Vibration Attenuation of the Satellite Attitude Control  
 Actuator Using a Vibration Isolator and Vibration Absorbers . . . . .** 683  
 Peng Tian and Rui Zhong

**Weight Calculation of Oil and Gas Pipelines Risk Factors  
 Based on Improved AHP . . . . .** 699  
 Tianyu Wang, Deyu Xu, Rujun Wang and Shujiao Tong

**Optimization for the Structure of Front Transmission Gearbox . . . . .** 709  
 Zhenqi Yu

**Study on the Hydrostatic Slide Film Temperature Field  
 and Bearing Capacity of Precision Grinding Machine. . . . .** 717  
 ChuanShe Guo and Yi Cui

**Study on Fuzzy Classifier Based on Genetic Algorithm  
 Optimization. . . . .** 725  
 Qian Gao and Nai-bao He

**Research on Automatic Identification of Color and Classification  
 Applied to Electric Online Monitoring . . . . .** 733  
 Yi Zhang, Feng Zhang, Bin-quan Zhu and Lv Tang

**Design of Control System for an Intelligent Closestool . . . . .** 743  
 Shuyun Zhu, Yan Chen, Hanhan Wang and Fangjuan Xie

**Research on Damage Assessment of Corroded Oil and Gas  
 Pipelines Based on Fracture Mechanics . . . . .** 751  
 Rujun Wang and Shujiao Tong

**The Research on Capacity Rise Phenomenon of the Cable Line  
 Under AC Voltage Withstand Test . . . . .** 759  
 Geqing Qi, Wenfeng Song, Dan Yuan, Zhuang Qi, Jianing Guo,  
 Wei Zhang and Lulu Wang

<b>Lyapunov-Based Control Strategy for Grid-Connected Inverter with Improved Transient Response</b> . . . . .	773
Jinhao Wang, Chaoying Yang and Yulong Wu	
<b>The Simulation of STATCOM for Distribution Systems Using a Mathematical Model Approach.</b> . . . . .	783
Wei Xie and Jian-Min Duan	
<b>The Design of Linear Three-Dimensional Calibration</b> . . . . .	791
Dequan Guo, Xinrui Zhang, Hui Ju, Hong Liu and Jin Chen	
<b>Design and Development of LED Dimming System Based on Wireless Remote and Bluetooth Control Technologies.</b> . . . . .	801
Yiwang Wang, Bo Zhang, Sikui Wu, Xiang Cang and Xiaoxiao Li	
<b>Open PID-Type Iterative Learning Control for Linear Time-Invariant System</b> . . . . .	809
Xuelian Zhou and Qiang He	
<b>Development of an Integrative Pointing Gimbal Mechanism for Space Application</b> . . . . .	817
Bo Pan, Shuyang Zhang, Lin Li, Fanxin Sun and Yongqiang He	
<b>Multuser Scheduling on Dual-Hop Relay Networks and Effect of Feedback Delay</b> . . . . .	827
Jiyao Wei and Xianyi Rui	
<b>Research on System Modeling and Starting Strategy of Inverter for Medium-Frequency Induction Heating</b> . . . . .	835
Sen-lin Cheng, Hu Xu, Chuan Wang and Qiang-zhi He	
<b>Optimal Configuration of Bypass Diodes for a High-Concentration Photovoltaic System</b> . . . . .	845
Ting-Chung Yu, Yao Ti Hung, Yih-Bin Lin, Chih-Hao Chen and Yan-Cheng Liou	
<b>Optimal Design and Analysis of a 3.3-MW Wind Turbine Gear Train.</b> . . . . .	857
Jianxin Zhang and Zhange Zhang	
<b>The Analysis of Battery Cooling Modes of EV</b> . . . . .	865
Yue Yang, Pengyu Wang, Guangming Lu, Hang Dong, Feng Li and Yanru Suo	
<b>The Research of Aviation Dangerous Weather Forecast for Fog and Haze Based on BP Neural Network.</b> . . . . .	877
Yanfen Cheng and Rui Wu	
<b>Small Power Sine Wave Inverter Design</b> . . . . .	885
Xuefeng Bai, Yongjian Ma, Hanqing Li and Pei Li	

**Uncertainty Quantification Using Random Set Based on IODM . . . . .** 893  
 Zhao Liang

**Coordinated Control Method of AGC and AVC in Power Grid . . . . .** 901  
 Shiguang Li, Zian Wang, Xinjing Wu and Jiatong Du

**Research into Key Points and Application Ideas of Reliability Assessment for Medium-Voltage Distribution Networks . . . . .** 911  
 Lingyun Wan, Tingting Wei, Jin Fu, Gaolin Wu, Qunying Yang and Wei Song

**Heat Transfer-Based Fault Diagnosis for Heat Exchanger of Aircraft Environmental Control System. . . . .** 921  
 H. Zhuohuan, W. Lulu and Y. Mo

**Direct Torque Control of Permanent Magnet Synchronous Motor at Low Speed Using a Variable PI Feedback Flux Observer . . . . .** 927  
 Suying Zhang, Wenshuai Cui, Yankai Shen and Huixian Liu

**Research on the Speed Synchronization Control Method of Double-HST Motor . . . . .** 937  
 Qian Ming Yang, Jian Li and Ling Qi Kong

**Design and Development of an In Situ Radioactivity Measuring System in the Marine Environment . . . . .** 949  
 Yingying Zhang, Bingwei Wu, Ying Zhang, Guoxing Ren, Dongyan Liu and Lu Cao

**The Design of Shield Posture’s Monitoring and Control System Based on Configuration Software. . . . .** 955  
 Yiping Shi and Yungen Wang

**Application Research of SuperCapacitance on Fuel Consumption Wheel Crane . . . . .** 963  
 Chao Li, Lu Niu and Aihong Tang

**Research on Elastic Characteristic of Interconnected Oil Gas Suspension . . . . .** 971  
 Y.J. Chen, L. Wang, Y.F. Zhang, G.H. Zheng and X. Zhang

**Impact of Switching Three-Phase Breaker at Different Period on Inter-turn Protection for High-Voltage Shunt Reactor . . . . .** 979  
 Sheng-Hong Lin, Shu-Yan Pan and Hua-Ren Wu

**The Application Software Framework About Distributed Intelligent Alarm Information in Intelligent Substation. . . . .** 989  
 Xin Xu, Zhiqiang Yao, RenHui Dou, Hao Ren, Mingzhi Geng and Hui Ren

<b>The Design and Implementation of Substation Graphic Gateway System Based on IEC61850 Technology . . . . .</b>	999
Mingzhi Geng, Renhui Dou, Yanping Wu, Zhiqiang Yao, Hao Ren and Xin Xu	
<b>An Improved Particle Swarm Optimization and Application . . . . .</b>	1007
Dongsheng Zhou, Lin Wang and Jiang Wei	
<b>Quantitative Analysis of Air Injection for Compressor Active Control . . . . .</b>	1015
Zhanheng Sun, Sanmai Su, Junjie Liu and Gao Rao	
<b>Thermocapillary Flows in Half-zone Liquid Bridges Under Axial Magnetic Fields . . . . .</b>	1023
Ruquan Liang, Linyang Zhu, Limin Kong, Fuqiang Yan and Shuo Yang	
<b>A Dual-Redundancy Thermal Backup Control Method for the Two-Wheeled Self-balancing Robot . . . . .</b>	1029
Yong Tao, Tianmiao Wang, Ye Wang, Jianhong Liang and Zhongyuan Chen	
<b>The Influence of Surface Roughness on the Aerodynamic Characteristics of Overhead Wire . . . . .</b>	1039
Zhangqi Wang and Lizhong Qi	
<b>Multi-objective Optimization Algorithm in Mission Planning of On-Orbit Servicing Spacecraft . . . . .</b>	1049
Qing Zhang, Jianxin Zhang, Qiang Zhang and Xiaopeng Wei	
<b>Product Conceptual Design Based on Polychromatic Sets Theory and Axiomatic Design . . . . .</b>	1061
Jianxin Zhang, Yangjie Zhou, Qiang Zhang and Xiaopeng Wei	
<b>Study on Dynamic Balance PID Control Algorithm and Its Application on the Quadrotor . . . . .</b>	1071
Hongwei Yan, Hongbin Li and Shaohua Song	
<b>The Electronic, Magnetic, and Vibrational Properties of <math>Ce_3Co_{29}Ge_4B_{10}</math> . . . . .</b>	1079
Liu-Tao Zhao, Xiao-Xu Wang, Jin-Rong Huo, Hai-Xia Cheng, Jian-Qiao Xie, Lu Li and Ying Liu	
<b>Effects of Activation Treatment on Interfacial Bonding in A356-10 wt% <math>B_4C</math> Composite Sheets Prepared by Rheo-Rolling . . . . .</b>	1089
Zhan Yong Zhao, Yang Zhang, Zhou Yang Zhao, Ren Guo Guan, Yuan Dong Li and Ben Chao Chen	
<b>LQR Optimal Control on the Positioning Accuracy and Rigidity for the Pneumatic Actuator . . . . .</b>	1097
Hongwei Yan, Hongbin Li and Shengjun Zhou	

**A Study of Visual Servo System Based on Binocular Camera . . . . .** 1105  
 Lei Hu and Chen Shen

**Exploration of the Gas-Liquid Separation Effect of Vortex Tool  
 in Downhole . . . . .** 1113  
 Zhijian Wang, YanBob Jia and Kai Liu

**Study on Hopping Height Control and Detection for the  
 Pneumatic Actuator . . . . .** 1121  
 Hongwei Yan, Hongbin Li and Shengjun Zhou

**An Interval-Reduced-Basis Approach for Predicting Acoustic  
 Response of Coupled Structural-Acoustic System . . . . .** 1129  
 Zheng Lv, Zhiping Qiu and Qi Li

**FE Research on Influence of Pouring Temperature on Thermal  
 Fatigue Depth for Aluminum Alloy Die Casting Die . . . . .** 1139  
 Chenggang Pan, Huqun Yang, Wenchao Ma, Qin Xiao  
 and Qingming Chang

**Analysis of the Protection of a Simplified Surge Protective Device  
 for Low-Voltage AC Power System . . . . .** 1147  
 Huiping Liu, Xiaoqing Zhang and Kejie Huang

**Investigation of Load Distribution Among Teeth of an Aero-engine  
 Spline Coupling . . . . .** 1155  
 Xiangzhen Xue, Sanmin Wang, Jian He and Hui Wu

**Dynamics Analysis of Linear Array Deployable Structure Based  
 on Symmetrical Scissor-Like Element . . . . .** 1163  
 Bo Li, San-Min Wang, Ru Yuan, Chang-jian Zhi and Xiang-zhen Xue

**Research and Development Analysis of Information Security  
 in Smart Grid Construction . . . . .** 1173  
 Yixin Ding, Ming Li, Li Yan and Junwei Ma

**The Multiobjective Optimization Model of Open Mill  
 Mastication Parameters. . . . .** 1179  
 Zhang Liang, Wang Qidong, Zhu Lihong and Zhao Han

**Precision Compensation Analysis of Spacecraft Assembly  
 Parallel Mechanism. . . . .** 1191  
 Guangtong Liu, Guotao, Yanlei Zhang and Laiying Tang

**Research on CAD/CAM Integration Methods Based  
 on the STL Model . . . . .** 1201  
 Huiqun Zhou and Jianjun Wu



**Investigation on the Characteristics of DC Air Discharge at Low Pressure Based on Hydrodynamics and Chemistry Model . . . . .** 1209  
Xing-hua Liu, Xue-Feng Sun, Ri-chang Xian, Yu-Feng Chen and Peng Yu

**Research on IOT Technology Applied to Intelligent Agriculture . . . . .** 1217  
Juntao Li, Weihua Gu and Hang Yuan

**Effective FPGA-Based Enhancement of Quantitative Frequent Itemset Mining . . . . .** 1225  
Xiaoqi Gu, Yongxin Zhu, Meikang Qiu, Shengyan Zhou and Chaojun Wang

**Image Classification Based on Deep Learning for Big Data of Power Grid . . . . .** 1233  
Jun Yin, Yongxin Zhu, Weiwei Shi, Yunru Qiu, Xingying Liu and Gehao Sheng

**Whether the High-Voltage Transmission Lines Have Enough Load Capacity After Wildfire . . . . .** 1243  
Tianzheng Wang, Zhen Tang, Xinwei Wang, Jinzhao Yang, Xiaogang Wu, Kechao Zhao, Chong Zuo and Weiyi Chen

**Design and Analysis of the Hydraulic System of the Small Slide Loader . . . . .** 1253  
Kailin Feng, Guanguo Ma and Yipeng Chen

**An Extended Kalman Filter Application on Moving Object Tracking . . . . .** 1261  
Yuan Niu and Lisheng Hu

# Individual Pitch Control Based on Radial Basis Function Neural Network

Bing Han, Lawu Zhou, Zhiwen Zhang, Meng Tian  
and Ningfeng Deng

**Abstract** As the increasing of structure in wind turbine (WT), the flapping vibration force of blade is more and more serious, and the output power will be unstable in operation of the merged power networks. In this paper, to improve the WT dynamic performance in running processes, by analyzing the WT aerodynamics, wind shear, and tower shadow effect, we have designed based on radial basis function neural network (RBFNN) control strategy for individual pitch control (IPC), using RBFNN approach pitch control system unknown nonlinear functions, and introduced into the adaptive law online adjustment the system error, to improve the dynamic performance of pitch control system and alleviate structure of fatigue loads. Finally, the results show that based on RBFNN for IPC produces adaptability dynamic performance. It can effectively improve power quality to reduce fatigue load in key components of WT.

**Keywords** Wind turbine · Coleman transform · Neural network · Blade moment

## 1 Introduction

In recent years, the exhaustion of the natural resources, the influence of environment and natural disasters and the energy crisis have appeared. However, from the technical maturity, the size of the market, or the perspective of cost price, the wind power is currently one of the most developed and the application prospect of new energy technology [1, 2]. Fixed pitch wind turbine (WT) have many problems in the development; variable pitch control not only solves the problem of the relia-

---

B. Han (✉) · Z. Zhang · M. Tian · N. Deng  
College of Electrical and Information Engineering, Hunan University,  
410082 Changsha, China  
e-mail: hanbing9107@qq.com

L. Zhou  
College of Electrical and Information Engineering, Changsha University of Science  
& Technology, 410000 Changsha, China

© Springer-Verlag Berlin Heidelberg 2016  
B. Huang and Y. Yao (eds.), *Proceedings of the 5th International  
Conference on Electrical Engineering and Automatic Control*, Lecture Notes  
in Electrical Engineering 367, DOI 10.1007/978-3-662-48768-6\_1

bility of the WT, and during startup the rotor speed can be controlled, after the interconnection of control, it puts the WT into the power system smoothly and rapidly and the output power of characteristic factor was improved significantly [3]. Variable pitch WTs have the advantages of high wind energy conversion efficiency, output power stability, flexible control, and small fatigue loads, then it has gradually become the mainstream of WTs; pitch control technology has become one of the key technology of large WT [4–6].

The variable pitch control of WT is divided into two kinds, collective pitch control and individual pitch control [7]. Collective pitch control is a control system using the same signal to control the pitch angle of the three blades. So much height difference in wind rotor plane is caused by the difference of wind speed, the resulting unbalanced force, and vibration in the rotating blade, which is a threat to the safety of the WT. Occurrence of individual pitch control offers the excellent method to solve this problem elegantly [8, 9]. Individual pitch control is the control system by giving three different blade pitch angle signal, and the aerodynamic force will offset imbalance of fatigue load.

In a word, domestic and foreign scholars study the various individual pitch control strategy [10–12]. They have achieved excellent results, but these methods have number of correlative questions. To improve the WT dynamic performance in running processes, by analyzing the WT aerodynamics, wind shear, and tower shadow effect, we have designed based on radial basis function neural network (RBFNN) control strategy for IPC, using RBFNN approach pitch control system unknown nonlinear functions, and introduced into the adaptive law online adjustment the system error, to improve the dynamic performance of pitch control system and alleviate structure of fatigue loads. Finally, the results show that based on RBFNN for IPC produces adaptability dynamic performance. It can effectively improve power quality to reduce fatigue load in key components of large WT.

## 2 Wind Turbine Model

The WT model is nonlinear aerodynamic characteristics, so it is necessary to establish the linear aerodynamic calculation model, the wind generator rotor rotation and linear model equations are [13]

$$J \times \frac{d(\Omega)}{dt} = M_{\text{rotor}} \quad (1)$$

$$M \times \frac{d^2(s_{\text{nod}})}{dt^2} + D \times \frac{d(s_{\text{nod}})}{dt} + S s_{\text{nod}} = F_{ax} - \frac{3}{2H} \times M_{\text{tilt}} \quad (2)$$

$$M \times \frac{d^2(s_{\text{nay}})}{dt^2} + D \times \frac{d(s_{\text{nay}})}{dt} + S s_{\text{nay}} = F_{sd} - \frac{3}{2H} \times M_{\text{rotor}} \quad (3)$$

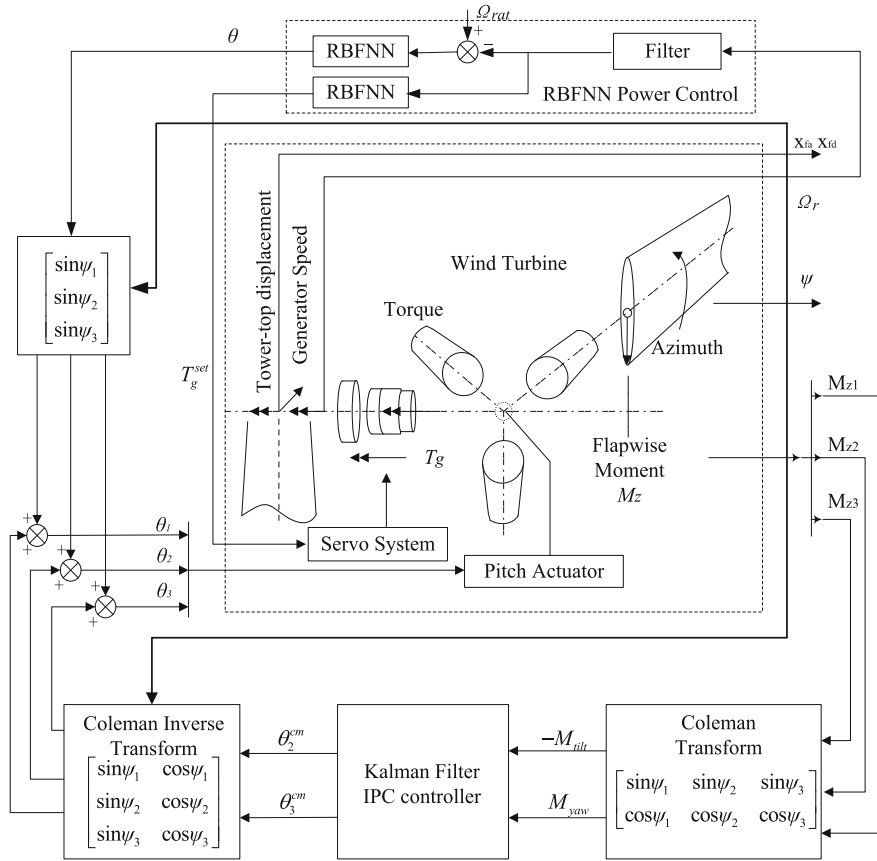


**Fig. 1** IPC based on RBFNN of schematic diagram

In which,  $J$  is moment of inertia of rotor,  $\Omega_r$  is rotor angular velocity,  $H$  is hub height,  $M$  is the tower total quality,  $M_{rotor}$  is shaft torque,  $s_{nod}$  is tower displacement,  $D$  is damping coefficient,  $F_{ax}$  is the axial force,  $F_{sd}$  is lateral force.

In this paper, the introduction of RBFNN controls to establish IPC system, the system schematic diagram is shown in Fig. 1. In the principle diagram,  $\theta_1^m$ ,  $\theta_2^m$ ,  $\theta_3^m$  are Coleman transform fine-tuning three blade pitch angles.  $\Omega_r$  is rotor rotating speed, as input RBFNN controller, the controller calculated to obtain pitch angle  $\theta$  and generator torque. While  $M_{z1}$ ,  $M_{z2}$ ,  $M_{z3}$  are IPC controller input signals, through Coleman coordinate transformation  $M_{tilt}$  and  $M_{yaw}$ . Finally, Coleman inverse transformation into three blade pitch angle  $\theta_i^m$ , and comparing collective pitch angle  $\theta$ , gives each blade pitch angle  $\theta_i$ .

In the IPC controller, the blade root moments  $M_{z1}$ ,  $M_{z2}$ ,  $M_{z3}$  are Coleman transformed from the rotating coordinates to the fixed reference frame  $M_{tilt}$  and  $M_{yaw}$  using equations as follows [14]:

$$\begin{bmatrix} M_{\text{tilt}} \\ M_{\text{yaw}} \end{bmatrix} = \begin{bmatrix} \sin \psi & \sin(\psi + 2\pi/3) & \sin(\psi + 4\pi/3) \\ \cos \psi & \cos(\psi + 2\pi/3) & \cos(\psi + 4\pi/3) \end{bmatrix} \begin{bmatrix} M_{z1} \\ M_{z2} \\ M_{z3} \end{bmatrix} \quad (4)$$

In which  $\psi$  is azimuth of wind rotor.

After transforming the  $M_{z1}$ ,  $M_{z2}$ ,  $M_{z3}$  to the fixed reference frame  $M_{\text{tilt}}$  and  $M_{\text{yaw}}$ , the next step is applied to the Kalman filter IPC controller. The pitch angles  $\theta^{\text{cm}}$  in the fixed reference frame can be obtained according to the IPC calculation in this paper. Finally, the fixed reference frame  $\theta^{\text{cm}}$  is reverse transformed to get the adjusting pitch signals  $\theta'$  in the rotating coordinates, the inverse Coleman transformation as follows [15]:

$$\begin{bmatrix} \theta'_1 \\ \theta'_2 \\ \theta'_3 \end{bmatrix} = \begin{bmatrix} \sin \psi & \cos \psi \\ \sin(\psi + 2\pi/3) & \cos(\psi + 2\pi/3) \\ \sin(\psi + 4\pi/3) & \cos(\psi + 4\pi/3) \end{bmatrix} \begin{bmatrix} \theta_1^{\text{cm}} \\ \theta_2^{\text{cm}} \\ \theta_3^{\text{cm}} \end{bmatrix} \quad (5)$$

The adjusting pitch signal  $\theta'_1$ ,  $\theta'_2$ ,  $\theta'_3$  is superimposed to the ones computed by a collective pitch and torque control implemented with the RBFNN controller. To optimize the collective pitch angles  $\theta_1$ ,  $\theta_2$ , and  $\theta_3$ , make the different blade pitch angle activity within a certain range, then compensate wind speed variations to achieve the purpose of fatigue load alleviate in WT.

### 3 Based on RBFNN of Design

Consider WT control system for the nonlinear system, using RBF neural network approximation method and the control output; neural network self-learning function realization of the control system is analyzed. The controller based on RBFNN structure as shown in Fig. 2.

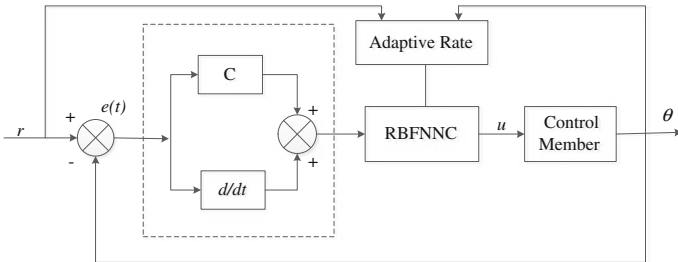


Fig. 2 Block diagram of RBFNN

And the pitch angle deviation is  $e = \theta_r^* - \theta_r$ , according to the predetermined trajectory motion. The design to guarantee that the system variable structure controller, the system of the state need to meet the requirements of Lyapunov stability control system stability conditions. RBFNN has good generalization ability, simple network structure, three layer feed forward network: input layer, hidden layer, and output layer, and the addition of RBFNN can be achieved by optimizing the equivalent mode control to improve the system variable structure controller output, to improve the larger interference caused by the earthquake shaking.

Sets the radial basis vectors of neural network to be  $h = [h_1, h_2, \dots, h_m]^T$ ,  $h_j$  as the gaussian function, then [16]

$$h_j = \exp\left(-\frac{\|s - C_j\|}{b_j^2}\right), \quad k = 1, 2, \dots, m \quad (6)$$

In which  $m$  is the number of hidden layer of neural, in the RBFNN structure,  $x_k$  is the input of RBF network;  $c_j = [c_{11}, c_{12}, \dots, c_{1m}]$ ;  $b = [b_1, b_2, \dots, b_m]$ .

The output of the RBF neural network is as follows [17]:

$$u_k = \sum_{k=1}^m \exp\left(-\frac{\|s - C_k\|^2}{b_k^2}\right) \quad (7)$$

However, when external disturbances join, in order to guarantee the robustness by RBFNN self-learning function, reduce the system of earthquake shaking, the RBFNN weights adjustment index for

$$d\theta_k = -\eta \frac{\partial V}{\partial \theta_k} = -\eta \frac{\partial (s\dot{s})}{\partial \theta_k} = -\eta \frac{\partial (s\dot{s})}{\partial u} \frac{\partial u}{\partial \theta_k} \quad (8)$$

Adaptive law is designed for

$$d\theta_k = \gamma s \exp\left(-\frac{\|s - C_k\|^2}{b_k^2}\right) = \gamma s h_k(s) \quad (9)$$

In which  $\gamma$  is the adaptive parameter of neural network.

Weights of the RBFNN are as follows:

$$\dot{L} = -s(\varepsilon + d(t) + \eta \text{sgn}(s)) \quad (10)$$

In this paper, we set the RBFNN initial weight value of 0.10, and it can well satisfy the control performance and guarantees the stability of the system.

## 4 Simulation Results

In this paper, we have used the MATLAB/Simulink and FAST to simulate the 2 MW horizontal axis WT. The turbulence wind speed model used Kaimal model, the mean of 13 m/s and a turbulence intensity of 14.1 % is used as shown in Fig. 3.

As seen in Fig. 3, the generator output power, rotor speed, and generator torque, respectively, have become much more reliable and efficient using RBFNN algorithm the WTs, because the neural network controller could introduce the system error into the adaptive law online adjustment. And the standard deviation of output power and rotor speed reduces 13.7 and 18.1 %, respectively. Thus it can be seen

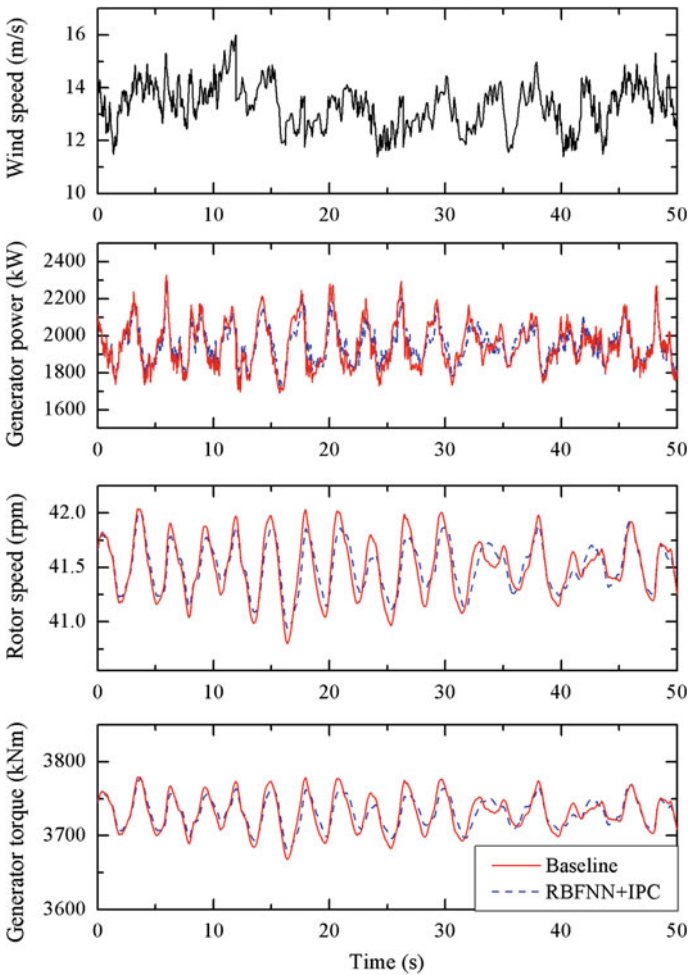


**Fig. 3** Performance comparison of the RBFNN + IPC and baseline

that the RBFNN controller shows better performances than baseline controller in optimizing the output power performance.

Simulation results are displayed in Fig. 4. It shows good regulations of generated power and rotational speed, compared to the baseline controller. The RBFNN + IPC are not only able to hold constant the generator power and rotor speed, but also reduces the tower and blade bending moments. RBFNN + IPC were used to mitigate the influence of wind speed fluctuation using the liability of self-study and self-adaptability of RBFNN in turning parameters of the system. As a result, the rotor speed variance reduced by 1.56 %, the tower base fore–aft moment showed significant reduction by 7.61 %, and tower base side-to-side moment reduced by 4.42 % compared with the baseline controller. Therefore, RBFNN + IPC have good control performance for alleviating fatigue load.

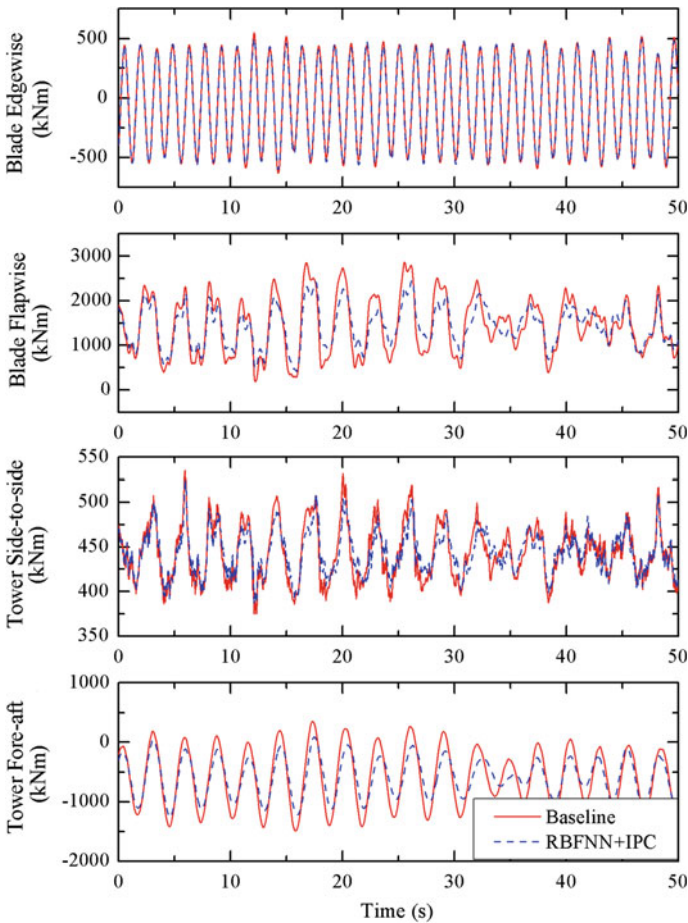


**Fig. 4** Loads of blade and tower comparison of the RBFNN + IPC and baseline



## 5 Conclusion

In this paper, to improve the WT dynamic performance in running processes, by analyzing the WT aerodynamics, wind shear, and tower shadow effect, we have designed based on RBFNN control strategy for IPC, using RBFNN approach pitch control system unknown nonlinear functions, and introduced into the adaptive law online adjustment the system error, to improve the dynamic performance of pitch control system and alleviate structure of fatigue loads. Finally, the results show that based on RBFNN for IPC produces adaptability dynamic performance. It can effectively improve power quality to reduce fatigue load in key components of WT and prolong its service life.

## References

1. Bossanyi E, Savini B, Iribas M et al (2012) Advanced controller research for multi-MW wind turbines in the UPWIND project. *Wind Energy* 15:119–145
2. Steffen R, David S, Frank S (2014) Nonlinear model predictive control of floating wind turbines with individual pitch control. In: American control conference, vol 6, pp 4434–4439
3. Hassan HM, Eishafei AL, Farag WA, Saad MS (2012) A robust LMI-based pitch controller for large wind turbines. *Renew Energy* 44:63–71
4. Zhang Y, Chen Z, Cheng M (2013) Proportional resonant individual pitch control for mitigation of wind turbines loads. *IET Renew Power Gener* 7(3):191–200
5. Yao XJ, Li H (2012) Individual pitch regulation for wind turbine. *Adv Mater Res* 383–390:4341–4345
6. Dou ZL, Shi G, Ling ZB (2014) Research on individual pitch control for reducing wind turbine torque fluctuation. *Trans China Electrotech Soc* 29(1):236–245
7. Philip C, Ma X (2014) Nonlinear system identification for model-based condition monitoring of wind turbines. *Renew Energy* 71:654–660
8. Boukhezzer B, Lupu L, Siguerdjane H et al (2007) Multivariable control strategy for variable speed variable pitch wind turbines. *Renew Energy* 32(8):1273–1287
9. Garelli F, Camocardi P, Mantz RJ (2010) Variable structure strategy to avoid amplitude and rate saturation in pitch control of a wind turbine. *Int J Hydrogen Energy* 35:5869–5875
10. Hand MM, Balas MJ (2007) Blade load mitigation control design for a wind turbine operating in the path of vortices. *Wind Energy* 10:339–355
11. Namik H, Stol K (2014) Individual blade pitch control of a spar-buoy floating wind turbine. *IEEE Trans Cont Syst Tech* 22(1):214–223
12. Houtzager I, van Wingerden JW, Verhaegen M (2012) Wind turbine load reduction by rejecting the periodic load disturbances. *Wind Energy* 16:235–256
13. Selvam K, Kanev S, Wingerden JW et al (2009) Feedback–feedforward individual pitch control for wind turbine load reduction. *Int J Robust Nonlinear Control* 19:72–91
14. Larsen T, Hanson D (2007) A method to avoid negative damped low frequent tower vibrations for a floating pitch controlled wind turbine. *J Phys Conf Ser* 75(1):2073–2079
15. Xing Z, Chen L, Sun H et al (2011) Strategy study of individual pitch control. *Proc CSEE* 31(26):131–138
16. Xia CL, Xiu J (2007) RBF ANN nonlinear prediction model based adaptive PID control of switched reluctance motor. *Proc CSEE* 27(3):57–62
17. Qin B, Zhou H, Du K et al (2007) Sliding mode control of pitch angle based on RBF neural-network. *Trans China Electrotech Soc* 27(3):37–41

# Study on the Distribution Automation System Terminal Automatic Test Method

Peng Li, Yimin Qian and Wei Li

**Abstract** With the widespread use of DAS, higher requirements for distribution automation terminal on-site testing have been put forward on account of limitations of field working conditions. Based on the requirement of relevant standards, this paper discusses automatic testing exploratory research, by analyzing the principal experimental objects and information transmission mode of the distribution automation terminal, which adopts IEC-60870-5-104 protocol. On this basis, this paper brings forward a set of feasible distribution automation terminal test method based on automatic information acquisition and predefined rules, by scheme design, process design, and building test environment. Finally, based on the test environment which divides into online and offline modes, the relevant automatic testing system has been studied and applied, achieves a fully automated power distribution terminal test process, and improves the efficiency of this test to ensure safe and stable running of power distribution automation terminal.

**Keywords** Distribution automation system (DAS) · Remote terminal unit of distribution automation · Automatic test · 104 protocol

## 1 Introduction

With the widespread use of distribution automation system (DAS) in China, higher requirements for detecting DAS have been put forward. Terminal unit is an important part of DAS [1]. Taking into account the working environment of distribution terminals, the power performance requirements of distribution terminal is more stringent than main station of DAS [2, 3]. The distribution automation terminal which accesses to DAS must be safe, stable, and reliable in order to meet the need of safe and stable operation of the power system. Because of limitations of field working conditions, the installation, debugging, and testing of distribution

---

P. Li · Y. Qian (✉) · W. Li  
State Grid Hubei Electric Power Research Institute, Wuhan, China  
e-mail: 61893790@qq.com

automation terminal must be completed in a short time, which puts forward higher demand to the efficiency of the distribution terminal test [4–6]. This paper studies the main test objects of distribution automation terminal and information transmission mode, puts forward a set of feasible automatically test method of distribution automation terminal to improve test efficiency, accurately and quickly complete the terminal device test, and ensure the safe and stable operation of distribution network terminal.

## **2 The Main Test Object and Information Transmission Mode**

Study of distribution automation terminal test first needs to determine the main test object and information transmission mode. The test objects include several aspects of the response time, the measuring accuracy, the switching input and output, which directly affect performance. In addition, the information transmission mode of distribution automation terminal is selected 104 protocol for communications statute.

### ***2.1 Overview of Test Objects***

According to several aspects of the response time, measuring accuracy, switching input and output, this paper brings forward the test objects of distribution automation terminal.

#### **2.1.1 Response Time**

The main testing objects of response time include the telemetry response time, the response time of remote communication, and the response time of remote control.

#### **2.1.2 Measuring Accuracy**

The measuring accuracy involves the current and voltage basic error, the reactive and active power basic error, the power factor basic error, and the basic error of harmonic component.

#### **2.1.3 Switching Input and Output**

The switching input involves the remote communication change, the SOE resolution, the remote communication storm, and the avalanche situation. On the other hand, the switching output involves the action accuracy of switching action signal.

## 2.2 Information Transmission Mode

In DAS, data communication between terminal and master station of DAS is used by communication network. And the main communication protocol of the communication network adopts IEC60870-5-104.

All information interactive contents between distribution automation terminal and master station use the standard 104 protocol to encode data. Therefore, it can be considered that any 104 packets between the distribution automation terminal and the master station contain the main information of transmission, such as telemetry values, remote status and remote control commands, and so on.

### 2.2.1 Introduction of IEC60870-5-104

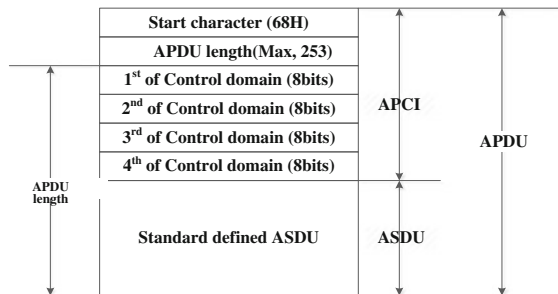
IEC60870-5-104 standard protocol applies to telecontrol equipment and systems with data transmission of serial bits encoding to monitor and control geographic wide process. Specific packet information of the 104 protocol is defined by the application protocol data unit (APDU), which includes the application protocol control information (APCI) and application service data unit (ASDU), as shown in Fig. 1.

The APCI defines the data stream starting point, length, and control information of APDU (such as packets no missing, no repeat, the transmission start/stop transmission connection monitoring, etc.). The ASDU consists of information unit and data unit identifier. Data unit identifier specifies the data type, ASDU length (optional), variable structure qualifier (optional), and ASDU public address (optional). Information unit is the main information carrier of information communication, provides information unit type, address, element set, and the time-scale.

### 2.2.2 The 104 Message Parsing of Distribution Automation Terminal

Data communication packet of distribution automation terminal contains its main information with collection and receiving. And it is parsed to get critical data of

**Fig. 1** Definition of APDU in companion standard for telecontrol



distribution automation terminal. For the use of 104 protocol, the transmission packet parsing focuses on the APDU. The APDU structure itself must meet the standard requirements, so it can easily use to describe the standard design of the corresponding parsing rules (Fig. 2).

### **3 Distribution Automation Terminal Automatic Test Method Design**

#### ***3.1 Design of Testing Scheme***

According to main test contents and information transmission mode of the distribution automation terminal, an automatic testing method is designed based on the automatic information acquisition and predefined rules. According to tested distribution automation terminal type, this scheme predefines test cases and evaluation rules. In an automatic test, test system directly injects testing energizing quantity to tested distribution automation terminal based on predefined test case. Meanwhile, the testing system obtains real-time response of distribution terminal. And test data is obtained from the 104 packet parsing module and computationally analyzed. Then this test system completes specified test project according to the test cases. After the test project is completed, the testing system forms a report according to test results and predefined evaluation rules. In this method, besides test cases and evaluation rules with artificial selection, all test procedures are done automatically.

Depending on whether the distribution automation terminal communicates with the main station by real-time data, automatic test process can be divided into online and offline modes. In online automatic test pattern, distribution automation terminals communicate with master station of DAS. The terminal test platform simulates the actual amount of electrical excitation to the distribution terminal, and acquires real-time response of distribution automation terminal through a network communication device with mirroring function, and completes the scheduled testing and evaluation of the project. In offline automatic test pattern, distribution automation terminal directly communicates with master station by disconnecting data to establish communication test platform. The terminal test platform simulates the actual amount of electrical excitation to the distribution terminal, and directly acquires real-time response of distribution automation terminal through network communication, and completes the scheduled testing and evaluation of the project.

#### ***3.2 Design of Testing Process***

According to the design features of testing scheme, automatic testing process of distribution automation terminal is shown in Fig. 3. Among them, the test

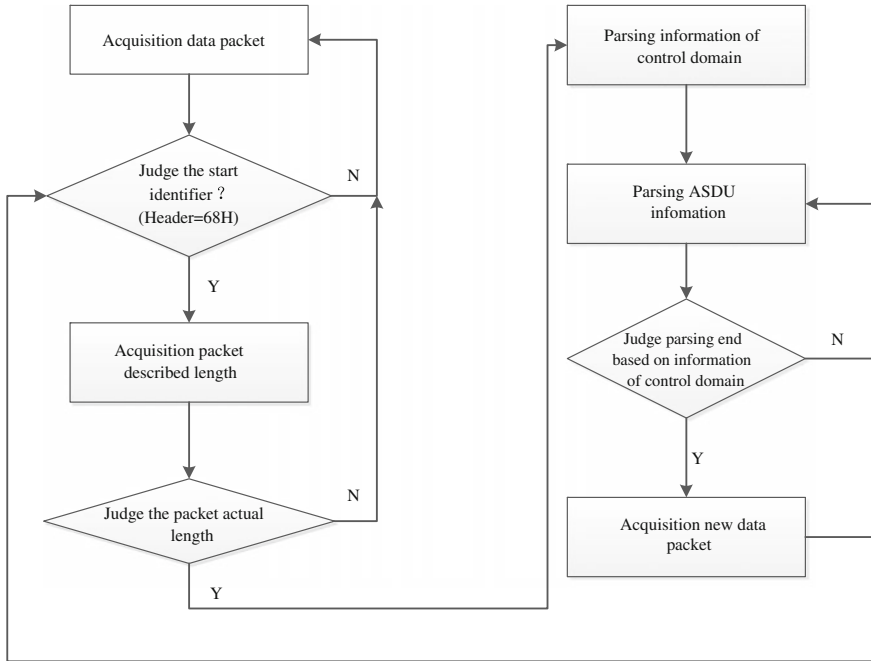


**Fig. 2** Communication data parsing rule of distribution automation terminal based on 104 protocol

configuration section needs to manually complete the basic test parameters (such as the tested distribution automation terminal type and specification, rated electrical quantities, communication parameters, etc.), test cases and evaluation rules configuration. Automatic test section itemizes automatic testing and calculations based on the configuration information. After all project specified by the test case is completed, the test system automatically completes evaluation and generates test reports.

### 3.3 Construction of Testing Condition

According to the test methods and test process design, testing system consists test console and test interface worktable. Among them, the test console completes several capabilities, including the basic configuration, testing project control, test results evaluation, and test report generation. The test interface performs two functions, including receiving test console control instructions and encouragement amount according to the control command of distribution automation terminal. Online and offline test environment of automatic test pattern are shown in Figs. 4 and 5.

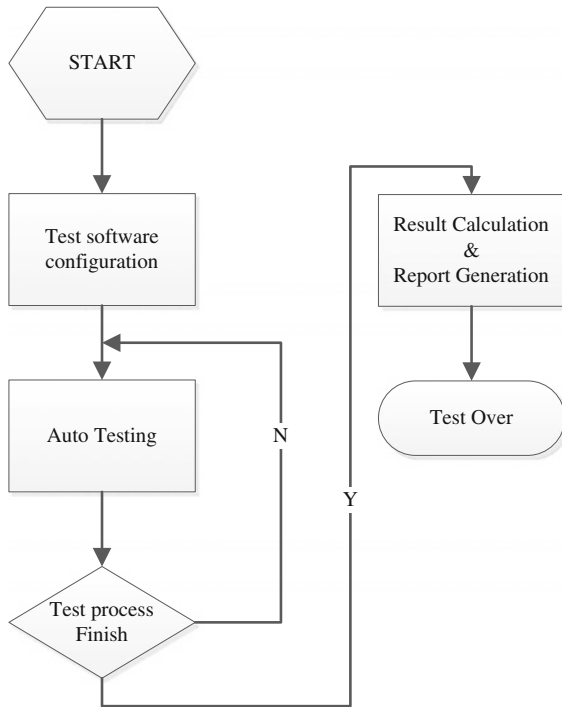


Fig. 3 Automatic test flow chat of distribution automation terminal

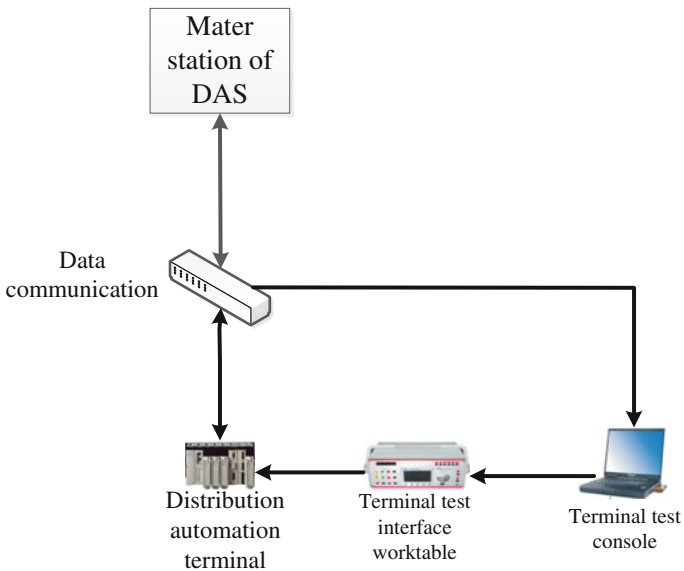
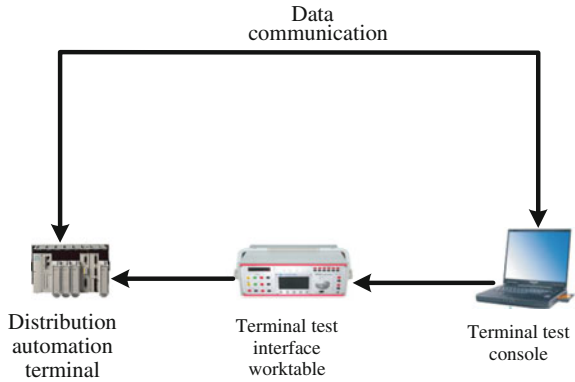


Fig. 4 Automatic online test pattern of distribution automation terminal

**Fig. 5** Automatic offline test pattern of distribution automation terminal



### 4 Research of Automation Testing System

According to the design ideas of distribution terminal automatic testing methods, a power distribution terminal automated test system based on information extraction can be designed and developed, which is shown in Fig. 6. The test system consists of three parts, Terminal Information Collector, Terminal Test Console, and Terminal Test Interface Worktable.

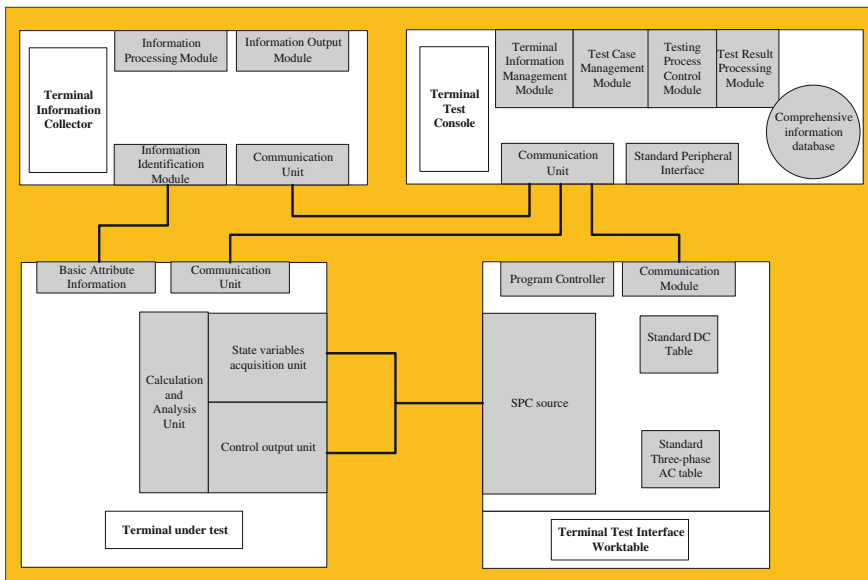


**Fig. 6** Power distribution terminal automated test system based on information extraction



### ***4.1 Terminal Information Collector***

Terminal Information Collector is used to automatically identify the basic attribute information of terminal under test, and complete the data collection, form a standard format to provide to Terminal Test Console.

### ***4.2 Terminal Test Console***

According to the basic attribute information terminal, Terminal Test Console finish test case matching, matching methods including standard cases and custom cases. After completion of test case configuration, console form control instruction according to the control rules, automatically implement test content, and complete the collection, calculation, analysis, and evaluation of test results. Terminal basic attribute information, test cases, test results, and the test evaluation are automatically saved in the test console database, and can be automatically exported in the form of general external interface and data format.

### ***4.3 Terminal Test Interface Worktable***

Test Interface Worktable receives control signals from Terminal Test Console, which is converted into real-time identifiable test excitation signal. The signal is automatically injected to the measured power distribution terminal. In the meantime, Test Interface Worktable automatically collected the response signal from terminal according to test cases, and automatically transferred to Terminal Test Console.

## **5 Conclusion**

According to the detailed analysis of the main test contents and information transmission mode of distribution automation terminal, this paper studies the feasibility of distribution terminal automatic testing methods, and process design of distribution automation terminal is designed. Additionally, the establishment of test environment about two automatic test mode is completed. At last, automatic test method of distribution automation terminal designed in this paper can effectively improve test efficiency, accurately and quickly completes the test terminal device, to ensure safe and stable running of power distribution automation terminal, with a high application value.

## References

1. Feng Q, Mao W (2009) Distribution network automation technology and analysis of engineering example. China Electric Power Press
2. Chen T, Zhao Z, Chen X, Hu D (2009) Power distribution system and its automation technology. China Electric Power Press
3. Yang W, Wen M, Zheng Z (2004) The automation of distribution network. China Water Power Press
4. Liu J, Ni J, Deng Y (2009) Distribution automation system. China Water Power Press
5. Liu J, Zhao S, Zhang X (2012) Development of distribution automation in China and some suggestions. Autom Electr Power Syst 36(19):6–10, 21
6. Xu L (2009) Summary of distribution automation network in China. Rural Electrification (3):5–7

# Identification for Acoustic Emission Signal of Crack Based on EMD Approximate Entropy and SVM

Zhen-hua Zeng, Shou-ming Zhang and Li Si

**Abstract** When cracks appear, material of the pipeline will deform, which is leading to the phenomenon of acoustic emission (AE). It is a kind of nonlinear, nonstationary complex signal. Based on this feature, an effective method of the signal identification based on empirical mode decomposition (EMD) approximate entropy (ApEn) and support vector machine (SVM) is applied in this paper. First, the signals are decomposed into some intrinsic mode function (IMF) signals using EMD algorithm; secondly, with simple processing of IMF, ApEn is used to calculate feature information; and lastly, the results are used as feature vector. The experimental results show that the method is an effective and convenient way to identify the signals.

**Keywords** Crack acoustic emission · EMD · Approximate entropy · SVM

## 1 Introduction

Pipeline is an important device used for the conveyance of gas, liquid, or powder, which is widely used in the supply of water and long distance transportation of oil and natural gas. In the midst of all this process, the temperature, corrosion, fatigue, and other factors can cause pipe to appear cracks. The expanding of crack may lead

---

Z. Zeng · S. Zhang (✉) · L. Si  
Faculty of Information Engineering and Automation, Kunming University  
of Science and Technology, No. 727 JingMing Road (South), Chenggong District,  
Kunming 650500, China  
e-mail: zsmingxm@sina.com

Z. Zeng  
e-mail: echozhenhua@sina.com

L. Si  
e-mail: silikm@163.com

to the leakage of the pipeline, which is a disaster for transportation and causes great economic cost. The signal source is created by a crack, overloading, or degradation of the material [1]. It is very important and necessary to diagnose the crack signal of pipeline timely and accurately. So, we can avoid severe damage and expensive repairs by the method.

Based on the above analysis, this paper focuses on the characteristics of signal. We use EMD algorithm to decompose the signal and calculate the ApEn of IMFs component as feature vectors. The experimental results show that the method is an effective and convenient way to identify the signals.

## 2 Introduction of Basic Theories

### 2.1 Empirical Mode Decomposition

It is a suitable method for processing nonlinear and nonstationary signal. The complex nonlinear signal can be decomposed into a series of structural components. The procedures to decompose a signal  $u(t)$  can be summarized as [4, 5]:

First, we identify all the local extrema of given signal  $u(t)$ , including maxima and minima. Then, we connect all the local extrema by a cubic spline line as the upper and lower envelope and calculate the mean of the two envelopes as  $m_1(t)$ . It is subtracted from the original signal  $h_1(t) = u(t) - m_1(t)$ . If  $h_1(t)$  satisfy the conditions, we get the first  $c_1(t)$ ; however, if  $h_1(t)$  do not satisfy, we use  $h_{11}(t) = h_1(t)$  as a new signal and repeat steps as before until the first  $c_1(t)$  is extracted. The  $c_1(t)$  is then subtracted from  $u(t)$ , as  $r_1(t) = u(t) - c_1(t)$ . The  $r_1(t)$  is treated as a new signal when we apply the above procedure to obtain the next one. After  $n$  times, we can get:  $u(t) = \sum_{i=1}^n c_i(t) + r_n(t)$ ,  $r_n(t)$  is a residue function.

### 2.2 Approximate Entropy

It used a non-negative number to measure the probability of signal that is generated in the new model. The more complex the signal, the greater the value. Supposing the original data of  $N$  points  $u(t) = [u(1), u(2), u(3), \dots, u(N)]$ , specific steps are as follows [3]:

1. Construct  $m$ -dimensional vector

$$U(i) = [u(i), u(i+1), \dots, u(i+m-1)], \quad i = 1 \dots N - m + 1 \quad (1)$$

2. Define the distance between  $U(i)$  and  $U(j)$  as

$$d[U(i), U(j)] = \max_{k=1 \dots m} [|x(i+k-1) - x(j+k-1)|] \quad (2)$$

3. Give a threshold, statistics the number of  $d[U(i), U(j)] < r$  to every  $i$ , then define

$$C_i^m(r) = \frac{1}{N - m + 1} \{\text{number of } d[U(i), U(j)] < r\} \quad (3)$$

4. Calculate

$$\phi^m(r) = \frac{1}{N - m + 1} \sum_{i=1}^{N-m+1} \ln C_i^m(r) \quad (4)$$

5. Finally, the value of is

$$\text{ApEn}(m, r, N) = \phi^m(r) - \phi^{m+1}(r) \quad (5)$$

The values of parameters  $m$  and  $r$  reference to the existing experience:  $m = 2$ ,  $r = 0.1 \sim 0.2 \text{ SD}_u$ ,  $\text{SD}_u$  is standard deviation of  $u(t)$ .

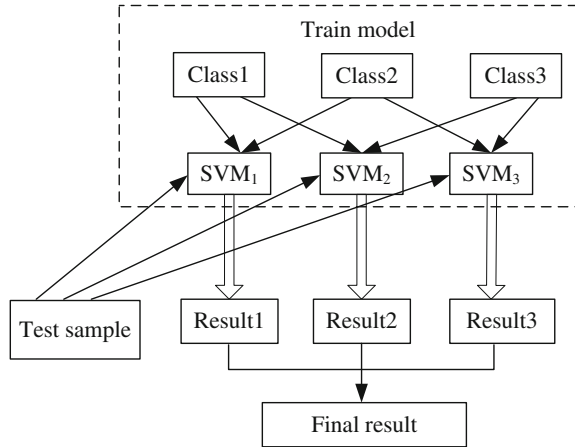
### 2.3 Support Vector Machine

Multiclass classification problem can be implemented by “one-against-one” approach. If  $k$  is the number of classes,  $k(k-1)/2$  classifiers are constructed. Each one trains data from two classes. For training data from the  $i$ th and the  $j$ th classes, we solve following two-class classification problem [2].

$$\begin{aligned} & \min_{\omega^{ij}, b^{ij}, \zeta_t^{ij}} \frac{1}{2} (\omega^{ij})^T \omega^{ij} + C \sum_t (\zeta_t^{ij}) \\ & \text{subject to } (\omega^{ij})^T \phi(x_t) + b^{ij} \geq 1 - \zeta_t^{ij} \quad \text{if } x_t \text{ in the } i\text{th class,} \\ & (\omega^{ij})^T \phi(x_t) + b^{ij} \leq 1 - \zeta_t^{ij}, \quad \text{if } x_t \text{ in the } j\text{th class,} \\ & \zeta_t^{ij} \geq 0 \end{aligned} \quad (6)$$

In classification, it can use a voting strategy: each binary classification is considered to be a voting where votes can be cast for all data points  $x$ —in the end a point is designated to be in a class with the maximum number of votes. For example, flow chart of three classification problems is showed in Fig. 1.

**Fig. 1** Schematic diagram of multiclass classification



### 3 Method of Identification for Acoustic Emission Signal

The flow chart of identification method has been shown in Fig. 2. The whole process includes five steps [6–9]:

1. Using digital signal emission system to collect experiment data. Three kinds of signal (crack; sandpaper; knocking) were simulated as original sample. Numbered lists should use the “Numbered Item” style.
2. Decomposing every signal into several IMFs. In order to reduce the amount of calculation, we select the first few components that contain the main information. The rest components add together into the last component.
3. Calculating the value of components as mentioned in step 2. If the number does not equal, the max number are  $m$ , we need to add zero value to make the number equal.
4. Using 70 % of original signal samples as training samples to construct multiclassifier.
5. Using the rest of 30 % original signal as testing samples to achieve signal classification.

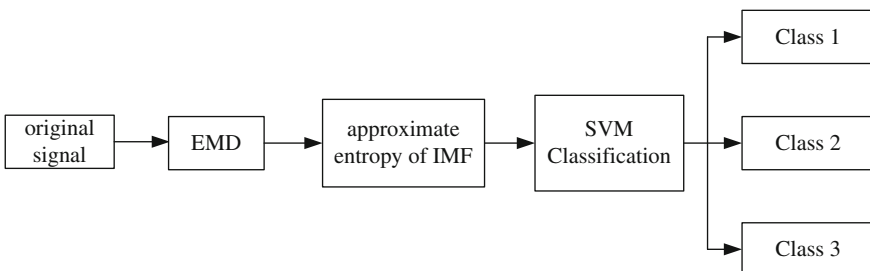


**Fig. 2** Flow chart of identification method

### 4 Analysis of Experimental Results

Experimental device is digital signal emission system SAEU2S designed by Beijing soundwel Technology Co., Ltd. Sensor is SR150M and its resonant frequency is 150 Hz. We set sampling parameters as follows: frequency of 2000 kHz, length of 10 ms, parameter interval of 2 ms, blocking time of 1 ms, waveform threshold of 50 db. We use Nielson source testing method to simulate a crack signal. At the same time, a metal knocking signal and a sandpaper signal are added into the sound sources. We collected 10 samples of each kind of signals and use only the beginning 1500 points to analyze. The signal waveform of three samples is shown in Fig. 3.

In the figure, three kinds of signal are different in magnitude. Amplitude of crack is maximum and sandpaper is minimum. Since the figure is only a partial signal, it is not accurate that we use the difference between the amplitude of three kinds of signal to identify the signals. With sandpaper signal, for example, the signal decomposition results are shown in Fig. 4.

We obtain eight main components and a residual component after decomposition. In the figure, it is obvious to the sharp drop in amplitude of the component after fifth subgraph. The main information of the signals focus on the first five components. In order to reduce the amount of calculation, the after four components are added into fifth components. According to the above method, if the number is not equal after processing, zero is served as component when the number is less

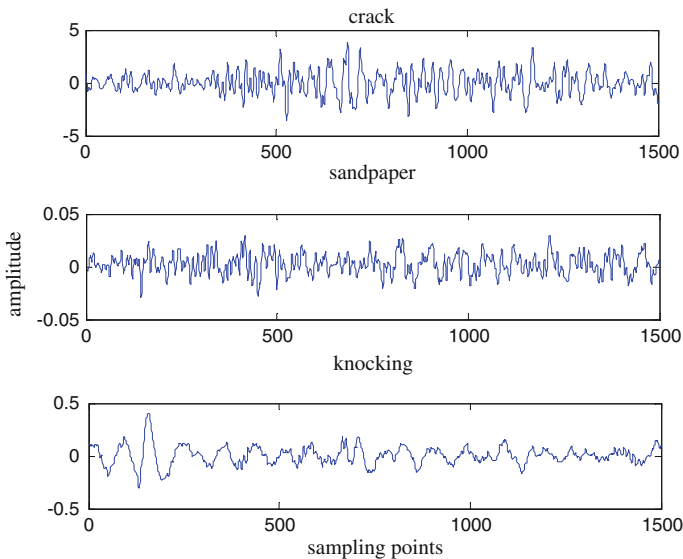
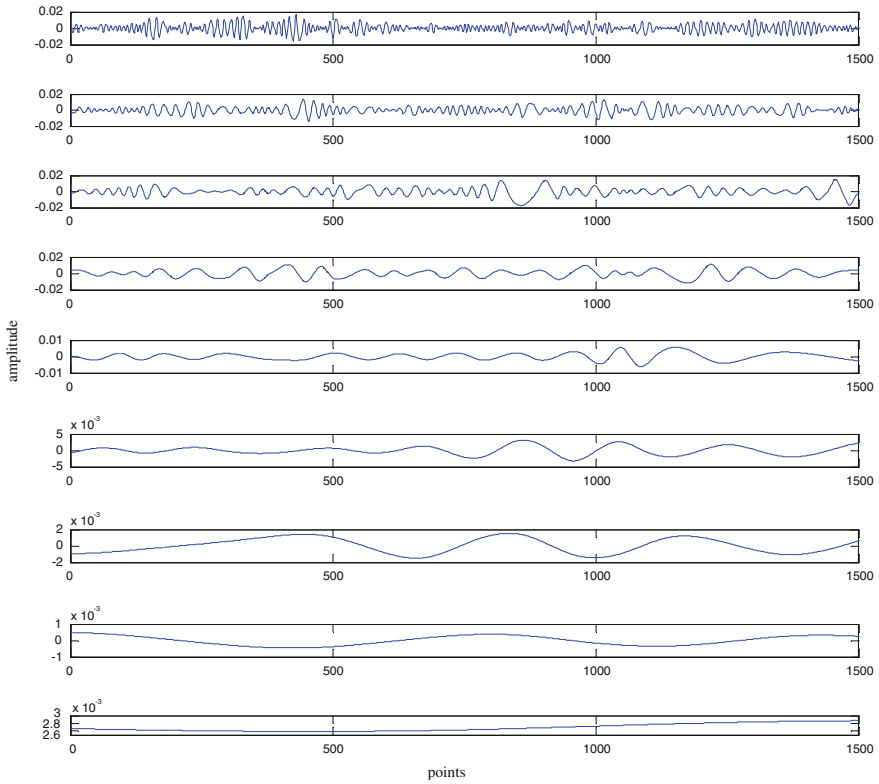


Fig. 3 The signal waveform of three samples



**Fig. 4** Decomposition results of sandpaper signal

**Table 1** Crack EMD approximate entropy calculation results

Crack	ApEn1	ApEn2	ApEn3	ApEn4	ApEn5	ApEn6
1	0.6226	0.5639	0.4275	0.1886	0.0794	0
2	0.6126	0.5809	0.5117	0.3004	0.1105	0
3	0.6203	0.5869	0.5328	0.3122	0.1146	0
4	0.6167	0.5803	0.4926	0.2081	0.0706	0
5	0.6338	0.6155	0.5499	0.4023	0.1749	0
Mean	0.6188	0.5855	0.5029	0.2823	0.11	0

than the maximum number. Calculating for each component, part of the calculation results are shown in Tables 1, 2 and 3.

From the results, although three types of data are different, it is not obvious. So, SVM which can deal with the classification of small samples is introduced.

In this experiment, we use libsvm toolbox which was designed by Professor Lin and his team in Taiwan University. Seven groups of each kind of the signal samples were taken as the training samples, and the rest of the three groups were test



**Table 2** Sandpaper signal EMD approximate entropy calculation results

Sandpaper	ApEn1	ApEn2	ApEn3	ApEn4	ApEn5	ApEn6
1	0.7752	0.6535	0.5852	0.4159	0	0
2	0.7639	0.6441	0.5935	0.3633	0	0
3	0.7459	0.6374	0.5617	0.349	0	0
4	0.7645	0.628	0.593	0.3431	0.1119	0
5	0.7475	0.6274	0.5988	0.4274	0.2391	0
Mean	0.7419	0.6381	0.5864	0.3797	0.0702	0

**Table 3** Beat signal EMD approximate entropy calculation results

Knocking	ApEn1	ApEn2	ApEn3	ApEn4	ApEn5	ApEn6
1	0.1176	0.3872	0.2216	0.1984	0	0
2	0.6992	0.3099	0.3902	0.2624	0	0
3	0.5844	0.1571	0.1687	0.2206	0.1216	0
4	0.0825	0.1409	0.2041	0.1627	0.0769	0.0156
5	0.0784	0.0961	0.2325	0.2129	0.1739	0
Mean	0.2120	0.2182	0.2434	0.2114	0.0745	0.0031

samples. The selection of the type of kernel function was a Gaussian radial basis function:  $K(\mathbf{x}_i, \mathbf{x}_j) = \exp(-\gamma \|\mathbf{x}_i - \mathbf{x}_j\|^2)$ . The  $\gamma$  parameter was 0.02, penalty factor C was 2. Nine groups of test sample were putted in classification, and the classification results are all correct, the accuracy rate of 100 %.

## 5 Summary

In this paper, an identification method for the signals was presented based on EMD ApEn and SVM. First, the collected signals are decomposed into some IMF signals using EMD algorithm; secondly, with simple processing, ApEn is used to calculate feature information; and lastly, using the results as feature vector to achieve the classification of the signals. They are introduced to detect the signals. It is effective to decompose nonlinear signal and can reveal the dynamics of signals deeply. SVM can solve small samples, nonlinear classification problem by selecting the appropriate kernel function and related parameters to train classifier. We can get high accuracy classification results. The experimental results show that the method is an effective and convenient way to identify the signals.

## References

1. Ammar IB, Mahi AE, Karra C et al (2005) Mechanical behaviour and damage evaluation by acoustic emission of composite materials. *Multidiscip Model Mater Struct* 9(1):100–115
2. Chang CC, Lin CJ (2011) LIBSVM: a library for support vector machines. *Acm Trans Intell Syst Technol* 2(3):389–396
3. Chen WT, Wang ZZ, Ren XM (2006) Characterization of surface EMG signals using improved approximate entropy. *J Zhejiang Univ Sci B* 7(10):844–848
4. Guo XH, Ma XP (2011). Fault diagnosis approach based on approximate entropy feature extraction with EMD and support vector machines. In: *Proceedings of 30th Chinese control conference, Yantai 22–24 July 2011*. IEEE, pp 4275–4279
5. Huang LZ, Guo XM, Ding XR (2008) Heart sound recogultion based on EMD approximate entropy and SVM. *J Vib Shock* 27(3):21–23
6. Mao YM, Que PW (2005) Application of Hilbert-Huang signal processing to ultrasonic non-destructive testing of oil pipelines. *J Zhejiang Univ Sci A* 7(2):130–134
7. Shen Y, Zhang YC, Wang ZH (2011) Satellite fault diagnosis method based on predictive filter and empirical mode decomposition. *J Syst Eng Electron* 22(1):83–87
8. Wang XH, Hu HW, Zhang ZY et al (2013) Extraction of weak crack signals by sparse code. *J Vib Eng* 26(3):311–317
9. Zhang XT, Tang LW, Wang P (2014) Acoustic emission fault diagnosis of rolling bearings based SVD and Fast Kurtogram algorithm. *J Vib Shock* 33(10):101–105

# Capacitors Optimization of Novel Series-Connected Capacitor-Run Three-Phase Induction Motor Fed by Single-Phase Supply

Hui Zhong, Xiuhe Wang and Dongwei Qiao

**Abstract** The phase-shift capacitors played the important role in the three-phase induction motor operation with single-phase power supply. This paper provided the capacitors optimization of three-windings in series connection motor. First, the capacitors are optimized with the golden section method by selecting the smallest negative-sequence current coefficient as objective function. Then capacitances are further optimized with simulated annealing method by taking the highest efficiency under rated loads as objective function. The combined optimization method enabled the proposed motor to operate with high efficiency and provided the method for capacitors determination. The calculation and test efficiency of the motor with the optimized capacitors were compared to valid the optimization. The effect of capacitance on the motor performance was investigated with simulation, which provided the evidence of the optimization.

**Keywords** Optimization method · The golden section method · Simulated annealing method · Capacitor · Single-phase motor

## 1 Introduction

Capacitor-run three-phase induction motors fed by single-phase power supply would improve the efficiency of single-phase induction motor without increasing its manufacturing cost. The novel approach with capacitor series connection was

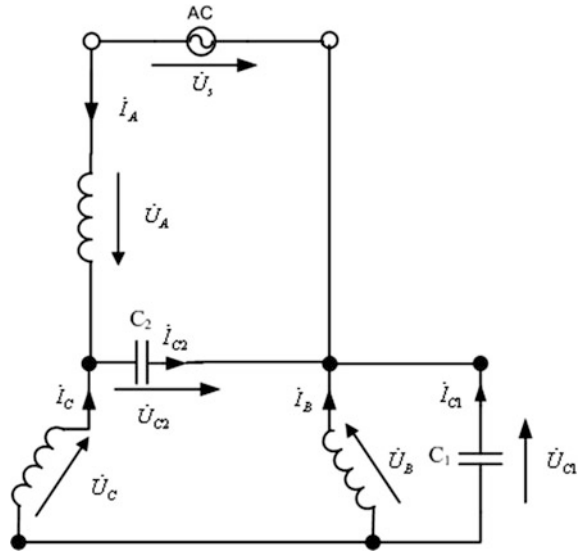
---

H. Zhong (✉) · X. Wang  
Electrical Engineering School, Shandong University, Jinan 250061, China  
e-mail: zhonghui@sdu.edu.cn

X. Wang  
e-mail: wangxh@sdu.edu.cn

D. Qiao  
School of Control Science and Engineering, Shandong University,  
Jinan 250061, China  
e-mail: 283453643@qq.com

**Fig. 1** Position of capacitors and windings



proposed in [1], shown in Fig. 1. The results of the steady and dynamic state performance analysis showed that the proposed motor can achieve approximately rated efficiency and higher power factor comparing to original three-phase induction motor [1, 2]. The capacitors used as phase converters are connected to the windings, which are the most important components for the performance of the proposed motor [3–5]. It is necessary to make a detailed study on the capacitor to ensure the performance of the motor.

In this paper, the capacitors parameters were optimized to get the best performance of the novel by selecting the smallest negative-sequence current coefficient or the highest efficiency under rated load as the objective functions. Considering of the importance of manufacture, economic and symmetry to the performance of the proposed motor, the ideal capacitors were determined by the combined using of the golden section searching and simulated annealing method. Investigations were undertaken to show the effect of the capacitance on torque fluctuation for the symmetry of the motor.

## 2 Optimization of Capacitors

When developing the simulation model of the motor shown in Fig. 1, the following assumptions are made: sinusoidal distributed air gap flux density, neglecting the harmonics, saturation and iron loss, and three-phase symmetrical stator windings. The balanced operation condition for the proposed motor is

$$\begin{cases} Z_{C_1} = \alpha^2 Z_f \\ Z_{C_2} = (\alpha^2 - 1) Z_f \end{cases} \quad (1)$$

where  $Z_{C_1}$  and  $Z_{C_2}$  are the impedances of the capacitors  $C_1$  and  $C_2$  respectively,  $\alpha = e^{j120^\circ}$ , and  $Z_f$  the positive-sequence equivalent single-phase impedance calculated from the  $T$  equivalent circuit of the induction motor.

$$Z_f = r_1 + jx_1 + jx_m \left( \frac{R'_2}{s} + jX'_2 \right) \Big/ \left[ \frac{R'_2}{s} + j(X'_2 + x_m) \right] \quad (2)$$

According to Eq. (1), impedances  $Z_{C_1}$  and  $Z_{C_2}$  are series connection of resistances and capacitances, which will increase the ohmic loss and decrease the efficiency of the motor. To avoid the additional ohmic loss, only capacitors will be connected in Fig. 1. In this case, the motor cannot operate symmetrically. What we need to do is to select suitable capacitors to enable the motor operate symmetrically as possible as we can.

To illustrate the determination of capacitances, calculation was performed on a three-windings reconnection model of a 2.2 kW, 190 V, 50 Hz, 4-pole, Y-connected three-phase induction motor. The rated slip is 0.05333 and power supply is 220 V. The machine parameters are as follows:  $R_1 = 0.8128 \Omega$ ,  $R'_2 = 0.7463 \Omega$ ,  $X_1 = 0.9927 \Omega$ ,  $X'_2 = 0.9927 \Omega$ ,  $X_m = 18.0923 \Omega$ . The calculated results show that impedances of the capacitors should be only capacitance. The capacitors are optimized by two methods to get to the suitable symmetry operation condition.

## 2.1 Theory

The capacitors are optimized with the golden section method and simulated annealing method.

The basic idea of golden section method is that of finding the minimum or maximum of a strictly unimodal function by successively narrowing the range of values inside which the extremum is known to exist [6]. The method uses an interval reduction strategy independent of the number of iterations, where the ratio between the sizes of two consecutive intervals is constant and makes use of the golden ratio  $\gamma = 0.618$  [7].

Simulated annealing (SA) is a generic probabilistic metaheuristic for the global optimization problem [8]. The method starts from a state and continues to either a maximum of steps or until a state with the minimum of energy is found. In the process, the call neighbor(s) should generate a randomly chosen neighbor of a given state; the call random (0, 1) should pick and return a value in the range [0, 1), uniformly at random.

## 2.2 Optimization with Golden Section Method

Mathematically, the performance of the novel motor can be described by a set of stator currents equations. Corresponding to a determined load, the positive-sequence, negative-sequence, and zero-sequence currents are the functions of the running capacitors value.  $k_{ib}$  is defined as the ratio of negative-sequence current to positive-sequence current, which are the functions of the capacitance  $C_1$  and  $C_2$ .

$$k_{ib}(Z_{C_1}, Z_{C_2}) = \frac{[(\alpha^2 - \alpha)Z_f + \alpha^2 Z_{C_2}](Z_0 + 2Z_{C_1}) + 2(\alpha^2 Z_f - Z_{C_1})Z_{C_2}}{[(\alpha^2 - \alpha)Z_b - \alpha Z_{C_2}](Z_0 + 2Z_{C_1}) - 2(\alpha^2 Z_b - Z_{C_1})Z_{C_2}} \quad (3)$$

When the slip is determined, according to Eq. (1), the relationship of the impedances can be derived as

$$Z_{C_2} = (\alpha^2 - 1)/\alpha^2 Z_{C_1} \quad (4)$$

Thus Eq. (3) can be changed to the function of capacitance  $C_1$

$$k_{ib}(Z_{C_1}) = \frac{[(\alpha^2 - \alpha)Z_f + (\alpha^2 - 1)Z_{C_1}](Z_0 + 2Z_{C_1}) + 2(\alpha^2 Z_f - Z_{C_1})\frac{\alpha^2 - 1}{\alpha^2} Z_{C_1}}{[(\alpha^2 - \alpha)Z_b - \frac{\alpha^2 - 1}{\alpha} Z_{C_1}](Z_0 + 2Z_{C_1}) - 2(\alpha^2 Z_b - Z_{C_1})\frac{\alpha^2 - 1}{\alpha^2} Z_{C_1}} \quad (5)$$

The golden section search method is used to find the optimal capacitor  $C_1$  which enables  $k_{ib}$  as small as possible for rated load. Table 1 shows the relationship between the capacitance and negative coefficients with rated slip. It can be seen that the minimum of the negative-sequence coefficient is correspondence to the capacitances as the slip determined. The ideal capacitors can be determined corresponding to the slip by golden section method.

Generally, single-phase induction motor runs with the slip varying from 0.03 to 0.08. According to the above method, ideal capacitance corresponding to the minimum negative-sequence coefficients with different slip is shown in Table 2.

It shows that the ideal capacitance value increases with the slip and changed little in the normal operating range of the motor, which provides a theoretical basis for the selection of a suitable capacitors. However the matched ideal capacitors cannot achieve the rated power output and need further optimization.

**Table 1** Capacitance and negative coefficients

$C_1/\mu\text{F}$	$C_2/\mu\text{F}$	$k_{ib}$
142	85	0.3969
224	134	0.1128
262	156	0.1436
307	183	0.2669
322	192	0.3014

**Table 2** Ideal capacitance corresponding to different slip

S	$C_1/\mu\text{F}$	$C_2/\mu\text{F}$	$k_{ib}$	$P_2/\text{W}$
0.03	183	97	0.111	953
0.04	210	118	0.0266	1278
0.05	2220	131	0.0808	1549
0.06	239	146	0.1412	1662
0.07	267	167	0.1846	1861
0.08	287	182.	0.2132	1982

### 2.3 Optimization with Simulated Annealing Method

Therefore, the calculation of efficiency can be built into a multivariable hybrid model. Using simulated annealing method to the impedance value of the variable capacitors  $C_1$  and  $C_2$  as optimization parameters, optimization intended to enable the motor efficiency at rated load maximized. Table 3 shows the comparison of the performance of the motor before and after optimization.

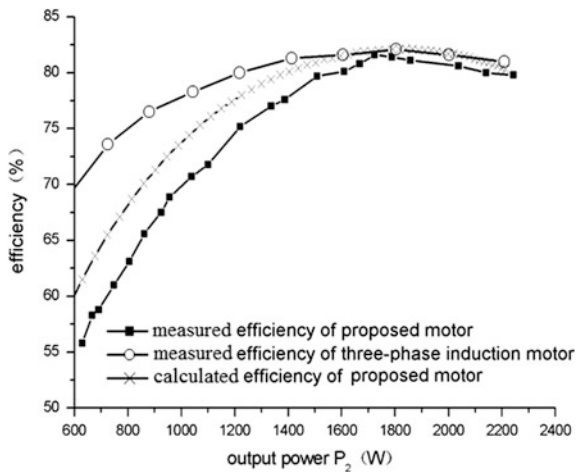
With above optimized capacitors, the efficiency calculation and test were carried out on the novel motor supplied with 220 V single-phase power source and test results were compared to those of three-phase symmetrical operation state with 110 V three-phase power supply, as shown in Fig. 2.

It can be seen that the efficiency of the proposed motor is much lower than the three-phase motor at light loads and heavy loads since the connected capacitors

**Table 3** Comparison of the performance of the motor before and after optimization

Optimization	$C_1/\mu\text{F}$	$C_2/\mu\text{F}$	Efficiency (%)	$k_{ib}$	$P_2/\text{W}$
Before	224	134	76.27	0.2675	2174
After	250	150	80.06	0.3167	2223

**Fig. 2** Efficiency comparison



were selected to satisfy the requirements of rated load. The calculated efficiency agreed to the measured one, which shows that the ohmic loss of the capacitors can be neglected.

### 3 The Effects of Capacitances on Motor Performances

Investigation was taken to show the effect of the capacitance on torque fluctuation, which could cause noise and decrease the performance of the proposed motor.

Figure 3 shows the steady torque fluctuation and steady speed fluctuation for different capacitances. Steady torque fluctuation  $\Delta T_e$  and speed fluctuation are defined as

$$\Delta T_e = (T_{\max} - T_{\min})/T_N \quad (6)$$

$$\Delta n = (n_{\max} - n_{\min})/n_s \quad (7)$$

where,  $T_{\max}$  and  $T_{\min}$  are the maximum and minimum of the steady torque, respectively,  $T_N$  the rated torque,  $n_{\max}$  and  $n_{\min}$  are the maximum and minimum of the steady speed, respectively,  $n_s$  the synchronous speed.

It can be seen that the speed fluctuation and steady torque fluctuation first decrease and then increase with capacitances in the given range. This can be explained as follows: smaller or larger capacitance than the value which enables the negative-sequence current to be minimum would cause the increase of the negative-sequence current, thus the electromagnetic torque caused by negative-sequence magnetic field increase and deduce the speed fluctuation and steady torque fluctuation.

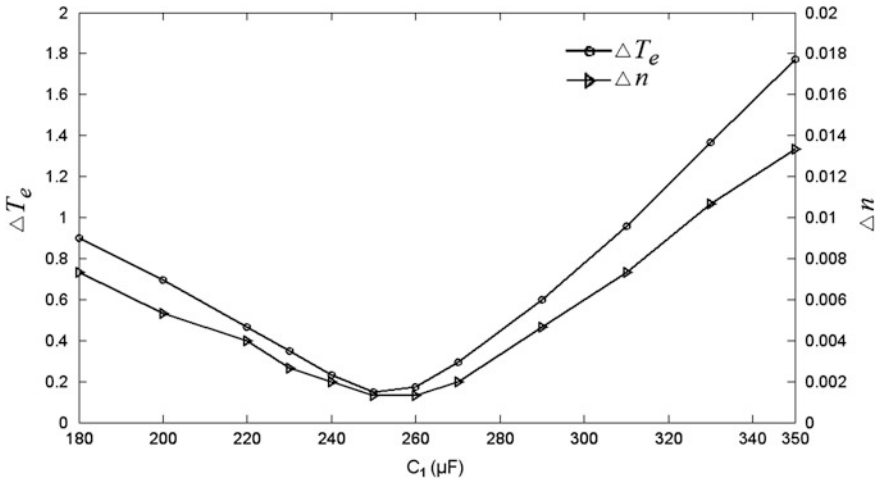


Fig. 3 Fluctuation of steady torque and speed for different  $C_1$



This suggests that there is a specific optimized capacitance of  $C_1$  which will achieve a near-optimal symmetrical operation state and produce the minimum negative-sequence current under rated load condition. In return, it produces the minimum fluctuation of the torque and speed. Any other capacitance, either larger or smaller than that value, will cause the negative-sequence current to grow, and thus larger fluctuation of torque and speed. With the capacitors, the novel single-phase motor would achieve approximately rated efficiency and a higher power factor compared with the original three-phase motor.

## 4 Conclusion

This paper presents the study of capacitors optimization for a novel energy efficient single-phase induction motor with three series-connected windings and two capacitors. Since the performance of the novel motor can be described by a set of stator currents equations, the ratio of negative-sequence current to positive-sequence current is defined, which is the function of the capacitors impedance.

The capacitors are optimized with the golden section method by selecting the smallest negative-sequence current coefficient as objective function at first. Then, capacitances are further optimized with simulated annealing method by taking the highest efficiency under rated loads as objective function. The combined optimization method enabled the proposed motor to operate with high efficiency and provided the method for capacitors determination. With above optimized capacitors, the efficiency calculation and test are carried out on the proposed motor and test results are compared to those of three-phase symmetrical operation motor. The effect of capacitance on the motor performance was investigated with simulation.

From the above studies, following conclusions can be drawn.

1. The validity of the proposed capacitor optimization method was verified by measured results on prototype motor, thus can be used to design and improve the performance of the novel single-phase motor.
2. The capacitances have great effects on transient and steady-state performances.

**Acknowledgments** The work has been supported by National Natural Science Foundation of China (NSFC) under grant #51307100.

## References

1. Zhong H, Wang XH, Zhang HB et al (2009) Single-phase induction motor with new type three-winding. Proc CSEE 29(21):69–73 (in Chinese)
2. Hui Z, Xiuhe W, Cheng Z et al (2011) Transient performance of a novel high efficiency single-phase induction motor with three series-connected windings. Diangong Jishu Xuebao 26 (4):32–39 (in Chinese)

3. Badr MA, Alolah AI, Abdel-Halim MA (1995) A capacitor start three phase induction motor. *IEEE Trans Energy Conversion* 10(4):675–680
4. Smith OJM (1992) High-efficiency single-phase motors. *IEEE Trans Energy Convers* 7(4):560–569
5. Umans SD (1994) Steady-state, lumped-parameter model for capacitor-run, single-phase induction motors. In: Industry applications society annual meeting, conference record of the 1994 IEEE 2–6 Oct 1994, vol 1, pp 164–174
6. Ta CM, Hori Y (2001) Convergence improvement of efficiency optimization control of induction motor drives. *IEEE Trans Ind Appl* 37(6):1746–1753
7. Kirschen DS, Novontny DW, Lipo TA (1987) Optimal efficiency control of an induction motor drive. *IEEE Trans Energy Conversion EC-2*(1):70–75
8. Kohoner J (1999) A brief comparison of simulated annealing and genetic algorithm approaches. Department of Computer Science, University of Helsinki

# Distributed Cooperative Secondary Control of Microgrids with Bounded Control Input

Xinsheng Wang and Tianyi Xiong

**Abstract** This paper proposes a distributed cooperative secondary control of microgrids (MG) operated in islanded mode with bounded control input. Although the primary control can maintain the voltage and frequency stable when the microgrid switches to islanded mode, it leads to the voltage and frequency of each DG deviations. The secondary control is applied to restore the voltage and frequency to their references and achieve power sharing. The MG can be considered as multi-agent systems since each DG is an agent and the communication network is modelled by a digraph. Considering the limitation of control input, a tracking strategy with bounded control input is adopted. The stability of the closed-loop system is proved in theory, and the simulation on an islanded microgrid verifies the effectiveness of the proposed control strategy.

**Keywords** Islanded microgrid · Secondary control · Bounded control input · Multi-agent systems

## 1 Introduction

As the main building blocks of smart grids, microgrids (MG) are small-scale power systems that facilitate reliable and effective integration of distributed generators (DGs) [3]. They can operate connected to the traditional centralized grid (macrogrid), but also can disconnect from the macrogrid and operate in an islanded mode due to the unplanned disturbances or preplanned scheduling [4]. However, once a microgrid is islanded from the macrogrid, the power balance between the supply and demand will not match, and the frequency and voltage of the microgrid will

---

X. Wang · T. Xiong (✉)

Harbin Institute of Technology at Weihai, Weihai 264209, Shandong, China  
e-mail: xty940430@163.com

X. Wang

e-mail: wangxsw@126.com

© Springer-Verlag Berlin Heidelberg 2016

B. Huang and Y. Yao (eds.), *Proceedings of the 5th International Conference on Electrical Engineering and Automatic Control*, Lecture Notes in Electrical Engineering 367, DOI 10.1007/978-3-662-48768-6\_5

fluctuate because of this mismatch, which may cause a blackout [9]. Therefore, control strategies play a significant role in the control of MGs.

Recently, hierarchical control for MGs in islanded mode has been proposed inspired by control architectures from transmission level power systems [12]. This control strategy is composed of three layers namely, primary, secondary and tertiary controls [6, 7, 14]. The application of primary control is able to maintain frequency and voltage in stable ranges in islanded MGs, however, primary control may lead voltage and frequency to deviate from their nominal values. To compensate the deviations and share the output power, the secondary control is applied, which leads to a track synchronization problem [2, 5, 11]. This paper focuses on the secondary control in islanded MGs.

The traditional secondary control is based on the MG centralized controller requiring a complex communication work, which may reduce the reliability and stability of the MG systems [1]. Compared to centralized control strategy, distributed control structure with sparse communication network is less sensitive to failures and error modelling [5, 16]. In addition, the cooperative control is applied in a power distribution system to regulate the output power of DGs [15].

Due to the flexibility and computational efficiency, networked multi-agent systems have gained wide attention. In MG systems, each DG can be considered as an agent, thus, a MG can be regarded as a multi-agent system. Through the communication network modelled by a direct graph (digraph), DGs can communicate with each other.

In this paper, a secondary control strategy of islanded MGs based on distributed cooperative control of multi-agent systems is presented. Considering the limitation on saturated control input, a tracking synchronization algorithm with a bounded control input is proposed to achieve the secondary control goal. Lastly, the validity and effectiveness of the proposed control strategies are verified by the simulation results.

## 2 Primary and Secondary Control Analysis in Islanded MGs

Figure 1 shows the block diagram of an inverter-based DG. It contains a primary dc source, a dc/ac inverter bridge, an LC filter, and an output connector [2]. The controller is composed of three control loops respectively named power, voltage and current controller, and the detailed descriptions of the three controllers are introduced in [10].

The target of primary control is to stabilize the voltage and frequency and mitigate circulating currents [2], which is realized in the internal control loops of DGs by adopting droop technique. The frequency and voltage droops implemented in power control loop for the  $i$ th DG are given by

$$\begin{cases} v_{o,\text{mag}}^* = V_{ni} - n_{Q_i} Q_i \\ \omega_i = \omega_{ni} - m_{P_i} P_i \end{cases} \quad (1)$$

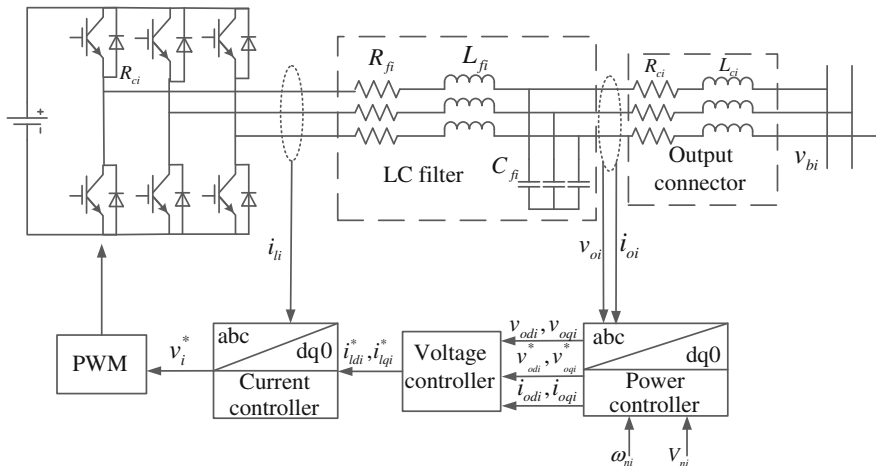


**Fig. 1** Block diagram of an inverter –based DG

where  $\omega_{ni}$  and  $V_{ni}$  are the references in primary control,  $\omega_i$  is the angular frequency calculated by power controller,  $v_{o,mag}^*$  is the output voltage magnitude reference value,  $m_{P_i}$  and  $n_{Q_i}$  are the droop coefficients,  $P_i$  and  $Q_i$  are the measured active and reactive power at the DG's terminal.

According to Guo et al. [8] and Simpson-Porco et al. [13], the frequency of MG under droop controller will be synchronized. However, once the total power output is not equal to the total consumption real power, the synchronized steady-state frequency may deviate from the nominal value  $\omega_{ref}$ . Similarly, if the reactive power is not equal to the desired value, the voltage will also deviate from its nominal value. Therefore, secondary control is necessary so as to restore the microgrid frequency and voltage to their nominal values.

Based on the primary control, the secondary control designs the control input  $V_{ni}$  and  $\omega_{ni}$  in (1) to restore the frequency and voltage to their nominal values.

Since the amplitude of the voltage can be described on direct-quadratic (d-q) reference frame as follows

$$\begin{cases} v_{o,mag} = \sqrt{v_{odi}^2 + v_{oqi}^2} \\ v_{oqi} = 0 \end{cases} \quad (2)$$

so the primary voltage control strategy is given by

$$\begin{cases} v_{odi}^* = V_{ni} - n_{Q_i} Q_i \\ v_{oqi}^* = 0 \end{cases} \quad (3)$$

where  $v_{odi}$  and  $v_{oqi}$  are the direct and quadratic components of  $v_{o,mag}$ .

According to (3), the secondary voltage control selects the appropriate  $V_{ni}$  so that  $v_{odi} \rightarrow v_{\text{ref}}$ . In the same way, the secondary frequency control selects  $\omega_{ni}$  to  $\omega_i \rightarrow \omega_{\text{ref}}$ . At the meantime, the active power of each DG is allocated to

$$m_{P_1} P_1 = m_{P_2} P_2 = \dots = m_{P_N} P_N \quad (4)$$

which is called as power sharing.

### 3 Distributed Cooperative Secondary Control with Bounded Control Input

Considering the condition requiring that the control input is within a range, distributed cooperative secondary control with bounded control input is proposed.

#### 3.1 Distributed Cooperative Secondary Control of Voltage with Bounded Control Input

As introduced in Sect. 2, the secondary voltage control is applied to synchronize the voltages of DGs to the reference, and bounded control input is required.

Due to the dynamics of the current and voltage controller are much faster than the dynamics of power controller [5, 10], we neglect the dynamics of the current and voltage controller and (3) can be written as

$$\begin{cases} v_{odi} = V_{ni} - n_{Q_i} Q_i \\ v_{oqi} = 0 \end{cases} \quad (5)$$

Differentiate the upper equation and define an auxiliary control  $u_{vi}$

$$\dot{v}_{odi} = \dot{V}_{ni} - n_{Q_i} \dot{Q}_i \equiv u_{vi} \quad (6)$$

This process is input-output feedback linearization, which transforms the secondary voltage control of a microgrid with N DGs to a first-order linear multi-agent system tracking synchronization problem [5]

$$\dot{v}_{odi} = u_{vi}, \quad i = 1, \dots, N \quad (7)$$

So the control goal synchronizing  $v_{odi}$  to the reference is achieved by designing the bounded auxiliary control input  $u_{vi}$ .

$u_{vi}$  can be designed as follows

$$u_{vi} = -c_v \left( \sum_{j \in N_i} a_{ij} \tanh(v_{odi} - v_{odj}) + \hat{g}_i \tanh(v_{odi} - v_{ref}) \right) \quad (8)$$

The communication network of a microgrid can be modelled by a digraph and each DG is assumed as a node. According to graph theory,  $N_j = \{j : (v_i, v_j) \in E\}$  set the neighbours of node  $i$ ,  $a_{ij}$  denotes the element of adjacency matrix,  $a_{ij} > 0$  if the  $i$ th DG can receive the information from the  $j$ th DG, otherwise,  $a_{ij}=0$ .  $\hat{g}_i$  is the pinning gain and  $\hat{g}_i > 0$  if the  $i$ th DG is connected to the reference, otherwise,  $\hat{g}_i = 0$ .  $c_v > 0$  is the control gain to improve the response time.

Since  $\|\tanh(\cdot)\| \leq 1$ ,  $\|u_{vi}\| \leq M_v = c_v \left( \sum_{j=1}^N a_{ij} + \sum_{j=1}^N \hat{g}_i \right)$ , that is, the auxiliary control input is bounded.

**Theorem 1** *The communication network of a microgrid is modelled by a digraph  $G_r$ , which is strong connected and meets the requirements of detailed balance that there exists vector  $w = [w_1 \ w_2 \ \dots \ w_N]^T$  satisfying  $w_i a_{ij} = w_j a_{ji}$ ,  $w_i > 0$ . Then, if the bounded auxiliary control input is designed as (9), the output voltage  $v_{odi}$  will track the reference  $v_{ref}$ .*

*Proof* Let  $\delta_{vi} = v_{odi} - v_{ref}$ , consider the following Lyapunov function candidate

$$V = \frac{1}{2} \sum_{i=1}^N w_i \delta_{vi}^T \delta_{vi} \quad (9)$$

Differentiate the Lyapunov function  $V$  along the trajectory with respect to time  $t$ , and when the digraph  $G_r$  is strong connected and satisfies detailed balance,  $\dot{V}$  is deduced as follows

$$\begin{aligned} \dot{V} &= \sum_{i=1}^N w_i \delta_{vi}^T \dot{\delta}_{vi} = \sum_{i=1}^N w_i \delta_{vi}^T \left[ -c_v \left( \sum_{j \in N_i} a_{ij} \tanh(\delta_{vi} - \delta_{vj}) + \hat{g}_i \tanh(\delta_{vi}) \right) \right] \\ &= -c_v \sum_{i=1}^N w_i \delta_{vi}^T \sum_{j \in N_i} a_{ij} \tanh(\delta_{vi} - \delta_{vj}) - c_v \sum_{i=1}^N w_i \hat{g}_i \delta_{vi}^T \tanh(\delta_{vi}) \\ &= -c_v \sum_{i=1}^N \sum_{j=1}^N w_i a_{ij} \delta_{vi}^T \tanh(\delta_{vi} - \delta_{vj}) - c_v \sum_{i=1}^N w_i \hat{g}_i \delta_{vi}^T \tanh(\delta_{vi}) \\ &= -\frac{1}{2} c_v \sum_{i=1}^N \sum_{j=1}^N w_i a_{ij} (\delta_{vi} - \delta_{vj})^T \tanh(\delta_{vi} - \delta_{vj}) - c_v \sum_{i=1}^N w_i \hat{g}_i \delta_{vi}^T \tanh(\delta_{vi}) \end{aligned} \quad (10)$$

Since  $\tanh(\delta_{vi} - \delta_{vj})$  and  $\delta_{vi} - \delta_{vj}$ ,  $\tanh \delta_{vi}$  and  $\delta_{vi}$  have the same sign componentwise,  $\dot{V} \leq 0$ . To this end, the overall auxiliary system is stable. Noticing that

$\dot{V} = 0$  implies  $\delta_{vi} = \delta_{vj} = 0, \forall i \neq j$ . According to LaSalle's Invariance principle, it follows that  $\delta_{vi} \rightarrow 0, t \rightarrow \infty$ , that is, the auxiliary closed-loop is asymptotical stable. Furthermore, since  $\delta_{vi} = v_{odi} - v_{\text{ref}}$ ,  $\lim_{t \rightarrow \infty} (v_{odi} - v_{\text{ref}}) = 0$  is obtained, that is, the output voltage  $v_{odi}$  can track the reference  $v_{\text{ref}}$ . The proof is completed.

### 3.2 Distributed Cooperative Secondary Control of Frequency with Bounded Control Input

As introduced in Sect. 2, the goal of secondary frequency control is to synchronize the angular frequency  $\omega_i$  to its reference  $\omega_{\text{ref}}$  and allocate  $m_{P_i} P_i$  to the same value. Moreover, in this section, bounded control input is required.

Differentiate equation (1)

$$\dot{\omega}_i = \dot{\omega}_{ni} - m_{P_i} \dot{P}_i \equiv u_{\omega_i}, \quad i = 1, 2, \dots, N \quad (11)$$

And let

$$m_{P_i} \dot{P}_i \equiv u_{P_i}, \quad i = 1, 2, \dots, N \quad (12)$$

where  $u_{\omega_i}$  and  $u_{P_i}$  are auxiliary controls.  $u_{\omega_i}$  is designed for  $\omega_i$  to track its reference  $\omega_{\text{ref}}$ , and  $u_{P_i}$  is to realize the active power sharing.

$u_{\omega_i}$  and  $u_{P_i}$  can be designed as follows

$$u_{\omega_i} = -c_{\omega} \left( \sum_{j \in N_i} a_{ij} \tanh(\omega_i - \omega_j) + \hat{g}_i \tanh(\omega_i - \omega_{\text{ref}}) \right) \quad (13)$$

$$u_{P_i} = -c_P \left( \sum_{j \in N_i} a_{ij} \tanh(m_{P_i} P_i - m_{P_j} P_j) \right) \quad (14)$$

where  $c_{\omega} > 0$  and  $c_P > 0$  are the coupling strength.

Similar to Sect. 3.1, the auxiliary control inputs  $u_{\omega_i}$  and  $u_{P_i}$  can be proved to be bounded. Moreover, the system can be proved to be asymptotic stable, and  $\omega_i$  can be proved to track its reference  $\omega_{\text{ref}}$ . Meanwhile, active power sharing can be realized.

## 4 Simulation

In this section, the validity and effectiveness of the proposed secondary control of islanded MG including four DGs is verified by simulation. Figure 2 shows the topology of the communication digraph.



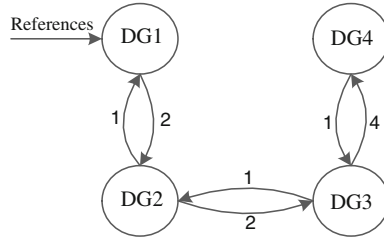


Fig. 2 The communication digraph topology

According to Fig. 2, the communication network digraph is strongly connected, and its adjacency matrix  $A_G$  is

$$A_G = \begin{bmatrix} 0 & 1 & 0 & 0 \\ 2 & 0 & 1 & 0 \\ 0 & 1 & 0 & 1 \\ 0 & 0 & 4 & 0 \end{bmatrix}$$

And there exists  $w = [w_1, w_2, w_3, w_4]^T = [4, 2, 1, 1/4]^T$  for  $w_i a_{ij} = w_j a_{ji}, \forall i, j$ , that is, detailed balance is satisfied.

Set the voltage and angular frequency references as  $v_{ref} = 380$  V and  $\omega_{ref} = 314.16$  rad/s, and the control gains  $c_v, c_\omega, c_p$  are all set to 400.

Assuming that the microgrid operates in island mode at  $t = 0$  s, the primary control is implemented at the beginning, and the proposed secondary control is applied at  $t = 0.6$  s.

Figures 3, 4 and 5 show the changes of DG voltages, frequencies and output active powers before and after applying the proposed secondary control. As seen in Fig. 3, 4 and 5, the voltages, angular frequencies and powers begin to deviate from their reference values after islanding. However, the deviation is compensated by distributed cooperative secondary control with bounded control input, that is voltages, frequencies respectively synchronize to their nominal values and active power sharing is realized.

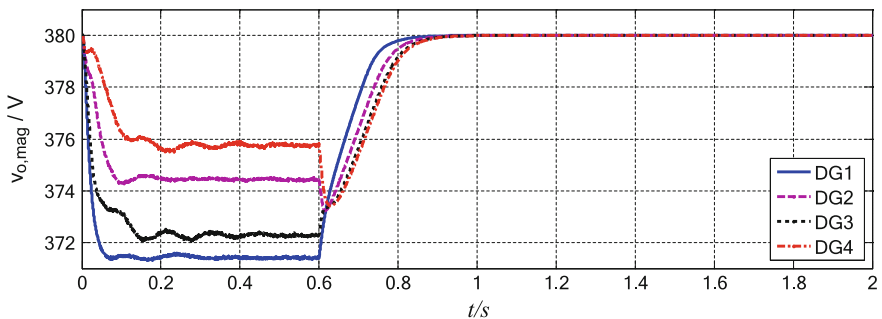


Fig. 3 DG output voltage magnitudes before and after applying secondary control

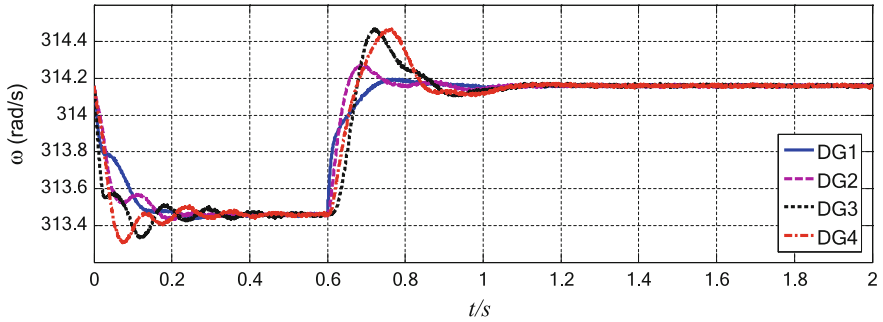


Fig. 4 DG angular frequencies before and after applying secondary control

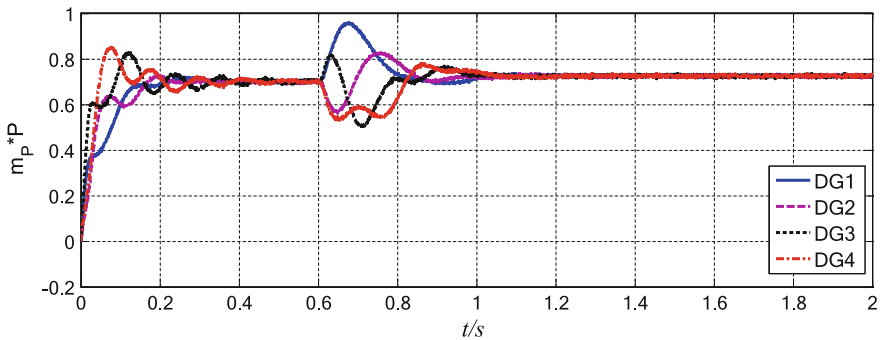


Fig. 5 DG output active power before and after applying secondary control

## 5 Conclusion

In this paper, the distributed cooperative secondary control of islanded MG based on multi-agent with bounded control input is adopted to achieve the secondary control goal that restores the voltage and frequency value to their references and achieve power sharing. In the end, the proposed strategy is proved to be reliable and effective by simulating on an islanded microgrid system.

## References

1. Bidram A, Davoudi A (2012) Distributed cooperative secondary control of microgrids using feedback linearization. *J IEEE Trans Power Syst* 2014:3462–3470
2. Bidram A, Davoudi A (2012) Hierarchical structure of microgrids control system. *J IEEE Trans Smart Grid* 3:1963–1976
3. Bidram A, Lewis FL (2014) Distributed adaptive voltage control of inverter-based microgrids. *IEEE Trans Energy Convers* 1–11

4. Bidram A, Lewis FL (2014) A multiobjective distributed control framework for islanded ac microgrids. *IEEE Trans Industr Inf* 10:1785–1798
5. Bidram A, Davoudi A, Lewis FL et al (2013) Secondary control of microgrids based on distributed cooperative control of multi-agent systems. *IET Gener Trans Distrib* 7:822–831
6. Guerrero J, Castilla M (2011) Hierarchical control of droop-controlled AC and DC micgrids—A general approach toward standardization. *IEEE Trans Industr Electron* 58:158–172
7. Guo FJ, Wen C (2014) Distributed control subject to constraints on control inputs: a case study on secondary control of droop-controlled inverter-based microgrids. In: *IEEE 9th conference on industrial electronics and applications*, pp 1119–1124
8. Guo F, Wen C et al (2015) Distributed secondary voltage and frequency restoration control of droop-controlled inverter-based microgrids. *IEEE Trans Industr Electron* 62:4355–4364
9. Mahmud M, Qo A (2014) Robust nonlinear distributed controller design for active and reactive power sharing in islanded microgrids. *IEEE Trans Energy Convers* 29:893–903
10. Pogaku N, Prodanovic M, Green T (2003) Modeling, analysis and testing of autonomous operation of an inverter-based microgrid. *IEEE Trans Power Electron* 22:613–625
11. Savahebi M, Jalilian A et al (2010) Secondary control scheme for voltage unbalance compensation in an islanded droop-controlled microgrid. *IEEE Trans Smart Grid* 3:797–807
12. Simpson-Porco J, Guerrero J et al (2013) Stability, power sharing, & distributed secondary control in droop-controlled micgrids. In: *IEEE SmartGridComm 2013 symposium-support for storage, renewable resources and micro-grids*, pp 672–676
13. Simpson-Porco JW, Dorfler F, Bullo F (2013) Synchronization and power sharing for droop-controlled inverters in islanded microgrids. *Automatica* 49:2603–2611
14. Vasquez J, Guerrero C et al (2010) Hierarchical control of intelligent microgrids J. *IEEE Ind Electron Mag* 4:23–29
15. Xin H, Qu Z, Seuss J et al (2011) A self-organizing strategy for power flow control of photovoltaic generators in a distribution network. *IEEE Trans Power Syst* 26:1462–1473
16. Zhang Z, Chow M (2012) Convergence analysis of the incremental cost consensus algorithm under different communication network topologies in a smart grid J. *IEEE Trans Power Syst* 27:1761–1768

# Distributed Robust Control of Uncertain Multi-agent Systems with Directed Networks

Wei Liu, Qingpo Wu and Shaolei Zhou

**Abstract** This paper investigates the distributed robust control problem of a class of uncertain linear time invariant multi-agent systems with directed networks. It is assumed that the agents have identical nominal dynamics while subject to different norm-bounded parameter uncertainties. Based on relative states information of the neighbor agents and a subset of absolute states of the agents, distributed robust controllers are constructed. Sufficient conditions are proposed based on bounded real lemma and algebraic graph theory. The effectiveness of the theoretical results is illustrated via a numerical simulation.

**Keywords** Multi-agent systems · Robust control · Directed networks · Bounded real lemma

## 1 Introduction

Recently, the distributed control problem of multi-agent systems has drawn great attention for its broad potential applications in many areas such as formation control [1–4], flocking control [5], and consensus control [6, 7]. Compared with traditional control systems, agents in the multi-agent systems are coupled through networks which usually are modeled by directed or undirected graphs. The system behavior depends not only on the individual agent dynamic, but also on the structure of the networks [7].

Due to some physical constrains such as limited resources and energy or short communication ranges, individual agent cannot get the global information of the system. Thus, only distributed controllers can be used with local information of neighbor agents. The distributed controllers have many advantages such as flexible scalability, high robustness, and low costs.

---

W. Liu (✉) · Q. Wu · S. Zhou  
Department of Control Engineering, Naval Aeronautical  
and Astronautical University, Yantai 264001, China  
e-mail: weiliu.sd.china@hotmail.com

The distributed control problem of ideal multi-agent systems without uncertainties has been studied from different perspectives and numerous results have been obtained [1–10]. However, in practical applications, real systems usually have uncertainties or subject to external disturbances such as sensor noise which may destroy the convergence property of the systems. Motivated by this observation, many works have been done. In [11], a decomposition approach was used to study the  $H_\infty$  control problem of identical dynamically coupled systems subject to external disturbances. Under undirected graphs, based on local relative output information, dynamic  $H_\infty$  controllers were proposed in [12]. As an extension of consensus regions, the notions of the  $H_\infty$  and  $H_2$  performance regions under undirected graphs were introduced and it was proved that the unbounded  $H_\infty$  performance region was independent of the communication topology as long as it was connected [13]. In [14], a control protocol was introduced to solve the  $H_\infty$  consensus problem synthesized with transient performance. In [15], under undirected networks, the distributed  $H_\infty$  robust control problem of linear multi-agent systems with parameter uncertainties was investigated, in which the agents have the same nominal dynamics while subject to different parameter uncertainties. Then the same problem was solved synthesized with transient performance with undirected networks [16].

Note that, the commutations topologies of the existing results relating to the distributed robust control problem of uncertain linear multi-agent systems [15, 16] are restricted to be undirected. However, the communication topologies in real application are usually modeled by directed graphs and the undirected topologies can be seen as a special class of directed topologies in which the edges among the agents are bidirectional.

Motivated by this, in this paper, we investigate the distributed robust control problem of uncertain linear multi-agent systems with directed networks. A directed graph is used to model the communication topology in the networks. It is assumed that the directed graph has a spanning tree and there is at least one root node has a loop. Based on local relative states information of the neighbor agents and a subset of absolute information of the agents, distributed robust controllers are constructed. Sufficient conditions are proposed based on the bounded real lemma and algebraic graph theory. Compared with the existing results in [15, 16] where the communication topologies are assumed to be undirected, a bright feature of this paper is that the networks are assumed to be directed.

The remainder of the paper is organized as follows. In Sect. 2, some necessary concepts and notation are introduced. In Sect. 3, the robust control problem of multi-agent systems is addressed. In Sect. 4, a simulation example is presented. Section 5 is the conclusion.

## 2 Preliminaries

Please use the ‘‘Equation’’ button for equations and positioned correctly using one tab space before and one after, as below.

In this paper, following notations will be used.  $\mathbb{R}^{n \times n}$  and  $\mathbb{C}^{n \times n}$  denote the set of  $n \times n$  real and complex matrices, respectively.  $\otimes$  denotes the Kronecker product. For  $\mu \in \mathbb{C}$ , the real part is  $\text{Re}(\mu)$ .  $I_n$  is the  $n \times n$  identity matrix.  $\|\cdot\|$  stands for the induced matrix 2-norm. For a square matrix  $A$ ,  $\lambda(A)$  denotes the eigenvalues of matrix  $A$ ;  $\text{rank}(A)$  denotes its rank. The inertia of a symmetric matrix  $A$  is a triplet of nonnegative integers  $(m, z, p)$  where  $m$ ,  $z$  and  $p$  are respectively the number of negative, zero and positive elements of  $\lambda(A)$ .  $\max\{\lambda(A)\}$  ( $\min\{\lambda(A)\}$ ) denotes the largest (smallest) eigenvalue of the matrix  $A$ .  $A > B$  ( $A \geq B$ ) means that  $A - B$  is positive definite (respectively, positive semidefinite).  $(A, B)$  is said to be stabilizable if there exists a real matrix  $K$  such that  $A + BK$  is Hurwitz.

A directed graph  $\mathcal{G} = (\mathcal{V}, \mathcal{E}, \mathcal{A})$  contains the vertex set  $\mathcal{V} = \{1, 2, \dots, N\}$ , the directed edges set  $\mathcal{E} \subseteq \mathcal{V} \times \mathcal{V}$ , the weighted adjacency matrix  $\mathcal{A} = [a_{ij}]_{N \times N}$  with nonnegative elements  $a_{ij}$ .  $a_{ij} = 1$  if there is a directed edge between vertex  $i$  and  $j$ ,  $a_{ij} = 0$  otherwise. The set of neighbors of  $i$  is defined as  $\mathcal{N}_i := \{j \in \mathcal{V} : a_{ij} = 1\}$ . A directed path is a sequence of ordered edges of the form  $(i_1, i_2), (i_2, i_3), \dots$ , where  $i_j \in \mathcal{V}$ . The Laplacian matrix of the topology  $\mathcal{G}$  is defined as  $\mathcal{L} = [\mathcal{L}_{ij}]_{N \times N}$ , where  $\mathcal{L}_{ii} = \sum_{j \neq i} a_{ij}$  and  $\mathcal{L}_{ij} = -a_{ij}$ . Then 0 is an eigenvalue of  $\mathcal{L}$  with  $\mathbf{1}_N$  as the eigenvector. A directed graph is called balanced if  $\sum_{j=1}^N a_{ij} = \sum_{j=1}^N a_{ji}$ . A directed graph is said to have a spanning tree if there is a vertex called the root such that there is a directed path from this vertex to every other vertex. A directed graph is said to be strongly connected if there is a directed path between every pair of distinct vertices.

**Lemma 1** (Bounded Real Lemma [17]) *For a positive scalar  $\gamma > 0$  and the transfer function  $G(s) = C(sI - A)^{-1}B + D$ , then the following are equivalent*

- (1)  $\text{Re}(\lambda(A)) < 0$  and  $\|G(s)\|_\infty < \gamma$ .
- (2)  $\bar{\sigma}(D) < \gamma$  and there exist a positive definite matrix  $P$  such that

$$A^T P + PA + C^T C + (PB + C^T D)(\gamma^2 I - D^T D)^{-1}(B^T P + D^T C) < 0.$$

**Lemma 2** (Schur Complement Lemma [18]) *Given a matrix  $S = \begin{bmatrix} S_{11} & S_{12} \\ S_{21} & S_{22} \end{bmatrix}$ ,*

*where  $S \in \mathbb{R}^{n \times n}$ ,  $S_{11} \in \mathbb{R}^{r \times r}$ ,  $S_{21} = S_{12}^T$ , then the following are equivalent*

- (1)  $S < 0$ .
- (2)  $S_{11} < 0, S_{22} - S_{21}S_{11}^{-1}S_{12} < 0$ .
- (3)  $S_{22} < 0, S_{11} - S_{12}S_{22}^{-1}S_{21} < 0$ .

### 3 Main Results

Consider a multi-agent system composed of  $N$  agents with following uncertain Lur'e type nonlinear dynamics

$$\dot{x}_i(t) = (A + \Delta A_i)x_i(t) + Bu_i(t), \quad i = 1, 2, \dots, N, \quad (1)$$

where  $x_i(t) \in \mathbb{R}^n$  and  $u_i(t) \in \mathbb{R}^p$  are the state and the control input of the  $i$ -th agent, respectively.  $A$  and  $B$  are constant system matrices with compatible dimensions.  $\Delta A_i$  is an unknown matrix representing the time-varying parameter uncertainty associated with the  $i$ -th agent. Here  $\Delta A_i = DF_iE$ , where  $D$  and  $E$  are known matrices of appropriate dimension which characterize the structure of the uncertainty.  $F_i$  is an uncertain matrix satisfying  $F_i^T F_i \leq \rho^2 I$  and  $\rho > 0$  is a given constant.

Here, a directed graph  $\mathcal{G}$  is used to model the communication topologies. The following assumption is introduced.

**Assumption 1** The directed graph  $\mathcal{G}$  has a directed spanning tree and there is at least one root node has a loop.

Based on this assumption, following distributed static consensus controller is proposed

$$u_i = cK \left( \sum_{j=1}^N a_{ij}(x_j - x_i) - g_i x_i \right), \quad (2)$$

where  $K \in \mathbb{R}^{p \times n}$  is the feedback matrix to be designed,  $c$  is the coupling strength to be selected,  $a_{ij}$  is the element of the adjacency matrix of the communication topology.  $g_i = 1$  means that agent  $i$  knows its own absolute state information,  $g_i = 0$ , otherwise. Then, according to Assumption 1,  $\sum_{i=1}^N g_i \neq 0$ .

Then, the closed-loop system dynamics of (1) using the controller (2) is

$$\begin{aligned} \dot{x} &= (I_N \otimes A - c(\mathcal{L} + G) \otimes BK)x + (I_N \otimes D)F(I_N \otimes E)x \\ &= (I_N \otimes A - c(\mathcal{L} + G) \otimes BK + (I_N \otimes D)F(I_N \otimes E))x \end{aligned}, \quad (3)$$

where  $x = [x_1^T, x_2^T, \dots, x_N^T]^T$ ,  $F = \text{diag}(F_1, \dots, F_N)$ ,  $\mathcal{L} \in \mathbb{R}^{N \times N}$  is the Laplacian matrix of the graph,  $G = \text{diag}\{g_1, g_2, \dots, g_N\}$ .

**Lemma 3** *Zero is a simple eigenvalue of  $\mathcal{L}$  and all the other nonzero eigenvalues have positive real parts if and only if the graph has a directed spanning tree [7]. Furthermore, if there is a root agent  $i$  such that  $g_i \neq 0$ ,  $G = \text{diag}\{g_1, g_2, \dots, g_N\}$ , then  $\text{Re}(\lambda(\mathcal{L} + G)) > 0$ .*

**Lemma 4** *Under the Assumption 1, there exist a positive definite matrix  $Q$  and a positive scalar  $\alpha$  such that*

$$(\mathcal{L} + G)^T Q + Q(\mathcal{L} + G) > \alpha Q, \quad (4)$$

where  $0 < \alpha < 2\min\{\text{Re}(\lambda(\mathcal{L} + G))\}$ .

*Proof* According to Lemma 3, one can obtain that  $\text{Re}(\lambda(\mathcal{L} + G)) > 0$ . Then  $\text{Re}(\lambda(\mathcal{L} + G - \frac{1}{2}\alpha I)) > 0$ . Thus, there exist a positive definite matrix  $Q$  such that  $(\mathcal{L} + G - \frac{1}{2}\alpha I)^T Q + Q(\mathcal{L} + G - \frac{1}{2}\alpha I) > 0$ . This completes the proof.

**Definition 1.** The system (1) with  $u_i = 0$  is quadratically stable if there exists a common Lyapunov matrix  $P > 0$  such that for all admissible uncertainty  $\Delta A_i$

$$(A + \Delta A_i)^T P + P(A + \Delta A_i) < 0.$$

**Lemma 5** (Small gain theorem) *The system (1) with  $u_i = 0$  is quadratically stable for all admissible uncertainties  $F_i$  satisfying  $F_i^T F_i \leq \rho^2 I$  if and only if  $A$  is Hurwitz and  $\|E(sI - A)^{-1}D\|_\infty < \frac{1}{\rho}$ .*

Based on Lemma 5, following conclusion is introduced.

**Theorem 1.** *Suppose that the quadratically stable problem of multi-agent system (1) with the controller (2) is solved if there exists a positive definite matrix  $P$  such that*

$$\begin{bmatrix} A^T P + PA - c\alpha P B B^T P & PD & E^T \\ D^T P & \frac{-1}{\rho^2 \varphi_1} I & 0 \\ E & 0 & -\varphi_2 \end{bmatrix} < 0, \quad (5)$$

where  $\varphi_1 = \max\{\lambda(Q)\}$ ,  $\varphi_2 = \min\{\lambda(Q)\}$ .  $Q$  is a positive definite solution of (4)  $0 < \alpha < 2\min\{\text{Re}(\lambda(\mathcal{L} + G))\}$  and the feedback matrix is designed as  $K = B^T P$ .

*Proof* According to Lemma 5, system (3) with is quadratically stable if and only if matrix  $I_N \otimes A - c(\mathcal{L} + G) \otimes BK$  is Hurwitz and

$$\|(I_N \otimes E)(sI - (I_N \otimes A - c(\mathcal{L} + G) \otimes BK))^{-1}(I_N \otimes D)\|_\infty < \frac{1}{\rho}.$$



According to bounded real lemma, if there exists a positive definite matrix  $\bar{P}$  such that

$$\bar{A}^T \bar{P} + \bar{P} \bar{A} + \bar{C}^T \bar{C} + \rho^2 \bar{P} \bar{B} \bar{B}^T \bar{P} < 0, \quad (6)$$

where  $\bar{A} = I_N \otimes A - c(\mathcal{L} + G) \otimes BK$ ,  $\bar{B} = I_N \otimes D$ ,  $\bar{C} = I_N \otimes E$ , system (3) is quadratically stable.

Here, we chose  $\bar{P} = Q \otimes P$  and  $K = B^T P$ , where  $Q > 0$  is a solution of (4),  $P > 0$  is a solution of the LMI (5). Then

$$\begin{aligned} & \bar{A}^T \bar{P} + \bar{P} \bar{A} + \bar{C}^T \bar{C} + \rho^2 \bar{P} \bar{B} \bar{B}^T \bar{P} \\ &= (Q \otimes (A^T P + PA)) - c((\mathcal{L} + G)^T Q + Q(\mathcal{L} + G)) \otimes P B B^T P \\ & \quad + I_N \otimes E^T E + \rho^2 (Q^2 \otimes P D D^T P) \end{aligned} \quad (7)$$

From Lemma 4, one has

$$((\mathcal{L} + G)^T Q + Q(\mathcal{L} + G)) \otimes P B B^T P > \alpha Q \otimes P B B^T P, \quad (8)$$

where  $0 < \alpha < 2 \min\{\text{Re}(\lambda(\mathcal{L} + G))\}$ .

It then follow from (7) using (8), one has

$$\begin{aligned} & \bar{A}^T \bar{P} + \bar{P} \bar{A} + \bar{C}^T \bar{C} + \rho^2 \bar{P} \bar{B} \bar{B}^T \bar{P} \\ & < (Q \otimes (A^T P + PA)) - c\alpha Q \otimes P B B^T P + I_N \otimes E^T E + \rho^2 (Q^2 \otimes P D D^T P) \end{aligned} \quad (9)$$

Since  $Q < \varphi_1 I_N$  and  $Q > \varphi_2 I_N$  where  $\varphi_1 = \max\{\lambda(Q)\}$ ,  $\varphi_2 = \min\{\lambda(Q)\}$ , one can obtain that

$$\begin{aligned} & \bar{A}^T \bar{P} + \bar{P} \bar{A} + \bar{C}^T \bar{C} + \rho^2 \bar{P} \bar{B} \bar{B}^T \bar{P} \\ & < (Q \otimes (A^T P + PA)) - c\alpha Q \otimes P B B^T P + \frac{1}{\varphi_2} Q \otimes E^T E + \rho^2 \varphi_1 (Q \otimes P D D^T P) \\ & = Q \otimes \left( A^T P + PA - c\alpha P B B^T P + \frac{1}{\varphi_2} E^T E + \rho^2 \varphi_1 P D D^T P \right) \end{aligned}$$

According to Schur complement lemma, inequality (5) implies that (6) hold. Thus, the quadratically stable problem for system (1) is solved.

*Remark 1* When the topology is undirected, the graph Laplacian matrix  $\mathcal{L}$  of undirected topology is symmetric positive semidefinite. Thus the matrix  $\mathcal{L} + G$  is diagonalizable and similarity transformation can be performed. These properties facilitated the derivation greatly. The quadratically stable problem of networked system can be converted into the quadratically stable problems of  $N$  individual systems associate with  $N$  eigenvalues of  $\mathcal{L} + G$ . As for the directed topology, the Laplacian matrix is not symmetric. Thus, the similarity transformation employed in

[15, 16] is not applicable. Here, based on Lemma 4 and the properly designed matrix  $\bar{P}$ , the quadratically stable problem of networked system is solved using bounded real lemma directly.

### 4 Examples

In this section, we provide an example to illustrate the effectiveness of the above theoretical results. A multi-agent system consisting four agents is considered. The system matrices are defined as

$$A = \begin{bmatrix} 0 & 1 \\ -2.8 & 0 \end{bmatrix}, B = \begin{bmatrix} 0 \\ 1 \end{bmatrix}, D = \begin{bmatrix} 0 \\ -0.4 \end{bmatrix}, E = [1 \ 0].$$

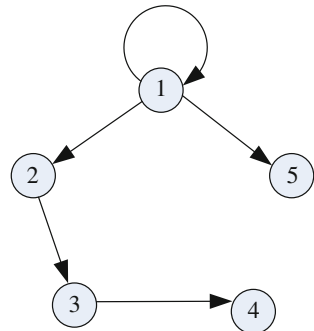
The uncertainty matrices are chosen as  $|F_i| < 10$ .

The directed communication topology is given in Fig. 1. Clearly, the communication topology has a directed spanning tree. Agent 1 is the root and agent 1 can obtain its own absolute state information. The Laplacian matrix of communication topology is

$$\mathcal{L} = \begin{bmatrix} 0 & 0 & 0 & 0 & 0 \\ -1 & 1 & 0 & 0 & 0 \\ 0 & -1 & 1 & 0 & 0 \\ 0 & 0 & -1 & 1 & 0 \\ -1 & 0 & 0 & 0 & 1 \end{bmatrix},$$

and  $G = \text{diag}\{1, 0, 0, 0, 0\}$ . The real part of the smallest eigenvalue of  $\mathcal{L} + G$  is 1. According to Lemma 5, we set  $\alpha = 00.5$  and get a feasible solution of (4)

**Fig. 1** Communication topology



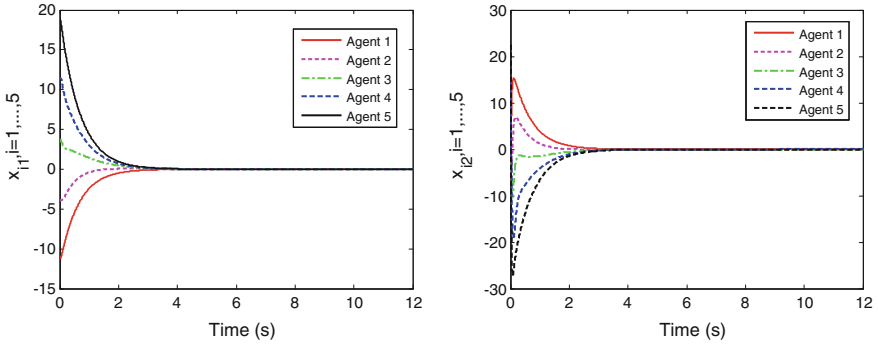


**Fig. 2** Trajectories of the states of all agents

$$Q = \begin{bmatrix} 1.3806 & 0.2799 & -0.0717 & -0.0920 & 0.2218 \\ 0.2799 & 0.9727 & 0.2399 & -0.0612 & -0.2111 \\ -0.0717 & 0.2399 & 0.8115 & 0.1455 & -0.1232 \\ -0.0920 & -0.0612 & 0.1455 & 0.6511 & -0.0498 \\ 0.2218 & -0.2111 & -0.1232 & -0.0498 & 0.7751 \end{bmatrix}.$$

Thus,  $\varphi_1 = 1.5539$ ,  $\varphi_2 = 0.4402$ . Let  $c = 80$ , solving the inequality (5), we get a feasible solution  $P = \begin{bmatrix} 0.9436 & -1.2799 \\ -1.2799 & 4.2009 \end{bmatrix}$ . According to Theorem 1, the feedback matrix can be chosen as  $K = [0.5503 \quad 0.4057]$ . Fig. 2 show the states trajectories of all the agents. It is shown that states of all the agents converge to zero.

## 5 Conclusions

In this paper, the distributed robust control problem of uncertain multi-agent systems have been investigated under directed communication topologies which have a spanning tree. Distributed robust controller has been constructed based on relative states information of neighbor agents. Sufficient conditions have been obtained using bounded real lemma.

## References

1. Jadbabaie A, Lin J, Morse AS (2003) Coordination of groups of mobile autonomous agents using nearest neighbor rules. *IEEE Trans Autom Control* 48:988–1001
2. Fax JA, Murry RM (2004) Information flow and cooperative control of vehicle formations. *IEEE Trans Autom Control* 49:1465–1476

3. Borrelli F, Keviczky T (2008) Distributed LQR design for identical dynamically decoupled systems. *IEEE Trans Autom Control* 53:1901–1912
4. Ajarlou A, Momeni A, Aghdam AG (2010) A class of bounded distributed control strategies for connectivity preservation in multi-agent systems. *IEEE Trans Autom Control* 55:2828–2833
5. Olfati-Saber R (2006) Flocking for multi-agent dynamic systems: algorithms and theory. *IEEE Trans Autom Control* 51:401–420
6. Vicsek T, Czirák A, Jacob EB, Cohen I, Schochet O (1995) Novel type of phase transitions in a system of self-driven particles. *Phys Rev Lett* 75:1226–1229
7. Ren W, Beard RW (2005) Consensus seeking in multiagent systems under dynamically changing interaction topologies. *IEEE Trans Autom Control* 50:655–661
8. Tuna SE (2008) Synchronizing linear systems via partial-state coupling. *Automatica* 44:2179–2184
9. Li Z, Duan Z, Chen G, Huang L (2010) Consensus of multiagent systems and synchronization of complex networks: A unified viewpoint. *IEEE Trans Circuits Syst–I Reg Pap* 57:213–224
10. Wen G, Yu W, Cao J, Hu G, Chen G (2013) Consensus control of switching directed networks with general linear node dynamics. In: *Proceedings of the 9th Asian control conference*, pp 1–6
11. Massioni P, Verhaegen M (2009) Distributed control for identical dynamically coupled systems: a decomposition approach. *IEEE Trans Autom Control* 54:124–135
12. Li Z, Duan Z, Huang L (2009)  $H_\infty$  control of networked multi-agent systems. *J syst Sci Complex* 22:35–48
13. Li Z, Duan Z, Chen G (2011) On  $H_\infty$  and  $H_2$  performance regions of multi-agent systems. *Automatica* 57:213–224
14. Wang J, Duan Z, Zhao Y, Qin G, Yan Y (2013)  $H_\infty$  and  $H_2$  control of multi-agent systems with transient performance improvement. *Int J Control* 86:2131–2145
15. Wang J, Duan Z, Wen G, Chen G (2015) Distributed robust control of uncertain linear multi-agent systems. *Int J Robust Nonlin* 25:2162–2179
16. Li Z, Duan Z, Xie L (2012) Distributed robust control of linear multi-agent systems with parameter uncertainties. *Int J Control* 85:384–396
17. Zhou K, Doyle J (1998) *Essential of robust control*. Prentice Hall, Upper Saddle River
18. Gahinet P, Apkarian P (1994) A linear matrix inequality approach to  $H_\infty$  control. *Int J Robust Nonlinear Control* 4:421–448

# Resonant Analysis and Depression in Multi-inverter Grid-Connection System

Jian Wu, Caihong Zhang, Rui Wang and Dianguo Xu

**Abstract** Interaction between multiple grid-connected inverters has a negative impact on the stable operation and power quality of the power grid. Interrelated influences of each inverter LCL filter make multiple inverters constitute a high order power network and excite more complex resonances at various frequencies. This paper first establishes a microgrid admittance matrix in which inverter uses hysteresis control. Multiple resonances can then be evaluated by modal analysis. Experimental results have confirmed that the modal analysis and the active damping are effective for resonance in multiple-inverters grid-connected system.

**Keywords** Modal analysis · Stability · Parallel inverters · LCL filter · Resonant · Hysteresis control · Active damping

## 1 Introduction

In recent years, as the environmental pollution and lack of energy are more and more serious, the development and employment of renewable energy, such as solar and wind power, become an urgent need of human society. Therefore, power quality of new energy has attracted more and more attention. Because of its good controllability and flexible operation mode, the inverter is used to deliver renewable and clean energy through LCL filters. Compared with the single reactance of L filter, LCL filter has a stronger inhibition ability of current high frequency com-

---

J. Wu (✉) · C. Zhang · R. Wang · D. Xu  
Harbin Institute of Technology, Harbin 15001, China  
e-mail: wujianhit@163.com

C. Zhang  
e-mail: zch110230131@163.com

R. Wang  
e-mail: 2548876553@qq.com

D. Xu  
e-mail: xudiang@hit.edu.cn

ponents, but the LCL filter is a three-order system with a resonant peak. A large number of literatures have studied the passive and active damping to restrain resonance, but they are only aimed at a single LCL inverter [1–4]. However, resonance characteristic of multi-inverters grid-connected system is clearly different from single inverters. Interrelated influences of each inverter LCL filter excite more complex resonances at various frequencies and lead to negative harm to the stable operation and power quality of grid. Some scholars have begun the research on resonance in multi-inverter grid-connected system [5–7]. Enslin and Heskes [5] ignore the influence of the inverter; this paper proposes a simplified passive circuit model to study the resonance problem. In [6], the effect of each other between multi-inverter is described and the opinion is presented that the grid series impedance is equivalent to  $N$  times than single inverter. Duarte et al. [7] introduced the control system into impedance modeling of the multi-inverters system and analyzed harmonic interaction between inverter and grid, but did not analyze the interaction between inverters.

In [8], inverter is controlled current source, in other words the inverter current is used to achieve virtual impedance. And then, inverter is introduced into the passive network model that is paralleled with output impedance, so the equivalent impedance model of multiple inverters is established. It can be found that the resonance peak changes with parallel sets. But, Norton equivalent circuit is too complex for analysis of resonant characteristics [9].

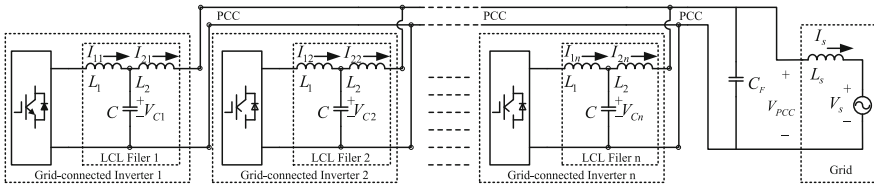
On the other hand, modal analysis method has been reported to analyse the power system resonance. Modal analysis method is suitable for microgrid resonance, which can evaluate not only the resonance frequency but also the extent of the resonance and scope based on the change of network matrix characteristic root. Meanwhile, the researchers have presented a lot of strategies to restrain the resonance phenomenon of paralleled-inverter grid-connected system, such as open-loop pole-zero compensation, double-loop current control, virtual impedance, etc.

In this paper, hysteresis controller is considered, and active damping method using voltage of capacitor to generate virtual impedance is chosen. First, the modeling and control of multiple inverter are analysed. Second, the modal analysis of resonance is described. Third, the  $z$ -domain stability of active damping based on parallel virtual resistance is discussed. Fourth, the theoretical study is validated through experiment. Finally, conclusion is obtained.

## 2 Modal Analysis of Multi-Inverter Grid-Connecter System

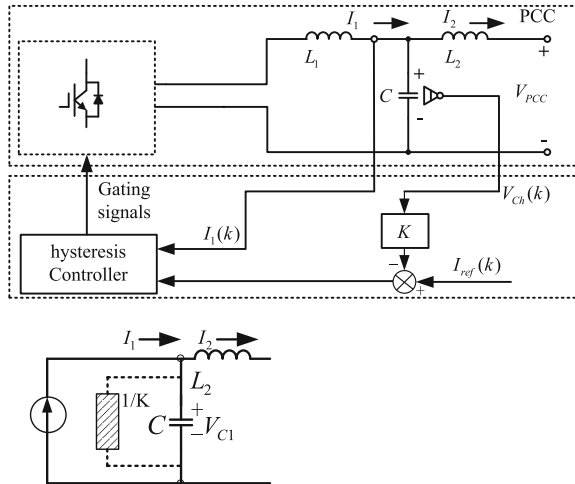
This section analyzes the possible resonance phenomenon where multiple inverters are centralized with current controlling.

Figure 1 indicates the configuration of many inverters which are all connected to grid. Every inverter contains an LCL filter, as well as is installed in the point of



**Fig. 1** Configuration of a multi-inverter grid-connected system

**Fig. 2** Configuration hysteresis controlled inverter system



common coupling (PCC) by LCL filter.  $L_1$  and  $L_2$  are respectively the inductor at inverter side and grid side,  $C$  is the capacitor. At the same time,  $L_s$  is the grid inductor. The inverter side current close-loop control based on hysteresis is used. Meanwhile, capacitor voltage feedback control is adopted to enhance the damping, as shown in Fig. 2.

### 2.1 Closed-Loop Multiple-Inverter Model

Due to the hysteresis control, the inverter can be considered as a current source, so its Norton's equivalent circuit system is unnecessary.

In simple model, the complex resonances can also be investigated. The inverter side reactor is not considered due to hysteresis current control, so the complexity of analysis is reduced.

When compensation capacitors are in the distribution power system, the resonance features of the multiple-inverter grid-connected system will be more complex. Through the proposed simple model, the behavior of the multiple-inverter

grid-connect system can be described using an admittance matrix or impedance matrix. The resonance has a relationship with singular of the inverted network admittance matrix.

## 2.2 Modal Analysis of Multiple-Inverter System

A singular Y matrix occurs only when an eigenvalue is very small, which could be real source of the resonance phenomenon and a serious resonance will lead to high nodal voltages.

So the analysis of harmonic resonance can be transformed into a study of critical resonance modes. The matrix can be expressed as

$$\begin{bmatrix} U_1 \\ U_2 \\ \vdots \\ U_n \end{bmatrix} = \begin{bmatrix} \lambda_1^{-1} & 0 & 0 & 0 \\ 0 & \lambda_2^{-1} & 0 & 0 \\ \vdots & \vdots & \ddots & \vdots \\ 0 & 0 & 0 & \lambda_n^{-1} \end{bmatrix} \begin{bmatrix} J_1 \\ J_2 \\ \vdots \\ J_n \end{bmatrix} \quad (1)$$

$U_i$  the modal voltage vector,  $J_i$  the modal current vector.

From (1), it can be easily seen that if  $\lambda$  is close to zero.  $U$  will be very big. In other words, the location and frequency of resonance can easily be detected.

When no active damping, the modal analysis of multiple-inverter grid-connected system with compensation capacitor is show in Fig. 3. Figure 3a shows the resonance features of multiple-inverter grid-connected system. When single inverter is in system, there is a fixed resonance peak. When paralleling several inverters and considering compensation capacitor, the system has three resonance peaks. In Fig. 3a, the one resonance frequency is fixed, and the second resonance frequency is caused by multiple-inverter paralleling at the fixed resonance peak left. If the

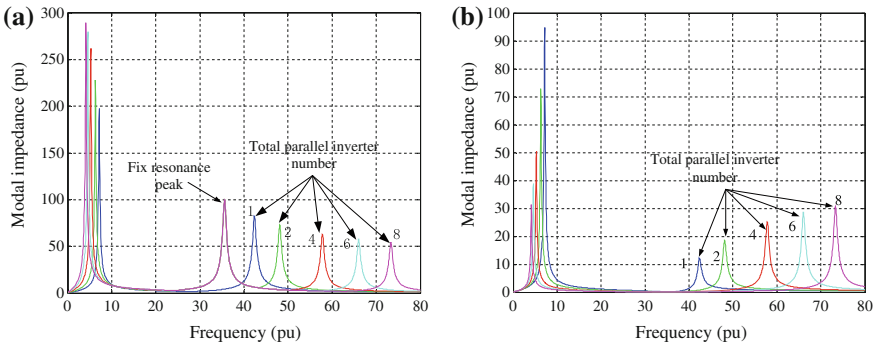


**Fig. 3** Resonance of multiple-inverter system with capacitor CF (without active damping) **a** parallel resonance **b** series resonances



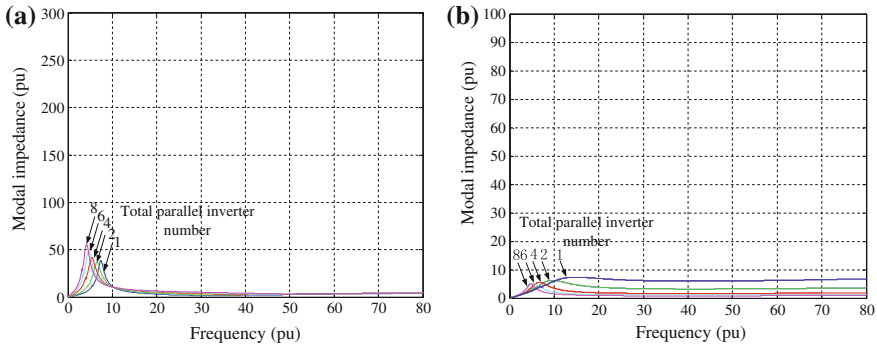


**Fig. 4** Parallel resonance of multiple-inverter system with capacitor CF (with active damping) **a** parallel resonance **b** series resonances

numbers of parallel inverters increase, the resonance frequency will decrease. While the third resonance frequency is at the fixed resonance peak right and is caused by compensation capacitor. If the numbers of parallel inverters increase, the resonance frequency will also increase.

The grid voltage will cause the series resonances phenomenon in multiple-inverter grid-connected system. From Fig. 3b, it can be found that the series resonance contains two kinds of resonance caused by interaction of parallel inverters and compensation capacitor. Meanwhile, the numbers of parallel inverter changing will cause resonance changing.

In Fig. 2, with the active damping on based virtual resistance, the filter capacitor is equivalently paralleled with a resistance which has value  $1/K$  in resonance frequency. The effectiveness of the active damping to multiple-inverter system resonances suppression is also verified using the modal analysis, as shown in Fig. 4.

It can be seen that, through selecting appropriate virtual damping ratio, the active damping based on virtual resistance is effective in restraining the three kinds of resonance: fixed resonance of single inverter, varying resonance caused by multiple inverter, and resonance of compensation capacitors.

### 3 Experiment Verification

The experiments have confirmed the developed modal analysis and stability domain calculation method. Table 1 indicates the model parameters; the experimental multi-inverter grid-connected system is composed of two three-phase inverters, and the digital control system incorporates DSP (TMS28335) and CPLD circuit.

The waveforms in Fig. 5 are the situation that the capacitor voltage feedback control is not adopted. The line current has a good quality by active damping to suppressing the parallel resonance peak.

**Table 1** System parameters

Description	Symbols	Value
Inverter side inductor	$L_I$ (mH)	3.5
Filter capacitor	$C$ ( $\mu$ F)	40
Grid side inductor	$L_2$ (mH)	0.2
Grid inductor	$L_s$ (mH)	0.14
Grid voltage	$V_s$ (V)	220
dc-bus voltage	$V_{DC}$ (V)	700
Sampling frequency	$f_s$ (KHz)	20
Compensation capacitor	$C_f$ ( $\mu$ F)	100
Active damping ratio	$K$	0.2

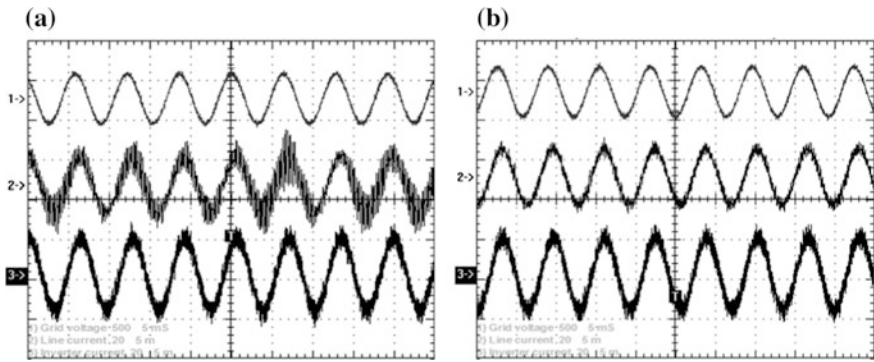


**Fig. 5** Parallel resonances in two inverter grid-connected system **a** with active damping **b** without active damping

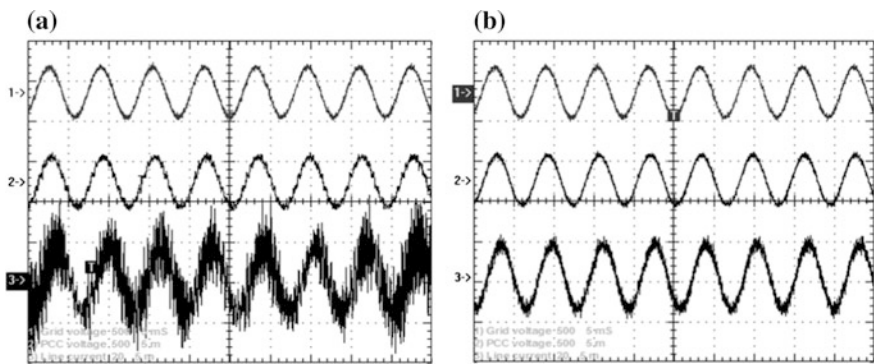


**Fig. 6** Series resonance of two inverter grid-connected system **a** with active damping **b** without active damping

Comparing experiment results of series resonances are shown in Fig. 6. The grid voltage contains 5 % 11th and 5 % 13th harmonics. When the capacitor voltage feedback control is not adopted, the series resonance can be restrained effectively, power quality of PCC voltage and line current of inverter has been clearly improved.

## 4 Conclusion

The relationship among the distribution, capacitance, and paralleled-inverter grid-connected system has been discussed with analysis and experiment. Due to good robustness and simple control, hysteresis still has a large number of applications in the field of grid-connected inverter and active power filter. So, this paper developed a simple model with considering the inverter as current source. The inverter side reactor does not need to be considered and the complexity of analysis is reduced. In addition, the paper indicates that there are more complex resonances in paralleled-inverter grid-connected system when there are compensation capacitors in the distribution power system. To identify the resonance frequency, this paper developed a modal analysis method based on proposed simple model.

**Acknowledgement** This paper and its related research are supported by grants from the Power Electronics Science and Education Development Program of Delta Environmental and Educational Foundation (DREM2014015) and the National Science Foundation of China (51407043).

## References

1. Bierhoff MH, Fuchs FW (2009) Active damping for three-phase PWM rectifiers with high-order line-side filters. *IEEE Trans Ind Electron* 56(2):371–379
2. Wu E, Lehn PW (2006) Digital current control of a voltage source converter with active damping of LCL resonance. *IEEE Trans Power Electron* 21(5):1364–1373
3. Dannehl J, Fuchs FW, Hansen S, Thøgersen PB (2010) Investigation of active damping approaches for PI-based current control of grid-connected pulse width modulation converters with LCL filters. *IEEE Trans Ind Appl* 46(4):1509–1517
4. Massing JR, Stefanello M, Grundling HA, Pinheiro H (2012) Adaptive current control for grid-connected converters with LCL filter. *IEEE Trans Ind Electron* 59(12):4681–4693
5. Enslin JHR, Heskes PJM (2004) Harmonic interaction between a large number of distributed power inverters and the distributed network. *IEEE Trans Power Electron* 19(6):1586–1593
6. Agorreta J, Borrega M, Lopez J, Marroyo L (2011) Modeling and control of N paralleled grid-connected inverters with LCL filters coupled due to grid impedance in PV plants. *IEEE Trans Ind Electron* 26(3):770–785
7. Fei W, Duarte JL, Hendrix MAM, Ribeiro PF (2011) Modeling and analysis of grid harmonic distortion impact of aggregated DG inverters. *IEEE Trans Power Electron* 26(3):786–797
8. He J, Li YW, Bosnjak D, Harris B (2013) Investigation and active damping of multiple resonances in a parallel-inverter-based microgrid. *IEEE Trans Power Electron* 28(1):234–246
9. Trinh QN, Lee HH (2013) An advanced current control strategy for three-phase shunt active power filters. *IEEE Trans Ind Electron* 60(12):5400–5410

# The Application of Power Electronic Switch in the Regulated Capacity Transformer

Hongxing Chen, Zhizhen Liu, Tong Hei, Xiaodong Qu  
and Guozheng Qi

**Abstract** The seasonal loads of rural, industrial, and mining enterprises vary sharply and their average load rate is at a low level. The replacement of the normal transformers by the ones able to regulate the power capacity and voltage can significantly reduce the no-load loss and the waste of electric energy. First, this paper analyzed the theory of the capacity and voltage regulating transformer (CVRT). Secondly, a simulation model is established by Simulink toolbox in Matlab to investigate the reduction of the impact of the current and voltage after the application of delay conduction.

**Keywords** Electronic power switch · Distribution transformer · Solid state relay · On-load capacity and voltage regulating

## 1 Introduction

At present, the loss of rural power transformer is quite large in our country. In order to avoid the occurrence of the loss, the characteristic of such a transformer should be consistent with the load characteristic of the rural power grid [1].

This paper focuses on the analysis of Simulink model for the arcless CVRT. Since the inevitable occurrence of arc in traditional transformers, we apply the power electronic switches, which can significantly reduce the probability of arc and ensure that the capacity and voltage can be safely transferred under the load condition.

---

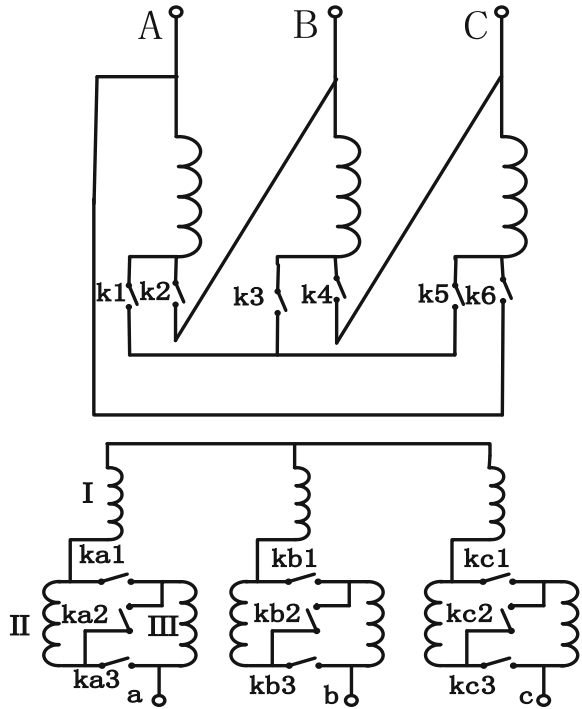
H. Chen · Z. Liu (✉) · T. Hei · X. Qu · G. Qi  
College of Electrical Engineering, Shandong University, Jinan 250061, China  
e-mail: liuzhizhen@sdu.edu.cn

## 2 System Theory Analysis

According to the winding connection as high or low voltage, the capacity ratio of the capacity regulating transformer can be set as 3:1 or 2:1, and a transformer with the former capacity ratio will be discussed in this paper.

The connection mode of the high and low voltage winding of the transformer is shown in Fig. 1. The voltage can be regulated by changing the turn's number of the high side which is not shown in the figure. The design principle of capacity regulation part is: when K2, K4, and K6 are closed, the high voltage windings are connected as the triangle (D) shape, which can provide a large capacity; when the other switches, K1, K3, and K5 are closed as the star (Y) shape, a smaller capacity can be provided. Each phase of the low voltage windings is a combination of three parts made up of coils: wire coils with a small number of turns are labeled as part I, and the other two parts are composed of sets of wires and labeled as part II and III [2]. When the transformer works in a large capacity, ka1, ka3, kb1, kb3, kc1, kc3 are closed to make part II being parallel with III and then in series with I.; when the transformer works in a small capacity, ka2, kb2, kc2 are closed to make part I being in series with II and III [3].

Fig. 1 Connection mode of high and low voltage winding



Due to the variation of the loads, when the working condition of the transformer transfers from providing large capacity to small capacity, the number of the low voltage winding turns increase about  $\sqrt{3}$  times as before, and the connection of the high voltage windings changes from D to Y to make the phase voltage  $1/\sqrt{3}$  times as before at the same time [2]. So the output voltage remains constant. At the same time, when the working condition changes as above, in accordance with the increase of the number of windings of the low voltage, the magnetic flux density of the core decreased, and the loss of silicon steel sheet is reduced, too. So the no-load loss and no-load current is reduced, which plays an important role in the energy saving [4].

At present, there are not many studies on the application of power electronic switches in transformer in our country [5]. Figure 2 is the structure of a power electronic switch, in which the commutation can be achieved through the solid state relay.

In Fig. 2, SCRa and SCRb are bidirectional thyristors; SSRa and SSRb are high power solid state relays. The switches' working principle is: assuming that the transformer is running at the high voltage winding position presented by X1, the SCRa is at the full state, the current path is X1, SCRa; SSRa, SSRb and SCRb are both at the state of disconnection. In order to guarantee the power supply quality of the secondary side during the voltage fluctuation of the system, the transformer is required to run at the position presented by X2 after the control system calculation and logical judgment. To start with, the SSRb should be triggered, and then the SCRa is switched off. The current path is changed to X2, SSRb, R. Finally the SCRb is triggered, and the current path is changed to X2, SCRb [6].

The power electronic switch discussed above has completely avoided the utilization of the mechanical and moving parts, the structure is simple, and it is convenient for application in the automatic control. Many advantages can be found when the switch is applied to the distribution transformers with voltage level of 35 kV and below.

Fig. 2 Power electronic switch by solid state relay

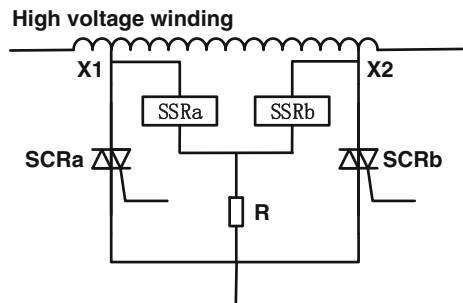
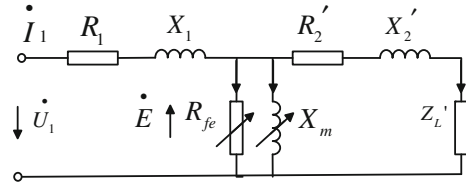


**Fig. 3** Transformer equivalent circuit



### 3 Circuit Model

Assuming the three phases of the transformer are in complete symmetry; the equivalent circuit of any phase is shown in Fig. 3.

In Fig. 3,  $R_1$  is the resistance of each phase winding on the primary side,  $X_1$  is the leakage impedance of each phase on the primary side, and  $R_{fe}$  is a equivalent resistance on behalf of iron loss of each phase of the core,  $X_m$  is the magnetic excitation reactance of each phase,  $R_2'$  is the resistance of each phase on the secondary side after reduction, and  $X_2'$  is the leakage reactance of each phase on the secondary side after reduction.

From Fig. 3, we can establish the following circuit equations.

$$\begin{cases} \dot{U}_1 = (R_1 + jX_1) \cdot \dot{I}_1 + (-\dot{E}) \\ \dot{I}_1 = \dot{I}' = \dot{I}_b + \dot{I}_o \\ -\dot{E} = (R_2' + jX_2') \cdot \dot{I}_2' + Z_L' \cdot \dot{I}_2' \\ -\dot{E} = R_{fe} \cdot \dot{I}_h = jX_m \cdot \dot{I}_o \end{cases} \quad (1)$$

According to the above equation and the basic parameters of the transformer, we can get characteristics of the transformer, and obtain the voltage and current of the transformer. Then the size of the transformer can be calculated.

### 4 System Simulation and Result Analysis

According to the working principle of the transformer, the simulation model of Simulink is shown in Fig. 4 [7]. The transformer starts running at large capacity, at 0.07 s, the load is reduced, and the transformer is adjusted to working at a small capacity. At 0.14 s, the load is increased; the transformer is adjusted to working at a large capacity. The waveforms of the voltage and current are shown in Fig. 5.

According to the waveforms in Fig. 5 we can know that: when the transformer is adjusted to working at a small capacity, the impact current of the high voltage side

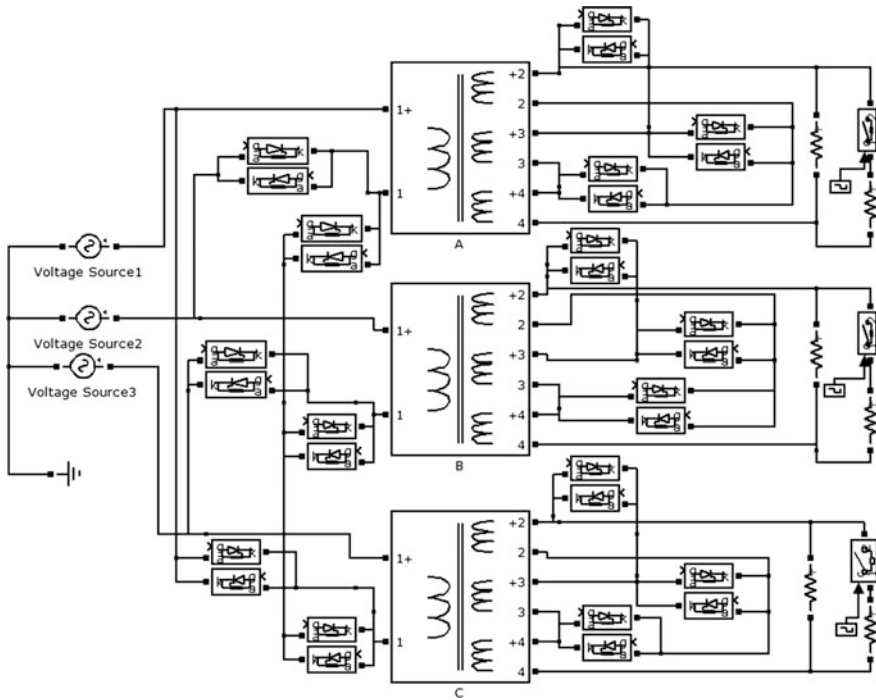
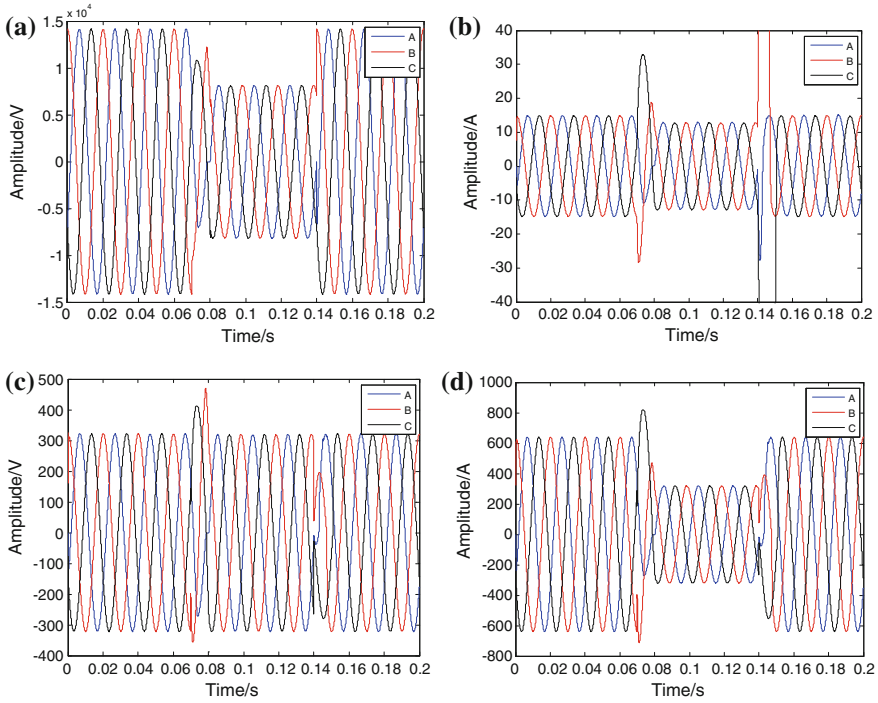


Fig. 4 Simulation model of arcless on-load capacity regulating transformer

is about two times of the normal current; when the transformer is adjusted to working at a large capacity, a very large impact current can be found on the high voltage side, and the impact current occurs only in two phases while no impact current can be found in the rest phase. By a comprehensive analysis, we know that, this phenomenon results from the application of the power electronic switches.

When the transformer capacity changes to follow the order of the control signals, one phase's current decreases to zero, the original thyristor is turned off, the new thyristor is turned on, and the winding connection is changed. However, the thyristors of the other two phases are still in the state of the conduction, the new thyristor has been switched on. Such an operation leaves the two phase windings in short circuit instantaneously and leads to a larger impact current [8]. Simulation shows that when the original thyristor is turned off, half a cycle's delay before the triggering of the new thyristor can significantly reduce the impact current of the high voltage side, but one phase will be in blackout for 1/3 to 1/2 cycles. Because the household electricity belongs to non-sensitive users, the blackout would have little influence on residential electricity [9].





**Fig. 5** Waveforms of the current and the voltage. **a** Voltage waveform in high voltage side. **b** Current waveform in high voltage side. **c** Voltage waveform in low voltage side. **d** Current waveform in low voltage side

## 5 Conclusion and Discussion

This paper analyzed the principle of reducing the loss of the regulated capacity transformer. One method about reduction of the impact current can be founded by model construction through the Simulink simulation and observation focused on the variation concerning voltage and current caused by the capacity regulation. Since load forecasting and other factors have not been taken into consideration in this system, the control precision needs to be improved and more researches on the load forecasting and control strategy should be held in further study.

**Acknowledgement** Supported by Shandong Science and Technology Development Plan (No: 13ny15)

## References

1. Shiyi L (2013) Discussion on the design of a load regulating transformer. *Sci Technol Vis* 31:91
2. Meng Z, Piao ZL (2013) Design of thyristor valve assembly in on-load automatic capacity regulating distribution transformer. *Appl Mech Mater* 325–326:417–423
3. Wang Y, Zhao T, Zhang L et al (2011) Intelligent control of on-load tap changer of transformer. In: 1st International conference on electric power equipment switching technology, vol 35(18), pp 98–102
4. Chen Y (1998) Principle and performance analysis of the power distribution transformer. *Transformer* 35(1):24–25
5. Huang J, Li X (2009) Non-inrush voltage regulating method for OL TC transformer based on power electronic technology. *Autom Electr Power Syst* 3(10):69–73
6. Wang J, Li J, Xu L (2006) Scheme of arcless on-load voltage regulation for distribution transformer using high power electronic switch. *Autom Electr Power Syst* 30(15):97–102
7. Wu T, Xie X (2004) MATLAB power system design and analysis. National Defence Industry Press, Beijing, pp 288–318
8. Wang J, Sheng W (2009) Simulation analysis of capacity regulating transformer. *Transformer* 46(7):19–23
9. Piao Z, Wang D, Zheng Y (2011) Simulation analysis of arcless on-load automatic capacity regulating for distribution transformer. *Trans Chin Soc Agric Eng* 27(2):224–229

# DC Fault Analysis and Protection Design in Shunt Modular Multilevel-Based MTDC System

Jian Wu, Yue Qi, Yanfei You and Dianguo Xu

**Abstract** Modular multilevel converters (MMC) are ideal next-generation multilevel converters well-suited for the high-voltage direct current (HVDC) transmission for multiterminal DC systems. However, the accidental DC faults in the cable or overhead lines, could give rise to safety concerns on transmission lines and converter stations. A protection design based on three-terminal voltage margin control method is proposed incorporating bypass thyristor and IGBT circuit breakers (IGBT-CBs) at DC side. In addition, IGBT-CBs isolate the DC line in case of a permanent fault utilizing the principle of handshaking method, making normal operation of the remaining system possible. This protection scheme is validated by the simulation studies on PSCAD/EMTDC, thereby demonstrating an improved DC fault reverse blocking capability of MMC-MTDC system.

**Keywords** DC fault · IGBT circuit breaker · MMC · MTDC · Voltage margin control

## 1 Introduction

Voltage-sourced converter (VSC) is currently one of the most dominant types of converters for HVDC transmission, as it offers fast dynamic response and independent power control [1–3]. In most occasions, it is the two-level and three-level neutral point clamped (NPC) converters that are employed in VSC-HVDC systems.

---

J. Wu (✉) · Y. Qi · Y. You · D. Xu  
Harbin Institute of Technology, Harbin 150001, China  
e-mail: wujianhit@163.com

Y. Qi  
e-mail: hitqiye@126.com

Y. You  
e-mail: yanfeihit@163.com

D. Xu  
e-mail: xudiang@hit.edu.cn

However, multilevel converters must be used to achieve a sinusoidal output voltage waveform at high voltage levels.

Contrary to cascaded H-bridge converter which has voltage drift phenomenon and cost high, MMC has a common DC-link, making itself a competitive candidate for the new power transmission and multiterminal HVDC transmission (MTDC) [4, 5]. MMC-MTDC has been a central issue for power transmission. However, DC-link faults, especially pole-to-pole fault, could cause DC voltage dips, leading to system consistency collapse, and are a major concern for the safety and consistency of MMC-MTDC system due to the control complexity of MTDC system [6].

A plethora of strategies have been proposed on the protection and maintenance of VSC-HVDC system. Some researchers made studies for the application of these strategies to the MMC-HVDC system. Protection strategies involve handshaking method, design of protective inductors, and full-bridge MMC with enhanced DC fault ride-through capability (DFRT) are also used on MMC-HVDC system [7–9]. But for MTDC system, due to the increase in the complexity of interstation coordination, research on DC fault protection is still exile.

The paper is structured as follows: Sect. 2 takes a closer look at the structure and control strategies of MMC-MTDC. Section 3 analyzes the procedure of the proposed protection strategy based on bypass thyristor and IGBT-CBs, as well as the process to rebuild the DC voltage and reload converter operation. Simulations of MMC-MTDC system on PSCAD/EMTDC are presented in Sect. 4 to demonstrate the system performance during both steady-state and DC fault conditions with the protection measures. Section 5 closes the paper with conclusion.

## 2 Principle of MMC-MTDC Under DC Fault

Three-terminal parallel-connected MTDC system based on half bridge MMC is shown in Fig. 1, which has a common DC-link capable of performing AC-to-DC and DC-to-AC power conversion. The  $V_{lP}$  ( $l = A, B, C$ ) are voltages of three-phase upper arm bridges, and  $V_{lN}$  ( $l = A, B, C$ ) are voltages of three-phase lower arm bridges.  $L$  is the arm bridge inductance, and  $V_{DC}$  and  $I_{DC}$  mean the DC voltage and DC current, respectively. The submodules (SM) could be switched in, inserted, bypassed, or blocked depending on the switching states of two IGBTs.

This paper uses parallel branch-type topology to give convenience to subgrid connection, as shown in Fig. 2. In order to maintain a promising performance of power transmission, the SM capacitor voltage in each arm has to be stable and balanced, which requires a hybrid averaging and balancing control and circulating current suppression. The averaging control enables the average voltage of all SM capacitors to follow the command value, whereas the balancing control is designed to maintain a balanced voltage for all the capacitors. To maintain a stable operation of the system, PI controller based on negative sequence double frequency characteristic of circulating current in  $d-q$  coordinate is used in each converter.

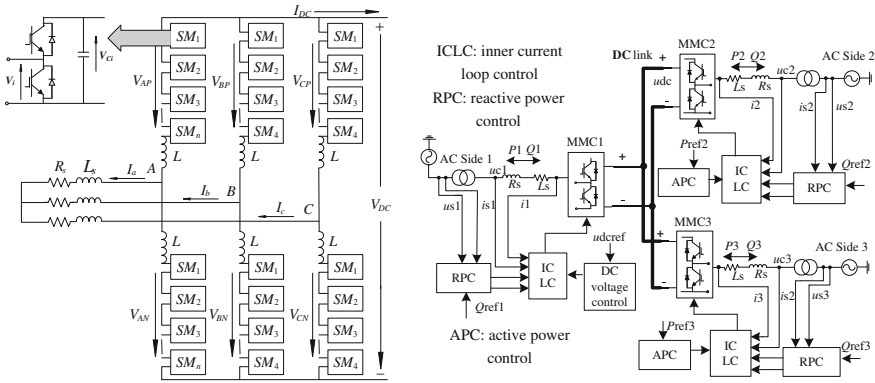


Fig. 1 Three-terminal MMC-MTDC system

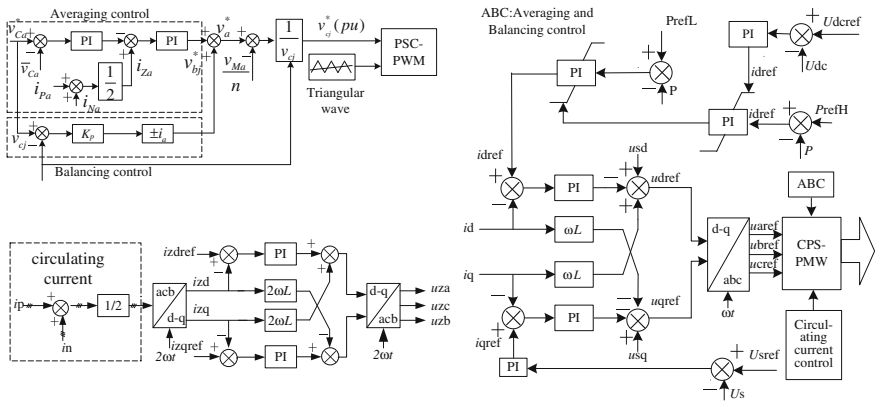


Fig. 2 Controller structure of converters

Direct current control strategy, also called vector control strategy, is applied for each converter station. The control strategy divides into inner current loop and outer voltage loop, which makes it suitable for high-power HVDC transmission. The inner current controller makes the current to track the reference current quickly. According to the control target of the converter station, outer controller can select active power or reactive power controller.

Direct current control comes from the mathematical models of multiterminal system under  $d-q$  coordinate by using Kirchhoff's law. After  $d-q$  transform of the differential equations,  $d$ -axis and  $q$ -axis reference value expression could be obtained as (1).

$$\begin{cases} u_{dref} = u_d + \omega Li_q - [k_{p1}(i_{dref} - i_d) + \int k_{i1}(i_{dref} - i_d)dt] \\ u_{qref} = u_q - \omega Li_d - [k_{p2}(i_{qref} - i_q) + \int k_{i2}(i_{qref} - i_q)dt] \end{cases} \quad (1)$$

The inner loop controller can be designed by (1) and the outer loop controller of each station has been marked in Fig. 1.

The  $u_{lref}$  is reference value of voltage. The  $i_{lref}$  ( $l = d, q$ ) is reference value of current. The  $u_l$  is measured value of voltage and current under  $d$ - $q$  coordinate. The  $i_l$  ( $l = d, q$ ) is measured value of voltage and current under  $d$ - $q$  coordinate. In order to make effective control of the three-station coordination, DC voltage margining control strategy is applied in outer controller, with upper communication and rapid coordination.

### 3 Protection Scheme

A hybrid protection scheme incorporating bypass thyristor and IGBT-CBs at DC side is demonstrated in Fig. 3. For parallel MTDC system, converter station running stably depends on maintaining a stable DC bus voltage. Once the DC voltage is out of control, all converter stations will be unable to maintain stable power and current and in turn cause the entire system out of control. Instantaneous DC voltage  $V_{dc}$  is detected throughout the operation and fault clearance procedures to determine the transition of three working states as shown in Fig. 4.

The overcurrent bearing capability of IGBTs is usually limited to around 2.5 p.u. for several milliseconds, hence the IGBTs should be blocked during DC fault for safety concerns, and thus large fault current would flow through the antiparalleled, freewheeling thyristor in each SM to withstand the overshooting current. Meanwhile, the signals for ac circuit breakers are also inhibited; demonstrating DC fault reverse blocking capability is blocked. By applying this strategy, the contribution of AC grid to the DC fault current is limited, which comprises only the SM capacitor discharging current at this time, with a much lower magnitude comparing with the former one with two currents combined. After the isolation of fault station,

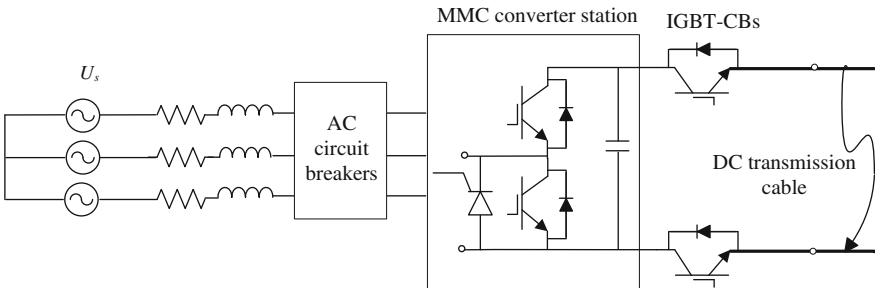
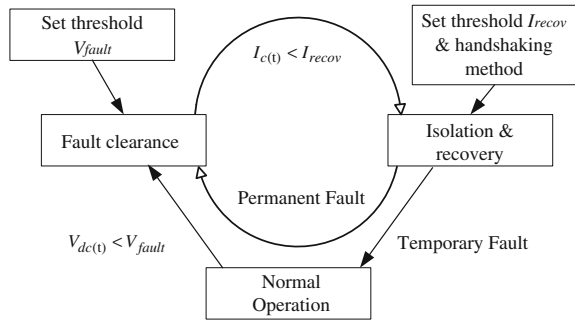


**Fig. 3** Protection scheme of dc pole-to-pole fault with H-bridge modules and IGBT-CBs

**Fig. 4** Switching state diagram of the proposed protection scheme



remaining system will restart and decides to switch master converter station or not by the identity of fault station.

For MTDC systems, the introduction of IGBT-CBs does favor to employ handshaking methods for locating and isolating DC faults by reaching a “healthy” hand to reclose IGBT-CBs after all the suspicious circuit breakers have been tripped. With the reclose of IGBT-CBs, the power transmission is resumed and the system returns to normal operation mode. Due to the topological characteristics of parallel-type MTDC system, the system is easy to return to normal working condition.

### 4 Simulation Results

The proposed strategy of bypass thyristor and IGBT-CBs has been proved by simulation studies performed on PSCAD/EMTDC model which is a three-terminal back-to-back MMC-MTDC, as shown in Fig. 1. Six IGBT-CBs are installed on the DC-link for isolating faulted lines. The simulation parameters are shown in Table 1. The MMC-1 as the master station, whereas the MMC-2 and MMC-3 as substations.

To verify the parameters this paper set is reasonable, the system starts to run under the steady normal operation mode. Under this mode, Fig. 5 demonstrates waveforms of MMC-MTDC system outputs. As shown in (a), DC voltage and DC current could be regulated as 9 kV. The active power and reactive power of three

**Table 1** Simulation parameters of three-terminal MMC-MTDC system

Quantity	Value	Quantity	Value
Nominal power of master station	2.5 MVA	Carrier frequency $f_c$	2 kHz
Number of SM per phase $n$	8	Rated frequency $f$	50 Hz
Grid voltage (line-to-line) $V_n$	3.5 kV	MMC submodule capacitance $C$	2.4 mF
AC inductance $L_s$	0.1 mH	DC voltage $V_{dc}$	9 kV
AC resistance $R_s$	10 mΩ	DC capacitor voltage command $V_{cl}^*$	2.25 kV
Arm inductance $L_a$	10 mH		

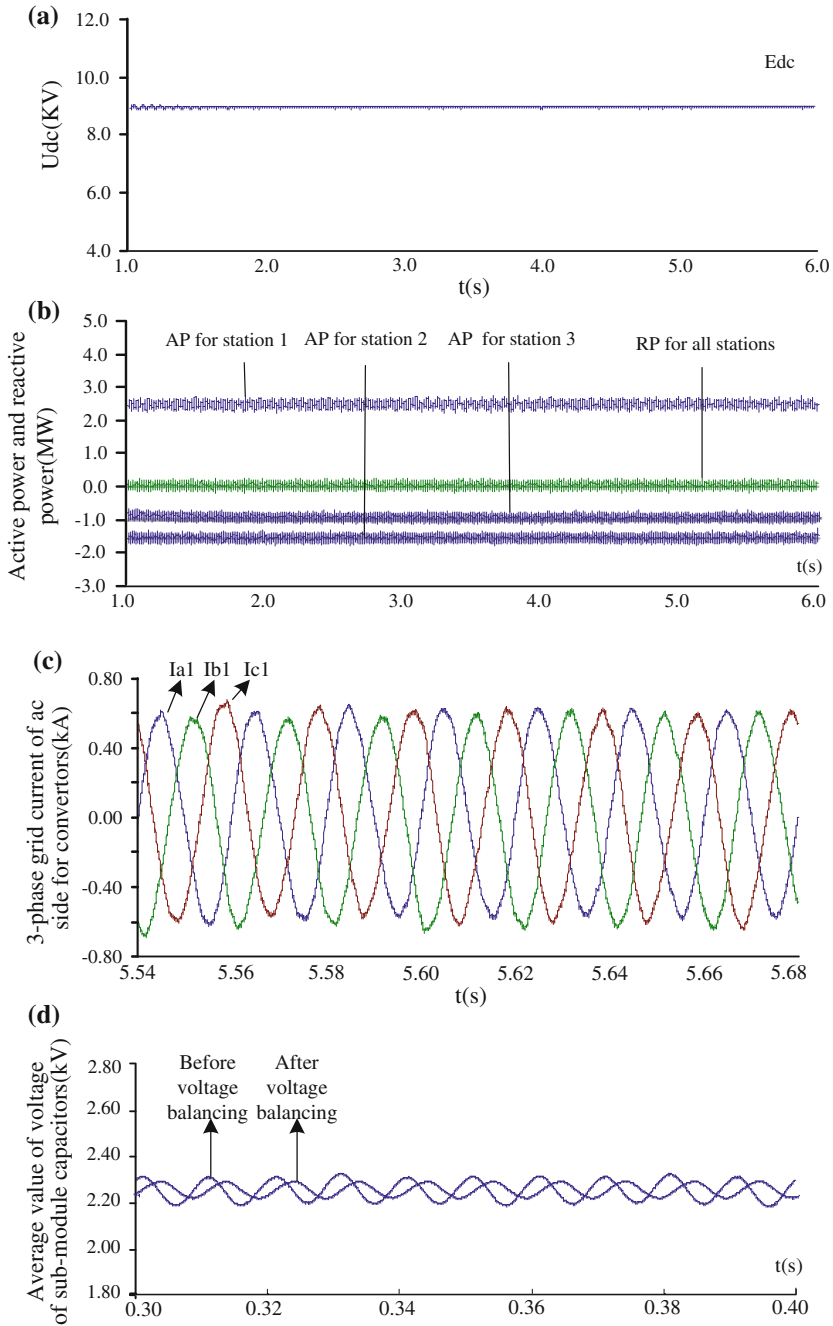
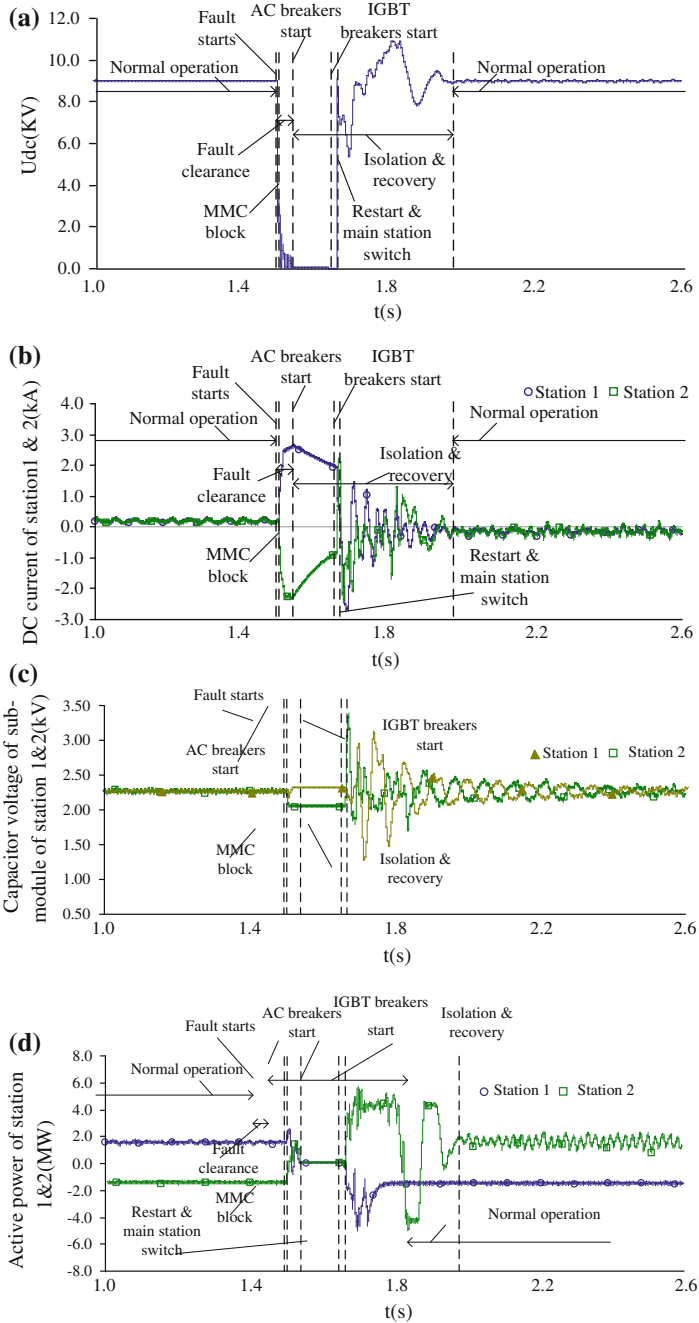


Fig. 5 Simulation results of MMC-MTDC system under normal operation mode





**Fig. 6** Simulation results of MMC-MTDC system under normal operation mode

stations are shown in (b), and reactive power of all station is close to zero. The peak value of ac current is around 600 A as shown in (c), whereas all the SM capacitor voltages before and after being averaged and balanced at the reference value of 2250 V are shown in (d). Fluctuations of SM capacitor voltage reduce by nearly 50 % by applying average and balance control. Under normal operation mode, DC voltage and power of every converter station are very stable, whereas fluctuations of output waveforms are very low, indicating an effective parameter selection.

Since this paper primarily studies the dynamic characteristics of the system concerning DC pole-to-pole fault and stability of parallel-type MTDC system depends on maintaining a stable DC voltage, therefore master station switching capability needs to be simulated. A DC pole-to-pole fault is introduced at  $t = 1.5$  s on station MMC-3 and after the fault is cleared, master station will switch from MMC-1 to MMC-2. Output parameters focus on MMC-1 and MMC-2 before and after DC pole-to-pole fault. Figure 6 illustrates the simulation results of three-terminal MMC-MTDC system under DC pole-to-pole fault with the proposed protection scheme.

The DC voltage quickly drops due to the fault, shown in (a), and the DC current suddenly experiences a severe surge, as shown in (b). Regarding the voltage threshold, the protection triggering voltage  $V_{\text{fault}}$  is set at 0.95 p.u.

When the DC voltage is under the threshold value, then all the gate signals for submodules are removed and submodules switch to bypassed condition, whereas SM capacitor voltage will remain unchanged until the system restarts as shown in (c). The protection changes to fault clearance procedure. After that the AC breaker will open, blocking the direct current path between AC and DC sides. When DC current drops below another threshold current  $I_{\text{rec}}$ , the IGBT-CBs are opened and ac breaker will reclose. When DC voltage is detected at both sides of the cables only between MMC-1 and MMC-2, indicating that the remaining system is still functional, the sub-module could restart and switch to inserted mode, leading the restart of the whole remaining system. Master station will change from MMC-1 to MMC-2 after the remaining system restarts, maintaining the DC voltage and providing power that substation needed, as shown in (d).

## 5 Conclusion

This paper reviews the research on DC fault clearance of MMC-HVDC, analyzed topology, and control strategy of three-terminal MMC-MTDC system. In addition, a hybrid protection scheme is also proposed incorporating bypass thyristor at ac side and IGBT-CBs at DC side. The bypass thyristor in the submodules would give the fault current a safe freewheeling channel, protecting SM and giving time for ac breakers to open to block the current path, and thus reduces the fault current in DC-links. IGBT-CBs are further implemented for the isolation of DC line. Simulations are carried out on PSCAD/EMTDC under both the normal and DC fault conditions, which suggest that the selected parameter based on the proposed

mathematical models is reasonable and functional. Implementation of such strategies of MMC-MTDC system enhances its dynamic performance on dc fault ride-through ability. Finally, the system is able to get back to normal operation mode with master station switching after fault clearance by reclosing IGBT-CBS and then rebuilds DC voltage and reloads power transmission under voltage margin control method.

**Acknowledgement** This paper and its related research are supported by grants from the Power Electronics Science and Education Development Program of Delta Environmental and Educational Foundation (DREM2014015) and the National Science Foundation of China (51407043).

## References

1. Flourentzou N, Agelidis VG, Demetriades GD (2009) VSC-based HVDC power transmission systems: an overview. *IEEE Trans Power Electron* 24(3):592–602
2. Anderson B, Xu L, Horton PJ, Cartwright P (2002) Topologies for VSC transmission. *Power Eng J* 16(3):142–150
3. Saeedifard M, Irvani R (2010) Dynamic performance of a modular multilevel back-to-back HVDC system. *IEEE Trans Power Del* 25(4):2903–2912
4. Peng FZ (2001) A generalized multilevel inverter topology with self voltage balancing. *IEEE Trans Ind Appl* 37(2):611–618
5. Xu L, Agelidis V (2005) VSC transmission system using flying capacitor multilevel converters and hybrid PWM control. *IEEE Trans Power Del* 22(1):427–434
6. Tang L, Ooi BT (2007) Locating and isolating dc faults in multiterminal DC systems. *IEEE Trans Power Del* 22(3):1877–1884
7. Deng F, Chen Z (2013) Design of protective inductors for HVDC transmission line within DC grid offshore wind farms. *IEEE Trans Power Del* 28(1):75–83
8. Tu Q, Xu Z, Xu L (2011) Reduced switching-frequency modulation and circulating current suppression for modular multilevel converters. *IEEE Trans Power Del* 26(3):2009–2017
9. Hagiwara M, Akagi H (2009) Control and experiment of pulse width modulated modular multilevel converters. *IEEE Trans Power Electron* 24(7):1737–1746

# The Simulation of Zero-Sequence Blocking Transformer (ZSBT)

Kai Xu, Zhi-zhen Liu, Xiao-dong Qu and Guo-zheng Qi

**Abstract** The problem of zero-sequence current in a three-phase four-wire distribution system is more and more serious. ZSBT is new zero-sequence current filter equipment. The existing literature is only a brief description about the structure and principle of ZSBT, there is no perfect design method. This paper proposes a design method of ZSBT. We build the 3D simulation model of ZSBT by Ansoft to analyze the parameters such as inductance, coupling factor, and flux density. The simulation results proved that the design method of ZSBT is feasible.

**Keywords** ZSBT · The design method · Ansoft simulation · Zero-sequence current filter

## 1 Introduction

In the three-phase four-wire distribution system, with the wide application of nonlinear load such as computer, LED lights, the zero-line current problem is more and more prominent. It makes transformer overheating, reducing efficiency.

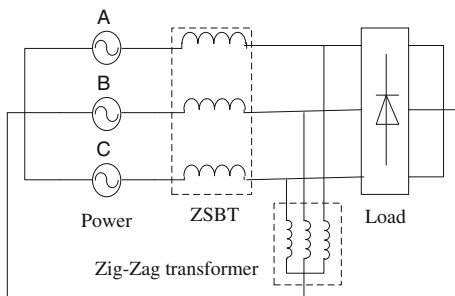
ZSBT was proposed in 2002 by Syafrudin [1]. It is mainly used for blocking the zero-sequence current flow into the system. After more than ten years of development, ZSBT in the zero-sequence current filtering technology is widely recognized. Literature [2] proposed an inhibition method of zero-sequence current by ZSBT and zigzag transformer; its structure is shown in Fig. 1.

Compared with literature [3], method of literature [2] does not need capacitance. Literature [4] introduced a simple structure and principle of ZSBT. There is no

---

K. Xu · Z. Liu (✉) · X. Qu · G. Qi  
College of Electrical Engineering, Shandong University, Jinan 250061, China  
e-mail: liuzhizhen@sdu.edu.cn

**Fig. 1** Zero-sequence filtering technology with ZSBT and zigzag transformer



literature that introduces design method of ZSBT. This paper proposes a design method of ZSBT. Through the analysis of ZSBT parameters by the simulation model, we prove that the design method is feasible.

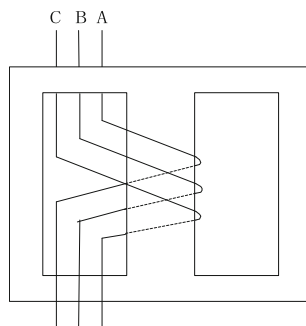
## 2 A Kind of Zero-Sequence Filtering Technology

This is a typical application of ZSBT in zero-sequence filtering technology, shown in Fig. 1. The current flowing through the zigzag transformer is only the zero-sequence; ZSBT only hinders the zero-sequence current. So, zero-sequence current flows through zigzag transformer instead of power without affecting the normal operation of system.

Structure of ZSBT is shown in Fig. 2. According to its structure, we can get coupling factor equal to 1 with the ideal case. It can also be expressed as

$$L_A = L_B = L_C = L = M \tag{1}$$

**Fig. 2** Structure of ZSBT



Ignoring the resistance, winding voltage equation is:

$$\begin{bmatrix} \dot{U}_A \\ \dot{U}_B \\ \dot{U}_C \end{bmatrix} = \begin{bmatrix} j\omega L_A & j\omega M & j\omega M \\ j\omega M & j\omega L_B & j\omega M \\ j\omega M & j\omega M & j\omega L_C \end{bmatrix} \cdot \begin{bmatrix} \dot{I}_A \\ \dot{I}_B \\ \dot{I}_C \end{bmatrix} \quad (2)$$

By applying (1) and (2), the voltage of ZSBT is

$$\dot{U} = \dot{U}_A = \dot{U}_B = \dot{U}_C = j\omega L (\dot{I}_A + \dot{I}_B + \dot{I}_C) \quad (3)$$

By the symmetrical component method [5], sum of three-phase currents  $i_A, i_B, i_C$  is three times as much as zero-sequence current  $i_0$ . So, Eq. (3) can also be expressed as

$$\dot{U} = j3\omega L \dot{I}_0 = j6\pi f L \dot{I}_0 \quad (4)$$

Equation (4) shows zero-sequence current that caused voltage drop of ZSBT. Positive-sequence and negative-sequence components of three-phase current cannot cause voltage drop of ZSBT.

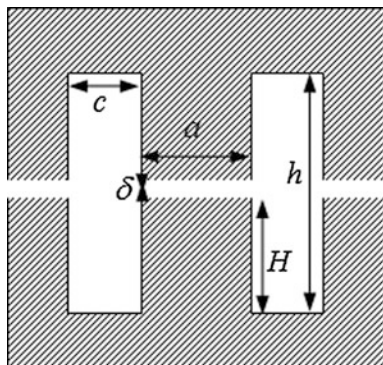
### 3 Design Method

For the convenience of description, label of core size is shown in Fig. 3.

We calculate core effective cross-sectional area  $S_F$ , winding circle number  $N$ , and cross-sectional area of wire  $\rho$  by classic methods in literature [5] and literature [6]. Air gap can maintain a constant inductance [7]. In order to ensure ZSBT with large overload capacity, magnetic flux density was selected as 0.45T. Each phase main inductance  $L_M$  approximately accounted for 85 % of the total inductance  $L$ . By applying Eq. (4), main inductance  $L_M$  is

$$L_M = 0.85L = \frac{0.85U}{6\pi f I_0} \quad (5)$$

Fig. 3 Core size of ZSBT



By applying magnetic Ohm's law [8], the magnetic circuit resistance  $R$  is

$$R = \frac{2\delta}{\mu S_q} \quad (6)$$

Coil inductance is proportional to the square of coil number of turns, and is inversely proportional to the magnetic circuit resistance [8]:

$$L_M = \frac{N^2}{R} \quad (7)$$

Replace air gap effective cross-sectional area  $S_q$  with iron core's. By applying (5), (6) and (7), calculated air gap is about

$$\delta^* = \frac{1.39I_0/N^2S_F}{U \times 10^7} \text{ cm} \quad (8)$$

Choose air gap  $\delta$  according to  $\delta^*$ , and calculate air gap width of the equivalent diffraction  $\varepsilon$ ,  $S_q$  [5]

$$\varepsilon = \frac{\delta}{\pi} \ln \left( \frac{H + \delta}{\delta} \right) \quad (9)$$

$$S_q = (a + 2\varepsilon) * (b + 2\varepsilon) \quad (10)$$

By applying (6), (7), calculated main inductance is:

$$L_c = \frac{\mu N^2 S_q}{2\delta} \times 10^{-2} \text{ H} = \frac{6.28N^2 S_q}{\delta \times 10^9} \text{ H} \quad (11)$$

If  $\Delta = \left| \frac{L_M - L_C}{L_M} \right| > 10\%$ , we need to recalculate main inductance  $L_C$  with different values of  $\delta$  until the requirement is met  $\Delta \leq 10\%$ .

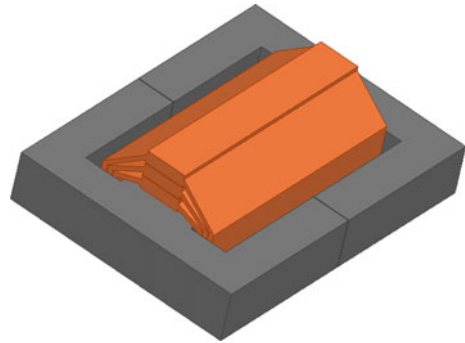
### 3.1 Simulation Model

According to the above methods, the ZSBT parameters can be calculated, shown in Table 1. Model of ZSBT was established, shown in Fig. 4.

**Table 1** Parameters of ZSBT

Core choose silicon steel sheet of 35W270 of E76-228 type								
$a$	$c$	$b$	$H$	$h$	$N$	$q$	$\delta$	$L_C$
76 mm	38 mm	50 mm	114 mm	228 mm	5 turns	180 mm <sup>2</sup>	0.8 mm	$8.10 \times 10^{-5} \text{ H}$

**Fig. 4** 3D model of ZSBT



### 4 Analysis of Winding Inductance and Coupling Factor

Coupling factor reflects the degree of a winding magnetic coupling. When it is close to 1, magnetic coupling is strong and mutual inductance is close to self-inductance. By Eq. (2), we concluded the influence of winding inductance and coupling factor on the voltage of ZSBT.

In the static field of Ansoft, we analyze the model of ZSBT that number of winding is set to a turn. Because the number of turns does not affect coupling factor. If the number of turns is different but the structure is the same, ZSBT will have the same coupling factor. So, the coupling factor of ZSBT is greater than 0.995, shown in Table 2. Coupling factor is large enough to meet the requirements. The inductance matrix is shown in Table 3. By Eq. (7), the inductance of the windings A, B, and C, respectively, is 0.08030, 0.08031, and 0.008033 mH. Meet the requirement:  $\Delta \leq 10\%$ .

**Table 2** The coupling factor matrix

	A	B	C
A	1	0.99855	0.99646
B	0.99855	1	0.99841
C	0.99646	0.99841	1

**Table 3** Winding inductance matrix

	A	B	C
A	0.003212	0.0032076	0.0032013
B	0.0032076	0.0032125	0.0032078
C	0.0032013	0.0032078	0.0032133



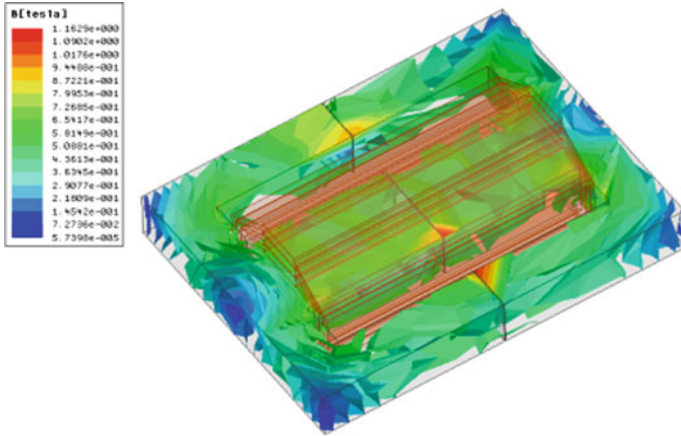


Fig. 5 Flux density distribution

### 4.1 Analysis of the Flux Density Distribution and Voltage

In the transient field of Ansoft, we analyze flux density distribution and voltage. Winding bubbled into 505A (including 20A of zero-sequence component) of three-phase alternating current. When instantaneous value of zero-sequence component is the largest, flux density distribution is shown in Fig. 5. The flux density of core column is about 0.7 T. We can get the average magnetic  $B = \frac{0.7 \times 2}{\pi} = 0.446$  T. Error of flux density is within the scope of the permit.

ZSBT voltage drop is produced by zero-sequence component of current. So winding induced voltage is the same, shown in Fig. 6. Induction voltage RMS of windings A, B, and C, respectively, is 1.796, 1.775, and 1.758 V. Meet requirement of the design:  $\Delta U \leq 10\%$ .

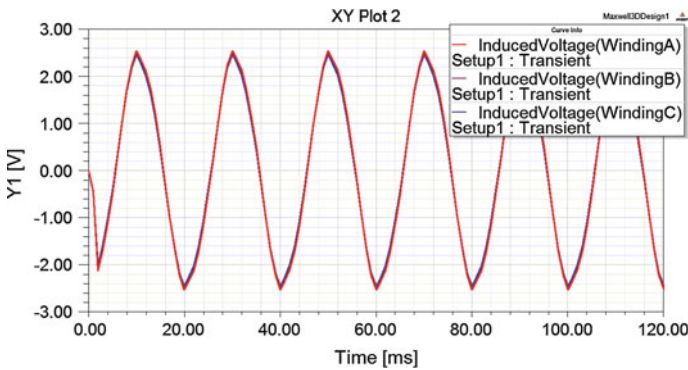


Fig. 6 Winding-induced voltage

**Acknowledgement** Supported by Shandong science and technology development plan (No. 13ny15).

## References

1. Syafrudin M, Hadzer CM, Sutanto J (2002) Zero-sequence harmonics current minimization using zero-blocking. Transformer Shunt LC Passive Filter. *IEEE Trans Ind Appl* 2(2):116–120
2. Song Q, Yin Z, Xue J, Zhou L (2008) Zero-sequence harmonics current minimization using zero-blocking reactor and zig-zag transformer. *IEEE Trans Ind Appl* 8(13):1758–1764
3. Fu X, Zhao M, Yao G (2011) A new type of neutral current suppression method research. *Build Electr* 11(30):62–66
4. Laka A, Barrena JA, Chivite-Zabalza J, Gorka C (2013) Novel zero-sequence blocking transformer (ZSBT) using three single-phase transformers. *IEEE Trans Energy Convers* 7 (18):234–242
5. Cui L (1995) Special transformer theory and design. Scientific and Technical Documents Publishing House, Beijing, pp 917–922
6. Fang D (2004) Transformer quick fast manual. China Water & Power Press, Beijing, pp 366–367, 375–376
7. Yu Y, Li X, Ge D (2014) Core reactor of the particularity of magnetic flux leakage and magnetic flux leakage loss. *Shandong Ind Techol* 15:90–91
8. Wang X (2009) Electrical machinery. China Machine Press, Beijing, pp 2–15, 63–64

# Design and Simulation of a Vivaldi Antenna Fed by Coplanar Waveguide

Lizhong Song, Weiwei Yin and Jia Li

**Abstract** This paper designed a Vivaldi antenna fed by coplanar waveguide (CPW) with band width. The designed antenna had simple structure, which was easy to fabricate. The discussed Vivaldi antenna in this paper was simulated by using the full-wave electromagnetic simulation software, and the specific simulation results were provided. The average voltage standing wave ratio (VSWR) was 2 within the frequency range of 2 to 6 GHz. The simulated axial ratio (AR) at the boresight direction within the working frequency range was higher than 20 dB. The wide beams and steady gains were also observed in accordance with the simulation results. The design and simulation results of Vivaldi antenna fed by CPW in this paper can provide a reference for the practical engineering application.

**Keywords** Vivaldi antenna · Wide band antenna · CPW · VSWR

## 1 Introduction

The ultra wide band (UBW) antennas were used in many cases such as UWB radar, and communication systems. The Vivaldi antenna was a kind of common wide band antenna, which has simple structure and good radiation performances including high gain, wide beam, and wide frequency band [1–5]. The Vivaldi antenna is a traveling-wave endfire planar antenna [6–8], which can be used in some particular cases such as the guidance radar on the missiles. By now, the Vivaldi antennas are still one of the research hotspots in antenna research field. For the design of Vivaldi antenna, the feeding structure was very important because it has great effect on the antenna radiation performances. The microstrip–slot line balun is usually employed in Vivaldi antenna design [9, 10]. Another feed method is that the coaxial cable was directly used to feed the Vivaldi antenna [11]. The

---

L. Song (✉) · W. Yin · J. Li

School of Information and Electrical Engineering, Harbin Institute of Technology,  
Weihai, Shandong 264209, People's Republic of China  
e-mail: songlizhong@hitwh.edu.cn

© Springer-Verlag Berlin Heidelberg 2016

B. Huang and Y. Yao (eds.), *Proceedings of the 5th International Conference on Electrical Engineering and Automatic Control*, Lecture Notes in Electrical Engineering 367, DOI 10.1007/978-3-662-48768-6\_11

coplanar waveguide (CPW) is an important kind of planar microwave transmission line, and its advantages include low loss, low dispersion, and convenience of connection with other microwave devices. It is convenient to feed the Vivaldi through CPW [12]. This paper discussed and simulated the traditional Vivaldi antenna fed by CPW. The antenna structure and parameters of the design were depicted and the simulation results of radiation performances were also provided. The simulation results revealed that it is an effective method to feed the Vivaldi antenna through CPW. The research result can provide a technical reference for some relative Vivaldi antenna design.

## 2 Geometry and Design of the Vivaldi Antenna Fed by CPW

The Vivaldi antenna model designed in this paper was shown in Fig. 1. The thickness of dielectric substrate was 1 mm and the relative dielectric permittivity was 2.2. The thickness of copper foil was 0.036 mm. The input port was CPW line, and the incident electromagnetic wave with wide band was radiated through tapered slot. For the frequency range of 2–6 GHz, the parameter design was carried out through full-wave electromagnetic simulation software. The designed Vivaldi antenna dimensions were shown in Fig. 2. The width of center conductor strip of CPW was  $w$ , the gap between center conductor strip and the metal ground at the sides was  $s$ , the effective dielectric permittivity  $\epsilon_{\text{eff}}$  and the characteristic impedance  $Z_{e0}$  can be expressed as the formula (1) and (2).

$$\epsilon_{\text{eff}} = \frac{C(\epsilon_r)}{C(\epsilon_r = 1)} \quad (1)$$

**Fig. 1** The simulation model of the discussed Vivaldi antenna fed by CPW

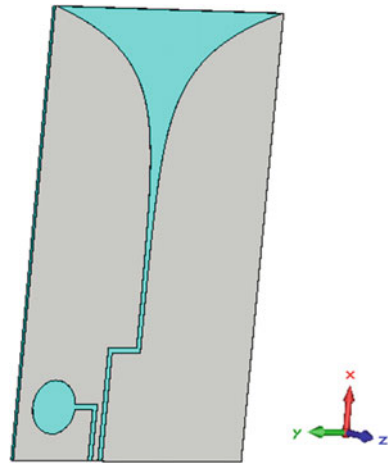
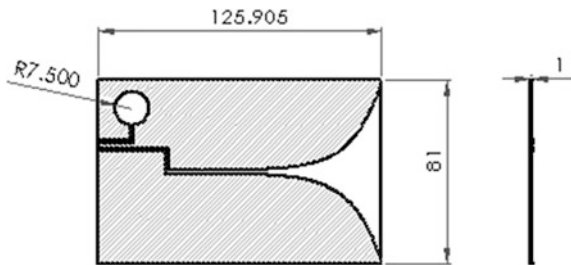


**Fig. 2** The structure and dimension of designed Vivaldi antenna fed by CPW



$$Z_{e0} = \sqrt{\frac{L}{C}} = \frac{\sqrt{LC}}{C} = \frac{\sqrt{\mu\epsilon}}{C} = \frac{\sqrt{\epsilon_{\text{eff}}\mu_0\epsilon_0}}{C} \quad (2)$$

where  $C$  is the unit capacitor of transmission line,  $C(\epsilon_r)$  is the unit capacitor when the space is filled up with dielectric material, and  $C(\epsilon_r = 1)$  is the unit capacitor when the space is filled up with air. In simulation, the parameters  $w$ ,  $s$ , and the radius  $R$  of the circular cavity were adjusted to match the input impedance of taper slot antenna. In this model,  $w$ ,  $s$ , and  $R$  were determined through software simulation, here  $R = 7.5$  mm,  $w = 2$  mm, and  $s = 1.5$  mm.

For the Vivaldi antenna, one of the curvatures of tapered slot follows the exponential function expressed as formula (3).

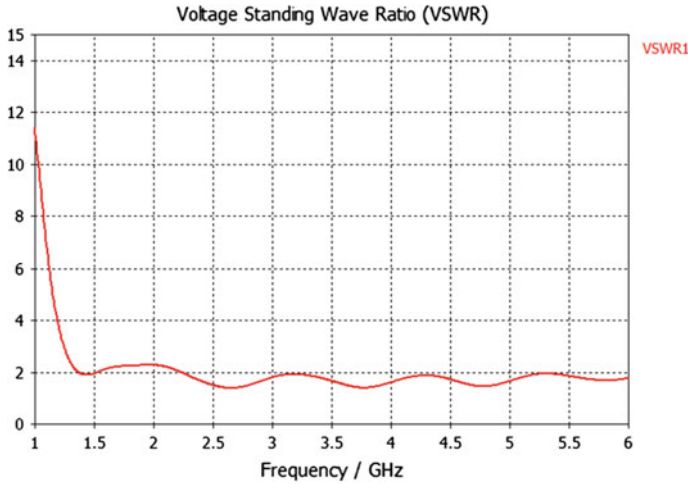
$$y = Ae^{rx} + B \quad (3)$$

where  $A$ ,  $B$ , and  $r$  were the constants which determined the size and shape of the Vivaldi antenna. In this section,  $r = 0.08$ , and the length and the width of whole antenna were 125.905 and 81 mm, respectively.

### 3 Simulation Results of the Vivaldi Antenna Fed by CPW

The designed Vivaldi antenna fed by CPW was simulated and optimized by using CST. The specific simulation results were shown in this section. Figure 3 was the simulated VSWR of the designed Vivaldi antenna. The average VSWR was about 2 within the frequency range between 1.4 and 6 GHz. In fact, the VSWR of the Vivaldi was approximately less than 2 within the operational frequency range of 2–6 GHz. When the frequency increased, the VSWR became lower. The VSWR of the designed Vivaldi fed by CPW revealed the steady performances.

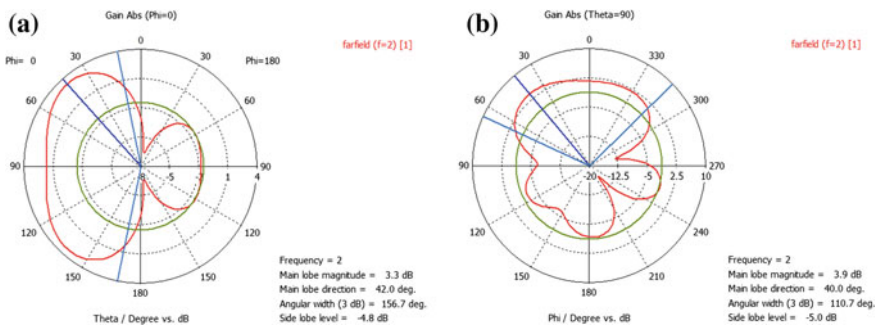
In this section, the radiation patterns of the designed Vivaldi antenna fed by CPW were provided and analyzed. The operational frequency range was from 2 to 6 GHz. Here, the simulation results of the radiation patterns at three typical frequencies were provided to reveal the radiation performances of the designed Vivaldi antenna. The simulated results of radiation patterns at 2 GHz were shown in Fig. 4.



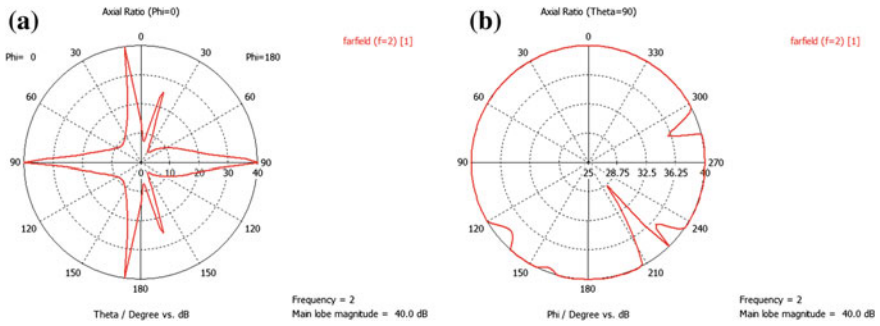
**Fig. 3** The simulated VSWR of the designed Vivaldi antenna fed by CPW

Figure 4a, b were the gain patterns at  $xoz$  plane and  $xoy$  plane, respectively. The half power beam widths at  $xoz$  plane and  $yoZ$  plane were  $156.7^\circ$  and  $110.7^\circ$ , respectively. Figure 5a, b were the axial ratio (AR) patterns at  $xoz$  plane and  $xoy$  plane, respectively, and the observed AR at the boresight direction for the frequency of 2 GHz was higher than 40 dB, so the linearly polarized radiation performance was obtained.

The simulated results of radiation gain patterns at 4 GHz were shown in Fig. 6. The half power beam widths at  $xoz$  plane and  $yoZ$  plane were  $141.5^\circ$  and  $85.2^\circ$ , respectively. Figure 7a, b were the axial ratio (AR) patterns at  $xoz$  plane and  $xoy$  plane, respectively, and the observed AR at the boresight direction for the frequency of 4 GHz was about higher 40 dB, which also indicated the Vivaldi antenna radiates linearly polarized electromagnetic wave at 2 GHz.



**Fig. 4** The simulated results of gain patterns at 2 GHz. **a** Pattern at  $xoz$  plane, **b** pattern at  $xoy$  plane



**Fig. 5** The simulated results of AR patterns at 2 GHz. **a** AR pattern at  $xoz$  plane. **b** AR pattern at  $xoy$  plane

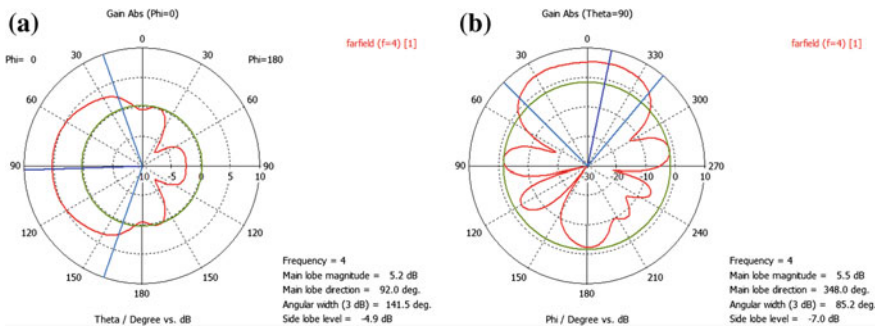


**Fig. 6** The simulated results of radiation gain patterns at 4 GHz. **a** Gain pattern at  $xoz$  plane. **b** Gain pattern at  $yoz$  plane

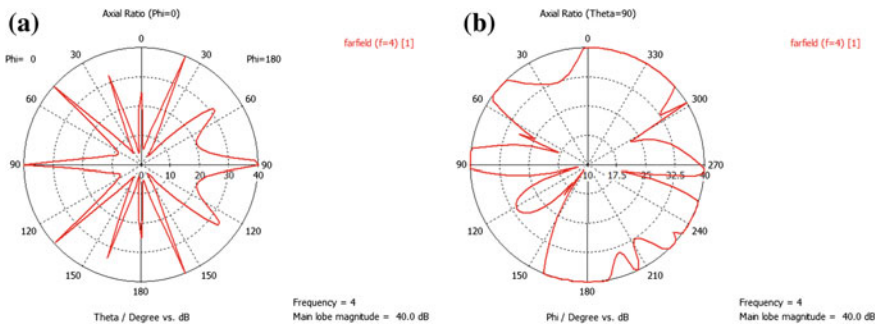


**Fig. 7** The simulated results of AR patterns at 4 GHz. **a** AR pattern at  $xoz$  plane. **b** AR pattern at  $xoy$  plane

The simulated results of radiation gain patterns at 6 GHz were shown in Fig. 8. The half power beam widths at  $xoz$  plane and  $yo z$  plane were  $126.1^\circ$  and  $73.1^\circ$ , respectively. Figure 8a, b were the axial ratio (AR) patterns at  $xoz$  plane and  $xoy$  plane, respectively, and the observed AR at the boresight direction for the frequency of 6 GHz was higher than 5 dB, which revealed that the AR decreased when the frequency increased for the designed Vivaldi antenna fed by CPW (Fig. 9).

The gain simulation results of designed Vivaldi antenna were shown in Fig. 10. According to simulation results, the observed gains and radiation patterns were steady for the frequency range from 2 to 6 GHz. When the frequency increased, the radiation gains approximately increased. The gains were higher than 3 dB within the operational frequency range of 2–6 GHz.

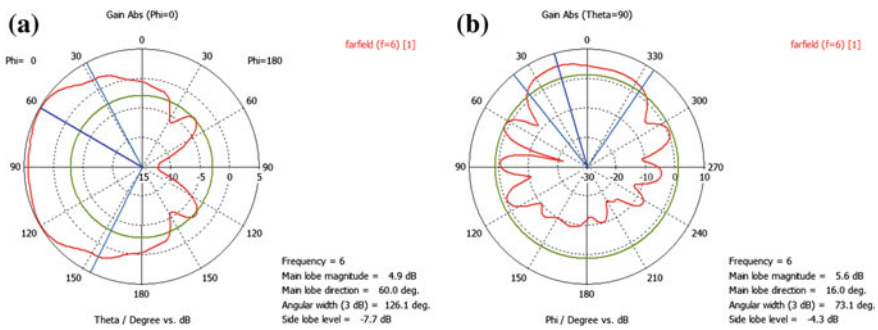


**Fig. 8** The simulated results of radiation gain patterns at 6 GHz. **a** Gain pattern at  $xoz$  plane. **b** Gain pattern at  $xoy$  plane

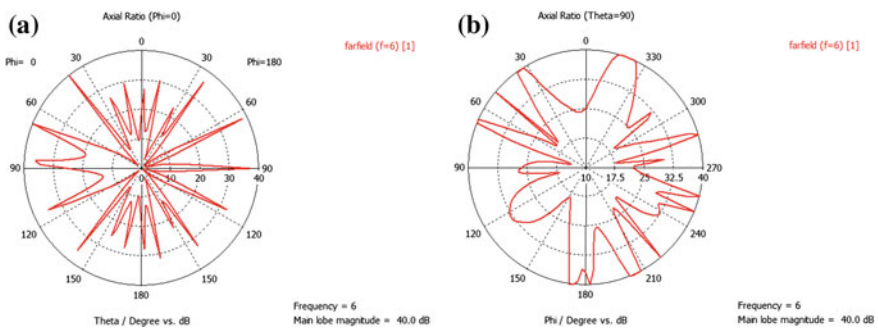


**Fig. 9** The simulated results of AR patterns at 6 GHz. **a** AR pattern at  $xoz$  plane. **b** AR pattern at  $xoy$  plane



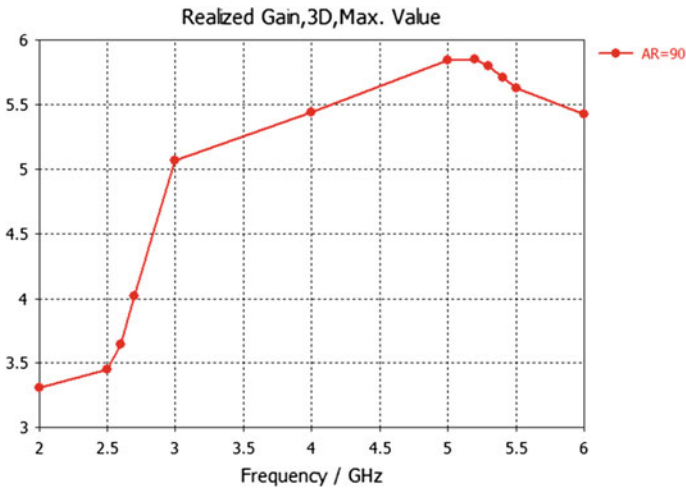


**Fig. 10** The gain simulation results of designed Vivaldi antenna

## 4 Conclusions

A wide band Vivaldi antenna fed by CPW was designed and simulated by using the electromagnetic simulation software in this paper. The designed Vivaldi antenna has simple structure and is low cost. Within the frequency range of 2–6 GHz, the designed Vivaldi antenna had acceptable VSWR and patterns according to the simulation results. The radiation performances of the designed Vivaldi antenna within the operational frequency range were provided. The CPW feeding structure of Vivaldi can be a candidate method for the design of wide band Vivaldi antenna at several practical applications.

**Acknowledgements** The research work was supported by the National Natural Science Foundation of China (61171181), the Science Foundation of Aeronautics of China (Grant No. 20131837001) and the Astronautical Supporting Technology Foundation of China (2013-HT-HGD06).

## References

1. He SH, Shan W, Fan C, Mo ZC, Yang FH, Chen JH (2004) An improved Vivaldi antenna for vehicular wireless communication systems. *IEEE Antennas Wirel Propag Lett* 13:1505–1508
2. Hamid MR, Peter G, Hall PS, Ghanem F (2011) Switched-band Vivaldi antenna. *IEEE Trans Antennas Propag* 59(5):1472–1480
3. Bourqui J, Okoniewski M, Fear EC (2010) Balanced antipodal Vivaldi antenna with dielectric director for near-field microwave imaging. *IEEE Trans Antennas Propag* 58(7):2318–2326
4. Congedo F, Monti G, Tarricone L, Bella V (2013) A 2.45-GHz Vivaldi rectenna for the remote activation of an end device radio node. *IEEE Sens J* 13(9):3454–3461

5. Bai J, Shi S, Prather DW (2011) Modified compact antipodal Vivaldi antenna for 4–50 GHz UWB application. *IEEE Trans Microw Theory Tech* 59(4):1051–1057
6. Wang P, Wen G, Zhang H, Sun Y (2013) A wideband conformal end-fire antenna array mounted on a large conducting cylinder. *IEEE Trans Antennas Propag* 61(9):4857–4861
7. Ludlow P, Fusco VF (2011) Antipodal Vivaldi antenna with tuneable band rejection capability. *IET Microwaves Antennas Propag* 5(3):372–378
8. Fei P, Jiao Y-C, Wei H, Zhang F-S (2011) A Miniaturized antipodal Vivaldi antenna with improved radiation characteristics. *IEEE Antennas Wirel Propag Lett* 10:127–130
9. Wu J, Zhao Z, Nie Z, Liu Q-H (2014) A printed UWB Vivaldi antenna using stepped connection structure between slotline and tapered patches. *IEEE Antennas Wirel Propag Lett* 13:698–701
10. Kasturi S, Schaubert DH (2006) Effect of dielectric permittivity on infinite arrays of single-polarized Vivaldi antennas. *IEEE Trans Antennas Propag* 54(2):351–358
11. Hu J, Chen H, Zhu R (2015) An antenna element for compact wide-band phased array. *Mod Radar* 37(1):52–55
12. Taringou F, Dousset D, Bornemann J, Wu K (2013) Broadband CPW feed for millimeter-wave SIW-based antipodal linearly tapered slot antennas. *IEEE Trans Antennas Propag* 61(4):1756–1762

# The PID Parameters Optimization Method Based on GA for NC Power Supply

Chenjia Wei, Zehao Liu, Peizheng Li, Jianfei Chen and Sheng Zhang

**Abstract** In the design of numerical control voltage source, the PID control parameters are usually determined by theoretical arithmetic or engineering setting method, which have some problems such as complex calculation, high demand experience, and low accuracy. This paper offers an intelligent optimization method with PID parameters  $k_p$  based on genetic algorithm. In terms of this optimization method, we design a PID parameter optimization system which consists of a microcontroller module, a host computer, and a LM2596 module. The microcontroller samples the output voltage, and receives the  $k_p$  parameters to set the LM2596 module. The host computer processes the real-time voltage value and evaluates the PID parameter based on ITAE. Meanwhile, optimal  $k_p$  parameters are generated by the genetic algorithm. The experimental results show that the mean value of ITAE reduces in the process of genetic algorithm, reflecting the fact that PID control effect is improved obviously and the parameters are becoming optimal. According to the test of full range  $k_p$  and ITAE table, we can conclude that  $k_p$  set by the genetic algorithm is superior to  $k_p$  set by Ziegler–Nichols (Z–N) method which is the optimal solution in the full scale. This paper is of instructive value in the field of setting parameters of PID control system.

**Keywords** PID · Parameter self-tuning · GA · ITAE

## 1 Introduction

Due to the fast response, high precision, and steady output, the numerical control power supply with PID control is widely used [1, 2]. However, how to set precise PID control parameters for getting efficient and steady output is an important research topic in the practical application. Nowadays, there are two main types of

---

C. Wei · Z. Liu · P. Li · J. Chen · S. Zhang (✉)  
Nanjing University of Post and Telecommunications, 210000 Nanjing, China  
e-mail: B12030536@njupt.edu.cn

methods for determining PID parameters: theoretical calculation setting method and engineering setting method, including Ziegler–Nichols (Z–N) method, indirect optimization method, and so on. Recently, utilizing intelligent algorithms including genetic algorithm to set PID parameters has been a new research issue [3, 4]. This paper applies the genetic algorithm into the optimization of numerical control voltage source PID parameter. We design a PID parameter optimization system which consists of a microcontroller module, a host computer, and a LM2596 module. Then, we prove the effectiveness of this algorithm by theoretical derivation and experimental verification. This paper also has important reference value when it comes to some other ways to set PID control parameters.

## 2 Methodology

### 2.1 The Numerical Control Power Supply System

This design is depended on LM2596 power converter and the adjustable output application circuit in its datasheet which is shown in Fig. 1.

The output voltage calculation formula is:

$$U_{\text{out}} = V_{\text{ref}} \cdot \left( 1 + \frac{R_2}{R_1} \right), \quad V_{\text{ref}} = 1.23 \text{ V} \quad (1)$$

where  $R_2$  is the variable resistor which controls the output voltage according to Eq. (1). In this paper, we replace  $R_2$  with digital potentiometer (AD5272) and adjust digital potentiometer to realize the adjustment of system output voltage.

### 2.2 Digital PID Controller

The fundamental idea of digital PID controller is to compare the measured and the reference values then correct the proportional coefficient  $k_p$ , integral coefficient  $k_i$ ,

**Fig. 1** Typical application of LM2596

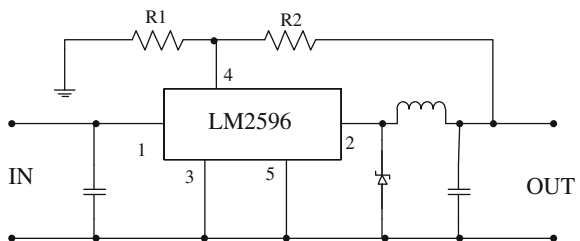




Fig. 2 System block diagram

and differential coefficient  $k_d$  to get the presupposed output value. The control laws are shown as Eq. (2).

$$u[k] = k_p \cdot \text{err}[k] + k_i \cdot \sum_n \text{err}[n] + k_d \cdot (\text{err}[k] - \text{err}[k - 1]) \quad (2)$$

where  $k$  is sampling sequence number,  $u[k]$  is the output of controller at sampling time  $k$ , and  $\text{err}[k]$  is the deviation at the sampling time  $k$ .

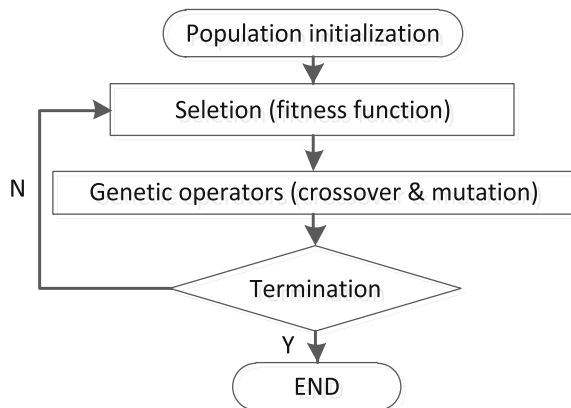
In this paper, the values of  $k_i$  and  $k_d$  are set to 1 and 0.2 according to experience. The value  $k_p$  is selected by the proposed optimization system. The system block diagram is shown in Fig. 2. The microcontroller samples the output voltage and sends it to host computer. The host computer processes the voltage value and realizes PID control. The microcontroller receives the output of PID controller so as to adapt the NC power supply.

### 2.3 PID Parameter Tuning Using GA

Genetic algorithm (GA) is a randomly global optimization search method [5], and the flow chart of GA is shown in Fig. 3.

In order to operate GA in this system, the parameters are encoded by binary code. The fitness function  $J$  adopts integral of time-weighted absolute value of the error (ITAE) which is shown as Eq. (3).

Fig. 3 Flow chart of GA



$$J = \sum_k k \cdot \text{err}[k] \quad (3)$$

In this paper, the value of ITAE is set by 1200 sampling voltage within 0.5 s after setting the parameter. Genetic operators include crossover and mutation. The crossover probability is set by ITAE and mutation probability is set by experience [6–8]. According to the bit weight characteristics of binary code, the ‘parent’ parameter will be divided into two equal lengths. The ‘child’ parameter is crossed by the head part of parameter which has higher crossover probability and the tail part of parameter which has less crossover probability. The mutation operation follows the principle of bit-flip which is based on setting probability.

#### 2.4 *The Implementation of PID Parameter Tuning by Using GA*

The system block diagram of the proposed PID parameter tuning system is shown in Fig. 2 and the flow chart of core optimization method (GA) is shown in Fig. 3. The concrete operations are listed as follows.

**Population initialization and encoding:** The host computer sets the output voltage and calculates the digital potentiometer according to Eq. (1). The value of potentiometer will be downloaded into a microcontroller to set the LM2596 NC power supply. Meanwhile, the initial generation of ‘parent’  $k_p$  parameter is generated randomly by the host computer. The digital potentiometer used in this system is 256-position. Thus, the value of  $k_p$  is set between 0 and 255 in this paper, corresponding to the 0–100 % range of  $k_p$  in Eq. (2).

**Dynamic adjustment of digital potentiometer using PID controller:** After setting the initial value of potentiometer, microcontroller samples then uploads the output voltage to the host computer. The host computer calls  $k_p$  parameters then calculates the value of potentiometer and downloads it to the microcontroller in order to adjust to the output value.

**Calculate the fitness function:** In order to calculate the fitness of the  $k_p$  parameter, this paper utilizes 1200 response voltage values to calculate ITAE value in Eq. (3). Then we will ergodic all the  $k_p$  parameters in the current generation and calculate the corresponding ITAE value.

**Genetic operator:** On the basis of the ITAE value of each ‘parent’  $k_p$  parameter, we can encode the  $k_p$  value and operate the crossover and mutation so as to generate the ‘child’ generation. Then, we will decode the ‘child’ generation and update the PID equation.

**Termination:** This generational process repeats until the termination condition has been reached. In this paper, the condition is set as that the mean ITAE value of the current generation is less than 4000.

### 3 Data

Experimental equipment: regulated power supply, host computer with MATLAB, MSP430 microcontroller, and LM2596 NC power supply.

Experimental conditions: input 9 V, initial output 3 V, setting output 5 V, load current 200 mA.

Tuning parameter:  $k_p$ .

#### 3.1 Full Range $k_p$ and Corresponding ITAE

Full range  $k_p$  and corresponding ITAE are tested in the experiment and the corresponding relation is shown in Fig. 4.

As shown in the Fig. 4, we can notice that the optimal  $k_p$  parameter value may be located within 3 interval: (35, 45), (80, 90), and (155, 175), and the global optimum may be located within 155 and 175.

#### 3.2 Parameter Tuning Based on Ziegler–Nichols Method

We utilize the Z–N method to tune the parameter and find that the optimal  $k_p$  value is 37. The corresponding ITAE value is 9563. The system response is shown in Fig. 5.

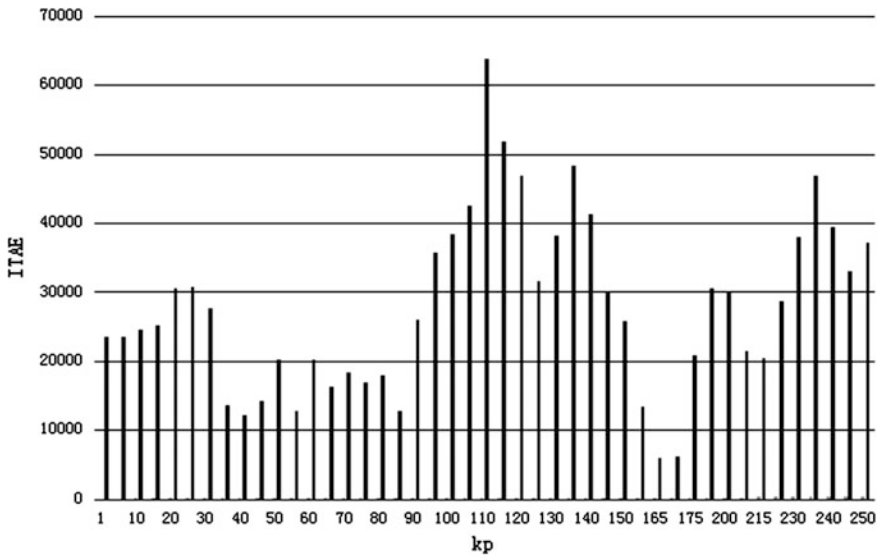
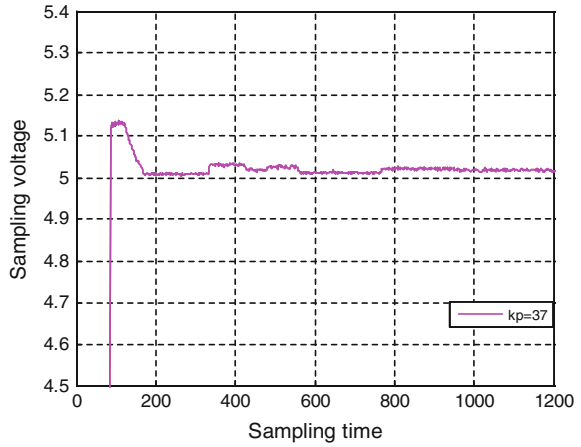


Fig. 4 Full range  $k_p$  and corresponding ITAE

**Fig. 5** System response of  $k_p$  parameter tuning by Z-N method



### 3.3 Generations of $k_p$ Parameter Tuned by GA and Corresponding ITAE Value

Table 1 and Fig. 6 show the mean ITAE value of each generation in GA optimization. According to the experiment, the optimal parameter value is 171 and corresponding ITEA value is 1517.

In the process of genetic algorithm, the mean value of ITEA is decreasing with the increase of generation. After 13 generations, the mean value decreased from 41,412.98 to 3696. It turns out that the genetic algorithm method is effective when tuning the  $k_p$  parameter. The system tends to be more stable and the output voltage tends to be more accurate.

Figure 7 shows the system response of the first generation, the fifth generation, and the 13th generation  $k_p$  parameter. It shows that the system response of the first generation is unstable, and the response is improved in the 5th generation. Up to the 13th generation, the response is stable and the transfer time is shorter than the former generations.

**Table 1** Mean ITAE value of each generation

Generation	ITAE	Generation	ITAE	Generation	ITAE
1st	41,412.98	6th	18,722.28	11th	10,131.51
2nd	38,933.31	7th	18,195.22	12th	6344.44
3rd	31,807.21	8th	14,120.56	13th	36,96.65
4th	23,546.87	9th	11,379.92		
5th	22,759.72	10th	12,528.04		



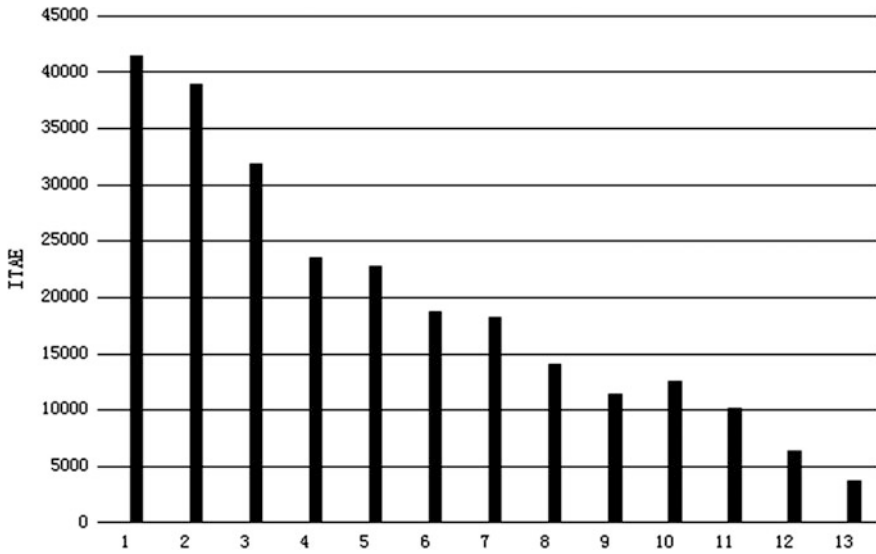


Fig. 6 Mean ITAE value of each generation

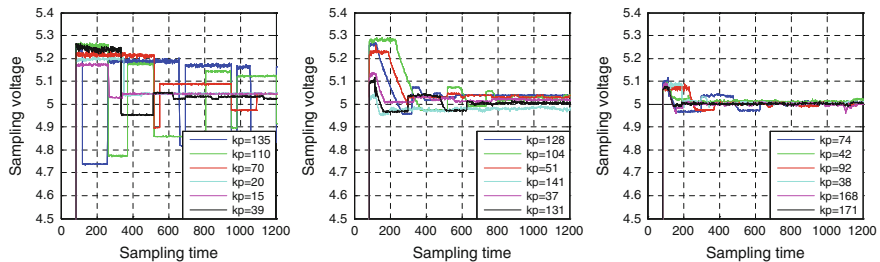


Fig. 7 System response of 1st generation, 5th generation and 13th generation

### 4 Conclusion

The result of the experiment shows that the  $k_p$  parameter tuned by GA ( $k_p = 37$ ) is global optimum, which is the same as the measured data and is better than  $k_p$  parameter tuned by the Z–N method ( $k_p = 37$ ). The efficiency of the GA used in PID parameter tuning is verified in the field of NC power supply. The proposed optimization method is efficient and not only can be used in the design of NC power supply, but also in the field of any other PID controller’s parameter tuning.

**Acknowledgements** The research work was supported by National Natural Science Foundation of China under Grant No. 31272511, and the foundation of Nanjing University of Posts and Telecommunications (JG00613JX07).

## References

1. Ali S, Kim DH (2015) Optimized power control methodology using genetic algorithm. *Wireless Pers Commun* 83–86
2. Elbayomy KM, Zongxia J, Huaqing Z (2008) PID controller optimization by GA and its performances on the electro-hydraulic servo control system. *Chin J Aeronaut* 21(4):378–384
3. Lin CL, Jan HY, Shieh NC (2003) GA-based multiobjective PID control for a linear brushless DC motor. *IEEE/ASME Trans Mechatronics* 8(1):56–65
4. McCall J (2005) Genetic algorithms for modelling and optimization. *J Comput Appl Math* 184(1):205–222
5. Niu X, Wang Y, Tang J (2010) Optimization parameters of PID controller parameters based on genetic algorithm. *Comput Simul* 27(11):180–184 (in Chinese)
6. Song S, Zuo D, Wang M, et al (2003) Study on technique of gas-based optimization of PID parameters. *Syst Eng Theory Practice* 9:135–138
7. Xiao L, Shao X, Zhang L et al (2010) PID parameter optimization using improved genetic algorithm. *Comput Eng Appl* 46(1):200–202 In Chinese
8. Zeng C, Zhao X (2009) Application of improved quantum genetic algorithm in PID parameter tuning. *Electr Power Autom Equip* 29(10):125–128 (in Chinese)

# Different Feature Combination Rules in CNNs for Face Detection

Qingyang Xu and Li Zhang

**Abstract** Convolutional neural network (CNN) is a very popular deep learning structure. It has kinds of merits in the feature learning, such as local reception region, sharing weights, subsampling, etc. CNN can learn the image by pixel without previous feature extraction, and then discover some more characteristics of the input by the feature combination. In this paper, we study the effect of different combination rules in the CNN training. The simulation tests exhibit the different kinds of combination rules in the CNN learning.

**Keywords** Deep learning · Convolutional neural network · Combinational rule · Face detection

## 1 Introduction

Face detection is a very popular problem in computer vision. It is difficult for face detection due to various backgrounds. Therefore, the robustness of the face detector is an important parameter. Effective methods in advanced features extraction are the key factors in face detection. Shallow neural network is an early way used to face detection [1–3].

The main deficiency of shallow neural networks for face detection is that they offered little or no invariance to translations, shifting, scaling, rotation, and local distortions of the inputs. CNNs are a deep neural network. CNNs can recognize patterns with extreme variability, with robustness to distortions, and simple geometric transformations like translation, scaling, rotation, squeezing, stroke width, and noise [4]. In this paper, we will adopt a CNN to detect the face, and study the effect of different feature combination methods to the feature extraction in the middle layer.

---

Q. Xu (✉) · L. Zhang  
Shandong University, Weihai 264209, China  
e-mail: qingyangxu@sdu.edu.cn

## 2 CNN Structure

Yann LeCun and Yoshua Bengio introduced the concept of CNNs in 1995 [5], which is a feedforward network with deep structure and the ability of extracting features from the input image without other preprocessing. CNNs combine three advanced operations to ensure some degree of shift, scale, and distortion invariance: local receptive fields, shared weights, and spatial or temporal subsampling (Fig. 1).

Convolution is a conventional operation in the digital image processing. A convolutional kernel is sliding on the image. The convolution layer will output a feature map to describe the characteristics of the image. In the convolutional layer, the convolution operation is realized by Eq. (1).

$$CFM_j^l = f \left( \sum_{i=1}^l X_i^l \otimes K_{ij}^l + b_j^l \right) \quad (1)$$

where  $CFM_j^l$  is the feature map of the  $l$ th convolutional layer,  $f$  is the active function,  $X_i^l$  is the input image,  $K_{ij}^l$  is the convolutional kernel, and  $b_j^l$  is the bias value.

For the input image, the convolutional kernel is fixed when it is sliding on the image. Therefore, the whole image shares the weights of the convolutional kernel. The convolutional kernel also simulates the local reception of eyes.

Another operation in the CNNs is the subsampling, the maximal pooling is the preferred one as Eq. (2)

$$PFM_{i,m}^l = \max_{n=1}^G CFM_{i,(m-1)*s+n}^l \quad (2)$$

where  $PFM_{i,m}^l$  is the feature map after the maximal pooling operation. In the training of the network, the pooling layer output will be the input of next convolutional layer, such as  $CFM_j^l = PFM_{i,m}^{l-1}$ . Therefore, the next layer's input will be the combination of the  $PFM$ . The combination method is different. We will study the different effects of different combination ways.

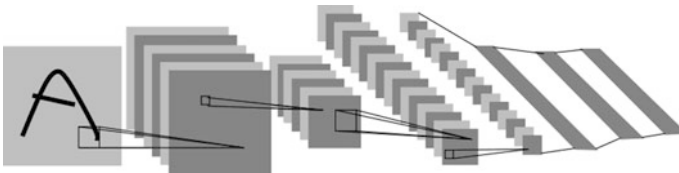


Fig. 1 CNNs structure

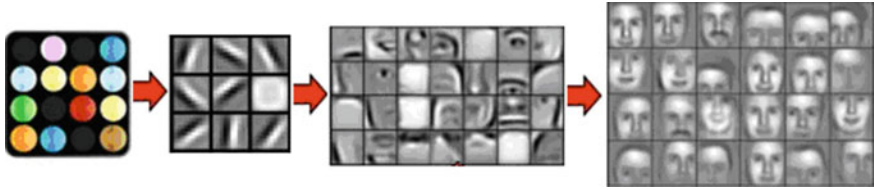


Fig. 2 Face detection flow of CNNs

### 3 Different Combination Method of Subsampling Layer

The principle of face detection by CNNs is shown in Fig. 2. The input of the CNNs is the original pixel image. Unlike other face detection algorithm, the CNNs handle the pixel image and not the features. The feature maps come from the convolution and subsampling operations of the CNNs [6]. The input of the next layer will be the combination of the feature maps of the previous layer.

For the input, a convolutional kernel is sliding on the image and the whole image shares the weights of the kernel. In CNNs, there are different convolutional kernels. Therefore, it will generate some feature maps after the convolution and subsampling operations. Supposing the first layer feature map after subsampling is  $PFM_1^1$ , and the next layer feature map output is  $PFM_2^2$ . In these CNNs, there are four feature maps after the subsampling, and then the input of next convolutional layer will have 14 maps by the combination of the four feature maps  $PFM_i^1$ . Table 1 is a simple combination rule of feature maps. For example, the new input is the combination of  $PFM_1$  and  $PFM_3$ . Different combination rules will generate different input features.

Therefore, the combination rule is very important for the generation of the follower layer input. In this paper, we adopt kinds of combination rules to generate the input image as Table 2. In Table 2, we adopt different combination rules, such as single  $PFM$ , combination of two  $PFMs$ , and the combination of three  $PFMs$ . Hence, the input features are more abundant.

Table 1 Combination method 1

New input	1	2	3	4	5	6	7	8	9	10	11	12	13	14
$PFM$														
$PFM_1$	*	*									*	*		*
$PFM_2$			*	*						*	*		*	
$PFM_3$					*	*			*	*				*
$PFM_4$							*	*	*			*	*	

**Table 2** Combination method 2

New input	1	2	3	4	5	6	7	8	9	10	11	12	13	14
<i>PFM</i>														
<i>PFM</i> <sub>1</sub>	*				*		*	*			*	*		*
<i>PFM</i> <sub>2</sub>		*			*	*		*		*	*		*	
<i>PFM</i> <sub>3</sub>			*		*	*	*		*	*				*
<i>PFM</i> <sub>4</sub>				*		*	*	*	*			*	*	

### 4 Simulation Test

In the simulation test, we adopt a face database including 1000 faces and other nonface images. These images are used to train the CNNs. The training process is shown in Fig. 3. The input image size of CNNs is  $32 * 36$  [7]. By a  $5 * 5$  convolutional operation, the images are converted to a size of  $28 * 32$  images. Then by a  $2 * 2$  subsampling, the feature maps of the first layer will be  $14 * 16$ . The following layer will follow the same principles, and then the output layer will be a face and nonface discrimination neuron. The feature maps combination rules follow Tables 1 and 2.

According to the two combination rules table, we do the simulation tests and the results are shown in Figs. 4 and 5. The two figures exhibit the effect of different combination rules to the CNNs learning.

The simulation has 500 iterations. From the simulation results, we can see that the combination rules of Table 1 are not the best one. In Table 1, there are some repeated combination rules, and some combination rules are neglected such as the combination of three *FP*Ms. From the learning process of CNNs, we can see that the feature extraction and combination are not well for the combination rules of

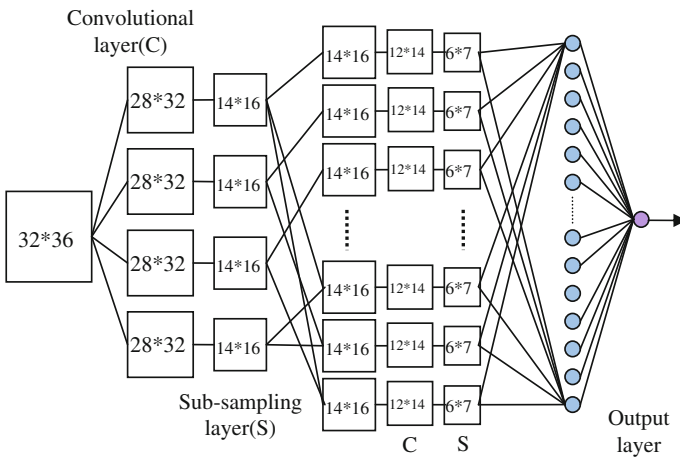


**Fig. 3** The images processing flow of CNNs

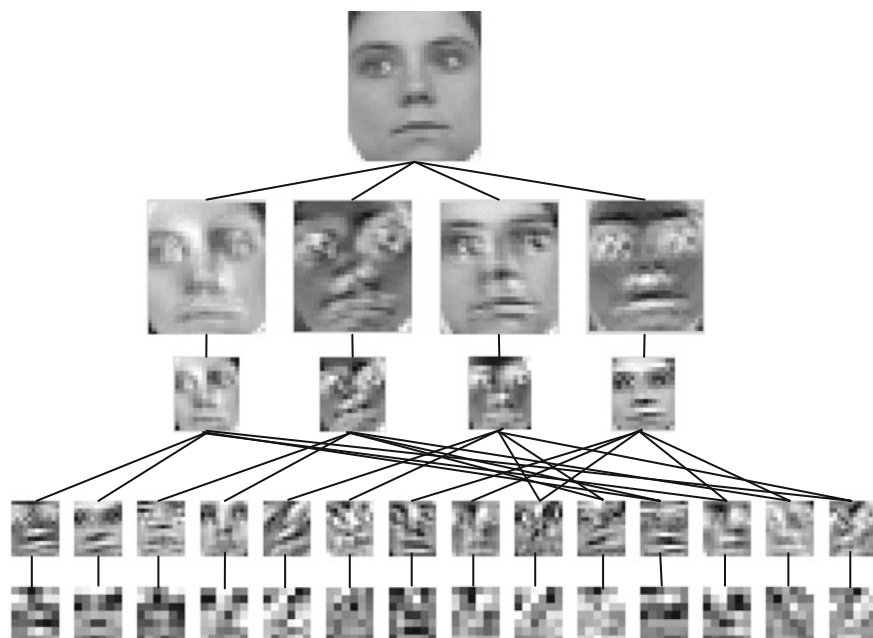


Fig. 4 Feature maps output by combination rule Table 1

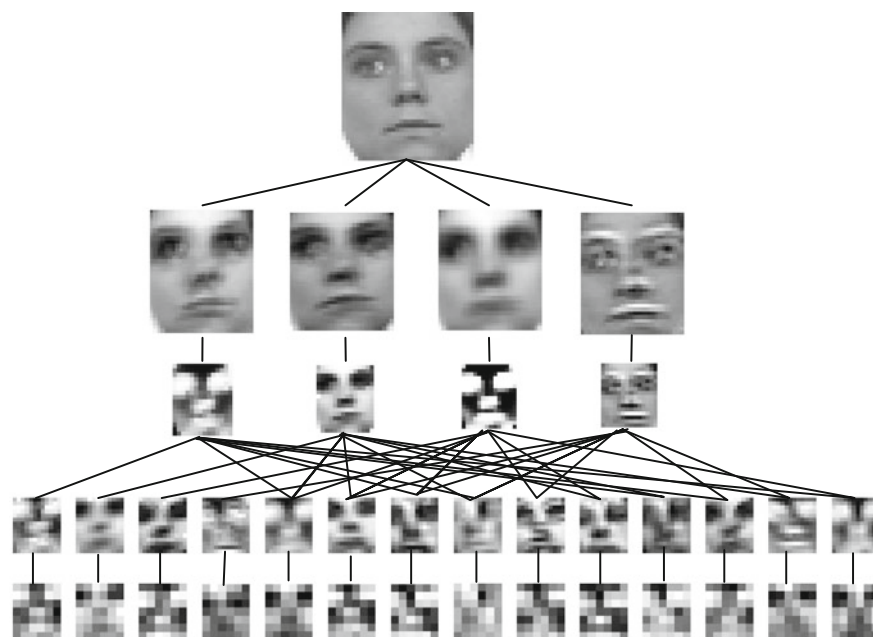


Fig. 5 Feature maps output by combination rule Table 2

Table 1 comparing with Table 2. By the combination rule of Table 2, the features of faces are effectively extracted and well combined. The feature extraction effect is more like the famous Gabor filter [8]. Therefore, the combination rules of Table 2 are the better one, and it considers every combination situation of one, two, and three combinations of *FPMs*.

## 5 Conclusion

CNN has kinds of merits, and it can handle the 2D image directly which is suitable for digital image processing. In order to study the feature learning and combination mechanism, different feature map combinations are adopted to exhibit the learning process of CNNs. Two typical combination rules tables are adopted. From the simulation results, we can see that the complete combination rules will extract better face features like the effect of the Gabor filter but the CNNs can handle the pixel images and be trained with better generalization ability.

**Acknowledgement** This work was supported in part by the National Natural Science Foundation of China under Grant No. 61174044, Natural Science Foundation of Shandong Province under Grant No. ZR2015PF009, and Independent Innovation Foundation of Shandong University under grant No. 2015ZQXM002.

## References

1. Rowley HA, Baluja S, Kanade T (1998) Neural network-based face detection. *IEEE Trans Patt Anal Mach Intell* 20(1):23–38
2. Feraud R, Bernier OJ, Viallet JE, Collobert M (2001) A fast and accurate face detector based on neural networks. *IEEE Trans Pattern Anal Mach Intell* 23(1):42–53
3. Jonsson K, Kittler J, Li YP, Matas J (2002) Support vector machines for face authentication. *Image Vis Comput* 20(5–6):369–375
4. Lawrence S, Giles CL, Tsoi AC, Back AD (1997) Face recognition: a convolutional neural network approach. *IEEE Trans Neural Netw* 8(1):98–113
5. LeCun Y, Jackel LD, Bottou LEO et al (1995) Learning algorithms for classification: a comparison on handwritten digit recognition. *Neural Netw Stat Mech Perspect* 261:276–291
6. Trinh H, Duranton M, Païndavoine M (2015) Efficient data encoding for convolutional neural network application. *ACM Trans Archit Code Optim (TACO)* 11(4):49(1–20)
7. Chen YN, Han CC, Wang CT et al (2010) A cnn-based face detector with a simple feature map and a coarse-to-fine classifier. *IEEE Trans Pattern Anal Mach Intell* 99:1–13
8. Huang L-L, Shimizu A, Kobatake H (2004) Classification-based face detection using Gabor filter features. In: Sixth IEEE international conference on automatic face and gesture recognition, pp 397–402



# The Contact Behavior Analysis Between Microcomponents on a Low-Frequency Reciprocating–Fretting Ball-on-Flat Tribometer

Zhongnan Wang, Wuyi Wang, Guangyu Zhang and Hejuan Chen

**Abstract** Fatigue failure between the reciprocating sliding microcomponents is the key factor that affects the performance and reliability of microelectromechanical system (MEMS) under alternative load. Sliding friction pairs on the smooth surface are at very slow scan rates and friction-induced vibration is caused by stick-slip phenomenon that is generated from nanometer clearance between the friction pairs. In this paper, a developed tribometer is applied to simulate the fretting friction with low-frequency reciprocation. Dynamic friction coefficient is measured with the normal load of 0–60 mN from a series of tribological tests of a small steel ball sliding on various flat surfaces such as PTFE, silicon wafer, and glass in a straight-line, oscillating motion configuration. The contact stress, contact force, and surface deformation with or without friction in these three configurations are calculated by the variation of friction coefficient according to the Hertz contact theory. Experimental results show that the friction force is not nearly dependent of the normal load and contact deformation is at nanoscale sizes in steel ball-on-silicon wafer configuration. Friction coefficient measured by the developed tribometer is combined with the contact stress calculation for the structural design of micro-components before manufacturing MEMS devices.

**Keywords** Tribometer · Microcomponents · Contact behavior analysis · Reciprocating–fretting · Ball-on-flat

---

Z. Wang · W. Wang (✉) · G. Zhang  
School of Mechatronics Engineering, Harbin Institute of Technology,  
Harbin 150001, China  
e-mail: wangwuyi@hit.edu.cn

Z. Wang  
e-mail: wzn198405@163.com

G. Zhang  
e-mail: zgyqx@hit.edu.cn

H. Chen  
School of Mechanical Engineering, Nanjing University of Science and Technology,  
Nanjing 210094, China  
e-mail: 601194143@qq.com

## 1 Introduction

Microcomponents in microelectromechanical system (MEMS) are mainly used for mechanical motion, such as the bending or vibration of the microcantilever, the rotation of microrotor, the reciprocating sliding of the actuator [1–4], etc. When microcomponents are in operation, alternative load is along with most of them, which is similar to the macrocomponents. As one of the important patterns of the failure, fatigue failure is the key factor that affects the performance and reliability of MEMS.

The majority of materials for microcomponents are brittle materials such as single-crystal silicon, polycrystalline silicon and nitrides, and the related failure is caused by the fracture and stiction that are relevant to friction. Sliding friction pairs between microcomponents are at very slow scan rates and the adhesive effects [5] on the smooth surfaces are strengthened by nanometer clearance between the friction pairs. The friction force and sliding speed will not remain in the constant state during the sliding friction process because of stick-slip phenomenon and the movement restriction, increased damage and less reliability in the microcomponents might be brought about from the resulting friction vibration. There is ample evidence that the contact force between surfaces is as dominate in MEMS, which makes stick-slip phenomenon more obvious, than that in macrocomponents. Moreover, friction force, viscosity resistance, and surface tension have more significant impacts on MEMS devices than those caused by the inertia force and electromagnetic force from the conventional machinery [6].

Therefore, the control of stick-slip and friction loss or even friction-free is essential for MEMS to keep the microcomponents in normal operation during the design process. However, as friction coefficient and friction force or friction torque will be increased due to great viscous force and shear force produced on the friction surfaces, the traditional lubrications are not always an effective way to resolve the lubrication problems of the slow sliding regime under the alternative load [7]. There is by far concern about the research on fatigue performance and friction measurement of microcomponents from MEMS researchers. The previously published research is mainly focused on the tests of mechanical properties for materials with microstructure in MEMS, and less is involved in the proper tests for fatigue performance between microcomponents.

Material properties are largely determined by the composition, as well as the structure which is also concerned with the fabrication process. The fabrication process of microcomponents is in a totally different way from that of bulk materials and thus there are significant property variations, even in the same materials. Differences may be caused by microstructure changes arising from various sizes of the components. In 1982, a new measurement technique about the fatigue properties of MEMS chip was introduced by Perkerson K.E. A comb-drive actuator is on one side of a huge mass connected with the notched samples and there is a comb-shaped capacitive displacement sensor on the other side. When a sinusoidal voltage at a half frequency is applied to the comb-drive actuator to control the vibration of the

mass, symmetrical tension–compression fatigue will occur at the sample notch by the resonance of the mass. Fatigue stress is dependent on the amplitude of the mass, while the latter is decided by voltage amplitude. Therefore, the fracture will appear at the notch of MEMS chips after  $N$ -times vibration. Fatigue limit or fatigue strength under certain cycles is determined from test data recorded by displacement sensor and tension–compression stress at the sample notch is calculated with the finite element analysis (FEA) method. Sundararajan [1] in 2001, introduced his research achievement that AFM probe with the frequency of 4 Hz is used for testing the fatigue property of structure components in nanoscale. The sample is a nanoscale beam with fixed ends and AFM probe is in alignment with the center of the top of the beam. Applied force on the beam is controlled by adjusting the deformation of piezoelectric crystal until the fracture of nanoscale beam appears in the  $N$ -times vibration. This approach with its experimental procedures is the same as the one introduced in the literature except for the load and test principles.

With the progress of MEMS applications, it is urgent to investigate tribological behavior for increasing amounts of micro-components and microrotating machineries which are manufactured by familiar materials. Although, a great many of novel microsystems are being developed by MEMS researchers, it is still difficult for the MEMS designers to acquire the fatigue property and tribological behavior of materials that they require from handbooks or references, and hence the measurement is necessary with the actual alternative load applied in the designed micro-components. For this purpose, measurement techniques of the sliding friction force and friction coefficient at a slow scan rate between microcomponents in MEMS are introduced in this paper and demonstration studies with load, displacement, and friction force using the self-developed tribometer are carried out to provide the MEMS designers with reliable measurement methods and data analysis in terms of tribological behavior.

## **2 The Low-Frequency Reciprocating–Fretting Ball-on-Flat Tribometer**

The low-frequency reciprocating sliding friction between the microcomponents is fretting that exists in the surfaces of tight mechanical parts which are approximately static at very low sliding speed. Microvibration and slow sliding on the contact surfaces are the key factor for the design of the tribometer, and the former is obtained by the power supply load while the latter is related to the motion platform which is used for fixed samples. Based on many years of experience in the design of the universal fretting wear test systems, a novel voltage-controlled measuring head with alternative load [2, 3] was developed at Warwick in 2011 and the absolute value of the ratio between its output current and input voltage is 100 mA/V. A developed low-frequency reciprocating test platform, in this paper, is combined with the above measuring head to compose a low-frequency reciprocating–fretting

ball-on-flat tribometer as illustrated in Fig. 1, including sample holder (1), magnetic coil (2), base (3), notch-hinge mechanisms (4), upper and lower samples (5), and laser placement sensor (6). The upper sample with alternative load is fixed to the sample holder in the measuring head and the test platform is actuated by drive coil with the action of sinusoidal voltage in order to simulate the fretting friction between the microcomponents.

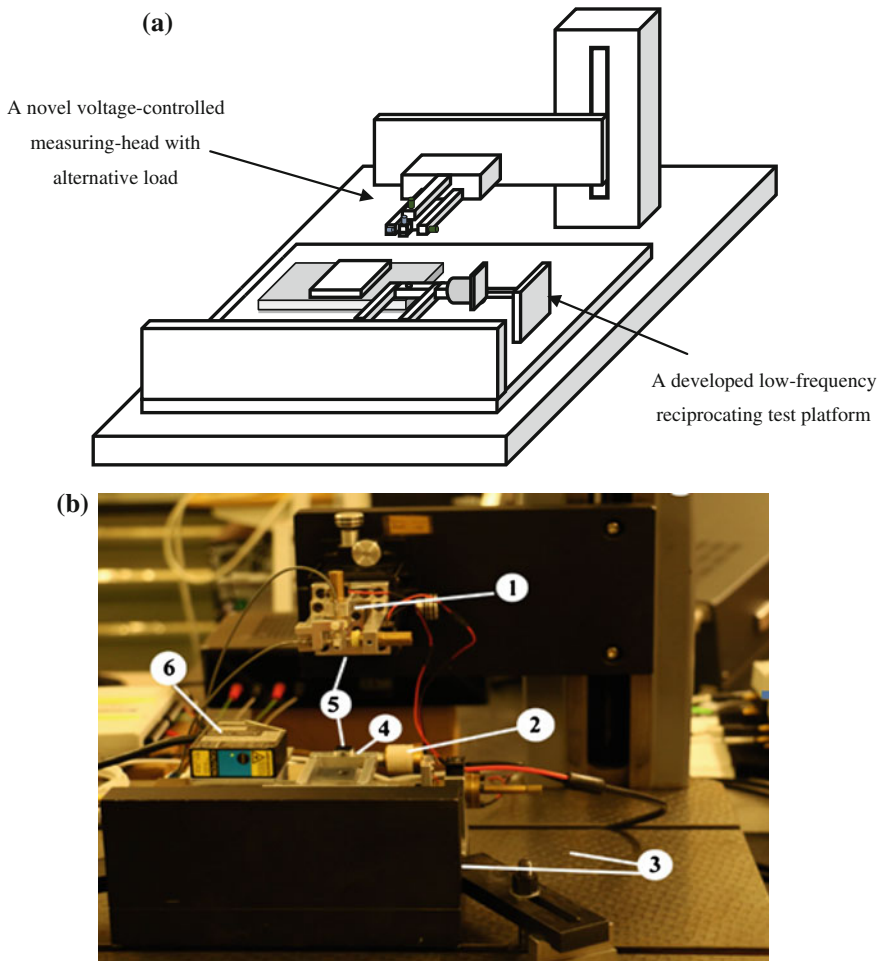


**Fig. 1** Low-frequency reciprocating-fretting ball-on-flat tribometer. **a** 3D model of the tribometer. **b** Image of the tribometer 1 Sample holder, 2 magnetic coil, 3 base, 4 notch-hinge mechanism, 5 upper and lower samples, 6 displacement sensor

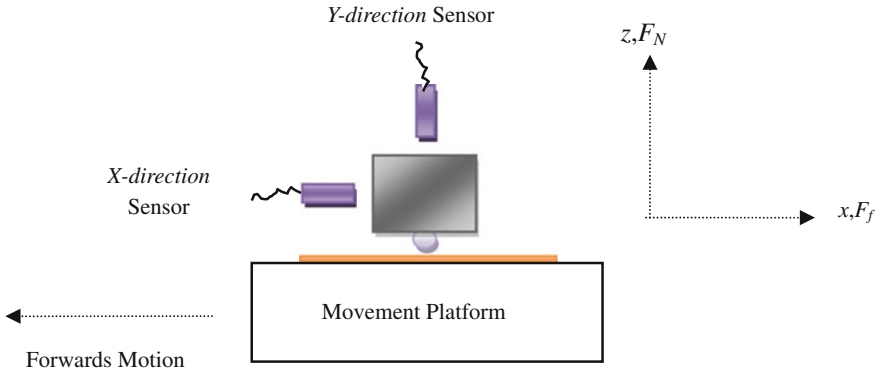


**Fig. 2** Schematic of the ball or platform in the forwards motion with its reference coordinates directions

The friction measurement is evaluated by the average peak-to-peak value of the signal, as shown in Fig. 2, and coefficient of friction is calculated with  $F_N$  and  $F_f$ ,

$$\mu = e \left| \frac{F_f}{F_N} \right| \tag{1}$$

where  $e = +1$  (forward motion) and  $e = -1$  (reverse motion).

### 3 The Influences of Friction on the Surface Contact Behavior in Ball-on-Flat Configuration

Take the well-known ball-on-flat configuration in the microcomponent (as shown in Fig. 3; [2]) as an example, a great surface contact force is brought between two surfaces at extremely low sliding speed to making their shapes change and thus it is not easy to be separated for them due to adhesion. As adhesive force is of the same order of magnitude as the normal load [5], the effect of friction force on the great contact force which is generated by adhesion cannot be neglected. As for multi-asperity contact in the ball-on-flat configuration, coefficient of friction is related to the scan speed during sliding. Hertzian contact theory is applied to the calculation of contact force between an elastic ball and a flat surface as shown in Fig. 3, and its simplified calculation formulas [8, 9] is,

$$P = P_0(1 - (r/a)^2)^{\frac{1}{2}} \tag{2}$$

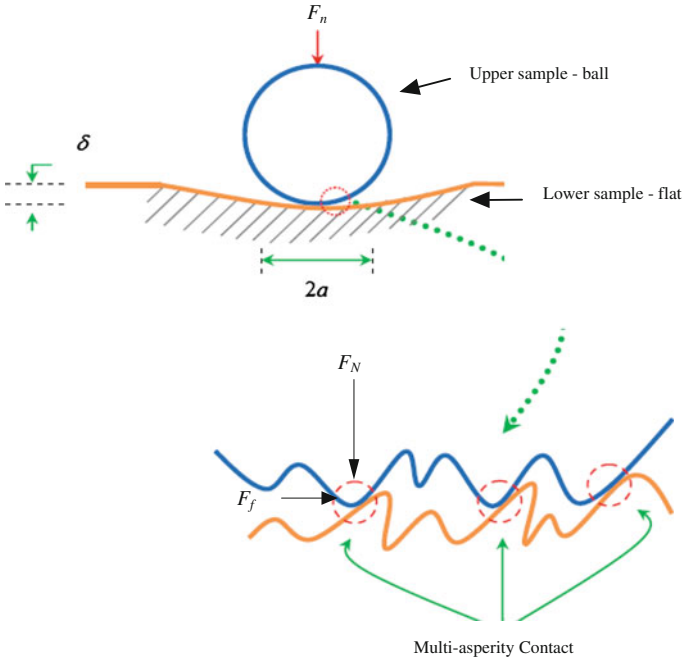


Fig. 3 Multi-asperity contact between a ball and a flat surface [2]

Hertzian contact stress and the maximum contact pressure are  $P$  and  $P_0 = \frac{3F_n}{2\pi a^2}$ , respectively. The contact area of an elastic ball on a flat is given by

$$a = \sqrt[1/3]{\frac{3F_n R_e}{4E_e}} \tag{3}$$

$F_n$  is the normal load and the radius of an equivalent ball on a flat is given by

$$\frac{1}{R_e} = \frac{1}{R_1} + \frac{1}{R_2} \tag{4}$$

$R_1$  and  $R_2$  are principal radii of curvature of the two bodies. Because  $R_2, R_e = R_1$ . Equivalent Young’s modulus of elasticity is given by

$$\frac{1}{E_e} = \frac{1 - \nu_{ball}^2}{E_{ball}} + \frac{1 - \nu_{flat}^2}{E_{flat}} \tag{5}$$

$E_{ball}, E_{flat}, \nu_{ball}$ , and  $\nu_{flat}$  are the elastic modulus and Poisson ratios of the two bodies in contact, respectively. The deflection (distance of approach of two far field points in the bodies) is given by

$$\delta = \left( \frac{9F_n^2}{16R_e E_e^2} \right)^{\frac{1}{3}} = \frac{a^2}{R_e} \quad (6)$$

the transverse contact stiffness is also given by

$$\lambda = \frac{dF}{d\delta} = (6E_e^2 F_n R_e)^{\frac{1}{3}} \quad (7)$$

when sliding friction occurs in contact between a ball and a flat surface, field of stress which is generated on the surfaces is in a condition of the surface strain. The tension which is caused by tangential tractive force,  $\sigma$ , is calculated by the formula given by Johnson [10], so maximum stress value is given by

$$\sigma_{\max} = 1.5 \frac{Q}{\pi a^2} \quad (8)$$

where the shearing traction at the contact surface is given by

$$Q = fF_n \quad (9)$$

for friction-free,  $Q = P$ .

Maximum normal contact stress, maximum normal contact force, and maximum deformation are calculated with friction-free or friction, respectively.

#### (1) Calculation of Contact Force without Friction in Ball-on-Flat Configuration

Hertz contact theory is applicable to nonconforming contact and its fundamental assumption is in a very small contact area. Rigid body motion will not occur between two bodies in contact and the contact surface should be smooth enough, regardless of the medium of the contact surface (lubricants) or the influence on dynamic friction [8].

Basic parameters of samples are shown in Table 1. Upper sample is a steel ball while lower specimens are flat surface materials including PTFE, silicon wafer and glass, with the sizes of  $10 \times 10 \times 1$  ( $\text{mm}^3$ ). FEA is used for the numerical solution and the numbers of nodes and elements of finite element model which are established by Hertz contacting theory are 47959 and 144778, respectively. Normal load is applied between 0 and 60 mN.

The maximum contact stress, the maximum contact force, and the maximum deformation, in Table 2, are calculated by Eqs. (1)–(5) when taking  $F_n$  for 9.65, 46.68, and 58.8 mN and the related variation can be seen from Figs. 5, 6, and 7. The curves of 1, 2, and 3 correspond to normalized curves of  $\lambda_{\max} - F_n$ ,  $P_{\max} - F_n$ , and  $\delta_{\max} - F_n$  from a steel ball sliding against PTFE, silicon wafer and glass, respectively. Among them,  $\delta_{\max}$  is the curve for normalization in Fig. 7 and the average value  $\delta_b$ , as the divisor, is taken from Table 2.

**Table 1** Physical conditions of Hertz contact

Name		Symbol	Value
Spherical radius (mm)		$R_e$	1
Elastic modulus (GPa)	Steel	$E_{ball}$	206
	Silicon wafer	$E_{flat}$	190
	PTFE		1.42
	Glass		88
Poisson ratio	Steel	$\nu_{ball}$	0.3
	Silicon wafer	$\nu_{flat}$	0.278
	PTFE		0.35
	Glass		0.215
Normal load (mN)		$F_n$	0–60
Coefficient of friction		See Fig. 6	

**Table 2** Calculations of maximum normal contact stress, maximum normal contact force, and maximum deformation with friction-free

Flat	$F_n$ /(mN)								
	9.65			46.68			58.83		
	$\lambda_{max}$ (MPa)	$P_{max}$ (mN)	$\delta_{max}$ ( $10^{-6}$ mm)	$\lambda_{max}$ (MPa)	$P_{max}$ (mN)	$\delta_{max}$ ( $10^{-6}$ mm)	$\lambda_{max}$ (MPa)	$P_{max}$ (mN)	$\delta_{max}$ ( $10^{-6}$ mm)
Steel ball-PTFE	1.24	9.63	96.4	5.98	46.6	466	7.53	58.7	587
Steel ball-silicon wafer	1.12	9.63	0.644	5.4	46.6	3.12	6.81	58.7	3.93
Steel ball-glass	1.05	9.63	2.37	5.07	46.6	11.5	6.39	58.7	14.5

1. The distribution trends of contact force are identical as noncircular for a steel ball sliding against a PTFE sample, a silicon wafer sample and a glass sample. Figure 4 is one of the most representatives of contact force distribution with the normal load of 58.83 mN. There have been polylines in the figure because meshing is not fine enough, while in theory, contact force distribution should be round with the increased normal load.
2. From Figs. 5, 6, 7, variations of  $\lambda_{max}$ ,  $P_{max}$ , and  $\delta_{max}$  from different material surfaces are basically in accordance, especially identical normalized curves of  $P_{max} - F_n$  and  $\delta_{max} - F_n$ . However, there is rapid change in the curves before  $F_n = 46.68$  mN while it shows the slow varying after  $F_n = 46.68$  mN. Moreover, nonlinearity is not very apparent due to the association with friction and wear between two contact surfaces, in addition to the elastic modulus and Poisson's ratio of the measured materials.
3.  $\delta_{max}$  increases with  $F_n$ . From Table 2, there is  $\delta_{max}$  with the maximum value in steel ball-on-PTFE configuration, reaching to microscale, while it is just at the nanoscale for a steel ball sliding on a silicon wafer sample surface and glass sample surface.



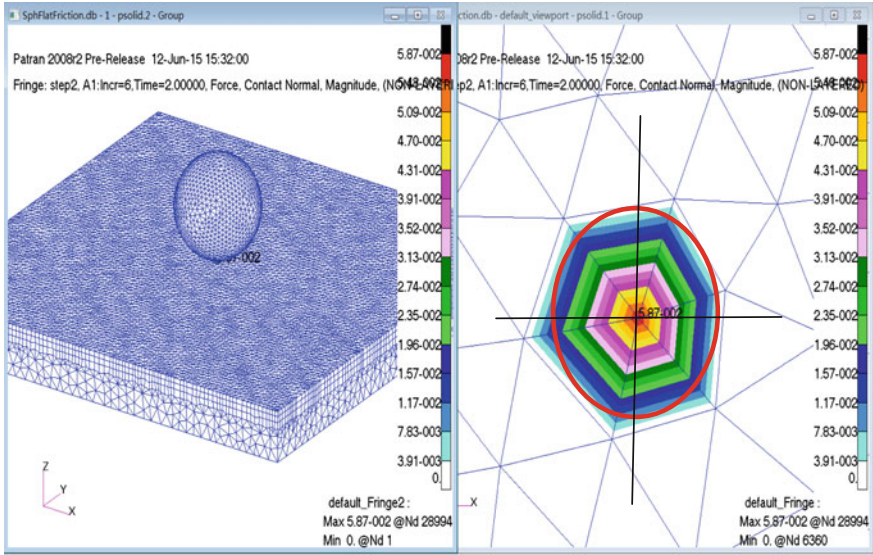


Fig. 4 Contact force distributions with the normal load of 58.83 mN

Fig. 5 Curves of  $\lambda_{max} - F_n$

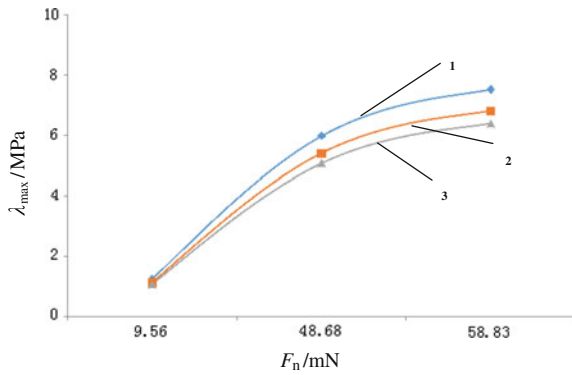
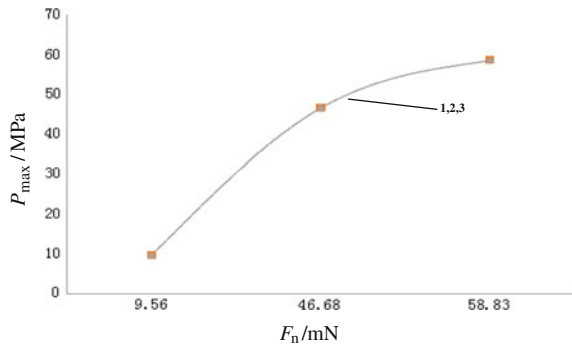
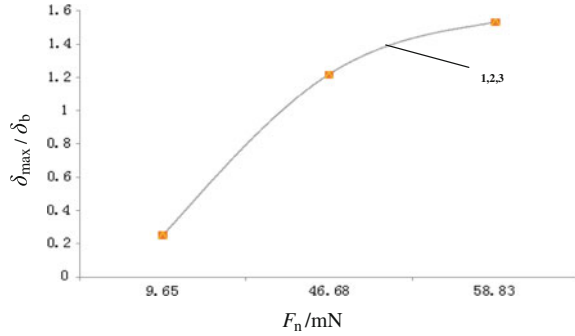


Fig. 6 Curves of  $P_{max} - F_n$



**Fig. 7** Normalized curves of  $\delta_{\max}$



(2) Calculation of contact stress and contact force with friction in ball-on-flat configuration

Hertz contact theory is not applicable to many contact problems in the real projects. As shown in Fig. 4, the contact problem is a nonlinear behavior [11] when there is any phenomenon of multiple elastic or nonelastic impacts and friction heat generated from the sliding contact between the surfaces. The maximum contact stress, the maximum contact force, and the maximum deformation are calculated with friction by Eq. (6) in the ball-on-flat configuration. The basic parameters of the samples are listed in Table 1. Reciprocating frequency of movement platform is 5 Hz and sliding speed is 2 mm/s through the tests. Figure 8 shows the measured friction coefficient for these samples and the curves of 1, 2, and 3 correspond to the

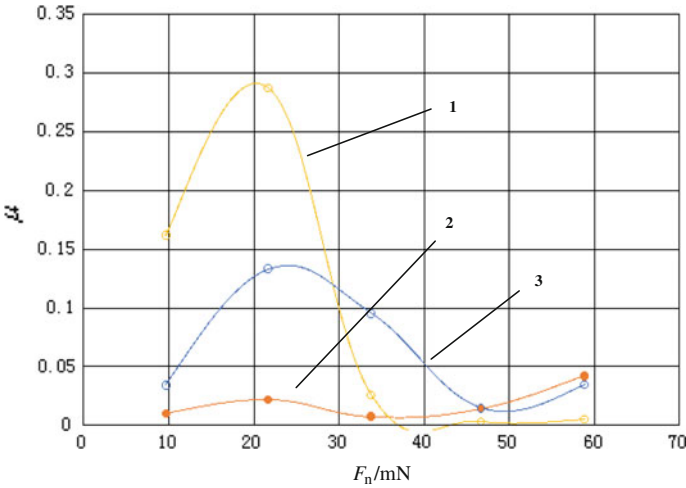


**Fig. 8** Curves of  $\mu - F_n$

changing curves of dynamic friction coefficient measured by the tribometer in Fig. 1 for a steel ball sliding on PTFE, silicon wafer and glass samples respectively, namely  $\mu - F_n$  curves.

The distribution trends of contact force calculated from Eq. (6) are identical for a steel ball sliding against a PTFE sample, a silicon wafer sample and a glass sample. Figure 9 shows the contact force distribution with the normal load of 58.83 mN for steel ball sliding on silicon wafer sample. The maximum contact stress, the maximum contact force, and the maximum deformation, in Table 3, are calculated when taking  $F_n$  for 9.65, 46.68, and 58.8 mN as well. Based on Table 3, Figs. 10, 11, 12, and 13 show that the curves of 1, 2, and 3 correspond to normalized curves of  $\lambda_{max} - F_n$ ,  $P_{max} - F_n$ , and  $\delta_{max} - F_n$  from a steel ball against PTFE, silicon wafer and glass, respectively and the results are as follows:

1. As can be seen from the contact force distribution in Fig. 9, the noncircular curves of contact force under dry friction condition are more obvious with the increase of the normal load for a steel ball sliding on a silicon wafer surface.
2. From Figs. 10, 11, 12, and 13,  $\lambda_{max}$ ,  $P_{max}$ ,  $\delta_{fmax}$ , and  $F_{fmax}$  fall down to nearly 0 with the increase in the normal load before  $F_n = 46.68$  mN, while there is hardly variable from  $F_n = 46.68$  mN. Therefore, friction has great impact on contact stress and contact pressure for a steel ball sliding on glass sample.
3. In terms of Figs. 10 and 11,  $\lambda_{max}$  and  $P_{max}$  increase with  $F_n$  for a steel ball sliding on PTFE and silicon wafer samples. The variation of  $\lambda_{max}$  and  $P_{max}$  in steel ball-on-silicon wafer configuration is similar to that of the situation without friction-free. The value and variation of  $\delta_{max}$  is very small and friction force is nearly constant.

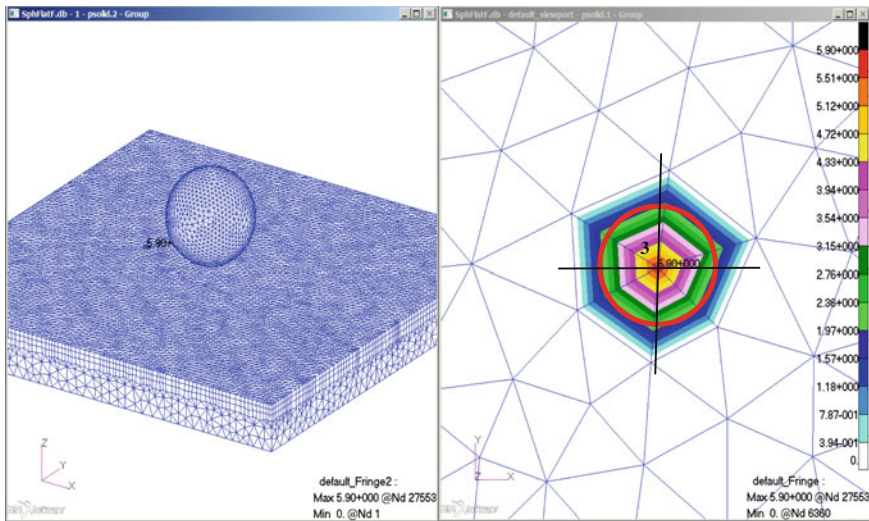


**Fig. 9** Contact force distributions with the normal load of 58.83 mN for a steel ball sliding on a silicon wafer

**Table 3** The maximum contact stress, the maximum contact force, and the maximum deformation when sliding with friction

	$F_n/(mN)$											
	9.65			46.68			58.83			58.83		
	$\lambda_{max}$ (MPa)	$P_{max}$ (mN)	$\delta_{fmax}$ (mm)	$F_{fmax}$ (mN)	$\lambda_{max}$ (MPa)	$P_{max}$ (mN)	$\delta_{fmax}$ (mm)	$F_{fmax}$ (mN)	$\lambda_{max}$ (MPa)	$P_{max}$ (mN)	$\delta_{fmax}$ (mm)	$F_{fmax}$ (mN)
Flat												
Steel ball-PTFE	0.66	9.34	0.26	3.53	3.25	45.60	0.99	3.80	4.16	57.8	0.97	4.5
Steel ball-silicon wafer	1.70	21.00	8.51	0.06	1.91	54.10	21.10	4.22	3.83	57.6	1.08	0.92
Steel ball-glass	570	5900	358	3110	4.16	50.20	6.23	4.25	8.57	72.5	23.10	6.87

**Fig. 10** Normalized curves of  $\lambda_{max} - F_n$

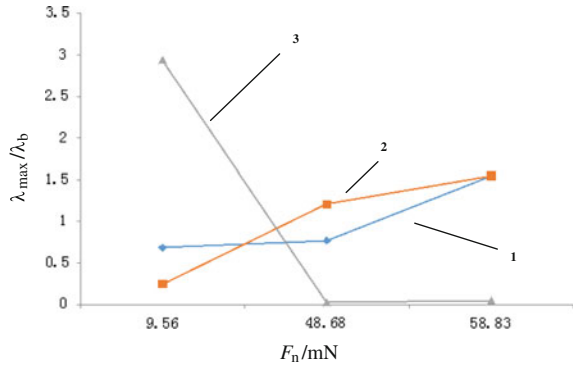


**Fig. 11** Normalized curves of  $P_{max} - F_n$

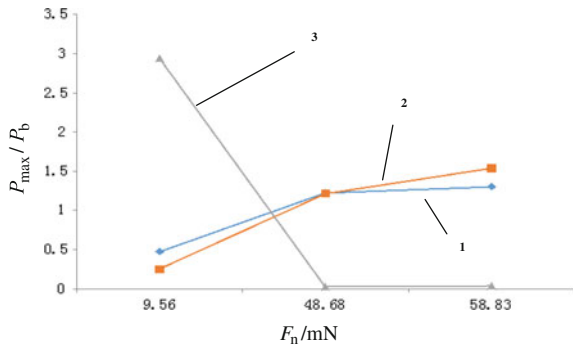
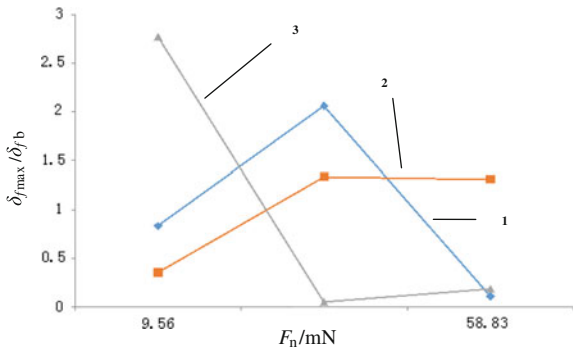
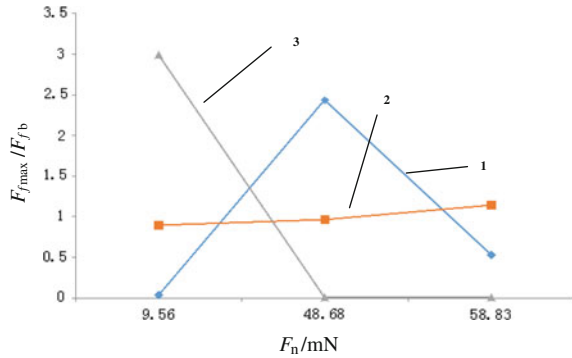


**Fig. 12** Normalized curves of  $\delta_{fmax} - F_n$



From the above results, we can infer that there is little influence on contact behavior for a steel ball sliding on the silicon wafer. As for the basic material in MEMS, the research results of silicon wafer samples will provide an important reference value for the design of microcomponents. Although the value of  $\delta_{max}$  is also small, there is a large wave in the related variation.  $F_{fmax}$  is far from steady and will arrive at the maximum value when  $F_n = 46.68$  mN, and this phenomenon may be related to material properties and surface quality.

**Fig. 13** Normalized curves of  $F_{fmax} - F_n$



## 4 Conclusion

The paper introduced the developed low-frequency reciprocating–fretting ball-on-flat tribometer and measured friction coefficient from a steel ball sliding against PTFE, silicon wafer and glass. Based on Hertz contact theory, the contact stress and contact force were calculated by varying dynamic friction coefficient and conclusion was drawn that the friction force is not almost dependent of the normal load and contact deformation is at the nanoscale for a steel ball sliding on silicon wafer sample. Combined with the contact stress calculation, friction coefficient of different materials was measured by the developed tribometer to provide important information for the structural design of microcomponents before manufacturing MEMS devices.

## References

1. Sundararajan S, Bhushan B (2001) Static friction and surface roughness studies of surface micromachined electrostatic micromotors using an atomic force/friction force microscope. *J Vac Sci Technol, A* 19:1777
2. Alsofi MS, Chetwynd DG (2010) A novel design of multi-function micro-tribometer for MEMS/NEMS materials. Presented at the 4th Saudi international conference (SIC-04), Manchester, UK
3. Alsofi MS (2011) A high dynamic response micro-tribometer measuring-head, Coventry, University of Warwick
4. Wang J, Lu X et al (1998) Progress of micro-friction and micro-wear of material. *Progress Tribol* 2:38–49
5. Pymuza Z (1999) Control tribological and mechanical properties of MEMS surface. *Microsyst Technol* 5:173–189
6. Ding T, Wang F, Ren G (2008) Summary of micro-machine design theory and workmanship. *Mach Design Manuf* 12:236–238
7. Dong Y, Liu Y, Wen S (2005) Experimental study on relation between micro friction and surface topography 6:542–545

8. Antoine JF, Visa C, Sauvey C, Abba G (2006) Approximate analytical model for Hertzian elliptical contact problems. *J Tribol* 3:660–664
9. Jamari J, Schipper DJ (2007) Deformation due to contact between a rough surface and a smooth ball. *Wear* 4:138–145
10. Johnson KL (1985) *Contacts mechanics*. Cambridge University Press, London
11. Feng J, Tan Y (2009) Analysis of the slipping contact between a cylinder and a plane on the base of Hertz theory. *Tribology* 4:346–350

# Single-Phase AC Voltage Control Circuit for Flow-Induced Acoustic-Vibration Piezoelectric Generator

Bo Chen, Jiacun Sun, Hejuan Chen, Jian Yang and Wei Qu

**Abstract** Energy harvesting from ambient excitation has attracted numerous interests with the purpose of implementing self-powered devices. The technology of piezoelectric energy harvesting from vibrations induced by airflow is innovative research in the field of energy harvesting. A new flow-induced acoustic-vibration piezoelectric generator (FAPG) without any mechanical moving parts using this technology is developed. It converts the vibration induced by acoustic wave of external airflow inside the pipe into electrical energy via a piezoelectric transducer. Based on the scheme of FAPG using short pipe at the inlet of airflow, an effective output power conditioning circuit is designed. Simulation and experiments show that with the new designed interface circuit, which can expand the conduction angle of the Alternating Current (AC) output by FAPG, the efficiency of energy harvesting is improved significantly. In the circumstance of high-speed inflow and impedance matching, the FAPG can get high output power at consistent impedance matching points under various inflow velocities with strong practicability and flexibility.

**Keywords** Piezoelectric energy harvesting · Power conditioning circuit · Flow-induced · Acoustic-vibration · Impedance matching

## 1 Introduction

The energy conversion methods that have been used to transform ambient energy into electrical energy for self-driven and self-powered system are various [1]. One promising method is to convert the ambient vibrations induced by airflow during the flight into electricity using piezoelectric materials. A new piezoelectric energy generator using this technology is developed; it converts the vibration induced by acoustic wave of external airflow inside the pipe into electrical energy via a

---

B. Chen · J. Sun · H. Chen (✉) · J. Yang · W. Qu  
School of Mechanical Engineering, Nanjing University of Science and Technology,  
Nanjing 210094, Jiangsu, China  
e-mail: hjchen@njjust.edu.cn



piezoelectric transducer [2]. As the velocity and pressure of the wind flow fluctuate randomly, the output voltage or power of the flow-induced acoustic-vibration piezoelectric generator (FAPG) is unstable without airflow regulation. Therefore, an annular air flow regulation inlet structure is adopted based on the numerical simulation of internal flow field and blowing experiment analysis [3, 4]. The result shows that the short inlet of annular nozzle at uniformed section has features of slowed flow, faster uniformly distribution of velocity by section achieved, and shorter initial transition position [5], which obviously shows the influence of air-flow rectification. Based on the scheme of FAPG using short pipe at the inlet of airflow, an effective power conditioning circuit is designed.

Designed by the principle of maximize transferred energy, the impedance of the piezoelectric generator and interface circuit should be matched for this purpose. Though single-phase alternating current (AC) could be generated stably from the generator, perfect impedance match between piezoelectric transducer and the interface circuit could not always be expected due to some possible deviations caused by structure, material, and process [6]. In the case of impedance mismatch, the output of the FAPG drops remarkably. On the other hand, the control circuit of the system is mostly in low-power or idle state, fully loaded state usually lasts for a short period. The power consumption varies from hundreds of nanowatts to dozens of milliwatts, or even a couple of watts. Distinguished from traditional power supply, the output impedance of the capacitive-piezoelectric transducer can reach thousands of ohms while the load impedance is usually in the range between tens and hundreds of ohms. This mismatch between the power supply and the load would cause loss during the power transmission. Impedance mismatch and wide range of power consumption will severely affect proper power supply, which is a seriously outstanding problem for power source generated from piezoelectric transducer. Therefore, a suitable energy harvesting interface circuit of impedance matching is necessary. However, the most used classic energy harvesting circuit only fits in with low frequency, while the vibration frequency of flow-induced vibration source is over 6 kHz. As a result, transformation of classic energy harvesting circuit is needed in order to match up with energy harvesting of high frequency.

## 2 Methods

### 2.1 *Operating Principle of FAPG*

Figure 1 shows the structure of FAPG. The air flow generates edge tone by hitting onto the resonant cavity edge (wedge structure) through an annular air flow modulation inlet structure, forcing the air inside the cavity resonating, then standing-wave resonance occurs in the cavity, where at the bottom the sound pressure is the greatest. Vibration from the bottom sound pressure acts on the surface of piezoelectric element, transduced into output voltage. On the basis of

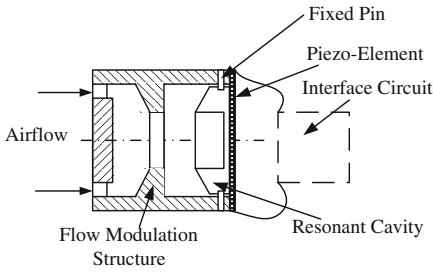


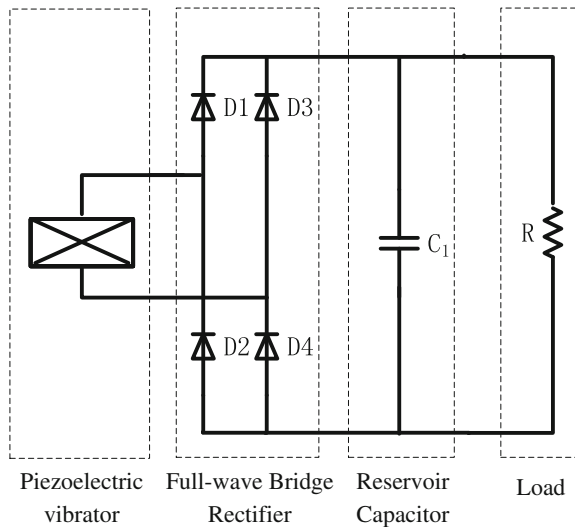
**Fig. 1** The structure of FAPG

resonance principle, the system is in resonance and the vibration amplitude as well as the output of the electric energy of piezoelectric transducer is maximized, on the condition that natural frequency of piezoelectric transducer equals to the excitation frequency. After power conditioning by the interface circuit, optimum matching between piezoelectric transducer and interface circuit (with load) can be obtained.

### 2.2 Interface Circuit Under Steady-State Sine Excitation

Classic energy harvesting circuit consists of full bridge rectifier, reservoir capacitor, and the load, as shown in Fig. 2. Under steady-state sine excitation, electric current will go through bridge rectifier and supply power for load  $R$  only when AC voltage in the piezoelectric elements is greater than voltage of reservoir capacitance  $C_1$  over

**Fig. 2** Classic energy harvesting circuit



a period of time. AC voltage generated by piezoelectric transducer charges  $C_1$  via bridge rectifier. Conduction angle of diode in bridge rectifier in this case is small, correspondently current distortion will happen, lowering the energy harvesting efficiency.

By adopting valley fill circuit [7, 8] shown in Fig. 3, cascading the combined circuit of diode and capacitor between bridge rectifier and the load, the distorted current waveform can be corrected to an almost perfect sine waves. As a result, valley fill circuit can increase on-time of circuit over a period of time, at the same time, conduction angle of rectifier diode expands from the original  $120^\circ$ – $150^\circ$ , achieving the goal of increasing energy harvesting efficiency.

### 2.3 Experimental System Setup

The experimental setup is shown in Fig. 4. The three main subsystems of the setup are airflow simulation system, electrical measuring system, and test specimen. Airflow simulation system mainly consists of air compressor, air drying machine, air tank, reducing valve, as well as, flow meter. Test specimens are mainly made up of air inlet, annular nozzle, resonate cavity, piezoelectric vibrator, and cover plate. Glue the PZT-5H piezoelectric ceramics of  $\varnothing 10$  mm to copper substrate of  $\varnothing 12$  mm, forming piezoelectric vibrator. During the experiment, open the valve of tank outlet, letting the airflow go through flow meter, injecting into FAPG. The flow

**Fig. 3** Valley fill energy harvesting circuit

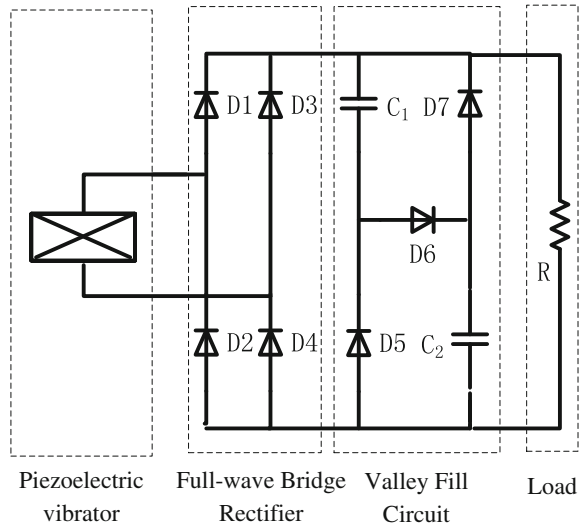


**Fig. 4** The experimental system diagram

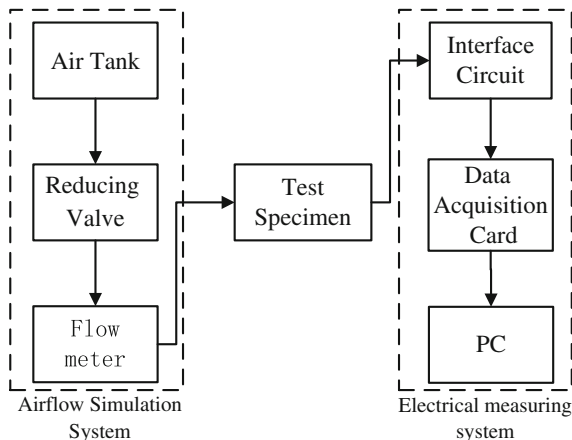


**Table 1** Relationship between volume flow ( $Q$ ) and airflow velocity ( $V$ )

Volume flow $Q$ (L/min)	160	180	200	220	240	260	280
Velocity $V$ (m/s)	106	119	133	146	159	172	186

velocity injected is controllable at the valve by observing the readout of the flow meter. Airflow enters test specimen, making the piezoelectric vibrator outputs voltage signal. Conditioned by the interface circuit, the output signal is sampled by data acquisition card and saved in the computer.

Relationship between airflow velocity ( $V$ ) and volume flow ( $Q$ ) can be expressed by  $V = Q/S$ , where  $S$  is the cross-section area of the annular nozzle, therefore, the airflow velocity can be obtained by measuring the inlet volume flow.

Table 1 shows the relationship between inlet volume flow and velocity of annular nozzle section of transducer.

## 2.4 Multisim Simulation

To determine the generator’s power flow characteristics, the piezoelectric vibrator can be modeled as sinusoidal current source  $I_p(t)$  in parallel with its internal electrode capacitance  $C_p$  [9]. Simulate classic energy harvesting circuit and valley fill energy harvesting circuit of FAPG through Multisim circuit simulation software of NI (as shown in Fig. 5 for classic circuit, where piezoelectric vibrator model is the same for the valley fill circuit, not shown), making simulation of FAPG harvesting energy from vibration under stationary excitation.

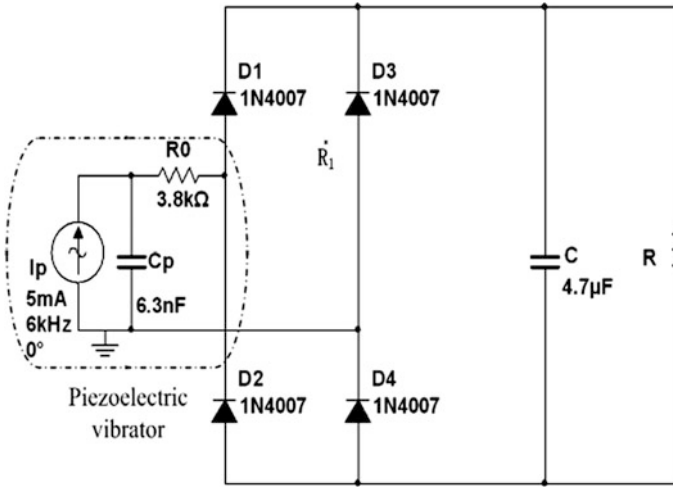


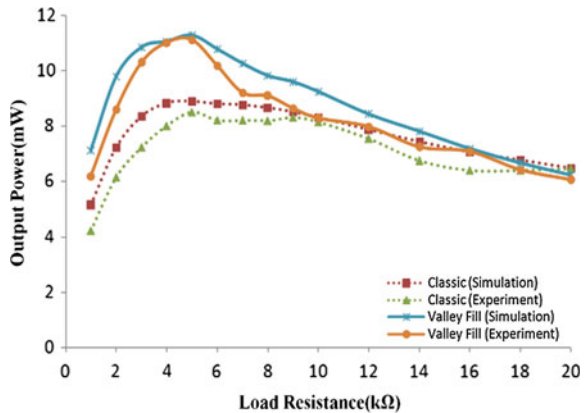
Fig. 5 Multisim simulation

### 3 Results

#### 3.1 Simulation Versus Experiment

The FAPG output signal keeps roughly the same with the output signal under multisim simulation parameters setting in Fig. 5 when airflow is at the high speed of 186 m/s. The experimentally measured and simulated variations of power output with increasing load are shown in Fig. 6. The simulation result is close to the experimental result, which shows the validity of the equivalent model of piezoelectric vibrator presented in Fig. 5.

Fig. 6 Experiment and simulation output power versus load resistance



### 3.2 Experiment Output Voltage and Power Versus Load Resistance at Various Inflow Velocity

Connect piezoelectric transducer to classic energy harvesting circuit and valley fill energy harvesting circuit separately and get the variation curve reflecting that output voltage ( $U$ ) and load power ( $P$ ) change with variant load ( $R$ ) at variable inflow velocity ( $V$ ) through regulating inflow volume ( $Q$ ).

As demonstrated in Figs. 7 and 8, voltage and power of each circuit, respectively, keep roughly the same change trend with load resistance no matter at high inflow velocity or low inflow velocity. As for the valley fill circuit, the output voltage increases rapidly with an increasing load resistance initially; when the load resistance reaches 5 k $\Omega$ , the output voltage increases slowly with increasing load

Fig. 7  $U$  versus  $R$

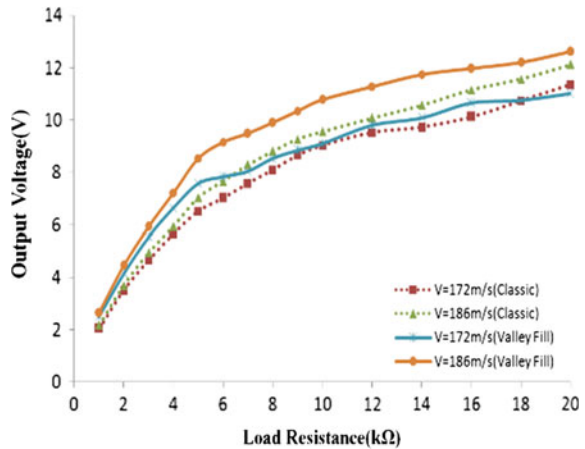
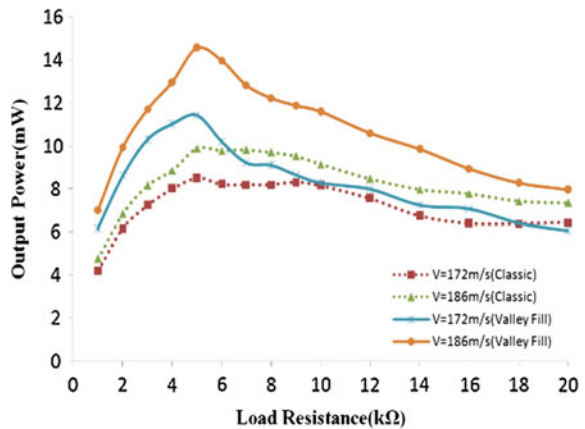


Fig. 8  $P$  versus  $R$



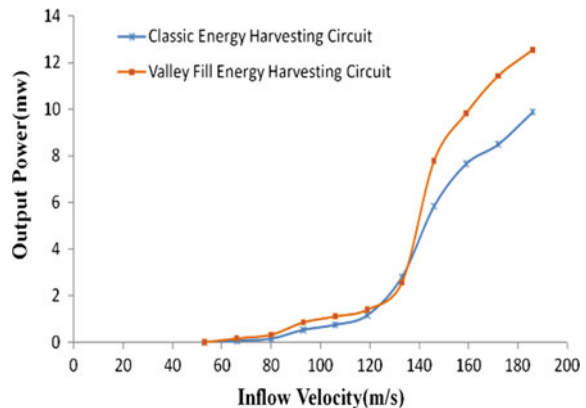
resistance. However, the output power increases gradually with an increasing load resistance until a critical value is reached and then decreases.

Nevertheless, at low inflow velocity ( $V$ ), output voltage and power of classic energy harvesting circuit turn greater than that of valley fill circuit after the load resistance has increased to a certain degree, due to the fact that the generator's output energy is not that great at low inflow velocity, while the valley fill circuit consumes more energy with more components than classic energy harvesting circuit, to this extent, the valley fill circuit shows no advantages. Therefore, when designing low-power piezoelectric generators, power dissipation in the electronic components needs to be considered. On the other hand, power dissipation due to diode voltage drop is also significant at lower generator output voltages, hence Schottky junction diodes, with lower drop compared to PN junction diodes, are often favored as the rectifying elements in applications.

As shown in Fig. 8, variant inflow velocity and interface circuit share the same matching point, impedance matching point of load power in both circuits keeps at 5 k $\Omega$ . It should be noted that once a unique peak power is detected at a specific inflow velocity ( $V$ ) (i.e. 172 m/s), the corresponding impedance matching point is safe to be employed for other inflow velocity ( $V$ ), as the impedance matching point for the FAPG with the two circuit remains constant with various inflow velocity ( $V$ ). Valley fill circuit outstrip classic energy harvesting circuit when the output power is around the impedance matching point, while rigorous impedance matching is necessary otherwise its output power would drop more dramatically.

Output power when impedance matched of both circuit under the excitation of variant inflow velocity is shown in Fig. 9. When the inflow velocity is below 140 m/s, the FAPG outputs insufficient energy, and the valley fill circuit shows no superiority over classic circuit due to more power dissipation in the electronic components of valley fill circuit. However, when the inflow velocity is over the critical speed of 140 m/s, the generator outputs enough energy so that the dissipation in the electronic components could be neglected. When the inflow velocity reaches 186 m/s, load output power of valley fill circuit ends up to 12.55 mW, a quarter more than that of the classic circuit, which is 9.89 mW.

**Fig. 9** Output power versus inflow velocity



## 4 Conclusion

When the inflow velocity is high, the FAPG without any mechanical moving parts holding excellent shock resistance and fast dynamic response has stable impedance matching points which remain unchangeable with variant inflow velocity and interface circuit, making it with strong practicability and flexibility. Simulation and experiment results indicate that the current conduction angle of valley fill circuit increases to  $150^\circ$  from  $120^\circ$  of classic energy harvesting circuit. Due to the component dissipation in the circuit, when the inflow velocity is high, more energy would get transduced, valley fill circuit surpasses in energy harvesting efficiency, and when the inflow speed is low, classic energy harvesting circuit with low-power dissipation is rather suitable.

**Acknowledgements** The research is financially supported by the National Natural Science Foundation of China under contract No. 51377084.

## References

1. Chen R (2011) New ambient energy harvesting technology. National Defence Industry Press, China
2. Zou H, Chen H, Liang Y et al (2015) Study of drive characterization of fuze vibration piezoelectric generator based on airflow-induced sound[J]. *Acta Armamentarii* 36(4):610–618
3. Na Lv (2012) Numerical simulation of turbulent flow in the airflow control inlet of the new pneumatic piezoelectric generator of missile-borne fuze. Nanjing University of Science and Technology, Nanjing
4. Zhu X (2012) Technologies for the airflow induced vibration and experimentation on the miniature vibration piezoelectric generator. Nanjing University of Science and Technology, Nanjing
5. He P (2012) Simulation of flow field in the airflow control inlet of the new pneumatic piezoelectric generator of missile-borne fuze. Nanjing University of Science and Technology, Nanjing
6. Priya S, Inman DJ (2009) Energy harvesting technologies. Springer Science and Business Media, Berlin
7. Wen D, Chen H, Cai J (2014) A method of compensating reactive power for high-specific piezoelectric power generator. *Ordnance Industry Automation* 2011(11):81–85
8. Qu W (2014) Energy harvesting technology for the fuze airflow induced vibration piezoelectric generator. Dissertation, Nanjing University of Science & Technology
9. Ottman G, Hofmann F, Bhatt A (2012) Adaptive piezoelectric energy harvesting circuit for wireless remote power supply. *IEEE Trans Power Electron* 17(5):669–675



# Medium and Long-Term Electric Power Planning Load Forecasting Based on Variable Weights Gray Model

Da Song and Xiaobo Liu

**Abstract** Based on the gray forecasting theory, the paper studies the influence of the buffer operator on the gray forecasting results, and solves the problems of the traditional gray model in the medium and long-term electric load forecasting. By constructing the buffer operator, the dynamic preprocessing of the raw load data is realized. Based on particle swarm optimization (PSO) algorithm, taking the maximum gray correlation degree between fitted value and actual values as the goal, to choose the optimal buffer operator and buffer system, which can reasonably weak the historical load data, improve precision of the model and make a prediction results more reasonable real.

**Keywords** Gray model · Buffer operator · Power planning load forecasting · PSO

## 1 Introduction

In medium and long-term power grid planning, the accuracy of load forecasting directly determines the construction goal of power grid in the next period of time [1], so load forecasting demand has enough accuracy and stability. The medium and long-term power load has not only a certain growth, but also an uncertainty fluctuation, it will go up and down depending on regional economic development, policy bias, natural factors, and so on. Overall, the load changing can still be considered nearly to be exponentially growth. So this kind of power load fore-

---

D. Song (✉)

Power System and Its Automation, Power Grid Planning,  
School of Electrical Engineering, GuiZhou University, Guiyang 550000, China  
e-mail: dsong1990@foxmail.com

X. Liu

High Voltage Technology, School of Electrical Engineering,  
GuiZhou University, Guiyang 550000, China  
e-mail: 799797284@qq.com

© Springer-Verlag Berlin Heidelberg 2016

B. Huang and Y. Yao (eds.), *Proceedings of the 5th International Conference on Electrical Engineering and Automatic Control*, Lecture Notes in Electrical Engineering 367, DOI 10.1007/978-3-662-48768-6\_16

137

casting can be regarded as a typical gray system [2]. However, its mutability predicted modeling which directly use original GM(1,1) model may cause the model error bigger, or better fitting effect but prediction effect is poorer. Building the GM(1,1) by using buffer operator to preprocess the original data, which can effectively improve the modeling sequence smooth ratio, weakens the randomness of the original load data, strengthens the overall trend in the development of load, and improves the prediction precision [3–5]. However, there are still problems in the application of buffer operator in practical load forecasting: first, the buffer effect of different buffer operator is different, which may lead to the decrease of prediction accuracy; second, the buffer operator is not adjustable, only through a qualitative judgment or subjective experience to choose a fixed buffer operator for data preprocessing, which often lead to the buffer effect too strong or too weak, poor adaptability and not be generalizable. Weak buffering effect will lead to the pretreatment effect which is not obvious, model predictive accuracy improvement limited. Strong buffering effect will change the inner rule of the original load sequence. Although it can realize high precision fitting of sequence after pretreatment, but it has deviated from the original load forecasting problem.

## 2 The Load Data Processing Based on Variable Weights Buffer Operator

Aiming at the shortage of the traditional buffer operator, the paper introduces the variable weights buffer weakening operator, which can reduce the original data adaptively and reduce the impact of accidental factors on the load data.

Given:  $X = [x(1), x(2), \dots, x(n)]$  is original data sequence,

$$Y = XD = [x(1)d, x(2)d, \dots, x(n)d] \quad (2.1)$$

where  $d$  is buffering operator;  $x(n) > 0$

$d$  is about the structure of  $\lambda$ ,  $\lambda$  is variable weights buffer coefficient.

This paper construct buffer operator as follows:

$$x(k)d_1 = \frac{\lambda x(k) + x(n)}{\lambda + 1} \quad \text{where } 0 < \lambda < 1, k = 1, 2, \dots, n. \quad (2.2)$$

$$x(k)d_2 = \lambda x(n) + (1 - \lambda)x(k) \quad \text{where } 0 < \lambda < 1, k = 1, 2, \dots, n. \quad (2.3)$$

$$x(k)d_3 = \frac{x(n)^{1+\lambda}}{x(k)^\lambda} \quad \text{where } 0 < \lambda < 1, k = 1, 2, \dots, n. \quad (2.4)$$

**Definition**  $X = [x(1), x(2), \dots, x(n)]$  is non-negative sequences of system behavior,  $r(k)$  is the average change rate from  $x(k)$  to  $x(n)$  which is included in  $X$ ,  $X$  with the buffer operator get the new sequence:

$$XD = [x(1)d, x(2)d, \dots, x(n)d] \tag{2.5}$$

and  $\delta(k) = \left| \frac{r(k)-r(k)d}{r(k)} \right|$ ,  $k = 1, 2, \dots, n$  is the degree of regulation which buffer operator  $D$  act on  $k$  point.

The degree of regulation  $\delta(k)$  reflects the action intensity of buffer operator to the original load data. By choosing an appropriate buffer operator model and the buffer coefficient  $\lambda$ , we can fine tune the strength of the buffer operator, and enhance the adaptability of the buffer operator in the load data preprocessing.

### 3 Modeling Process of Variable Weights Buffer GM(1,1) Model

In order to weaken the random fluctuations of the data, highlight the inherent law of the sequence, improve the prediction accuracy, using the variable weight buffer operator and background value optimization to improve the traditional GM(1,1), build the variable weights buffer GM(1,1), and model the variable weight buffer model. Taking the type (2.3) model as an example, build the model as follow:

1. The original load data is

$$X^{(0)} = [x^{(0)}(1), x^{(0)}(2), \dots, x^{(0)}(n)] \tag{3.1}$$

2. Using the variable weights buffer operator ( $D$ ) to preprocess the original data sequence weakens the randomness and enhances the trend.

$$\begin{cases} Y^{(0)} = [y^{(0)}(1), y^{(0)}(2), \dots, y^{(0)}(n)] \\ y^{(0)}(k) = \lambda x^{(0)}(n) + (1 - \lambda)x^{(0)}(k), \quad k = 1, 2, \dots, n \end{cases} \tag{3.2}$$

3. AGO, forming the weakening data sequence model

$$\begin{cases} Y^{(1)} = [y^{(1)}(1), y^{(1)}(2), \dots, y^{(1)}(n)] \\ y^{(1)}(k) = \sum_{i=1}^k y^{(0)}(i), \quad k = 1, 2, \dots, n \end{cases} \tag{3.3}$$

4. Build the variable weights background value ( $Z^{(1)}$ )

$$\begin{cases} Z^{(1)} = [z^{(1)}(2), z^{(1)}(3), \dots, y^{(1)}(n)] \\ z^{(1)}(k) = \eta y^{(1)}(k - 1) + (1 - \eta)y^{(1)}(k), \quad k = 2, 3, \dots, n \end{cases} \tag{3.4}$$

where  $\eta$  is the weight coefficient of the background,  $0 \leq \eta \leq 1$ .

### 5. Build GM(1,1) model

$$y^{(0)}(k) + az^{(1)}(k) = b \quad (3.5)$$

where  $a, b$  are model parameters, using least square method to get the value of  $a, b$

$$[a, b]^T = (B^T B)^{-1} B^T Y \quad (3.6)$$

$$B = \begin{bmatrix} -z^{(1)}(2) & 1 \\ -z^{(1)}(3) & 1 \\ \vdots & \vdots \\ -z^{(1)}(n) & 1 \end{bmatrix}, \quad Y = \begin{bmatrix} y^{(0)}(2) \\ y^{(0)}(3) \\ \vdots \\ y^{(0)}(n) \end{bmatrix} \quad (3.7)$$

### 6. The time response function model

$$\hat{y}^{(1)}(k) = \left( y^{(0)}(1) - \frac{b}{a} \right) e^{-a(k-1)} + \frac{b}{a}, \quad k = 1, 2, \dots, n \quad (3.8)$$

IAGO, get the forecast results

$$\hat{y}^{(0)}(k) = \hat{y}^{(1)}(k) - \hat{y}^{(1)}(k-1) \quad (3.9)$$

when  $\lambda$  and  $\eta$  equals 0.5, the model is the traditional GM(1,1) model.

## 4 Optimization of Model Parameters Based on Gray Correlation Analysis

From the formula (3.1) to (3.5), it is can be seen that buffer operator mode and background function are the most important factors which can affect the gray model forecasting precision. In order to find the optimal value of  $\lambda$  and  $\eta$ , the particle swarm optimization (PSO) is used to solve the problem, and the influence of different buffer operators on the prediction results is compared with different buffer operators [6–8].

When building the particle fitness function, the method with the average fitting error minimum as the objective often is used. But, this method is easy to fall into local optimum, which leads to higher accuracy of fitting precision and poor prediction accuracy. At the same time, considering the variable weights buffer gray model which uses the weakening data, preprocessing data, to build the GM(1,1) mode could lead to the predicted value to highly fit the weakening data, but deviate the original load if the minimal average relative error which it gets from comparing with the weakening data is seen as the goal. To avoid these problems, this paper

based on the gray relational analysis, the maximum gray relational between fitted and actual value is treated as the goal to construct a function. To ensure that prediction results maximally keep inherent variation rules of the original load sequence, and to avoid the local optimum.

Let  $X^{(0)} = [x^{(0)}(1), x^{(0)}(2), \dots, x^{(0)}(n)]$  be an original load sequence,  $\hat{Y} = [\hat{y}(1), \hat{y}(1), \dots, \hat{y}(n)]$  is the fitted sequence based on  $X$  modeling. So the gray correlation degree between  $X$  sequence and  $\hat{Y}$  sequence is:

$$\gamma(X, \hat{Y}) = \frac{1}{n} \sum_{k=1}^n \gamma(x(k), \hat{y}(k)) \tag{4.1}$$

$$\gamma(x(k), \hat{y}(k)) = \frac{\min_k |x(k) - \hat{y}(k)| + \rho \max_k |x(k) - \hat{y}(k)|}{|x(k) - \hat{y}(k)| + \rho \max_k |x(k) - \hat{y}(k)|} \tag{4.2}$$

where  $\rho$  is resolution ratio,  $0 < \rho < 1$ .

Gray correlation degree reflects the sequence curve similar degree. The greater gray correlation degree between fitted sequence and original load sequence is, the better the result is. So, the model considers both fitting and prediction. Let the maximum value of gray correlation degree between fitted sequence and load sequence is the object, the fitness function got is.

$$f[(\lambda, \eta)_i] = \max \left[ \frac{1}{n} \sum_{k=1}^n \gamma(x^{(0)}(k), \hat{y}^{(0)}(k)) \right] \tag{4.3}$$

Using MATLAB, PSO algorithm with gray correlation fitness function can be realized, to improve the traditional gray model and improve the accuracy of load forecasting.

## 5 Computational Analysis of Examples

In order to verify the validity and the accuracy of the gray model in the medium and long-term power load forecasting. 2005–2014 total social electricity consumption data are used as example. Compared the traditional GM(1,1) and the variable weight buffer GM model with the formulas (2.2)–(2.4) as the buffer operator, we can analysis the advantage of the model.

With the 2005–2011 load data as the raw data (see Table 1), the 2012–2014 load is predicted. From Table 1, we can see that the growth of electric power load is random, but also has a stable growth trend. Using (2.2)–(2.4) as the buffer operator build three optimizing models, respectively. The fitted results are shown in Tables 1, 2 and 3.

**Table 1** 2005–2011 total electricity consumption data of China and model 1 fitting results

Year	Actual value	Optimization model 1			
		Weakening data	Fitted value	The relative error compared to weakening data (%)	The relative error compared to actual data (%)
2005	2.494	2.6340	2.634	0.00	5.61
2006	2.9368	3.0960	3.0821	-0.45	4.95
2007	3.2458	3.4081	3.3846	-0.69	4.28
2008	3.4268	3.5362	3.5786	1.20	4.43
2009	3.643	3.6882	3.7531	1.76	3.02
2010	4.1923	3.9577	3.9343	-0.59	-6.15
2011	4.6928	4.5715	4.7224	3.30	0.63
Average relative error (%)	-	-	-	1.14	4.15
Gray correlation degree	0.6914				

**Table 2** 2005–2011 total electricity consumption data of China and model 2 fitting results

Year	Actual value	Optimization model 1			
		Weakening data	Fitted value	The relative error compared to weakening data (%)	Weakening data
2005	2.494	2.5164	2.5164	0.00	0.90
2006	2.9368	2.9522	2.9861	1.15	1.68
2007	3.2458	3.3940	3.4283	1.01	5.62
2008	3.4268	3.4984	3.5404	1.20	3.32
2009	3.643	3.8206	3.7996	-0.55	4.30
2010	4.1923	4.1074	4.0778	-0.72	-2.73
2011	4.6928	4.3616	4.3764	0.34	-6.74
Average relative error (%)	-	-	-	0.71	3.61
Gray correlation degree	0.8119				

The results obtained by the three different buffer models can be seen in the use of PSO algorithm for the global optimization of the buffer coefficient and background values, the average fitting error is smaller, the same prediction error is within a reasonable range, and the long-term load forecasting results are stable and the accuracy is higher. Compared with the results of Tables 1, 2 and 3, it is seen that model 3 fitted effects is better than that of model 1 and model 2. The average fitted relative error of model 3 is 0.69. The relative prediction error of model 3 is 3.1 %, which is obviously better than the model 1, but the gray correlation degree of model 2 is 0.8119, which is obviously larger than model 1 and model 3. The model 2 reflects the relevance of the original load data, better grasps the development trend

**Table 3** 2005–2011 total electricity consumption data of China and model 3 fitting results

Year	Actual value	Optimization model 1			
		Weakening data	Fitted value	The relative error compared to weakening data (%)	Weakening data
2005	2.494	2.6117	2.6117	0.00	4.72
2006	2.9368	2.9391	2.9591	0.68	0.76
2007	3.2458	3.2724	3.24526	-0.83	-0.02
2008	3.4268	3.5039	3.45169	-1.49	0.73
2009	3.643	3.7009	3.70086	0.00	1.59
2010	4.1923	3.9316	3.97725	1.16	-5.13
2011	4.6928	4.2543	4.2828	0.67	-8.74
Average relative error (%)	-	-	0.69	-	3.10
Gray correlation degree	0.6569				

**Table 4** Forecasting results of three models

Year	Actual value	Optimization model 1		Optimization model 2		Optimization model 3	
		Predicted value	Relative error (%)	Predicted value	Relative error (%)	Predicted value	Relative error (%)
2012	4.9591	5.3176	7.23	4.6968	-5.29	4.8199	-2.81
2013	5.3223	5.5203	3.72	5.0406	-5.29	5.0199	-5.68
2014	5.5233	5.7308	3.76	5.4097	-0.02	5.3983	-2.26
Average relative error (%)	-	4.90	-	3.53	-	3.58	-

of load data, maintains the intrinsic development trends, and changes, more consistent with the law of long-term load development.

2005–2011 total social electricity consumption data are used as the model data, to forecast 2012–2014 national total social electricity consumption with the three kinds of optimization model. The results are shown in Table 4.

The prediction result of Table 4 shows that the average relative error for the optimization model 2 is 3.53 %. In the three models, the prediction result for model 2 is the best. So, this confirms the above analysis result, it will meet the requirements of medium and long-term load forecasting and provide a good load basis for power grid planning.

## 6 Conclusions

1. In this paper, it introduces the variable weight buffer operator to preprocess dynamically the original load data and constructs three different kinds of buffer models to obtain the optimal buffer gray model and buffer effect.

2. The gray correlation degree is introduced as the optimal object, with PSO to optimize parameters; it can save the data intrinsic change rule possibly and make the forecast results more accurate.

## References

1. Niu D, Cao S, Zhao L (1998) Power load forecasting technology and its application. China Electric Power Press, Beijing
2. Liu S, Xie N et al (2008) The grey system theory and its application, 4th edn. Science Press, Beijing
3. Wang Z, Dang Y, Liu S (2009) Buffer operators with variable weights and the complement of axioms. *Syst Eng* 27(1):113–117
4. Liu S (1997) The trap in the prediction of a shock disturb system and the buffer operator. *J Huazhong Univ Sci Technol* 25(1):25–27 (in Chinese)
5. Dang Y, Liu S et al (2004) Study on the buffer weakening operator. *Chin J Manage Sci* 12(2):108–111
6. Yang H, Bi Z (2011) Particle swarm optimization-based grey model for long term load forecasting. *Electr Measur Instrum* 48(2):40–44 (in Chinese)
7. Bunn DW (1989) Forecasting with more than one model. *J Forecast* 8(3):161–166
8. Granger CWJ (1989) Combining forecasts-twenty years later. *J Forecast* 8(3):167–173



# Combination and Optimization Load Forecasting Based on Credibility

Jia-liang Chen, Shu-bo Hu, Wei Zhou, Lin Zhao, Jian-ming Yu,  
Guo-hui Shen and Jing-jie Sun

**Abstract** Load forecasting is based on the known history of electricity demands, and it considers political, economic, and climate factors to make forecasting for the future electricity demands. This article first analysis the trends of history power load, and then choose load forecasting methods according to the trends. Through the analysis and comparison of the load forecasting methods' credibility, assess the adaptability between forecasting methods and power load integrated. Higher credibility load forecasting methods are got through credibility sorting and then weights for each method are solved by optimization. The sorted load forecasting methods are combined together to forecast load power. Then to make the forecasting result more accuracy, after-test residue checking method is used to test the forecasting results. Forecasting electricity consumption of local actual operation power load and getting high credibility forecasting results can ensure the construction of local power grid develop with correct direction.

**Keywords** Combination forecasting · Credibility · Mid-long term load forecasting · Optimization forecasting · Electricity consumption forecasting

---

J. Chen (✉)

State Grid Putian Electric Power Supply Company, Putian 351100, China  
e-mail: 562589482@qq.com

S. Hu · W. Zhou

School of Electrical Engineering,  
Dalian University of Technology, Dalian 116024, China

L. Zhao · J. Yu · G. Shen

China Electric Power Research Institute, Beijing 100192, China

J. Sun

State Grid Dalian Electric Power Supply Company, Dalian 116000, China

© Springer-Verlag Berlin Heidelberg 2016

B. Huang and Y. Yao (eds.), *Proceedings of the 5th International Conference on Electrical Engineering and Automatic Control*, Lecture Notes in Electrical Engineering 367, DOI 10.1007/978-3-662-48768-6\_17

## 1 Introduction

Mid-long term load forecasting is an important part of power system planning. Scientific and reasonable load forecasting is important for power system planning, electricity consumption, and other work. Each load forecasting method has its own special trend. In the actual application load forecasting, historical data do not meet only one trend and characteristic. Single forecasting method would not be suitable for all power load trends. It will lead to large errors. So, combination load forecasting method is needed to analysis power load synthetically.

Various techniques and methods have been developed to solve load forecasting in power system. Reference [2] presented to the residual sum of squares and to minimize the objective function of the integrated model for load forecasting, and according to the characteristics of the model, given easily approximate solving method of comprehensive prediction model. Reference [8] gives the traditional electricity consumption elasticity coefficient method which is improved, combined with grey prediction model and the second moving average forecasting method, and establishes a new comprehensive prediction model and a genetic algorithm to optimize the weight of each single model. Reference [5] presents a method based on least squares methods. Reference [7] proposes a method based on two indexes to calculate the weight of each single model. Reference [1] proposes a combined forecasting algorithm based on Markov model using linear phase bi-orthogonal Wavelet features, the load time series wavelet multi-resolution decomposition. It uses soft-threshold method to detect and deal with bad signal, using the signal fuzzy Markov prediction model is established, by the prediction of the load sequence values are combined to get the final result. Also intelligence algorithms model can be used to establish the credibility evaluation or to select the credibility of related factors of prediction error [3, 4].

In this article, credibility of single forecasting method in combination is sorted and selected. According to this, this article presents a mid-long term combination load forecasting method based on credibility assessment of power system. Then optimization model based on interior point method is built to obtain weights of the combination method, and more accurate forecasting results are got. Assess the results through the after-test residue checking method and the accuracy level of the forecasting methods can be got.

## 2 Credibility Assess of Load Forecasting Methods

Credibility of forecasting methods is different from forecasting accuracy and relative error. The errors come from forecasting results and actual values. Relative errors cannot assess the adaptation of forecasting methods and load data, as well as

the credibility of the results comprehensively. Credibility is based on the load forecasting error, but more comprehensive than error. The method is defined as credibility of standard relative error, such as Eq. (1.1):

$$E_i = \frac{D_{\text{forecast}}^i - D_{\text{actual}}^i}{D_{\text{actual}}^i}, \quad R_i = \sqrt{E_{i1}^2 + E_{i2}^2 + E_{i3}^2 + \cdots + E_{im}^2} \quad (1.1)$$

$$\text{Con}_i = \frac{1}{R_i} \quad (i = 1, 2, 3, \dots, n)$$

In this formula: Con is forecasting credibility;  $R$  is the standard relative error of forecasting result;  $E$  is the relative error;  $D_{\text{forecast}}$  is load forecasting result;  $D_{\text{actual}}$  is the actual load value.

## 2.1 Combination Load Forecasting Mathematical Model

The key of combination load forecasting is to determine the weights distribution of the selected forecasting methods. The optimization function, which is the fitting standard variance of forecasting results, is minimal. The optimization function is like Eq. (1.2):

$$\min f(x) = \sqrt{((x_1 D_{\text{forecast}}^1 + x_2 D_{\text{forecast}}^2 + \cdots + x_n D_{\text{forecast}}^n) - D_{\text{actual}})^2} \quad (1.2)$$

In this formula:  $x_n$  is the weight of the  $n$ th forecasting method;  $D_{\text{forecast}}^n$  is the forecasting value of the  $n$ th forecasting method and  $D_{\text{actual}}$  is the actual load value. The equality constraint is like Eq. (1.3):

$$x_1 + x_2 + \cdots + x_n - 1 = 0 \quad (1.3)$$

Namely, all weights sum together as 1. The inequality constraint is as Eq. (1.4):

$$0 \leq x_i \leq 1 \quad (1.4)$$

The single weight value can take 0 or 1. When the fitting standard variance of forecasting results of the selected method is much higher than the other methods, the weight takes 0. When the fitting standard variance of forecasting results of the selected method is much lower than the other methods, the weight can take 1. The weights are solved and optimized through the primal-dual Interior point method [11].

## 2.2 After-test Residue Checking

How to choose the forecasting method is not only based on credibility assessment, but also based on multiple checking to judge the reasonability and effectiveness. Only the method through the checking can be used in practical load forecasting.

$X$  is the original load series and  $\hat{X}$  is the forecasting load series, Eq. (1.5) are given on mathematical definition:

$$\begin{aligned} \bar{X} &= \frac{1}{n} \sum_{k=1}^n X(k), & S_1^2 &= \frac{1}{n} \sum_{k=1}^n (X(k) - \bar{X})^2, & \bar{\varepsilon} &= \frac{1}{n} \sum_{k=1}^n \varepsilon(k), \\ \varepsilon(k) &= X(k) - \hat{X}(k), & S_2^2 &= \frac{1}{n} \sum_{k=1}^n (\varepsilon(k) - \bar{\varepsilon})^2 \end{aligned} \quad (1.5)$$

In this formula:  $\bar{X}$  is the average value of the original load series and  $S_1^2$  is the variance of the original load series.  $\varepsilon(k)$  is the error of the original load series and  $\bar{\varepsilon}$  is the average value of the residual error series.  $S_2^2$  is the variance of the residual error series.

In the after-test residue checking, two checking parameters are defined: average variance ratio and small error probability. The average variance ratio is expressed as Eq. (1.6):

$$C = \frac{S_2}{S_1} \quad (1.6)$$

In this formula:  $S_1$  is the standard deviation of the original load series and  $S_2$  is the standard deviation of the original residual error series.

The small error probability is expressed as Eq. (1.7):

$$p = P(|\varepsilon(k) - \bar{\varepsilon}| < 0.6745S_1) \quad (1.7)$$

In this formula:  $\varepsilon(k)$  is the error of the original load series and  $\bar{\varepsilon}$  is the average value of the residual error series.

In this two checking parameters, the average variance ratio  $C$  is the smaller the better. The smaller  $C$  is, the smaller  $S_2$  is, and the bigger  $S_1$  is. Then the volatility of original load is large, and the volatility of forecasting load is small, for which the forecasting results are concentration and the forecasting effect is better. In the other side, the small error probability  $p$  is the larger the better. The larger  $p$  is, the more small error probable rates are. The error of the whole forecasting is small.

The accuracy calibration table of after-test residue checking [6] is as Table 1.

**Table 1** Accuracy calibration table

Accuracy calibration	Critical value	
	Average variance ratio	Small error probability
First	0.35	0.95
Second	0.5	0.8
Third	0.65	0.7
Fourth	0.8	0.6

**Table 2** The comparison table of electricity consumption forecasting methods' credibility

Forecasting method	Credibility	Sorting	Forecasting method	Credibility	Sorting
Least square	9.09	1	Tangent function	2.70	4
Quadratic function	1.69	6	Exponential fitting	5.56	3
Cubic function	2.17	5	Grey theory method	6.40	2

Table 2 shows the credibility sorting of the selected load forecasting methods. In combination forecasting, the first three high credibility forecasting methods are selected and combined together. Then the area electricity consumption is forecasted.

### 2.3 Combination Forecasting

The forecasting results and relative error comparison table of electricity consumption forecasting from January to June in 2013 show that combining the higher credibility forecasting methods together and doing the combination forecasting can make the overall forecasting results' relative error smaller. Judging from the overall forecasting results, the relative error of combination forecasting is smaller, and the credibility of combination forecasting is 17.63 which is far higher than other methods (Table 3).

In this article, the selected forecasting methods and the proposed combination and optimization load forecasting method are assessed by after-test residue checking method and the results of checking parameters are shown in Table 4.

Through comparing the results in Table 4 with the accuracy calibration in Table 1, we can know that the grey theory method, least square, and combination forecasting method all will reach the first level. The exponential fitting method is near the second and third level. Based on the after-test rule, the smallest average variance ratio is combination forecasting method, and secondly least square, grey theory method. The worst one is exponential fitting method.

**Table 3** The comparison table of electricity consumption forecasting from January to June in 2013

Month	Forecasting value				Actual value				Relative error			
	Grey	Least square	Exponential	Combination	Grey (%)	Least square (%)	Exponential (%)	Combination (%)	Grey (%)	Least square (%)	Exponential (%)	Combination (%)
January	24.29	23.92	21.03	23.17	23.62	1.27	10.97	1.93	2.82	1.27	10.97	1.93
February	21.30	21.01	20.37	20.59	19.78	6.21	2.98	4.09	7.68	6.21	2.98	4.09
March	22.92	22.36	20.85	22.00	21.67	3.19	3.78	1.51	5.74	3.19	3.78	1.51
April	23.41	22.82	21.19	22.49	22.19	2.84	4.51	1.35	5.51	2.84	4.51	1.35
May	22.06	21.57	20.03	21.25	20.96	2.91	4.43	1.41	5.26	2.91	4.43	1.41
June	22.57	21.96	20.31	21.83	21.58	1.73	5.89	1.14	4.55	1.73	5.89	1.14

**Table 4** Results of after-test residue checking method

Forecasting methods	Average variance ratio $C$	Small error probability $p$
Grey theory	0.2745	1
Least square	0.2423	1
Exponential fitting	0.6953	0.75
Combination forecasting	0.2397	1

### 3 Summary

Through credibility assessment and sorting of several load forecasting methods select adaptation load forecasting methods with power load data. Then high credibility forecasting methods are combined and optimized, and also the limitations of single forecasting method are weakened. After weights distribution, more credible results are given synthetically. Through assessment of credibility and combination load forecasting, the overall load forecasting credibility improved and the forecasting results are more accurate than the traditional single load forecasting.

### References

1. Guo K-L, Tan L-N, Huang H (2011) The application of wavelet packet based Markov Chain in short-term load forecasting. *Power Syst Prot Control* 39(6):66–701
2. Kang C, Xia Q, Shen Y et al (1999) Integrated model of power system load forecasting. *J Tsinghua Univ (Sci Technol)* 39(1):8–11
3. Li P, Yan Y, Zheng W-J et al (2010) Short-term load forecasting based on quantum neural network by evidential theory. *Power Syst Prot Control* 38(16):49–53
4. Ma X-S, Shi T-J (2008) Credibility theory based approach to build optimal bidding strategies with risk management for generation companies. *Power and energy society general meeting—conversion and delivery of electrical energy in the 21st century, 2008 IEEE*, pp 1–5
5. Miao Z, Wu H, Li T et al (2009) Application of combination determining weights method based on LAD to the power mid-long term load forecasting. *Power Syst Prot Control* 37(2):28–31
6. Ning X-X, Liu S-F (2009) *Management forecasting and decision-making method*. Science Press, Beijing, pp 113–145
7. Wen Q, Zhang X, Yang X (2011) The application of combination forecasting model in medium-long term load forecasting based on load error and economic development trend. *Power Syst Prot Control* 39(3):57–61
8. Yuan T-J, Yuan J-D, Chao Q et al (2012) Study on the comprehensive model of mid-long term load forecasting. *Power Syst Prot Control* 40(14):143–151

# Actuated Signal Control System for Pedestrian Street Crosswalk at Midblock Crossings

Longjian Wang, Yonggang Wang and Mengyang Xin

**Abstract** In order to enhance the midblock crossing safety of pedestrians at special locations, such as entrance of schools, hospitals, and supermarkets, the actuated signal control system is proposed to provide the special signal for vulnerable pedestrians' crossing behavior, especially for the peak hours. Pressure sensors and inductive loops are applied to detect the number of pedestrians and the volume of approaching vehicles, and system function principle is designed to improve the efficiency and accuracy of signal control with a signal timing model. A roadway segment near Cuihua Road School is chosen as an example and the corresponding signal timing model is calibrated according to the geometrics of Cuihua Road. The layouts of detectors and facilities are allocated to protect pedestrians' crossing at midblock crossings. The analysis result shows the efficiency of this method.

**Keywords** Actuated signal control · Pedestrian street-crossing · Pressure sensor · Crosswalk barrier

## 1 Introduction

During the past years, a large number of pedestrians died and were injured [1]. Statistics released by the Global Status Report on Road Safety 2013 found that the number of people killed in road accidents is as high as 1.24 million in each year and 270 thousands of them are pedestrians, which account for 22 % of the total number. In China, according to statistics, the pedestrian casualty numbers accounted for

---

L. Wang (✉) · Y. Wang · M. Xin  
School of Highway, Chang'an University, 710064 Xi'an, China  
e-mail: wanglongjianwin@163.com

Y. Wang  
e-mail: wangyg@chd.edu.cn

M. Xin  
e-mail: 728522574@qq.com



about 20 % of all traffic accident casualties, 50 % of them are injured or died while crossing the street. Overall, pedestrians street-crossing still face a high risk of accident [2–4]. It is estimated that accidents on crosswalk slightly decrease but the casualty rate is still high.

Nowadays, the design of traffic signal facilities does not consider the demand of pedestrian crossing, which not only reduces the efficiency of vehicles travel, but also lowers the safety and efficiency of pedestrians cross. Some previous works have already addressed this problem from a more general perspective. For example, button type signal control system for pedestrian crossing considering pedestrian crossing demand, but it appears that pedestrians ignored button to cross the street when it is a red light for pedestrian [5, 6]. The fixed signal control system takes the right of pedestrians and vehicles into account [7–9], but it can cause a great delay when few pedestrian cross [10, 11]. How to consider the right of pedestrians and vehicles and enhance the safety and efficiency of pedestrian street-crossing is an extremely complex problem.

Therefore, the purpose of this research is to establish the signal timing model and design the system to control the actuated signal, and it is structured as follows: after this brief introduction, Sect. 2 describes the system architecture and work principle, and Sect. 3 presents its application in actuated signal control of Cuihua Road. Finally, conclusions and discussions are summarized in Sect. 4.

## 2 System Architecture

### 2.1 Actuated Signal Control System Framework Design

In this study, the components of actuated signal control system include data acquisition module, signal control module, and street-crossing facilities module, as Fig. 1 shows. Data acquisition module is mainly used to collect the number of pedestrian in pedestrian waiting zone and the number of vehicles on the road. It consists of resistance strain weighing pressure sensor and inductive-loop detectors. The components of signal control module are ADC0809 A/D converter and ATmega16 MCU. The A/D converter converts the analog signal of the pedestrian and vehicle collected

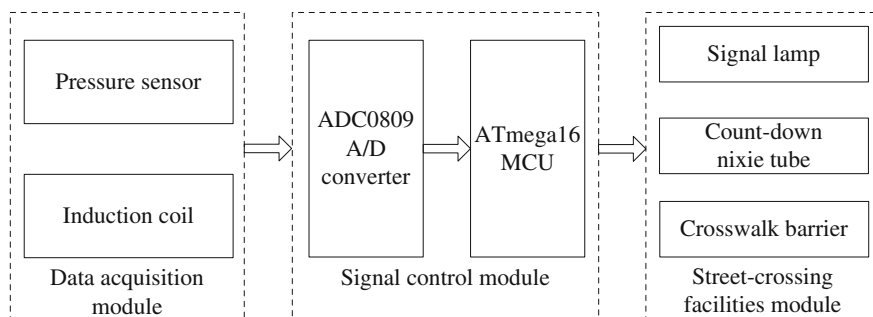


**Fig. 1** Framework of actuated signal control system for road pedestrian street-crossing

by pressure sensor and inductive-loop detectors into the digital signal and sends it to the MCU. Then MCU will process digital signal and sends control command to control street-crossing facilities, including signal lamp, count-down nixie tube, and crosswalk barrier so as to provide dynamic signal timing.

1. Pedestrian detection

Pedestrian detection is mainly used as resistance strain weighing pressure sensor to obtain the weight of pedestrian. The pressure sensor lay in pedestrian waiting zone. The layout of pressure sensor is shown in Fig. 2. When pedestrian stands on the pedestrian waiting zone, the resistance strain gauge will deform, and the resistance value will change. Then the resistance signal will turn into voltage signal sent out from output pin. We will use ADC0809 A/D converter to convert the voltage signal into digital signal and transmit it to the ATmega16 MCU, and MCU will calculate the number of pedestrians according to the average given weight. The structure of resistance strain weighing pressure sensor is shown in Fig. 3.

2. Vehicle detection

Road vehicle detection is mainly by the inductive-loop detectors that are buried under the road surface. The inductive loop detects the oscillating frequency of the

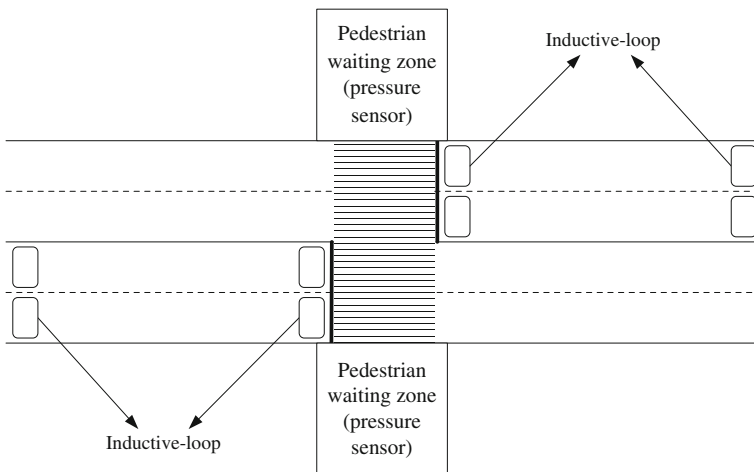
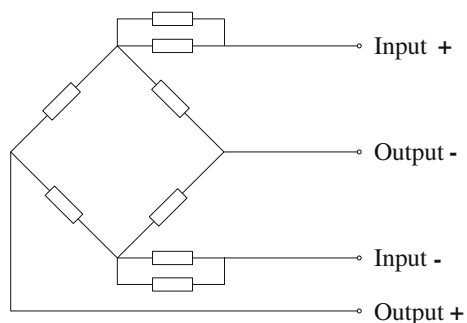


Fig. 2 Layout of detectors

Fig. 3 Weighing pressure sensor



oscillating circuit, which is composed of annular coil, coil lead, and capacitor. When the vehicle passes the inductive loop, the oscillating frequency will change relative to the reference frequency. We bury two inductive loops in each lane: the first inductive loop is buried close to the stop line to detect the number of vehicles leaving; the second inductive loop is buried on the position at a tolerable queue length from the first inductive loop to detect the number of vehicles entering. The difference between two numbers of vehicles is the number of the queue in this lane. It is the basis for the control of street-crossing facilities. The layout of inductive loop is shown in Fig. 2.

3. Signal control module

The signal control module realizes dynamic signal timing by adopting AVR series ATmega16 MCU as major control chip. The system's control core is composed of the minimum system of MCU and the ADC0809 A/D converter. The minimum system of MCU includes reset circuit, crystal oscillating circuit, download port, power supply, and serial interface circuit, as shown in Fig. 4.

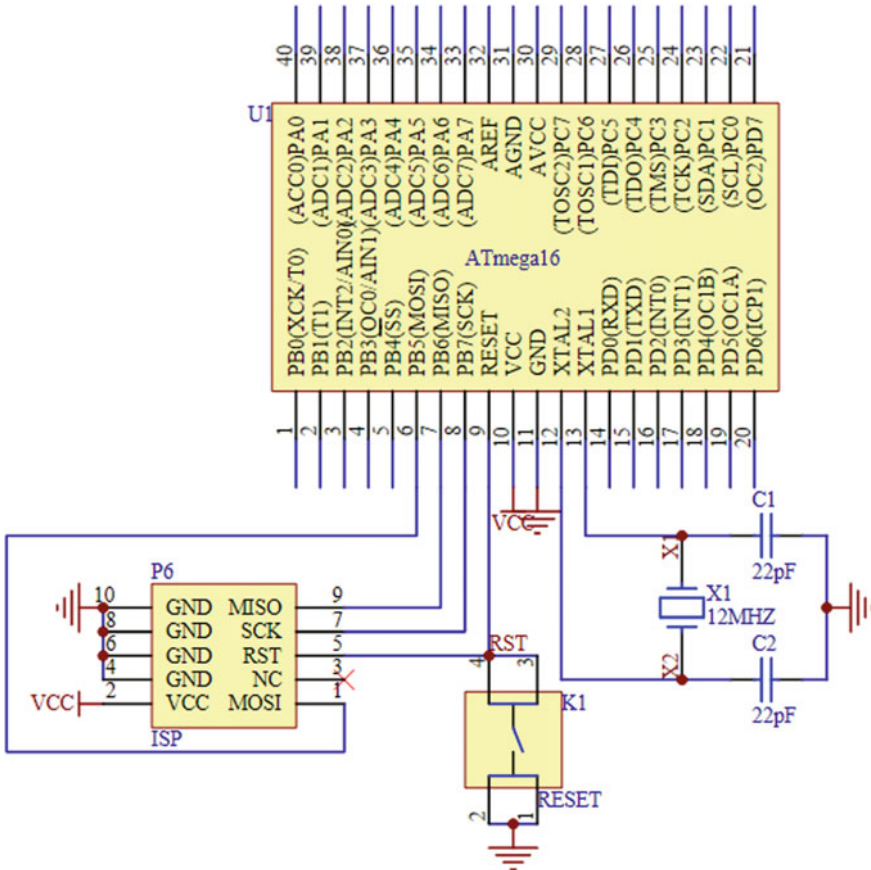
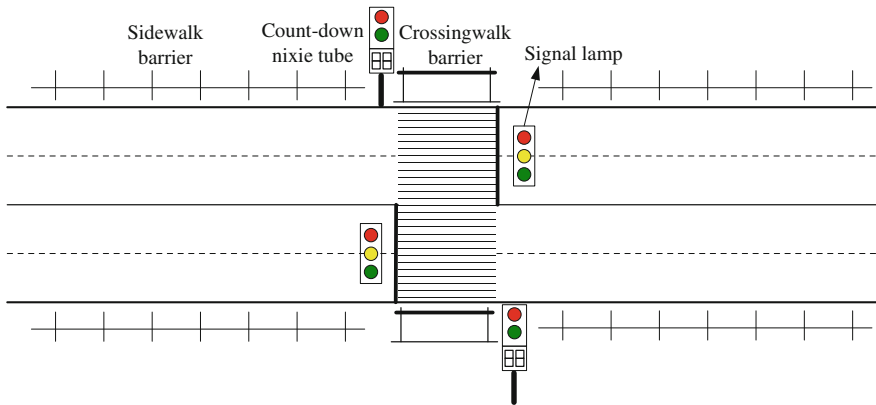


Fig. 4 MCU minimum system



**Fig. 5** Layout of street-crossing facilities

4. Street-crossing facilities

The street-crossing facilities include signal lamp, count-down nixie tube, and crosswalk barrier, and its main function is to control pedestrians and vehicles' running by the number of street-crossing pedestrians and the number of queue vehicles. The count-down nixie tube will display the rest time for street-crossing. The crosswalk barrier will open when pedestrian signal lamp displays green, and it will close when pedestrian signal lamp displays red. We should set sidewalk barrier [12] on both sides of crosswalk barrier. This facilities can prevent pedestrian from violating traffic rules when crossing road, and protects pedestrians' safety. The layout of street-crossing facilities is shown in Fig. 5.

**2.2 Principle of Actuated Signal Control System**

The adjustment of pedestrian signal timing is based on the real-time pedestrian and vehicle information. The actuated signal timing flow of the system is as follows:

1. When detector does not detect pedestrian, signal implements the motor phase. Vehicle signal lamp displays green and pedestrian signal lamp shows red.
2. When pedestrian detector detects pedestrian, MCU will judge whether the pedestrian weight exceeds threshold. If the pedestrian weight exceeds threshold, the pedestrian weight is converted into pedestrian number. If the pedestrian weight is less than its threshold, signal continues to implement the motor phase. The pedestrian weight threshold is based on the actual traffic situation of different roads.

Let  $M_p$  be the weight of pedestrians in waiting zone (kg),  $M$  represents pedestrian average weight (kg), so the number of pedestrians  $N$  can be written as

$$N = M_p/M \quad (1.1)$$

3. Judge whether the number of pedestrian exceeds its threshold. If not, it calculates pedestrian green time, and then implements pedestrian phases. If the number of pedestrians is greater than the threshold, implement maximum pedestrian green time, and then implement pedestrian phases. The value of maximum pedestrian green time is determined by road traffic situation.

Let  $g$  represent pedestrian green time (s),  $n$  represent the number of lanes in two directions,  $D$  represent the width of each lane (m),  $v$  represent pedestrian crossing speed (m/s),  $N$  represent the number of pedestrians,  $S$  represent pedestrian flow rate per unit width with the unit of p/(s m),  $W$  represent the width of crosswalk (m), and  $t_r$  represent pedestrian reaction time (s). Thus  $g$  is given by:

$$g = n \cdot D/v + N/(S \cdot W) + t_r \quad (1.2)$$

4. Pedestrian lamp display green, nixie tube begin count-down and open the crosswalk barrier. Pedestrian begin to street-crossing and vehicles stop.
5. Judge whether the number of vehicle queues exceeds its threshold. If the number of vehicle queues is greater than the threshold, the pedestrian green time ends. If it is less than the threshold, turn to the next step.

Let  $N_0$  represent vehicle number on the detected section at the initial time,  $N_U(t)$  represent cumulative vehicle number through the upstream detector at time  $t$ , and  $N_D(t)$  represent cumulative vehicle number through the downstream detector at time  $t$ . So, vehicle number between two detectors at time  $t$  can be expressed as

$$\Delta N(t) = N_0 + N_U(t) - N_D(t) \quad (1.3)$$

6. Judge whether the pedestrian green time exceeds threshold. If pedestrian green time is greater than the threshold, the pedestrian green time ends. If pedestrian green time is less than the threshold, go to the previous step.
7. At the end of the pedestrian green time, the crosswalk barrier closing and pedestrian lamp displays red. Then signal implements motor phases. The flow chart of actuated signal control system is shown in Fig. 6.

### 3 Illustrative Examples and Analysis

Cuihua Road is located between South 2nd Ring Road and South 3rd Ring Road in Xi'an, China. There are three major schools in this road. In this paper, the section of Cuihua Road surrounding the Cuihua Road Primary School is an example and is analyzed. There are four motorized lanes and two non-motorized lanes in two

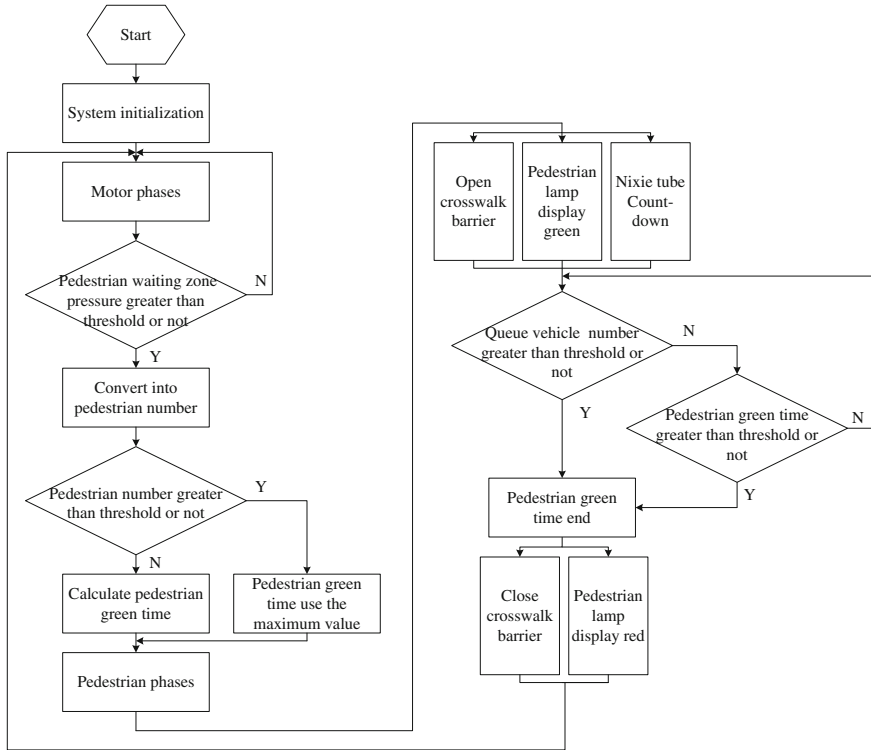


Fig. 6 Flow chart of actuated signal control system

directions and two greenbelts between them. Each lane width is 3.5 m and each greenbelt width is 2.5 m. This section has a crosswalk and central reserve, and does not have signal control. The width of crosswalk is 3 m. There are many pupils crossing when they go to and come back from school but few cross from here in other time. In peak hour, vehicle volume from north to south is 744 pcu/h, and it is 1112 pcu/h in another direction, street-crossing volume is 1077 p/h. There is a big security risk and endangering the safety of pupils. This paper proposes set actuated signal control system at this section to improve the efficiency and the safety level of pedestrian crossing.

1. The layout scheme of facilities

The pedestrian waiting zone is set up close to the non-motorized lane. The width of pedestrian waiting zone is 4 m, and the length of it is 4 m. The pressure sensor lay in pedestrian waiting zone. Its rated load is 800 kg, so we use two pressure sensors to gain the measurement range. We bury two inductive loops in each motorized lane. The detector layout of Cuihua Road is shown in Fig. 7. The street-crossing facilities of Cuihua Road are shown in Fig. 8.

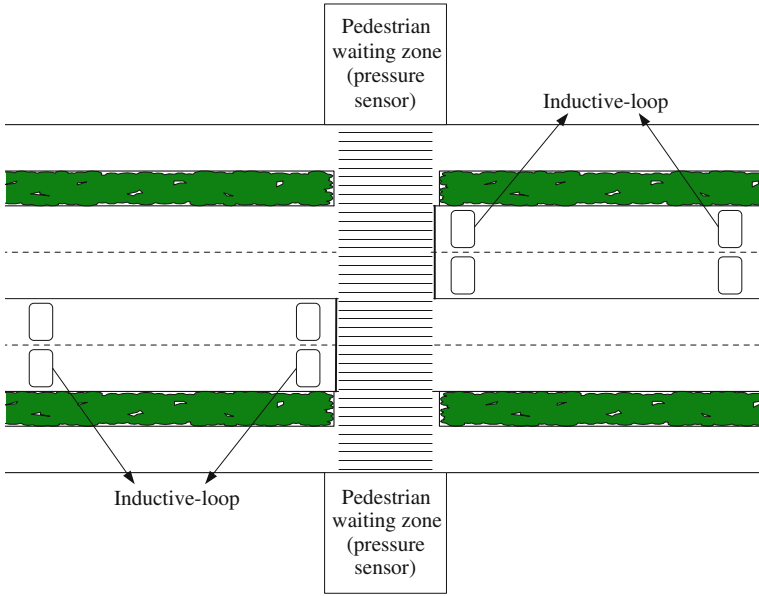


Fig. 7 Detector layout of Cuihua Road

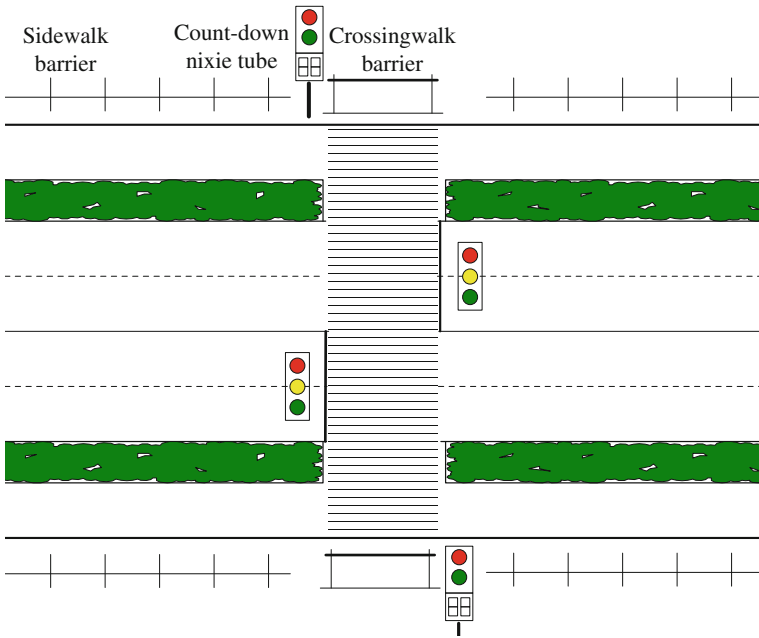


Fig. 8 Street-crossing facilities of Cuihua Road

## 2. Parameter calibration

Because of the purpose of improvement to meet the pupils' street-crossing demand, the pedestrian average weight  $M$  value is 35 kg. The number of lanes in two directions  $n$  is 6; each lane width  $D$  is 3.5 m; each greenbelt width is 2.5 m. So the length of street-crossing is  $6 \times 3.5 + 2.5 \times 2 = 26$  m. The pupil crossing speed  $v$  is 1.2 m/s, the pupil flow rate per unit width  $S$  is 1.23 p/s/m, the width of crosswalk  $W$  is 3 m, pedestrian reaction time  $t_r$  is 2 s. So pedestrian green time  $g$  can be expressed as

$$g = 26/1.2 + M_p/(35 \times 1.23 \times 3) + 2 = M_p/129.15 + 71/3 \quad (1.4)$$

The threshold of pedestrian waiting zone pressure is 350 kg, that is, to say about ten pupils waiting to cross. The threshold of pedestrians' number on pedestrian waiting zone is 15. The maximum value of pedestrian green time is 40 s. The threshold of vehicle queue number is 20 [13].

## 4 Conclusions and Discussions

Aiming at improving the safety level and efficiency of pedestrian crossing at special section, such as the entrance of schools and organizations, there are many pedestrians crossing the street in the some time, but few in other time, the pedestrian crossing actuated signal control method is proposed. In order to improve the effective of control and the accuracy of signal timing, the pressure sensor and inductive loop is applied to detect pedestrian weight and vehicle queue length. By this research, we proposed an effective method to provide convenience for pedestrians. Surely, this method is only applicable with a large number of demands of pedestrian crossing the section within a short period of time. If there are a large number of demands of pedestrian crossing the section still needs further research. Therefore, we should make more quantitative and simulation researches to overcome this or other similar difficult issues in our further deep study.

**Acknowledgments** This research is supported by the Key Programs of Department of Transport of Shaanxi, China (No. 15-42R).

## References

1. Perumal V (2014) Study on pedestrian crossing behavior at signalized intersections. *J Traffic Transp Eng* 1:103–110
2. Chang YL, Sun F (2012) Signal optimization design of the mid-block crosswalk. *Appl Mech Mater* 178:2708–2712
3. Lobjois R, Benguigui N, Cavallo V (2013) The effects of age and traffic density on street-crossing behavior. *Accid Anal Prev* 53:166–175



4. Wang T (2006) A study on the improvement of the safety of pedestrians crossing the street. *Planners* 10:78–80
5. Boudet L, Midenet S (2009) Pedestrian crossing detection based on evidential fusion of video-sensors. *Transp Res Part C Emerg Technol* 17:484–497
6. Zou ZY, Zhou ZH, Huan GE (2009) Optimization of road section crosswalk signal design. *J Transp Syst Eng Inf Technol* 9:142–147
7. Li L, Yang X, Yin L (2010) Exploration of pedestrian refuge effect on safety crossing at signalized intersection. *Transp Res Rec* 2193:44–50
8. Liu JM, Li X, Zhang R (2011) Empirical analysis of optimizing pedestrian crossing traffic at signalized intersections. *J Transp Syst Eng Inf Technol* 11:221–227
9. Wall RS, Ashmead DH, Billie Louise B et al (2004) Directional guidance from audible pedestrian signals for street crossing. *Ergonomics* 47:1318–1338
10. Feng SM, Pei YL (2007) Analysis of vehicle delay on road sections under the condition of pedestrian crossing. *J Transp Syst Eng Inf Technol* 7:73–77
11. Lu S (2009) Maximum waiting time for pedestrian crossing based on survival analysis. *J Transp Inf Saf* 27:69–76
12. Hine J, Russell J (1993) Traffic barriers and pedestrian crossing behaviour. *J Transp Geogr* 1:230–239
13. Li M (2012) Threshold of waiting-time for pedestrian crossing based on psychological time. *J Chongqing Jiaotong Univ* 31:612–614

# Study of a Unidirectional Hybrid Three-Phase Voltage Source Rectifier

She Dongjin, Wang Jiuhe and Zhai Dandan

**Abstract** This paper studies a unidirectional hybrid three-phase voltage source rectifier (UHTPVSR), improves the topology, and the power distribution method of UHTPVSR. The Euler–Lagrange mathematical models of the boost converter and VIENNA rectifier are set up. A hybrid control strategy based on passive control is proposed. The hybrid control strategy makes UHTPVSR having good current tracking ability, strong robustness, and is easy to implement. The simulation results show that UHTPVSR can realize voltage control at DC side and achieve sinusoidal current and unit power factor at AC side, and are able to distribute power at predetermined rate.

**Keywords** Hybrid rectifier · Passivity-based control · Vienna rectifier · Power distribution · Damping injecting

## 1 Introduction

The application of three-phase voltage source rectifier (TPVSR) in industry is increasingly widespread. Industrial applications have a more demanding standard in efficiency, power density, reliability, AC current harmonics, power factor, DC voltage control, and electromagnetic interference of TPVSR. To meet the industry standard of rectifiers' overall performance, scholars proposed a unidirectional hybrid three-phase voltage source rectifier (UHTPVSR) [1]. UHTPVSR is constructed by a three-phase single-tube rectifier (Z1) and a two or three level PWM

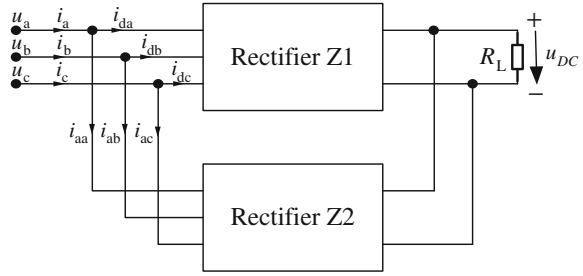
---

S. Dongjin (✉) · W. Jiuhe (✉) · Z. Dandan (✉)  
School of Automation, Beijing Information Science  
& Technology University, Beijing 100192, China  
e-mail: jade\_1228@163.com

W. Jiuhe  
e-mail: wjhyhrwm@163.com

Z. Dandan  
e-mail: zhaidandan\_happy@126.com

**Fig. 1** The composition of UHTPVSR



rectifier (Z2) in parallel connection (Fig. 1), input currents of Z1 and Z2 are combined into three-phase sinusoidal line current. Typically rectifier Z1 is set to operate with a low frequency, bearing higher proportion of load power, while the rectifier Z2 is set to a high frequency, bearing a lower proportion of load power. Load power is distributed by the two rectifiers at a reasonable proportion.

At present, scholars have studied the topology and the control scheme of UHTPVSR. Two or three level structures of UHTPVSR and the multi-loop control structure based on PI controller or the repetitive control theory-based PR controller are used in document [1–4]. But based on the control schemes, the current distortion in the current switching point is still not eliminated. Therefore, the performance of the UHTPVSR is not improved comprehensively.

This paper made improvements on the topology, improved the input current distortion; made optimal power allocation method. A hybrid control scheme using passivity-based control [5] in inner loop and PI controller in outer loop was applied. The strategy can make UHTPVSR perform better.

## 2 Topology and Working Principle of UHTPVSR

### 2.1 Circuit Topology of UHTPVSR

Topology in this paper chooses the high efficiency three-level VIENNA rectifier as the rectifier Z2, as shown in Fig. 2.

In Fig. 2, the diode-based rectifier Z1 is operating in continuous conduction mode (CCM).  $i_{da}$ ,  $i_{db}$ ,  $i_{dc}$  are input currents of the three-phase diode-based rectifier;  $i_{aa}$ ,  $i_{ab}$ ,  $i_{ac}$  are input currents of VIENNA rectifier,  $SW_i$  ( $i = a, b, c$ ) are bidirectional switches assembled by one power switch and four diodes.

But in the current topology, the input current of UHTPVSR is combined by the input current  $i_{da}$  and  $i_{aa}$ . In the conventional topology of UHTPVSR,  $i_{da}$  and  $i_{aa}$  is difficult to track the desired current, which will bring more serious distortions on the switching points in current  $i_a$ , as shown in Fig. 3a.

Therefore, in order to eliminate the current distortion on switching points, a small filter inductor  $L_{d1}$  (dashed box in Fig. 2) is added in AC side of three-phase

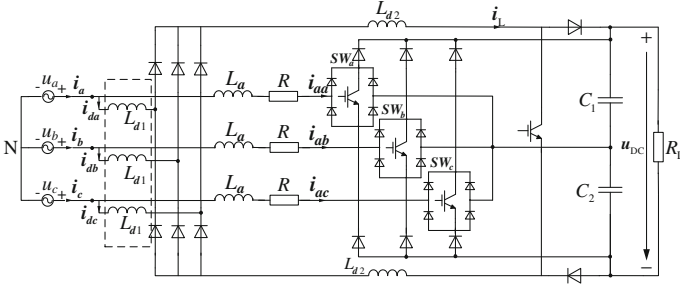


**Fig. 2** The improved topology of UHTPVSR

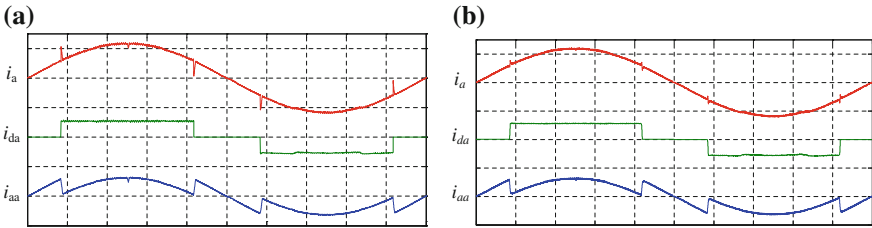


**Fig. 3** **a** Simulation current of phase *a* without the small filtering inductances based on passive controller. **b** Simulation current based on passive controller after adding small filter inductors

diode-based rectifier, so  $i_{da}$  and  $i_{aa}$  will be smooth on the switching point, while restraining the input current distortion of each phase in UHTPVSR’s AC side, improved the power factor and reduced the THD. Figure 3b shows the simulation current waveform of phase *a* after adding the small filtering inductors.

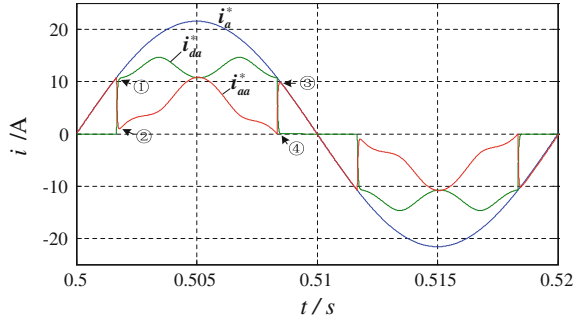
**2.2 Power Distribution Principle of UHTPVSR**

Rectifier Z1 and Z2 supply power to the load in parallel, line currents  $i_a, i_b, i_c$  are synthesized by  $i_{di}$  ( $i = a, b, c$ ) and  $i_{ai}$ , such that  $i_i = i_{di} + i_{ai}$ , and to ensure UHTPVSR operates at high power factor,  $i_a, i_b, i_c$  should be sinusoidal input currents which synchronized with the three-phase AC voltage.

Average power per phase of UHTPVSR is  $P_a = P_{a1} + P_{a2}$ , in the formula,  $P_{a1}$  and  $P_{a2}$  are average power of rectifiers Z1 and Z2,  $P_{a1} = U_a I_{da}$ ,  $P_{a2} = U_a I_{aa}$ .

In this paper, the power allocation method is improved. As shown in Fig. 4, the 6-pulse current waveform  $i_u$  is added on the desired DC current, which formed the new desired input current  $i_{da}^*, i_{aa}^*$ . Since the amplitude of 6-pulse frequency waveform is controllable, the amplitude of current  $i_u$  is adjusted by the factor  $k$ , meanwhile, the RMS of  $i_{da}$  will be adjusted too. By the formula  $P_{a1} = U_a I_{da}$ ,

**Fig. 4** Desired phase *a* current of three-phase diode-bridge rectifier and VIENNA rectifier



$P_{a2} = U_a I_{aa}$ , it can be concluded that the active power allocation ratio of two parts can be adjusted by the regulation of  $k$ . In order to make the current wave smoother on commutation points,  $i_u$  is filtered to make it close to the sine wave which is six times of the power frequency.

For example of phase A, boost converter's current expectation  $i_{da}^*$  is

$$i_{da}^* = \frac{1}{2} I_{mr} + k i_{uP} \tag{1}$$

In function (1),  $k$  is the waveform coefficient of  $i_u$ ,  $i_{uP}$  is the amplitude of  $i_u$ ,  $I_{mr}$  is the peak value of single-phase line current. The active power allocation ratio of two rectifier units is

$$k_1 = \frac{P_{a1}}{P_a} = \frac{\sqrt{3}}{\pi} + \frac{72\sqrt{3} K i_{uP}}{35\pi I_{mr}} \tag{2}$$

$$k_2 = \frac{P_{a2}}{P_a} = 1 - \frac{\sqrt{3}}{\pi} - \frac{72\sqrt{3} K i_{uP}}{35\pi I_{mr}} \tag{3}$$

In the formulas (2) and (3), it is shown that by controlling the desired current wave rectifier Z1, that is, adjust  $k$ , the active power allocation ratio of two rectifier units,  $k_1 \cdot k_2$  can be adjusted.

### 3 Mathematical Model and Control Strategy of UHTPVS

#### 3.1 Controller Design of Boost Type DC-DC Converter

**Mathematical model of Boost type DC-DC converter** The dynamic equation of the converter is obtained from Fig. 2

$$\begin{cases} L di_L/dt = U_S + (u_G - 1)u_o \\ C du_o/dt = (1 - u_G)i_L - u_o/R_L \end{cases} \quad (4)$$

Take the inductor current  $i_L$  and capacitor voltage  $u_o$  as state variables, set  $[x_1 \ x_2] = [i_L \ u_o]$ . The EL model of the converter is obtained from (4).

$$\mathbf{M}_1 \dot{\mathbf{x}}_1 + \mathbf{J}_1 \mathbf{x}_1 + \mathbf{R}_1 \mathbf{x}_1 = \mathbf{u}_1 \quad (5)$$

$$\mathbf{M}_1 = \begin{pmatrix} L & 0 \\ 0 & C \end{pmatrix}, \mathbf{x}_1 = \begin{pmatrix} x_1 \\ x_2 \end{pmatrix}, \mathbf{J}_1 = \begin{pmatrix} 0 & 1 - u_G \\ u_G - 1 & 0 \end{pmatrix}, \mathbf{R}_1 = \begin{pmatrix} 0 & 0 \\ 0 & 1/R_L \end{pmatrix},$$

$$\mathbf{u}_1 = \begin{pmatrix} U_S \\ 0 \end{pmatrix}.$$

where the  $\mathbf{J}_1 = -\mathbf{J}_1^T$  is skew-symmetric matrix and  $\mathbf{R}_1$  is positive definite matrix, so that Eq. (5) has the characteristics of EL model.

**Passive-based controller design** According to EL model (5), let  $\mathbf{x}_{e1} = \mathbf{x}_1 - \mathbf{x}_1^*$ , the transient desired equilibrium point  $\mathbf{x}_1^* = [x_1^* \ x_2^*]^T = [I_L^* \ U_o^*]^T$ , let  $\mathbf{H}_{e1}$  denotes the error storage function

$$\mathbf{H}_{e1}(\mathbf{x}_1) = \frac{1}{2} \mathbf{x}_{e1}^T \mathbf{M}_1 \mathbf{x}_{e1} \quad (6)$$

In order to accelerate  $\mathbf{H}_{e1}$  to zero, it required damping injecting  $\mathbf{R}_{a1}$ , damping injection dissipation is  $\mathbf{R}_{d1} \mathbf{x}_{e1} = (\mathbf{R}_1 + \mathbf{R}_{a1}) \mathbf{x}_{e1}$ , the positive definite diagonal damping matrix  $\mathbf{R}_{a1} = \text{diag}\{r_{a1}, 1/r_{a0}\}$  ( $r_{ai} > 0$ ).

The formula (5) can be expressed as

$$\mathbf{M}_1 \dot{\mathbf{x}}_{e1} + \mathbf{R}_{d1} \mathbf{x}_{e1} = \mathbf{u}_1 - (\mathbf{M}_1 \dot{\mathbf{x}}_1^* + \mathbf{J}_1 \mathbf{x}_1 + \mathbf{R}_1 \mathbf{x}_1^* - \mathbf{R}_{a1} \mathbf{x}_{e1}) \quad (7)$$

Select the control law  $\mathbf{u}_1 = \mathbf{M}_1 \dot{\mathbf{x}}_1^* + \mathbf{J}_1 \mathbf{x}_1 + \mathbf{R}_1 \mathbf{x}_1^* - \mathbf{R}_{a1} \mathbf{x}_{e1}$ , due to  $\mathbf{R}_{d1}$  is positive definite matrix, there is  $\dot{\mathbf{H}}_{e1}(\mathbf{x}_1) = \mathbf{x}_{e1}^T \mathbf{M}_1 \dot{\mathbf{x}}_{e1} = -\mathbf{x}_{e1}^T \mathbf{R}_{d1} \mathbf{x}_{e1} < 0$ .

The switching function can be expressed as

$$u_G = 1 - \frac{U_S - L \frac{di_L^*}{dt} + r_{a1}(i_L - I_L^*)}{u_o} \quad (8)$$

### 3.2 Mathematical Model and Passive-Based Controller Design of VIENNA Rectifier

**Mathematical model of VIENNA rectifier** VIENNA rectifier's voltage state in AC side depends on the direction of the AC current and the switch state. The switch function of VIENNA rectifier is provided as follows:

$$S_i = \begin{cases} +1 & \text{SW}_i = 0, \quad i_i > 0 \\ 0 & \text{SW}_i = 1, \quad i_i = a, b, c \\ -1 & \text{SW}_i = 0, \quad i_i < 0 \end{cases}$$

The mathematical model of Vienna rectifier in two-phase synchronous rotating  $d$ - $q$  coordinate frame can be written as

$$\begin{cases} L_a \dot{i}_d - \omega L_a i_q + R i_d + d_d \frac{u_{DC}}{2} = u_d \\ L_a \dot{i}_q + \omega L_a i_d + R i_q + d_q \frac{u_{DC}}{2} = u_q \\ \frac{C}{3} \dot{u}_{DC} + \frac{2u_{DC}}{3R_L} - \frac{d_d}{2} i_d - \frac{d_q}{2} i_q = 0 \\ \frac{C}{3} \Delta u_{DC} = \frac{1}{3} \alpha d_0 i_d - \frac{\Delta u_{DC}}{3R_L} \end{cases} \quad (9)$$

In formula (9),  $S_d, S_q$  are components of switching function on  $d, q$  axis;  $i_d, i_q, u_d, u_q$  are the currents and voltages on the  $d$  axis and  $q$  axis.  $d_i$  is defined as a new switching variable and its relationship with  $S_i$  is  $d_i = (1 - S_i) \left[ \text{sign}(i_i) + \frac{\Delta u_{DC}}{u_{DC}} \right]$ .  $\alpha$  is equal to  $2/\pi$ .

By formula (9), the VIENNA rectifier can be modelled by EL equations in the following form:

$$\mathbf{M}_2 \dot{\mathbf{x}}_2 + \mathbf{J}_2 \mathbf{x}_2 + \mathbf{R}_2 \mathbf{x}_2 = \mathbf{u}_2 \quad (10)$$

$$\mathbf{M}_2 = \begin{pmatrix} L_a & 0 & 0 & 0 \\ 0 & L_a & 0 & 0 \\ 0 & 0 & \frac{C}{3} & 0 \\ 0 & 0 & 0 & \frac{C}{3} \end{pmatrix}, \mathbf{J}_2 = \begin{pmatrix} 0 & -\omega L & \frac{d_d}{2} & 0 \\ \omega L & 0 & \frac{d_q}{2} & 0 \\ -\frac{d_d}{2} & -\frac{d_q}{2} & 0 & 0 \\ 0 & 0 & 0 & 0 \end{pmatrix}, \mathbf{R}_2 = \begin{pmatrix} R & 0 & 0 & 0 \\ 0 & R & 0 & 0 \\ 0 & 0 & \frac{1}{3R_L} & 0 \\ 0 & 0 & 0 & \frac{1}{3R_L} \end{pmatrix}$$

$$\mathbf{x}_2 = (i_d \quad i_q \quad u_{DC} \quad \Delta u_{DC})^T, \mathbf{u}_2 = (u_d \quad u_q \quad 0 \quad \frac{2}{3} d_0 i_d)^T.$$

Approximately the voltage of VIENNA rectifier in the  $dq$  coordinate system  $v_{d0}, v_{q0}$  can be written as  $v_{rd} = d_d * (u_{DC}/2) + u_{ON}$ ,  $v_{rq} = d_q * (u_{DC}/2) + u_{ON}$ ,  $v_{ro} = d_o * (u_{DC}/2) + u_{ON}$ .

**Passive-based controller design** Set  $\mathbf{x}_{e2} = \mathbf{x}_2 - \mathbf{x}_2^*$ , the desired value of  $\mathbf{x}_2^*$  is  $\mathbf{x}_2^* = [x_1^* \quad x_2^* \quad x_3^* \quad x_4^*]^T = [i_d^* \quad i_q^* \quad u_{DC}^* \quad \Delta u_{DC}^*]^T$ . In order to accelerate the error energy to zero, the damping  $\mathbf{R}_{a2}$  is injected into the system, set  $\mathbf{R}_{d2} \mathbf{x}_{e2} = (\mathbf{R}_2 + \mathbf{R}_{a2}) \mathbf{x}_{e2}$ , the formula (10) can be described as

$$\mathbf{M}_2 \dot{\mathbf{x}}_{e2} + \mathbf{R}_{d2} \mathbf{x}_{e2} = \mathbf{u}_2 - (\mathbf{M}_2 \dot{\mathbf{x}}_2^* + \mathbf{J}_2 \mathbf{x}_2^* + \mathbf{R}_2 \mathbf{x}_2^* - \mathbf{R}_{a2} \mathbf{x}_{e2}) \quad (11)$$

Let the error storage function be  $\mathbf{H}_{e2}(\mathbf{x}) = \frac{1}{2} \mathbf{x}_{e2}^T \mathbf{M}_2 \mathbf{x}_{e2}$ , in order to make the error energy becomes zero fast, passive-based controller is obtained by

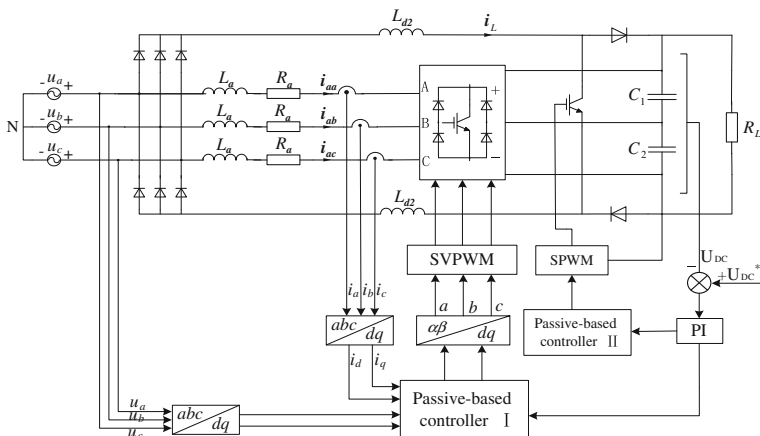


Fig. 5 Control block diagram of unidirectional hybrid three-phase voltage source rectifier

$$u_2 = M_2 \dot{x}_2^* + (J_2 - R_{a2})x_2 + R_{d2}x_2^* \tag{12}$$

The control law is described as (13). The structure of the proposed UHTPVSRC control scheme is shown in Fig. 5.

$$\begin{cases} d_d = \frac{2}{u_{DC}} [e_d - Li_d^* - (R + r_{a2})i_d^* + r_{a2}i_d + \omega Li_q] \\ d_q = \frac{2}{u_{DC}} [e_d - Li_q^* - (R + r_{a2})i_q^* + r_{a2}i_q - \omega Li_d] \\ d_o = -\frac{\Delta u_{DC}}{r_{a3} \omega i_d} \end{cases} \tag{13}$$

### 4 Simulation Results and Discussion

The UHTPVSRC's simulation in 10 kW is done by using MATLAB/Simulink software. In simulation, the rms of three-phase voltages are 220 V, frequency  $f = 50$  Hz;  $L_{d1} = 10 \mu H$ ,  $L_{d2} = 7$  mH;  $L_{a1} = L_{a2} = L_{a3} = 1.3$  mH, capacitor  $C_1 = C_2 = 1300 \mu F$ . The switching frequency of rectifier Z1 is 10 kHz, while of Z2 is 20 kHz,  $u_{DC}^* = 800$  V.

**Simulation results in the case of rated load  $R = 64 \Omega$**  In passive controller, the injecting damping  $r_{a1} = 1000$ ,  $r_{a2} = 2000$ . PI parameter is  $K_p = 0.0005$ ,  $K_i = 10.7$ . The waveform coefficient is  $k = 5$ . Power distribution ratio of two-part is  $k_1:k_2 \approx 0.6:0.4$ . Figures 6, 7, and 8 show the simulation results of UHTPVSRC.



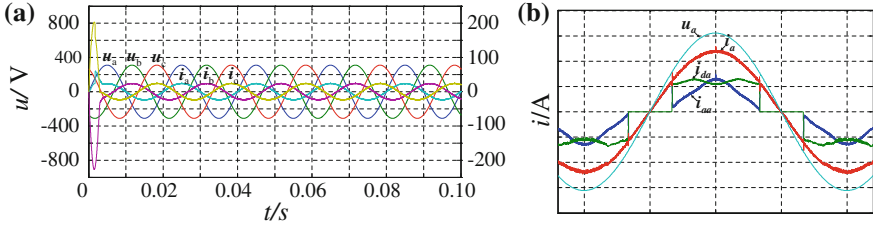


Fig. 6 a Three-phase voltage and current of UHTPVSR. b Zoomed graph of phase *a* current

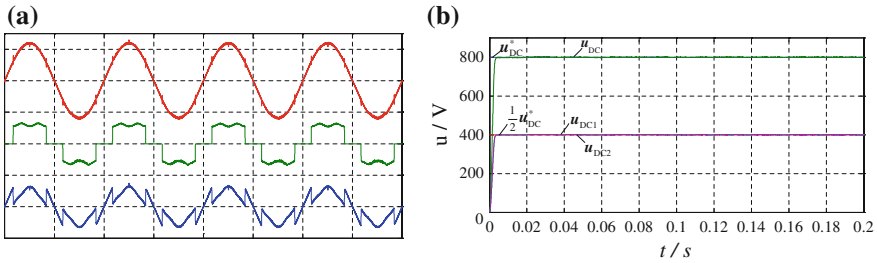


Fig. 7 a Phase *a* current of UHTPVSR and rectifier Z1, Z2. b Output voltage of UHTPVSR

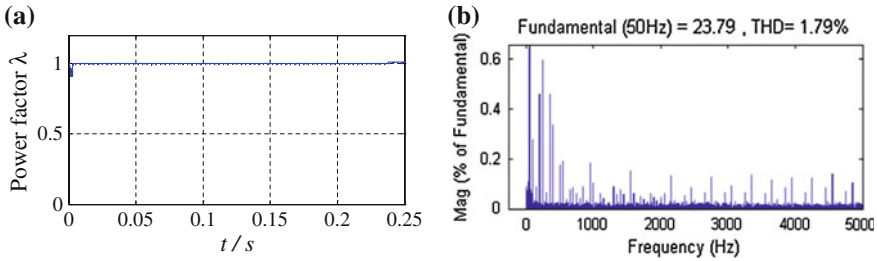


Fig. 8 a Power factor of UHTPVSR. b FFT analysis of UHTPVSR

Figures 6, 7, and 8 show that, THD = 1.79 %, power factor is  $\lambda = 0.9997$ ,  $u_{DC} = u_{DC}^* = 800$  V. Simulation achieved the goal of sinusoidal input current, stable DC output voltage and unity power factor, and achieved the goal of THD < 5%.

**The simulation results in the case of load disturbance** In the case of load disturbance (load resistance changed from 64 to 32  $\Omega$  at the time of 0.2 s and then changed from 32 to 64  $\Omega$  at 0.6 s); simulation results are shown in Fig. 9, which shows UHTPVSR controlled by the proposed strategy has strong robustness.

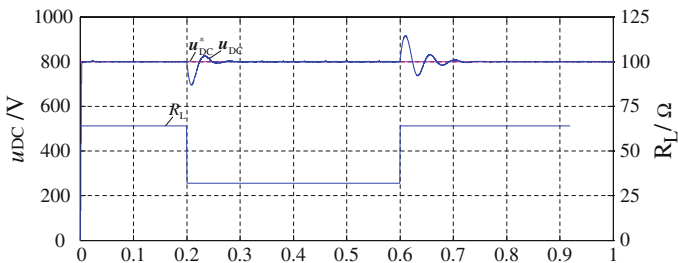


Fig. 9 Simulation of UHTPVSr when  $R_L = 64 \Omega$  for load disturbance

**Acknowledgements** This work is supported by national natural science foundation of China (51477011)/by program of Beijing Natural Science Foundation (KZ201511232035)/Funding Project for Science and technology innovation ability enhancement in Institutions under the Jurisdiction of Beijing Municipality (TJSHG201310772024).

## References

1. Alves RL, Barbi I (2006) A new hybrid high power factor three phase unidirectional rectifier. In: IEEE International symposium on industrial electronics, Montreal, Quebec, Canada, pp 1046–1051
2. Costa AV, Rodrigues DB, de Lima GB et al (2013) New hybrid high-power rectifier with reduced THDI and voltage-sag ride-through capability using boost converter. IEEE Trans Ind Appl 49(6):2421–2436
3. Soeiro TB, Kolar JW (2013) Analysis of high-efficiency three-phase two- and three-level unidirectional hybrid rectifiers. IEEE Trans Ind Electron 60(9):3589–3601
4. Bai L, Wang D, Zhou Y (2013) Study on the current control strategy of hybrid rectifier based on the PR controller. In: International conference on electrical machines and systems (ICEMS), Busan, Korea (South), pp 1693–1696
5. Jiuhe W (2014) Power converter and its passive-based control. Science Press, Beijing in Chinese

# The Heading Control of POD-Driven Ship Using Adaptive Integrator Backstepping

Yacong Zhao, Haibin Huang and Yufei Zhuang

**Abstract** This paper proposes a controller for pod-driven surface ships based on adaptive backstepping with integrator. The pod propulsion has the advantages of higher efficiency and better maneuverability compared with the conventional propulsion, and large steering-induced heeling angle with the possibly large steering forces. The adaptive backstepping is normally used in the systems including uncertainty information or unknown parameters and the integrator can be added to eliminate the constant static error. Simulation results show that compared with the PID controller, the adaptive backstepping with integrator is much better in overshoot, adjusting time, and static error without disturbance and in chattering with disturbance.

**Keywords** POD-driven ship · Heading control · Adaptive backstepping with integrator · Modeling simulation

## 1 Introduction

For the past few years, an increasing number of ships are equipped with podded propulsions. The pod propulsion has the advantages of increasing the efficiency and the maneuverability of the ship. Besides, pod propulsion increases the flexibility and the location of the engine room. Due to the possibly large steering forces, large steering-induced heeling angles can occur. Additionally, the directional stability of ships with pods tends to be less than comparable ships with conventional propulsion [1].

The backstepping procedure is a systematic design technique for globally stable and asymptotically adaptive. When systems include uncertainty information or unknown parameters, adaptive control based on backstepping is more convenient [2]. Recently, the backstepping control has been used for the maneuvering of ships,

---

Y. Zhao · H. Huang · Y. Zhuang (✉)

Harbin Institute of Technology at Weihai, Weihai 264209, Shandong, China  
e-mail: yufeizhuang9@gmail.com

© Springer-Verlag Berlin Heidelberg 2016

B. Huang and Y. Yao (eds.), *Proceedings of the 5th International Conference on Electrical Engineering and Automatic Control*, Lecture Notes in Electrical Engineering 367, DOI 10.1007/978-3-662-48768-6\_20

173

like the modified observer backstepping [3], the backstepping dynamical sliding mode control [4], and adaptive backstepping with integrator [5]. In this paper, the adaptive backstepping with integrator is used for the heading control of podded ship.

## 2 Problem Statement

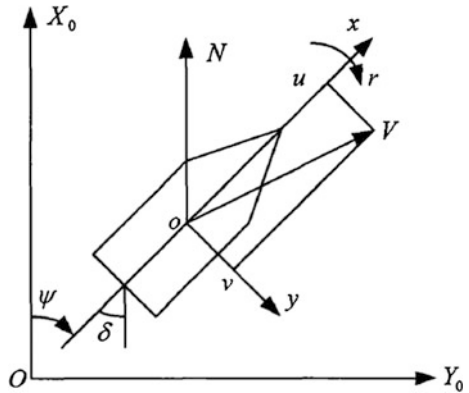
### 2.1 Ship Model

For ships' moving, there are six degrees of freedom (DOF), six independent coordinates are necessary to determine the position and orientation. The first three coordinates and their time derivatives correspond to the position and translation motion along the  $x$ ,  $y$ ,  $z$  axes [6]. When analyzing the motion of ships in six DOF, it is convenient to define two Earth-centered coordinate frames.  $OX_0Y_0Z_0$  is an Earth-fixed frame that can be considered as inertial for the present problem.  $oxyz$  is a body-fixed one whose axes coincide with the ship's principal axes of inertia. While for most surface ships three DOF are enough (Fig. 1).

The position and the velocity of the ship are represented by  $\eta = [X_0 \ Y_0 \ \psi]^T$  and  $v = [u \ v \ r]^T$ , respectively. The change of  $\psi$ ,  $X_0$ ,  $Y_0$  is determined by  $u$ ,  $v$ ,  $r$ . Only considering the surge, sway, and yaw, and using MMG, the ship path following mathematical model can be described as follows [7]:

$$\begin{cases} (m + m_x)\dot{u} - (m + m_y)vr = X_H + X_P \\ (m + m_y)\dot{v} + (m + m_x)ur = Y_H + Y_P \\ (I_Z + J_Z)\dot{r} = N_H + N_P \\ \dot{x} = u \cos \psi - v \sin \psi \\ \dot{y} = u \sin \psi + v \cos \psi \\ \dot{\psi} = r \end{cases} \quad (1)$$

**Fig. 1** Motion variables for a surface ship



where  $H$  represents the viscous hydrodynamics,  $P$  represents the thrust of the pod propulsion.

$$\begin{cases} X_H = X(u) + X_{vv}v^2 + X_{vr}vr + X_{rr}r^2 \\ Y_H = Y_vv + Y_r r + Y_{vvv}v^3 + Y_{rrr}r^3 + Y_{vvr}v^2r + Y_{vrr}vr^2 \\ N_H = N_vv + N_r r + N_{vvv}v^3 + N_{rrr}r^3 + N_{vvr}v^2r + N_{vrr}vr^2 \end{cases} \quad (2)$$

The viscous hydrodynamics are expressed in Eq. (2) [8], at the situation without controller, running the simulation in Simulink/Matlab founded the general proportional relation between  $v$  and  $r$ . The  $N_H$  can be expressed as

$$N_H = \theta_{11}r + \theta_{21}r^3 \quad (3)$$

where  $\theta_{11}$ ,  $\theta_{21}$  are unknown parameters.

## 2.2 POD Propulsion

There is no conventional rudder in the pod-driven ships. Pod turning an angel products the vectored thrust, component of the force along the latitude of the ship. When  $T_P$  is the effective thrust of the pod propulsion, the component force along or roll the axes can be expressed as

$$\begin{cases} X_P = T_P \cos(\delta) \\ Y_P = -T_P \sin(\delta) \\ N_P = \mathbf{x}_P(-T_P \sin(\delta)) \end{cases} \quad (4)$$

where  $\mathbf{x}_P$  represents the vectored position along the  $y$  axes,  $\delta$  is the turning angel of the pod.

The expression of  $\delta$  is that,

$$T_E \dot{\delta} = -\delta + \delta_c \quad (5)$$

## 3 Heading Control

According to Eqs. (1), (3), and (4) and making that  $x_1 = \psi$ ,  $x_2 = r$ ,  $T = (-x_P T_P)/(I_Z + J_Z)$ ,  $\theta_1 = \theta_{11}/(I_Z + J_Z)$ ,  $\theta_2 = \theta_{21}/(I_Z + J_Z)$ ,  $\sin(\delta) = u$ , the expression can be written as

$$\begin{cases} \dot{x}_1 = x_2 \\ \dot{x}_2 = \theta_1 x_2 + \theta_2 x_2^3 + Tu \\ y = x_1 \end{cases} \quad (6)$$

Step 1: Assume the reference trajectory is  $\psi_d$ . Define the tracking error as  $z_1 = x_1 - \psi_d$ , in order to eliminate the constant static error, defining  $\dot{\xi} = z_2$  imports the integrator.

$$\begin{cases} \dot{\xi} = z_2 \\ z_1 = x_1 - \psi_d \\ z_2 = x_2 - \alpha_1 \\ y = x_1 \end{cases} \quad (7)$$

The  $\alpha_1$  is the virtual control, to obtain this stabilizing function, the first Lyapunov function is chosen as

$$V_1 = \frac{1}{2} z_1^2 \quad (8)$$

Taking the time derivative of  $V_1$ ,

$$\dot{V}_1 = z_1 (z_2 + \alpha_1 - \dot{\psi}_d) \quad (9)$$

Select  $\alpha_1 = -c_1 z_1 + \dot{\psi}_d$ ,  $c_1$  is positive. Yield

$$\dot{V}_1 = -c_1 z_1^2 + z_1 z_2 \quad (10)$$

When  $z_2 \rightarrow 0$ ,  $V_1 \rightarrow 0$ , the subsystem of  $z_1$  is stable.

Step 2: The second Lyapunov function is chosen as

$$V_2 = V_1 + \frac{1}{2} z_2^2 + \frac{\lambda}{2} \xi^2 \quad (11)$$

Taking the time derivative of  $V_2$ ,

$$\begin{aligned} \dot{V}_2 &= -c_1 z_1^2 + z_2 (z_1 + \dot{z}_2 + \lambda \xi) \\ &= -c_1 z_1^2 + z_2 (z_1 + \lambda \xi + \theta_1 x_2 + \theta_2 x_2^3 + Tu - \dot{\alpha}_1) \\ &= -c_1 z_1^2 + z_2 (z_1 + \lambda \xi + \hat{\theta}_1 x_2 + \hat{\theta}_2 x_2^3 + Tu - \dot{\alpha}_1) \\ &\quad + z_2 (\tilde{\theta}_1 x_2 + \tilde{\theta}_2 x_2^3) \end{aligned} \quad (12)$$

Select the control law,

$$u = \frac{1}{T} \left( -z_1 - \lambda \xi - \hat{\theta}_1 x_2 - \hat{\theta}_2 x_2^3 + \dot{\alpha}_1 - c_2 z_2 \right) \quad (13)$$

$c_2$  is positive. Yield,

$$\dot{V}_2 = -c_1 z_1^2 - c_2 z_2^2 + z_2 (\tilde{\theta}_1 x_2 + \tilde{\theta}_2 x_2^3) \quad (14)$$

Step 3: Select the Lyapunov function of the total plant

$$V = V_2 + \frac{1}{2r_1} \tilde{\theta}_1^2 + \frac{1}{2r_2} \tilde{\theta}_2^2 \quad (15)$$

where  $\hat{\theta}(t)$  is an estimate of the unknown parameter  $\theta$  and  $\tilde{\theta} = \theta - \hat{\theta}$ .

Taking the time derivative of  $V$ ,

$$\begin{aligned} \dot{V} &= -c_1 z_1^2 - c_2 z_2^2 + z_2 (\tilde{\theta}_1 x_2 + \tilde{\theta}_2 x_2^3) - \frac{1}{r_1} \tilde{\theta}_1 \dot{\tilde{\theta}}_1 - \frac{1}{r_2} \tilde{\theta}_2 \dot{\tilde{\theta}}_2 \\ &= -c_1 z_1^2 - c_2 z_2^2 + \frac{1}{r_1} \tilde{\theta}_1 (r_1 z_2 x_2 - \dot{\tilde{\theta}}_1) + \frac{1}{r_2} \tilde{\theta}_1 (r_2 z_2 x_2^3 - \dot{\tilde{\theta}}_2) \end{aligned} \quad (16)$$

Define the  $\hat{\theta}(t)$  and  $u$

$$\begin{cases} \dot{\hat{\theta}}_1 = r_1 \left[ x_2 (c_1 x_1 - c_1 \psi_d + x_2 - \dot{\psi}_d) - p_1 (\hat{\theta}_1 - \theta_{10}) \right] \\ \dot{\hat{\theta}}_2 = r_2 \left[ x_2^3 (c_1 x_1 - c_1 \psi_d + x_2 - \dot{\psi}_d) - p_2 (\hat{\theta}_2 - \theta_{20}) \right] \\ u = \frac{1}{T} [-\hat{\theta}_1 x_2 - \hat{\theta}_2 x_2^3 + (1 + c_1 c_2 + \lambda)(\psi_d - x_1) \\ \quad + \lambda c_1 \int (\psi_d - x_1) dt + (c_1 + c_2)(\dot{\psi}_d - x_2)] \end{cases} \quad (17)$$

Yield

$$\dot{V} = -c_1 z_1^2 - c_2 z_2^2 \quad (18)$$

According to the Lyapunov stability theorem, the stability of the plant is guaranteed [9].

## 4 Simulation

The controller performance is evaluated and compared here through numerical simulation in Simulink/Matlab. The initial values are  $\eta = [0 \ 0 \ 0]^T$  and  $v = [7.6 \ 0 \ 0]^T$ . The ship main parameters are shown in Table 1 [10].  $k_1 = 0.001$ ,  $k_2 = 0.9$ ,  $\lambda = 0.001$ ,  $r_1 = r_2 = 50$ ,  $p_1 = p_2 = 1.3e-6$  are the control parameters, the results of the simulation compared to PID control.

**Table 1** Ship parameters

Length (m)	175
Beam (m)	25.4
Draft (m)	8.5
Total displacement (kN)	$2.13 \times 10^8$

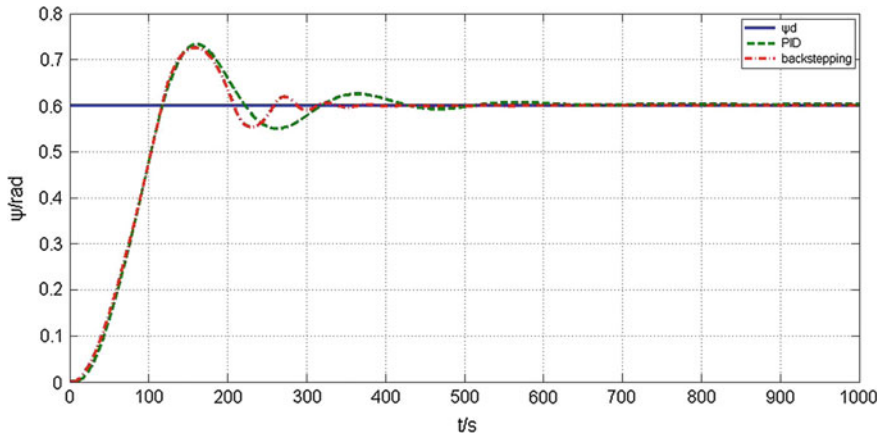


**Fig. 2** The result without disturbance

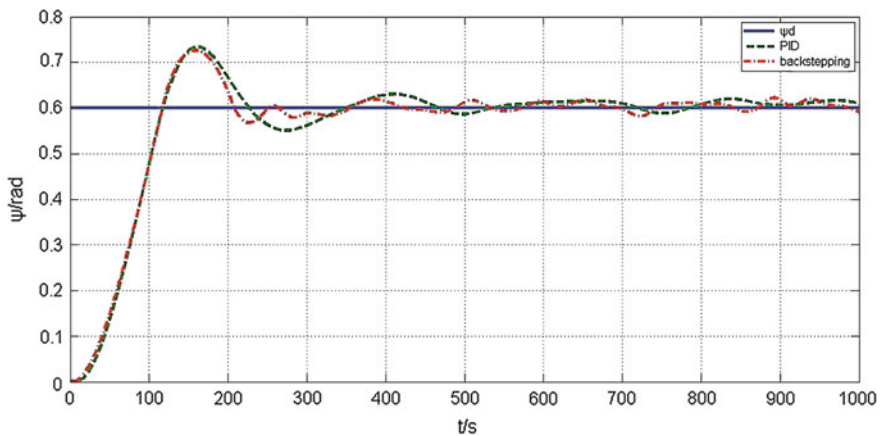


**Fig. 3** The result with disturbance

From Figs. 2 and 3, it is shown that the two kinds of controllers can make the system stable. While the overshoot of the adaptive backstepping with integrator is a litter smaller than PID, the adjusting time is shorter, and the static error is smaller when there is no disturbance. Furthermore, the chattering of the proposed control is smaller compared to the PID.



## 5 Conclusion

This paper designed a control for the heading tracking of the pod-driven ship using adaptive backstepping with integrator control. From the simulation it can be seen that the proposed controller is better than PID controller. While designing the controller, the mathematical model that is simplified has a certain gap in contrast with actual motion. The further study is necessary.

**Acknowledgments** This work was supported in part by the Fundamental Research Funds for the Central Universities under Grant nos. HIT.NSRIF.2013135 and HIT.KISTP.2014029, the Natural Scientific Research Innovation Foundation in Harbin Institute of Technology under Grant no. HIT.NSRIF.2014139, and the Science and Technology Foundation for the Universities in Shandong Province under Grant no. J14LN93.

## References

1. Serge T, Giedo L (2002) Manoeuvring aspects of fast ships with pods. In: 3rd International Euro conference on high-performance marine vehicles HIPER'02, Bergen, 14–17 Sept 2002, pp 392–406
2. Ali JK, Alan SIZ (2000) Adaptive backstepping control of nonlinear systems with unmatched Uncertainty. In: Proceedings of the 39th IEEE conference on decision and control. Sydney, Australia, December 2000
3. Morishita HM, Souza CES (2014) Modified observer backstepping controller for a dynamic positioning system. *Control Eng Pract* 33:105–114
4. Liao Y-L, Wan L, Zhuang J-Y (2011) Backstepping dynamical sliding mode control method for the path following of the underactuated surface vessel. *Proc Eng* 15:156–263
5. Wang J (2011) Study on adaptive control of ship course based on backstepping. Harbin Engineering University
6. Thor IF (2002) Marine control systems: guidance, navigation and control of ships, rigs and underwater vehicles. *Marine Cybernetics*, Trondheim, pp 17–46
7. Jia X, Yang Y (1999) Ship motion mathematical model. Dalian Maritime University Press, pp 141–144
8. Jia X, Yang Y (1999) Ship motion mathematical model. Dalian Maritime University Press, pp 49–98
9. Hassan KK (2001) *Nonlinear systems*, 3rd edn. Prentice Hall, pp 111–180
10. Jia X, Yang Y (1999) Ship motion mathematical model. Dalian Maritime University Press, pp 169–170

# Dynamic Modeling of RR-RRR Spherical Parallel Manipulator for Vector Thruster

Han Xu, Yuan Chen and Jun Gao

**Abstract** Thrust vectoring technology with single manipulator and multidimensional attitude is a novel thrust vectoring method in underwater vehicle. In order to complete both the rotational transmission and attitude adjustment, a two degree of freedom (DOF) spherical thrust vectoring parallel manipulator are proposed. Its forward and inverse kinematic solutions are formulated. And the dynamic model is established by Lagrange's formulation and the principle of energy equivalence. Finally, numerical simulation results validate the efficiency of kinematic and dynamic models.

**Keywords** Spherical parallel manipulator · Autonomous underwater vehicle · Thrust vectoring technology · Kinematic and dynamic model

## 1 RR-RRR Spherical Parallel Manipulator for Vector Thruster

Spherical parallel robots have been applied in lots of aspects [1, 2]. Agile Eye and a 2-DOF SPM for a given set of inputs have been proposed in [1, 3, 4]. It has also been revealed in [5] that the 2-DOF SPM always undergoes self-motion in a singular configuration. Inspired by [5], this paper discusses a type of 2-DOF vector thruster parallel manipulator.

As is depicted in Fig. 1 the 2-DOF spherical parallel manipulator is a kind of spatial five-bar mechanism, which is composed of a R-R transmission chain and a R-R-R transmission chain. The two transmission chains are both rotating pair, whose all axes intersect at the coordinate origin. Two yaw motors are fixed to the frame, and their axes are perpendicular to each other. A propulsion motor is fixedly connected to the movable platform. The axis of the propulsion motor is perpendicular to the moving

---

H. Xu · Y. Chen (✉) · J. Gao

School of Mechanical, Electrical and Information Engineering, Shandong University, Weihai 264209, China

e-mail: cyzghysy@sdu.edu.cn

© Springer-Verlag Berlin Heidelberg 2016

B. Huang and Y. Yao (eds.), *Proceedings of the 5th International Conference on Electrical Engineering and Automatic Control*, Lecture Notes in Electrical Engineering 367, DOI 10.1007/978-3-662-48768-6\_21

181

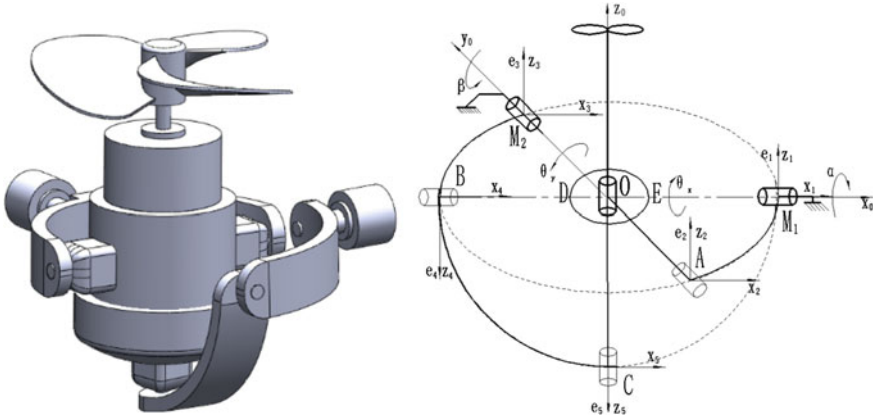


**Fig. 1** Three-dimensional model and schematic of the spherical parallel manipulator

platform. The manipulator is simplified to a five-bar structure including the chains  $M_1A$ ,  $M_2B$ ,  $BC$ ,  $AO$ , and  $CO$ . All axes of revolute joints intersect at the coordinate origin, and the axes of adjacent revolute joints are perpendicular to each other. Two yaw motors are fixedly connected with external agencies at point  $M_1$  and  $M_2$ , respectively. Two chains  $AO$  and  $CO$  are connected to the moving platform. Figure 1 illustrates the coordinate system. The origin of the coordinates is defined as the  $O$  point.

## 2 Kinematic Solutions of Vector Thruster

The simplified five bar spherical manipulator of the vector thruster is composed of a R-R drive chain and a R-R-R transmission chain which are driven by two yaw motors, and the motor shaft is perpendicular to each other and to a point  $O$ .

### 2.1 Forward Kinematic Solutions

Two input angles of deflection motor are defined as  $\alpha$  and  $\beta$ , and the rotation angle of  $X_0$  and  $Y_0$  axis of the moving platform are designed as  $\theta_x$  and  $\theta_y$ . Since the spherical surface is related to the rotation of the manipulator, its kinematics' positive solution can be transformed into the displacement transformation matrix of the moving platform.

The moving platform is driven by two parallel transmission chains. The direction vector of chain  $CO$  can be expressed as  $e_5 = (-\sin \phi \ 0 \ -\cos \phi)^T$ . If the yaw motor

1 rotates at an angle  $\alpha$ , for chain AO, we have  $e_2 = (0 - \cos \alpha \sin \alpha)^T$ . Substitution of the definitions of  $e_5$  and  $e_2$  into  $r = e_2 \times e_5$  yields

$$r = (\cos \alpha \cos \phi - \sin \alpha \sin \phi - \cos \alpha \sin \phi)^T \tag{1}$$

For the moving platform DOE, the normal vector  $t$  can be expressed as  $t = e_2 \times r$ , and substitution of Eq. (1) into it yields

$$t = (\sin \phi \sin \alpha \cos \alpha \cos \phi \cos^2 \alpha \cos \phi)^T \tag{2}$$

Since the three rotation axes of the chains BC, AO, and CO are perpendicular to each other and intersect at O point and the input angle  $\phi$  equals  $\beta$ , we have

$$t = (\sin \beta \sin \alpha \cos \alpha \cos \beta \cos^2 \alpha \cos \beta)^T \tag{3}$$

### 2.2 Inverse Kinematic Solutions

The inverse kinematics solution of the five-bar structure is referenced as the two input angles  $\alpha$  and  $\beta$  of the two yaw motors. It is assumed that the final attitude matrix of the moving platform is expressed as  $T = (i \ j \ k)^T$ , where the three-unit vectors are defined as  $i = r, j = -e_2, k = t$ , respectively. From Eqs. (1)–(3), the three-unit vectors can be expressed as

$$\sin \beta = i \quad \sin \alpha \cos \alpha \cos \beta = j \quad \cos^2 \alpha \cos \beta = k \tag{4}$$

Thus, the inverse kinematics solution can be derived as follows:

$$\alpha = \arctan j/k \quad \beta = \arcsin i \tag{5}$$

### 2.3 Jacobian Matrix

The angles  $\theta_x$  and  $\theta_y$  is defined as the angles that the moving platform rotates about the  $X_0$ -axis and the  $Y_0$ -axis, respectively. The relationship of the final attitude matrix of the moving platform and the angles  $\theta_x$  and  $\theta_y$  can be expressed as  $\tan \theta_x = j/k \tan \theta_y = k/i$ , where  $\theta_x = \frac{\pi}{2} - \alpha \theta_y = \arctan \frac{\cos^2 \alpha \cos \beta}{\sin \beta}$ . The relationships among  $\dot{\alpha}, \dot{\beta}, \theta_x$  and  $\theta_y$  can be derived as a form of matrix

$$\begin{bmatrix} \dot{\theta}_x \\ \dot{\theta}_y \end{bmatrix} = \mathbf{J} \begin{bmatrix} \dot{\alpha} \\ \dot{\beta} \end{bmatrix} \quad (6)$$

Thus the Jacobian matrix of the mechanism is expressed as

$$\mathbf{J} = \begin{bmatrix} -1 & 0 \\ \frac{2 \sin \alpha \cos \alpha \sin \beta \cos \beta}{\cos^2 \alpha \cos^2 \beta + \sin^2 \beta} & \frac{\cos^2 \alpha}{\cos^4 \alpha \cos^2 \beta + \sin^2 \beta} \end{bmatrix} \quad (7)$$

### 3 Dynamic Modeling of Vector Thruster

The dynamic equations of the vector thruster manipulator can be derived using Lagrange's formulation and the principle of energy equivalence [6–8]. The total potential energy of the manipulator is defined as follows:

$$E_p = E_{p0} + E_{p1} + E_{p2} + E_{p3} \quad (8)$$

where  $E_{p0}$ ,  $E_{p1}$ ,  $E_{p2}$ , and  $E_{p3}$  are defined as the potential energy of the moving platform, the chains  $M_1A$ ,  $M_2B$ , and  $BC$ , respectively.

After  $\alpha$  and  $\beta$  angle rotating about the  $X$ -axis and  $Y$ -axis, the center of mass of the propeller can be calculated as

$$\mathbf{C}_{m0} = (\cos \alpha \sin \beta \cdot z \quad -\sin \beta \cdot z \quad \cos \alpha \cos \beta \cdot z)^T \quad (9)$$

After  $\beta$  angle about the  $Y$ -axis of the chain  $M_2B$ , the center of mass of the chain  $M_2B$  is defined as

$$\mathbf{C}_{m2} = \left( -\frac{\sqrt{2}}{2}R \cos \beta \quad \frac{\sqrt{2}}{2}R \quad \frac{\sqrt{2}}{2}R \sin \beta \right)^T \quad (10)$$

After  $\alpha$  and  $\beta$  angle rotating about the  $X$ -axis and  $Y$ -axis of the chain  $BC$ , we have the following center of mass of the chain  $BC$

$$\mathbf{C}_{m3} = \left( -\frac{\sqrt{2}}{2}R(\cos \alpha \sin \beta + \cos \beta \frac{\sqrt{2}}{2}R \sin \alpha - \frac{\sqrt{2}}{2}R(\cos \alpha \cos \beta - \sin \beta))^T \right) \quad (11)$$

The potential energy of each part can be expressed as

$$\begin{cases} E_{p0} = m_0 g \cos \alpha \cos \beta \cdot z \\ E_{p1} = 0 \\ E_{p2} = \frac{\sqrt{2}}{2} m_2 R \sin \beta \\ E_{p3} = -\frac{\sqrt{2}}{2} m_3 g R (\cos \alpha \cos \beta - \sin \beta) \end{cases} \quad (12)$$

where  $m_0$ ,  $m_2$ , and  $m_3$  represent the total mass of the motor and the propeller, the mass of the chain  $M_2B$  and the mass of the chain  $BC$ . The total kinetic energy of the manipulator is defined as

$$E_k = E_{k1} + E_{k2} \quad (13)$$

where  $E_{k1}$  represents the total kinetic energy of the propeller and  $E_{k2}$  represents the total kinetic energy of the chains  $M_1A$ ,  $M_2B$ , and  $BC$ .

The angular velocity vector of the moving platform can be defined as  $\mathbf{w} = (\dot{\theta}_x \quad \dot{\theta}_y)^T$ .  $E_{k1}$  and  $E_{k2}$  can be expressed as

$$E_{k1} = \frac{1}{2} \mathbf{w}^T \mathbf{I}^0 \mathbf{w} = \frac{1}{2} [\dot{\alpha} \quad \dot{\beta}] \mathbf{J}^T \mathbf{I}^0 \mathbf{J} [\dot{\alpha} \quad \dot{\beta}]^T \quad (14)$$

$$E_{k2} = (\mathbf{I}_1 + \mathbf{I}_3) \dot{\alpha}^2 + (\mathbf{I}_2 + \mathbf{I}_3) \dot{\beta}^2 \quad (15)$$

The driving torque of the two paw motors can be derived from the following Lagrange equation:

$$\frac{d}{dt} \frac{\partial \mathbf{L}}{\partial \dot{\theta}} - \frac{\partial \mathbf{L}}{\partial \theta} = \boldsymbol{\tau} \quad (16)$$

where  $\mathbf{L}$  represents the Lagrange function of the manipulator, which is defined as  $\mathbf{L} = E_k - E_p$  and  $\boldsymbol{\tau} = (\tau_1 \quad \tau_2)^T$  is the driving torque of the two motors.  $\theta = (\alpha \quad \beta)^T$  and  $\dot{\theta} = (\dot{\alpha} \quad \dot{\beta})^T$  are the angle and angular velocity of the two drive motors. Substituting Eqs. (9)–(15) into Eq. (16) yields the dynamic model.

## 4 Numerical Simulation and Discussion

The total mass of the propeller is equal to 3 kg. The distance between the mass center of the moving platform and the origin of coordinate ( $R$ ) is designed as 200 mm, and all masses of the chains  $M_1A$  ( $m_1$ ),  $M_2B$  ( $m_2$ ), and  $BC$  ( $m_3$ ) is equal to 1 kg.

The extension length of the propeller shaft is set as 60 mm. According to formula (6), the change of the spatial location of the propeller can be obtained which is shown in Fig. 2. The maximum input angle of the two deflection motor  $\alpha$  and  $\beta$  is  $\pm 40^\circ$ . Analyzing from the MATLAB the workspace position of the manipulator is also shown in Fig. 2. It is assumed that the angle  $\alpha$  varies from  $-\pi/4$  to  $\pi/4$  at the rate of 0.1 rad/s, the angle  $\beta$  remains constant as  $\pi/6$ . As shown in Fig. 3, the driving torque curve of the manipulator is obtained.

During the variation of  $\alpha$ , the maximum value of the driving torque  $\tau_1$  is 4500 N mm, the driving force  $\tau_2$  changes gently in the 6 s before, reaches the

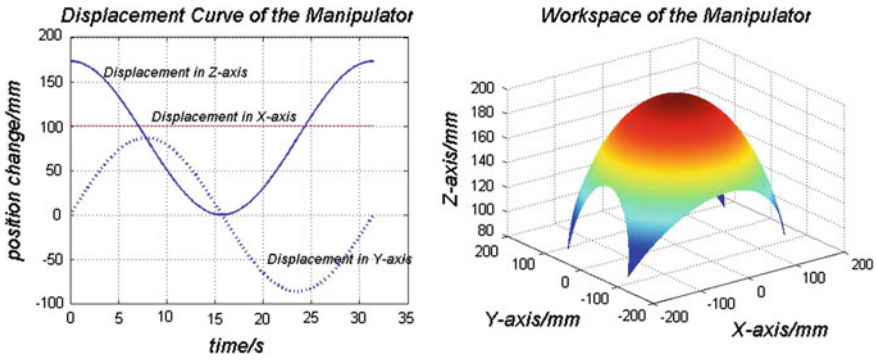


Fig. 2 Motion law of spatial and the workspace position of the manipulator

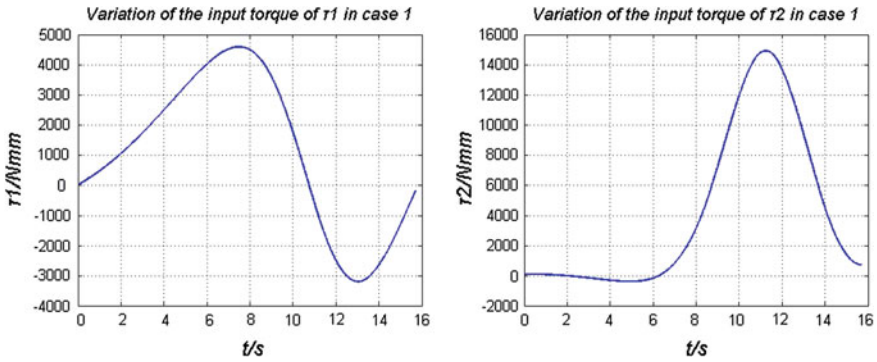


Fig. 3 Driving torque versus time curve of  $\tau_1$  and  $\tau_2$ , respectively, in case 1

maximum near 14500 N mm at 11 s. The analysis of the input torque can provide important reference for the following motor selection and propulsion performance analysis.

### 5 Conclusion

As parallel manipulators have the merits both of being able to implement complicated DOFs and of having the ability to perform the movements very fast, in this paper the parallel manipulators are selected for study as the vector thruster manipulator of underwater vehicle. By conceptual design a 2-DOF spherical parallel manipulator is developed. The inverse and forward kinematics and a velocity analysis of the novel spherical parallel manipulator are carried out. The simulation results show the deflection in both directions reaching  $\pm 45^\circ$ , which greatly improves the deflection angle in both directions, so as to guarantee a large range

control of the main push propeller and a more flexible for underwater vehicle. Dynamic model of the spherical parallel manipulator is developed. The numerical simulation results verify that the proposed parallel manipulator can realize the rotational transmission and attitude adjustment, and is suitable for vector thruster.

**Acknowledgments** Grateful acknowledgement is given to the financial supports from the National Natural Science Foundation of China with Grant No. 51375264. This work was also partially supported by State Key Laboratory of Robotics and System (HIT) with Grant No. SKLRS-2015-MS-06, and Research Awards Fund for Excellent Young and Middle-aged Scientists of Shandong Province with Grant No. BS2013ZZ008.

## References

1. Kong X, Gosselin CM (2009a) Forward displacement analysis of a quadratic spherical parallel manipulator: the agile eye. In: Proceedings of the ASME 2009 international design engineering technical conferences and computers and information in engineering conference, paper DETC2009-87467, August 30–September 2, San Diego, California, USA
2. Wu K, Yu J, Zong G, Kong X (2014) A family of rotational parallel manipulators with equal-diameter spherical pure rotation. *J Mech Robot* 6(1):011008
3. Kong X, Gosselin CM (2009b) Forward displacement analysis and singularity analysis of a 2-DOF 5R spherical parallel manipulator. In: Proceedings of the ASME 2009 international design engineering technical conferences and computers and information in engineering conference, paper DETC2009-87654, August 30–September 2, San Diego, California, USA
4. Ueda K, Yamada H, Ishida H, Hirose S (2013) Design of large motion range and heavy duty 2-DOF spherical parallel wrist mechanism. *J Robot Mechatron* 25(2):294–305
5. Gosselin CM, Geron F (1999) Two degree-of-freedom spherical orienting device: US, 596691
6. Abdellatif H, Heimann B (2009) Computational efficient inverse dynamics of 6-dof fully parallel manipulators by using the Lagrangian formalism. *Mech Mach Theory* 44:192–207
7. Khalil W, Ibrahim O (2004) General solution for the dynamic modeling of parallel robots. In: Proceedings of the IEEE international conference on robotics and automation, New Orleans, LA, USA, pp 3665–3670
8. Saltaren RJ, Sabater JM, Yime E, Azorin JM, Aracil R, Garcia N (2007) Performance evaluation of spherical parallel platforms for humanoid robots. *Robotica* 25(03):257–267



# Synchronous Generator-Based Design of Damping Emulation Controller for DFIG

Zhang Yan, Yang Chunhua and Sun Hui

**Abstract** The present work is based on developing the effect from doubly fed induction generator (DFIG) connected to the grid. The dynamic model, small signal stability analysis, and damping characteristic are conducted. By comparison with synchronous generator, there is insufficient damping performance from DFIG. The paper proposes the idea of designing a damping controller emulating synchronous generator by pole placement technique in order to improve damping. Furthermore, a mirror pole assignment solution is particularly put forward in view of instability system. The theoretical analysis and controller effectiveness are confirmed via simulation results for a size 9 MW DFIG operating under varied converter conditions, and the damping improvement observed in time domain support the result obtained from eigenvalue analysis.

**Keywords** DFIG · Damping analysis · Mirror pole placement · Small signal

## 1 Induction

As the wind powers' penetration level is increasing, power system will make adjustments. Variable speed wind turbine, connected to the grid by electronic devices, has the characteristics of turbulent and randomness. Because the characteristics are very different from those of conventional power plants, small signal stability problems can become an issue. It is necessary to study of the dynamic model of turbine in order to investigate the aspects of damping and stability by comparing with synchronous. In the early stage, the wind generator was often modeled equivalent to asynchronous generator lumped model [1]. However, one-mass model is insufficient to analyze the transient behavior of wind turbine generator systems (WTGS), multi-mass shaft model was studied [2, 3]. According

---

Z. Yan (✉) · Y. Chunhua · S. Hui  
School of Electrical Engineering, Dalian University of Technology,  
Dalian 116023, China  
e-mail: ivy\_zhy@yeah.net

to the conclusion from Muyeen et al. [4], this paper expresses doubly fed induction generator (DFIG) by two-mass shaft model which is suitable for the stability analysis.

Increasing attention has been focused recently on the damping of oscillations which characterize the phenomena of stability. Research has suggested that the integration of wind power can impact on system stability [5]. It is clear that DFIG cannot provide the same damping as synchronous systems, because its kinetic energy characteristics have been isolated by inverters connected with grid. Therefore, the damping controller has become a favorite topic for stability.

There are several papers exploring the related subjects. The converters in [6] are controlled to behave like a synchronous generator by using energy storages. However, the efficiency is limited to the capacity and service life of storages. In [7], pole assignment method is employed, but the focus of many controllers did not consider the instability condition.

This paper proposes a two-mass shaft model in Sect. 2. Section 3 analyzes static stability and damping characteristic between DFIG and synchronous. The damping controller is presented by improved pole assignment method under stability and instability condition. Both controllers are tested upon the mathematical model and validated using MATLAB/Simulink in Sect. 4. Finally, a conclusion is drawn that the obtained results show better damping compared to before, particularly in terms of stabilization system.

## 2 DFIG Wind Turbine Model

The wind generation system consists of variable speed wind turbine, wind wheel gear box, doubly fed induction generator, and grid and generator side converters. The stator winding is directly connected to the grid, and rotor winding is connected to the grid through back-to-back PWM voltage source converters.

- Electromagnetic Equations of DFIG

The electrical part of the DFIG is represented by a fourth order state space model, which is constructed using the synchronously rotating reference frame (dq frame). The voltage and flux linkage equations of the DFIG can be written as follows [8]:

$$\begin{aligned} \text{stator: } u_{ds} &= p\psi_{ds} - \psi_{qs} + r_s i_{ds}, & u_{qs} &= p\psi_{qs} + \psi_{ds} + r_s i_{qs} \\ \text{rotor: } u_{dr} &= p\psi_{dr} - s\psi_{qr} + r_r i_{dr}, & u_{qr} &= p\psi_{qr} + s\psi_{dr} + r_r i_{qr} \end{aligned} \quad (1.1)$$

$$\begin{aligned} \text{stator: } \psi_{ds} &= L_{ss} i_{ds} + L_m i_{dr}, & \psi_{qs} &= L_{ss} i_{qs} + L_m i_{qr} \\ \text{rotor: } \psi_{dr} &= L_{rr} i_{dr} + L_m i_{ds}, & \psi_{qr} &= L_{rr} i_{qr} + L_m i_{qs} \end{aligned} \quad (1.2)$$

where subscripts ss, rr, and m stand for stator, rotor, and mutual inductances, respectively. s is slip. From the Eqs. (1.1) and (1.2), the voltage–current matrix

equation can be written where voltages as independent variables and currents as dependent.

- Two-mass Shaft Model

The investigated two-mass-system can be described by the following set of elementary mechanical equations [9]:

$$\begin{cases} H_w p \omega_w = -k_s \theta_s - D p \theta_s + T_w \\ H_g p \omega_g = k_s \theta_s + D p \theta_s - T_e \\ p \theta_s = \omega_w - \omega_g \end{cases} \quad (1.3)$$

Equations for the rotation taking into account the different angular velocities at the turbine side with the index w and at the generator side with g. Where p represents the differential operator, T is the torque, ω is the angular velocity, θ the angular position, k the stiffness coefficient, and D the internal damping.

- Model of the Converters

The generator side converter controls the active and reactive power of the DFIG, and the grid side converter is controlled in such a way as to maintain the DC link capacitor voltage in a set value and to maintain the converter operation with a desired power factor (Fig. 1).

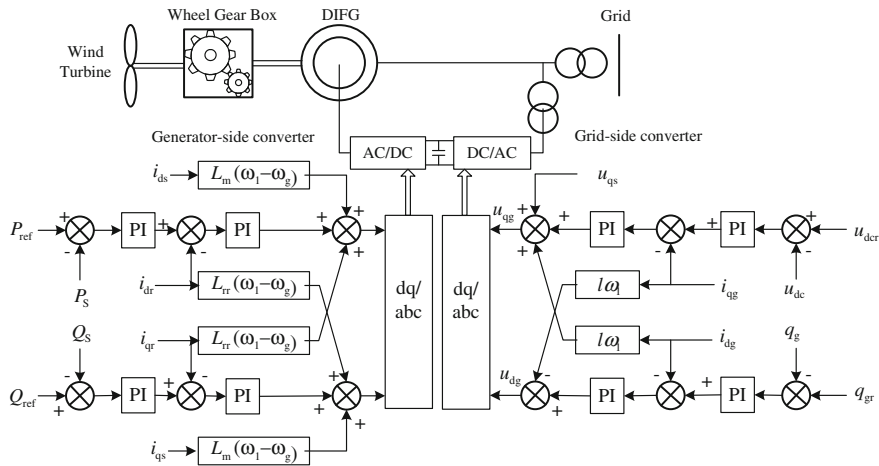


Fig. 1 Generator side and grid side converters

### 3 Stability Analysis and Damping Control

#### 3.1 Stability and Damping Analysis

According to Sect. 2, we can get the state matrix by small signal analysis so as to study the effects of a disturbance on a linear system. They are

$$\begin{aligned} p\Delta x &= A\Delta x + B\Delta\omega \\ \Delta P &= K_p\Delta x \end{aligned} \quad (1.4)$$

where  $\Delta x = [\Delta\omega_w \ \Delta\omega_g \ \Delta\theta_s \ \Delta\psi_{ds} \ \Delta\psi_{qs} \ \Delta i_{dr} \ \Delta i_{qr} \ \Delta x_1 \ \Delta x_2 \ \Delta x_3 \ \Delta x_4]^T$ .  $\Delta x_1$ – $\Delta x_4$  are state variables dependent from converters. Solving for the Eq. (1.4), we have the transfer function of DFIG which is as follows:

$$G_w(s) = K_p(sI - A)^{-1}B \quad (1.5)$$

The study is carried out to compare the stability and damping between DFIG and synchronous. The parameters are as follow:  $r_r = 0.005$ ,  $r_s = 0.0071$ ,  $L_m = 2.9$ ,  $L_{ss} = 3.071$ ,  $L_{rr} = 3.056$ ,  $H_w = 4.54$ ,  $H_g = 0.5$ ,  $k_s = 0.3$ ,  $D = 2$ . The eigenvalues of the system matrix A characterize the stability of the system are shown in Table 1. It summarizes the variation of damping without obvious changing (–3.4127 to –3.9745) when PWM controllers are operated at different conditions. It means DFIG imparts significant effect on the damping performance. It is worth noting that the system is unstable because of positive eigenvalues of mode #2 and #3. Additional approach is required particularly for keeping system stable.

**Table 1** Eigenvalues of the DFIG system

Mode number	#1	#2	#3
$\lambda_1$	–3.0475	–3.0475	–3.0475
$\lambda_2$	–0.0199+1.2554i	–0.0253+0.3981i	–0.1459+1.3128i
$\lambda_3$	–0.0199–1.2554i	–0.0253–0.3981i	–0.1459–1.3128i
$\lambda_4$	–0.0191+1.2529i	–0.0593+0.3920i	–0.3184+1.0712i
$\lambda_5$	–0.0191–1.2529i	–0.0593–0.3920i	–0.3184–1.0712i
$\lambda_6$	–0.1414+0.0410i	–0.1414+0.0410i	0.3783
$\lambda_7$	–0.1414–0.0410i	–0.1414–0.0410i	–0.1414+0.0410i
$\lambda_8$	–0.0006+0.0042i	0.0501	–0.1414–0.0410i
$\lambda_9$	–0.0006–0.0042i	–0.0292	–0.1085
$\lambda_{10}$	–0.0030	0.0100	0.0147
$\lambda_{11}$	–0.0000	–0.0000	–0.0000
Damping	–3.4127	–3.4688	–3.9745

### 3.2 Controller Design and Mirror Approach

The article prefer to the pole placement technique, which uses root locus rules to shift a pair of dominant poles to a newly assigned location in the  $s$ -plane.

Let  $G_w(s)$  construct closed-loop plant with a controller denoted by  $H(s)$ . The controller consists of a washout and a series of lead and/or lag functions, as shown in Fig. 2. Assume that the eigenvalue is to be placed to a new location denoted by  $\lambda_0$ . So  $\lambda_0$  must satisfy the characteristic equation  $1 + G_w(\lambda_0)H(\lambda_0) = 0$ . It means

$$\begin{aligned} |H(\lambda_0)| &= 1/|G_w(\lambda_0)| \\ \arg(H(\lambda_0)) &= 180^\circ - \arg(G_w(\lambda_0)) \end{aligned} \tag{1.6}$$

The key question is how to choose the new pole  $\lambda_0$ . Since bandwidth impact on anti-interference performance, the objective location cannot be as far as possible away from the virtual axis. This paper explored the possibility of the similar controlling, based on state space model of synchronous system with PSS.

The state vector is defined as  $X = [\Delta\delta \ \Delta\omega \ \Delta E'_q \ \Delta E \ \Delta x_1 \ \Delta x_2]^T$ , where  $\Delta x_1$  and  $\Delta x_2$  are dependent variables. The eigenvalues are shown in Table 2.

Notice that the damping of system is over  $-30$ . The imaginary part of new pole is usually chosen slightly larger than before [10]. The magnitude and phase of the transfer function are computed for values of  $\lambda_{02}-\lambda_{05}$ . The eigenvalues of closed-loop system are shown in Table 3.

By addition controller, the damping performance of all modes is enhanced-based eigenvalues from synchronous (Table 3). However, it has been observed mode #2 and #3 keeping instability. An additional approach focusing on positive eigenvalues with a goal of designing a controller capable of all modes is presented. We refer to the technique as mirror pole placement, which shifts positive poles to specific locations in the mirror image. Then, the proposed control operation was used. From

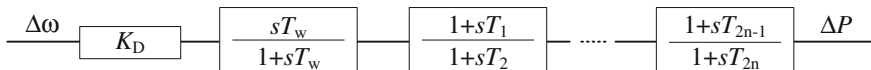


Fig. 2 Structure of attach DFIG controller

Table 2 Eigenvalues of the synchronous system with PSS

Eigenvalues	Damping ratio	Frequency of oscillation
$\lambda_{01}$	-18.0633	1.00e+000
$\lambda_{02}$	-4.7573+8.8833i	4.72e-001
$\lambda_{03}$	-4.7573-8.8833i	4.72e-001
$\lambda_{04}$	-1.9670+4.453i	3.30e-001
$\lambda_{05}$	-1.9670-4.453i	3.30e-001
$\lambda_{06}$	-0.3393	1.00e+000

**Table 3** Damping of the closed-loop system

Mode	$\lambda_{02}$	$\lambda_{03}$	$\lambda_{04}$	$\lambda_{05}$
#1	-23.8408	-17.3553	-12.1125	-8.3282
#2	-23.8969	-14.5404	-12.1685	-8.3842
#3	-24.4026	-15.0464	-12.6743	-8.8903

**Table 4** Comparison of eigenvalues with mirror placement and original placement

$\lambda_{02}$		$\lambda_{03}$	
Mirror position	Original position	Mirror position	Original position
-10.2754	-10.9587	-5.0830+8.2644i	-4.4760+8.8993i
-4.6066+8.8525i	-4.8122+8.9316i	-5.0830-8.2644i	-4.4760-8.8993i
-4.6066-8.8525i	-4.8122-8.9316i	-5.4057	-3.0475
-3.0475	-3.0475	-3.0475	-0.3647+2.4050i
-0.1459+1.3128i	-0.1459+1.3128i	-0.9979+1.5029i	-0.3647-2.4050i
-0.1459-1.3128i	-0.1459-1.3128i	-0.9979-1.5029i	-2.0627
-0.0614+0.3864i	-0.2036+0.4809i	-0.1458+1.3128i	-0.1459+1.3128i
-0.0614-0.3864i	-0.2036-0.4809i	-0.1458-1.3128i	-0.1459-1.3128i
-0.1414+0.0410i	0.3037	-0.1414+0.0410i	0.4137
-0.1414-0.0410i	-0.1414+0.0410i	-0.1414-0.0410i	-0.1414+0.0410i
-0.1085	-0.1414-0.0410i	-0.1085	-0.1414-0.0410i
-0.0147	-0.1085	-0.0147	-0.1085
-0.0010	0.0147	-0.0010	0.0147
-0.0000	-0.0000	-0.0000	-0.0000
-23.3576	-24.4026	-21.3137	-15.0464

Table 4, there is no significant change of damping values after shifting the positive poles, but the system gets pushed to stable.

## 4 Simulation Results

Two examples for stability system (mode #1) and instability (mode #2) are presented in simulation studies. Figure 3 shows the step response provided by different damping. We can observe that the stabilized system with sufficient damping performance and low frequency oscillation is better.

From Fig. 4, the pole at right part of  $s$ -plane does not move and the system remains instable over the entire range. It is important to take into account removing positive poles by mirror pole placement method.

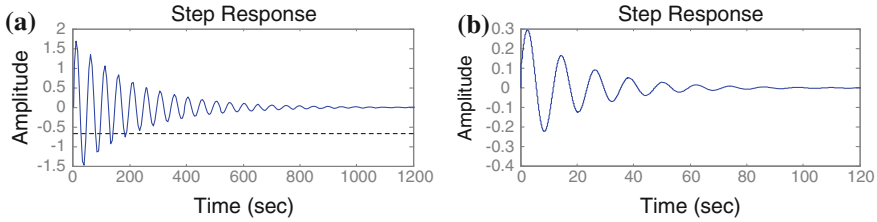


Fig. 3 Simulation of mode 1#. a Damping:  $-8.3282$ . b Damping:  $-23.8408$

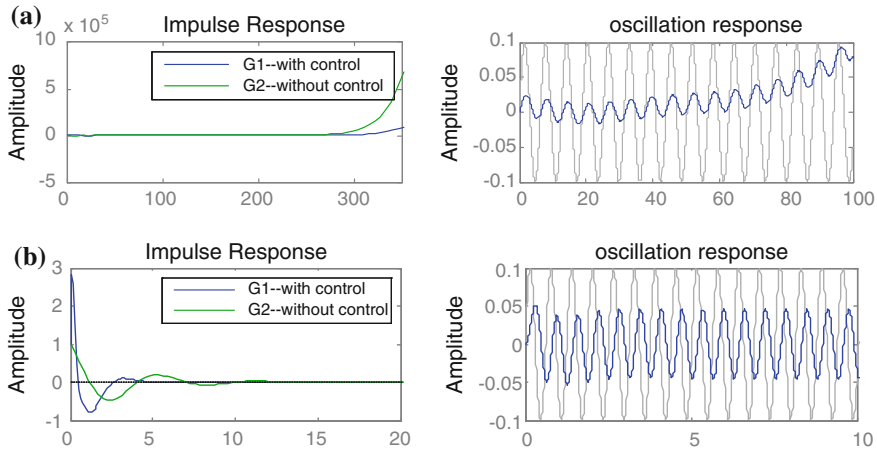


Fig. 4 Simulation of mode 2#. a Damping control without mirror placement. b Damping control with mirror placement

### 5 Conclusion

This paper has presented the wind system of DFIG model and damping analysis for converter additional controller, which makes stability and performance damping more sufficient. Eigenvalue analysis results show that the doubly fed wind turbine provides the insufficient damping to system, and it is possible impact the system stable. Based on the synchronous model, eigenvalues from the state space equations can be obtained in order to help the designer to define the target poles, and improving the damping. The mirror pole assignment approach is making the system stable and easy to control damping.

## References

1. Akhmatov V (2002) Variable-speed wind turbines with doubly-fed induction generators. Part I: modelling in dynamic simulation tools. *Wind Eng* 26(2):85–108
2. Leithead WE, Connor B (2000) Control of variable speed wind turbines: dynamic models. *Int J Control* 73(13):1173–1188
3. Petru T, Thiringer T (2002) Modeling of wind turbines for power system studies. *IEEE Trans Power Syst* 7(4):1132–1139
4. Muyeen SM, Ali MH et al (2007) Comparative study on transient stability analysis of wind turbine generator system using different drive train models. *IET Renew Power Gener* 1(2):131–141
5. Muljadi E, Butterfield CP, Parsons B et al (2007) Effect of variable speed wind turbine generator on stability of a weak grid. *IEEE Trans Energy Converters* 22(1):29–35
6. Shintai T, Miura Y, Ise T (2014) Oscillation damping of a distributed generator using a virtual synchronous generator. *IEEE Trans Power Delivery* 29(2):668–676
7. Tang Y, He H et al (2013) Comparative study between HDP and PSS on DFIG damping control. In: *Computational intelligence applications in smart grid*, vol 16, pp 59–65
8. Chowary BH, Chellapilla S (2006) Doubly-fed induction generator for variable speed wind power generation. *Trans Electr Power Syst Res* 76:786–800
9. Salman SK, Teo ALJ (2003) Windmill modeling consideration and factors influencing the stability of a grid-connected wind power-based embedded generator. *IEEE Trans Power Syst* 18(2):793–802
10. Kundur P (1994) *Power system stability and control*. McGraw-Hill, New York



# Study on Control Strategy of Harmonic Suppression in a Wide Power Range Based on V2G Bidirectional Onboard Charger

Fuhong Xie, Weifeng Gao, Xiaofei Liu and Shumei Cui

**Abstract** With the development and widespread use of electric vehicle (EV), the vehicle-to-grid technology (V2G) has become increasingly attractive. Considering the case of V2G bidirectional onboard charger has involved in power grid frequency regulation service and the characteristics of frequency regulation signal, this paper propose a control strategy for wide power range bidirectional current harmonic suppression by combining with the quasi proportional resonant (QPR) control and the weighted feedback current (WFC) control and introducing a peak restrained LCL filter. Simulation and experimental results are provided to validate the feasibility and correctness of the proposed control strategy.

**Keywords** EV · V2G · Bidirectional onboard charger · Harmonic suppression

## 1 Introduction

Electric vehicle (EV) power battery can provide energy for the power grid in the peak load time and store the excess power when the power load is low, which can effectively regulate the difference between peak and valley load of the grid, reducing the reversed capacity for peak load regulation and frequency regulation in the traditional grid, as well as, contributing to the absorbency of renewable energy in power grid, in which all improve the efficiency and stabilization of grid operation [1]. This bidirectional exchange of energy and information between EV and power grid is called the vehicle-to-grid (V2G) technology [2].

---

F. Xie (✉) · W. Gao · X. Liu · S. Cui  
Harbin Institute of Technology, Harbin, China  
e-mail: xiefuhong2@126.com

Brooks [3], Kempton and Tomić [4] evaluated that V2G was highly competitive for frequency regulation. Xiaofei et al. [2] indicated that the research focus of bidirectional charger were improvement in efficiency and ability of grid current harmonic suppression, reduction in costs, volume, and weight. Therefore, researchers had conducted corresponding study for the V2G bidirectional charger. Wang et al. [5] presented a sectional optimized modulation strategy of AC/DC matrix converters for V2G applications. Tang and Su [6] described a low-cost onboard charger for plug-in hybrid electric vehicles. Zhou et al. [7] studied a new multi-function bidirectional battery charger for plug-in hybrid electric vehicles.

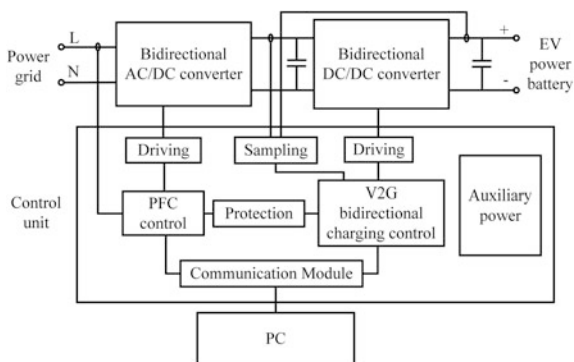
When V2G technology participates in frequency regulation service, however, the volatility of power demand signal in grid side requires frequent switch between output and input power, which makes the charger's working point unfixed and may result in a wide bidirectional power range. The proportional integral (PI) controller is widely used in AC/DC converter for grid current control. In general, the PI controller parameters are designed only for the system's rated operating point. When the working point is not at the approximate linear region of the rated operating point, it will lead to poor performance and steady-state error increases, which results in high current total harmonic distortion (THD).

Based on the aforementioned analyses, considering the characteristics of frequency regulation signal in grid side, this paper proposes a control strategy of current harmonic suppression in a wide power range for V2G bidirectional charger.

## 2 Design of V2G Bidirectional Charger

The overall structure of V2G bidirectional charger is shown in Fig. 1. The control unit achieves the power factor correction (PFC) in grid side, the domination of power flow direction and the controllable output in battery side. The personal computer (PC) is used to simulate the upper power grid control system for transmitting the power demand signal to the charger.

**Fig. 1** Diagram of overall structure for charger system



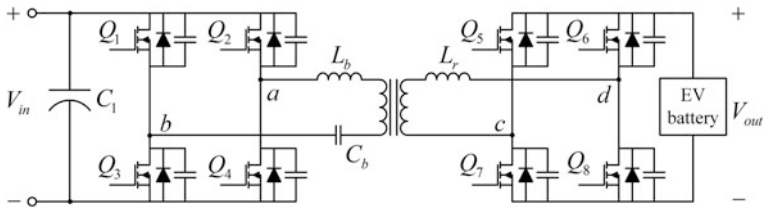


Fig. 2 Diagram of the dual active bridge structure

### 2.1 Bidirectional DC/DC Converter

The dual active bridge (DAB) structure is selected as the bidirectional DC/DC converter for its advantage of low switch stress and electrical isolation, the circuit topology is shown in Fig. 2. The DAB structure is composed of two full bridges connected by a high frequency transformer. In Fig. 2, the  $V_{in}$  is the high-voltage side which is attached to the output DC bus of bidirectional AC/DC.

### 2.2 Bidirectional AC/DC Converter and Grid-Connected Filter

The bidirectional AC/DC converter is composed of single-phase reversible PWM rectifier and its grid-interconnected LCL filter. Figure 3 shows the main structure of bidirectional AC/DC converter and its output  $U_{DC}$  connected to the input of bidirectional DC/DC converter in the second stage. In the picture, the  $L_g$  is winding inductance in grid side and the  $R_f$  is filter damping resistance.

However, the LCL filter is a three-order system that it has a resonance point in its amplitude-frequency characteristic curve, which may result in system instability in high frequency band. Therefore, a peak restrained measure is introduced into traditional LCL filter design. A typical LCL filter is shown in Fig. 4a.

Fig. 3 Diagram of single-phase reversible PWM rectifier with LCL filter

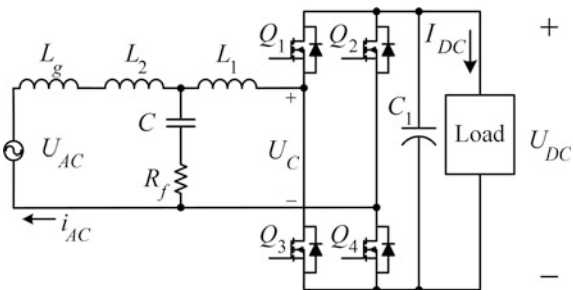
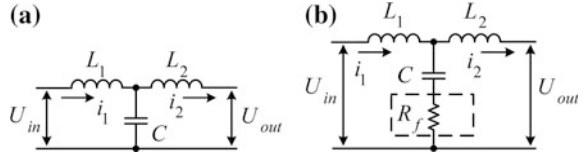


**Fig. 4** Diagram of structure for LCL filters. **a** LCL filter. **b** Peak restrained LCL filter



The transfer function of the typical LCL filter in Fig. 4a is obtained as

$$G_{LCL}(s) = \frac{i_2(s)}{U_{in}(s)} = \frac{1}{L_1 L_2 C s^3 + (L_1 + L_2)s} \tag{1}$$

In general, for small and medium power level application, passive damping method is widely used for resonance peak elimination that inserts a damping resistor into the capacitor branch in a LCL filter [8], as shown in Fig. 4b. In this case, the transfer function is changed to

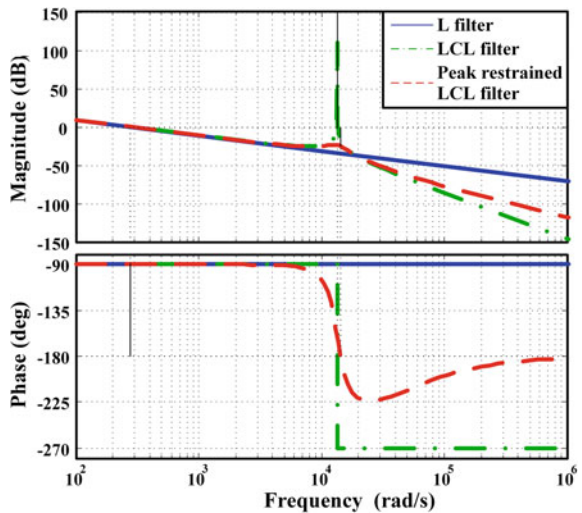
$$G_{pr-LCL}(s) = \frac{1 + CR_f s}{L_1 L_2 C s^3 + (L_1 + L_2)CR_f s^2 + (L_1 + L_2)s} \tag{2}$$

Moreover, the damping resistance  $R_f$  is obtained as

$$R_f = \frac{1}{3\omega_r C} = \frac{1}{3C} \sqrt{\frac{L_1 L_2 C}{L_1 + L_2}} \tag{3}$$

According to Eqs. (1) and (2), the amplitude-frequency characteristic curve of filters can be drawn in Fig. 5. It can be seen that the introduction of damping resistance successfully inhibits the resonance peak in the dotted red line.

**Fig. 5** Diagram of amplitude-frequency characteristic curve for filters



The change of features is mainly reflected in resonance point and frequency band above, given that, in general, the quadratic coefficient,  $(L_1 + L_2)CR_f$ , is much less than the monomial coefficient,  $(L_1 + L_2)$ . In order to simplify the calculation process, considering the low frequency of controlled grid current, this paper calculated the weighted coefficient still in a case of no damping resistor.

### 3 Control Strategy of Harmonic Suppression

#### 3.1 Design of Weighted Feedback Current Control

Furthermore, considering that LCL filter is a three-order system which cannot realize great control performance no matter direct current control or indirect current control, therefore, in order to improve the stability margin of the system, reduce the control error caused by the current sampling and so as to restrain the harmonic content of the grid current, a weighted feedback current (WFC) control is adopted in this paper. The  $i_s$  is defined as the WFC, while  $\alpha$  is the weighted coefficient of output current for the converter,  $\beta$  is the weighted coefficient of the current in grid side, as shown in Fig. 6. So it is

$$i_s = \alpha i_1 + \beta i_2 \quad (4)$$

From Fig. 6, the state equations are obtained as follows:

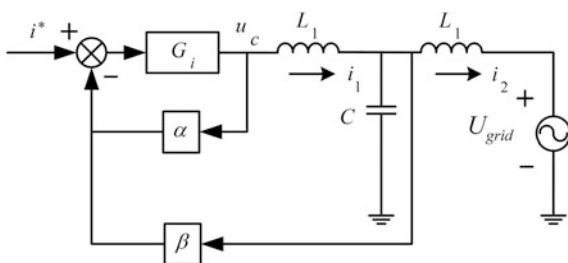
$$u_c = sL_1 i_1 + sL_2 i_2 \quad (5)$$

$$u_c = sL_1 i_1 + \frac{1}{sC} (i_1 - i_2) \quad (6)$$

The transfer function between the converter output voltage  $u_c$  and  $i_s$  is

$$G_{is}(s) = \frac{i_s(s)}{u_c(s)} = \frac{\alpha L_2 C s^2 + (\alpha + \beta)}{L_1 L_2 C s^3 + (L_1 + L_2) s} \quad (7)$$

**Fig. 6** Diagram of weighted feedback current control based on LCL filter



The WFC control can adjust the weighted coefficient, affecting the location of the conjugate zero points, and thus change the system's performance. Equation (7) is rewritten into the following form:

$$G_{is}(s) = \frac{i_s(s)}{u_c(s)} = \frac{1}{(L_1 + L_2)s} \times \frac{\alpha L_2 C s^2 + (\alpha + \beta)}{1 + L_1 L_2 C s^2 / (L_1 + L_2)} \quad (8)$$

In order to achieve great control performance, according to WFC control, the location of system's zeros and poles are usually configured to make cancelation or closed position by selecting proper weighted coefficient, so that a three-order system can be reduced to a first-order one, which can reduce the control difficulty of the system and improve the static control accuracy. In the right side of Eq. (8), let the coefficient of numerator equal to the denominator's coefficient, so that the equations about  $\alpha$  and  $\beta$  are obtained and solved.

$$\begin{cases} \alpha = \frac{L_1}{L_1 + L_2} \\ \beta = \frac{L_2}{L_1 + L_2} \end{cases} \quad (9)$$

Equation (8) is simplified into the following form finally:

$$G_{is}(s) = \frac{i_s(s)}{u_c(s)} = \frac{1}{(L_1 + L_2)s} \quad (10)$$

### 3.2 Design of Quasi Proportional Resonant Controller

PI controller cannot achieve no steady-state error control for alternating current (AC) system transient feedback application, given that the tracking signal is a fast changing sine wave and it is an error system in theory [9]. In order to overcome this control defect, the proportional resonant (PR) controller is proposed [10]. PR controller has infinite gain at the resonance frequency, and thus the system will have a great ability for sinusoidal reference signal tracking.

However, for actual system applications, the implementation of PR controller is restrained by the limitation of parameter accuracy and the low gain in nonfundamental frequency, which makes it unable to effectively suppress the current harmonic. Therefore, based on the PR controller, in order to make the V2G bidirectional charger more suitable for V2G frequency regulation service application and less sensitive to the grid frequency fluctuations, an easily implementary quasi proportional resonant (QPR) controller is adopted in this paper, which it not only has a great gain at the resonant frequency as PR controller does, but also can

lower the impact, caused by grid frequency offset, on the output current of converter. The transfer function of QPR controller is

$$G_{\text{QPR}}(s) = K_P + \frac{2K_I\omega_c s}{s^2 + 2\omega_c s + \omega_0^2} \quad (11)$$

Equation (11) describes that QPR controller can obtain enough gain at resonant point by adjusting the variable  $K_I$ , and thus ensuring a small steady-state error. On the other hand, compared to the PR controller, QPR controller has a broader bandwidth which can reduce the influence results from grid frequency fluctuation.

## 4 Verification and Analysis of the System

### 4.1 Simulated Results and Analysis

Simulation model of reversible PWM rectifier and DAB converter have been built by using Matlab and Simulink, the input of the system connect to the grid while the output is attached to a battery. The capability of current harmonic suppression for PI control, PI with WFC control, QPR control, QPR with WFC control at different power condition is verified and compared in the simulation experiment. Table 1 shows the simulation parameters setting.

In order to overcome the shortcoming of local linearization of the controller, the whole power range is divided into several sections and the respective optimal PI or QPR parameters are used in different power segments. Figure 7 shows that, with the decrease of power, although the increase of the proportion of current harmonic content leads to a corresponding growth of THD of grid current, the introduction of QPR with WFC control can make the grid current THD remain in a very low level in a wide power range, which can achieve EV clean grid-connection without adding additional EMI equipment.

**Table 1** Parameters setting of simulation model for V2G bidirectional charger

Parameters	Value
Rated grid rms voltage	AC220 V, 50 Hz
DC-bus voltage	390 V
Output voltage in battery side	280 V
Rated power of system	3.3 kW
Filter inductance $L_1, L_2$	3 mH, 600 $\mu$ H
Filter capacitor $C$	11 $\mu$ F
Switching frequency of reversible PWM rectifier	40 kHz
Switching frequency of DAB converter	80 kHz

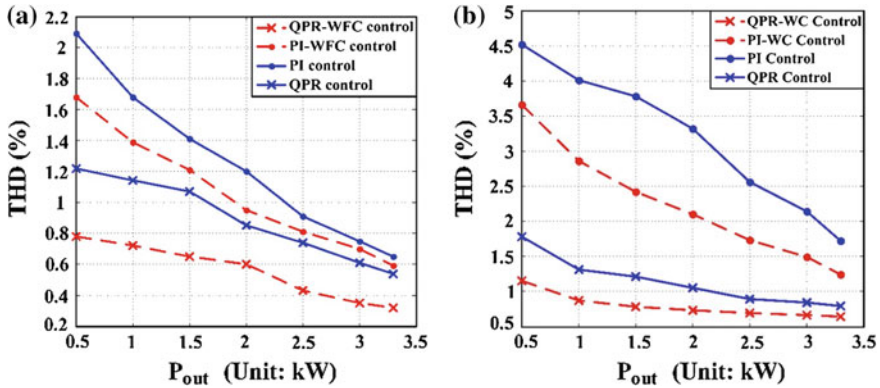
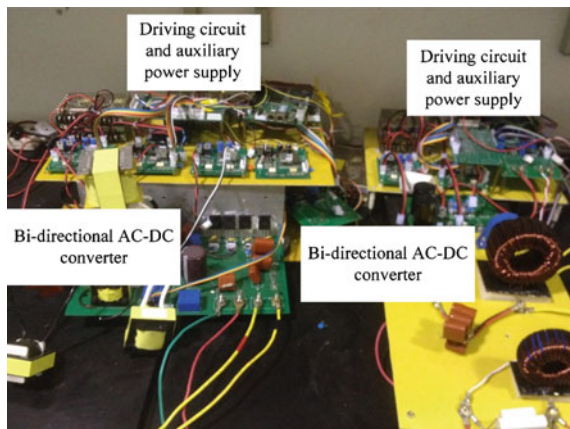


**Fig. 7** The simulation results of grid current THD of V2G bidirectional charger. **a** Simulation results of discharging grid current THD of four kinds of control method at different output power condition. **b** Simulation results of charging grid current THD of four kinds of control method at different input power condition

### 4.2 Experimental Results and Analysis

In order to further verify the feasibility of the control strategy, this paper has built an experimental platform for V2G bidirectional charger. The rated single-phase grid rms voltage is 220 V and its frequency is 50 Hz, isolated grid-connection is realized by using a voltage regulator. The other parameters are set as the same as the simulated parameters. The experimental platform is shown in Fig. 8, the grid voltage and current in discharging and charging are presented in Figs. 9 and 10 shows the experimental results of grid current THD of four kinds of control strategy for two-way power flow.

**Fig. 8** Experimental platform of V2G bidirectional charger





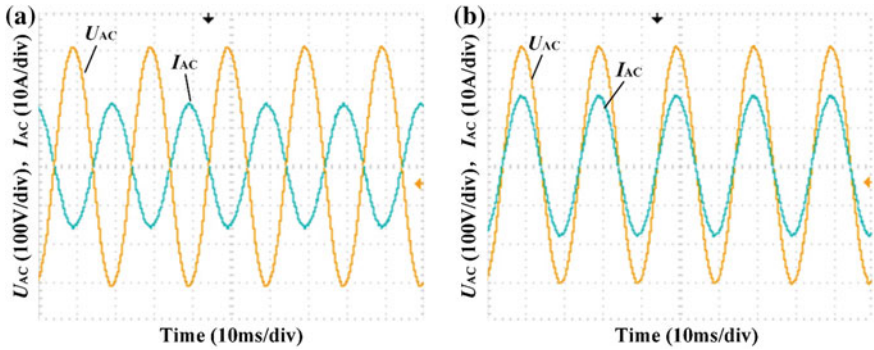


**Fig. 9** Wave forms of grid voltage and current with QPR and WFC control. **a** Waveforms of grid voltage and discharging current. **b** Waveforms of grid voltage and charging current

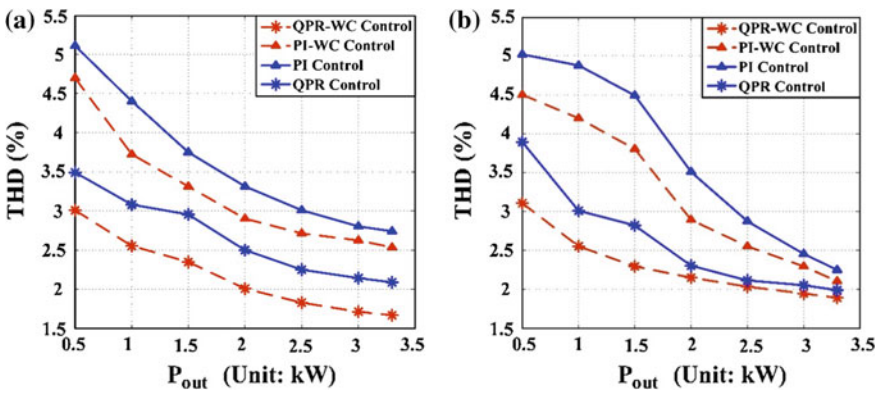


**Fig. 10** The experimental results of grid current THD of V2G bidirectional charger. **a** Experimental results of discharging grid current THD of four kinds of control method at different output power condition. **b** Experimental results of charging grid current THD of four kinds of control method at different output power condition

It can be seen that the experimental results are similar with the simulated ones, the adoption of QPR with WFC control can achieve synchronusness between grid voltage and current and current harmonic suppression in a wide power range.

## 5 Conclusion

According to the adaptability for smart grid frequency regulation service, this paper proposed a control strategy of grid current harmonic suppression in a wide power range for V2G applications based on the peak restrained LCL filter and the QPR with WFC control. Theoretical basis and implementation method were presented;

simulation and experiment results verified the feasibility. Compared to others, the features of the new control strategy are

- (1) Low steady-state error and great current harmonic suppression capability, the grid current THD can be limited to a minimum of about 0.32 % in simulation and about 1.67 % in experiment.
- (2) No programming difficulty exacerbation and no additional hardware, thus no reduction of the power density of the system.
- (3) No complex calculation of the proposed control strategy, thus short control delay which is suitable for both low and high switch frequency applications.

## References

1. Marra F, Sacchetti D, Træholt C, Larsen E (2011) Electric vehicle requirements for operation in smart grids. In: 2nd IEEE PES international conference and exhibition on innovative smart grid technologies (ISGT Europe) 2011. IEEE, pp 1–7
2. Xiaofei L, Qianfan Z, Shumei C (2012) Review of electric vehicle V2G technology. *Trans China Electrotechnical Soc* 27(2):121–127
3. Brooks AN (2002) Vehicle-to-grid demonstration project: grid regulation ancillary service with a battery electric vehicle. California Environmental Protection Agency, Air Resources Board, Research Division
4. Kempton W, Tomić J (2005) Vehicle-to-grid power implementation: from stabilizing the grid to supporting large-scale renewable energy. *J Power Sources* 144(1):280–294
5. Wang H, Su M, Sun Y, Li X, Han H, Zhang G (2013) AC/DC matrix converters for V2G applications. *Proc CSEE* 9:006
6. Tang L, Su GJ (2009) A low-cost, digitally-controlled charger for plug-in hybrid electric vehicles. In: Energy conversion congress and exposition, 2009. ECCE 2009. IEEE, pp 3923–3929
7. Zhou X, Wang G, Lukic S, Bhattacharya S, Huang A (2009) Multi-function bi-directional battery charger for plug-in hybrid electric vehicle application. In: Energy conversion congress and exposition, 2009. ECCE 2009. IEEE, pp 3930–3936
8. Wang TC, Ye Z, Sinha G, Yuan X (2003) Output filter design for a grid-interconnected three-phase inverter. In: IEEE 34th annual power electronics specialist conference, vol 2, pp 779–784
9. Chunjiang Z, Jing Z, Weiyang W (2008) High-frequency link inverter waveform control with resonant controller based on delta operator. *Trans China Electrotechnical Soc* 23(7):81–85
10. Zhao QL, Guo XQ, Wu WY (2007) Research on control strategy for single-phase grid-connected inverter. In: *Zhongguo Dianji Gongcheng Xuebao* (Proceedings of the Chinese society of electrical engineering, vol 27(16), pp 60–64

# Snow Removal of Video Image Based on FPGA

H.H. Li, S. Liu and Y. Piao

**Abstract** With the development of science and technology, outdoor surveillance systems are applied in many fields widely. However, due to the bad weather (such as snow, fog, rain, dust), it degrades the quality of video image and the function of surveillance system. The traditional methods of snow removal are largely realized with software and cannot meet the real-time processing requirements. They are difficult to get a wide range of applications. The cause of the noise generated by the snow is analyzed. According to the improved frame difference algorithm, we propose a snow removal technology of video image based on FPGA. Compared to the traditional methods, it can process the snow video image with minimum resolution  $640 \times 480$  in real time. At last, the results show that the snow removal technology of video image based on FPGA can remove the snow effect efficiently. Furthermore, it can improve the contrast and enhance the image details.

**Keywords** Snow removal · Real time · FPGA · Video processing

## 1 Introduction

Most of the video surveillance system is sensitive to the weather. On a clear day, it can work normally. But in bad weather (such as fog, rain, snow), the function of video monitoring system is greatly limited. The images quality captured degrades severely. Therefore, it is difficult to distinguish effective information in real time. The effect of snowflake on the video images is mainly to cover the target pixels. The brightness pixel which is contaminated by snowflake is much brighter. It affects the image quality of outdoor vision systems seriously. Inclement weather video image processing is one of the key research topics among digital image processing,

---

H.H. Li · S. Liu

Jilin University of Finance and Economics, Changchun, Jilin, China

Y. Piao (✉)

Changchun University of Science and Technology, Changchun, Jilin, China

e-mail: piaoyan66@126.com

© Springer-Verlag Berlin Heidelberg 2016

B. Huang and Y. Yao (eds.), *Proceedings of the 5th International Conference on Electrical Engineering and Automatic Control*, Lecture Notes in Electrical Engineering 367, DOI 10.1007/978-3-662-48768-6\_24

207

computer vision, target tracking, and other areas. It has been the hot research content to reduce the influence of the bad weather in video image and improve the reliability of the system.

In the snow, the distribution of snowflake is random, and the size and shape of snowflake is complex. That makes it difficult to remove snowflakes in the video image effectively due to the nature of random distribution of the snowflake. Xiang [1] captures snowflake sports using the correlation model. A new video image detection and removal algorithm in the snow is proposed. It can remove the snowflake effect from the video efficiently. However, it does not meet the real-time requirements. Ding [2] proposes single image rain and snow removal via guided L0 smoothing filter. Although the snow removal effect is better, it is difficult to process the video image. Xiao [3] discusses snow removal situation under static scene and dynamic scene theoretically. Under dynamic scene, the rain or snow pixels and moving object pixels are classified successfully based on space and time model of rain or snow. According to the classification, the snow or rain is removed. But this method is complex and cannot remove the snow or rain in real time. Xin [4] detects and removes the snowflake by using moving detection algorithm. Then the background pixels are reconstructed. But this method removes the snow of video image with low resolution  $352 \times 288$  at the speed of 21.8 ms per frame.

Traditional snow removal technology of video image is mostly based on software simulation and theory analysis. These methods often process the video image with low resolution and cannot meet the requirements of real-time processing. They are difficult to be applied in people's daily life. But snow removal technology of video image based on FPGA can realize the simple algorithm rapidly with pipelining operation. In addition, this technology can process the snow video image with high resolution in real time. It enables to remove the noise introduced by snowflake quickly and enhance the visual effect. Therefore, it can be applied in remote sensing, navigation, target recognition, intelligent monitoring, and other fields widely.

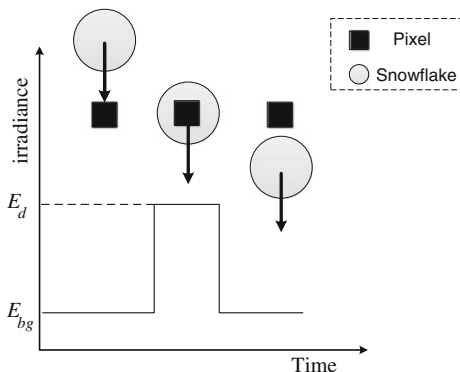
## 2 Characteristics and Effects of Snowflake

Snowflake is an unstable medium. It has a variety of shapes such as: column, star, circle, line type, etc. Due to the different internal structures, the reflection characteristic on the surface of snowflake is also variant. The diameter of most snowflake crystal is between 0.2 and 10 mm, some even more than 20 mm. The speed of the fallen snowflake can be described as a function of radius [5].

$$v(\varphi) = \lambda\varphi^\varepsilon \quad (1)$$

where  $\varphi$  is the radius of snowflake,  $\lambda$  and  $\varepsilon$  are constants. Generally, the density of snowflake is low, and the speed of motion is slow. In three-dimensional space, it is mainly regarded as snowflake or snow line, and usually produces the effect of motion blur. Generally, the brightness of snowflake is strong. Snowflakes that are

**Fig. 1** The effect of snowflake



distributed randomly have an impact on video image. The influence mainly generates blocking for target, and makes the brightness of pixels stronger. Finally, snowflake affects the image quality of the visual system seriously.

When the snowflakes are falling in the air, the time that they pass one pixel is very short. In the visual system imaging process, the falling snowflakes will cover the object in the background, and coincide with pixels, making the image blurry, that will affect the function of the system. In the interval  $[t_n, t_n + T]$ , the process of the falling snowflakes is shown in Fig. 1.

In the process of the snowflakes falling, the intensity value of one pixel can be seen as a linear combination of the background intensity and the snowflake intensity.

$$I_d(x, y, t) = \int_0^{\tau} E_d dt + \int_{\tau}^T E_{bg} dt \quad (2)$$

where  $I_d(x, y, t)$  is the intensity value of one pixel at  $t$  time,  $E_d$  is the radiation intensity of the background reflecting light,  $E_{bg}$  is the radiation intensity of the snowflake. In the snow visual system, the intensity of the snowflake is usually higher than the background pixels. Therefore the intensity of pixels covered by snowflake will become larger. The changed value [1] is:

$$\Delta I = I_d - I_{bg} \quad (3)$$

### 3 System Modules Design

With the development of science and technology, the logic gates of FPGA chip have exceeded hundreds of millions, there are many types of Ram memory block and embedded functional modules. Snow removal system of video image based on

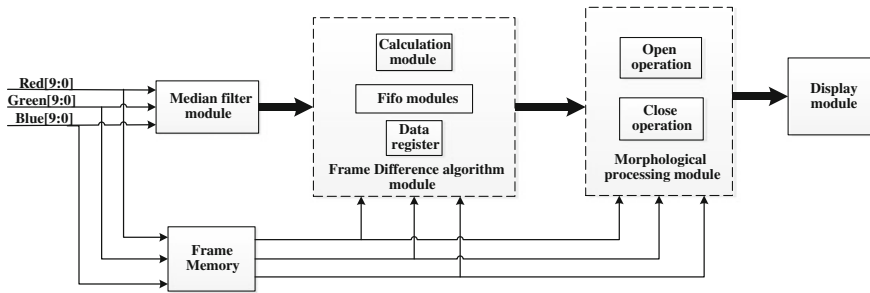


**Fig. 2** The hardware structure of system modules

FPGA is designed by hardware description language. It has many advantages, such as parallel processing, low delay, easily debugging. And the system can remove noise caused by snow real time and restore the real natural scenery.

Snow removal system of video image based on FPGA mainly consists of two parts: snow detection and snow removal. Snowflake can be seen as the moving object in the snow. The improved frame difference algorithm can effectively detect snowflake quickly. And it has low computational complexity, easy implementation, insensitive to light intensity in the scene and high noise endurance. The system modules include: median filter module, frame memory module, frame difference module, morphological processing module, and display module. Figure 2 shows the hardware structure of system modules.

### 3.1 Median Filter Module

Median filter is a nonlinear smoothing filter. It can preserve the edge information effectively and reduce the salt and pepper noise. Based on the principle, the current pixel value is replaced by the center value after all the pixel values are sorted in the neighborhood. Therefore, the filter can eliminate the isolated noise points. The modules of median filter mainly include window module and sort module.

The window size of median filter is  $3 \times 3$ . All the pixels within the window are provided at the same time. First of all, to sort the pixel per line, we can obtain the maximum value, median value, and minimum value of each line. Afterward, the maximum values of three lines are sorted to obtain one median value of the maximum pixel values. By the same way, the other two median values are obtained. At last, to sort the three median values can obtain the median value as the output of median filter. Figure 3 shows the modules of median filter.

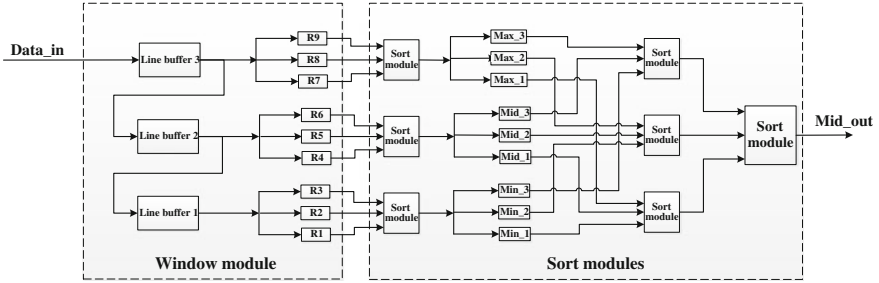


Fig. 3 The module of median filter

### 3.2 Improved Frame Difference Module

Frame difference algorithm is realized very simple, low computational complexity. It can implement processing of video image in real time. The traditional frame difference algorithm processes the two adjacent frames. According to the displacement of moving target, the corresponding pixels do subtraction. The absolute value in the target area is large. While the value of background region is merely zero (ideal state). At time  $t$ , the current frame and a previous frame image do subtraction based on the formula (4).

$$\Delta I(x, y, t) = |I(x, y, t) - I(x, y, t - 1)| \tag{4}$$

where  $I(x, y, t)$  is the pixel value of current frame at  $(x, y)$ ,  $I(x, y, t - 1)$  is the pixel value of previous frame at  $(x, y)$ . In the absence of snow scene, when the change is stable in the background, the difference value  $\Delta I(x, y, t)$  is 0. However, in the snow scene, the difference value is generally not equal to 0. Then, the snow can be detected through binary processing operation. By setting the threshold value  $T$ , if the absolute value is greater than or equal to  $T$ , it is the pixel of moving target. Inversely, the pixel is in the background.

$$D_t(x, y) = \begin{cases} 1 & |\Delta I_t(x, y)| \geq T \\ 0 & |\Delta I_t(x, y)| < T \end{cases} \tag{5}$$

The original frame difference algorithm can detect some snowflakes. But the snowflake is not detected totally. Moreover, the position of the detected snowflake is not accurate. The detected area becomes large and the effect of snow removal is less effective. The improved frame difference algorithm processes the three consecutive frames directly. First, the corresponding pixels of the adjacent frames do subtraction. And the results whose absolute value do OR operation. This method can overcome the disadvantages of traditional frame difference algorithm and detect the moving target accurately.

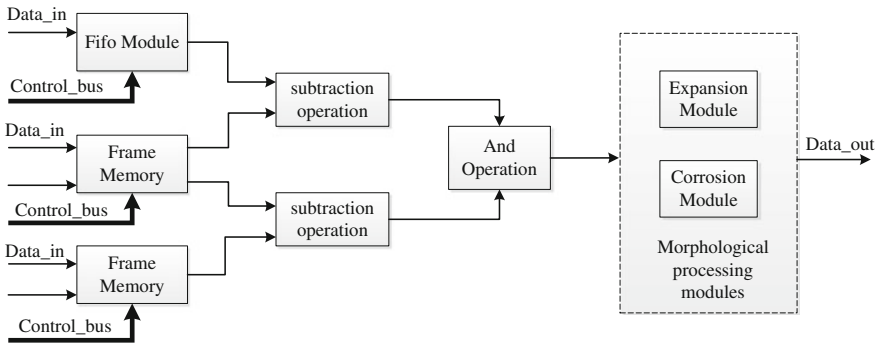


Fig. 4 The structure of improved frame difference module

The improved frame difference algorithm easily meets the requirement of hardware development. The modules of improved frame difference algorithm mainly include the memory module, frame difference module and morphological processing modules. Figure 4 shows the structure of improved frame difference modules.

After traditional frame difference operation, the output image often appears noise and cavitation phenomenon. For enhancement of output image, we introduce the morphology processing method. The experiment shows that this method can reduce the cavitation phenomenon and decrease the noise. Morphology processing operation mainly includes open operation and close operation. Open operation is that do the erosion first and then do the expansion. While close operation performs the reverse computing. Expansion operation is that all the pixels in a neighborhood do OR operation. And the result is as the center pixel value. For example, if one pixel value is 255 for 8-bit image data, then the center pixel value becomes 255. Figure 5 shows the expansion module.

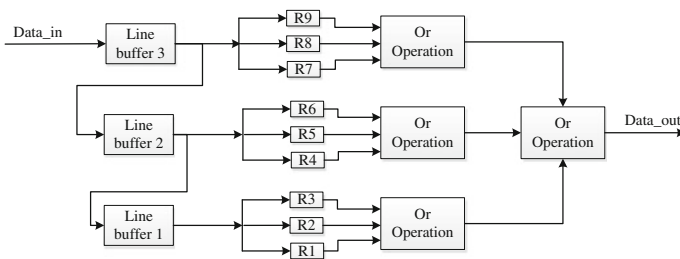
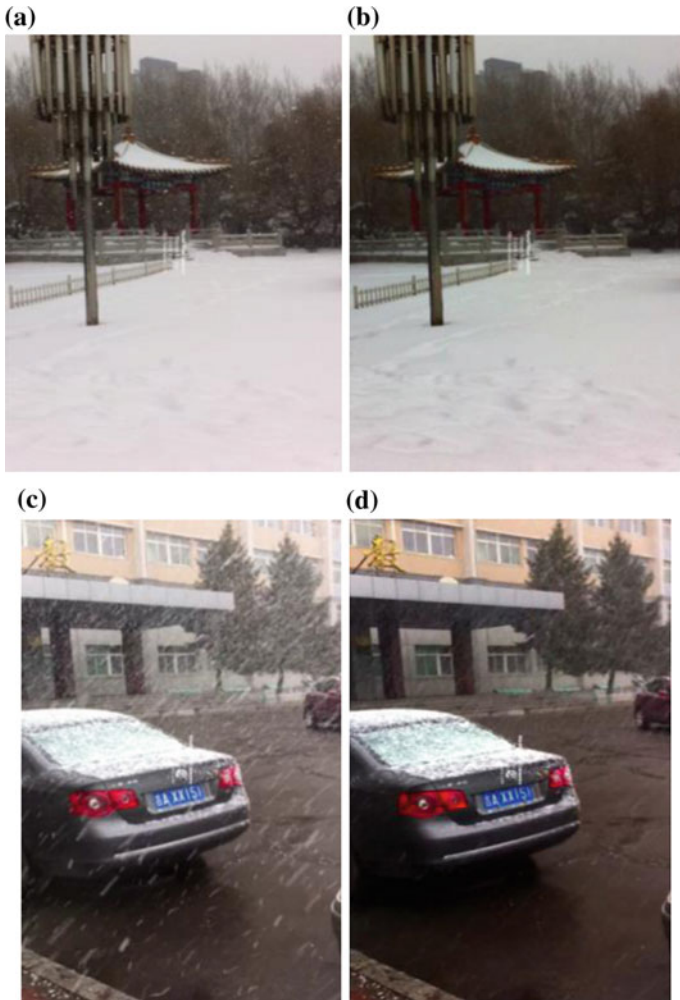


Fig. 5 The expansion module





**Fig. 6** The results of snow removal. **a** The original frame of light snow video. **b** The snow removal frame. **c** The original frame of heavy snow video. **d** The snow removal frame

## 4 Experimental Results and Analysis

The improved frame difference algorithm is realized with Verilog HDL. It can detect and remove the snowflake in real time. It also improves the degree of clarity of the video image and gets good system visualization.

The snow removal system of video image based on FPGA has lots of advantages, such as high stability, strong flexibility, and debugging easily. Before the experiment, first, the snow video image is captured by ordinary camera with high resolution  $640 \times 480$  at 25 frames per second. Figure 6a shows the original frame

of light snow video. Figure 6b shows the snow removal frame. Figure 6c shows the original frame of heavy snow video. Figure 6d also shows the snow removal frame. The results show that the snow removal system of video image based on FPGA can reduce the quantity of snowflake efficiently and improve the contrast largely. Furthermore, it also decreases the noise and enhances the visual effects of system.

## 5 Conclusion

In video surveillance system, due to the effects of snowflakes, the pixel value of video image is increased. In this article, we analyze the reasons of noise generated by snowflake. Combined the module of snowflake, we proposed the snow removal technology of video image based on FPGA. In addition, we design and realize the system function modules based on the improved frame difference algorithm. Finally, according to the result of experiment, this method proposed can reduce the effect of noise efficiently and restore the real natural scenery. The system of snow removal based on FPGA can process the video image with high resolution in real time. And it has high stability and also can be debugged easily. Therefore, it can be applied in many fields widely, such as intelligent transportation, navigation, outdoor surveillance, vehicle license recognition.

**Acknowledgments** This work is mostly supported by Ministry of Science and Technology of China Project (NO: 2015DFR10670), Jilin Province Science and Technology Development Project (NO: 20140204045GX), Jilin Province Development and Reform Commission Project (NO: 2014Y109), and Changchun Science and Technology Project (NO: 2014215).

## References

1. Liang X, Zhen HJ, Xi ZQ (2007) Detection and removal of snow from videos. *J Optoelectron Laser* 18(4):478–481
2. Xing HD, Li QC, Xian HZ et al (2015) Single image rain and snow removal via guided L0 smoothing filter. *Multimedia Tools Appl* 1–16. doi:10.1007/s11042-015-2657-7
3. Xiao BC (2014) The removal of rain and snow from video images based on statistical learning of spatiotemporal property. Dissertation, Beijing University of Posts and Telecommunication
4. Xin J (2013) The research on fog and snow images clearness methods. Dissertation, Wuhan University of Technology
5. Pei SC, Tsai YT, Lee CY (2014) Removing rain and snow in a single image using saturation and visibility features. In: *IEEE international conference on multimedia and expo workshops (ICMEW)*, 2014. IEEE, pp 1–6
6. Xian HZ, Ying HL, Wei G et al (2013) Single-image-based rain and snow removal using multi-guided filter. In: *20th international conference, ICONIP 2013*, pp 258–265
7. Muramoto KI, Matsuura K, Shiina T (1995) Measuring the density of snow particles and snowfall rate. *Electron Commun Jpn (Part III: Fundam Electr Sci)* 78(11):71–79
8. Xu J, Zhao W, Liu P et al (2012) An improved guidance image based method to remove rain and snow in a single image. *Comput Inf Sci* 5(3):49–55

9. Barnum PC, Narasimhan S, Kanade T (2010) Analysis of rain and snow in frequency space. *Int J Comput Vision* 86(2–3):256–274
10. Bossu J, Hautière N, Tarel JP (2011) Rain or snow detection in image sequences through use of a histogram of orientation of streaks. *Int J Comput Vision* 93(3):348–367

# A New Concept: Azimuth Dilution of Precision for Monocular Observational Tracking System

Bing Liu, Dong Wang, Zhen Shen, Taihe Yi and Dongyun Yi

**Abstract** The single satellite missile warning system is a monocular observational tracking system which is an inevitable transition state for the satellite missile warning network. Inspired by the idea of geometry dilution of precision (GDOP) in GPS system, a new concept named azimuth dilution of precision (ADOP) which specifies the amplification effect of the geometry between satellite and trajectory on the accuracy of the launch azimuth estimation is defined. A rapid global ADOP analysis method based on the geometry symmetry is proposed. This technique can be applied for the performance analysis and allocation optimization of monocular observational tracking observation.

**Keywords** Tracking system · Monocular observation · Geometry symmetry · Performance analysis

## 1 Introduction

The tracking system such as Defence Support Programme (DSP) or Space Based Infrared System High Component (SBIRS-High) can provide ambiguous information of the tactical parameters which mainly includes the time of launch, launch point geodetic latitude and longitude, trajectory azimuth [1]. Deploying only one satellite is an inevitable transition state of the satellites network. Besides, satellite network may be attacked by the hostile and then the system may degrade into a single satellite system partially. Therefore, the study on the performance analysis for the single satellite system is of significant practical utility.

In literatures, researchers mainly focus on the estimation algorithm with space-based line-of-sight (LOS) measurements. The problem can be modeled as a nonlinear programming in which the tactical parameters should be estimated. But researchers find it is an unobservable system to track the missile by only one

---

B. Liu (✉) · D. Wang · Z. Shen · T. Yi · D. Yi  
National University of Defense Technology Changsha, Changsha 410073, Hunan, China  
e-mail: liubeing@126.com

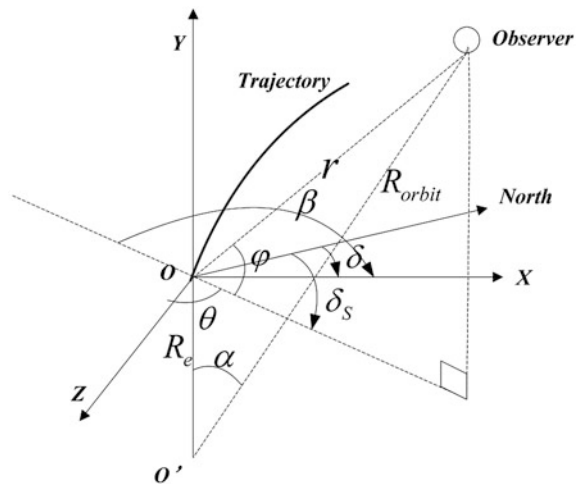
bearing-only sensor [2, 3]. They have to incorporate the model of boost phase as the constraint of estimation. The model can be classified into two types: profile-based model [4, 5] and profile-free model [6, 7]. The overview of these methods can be found in [8].

Besides the research on the algorithm, satellite-target geometry is the factor of error propagation, which is seldom studied to authors' knowledge. In [6], the accuracy of azimuth estimation is studied by two kinds of algorithms which are called standard profile-based algorithm and model-based algorithms. The computational results indicate that the accuracy of azimuth estimation is related to the relative satellite-trajectory geometry. We found that although the algorithms differ, the accuracy of trajectory estimation in polar coordinate system has some common points, in which the distribution is nearly symmetrical. So we want to study on this phenomenon in depth. Inspired by the idea of geometry dilution of precision (GDOP) in GPS system, we want to define a term which specifies the amplification effect of the geometry between satellite and trajectory on the accuracy of the launch azimuth estimation. To our knowledge, similar idea has not been reported in other literatures.

## 2 Geometry of Monocular Observation (GMO)

We shall define the relative geometry relationship between the observer and a trajectory. Assuming we have a three-dimensional Cartesian system in which there is a trajectory and an observer. Without loss of generality, we use the launching coordinate system, in which the origin is the launch point,  $Y$ -axis is the vertical direction and  $X$ -axis is the horizontal direction, and the trajectory lies nearly in the plane of  $XOY$  (see Fig. 1). Then in this coordinate system, the position of the missile is fixed at any time no matter where the launch point is and what trajectory

**Fig. 1** Geometry of monocular observation



azimuth is. Then the geometry between the observer and the trajectory is determined by the position of the observer in the launching coordinate system. That is to say the relative satellite-trajectory geometry can be defined by the spherical coordinate  $(\theta, \varphi, r)$  of the observer.

However, for launch detection satellite system, geocentric coordinate system usually brings about much convenience. So we introduce other parameters which are related to the geocenter to represent the geometry. In Fig. 1,  $O'$  is the geocenter,  $R_e$  is the radius of the Earth,  $R_{orbit}$  is the radius of the geostationary orbit. Then  $\varphi$ ,  $\theta$ , and  $r$  can be uniquely identified by  $\alpha$ ,  $\beta$ , and  $R_{orbit}$  as follows:

$$\begin{aligned} r &= \sqrt{R_e^2 + R_{orbit}^2 - 2R_e R_{orbit} \cos \alpha} \\ \varphi &= \frac{\pi}{2} - \alpha - \arcsin\left(\frac{R_e \sin \alpha}{r}\right) \\ \theta &= \begin{cases} \beta - \frac{\pi}{2}, & \text{if } 0 \leq \beta \leq \frac{3\pi}{2} \\ \beta - \frac{5\pi}{2}, & \text{if } \frac{3\pi}{2} \leq \beta \leq 2\pi \end{cases} \end{aligned} \quad (2.1)$$

where  $\alpha \in [0, \pi]$  is the included angle between the vectors of observer and launching point, and  $\beta \in [0, 2\pi]$  is the angle from the plane formed by observer, launching point and geocenter to the plane of trajectory in clockwise. For the geostationary satellite,  $R_{orbit}$  is constant. Then the geometry can be defined by  $\alpha$  and  $\beta$  which have the clear geometric meaning.  $\alpha$  is the angle (in radian) from geocenter between the satellite and the launch point. Then  $R_e \alpha$  is the great circle distance between the subastral point of the satellite and the launching point. If we define the launch azimuth ( $\delta$ ) and the azimuth of observer ( $\delta_s$ ) by the angle from the north to the  $OX$  and the observer, respectively, in a clockwise direction, we have  $\delta = \beta + \delta_s - \pi$ . Noticing that if  $\alpha$  is fixed, the relative geometry is only related to  $\beta$  which is determined by  $\delta - \delta_s + \pi$ . Then, for any two different monocular observation evens, if the radius of the orbit and the trajectories in launching coordinate system are the same, the observation geometries are equivalent as long as their  $\alpha$  and  $\beta$  are equal.

### 3 Problem Formulations

Firstly, the measurement model should be introduced. For the passive observation system, the measurements are azimuth  $A$  and elevation  $E$  (in radians) of the target seen from an observation platform. The measurement function is denoted as

$$h(X_T) = \begin{pmatrix} A \\ E \end{pmatrix} = \begin{pmatrix} \arctan(y_T/x_T) \\ \arctan\left(z_T/\sqrt{x_T^2 + y_T^2}\right) \end{pmatrix} \quad (3.1)$$

where  $X_T = [x_T, y_T, z_T]^T$  is the vector for the sensor to the target in Earth-center-fixed coordinate system (ECF-CS). To reduce the nonlinearity of the measurements  $A$  and  $E$ , we take the new form  $u$  and  $w$  as alternatives.

$$H(X_T) = \begin{pmatrix} u \\ w \end{pmatrix} = \begin{pmatrix} y_T/x_T \\ z_T/x_T \end{pmatrix} \quad (3.2)$$

Secondly, we introduce the concept of azimuth dilution of precision (ADOP) for monocular observational tracking system. The concept of geometric dilution of precision (GDOP) represents how measurement error affects the estimation in position. Imitating the definition of GDOP, we define the azimuth DOP as

$$\text{ADOP} = \frac{\Delta(\text{Output trajectory azimuth})}{\Delta(\text{Measured Data})} \quad (3.3)$$

According to Sect. 2, the GMO can be represented by two parameters  $\alpha$  and  $\beta$ , then in this section, we shall deduce the ADOP as the function of  $\alpha$  and  $\beta$ . Assume the trajectory in launching coordinate system is as a function of time, i.e.,  $f(t) = [x_L(t), y_L(t), z_L(t)]^T$ . Because the trajectory in boost phase is nearly in a plain, we assume  $z_L(t) \approx 0$ . We choose the ECF-CS as the coordinate system, and assume the observer locates on the  $x$ -axis. Its coordinate is  $O_s = [R_o, 0, 0]^T$ , where  $R_o$  is the radius of the orbit. Provided that the launch point is at  $0^\circ$  in longitude and  $B$  degrees in latitude, and the trajectory azimuth is  $\delta$ . Then the observer and the launch point are both in the  $XOZ$  plane. This kind of setting brings about some convenience, because  $B = \alpha$ , and  $\delta = \beta$ . The vector from the sensor to the target is

$$[x_T \ y_T \ z_T]^T = R_z(\pi/2)R_x(-\alpha)R_y(\pi/2 + \beta)f(t) + O_L - O_s \quad (3.4)$$

In which  $R_x, R_y, R_z$  are the rotation matrixes. According to Eqs. (3.2) and (3.4), the measurements are the nonlinear function of parameters  $\alpha, \beta, x_L, y_L$  as follows.

$$H_i = \begin{pmatrix} u(t_i) \\ w(t_i) \end{pmatrix} = \begin{pmatrix} \frac{x_L(t_i) \sin \beta}{R_f \cos \alpha - R_o + y_L(t_i) \cos \alpha - x_L(t_i) \sin \alpha \cos \beta} \\ \frac{R_f \sin \alpha + y_L(t_i) \sin \alpha + x_L(t_i) \cos \alpha \cos \beta}{R_f \cos \alpha - R_o + y_L(t_i) \cos \alpha - x_L(t_i) \sin \alpha \cos \beta} \end{pmatrix} \quad (3.5)$$

Assuming the set of unknown parameters is  $\Lambda$  which would be introduced latter, and then we define the launch azimuth DOP (ADOP) in monocular system as follow:

$$\text{ADOP}_\Lambda = \sqrt{Q_{1,1}} \quad (3.6)$$

The subscript of matrix  $Q$  indicates the element in the first row and first column, and  $Q$  is

$$Q = \left[ \sum_{i=1}^n (\nabla_A H_i^T) (\nabla_A H_i) \right]^{-1} \quad (3.7)$$

$A$  is the unknown parameter which determined the trajectory. For the profile-based method,  $f(t)$  is a known function or its second derivative (acceleration). In [4],  $A = \{\text{lat}, \text{lon}, H_0, t_0, L, \delta\}$ , in which lat and lon represent the latitude and longitude of the launch point,  $H_0$  is the altitude of first detection,  $t_0$  is the time of first detection after launch,  $L$  is the loft parameter which corrects the difference between the certain trajectory and the profile,  $\delta$  is the launch azimuth. Because we only analyze the GMO effect on the estimation of  $\beta$ , so we neglect the blocking effect of the clouds on the first detection. Then for the profile-based method, the missile can be detected as long as it launches, i.e.,  $R_f = R_e$ . Consequently, the detection time is set to be zero as a known parameter and the position of launching point is easy to get by computing the cross point of the LOS and the Earth's sphere. So the position of the launch point can be treated as a known parameter as well. Only  $\beta$  is the unknown parameter. Then we have

$$\nabla_A H = \frac{dH}{d\beta} = \nabla_{x_r} H \cdot \frac{dH}{d\beta} = \nabla_{x_r} H \cdot \frac{dR(\alpha, \beta)}{d\beta} f(t) \quad (3.8)$$

Using Eqs. (3.4), (3.5) and (3.8), we get

$$\frac{dH}{d\beta} = \left( \begin{array}{c} -x_L \cos \beta [R_{\text{orbit}} - \cos \alpha (R_e + y_L)] + x_L \sin \alpha \\ [R_{\text{orbit}} - \cos \alpha (R_e + y_L) + x_L \sin \alpha \cos \beta]^2 \\ -x_L (R_e + y_L) \sin \beta - x_L R_{\text{orbit}} \cos \alpha \sin \beta \\ [R_{\text{orbit}} - \cos \alpha (R_e + y_L) + x_L \sin \alpha \cos \beta]^2 \end{array} \right) \quad (3.9)$$

Finally, we have the criterion of GMO

$$\text{ADOP}_\beta = \left[ \sum_{i=1}^n \left( \frac{dH_i}{d\beta} \right)^T \left( \frac{dH_i}{d\beta} \right) \right]^{-1} \quad (3.10)$$

This criterion can evaluate GMO with any trajectory in plain as long as  $x_{L_i}$  and  $y_{L_i}$  are substituted. For the profile-free method,  $f(t)$  can be modeled with a few unknown parameters based on the missile momentum equation and the basic physics restrictions in missiles manufacture and flight. The general form can be described as  $f(t) \approx \tilde{f}(A, t)$ , in which  $A$  is the unknown parameter. In [7],  $A = [u_0, w_0, H_0, \delta, v_0, \theta_0, a]$ , in which  $u_0$  and  $v_0$  are the measurements of the first detection,  $w_0$  is the speed of the first detection,  $\theta_0$  is the speed angle of the first detection. In this paper, we define  $A = \{\beta, v_0, \theta, a\}$ . Because  $u_0, w_0, H_0$  affect little to the precision of the azimuth estimation and can be estimated roughly without the



algorithm. For the analytical form for this  $\mathcal{A}$  is too long and the derivation is tedious, we can take the numerical differentiation instead.

### 4 Geometry of Monocular Observation Analysis

We generate trajectories by the gravity turn constant acceleration model, and then the ADOP with different  $\alpha$  and  $\beta$  is computed. Figure 2 is the ADOP in polar system. The polar angle represents  $\beta$ , the polar radius represents ADOP. The different curves represent different  $\alpha$ . Comparing (a) and (b), we find that the ADOP distributions are different. But there are some common points as well. In these two figures, we can see that the bigger  $\alpha$  is, the bigger ADOP is. Further more, when the target shoots towards or opposite to the observer, the ADOP is smaller than other directions. That is to say, when the observer is located nearby the direction of the moving target, we can get a good observation of the direction of the moving target. The difference of the two figures is that, the worst GMO of  $ADOP_\beta$  is  $\beta = 90^\circ$  and  $270^\circ$  with any  $\alpha$ , but the worst GMO of  $ADOP_{\mathcal{A}}$  is that  $\beta$  is nearby  $90^\circ$  and  $270^\circ$ , but it differs with different  $\alpha$ . Further more, if the target is near the observer, when it moves towards the observer, the GMO is better. If the target is far away from the observer, when the target moves away from the observer, the GMO is better.

According to Eq. (3.5), the observation geometry is also influenced by the shape of the trajectory. We generate trajectories by the gravity turn constant acceleration model. We shall find an index which is independent with the trajectory to specify the GMO. The trajectories which obey the constant acceleration model with range from 3000 to 14,000 km under the minimum energy law are computed. Then we compute  $ADOP_\beta(\alpha, \beta, \text{range})$  in which  $\alpha = 3^\circ, 6^\circ, \dots, 60^\circ, \beta = 0^\circ, 10^\circ, \dots, 350^\circ, \text{range} = 3000, 3500, \dots, 14,000 \text{ km}$ , and then get a tensor  $ADOP_{i,j,k}$ . For any fixed

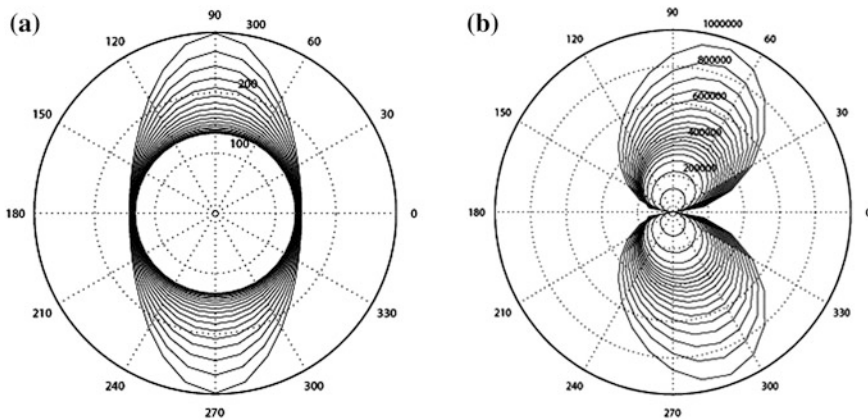


Fig. 2 a  $ADOP_\beta$  distribution. b  $ADOP_{\mathcal{A}}$  distribution

$i$  and  $j$ , ADOP is decreasing with  $k$  which means that the ADOP is decreasing with range at any GMO. We define the uniformed GMO index as follows:

$$I_{GMO}(\alpha, \beta, \text{range}) = \frac{\min_{\alpha \in A, \beta \in B} \{ADOP(\alpha, \beta, \text{range})\}}{ADOP(\alpha, \beta, \text{range})} \tag{4.1}$$

Using Eq. (4.1), we compute the uniformed index of  $ADOP_{i,j,k}$ , and then we find that  $I_{GMO_{i,j,k}} \approx I_{GMO_{i,j,k'}}$ , ( $\forall k \neq k'$ ), i.e.,  $I_{GMO}$  is nearly independent with the trajectory. So  $I_{GMO}$  can be used as the relative evaluation of GMO of single satellite system.

### 5 Compass of ADOP

We can use ADOP to evaluate the GMO of single satellite missile warning system. A good GMO is good at estimating the trajectory azimuth for an incoming missile. The basic processing route is showed in Fig. 3a. First, we set the satellite’s location and the area of defense we concerned. This is a basic setting for the scenario of missile warning. Assuming the missile may launch from anywhere in the field-of-view (FOV) of the satellite, then the surveillance area can be set as the entire area in the FOV. According to these settings, we can compute the GMO which the missile launches from anywhere to the defense area. Secondly, we build the trajectory of boost phase and compute of  $ADOP_{\beta}$ . Finally, we use  $I_{GMO}$  as the index of GMO to analyze the observational geometry of this single satellite system.

In Fig. 3b, The area of good GMO is distributed along the line which crosses the impact area and the subastral point.

The GEO satellite is located at  $152^{\circ}$  E in longitude. The color contour map indicates the  $I_{GMO}$  where the missile flies from the coverage area to the U.S west coast. We can see that, there is a high precision belt (red) from the west of Australia to the USA. The GMO for trajectory azimuth estimation get worse when the launch point is far way from the belt.

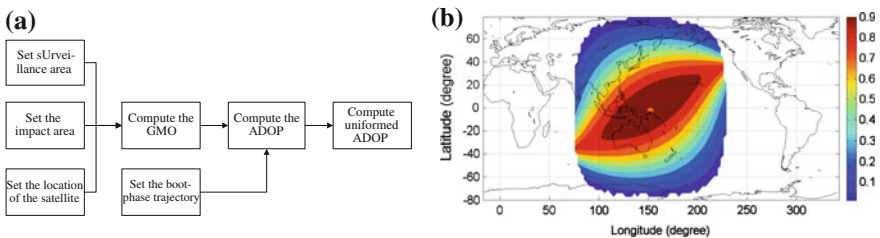


**Fig. 3** a Basic idea of GMO analysis for missile warning. b  $I_{GMO}$  distribution

## 6 Conclusions

In this paper, a new concept named ADOP which specifies the amplification effect of the geometry between satellite and trajectory on the accuracy of the launch azimuth estimation is defined. The uniformed ADOP is defined as an index to evaluate the geometry of observation in trajectory azimuth measurement. A rapid global ADOP analysis method based on the geometry symmetry is proposed to analyze the observation geometry of the entire coverage area. This technique can be applied on the performance analysis and allocation optimization of single satellite missile warning system.

## References

1. Beaulieu MR, Alfriend KT (1998) Launch detection satellite system engineering error analysis. *J Spacecraft Rockets* 35(4):487–497
2. Song TL (1996) Observability of missile tracking with bearings-only measurements. *IEEE Trans Aerosp Electron Syst* 32(4):1468–1472
3. Jauffret C, Pillon D (1996) Observability in passive target motion analysis. *IEEE Trans Aerosp Electron Syst* 34(4):1290–1300
4. Beaulieu MR (1996) Launch detection satellite system engineering error analysis. Naval Postgraduate School, Monterey, CA
5. Li Y, Yi D, Wu Y (2003) A new method of estimating trajectory measured by a single satellite. *J Ballistics* 15:38–44
6. Shen Z (2010) The single satellite early warning Ballistic missile parameter estimation research. National University of Defense Technology, People's Republic of China
7. Shen Z, Qiang S, Zhang Y, Yi D (2011) New method on course heading estimation with single satellite's passive detection. *J Astro* 32(7)
8. Yu D, Wang H, You Y, Chen L (2014) Review for the method of single satellite early warning Ballistic missile parameter estimation. *Mod Defence Technol* 4:62–68

# Study on Self-adaptive Packet Scheduling Algorithm of TD-LTE System's Downward Frequency Domain

Jia-liang Ling, Jian-zhong Cao and Tian-fa Liao

**Abstract** Round robin (RR) algorithm has best user fairness, but the system throughput is low, Max C/I algorithm has highest throughput, but poor fairness, Proportional fairness (PF) algorithm makes a compromise between throughput and fairness, but focuses on the average throughput fairness. This paper proposes a frequency domain scheduling algorithm for TD-LTE under different loads (light, medium, and heavy loads), which is called M-RR algorithm. Simulation results show that the algorithm emphasizes on fairness in terms of resource usage, and ensure the system throughput.

**Keywords** LTE · Proportional fair · Self-adaptive · Packet scheduling · Throughput

## 1 Three Common Resource Scheduling Algorithms and Analysis on Their Performance

### 1.1 Three Resource Scheduling Algorithms

Round robin (RR) algorithm: in this algorithm, the base station would serve users within the sector in a rotating manner. The major philosophy is [1]: providing resources to every user in the system in a fair manner at the price of the throughput.

---

J. Ling (✉) · J. Cao (✉) · T. Liao (✉)  
Huizhou University, Huizhou 516007, China  
e-mail: jia@hzu.edu.cn

J. Cao  
e-mail: cjz@hzu.edu.cn

T. Liao  
e-mail: liaotianfa@163.com

Max C/I algorithm: when selecting the scheduled users, this algorithm only eyes users with the maximum C/I and eNodeB only serves users with the best channel conditions at the moment [2].

Proportional fair algorithm: the priority calculation equation of the proportional fair scheduling algorithm is [3, 4]:

$$k = \arg \max_{n=1, \dots, K} \left\{ \frac{r_n(t)}{R_n(t)} \right\} \quad (1.1)$$

In the equation above,  $r_n(t)$  is the instant speed of User  $n$  at current moment decided by User  $n$ 's channel status information;  $R_n(t)$  is the average speed of User  $n$  in time window  $T_c$ . The updated equation of the average transmission speed of User  $i$  is:

$$R_n(t+1) = \left( 1 - \frac{1}{T_c} \right) R_n(t) + \frac{r_n(t)}{T_c} \quad (1.2)$$

$T_c$  is a time constant meaning the size of the time window. The size of the time window reflects the tolerating capacity of users for failing to receive data transmission. A big  $T_c$  means users could wait longer until their channel conditions improve, which could help increase the system's throughput, but additional time delay as well.

## 1.2 The Performance of the Three Algorithms

The advantage of RR algorithm is that it ensures fairness between users in terms of resource usage, while its disadvantage is that it fails to consider the differences of channel conditions between users, leading to low throughput of the system. Max C/I algorithm's advantage is that it could conduct scheduling according to the changing channel conditions of the users and increase the usage rate of frequency spectrum to the maximum extent. The disadvantage is that it could not guarantee fairness between users. PF scheduling algorithm takes a comprehensive consideration of the differences of channel conditions between users and the requirement on fairness and makes a compromise between throughput and fairness. Besides, when calculating the priority grade of a user, the average transmission speed of the ser in the previous time is taken into consideration by the PF algorithm, so the algorithm has memory.

Therefore, from the perspective of throughput, RR algorithm has the lowest throughput, while Max C/I algorithm has the highest throughput. PF algorithm is between the two algorithms; in terms of fairness, RR algorithm is the best while Max C/I algorithm is the worst, with PF algorithm again falling between them; considering the complexity of the algorithm, RR algorithm is the simplest and PF algorithm is the most complicated, with Max C/I algorithm falling between them.

## **2 TD-LTE Downward M-RR Scheduling Algorithm and Simulation**

Based on the analysis on the three classic algorithms, RR, Max C/I, and PF, we can see the advantages and disadvantages of these three algorithms. Based on the analysis on these advantages and disadvantages, considering the changes of system load, this paper proposes a new scheduling algorithm combining the advantages of RR algorithm and Max C/I algorithm, named M-RR algorithm.

### ***2.1 Definition of User Demand and Load***

The algorithm defines three grades of user service quality: the lowest service quality, medium service quality, and the highest service quality. Meanwhile, according to the system's total amount of resources (one TTI) and the amount of resources demanded for ensuring the quality of different services to users, the algorithm defines three types of load: light load, when the system resources could ensure medium service quality or above to all users; medium load, when the system resources could ensure lowest service quality to all users, but not medium service quality; heavy load, when the system resource could only ensure lowest service quality to some users. Under these different loading conditions, the M-RR algorithm would adopt different allocation strategies.

### ***2.2 Algorithm Design***

In the design of M-RR algorithm, to facilitate analysis, we would only consider the status of single business, as the amount of resources required to ensure the same level of service quality to different users is the same. Meanwhile, the algorithm sets the initial requirement of all connected users all at the highest level. However, as the system has limited resources, increasing number of users would gradually increase the load. To ensure the fairness between users, the service quality level of some or all users may be reduced.

### ***2.3 Resource Allocation Strategies Under Three Types of Load***

Light load. Under light load, the algorithm's priority is to ensure medium service quality to all users with demand by allocating the same amount of resources needed

for ensuring medium service quality. If there are still residual resources afterwards, they would be allocated to users selected as per the maximum C/I. In this way, the fairness could be ensured and current channel conditions of the users could be well used to increase the throughput.

Medium load: under medium load, the algorithm's priority is to ensure the lowest service quality for all users and allocate resources needed for the lowest service quality to all users with need. As under medium load, the resources could no longer ensure medium service quality to all users. Therefore, if there are still residual resources, the proportional fair algorithm would be used to calculate the priority grade and allocate resources accordingly. Thus, on the basis of ensuring fairness, current channel conditions of the users could be well used to increase the throughput.

Heavy load: under heavy load, the resources could no longer ensure the lowest service quality to all users. So, to ensure fairness, same amount of resources used to maintain lowest level of service quality shall be provided to users in turn.

## 2.4 Resource Block (RB) Allocation Strategy

M-RR algorithm's resource block is subject to following allocation strategy: The first stage: initialization.

Initialization includes reading and accessing user information, amount of resources matching each level of service quality, channel quality feedback, and total amount of resources. This stage would judge current loading status, obtaining resource block set  $R$ , undistributed resource block set  $R_u$ , distributed resource block  $R_c$ , user set  $U$  waiting for scheduling, No.  $n$  user  $U_n$ , and would define the scheduling priority  $k$ , the minimum number of resource blocks each user could receive under the lowest service quality—Min\_RB, and the minimum number of resource blocks each user could receive under medium service quality—Mid\_RB.

The second stage: distributing resource blocks to each user.

- Step 1: Judge if  $U \times \text{Mid\_RB} > R$ ? If it is less than resources block  $R$ , turn to Step 3; otherwise distribute each user with resource block Mid\_RB;  $R_c = \text{Mid\_RB}$  and turn to Step 2.
- Step 2: Judge if  $R_u = R - R_c = 0$ ? If yes, end the distribution of resources; otherwise, calculate the priority level  $k = \arg \max_{j=1, \dots, K} \left\{ \left( \frac{C}{T} \right)_j(t) \right\}$  and distribute residual resource blocks in the descending order of the priority level and terminate resource distribution.
- Step 3: Judge if  $U \times \text{Min\_RB} > R$ ? If it is less than resource block  $R$ , turn to Step 5; otherwise distribute to each user resource blocks Min\_RB;  $R_c = \text{Min\_RB}$ .

- Step 4: Judge if  $R_u = R - R_c = 0$ ? If yes, stop resource allocation; otherwise, calculate priority level  $k = \arg \max_{n=1, \dots, K} \left\{ \frac{r_n(t)}{R_n(t)} \right\}$ ,  $R_n(t+1) = \left( 1 - \frac{1}{T_c} \right) R_n(t) + \frac{r_n(t)}{T_c}$  and distribute residual resource blocks in the descending order of the priority level and terminate resource distribution.
- Step 5: Distribute to each user resource block Min\_RB in turn until  $R_u = R - R_c = 0$  and then end resource distribution.

### 3 Simulation Result

Simulation parameters settings are shown in Table 1.

We know from the setting of band width that each TTI in the sector of eNodeB has 25 resource blocks. While simulating the M-RR algorithm, according to the total amount of resources and number of users: the resourced block required by the lowest service quality is set to be Min\_RB = 1; the resourced block required by the medium service quality is set to be Mid\_RB = 2; the resourced block required by the highest service quality is set to be 25. Such setting is to facilitate the comparison with three classic algorithms, because when using the three classic algorithms, each resource block would be allocated to a certain user. Each sector has 11 groups of users, covering three loading scenes. 3, 5, and 10 users would be of light load; 15, 20, and 25 users would be of medium load; 30, 35, 40, 45, and 50 users would be of heavy load. Each user group’s simulation time is 500 TTI.

This paper mainly evaluates the system throughput [5], average throughput fairness, average number of users served by each TTI, and the average satisfaction degree of customers in each TTI users are used to evaluate the performance of scheduling algorithm. Wherein, fair indication (FI) of average throughput [6, 7] is defined as follow:

**Table 1** Simulation parameters setting

Parameter name	Parameter setting
eNodeB	1 eNodeB, 3 sectors
Frequency	2 GHz
Bandwidth	5 MHz
TX mode	Single antenna
BS antenna gain	0 dBi
UE speed	5 km/h
Macroscopic pathloss model	TS36942 urban
Thermal noise density	-174 dBm/Hz
Receiver noise figure	9 dB
Simulation length	200 TTIs



$$FI = \frac{(\sum_{i=1}^U X_i)^2}{U \sum_{i=1}^U X_i^2} \tag{1.3}$$

wherein,  $X_i$  is User  $i$ 's average throughput,  $U$  is the total number of users. FI's range of values is [0 1]. The lower FI is, the less fair it would be. If  $FI = 1$ , it means every user has the same average throughput, and the system has the best fairness.

Figures 1, 2, 3 and 4 respectively show the average throughput, average throughput fairness, average number of users served by each TTI and average satisfaction degree of users in each TTI. The four figures above show that M-RR algorithm is also a compromise between RR algorithm (fairness) and MAX C/I algorithm (throughput), but has different focuses from the PF algorithm which emphasizes the fairness in average throughput, and M-RR algorithm emphasizes on fairness in terms of resource usage.

**Fig. 1** The throughput curves

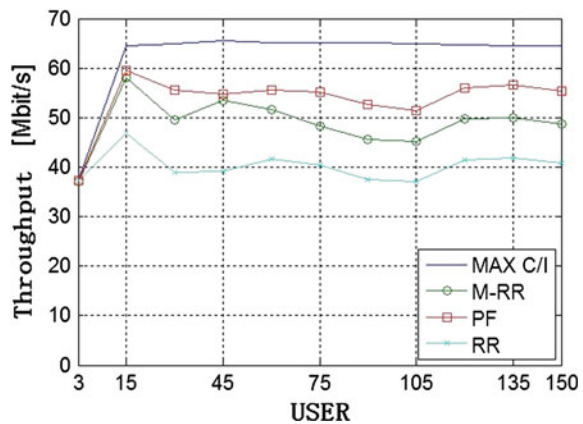


**Fig. 2** The fairness curves

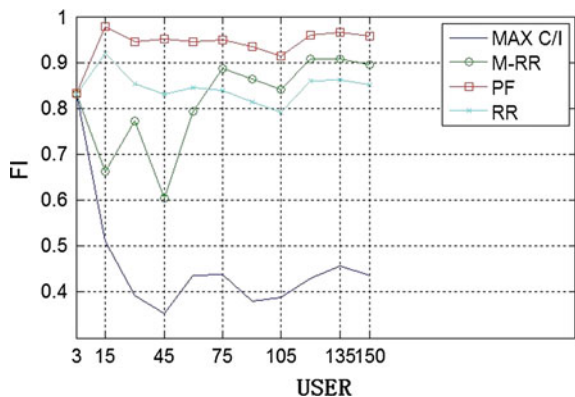


**Fig. 3** Average number of users per TTI

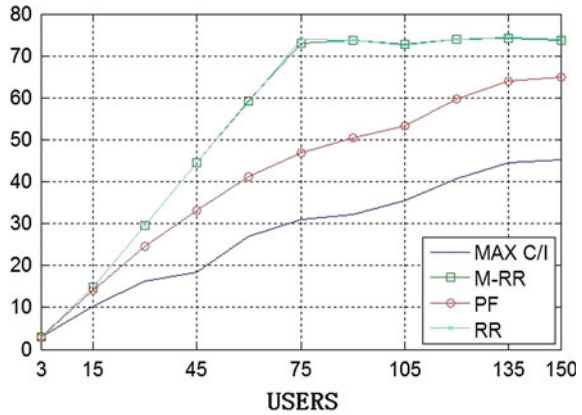
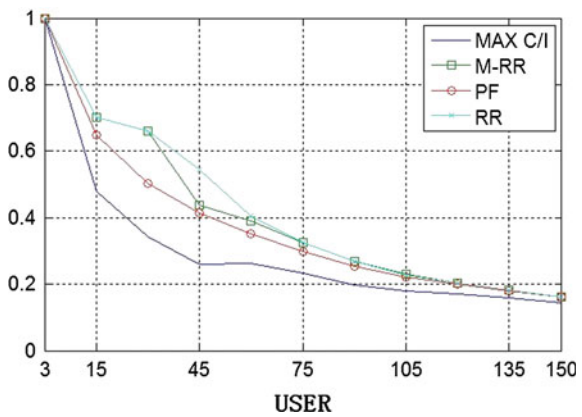


**Fig. 4** Average satisfaction degree of users in each TTI



### 4 Conclusions

Following conclusions could be drawn out from the simulation results

MAX C/I algorithm has the highest throughput, followed by PF algorithm and then M-RR algorithm, with the RR algorithm registering the lowest throughput. Although the M-RR algorithm takes into consideration the difference of users' channel conditions and distributes residual resources to users with better channel conditions under light load, medium load, and heavy load, to increase the system's throughput, However, as it aims at serving as many users as possible, the throughput is less than that of the PF algorithm.

The PF algorithm's has the best fairness of average throughput, and the MAX C/I algorithm is the worst in this regard. RR algorithm comes second in terms of average throughput fairness under light load, medium load, and heavy load, but could not match M-RR algorithm under heavy load. This is because, under light load and heavy load, RR algorithm distributes resources to users it serves on an

equal basis, but M-RR algorithm would, after meeting certain demand of served users, distribute residual resources to users with better channel conditions to increase the system's throughput; under heavy load, M-RR algorithm and RR algorithm distribute resources to their served users, but M-RR algorithm also considers users' channel conditions and tries to make the use of each resource block in the most effective manner, reducing the differences of average throughput between users, so the fairness of the average throughput at the time is better than the RR algorithm. The PF algorithm uses average throughput of users in the past time interval, so it has the best fairness in terms of average throughput. MAX C/I only serves users with the best channel conditions so users differ the most in terms of average throughput, meaning it has the worst fairness for average throughput.

The combination of average number of users served by each TTI and the average satisfaction degree of users in each TTI users could be viewed as the short-term fairness of resource occupation. Under heavy load, M-RR's fairness of resource occupation is the same as RR algorithm; under not heavy load, although it also serves as many as users, it would lean toward users with better channel conditions after meeting certain demand of all users and the distribution of resources is not so even as RR algorithm. Therefore, the fairness of resource occupation at this time is not as good as RR algorithm. PF pursues for long-term fairness of average throughput and does not perform well in short-term distribution of resources, so the fairness of resource occupation is not as good as RR algorithm and M-RR algorithm.

## References

1. Lee SB, Choudhury S, Khoshnevis A (2009) Downlink MIMO with frequency-domain packet scheduling for 3GPP LTE. In: IEEE INFOCOM 2009 proceedings. 978-1-4244-3513-5/09
2. Ramli HAM, Basukala R, Sandrasegaran K (2009) Performance of well known packet scheduling algorithms in the downlink 3GPP LTE system. In: The 2009 IEEE 9th Malaysia international conference on communications, 15–17 Dec 2009, Kuala Lumpur, Malaysia. 978-1-4244-5532-4/09
3. Li X, Li B, Lan B (2010) Adaptive PF scheduling algorithm in LTE cellular system. In: 2010 International coverage and transmission conference (ICTC2010). 978-1-4244-9807-9/10
4. Zhaohua Z (2010) Performance of the frequency domain packet scheduling for LTE downlink. In: 2010 2nd international conference on future computer and communication. 978-1-4244-5824-0
5. Diaz IF, Dimitrova DC, Spaey K et al. (2010) Sensitivity analysis of the optimal parameter settings of an LTE packet scheduler. IEEE-VTC. Taipei, Taiwan, pp 1–6
6. Fraimis IG, Kotsopoulos SA (2011) QoS-based proportional fair allocation algorithm for OFDMA wireless cellular systems. *Commun Lett IEEE* 15(10):1091–1093
7. Qian G, Ren C, Tang S (2010) Multiservice QoS-based downlink cross-layer resource block allocation algorithm in LTE system. *Commun Technol* 43(4):190–192

# The Research and Simulation of Three-Level NPC Inverter

Yuan Deng and Guangyao Jin

**Abstract** Compared with the commonly used sine-wave pulse width modulation (SPWM) method, the space vector pulse width modulation (SVPWM) method has higher utilization rate of DC voltage and smaller output waveform distortion. This paper describes the basic principle and control algorithm of three-level SVPWM. The topology of the system is a diode-clamped parallel (NPC) inverter, which is built on the PSCAD software platform. The simulation waveforms are obtained through the self-built model, which verifies the correctness of the system and provides reference for the further research.

**Keywords** SVPWM · Inverter · PSCAD · Simulation

## 1 Introduction

Compared with sine-wave pulse width modulation (SPWM), space vector pulse width modulation (SVPWM) can improve the utilization of DC voltage, and has the advantages of low harmonic components, low switching frequency, and low power consumption. SVPWM can better combine the vector control algorithm, which provides a better solution for the vector control and can maximize the performance of the equipment. In this paper, a diode-clamped three-level inverter is used as the topology and the SVPWM algorithm is used to obtain the desired current voltage output. The inverter does not need voltage-sharing. Each switching device is only able to withstand the  $1/2$  DC voltage, which can generate 1, 0, -1 three switching

---

Y. Deng (✉) · G. Jin  
Pinggao Group Co., Ltd, Henan Province, Pingdingshan 467001, China  
e-mail: 13700755137@163.com

G. Jin  
e-mail: pgjingy@163.com

state. Twenty-seven output voltage vectors can be selected. Compared with two-level voltage vector, the three-level inverter can output more voltage step and get a lower total harmonic distortion (THD).

## 2 The Basic Structure of the Diode-Clamped Three-Level Inverter

The basic structure consists of three-phase power supply, nonlinear load, and inverter. Due to the existence of nonlinear load, the transmission line can produce a large number of harmonics in addition to the fundamental component of the power source which can cause additional loss of transmission line. The three-level inverter is equivalent to a controlled current source. It generates the same size as the harmonic current but the direction is opposite, so as to reduce the harmonic components in the line.

From Fig. 1, the inverter bridge arm of each phase is composed of parallel diodes, power tubes, and clamp diodes. The power tube is mainly used IGBT or IGCT and two clamping diodes are composed of fast recovery diodes. The DC side of the inverter is connected in series with two capacitors, which is half of the DC side voltage. The capacitance value is limited, so the midpoint current on the capacitor charge and discharge power will have the midpoint voltage offset. Taking into account the three-phase bridge arm, there are 27 kinds of switching states of the inverter. Park vector formula for three-level inverter is

$$U = 2/3(u_a + u_b e^{j2/3\pi} + u_c e^{j4/3\pi}) \tag{1}$$

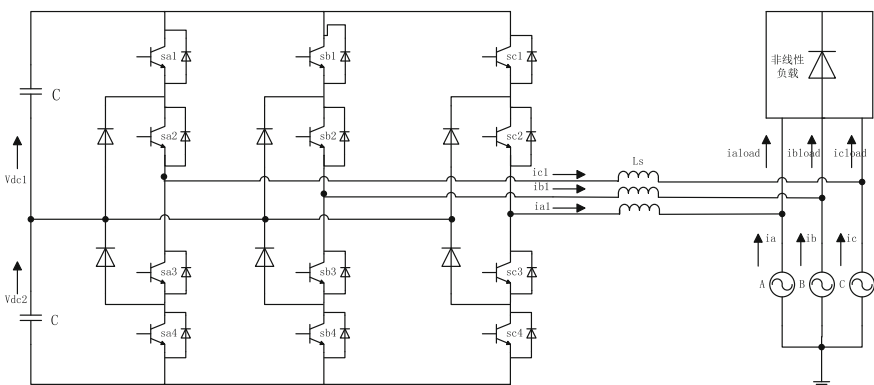
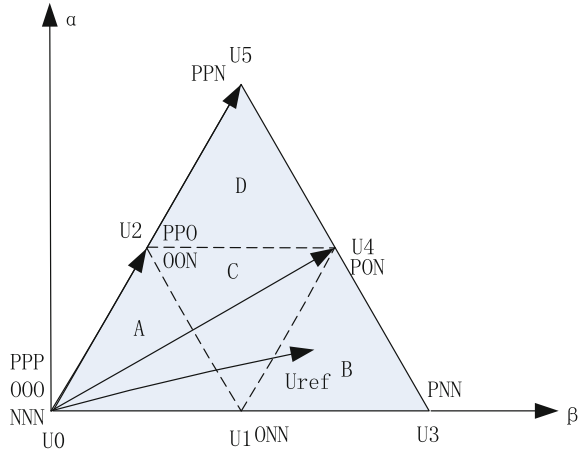


Fig. 1 Diode-clamped three-level inverter topology



**Fig. 3** Space vector



small vector. When the reference vector is located in the region A and C, two sets of voltage vector can be selected. In the case of region C, the ONN–OON–PON–POO–PON–OON–ONN and OON–PON–POO–PPO–POO–PON–OON are available in vector order.

## 4 Self-Built Model and Main Program Flow

### 4.1 The Creation of Custom Functional Components

PSCAD/EMTDC is a powerful simulation tool, because the software has the function of creating a custom function. The user can build the system model according to the requirements of the simulation. You can also use the FORTRAN to create a functional element to realize the logic function of the component. Creating SVPWM element in PSCAD, the element has 13 inputs and 12 outputs, including the Udc for DC voltage, reT for triangular wave pulse signal, UaUbUc for three-phase voltage inputs, TP1–TP6 for six control signals, g1–g12 for the power device driving signal. They are shown in Fig. 4.

### 4.2 Main Program Flow

The main program flow is shown in Fig. 5. Control algorithm is the use of FORTRAN language programming. Mainly it contains the following functions: initialization, completing a switching cycle, judging sector, computing working time of space vector, judging period of time, working time of space vector, and switching control pulses.

**Fig. 4** SVPWM custom model

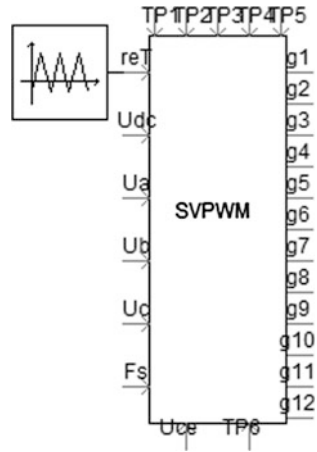
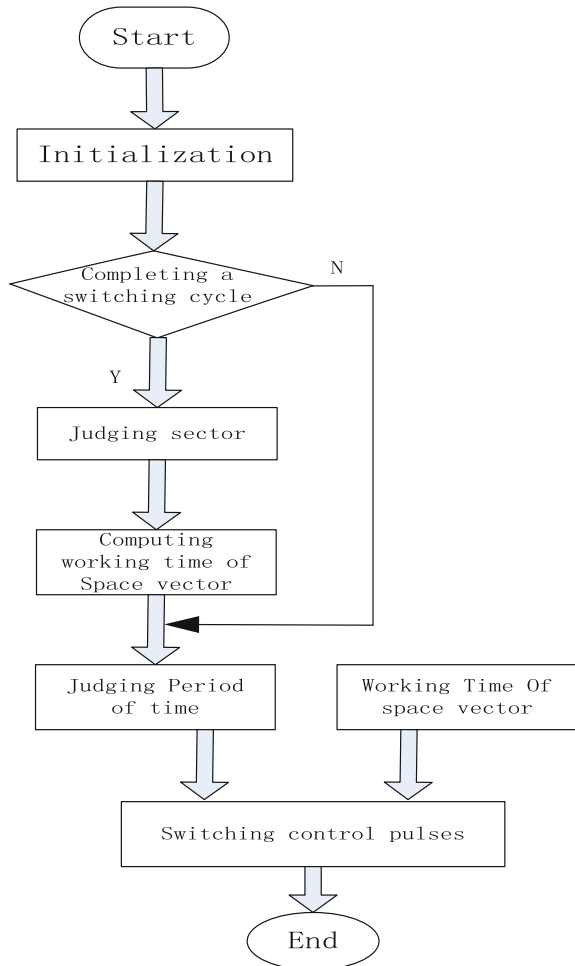


**Fig. 5** Program flowchart of self-defined SVPWM component





### 5 Simulation Result Analysis

In order to detect the inverter performance, the feasibility of the model and the control algorithm are verified in PSCAD. The simulation circuit is shown in Fig. 6. Before the operation of the system, the power charges the DC side capacitor of the inverter until the voltage to the reference voltage. Three-phase power supply voltage is 380 V, line inductance is 0.2 mH, line resistance is 20, inverter capacitor is 4700  $\mu$ F, switching frequency is 4.8 kHz. Figure 7 is a nonlinear load current waveform; Fig. 8 is the midpoint voltage waveform of the inverter and Fig. 9 is

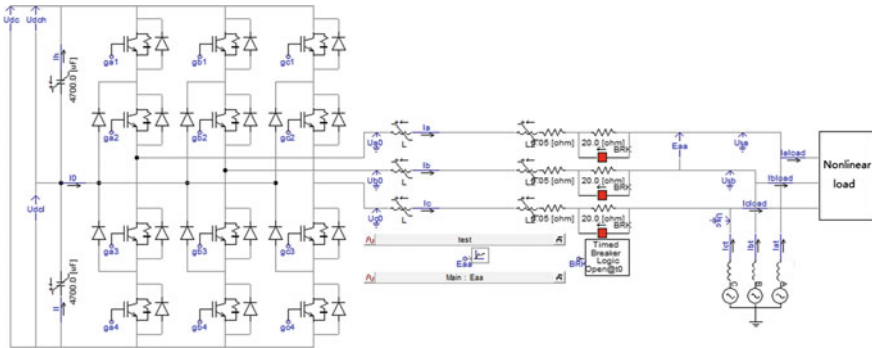


Fig. 6 System simulation model

Fig. 7 Nonlinear load current

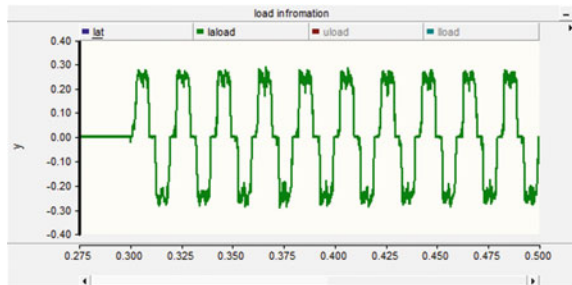


Fig. 8 Midpoint voltage

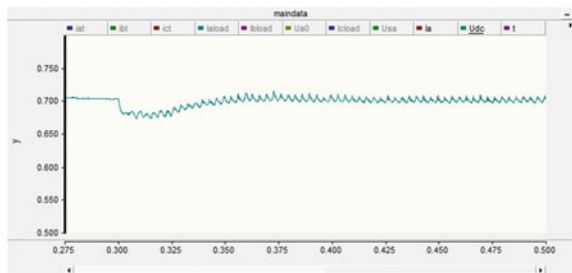


Fig. 9 Compensation current

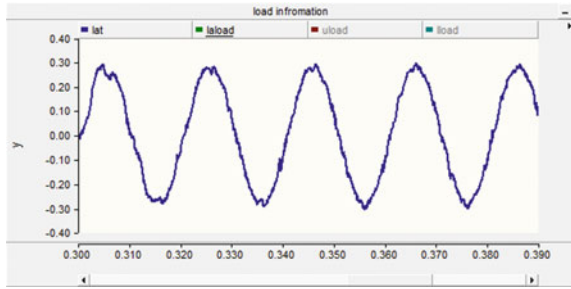
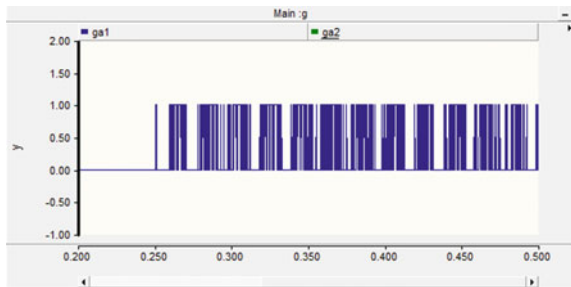


Fig. 10 Switch signals



compensated for the system current waveform; Fig. 10 is a switch signal. Closing the circuit breaker in 0.2 s and put the inverter into the system. The nonlinear load is put into at 0.3 s. As can be seen from the waveforms, the inverter can accurately track the load harmonics and compensate the harmonic current.

## 6 Conclusion

In this paper, a simulation model of the diode-clamped three-level inverter based on PSCAD/EMTDC simulation platform is built. A self-built SVPWM component is created and its function is realized using the program. Finally, it uses simulation experiment of system to verify the correctness and effectiveness of the inverter and self-defined component.

## References

1. Nabae A, Takahashi I, Akagi H (1981) A new neutral-point clamped PWM inverter. IEEE Trans Ind Appl 17:518–523
2. Zhang H, Finney SJ, Massoud A et al (2008) An SVM algorithm to balancing the capacitor voltages of the three-level NPC active power filter. IEEE Trans Power Electron 23 (6):2694–2701

3. Song W, Ding XY, Shu MT et al (2005) Study on SVPWM method and its implementation for three-level neutral-point-clamped inverter. *Power Electron* 39(5):13–14, 30
4. Hua XP, Wang B, Meng LL et al (2006) Simulation of algorithm of voltage space vector PWM. *Electr Switchgear* 2006:26–28
5. Liangzhen Lin, Lin Ye (2000) An introduction to PSCAD/EMTDC. *Power Syst Technol* 24 (1):65–66
6. Manitoba HVDC Research Center (2005) PSCAD on-line help system
7. Busquets-Monge S, Bordonau S, Boroyevich D, Somavilla S (2004) The nearest three virtual space vector PWM—a modulation for the comprehensive neutral-point balancing in the three-level NPC inverter. *IEEE Power Electron Lett* 2 (1):11–15
8. Lin BR, Yang KT (2004) Active power filter based on NPC inverter for harmonic and reactive power compensation In: *IEEE Region 10 Conference on TENCN 2004*. vol (4), pp 93–96

# Research and Application of 350 MW Unit Water Wall Crack Failure

Rui Zhang and Chunying Wu

**Abstract** A vast number of cracks have appeared at the exit of the boiler vertical water wall, which causes the boiler outage during the 350 MW supercritical unit. To solve this problem, we analyze the characteristics of cracks and boiler-related operating curve is in operation. The study found that the main factor leading to the cracks at the exit of the boiler vertical water wall is thermal stress resulted from large-scale temperature deviations between pipes and rapid changes in pipe temperature. The thermal stress generally emerged under the low-load condition after the boiler turns to dry state. In addition, there is a correspondence between vertical water wall tube temperature fluctuations and changes in boiler feed water. We made the three following recommendations for the causes and characteristics of cracks at the exit of boiler vertical water wall. First, it is to minimize this type of boiler long-term low-load operation in the dry state. Second, the operating personnel shall monitor the vertical water wall outlet temperature under the low-load after the boiler turns to dry state. Finally, we increase the adjustment ability of automatic water supply and automatic coal supply to coal–water ratio.

**Keywords** Thermal stress · Vertical water wall · Temperature difference · Supercritical boiler

## 1 Introduction

The power required by industrial production and daily life is all production and supply from the power plant. At present, our country still takes coal as the main source of energy to generate electricity [1]. However, China has entered an era of

---

R. Zhang (✉)  
Jilin Provincial Electric Power Research Institute,  
Changchun 130021, Jilin Province, China  
e-mail: lgq109@163.com

C. Wu  
Northeast Dianli University, Jilin 132012, Jilin Province, China

sustainable development in terms of energy utilization and environmental protection; the power must be greatly based on the reduced coal consumption. Today, supercritical and ultra-supercritical thermal power units have a significant effect on energy saving and environmental improvement. It is a large coal-fired thermal power generating units of the rapid development in recent years. With the application of supercritical and ultra-supercritical technology in boiler, the planning of the boiler and the actual installation methods also has changed to some extent. Using the structure of the coil water wall in the radiation zone of the furnace and the vertical tube screen structure in the low heat intensity region of the radiant area of the furnace has been the common method of supercritical and ultra-supercritical boiler [2, 3]. The design and operation mode of supercritical and ultra-supercritical boilers have many advantages, but the problems of heat deterioration and thermal deviation tend to occur [4, 5]. There are many cracks in the outlet of the vertical water wall in a power plant supercritical boiler. It leads to the vertical water wall failure and boiler outage. In this paper, we make an analysis of operating parameters curve for the characteristics of the power plant boiler vertical water wall at the exit of the crack and vertical water wall at the outlet of the tube wall temperature, boiler water, coal quantity and separator outlet pressure in order to find out the cause and feature of the crack. And then, the countermeasures of controlling the crack are proposed. It provides technical support and assistance to the normal operation and reconstruction of the boiler.

## 2 Equipment Introduction

The boiler of the plant is 350 MW supercritical once-through boiler and the model is HG-1110/25.4-HM2 type. The boiler is the product of  $\Pi$  type arrangement, balanced ventilation, single reheat, solid slag, steel frame and full suspension structure.

Boiler is single furnace which is 14.6273 m in width and 14.6273 m in depth. Under the BMCR condition, boiler super heater outlet steam pressure is 25.4 MPa and temperature is 571 °C; reheat steam outlet pressure is 4.287 MPa and temperature is 569 °C; water temperature is 284.1 °C.

Boiler milling system is medium-speed mill positive pressure direct firing system configured six HP863 type medium-speed coal mill. Coal fineness  $R_{90} = 37\%$ . SOFA burner is arranged in the main combustion chamber that is above the four corner areas, in order to achieve staged combustion and to reduce NOX emissions.

Boiler vapour and water process use a built-in steam separator into double process, boiler start-up system is composed of built-in steam separator, water storage tank, water control valves, etc. Spiral water wall is between the import from the ash hopper and middle mixed container, the intermediate header tube screen transition is converted to vertical tube panels, and it forms the furnace front wall, side walls, hanging back wall and the water pipe; a temperature measuring point is installed in the vertical water wall outlet for every eight root canal, wall outlet header through a small tube connected to the drop tube inlet collection. It enters the

flame tube situated at the angle of flame. There is a split into two, one leading to the water wall convection tube bundle via the folding flame angle and the other to the horizontal flue side wall via flue inlet header. They finally move to the steam separator.

### 3 Characteristics of the Crack in the Vertical Water Wall Outlet

The leakage of the vertical water wall outlet of a supercritical boiler in a power plant is found in the operation, it cause the failure of vertical water wall and boiler outage. Checking after stopping the furnace, we found that multiple transverse cracks appeared at front, rear, left and right side of vertical water wall outlet, shown in Fig. 1 circle.

Figure 1a is a picture of crack at the exit of vertical water wall vision picture. Figure 1b is the close-range picture. Cracks appeared in the vertical water wall outlet, set near the weld box and located in the non-heated boilers. All crack positions are located between the two tubes and presents the transverse state. Left and right sides are both present and steam is blown out from the cracks and makes water wall tube thinner.

## 4 Analysis of Crack Reason and Countermeasures to Control

### 4.1 Analysis of Crack Reason

To find out the cause of boiler water wall at the exit of the vertical cracks, we obtain a temperature curve of adjacent temperature measurement points from 50 % BMCR

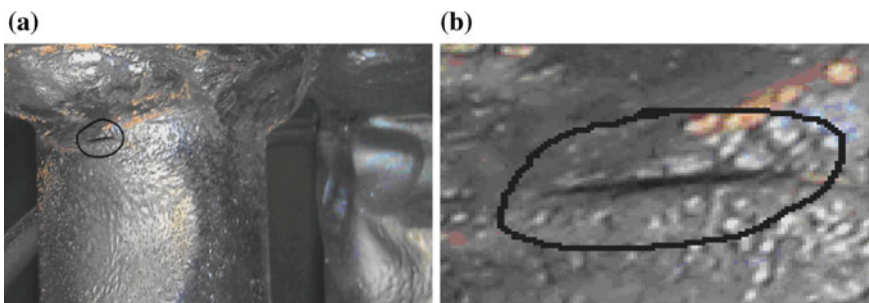
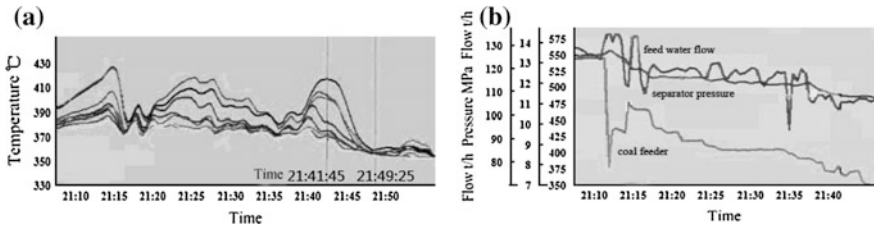


Fig. 1 Crack vision (a) and cracks close-range (b) at vertical water wall outlet

**Table 1** Corresponds to low temperature curve value table

Name	Temperature 1	Temperature 2	Temperature 3	Temperature 4	Temperature 5	Temperature 6	Temperature 7	Temperature 8
Value (°C)	415.6	394.1	390.7	362.1	351.8	347.0	344.6	340.5



**Fig. 2** Vertical water wall at the outlet temperature (a) and sliding boiler stop parameters (b) of boiler slip process stops running

unit to 35 % BMCR conditions at the vertical water wall outlet when the running of slippery pressure shuts down. It corresponds to the water supply, coal supply and the outlet pressure curve, shown in Fig. 1. Vertical water wall outlet when the boiler slipping shuts down. 21:41:45 corresponding time temperature values is in Table 1, the temperature value at 21:49:25 is in Table 1. As can be seen from Fig. 2a in a graph, there is a big temperature difference between vertical water wall tube. The temperature value at 21:41:45 can be found in Table 1. The maximum temperature difference reaches 75.1 °C. Taking into account that not every root canal temperature measuring points are installed, the temperature deviation portion of the tube may be greater. The temperature deviation between the tubes lead to different flex of tube and stress generated between the tubes. By comparing Tables 1 and 2 it is found at the exit of vertical water wall tube that temperature decreases and it changes quickly, declining magnitude is up to 79.9 °C, changing rate reached 10.4 °C/min, which is larger than vertical water wall tube temperature. The temperature’s allowed change rate is 2.5 °C/min. Rapid changes in tube temperature will have a greater thermal shock for pipes and collecting box.

Figure 2b is the graph of the feed water flow, steam water separator outlet pressure and boiler operating parameters for the total amount of coal in the corresponding period of the boiler wall temperature. By comparing Fig. 2a, b it is found that there is a corresponding relationship between the changes in the boiler water flow and vertical water wall tube temperature fluctuations.

### 4.2 Characteristics of Pipe Temperature Deviation

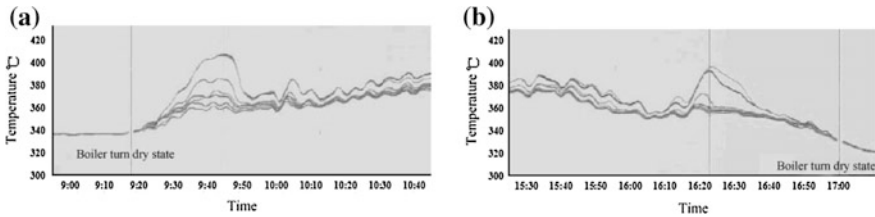
To find out the relationship between the vertical water wall temperature deviations and load, we, respectively, obtain a temperature curve at the exit of vertical water wall during the intact load-up and load-down of boiler.

Figure 3 is a temperature curve diagram at vertical water wall outlet of boiler raising and lowering load. Figure 3a is raising load temperature curve diagram at vertical water wall outlet and Fig. 3b is the lowering load graph. From Fig. 3, it can



**Table 2** Corresponds to low temperature curve value table

Name	Temperature 1	Temperature 2	Temperature 3	Temperature 4	Temperature 5	Temperature 6	Temperature 7	Temperature 8
Value (°C)	335.7	329.8	328.5	329.2	326.6	327.3	327.0	326.6



**Fig. 3** Boiler load temperature rise curve (a) and boiler load drop temperature graph (b) at the exit of the vertical temperature profile wall

be found that large deviation between the tube temperature and pipe temperature rapid change usually occur in the low-load condition that the boiler turns into the dry state. The temperature values of the boiler vertical water wall outlet under the condition of 80 % BMCR correspond to Fig. 2 and are shown in Table 3. The temperature values of the boiler vertical water wall outlet under the condition of 25 % BMCR correspond to Fig. 2 and are shown in Table 4.

From Table 3, it is found that at the exit the vertical water wall temperature deviation is small—a maximum of 9.7 °C. In the boiler operating condition, the temperature is high, but the deviation is not large. From Table 4, it can be found that in the boiler wet operating conditions, the vertical water wall outlet temperature is equally distributed, the deviation is small and the maximum value is 3.6 °C. Integrated 4.2, large deviation between the tube temperature and pipe temperature and rapid change generally occur under the low-load conditions that the boiler turns into dry state.

### 4.3 Control Measures for Cracks

Since there is a large-scale temperature deviation inside the vertical water wall and rapid changes in temperature generally appear under the low-load conditions that the boiler turns into dry state, we should reduce boiler long-term low-load operation in the dry state. In the condition of low-load boiler under dry state, the operation staff should increase the presence of surveillance over the vertical water wall outlet and adjust in time in case of deviation. Owing to the corresponding relationship between boiler water flow variation and vertical water wall tube temperature fluctuations, recommendations are given to further improve automatic feed water and automatic feed coal for coal–water ratio adjustment capacity in boiler operation.

**Table 3** 80 % BMCR conditions of temperature table

Name	Temperature 1	Temperature 2	Temperature 3	Temperature 4	Temperature 5	Temperature 6	Temperature 7	Temperature 8
Value (°C)	433.6	430.1	430.7	428.9	428.3	427.7	427.2	423.9

**Table 4** 25 % BMCR conditions of temperature table

Name	Temperature 1	Temperature 2	Temperature 3	Temperature 4	Temperature 5	Temperature 6	Temperature 7	Temperature 8
Value (°C)	325.6	323.4	322.7	321.8	320.7	320.4	320.2	322.0

## 5 Conclusion

In the operation of 350 MW supercritical units, there are many cracks in the outlet of the vertical water wall of the boiler. It cause failure and boiler shutdown. In this paper, the characteristics of the cracks and the boiler operation parameter curve are analyzed, which have found out the reason and the characteristic of the cracks. The measures to control the crack are also put forward. The following conclusions are safely reached:

- (1) The cracks in the outlet of the boiler vertical water wall are caused by the large deviation of the tube temperature and the thermal stress caused by the rapid change of the tube temperature.
- (2) Thermal stress caused by large deviation of the vertical water wall of boiler and the rapid change of the tube temperature generally appear in the low-load conditions after the dry state of the boiler.
- (3) There is a corresponding relationship between the changes in the boiler feed water flow and vertical water wall tube temperature fluctuations.
- (4) Based on the cause and characteristics of crack initiation, this paper presents 350 MW supercritical unit boiler to reduce the chances of turning dry after long-term low-load operation. Operating crew should increase the presence of surveillance over vertical water wall outlet temperature and make timely adjustments to avoid a large deviation. The adjustment is made to improve the automatic water and coal feed in the due water–coal ratio, so as to avoid the imbalance between water and coal during the load change.

## References

1. Sheng W (2007) Thermal power plant equipment and operation. China Electric Power Press, Beijing
2. Gao P (2014) Risk assessment and management of ultra supercritical boiler water wall. *Zhe Jiang Power* 1:47–50
3. Bowen BD, Fournier M, Grace JR (1991) Heat transfer in membrane water walls. *Int J Heat Mass Transf* 34:1043–1057
4. Liu X, Sheng W, Guan D (2010) Thermal stress analysis of a 600 MW supercritical boiler membrane wall. *Boiler Technol* 41(6):11–17
5. Ahmad J, Purbolaksono J, Beng LC et al (2009) Failure investigation on rear water wall tube of boiler. *Eng Fail Anal* 16(7):2325–2332

# Optimal Design of a Linear Induction Motor for Traction Application

J. Gong, F. Gillon and H. Zhong

**Abstract** In traction application, the electric motor design methodology is not trivial. This paper presents a design approach using rated point. Based on a 2D finite element model, design optimization of a double-sided linear induction motor is achieved using an efficient global optimization algorithm.

**Keywords** Finite element model · Design optimization · Efficient global optimization

## 1 Introduction

Direct linear motor can be observed in a wide range of applications, from industry field to the public transportation system. Simple structure, easy maintenance, and less environmental pollution are the advantages of linear motors. For demanding applications, the linear motors are mostly of the induction type, especially in public transportation system. However, it is difficult to design a linear induction motor (LIM) because of the end and edge effects. The numerical methods such as finite element method allow overcoming these difficulties. 3D finite element method (FEM) can take into account both the longitudinal end effects and the transverse edge effects; however, it results in very high computation burden. The optimal design of an electrical machine with a high fidelity model, such as finite element model, runs into the wall of the computation time and of the number of parameters. Indeed, FEM is sensitive to numerical noise, its results depend on the mesh quality and a single evaluation of this model is computationally expensive. The Efficient Global Optimization (EGO) based on the progressive construction of a Kriging

---

J. Gong (✉) · H. Zhong

Electrical Engineering School, Shandong University, Jinan, China  
e-mail: gongjinlin@sdu.edu.cn

F. Gillon

ECLille, L2EP, F-59650, Villeneuve d'Ascq, France

© Springer-Verlag Berlin Heidelberg 2016

B. Huang and Y. Yao (eds.), *Proceedings of the 5th International Conference on Electrical Engineering and Automatic Control*, Lecture Notes in Electrical Engineering 367, DOI 10.1007/978-3-662-48768-6\_29

251

model used to drive the optimization problem allows for an affordable optimization time [3].

In this paper, a LIM with double primaries for the traction application is designed, based on the validated 2D finite element model at reduced scale and the tramway's needs. The optimal design problem of LIM is formulated using the rated point design approach and achieved using the EGO algorithm.

## 2 Finite Element Model Analysis

### 2.1 LIM Structure Description

Figure 1 shows the basic structure of the double-sided linear induction motor. Two identical primaries are placed face to face. Three concentrated windings, forming the primary, are fed by three-phase AC voltage. An aluminum sheet is placed in the middle of the two primaries. This motor is mechanically very simple. Its great advantage is its robustness coming from the simplicity of its construction. The supply part is similar to that of a toothed synchronous motor and the difference between them is in the reaction part. This electrical conducting layer or squirrel cage allows the circulation of induced currents produced by the stator winding magnetomotive force. The interaction of these induced currents with the winding creates a propulsion force. It is designed for the railway system application. For this application, the static part is the aluminum plate which is installed on the ground, while the moving part is represented by the two primaries that are installed in the train.

### 2.2 2D Finite Element Analysis

The fundamental difference between a rotating induction motor and LIM is the finite length of magnetic and electric circuit of LIM in the direction of traveling

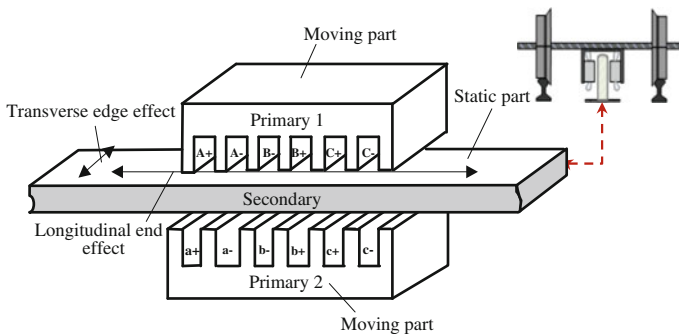


**Fig. 1** Basic structure of double-sided linear induction motor

field [1]. An analytical solution is barely achieved to analyze a LIM, due to the end effects and the nonlinear characteristic of the materials and complex geometry of machine. Many numerical approaches are widely used to model linear motors. The 2D FEM is most frequently encountered to study the behavior of electromagnetic devices. It can consider the longitudinal end effect but not the transverse edge effect. The conductivity of secondary can be adjusted in order to compensate the transverse edge effect. Moreover, the leakages of winding overhang are taken into account in the improved 2D model.

The FEM is achieved with Vector Fields software [8]. The supplied voltage is realized by three external circuits imposed on the phases in the slots. The AC solver is chosen to analyze the model.

The longitudinal end effect is caused both by the interference of the magnetic flux density waves and the step change in the reluctance for magnetic flux at each end of the magnetic circuit [1]. Figure 2 shows the amplitude of the flux density distribution in the air gap of LIM along the X direction. The flux distribution is nonuniform and the flux at the exit of LIM is stronger than the flux at the entrance of LIM. This gives a good representation of the longitudinal end effects within the linear motor.

### 2.3 Simulation Taking into Account the Movement

A linear induction motor with reduced scale is first studied using FEM. Figure 3 shows the evolution of the mechanical characteristics of LIM according to the relationship between the fed voltage and frequency  $V/f$ . Compared to the traditional rotating motor design scheme, the flux leakage of the stator of the LIM is important

**Fig. 2** Amplitude of flux density distribution in the air gap

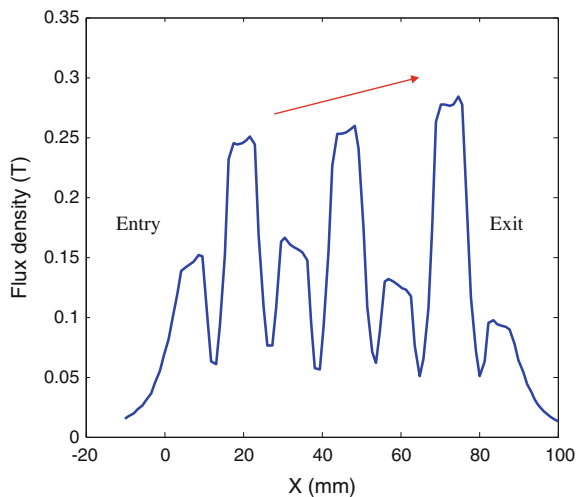
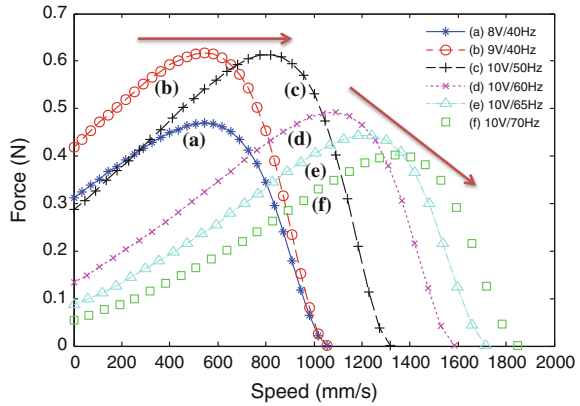




**Fig. 3** Evolution of the mechanical characteristics of LIM according to different V/f supplies



and cannot be neglected. The magnetization flux cannot be kept constant; nevertheless the V/f is kept constant in the so-called constant thrust region. For the LIM, the ratio of V/f has to be increased in order to have the same maximal thrust force when the frequency increases. This phenomenon can be presented with the blue curve (a), the red curve (b), and the black curve (c) of Fig. 3.

### 3 Optimal Sizing Using EGO

#### 3.1 Optimization-Based Design Process

There exists a variety of different approaches for the design of electromagnetic devices. A classic approach called manual design process is illustrated in Fig. 4. The manual design process involves an engineer in the iteration process and it is the most used in industry before the appearance of computer aided design. Unfortunately, it requires a great deal of engineering experience and it cannot guarantee for the best design.

With the development of the computer and the optimization tools, there is a great revolution of design approaches. An optimization-based design process is shown in Fig. 5. Unlike the manual design process, the detailed analysis is used to calculate design metrics such as mass, cost, and loss, which would be considered as the objective functions. An optimization engine such as different optimization algorithms will select the parameters of the design so as to maximize or minimize the

**Fig. 4** A manual design process [7]

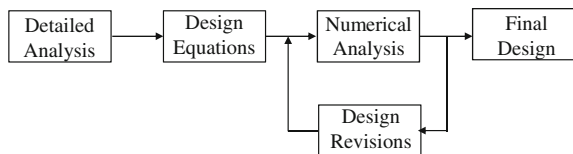
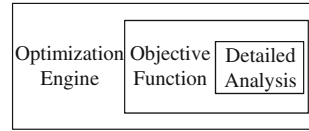


**Fig. 5** Optimization-based design process [7]



objective function that is calculated based on the detailed analysis. Compared to manual design process, this process can not only save lots of engineering time but also make sure for the best design.

In this paper, the design of the LIM for the subway system is optimized using EGO optimization algorithm, based on the validated 2D FEM at reduced scale and the tramway’s needs.

### 3.2 Design Approach Using Rated Force and Speed

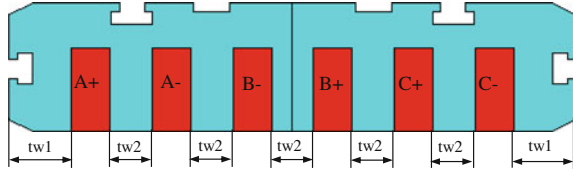
There are several different approaches by which motors may be designed, such as approaches using rated torque and speed, approach using torque versus speed curve, and approach using load cycle [6]. For design of a traction motor, the approach using rated torque and speed perform quite well due to the fact that the load is generally constant [5]. The rated torque can also be determined as a percentage of the maximal torque requirement to avoid an oversize motor, but this depends on lots of experience to decide how many percentages should be taken. In our work m, the rated thrust and speed is used for the design.

In order to present the optimal design approach based on the 2D FEM at reduced scale, the rated speed is fixed at 1 m/s, which is 36 % of the rated speed of the tramway. The rated thrust force is reduced to 0.1 N in order to be in the range of our prototype. The mono-objective optimization problem in the mathematical form is presented in (1).

$$\begin{aligned}
 & \min_{tw1, tw2, U, Speed} \text{ Losses} \\
 \text{s.t.} \quad & Eq = \left| \frac{I}{I_2} - 1 \right| + \left| \frac{I}{I_2} - 1 \right| \leq 10 \%, \text{ Mass} \leq 1 \text{ kg}, \left\| \frac{\text{Force}}{0.1} - 1 \right\| \leq 0.05 \quad (1) \\
 & \text{with } tw1 \in [5, 12], tw2 \in [5, 10], U \in [0, 20], \text{ Speed} = 1 \text{ m/s}
 \end{aligned}$$

The objective of the optimization problem is to minimize total motor losses, i.e., the sum of joule losses and iron losses while satisfying three constraints. The first constraint parameter Eq represents the non-balance of the currents between three phases. Though the three phases of the LIM are fed by the balanced voltages, i.e., the same amplitude with 120° difference between the phase angles, the currents in the three phases are not balanced due to the longitudinal end effects. The more important the Eq, the more the longitudinal end effects influence the motor’s performance. It is therefore limited to less than 10 %. The second constraint parameter Mass represents the mass of the LIM which should be less than 1 kg. The third

**Fig. 6** Geometrical variables of the optimization problem



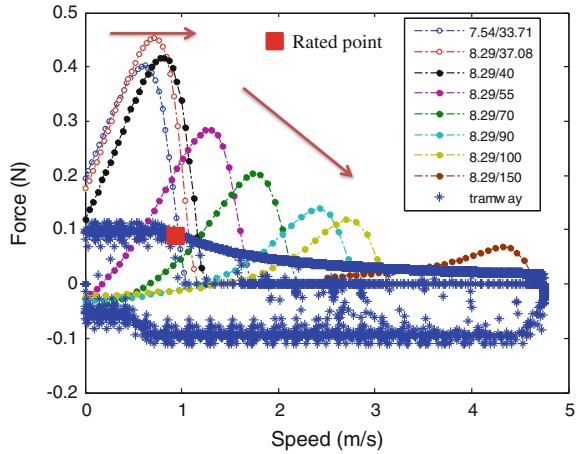
constraint parameter Force represents the thrust force of the rated point provided by the interaction between the slip and induced current in the aluminum plate. It is imposed around 0.1 N. There are four design variables, among which two are geometrical variables:  $tw1$ ,  $tw2$  represent the width of the motor teeth shown in Fig. 6.  $U$  represents the fed voltage of the primary for the motor control and Speed represents the speed of the secondary which is imposed to 1 m/s according to the selected rated point.

### 3.3 Design Optimization Using EGO Algorithm

The direct integration of a high fidelity model such as FEM within an optimal design process is difficult because of the large number of model evaluations required by the optimization algorithms. Surrogate model-assisted optimization approach allows replacing the high fidelity model by fast analytical surrogate model during the optimization process [2, 4], where a surrogate model is constructed using the sampling data computed by a high fidelity model in order to approximate the performance. However, due to the inaccuracy of the surrogate model, the solution found is not accurate enough. In order to benefit from both the accuracy offered by the 2D FEM and the fast prediction of a surrogate model, within the optimization loop, EGO algorithm is used. EGO is a surrogate-based optimization algorithm which uses Kriging models as surrogates for the fine model, and allows adding sample points (infill points) into the Kriging surrogate model during the optimization process. Since this algorithm does not use gradient information, it can easily cope with the noisy model. This way, the number of fine model (FEM) calls is drastically reduced, obtaining though the optimal trade-off solutions with an affordable computational cost. The role of the surrogate model within the algorithm is to guide the search for improving solutions; the final optimal design is evaluated by the FEM.

The working characteristic of the tramway traction motor at the reduced scale is marked with blue stars in Fig. 7. It is compared with the results of the optimal motor. The evolution of the mechanical characteristics of the optimal solution is marked with blue circles, and that passing the rated point is marked with red square. The working characteristic of the optimal motor can attain all the working points of the tramway traction motor. It is said that the obtained optimal motor can satisfy all the traction requirements of the tramway. However, the case using the maximal thrust force and the rated speed approach leads to oversize motors as the motor never operates permanently at the maximal thrust force.

**Fig. 7** Thrust force as a function of speed with different fed frequencies



## 4 Conclusion

Based on finite element method, the double-sided LIM is presented and studied. A 2D FEM of LIM is achieved, which allows taking into account both the transverse edge effects and the longitudinal end effects. Using the rated point design approach, an optimization problem is formulated according to the needs of a tramway. Then, the LIM is optimal sized using the EGO algorithm. Compared to the initial solution, the optimal solution allows decreasing of the losses by 41 % with the same performance of LIM. The obtained optimal motor can satisfy all the traction requirements of the tramway at the reduced scale. The results confirm the advantages of EGO for optimal design problem. It allows obtaining the results with affordable time using the FEM. Moreover, the surrogate models of objective and constraint functions are available after the optimization. They can be used later in an analysis process. Therefore, EGO optimization algorithm has proved its efficiency for the design of electromagnetic devices using a high fidelity model.

**Acknowledgment** This work was supported by National Nature Science Foundation of China (51307099) and (51307100).

## References

1. Gieras JF (1994) Linear induction drives. Oxford Science Publications, Oxford
2. Gong J (2011) Conception optimale d'un moteur linéaire à induction pour le système de traction ferroviaire, Ph.D. dissertation 2011, Ecole Centrale de Lille, France (online available)
3. Gong J, Aslan B, Gillon F, Semail E (2014) High speed functionality optimization of five-phase pm machine using 3rd current harmonic, Int J Comput Math Electr Electron Eng 33(3):879–893

4. Hawe GI, Sykulski JK (2006) A hybrid one-then-two stage algorithm for computationally expensive electromagnetic design optimization. In: Proceeding of 9th workshop on optimization and inverse problems in electromagnetism, Sorrento (OIPE), pp 191–192
5. Kreuawan S, Gillon F, Brochet P (2008) Comparative study of design approach for electric machine in traction application. *Int Rev Electr Eng* 3(3):455–465
6. Kreuawan S, Gillon F, Brochet P (2008) Comparative study of design approach for electric machine in traction application. *Int Rev Electr Eng* 3(3):455–465
7. Sudhoff SD (2014) Power magnetic devices: a multi-objective design approach. Wiley, Hoboken. ISBN 978-1-118-48999-4
8. Vector fields software: 2D AC, 3D Electra/SS manuals

# Simulation on the Boost-Buck Current Compensation Device of PV Grid Connection and Active Power Filter All-in-One Machine

Tian-fa Liao, Zhao-quan Cai, Jia-xiang Xue and Hong-wei Zhang

**Abstract** This paper first analyzed the alternating current AC/DC power decoupling working mechanism of photovoltaic (PV) grid connection and active power filter all-in-one machine, then put forward Boost-Buck parallel current compensation circuit and analyzed its working principle. Simultaneously, the thin-film capacitor  $C_{dc}$  in DC side was calculated, and finally the simulation model of current compensation device based on the Boost-Buck was established. The simulation results show that the thin-film capacitor with a small capacity (100–200  $\mu\text{F}$ ) can reduce the voltage fluctuation and stabilize MPPT working point as well as solve the dilemma that the life of grid-connected system is limited by power decoupling electrolytic capacitor, which provides a reliable hardware foundation for realizing the PV grid-connected and active power filter all-in-one machine.

**Keywords** PV grid-connected · Active power filter · Boost-buck · Current compensation

## 1 General Instructions

At present, installed capacity of photovoltaic (PV) grid-connected system is growing rapidly [1–3], but PV inverter utilization rate is not high due to the limitation of its application scale. Meanwhile, harmonic pollution of power grid becomes more serious [4, 5], and the active power filter is the key for the harmonic governance as a result of good dynamic performance and compensation effect, but the expensive cost limits its application. Therefore, the second generation product

---

T. Liao (✉) · Z. Cai  
Department of Electronic Engineering, Huizhou University,  
Huizhou 516007, China  
e-mail: liaotianfa@163.com

J. Xue · H. Zhang  
Mechanical and Automobile Engineering College, South China University  
of Technology, Guangzhou 510640, China

of PV grid-connected inverter is the PV grid connection and active power filter all-in-one machine, which has a great application value for using the solar energy and improving the quality of power grid. During the development of PV grid connection and active power filter all-in-one machine, both the traditional electrolytic capacitor and thin-film capacitor are not applicable due to the reasons of the service life and volume size. Therefore, the key to develop the PV grid connection and active power filter all-in-one machine is to design an energy storage device in the DC side of inverter circuit [6].

## 2 Working Mechanism of AC/DC Power Decoupling [7]

When the PV grid-connected inverter converts the DC to the AC which has the same frequency and phase with the grid voltage, the output power will generate 100 Hz power pulse, and its expression is

$$P_{ac}(t) = u_{ac}(t)i_{ac}(t) = U_{rms}I_{rms}(1 - \cos 2\omega t) \quad (1)$$

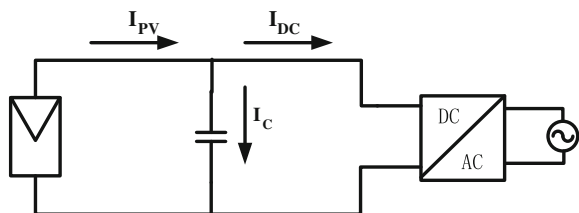
where  $P_{ac}(t)$ ,  $u_{ac}(t)$ , and  $i_{ac}(t)$  are the instantaneous values of grid-connected power, grid voltage, and grid-connected current, respectively. In addition,  $U_{rms}$  and  $I_{rms}$  are the effective values of grid voltage and grid-connected current, respectively, and  $\omega$  is the base wave angle frequency of the grid voltage.

The output power fluctuations will lead to considerable oscillation of output voltage and current of photovoltaic array, thus the maximum power point tracking control cannot be implemented and the system operation power is greatly reduced. Hence, it is necessary to join an energy storage device in the DC side of inverter circuit for implementing decoupling between DC power and AC power, filtering the current pulsation in the DC side, and maintaining stable DC voltage on the DC side so as to smoothly realize the maximum power point tracking of preceding stage. A commonly used method is to join an electrolytic capacitor with the large capacity in the DC side, as shown in Fig. 1.

In Fig. 1, the relation among the decoupling capacitor current, output current of preceding stage, and the input current of inverter is as

$$I_C = I_{PV} - I_{DC} \quad (2)$$

**Fig. 1** The current relationship in the DC side



where  $I_{DC}$  is the average input current of inverter,  $I_{PV}$  is the average output current of photovoltaic array, and  $I_C$  is the average current of passing through the electrolytic capacitor.

After capacitor filtering, input current of inverter is expressed as

$$i_{DC}(\omega t) = \frac{\pi}{2} I_{DC} |\sin \omega t| = I_{DC} \left( 1 - 2 \sum_{n=2,4,6}^{\infty} \frac{\cos n\omega t}{n^2 - 1} \right), \quad \omega t \in [0, 2\pi] \quad (3)$$

From formula (1), the fundamental wave expression of current pulsation in the DC side generated by the output power fluctuation is as follows.

$$i(\omega t) = \frac{2}{3} I_{DC} \cos 2\omega t \quad (4)$$

Therefore, the capacitance values which are needed to filter the current pulsation two times the fundamental wave frequency of grid can be calculated by the following formula:

$$\frac{1}{2\omega C_{in}} = \frac{\tilde{u}}{2 \left( \frac{2I_{DC}}{3} \right)} \quad (5)$$

In the formula,  $\tilde{u}$  is the allowed maximum voltage pulsation amplitude in the DC side as the system stably operates in the maximum power point. Then,

$$C_{in} = \frac{2P_{PV}}{3\omega V_{PV}\tilde{u}} \quad (6)$$

Taking  $P_{PV} = 3000$  W,  $V_{PV} = 270$  V,  $U = 1$  V,  $\omega = 314$  rad/s, so the required capacitance size is  $C_{in} = 2 \times 3000 / (3 \times 314 \times 270 \times 410) = 2.359$  mF.

Electrolytic capacitor has the advantages such as large capacity, small volume, and low cost, as well as, it can easily solve the decoupling problem before and after the AC/DC power, but its life is sensitive to temperature. For the new system with working around the clock, it is far from the requirements that electrolytic capacitor is used as decoupling element; therefore, the life and reliability of PV grid-connected inverter are directly affected. Usually, the thin-film capacitor is used to replace the electrolytic capacitor to solve the problem of life. Compared with the electrolytic capacitor, the volume of thin-film capacitor is about 20 times as much as the electrolytic capacitor under the same capacity. Meanwhile, the cost is also much higher. Hence, it is impossible for the direct replacement to fundamentally solve the problem.

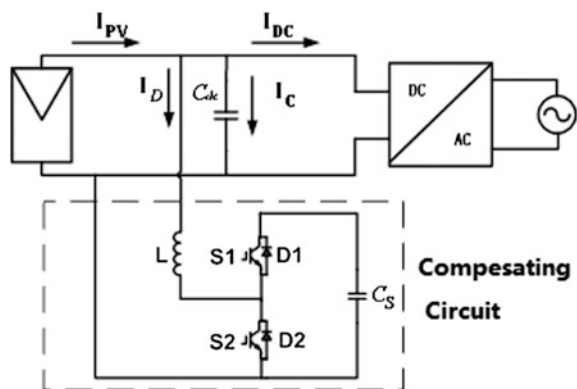


### 3 Parallel Current Compensation Circuit Based on the Boost-Buck

It is an ideally alternative method that the thin-film capacitor with a small capacity is used as the decoupling capacitor in DC side, which certainly causes the intense pulsation of decoupling current. Therefore, this paper studies a kind of parallel current compensation device based on Boost-Buck [8], which can eliminate the pulsation of decoupling current to maintain the stability of voltage in the side of DC, as shown in Fig. 2. The device is equivalent to a controlled current source as well as independent of the grid-connected system control. It consists of two small power MOS tubes and two capacitors with small capacity. Moreover, the film capacitor  $C_{dc}$  with a small capacity replaces the traditional electrolytic capacitor with the large capacity.  $C_s$ , as the energy storage capacitor, allows voltage pulsation with larger amplitude. So, the capacitor with small capacity also can be used.

As shown in Fig. 3, working principle of Boost-Buck current compensation circuit is as follows. When  $I_{PV} > I_{DC}$ , switch tube  $S_2$  works and constitutes the Boost boosted circuit with the backward diode  $D_2$  of  $S_1$ . At the moment, the excess energy will be poured into the energy storage capacitor  $C_s$ . When  $I_{PV} < I_{DC}$ , switch tube  $S_1$  works and constitutes the Buck step-down circuit with the backward diode  $D_2$  of  $S_2$  which is the freewheel diode. Simultaneously, the energy storage capacitor releases the energy to DC side to compensate the insufficient output energy in the preceding stage. Thus, energy storage diode voltage will be always higher than or equal to the capacitor voltage in DC side, and is in the charging and discharging state of circulation, which is equivalent to transfer the voltage pulsation in DC side to the energy storage capacitor. This realizes the small capacity for the capacitor in DC side as well as better solves the life problem of energy storage device in DC side.

Fig. 2 Parallel current compensation circuit based on the Boost-Buck



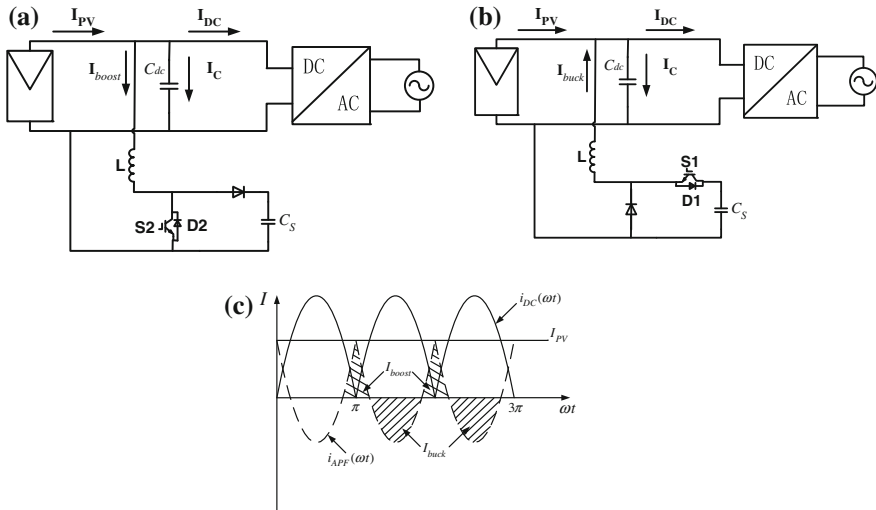


**Fig. 3** The working principle of Boost-Buck current compensation circuit. **a** The Boost working mode; **b** the Buck working mode; **c** modulating principle

## 4 Current Compensation Device Simulation Based on Boost-Buck

The simulation model of current compensation device based on Boost is constructed by using the PSIM software in DC side of PV grid-connection and active power filter all-in-one machine, as shown in Fig. 4. Where the maximum power of solar battery is 2330 W, switch frequency of Boost is 20 kHz, the capacitor in DC side is 100  $\mu\text{F}$ , energy storage capacitor is 200  $\mu\text{F}$ , and the inductance is 0.1 mH.

### 4.1 100 $\mu\text{F}$ Capacitance in DC Side

The DC side capacitance is set as 100  $\mu\text{F}$  capacitance of small capacity in the PV grid-connected simulation system in Fig. 3a and the simulation results obtained by operation are shown in Fig. 6. As seen in Fig. 5, voltage pulsation amplitude in the DC side is 40 V, and the pulsation amplitude of decoupling current can be up to 40 A. Finally, the grid-connected current would be distorted and the system input power has 300 W oscillations.

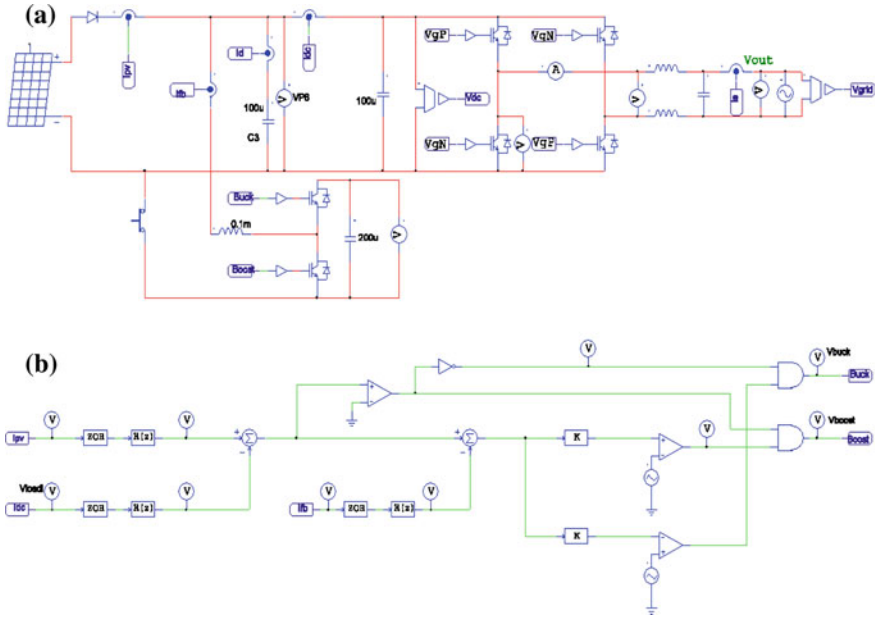


**Fig. 4** Simulation model based on Boost-Buck current compensation. **a** The main circuit of compensation device, **b** the control part of compensation device

### 4.2 Current Compensation Device Simulation Based on Boost-Buck

Compensation device control is carried out according to the polarity of decoupling current. When  $I_C > 0$ ,  $S_2$  is driven the energy storage capacitor absorbs energy. When  $I_C < 0$ ,  $S_1$  is driven the energy storage capacitor releases energy. In Fig. 2, it is needed to detect the compensation current  $I_d$  and the input current  $I_{DC}$  of last stage for controlling the compensation current.

The two feedback variables include the high-frequency current component generated by the make and break of the semiconductor device, as shown in Fig. 6b. Hence, this paper uses a second order butterworth low-pass filter to detect two kinds of current. And the simulation results of detection are shown in Fig. 6.

The simulation results of compensation device and the simulation results that the electrolytic capacitance 2.359 mF calculated by using formula (5) conducts the power decoupling are shown in Fig. 7.

The simulation results show that:

- (a) Voltage oscillation generated by the power fluctuation is transferred to the energy storage capacitor; voltage fluctuation amplitude in DC side is reduced to about  $\pm 10$  V.

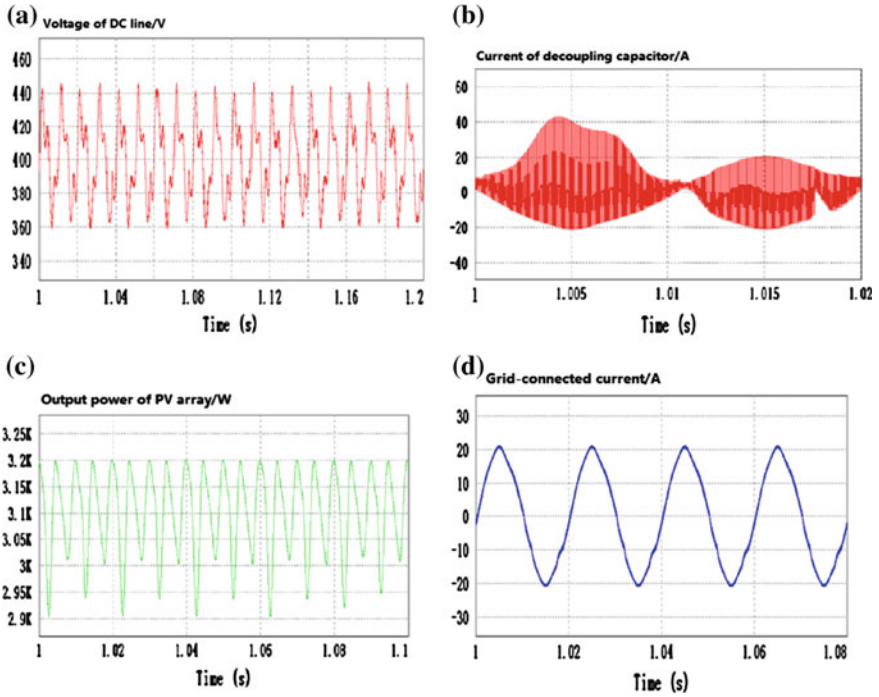


**Fig. 5** The simulation of DC side voltage pulse influence. **a** Voltage waveform of DC line, **b**  $I_C$  of decoupling capacitor, **c** the output power curve of PV array, **d** grid-connected current waveform

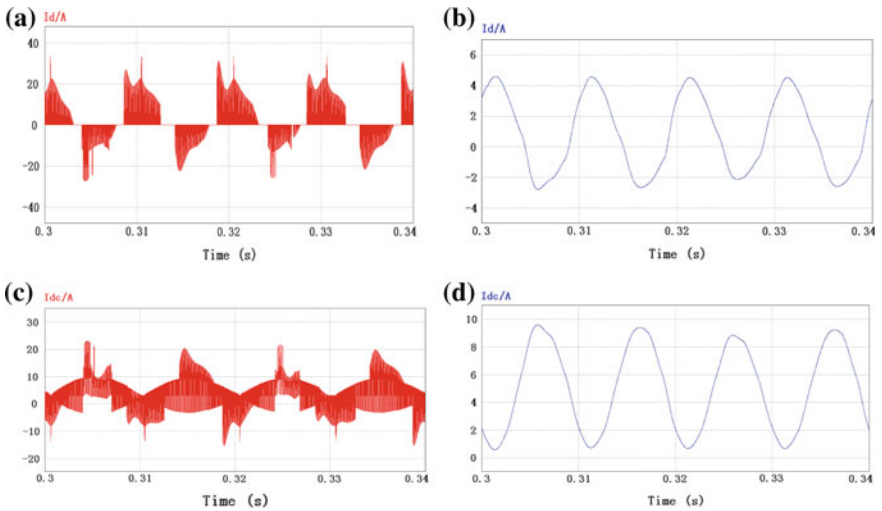


**Fig. 6** The simulation of pulse current detection. **a**  $I_d$  before the filtering, **b**  $I_d$  after the filtering, **c**  $I_{DC}$  before the filtering, **d**  $I_{DC}$  after the filtering

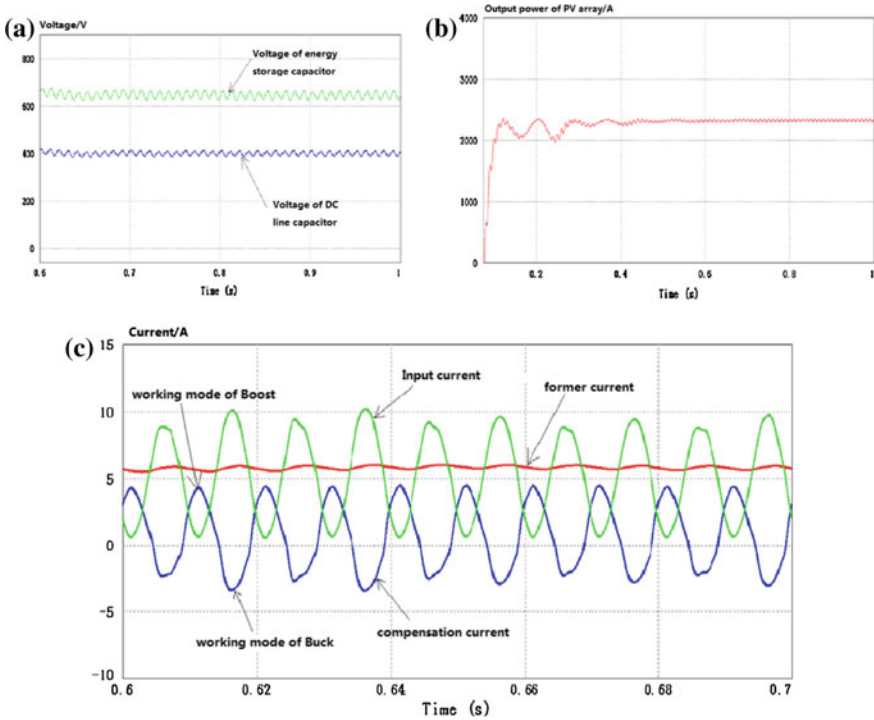


**Fig. 7** The simulation waveform of current compensation device based on Boost-Buck, **a** Voltage waveform of DC line, **b** output power curve of PV array, **c** the compensation current waveform

- (b) System works stably in the maximum power point of PV array, and the power fluctuates about 20 W.
- (c) The electrolytic capacitor with the large capacity (2.359 mF) can be replaced by the electrolytic capacitor with the small capacity (100  $\mu$ F). Under the premise without affecting the stability and reliability of system, the dilemma that the grid-connected system life is limited by power decoupling electrolytic capacitor is solved, and the reliable hardware foundation is provided for realizing the new system with the cooperative control between the PV grid connection and the active power filter.

## 5 Conclusion

This paper presents a study on the optimization method that current compensation device based on Boost-Buck replace electrolytic capacitor with a large capacity. This method adopts the thin-film capacitor as the energy storage component, breaks

through the system application bottleneck of original structure due to the electrolytic capacitor life limitation, and lays the hardware foundation for the all-weather work realization of new system with the cooperative control. Plenty of simulation results in this study provide abundantly theoretical basis for system hardware realization.

## References

1. Cui R, Wang J, Meng F et al (2008) The future of PV power generation. *Renew Energy Res* 26 (3):96–101
2. Ding M, Wang W, Wang X et al (2014) A review on the effect of large-scale PV generation on power systems. *Proc CSEE* 34(1):1–14
3. Sun Y, Wang R, Xiao L et al (2011) Economical and environmental analysis of grid-connected photovoltaic systems in China. *China Popul Resour Environ* 21(4):88–94
4. Chen W, Ai X, Wu T et al (2013) Influence of grid-connected photovoltaic system on power network. *Electr Power Autom Equip* 33(2):26–32, 39
5. Liao T, Yi C, Xie J et al (2015) Design and simulation of low-pass filter for ip-iq harmonic current of photovoltaic (PV) grid inverter. *J Huizhou Univ* 35(3):51–55
6. Guo J, Li Z, Cheng Y et al (2013) A design of grid-connected PV and reactive power compensation device. *Sci Technol Eng* 13(24):7162–7165
7. Li D, Jiang C, Chen M et al (2012) Review of decoupling techniques for photovoltaic micro-inverters. *J Power Supply* 2:57–61, 71
8. Xiao H, Xie S (2010) An interleaving double-switch Buck-Boost converter for PV grid-connected inverter. *Proc CSEE* 30(21):7–12

# An Improved DV-Hop Node Localization Algorithm Combined with RSSI Ranging Technology

Hongyu Shi and Ling Peng

**Abstract** DV-Hop algorithm is a typical rang-free localization algorithm in wireless sensor network (WSN). On the basis of the localization principle and localization process of DV-Hop algorithm, this paper proposes an improved DV-Hop algorithm. The improved DV-Hop algorithm uses cluster strategy to reduce communication overhead and probability of group conflict in the first stage of DV-Hop algorithm; the Received Signal Strength Indicator (RSSI) ranging technique is employed to replace the distance measurement of one hop away from the anchor node in DV-Hop algorithm; then, estimate the node positions with quasi-Newton optimization method instead of Least square method. MATLAB7.0 simulation results indicated that this improved DV-Hop algorithm can significantly reduce the localization error without increasing computing complexity.

**Keywords** WSN · DV-Hop · RSSI · The quasi-Newton method · Localization error

## 1 General Instructions

In all applications of wireless sensor networks (WSNs) [1], the node monitoring data must be combined with its own position information, at the same time the node position information also plays a key role in other applications. So, the problem of node localization is one of the key supporting technologies of WSNs, and it is also one of the hotspots in the research of WSNs.

According to the information of the distance and the angle of the localization, the node localization method in wireless sensor network can be divided into two kinds: range-based method and rang-free method. In the range-based localization

---

H. Shi (✉) · L. Peng

Department of Electronic Science, Huizhou University, Huizhou 516007, China  
e-mail: shyshy2000@126.com

L. Peng

e-mail: pl@hzu.edu.cn

© Springer-Verlag Berlin Heidelberg 2016

B. Huang and Y. Yao (eds.), *Proceedings of the 5th International Conference on Electrical Engineering and Automatic Control*, Lecture Notes in Electrical Engineering 367, DOI 10.1007/978-3-662-48768-6\_31

269

algorithm, the time of arrival (TOA), the time difference of arrival (TDOA), and the signal arrival of angle (AOA) are the main ranging techniques, although the positioning accuracy is high, the cost and energy consumption is high too, and it usually requires additional hardware support, so it is not suitable for large-scale WSNs.

RSSI [2] is one of the simplest ranging methods, which converts the received signal strength to a distance which is based on the theoretical and empirical model. Since this technique is easy to implement and does not require additional hardware support, it is widely used in many fields [3]. DV-HOP (distance vector-hop) localization method has become a classic distance rang-free node positioning method in wireless sensor network due to the high requirement of the ratio of beacon nodes and high positioning accuracy and simple algorithm process [4].

At present, there are a lot of improvements on the classical DV-Hop algorithm, such as Kezhong Liu who proposed a determination method of adaptive collinear threshold based on local network topology by introducing the concept of collinearity degree to the selection stage of beacon nodes [5]. Jia Zhang made correction in the estimated distance between unknown nodes and anchor nodes, which is composed of the multi hop correction value and the average distance error of the anchor node per hop and improve positioning accuracy by using the total least squares method at the same time [6]. Yanheng Liu introduced RSSI technology to replace the measurement of one hop distance of the anchor nodes in the DV-Hop algorithm. Meantime, hyperbolic 2D algorithm is used to replace the three edge measurement method in the DV-Hop positioning algorithm [7].

Although the modified algorithm can improve the positioning accuracy to a certain extent, it is inevitable to increase the communication cost and computation of the system. The improved algorithm proposed in this paper can significantly improve the positioning accuracy by adding some improvement measures in the three stages of the original positioning algorithm, which does not change the localization process of the traditional DV-Hop algorithm.

DV-Hop positioning algorithm, which is proposed by D. Niculescu and B. Nath, is the most successful and widely used method in APS series, which mainly depends on the distance vector routing protocol.

DV-Hop positioning algorithm can be divided into the following three stages [8]:

- (1) Determining the minimum number of hops between the unknown node and each beacon node

First, by using the typical distance vector exchange protocol, the beacon node broadcast position packet information to the neighbour node. Then, after receiving this information, the neighbour node records the minimum hop count of each beacon node, and ignores the grouping of the larger hops from the same beacon node. Finally, the jump value, which is 1, is transmitted to the neighbour node. All nodes in the network can record the minimum hops of each beacon node.



(2) Calculating the actual hop distance between the unknown node and the beacon node

Each beacon node estimates the actual distance per hop with the record of the location information and the number of hops in the first phase. Then beacon nodes packet broadcast the average of each hop distance with a survival period to the network, the unknown node only records and receives the first hop average distance and forwards it to the neighbour node. This method can ensure that most of the unknown nodes can receive the average distance from the nearest beacon nodes. After receiving the average hop distance, the unknown node multiply the average hop distance to the minimum hop count of the first stage, and then the distance between each beacon node is obtained.

(3) Calculating the position coordinates of the unknown node

After the jump distance between the nearby beacon nodes and the unknown nodes are obtained, they calculate their own coordinates using the three edge measurement method or maximum likelihood estimation method. Assume that the coordinates of nodes 1, 2, 3, ...,  $n$  are  $(x_1, y_1), (x_2, y_2), (x_3, y_3), \dots, (x_n, y_n)$ , the distance between each of them to the node  $D$  is  $d_1, d_2, \dots, d_n$ , the coordinates of the node  $D$  is  $(x, y)$ , then you can get the equation group as shown in formula (1)

$$\begin{cases} (x_1 - x)^2 + (y_1 - y)^2 = d_1^2 \\ \vdots \\ (x_n - x)^2 + (y_n - y)^2 = d_n^2 \end{cases} \tag{1}$$

In the formula (1), the last equation is subtracted from the first equation, which is available

$$\begin{cases} x_1^2 - x_n^2 - 2(x_1 - x_n)x - y_1^2 - y_n^2 - 2(y_1 - y_n)y = d_1^2 - d_n^2 \\ \vdots \\ x_{n-1}^2 - x_n^2 - 2(x_{n-1} - x_n)x + y_{n-1}^2 - y_n^2 - 2(y_{n-1} - y_n)y = d_{n-1}^2 - d_n^2 \end{cases} \tag{2}$$

The formula of the linear equation is:  $AX = b$ , the value of  $A, b, X$ , as shown in the formula (3).

$$A = \begin{bmatrix} 2(x_1 - x_n) & 2(y_1 - y_n) \\ \vdots & \vdots \\ 2(x_{n-1} - x_n) & 2(y_{n-1} - y_n) \end{bmatrix}, \tag{3}$$

$$b = \begin{bmatrix} x_1^2 - x_n^2 + y_1^2 - y_n^2 + d_n^2 - d_1^2 \\ \vdots \\ x_{n-1}^2 - x_n^2 + y_{n-1}^2 - y_n^2 + d_n^2 - d_{n-1}^2 \end{bmatrix}, X = \begin{bmatrix} x \\ y \end{bmatrix}$$

The equation  $AX = b$  can be solved by the standard of least square method. But in some cases, it may not be possible to get the inverse matrix, which causes the method to be invalid. The location of the unknown nodes can be estimated by the method of optimization. In Sect. 2.3, we will introduce how to estimate the node position using the quasi-Newton method instead of the least square method.

## 2 Improved DV-HOP Algorithm

This improved algorithm does not change the localization process of the DV-Hop algorithm; some improved measures are added only in the three stages of the DV-Hop analysis.

### 2.1 *Reducing the Packet Conflict by Using Clustering Method*

In determining the minimum hop count between the unknown nodes and each beacon node, because of the random distribution of sensor nodes, there are conflicts in the packet process when the location information to the neighbour nodes are broadcasted by the beacon node. So, there is a deviation of minimum hop count and hop count more, deviation is larger, while the global flood will cause greater communication costs.

In the improved algorithm, some of the beacons nodes are selected as the cluster head, the other nodes join the cluster in nearest neighbour rules. Beacon nodes broadcast their location information only in the cluster; the receiving node, then record the minimum hops count to each beacon node.

### 2.2 *Correcting Average Hop Distance by Introducing RSSI Ranging Technique*

The location of the unknown nodes, which are out of the anchor node range, can be calculated in the original algorithm and need not accurate distance information. However, if only the number of hops is calculated, the error of the average per hop is very large, which will directly affect the positioning accuracy of the unknown nodes. In this new algorithm, the signal strength indicator (RSSI) ranging technology is introduced, which can correct the distance error to the anchor node of phase 2 in the DV-Hop algorithm.

RSSI is a kind of distance measurement technology which is used to attenuate the signal attenuation. RSSI is used to limit the number of hops and the average jump distance as an assistant positioning method in DV-HOP algorithm.

In order to estimate the distance between the nodes and the adjacent nodes, a linear RSSI model is first established in order to make use of the RSSI value.

For simplicity, a linear model is established:

$$\bar{d} = \alpha * \gamma + \beta \tag{4}$$

In formula (4),  $\gamma$  is the RSSI value. Using the least square method to estimate the coefficients in the model:

$$\hat{\alpha} = \frac{\sum_{i=1}^n r_i d_i - n\bar{r}\bar{d}}{\sum_{i=1}^n r_i^2 - n\bar{r}^2} = \frac{\sum_{i=1}^n (r_i - \bar{r})(d_i - \bar{d})}{\sum_{i=1}^n (r_i - \bar{r})^2} \tag{5}$$

$$\hat{\beta} = \bar{d} - \hat{\alpha} * \bar{r} \tag{6}$$

In formula (5),  $n$  is the capacity of the sample;  $(r_i, d_i)$  is the samples of the sets of  $i$ .  $\bar{r} = \frac{1}{n} \sum_{i=1}^n r_i$ ,  $\bar{d} = \frac{1}{n} \sum_{i=1}^n d_i$ ;  $\hat{\alpha}$ ,  $\hat{\beta}$  are, respectively, the least square estimation of  $\alpha$ ,  $\beta$ .

After computing the average distance per hop in the network, the anchor node broadcast it to the network; the unknown nodes calculate the distances to the anchor nodes based on the hop count information and average distance per hop. Meantime, the RSSI ranging technology is used to replace measurement of per hop distance to the anchor node.

### 2.3 Calculating the Node Position Coordinates by Introducing the Quasi-Newton Optimization Method

In the third stage of the original DV-Hop algorithm, after the estimated distance of the unknown node to the nearby beacon nodes is obtained by means of the product of the average hop distance and the minimum hop count of the beacon nodes, the maximum likelihood method is used to estimate position coordinates. That is, the equation  $AX = B$  can be solved by the standard least squares method:

$\hat{X} = (A^T A)^{-1} A^T b$ . However, in some cases, the inverse matrix  $(A^T A)^{-1}$  may not be obtained, which causes the method to be invalid. So, we can consider the introduction of optimization method to estimate the location of the unknown nodes.

The quasi-Newton method, which was developed in the 1960's of the twentieth century [9], is a very effective method in solving the optimization problem. It overcomes the limitations of Newton method which need the derivation and inversion, simplifies the process of the algorithm and can speed up the convergence rate. So, this method is widely used in solving the optimization problems.

To construct the objective function by the difference between measuring distance and estimating distance between the nodes:

$$f(x) = \min \sum_{i,j \in E} (\hat{d}_{ij} - \|p_i(x_i, y_i) - p_j(x_j, y_j)\|)^2 \quad (7)$$

In formula (7),  $p_i(x_i, y_i)$  and  $p_j(x_j, y_j)$  are the position coordinates of nodes  $i$  and  $j$ ,  $\hat{d}_{ij}$  is the estimated distance between node  $i$  and  $j$ . When  $f(x) = 0$ ,  $X$  is the optimal solution.

The steps of using quasi-Newton method to solve the optimal solution are:

- (1) An initial value is given:  $x_0 \in R^n$ ,  $H_0 \in R^{n \times n}$ ,  $0 \leq \varepsilon \leq 1$ ,  $K = 0$ ;
- (2) If  $\|g_K\| = \|\nabla f(x_K)\| \leq \varepsilon$ , stop calculation, otherwise calculate  $d_K \in -H_K g_K$ ;
- (3) Conduct linear search along the  $d_K$  direction, and then calculating  $\alpha_K$ , setting  $x_{K+1} = x_K + \alpha_K d_K$ ;
- (4) Correct  $H_{K+1} = H_K$  to make the quasi-Newton conditions establishment;
- (5) Make  $K = K + 1$ , repeat (2).

### 3 Simulation and Analysis

MATLAB7.0 is used to verify the effectiveness and availability of the improved algorithm by simulating the typical DV-Hop algorithm and the improved algorithm (IDV-Hop), and then of the localization error and the number of data packets are analyzed as the simulation results.

Assuming 200 nodes are uniformly random and distributed in a square area length of 100 units, which the ratio of beacon nodes is 5 %. In the same network scenario, the connectivity of the network is changed by changing the total number of nodes, and localization error of the two algorithms is obtained. In order to minimize the random error, the average of 100 times of the simulation results is obtained under the same parameters.

The localization error (LE) is the primary indicator of the evaluation of the positioning technology; it is usually expressed as the ratio of the error value to the node communication radius [10]. In order to measure the effectiveness of the localization algorithm, the localization error (LE) which is shown by the formula (8), is defined as the Euclidean distance between the actual position and the estimated position.

$$LE = (\hat{X} - X_a) + (\hat{Y} - Y_b) \quad (8)$$

In formula (8),  $(\hat{X}, \hat{Y})$ ,  $(X_a, Y_b)$  are the estimated position coordinates and the actual position coordinates of unknown node.

When the sensor nodes are evenly distributed, the comparison results of the DV-Hop algorithm and the improved algorithm (IDV-Hop) are shown in Fig. 1 in different degrees of connectivity and different beacon nodes, obviously, the improved algorithm is superior to the original algorithm when network connectivity and the ratio of beacon nodes are same.

When Network connectivity is, respectively, 9 and 12, the comparison of the improved algorithm IDV-Hop and DV-Hop algorithm in data packet transmission is shown in Fig. 2, in which horizontal coordinates represent the proportion of beacon nodes. As can be seen from Fig. 2, when the ratio of the beacon nodes and the network connectivity increase, the data traffic of the network also increases.

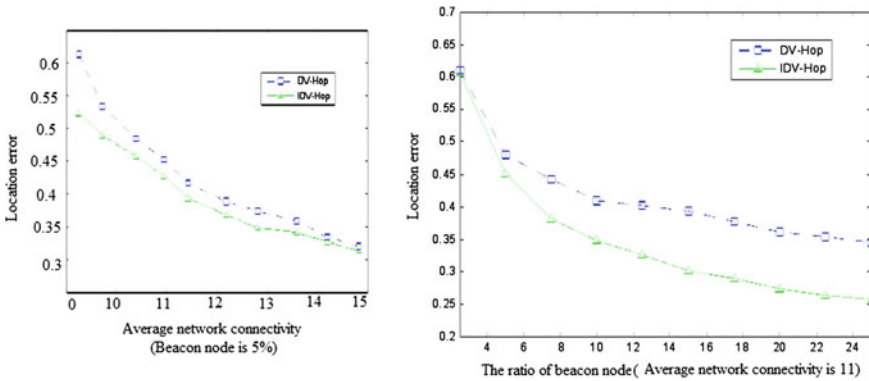


Fig. 1 Localization error

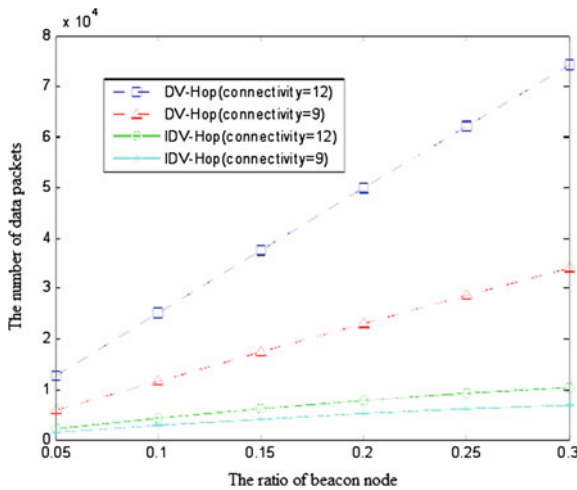


Fig. 2 The number of data packets

When the network parameters are the same, the data communication of IDV-Hop algorithm is significantly less than that of DV-Hop algorithm. This is mainly due to the IDV-Hop which uses clustering strategy in the first stage of the algorithm, and uses the partial flooding instead of whole network wide flooding.

### **3.1 Concluding Remarks**

According to the characteristics of WSNs and the limitation of traditional DV-Hop localization algorithm, on the basis of the positioning principle and positioning process of DV-Hop algorithm, an improved DV-Hop algorithm is proposed.

This improved algorithm proposed in this paper does not change the positioning process of the DV-Hop algorithm and does not need additional information. Experiment results simulated by MATLAB7.0 indicated that this improved algorithm can significantly reduce the localization error without increasing traffic.

## **References**

1. Sun L-M, Li J-Z, Chen Y (2005) *Wireless sensor networks*. Tsinghua University Press, Beijing, pp 135–155
2. Liu Y-J, Jin M-L, Cui C-Y (2010) Modified weighted centroid localization algorithm based on RSSI for wireless sensor networks. *J Sens Technol* 23(5):717–721
3. W-K Chen, Li W-F, Shou H (2011) Weighted centroid localization algorithm based on RSSI for wireless sensor network. *J Wuhan Univ Technol* 30(12):265–268
4. Zeng F-Z, Sun Z-Z, Luo J (2008) Node localization in wireless sensor network. *Commun J* 29(11):62–66
5. Liu K, Wang S, Hu F (2006) An improved DV-HOP node localization method in wireless sensor networks. *Inf Control* 12(6):788–792
6. Zhang J, Wu YH, Shi F (2010) Wireless sensor network localization algorithm based on DV-Hop. *Comput Appl* 30(2):323–326
7. Liu Y, Liu B, Sun D (2010) An improved DV-HOP localization algorithm. *Comput Appl* 30(2):763–767
8. Niculescu D, Nath B (2003) *Ad hoc positioning system (APS) using AoA*. IEEE INFOCOM 2003, vol 3. San Francisco, pp 1734–1743
9. Ye H, Ma C (2010) Hybrid genetic algorithm in solving nonlinear inequalities. *J Fujian Norm Univ (Nat Sci)* 26(1):18–21
10. Sichertu ML, Veerari tiphan C (2013) Simple, accurate time synchronization for wireless sensor networks. In: *IEEE wireless communications and networking conference (WCNC'03)*. IEEE Press, Piscataway, NJ, US, pp 1266–1273

# Processing to the Commutation Failure in Multi-infeed Direct Current System

Xuan Wang, Hui Yan, Yuhong Wang, Junfeng Gui, Mingchao Xia, Xiaogang Hu and Pingzhu Liu

**Abstract** The commutation failure in multi-infeed DC system will result in serious consequences. Influence factors are analyzed in this paper including the principle of inverter and influence failure factors for single-feed system. The countermeasures for the failure are introduced. The response for commutation failure includes precaution before failure and recovery strategy after failure. The influence to transmission power by electrical distances is studied. Engineering practice shows that STATCOM can effectively improve steady-state and transient operation characteristics of multi-infeed DC system. It will reduce the probability of commutation failure.

**Keywords** Multi-infeed · DC system · Commutation failure · STATCOM

## 1 Introduction

High-voltage direct current transmission (HVDC) has the advantages of high stability, large transmission capacity, low loss, high power regulation, and nonsynchronous communication. With the development of technology, HVDC technology has many bright technical and economic advantages to the national network for the development of China's power industry in long-distance and large-capacity power transmission. China Southern Power Grid and East China Power Grid have placed multi-circuit DC transmission lines. In April 2014, the world's first five terminal flexible DC transmission demonstration projects were built in Zhoushan China. Multiple DC transmission lines placed on the same AC power system formed the so-called multi-infeed DC system (MIDC).

---

X. Wang (✉) · H. Yan · Y. Wang · J. Gui · M. Xia · X. Hu · P. Liu  
China Epri Science and Technology Co. Ltd., Beijing, China  
e-mail: k2011@139.com

© Springer-Verlag Berlin Heidelberg 2016  
B. Huang and Y. Yao (eds.), *Proceedings of the 5th International Conference on Electrical Engineering and Automatic Control*, Lecture Notes in Electrical Engineering 367, DOI 10.1007/978-3-662-48768-6\_32

DC transmission system includes converter device, DC transmission line, and AC converter. The failure of any part will affect the safety of the operation of HVDC transmission system's reliability and related equipment. Commutation failure is a common fault of DC transmission system. It may cause DC magnetic bias of converter transformer, overheating, operation of relay protection, overvoltage, sub-synchronous resonance, and other consequences. Some failure cases can recover on their own, but the secondary change of the failure and continuous commutation failure may lead to DC system locking and cause greater impact to the grid.

Analysis model and method for MIDC system can provide the technical support for complete sets of filter design, DC control strategy optimization, and AC/DC hybrid power grid operation and coordination. It has an important significance to improve the safe operation level of the system. It can prevent MIDC system accident and improve the power grid security and stability of MIDC hybrid grid [1–12].

## 2 Reason of the Commutation Failure

AC system failure is the main cause of commutation failure. However, the reason is different due to operating conditions and AC system fault types. With the increasing DC transmission project in China, MIDC increased the complexity of the system structure. It has brought new problems to the safe and stable operations of the power system.

For MIDC systems, the failure will be more complicated because of the small electrical distance and low AC system strength. In this paper, we will analyze failure factors of the MIDC failure region from the following aspects.

### 2.1 Principle of Inverter Commutation Failure

Since the rectifier valve will carry the reverse voltage for a longer period of time after the current turns off, when the trigger circuit fails commutation failure will occur in the rectifier. Most of the commutation failures in DC transmission system occur in the inverter, which is the common failure.

Common faults of the converter include the short circuit of the bridge leg, false firing, when the valve does not open, and the short circuit of the converter bridge. In these failures, the probability of failure occurrence is higher. In addition to the failure of the DC system, they will lead to the failure of the connected AC system which may also result in commutation failure.

Success of commutation requires two conditions: one is sufficient voltage–time area during the commutation process with two converter valves; and the other is enough shut-off time for carrier recombination after the commutation process of thyristors.



According to the basic conditions, the process of the inverter is analyzed as follows. When the system is in normal operation, trigger angles are determined by HVDC system gate layer controller, their relationship is

$$\beta = \pi - \alpha = \gamma + \mu \quad (1)$$

where  $\alpha$  is trigger delay angle,  $\beta$  is trigger leading angle,  $\gamma$  is turn off angle, and  $\mu$  is commutation angle.

In a symmetrical system, the inverter's turn off angle is

$$\gamma = \arccos \frac{\sqrt{2}KI_dX_c}{U_L} + \beta \quad (2)$$

where  $I_d$  is the DC current,  $X_c$  is the commutated reactance,  $U_L$  is the converter bus voltage (RMS value), and  $K$  is the turns ratio of converter transformer.

In an asymmetrical system, turn off angle is also affected by the zero phase angle of the voltage. The commutation failure is related to the setting of the arc extinction angle. So, amounts of this angle are the influence factors for the commutation failure.

## 2.2 Influence Failure Factors for Single-Feed System

For commutation failure of the single-infeed HVDC, AC voltage drop, sudden increase of DC current, and zero phase offset of AC voltage are the underlying causes.

In MIDC system, the electrical distance between inverter stations is small. When AC system fault causes AC voltages of multiple buses to drop at the same time, it may lead to the commutation failure in many inverter stations. Faults in single AC or DC system may also affect the multiple circuits of the DC line, resulting in commutation failure at the same time.

Commutation failure has the modes of the once failure, two continuous, and two discontinuous failures. In the process of once failure, discharge of capacitors at inverter side made the current uncontrollable on the side of the bridge rectifier and the probability of failure will greatly increase. Two continuous failures are caused by the increasing DC current of the inverter. When the failure is due to AC voltage drop, another commutation failure will occur if the drop element does not get eliminated. Further, the inverter will be with continuous commutation failures if the AC system has a serious failure with very low voltage. The system will be unable to recover by itself. When failures occur more than once, DC system will temporarily stop running.

### ***2.3 Response for the Commutation Failure***

The response mode includes precaution before failure and recovery strategy after failure.

The main precaution for the failure is to improve the reliability of the system. Main equipment should be with a reasonable structure design and in-depth research. The control strategy should be dual and independent. Furthermore, the voltage support of the AC channel in parallel with the DC system should be strengthening. It means that operation and maintenance could maintain the stability of the AC voltage. The distortion of the AC waveform should be undermined.

Another way, protective measures should be controlled. The inverter commutation failure will be difficult to recover after serious fault in AC system. Continuous failures are extremely unfavorable to the operation of the DC system. At present, corresponding protection devices are equipped with the HVDC project of State Grid Corporation. In addition, development and application of new commutation devices, such as the capacitor commutation device and controllable IGBT, can significantly reduce or even completely avoid HVDC commutation failure occurs.

## **3 Analysis of MIDC with STATCOM**

Compared with the traditional reactive power compensation device, STATCOM based on the voltage source converter technology has the continuous regulation, small harmonic, low loss, wide operating range, and high reliability. It will improve the stability of AC voltage when STATCOM is connected to the inverter of MIDC.

Here an engineering example is used to analyze how STATCOM can improve the steady and transient operation for the characteristics of double-infeed HVDC system.

### ***3.1 The Example Analysis of STATCOM***

A double-infeed HVDC system with STATCOM is shown in Fig. 1. HVDC1 and HVDC2 have both control modes of constant rectifier current and trigger angle limitation. The STATCOM system uses modulation strategy of sinusoidal pulse width modulation (SPWM), and its control method is constant DC voltage and AC voltage. The AC voltage controlled by STATCOM is at the inverter side of HVDC1. The capacity of STATCOM is 300 Mvar; the capacity of HVDC1 is 1000 MW; and the capacity of HVDC2 is 2000 MW. STATCOM is directly connected to DC subsystem of HVDC1. AC buses of HVDC1 and HVDC2 are connected between certain electrical distances.

Due to the system in Fig. 1, influence of MAP is studied from various STATCOM capacity and distance L12. L12 is the distance from the back to DC points of HVDC1 and HVDC2. Here, L12 is set as 39 and 117 km, respectively.

Results in Fig. 2 show that when STATCOM has been put into the inverter AC bus of a double-infeed DC system, HVDC will get higher operation stability with the greater capacity and smaller electrical distance.

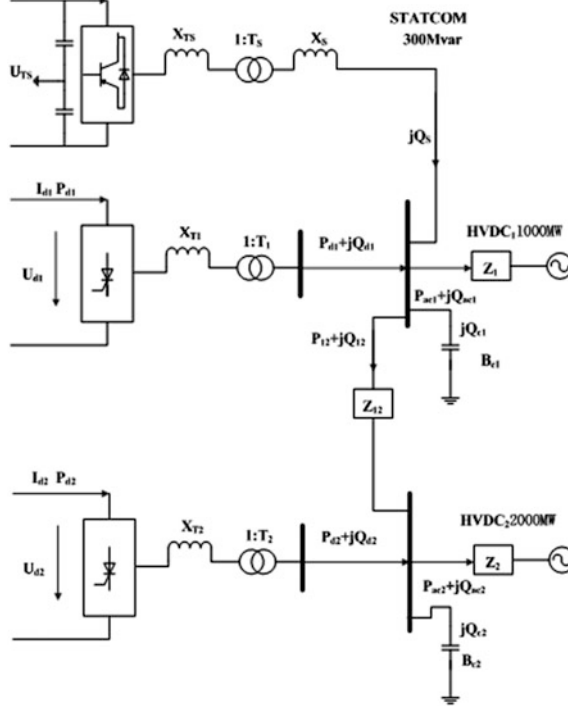


Fig. 1 Double-infeed HVDC system with STATCOM

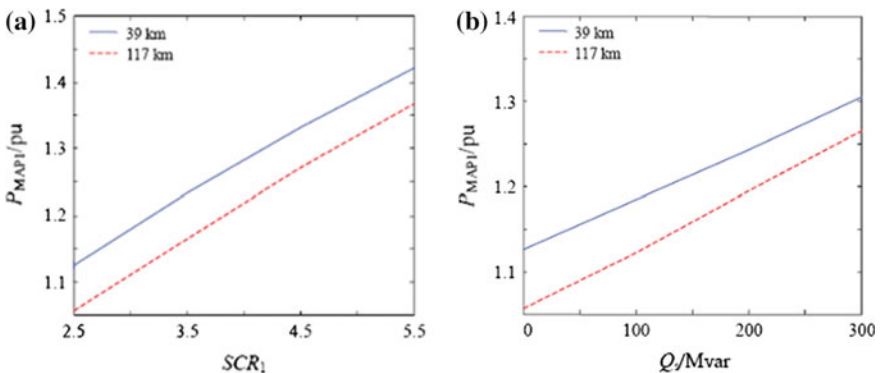


Fig. 2 MAP of MIDC. a Without STATCOM. b With STATCOM

### 3.2 *Effect Analysis of STATCOM*

STATCOM can provide positive effect on commutation failure in many aspects.

1. For double-infeed HVDC system, STATCOM can equivalently increase the AC system strength energy of HVDC1 and HVDC2, so that the anti-failure for two circuits of DC transmission lines can be improved. Therefore, STATCOM can effectively reduce the probability for the access of double-infeed HVDC system by commutation failure.
2. STATCOM can reduce the system's equivalent reactance and increase the critical phase voltage drop and reduce the probability of failure in the weak AC system. This has been approved by the simulation results above.
3. Rapid dynamic response of STATCOM for reactive power compensation can enhance the voltage stability. To optimize the use of STATCOM placement, the scale of DC system can improve the accepting capacity of the power grid.

## 4 Conclusions

Failure in any of DC transmission system, DC transmission line, and AC part of MIDC can cause commutation failure; all the influence factors are analyzed. Strengthening the structure and parameters of main equipment, optimizing the control strategy, and improving the level of protection measures can reduce the loss of failure. The influence to transmission power by electrical distances is studied. Engineering practice shows that STATCOM can effectively improve steady-state and transient operation characteristics of multi-infeed DC system. It will reduce the probability of commutation failure.

The multi-infeed AC/DC hybrid power grid has rare examples in the worldwide. At present, the domestic and foreign researches to solve these problems are unusual. Complete theory and analysis system have not yet been formed. It needs to be further studied and perfected.

**Acknowledgements** This research was financially supported by Science Foundation of China State Grid, Project No. 52094014000U.

## References

1. Shao Y, Tang Y, Guo X et al (2011) Analysis on commutation failures in multi-infeed HVDC transmission systems in North China and East China power grids planned for UHV power grids in 2015. *Power Syst Technol* 35(10):9–15
2. Hansen A, Havemann H (2000) Decreasing the commutation failure frequency in HVDC transmission systems. *IEEE Trans Power Delivery* 15(3):1022–1026

3. McArthur SD, Catterson VM, Hatziagyriou ND et al (2007) Multi-agent systems for power engineering applications—Part I: concepts, approaches, and technical challenge. *IEEE Trans Power Syst* 22(4):1743–1752
4. McArthur SD, Catterson VM, Hatziagyriou ND et al (2007) Multi-agent systems for power engineering applications—Part II: technologies, standards, and tools for building multi-agent systems. *IEEE Trans Power Syst* 22(4):1753–1759
5. Rahimi E, Gole AM, Davies JB et al (2011) Commutation failure analysis in multi-infeed HVDC systems. *IEEE Trans Power Delivery* 26(1):378–384
6. Bernd MB, Cigré DP (2002) Stability and control of HVDC and AC transmissions in parallel. *IEEE Trans on power delivery* 17(4):1113–1120
7. de Toledo PF (2002) Multiple-infeed short circuit ratio aspects related to multiple HVDC into one AC network. *IEEE Trans on Power Delivery* 17(1):248–253
8. Wang C, Liu B (2013) Effects of commutation failure in multi-circuit HVDC transmission system interconnecting regional power grids on AC power system at sending end. *Power Syst Technol* 37(4):1052–1057
9. Yuan Y, Wei Z, Lei X et al (2013) Research survey on commutation failure in DC transmission system. *Electr Power Autom Equipment* 33(11):140–147
10. He C, Li X, Jin X et al (2007) Simulation analysis on commutation failure criteria for HVDC transmission systems. *Power Syst Technol* 31(1):20–24
11. Ren J, Li X, Jin X et al (2008) Simulation study on commutation failure caused by switching AC filters of inverter stations in multi-infeed HVDC system. *Power Syst Technol* 32(12):17–22
12. Liu J, Li X, Wu C et al (2009) Research on critical index of commutation failure in HVDC system. *Power Syst Technol* 33(8):8–12

# Research on Friction and Thermal Load Performance of Hydro-viscous Clutch

Li-gang Ma, Chang-le Xiang, Ming-gang Du and Liu-yang Guo

**Abstract** In this paper, the theory of friction coefficient and thermal loads in slip state of a new hydro-viscous clutch has been studied and the influencing factors are determined. Furthermore, the friction characteristics test is designed. The test results show the variation tendency of friction coefficient when the hydro-viscous clutch operates at the difference temperature, difference normal pressure and difference rotating speed. The formula of different rotating speed on the impact of the coefficient of friction is fitted. The thermal load theory calculation reflects the temperature rising trend under different thermal loads of hydro-viscous clutch. Comparing the theoretical calculation and experimental results and analyzing the heat dissipation way of hydro-viscous clutch, it shows that the equation to calculating the thermal load that described the frictional state of frictional disk of hydro-viscous needs to be developed.

**Keywords** Hydro-viscous clutch · Friction coefficient · Thermal load · Testing by experiment

## 1 Introduction

Hydro-viscous clutch has the advantages of stepless speed regulation, small volume, high transmission power, and high reliability. Hydro-viscous clutch has been widely used in civil industry, mainly used in pumps, fans, and other large mechanical equipments in domestic. Its application fields are usually industries like coal and oil. Nowadays, it is widely used in the speed control device of tracked vehicles cooling fan in the military industry.

---

L. Ma (✉) · C. Xiang  
School of Mechanical Engineering, Beijing Institute of Technology,  
Beijing 100081, China  
e-mail: maligang201@163.com

M. Du · L. Guo  
China North Vehicle Research Institute, Beijing 100072, China

The hydro-viscous clutch applies internal lubricant of transmission as a medium whose temperature is up to 120 °C. Therefore, the copper-based friction plates with high temperature resistance are chose as the friction element. In view of the characteristics of lubricating medium and friction element, the friction characteristics and thermal load of the hydraulic clutch are studied in this paper.

The hydro-viscous clutch works in the friction state over long term. The friction state of active and passive plates, as Stribeck curves shown can be divided into three states—boundary lubrication, mixed lubrication, and hydrodynamic lubrication—as shown in Fig. 1.

The processes from difference speed to combining of the hydro-viscous clutch are mainly in hydraulic lubrication and mixed lubrication region. According to the different lubrication states corresponding to the typical value of the friction coefficient, as shown in Fig. 2, the friction coefficient of the hydro-viscous clutch should be less than 0.1, especially when the hydro-viscous clutch is completely working in the phase of the hydraulic lubrication and the friction coefficient is less than 0.05.

Due to the long-term friction of the friction plate, a large amount of heat is generated in the hydraulic and mixed lubrication region. If there is no enough oil to take away the heat, the heat of the clutch will gradually accumulate. Once reaching a certain limit value, the friction will stick together or even burn out. Therefore, it is necessary to study the thermal load bearing capacity of the clutch under the limited lubrication. In this paper, the friction and thermal load characteristics of the clutch are studied.

Fig. 1 Stribeck curve

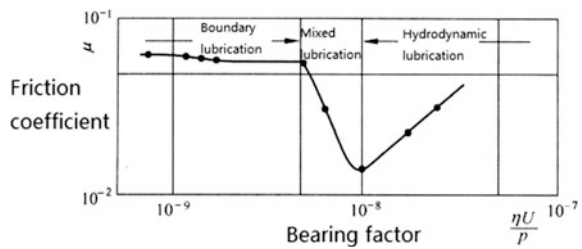
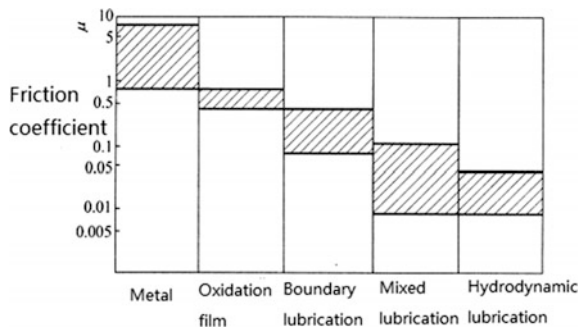


Fig. 2 Friction coefficient in various friction regions



## 2 The Theoretical Analysis and Experimental Study on Friction Characteristics

### 2.1 Theoretical Analysis

Because of the certain friction state of the clutch, the friction coefficient of the hydro-viscous clutch is analyzed by using the fluid mechanics and heat transfer. According to the working mechanism of the clutch, the torque of the transmission is

$$M = Kn2\pi\mu p \int_{R_1}^{R_2} R^2 dR = Kn\mu F \frac{2(R_2^3 - R_1^3)}{3(R_2^2 - R_1^2)} \quad (1)$$

$$M = Kn\mu F \frac{2(R_2^3 - R_1^3)}{3(R_2^2 - R_1^2)} \quad (2)$$

where the friction coefficient is calculated as following:

$$R = \frac{2(R_2^3 - R_1^3)}{3(R_2^2 - R_1^2)} \mu = \frac{M}{FRnK} \quad (3)$$

where  $\mu$  is the friction coefficient of the hydro-viscous clutch plate,  $M$  is friction torque,  $F$  is positive pressure,  $n$  is number of friction pairs,  $K$  is the pressing force coefficient, take 0.9,  $R_2$  and  $R_1$ . Respectively, is the outer ring radius and the inner radius of the friction surface,  $R$  is the equivalent radius of the friction surface.

### 2.2 Test Method

According to the results of theoretical analysis, the friction coefficient can be calculated by the torque and positive pressure through the test. According to the Stribeck curve, the friction coefficient is related to the viscosity, the rotational speed, and the thickness of the oil film. Therefore, the load will be locked. Testing the friction coefficients of the different initial entry temperature and the same inlet temperature by adjust the speed difference.

### 2.3 Test Device

The test device of hydro-viscous clutch is shown in Fig. 3. Changing the input speed by DC motor and maintaining input speed in a constant during the test while locking the output shaft of the clutch to guarantee output speed is zero. Adjusting



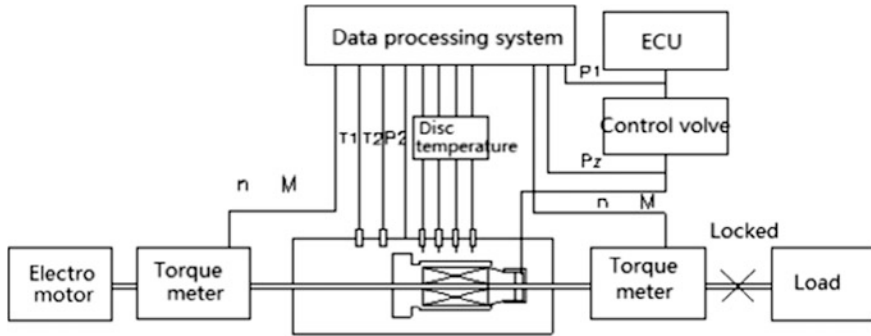


Fig. 3 Test bench sketch

control pressure the clutch until the motor’s input torque to achieve the corresponding torque value.

## 2.4 Test Result

### 2.4.1 Effect on Friction Coefficient by Difference Speed

As shown in Fig. 4, the variation of friction coefficient with the difference speed under control oil pressure is 0.66 MPa and oil temperature is 90 °C. Assuming the effect of temperature is ignored, the friction coefficient curve is fitted at a given

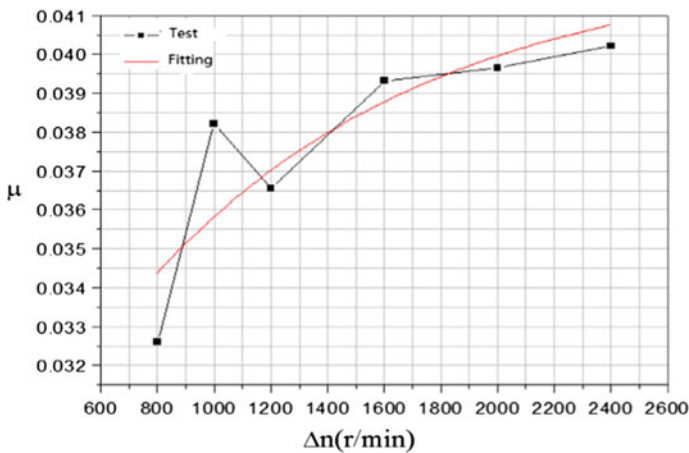


Fig. 4 The curve of friction coefficient under speed difference by experimental data and fitting

temperature. The red line in Fig. 4 is the friction coefficient fitting curve, where the fitting formula is

$$\mu = \mu_0 + ae^{\frac{\Delta v}{b}} \tag{4}$$

as seen from the fitting curve, the friction coefficient is a function of the difference speed, the formula is

$$\mu = \mu_0 + ae^{\frac{\Delta v}{cR}} \tag{5}$$

where  $c = \frac{\pi b}{30}$ ,  $R$  is the equivalent radius of the friction surface.

Because of the relationship between the friction coefficient and friction materials, lubricants, and test temperature, the formula is not general only for the hydro-viscous clutch and oils in this test.

### 2.4.2 Effect on the Friction Coefficient by Positive Pressure

The positive pressure does not affect the friction coefficient. In fact, the friction gap is small, carrying capacity is relatively large and the friction coefficient is changing with positive pressure. As shown in Fig. 5, the changes of the friction coefficient are due to the changes of friction pair clearance, heat, and temperature caused by the positive pressure changes. Therefore, although positive pressure has nothing to do with the friction coefficient in theory, the actual friction coefficient is affected by positive pressure in certain extent.

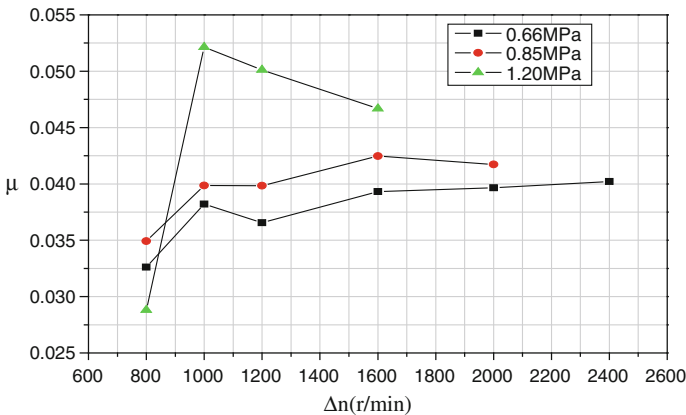
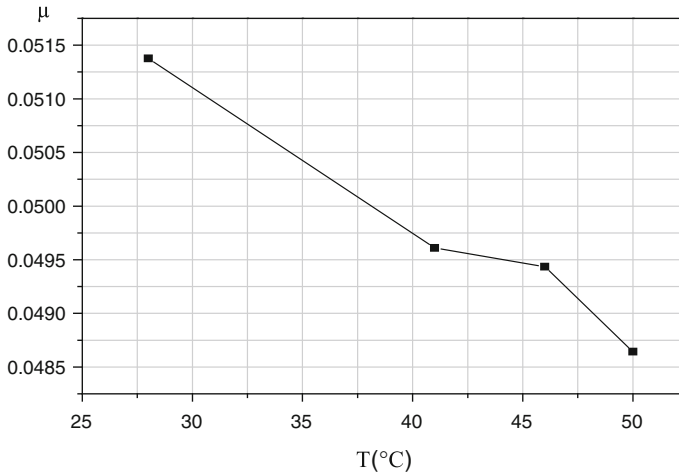


Fig. 5 The curve of friction coefficient under speed difference and different control oil pressures



**Fig. 6** The curve of friction coefficient under the same speed difference and different oil temperature

### 2.4.3 Effect on Friction Coefficient by Initial Oil Temperature

As shown in Fig. 6, it is the curve of the friction coefficient with temperature that varies at a given speed. It can be seen that the temperature is an important factor affecting the friction coefficient. Because the temperature in friction process will rise rapidly, it is difficult to eliminate friction effect of heat on the initial temperature in the test. The friction heat temperature rises reduce the effect of initial temperature on the friction coefficient to some extent. So the change of friction coefficient is very small under the initial temperature change form 20 to 50 °C. However, the trend of friction coefficient changing is reasonable, that is, when the temperature is higher, the viscosity, the shear resistance, and the friction coefficient are smaller.

## 3 Theoretical Analysis and Experimental Study on Thermal Load Characteristics

### 3.1 Theoretical Calculations Assume

1. Assuming that the friction power of clutch completely converted into heat;
2. Assuming that the heat in the operating process of hydro-viscous clutch is completely taken away by the flow of oil.

### 3.2 Frictional Power Calculation

According to the assumptions above, the friction energy of the clutch can be calculated:

$$W_f = \int_0^t N_H dt = \int_0^t M_1(\omega_1 - \omega_2) dt \tag{6}$$

The theoretical loss power of the clutch is

$$N_H = (1 - i) \cdot n_1 \cdot M_1 / 9549 \tag{7}$$

where  $i$  is the speed ratio, namely the ratio of the output speed and input speed,  $n_1$  is the input speed,  $\omega_1$  and  $\omega_2$  is, respectively, the input angular velocity and output angular velocity,  $M_1$  is the input torque,  $N_H$  is the loss power,  $W_f$  is the friction energy.

As shown in Fig. 7, assuming that all the loss power is converted to heat, the theoretical power consumption of the hydro-viscous clutch is calculated according to the load. The largest loss power is about 28 kW when the ratio is 0.7. The limited value should be covered in the friction characteristic test of hydro-viscous. The inertia of load and the power transfer gear pair can also cause the loss power. Therefore, the maximum test load is 35 kW, which is 1.25 times larger than the theoretical power of the clutch.

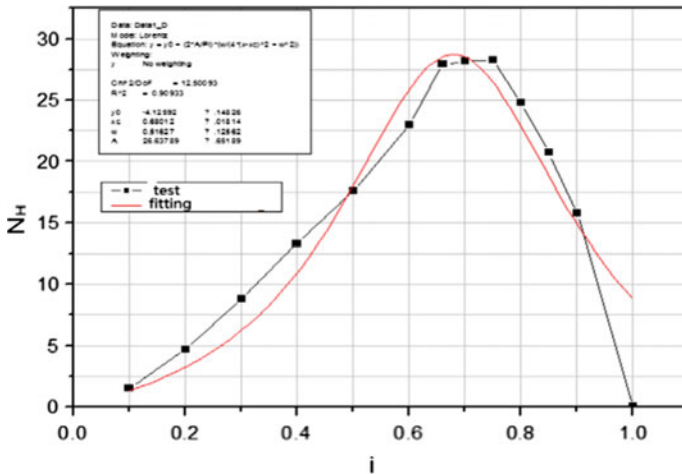


Fig. 7 Theoretical power loss of viscous clutch

### 3.3 Test Methods

According to the maximum thermal load of the calculation, the loss power of clutch is divided into four points, that is, 35, 20, 30, and 10 kW. Maintaining the friction work of clutch for some time at each point in the test, then getting the heat energy of hydro-viscous clutch through monitoring and measuring the temperature of the friction plate export, which is the thermal load characteristics.

### 3.4 Test Results

#### 3.4.1 The Comparative Analysis Between the Calculation and Test Results

Assuming that all the heat is taken away by the oil, the temperature rise of the oil is based on the following formula,

$$\Delta T = \frac{N_H}{\rho \cdot Q \cdot C} \quad (8)$$

where  $\Delta T$  is the average temperature of lubricating oil, °C,  $C$  is the specific heat of lubricating oil, 1161 J/kg °C,  $Q$  is the flow of lubricating oil, m<sup>3</sup>/s,  $\rho$  is the density of lubricating oil, 862 kg/m<sup>3</sup>.

As shown in Fig. 8, the temperature of lubricating oil is less than the calculated values. It is about half of the calculated value. It is indicated the heat generated in the clutch is not only taken away by lubricating oil, but also through the friction plate itself and the heat conduction of the box, as well as air heat convection and heat radiation in a variety of ways to take away a lot of heat.

#### 3.4.2 The Test of Friction Plate Outlet Oil Temperature

The Fig. 9 shows the installation location of temperature sensor for the friction plate outlet. As shown in Fig. 10, though comparing the temperature rise of lubricating oil on the friction plate export, the heat is the largest where far from the piston of clutch. The temperature rises up to 45 °C on TO3 position. The following is the TO2 and TO1 position, the minimum heat is the friction pair which is the closest to the piston and the maximum temperature rise is less than or equal to 25 °C. This phenomenon reflects the real situation of friction heat. Due to large number of friction pair, the accumulation heat is more. Especially the heat of friction will be more concentrated in the central of axial. At the same time, the installation position of the oil temperature sensor has a certain influence on the accuracy of temperature measurement. The outer ring of the clutch outer hub will block the splashing of oil,

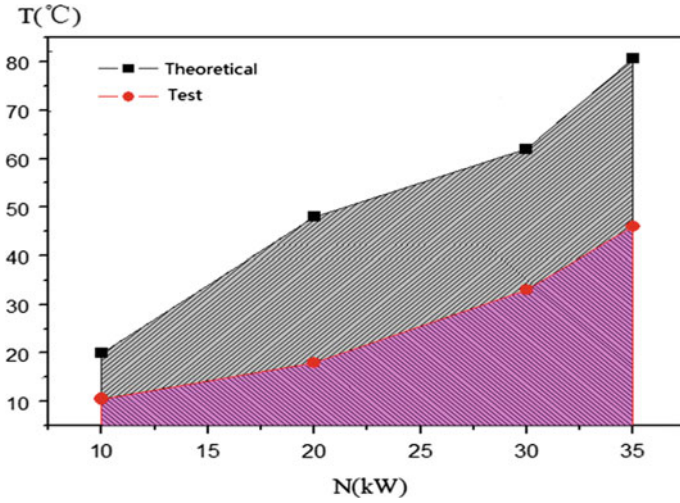


Fig. 8 Temperature rise by test and calculation

Fig. 9 Diagram for installation location of temperature sensor in friction plate outlet

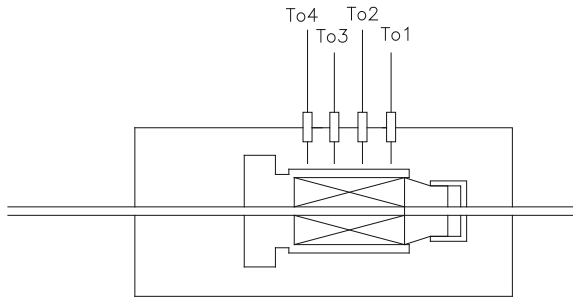
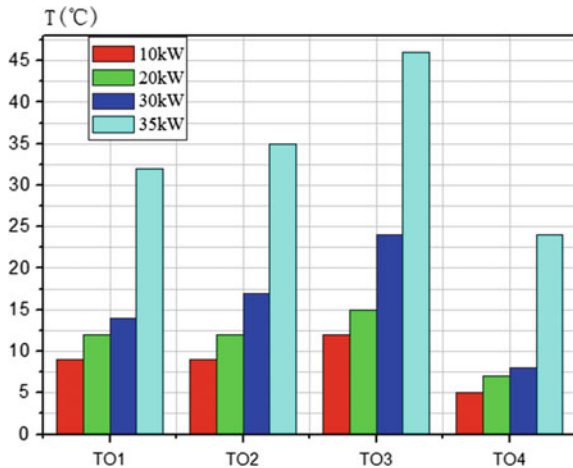


Fig. 10 Temperature rise of lubricant at thermal load of 10, 20, 30, and 35 kW



thus affecting the temperature of the oil temperature sensor. Therefore, during the structural design, it is necessary to change the position of the outer ring. At the same time, it is also necessary to increase the number and density distribution of lubrication holes in the axial center. To optimize the lubrication flow matching, it will reduce the number of lubrication hole in intermediate shaft at TO4 and TO1 which close to the ends of the friction plate.

## 4 Conclusions

In the paper, according to the friction principle, the friction state of the clutch and the range of the friction coefficient are estimated.

In the friction characteristic test of hydro-viscous clutch, it can be concluded the dynamic coefficient of friction of the clutch. The friction coefficient formula is fitted out at given temperature. It is a technical foundation for the further research in the future.

According to the test results, the friction coefficient of the clutch is not only affected by the speed difference, but also by the temperature and positive pressure. Due to the friction condition is more complex, the temperature, normal pressure, and difference rotating speed are related. It is difficult to obtain a formula to represent the friction coefficient.

Comparing the theoretical calculation and experimental results, it shows that the thermal load theory calculation reflects the temperature trend under different thermal loads of hydro-viscous clutch. But, it is not appropriate to calculate the heat convection only by a simple formula. It is necessary to introduce the coefficient or update the formulas.

## References

1. Maki R (2005) Wet clutch tribology-friction characteristics in limited slip differentials. Lulea University of Technology, Sweden
2. Lund M (2009) Wet clutch performance and durability. Lulea University of Technology, Sweden
3. Marklund P (2008) Wet clutch tribological performance optimization methods. Lulea University of Technology, Sweden
4. Marklund P, Larsson R (2007) Wet clutch under limited slip conditions-simplified testing and simulation. Proc Inst Mech Eng Part J J Eng Tribol 221
5. Yuan Y, Attipbele P, Dong Y (2003) CFD simulation of the flows within disengaged wet clutches of an automatic transmission. SAE Paper 2003-01-0320
6. Jang JY, Khonsari MM (1999) Thermal characteristics of a wet clutch. J Tribol Trans ASME 121(3):610-617

# A Comprehensive Evaluation Model for Switchgear Based on the Normal Cloud Model and D–S Evidence Theory

Y. Jia, D. Liu and H. Sui

**Abstract** A hierarchical evaluation method based on normal cloud model and D–S evidential theory is proposed. By hierarchical clustering the indicator of switchgear, normal cloud model is used to determine the correlation degree of indicator and evaluation level, and improved fuzzy algorithm is applied to evaluate the first layer. On this basis, D–S evidential theory is used to assess the overall state of the switchgear. As an example, one group of data of the KYN28A-12 model switchgear is analyzed. The simulation result demonstrates the effectiveness of the assessment algorithm. The assessment model is clear and does not need a lot of historical data, which offers a new thinking to assess the operating state of high voltage switchgear.

**Keywords** High voltage switchgear · State assessment · Normal cloud model · Weighting · D–S evidential theory

## 1 Foreword

Condition-based maintenance is an important means to maintain the good status of high voltage switchgear (HVS). Evaluating the state of HVS is the necessary prerequisite for condition-based maintenance. Otherwise, the structure of HVS is complex, and it has lots of status information. The inaccurate measurements and imperfect evaluation criteria result significant uncertainty of HVS' state assessment.

Reference used the fault tree analysis method to analyze the probability of switchgear fault, and described the impact of component failure on the switchgear failure. According to the different forms of data, reference combined with equipment scoring method, proposed a hierarchical fuzzy comprehensive evaluation

---

Y. Jia (✉) · H. Sui

School of Electrical Engineering, Shandong University, Jinan 250061, China  
e-mail: 285116377@qq.com

D. Liu

Yantai Power Supply Company of Shandong Province, Yantai 264000, China

© Springer-Verlag Berlin Heidelberg 2016

B. Huang and Y. Yao (eds.), *Proceedings of the 5th International Conference on Electrical Engineering and Automatic Control*, Lecture Notes in Electrical Engineering 367, DOI 10.1007/978-3-662-48768-6\_34

295



model. However, this method only relates to the ambiguity of uncertainty, the effects of randomness is ignored.

Cloud model considers two kinds of uncertainty of the objective world things and concepts of human knowledge, the fuzziness and randomness, and fully integrates them, constitutes the mapping of qualitative and quantitative. This model conforms to the operating conditions of all switchgear and the fact that the measurement error of status information is random.

Based on consideration of randomness and ambiguity in the assessment process, optimal weight method is used to determine the weights for each indicator. The switchgear operating state evaluation model which is based on normal cloud model and DS evidence theory is established.

## 2 Overall Structure of State Assessment

In order to assess the state of switchgear accurately as far as possible, by referencing the existing research and the Q/GDW613-2011 standard (12 (7.2) kV ~ 40.5 kV AC metal-enclosed switchgear State Evaluation Guidelines) of the State Grid Corporation of China, a two-level evaluation system for switchgear is established, as shown in Fig. 1.  $H_1, H_2, H_3$  and  $H_4$  are four state levels of switchgear. The first layer is subsystem assessment, comprises insulating state, electrical state, mechanical state, and so on. The indicator of each subsystem is shown in Table 1. This layer evaluates the status of subsystems according to the data of indicator. The second layer is the overall assessment of switchgear, which merges evaluation results of subsystems.

Since the evaluation system comprises a plurality of evaluation indicator, and the unit of each indicator is not the same. Therefore, each indicator should to be normalized. This model employs the relative deterioration degree method. After normalization, four evaluation grades are shown in Table 2.

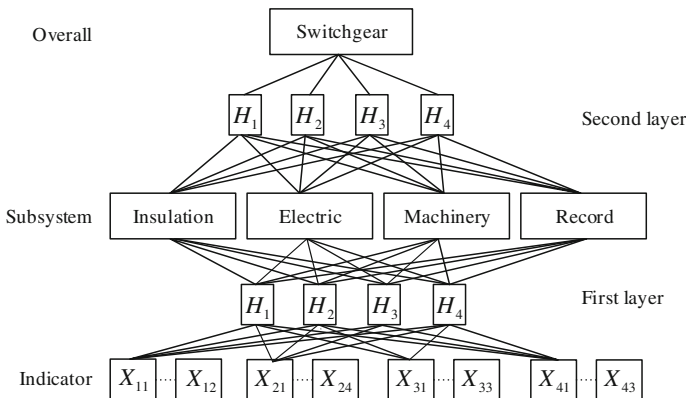


Fig. 1 Assessment structure of switchgear state

**Table 1** Indicator category

Subsystem	Evaluation indicator
Insulation $U_1$	TEV detection
	Ultrasonic detection
	Bus insulation resistor
Electrical $U_2$	Closing synchronization
	Opening synchronization
	Closing coil current
	Contact resistance
Mechanical $U_3$	Average opening speed
	Average closing speed
	Closing spring state
Historical record $U_4$	Breaking times
	Number of using years
	Cumulative electrical wear

**Table 2** Assessment level of different relative deterioration degree

Relative deterioration degree	Operational status and maintenance proposal
[0, 0.2]	Switchgear running in a good condition, can be appropriately postpone the maintenance plan
[0.2, 0.5]	Switchgear operating status is normal, but there is a tendency to close to the standard limits. It should be monitored intentionally and can be maintained as planned
[0.5, 0.8]	Switchgear has potential accidents; it can also run with fault in short term. The switchgear should be arranged outage maintenance by timely
[0.8, 1]	Switchgear has major potential accidents. It needs to be remeasured for fault acknowledgment, and performed outage maintenance immediately

### 3 Distribution of Weights

Suppose there are  $p$  methods of subjective empowerment of the indicator, and  $p$  methods of objective empowerment. Each of these methods satisfies that the weights of the indicator sum to 1. Assume the same subsystem contains  $l$  evaluation indicators.  $\omega_k (k = 1, 2, \dots, l)$  is the optimum combination weight, and satisfies following formula:

$$\min H(\omega_k) = \alpha_k \sum_{i=1}^p (\omega_{ik} - \omega_k)^2 + \beta_k \sum_{j=1}^q (\omega_{jk} - \omega_k)^2 \tag{1}$$

$\alpha_k$  and  $\beta_k$  indicate the relative importance of primary weighting methods and objective weighting methods. According to moment estimation theory, values of  $\alpha_k, \beta_k$  can be solved by the expectation of subjective and objective weights of each indicator.

$$\begin{cases} \alpha_k = \frac{E(\omega_{ik})}{E(\omega_{ik}) + E(\omega_{jk})} \\ \beta_k = \frac{E(\omega_{jk})}{E(\omega_{ik}) + E(\omega_{jk})} \end{cases} \quad (2)$$

Further, formula (3) can be obtained, which describes the relative importance of subjective and objective weights of each indicator in the same subsystem.

$$\begin{cases} \alpha = \frac{1}{l} \sum_{k=1}^l \alpha_k \\ \beta = \frac{1}{l} \sum_{k=1}^l \beta_k \end{cases} \quad (3)$$

Meanwhile the optimal combination weight of each indicator satisfies the formula (1), also satisfies  $\sum_{i=1}^l \omega_k = 1$ . Therefore, it is needed to solve the overall optimal value, as shown in formula (4):

$$\begin{cases} \min H(\omega) = \alpha \sum_{k=1}^l \sum_{i=1}^p (\omega_{ik} - \omega_k)^2 + \beta \sum_{k=1}^l \sum_{j=1}^q (\omega_{jk} - \omega_k)^2 \\ s.t. \quad 0 \leq \omega_k \leq 1 \\ \sum_{i=1}^l \omega_k = 1 \end{cases} \quad (4)$$

Easy to know that the formula (4) is a nonlinear convex programming, the optimal combining weights can be solved by Karush-Kuhn-Tucker Conditions:

$$\omega_k = \frac{\alpha \sum_{i=1}^p \omega_{ik} + \beta \sum_{j=1}^q \omega_{jk}}{\alpha p + \beta q} \quad (5)$$

Optimal weights of the first layer adopt the experts weighting method of subjective weighting method, maximum variance weighting, and entropy weight method of objective weighting method, through the Eqs. (2–5) it can be obtained. Due to the lack of objective data, the second layer assessment only uses subjective weighting method. Its impact on the result of assessment can be abated by using the method of DS evidence theory.

## 4 Assessment Model

### 4.1 Assessment of Subsystem

Let  $A$  be a precise numerical quantitative domain.  $C$  is the qualitative concept on  $U$ . If the quantitative value  $x \in U$ , and  $x$  is a random realization of stable tendency in  $C$ . Let the correlative degree between  $x$  and  $C$  is  $\mu(x)$  ( $\mu(x) \in [0, 1]$ ). It should be claimed that the distribution function of  $\mu(x)$  on  $U$  is the cloud model. Let  $N(A, B)$  express a normal distribution function, and its expectation is  $A$ , the standard deviation is  $B$ . Obtain following formulas:

$$x_i = N(Ex, En) \tag{6}$$

$$En' = N(En, He) \tag{7}$$

$$\mu_i = \exp\left[-(x_i - Ex)^2 / 2(En')^2\right] \tag{8}$$

Explanation:  $Ex$  is the expectation;  $En$  is the entropy;  $He$  is the ultra-entropy. They expressed the relationship between variables  $\mu_i$  and  $x_i$ . If the cloud model composed of data pair drop( $x_i, \mu_i$ ) ( $i = 1, 2, \dots$ ) satisfies Eqs. (6), (7), and (8). It is called the normal cloud model. Recorded as  $(Ex, En, He)$ .

Let the threshold value of relative deterioration degree be extended based on the normal cloud model. Thereby every grade normal cloud model is obtained, as shown in Table 3.

The correlation function of the normal cloud model is shown in Fig. 2.

If a new measurement data of an indicator is collected, its relative deterioration degree should be calculated, then according to the formula (6), (7), and (8) the correlation degree of each grade is found out. To meet the condition of evidence fusion,  $\mu_g$  need to be normalized by formula (9).

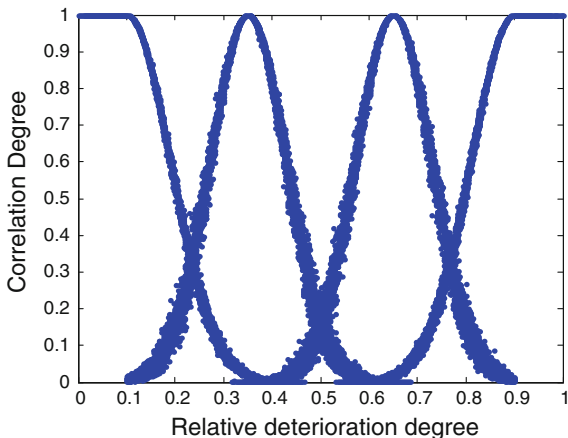
$$\mu'_g = \frac{\mu_g}{\sum_{i=1}^4 \mu_i} \tag{9}$$

**Table 3** Corresponding normal cloud model

Assessment level	Normal cloud model
Good	(0.1,1/30,0.001)
General	(0.35,1/20,0.002)
Abnormal	(0.65,1/20,0.002)
Serious	(0.9,1/30,0.001)

If the relative degradation is less than 0.1, corresponding association vector is [1, 0, 0, 0]. While the relative deterioration degree is greater than 0.9, the corresponding correlation vector is [0, 0, 0, 1]

**Fig. 2** Correlative degree diagram of the normal cloud model



After determining the optimal combination weights of each indicator, the first layer assessment will be carried out with the improved fuzzy evaluation algorithm, as shown in formula (10). So, the correlation degree between subsystems and different levels is arrived.

$$\mu_{rg} = \sum_{i=1}^l \omega_i \mu'_g \tag{10}$$

If the measurement data of one indicator is missing, this indicator should be removed from this model, and the optimal weights for evaluation are recalculated.

### 4.2 Overall Assessment of Switchgear

In the evidence theory, suppose  $\Theta$  is a sample space formed by a series of any two mutually exclusive propositions, as shown in the following:

$$\Theta = \{A_1, A_2, \dots, A_i, \dots, A_n\} \tag{11}$$

Then  $\Theta$  is called the frame of discernment,  $2^\Theta$  is a collection constituted by all samples subsets; is called basic probability distribution function; and satisfies the following condition:

$$\begin{cases} m(\phi) = 0 \\ \sum_{A \subset \Theta} m(A) = 1 \end{cases} \tag{12}$$

When there are  $n$  mutually independent distribution functions, the fusion rules of D–S evidence theory is shown in formula (13):

$$m(A) = \begin{cases} \frac{1}{1-K} \sum_{\cap A_i=A} \prod_{1 \leq j \leq n} m_j(A_i) & A \neq \phi \\ 0 & A = \phi \end{cases} \tag{13}$$

Note:  $m = m_1 \oplus m_2 \oplus \dots \oplus m_n$ ;  $K = \sum_{\cap A_i=\phi} \prod_{1 \leq j \leq n} m_j(A_i)$ .

Four evaluation grades constitute the assessment identification frame of switchgear. Which is  $\Theta = \{H_1, H_2, H_3, H_4\}$ . Let  $m(H)$  be expressed as correlation degree between the status of switchgear and each grade. Due to the different importance of each subsystem, set the subsystem with maximum weights as the key evidence. Process the original evidence according to formula (14).

$$\begin{cases} \omega_{\max} = \max\{\omega_1, \omega_2 \dots \omega_n\} \\ \bar{\omega}_i = \frac{\omega_i}{\omega_{\max}} \\ m'_i(H_g) = \bar{\omega}_i m_i(H_g) \\ m'_i(\Theta) = (1 - \bar{\omega}_i) \end{cases} \tag{14}$$

Where  $\omega_i$  is the weights of  $i$ -th evidence;  $m_i(H_g)$  is the reliability function value between  $i$ -th evidence and  $H_g$  assessment level;  $m'_i(H_g)$  is correlation degree of processed;  $m'_i(\Theta)$  is uncertainty credit assign of  $i$ -th evidence.

Fuse the assessment result of each subsystem by formula (15), the overall operation assessment of switchgear is obtained. The assessment result of the switchgear is processed by using the maximum correlation degree norms.

## 5 Experiments and Analysis

Choose one data to assess the state of the switchgear of KYN28A-12 type. According to expert weighting method, subjective the weights of each indicator as shown in Table 4; the weights vector of subsystems is [0.1727, 0.3318, 0.2909, and 0.2045].

Through calculation, evaluation matrix of each subsystem is shown in Table 5.

According to the principle of maximum correlative degree, it can be seen that the running status of  $U_1, U_2$ , and  $U_3$  is H3, and the running status of  $U_4$  is H2.

**Table 4** Subjective weights of each indicator

Subsystem	The vector of weight
$U_1$	[0.4268, 0.1829, 0.3902]
$U_2$	[0.2979, 0.2680, 0.2212, 0.2128]
$U_3$	[0.3784, 0.3405, 0.2811]
$U_4$	[0.2810, 0.2893, 0.4298]

**Table 5** Evaluation results of each subsystem

Subsystem	Correlative degree			
	$H_1$	$H_2$	$H_3$	$H_4$
$U_1$	0.0000	0.0810	0.9179	0.0011
$U_2$	0.0000	0.1019	0.5565	0.3416
$U_3$	0.0000	0.0009	0.8884	0.1107
$U_4$	0.0501	0.5914	0.3518	0.0067

**Table 6** Overall assessment of switchgear

$m(\Theta)$	Correlative degree			
	$H_1$	$H_2$	$H_3$	$H_4$
0	0	0.03397	0.9660	2.783e-06

Then obtain the overall rating of switchgear as shown in Table 6. It can be seen that the overall assessment of switchgear is  $H_3$ , which showed that switchgear has potential accidents, but can also run for some time; it should be arranged maintenance outage by timely. After maintenance, it is found that circuit breaker operating mechanism of the switchgear is clamping stagnation and insulation is aging. Through timely maintenance, the further development of the switchgear faults is avoided, the safe operation of the power system is protected.

## 6 Conclusion

The example certified that the evaluation method based on normal cloud model and D–S evidential theory has the following advantages. (1) It considers the fuzziness and randomness of uncertainty, overcomes the shortcomings of ignoring randomness in the previous evaluation model. (2) It has a clear structure, and the evaluation indicator is easily obtained. This model does not require a large amount of historical data, can evaluate the status of switchgear accurately. It provides a new way to assess the status of switchgear.

## References

1. He J (2011) Research on condition-based maintenance of high voltage switchgear. Technol Square 11:166–168
2. Tian D, He J (2000) Online monitoring of insulation and condition-based maintenance of the electrical equipment. Electr Power China 33(3):46–50
3. Wang Z, Huang H, Zhang B (2014) Status overhaul of high voltage switchgear based on fault tree theory. J Shanghai Univ Electr Power 30(4):21–25
4. Xie J, Shu H, Wang K (2014) State evaluation based on AHP fuzzy theory of high voltage switchgears. High Voltage Eng 40(10):3192–3196
5. Jiang J (2008) Cloud theory and its application. Guangxi University, GuangXi

6. Q/GDW613-2011, 12 (7.2) kV~40.5 kV AC metal-enclosed switchgear State Evaluation Guidelines. Enterprise standard of China State Grid Corp
7. Zheng N (2007) Study on condition assessment and fault diagnosis of power transformer. North China Electric Power University, BaoDing
8. Jin J (2008) Engineering judgment model based on normalized method. *J Changshu Inst Technol* 2008(4):39-43
9. Liao R, Wang Q, Luo S (2008) Condition assessment model for power transformer in service based on fuzzy synthetic evaluation. *Autom Electr Power Syst* 32(3):70-75
10. Chen K (1991) Nonlinear programming. Fudan University publishing house, ShangHai, pp 27-38
11. Chi G, Qi F (2012) The City's ecosystem evaluation model based on optimal combination weights and its application operations research and management science 21(2)
12. Mao D (2002) A combinational evaluation method resulting in consistency between subjective and objective evaluation in the least squares sense. *Chin J Manage Sci* 5:95-97
13. Li D, Liu C (2004) Study on the universality of the normal cloud model. *Eng Sci* 8:28-34
14. Xiong D (2003) Improvement of fuzzy comprehensive evaluation method. *J Chongqing Univ Nat Sci Edition* 26(6):93-96
15. Yao M (1991) The principle of biggest association membership and its application. *Control Decis* 6(4):283-288



# Target Tracking Based on Audio and Video Information Fusion

H. Wang

**Abstract** Particle filter is an effective technique to deal with the state estimation of nonlinear and non Gauss dynamic systems. Aiming at the problem of moving target tracking under the condition of illumination and occlusion, a particle filter algorithm based on audio and video information fusion is studied. This algorithm overcomes the deficiency of the algorithms based on a single signal source by using the time—space relativity and the complementarity of the audio and video. Pedestrian tracking experiment based on audio and video information fusion shows that the fusion algorithm is more stable and accurate than the single video tracking algorithm.

**Keywords** Target tracking · Particle filter · Audio and video information fusion · Time delay estimation

## 1 Introduction

Target tracking has an important role in the field of civil and military. Single audio sensor has a full range of positioning capability, but the discontinuity of audio information can easily lead to tracking failure. Single video tracking system affected by the change of illumination and occlusion, will also appear the tracking error or even the loss of tracking target. The fusion of audio and video information, can overcome the deficiency of single source by using the time—space relativity and the complementarity of the audio and video and improve the effectiveness and robustness of the moving target tracking. Target tracking algorithm based on audio and video information fusion is discussed in this paper, and is used to solve the problem of moving target tracking under the condition of illumination and occlusion.

---

H. Wang (✉)

School of Automation, Nanjing University of Science and Technology  
NUST, 200 Xiao Ling Wei, Nanjing, People's Republic of China  
e-mail: whm163mail@163.com

© Springer-Verlag Berlin Heidelberg 2016

B. Huang and Y. Yao (eds.), *Proceedings of the 5th International Conference on Electrical Engineering and Automatic Control*, Lecture Notes in Electrical Engineering 367, DOI 10.1007/978-3-662-48768-6\_35

305

## 2 Audio Target Tracking Principle

Target tracking based on audio signal is to determine the location of the sound source using sound receiving device. Compared with a single microphone, using array microphone not only can meet the strict requirements of the system to the target distance, direction, but also filter the noise in the environment.

### 2.1 Signal Model of Microphone Array

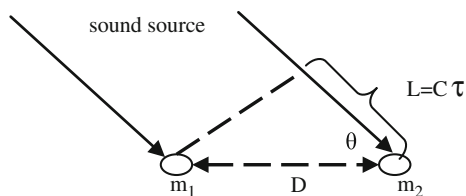
Figure 1 shows the simplest microphone array which consists two microphones  $m_1$ ,  $m_2$ . Assume the distance between the two microphones is  $D$ , the angle between the beam and the two microphones connection is  $\theta$ , then the sound source can be positioned by considering time delay and the geometry of microphone array. If the distance between the sound source and the microphone is much greater than that of two microphones, the sound beams from source to two microphones can be regarded as parallel, and the relationship between the direction  $\theta$  of the sound source and the time delay  $\tau$  of the sound source to the two microphones is shown in the formula (1),  $c$  is sound speed.

$$\theta = \arccos \frac{L}{D} = \arccos \frac{c\tau}{D} \quad (1)$$

### 2.2 Generalized Cross Correlation Time Delay Estimation

Generalized cross correlation time delay estimation is the most widely used method of sound source localization [1]. The idea of this method is described as follows: (1) The sound signal is separately received by two microphones, and then be processed into discrete signals; (2) Above two discrete signals are Fourier transformed and the cross power spectrum  $G_{12}(\omega)$  of the two signals is obtained; (3) Weight the cross power spectrum and use Fourier inverse transform, the cross correlation functions  $R_{12}(\tau)$  of the frame is obtained; (4) Time difference  $\tau$  that sound reach to the two microphones is obtained by the peak detection.

**Fig. 1** Double microphone array



Based on Matlab7.0 software, the generalized cross correlation time delay estimation algorithm with phase transformation is used to obtain the time delay between two microphones by simulation. Assuming that the analog sound source is expressed as:

$$S = 3 \sin(2\pi \times 17 \times tt/fs) + 2.5 \sin(2\pi \times 35 \times tt/fs) + 1.5 \sin(2\pi \times 51 \times tt/fs) + \sin(2\pi \times 102 \times tt/fs) \tag{2}$$

here:  $tt$  indicates the signal length, range from 1 to 4096;  $fs$  indicates the sampling frequency, let it be 1000 Hz. Figure 2 shows the results of the delay when the signal to noise ratio (SNR) is  $-20, -10, 0, 10, 20$ , respectively.

From Fig. 2, time delay obtained by the generalized cross correlation estimation algorithm with phase transformation can be seen. When the SNR is high, the signal fluctuations become small, and the peak become sharp. With the decrease of the SNR, the disturbance is gradually increasing, but the algorithm also shows strong anti-interference ability. The peak value of the graph shows that the delay is  $-0.031$  s. (“-” indicates that the other sensor received signal earlier than the reference sensor).

The experiment shows, with a microphone array for sound source localization, the delay between two microphones can be obtained by generalized cross correlation time delay estimation algorithm, and then the specific location of moving object can be determined.

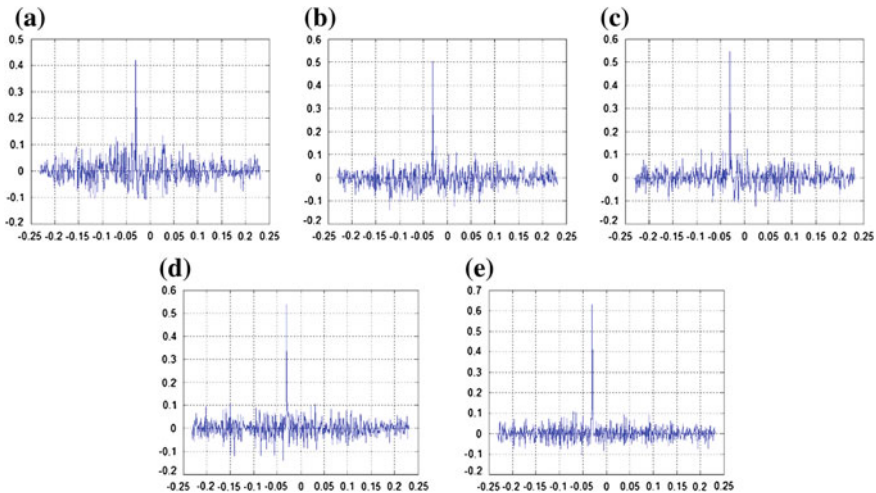


**Fig. 2** Time delay estimation results under different SNR. **a** SNR =  $-20$ . **b** SNR =  $-10$ . **c** SNR =  $0$ . **d** SNR =  $10$ . **e** SNR =  $20$

### 3 Tracking Algorithm Based on Audio and Video Information Fusion

As a nonlinear filter technique, particle filter algorithm has good applicability to nonlinear stochastic systems with non Gauss background [2]. Using particle filter algorithm in the audio and video fusion algorithm can guarantee the robustness of target tracking.

#### 3.1 System Initialization

Assume that the pixels in target area is  $\{x_i\}_{i=1, \dots, M}$ ,  $M$  is the number of pixels within the target area, then the probability distribution of the target color can be expressed as:

$$\hat{q}_u = \sum_{i=1}^M \delta(b(x_i) - u) \quad u = 1, \dots, H \quad (3)$$

here:  $b(x_i)$  is a color index function for  $x_i$  pixel,  $u$  is the characteristic value of target image. For the spatial distribution information of pixels, assume that the contribution of a pixel to the target feature description is inversely proportional to the distance between it and the center of the target, the closer the distance, the more obvious the effect to the target feature description. So, for the pixels in the target area, the weighted kernel function can be used to define its effect as shown in formula (4), where:  $r$  is the distance between pixels to the center of the target.

$$k(r) = \begin{cases} 1 - r^2 & r < 1 \\ 0 & r \geq 1 \end{cases} \quad (4)$$

Let  $x_0$  be the center position of the reference target,  $x_i$  is any point in the target area, then the color probability distribution with spatial position information of the target model is:

$$\hat{q}_u = C_q \sum_{i=1}^M k\left(\left\|\frac{x_0 - x_i}{d}\right\|^2\right) \cdot \delta(b(x_i) - u) \quad u = 1, \dots, H \quad (5)$$

here:  $C_q$  is normalized coefficient. Let  $C_q = \left[\sum_{i=1}^M k\left(\left\|\frac{x_0 - x_i}{d}\right\|^2\right)\right]^{-1}$  to make  $\sum_{i=1}^M \hat{q}_u = 1$ ,  $d$  is the size of the target area.

Similarly, in the current frame, the color probability distribution with spatial position information of the candidate target which center position is  $y$  can be defined as:

$$\hat{p}_u(y) = C_p \sum_{i=1}^M k \left( \left\| \frac{y - y_i}{d} \right\|^2 \right) \cdot \delta(b(y_i) - u) \quad u = 1, \dots, H \quad (6)$$

here:  $\{y_i\}_{i=1, \dots, M}$  represents the pixels of the candidate target region.

### 3.2 System State Transfer

Select the target template from the initial frame, obtain the initial state parameters of the target, select  $N$  particles  $\{s_1^i\}_{i=1}^N$  near the target randomly, and initialize the particle weights:  $w_1^i = 1/N$ ,  $i = 1, \dots, N$ . In the paper, the position parameters are concerned, so the state transfer model of the system is described by first order equation as follows:

$$S_k = AS_{k-1} + Bw_k \quad (7)$$

here:  $S_k$  represents the target state at the moment  $k$ ,  $w_k$  represents noise,  $A$ ,  $B$  are constants. After the system state transfer, the particle set is transferred from  $\{s_{k-1}^i\}_{i=1}^N$  at the moment  $k-1$  to  $\{s_k^i\}_{i=1}^N$  at the moment  $k$ . In order to overcome the problem of particle degradation, the Mean Shift algorithm is integrated into the particle filter. That is, convergence operation is performed to each particle by Mean Shift algorithm after the state transfer, so as to make each particle more close to the true location of the target. The method reduces the computation of the tracking algorithm, and improves the real-time performance of the algorithm.

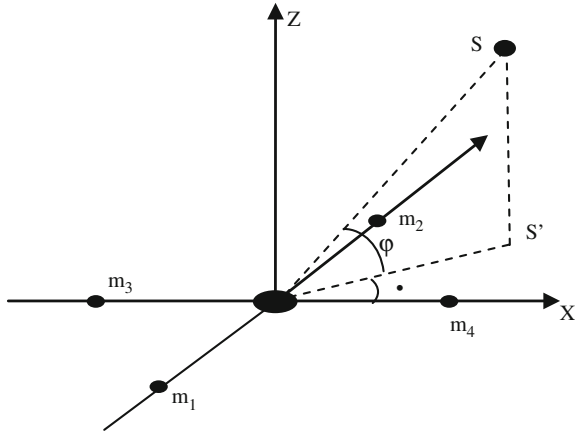
### 3.3 System Observation

The aim of the system observation is to ensure the reliability of the results of the particles state transfer. When there is no true position of the target, the similarity of target feature can be used to construct the likelihood probability of the target. The particles close to the real state of the target are given larger weights by using the likelihood probability.

In order to improve the tracking accuracy, a tracking method of audio and video information fusion is adopted in this paper. A tracking system consisting of a camera and four microphones is arranged as Fig. 3.

$m_1$  to  $m_4$  are four microphones,  $m_1, m_2$  is a pair,  $m_3, m_4$  is another pair, and they are arranged in the  $X$  axis and the  $Y$  axis, respectively. Distance between two microphones of a pair is  $D$ , two pairs form a microphone array. Camera is located at the origin of coordinates, focal length is  $f$ , planar imaging is  $L_x \times L_y$ . Assume that the coordinates of the center pixel of the image is  $(x_{cx}, x_{cy})$ , the number of pixels in

**Fig. 3** Sensor array diagram of the target tracking system



the horizontal direction and the vertical direction is  $N_x, N_y$  respectively.  $S$  is the tracking target,  $S'$  is the projection of  $S$  in the  $XY$  plane. The azimuth and pitch angles of the sound source are  $\theta$  and  $\phi$  respectively.

According to the geometric position relationship, the coordinates that sound source mapped to the image is:

$$\begin{cases} x_x = af \cdot \tan \theta + x_{cx} \\ x_y = bf \cdot \frac{\tan \phi}{\cos \theta} + x_{cy} \end{cases} \quad (8)$$

here:  $a = N_x/L_x, b = N_y/L_y$ . From formula (8):

$$\begin{cases} \theta = \arctan \frac{x_x - x_{cx}}{af} \\ \phi = \arctan \frac{x_y - x_{cy}}{bf} \cos \theta = \frac{a(x_y - x_{cy})}{b\sqrt{(x_x - x_{cx})^2 + a^2 f^2}} \end{cases} \quad (9)$$

Let  $\tau_{12}, \tau_{34}$  be the delay between  $m_1$  and  $m_2, m_3$  and  $m_4$  respectively. According to generalized cross correlation time delay estimation theory, the relationship between  $\tau_{12}, \tau_{34}$  and  $\theta, \phi$  is:

$$\begin{cases} \tau_{12} = \frac{D}{c} \sin \phi \\ \tau_{34} = \frac{D}{c} \sin \theta \cos \phi \end{cases} \quad (10)$$

Assume that the measuring position variance of the sound source is  $\sigma_{\text{aud}}^2$ , calculate the time delay estimation  $\hat{\tau}_{12}, \hat{\tau}_{34}$  of two pairs of microphones at the moment  $k$ , and the likelihood function  $p(z_k^{\text{aud}} | s_k^i)$  of the particle  $\{s_k^i\}_{i=1}^N$  can be obtained according to the formulas (9) and (10):

$$p(z_k^{\text{aud}}|s_k^i) = \frac{1}{\sqrt{2\pi\sigma_{\text{aud}}^2}} \exp\left(\frac{-[(\tau_{12} - \hat{\tau}_{12}) + (\tau_{34} - \hat{\tau}_{34})]^2}{2\sigma_{\text{aud}}^2}\right) \quad (11)$$

For the observation model based on video information, Because of the color probability distribution of the target template is obtained by the formula (5), combining with particle filter algorithm and Mean Shift algorithm, the Bhattacharyya coefficient of the candidate model and the target model which takes the particle  $\{s_k^i\}_{i=1}^N$  as the center is expressed as:

$$\rho_i[\hat{q}_u, \hat{p}_u^i(s_k^i)] = \sum_{u=1}^H \sqrt{\hat{q}_u \hat{p}_u^i(s_k^i)} \quad (12)$$

Then the distance between the candidate model and the target model is:

$$d_i = \sqrt{1 - \rho_i} = \sqrt{1 - \sum_{u=1}^H \sqrt{\hat{q}_u \hat{p}_u^i(s_k^i)}} \quad (13)$$

Assume that the measuring variance of the video tracking is  $\sigma_{\text{vid}}^2$ , then the likelihood function of the color feature tracking of the candidate template which takes  $s_k^i$  as the center is:

$$p(z_k^{\text{vid}}|s_k^i) = \frac{1}{\sqrt{2\pi\sigma_{\text{vid}}^2}} \exp\left(\frac{-d_i^2(s_k^i)}{2\sigma_{\text{vid}}^2}\right) \quad (14)$$

According to the formulas (11) and (14), The likelihood function fusing audio and video information can be obtained as follow:

$$p(z_k|s_k^i) = p(z_k^{\text{aud}}|s_k^i) \cdot p(z_k^{\text{vid}}|s_k^i) \quad (15)$$

Then particle weights are updated as:  $w_k^i = w_{k-1}^i p(z_k|s_k^i)$

### 3.4 Determination of Target Location and Resampling

To estimate the posterior probability density of the target state, there:

$$p(s_k|z_{1:k}) \approx \sum_{i=1}^N w_k^i \delta(s_k - s_k^i) \quad (16)$$

$z_{1:k} = \{z_1, \dots, z_k\}$  represents the measurement vector of system until the moment of  $k$ . The target state of the current frame is estimated by summing the weighted particles state, as follow:

$$s_k = \sum_{i=1}^N w_k^i s_k^i \quad (17)$$

Usually, after the Mean Shift algorithm, the sampling particles will be convergent, and the influence of particle degradation will be weakened. However, in order to prevent the occurrence of small weight particles, a threshold will be set in the algorithm, when the size of effective sample is less than the given threshold, it will be resampled.

## 4 Tracking Experiment Based on Audio and Video Information Fusion

### 4.1 Sound Source Detection

Detection of the target's sound is the most direct method for detecting sound source, the method can reduce the influence of changing background as much as possible. Steps using microphone array and camera to detect the sound source are described as follow:

1. Capture the static image of background using camera, when the target appears in the picture, the change of the image can be immediately detected;
2. In order to enhance the robustness of the audio signal from the target, only when the sound lasts for a while, the audio signal can be identified from the tracking target;
3. Map the audio information from the microphone array to the corresponding image.

The results of sound source detection are shown in Fig. 4, the vertical line represents the position of the target by the microphone array.

### 4.2 Tracking Experiment Based on Information Fusion

In the experiment, a sensor system consisting of a microphone array and a camera is placed in a position about 2 m away from the tracking target. RGB color space is quantified as  $16 \times 16 \times 16$ . In the algorithm, the initial particle number is set 30, the experimental results of the fusion algorithm are shown in Fig. 5. Experimental results show that the tracking performance is good, the algorithm can ensure the robustness of tracking results especially in the presence of occlusions.



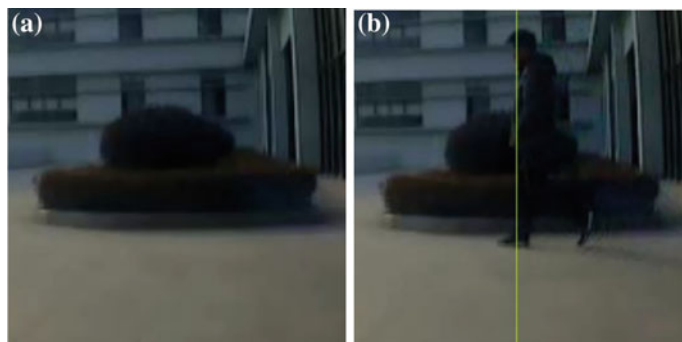


**Fig. 4** Test results of sound source (speaker). **a** Static background image. **b** The speaker is detected

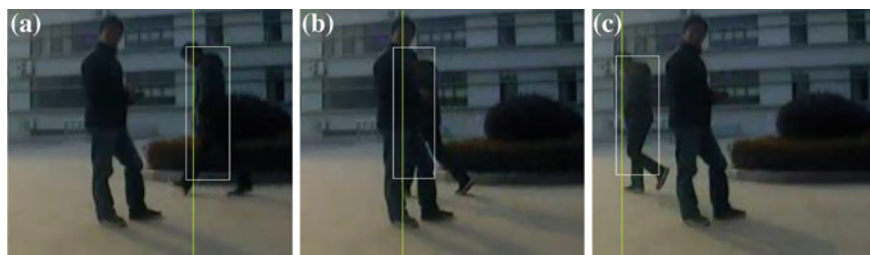


**Fig. 5** Target tracking results based on audio and video information fusion. **a** Situation of no occlusion. **b** Occlusion case. **c** Continue tracking after occlusion

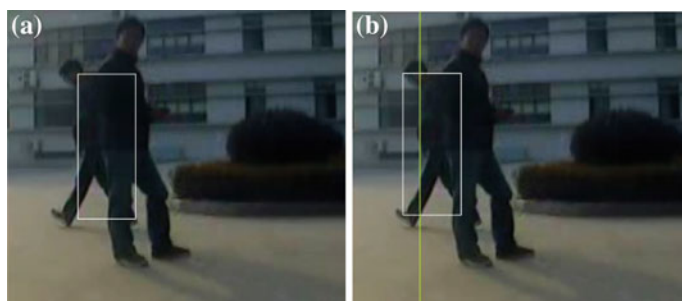


**Fig. 6** Comparison of two algorithms. **a** On a single video information. **b** On audio and video information fusion

Compared with the particle filter tracking algorithm based on a single video information, the algorithm based on audio and video information fusion is more accurate. The tracking effect for the same video (take 1 frames as an example 1) is shown in Fig. 6.

## 5 Conclusion

When the background is more complex, such as the changing illumination or occlusion, target tracking based on a single video information will easily lose the target. In order to solve the above problems, the paper studies the target tracking algorithm based on audio and video information fusion. The experimental results show that the particle filter algorithm based on the fusion information is greatly enhanced in tracking accuracy and stability compared with the particle filter algorithm based on single video information.

## References

1. Tianshuang Q, Hongyu W (1996) Relationship among methods of time delay estimation. *J Dalian Univ Technol* 36(4):493–497
2. Nan X, Tianshuang Q (2013) A nonlinear filtering algorithm combining the Kalman filter and the particle filter. *Acta Electronica Sin* 41(1):148–152
3. Lu J (2008) The research on acoustic source localization based on microphone arrays. Master thesis of Tianjin University

# Experimental Research on Fatigue Damage of Composite Solid Propellant with Constant Constraint

Jinfei Li, Weidong Huang, Kai Qu, Wenshuang Wang  
and Ming Yang

**Abstract** In order to study the effect of fatigue load on composite solid propellant with constant strain, three sets of experiments on propellant with different constant strains (20, 16.4, 10.9, 5.5, and 2.7 %) and different fatigue frequencies (10, 15, and 20 Hz) were conducted. Based on the uniaxial tension test, the mechanical properties' changing law were obtained. It was shown by the results that the maximum tensile strength and the initial modulus of propellant decreased with fatigue load and constant strain, and the damage behavior under fatigue load with constant strain can be divided into three stages, stage one is that the initial modulus was decreased quickly (the fatigue times less than 600), stage two is that the initial modulus was diminished slowly, and stage three is that the modulus was cut down seriously again (the fatigue time is more than 72,000). The connection between the initial modulus and fatigue factors is confirmed at the second damage stage.

**Keywords** Composite solid propellant · Fatigue damage · Mechanical property · Initial modulus

---

J. Li (✉) · W. Huang · K. Qu · W. Wang · M. Yang  
Naval Aeronautical and Astronautical University, 264001 Yantai, China  
e-mail: lijinfai\_03@163.com

W. Huang  
e-mail: wdhuang103@yahoo.com

K. Qu  
e-mail: qu\_kai\_1980@sina.cn

W. Wang  
e-mail: 452845454@qq.com

M. Yang  
e-mail: tomorrowyoung@163.com

## 1 Introduction

Shipboard solid rocket motor suffers low frequency vibration load which is caused by ocean wave and high frequency vibration load which is caused by the engine system of naval vessel for long time, the vibration load will have an influence on the mechanical properties of grain. To get the mechanical properties' changing law of grain under fatigue load, the accelerated fatigue experiment on propellant is needed. Recently, much work about fatigue damage of propellant have been done, nevertheless how the load value and loading ways work on propellant is ignorant.

Currently, some related literature has carried out research on the damage of composite solid propellant [1–5]. Both the nonlinear mechanical property of binder and the adhesive surface invalidation result in the nonlinear characteristics of propellant's uniaxial tension curve. Due to the anomaly in shape of particle, the stress concentrates at the edges of particle when extended, and moreover, the stress is too large to destroy the adhesive surface, the particle modulus reinforced effect is reduced and the impactful modulus of propellant is cut down [6–11]. For the fatigue load which can promote the binder break down and the particle dewetting bring on bad mechanical properties, the fatigue damage experiment of composite solid propellant is designed.

In this paper, by choosing the maximum strain and load frequency as fatigue factors, the fatigue experiment was conducted. The mechanical properties were measured by uniaxial tension test, the damage peculiarity of propellant with different maximum strains and frequencies was analyzed, the fatigue model of propellant based on the initial modulus was obtained.

## 2 Experiment

### 2.1 Material and Equipment

The solid particle's mass fraction of composite solid propellant is 86 %, including 69 % AP, and 17 % Al powder, the binder system's is 11.5 %, and the function reagent's is 2.5 %. The initial mechanical properties of propellant were tested, such as the maximum tensile strength is 1.272 MPa, the maximum elongation is 50.42 %, the initial modulus is 3.20 MPa.

Due to the limit of tension velocity (less than 500 mm/min) of the almighty material test machine, the fatigue load work on by the electric vibration system, the vibration frequency ranges from 5 to 3000 Hz. The specimens were made according to the standard QJ924-85, and then peg them on the test fixture.

## 2.2 Scheme of Experiment

To reduce the error of experiment, every five specimens were pegged together on the fixture. The upper of fixture is fixed, and the bottom connects to the vibration stand. In this way, when the vibration stand exports sine wave load with a different frequency, the specimens' bottom can be moved periodically. Each group of specimens is tested in turn.

1. To study the effect of fatigue times and frequency on mechanical properties of propellant, three set of different fatigue frequency experiments of propellant with 20 % constant strain were conducted, and the fatigue times under each frequency is 600, 6000, 30,000, and 60,000. Each group has five specimens, and the specimens should be kept in the ainer for 24 h after the fatigue experiment. The mechanical properties were tested by uniaxial tension test.
2. To study the effect of maximum strain on mechanical properties of propellant, five set of different strain experiments of propellant with 10 Hz fatigue frequency were conducted, and the fatigue times under each strain is 600, 6000, 30,000, and 60,000. Each group has five specimens, and the specimens should be kept in the ainer for 24 h after the fatigue experiment. The mechanical properties were tested by uniaxial tension test.

## 3 Result and Analysis

### 3.1 The Fatigue Times' Influence

The specimens were loaded under different fatigue times with 20 % strain and 10 Hz frequency, and then tested by the almighty material test machine. The measured results were recorded in Table 1.

**Table 1** The mechanical properties of propellant under different fatigue times

Fatigue times	Initial modulus/MPa	Maximum strength/MPa	Maximum elongation/100 %
60	2.96	1.21	48.80
120	2.85	1.24	51.61
600	2.21	1.23	53.22
1200	2.18	1.22	51.03
6000	2.16	1.21	50.22
12,000	2.14	1.18	52.34
30,000	2.04	1.19	51.46
60,000	1.85	1.03	44.73
72,000	1.76	0.83	40.17

It is shown that the maximum tensile strength and elongation do not have great diversification when the fatigue times is less than 60,000, and they were seriously reduced with increasing fatigue times. On the other hand, the initial modulus was quickly cut down at first and then changed drastically. In order to research how the fatigue times influence on initial modulus, five specimens were tried with 20 % strain and 10 Hz frequency. They were not broken at the same time, the average broken times was 78,708.

The relationship between fatigue time and initial modulus is showed in Fig. 1. Because of the 20 % strain, the microcracks are present between binder and particle, subsequently, the microcracks grew up and were aggregated; the stress field in the propellant is distributed again, the stress is gathered intensively, so that the macrocracks appear and the specimens break. The cracks were produced obviously in the specimen when the fatigue times reached 72,000.

Due to the facts that the fatigue damage cumulation process is a long period and the initial modulus dropped abruptly at first, the slow decreased process of the initial modulus was studied emphatically. A linear equation would be used to describe the relationship between initial modulus and fatigue times. According to the data in Table 1, the initial modulus' changing law was written as the following equation:

$$E = (-6.01227 \times 10^{-6})N + 2.20472 \tag{1}$$

In Eq. 1,  $E$  is the initial modulus,  $N$  is the fatigue times the correlative coefficient is 0.994.

**Fig. 1** The relationship between fatigue times and initial modulus

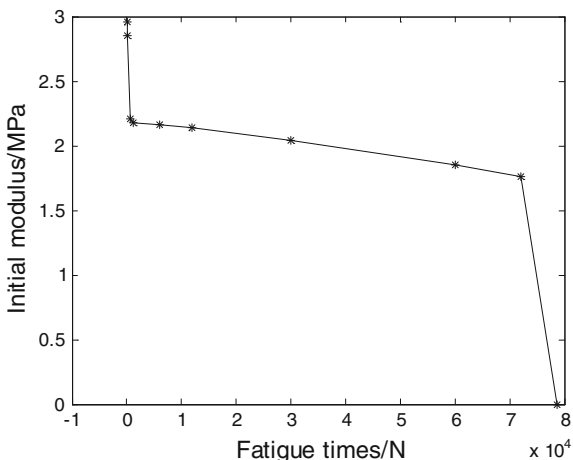


**Table 2** The initial modulus of specimens with constant strain

Frequency/Hz	Fatigue times					
	60	120	600	1200	6000	12,000
10	2.96	2.85	2.21	2.18	2.16	2.14
15	2.90	2.80	2.22	2.20	2.11	2.12
20	2.89	2.79	2.19	2.21	2.07	2.10

**Table 3** The correlative ratio of different fatigue frequencies

Frequency/Hz	Relative error/100 %								
	60	120	600	1200	6000	12,000	30,000	60,000	72,000
10	1.47	1.31	0.18	0.75	2.21	0.94	0.77	2.77	1.96
15	0.57	0.46	0.63	0.15	0.14	0.00	1.16	0.55	1.39
20	0.91	0.82	0.72	0.64	2.03	0.94	0.29	1.66	3.24

### 3.2 The Fatigue Frequency’s Influence

To study the effect of fatigue frequency on mechanical properties of specimen with 20 % strain, three sets of different frequency experiments were conducted. The fatigue frequency is 10, 15, and 20 Hz, and the initial modulus was tested. The measured results are recorded in Table 1.

To analyze the effect of different frequency on the result, the mean value of initial modulus of specimens under same fatigue times were calculated, the calculated way is presented as

$$\delta = |E(N, \varepsilon, f) - \bar{E}(N, \varepsilon)| / \bar{E}(N, \varepsilon) \times 100 \% \tag{2}$$

In Eq. 2,  $\delta$  is the relative error,  $\bar{E}(N, \varepsilon)$  is the mean value of initial modulus of specimens with same strain ( $\varepsilon$ ) and fatigue times ( $N$ ) under different frequency,  $E(N, \varepsilon, f)$  is the initial modulus of specimens (Table 2).

The data in Table 3 shows that the relative error is less than 5 %, that is to say that the fatigue frequency had a little influence on specimens with same initial strain and fatigue times, so the 10 Hz fatigue frequency was selected to consider.

### 3.3 The Initial Strain’s Influence

To study the initial modulus changing law of specimens under different initial strain, the specimens were loaded with constant strain (16.4, 10.9, 5.5, 2.7 %), and the fatigue times is 600, 6000, 30,000, and 60,000. The measured results were recorded in Table 4.

**Table 4** The initial modulus of specimens

Initial strain/%	Fatigue times			
	600	6000	30,000	60,000
20	2.21	2.16	2.04	1.85
16.4	2.29	2.26	2.17	2.05
10.9	2.42	2.41	2.38	2.34
5.5	2.69	2.69	2.67	2.66
2.7	2.93	2.93	2.92	2.91

Like the Eq. 2, the data in Table 4 were fitted by linear equation, the fitting curves were showed in Fig. 2, and the fitting parameter was showed in Table 5.

It is shown that the quotiety of linear equation increases with the initial strain growth, and the constant of equation is the mutational modulus under different strain. The specimens were damaged a little with a small initial strain, and the initial modulus declined slowly with the fatigue times increasing. The exponent equation is used to explain the connection between the strain displacement, initial mutational modulus and slope of fitting curves, the form of the exponent equation which can be described as below:

$$Y = a \cdot e^{-X/b} + c \tag{3}$$

In Eq. 3,  $X$  is the strain displacement,  $Y$  is the slope of fitting curves or mutational modulus,  $a$ ,  $b$ , and  $c$  are the parameters of the exponent equation.

The relation between strain displacement, the slope of fitting curves, and mutational modulus is given by Eqs. 4 and 5.

$$K = -5.7139 \times 10^{-7} * \exp(d_c / - 4.48) + 5.6773 \times 10^{-7} \tag{4}$$

**Fig. 2** The fitting curves of initial modulus versus fatigue times

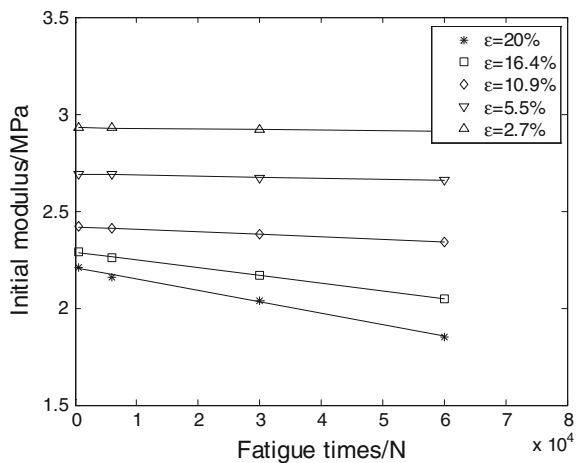




**Table 5** Fitting parameters

Initial strain/%	Equation parameter		Correlative coefficient
	a	b	
16.4	$-3.97623 \times 10^{-6}$	2.28853	0.9984
10.9	$-1.32541 \times 10^{-6}$	2.41951	0.9984
5.5	$-5.41192 \times 10^{-7}$	2.69057	0.98416
2.7	$-3.51945 \times 10^{-7}$	2.931	0.98873

$$E_b = 1.1256 * \exp(d_e/ - 4.48) + 2.115 \tag{5}$$

Thus, the initial modulus of specimen under different constant strain and fatigue times can be denoted as

$$E = (-5.71 \times 10^{-7} * \exp(\varepsilon/ - 4.48) + 5.68 \times 10^{-7})N + 1.1256 * \exp(\varepsilon/ - 4.48) + 2.12 \tag{6}$$

## 4 Conclusions

First, the main damage phenomena of composite solid propellant under fatigue load with constant strain are particle dewetting and binder rupture, and the damage behavior can be divided into three stages, stage one is that the initial modulus was decreased quickly (the fatigue times less than 600), stage two is that the initial modulus was reduced slowly, and stage three is that the modulus was cut down seriously again (the fatigue times more than 72,000).

Second, the mechanical properties of propellant with different constant strains were measured by uniaxial tension test, the initial modulus of propellant can be regarded as an damage parameter, and the connection between the initial modulus and fatigue factors is confirmed when it decreases slowly.

## References

1. Grythe KF, Hansen FK (2007) Diffusion rates and the role of diffusion in solid propellant rocket motor adhesion. *J Appl Polym Sci* 103(3):1529–1538
2. Johnson JL (2006) Data collection requirements for quality evaluation of energetic materials and methods. In: 37th International annual conference of ICT. Karlsruhe, Germany
3. Little RR, Chelner H, Buswell HJ (2006) Development, testing and application of embedded sensors for solid rocket motor health monitoring. In: 37th International annual conference of ICT. Karlsruhe, Germany
4. Matous K, Inglis HM, Gu X et al (2007) Multiscale modeling of solid propellants: from particle packing to failure. *Compos Sci Technol* 67:1694–1708

5. Metzner AP (2001) Yielding of polymers filled with large-diameter particles. *J Appl Polym Sci* 85:455–465
6. Matous K, Inglis HM, Xiaofang G (2005) Multiscale damage modeling of solid propellants: theory and computational framework. AIAA 2005-4347
7. Onsoy N, Yigitsoy B, Tinaztepe HT (2010) Accelerated aging studies of the aluminized HTPB/AP based composite propellant. Antalya: the RTO applied vehicle technology panel symposium
8. Sakovich GV (1995) Design principles of advanced solid propellants. *J Propul Power* 11(4):830–837
9. Tan H (2005) The Mori-Tanaka method for composite materials with nonlinear interface debonding. *Int J Plast* 21:1890–1918
10. Wong FC (1997) Analysis and prediction of particulate composite mechanical behavior using a nonlinear micromechanical theory. The University of Canada, Canada
11. Zisman WA (2001) Surface chemistry and surface energy of binders. *Ind Eng Chem* 55(10):19–23

# Impacts and Analysis of Electric Vehicles and Photovoltaic Integration into Power Systems

Cheng Gong, Zhongjun Chi, Baoqun Zhang, Longfei Ma, Rui Shi and Ran Jiao

**Abstract** Electric vehicle (EV), photovoltaic (PV) load will affect the power grid in a certain extent when is connected to grid, such as the change of load characteristics, increase the peak valley difference. At the same time the application of inverter will bring about reverse power threat to the operation and maintenance of power grid. To weaken the influence, V2H (Vehicle to Home) technology is used to EV and grid interaction, which can control EV charging load to a specific value as well as control the EV discharge to grid. In order to actively respond to the impact of EV and distributed PV application access to the power grid, based on the actual home users, the data of household electricity load and the user level transformer are collected and analyzed. At the same time, with the peak and valley price, based on the quantitative analysis of the influence of electric cars, solar access to the grid, the interactive applications are put forward. Calculation and interactive analysis results show that the implementation of V2H can not only bring economic benefits to users but also reduce the peak valley ratio and the risk of peak on peak which result on the electric vehicle charging in disorder.

**Keywords** Electric vehicle · Photovoltaic · Load characteristics · Interaction analysis

## 1 Introduction

As the effects of the global energy shortage, environmental pollution, and serious climate change, energy-saving emission reduction policies attract more attention by various departments. Electric vehicles, as new energy vehicles, have low noise, high energy utilization efficiency, and no mobile source emissions. Thus, EV is bound to become China's important support for one of the strategic emerging industries. At present, the exploration and establishment of electric vehicle charging

---

C. Gong (✉) · Z. Chi · B. Zhang · L. Ma · R. Shi · R. Jiao  
State Grid Beijing Power Research Institute, Beijing, China  
e-mail: 123.gc@163.com

© Springer-Verlag Berlin Heidelberg 2016  
B. Huang and Y. Yao (eds.), *Proceedings of the 5th International Conference on Electrical Engineering and Automatic Control*, Lecture Notes in Electrical Engineering 367, DOI 10.1007/978-3-662-48768-6\_37

and switching facilities to meet the diverse needs of electric vehicles have become an important issue for the development of electric vehicles in the world [1–3].

The state has introduced a series of policies to speed up the development of energy saving and environmental protection industry. In order to encourage distributed PV access grid, power grid companies are persuaded to purchase the full amount of photovoltaic power generation. While in Europe, the government uses policy subsidies to support the development of photovoltaic in the construction phase. In the future, distributed PV power supply will be common in the family, becoming an important part of the power grid. With the amount of PV users, the requirement of power network operation management and security protection will be stricter. The traditional marketing mode of state grid company needs to update as the change of the home and grid electrical characteristics [4, 5].

As the EV and PV users increased year by year, researches on the effect of grid when EV and PV load is connected to household user load has become a new topic. To formulate a reasonable policy and electricity price mechanism, orderly guide to the access of photovoltaic, energy storage, and electric vehicle load can improve the influence of the new load to the power grid. In Japan, the United States, and other countries, V2H technology has been practically used, which can guide the rational use of electricity, based on the peak and valley price [6].

In order to actively respond to the impact above, data acquisition and analysis are carried out in this paper. To collect the basic data, a new data acquisition system is developed and deployed in the real family, which can get the data of the family and the transformer. Based on the data of about 8 months, the effect of EV and PV access to grid is studied. Moreover, combined with the mechanism of electricity price, the application scheme of electric vehicle and photovoltaic is put forward.

## 2 The Research Object

To get real data for the research, the user in a villa, Changping District, Peking is selected as the research object. In the house, the photovoltaic power generation system and the energy storage system are installed. Some main electrical equipment is used such as electric heating, air conditioning, refrigerators, television sets, washing machines, treadmill lighting lamps, etc. Moreover, two fuel cars and one electric car are used for travel. To get the data, acquisition devices are deployed in the house which is shown in Fig. 1.

The data acquisition system can collect the data we need such as the electricity usage, the instantaneous power, the current, the voltage, and so on. All the data is uploaded to the server in real-time through the 3G module.

The diagram of the photovoltaic power generation system and the energy storage system is shown in Fig. 2. As is shown, through the control unit, we can achieve the overall control.

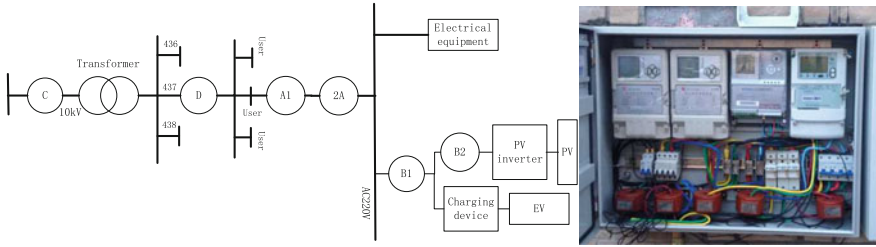
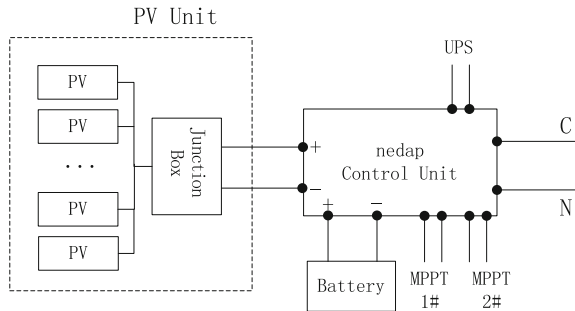


**Fig. 1** Figure of connection mode of data acquisition system

**Fig. 2** Figure of PV and energy storage system



The battery capacity of the EV is 23 kWh, which can make sure that the car runs 130 km for the top.

### 3 Data Analysis

For a home user, photovoltaic, energy storage and electric vehicle access of 10 kV power network mainly affects performance in two aspects: changing the load characteristics of the user side and influencing the power quality of the grid.

To study the effects above, based on the data from January 1, 2014 to August 31, 2014, the information of the grid load and the user load is analyzed, which is shown below.

#### 3.1 Effect of Photovoltaic Energy Storage on Load Characteristics of Power Network

The influence of the load of the original station after the installation of the PV power generation with no energy storage is shown in Fig. 3.

When the PV power generation system and the energy storage device are used, the influence of the load is shown in Fig. 4.

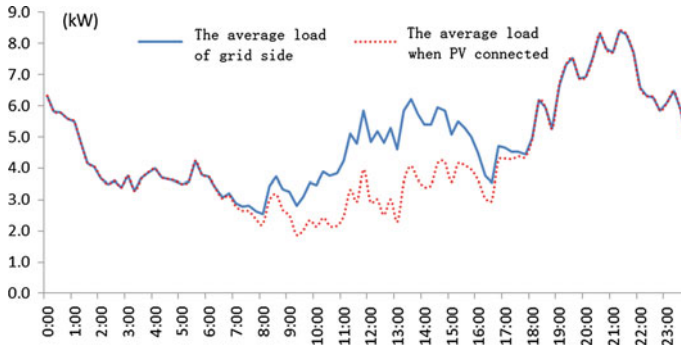


**Fig. 3** Curve of the influence on power grids (only PV)

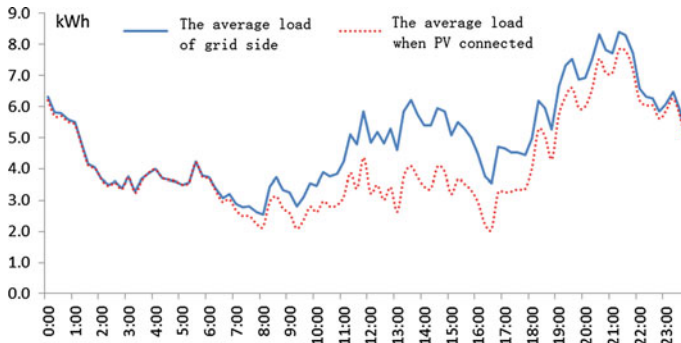


**Fig. 4** Curve of the influence on power grids (PV and energy storage device)

From Figs. 3 and 4 load curve comparison, we can get the conclusion below.

1. The effect of PV generation on the grid at the valley time is larger. While at the peak period, the effect is significantly reduced. The valley time is offset and the power grid peak and valley difference is increased.
2. As for the energy storage system, the effect on the grid at the evening peak time is larger and that of peak valley difference compared with previous (not access storage) decreased.

### ***3.2 Effect of Electric Vehicle Load on Load Characteristics of Electric Network***

The effect of the EV charging load on the grid is mainly reflected in three aspects: charging time, charging load, and the number of electric vehicles. Through the

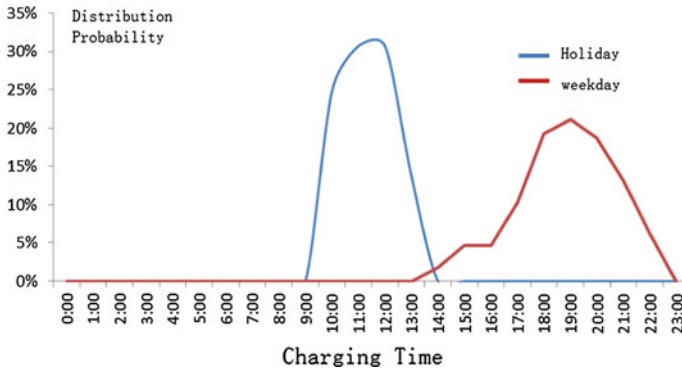


Fig. 5 The charging time distribution curve

analysis, it is found that the working day and holiday travel law, and the law of the charge of the pilot users show strong consistency, as shown in Fig. 5. At working days, the charging behavior mainly concentrated in the evening 17:00–23:00, while at holidays, charging behavior concentrated at noon 10:00–13:00.

Therefore, the data is divided into two kinds—the working days and holidays. The daily load curve of the electric vehicle charging station is studied. The load curve of the 10 kV low voltage station is shown in Fig. 6 on weekdays, and shown in Fig. 7 at weekends.

Through the analysis, we can conclude that: at the working day and holiday, electric vehicle users behave differently when charging, but show consistency in some way. The peak valley difference will increase when charging at weekday and decrease at holiday.

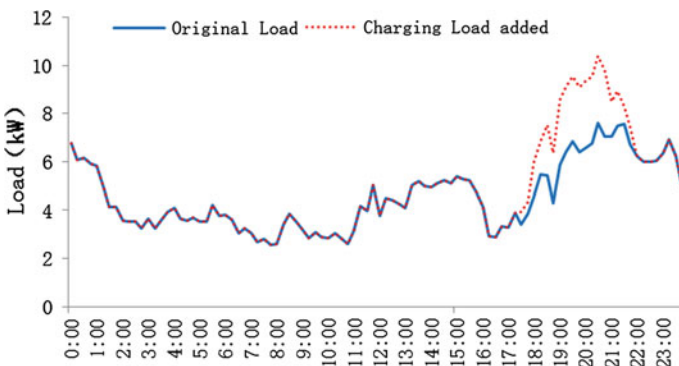


Fig. 6 The superposition of the electric vehicle charging load curve on weekdays

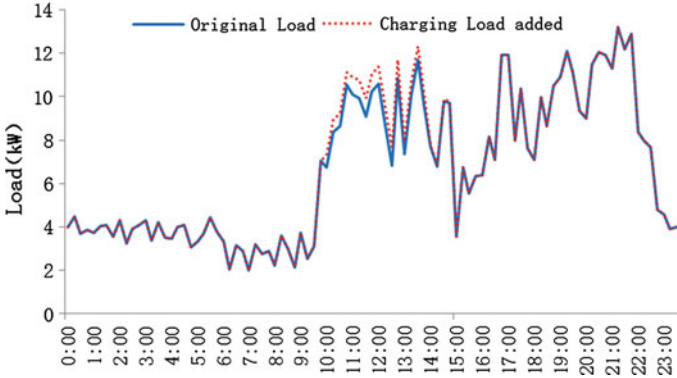


Fig. 7 The superposition of the electric vehicle charging load curve at weekends

### 3.3 Analysis on the Comprehensive Effect of Load Characteristics of Power Network

Based on the analysis result above, the comprehensive effect of the PV, EV, and the energy storage system on the grid is researched.

(a) The working days

The comprehensive effect of the PV, EV on the grid in the working days is shown in Fig. 8. When the energy storage system added, the effect is shown in Fig. 9.

From Figs. 8 and 9, we can draw the following conclusions

- The working day has a great influence on the peak load of the power grid.
- The peak period of day load is affected by the photovoltaic power generation, which can be stabilized.

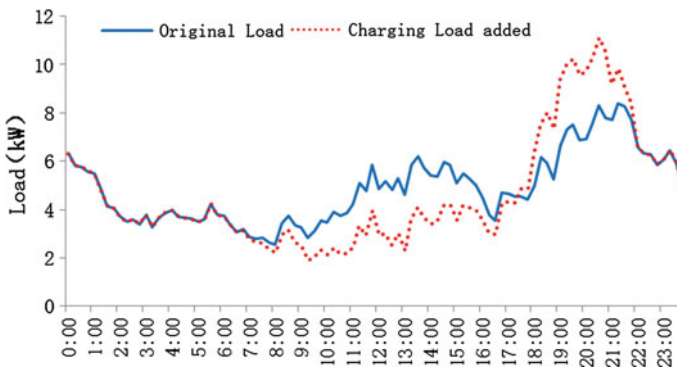
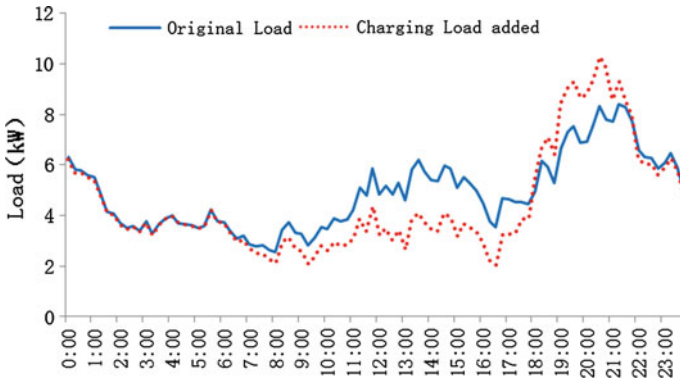


Fig. 8 Curve of the comprehensive effect of PV and EV on weekdays





**Fig. 9** Curve of the comprehensive effect when the energy storage system added on weekdays

- Because of the electric vehicle charging load, the evening peak load will increase, which can increase by 41 %.
- The area of the peak valley ratio further increases, which can be up to 77.5 %.
- The storage device can weaken the effect of the evening peak to a certain extent, and the peak valley ratio can be improved.

(b) The holidays and vacations

Similarly, the comprehensive effect of the PV, EV on the grid in holidays is shown in Fig. 10. When the energy storage system added, the effect is shown in Fig. 11.

Seen from Figs. 10 and 11, due to the charging load occurs at noon peak period and the use of photovoltaic power generation, the comprehensive effect in holidays

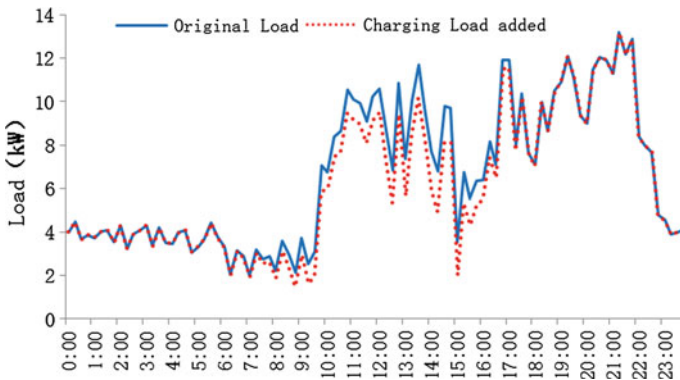


**Fig. 10** Curve of the comprehensive effect of PV and EV at weekends

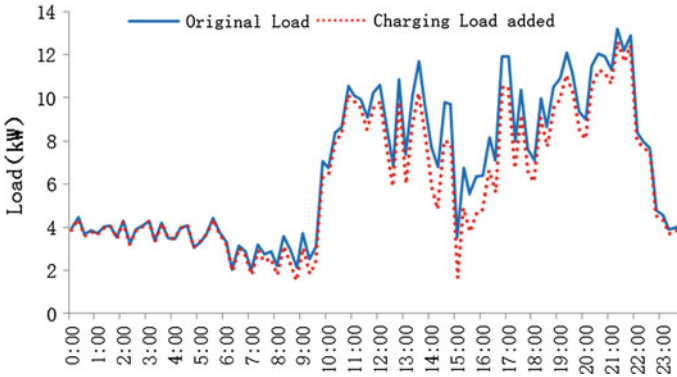


**Fig. 11** Curve of the comprehensive effect when the energy storage system added at weekends

is not obvious, and the risk of noon peak can be avoided. While at night, because of the application of energy storage device, the evening peak load is weakened to some extent.

### 4 Interactive Calculation and Analysis

According to July 30, 2014, National Development and Reform Commission issued “on the electric vehicle with electric power price policy related issues notice” to determine the electric vehicle charging for electric facilities for electric power and the implementation of peak and valley time of use price policy. The power of the user’s use of electricity belongs to the residents’ electricity, not in accordance with the peak valley electricity price. If the future of user electric energy characteristics and home users of the new energy release peak and valley price can not only promote the development of new photovoltaic energy, automobile to the user, but also can produce certain economic benefits and to guide the rational use of electricity, so that the new energy can better interact with the grid.

Assuming that the user electricity price of peak and valley is implemented, which is shown in Table 1, we can calculate the cost of charging. According to

**Table 1** Charging electricity measurement

Charging time	Flat period	Peak period	Valley period
Time	7:00–10:00 15:00–18:00 21:00–23:00	10:00–15:00 18:00–21:00	23:00–7:00
Unit price (RMB/kWh)	0.8395	1.3222	0.3818
Annual power (kWh)	2316		
Price (RMB)	2175	3062	884

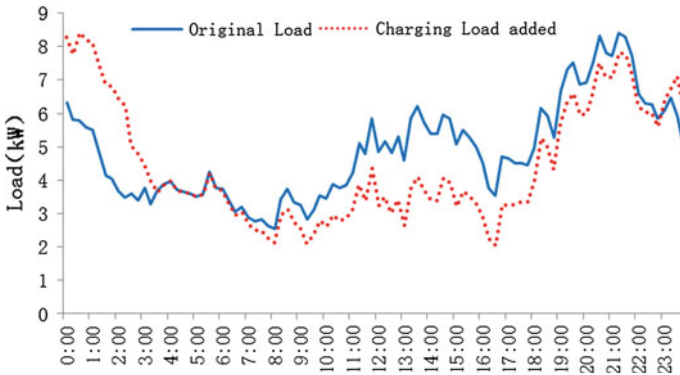


**Fig. 12** Curve of the comprehensive effect after the implementation of V2H

preliminary statistics, the electric vehicle power consumption per hundred kilometers is 20 kWh.

According to the user’s electric vehicle charging behavior analysis, 62 % of the charging behavior occurs in the peak period, and 35 % in the flat section, 3 % in the valley section, converted down, a year of charging electricity for 2686 RMB. Assume that all the electric car users in the valley segment charge only RMB 884 a year to save electricity 1802 RMB.

When the technology of timing charging is used, the EV will be charged at the time of the valley, the curve of the comprehensive effect is shown in Fig. 12.

From Figs. 8 and 12 contrast can be seen, considering power grid peak and valley time, orderly guide for electric vehicle charging load due to the application of energy storage device, the evening peak period can weaken, the user and peak time delayed, and avoid the peak and peak phenomenon.

## 5 Conclusion

In this paper, from the research on the actual data analysis of the actual user, we can get the conclusions as follows:

1. The effect of the PV on the grid is larger, and the peak segment length is significantly reduced, valley time completely offset. When the energy storage system added, the evening peak load effect greatly, and that of peak valley difference is decreased.
2. At the working day and holiday, electric vehicle users behave differently when charging, but show consistency in some way. The peak valley difference will increase when charging at weekday and decrease at holiday.

3. When the technology of V2H is used, the influence of peak load on the 10 kV power network is greater on weekdays, the load curve is stabilized during the day due to the effect of PV, and the load curve is pulled at night due to the EV charging load.
4. Perform electric vehicle charging peak valley electricity price and distributed power tariff, orderly guide users to a reasonable use of new power, in bringing economic benefits to users, at the same time, can reduce the electric vehicle charging peak and peak risk, reduce the difference between peak and valley, to ensure safe and stable operation of power grid.

## References

1. Clement-Nyns K, Haesen E, Driesen J (2010) The impact of charging plug-in hybrid electric vehicles on a residential distribution grid. *IEEE Trans Power Syst* 71–80
2. Haines G, McGordon A, Jennings P (2009) The simulation of vehicle-to-home system—using electric vehicle battery storage to smooth domestic electricity demand. *EV-ER MONACO Ecol Veh Renew Energies*
3. Hu Z, Song Y, Xu Z (2012) Impacts and utilization of electric vehicles integration into power systems. *Proc CSEE* 32(4):1–10 (in Chinese)
4. Wanlu LI (2012) Electric vehicles V2H energy management and optimization system. *Heilongjiang Electr Power* 34(1):78–80
5. Letian T, Weiguo H, Chenggang D et al (2009) Power supply modes for electrical vehicles and their impacts on grid operation. *East China Electr Power* 37(10):1675–1677 (in Chinese)
6. Zhao J, Wen F, Xue Y et al (2010) Power system stochastic economic dispatch considering uncertain outputs from plug-in electric vehicles and wind generators. *Autom Electr Power Syst* 34(20):22–29 (in Chinese)

# A Wireless Multipoint Parameter Monitoring System for Greenhouse Environment

Xiaoqing Zhang and Yudong Jia

**Abstract** A system of real-time monitoring and wireless transmission of illuminance, temperature and humidity parameters for a greenhouse environment is achieved in the framework of ZigBee protocol stack. It mainly includes two kinds of minimum systems with the cores of Texas Instruments CC2530 chip and ARM STM32F103 chip. CC2530 minimum system completes network nodes function of multipoint parameter monitoring. BPW34S sensors are used to construct the illuminance collection module and SHT10 sensors are used to construct the temperature and humidity collection module. Multipoint parameter data are sampled by CC2530 nodes. A node chip transmits measured data wirelessly to another node based on ZigBee technology. The STM32 minimum system contains a CC2530 which is used to receive data from other sensor node modules through serial port. After the system processes the data, the result is displayed on LCD12864 screen. Experiment shows that data loss rate of this system are zero within 15 m communication distance. This system is suitable for a greenhouse of about 20 m × 25 m area and it has several advantages of low cost, easy installation, and high efficiency.

**Keywords** Wireless sensor networks · Multipoint parameter · Monitoring nodes · ZigBee · Low energy consumption

---

X. Zhang (✉) · Y. Jia  
Beijing Information Science & Technology University,  
Qinghe Xiaoying East Road 12,  
Haidian District, Beijing 100192, China  
e-mail: zxqbim@163.com

Y. Jia  
e-mail: jiayudong@bistu.edu.cn

# 1 Introduction

Multipoint parameter monitoring system for a greenhouse environment needs to acquire a large number of data which are derived from monitoring sensors [1]. The monitoring network constituted by traditional wired sensors exist some problems, such as extraordinary requirements of wiring and installation, high maintenance funds, and difficulty of function extension.

ZigBee is a quickly developing technology in today’s wireless network, and it has the advantages of low power, short distance, and better connectivity transmission [2, 3]. Based on ZigBee technology, a multipoint parameter wireless monitoring and self-organizing network system for greenhouse is built, which uses the MCU STM32F103 chip as a core and universal CC2530 chips to complete the data collection and wireless transmission of multi points. At last, the STM32F103 chip realizes data processing and displaying. Significant advantages are low power consumption, low maintenance cost, relatively simple installation and updating, and easy to add functional module.

## 2 Overall Design of System

### 2.1 The Composition Diagram of the System

The design sketch of a complete nodes network system is shown in Fig. 1.

The system can be divided into two modules: master module and slave module. Master module which includes STM32F103, a CC2530, and LCD displaying circuit is responsible for the operation of whole system. Its main function is responsible for receiving data from the wireless antenna and displaying all kinds of data on the

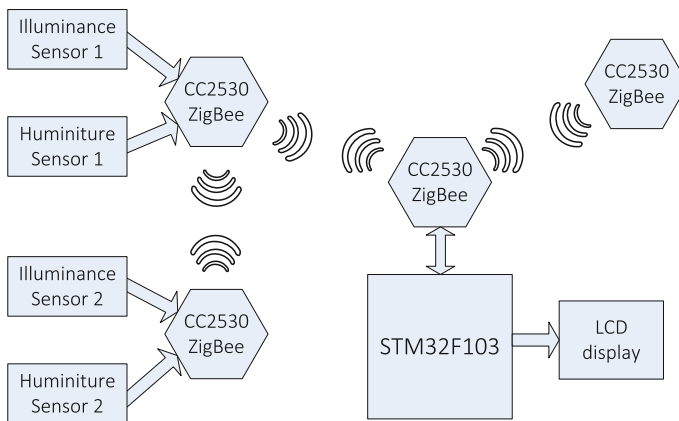


Fig. 1 Wireless monitoring network of multi point parameters

LCD screen in real-time. Slave module includes node sensors at multi points. The sensor chip collects the data of temperature, humidity, and intensity of illumination. Multiple CC2530 chips are responsible for collecting data of temperature, humidity, and intensity of illumination from sensor chips. Then they transmit the measured data from every node to master module accurately through the wireless antenna [4].

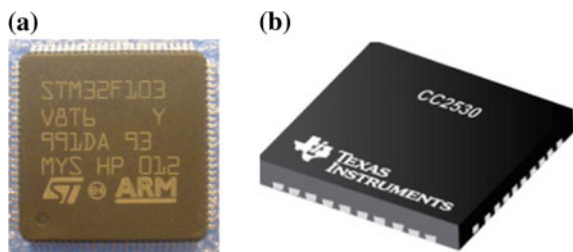
## 2.2 Main Control Chips

With the development of the semiconductor and information technology, embedded technology becomes the popular trend of digital products today. As a representative product, Cortex-M3 core of STM32 single-chip computer is a 32-bit microprocessor based on ARM framework, shown in Fig. 2a. Cortex-M3 is widely used in the field of electronic intelligence. STM32F103 series have strong performance in aspects of signal processing, superior control, and connection function. Enhanced series with clock frequency up to 72 MHz have the strongest performance in the same type of the chip. It is configured with 32 to 128 K RAM. Current consumption of STM32 is only 36 mA and it is the lowest power consumption products on the market at present. The core of the Cortex-M3 processor reaches 32-bit internal data length, so register address, the interface of storage address is also 32-bit.

In this system, Cortex-M3 is used to receive and process data. Fourteen interrupting channels with eight priority levels have faster responsive speed. It has stronger ability to process data compared with the ordinary single-chip micro-computer. ZigBee application solution of CC2530 SOC developed by TI Company is adopted because it is of convenience and low power consumption which greenhouse parameters wireless monitoring network requires. It is suitable for IEEE 802.15.4 ZigBee remote-control standards and protocol application of 2.4 GHz [5].

CC2530 chip integrates with professional RF transceiver of high practicality and stability. It includes an 8051 MCU in which the capacity of powerful, programmable Flash is optional. It has an 8 KB RAM and many other powerful features. Its appearance is shown in Fig. 2b. In this system, CC2530 on each node realizes DAQ function of illumination, temperature, and humidity. ZigBee nodes constitute sensing control nodes with corresponding sensors. The monitoring

**Fig. 2** Two control core chips of the system  
**a** STM32F103. **b** CC2530



system real-time monitors illumination, temperature, and humidity in the greenhouse. STM32 minimum system receives data through serial port by adding a piece of CC2530, and the processed data is displayed by the LCD module.

### 3 Hardware Design

#### 3.1 *Wireless Transmission Antenna*

The realization of wireless data transceiver based on ZigBee technology needs 2.4 GHz band frequency. With the data transceiver rate of up to 250 K bits per second, its theoretical transmission distance is within the range of 50 m or less. To complete the monitoring and data transmission function, the CC2530 minimum system requires adding light detection module, temperature and humidity detection module and RF transceiver module to realize the function of sending and receiving data.

The key of antenna design is antenna matching circuit, which affects transmitting distance directly. Because the ZigBee in our system works in the 2.4 GHz band, we should consider the impact of electromagnetic compatibility, the length, and location of the antenna and other factors when PCB wiring.

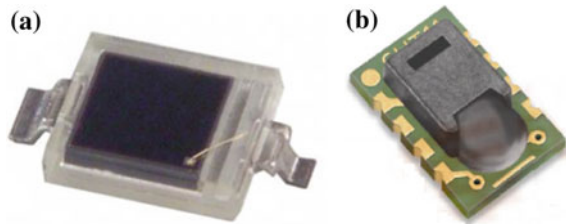
RF signal of CC2530 works with differential way. If the optimal differential load requirements be consistent, signal reflection interference will not occur on the signal transmission and the signal of antenna reaches the strongest. Because there is relationship between the output impedance, the production materials, and circuit layer spacing, we should refer to the relationship between the location of the antenna and the attenuation of signal when making PCB.

#### 3.2 *The Illuminance Data Acquisition Node*

We adopt silicon light battery BPW34S of Siemens Company as the light sensor, shown in Fig. 3a. The output voltage of the photosensitive probe is 10–1100 mV, the measured wavelength range is 400–1100 nm, its sensitivity is 0.62 A/W, and the maximum power dissipation is 0.15 W. So it has the advantage of low energy consumption. The BPW34S device converts light signal into electrical signal, magnified by 3 times by the amplifier TLV2372, and provides the sampling voltage to the AD in CC2530, which is in the range of 30–3300 mV. The measured data is sent to the serial port by AD, which is read by CC2530 through two wires serial directly. Voltage data for monitoring the indoor illumination should be processed by Cortex-M3 main MCU so as to be converted into illumination data.



**Fig. 3** Node sensor devices  
**a** BPW34S. **b** SHT10



### **3.3 The Temperature and Humidity Data Acquisition Node**

The chip of SHT10 is the main chip of temperature and humidity sensor module, which is used to detect temperature and humidity parameter. It is a digital sensor of temperature and humidity with high precision which is developed by Sheng Sirui of Switzerland Company. The output resolution of temperature value is 12 bits and the output resolution of the humidity value is 14 bits. The sensor supply voltage range is from 2.5 to 5.0 V. Its average current consumption of monitoring data is only about 30  $\mu$ A and its shape is shown in Fig. 3b.

### **3.4 Data Processing Module**

With the power supply module, wireless transmission module, sensor module, LCD display module based on the minimum system of STM32, we constitute a complete multipoint parameter monitoring system for greenhouse. In order to make two minimum systems of CC2530 and Cortex-M3 be low energy consumption and efficient operation, the stable power supply should be taken into account in system design. Specifically, at first a USB interface is used to supply 5 V DC power, and then 5 V voltage is converted into 3.3 V for CC2530 and Cortex-M3 power supply by TPS62203 chip. The node modules are provided 3 V voltage supply by small rechargeable lithium batteries.

The system displays the final results by LCD12864 liquid crystal. It is a LCD screen with serial interface mode, including 4 bit/8 bit parallel 2-wire or 3-wire. Compared with the liquid crystal module with the same function, the LCD12864 with the resolution of  $128 \times 64$  dots has lower cost and comparable functions.

## 4 System Software Design

### 4.1 System Software Flow Chart

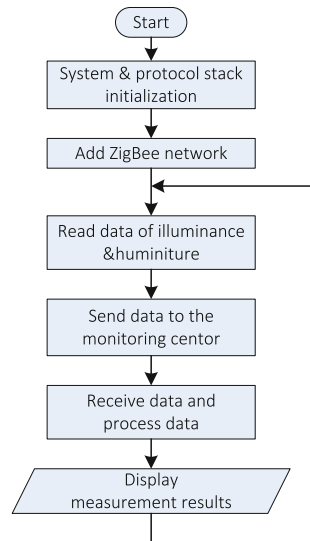
The entire system software is divided into two parts. One is ZigBee technology programming about the CC2530, based on the development platform of TI Z-Stack [6]. The other part is the STM32 data processing and LCD programming based on an integrated development environment provided by MDK4.1. In the overall design we have to take into account the work order of each module, as well as the cooperation between the various modules. The system flow chart is shown in Fig. 4.

First, initialize the system and ZigBee wireless communication protocol stack. Secondly, collect data (temperature, humidity, and light intensity) by the minimum system CC2530 chip joined sensing module. Thirdly, get the data package and transfer to the relay chip CC2530 by wireless communication technology based on ZigBee. Fourthly, pass the data into the Cortex-M3 from the relay CC2530 through the serial port. Fifthly, process the data by Cortex-M3 processor core. Finally, the received data is printed on the LCD screen.

### 4.2 Initialization of ZigBee Protocol Stack

ZigBee protocol stack consists of four layers from bottom to top: physical (PHY) layer, media access (MAC) layer, network (NWK) layer, and application

Fig. 4 Software flow chart of the system



(APL) layer [7]. ZigBee alliance developers establish the top-level design, including the network layer and application layer; IEEE standards developers establish the low-level design, including the physical layer and media access layer [8].

Based on the IEEE 802.15.4 standard and ZigBee 2006 standard, a more complete ZigBee 2006 stack has been developed by TI Company and has been recognized by the ZigBee alliance. It moves the operating system design concept of the ZigBee protocol stack into IAR integrated development environment for research and engineering. It adopts the event polling mechanism. The system enters hibernation standby mode after the four-story structure initialization. Once an event is triggered, it will wake up the system from sleep mode into the operating mode to solve an interrupt event. Then it continues into sleep mode when the event is finished. If there are several events occurring together at some point, discrimination processing is taken according to the priority step by step, which reduces the power consumption of the system greatly.

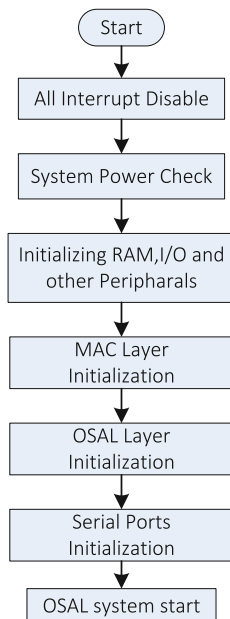
TI Z-Stack is an operating system based on rotary query [9]. Its operating mechanism is that when there is an event, operating system abstraction layer (OSAL) distributes this event to the task that is able to handle this event responsibly, and then this task determines the type of the event and calls that are appropriate processing program to handle the event.

In general, Z-Stack has two functions. One is the system initialization and the other is starting operating system entity. Z-Stack operating system entity only has one line of code, namely "*osal\_start\_system()*:". *osal\_start\_system()* calls (*tasksArr[idx]*) (*idx,events*) to perform specific processing functions. *tasksArr[]* is an array of function pointers and performs different functions depending on different variable *idx*. OSAL is the core of the protocol stack. Each task of OSAL is planned to a subsystem of Z-Stack in the initialization process of OSAL layer. *sosal\_Add Tasks()* of *osal\_inti\_system()* provides mission lists and adds tasks that meet the need of users to operating system timely.

The flow chart of system initialization is shown in Fig. 5. Generally, the system initialization includes several main functions listed as below.

- Initializing the system clock
- Detecting the chip working voltage
- Initializing the stack and each hardware module
- Initializing flash storage
- Forming MAC address
- Initializing nonvolatile variable and the MAC layer protocol
- Initializing the operation system
- Initializing the application frame protocol

**Fig. 5** Initialization process of ZigBee protocol stack



## 5 Monitoring Experiment

Testing experiment is carried out in a greenhouse of 20 m × 25 m. Test system, which is a star-like network structure, is made up of one central node and eight sensor nodes. The ZigBee sensor nodes transmit the monitoring data to the central ZigBee wireless module that is connected with STM32 in time. Finally, STM32 deals with the data and then displays them on LCD screen.

Experiment results show that data transmission is accurate and reliable and data loss rate is zero within 15 m communicating distance. The measuring range of temperature is about 10–50 °C, that of relative humidity is about 20–60 % RH, and that of illuminance is about 100–1000 Lx.

## 6 Conclusion and Discussion

The core chips of main module of the system are STM32F103 and CC2530. The main chip of the slave module is CC2530. System software design adopts IAR and MDK integrated development environment, and their compiling language is C language which has the best performance in both running efficiency and speed. Programming of CC2530 chip mainly compiles the ZigBee protocol stack and realizes wireless transmission. Programming of STM32 chip mainly realizes receiving CC2530 data by serial port and displaying them on the LCD screen.

Modular form of the software design can help break the difficult task into small targets one by one according to modules. In this way, it can not only improve work efficiency, but also be convenient for debugging.

The successful implementation of multipoint parameter monitoring system for greenhouse based on ZigBee technology explains that the combination of the CC2530 and STM32 makes full use of their advantages. In addition, adopting wireless auto-network technology solves a series of problems, such as removing redundant wiring nodes in greenhouse, transmitting node information wireless, implementing efficient monitoring and updating system in real-time and so on.

## References

1. Kalaivani T, Allirani A, Priya P (2011) A survey on Zigbee based wireless sensor networks in agriculture. In: Proceedings of the 3rd international conference on Trendz in information sciences and computing, pp 85–89
2. Avide C, Wei H (2004) Wireless sensor networks. *Commun ACM* 47(06):30–33
3. Gislason D, Gilman T (2004) ZigBee wireless sensor networks. *Dr.Dobb's J* 29(11):40–42
4. Sung TW, Yang CS (2010) An adaptive joining mechanism for improving the connection ratio of ZigBee wireless sensor networks. *Int J Commun Syst* 23(2):231–251
5. Lee J, Huang YC (2006) Design and implementation of ZigBee/IEEE 802.15.4 nodes for wireless sensor networks. *Meas Control* 39(7):204–208
6. Chipcon Semiconductor (2006) Z-Stack API
7. Edgar HC (2004) *Wireless sensor networks: architectures and protocols*. CRC Press, Boca Raton
8. ZigBee Alliance (2004a) ZigBee alliance network specification version 1.0
9. ZigBee Alliance (2004b) ZigBee specification version 1.0-ZigBee document 05347r06

# A Survey of Fault Location for Distribution Systems

Yongjun Liu, Min Liu, Cheng Lin and Kefeng Ou-yang

**Abstract** Accurate distribution network fault location technology is the key to achieving a smart grid. Due to its complex network topology, multi-branch, load-time variant and characteristics of the different features, existing distribution network fault location methods are not applicable. In this paper, fault location methods are summarized from three perspectives: fault line selection, fault section location and fault ranging, and the developmental trends in fault location for distribution networks are considered.

**Keywords** Smart grid · Fault location · Distribution systems · Survey

## 1 Introduction

The construction of smart distribution systems with the characteristics of self-healing control is the inevitable trend of future power-grid technology [1]. One of the key techniques of self-healing control is the fault-location technique for distribution networks. Currently, distribution network fault location methods do not quickly and effectively solve various types of faults occurring in actual power distribution networks, especially the single-phase ground fault. Indeed, the main problem of fault location for distribution networks is to solve the accurate location of single-phase-to-earth fault. Consequently, the technology of distribution systems fault location has been a research hotspot at home and abroad.

Research into fault location for distribution systems can be divided into three directions: first, fault line selection, in which the fault feeders among multiple line

---

Y. Liu · M. Liu (✉)  
College of Electrical Engineering, Guizhou University,  
Guiyang 550003, Guizhou Province, China  
e-mail: minliu666@qq.com

C. Lin · K. Ou-yang  
Power Dispatching Control Center of Guizhou Power Grid Corporation,  
Guiyang 550003, Guizhou Province, China

outlets of a bus bar are evaluated; second, fault section location, which determines where the fault feeder section lies; third, fault ranging, in which the distance between the measuring end and the fault point is estimated. The three aspects comprise the essence of fault location, but the difficulty for achieving fault location is gradually increasing. In this paper, the existing distribution network fault location techniques and the advantages and disadvantages of each method are summarized. Finally, a future developmental direction for the fault location technology is proposed.

## **2 Fault Line Selection**

### ***2.1 Steady-State Components Based Fault Line Selection***

Fault line selection methods based on the fault stable components include: the zero sequence current amplitude method, the zero sequence current ratio method, the zero sequence current population ratio method and the zero sequence reactive power direction method, among others.

Since the above methods are only applicable to ungrounded systems, there is a problem of applicability for neutral point grounding system. It is difficult to select the fault line through zero-sequence current magnitudes and polarities of fault lines [2]. To overcome this drawback, a zero-sequence current active power method is proposed [3]. However, the fault signal used is weak, and the method is largely affected by the system line length, the size of the transition resistance and other factors. Reference [4] points out that the fault line can be selected by comparing the magnitude and direction of the negative sequence current.

Overall, methods based on steady-state components without stable steady-state information, which lead to the reliability of line selection, is not high.

### ***2.2 Transient Components Based Fault Line Selection***

Firstly, at present, fault line selection methods based on fault transient components mainly include the first half-wave method. The first half-wave method proposed in [5] uses the characteristics of the first half-wave reverse phase of a ground fault fundamental transient current and transient voltage to determine the fault, but the algorithm anti-interference ability is not strong in practical application. Secondly, fault line selection methods include the wavelet method. Finally, wavelet transform of the transient zero sequence current is implemented by using appropriate wavelet and wavelet base. According to a transient current component in the line, the fault amplitude envelope is greater than the healthy line amplitude, and the characteristic of two opposite polarity to select fault line [6].

But both the size and composition of the transient components are affected by the system operation modes, fault types, fault time and other factors. So, the transient

components algorithm, influenced by the line structure, parameters and fault conditions, remains to be tested in practice, due to the shortness of the transient process.

### ***2.3 External Injection Signal Based Fault Line Selection***

Fault line selection methods based on an external injection signal mainly include S signal injection and the pulse injection method. The principle of S signal injection method is to inject an S current signal to the grounding line grounding phase via a bus voltage transformer, and then use the dedicated signal current detector to find the fault line [7]. The pulse injection method works similarly to the S signal injection, but the injected signal is periodically intermittent, lower frequency and controllable [8].

But, the method needs to configure the dedicated injection signal source and assistant detection device, so this causes a high investment cost. At the same time, signal detection of the intermittent arc grounding fault is difficult.

## **3 Fault Section Location**

### ***3.1 Matrix-Based Fault Section Location Algorithm***

A method for judging the fault region of the distribution network based on directed graph is proposed in [9]. This method avoids the matrix multiplication and normalization processing and establishes a new matrix algorithm for a fault section detection, and also expands the processing capacity of multi-power network. A new algorithm for multi-power complex distribution network fault location, without matrix multiplication and normalization process, is proposed in [10]. In order to avoid nonexistent or false alarms of fault information under a harsh environment, that requires fault location techniques having fault-tolerant, fault handling must be implemented under incomplete fault information. Reference [11] presents a method based on Bayesian analysis, using correlation of multi-phase fault information for fault-tolerant fault location.

The adaptability of the matrix algorithm for changes in network topology is poor. The algorithm requires a large amount of information and causes the phenomenon of storage redundancy. Therefore, research on the matrix algorithm with high adaptability, high fault tolerance and fast and accurate algorithm needs to be further carried on.

### ***3.2 Artificial Intelligence Algorithm***

The primary Artificial intelligence methods include the Genetic Algorithm, Particle Swarm Optimization, Neural Networks, and the Ant Colony Algorithm. The fault



location method based on the Genetic Algorithm with reliable fault-tolerant ability for distribution network is studied in [12]. A method based on the BPSO algorithm is proposed in [13], which has fast convergence rate, and can accurately locate the single-point and multi-point faults in a radial distribution network.

While such methods can still be able to accurately locate the fault section under the case of network topology changes, the real-time information uploaded is incomplete. But, other weaknesses are that model building is relatively complicated, the models are not perfect, and the positioning is inefficient, among others.

## **4 Fault Ranging**

### ***4.1 Injection Based Fault Ranging Method***

Injection methods for fault ranging mainly include: the S injection method, the single-ended injection method and port fault diagnostics, etc. The principle is that a special signal is injected into a post-fault system through the voltage transformer, and then the detected signal is used to locate the fault location. Paper [14] proposes the ‘DC open circuit, AC pursuit’ off-line fault location method based on the S injection method.

The current S injection method has a high investment cost and is greatly influenced by the wires’ distributed capacitance, grounding resistance and so on. Also as the robustness of the transition resistance is poor, further research is needed in this area.

### ***4.2 Traveling Wave Based Fault Ranging Method***

Compared with the impedance-based method, the advantages of the traveling wave method are not affected by system parameters, transition resistance, system operation mode and line loads. A new location method for distribution networks, based on mutation of the line mode traveling wave after a synchronous injection of a three-phase high-voltage pulse, is presented in [15]. A method of on-line fault ranging for small current grounding system based on HHT is proposed in [16]. The influences of wave velocity and line sag were eliminated based on improved HHT in [17]. The method of modulus maximum of wavelet transform is proposed to eliminate the noise and use of single speed method based on equivalent circuit is proposed to eliminate the influence of wave velocity discontinuity in [18].

But the traveling wave method requires expensive high-frequency sampling devices, and it is difficult to achieve adequate configuration. The detection of traveling waves and the reflected wave are not always not resolved, so practical applications are still problematic.

### ***4.3 Impedance Based Fault Ranging Method***

Fault ranging based on the impedance method requires only the substation outlet voltage and current as input. The performance of ten fault ranging techniques based on impedance has been compared and summarized in [19]. Paper [20] takes into account the feeder laterals, single or multi-phase load and dynamic nature of the load, as well as the proposed fault ranging method for radial distribution network based on fundamental components as measured from a line terminal. Moreover, the average range of accuracy is higher than that of the fault location method based on the reactive component method. Paper [21] presents the use of a synchronous phasor measurement unit (PMU) to achieve precise fault ranging in distribution networks, with ranging accuracy in the magnitude of less than 1 %.

However, because of the complexity and the variety of distribution network topology, employing the fault ranging algorithm based on impedance can produce many possible fault locations. How to eliminate so much uncertainty is worth further study.

### ***4.4 Intelligent Ranging Principle***

With the ongoing development of mathematical tools, some researchers apply the latest research results from related disciplines, such as expert systems, neural networks, fuzzy theory, simulated annealing, the optimization algorithm, pattern-recognition technology and wavelet analysis, to the fault location of power systems. Different intelligent ranging methods are proposed in [22], but these fault ranging methods are not mature enough yet to be further studied.

## **5 Summary and Outlook**

In terms of the current distribution network fault location techniques, one may summarize that: fault line selection techniques are relatively mature, but their reliability and sensitivity still need to be improved in the practical application; fault section location algorithms are rather more mature, but still need further study as regards the algorithm with fault tolerance and suitability, etc.; fault ranging is the most difficult aspect of fault location, and there is no good method to achieve accurate fault ranging of distribution networks.

For distribution network particularity, the fault location algorithm based on single terminal is difficult to achieve a balance between accuracy positioning and economic. Besides, a combination of fault location technology and the existing distribution network feeder automation to achieve effective and accurate fault location is a worthy field of study. Finally, research on PMU-based fault location in distribution networks has made some progress, and how to apply the powerful function of PMU for fault location accurately is a new field also worth studying

**Acknowledgment** This research has been supported by the Power Dispatching Control Center of Guizhou Power Grid Corporation (the Study of a variety of Electricity Price Mechanism) (gzdwDD[2014]0301FS048-K)

## References

1. Dong X, Huang S et al (2012) Self-healing control technology for distribution system. *Autom Electr Power Syst* 18:17–21
2. Qing S (2012) A new method of fault line selection for small current grounding system. KunMing University
3. Zhao F, Yan T, Sun L (2007) Zero sequence transient reactive power for a single-phase-earth feeder on non-solid distribution. *Relay* s1:59–62
4. Zeng X, Yin X et al (2001) Study for negative sequence current distributing and ground fault protection in middle voltage power systems. *Proc CSEE* 06:85–90
5. Xue Y, Feng Z et al (2003) Earth fault protection in non-solidly earthed network based on transient zero sequence current comparison. *Autom Electr Power Syst* 09:48–53
6. Zhang W, Zhang B, Hu H et al (2009) Application of wavelet packet analysis in phase-to-ground fault detection of distribution networks. *Autom Electr Power Syst* 23:60–64
7. San Z, Pan Z, Ding L, Zhang H (1997) The principle and application of “s injection method” for faulty line selection. *Electr Power* 06:44–45
8. Wang F, Kang Y (2008) Pulse signal injection based faulty line detection for small current neutral grounding system. *Power Syst Technol* 15:90–93
9. Liu J, Cheng H, Dong H, Cai J (2002) Fault section identification and load balancing of distribution network. *Autom Electr Power Syst* 22:34–38
10. Wei Z, He H, Zheng Y (2001) A novel algorithm for fault location in power distribution network. *Autom Electr Power Syst* 14:48–50
11. Liu J, Dong X, Chen X et al (2012) Robust fault isolation and restoration for distribution systems. *Power Syst Technol* 01:253–257
12. Du H, Sun Y et al (2000) Fault section diagnosis and isolation of distribution networks based on genetic algorithm. *Power Syst Technol* 05:52–55
13. Li C, He Z et al (2009) Fault location for radialized distribution networks based on BPSO algorithm. *Power Syst Protect Control* 07:35–39
14. Zhang H, Pan Z et al (2004) Injecting current based method for fault location in neutral isolated power system. *Autom Electr Power Syst* 03:64–66
15. Zhou C, Shu Q, Han X (2014) A single-phase earth fault location scheme for distribution network based on mutation of line mode traveling wave. *Power Syst Technol* 07:1973–1978
16. Wang J, Ju M, Xu Z, Moran Ju (2014) An HHT method of fault line selection and online fault location in neutral point ineffectively grounded power system. *Electr Measure Instrum* 15:48–54
17. Zhang Y, Su H (2015) New method of fault location in small current grounding system. *Proc CSU-EPSA* 02:32–38
18. Ding J, Yuan Z (2008) Application of traveling wave fault location for the small neutral earthed system. *Electr Measure Instrum* 06:15–19
19. Mora-Florez J, Melendez J, Garrillo-Caicedo G (2008) Comparison of impedance based fault location methods for power distribution systems. *Electr Power Syst Res* 78(4):657–666
20. Sachdev MS, Das R, Sidhu TS (1997) Determining locations of faults in distribution systems. In: Conference Publ no. 434, pp 188–191. doi:10.1049/cp:19970060
21. Ren J, Venkata SS, Sortomme E (2014) An accurate synchrophasor based fault location method for emerging distribution systems 297–298. doi:10.1109/TPWRD.2013.2288006
22. Zhang Z, Lü Y, Wang J et al (2010) A new two-terminal traveling wave fault location method based on wavelet transform. *Power Syst Technol* 34(1):203–207

# Numerical Simulation of Flow Field of a Centrifugal Compressor with a High Pressure Ratio

Zhipeng Xu, Wei Shen, Yong Zhang and Longbo Gao

**Abstract** In order to study the characteristics of a type of centrifugal compressor with a high pressure ratio and the distribution of the flow field parameters in the design points, CFX software was used to simulate its flow field. According to the results, the pressure ratio and the efficiency of the compressor are high at high RPMS, and the range of mass flow rate is wide at lower RPMS. So the capacity to adapt different working conditions of this compressor is good. At the aspect of the flow field in the design points, the distribution of the overall flow field parameters is homogeneous, but the shock waves exit in the first stator entrance, making the passage narrower and bring much energy loss, which is the one of the reasons to decline the compressor efficiency.

**Keywords** Centrifugal compressor · High pressure ratio · Characteristics · Flow field · Simulation

## 1 Introduction

The centrifugal compressor is widely used because of its advantages such as higher pressure ratio of single stage, good capacity to adapt the conditions with small mass rate. However, it is much more difficult to design and analyze the centrifugal compressor because of the complex shape of the blade, supersonic flow, the shock waves, and so on. With the development of the computer and computational fluid dynamics (CFD) [1–4], the numerical simulation technique is more widely used in the design and analysis stages, which can both save the expenses of tests and shorten the development cycle.

The way to pressurizing by a single centrifugal impeller is used in the design of a type of centrifugal compressor, and the value of the pressure ratio at the design

---

Z. Xu (✉) · W. Shen · Y. Zhang · L. Gao  
Naval Aeronautical and Astronautical University, Yantai 264001, China  
e-mail: 1071216554@qq.com

RPMS is bigger than 8 with high efficiency [3, 5]. In order to study the compressor characteristics and the distribution of the flow field parameters in the design points, simulation is made of its fluid flow [6].

## 2 The Building of the Model

### 2.1 The Building of the Model

This centrifugal compressor mainly comes in three parts, the single centrifugal impeller with splitters, the first stator, and the second stator [6–8]. Bladegen software is used to anti-design the whole compressor model according to the structure dimension and blade information, as shown in Figs. 1, 2 and 3.

**Fig. 1** The model of the impeller

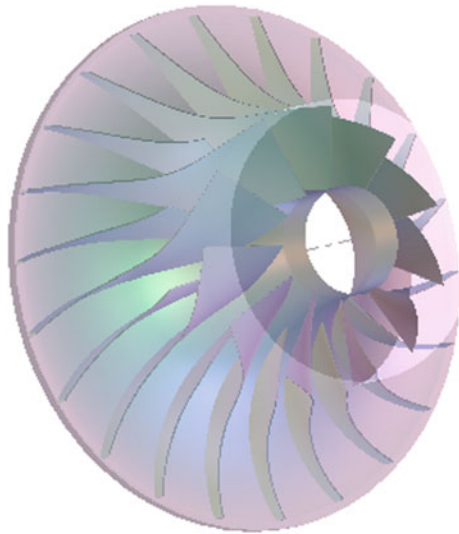


**Fig. 2** The model of the first stator

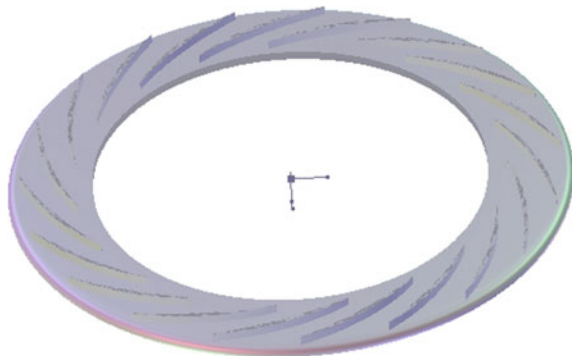
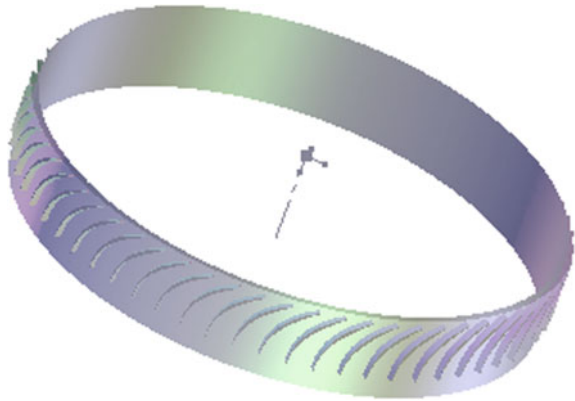


**Fig. 3** The model of the second stator



### 2.2 Mesh Generation

The model is imported into the software of Turbogrid, and then the mesh can be quickly generated. Based on the mesh [9], the standard atmospheric conditions are set. Next, numerical simulations are made of different flow field at different RPMS by CFX software.

## 3 Results Analysis

### 3.1 Characteristic Analysis

Different flow field of design RPMS of 100, 90, 80, and 70 % are simulated, and then the characteristic curves of pressure ratio-mass rate and isen efficiency-mass rate can be obtained as shown in Figs. 4 and 5 (The mass rate has been non-dimensionalized).

**Fig. 4** The characteristic curves of pressure ratio-mass rate

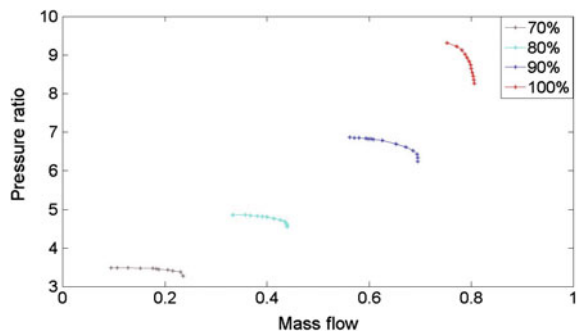
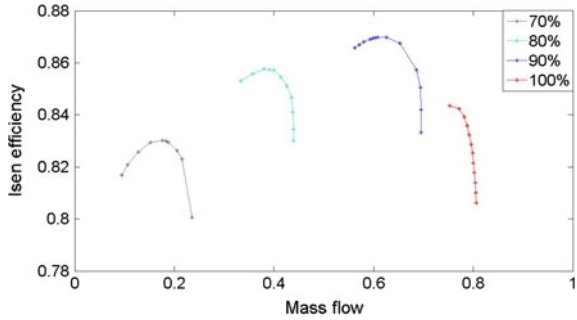


**Fig. 5** The characteristic curves of isen efficiency-mass rate



As can be seen from Fig. 4, the characteristic curves of pressure ratio-mass rate become steeper with the increase of the RPMS. Especially at the design RPMS, the range of mass rate in the steady operation conditions reduces to approximately 0.1 kg/s. At aspect of the capacity to pressurize, the maximum of p-ratio reaches 9.2. The calculated values is generally greater than the measured ones, and in the design points, the deviation between them is 5.6 %, because the influence of the blade roughness and the tip clearance has not been fully considered during the simulation.

As can be seen from Fig. 5, the ranking results of the four RPMS from highest to lowest by the isen efficiency are design RPMS of 90, 80, 100, 70 %. The calculated efficiency value is generally greater than 80 %, and it reaches 84.5 % in the design points greater than the measured value at 4.3 %.

Based on above analysis, the pressure ratio and the efficiency of the compressor are high at high RPMS, and the range of the mass flow rate is wide at lower RPMS. So the capacity to adapt different working conditions of this compressor is good.

### 3.2 Analysis of the Fluid Field in the Design Points

As can be seen from Figs. 6 and 7, the distribution of the Mach number and the static pressure in the flow field in the design points is well uniform. There is respectively a range of high speed and low speed at the leading edge and the trailing edge of the impellor blades; the value of the velocity of the flow is up to supersonic when entering the channel of the first stator, with a shock waves and a range of low speed at the leading edge of the blades. The velocity gradually declines along with the flow in the first stator. The value of the velocity of the fluid reduces to subsonic when entering the channel of the second stator, and it further declines along with the flow. There is a range of low speed on the leading edge obviously.

As can be seen from Fig. 8, the attack angle of the velocity vector of the flow and the distribution of the relative velocity are basically rational. The splitter well diminishes the flow separation at the back end of high-load blade. However, the

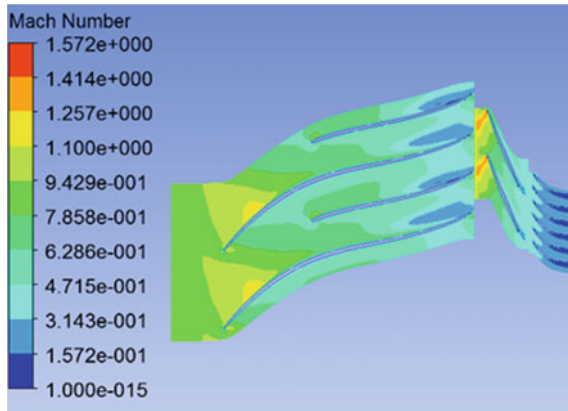


Fig. 6 The distribution of the Mach number of the whole compressor

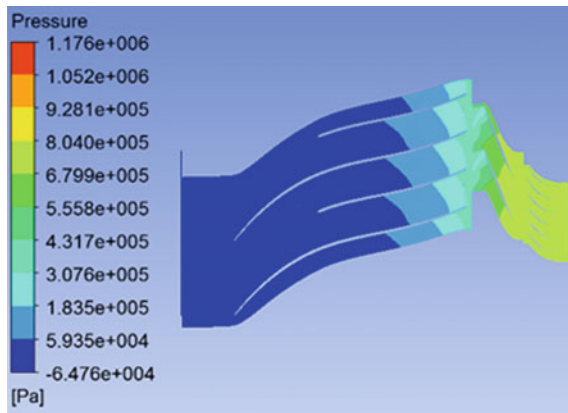


Fig. 7 The distribution of the static pressure of the whole compressor

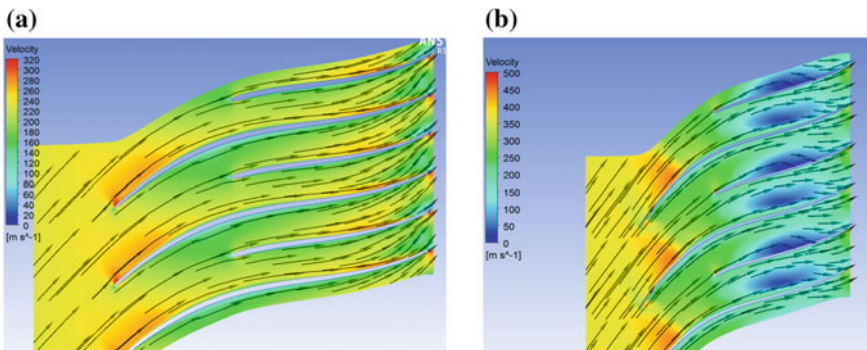
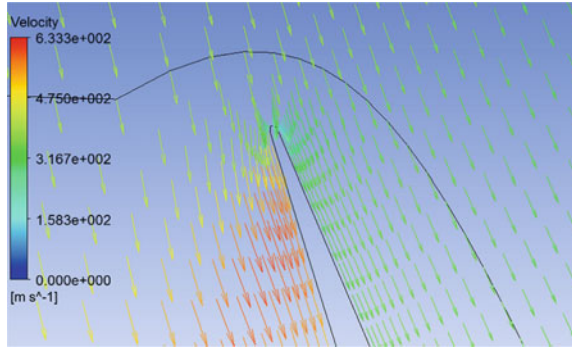


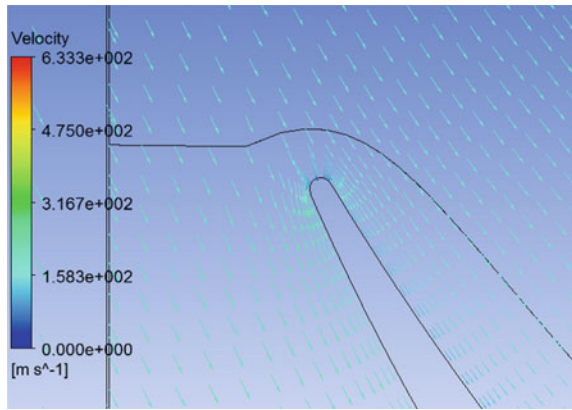
Fig. 8 The distribution of the relative velocity of the impeller. **a** 20 % of the height of blade. **b** 80 % of the height of blade



**Fig. 9** The distribution of the velocity at the leading edge of the first stator blade



**Fig. 10** The distribution of the velocity at the leading edge

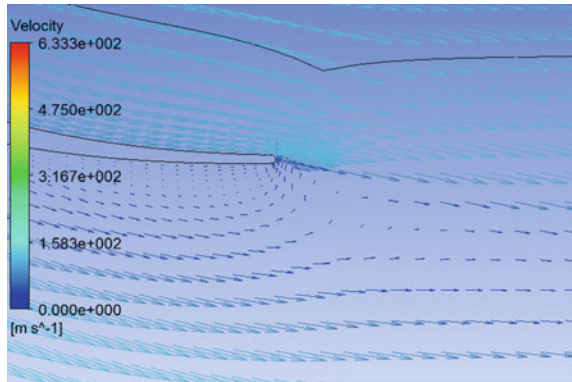


trend of flow separation at 80 % of the height of blade becomes obvious, bringing much flow loss and limiting the range of steady working.

The type of blade of the first stator is straight blade. As can be seen from Fig. 9, the value of the velocity of the fluid is up to supersonic when entering the channel of the first stator. Because the inlet angle of the leading edge is a little inappropriate, the flow separates slightly, which narrows down the channel and forms a range of high speed and low-pressure, bring much flow loss. It is also one of the reasons for the reduce of efficiency.

As can be seen from Figs. 10 and 11, the value of the velocity of the fluid has reduced to subsonic when entering the channel of the second stator. Because the inlet angle of the leading edge is well appropriate, the flow does not separate. At the trailing edge of the blade, the two streams with different velocity mix. Although there exists swirling flow, the flow loss caused is little because the speed is low.

**Fig. 11** The distribution of the velocity at the trailing edge



## 4 Conclusions

Numerical simulations of the different flow field of design RPMS of 100, 90, 80, and 70 % are made by CFX software. And some conclusions have been given below.

- (1) The pressure ratio and the efficiency of the compressor are high at high RPMS, and the range of mass flow rate is wide at lower RPMS. So the capacity to adapt different working conditions of this compressor is good.
- (2) The distribution of the Mach number and the static pressure in the flow field in the design points is well uniform. There is respectively a range of high speed and low speed at the leading edge and the trailing edge of the impellor blades. Because the inlet angle of the leading edge is a little inappropriate, the flow separates slightly, which narrows down the channel and forms a range of high speed and low-pressure, bring much flow loss.
- (3) In order to improve the capacity of the compressor, some measures can be done, such as adjusting of the incidence angle, improvement of the blade profile and so on.

## References

1. Hirsch CH, Kang S, Pointel G (1996) A numerically supported investigation of the 3D flow in centrifugal impeller. Part I and II. ASME-Papers 96-GT-151 and 96-GT-152
2. Acosta AJ, Bowerman RD (1957) A experimental study of centrifugal pump impeller. Trans ASMME 79:1821–1839
3. Krain H (1988) Swirling impeller flow. ASME J Turbomach
4. Versteeg HK, Malalasekera W (1995) An introduction to computational fluid dynamics: the finite volume method. Wiley, New York
5. Japikse D, Marscher WD, Furst RB (1997) Centrifugal pump design and performance. Concepts ETI, White River Junction, Vt, USA

6. Gui L, Gu C, Chang H (1989) Influences of splitter blades on the centrifugal fan performances. In: ASME, the gas turbine and aero engine congress and exposition, Torpnto. 89 GT33
7. Miyamoto H, Nakashima Y (1992) Effects of splitter blades on the flows and characteristics in centrifugal impeller. *JSME Int Ser* 35(2):238–246
8. Ibaraki S, Matsuo T, Kuma H et al (2003) Aerodynamics of a transonic centrifugal compressor impeller. *ASME Journal of Turbomachinery* 125(2):346–351
9. Epstein AH (2003) Millimeter-scale, MEMS Gas Turbine Engines. In: Atlanta: Proceedings of ASME Turbo Expo 2003, No.GT-2003-38866

# Render Synthetic Objects with Background Image According to Image-Based Lighting

Binling Luo, Shuting Cai, Shaojia Wen and Daolin Hu

**Abstract** Image-based lighting (IBL) technique helps people integrate synthetic object into real-world environment. The general IBL method renders object using the captured omnidirectional high dynamic range (HDR) image as lighting condition. This paper extends the general IBL technique to employing single-view background image in HDR format to produce environment light. This idea is different from the general IBL technique which limits the input in omnidirectional light probe image. Besides, the proposed method can modify the background image slightly for special purpose based on texture transplanting. The created texture is saved in database; when people wish to modify the background image, they call texture from database and transfer it to the target surface. The method provided in this paper can produce visual effect just as real objects would.

**Keywords** High dynamic range image · Image-based lighting · Local scene · Texture transplanting

## 1 Introduction

Adding synthetic objects in a background image is more and more popular in visual effects domains. A perfect visual effect is based on proper light simulation between the objects and their ambient. Image-based lighting (IBL) technique employs high dynamic range (HDR) images as light sources to lit synthetic objects in visual

---

B. Luo (✉) · S. Cai · S. Wen · D. Hu  
School of Automation, Guangdong University of Technology, Guangzhou 510006, China  
e-mail: 530039473@qq.com

S. Cai  
e-mail: shutingcai@gdut.edu.cn

S. Wen  
e-mail: 429641744@qq.com

D. Hu  
e-mail: 1204408659@qq.com

environment, and they look like illuminated by real-world light. The basic frame of IBL technique was proposed by Debevec [1–2]: to begin with, he captured real-world illumination as an omnidirectional HDR image; in the next step, he mapped the light probe image onto the inner surfaces of the a large box to reconstruct light source; at last, he added the synthetic object to the environment and simulated the light from the environment to lit synthetic object.

In most visual effects domains, people wish to take a real-world image as background image. However, most available background image are captured by single-view instead of omnidirection, which do not conform to the set up condition of the general IBL technique. At this point, people cannot directly employ the general IBL technique. As a solution, we provide a method which projects the single-view image to the inner surfaces of a hollow ball and repeats the image until it covers the whole surface to simulate the consistent light environment. This method is suited for an outdoor image which was taken at noon or on a cloudy day when the solar radiation was evenly distributed in all directions. In this condition, the light information can be copied from the single-view image to all directions to develop light environment since all directions share similar radiation distribution. This approximately simplifies IBL method so that everyone can carry out IBL with a traditional cameral at anytime and anywhere, if people want to modify the background image slightly for special purpose (such as to improve visual interest). The general IBL technique does not provide this function, and we also propose a method to modify the background image slightly based on IBL. In our method, a texture image is computed and then it was transferred to the target surface in background image to modify the background.

The main advantages of our methods are: (1) it copy lights information from a single-view image to all directions to develop light environment, so people do not have to set up IBL from an omnidirection image which needs special drivers and skill; (2) it can modify the background image for special purpose by texture transplanting; (3) it uses texture image to develop local scene [2] to support synthetic objects, which can keep the level of realism.

This paper is organized as follows. Section 1 gives a brief instruction on general IBL technique; in Sect. 2, we discuss the extension IBL method in detail; we present the experiment result in Sect. 3; the last section is the conclusion of our work.

## 2 Our Proposed Method

We extend the general IBL technique to use single-view background image to produce environment light. Besides, it provides a method based on texture transplanting to modify the background. To begin with, we project the single-view background image to the inner surface of a hollow ball, then copy and paste the background image until they cover the whole surface of the hollow ball. This method is suited for outdoor image which is taken in the condition that the solar

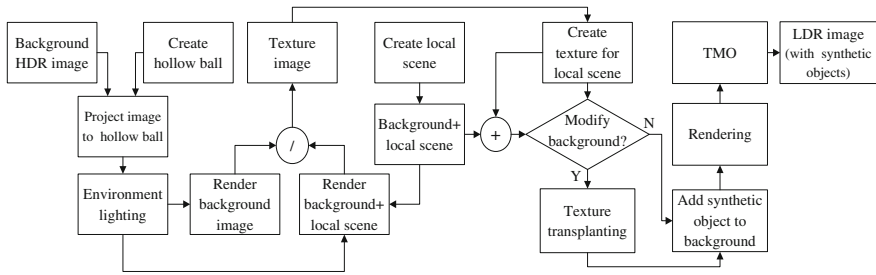


Fig. 1 The framework of our method

radiation was evenly distributed in all directions; so the method can copy light information from one direction to all directions. HDR image records the correct lighting information in real world. So when using the hollow ball mapped with HDR image as lighting model, we can approximate that the environment light comes from the same direction as our hollow ball. Then we created a local scene [2] together with synthetic objects in the background, local scene is used to support synthetic objects which will produce interacted effect with synthetic objects, so it will show shadows and reflect lights which are caused by synthetic objects. Local scene can improve the realism of the scene. And then a texture is computed for the local scene to make local scene dissolve in the background. If people want to modify the background image, they can employ texture transplanting which will be discussed in Sect. 2.3. The framework is showed in Fig. 1.

### 2.1 Create Hollow Ball

As mentioned in Sect. 1, in IBL technique, Paul Debevec projected the light probe image to the inner surfaces of a large box to simulate lighting environment, the position of the light probe image within box was measured manually. As it is known, the real scene is surrounded by an infinite sphere, so we prefer to use a hollow ball to reconstruct the surrounded light instead. The hollow ball should be big enough to envelop the synthetic object, and the surface is set to white diffuse material.

### 2.2 Project Background Image onto the Inner Surface of the Hollow Ball

The initial condition in our method is employing the single-view background image in HDR format to recreate the physical lighting conditions. We first project the background image onto the inner surface of the hollow ball in planar mode, see

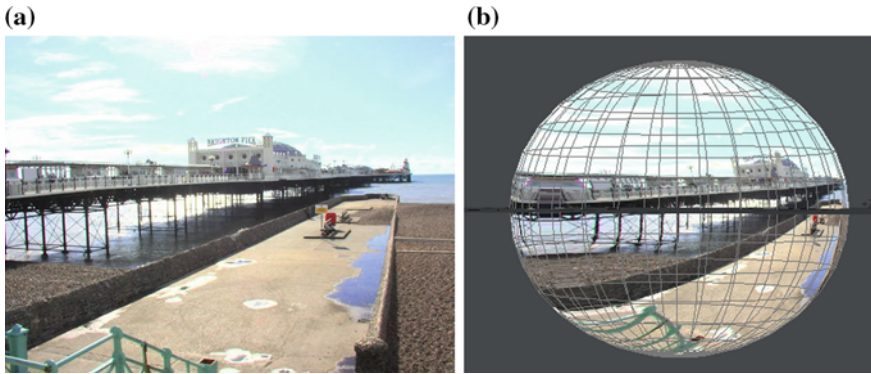


**Fig. 2** Project background image to hollow ball. **a** Background image. **b** Background image is projected to hollow ball

Fig. 2, this project function is provided by light wave [4]; we repeat copy of the background image and paste them along Z axis until they cover the whole surface of the hollow ball. The goal is to copy light information from one direction to all directions as the solar radiation was evenly distributed in all directions. At this point, the light from the ball would have the similar directions as it would have in the real environment. The hollow ball is treated as a map of light.

### 2.3 Create Local Scene

Local scene is used to support the synthetic objects in IBL environment. It will produce interacted effect with synthetic objects, and can show shadows and reflect lights which are caused by synthetic objects. In common case, a local scene is a flat surface, and its optical characteristic should be known since it participates in the illumination solution. In our method, the optical characteristic of the local scene is approximated according to background image. We do not strictly require the geometry type of the local scene, just a simple flat surface with suitable size to support the synthetic objects will be acceptable.

Figure 3 shows an example of local scene. From Fig. 3, we can find that unlike background, the local scene contains only one color and lacks color variations, so the local scene is distinguished from background obviously. As how to dissolve the local scene in background image and the solution will be discussed in the following section.

**Fig. 3** Create local scene

## 2.4 Compute Texture for Local Scene

IBL has special demands on local scene, it must possess accurate color varying as well as optical characters. Otherwise, the local scene profile will distinguish obviously in background, as shown in Fig. 3. As a solution, Reinhard [3] provided a method based on texture projecting to improve the quality. He rendered the background image at first, and then set the local scene to diffuse surface with white color and rendered the image of local scene in background. He divided the background image by the image of local scene in background to produce the texture image. The process is shown in Eq. (1):

$$I_{\text{texture}} = I_{\text{background}} / I_{\text{background} + \text{local\_scene}} \quad (1)$$

where  $I_{\text{texture}}$  denotes the appearance of the texture image in light system,  $I_{\text{background}}$  is the background image in light system, and  $I_{\text{background} + \text{local\_scene}}$  represents the image of local scene in background within light system. Finally, he mapped the local scene with the produced texture image.

Our work is based on that of Paul Debevec's but more robust than it. On one hand, in Paul Debevec's method, the geometry of the local scene should be known so as to make it fit the background. However, to gain geometry information is not an easy work. In our method, we do not strictly require the geometry of the local scene, just a simple flat surface at any shape is acceptable. After computing the texture using (1), we copy the texture areas and paste all of them to the local scene with planar mode until the whole surface of the local scene is covered by the texture. In this way, people do not have to know the geometry of the local scene accurately, and can make it fit the background. On the other hand, our method can transplant the texture from a source surface to a target surface to modify the background. We first place the local scene on a source surface in background to calculate the texture image using (1), texture image have blank space which we cut off (supported in most plot tools) to produce a pure texture image. And then, the local scene is moved to the target surface in the background; then project the pure



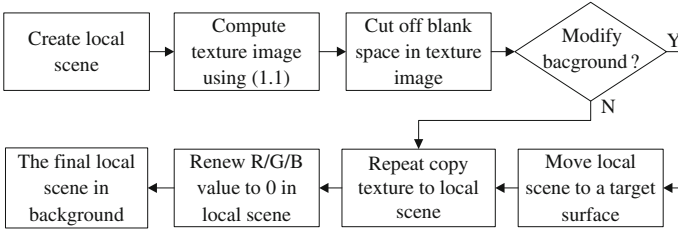


**Fig. 4** Compute texture for local scene

texture to the local scene in planar mode and repeat the texture until they cover the whole surfaces of the local scene. Project equation is

$$I_{f\_local\_scene} = I_{local\_scene} + I_{texture} \quad (2)$$

where  $I_{f\_local\_scene}$  is the final local scene in background image within lighting system,  $I_{local\_scene}$  is the original diffuse white local scene in lighting system,  $I_{texture}$  is the computed texture for the local scene. As mentioned in the last section, in order to gain a diffused white surface, we set the R/G/B value to 255 at the beginning, now we have to renew them to 0. The process is showed in Fig. 4.

## 2.5 Add Synthetic Object

In this section, we create four balls and place them under the local scene

1. Rubber ball: R/G/B (200/40/40), Diffuse (100 %), Specularity (20 %), Glossiness (50 %), Reflection (0 %), Transparency (0 %).
2. Rock ball: R/G/B (50/50/50), Diffuse (100 %), Specularity (20 %), Glossiness (50 %), Reflection (0 %), Transparency (0 %).
3. Metal ball: R/G/B (20/50/90), Diffuse (54 %), Specularity (100 %), Glossiness (15 %), Reflection (18 %), Transparency (0 %).
4. Glass ball: R/G/B (60/255/255), Diffuse (60 %), Specularity (60 %), Glossiness (80 %), Reflection (20 %), Transparency (70 %).

We can learn material characters from [4] or buy them from the third party.

## 2.6 Render Synthetic Object Based on Ray Tracing

In this section, we discuss rendering process. In general, render algorithm calculates the total light arrived at each point on object surface. Debevec [2] proposed a ray-tracing method for IBL. In which,  $R$  is a ray that must be traced, and it hits a

surface in the scene,  $L$  represents the pixel color in the scene rendering. There are three cases for a ray

A ray  $R$  hits IBL environment: A ray  $R$  hits IBL environment instead of synthetic object during its travel. In this case, the color from HDR background image is used as the pixel color  $L$ .

A ray  $R$  hits surface with specular property: In this case, A ray  $R$  is reflected or refracted from the contacted surface, and the travel type is decided by material properties [5, 6]. In this case,  $r$  is calculated as a reflected or refracted vector, and then,  $r$  is multiplied by the pixel color of the synthetic object to calculate  $L$ .

A ray  $R$  hits surface with diffuse property: In this case, lighting intensity  $E$  on object surface point  $x$  is calculate as

$$E(x, n) \approx \frac{1}{k} \sum_{i=0}^{k-1} r_i \cos \theta_i \quad (3)$$

where  $k$  is the total number of the reflected ray  $r_i$  emitted from object surface point  $x$ . In our experiment, we employ ray trace reflection and refraction algorithms since they allow very fast and good quality rendering.

## 2.7 Tone Map Image

Since we use HDR image to lit synthetic object at the beginning, the rendered image has to be tone mapped into LDR image so as to show it on traditional displays. Any tone map operator introduced in [5] can be used in this step. In our experiment, we employ Bilateral filter TMO which is proposed by Durand and Dorsey [7].

## 3 Experiment and Discussion

We employ Light Wave V11.6 as well as MATLAB R2012b on an Intel Core i5-3230M CPU @ 2.6 GHz, 4.00 GB RAM, win7 system to perform our experiment. Light Wave is used to create synthetic object and render the scene and MATLAB is used for image processing.

In Fig. 5a, is an IBL image without local scene, we find that synthetic objects can reflect surrounding environment (see glass ball). However, all balls are somewhat strange since there are no ball shadow casts on their supported surface, the balls appear to float above the ground. In Fig. 5b, a local scene is created to support the synthetic object and the scene exhibits appropriate interaction, and people can see the shadow on the snowfield as well as on the surface of the ball

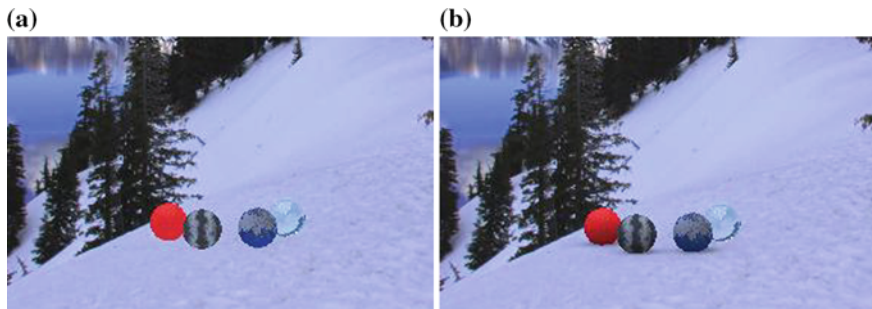


**Fig. 5** IBL image. **a** IBL image without local scene. **b** IBL image with local scene

where it gets in contact with the snowfield. The local scene improves the level of realism and visual interest of the scene.

Besides, comparing to Paul Debevec's algorithm, our method can modify background image by texture transplanting, and it does not require accurate geometric information for the local scene, shown in Fig. 6a. There is a puddle of water on the location of the synthetic object in background, and people wish to remove this puddle of water from background and place the synthetic object under the ground, the method instructed in Sect. 2 can realize this requirement. Experiment result is exhibited as shown Fig. 6b. We can see that the water has been removed and there is shadow on the ground. It produces visual effect just as real objects would.

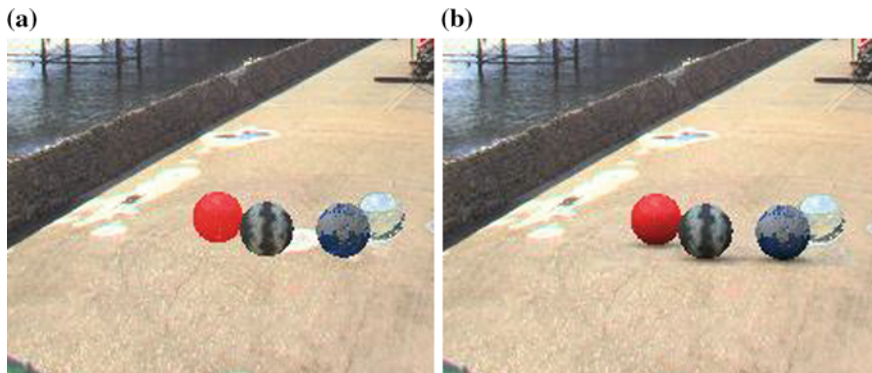


**Fig. 6** Modify background image based on texture transplanting. **a** Rendering with the original background. **b** Rendering with the modified background

## 4 Conclusion

In this paper, we provide an IBL method that uses single-view background image in HDR format to reproduce environment light. Besides, it modifies the background image for personal preference thanks to texture transplanting. This proposed method is an extensive use of the general IBL technique. We hoped our work will be useful for further assisting artists and visual effect study such as light-based graphics [8].

## References

1. Debevec P (2002) Image-based lighting. *IEEE Comput Graph Appl* 22(2):26–34
2. Debevec P (1998) Rendering synthetic objects into real scenes: bridging traditional and image-based graphics with global illumination and high dynamic range photography. In: SIGGRAPH '98: Proceedings of the 25th annual conference on computer graphics and interactive techniques. ACM, New York, NY, pp 189–198
3. Reinhard E, Ward G, Pattanaik S, Debevec P, Heidrich W, Myszkowski K (2010) Image-based lighting. *High dynamic range imaging*, 2nd edn. Morgan Kaufmann, Burlington, pp 501–593
4. Ablan D (2004) Texture. *Inside lightwave V8*. New Riders Press, Upper Saddle River, pp 210–258
5. Banterle F, Artusi A, Debattista K, Chalmers A (2011) Image-based lighting. *Advanced high dynamic range imaging*. Natick, A K Peters, pp 149–179
6. Blinn JF (1976) Texture and reflection in computer generated images. *Comm ACM* 19 (10):542–547
7. Durand F, Dorsey J (2002) Fast bilateral filtering for the display of high dynamic range images. *ACM Trans Graph* 21(3):257–266
8. King SY, Kim KY, Soh BS, Yang G (2006) Vibrotactile rendering for simulating virtual environment in a mobile game. *IEEE Trans Consum Electron* 52(4)

# Reliability Evaluation of Distribution Systems Incorporating Distributed Generators Using Monte Carlo Simulation

Zhenpeng Wu and Aoying Ji

**Abstract** To evaluate the reliability of distribution network containing distributed generations (DGs), at first the stochastic characteristics of power output of wind power generation and microturbine (MT) are researched, and a reliability model of hybrid generation consisting of DG is built. The Monte Carlo simulation (MCS) algorithm is applied to a modified main feeder of RBTS Bus 6 distribution network. The wind turbine (WT) generator is an example to establish the reliability of distributed power intermittent assessment model. Finally, the reliability of RBTS Bus 6 is evaluated by the built model and the proposed algorithm. This evaluation results show that the penetration of DG can improve the reliability indices of the distribution network.

**Keywords** Reliability evaluation · Monte Carlo simulation · Distributed generation

## 1 Introduction

In recent years, with the development of distributed generation (DG) technology and national energy saving and emission reduction policies, DG supply has been widely used in power system, the access of distributed power supply makes the power system more efficient and flexible [1, 2].

Distributed generation due to the flexible installation location near the load is of positive significance to alleviate the grid peak power shortage [3]. Many power

---

Z. Wu (✉)  
Guizhou University, Huaxi, Guiyang, China  
e-mail: 472779434@qq.com

A. Ji (✉)  
State Grid Lishui Electric Power Company, Lishui, Zhejiang, China  
e-mail: 843024272@qq.com

energy experts believe that the combination of power grid and DG is the main way to save investment, reduce energy consumption, and improve the reliability and flexibility of power system, it is the development direction of electric power industry in this century. However, the access of DG changes the structure and operation mode of the traditional distribution network, which makes the distribution network from the traditional single power supply network to multi power and the user's interconnection [4, 5]. When the components in the system failure, the distribution network may appear in the isolated island operation mode, continue to load power supply point. Compared with the traditional power supply, the DG output power is more random, so the reliability evaluation model and the method of the distribution network must be changed [6].

On the basis of studying the reliability assessment model, method, and DG technology of the traditional distribution network, the reliability of distribution network with DG is evaluated by using the Monte Carlo simulation (MCS) algorithm. The reliability of RBTS Bus 6 is evaluated by the built model and the proposed algorithm, the validity of the method is verified. This evaluation results show that the penetration of DG can improve the reliability indices of the distribution network.

## 2 DG Model and Load Model

Distributed power according to its power generation energy is divided into two categories: one is the use of intermittent energy DG, including wind, solar energy, geothermal energy, ocean energy, and other forms of power generation; and the other is the use of nonintermittent energy DG, mainly including internal combustion engine, heat and power, micro gas turbine, fuel cell, and other power generation form. In this paper, wind turbine (WT) generator and microturbine (MT) are used as the research objects.

### 2.1 Intermittent Energy DG

Taking the WT as an example, the model of intermittent DG is established. Existing research that the wind speed has statistical properties is generally a positive skew distribution used, to describe the wind speed distribution function. The Weibull distribution and normal distribution are widely used. If the wind speed approximation is described by using Weibull distribution, most of the time, wind speed is located between the cut in the wind speed and the rated wind speed; the relationship between the output power and wind velocity can be expressed by the following equation [7]:

$$f(P_W) = \frac{K}{bC} \left( \frac{P_W - a}{bC} \right)^{K-1} e^{\left[ -\left( \frac{P_W - a}{bC} \right)^K \right]} \tag{1}$$

where  $K$  and  $C$  are the scale and shape parameters of Weibull distribution, and  $a = P_r v_{ci} / (v_{ci} - v_r)$ ,  $b = P_r / (v_r - v_{ci})$ ,  $P_r$  is the rated output power of WT,  $v_r$  and  $v_{ci}$  the cut in the wind speed and the rated wind speed.

If the wind speed is described by normal distribution, therefore, it can be expressed by the following equation [7]:

$$f(P_W) = \frac{1}{\sqrt{2\pi}\sigma_v b} e^{\left[ -\frac{(P_W - a - b\mu_v)^2}{2(b\sigma_v)^2} \right]} \tag{2}$$

where  $\mu_v$  and  $\sigma_v$  are the mean and variance of wind speed, respectively.

### 2.2 Nonintermittent Energy DG

Taking the MT as an example, the reliability assessment model of nonintermittent distributed power supply is established. It consists of  $n$  sets of micro gas turbine generator group and the normal operation of the units obeys the binomial distribution. The output power of MTs can be expressed by the following equation [7]:

$$P\{P_d = kP_r\} = C_n^k p^k q^{n-k} P_r, \quad k = 0, 1, 2, \dots, n \tag{3}$$

where  $n$  is the total number of MTs,  $q$  is the forced outage rate of MTs and  $q = 1 - p$ , and  $P_r$  is the rated output power of MTs.

### 2.3 Load Model

In a lot of power companies, the detailed timing load consumption data is usually not accurate. The method of building a time-varying load model is a method to analyze the load characteristics of individual users and combine with the annual peak load to produce a load model which is based on the hourly variation. Using statistical data provided by the power sector and typical daily load, monthly load, and annual load, the load value of each load point is calculated by using the following equation:

$$L(t) = L_y P_w P_d P_h(t) \tag{4}$$

where  $L_y$  is the annual peak load,  $P_w$  is the week load percentage of annual peak load,  $P_d$  is the percentage of daily load to the week peak load, and  $P_h$  is the percentage of hourly load of day peak load.

### 3 Monte Carlo Simulation

#### 3.1 The Conditions of Simulation

DG uses uninterruptible power island operation mode, when the fault occurs, if the DG's capacity is greater than the load demand, the island operation can be carried out. If the DG's capacity is less than the load demand, it takes the load shedding strategy. According to the priority of cutting load, the load level is removed from the lowest load until the power constraint is met.

Only consider the single fault model system.

#### 3.2 Simulation Procedure

1. Read the data and initialize it to form a load level of 8760 h. Set the number of simulation years, and set up the simulation time.
2. Down times randomly for the system components. Time to failure (TTF) is the duration that would take the component to fail. This time is predicted randomly by (5) [6].

$$\text{TTF} = -\frac{1}{\lambda_i} \ln U_i \quad (5)$$

3. Time to repair (TTR) is the time required to repair or replace a failed component. Also, this time is predicted randomly by (6) [6].

$$\text{TTR} = -\frac{1}{\mu} \ln U_i \quad (6)$$

where  $\lambda$  and  $\mu$  are failure and restoration rates of system component, respectively.  $U_i$  is a uniformly distributed random number.

4. According to the system structure, the load points are determined by the components. Determine whether there can be a complex point of continuous power supply by DG island operation.
5. During the period of the isolated island operation, determine the output power of DG, meet the operation mode of island, and calculate the index of each load point.
6. Judge the total simulation time to meet the conditions and then calculate the reliability index of the system.



### 3.3 Reliability Indices

Mostly, forced interruptions in power service are included in reliability evaluation. These interruptions occur due to the failure of network components. In this study, some common indices are used to evaluate the reliability of power networks. These include SAIFI, SAIDI, and ASAI. These indices can be calculated from the reliability indices calculated above.

## 4 Case Study

Many distribution network reliability studies reported in the literature have used the IEEE-BRTS Bus4 or Bus6. These networks offer the information needed to conduct a reliability study. In this study, a modified main feeder of R BTS Bus 6 is used. The system is shown in Fig. 1. Set simulation time for 1000 years. The peak loads of island 1 and island 2 are 3.6 and 4.5 MW, respectively. The rated output power of WTs is 1 MW, the rated velocity of WTs is 14 m/s, the cut-in velocity of WTs is 4 m/s, and the cut-off velocity of WTs is 4 m/s. The failure rate and average repair time of WTs are 0.22 f/year and 70 h, respectively. The rated output power of MTs is 1 MW, the failure rate and average repair time of MGTs are 0.18 f/year and 12 h, respectively. The distributed power supply is connected to it as shown in Fig. 1, when the fault occurs, the island 1 and the island 2 can be run independently.

The reliability evaluation of distribution network with DGs is carried out according to the MCS algorithm:

- Case1: without any DG.
- Case2: install three sets of WTs in island 1 and island 2.
- Case3: install three sets of MTs in island 1 and island 2.

The reliability indices of five typical load points are shown in Figs. 2, 3, and 4 and Tables 1, 2, and 3, 4.

The following table is the reliability index of the system under three cases.

- From the results of reliability index, it can be seen that the failure rate of the load point can be reduced, and the reliability of the system can be improved.
- Compared with DG and no DG case, the access of DG only has effect on the reliability of the load point of the island, and has no effect on the reliability of the load point outside the island. By improving the failure rate and outage time of the load points in the island, the reliability index of the system SAIDI and ASAI were improved.
- Compared with case 2 and case 3, due to the uncertainty and randomness of the intermittent DG output, the same capacity of nonintermittent DG than intermittent DG can improve the reliability of the system.

**Fig. 1** Main feeder of RBTS Bus 6

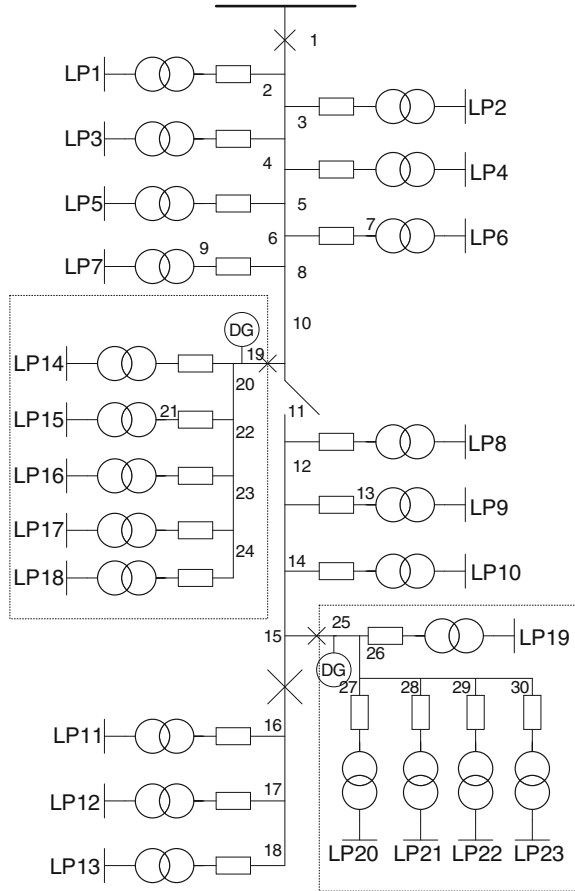


**Fig. 2** Failure rate for some special load points

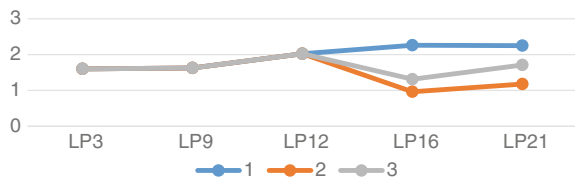


**Fig. 3** Average repair time for some special load points

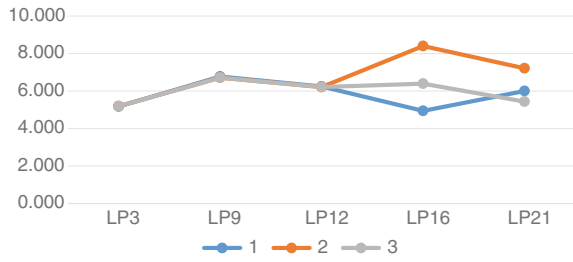


**Fig. 4** Outage time for some special load points

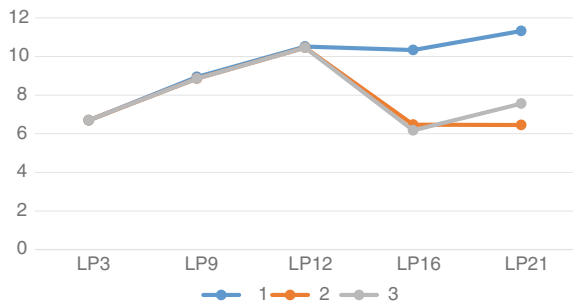


**Table 1** Failure rate for some special load points

Case	LP3	LP9	LP12	LP16	LP21
1	1.602	1.629	2.026	2.261	2.253
2	1.602	1.629	2.026	0.962	1.177
3	1.602	1.629	2.026	1.312	1.713

**Table 2** Average repair time for some special load points

Case	LP3	LP9	LP12	LP16	LP21
1	5.177	6.777	6.243	4.942	6.006
2	5.190	6.713	6.213	8.403	7.218
3	5.190	6.713	6.213	6.394	5.437

**Table 3** Outage time for some special load points

Case	LP3	LP9	LP12	LP16	LP21
1	6.687	8.942	10.514	10.336	11.321
2	6.703	8.853	10.458	6.471	6.449
3	6.704	8.854	10.457	6.173	7.560

**Table 4** Reliability indices of RBTS Bus 2

Index	Case 1	Case 2	Case 3
SAIFA	1.638	1.320	1.445
SAIDI	8.052	6.895	7.133
ASAI	0.9991	0.9992	0.9992

## 5 Conclusion

Firstly, the reliability evaluation of distribution network with DG is solved by using the MCS algorithm combined with the different operating characteristics of the MTs and the WTs. Finally, taking the main feeder of RBTS Bus6 F4 system as an example, the reliability evaluation index of the DG system is calculated, the role of DGs in improving the reliability of the distribution network is proved. The implementation of variable DGs such as MT and WT can positively influence the reliability of the system.

## References

1. Li Z, Xu Q, Li Z (2011) Reliability analysis of distributed system with DGs. 4th international conference on electric utility deregulation and restructuring and power technologies (DRPT), China
2. Lin S, Han M, Fan R Hu X (2011) Configuration of energy storage system for distribution network with high penetration of PV. IET renewable power generation conference (RPG 2011), Edinburgh, September 2011
3. Liang HS, Su J, Liu SG (2010) Reliability evaluation of distribution system containing microgrid. China international conference of electricity distribution (CICED), China, September 2010
4. Billinton R, Wang P (1999) Teaching distribution system reliability evaluation using Monte Carlo simulation. *IEEE Trans Power Sys* 14(2):397–403
5. Longyun K, Hongxia G et al (2010) Characteristics of distributed generation system and related research issues caused by connecting it to power system. *Power Sys Technol* 34(11):43–47 (in Chinese)
6. Wu Y (2011) Reliability evaluation of distribution system with distributed generators. Beijing, China
7. Lu J, Zhao Y (2013) A Point estimation method for reliability evaluation of distribution network with distributed generation. *Power System Technology*, China

# Circular Synthetic Aperture Sonar Imaging Using Isometric Angle Characteristic

Guo-hui Di, Jun Wang and Fu-lin Su

**Abstract** Circular synthetic aperture sonar (CSAS) can provide fine image of interest region in three dimensions through the sonar movement along a circle at a fixed height. The severe computation complexity of the state-of-the-art imaging algorithms is of great trouble during the usage process of CSAS. According to the relationship between the azimuth and the peak-valued curve of the returns of CSAS, the isometric angle characteristic is revealed in the paper. A fast inverse algorithm of CSAS imaging employing the isometric angle characteristic is proposed combined with CLEAN algorithm. The numerical experiments show the effectiveness and the low computational complexity of the proposed algorithm.

**Keywords** Circular synthetic aperture sonar (CSAS) · Isometric angle · Inverse approach · Imaging algorithm

## 1 Introduction

Circular synthetic aperture sonar (CSAS) technique can provide high-resolution image of the interest region on three dimensions (3-D), which is first proposed in [1]. The circular synthetic aperture framework has been deeply studied in the field of radar imaging [2–6]. The pop imaging algorithms include back-projection algorithm and point-to-point correlation algorithm in time domain, and the wave front reconstruction algorithm in the wave number domain. The algorithms in time domain are widely employed because of its clear logical process, however these

---

G. Di · F. Su (✉)  
Harbin Institute of Technology, 92 West Dazhi Street,  
Nan Gang District Harbin, China  
e-mail: 13B905021@hit.edu.cn

G. Di  
Heilongjiang Bayi Agricultural University, Daqing, China

J. Wang  
Harbin Institute of Technology, Weihai, China

algorithms suffer severe computation complexity. To resolve the computational burden, some modified algorithms are developed such as the back-projection approach using fast factorization [7] and the precise polar formation algorithm (PFA) [8]. Nevertheless, none of the modified algorithms takes advantage of the geometry of the circular trajectory of CSAS. In this paper, a fast inverse algorithm of CSAS imaging algorithm employing the characteristic of circular trajectory is proposed combined with CLEAN algorithm, and the inversion formula of the point target is developed.

## 2 Analysis of the Returns of CSAS

As shown in Fig. 1, the sonar platform navigates along a circle with a radius  $R$  which is located in the plane on a fixed height  $h$ . Assuming that the projection of imaging scenario onto the bottom plane with height  $h = 0$  is a round cake with a radius  $r$ , the beam of sonar always points to the center of the round cake while moving along the circular trajectory. The angular velocity of the sonar is  $\omega = v/R$ , where  $v$  denotes the linear velocity. For simplicity, we define the elevation angle  $\theta_z = \arctan(h/R)$ , the target angle along the track  $\theta_x = \arcsin(r/R)$ , and the slant distance of scenario center  $R_0 = \sqrt{R^2 + h^2}$ .

In the following, the formulation of CSAS returns will be addressed. In theory, the resolution of CSAS in the range and azimuth dimensions is relevant with the carrier frequency, and the resolution in the height dimension depends on the bandwidth of illuminating signal. The sonar signal can be expressed as

$$p(t) = \exp(j2\pi f_0 t) \exp(j\pi\gamma t^2) \quad (0 \leq t \leq T) \tag{1}$$

where  $T$  denotes the pulse width and  $f_0$  denotes the carrier frequency.

With regard to the underwater target  $P(x, y, z)$  with omnidirectional scattering function  $f(x, y, z)$  when the variation of the instantaneous distance between the target and sonar is ignored, the return can be formulated as  $s(t, \theta)$  follows:

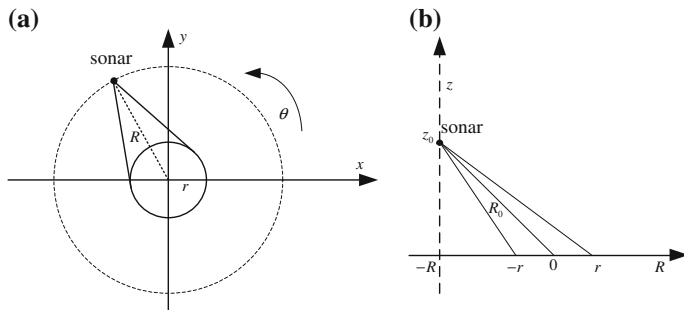


**Fig. 1** The geometry of CSAS. **a** Top view. **b** Side view

$$s(t, \theta) = \iiint f(x, y, z) \cdot p[t - 2R_p(\theta)/c] dx dy dz \tag{2}$$

where  $\theta$  denotes azimuth,  $t$  denotes the fast time, and  $c$  denotes the wave speed. The slant distance between sonar and the target whose coordinate is  $(x, y, z)$  as the motion of sonar platform is

$$R_p(\theta) = \sqrt{(x - R \cos \theta)^2 + (y - R \sin \theta)^2 + (z - h)^2} \tag{3}$$

### 3 The Imaging Using Isometric Angle Characteristic

In the following, the influence on the return waveforms of the distribution of point target in three dimensions will be addressed. Based on the Eq. (2), Fig. 2a depicts the waveform of scatters which are located in different azimuths but at the same range and height. Similarly, Fig. 2b, c illustrate the waveform of scatters which are only distributed in different ranges and different heights, respectively. As a benchmark, the return of the scatterer located in  $(0, 0, 0)$  is present in the figures. Some useful remarks can be summarized as follows:

For the targets located in different azimuths, the amplitudes of the returns are identical while the initial phases are different; for the targets located in different ranges, the amplitudes are proportional to their ranges and the initial phases are identical; for the targets located in different heights, both the amplitudes and initial phases are identical, but the delays of the returns are different.

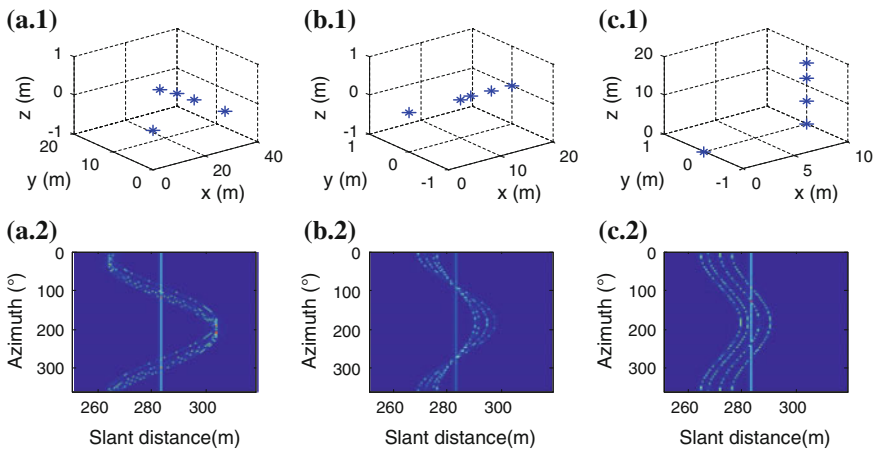


**Fig. 2** The returns of targets ( $SNR = \infty$ ). **(a.1)** Original target scenario on different azimuths. **(b.1)** Original target scenario at different ranges. **(c.1)** Original target scenario at different heights. **(a.2)** **(b.2)** **(c.2)** the returns after range compression

The distance between the target and the platform of CSAS varies while the platform moves along the circular trajectory. For convenience, the azimuth of the platform when the distance between the target and the platform takes the maximum value  $R_{\max}$  is denoted as  $A_{\max}$ , and the azimuth corresponding to the minimum distance  $R_{\min}$  is denoted as  $A_{\min}$ . Based on the Eq. (3), the distance curve between the platform and the target is a sine function; moreover the amplitude of the sine function is subject to the distance  $\rho_p$ . The amplitude of the sine function, i.e., the difference  $D(\rho_p) = R_{\max} - R_{\min}$ , is a nonreduction function of the variable  $\rho_p$ . The distance difference  $D(\rho_p)$  can be written as

$$D(\rho_p) = \sqrt{(R + \rho_p)^2 + h^2} - \sqrt{(R - \rho_p)^2 + h^2} \tag{4}$$

Based on the analysis about the distance between target and platform, the back-projection algorithm can be implemented as the following description. Considering the target on the bottom plane, the echo delay when the platform is at the azimuth  $\theta$  will be the same as the echo delay of the point target at the imaging center as the following

$$R_0 = \sqrt{R^2 + h^2} = \sqrt{(x - R \cos \theta)^2 + (y - R \cos \theta)^2 + (0 - h)^2} \tag{5}$$

In nature, when the projection of the platform lies in the middle vertical line of the line connecting the imaging point target and the image center, the distance between the platform and the imaging target will be the same as the distance between the platform and the imaging center. As illustrated in Fig. 3 about the point target  $P_1$ , the line  $OP_1$  is the line connecting the imaging center  $O$  and the target  $P_1$ , and the line  $A_1B_1$  is the middle vertical line of the line  $OP_1$ . Only when the platform moves at the position corresponding to  $A_1$  and  $B_1$ , the distance between the platform and the point target  $P_1$  is the same as the distance between the platform and the imaging center  $O$ . At this moment, both the angles,  $\theta_1 = \angle P_1OA_1$  and  $\theta_2 =$

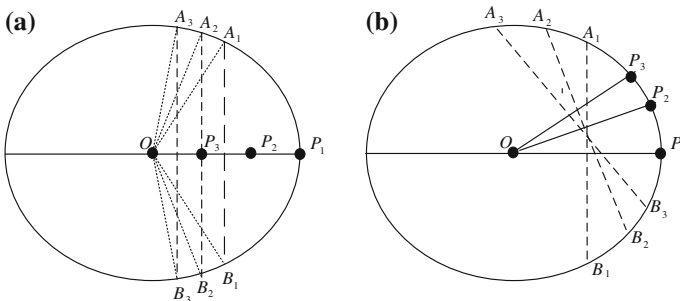


**Fig. 3** The sketch of isometric azimuths. **a** The targets which are located at different ranges. **b** The target which on different azimuths



$\angle P_1OB_1$  are defined as the isometric angles. According to the isometric azimuths  $\theta_1$  and  $\theta_2$ , the polar coordinate of the target can be shown as

$$\begin{cases} \rho_P = 2R \cos[(\theta_1 - \theta_2)/2] \\ \theta_P = (\theta_1 + \theta_2)/2 \end{cases} \quad (6)$$

On the basis of Eqs. (4) and (6), the difference of the distance  $D(\rho_P)$  is the function of the included angle, i.e., the included angle  $\delta$  can be expressed using  $D(\rho_P)$

$$\delta = 2rac \cos \left[ (D/4R) \cdot \sqrt{(4R^2 + 4h^2 - D^2)/(4R^2 - D^2)} \right] \quad (7)$$

In the above equation, the distance difference  $D(\rho_P)$  is abbreviated as  $D$ . Considering the imaging region consisting of  $N$  point targets, the number of the isometric azimuths will not exceed  $2N$ , therefore the number of included azimuth may be  $N * (2N - 1)$ . In order to acquire all the target coordinates, the true  $N$  number of isometric azimuths must be determined. The CLEAN algorithm is employed to obtain the information of the targets through iterative inverse approach as follows:

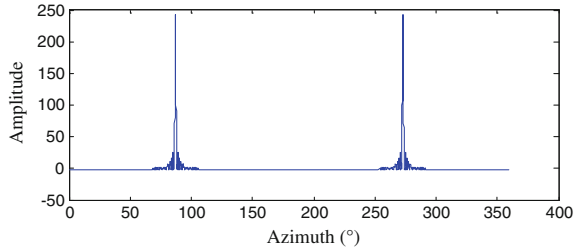
1. Based on the returns after the procedure of range compression, construct the azimuth assemble  $\Delta_1 = \{\theta_1, \theta_2, \dots, \theta_k\}$  of the points which correspond to the distance of  $R_0 = \sqrt{R^2 + h^2}$  from the imaging center  $O$ .
2. Determine the maximum range difference  $D_1$  of every return curve.
3. Calculate the included angle  $\delta_1$  based on the range difference  $D_1$  using the Eq. (6), and estimate the azimuths  $\hat{\theta}_i$  and  $\hat{\theta}_j$  of the points on the return curve which correspond to the distance  $R_0$ . Search the angles  $\theta_i$  and  $\theta_j$  in the assemble  $\Delta_1$  which are closed to the estimated azimuths  $\hat{\theta}_i$  and  $\hat{\theta}_j$  on the above step, and then the target position  $P(x_i, y_j)$  based on Eq. (6).
4. Recalculate the returns of target  $P(x_i, y_j)$ , and then remove the return of target  $P(x_i, y_j)$  from the return.
5. The Step 1-Step 5 should be executed until the maximum amplitude of returns is less than the threshold  $T_a$ , the return which is less than the threshold  $T_a$  can be treated as noise.

## 4 Numerical Experiments

### 4.1 A Simple Imaging Example

In the subsection, the performance of the proposed inverse approach is evaluated through numerical experiments. In the experiments, the height of platform  $h$  is 200 m and the radius  $R$  is 200 m, the sonic velocity is 1480 m/s. The illuminated signal is a linear frequency modulation (LFM) signal whose bandwidth is 10 kHz,

**Fig. 4** The target returns at the distance of  $R_0$



the pulse width is 6.2 ms, and the carrier frequency is 22 kHz. The sampled interval on the azimuth dimension is  $0.1^\circ$ , the sampled frequency on the range dimension is 160 kHz. Figure 4 depicts the part of the returns at the distance  $R_0$  of the single target at  $(20, 0)$  on the azimuth dimension.

The corresponding azimuths can be obtained,  $87.1^\circ$  and  $272.9^\circ$ , and then the estimating coordinate of the target  $\rho_p = 20.2372$  and  $\beta = 0$ . The error between the estimated and actual coordinate of the target is 0.01186 %.

## 4.2 The Resolution of the Inverse Approach

The resolution of the proposed inverse approach is analyzed in the following. The target return after demodulation, the output of the matching filter is

$$s(t, \theta) = T_r \sin c \left[ \pi \gamma T_r \left( t - \frac{2R_p(\theta)}{c} \right) \right] \exp \left[ j2\pi f_0 \left( t - \frac{2R_p(\theta)}{c} \right) \right] \quad (8)$$

Observing the image on the azimuth dimension when  $t = 2R_0/c$  as follows

$$s(\theta, R_0) = T_r Sa \left[ 2\gamma T_r \rho_p \cos \theta_z \sin(\theta + \alpha) / c \right] \cos \left[ 4\pi f_0 \rho_p \cos \theta_z \sin(\theta + \alpha) / c \right] \quad (9)$$

Based on the symmetrical characteristic of the circle, there is no influence onto the feature of the return except for the time of arrival when only the azimuth  $\theta$  changes. Using the approximation  $\sin \theta \approx \theta$  when  $\theta$  tends to zero, the first zero-value point of the function  $\sin c(\cdot)$  is

$$2\pi \gamma T_r \rho_p \cos \theta_z \cdot \theta_B = \pm \pi \quad (10)$$

Consequently, the main lobe width can be formulated as

$$|\theta_B| = c / (2B_r \rho_p \cos \theta_z) \quad (11)$$

According to Eq. (11), the resolution of CSAS using the proposed inverse approach is determined by the signal bandwidth and the target-center distance  $\rho_p$ .

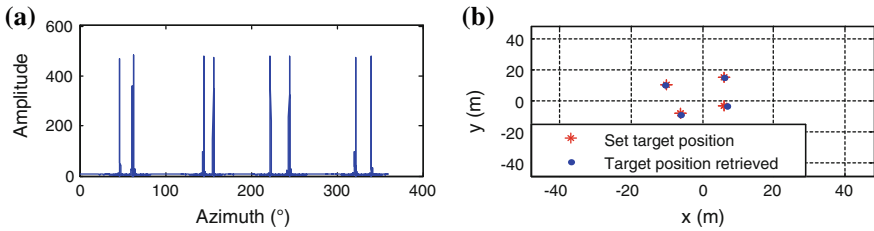


**Fig. 5** The image using the inverse approach including four targets. **a** The target returns at the distance of  $R_0$ . **b** The estimated target coordinates using the proposed approach

With the increase in  $\rho_p$ , the resolution performance is improved. The imaging variation on the azimuth dimension may appear with respect to the target located in the imaging center. Figure 5 shows the CSAS image using the proposed approach including four targets; it is clear that the imaging performance decreases with the increase in target-center distance.

### 4.3 Computation Complexity

Considering the imaging scenario is discretized into  $M \times N$  grids, where  $M$  denotes the grid number on azimuth dimension and  $N$  the grid number on range dimension. The computation complexity of the proposed approach and other algorithms is shown in Table 1.

The computation complexity of the inverse approach is proportional to the number of targets, and has nothing to do with the size of the imaging scenario. In consequence, the proposed approach is especially fit for using in sparse scenario.

For the sake of improving the accuracy of inverse operation, we can take advantage of the image on the azimuth dimension at other range cell. For an arbitrary fast time  $t = 2(R_0 + \Delta R)/c$ , the image on the azimuth dimension can be shown as

**Table 1** The computation complexity

	Back-projection algorithm	Modified back-projection algorithm	The proposed inverse approach
Computation complexity	$O(M^2N)$	$O(NM \log_2 M)$	$O(MN)$

$$s(\theta, \Delta R) = T_r \sin c\{2\pi\gamma T_r[\Delta R + (x \cos \theta + y \sin \theta) \cos \theta_z]/c\} \cdot \cos\{4\pi f_0 \cos \theta_z[\Delta R + (x \cos \theta + y \sin \theta) \cos \theta_z]/c\} \quad (12)$$

In the case that the projection of the platform is not located on the perpendicular bisector of the line  $OP$ , the distance between the target  $P$  and the platform is not equal to  $R_0$ . Supposing the distance is  $R_0 + \Delta R$ , and the distance between the point  $A$  and the platform position  $B$  is  $R_0 + \Delta R$ , the polar coordinate of the target can be shown as

$$\begin{cases} \rho_P = R \cos[(\theta_1 + \theta_2)/2] + \sqrt{(R + \Delta R)^2 - h^2 - R^2 \sin^2[(\theta_1 + \theta_2)/2]} \\ \theta_P = (\theta_1 + \theta_2)/2 \end{cases} \quad (13)$$

Combining the estimated target position according to the Eq. (13) and the estimated result according to the Eq. (6), we can achieve more accurate estimated coordinate of the target.

## 5 Conclusion

In the paper, the inverse approach is proposed to accomplish the CSAS imaging which exploits the isomeric angle characteristic on the azimuth dimension. Comparing the traditional CSAS imaging methods, the proposed approach has lower computation complexity and higher resolution. Numerical experiments show the effectiveness of the proposed inverse approach. Due to the number of samples on the range dimension and the quantization series, the imaging variation on the azimuth dimension may appear with respect to the target located in the imaging center.

## References

1. Soumekh M (2001) Synthetic aperture radar signal processing. Wiley, New York
2. Axelsson SRJ (2004) Beam characteristics of the three-dimensional SAR in curved or random paths. *IEEE Trans Geosci Remote Sens* 42(2):2324–2334
3. Broquetas A, De Porrata R, Sagués L et al (1997) Circular synthetic aperture radar (C-SAR) system for ground-based applications. *Electron Lett* 33(11):988–989
4. Ponce O, Prats-Iraola P, Pinheiro M, Rodriguez CM et al (2014) Fully polarimetric high-resolution 3-D imaging with circular SAR at L-band. *IEEE Trans Geosci Remote Sens* 52(6):3074–3090
5. Frolind P, Gustavsson A, Lundberg M et al (2012) Circular-aperture VHF-band synthetic aperture radar for detection of vehicles in forest concealment. *IEEE Trans Geosci Remote Sens* 50(4):1329–1339

6. Lin Y, Hong W, Tan W, Wang Y et al (2012) Airborne circular SAR imaging: results at P-band. In: IEEE international geoscience and remote sensing symposium, Munich, Germany, pp 5594–5597
7. Ponce O, Prats P, Cassola MR et al (2011) Processing of circular SAR trajectories with fast factorized back-projection. In: IEEE international geoscience and remote sensing symposium, Vancouver, Canada, pp 1021–1027
8. Lin Y, Hong W, Tan W et al (2011) Interferometric circular SAR method for three-dimensional imaging. *IEEE Trans. Geosci Remote Sens* 8(6):1026–1030

# Analysis of the Choice of a Serial Reactor in a Parallel Capacitor Device

Xianzhong Long, Xiaobo Liu and Da Song

**Abstract** When there are harmonic sources in a system, a parallel capacitor will enlarge the harmonics, producing harmonic resonance. Since it is an effective strategy to install a suitable reactance rate of reactor into the capacitor to restrain the harmonics, further analysis is necessary on the choice of reactance rate. This article analyzes the relationship between the effective capacity, the ability to suppress the harmonic, the insulation of the parallel capacitor and the series the reactor in capacitor. On this basis, the article studies the deficiency of the existing reactance rate in capacitor and provides more detailed options. Generally it is a very good remedy for harmonic suppression to string a reactor in the capacitor. So, analyzing the reactance rate of the parallel capacitor is very important.

**Keywords** Parallel capacitor · Reactance rate · The insulation of the capacitor · The effective capacity of the capacitor · Reactor

## 1 Introduction

The parallel capacitor provides reactive power compensation to ensure the stability of the system's voltage. When the parallel capacitor is placed into the system, it will produce large switching inrush current, which must be less than twenty times the rated current. When the harmonic sources exists in the system, the capacitance value of a capacitor and the system's equivalent reactance value change, which may

---

X. Long (✉) · D. Song  
Power System and its Automation, School of Electrical Engineering,  
GuiZhou University, Guiyang 550000, China  
e-mail: 15885034782@163.com

X. Liu  
High Voltage Technology, School of Electrical Engineering,  
GuiZhou University, Guiyang 550000, China

enable systematic harmonic amplification and resonance. The installation of an inductor into parallel capacitors can be used to suppress the capacitors' switching inrush current and can also play a function to suppress the harmonics of a specific frequency. However, while the selection of reactance rate in the design specification of the parallel capacitor device is relatively simple, in practice, it is not easy to grasp. Therefore, it is necessary to carry out more specific analysis on the selection of the reactance rate under various harmonic sources.

Most of the existing research studies are aimed at the specific power system for the selection of parallel capacitor reactance rate, so the promotion of the results is not strong. Also, a part of the research starts from the principle to avoid the capacitor resonance and reduce the magnification times of the harmonic magnification, so the selection of reactance rate of parallel capacitor is analyzed and verified [1–3]. In reference [3], the reactance rate combinations of 4.5–6 % and 12–13 % are proposed to suppress the third harmonic amplification. In the reference [3–6], a practical application of the reactance rate selection principle is put forward, which is based on the magnification times of specific harmonics of different reactance ratios.

However, the results obtained from these studies have not considered the relationship between the insulation of parallel capacitor and the capacity of the capacitor and the ability to suppress harmonics of the capacitor, so the selection of the reactance rate is not the most ideal.

## 2 Resonance Analysis of a Capacitor

The circuit model and the equivalent diagram of a capacitor device with reactor in series are shown in Fig. 1, where the device is connected with the harmonic source on the bus [4–6]. In Fig. 1, the  $I_n$  are harmonic sources, the  $I_{sn}$  is the harmonic

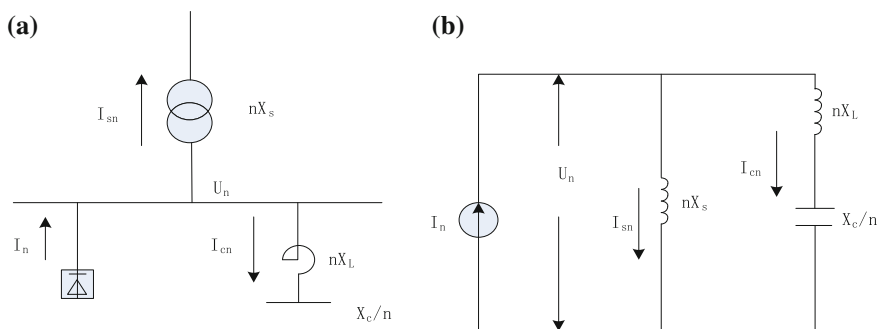


**Fig. 1** Circuit diagram of parallel capacitor device with harmonic source. **a.** Schematic diagram **b.** Equivalent circuit diagram

current flowing through the system, the  $I_{cn}$  is harmonic current flowing through the capacitor branch,  $nX_s$  is the reactance value of the system when the  $n$ th harmonic exists,  $nX_L$  is the reactance value of reactor when  $n$ th harmonic is in the capacitor branch, and  $X_c/n$  is the capacitance value of a capacitor when the  $n$ th harmonic is in the capacitor branch.

From Fig. 1:

$$I_{cn} = I_n \frac{nX_s}{nX_s + nX_L - X_c/n} \quad (1)$$

$$I_{sn} = I_n \frac{nX_L - X_c/n}{nX_s + nX_L - X_c/n} \quad (2)$$

$$Z_n = \frac{nX_s(nX_L - X_c/n)}{nX_s + nX_L - X_c/n} \quad (3)$$

Series resonant point of capacitor branch:  $n = \sqrt{X_c/X_L}$ ;

Parallel resonant point of capacitor branch:  $n = \sqrt{X_c/(X_L + X_s)}$ ;

The expression of the reactance rate in the capacitor device is:  $K = X_L/X_C$ .

When the harmonic in the power network is required to be suppressed, this can be realized by changing the reactance rate of the capacitor to make the capacitor branch to the present sensibility to the lowest harmonics in all of the harmonic [1–3]. Because  $X_L$  is very large relative to  $X_s$ , in order to avoid the system sliding into parallel resonance for various reasons, the value of  $K$  should be  $K > 1/n^2$  [7–10]. The general selection rules for the reactance rate are as follows:

1. for switching the inrush current of capacitor, the reactance rate can be chosen from 0.1 to 1 %;
2. if the system mainly consists of third and higher harmonics, the reactance ratio combination of 12 % or two 12 % and 4.5–5 % are chosen;
3. if the system mainly consists of fifth and higher harmonics, choose the reactance rate between 4.5 and 5 %.

While these are more general considerations, the operability is not strong in practical application. This paper considers three approaches; the combination of the insulation of the capacitor; the effective capacity of the capacitor; and the ability of the capacitor to suppress the harmonics, all of which can make the reactance rate selection rules more specific. This scheme is more reasonable and more practical for the practical requirements of the capacitor, which is based on the insulation of the capacitor, the capacity of the capacitor and the ability to suppress the harmonics.



### 3 Analysis of the Influence of the Reactance Rate

#### 3.1 Effect of a Reactor on the Capacity of a Capacitor

The capacity of the capacitor whose series reactance rate is  $K$  is as follows:

$$Q_{cn} = S_d \left( \frac{1}{n^2} - K \right) \quad (4)$$

In the above formula,  $S_d$  is the short circuit capacity of the capacitor connected to the bus.

It can be seen that, with the increase of the reactance rate, the effective capacity of the capacitor is reduced, which means that the reactive power compensation capacity of the power system is reduced. The capacity of reactive power compensation in a power system is designed in advance, so the larger reactance rate will not only result in a greater waste of capacity, but it will also cause great economic losses to the power network, and it will add some difficulties to the design and manufacture of capacitors. Therefore, under the premise of meeting the technical requirements, the smaller the reactance of the capacitor, the better the economy.

#### 3.2 Effect of Reactor on Harmonic Voltage Amplification

When the reactance rate of  $K$  of the reactor is connected to the capacitor, the amplification rate of the harmonic voltage is as follow:

$$F_n = \left| \frac{n^2 K - 1}{n^2 (S + K) - 1} \right| \quad (5)$$

In the above formula:  $S = Q_{cn}/S_d$ .

It can be seen that, with the increase of the reactance rate, the amplification times of the specific harmonic are reduced.

#### 3.3 Effect of Reactor on the Voltage at the End of the Capacitor

The voltage of the capacitor, after being strung into a reactor with a reactance rate of  $K$  at the end of the reactor, is as follow:

$$U_{cn} = U_n / (1 - K) \quad (6)$$

It can be seen that the voltage at the end of the capacitor increases with the increase of the reactance rate, and then the insulation requirements of the capacitor are also improved. The voltage of a capacitor which has the series reactor will be increased, and the amplitude of the increase is related to the percent of the series reactor.

That is, for fifth or higher harmonic,  $K > 4\%$  should be taken; for the third or higher harmonic,  $K > 11.1\%$  should be taken. As can be seen, when the reactance rate is 0.1–1 %, it has very good inhibitory effect on the switching current of a capacitor, and the amplification of the 3rd, 7th and 5th harmonics are large, which can lead to 5th and 7th harmonic resonance; when the reactance rate is 4.5–5 %, it has very good inhibitory effect on the 7th and 5th harmonics, and the amplification of 3rd harmonic is great, which may lead to the third harmonic resonance; when the reactance rate is 12–13 %, it has very good inhibitory effect on the third and higher harmonics.

## 4 Reactance Rate Selection

### 4.1 *When There Is no Harmonic in the System*

In order to limit the inrush current of capacitor, a reactance rate can be selected from 0.1 to 1 %. Because of the reactance rate is high, the capacitor insulation requirements are also higher, and the effective capacity of capacitor will decrease, so the low reactance rate is selected to suppress the inrush current. For example, a reactance rate can be taken as 0.1–0.5 %.

### 4.2 *When the System Is Mainly of 3rd Harmonic and Higher*

1. If the contents of the 3rd and higher harmonics are small (i.e., the allowable value of harmonic content has not been achieved), consideration of the harmonic content is small, so the capacitor insulation requirements and capacitor effective capacity should be of primary consideration. The reactance rate of 1–0.5 % can be used, and amplification of 5th and 7th harmonics should be verified to ensure the amplification of 5th and 7th harmonics are in the acceptable range.
2. If the contents of the 3rd and higher harmonics are large (i.e., the harmonic content is not limited or near it), then the ability to suppress harmonics should be put the primary consideration. Taking into account the 3rd harmonic does not exceed the standard, and, while the reactance rate of 4.5–5 % has a great amplification effect

on the 3rd harmonic, the reactance rate combination of 12–13 % and 4.5–5 % is considered.

3. If the content of the 3rd or higher harmonics is very large (i.e., the harmonic content exceeds the limit value), then the ability to suppress harmonics should be put into first place. Taking into account that the 3rd harmonic exceeds the limit, the reactance rate of 12–13 % should be used.

### ***4.3 When the System Is Mainly of 5th Harmonic and Above***

1. If the contents of 5th and higher harmonic are small (i.e., the allowable value of harmonic content has not been achieved), consideration of the harmonic content is small, so the capacitor insulation requirements and capacitor effective capacity should assume primary consideration. The reactance rate of 0.5–1 % can be used, and amplification of the 5th and 7th harmonic should be verified to ensure the amplification of 5th and 7th harmonic are in the acceptable range.
2. If the contents of the 5th and higher harmonics are large (i.e., the harmonic content is not limited or near it), then the ability to suppress harmonics should be put of primary importance. Taking into account that the 5th harmonic does not exceed the standard, the reactance rate of 4.5–5 % is considered. Considering the capacitor insulation requirements and capacitors' effective capacity, the reactance rate of 4.5 % should be used.
3. If the content of the 5th or higher harmonics is very large (i.e., the harmonic content exceeds the limit value), then the ability of suppress harmonics should be put first. Taking into account that the 5th harmonic exceeds the limit, the reactance rate of 5 % should be used.

## **5 Conclusion**

The parallel capacitor reactance rate of a capacitor has great influence on switching inrush current, harmonic suppression, a capacitor' effective capacity and the capacitor's insulation requirements. Through theoretical analysis, with the increase of the reactance rate, the capacity of a capacitor is reduced, the ability to restrain harmonics is enhanced, and the insulation requirement of a capacitor is increased. For the selection of the reactance rate, the conclusions are as follows:

1. when the system has no harmonics, the reactance rate of 0.5–0.1 % should be taken;
2. when the system is mainly of 3rd harmonic and above, if the contents of the 3rd and higher harmonics are small, the reactance rate of 0.5–1 % can be used; if the

contents of the 3rd and higher harmonics are large, the reactance rate combination of 12–13 % and 4.5–5 % is considered; if the content of the 3rd or higher harmonics is exceeded, the reactance rate of 12–13 % should be used.

3. when the system consists mainly of the 5th harmonic and above, if the contents of the 5th and higher harmonics are small, the reactance rate of 0.5–1 % can be used; if the contents of the 5th and higher harmonics are large, the reactance rate of 4.5 % is considered; if the content of the 5th harmonics or higher is exceeded, the reactance rate of 5 % should be used.

Through theoretical analysis combined with the actual situation of power networks, this paper analyzes the effective capacity of the capacitor, the capacity of the capacitor to restrain the harmonic power, and the insulation requirements of capacitor, so that the selection principle of the reactance rate of a capacitor is obtained. Compared with the currently used method of selecting the reactance rate of a capacitor in a power network, the selection principle of the reactance rate of a capacitor in this paper is more specific and reasonable. In this paper, the selection principle of the reactance rate of capacitor not only considers the suppression of harmonics, but also takes into account the effective capacity of the capacitor and the insulation requirements. By taking into account these three aspects, the final choice will yield better economic and other practical consequences. The selection principle of the reactance rate of capacitor in this paper has great reference value for the design and planning of power networks.

## References

1. Lin H, Sun S (1998) The harmonic in the power grid. China Electric Power Press, BeiJing
2. Wu J (1998) Power supply system harmonics. China Electric Power Press, BeiJing
3. Yang C (1994) Harmonic response of parallel capacitor device and its countermeasures. Zhejiang Electr Power 1:22–30
4. Zhou S, Lin H (2009) The simplify analysis and calculation of parallel capacitor devices harmonic. Distrib Util 26(1):4–9
5. Yi C (2008) The harmonic amplification analysis and capacitance parameter selection of parallel capacitor. Guangxi Electr Power 1:43–46
6. Wu G, Xu Y, Hong W, et al (2014) Study on the method of reactance rate's selection on parallel capacitor option. Electr Eng Autom 6:21–23
7. Daut I, Eng E, Univ D, et al (2008) Investigation on the effect of shunt capacitor and shunt filter on harmonic in distribution system. In: Power and energy conference
8. Richards GG, Yang H (1993) Distribution system harmonic worst case design using a genetic algorithm. IEEE Trans Power Delivery 8(3):1484–1491
9. Hong S, Zheng C, Lei F, et al (2012) Research on the parallel capacitor series reactance rate parameter design
10. Park J (2012) Filters based on asymmetric coupled lines with equal reactance. Microwave Theory Tech IEEE Trans 261–269

# Decision Fusion Moving Target Detection of Radar Video Based on D-S Evidence Theory

Xiaohan Yu, Wei Zhou, Jian Guan and Wenchao Hu

**Abstract** In dense clutter and complex multi-objective situation, radar automatic detection and tracking will produce many false tracks. In order to solve this problem, first, using iterative threshold segmentation method to rapidly detect the suspected targets from a single frame radar video image, and gaining the continuous multiframe detection results by accumulation. Then, synthesize single frame detection results and multiple frames accumulation results to extract the area change ratio and energy density of targets, and build their basic probability assignment (BPA) functions, respectively. In addition, D-S evidence theory is adopted to carry out decision fusion, to obtain the optimal decisions in order to realize the automatic detection of moving targets. Finally, the effectiveness of the algorithm is verified by experimental results.

**Keywords** Area change ratio · Energy density · BPA · D-S evidence theory · Decision fusion · Moving target detection

## 1 Introduction

Radar plays a vital role in ocean surveillance, and moving target detection and tracking is the most basic function of radar [1]. In recent years, most of the new radars have the function of automatic detecting and tracking. But in dense clutter and complicated multi-objective situation, the target detection false alarm rate is high, track processing is difficult, and it is easy to form false tracks [2]. Therefore, studying a steady method for automatic detection of marine moving targets is of great significance.

---

X. Yu (✉) · W. Zhou · J. Guan · W. Hu  
Naval Aeronautical and Astronautical University, Yantai, China  
e-mail: 2953164562@qq.com

Compared with traditional radar signal processing, it can view the sequence consisting of graphic display radar echo signal in chronological order as radar video and research the radar target detection from the perspective of computer vision. Its advantage is that the time and space attribute of target can be comprehensively considered to improve detection speed and accuracy [3]. At present, commonly used moving target detection methods based on image are interframe difference method [4], optical flow field method [5], background difference method [6], etc. Different from above methods, this paper introduces the information fusion ideas to moving target detection, and D-S evidence theory is adopted to carry out decision fusion.

## 2 Algorithm Description

### 2.1 Single Frame Detection

Radar images are gray images, the gray values of land area and ship targets in images are higher, the gray values of surface areas are lower. There is no overlap between targets, so the suspected targets can be segmented from background by threshold segmentation. This paper uses the iterative threshold segmentation method for radar image's segmentation. After threshold segmentation, radar image contains some independent points and tiny holes, it needs morphological processing. This article adopts the method of morphological expansion to fill holes and bridge cracks. Figure 1 shows the single frame detection results of two sets of typical radar image data, from left to right in turn are original radar image slices, threshold segmentation results, and morphology processing results.

From Fig. 1, we can find that through iterative threshold segmentation, the sea clutter and noise are eliminated effectively, but it is still unable to determine whether the detection results of suspected targets are moving targets or not, which needs further judgment.

### 2.2 Multiframe Accumulation

Radar video is composed of radar images sequence in chronological order. If we accumulate the detection results of continuous multiple frames, obtain the historical routes of targets, the features can be extracted through different historical routes' characteristics of moving targets and static targets. Suppose the  $i$ th frame detection result is  $I_i$ , the continuous  $i$  frames accumulation result is  $I_i = I_1 \cup I_2 \cup \dots \cup I_i$ . Figure 2 shows 20 frames' accumulation results of Fig. 1, marked area is the 20th frame detection result.

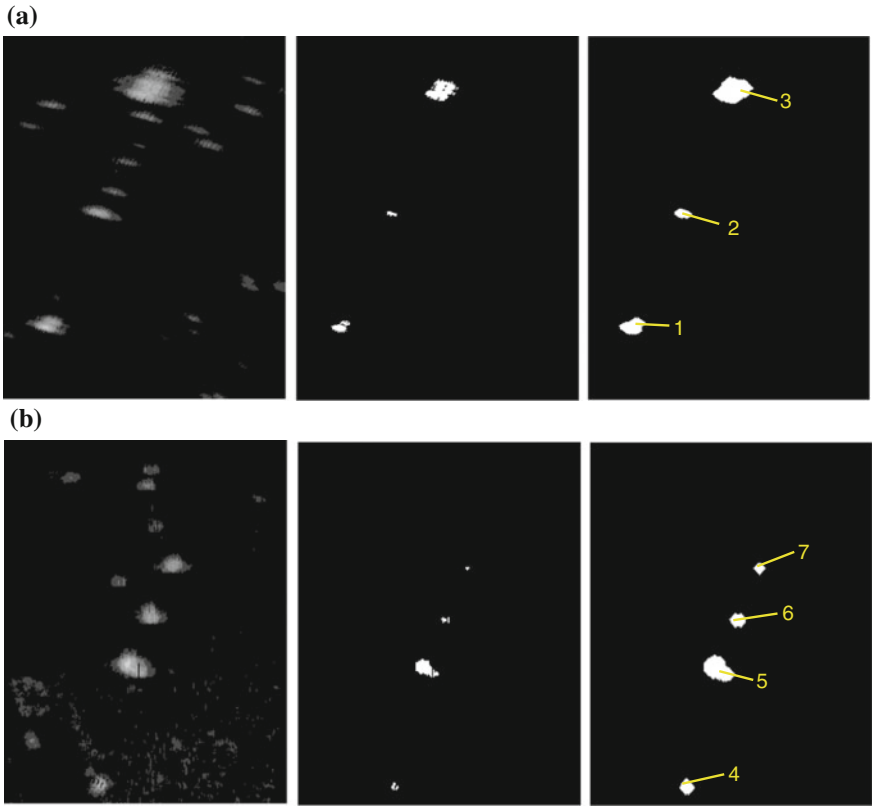


**Fig. 1** Single frame detection results of typical radar images **a** The first set of data. **b** The second set of data

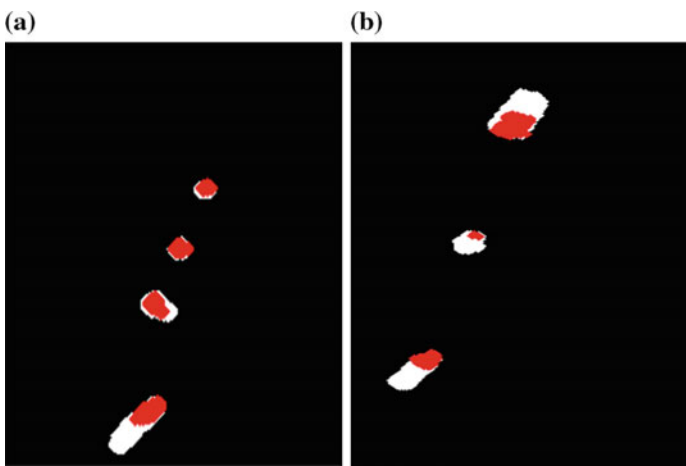


**Fig. 2** Multiframe accumulation results of typical radar images **a** The first set of data. **b** The second set of data

## 2.3 Target Feature Extraction

From Fig. 2, we can find that the most visible difference between moving target and static target is the proportion of target contour in target trajectory. In addition, from energy viewpoint, their energy distribution will be different. Next, we will synthesize single frame detection results and multiple frames accumulation results to extract the area change ratio and energy density of targets.

### 2.3.1 Area Change Ratio

We introduce the concept area change ratio to describe the proportion of target contour in target trajectory. Area change ratio can be defined as the ratio of target area and connected trajectory region's area. After threshold segmentation, radar image becomes binary image. Target area is the pixels number in binary image, that is  $A = \sum_{x=0}^{m-1} \sum_{y=0}^{n-1} f(x, y)$ . The area change ratio of  $i$ th frame is  $A_{ri} = \frac{A_i}{A_{si}}$ ,  $A_i$  is the target area of  $i$ th frame, and  $A_{si}$  is the connected region's area after  $i$  frames accumulation.

### 2.3.2 Energy Density

For static target, the target position almost remains unchanged, continuous radiation of electromagnetic wave will build up energy at the target area; but the position of moving object is constantly changing, energy will disperse in the target trajectory. Therefore, the energy distribution of moving target and static target must be different. We introduce the concept energy density to describe the energy distribution of target. Reflected on the radar image after binarization, energy can also be quantitatively described by pixels number, the  $i$ th frame's target energy density is

$$P_{ri} = \frac{\sum A_i}{A_{si}}.$$

## 2.4 Feature Decision Fusion

Decision-level image fusion is a further fusion process after the characteristic information classification, identification, and other processing of each image. It is a higher level information fusion, its final decision result is the global optimal decision [7]. Decision fusion always uses all kinds of uncertainty reasoning technology. This paper adopts D-S evidence theory to fuse the area change ratio and the energy density extracted from Sect. 2.3, the fusion result is the final judgment criteria of moving targets.



### 2.4.1 D-S Evidence Theory

D-S evidence theory is a kind of inexact reasoning method, which fuses belief functions coming from two or more evidence body together through certain combination rules, and gets a new belief function as decision criterion. The theory has strong flexibility on distinguishing the uncertain and correct reflection of evidence collection [8].

Suppose  $\Theta$  is a recognition framework,  $C$  and  $D$  are different evidences in  $\Theta$ , their BPA are  $m_1$  and  $m_2$ , the combination formula is

$$m(B) = \begin{cases} 0 & B = \emptyset \\ \sum_{C_i \cap D_j = B} m_1(C_i)m_2(D_j)/(1-K) & B \neq \emptyset \end{cases} \quad (1)$$

$$K = \sum_{C_i \cap D_j = \emptyset} m_1(C_i)m_2(D_j) < 1 \quad (2)$$

In the formula,  $K$  means normalizing factor. If  $K \neq 1$ ,  $m$  confirms a combination of BPA; if  $K = 1$ ,  $m_1$  and  $m_2$  are contradictory, the BPA cannot be combined.

### 2.4.2 BPA Construction

Before feature decision fusion of area change ratio and energy density, we need to build their BPA functions, respectively. Based on the analysis of abundant radar image slices data, we can obtain their moving targets probability piecewise functions  $y_1$  and  $y_2$ , and corresponding confidence coefficient  $Q_1$  and  $Q_2$ . The BPA is

$$\begin{cases} m_i = Q_i \times y_i \\ m_i(\Theta) = 1 - Q_i \end{cases} \quad (3)$$

### 2.4.3 Optimal Decision Rule

The result of feature decision fusion is the global optimal decision, such as the final judgment standard of moving targets. Set  $\exists B_1, B_2 \subset \Theta$ , if they meet

$$\begin{cases} m(B_1) = \max\{m(B_i), B_i \subset \Theta\} \\ m(B_2) = \max\{m(B_i), B_i \subset \Theta, B_i \neq B_1\} \end{cases} \quad (4)$$

$$\begin{cases} m(B_1) > \varepsilon_1 \\ m(B_1) - m(B_2) > \varepsilon_2 \end{cases} \quad (5)$$

$B_1$  is the optimal decision,  $\varepsilon_1, \varepsilon_2$  are predefined thresholds. In this paper,  $\varepsilon_1 = 0.9$ ,  $\varepsilon_2 = 0.1$ .

### 3 Experimental Results and Analysis

Above algorithm is realized by programming on MATLAB 2010 platform. Select part of radar image collected from a certain type of shore-based radar as the experimental data, the total amount of images are 300 frames. The first 200 frames are used for prior analysis to obtain the optimal decision, the remaining 100 frames are used for algorithm validation. For illustration purpose, we cut out two set of image data from the original radar image (as shown in Fig. 1), Fig. 3 shows the area change ratio curve of the first 50 frames. For the target which suddenly disappears on or two frames but appears again on the back frames, we use the result of previous frame.

From Fig. 3, we can find that with the increase of accumulation of frames, the area change ratios of targets 1, 2, 3, 4 have been showing a tendency of decline starting from 1; the area change ratios of targets 5, 6, 7 are volatile without obvious changing rules, but are all above 0.5.

Table 1 shows the energy density of typical frames chosen from the first 50 frames. The information we can get from it is the energy densities of targets 1, 2, 3,

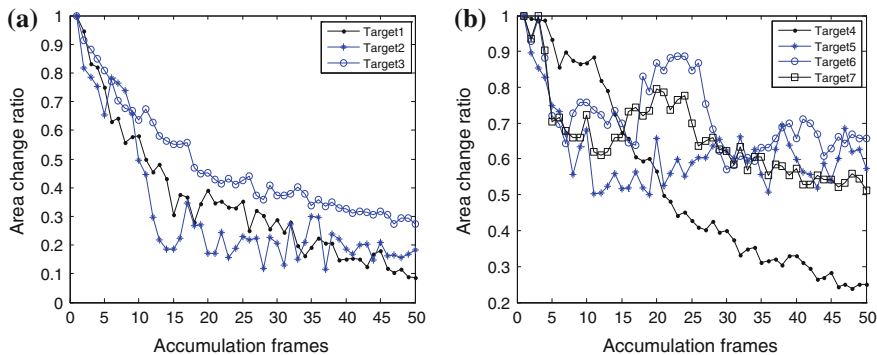


Fig. 3 Area change ratio curve of targets a The first set of data. b The second set of data

Table 1 Energy density of targets

Frame	1	3	5	7	10	15	20	30	40	50
Target 1	1.00	2.63	3.61	4.31	5.30	6.96	7.63	8.97	9.35	9.74
Target 2	1.00	2.03	2.69	3.28	5.05	5.96	6.28	6.63	6.90	7.26
Target 3	1.00	2.65	4.00	5.26	6.47	8.10	9.64	10.37	10.82	10.96
Target 4	1.00	2.33	3.37	4.41	6.63	7.45	8.76	10.05	10.94	11.15
Target 5	1.00	2.72	4.16	5.56	7.44	10.04	12.61	16.33	21.07	26.82
Target 6	1.00	2.41	3.84	5.18	5.71	8.35	11.17	18.15	22.32	27.38
Target 7	1.00	1.75	3.25	4.68	5.23	7.29	9.73	13.23	16.37	20.17

4 increase slowly starting from 1 and gradually stabilize at about 10; the energy densities of targets 5, 6, 7 keep growing starting from 1.

Ideally, according to the physical meanings, the area change ratio of moving targets should keep decreasing starting from 1, and be more and more close to zero at last, the energy density should be stable at a fixed value; the area change ratio of static targets should be close to 1, the energy density should keep increasing. But for measured data, the area of one same target on two consecutive frames may not totally be the same because of the influence of the target fluctuation. The binarization processing of original image may cause energy attenuation to some extent. These factors lead to the differences between extracted characteristic values and the ideal state. But it basically meets the change rule, and will not have a significant impact on the experimental results.

Through analyzation of the first 200 radar images and consideration of the artificial interpretation results, we can get the moving targets probability piecewise functions of area change ratio and energy density are, respectively,

$$y_1 = \begin{cases} 1 & 0 < A_{ri} \leq 0.3 \\ 0.7 & 0.3 < A_{ri} \leq 0.6 \\ 0.15 & 0.6 < A_{ri} \leq 1 \end{cases}, \quad y_2 = \begin{cases} 0.9 & 0 < P_{ri} \leq 8 \\ 0.5 & 8 < P_{ri} \leq 15 \\ 0.05 & P_{ri} > 15 \end{cases} \quad (6)$$

And their corresponding confidence coefficients are  $Q_1 = 0.75$ ,  $Q_2 = 0.7$ . The combination result obtained from formula (1) is as follows:

$$m(B) = \begin{cases} 0.9815 & 0 < A_{ri} \leq 0.3, 0 < P_{ri} \leq 8 \\ 0.8814 & 0 < A_{ri} \leq 0.3, 8 < P_{ri} \leq 15 \\ 0.6683 & 0 < A_{ri} \leq 0.3, P_{ri} > 15 \\ 0.8774 & 0.3 < A_{ri} \leq 0.6, 0 < P_{ri} \leq 8 \\ 0.6831 & 0.3 < A_{ri} \leq 0.6, 8 < P_{ri} \leq 15 \\ 0.4038 & 0.3 < A_{ri} \leq 0.6, P_{ri} > 15 \\ 0.5709 & 0.6 < A_{ri} \leq 1, 0 < P_{ri} \leq 8 \\ 0.3195 & 0.6 < A_{ri} \leq 1, 8 < P_{ri} \leq 15 \\ 0.1345 & 0.6 < A_{ri} \leq 1, P_{ri} > 15 \end{cases} \quad (7)$$

In the formula,  $m(B_1) = 0.9815$ ,  $m(B_2) = 0.8814$ , put them into formula (5), they meet the optimal decision rules. So, the optimal decision is

$$0 < A_{ri} \leq 0.3, \quad 0 < P_{ri} \leq 8 \quad (8)$$

Namely when the area change ratio and energy density of target meet formula (13), the target is a moving target.

Next, we use the remaining 100 radar images to verify this algorithm. It can be found in Fig. 3 and Table 1 that the characteristic values extracted from the first 10 frames are not stable, which cannot be seen as judge standard. Therefore, we output the moving target detection results beginning from the 211th frame. Figure 4 shows the detection results of several key frames.

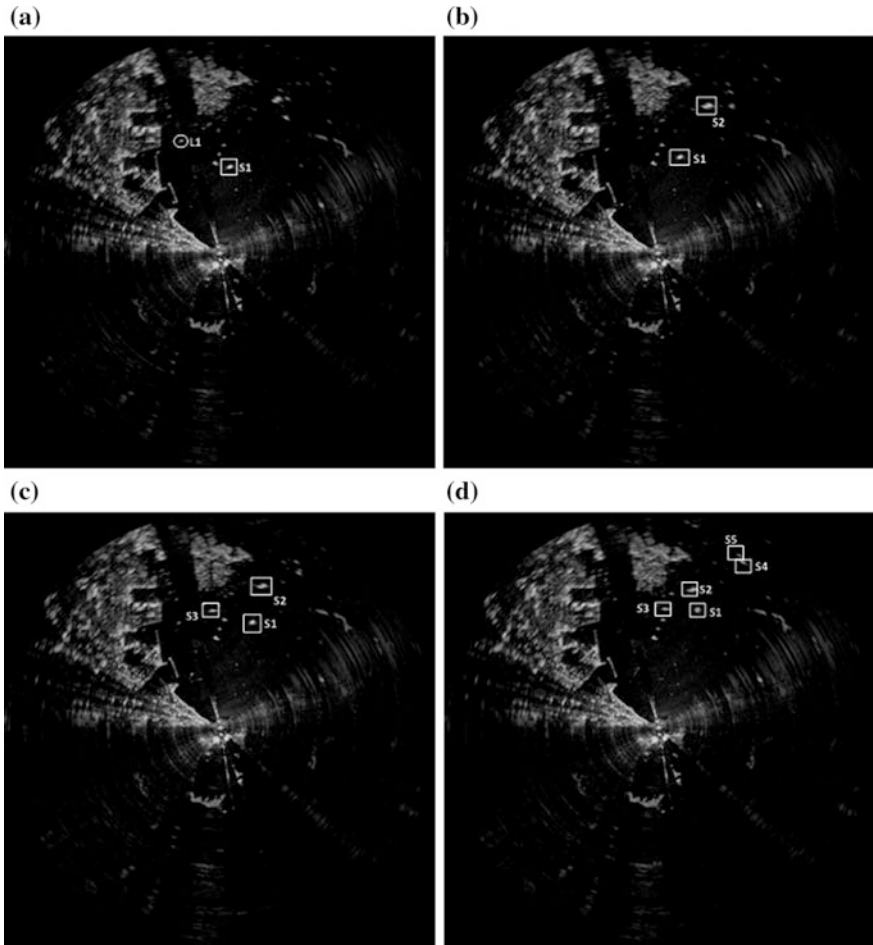


**Fig. 4** Moving target detection results **a** The 219th frame. **b** The 246th frame. **c** The 275th frame. **d** The 300th frame

Figure 4 shows that the algorithm detected five moving targets S1, S2, S3, S4, S5 in order. According to the artificial interpretation results, after the 300th frame image was processed, all moving targets were detected effectively except the target L1 on the 219th frame, which only appeared on a few frames and quickly disappeared. Therefore, with low false alarm rate, the algorithm has good detection effects for the stability moving targets. It effectively solves the problem of high false track rate of radar automatic detection and tracking in dense clutter and complex multi-objective situation. For the detection of maneuvering moving targets, its performance remains to be further improved.

## 4 Conclusion

This paper introduces the information fusion ideas to radar video moving target detection and extracts two effective features to describe targets and fuses them using D-S evidence theory to obtain the optimal decision rule as the standard of moving target automatic detection. The effectiveness of the algorithm is verified by the collected marine radar data. Next, we will consider extracting more features for fusion, in order to enhance the algorithm's detection performance for maneuvering fast moving targets. At the same time, the algorithm's combination with tracking algorithm and application to actual radar system will also be our future research directions.

## References

1. Xu H (2012) The research on target detection technology for marine radar in image processing. Wuhan University of Technology, Wuhan
2. He Y, Guan J, Meng XW et al (2011) Radar target detection and CFAR processing. Tsinghua University Press, Beijing, pp 6–9
3. Zhou W, He D, Guan J et al (2012) Ship detection in radar video based on visual saliency. Radar Science and Technology 10(1):54–58
4. Ke T, Li Y (2014) Research of object detection and tracking algorithm on the video surveillance in electric power system. Electr Power Sci Eng 30(1):42–46
5. Bao W, Li H, Li N et al (2009) A liveness detection method for face recognition based on optical flow field. In: IASP 2009. International conference on image analysis and signal processing, Taizhou, China, pp 233–236
6. Hu B, Gong X (2010) Moving objects detection based on improving background subtraction. Comput Eng Des 31(17):3841–3844
7. He Y, Wang G, Guan X et al (2010) Information fusion theory with applications. Publishing House of Electronics Industry, Beijing, pp 329–331
8. Yin S, Liu Y, Huo K (2014) Multi-sensor fusion recognition method based on improved D-S evidence theory. In: International conference on information and communications technologies (ICT 2014), Nanjing, China, pp 1–7

# Effect of Co-doping on the Electronic Structure and Absorption Spectrum of Wurtzite ZnO Under Pressure

Jing Leng, De-jun Wang, Zheng-hao Sun, Wei-jie Liu and Run-ru Liu

**Abstract** The effect of Co content and hydrostatic pressure on the electronic structure and absorption properties of wurtzite ZnO has been investigated by first principles calculations. The results reveal that the splitting between the energy levels of Co 3d states increased with pressures, which indicate the enhanced action of the crystalline field. In comparison to pure ZnO, a new peak appears in the low-energy region of the optical absorption spectrum in the system doped with Co and hydrostatic pressure is found to have great influence on the electronic transition of  $d-d$  orbital of Co atom in this system.

**Keywords** First principles · Electronic structure · Optical properties · Co-doped ZnO

---

J. Leng (✉) · Z. Sun · W. Liu  
School of Basic Sciences, Changchun University of Technology,  
Changchun 130012, China  
e-mail: lengjing.602@163.com

Z. Sun  
e-mail: sunzhenghao@ccut.edu.cn

W. Liu  
e-mail: liuweijie@ccut.edu.cn

D. Wang · R. Liu  
College of Continuing Education, Changchun University,  
Changchun 130022, China  
e-mail: wdj109@sina.com

R. Liu  
e-mail: l2004mmm@hotmail.com

## 1 Introduction

In recent years, zinc oxide (ZnO) doped with transitional metals has attracted a great deal of attention because of their potential in modern technology for things such as transparent conducting films, piezoelectric transducers, varistors, and phosphors. In particular, intensive investigations have been made into ZnO:Co system. A number of works have been carried out to investigate the physical properties of this doped system. However, most studies focus on its magnetic characters and Co-doping effect at ambient pressures, there are few reports about the electronic and optical properties with hydrostatic pressure. Motivated by this, we have carried out first principles investigation of electronic density and the absorption spectrum of Co-doped ZnO for wurtzite phases under different hydrostatic pressures in this study, the possible mechanisms responsible for the diversification in the UV-visible emission bands have been discussed in detail.

Transition metal (TM) ions-doped semiconductors possess rich electronic structures that combine the features of highly localized impurities, which have potential applications in many magnetic and optoelectronic devices [1–3]. In particular, ZnO-based materials have been of special interest due to its abundance and environment friendly nature and also due to its potential as a promising candidate material for the next generation of spintronic devices utilizing electronically or optically controlled magnetism [4–6]. Among the various singly doped ZnO systems,  $\text{Zn}_{1-x}\text{Co}_x\text{O}$  is a widely investigated TM-doped semiconductor currently in this context. Experimental studies of  $\text{Zn}_{1-x}\text{Co}_x\text{O}$  revealed that thin films or nanocrystals have ferromagnetic properties and the Curie temperatures higher than room temperature. Moreover,  $\text{Zn}_{1-x}\text{Co}_x\text{O}$  can change its magnetic state by p- or n-type doping [7]. Further studies showed that bulk  $\text{Zn}_{1-x}\text{Co}_x\text{O}$  with a low defect density and  $x$  in the range used in experimental exhibits ferromagnetic properties only at very low temperatures [8]. In parallel, theory has revealed that insulating  $\text{Zn}_{1-x}\text{Co}_x\text{O}$  without defect is not ferromagnetic whereas the role of n- or p-type carriers remains under debate. There are still many controversies ranging from ferro- and antiferromagnetic coupling to oscillatory behavior with Co–Co distance [9]. Up to date, most studies focus on its magnetic characters and Co-doping effect at ambient pressures, but there are few reports about its electronic and optical properties with hydrostatic pressure. Motivated by this, we have investigated electronic density and the absorption spectrum of Co-doped ZnO for wurtzite phases under different hydrostatic pressures in this study.

## 2 Computational Models and Method

The theoretical calculations were performed within the density functional theory as implemented in the Cambridge Serial Total Energy Package (CASTEP) code. We used the generalized gradient approximation (GGA) with the Perdew–Burke–Ernzerh

(PBE) scheme to describe the core region and valence electrons of the atoms in the supercell of pure and doped ZnO. A plane wave expansion up to a 700 eV cutoff energy was used. The Co-doped ZnO was constructed from a bulk ZnO ( $3 \times 2 \times 2$ ) supercell by replacing two O atoms with two Co atoms.

When the pressure is below 9 Gpa, the stable phase of ZnO crystal has a hexagonal structure with a P63mc space group [10, 11]. The  $3 \times 2 \times 2$  supercell containing 48 atoms is adopted for pure ZnO. A  $3 \times 2 \times 2$  supercell of  $\text{Zn}_{0.9176}\text{Co}_{0.0833}\text{O}$  is used for the Co-doped ZnO structure, which is obtained by replacing two O atoms with two Co atoms.

The electronic and optical properties were studied by using plane-wave pseudopotential method with CASTEP code, which is based on the density function theory (DFT). The GGA with the PBE scheme is adopted for describing the core region and valence electrons of the atoms in the supercell of pure and doped ZnO. The valence electron configurations for O, Zn, and Co atoms are considered as  $\text{O}2s^2p^4$ ,  $\text{Zn}3d^{10}4s^2$ , and  $\text{Co}3d^74s^2$ , respectively. The numerical integration of the Brillouin zone is sampled by  $4 \times 6 \times 4$  Monkhorst–Pack k-point meshes for all the models and the cutoff energy of the plane wave was set to 700 eV. In the optimization process, the energy changes, as well as the maximum tolerances of the force, stress, and displacement were set to  $5 \times 10^{-6}$  eV/atom, 0.01 eV, 0.02 GPa, and  $5 \times 10^{-4}$  eV/Å, respectively.

### 3 Results and Discussion

The band structure, density of states, and optical properties of Co-doped ZnO under high pressure were investigated according to first principles. The results show that the conduction band minimum (CBM) always moves to higher energy, whereas the valence band maximum moves to lower energy with increasing pressure, so the band gap broadens. The splitting between the energy levels of Co 3d states increased with pressures, which indicates the enhanced action of the crystalline field. In comparison to pure ZnO, a new peak appears in the low-energy region of the optical absorption spectrum in the system doped with Co. The curve shape for optical absorption spectrum is almost unchanged with increasing pressure, but all the peaks move to higher energy (blue shift).

#### 3.1 Band Structure and Electronic Properties

Figure 1a shows the band structure of pure ZnO under 0 Gpa. It can be observed that the top of valence band and the bottom of the conduction band locate at the same G-point, which means that pure ZnO with wurtzite structure is a direct gap material. The calculated band gap is about 0.749 eV, which is very close to the value calculated previously [11]. However, it is smaller than the experimental result



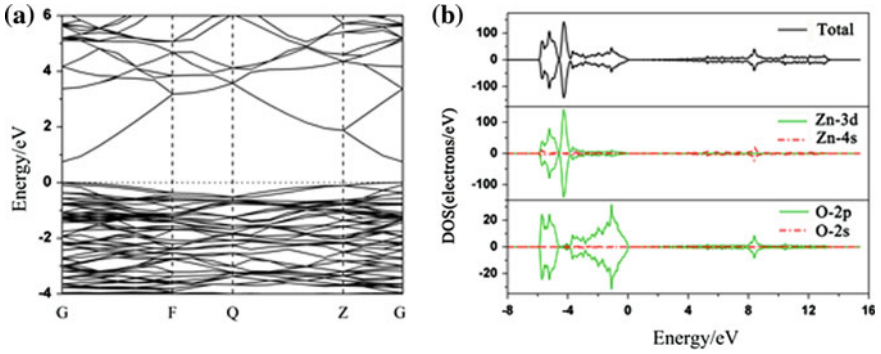


**Fig. 1** Band structure TDOS (a) and PDOS (b) of pure ZnO under 0 GPa. Fermi level is set to zero

of 3.37 eV due to the well-known intrinsic factor of DFT in GGA [6]. Although the band gap is underestimated, it does not affect the qualitative analysis of physical properties since only the relative positions of the occupied states and empty states need to be taken into account. Figure 1b presents the total density (TDOS) and the partial density states (PDOS) of pure ZnO. It can be seen that the valence band from  $-6$  to  $-0.01$  eV is mainly formed by O 2p states and Zn 3d states and the conduction band are built up from Zn 4s states and O 2s states.

Moreover, the upper valence band and the lower conduction band are dominated by Zn 4s and O 2p states. Here, we can conclude that the transition between VB and CB is due to the O 2p and Zn 4s states.

To investigate the effect of Co-doping on the electronic structure of ZnO, the band structure of Co-doped ZnO calculated at ambient pressure is shown in Fig. 2. It can be clearly seen that, both the valence band and conduction band apparently shift toward the low-energy region compared with pure ZnO. Moreover, the Fermi

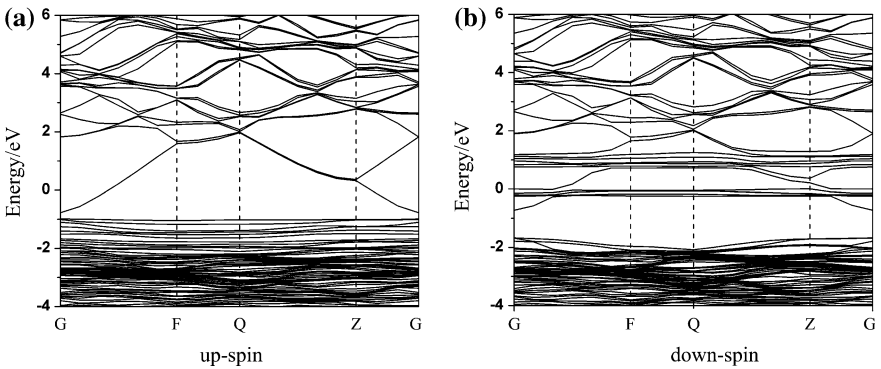


**Fig. 2** Band structures of the up spin (a) and down spin (b) of ZnO doped with Co under 0 GPa. Fermi level is set to zero

energy has accessed to valence band obviously and a metallic behavior is shown with up and down spin. These results are consistent with reports in other studies on cobalt-doped ZnO [9, 10]. As previously reported, due to the DFT underestimation of the CBM of the ZnO, there is partial occupation of both the ZnO CBM and the Co  $e_d$  states producing an incorrect metallic electronic structure.

In order to get more physical insight of electronic band structure and to further investigate the effect of hydrostatic pressure, the total density of states (TDOS) and the partial density of states (PDOS) for Co-doped ZnO are inspected in Fig. 3a–f.

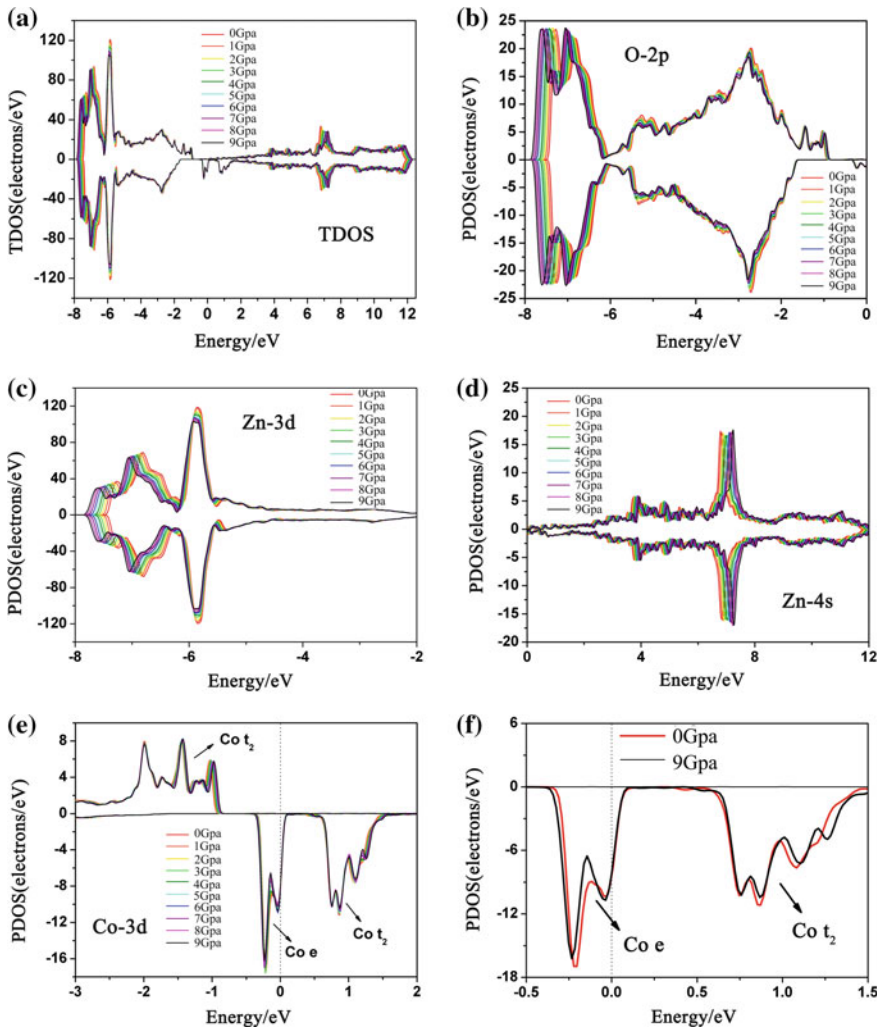


**Fig. 3** Total DOS for Co-doped ZnO (a), PDOS for O-2p (b), Zn-3d (c), Zn-4s (d) and Co-3d (e, f) at pressures ranged from 0 to 9 GPa

As shown in Fig. 3a, total density of states is extended from about  $-7.92$  to  $12.38$  eV. With pressure increasing, all energy bands have been expanded. Figure 3b–e is defining the character of PDOS with increasing pressure. It can be seen that the Zn3d states is dominant at high binding energy, which are followed by the main O2p valence band. The topmost occupied states are the minority Co  $e_d$  states, with the unoccupied  $t_{2d}$  states present around the onset of the ZnO conduction band. However, the Zn4s state plays a major role in the construction of conduction band. The pressure, when applied on DOS, results in the broadening of the bandwidth of O2p, Zn3d, and Zn4s band. Moreover, the valance bands shift obviously to low-energy levels and conduction band to higher ones. The Co 3d states under 0 and 9 Gpa is presented in Fig. 3f, in order to get a detailed investigation on the effect of hydrostatic pressure. One can see that, as the pressure increased, the lower  $e_d$  states and the upper  $t_{2d}$  states shifting to opposite direction to each other. It indicated that the splitting between the energy levels of Co 3d states increased, which can be attributed to the enhanced action of the crystalline field under pressure.

### 3.2 Optical Properties

The absorption coefficient is an important parameter, which tells the decay of light intensity spreading in unit distance in medium. Figure 4a shows the variations of absorption coefficient  $\alpha(E)$  with energy of Co-doped ZnO at pressures from 0 to 9 Gpa. Compared with pure ZnO, the absorption peaks position and shape of Co-doped ZnO changed a little in the spectrum in an energy range of  $4.0$ – $13.0$  eV. One can see that as the pressure increases, the absorption increases and small blueshift emerges in the absorption spectrum. Besides, it is noted that a new absorption peak appeared in the low-energy region. This peak is obtained from the electron transition of  $d$ – $d$  orbital of Co atom, which agrees with the experimental

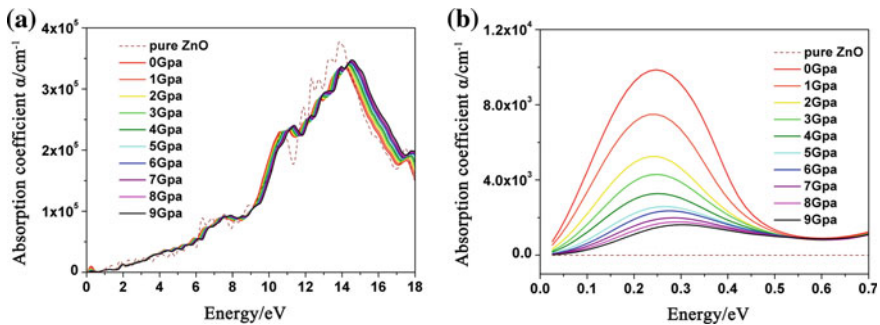


**Fig. 4** Optical absorption spectra of Co-doped ZnO (a) and the absorption peak obtained from the electron transition of  $d$ – $d$  orbital of Co atom (b)

results [8]. The calculated results implied that the photocatalytic activity of ZnO in the UV-visible light range will be improved by doping with Co. Moreover, it can be clearly seen in Fig. 5b that the absorption intensity decreases obviously when pressures increase. As we know, the absorption intensity is directly determined by the electron transition probability [11]. Since it is affected by the pressures, it indicated that the hydrostatic pressure could have great influence on the electronic transition of  $d-d$  orbital of Co atom. The electron transition probability will decrease with the increasing of hydrostatic pressures. The results suggested that the applied pressure can be used as a probe of the optical characters to tune the absorption properties of semiconductors.

## 4 Conclusion

These calculated results indicated that Co-doping is crucial to improve the photocatalytic activity of ZnO in the UV-visible light range. Besides, hydrostatic pressures have great influence on the electronic transition of  $d-d$  orbital of Co atom in this singly doped ZnO system. The applied pressure can be used as a probe of the properties of semiconductors as well as an engineering technique of defects in them.

In summary, first principles calculations have been carried out to study the band structure and optical properties of Co-doped ZnO system under different hydrostatic pressures. The calculated band gap is in good agreement with the available theoretical values. The electronic structures of Co-doped ZnO reveal that the splitting between the energy levels of Co 3d states increased with pressures, which indicate the enhanced action of the crystalline field. The absorption spectrum shows that a new peak is observed in the low-energy region, which originates from the electron transition of  $d-d$  orbital of Co atom. Moreover, its intensity decreases gradually with increasing pressures. These calculated optical properties suggest that Co-doping is crucial to improve the photocatalytic activity of ZnO in the UV-visible light range. Besides, hydrostatic pressures have great influence on the electronic transition of  $d-d$  orbital of Co atom in this singly doped ZnO system. The applied pressure can be used as a probe of the properties of semiconductors as well as an engineering technique of defects in them. It also offers a new method to tune the optical absorption properties conveniently, which still need further studies and experimental verification.

**Acknowledgment** This work was supported by National Natural Science Foundation of China (51302019), The Science and Technology Research Projects of Education Department of Jilin Province, China(No. 2014133) and The Research Funds of Science and Technology Development Program of Changchun city under Grant (No. 13GH11 and No. 14KG108).

## References

1. Cui XY, Delley B, Freeman AJ (2007) Neutral and charged embedded clusters of Mn in doped GaN from first principles. *Phys Rev B* 76:045201
2. Dietl T, Ohno H, Matsukura F, Cibert J, Ferrand D (2000) Zener model description of ferromagnetism in Zinc-Blende magnetic semiconductors. *Science* 287:1019
3. Bougeard D, Ahlers S, Trampert A, Sircar N, Abstreiter G (2006) Clustering in a precipitate-free GeMn magnetic semiconductor. *Phys Rev Lett* 97:237202
4. Johnson CA, Kaspar TC, Chambers SA, Salley GM, Gamelin DR (2010) Sub-band-gap photoconductivity in  $\text{Co}^{2+}$ -doped ZnO. *Phys Rev B* 81:125206
5. Ghosh S, Wang Q, Das GP, Jena P (2010) Magnetism in ZnO nanowire with Fe/Co codoping: first-principles density functional calculations. *Phys Rev B* 81:235215
6. Ney A, Ney V, Ye S, Ollefs K, Kammermeier T (2010) Clustering in a precipitate-free GeMn magnetic semiconductor. *Phys Rev B* 82:041202R
7. Gacic M, Jakob G, Herbolt C, Adrian H (2007) Magnetism of Co-doped ZnO thin films. *Phys Rev B* 75:205206
8. Sanchez N, Gallego S, Muñoz MC (2008) Magnetic states at the oxygen surfaces of ZnO and Co-doped ZnO. *Phys Rev Lett* 101:067206
9. Iuşan D, Knut R, Sanyal B, Karis O, Eriksson O, Coleman VA, Westin G, Wikberg JM, Svedlindh P (2008) Electronic structure and chemical and magnetic interactions in ZnO doped with Co and Al: experiments and ab initio density-functional calculations. *Phys Rev B* 78:085319
10. Pua CY, Tang X, Zhang QY (2011) First principles study on the structural and optical properties of the high-pressure ZnO phases. *Solid State Commun* 151:1533–1536
11. Maensiri S, Laokul P, Klinkaewnarong J, Thomas C (2009) Structure and magnetic properties of  $\text{Zn}_{0.9}\text{Co}_{0.1}\text{O}$  nanorods synthesized by a simple sol-gel method using metal acetylacetonate and poly(vinyl alcohol). *Appl Phys A* 94–3:601–606

# Fitting Formula of Sheath Currents and Arrangement Optimization of Cables

Yong-zhi Wang, Wei Cao, Hai-sheng Liang and Fan Li

**Abstract** There will be circulating currents in metal sheaths of cross bonding cables when length or arrangements of three segments are different. The phasor sums of sheath-induced voltages in sheath cross bonding cables are first analyzed. Then, the circulating currents are calculated by EMTP with varied lengths of three segments to get the sample data, which are in turn used to fit out the empirical formula for evaluating sheath circulating currents. Finally, the principle of mixed arrangements is proposed to reduce sheath circulating currents in sheath cross bonding cables when the lengths of cable segments are not equal.

**Keywords** High-voltage cable · Sheath currents · Empirical formula · Arrangement

## 1 Introduction

With the development of urbanization, many high-voltage cables are applied in urban transmission area. Sheath-induced voltages should be less than 50 V without safety measures, and which should be less than 300 V when there are safety measures [1]. Sheath cross bonding is used widely [2–5]. However, due to the limitation of environment, it is difficult to ensure that three segments of cable get completely transposition. So, there will be sheath currents in cables, which will reduce cable transmission capacity and shorten cable life [6–8].

At present, there are three methods for calculating sheath currents: first, EMTP was used to calculate sheath currents, and cable models should be built in EMTP, in addition, parameters selection and setting are complex. So, it is difficult to be mastered

---

Y. Wang (✉) · W. Cao  
Shanghai University of Electric Power, Shanghai 200090, China  
e-mail: wangyongzhi0315@163.com

H. Liang · F. Li  
State Grid of Shanghai Electric Power Economic Institute of Technology,  
Shanghai 2000002, China

by project workers. Secondly, lumped parameter builds loop equations, and computer program is needed to acquire equation results [9–11]. This method needs more works and it is still difficult for unprofessional engineers. Lastly, electrical engineers usually estimate sheath currents using work experience [12]. As a result, the results will not be accurate and the engineers without experience will be helpless.

The article uses dates simulated by EMTP fits current formula which is easily mastered by electrical engineers. In addition, it proposes a method that the longer segment uses vertical (flat) arrangement and the shorter segment uses triangle arrangement to decrease sheath currents.

## 2 Analysis of Sheath-Induced Voltages

### 2.1 Sheath-Induced Voltages of Cables in Single Segment

Cables are laid in pipes which are modified as  $3 \times 7$  or  $2 \times 10$ . HV cables are required to lie in the outside of pipes for the purpose of cooling. So, cables in pipes can only be arranged in flat arrangement, vertical arrangement, and triangle arrangement, see Fig. 1.

Calculation of sheath-induced voltages per km is showed in formula (1)

$$\left. \begin{aligned} E_{SA} &= 2\omega I \times 10^{-4} \left[ \frac{\sqrt{3}}{2} \ln n + j\frac{1}{2} \ln \frac{nS^2}{GMR_s} \right] \\ E_{SB} &= 2\omega I \times 10^{-4} \left[ \frac{\sqrt{3}}{2} \ln \frac{mS}{GMR_s} - j\frac{1}{2} \ln \frac{S}{m \times GMR_s} \right] \\ E_{SC} &= 2\omega I \times 10^{-4} \left[ -\frac{\sqrt{3}}{2} \ln \frac{mS}{GMR_s} - j\frac{1}{2} \ln \frac{n^2 S}{m \times GMR_s} \right] \end{aligned} \right\} \quad (1)$$

$I$  is cable load current;  $GMR_s$  is Geometric radius;  $S$  is cable distance between phase A and phase B;  $mS$  is cable distance between phase B and phase C;  $nS$  is cable distance between phase A and phase C.

When load currents are 698 A, which is the rating value, sheath-induced voltages per km of different arrangements are calculated by formula (1), see Table 1.

From Table 1, we can see that sheath-induced voltages of flat arrangement are more than the voltages in right triangle arrangement, in Table 1.

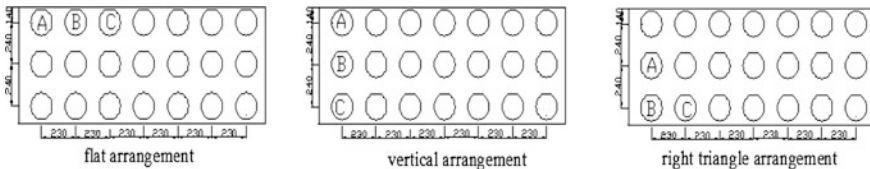


Fig. 1 Cable arrangements

**Table 1** Induced voltages in metal sheath of single segment

Arrangement	Sheath-induced voltages of phase A(V)	Sheath-induced voltages of phase B(V)	Sheath-induced voltages of phase C(V)
Flat	$89.8\angle 72.9$	$70.8\angle -30$	$89.8\angle -135.9$
Vertical	$91.6\angle 73.3$	$72.4\angle -30$	$91.6\angle -133.3$
Right triangle	$80.6\angle 81.2$	$71.6\angle -31.3$	$79.8\angle -133.3$
Trefoil	$70.6\angle 90$	$70.6\angle -30$	$70.6\angle -150$

## 2.2 Analysis of Sheath-Induced Voltages in Cross Bonding Cables

Using formula (1), calculate sheath-induced voltages of single segment, and get the summation of the major section consisting three minor segments according cross bonding theory. Then phasor sums of induced voltages will be obtained and the distribution of sheath-induced voltages along the cable distance also can be obtained.

From Table 1, sheath-induced voltages of three phases are equal in size and the phase angles are  $120^\circ$  in difference. So, only the lengths of three segments are equal and the arrangements of three segments are the same, phasor sums of sheath-induced voltages in three segments are 0 in the trefoil arrangement, such as Fig. 2. The distribution of induced voltages when the three segments are not equal is shown in Fig. 3. Therefore, if cable arrangements and three segments of cables are imbalance, the phasor sums of sheath-induced voltages are not 0 after cross bonding, then there will be currents in metal sheaths, and the sizes of currents are related to phasor sums of sheath-induced voltages.

**Fig. 2** Induced voltage profile of three equal length segments in trefoil arrangement

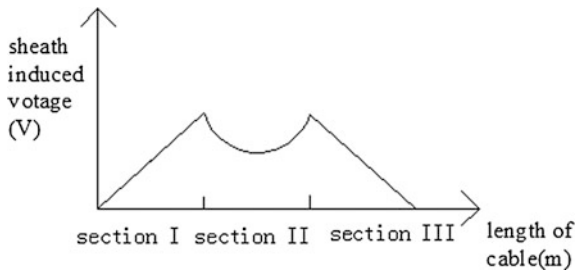
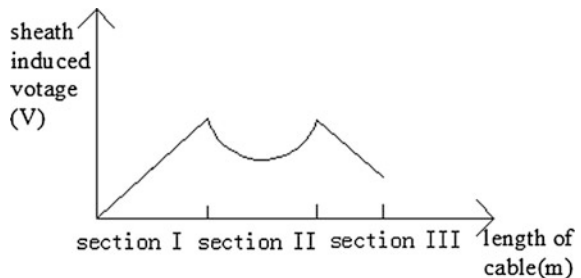


**Fig. 3** Induced voltage profile of three unequal length segments in trefoil arrangement





### 3 Analysis of Sheath Currents in the Same Arrangement After Cable Sheaths Cross Bonding

According to the theory of sheath current calculation, sheath currents are proportional to the differences of sheath voltages in the two sides of cable. Combining with the above conclusions, the relationship between sheath currents and the differences of three segments is approximately linear. Therefore, data samples simulated by EMTP can be used to fit current formula.

#### 3.1 Method of Curve Fitting

For given dates  $(x_i, y_i)$  ( $i = 1, 2, \dots, N$ ), the formula of  $y = a+bx$  should be found and make sure that total error of  $Q = \sum_{i=1}^N [y_i - (a + bx_i)]^2$  is minimum.

The parameters of  $a$  and  $b$  making  $Q$  get the minimum should meet  $\partial Q/\partial a = 0$ ,  $\partial Q/\partial b = 0$ , then equation group obtained is

$$\begin{aligned} aN + b \sum_{i=1}^N x_i &= \sum_{i=1}^N y_i \\ a \sum_{i=1}^N x_i + b \sum_{i=1}^N x_i^2 &= \sum_{i=1}^N \Delta x_i y_i \end{aligned} \quad (2)$$

Solve two element equation and get the parameters of  $a$  and  $b$ , then the formula describing the data curve will be obtained.

#### 3.2 The Induction of Sheath Current Formula in Single Arrangement

According to the method of curve fitting, take the differences of three segments ( $\Delta L$ ) into  $x$ , and take sheath currents ( $I_S$ ) into  $y$ . By setting different values of  $\Delta L$ , sheath currents of cross bonding cables will be obtained through EMTP simulation. Then data samples will be obtained, and relation curves between  $\Delta L$  and  $I_S$  can be described by MATLAB, see Figs. 4 and 5, in which the linear relationship between  $\Delta L$  and  $I_S$  is easily seen, then sheath current formula can be obtained according to the method of 2.1.

When load currents are 698 A, length of single segment cable is in the range of 200–600 m, using curve fitting method, sheath current formula of vertical (flat) arrangement is shown in the formula (3):

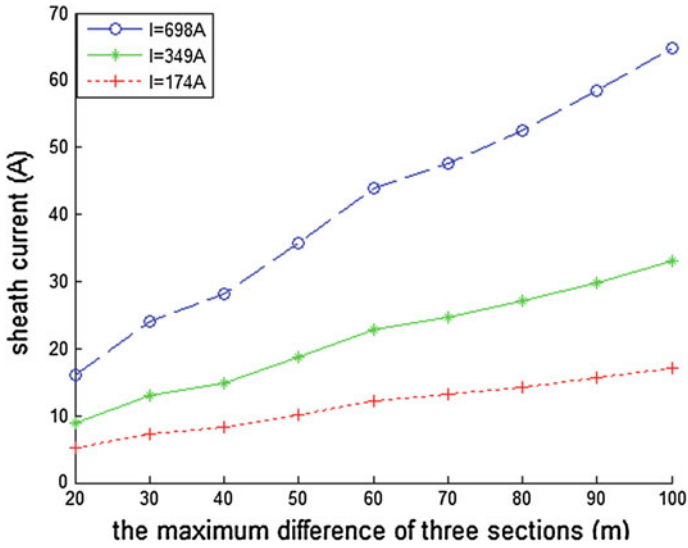


Fig. 4 The curve between  $I_s$  and  $\Delta L$  under vertical arrangement

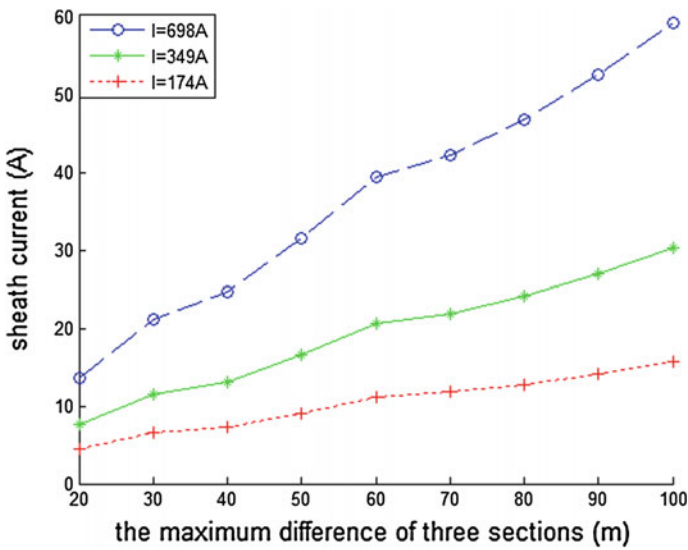


Fig. 5 The curve between  $I_s$  and  $\Delta L$  under right triangle arrangement

**Table 2** Comparison between EMTP simulation and formula calculation under vertical arrangement

Differences of three segments length	Sheath currents when load current are 698.1 A			Sheath currents when load current are 349.2 A			Sheath currents when load current are 74.6 A		
	EMTP simulation (A)	Formula calculation (A)	Relative error (%)	EMTP simulation (A)	Formula calculation (A)	Relative error (%)	EMTP simulation (A)	Formula calculation (A)	Relative error (%)
0	4.9	5.49	12	3.34	2.75	17.8	2.53	1.37	45.9
20	16.14	17.41	7.9	8.85	8.71	1.7	5.22	4.35	16.7
40	28.21	29.33	4.0	14.86	14.67	1.3	8.19	7.34	10.4
60	43.82	41.25	5.9	22.80	20.63	9.5	12.28	10.32	15.9
80	52.55	53.17	1.2	27.02	26.59	1.6	14.26	13.3	6.7
100	64.74	65.09	0.5	32.98	32.55	1.3	17.11	16.28	4.9
150	95.1	94.89	0.2	48.19	47.45	1.5	24.72	23.73	4.0

**Table 3** Comparison between EMTP simulation and formula calculation under right triangle arrangement

Differences of three segments length	Sheath currents when load current are 698.1 A			Sheath currents when load current are 349.2 A			Sheath currents when load current are 74.6 A		
	EMTP simulation (A)	Formula calculation (A)	Relative error (%)	EMTP simulation (A)	Formula calculation (A)	Relative error (%)	EMTP simulation (A)	Formula calculation (A)	Relative error (%)
0	3.27	3.60	10.2	2.471	1.80	27.2	2.08	0.90	56.6
20	13.58	14.65	7.8	7.556	7.325	3.1	4.56	3.66	19.7
40	24.6	25.70	4.5	13.04	12.85	1.4	7.27	6.43	11.6
60	39.32	36.75	6.5	20.54	18.38	10.5	11.15	9.19	17.6
80	46.72	47.80	2.3	24.10	23.90	0.8	12.80	11.95	6.6
100	59.20	58.85	0.2	30.19	29.43	2.5	15.69	14.72	6.2
150	87.67	86.48	1.4	44.45	43.24	2.7	22.84	21.62	5.3

$$I_s = 5.491 + 0.596 \times \Delta L \quad (3)$$

If arrangements and cable length of three segments are determined, sheath currents are proportional to load currents. So, the formula applied to any load currents of vertical (flat) arrangement will be deduced, see formula (4)

$$I_s = \frac{I_c}{698} [5.49 + 0.60 \times \Delta L] \quad (4)$$

Similarly, Fig. 5 sheath current formula of right triangle arrangement will be obtained see formula (5)

$$I_s = \frac{I_c}{698} [3.60 + 0.55 \times \Delta L] \quad (5)$$

In the formula,  $I_s$  is sheath current;  $I_c$  is cable load current;  $\Delta L$  is the maximum difference of three segment cables.

Sheath currents are calculated by formula (4) and formula (5), when  $\Delta L$  are different, and the calculation results are compared with simulation dates, see Tables 2 and 3.

In Tables 2 and 3, the relative error between EMTP simulation and formula calculation is less than 8 %, and the relative error of individual point is larger, which is due to smaller values of sheath currents that even 1–2 A of current will cause relative error large. However, the absolute error is less than 3 A, which is 0.3 % of load currents, the error is accepted when calculating sheath currents in project area.

## 4 Influence of Mixed Arrangements on Sheath Currents

In cross bonding system, it is difficult to ensure three segments of cables same in length and in arrangements due to the limitation of environment. From 1, sheath-induced voltages of vertical (flat) arrangement are more than sheath-induced voltages of right triangle arrangement in the same situation. Therefore, when three segments are unequal, the longer segment of cable uses right triangle arrangement in which the sheath-induced voltages per km are lower, and the shorter segment of cable uses vertical (flat) arrangement in which sheath-induced voltages per km are larger. Then, voltage phasor sums of three segments and sheath currents will be reduced.

When load currents are 698 A, sheath-induced currents with different  $\Delta L$  are simulated by EMTP in different arrangement combinations. In Table 4, sheath currents of recommend arrangements that the shorter segment uses vertical (flat) arrangement and the longer one uses right triangle arrangement are the least. On the contrary, when the longer segment uses vertical (flat) arrangement and the shorter one uses right triangle arrangement, sheath currents will be increased more than 30 %.

**Table 4** Influence of different arrangements on sheath currents when three segments are not equal

Length of three segments (m)	Vertical arrangement of each segment	Right triangle arrangement of each segment	Vertical arrangement of each segment	Right triangle arrangement of each segment	Mixed arrangement I (vertical-right triangle-vertical)	Mixed arrangement II (right triangle-vertical-flat)
350–450–400	Currents of formula calculation (A)	Currents of formula calculation (A)	Currents of EMTP simulation (A)	Currents of EMTP simulation (A)	Currents of EMTP simulation (A)	Currents of EMTP simulation (A)
	65.49	58.6	64.74	56.19	17.15	98.25
			52.61	47.42	43.08	37.89
			44.31	49.40	56.58	79.16

## 5 Conclusion

The segments of cables are determined by project workers according to experience in cross bonding cables. Usually the length differences between two segments should be less than 100 m, which can make sure sheath currents lower than 10 % of load currents. The article gives an empirical formula to calculate sheath currents and provides a new method that uses mixed arrangements to reduce sheath currents when three segments are unequal in cross bonding system.

1. Using curve fitting method to get the sheath current formula which is easily mastered by electrical project workers and, the calculation is accurate in project.
2. Considering the characteristics that three segments of cables in cross bonding system are unequal, phasor sum is analyzed through phasor diagram and the method that longer segment of cable uses right triangle arrangement and the shorter one uses vertical (flat) arrangement reducing sheath current is obtained to reduce sheath current.

**Acknowledgments** This work was supported by The National High Technology Research and Development Program of China (863 Program) (2011AA05A106)

## References

1. National Standard of the People's Republic of China GB/50217-2007 (2007) Code for design of cables of electric engineering
2. ANSI/IEEE Std575-1988 (1988) An American national standard IEEE guide for the application of sheath-bonding methods for single-conductor cables and the calculation of induced voltages and currents in cable sheaths
3. Du B, Li Z, Zhang K et al (2013) Calculation and application of grounding current of 220 kV XLPE cables. *High Volt Eng* 39(5):1034–1039
4. Wang J (1993) Metal sheath connection mode of single-core cables. *East China Electr Power* 10:49–52
5. Zhou W (2012) Analysis of grounding mode of high voltage cable system based on engineering project. *Electr Power Electr* 32(1):38–40
6. Niu H, Wang X, Yi Z et al (2005) Study on circulating current of 110 kV single-core cable. *High Volt Eng* 31(8):15–17
7. Xu X, Chen Y (2010) Investigation of the induced current in the metallic sheath of single core HV power cables, part 1. *Electr Wire Cable* 5:42–46
8. Wang B, Luo J, Huang H et al (2009) Analysis of circulating current in sheaths of 220 kV XLPE single-core cables. *High Volt Appar* 35(5):141–145
9. Feng C, Wang P, Ma L et al (2015) Analysis on the circulation of metal sheath in the multi loop single core XLPE power cable. *Qinghai Electr Power* 34(1):31–35
10. Luo Z, Zhan W, Wutao et al (2014) Development and application of the software for the calculation of the metal sheath circulation in the multi loop cable. *Electr Wire Cable* 2(2):36–40
11. Zhang K (2011) Mechanism and failure analysis of high voltage cross linked polyethylene cable grounding current. Master Thesis of Tianjin University, Tianjin
12. China Southern Grid Corp Enterprise Standard Q/CSG114002-2011 (2011) Electrical equipment preventive test procedures

# Analysis and Simulation of Electric Vehicle Power Battery

Longfei Ma, Baoqun Zhang, Cheng Gong, Ran Jiao, Rui Shi  
and Zhongjun Chi

**Abstract** Energy and the environment have become the most current concerns in the world, and many countries have considered developing electric vehicles as an important means to solve the problem of energy and the environment. So, it is very necessary to research the effect on grid by electric vehicle charge and discharge but it must build a suitable model of batteries of electric vehicle. This paper built a PNGL and Thevenin simulation model, and compared the simulation curve with the actual measure curve. The results prove that the two methods on two occasions applications are more appropriate.

**Keywords** Battery · Simulation · GNL · Thevenin

## 1 Introduction

Energy and the environment have become the most current concerns in the world, and many countries have considered developing electric vehicles as an important means to solve the problem of energy and the environment. Batteries are key components in electric vehicles, which have significant impact on the vehicle power

---

L. Ma (✉) · B. Zhang · C. Gong · R. Jiao · R. Shi · Z. Chi  
State Grid Beijing Electric Power Research Institute, Beijing, China  
e-mail: malongfei1987@163.com

B. Zhang  
e-mail: davehilbert@163.com

C. Gong  
e-mail: 123.gc@163.com

R. Jiao  
e-mail: jiaoran0418@sina.com

R. Shi  
e-mail: shirui\_56@163.com

Z. Chi  
e-mail: czjtsh@163.com



performance, fuel economy, and safety. In order to develop EV in China, as well as the corresponding grid control strategy and digital real-time simulation method, reveal that the influence of grid, the electric car charging research power battery model is established and the simulation calculation is very necessary [1].

## 2 Battery Simulation Model

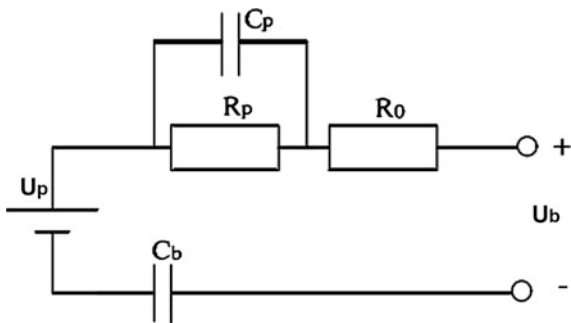
This paper focuses on the equivalent model of batteries, which are internal resistance model, Thevenin model, resistance capacity model, PNGV (The Partnership for a New Generation of Vehicles) model, and GNL (General nonlinear model) model. However, the resistance model can only reflect the effect of the internal resistance of the battery charge, which cannot describe the battery performance. Thevenin model can make a prediction reflecting the influence of the internal resistance of the battery on the battery charge and discharge performance, but does not reflect the cell polarization effect [2]. Resistance capacitance model can reflect differences in the process of charge and discharge the battery internal resistance by adding the RC link, but the model cannot reflect the influence of polarization effect of battery on the battery charge and discharge process. PNGL model and GNL model are improved from Thevenin model. The PNGV model increases a capacitor based on the resistive capacitive circuit model, which can reflect the change of the battery terminal voltage generated by the current with time. The GNL model based on the electrochemical mechanism describes the polarization, electrochemical plan, and concentration difference polarization in detail. However, because of the introduction of a number of resistance and capacitance and the nonlinear link, it is very complex in parameter identification.

In general, the model of the equivalent circuit model of the battery is different, and the simulation accuracy is different [3]. The GNL model can be used to model the battery, but the circuit topology is too complex, and the testing and parameter identification of the battery is very high, which is not suitable for the application. The internal resistance of the battery model is too simple, which cannot reflect the cell polarization effect on the model. Taken together, this paper chooses the Thevenin model as the constant current charging simulation model and the PNGV model as the dynamic simulation model.

## 3 Identification Principle of Battery Parameters

Figure 1 is a typical PNGV battery model circuit diagram. Ideal voltage source  $U_0$  indicates the electrode potential of the battery. Polarization resistance  $R_p$  and polarization capacitance  $C_p$  are shunt connection which can describe transient process caused by cell polarization effect including transient process of dynamic current response and recovery effect of charge and discharge.  $R_0$  is the internal

**Fig. 1** PNGV battery model circuit diagram.



resistance of the battery and  $C_b$  reflects the shift of the battery terminal voltage with time in the process of battery charging and discharging.

According to the Fig. 1, combined with the circuit principle of differential equation model is as follows.

$$\begin{cases} \begin{bmatrix} \frac{dU_b}{dt} \\ \frac{dU_p}{dt} \end{bmatrix} = \begin{pmatrix} 0 & 0 \\ 0 & -\frac{1}{C_p R_p} \end{pmatrix} \begin{bmatrix} U_b \\ U_p \end{bmatrix} + \begin{bmatrix} \frac{1}{C_b} \\ \frac{1}{C_p} \end{bmatrix} [I_L] \\ [U_L] = [-1, -1] \begin{bmatrix} U_b \\ U_p \end{bmatrix} + [-R_o][I_L] + [U_{OC}] \end{cases} \quad (1)$$

where  $U_b$  is the battery voltage, and  $U_p$  is the electrode potential.  $C_b$  is the series capacitance, and  $C_p$  is the polarization capacity.

If left batteries stand enough before they charge and discharge, the initial charge of  $C_b$  and  $C_p$  will be 0.

$$\bar{U}_{L,i} = U_{OCV} - \frac{1}{C_b} \sum (I_L \Delta t)_i - R_o I_{L,i} - R_p I_{p,i} \quad (2)$$

And,

$$\begin{aligned} i_p &= \frac{Q_p}{C_p R_p} \\ Q_p &= \int (i_L - i_p) dt \end{aligned} \quad (3)$$

$$\sum (I_L \Delta t)_i = \sum (I_L \Delta t)_{i-1} + \frac{I_{L,i} + I_{L,i-1}}{2} \Delta t \quad (4)$$

$$I_{p,i} = \left( 1 - \frac{1 - e^{-\frac{\Delta t}{\tau}}}{\frac{\Delta t}{\tau}} \right) \times I_{L,i} + \left( \frac{1 - e^{-\frac{\Delta t}{\tau}}}{\frac{\Delta t}{\tau}} - e^{-\frac{\Delta t}{\tau}} \right) \times I_{L,i-1} + e^{-\frac{\Delta t}{\tau}} \times I_{p,i-1} \quad (5)$$

$U_L$  and  $I_L$  can be obtained by measuring the voltage of the battery and  $I_p$  can be obtained from Eqs. (3) and (4).  $C_b, R_o, R_p$  can be regarded as the unknown coefficient of the linear equation. Then all of the equations can be regarded as system of linear equations, from which it can get unknown coefficient [4].

Equations (6), (7), (8) are discretization handled from Eqs. (2) and (3).

$$U_L = U_{OC} - \frac{1}{C_b} \sum i_L \Delta t - R_p i_L - R_p i_p \tag{6}$$

$$i_{p,i} = \frac{Q_{p,i}}{C_p R_p} \tag{7}$$

$$Q_{p,i} = \sum (i_{L,i} - i_{p,i}) \Delta t \tag{8}$$

### 4 The Simulation of Battery

According to the analysis results, it can be obtained from the simulation model of battery on the Simulink [5]. Figure 2 is the simulation model of PNGV, which generates the PNGV wave, Fig. 3 is the simulation model of battery in PNGV, which can simulate the battery wave under the condition that input is transient current.

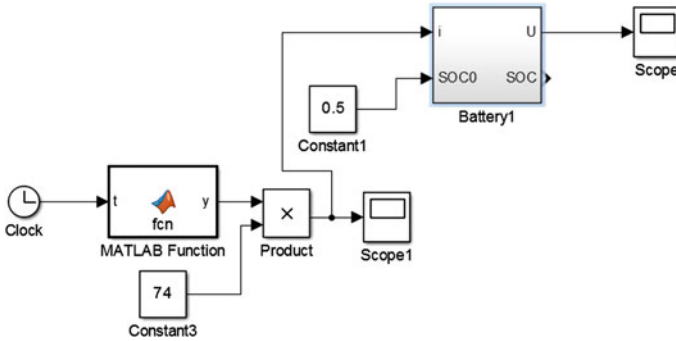


Fig. 2 The simulation model of PNGV

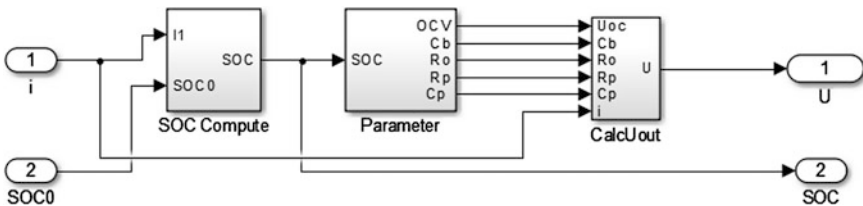
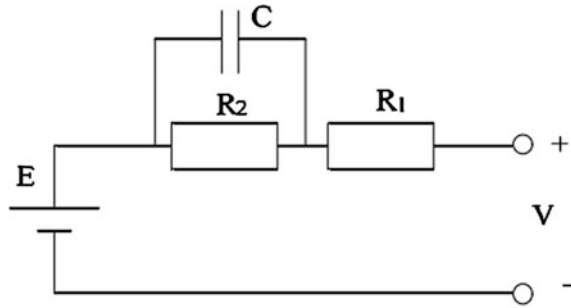


Fig. 3 The simulation model of battery in PNGV

**Fig. 4** The model of Thevenin



**Fig. 5** The 5 V/100 A lithium battery discharge test cabinet



The constant current charge and discharge of battery simulation model are based on Thevenin model in Fig. 4 which is very similar to PNGV model [6, 7]. The equation of Thevenin model can be obtained from PNGV equation easily, so here only the simulation results are given (Fig. 5).

### 5 The Actual Measurement of Power Battery

This paper uses the 5 V/100 A lithium battery discharge test cabinet to test batteries [8]. It can take the largest 100 A charge and discharge test, and is suitable for the comprehensive performance test of lithium polymer, lithium ion, nickel metal hydride, nickel cadmium batteries, and battery materials research [9]. The instrument is as follows, and the test results are in Figs. 6 and 7.

Fig. 6 The HPPC curve of simulation and actual test

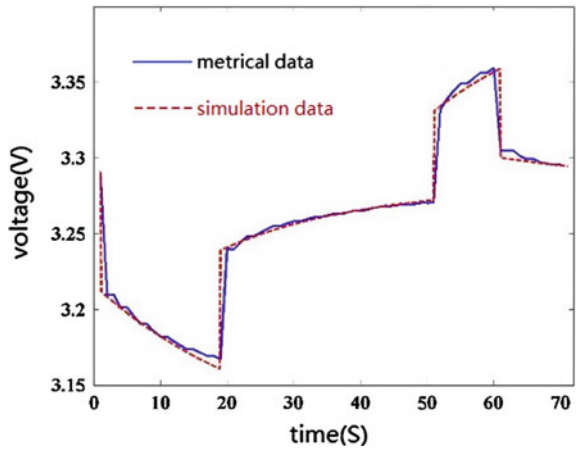
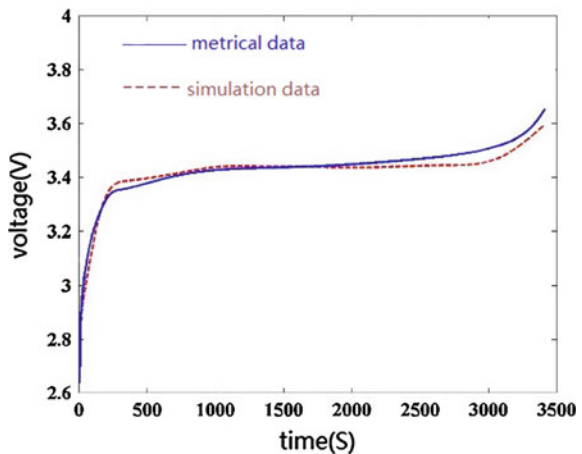


Fig. 7 The battery charging curve of simulation and actual test



## 6 The Simulation Results and the Actual Measurement Results

According to the research and simulating, the simulation curves and the actual measurement curves are as follows.

From the curve, the simulation curve fits the actual measure curve very well, especially the curve between 0 and 2000s is in good agreement.

## 7 Conclusion

This paper built Thevenin model and PNGV model based on parameter identification of battery. Then, it simulated the electric vehicle battery character under the condition of constant current charge and discharge and pulse charging and discharging. According to the simulation curve and actual measure curve, they fit well, so Thevenin model can describe the constant current charging simulation model and the PNGV model can describe the dynamic simulation model.

## References

1. Freedom C (2003) Battery test manual for power-assist hybrid electric vehicles. Department of Energy, October 2003, DOE/ID-11069, 20032900-2911
2. Ceraolo M (2000) New dynamical models of lead-acid batteries. *IEEE Trans Power Syst* 15(4):1184–1190
3. Dubarry M, Vuillaume N, Liaw BY (2010) Origins and accommodation of cell variations in Li-ion battery pack modeling. *Int J Energy Res* 34(2):216–231
4. Anderson TW (1957) Maximum likelihood estimates for a multivariate normal distribution when some observations are missing. *J Am Stat Assoc* 52(278):200–203
5. Park SH, Park KB, Kim HS et al (2012) Single-magnetic cell-to-cell charge equalization converter with reduced number of transformer windings. *IEEE Trans Power Electr* 27(6): 2900–2911
6. Pecas Lopesa JA, Polenzb SA, Moreiraa CL et al (2010) Identification of control and management strategies for LV unbalanced microgrids with plugged-in electric vehicles. *Electr Power Syst Res* 80(8):898–906
7. Kisacikoglu MC, Ozpineci B, Tolbert LM (2010) Examination of a PHEV bidirectional charger system for V2G reactive power compensation. In: Power electronics conference and exposition (APEC) twenty-fifth annual IEEE
8. Mets K, Verchuern T, Haerick W et al (2010) Optimizing smart energy control strategies for plug-in hybrid electric vehicle charging. *IEEE/IFIP Network Operations and Management Symposium Workshops*, Osaka, Japan
9. Logghe S, Van Herbruggen B, Zeebroeck BV (2006) Emissions of road traffic in Belgium. *Transport & Mobility Leuven*, Brussels

# Vibration Suppression of a 3-DOF Parallel Manipulator Based on Single-Mode Input Shaping Combined with PD

Bing Li and Yulan Wei

**Abstract** The residual vibration of flexible systems limits accuracy of motion trajectory and motion response speed. This paper presents the methodology of input shaping combined with PD control strategy to suppress the residual vibration of a 3-DOF parallel manipulator. First, the manipulator is introduced, and natural frequency and damping ratio of the 3-DOF parallel manipulator are obtained by experimental modal tests. Then, the theories of input shaping, PD and input shaping combined with PD are presented. Finally, the response curves of manipulator of the PD and Zero-Vibration input shaper combined with PD approaches are expressed by numerical simulation. At last, a comparison of response curves with different  $k_p$  is carried out.

**Keywords** Input shaping · Manipulator · PD · Vibration suppression · Single-mode

## 1 Introduction

In aerospace, manufacturing, and industry, parallel manipulators are widely used. However, residual vibration is caused by light weight linkages. The accuracy of motion trajectory is often depressed by the residual vibration in the process of the movement of manipulator. Moreover, the response time of manipulator are increased because of the residual vibration [1, 2]. Input shaping control method can effectively suppress the residual vibration of the structures and manipulators. The control strategy can be applied to uncertain modeling of the system, closed-loop system, or nonlinear system [3–5]. Some new input shaping control strategies have

---

B. Li (✉) · Y. Wei

School of Engineering, Huzhou University, Huzhou 313000, People's Republic of China  
e-mail: bingli@hutc.zj.cn

© Springer-Verlag Berlin Heidelberg 2016

B. Huang and Y. Yao (eds.), *Proceedings of the 5th International Conference on Electrical Engineering and Automatic Control*, Lecture Notes in Electrical Engineering 367, DOI 10.1007/978-3-662-48768-6\_49

429

been proposed [6–8]. The classical input shapers can effectively and quickly eliminate the residual vibration, but the sensitivity of input shaper is high. When the system parameters are changed or influenced by the external environment, the capability of vibration suppression of the control strategy is decreased. EI input shaper can obtain a wide range of frequencies to suppress vibration, but the input shaper increases the stability time of system and reduce the working efficiency of the system [9]. PD control strategy possesses strong adaptability and robustness, and its control effect is less affected when the system parameters are changed. But the method causes system overshoot, resulting in residual vibration. A new hybrid control method, input shaping combined with PD control strategy can effectively suppress residual vibration [10, 11]. Moreover, it can improve the robustness of the control strategy, and the influence of system is reduced by the external environment. In this paper, a 3-DOF parallel manipulator is analyzed, and the input shaping combined with PD control strategy of the manipulator is established. The system response, stability time, and robustness are analyzed by numerical simulation.

## 2 3-DOF Parallel Manipulator

Figure 1 shows a 3-DOF parallel manipulator. Light weight flexible linkages are used for decreasing the weight of manipulator and obtaining high speed motion. However, these linkages lead to residual vibration. The faster the movement speed, the more the residual vibration [12]. The flexible linkages are manufactured by an aluminum alloy; the parameters of the linkages are shown in Table 1. The natural frequency and damping ratio of the 3-DOF manipulator that is obtained by experimental modal tests are 76.6 Hz and 0.057 for the first mode, respectively.

**Fig. 1** 3-DOF parallel manipulator

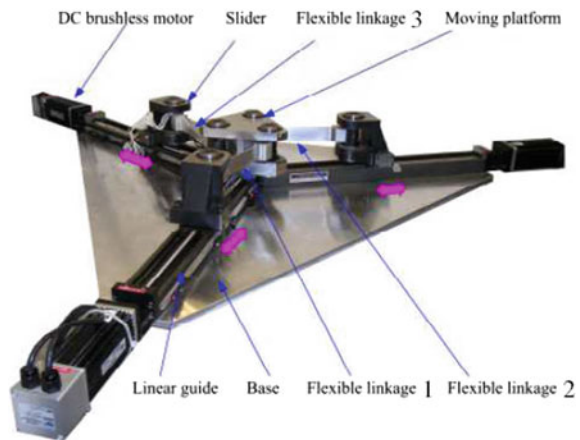




**Table 1** Parameters of linkages

Parameters	Values
Length (mm)	200
Cross-section height (mm)	30
Width of cross-section (mm)	2
Elastic modulus (N/m <sup>2</sup> )	$7.1 \times 10^{10}$
Mass density (kg/m <sup>3</sup> )	$2.77 \times 10^3$
Concentrated rotational inertia (kg m <sup>2</sup> )	$5.815 \times 10^{-5}$

### 3 Methodologies

#### 3.1 Input Shaping

In frequency domain, the impulses of input shaper can be expressed as [12]

$$H_{IS}(s) = \sum_{i=1}^n A_i e^{-t_i s} \quad (1)$$

And in time domain, it can be written as

$$h(t) = \sum_{i=1}^n A_i \delta(t - t_i) \quad (2)$$

A single-mode vibration system can be represented as a decaying sinusoidal response

$$y(t) = \left[ A \frac{\omega}{\sqrt{1 - \zeta^2}} e^{-\zeta\omega(t-t_0)} \right] \sin \left[ \omega \sqrt{1 - \zeta^2} (t - t_0) \right] \quad (3)$$

Inputting  $n$  impulses, the response of system can be expressed as

$$y_{IS}(t) = \sum_{i=1}^n \left( A_i \frac{\omega}{\sqrt{1 - \zeta^2}} e^{-\zeta\omega(t-t_i)} \sin \left[ \omega \sqrt{1 - \zeta^2} (t - t_i) \right] \right) \quad (4)$$

where  $A_i$  is the amplitude of the  $i$ th impulse,  $t_i$  is the time location of the  $i$ th impulse,  $\zeta$  is the modal damping ratio, and  $\omega$  is the modal angular frequency.

After the input shaper convolved with the input signal, the residual vibration of system is zero. For example, two impulses zero-vibration (ZV) input shaper is used, then (4) can be expressed as

$$y_{IS}(t) = B_{AMP} \sin(\omega_d t + \psi) \quad (5)$$

The amplitude and initial angle of vibration are

$$B_{AMP} = \sqrt{[B_1 \cos(\phi_1) + B_2 \cos(\phi_2)]^2 + [B_1 \sin(\phi_1) + B_2 \sin(\phi_2)]^2} \quad (6)$$

$$\psi = \tan^{-1} \left[ \frac{B_1 \sin(\phi_1) + B_2 \sin(\phi_2)}{B_1 \cos(\phi_1) + B_2 \cos(\phi_2)} \right] \quad (7)$$

where

$$B_i = A_i \frac{\omega}{\sqrt{1-\zeta^2}} e^{-\zeta\omega(t-t_i)} \quad \phi_i = \omega\sqrt{1-\zeta^2}t_i \quad \omega_d = \omega\sqrt{1-\zeta^2} \quad (8)$$

After the impulse ends,  $B_{AMP}$  should be equal to zero in order to ensure that the vibration of the system is equal to zero. In order to minimize the sequence of impulses, the time location of the first impulse is set arbitrarily to 0 ( $t_1 = 0$ ). Otherwise, in order to normalize the sequence of impulses, the sum of all impulse amplitude is set equal to 1, and the amplitude of each impulse is greater than zero. Then, the impulse amplitude and time location of a two impulses ZV input shaper can be expressed as

$$A_1 = \frac{1}{1+k} \quad A_2 = \frac{k}{1+k} \quad t_1 = 0 \quad t_2 = \frac{\pi}{\omega\sqrt{1-\zeta^2}} \quad k = e^{-\frac{\zeta\pi}{\sqrt{1-\zeta^2}}} \quad (9)$$

### 3.2 PD Control Method

When PD feedback control strategy is used in a single-mode vibration system, its transfer function is expressed as [7]

$$H_{PD}(s) = \frac{\omega^2(k_d s + k_p)R(s)}{s^2 + (2\zeta\omega + k_d\omega^2)s + (1 + k_p)\omega^2} \quad (10)$$

where,  $k_d$  is differential gain,  $k_p$  is proportional gain. The modal angular frequency and the modal damping ratio of the system are changed from  $\omega$  and  $\zeta$  to  $\omega_n$  and  $\zeta_n$  due to proportional gain  $k_p$ .

$$\omega_n = \omega\sqrt{1+k_p} \quad \zeta_n = \frac{2\zeta\omega + k_d\omega^2}{2\omega\sqrt{1+k_p}} \quad (11)$$

Evaluating the Laplace inverse transform of (10), its system response can be expressed as

$$y_{PD}(t) = y_{PD1}(t) + y_{PD2}(t) \quad (12)$$

The system response consists of two parts. Where,  $y_{PD1}(t)$  is the forced vibration response,  $y_{PD2}(t)$  is the natural vibration response. The vibration amplitude of  $y_{PD}(t)$  is related to the initial state and the parameters of system. If the initial state is set arbitrarily to be 0, then

$$y_{PD2}(t) = A_{SYS} \sin(\omega_d t + \theta) \quad (13)$$

where  $A_{SYS}$  is the vibration amplitude of the system,  $\theta$  is the initial angle of vibration, its value is related to the parameters of the system. If the input signal of the system is the unit step signal, then

$$A_{SYS} = \frac{(-k_d \omega_n + 2k_p \zeta_n) \sqrt{(c - c_0)^2 + \omega_d^2}}{\omega_n^3 \omega_d} e^{-c_0 t} \quad (14)$$

$$\theta = \arctan\left(\frac{\omega_d}{c - c_0}\right) \quad (15)$$

where

$$c = \frac{(-k_p - 2k_d \zeta_n \omega_n + 4k_p \zeta_n^2) \omega_n}{-k_d \omega_n + 2k_p \zeta_n} \quad c_0 = \frac{2\zeta_n \omega_n + k_d}{2} \quad (16)$$

### 3.3 Input Shaping Combined with PD

Typically, the input shaper is placed in front of the PD feedback control system, as shown in Fig. 2.

When input shaping combined with PD feedback control strategy is applied to a single-mode vibration system, the transfer function of the system can be presented as

$$H(s) = H_{IS}(s) \cdot H_{PD}(s) = \sum_{i=1}^n A_i e^{-t_i s} \frac{\omega^2 (k_d s + k_p) R(s)}{s^2 + (2\zeta \omega + k_d \omega^2) s + (1 + k_p) \omega^2} \quad (17)$$

The system response includes two parts

$$y(t) = y_1(t) + y_2(t) \quad (18)$$

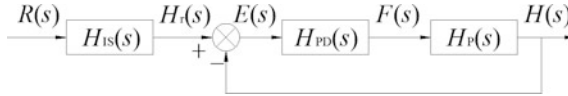


**Fig. 2** Control system of input shaping combined with PD

where  $y_1(t)$  is the forced vibration response of the system, and its initial value is 0,  $y_2(t)$  is the natural vibration response of the system.

$$y_2(t) = A_{SYS}B_{AMP} \sin(\omega_d t + \theta + \psi) \tag{19}$$

To ensure that the system possesses better working performance, the parameters  $k_d$  and  $k_p$  of PD controller should be chosen reasonably.

Assuming that the stability error of the residual vibration of system is 5 %, and the input signal is divided into two impulses using ZV input shaper. After the last impulse ends, the residual vibration of the system will be eliminated, then the system can reach the stable state.

The time constant of the closed-loop system represents the capacity of resisting disturbance. The time constant of the input shaping combined with PD controller is the same as the PD feedback controller. It can be obtained by (20)

$$t_c = \frac{2}{2\zeta\omega + k_d\omega^2} \tag{20}$$

The relationship between the time constant and the differential gain of the system can be obtained by (20).

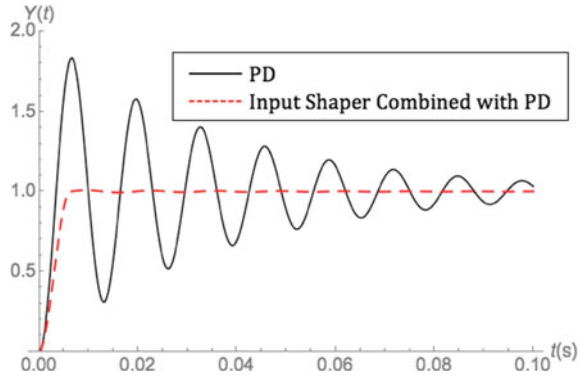
### 4 Numerical Simulation

According to the parameters of the 3-DOF parallel manipulator, the parameters of the two impulse ZV input shaper are

$$\begin{bmatrix} A_i \\ t_i \end{bmatrix} = \begin{bmatrix} 0.544721 & 0.455279 \\ 0 & 0.0065 \end{bmatrix} \tag{21}$$

In order to make an easy comparison between PD control strategy and input shaping combined with PD control strategy, the same time constant  $t_c$  of 0.0047 s is adopted. The first order mode damping ratio and natural frequency of the linkages of the 3-DOF parallel manipulator are  $\zeta = 0.057$  and  $f = 76.6$  Hz. Differential gain is  $k_d = 0.1827$ , proportional gain changes are between 15 and 25. When the

**Fig. 3** Comparison curves of system response



proportional gain is defined as 25, the comparison of system response between PD control strategy and input shaping combined with PD control strategy are shown in Fig. 3.

As shown in Fig. 3, in the same feedback gain, the strong residual vibration is obvious with PD control strategy. The residual vibration of input shaping combined with PD control strategy is reduced significantly. The system can reach the stable state in the half vibration period, and the response speed of the system is fast and the overshoot is small.

Under different proportional gain, the system response of the PD control strategy and the input shaping combined with PD control strategy are shown in Figs. 4 and 5.

As shown in Figs. 4 and 5, it can be seen that in the case of different differential gain, the system response of the PD control strategy has obvious residual vibration, and the greater the value of  $k_p$ , the greater the vibration amplitude. But the change of the  $k_p$  value has little influence on the system response when using input shaping combined with PD control strategy. Moreover, the effect of vibration suppression is good in all the three different  $k_p$  values, and the higher the  $k_p$ , the shorter the response time of the system.

**Fig. 4** System response with PD feedback control

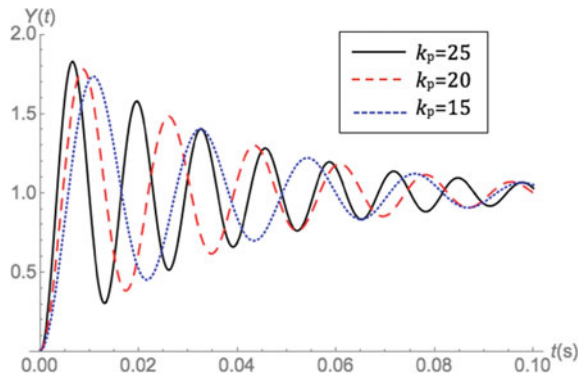
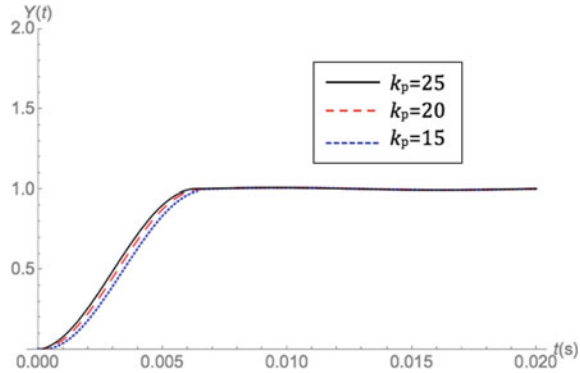


**Fig. 5** System response with input shaping combined with PD feedback control



## 5 Conclusions

A theoretical analysis of the input shaping combined with PD control strategy is carried out. The input shaping combined with PD controller of the 3-DOF parallel manipulator is established. The input shaping combined with PD controller can significantly reduce the residual vibration of the system by numerical simulation in the case of the same differential gain, under the action of the unit step signal. The system can reach the stable state in the half vibration period. The response speed of the system is fast and the overshoot is small. The change of the  $k_p$  value has a minimal effect on the response of the system. The performances of vibration suppression are all effective. In addition, the higher the  $k_p$  value, the shorter the response time of the system.

**Acknowledgement** This project is supported by Zhejiang Provincial Natural Science Foundation of China (LQ12E05008).

## References

1. Mohamed Z, Chee AK, Mohd-Hashim AWI et al (2006) Techniques for vibration control of a flexible robot manipulator. *J Robot* 24:499–511
2. Kapucu S, Nihat Y, Yavuz H (2008) Suppression of residual vibration of a translating-swinging load by a flexible manipulator. *Mechatronics* 18:121–128
3. Singhose WE, Seering WP, Singer NC (1997) Time-optimal negative input shapers. *J Dyn Measure Control* 19(2):198–205
4. Huey JR, Sorensen KL, Singhose WE (2008) Useful applications of closed-loop signal shaping controllers. *Control Eng Pract* 16(7):836–846
5. Mohammed FD, Ziyad NM (2006) Nonlinear input-shaping controller for quay-side container cranes. *Nonlinear Dyn* 45:149–170
6. Pengxiao Jia, En Li, Zize Liang et al (2013) Adaptive PD control combined with input-shaping for suppressing vibration of a single-mode flexible mechanism. *J Vibr Shock* 32(17):189–193

7. Dong M, Song C, Mei X (2010) Simulation research on PD combined with input-shping for suppressing the vibration of single-mode flexible mechanical structures. *J Mech Eng* 46(13):135–140
8. Ma K, Ghasemi-Nejhad MN (2007) Adaptive input shaping and control for simultaneous precision positioning and vibration suppression of smart composite plates. *Smart Mater Struct* 16:1870–1879
9. Singhose WE, Derezinski S, Singer NC (1996) Extra-insensitive input shapers for controlling flexible spacecraft. *J Guid Control Dyn* 19(2):285–291
10. Kenison M, Singhose W (2002) Concurrent design of input shaping and proportional plus derivative feedback control. *ASME. J Dyn Syst Measure Control* 124(3):398–405
11. Li R, Xu T, Zou W et al (2010) Analysis on force and energy consumption for elastic mechanisms with a rigid mode motion based on PD combined with input-shaping control. *J Vibr Shock*. 29(12):158–161
12. Li B, Zhang X , Mills JK et al (2009) Vibration suppression of a 3-PRR flexible parallel manipulator using input shaping, vol 4. In: *IEEE international conference on mechatronics and automation*, Changchun, China, pp 3539–3544

# Hybrid Dual-Loop Control for a Three-Phase PWM Rectifier

Jing Cao, Chaonan Tong and Hongtao Li

**Abstract** This paper investigates a novel control strategy for a three-phase voltage source PWM rectifier (VSR) system with sliding mode control (SMC) and repetitive control (RP). To achieve the aim of well-controlled output DC-bus voltage, sinusoidal input currents, controlled power factor and bidirectional power flow, double closed loops control strategy are realized: i.e., outer voltage loop control with SMC and inner current loop control with the combination method of RP with PI control. The entire simulation results and experiment results are provided to demonstrate the effectiveness of the proposed control method and shows that it is in good agreement with the desired performances. In addition, the proposed method is convenient to realize and thus has a wide range of industrial applications.

**Keywords** Sliding mode control · Three-phase rectifiers · Repetitive control · Dual-loop control

## 1 Introduction

The three-phase PWM rectifier is used increasingly in a wide diversity of applications in recent years, for it can provide constant dc bus voltage, low harmonic distortion of the currents, controllable power factor, and bidirectional power flow as compared to a simple diode or a phase commutated rectifier. For instance, in ac/dc/ac converters in typical AC drive system, it is noted that PWM rectifiers,

---

J. Cao (✉) · C. Tong  
School of Automation and Electrical Engineering,  
University of Science and Technology Beijing, Beijing, China  
e-mail: caojing7997@163.com

J. Cao · H. Li (✉)  
School of Electrical Engineering and Control,  
North China University of Technology, Beijing, China  
e-mail: hontel@163.com



which are designed bidirectional power flow, play a significant role in saving energy, because they enable the motor to work in a four-quadrant, excess-energy-feed forward network.

Various new control strategies have been proposed in recent works about this kind of PWM rectifier, such as sliding mode control (SMC) [1], predictive control [2], repetitive control (RP) [3], hysteresis control [4] etc. In terms of control structure, the normal form contains two parts: outer voltage loop and inner current loop. On the one hand, while the SMC method has good robustness, and usually is applied to the current loop, outer voltage loop is limited to PI controller [5] and a full sliding mode controller for two closed loops [6] is difficult to design. On the other hand, RP, which is based on the internal model principle, can achieve zero-error tracking or disturbances rejection for any periodic signals, and shows good characteristics on tracking performance and improving the THD of the ac line side current [7]; both of these two methods are easy to be implement in practice and can be applied to improve the performance of three-phase PWM rectifier.

In this paper, SMC is applied to the dc link voltage loop and inner current loop control is applied in a combined method of RP and PI control. The control scheme was verified in a 5 kW lab prototype. The simulation and experimental results show that the proposed control scheme has the superior dynamic response and robustness.

## 2 Modeling of the Three-Phase PWM Rectifier

The three-phase voltage-source PWM rectifier is show in Fig. 1.

Here,  $e_k$  represents the source voltage and  $i_k$  represents the input current,  $k = a, b, c$ , respectively.  $C_{dc}$  is the capacity of the dc-side filter capacitance,  $R_L$  and  $L$  denote the resistance and inductance, and  $u_{dc}$ ,  $i_{dc}$  is the voltage and the current of the dc side.

The switching states of the rectifier are determined by the gating signals  $s_k$ . The switches of the upper-half bridge is on and the lower-half bridge is off when  $s_k = 1$ , and the switches of lower-half bridge is on and the upper-half bridge is off when  $s_k = 0$ .

Using the Park transformation, the ac-side quantities can be transformed into a rotating d-q frame, and the time-invariant model can be written as function (1),

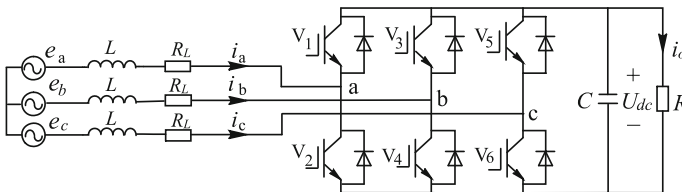


**Fig. 1** The three-phase voltage-source PWM rectifier

$$\frac{d}{dt} \begin{bmatrix} i_d \\ i_q \\ u_{dc} \end{bmatrix} = \begin{bmatrix} -\frac{R_L}{L} & \omega & 0 \\ -\omega & -\frac{R_L}{L} & 0 \\ 0 & 0 & -\frac{1}{CR_L} \end{bmatrix} \begin{bmatrix} i_d \\ i_q \\ u_{dc} \end{bmatrix} + \begin{bmatrix} -\frac{u_{dc}}{C} & 0 \\ 0 & -\frac{u_{dc}}{C} \\ \frac{i_d}{L} & \frac{i_q}{L} \end{bmatrix} \begin{bmatrix} S_d \\ S_q \end{bmatrix} + \begin{bmatrix} \frac{1}{L} & 0 \\ 0 & \frac{1}{L} \\ 0 & 0 \end{bmatrix} \begin{bmatrix} e_d \\ e_q \end{bmatrix} \tag{1}$$

where,

$$A = \begin{bmatrix} -\frac{R_L}{L} & \omega & 0 \\ -\omega & -\frac{R_L}{L} & 0 \\ 0 & 0 & -\frac{1}{CR_L} \end{bmatrix}, \quad B(x) = \begin{bmatrix} -\frac{u_{dc}}{C} & 0 \\ 0 & -\frac{u_{dc}}{C} \\ \frac{i_d}{L} & \frac{i_q}{L} \end{bmatrix}, \quad u(x) = \begin{bmatrix} S_d \\ S_q \end{bmatrix},$$

$$D = \begin{bmatrix} \frac{1}{L} & 0 \\ 0 & \frac{1}{L} \\ 0 & 0 \end{bmatrix}$$

The whole closed-loop control system is shown in Fig. 2. The outer voltage loop is achieved by the SMC method while the inner current loop is achieved by the combination method. Phase-locked loop (PLL) is applied to calculate the initial angle  $\theta$  which is needed in the conversion of co-ordinates, for instance, the conversion between three-phase static reference frame (3s) and two-phase rotating reference frame (2r) or the conversion between two-phase static reference frame (2s) and two-phase rotating reference frame (2r).

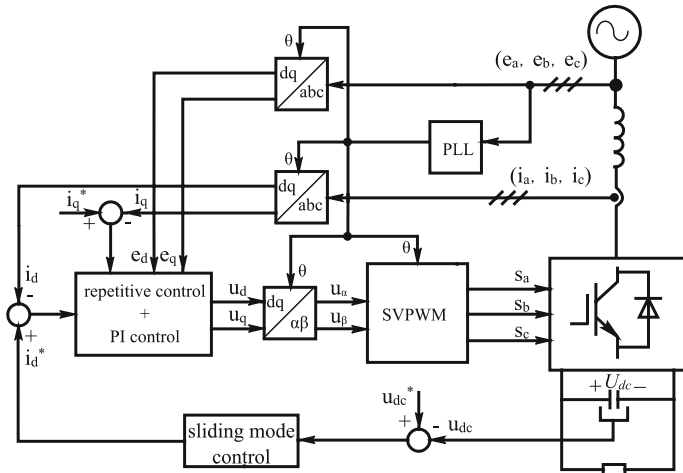


Fig. 2 The whole closed-loop control system

### 3 System Control Strategy

#### 3.1 Proposed SMC for DC Link Voltage Regulation of a PWM Rectifier

DC bus voltage stability can enhance robustness of the three phase PWM rectifier, especially when the mutation of grid voltage or DC bus voltage is large. If not properly controlled, it will seriously threaten the security of the system and reliable operation. SMC has been used for adjusting the DC voltage in this paper, instead of the common PI control to avoid overshoot and parameter adjustment complexity. Sliding mode control (SMC) has been proven to be a useful tool to control the complex nonlinear systems. The concept of the SMC is to formulate a variable structure control law such that the system state is forced to a certain predefined surface, called the sliding surface, and thereby forces the system state to stay with appropriate switching of the control structure [7].

According to the power balance principle, neglecting the losses of the inductances and switching devices, the voltage function in Eq. (2) can be expressed so:

$$\frac{3}{2}e_d i_d + \frac{3}{2}e_q i_q = u_{dc} i_{dc} + \frac{u_{dc}^2}{R_L} \quad (2)$$

Equation (2) indicates that only the fundamental of the AC side can bring the change in the DC side, so the reference current  $i_q = 0$ , and, as the given signal of the current active component, changes of the DC voltage involved in inner current control. Let  $x_1 = U_{dc} - U_{dc}^*$ ,  $x_2 = \frac{d u_{dc}}{dt} = \Delta u(t)$ , the following state-space model of three-phase rectifier DC-link voltage dynamic response can be obtained by Eq. (3).

$$\begin{bmatrix} \dot{x}_1 \\ \dot{x}_2 \end{bmatrix} = \begin{bmatrix} 0 & 1 \\ 0 & 0 \end{bmatrix} \begin{bmatrix} x_1 \\ x_2 \end{bmatrix} + \begin{bmatrix} 0 \\ k \end{bmatrix} u(x) \quad (3)$$

where  $k = -e_d / C U_{dc}$ ,  $u(x) = \Delta i_d$ .

The first step of designing the sliding-mode controller is to select the sliding surface [8]. A first-order sliding surface is selected as:

$$\sigma(x) = c x_1 \quad (4)$$

where,  $c$  is constant. To control the chattering caused by limited switching frequency, we assume:

$$\dot{\sigma} = -\varepsilon \text{sat}(\sigma) - q \sigma \quad (5)$$

$$\text{sat}(\sigma) = \begin{cases} +1, \sigma > \Delta \\ \beta\sigma, |\sigma| \leq \Delta \\ -1, \sigma < -\Delta \end{cases} \quad (6)$$

where,  $q, \varepsilon$  are constant,  $q > 0, 0 < \varepsilon \ll 1, 1 - qT > 0, \Delta$  is a sufficiently small positive constant, which is called the boundary layer,  $\Delta * \beta = 1$  and the system can be driven to the boundary layer when it is in a stable state.

The equivalent control  $u(x)$  can be obtained, assigning  $i_{qref} = 0$  to achieve unity power factor:

$$u(x) = [2u_{dc}u_{dc}/3e_dR_L + \varepsilon\text{sat}(\sigma) + q\sigma] \quad (7)$$

By choosing the Lyapunov function,  $V(x) = \frac{1}{2}\sigma^2(x)$ , the sliding mode condition exists if and only if  $\dot{V}(x) = \dot{\sigma}(x)\sigma(x) < 0$ . Substituting Eq. (4), we obtain Eq. (8) which verifies that the existence condition can be fulfilled:

$$-\varepsilon\text{sat}(\sigma) * \sigma - q\sigma^2 = -\varepsilon|\sigma| - q\sigma^2 < 0 \quad (8)$$

### 3.2 Proposed Combination Method for an Inner Current Loop

The aim of an inner current loop is to track the current reference which is given by the out loop and to adjust the current so as to improve the power factor. Repetitive control uses the information from the preceding cycle to improve the control performance in the present cycle. According to the model Eqs. (1), the decoupling current system model and the proposed current control scheme consist of a plug-in type repetitive controller for a PWM rectifier as shown in Fig. 3.

$G_p(z)$  is the transformation of control object,  $G_{PWM}(z)$  is the equivalent model of a PWM transformer,  $G_s(z)$  is equivalent channel of feedback filter,  $G_{PI}(z)$  is the PI

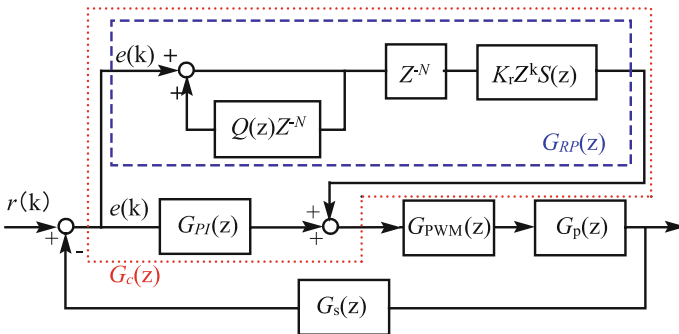


Fig. 3 Construct of a plug-in repetitive controller

controller, and  $G_{RP}(z)$  is the repetitive controller. The transfer function of the plug-in repetitive controller is shown in Eq. (9):

$$G_{RP}(s) = \frac{z^{-N+K}K_rS(z)}{1 - Q(z)z^{-N}} \quad (9)$$

The transfer function of the combination controller is shown in Eq. (10):

$$G_c(z) = \frac{z^{-N+K}K_rS(z)(z-1) + K_p(1 - Q(z)z^{-N})(z-1) + K_i z}{(1 - Q(z)z^{-N})(z-1)} \quad (10)$$

The error function with feed forward system is Eq. (11),

$$E(z) = R(z) * \frac{1 - G_p(z)}{1 + G_c(z)G_p(z)} \quad (11)$$

The system stability required to meet the root of the characteristic Eq. (11) is within the unit circle, while the sufficient condition for the control system stability is the function (12):

$$|Q(z)(1 + K_p G_p(z)) - z^k K_r S(z) G_p(z) - K_p G_p(z)| < 1 \quad (12)$$

## 4 System Control Strategy Simulation and Experimental Verification

To verify the proposed controller method, both a simulated model of a power circuit and a real prototype have been built. Control and circuit parameters are illustrated in Table 1.

The simulation result curve of the system under hybrid control is shown in Figs. 4 and 5. By applying hybrid control to the PWM rectifier, the SMC voltage controller presents no steady error, no voltage overshoot and no current oscillation, while the current waves exhibit sinusoidal form and unit power factor.

Figure 6 shows the experiment results with the DC link voltage under load variations using the sliding mode controller. Compared with a PI controller, SMC is less sensitive to parameters and has stronger robustness. Meanwhile, due to the chattering effect, the system required more current to maintain the steady-state

**Table 1** Control and circuit parameters

Parameter	Value	Parameter	Value
Frequency	50 Hz	$R_L$	20 $\Omega$
$L$	0.1 mH	Ac voltage	220 V
$C$	4000 $\mu$ F	Dc link voltage	750 V

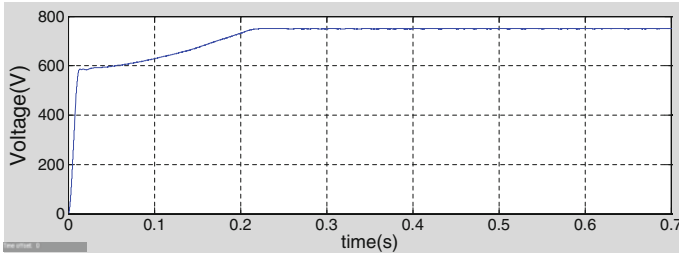


Fig. 4 Simulation results of voltage control using SMC

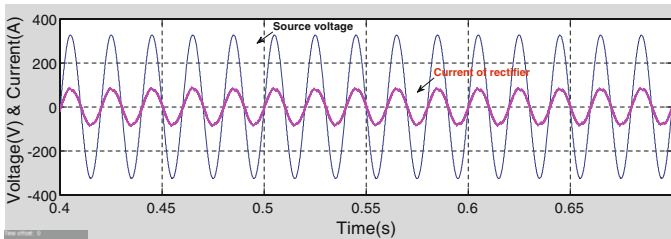


Fig. 5 Simulation results of current control using a combination control method

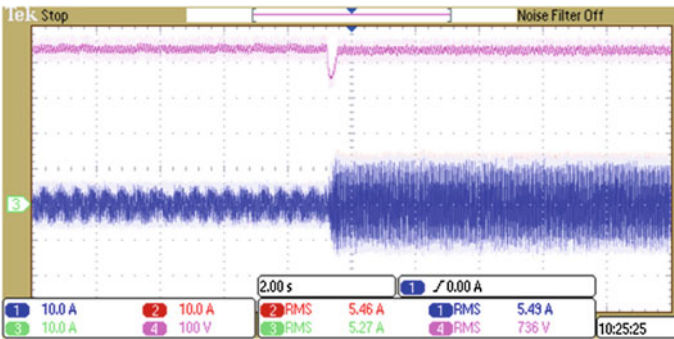


Fig. 6 Experiment results of DC link voltage under load variations using SMC control

with the same load changes, and the difference can be controlled at 3 % or less. Figure 7 shows that combination method of RP and PI control can achieve unit power factor control, and the input current is synchronized with input voltage and is sinusoidal.

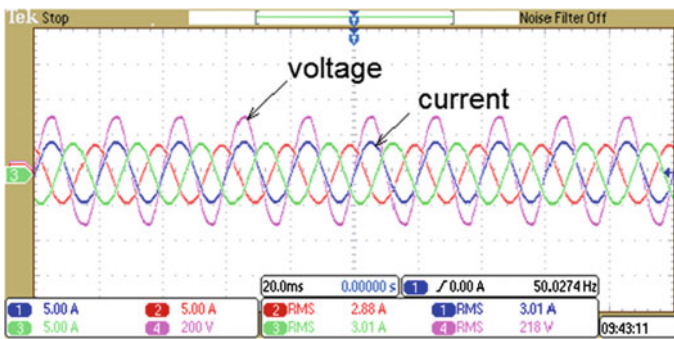


Fig. 7 Experiment results of current control using combination control method

## 5 Conclusion

This paper proposes a new hybrid control scheme for the three-phase PWM rectifier. A sliding-mode control algorithm on synchronous rotating reference frame for the external voltage loop has been proposed, and a combination method of RP and PI control is applied to the inner current loop. Experimental and simulation results show that the proposed controller can offer an excellent steady-state performance, very fast dynamic response, and a unit power factor. In addition, the proposed method is convenient to realize and thus has a wide range of industrial applications.

## References

1. Yu H, Hu Q, Ding XY (2007) Fuzzy sliding mode variable structure control of three-phase rectifier. In: FSKD conference, pp 581–585
2. Rodríguez J, Pontt J et al (2007) Predictive current control of a voltage source inverter. *IEEE Trans Ind Electron* 54:495–503
3. Keliang Z, Danwei W (2003) Digital repetitive controlled three-phase PWM rectifier. *IEEE Trans Power Electron* 18(1):309–316
4. Dawande MS, Kanetkar VR, Dubey GK (1996) Three phase switch mode rectifier with hysteresis current control. *IEEE Trans Power Electron* 11:466–471
5. En-de W, Shenhua H (2012) A novel double closed loops control strategy of three-phase voltage source PWM rectifier. *Proc CSEE* 32(15):24–30
6. Jin Y, Xu Y et al (2010) Full discrete sliding mode controller for three phase PWM rectifier based on load current estimation. *Energy Convers Congr Exposition*, pp 2349–2356
7. Xinhui W, Panda SK, Jianxin X (2008) Design of a plug-in frequency domain based repetitive current controller for three phase PWM boost rectifier under distorted and unbalanced supply voltages. *Proc PESC*
8. Young KD, Utkin VI, Ozguner U (1999) A control engineer's guide to sliding mode control. *IEEE Trans Control Syst Technol* 7(3):328–342

# A Voltage Regulating Electronic Transformer with High Power Factor and Wide Working Voltage

Hui Su, Yonggao Jin and Xiaodong Qu

**Abstract** An electronic transformer using IR2155 has the advantages of simple structure, high output power, large current conduction angle and stable work, but it has no regulating function. When the alternating voltage range is from 180 to 250 V, output voltage also changes, so its use is limited. This paper presents the integration of APFC rectifying mode into an electronic transformer. This electronic transformer can work over a wide voltage range from 180 to 250 V; it can stabilize output voltage and has a high power factor, high output voltage, and requires only simple maintenance as well.

**Keywords** Electronic transformer · APFC rectifier · High power factor · Wide voltage range

## 1 Introduction

The electronic transformer using IR2155 has the advantages of simple structure, high output power, stable work, large current conduction angle and high rectification efficiency, but it can't regulate the output voltage [1, 2]. When the alternating voltage range is from 180 to 250 V, output voltage also changes. If the rectifying part adopts a bridge rectifier, it could generate large pulse current, and the power factor is only about 0.56 [3]. Another problem is that an electronic transformer has residual energy because in a high-frequency transformer, output voltage would be up when the load is light.

The APFC rectifying mode has a high power factor and large output power, and, when alternating input voltage changes in the range of 180–250 V, it can output

---

H. Su (✉) · Y. Jin (✉) · X. Qu  
Department of Electronic Information and Engineering,  
Yanbian University, Yanji 133000, China  
e-mail: suhui212212@163.com

Y. Jin  
e-mail: ygao@ybu.edu.cn



stable direct current voltage. It could be work stable as long as the output voltage is 1.4 times greater than the input direct current voltage [4]. The electronic transformer has the ability of outputting 350–600 V through controlling.

In order to solve the problems of the low power factor and no regulating function, a voltage regulating electronic transformer integrates an electronic transformer into the APFC rectifying mode, so this electronic transformer has the advantages of both.

The first stage of this electronic transformer adopts APFC rectifying mode; it transforms alternating input voltage (180–250 V) into controllable direct current voltage(350–450 V); the voltage changes can compensate for output voltage changes of an electronic transformer in the second stage, so this method can improve the power factor by as much as 0.9. So this electronic transformer can work in a wide alternating input voltage range, from 180 to 250 V, and has stable output voltage.

## 2 Characteristics Analysis of the Electronic Transformer Composed of IR2155

### 2.1 Analysis of Residual Energy

Figure 1 depicts the electronic transformer circuit composed of IR2155. This chip can output pulse with a 50 % duty cycle, its dead time  $T_{DT}$  is about 1.2  $\mu$ s, the maximum working voltage to drive MOSFET is 600 V, and the working frequency ranges from 20 to 100 kHz, calculated by Eq. (1) [5–7].

$$f = \frac{1}{1.4(R + 150)C} \tag{1}$$

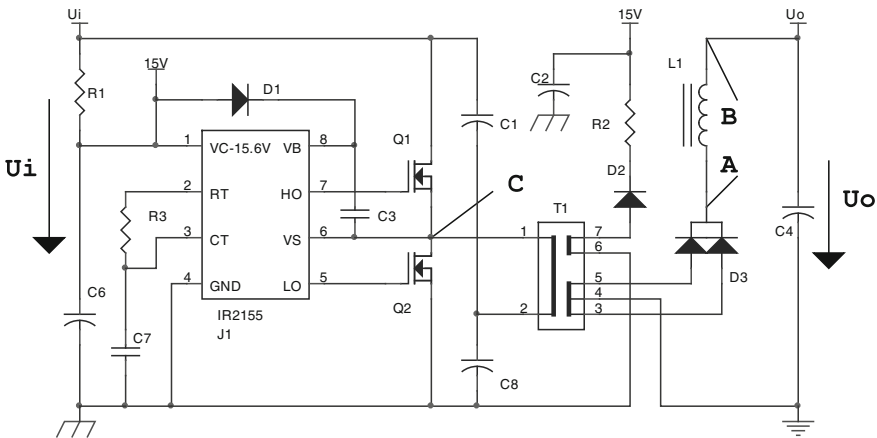


Fig. 1 The electronic transformer circuit

**Table 1**  $D_L$  in different working frequencies

$f$ (kHz)	$T$ ( $\mu$ S)	$T_{DT}$ ( $\mu$ S)	$D_L$
50	10.0	1.2	0.88
75	6.7	1.2	0.82
100	5.0	1.2	0.76

The output voltage driving the rated voltage is calculated by Eq. (2).  $N$  is the ratio of the primary and secondary coil, and  $D_L$  is the rated duty cycle generated by  $T_{DT}$  when driving the rated load.

$$U_O = \frac{D_L U_i}{2N} \tag{2}$$

The duty cycle  $D_L$  of point A after rectification of the driving rated load is described by Eq. (3). It is obvious to see that the higher is the working frequency, the smaller is  $D_L$ . Table 1 shows different values of  $D_L$  calculated by Eq. (3) for different working frequencies.

$$D_L = \frac{T - 2T_{DT}}{T} = 1 - 2T_{DT}f \tag{3}$$

Equation (2) can be expressed by Eq. (4): the higher is the working frequency is, the smaller is the output voltage.

$$U_O = \frac{(1 - 2T_{DT}f)U_i}{2N} \tag{4}$$

We know from Eq. (4), that the output voltage is unchanged when the working frequency is unchanged. But Eq. (4) can't determine the residual energy effect in a high-frequency transformer or the influence of the ringing pulse effect caused by the on-off status to  $U_O$ , i.e., the lighter is the load, the larger is the influence on to  $U_O$ .

The influence of residual energy on  $U_O$  due to different loads is shown in Figs. 2 and 3. When driving the rated load,  $T_{DT}$  is about zero and the residual energy is almost zero. While  $T_{DT}$  slowly decreases as the load is light, residual energy is large

**Fig. 2** Residual energy with rated load

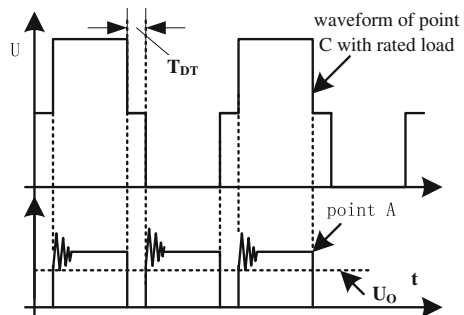


**Fig. 3** Residual energy with light load

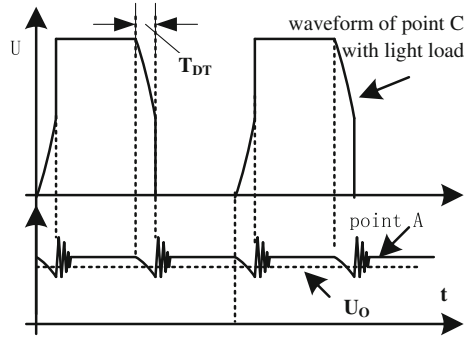
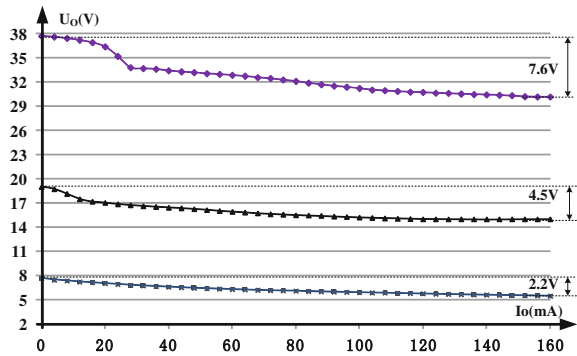


**Fig. 4** Change curve of output current  $I_O$  and  $U_O$



and this result leads to an increase of output voltage, i.e., the smaller is the load, the greater is the impact.

When the input voltage is constant and the rated output voltage is 5, 15 or 30 V, changing output current  $I_O$  produces a series of change curves about  $U_O$ , shown in Fig. 4.  $U_O$  changes considerably as  $I_O$  ranges from 1 to 160 mA, yet the changes in  $U_O$  are small above 160 mA.

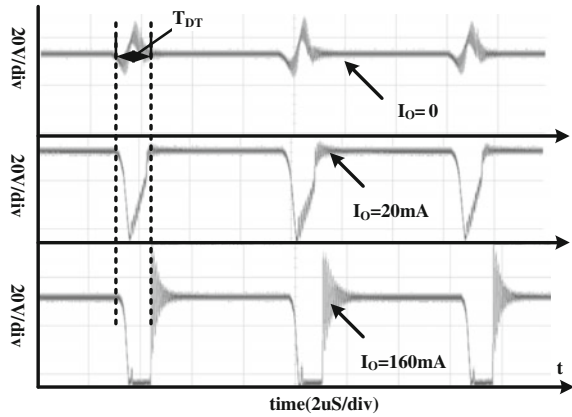
Figure 5 shows that, for the working waveform of point A when  $I_O$  is different, the smaller is  $I_O$ , the greater is the impact of residual energy.

## 2.2 Setting of the APFC Output Voltage

When the first stage of this electronic transformer adopts an APFC transformation mode, it transforms alternating input voltage (180–250 V) into controllable direct current voltage ( $U_i = 350\text{--}450$  V). In this case the voltage changes can compensate for output voltage changes caused by the residual energy effect of an electronic transformer in the second stage.

In order to ensure the limits of an APFC converter output voltage  $U_i$ , when  $I_O$  is smallest, adopting “equivalent duty cycle”  $D_N$  calculate duty cycle  $D_M$  and  $D_L$

**Fig. 5** Working waveform of point A when  $I_O$  is different



with rated load, so we can get minimum  $U_i$  and maximum  $U_i$ , Eq. (5) can be derived from Eq. (2).

$$D_N = D = 2N \frac{U_O}{U_i} \tag{5}$$

Table 2, for  $U_i = 460$  V, which displays the rated output voltage  $U_O = 15$  V, changing  $I_O$  determines the listed  $U_O$  and  $D_N$ . In Table 3, for  $U_i = 460$  V at a rated output voltage of  $U_O = 30$  V, changing  $I_O$  produces the tabulated values of  $U_O$  and  $D_N$ .

From Tables 2 and 3, we can see that no matter how much is the output voltage,  $D_N$  gradually becomes larger than the rated value  $D_L$  when  $I_O$  changes.

Formula (6) can be derived from formula (5):

**Table 2**  $D_N$  values  
( $U_O = 15$  V)

$I_O$ (mA)	$U_O$ (V)	$U_i$ (V)	$N$	$D_N$
0	19.1	460	12	1.00
12	17.5	460	12	0.91
32	16.6	460	12	0.87
80	15.5	460	12	0.81
160	15.1	460	12	0.79

**Table 3**  $D_N$  values  
( $U_O = 30$  V)

$I_O$ (mA)	$U_O$ (V)	$U_i$ (V)	$N$	$D_N$
0	37.8	460	6	0.99
40	33.4	460	6	0.87
80	32.1	460	6	0.84
120	30.7	460	6	0.80
160	30.2	460	6	0.79

$$U_i = 2N \frac{U_O}{D_N} \tag{6}$$

If  $D_N = D_M$ ,  $U_i$  is the minimum;  $D_N = D_L$  and  $U_i$  is the maximum, we can ensure that the range of  $U_i$ .  $U_i$  will satisfy the relationship as shown in Eq. (7).

$$2N \frac{U_O}{D_M} < U_i < 2N \frac{U_O}{D_L} \tag{7}$$

Set  $D_M = 1$  (the maximum value) and  $D_L = 0.79$ , so when  $U_O = 15$  V,  $N = 12$ ; and when  $U_O = 30$  V,  $N = 6$ . By means of Eq. (7),  $360$  V  $< U_i < 456$  V. An APFC transformer can work regularly when the alternating input voltage has a range in 180–250 V.  $U_i$  should be more than 350 V ( $250 \times 1.4$ ), considering a margin, and take the value of  $U_i$  in 350–480 V.

To design a high power factor electronic transformer when  $U_O = 15$  V, first calculate  $D_L$  by Eq. (3) after determining the working frequency, and then, assuming  $U_i = 460$  V, ascertain the ratio  $N$ .

### 3 Voltage Regulating Electronic Transformer with High Power Factor

Figure 6 is the complete circuit diagram of the voltage regulating electronic transformer with high power factor, using an NCP1200 designed APFC transformer. NCP1200 has a self-power supply function and FB feedback terminal and its frequency is fixed, so the whole circuit is simple and work stable [8]. The output voltage  $U_O$  depends on the voltage-stabilizing value of VR-tube D5. When IR2155 starts, the working voltage is supplied by R1, and then supplied by the auxiliary winding of transformer after starting.

$U_O$  is fed back to the FB terminal of NCP1200 to control  $U_i$  after it has been isolated by photoelectric coupler P1, so as to stabilize the output voltage  $U_O$  of electronic transformer. P1 and R5 control the sine-wave amplitude supplied by R4

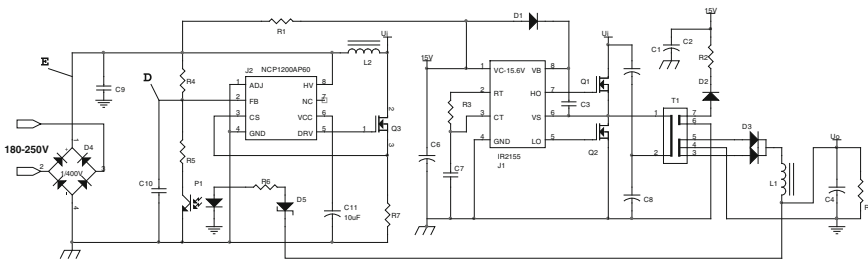
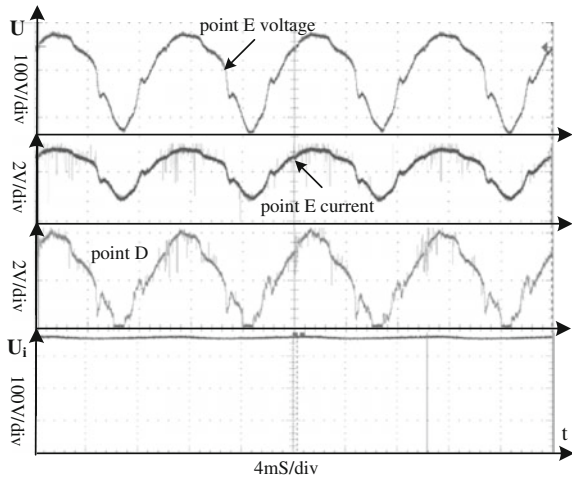


Fig. 6 The circuit of a voltage regulating electronic transformer with high power factor

and then generate sine-wave voltage with a variable amplitude at *D* point. PWM waveform is generated inside the NCP1200 after the *D* point voltage has been compared with the voltage of R7, thus controlling the conduction time of switch tube Q3.

Figures 7 and 8 show every point of the working waveform for input voltage respectively 220 and 250 V. It is obvious to see that the input current is closer to the input voltage, so the power factor can be as high as 0.9.

**Fig. 7** Every point working waveform ( $U_i = 220\text{ V}$ )



**Fig. 8** Every point working waveform ( $U_i = 250\text{ V}$ )

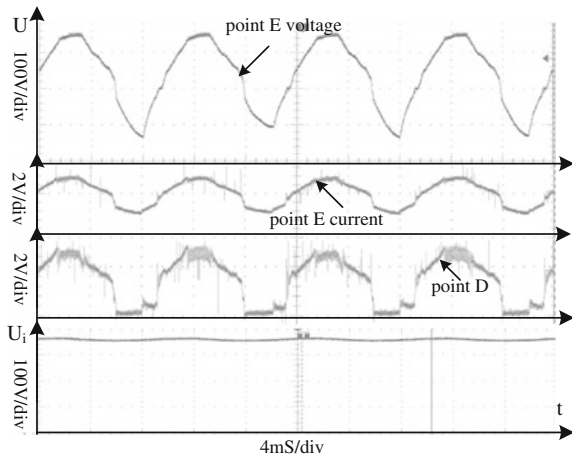


**Table 4**  $U_O$  values when alternating input voltage ranges from 180 to 250 V

AC $U_i$ (V)	$U_O$ (V)	$I_O$ (A)
180	23.5	4.1
200	23.7	4.1
220	23.9	4.1
250	24.2	4.1

**Table 5**  $U_O$  values when input voltage is 220 V and  $I_O$  changes

AC $U_i$ (V)	$I_O$ (A)	$U_O$ (V)
220	0.2	24.8
220	1.2	24.6
220	2.8	24.2
220	4.1	23.9

## 4 Analysis of the Experimental Results

Designing the electronic transformer whose output power factor is 100 W and output voltage is 24 V, we measured the voltage stability, load stability, power factor and efficiency. Table 4 shows the measured  $U_O$  values when the alternating input voltage ranges from 180 to 250 V. From Table 4, we calculated the voltage regulation rate as 2.9 %, the power factor is 0.91–0.93, and the efficiency is 83–86 %.

Table 5 lists the measured  $U_O$  values when the input voltage is 220 V and  $I_O$  varies. From Table 5, we calculated the load regulation rate as 3.6 %, the power factor as 0.93, and the efficiency as 83–86 %.

## 5 Summary

According to the experimental results, the electronic transformer with a high power factor has an excellent voltage stabilizing function when alternating input voltage ranges from 180 to 250 V. The input current is closer to input voltage over the entire input voltage range, so the power factor can be as high as 0.9. This circuit has a simple structure and high efficiency, so we can design a voltage regulating electronic transformer with 50–200 W output power, which can work over a wide voltage range and be used in diverse applications to drive all kinds of high-power light sources.

## References

1. Wang W, Zhang W, Gao G (2001) Design of electronic ballast for high pressure sodium lamp based on IR2155. *J Harbin Inst Technol* 6(33):791–795
2. Zhang K (2014) Development of high efficiency and low cost laboratory power supply based on electronic transformer. Yanbian University

3. Jing Y, Zheng W (2014) Capacitive characteristics of single-phase uncontrollable bridge rectifier filter circuit. *Autom Electr Power Syst* 10(38):113–119
4. Wang L, Jin Y (2014) Design of high-power LED drive circuit with economical high power factor based on NCP1200. *MMC* 1806–1810
5. Yunlong Y (2002) Reverse analysis of electronic ballast driving chip IR2155. In: Zhejiang University
6. Li Z, Wang P, Chu Z, Zhu H, Li Y (2013) Research on medium and high-voltage smart distribution grid oriented power electronic transformer. *Power Syst Technol* 9(37):2592–2601
7. Zhang X, Zhang D (2014) Control strategy of power electronic transformer for power grid fault. *Proc CSU-EPSA* 1(26):39–43
8. Yonggao J, Yinshi J (2014) Design of high-power LED drive circuit with high-power-factor and constant-current based on the NCP1200. *China Illuming Eng J* 2(25):35–38



# The Quantitative Assessment Study on the ‘First-Class’ of the Key Indices of Grid Evaluation

Zheng Wu, Ming Zeng, Junhui Huang, Jan Tan, Jun Han, Wenqi Gu and Han Xu

**Abstract** Carrying out international benchmarking on the operating management of the grid can clear goal orientation, which has targeted to enhance the performances of the power grid. How to do the quantitative assessment on the key indices of grid evaluation and determine the ‘first-class’ of the international power grid has become an important issue which is worthy of study. Under this background, this paper selects eight key indices which are internationally accepted and can comprehensively reflect the overall development and operation of the grid. Furthermore, this paper does the quantitative assessment on each key index by quintile method, optimal segmentation method, and K-means clustering method in order to draw the appropriate “first-class” interval. On this basis, this paper analyzes the advantages and disadvantages of assessing different types of indices by different methods and determines the top level of each key index to a reference for the grid assessment with the combination of the actual situation.

**Keywords** Key indices · Databases · First class · Quantitative assessment

## 1 Introduction

With the development of social economic and technical equipment, power grid capabilities become more and more rich and diverse [1–3]. Grid should meet the increasingly high limit about services, which order the grid not only to service the

---

Z. Wu

State Grid Jiangsu Power Company, Nanjing 210000, Jiangsu, China

M. Zeng · W. Gu (✉) · H. Xu

College of Economics and Management, North China Electric

Power University, Beijing 102206, China

e-mail: guwenqiguwenqi@163.com

J. Huang · J. Tan · J. Han

State Grid Jiangsu Economic Research Institute, Nanjing, Jiangsu 210000, China

© Springer-Verlag Berlin Heidelberg 2016

B. Huang and Y. Yao (eds.), *Proceedings of the 5th International Conference on Electrical Engineering and Automatic Control*, Lecture Notes in Electrical Engineering 367, DOI 10.1007/978-3-662-48768-6\_52

consumers and the power supplies and to get closed with the government but also to adapt to climate and energy resources changes and promote ecological optimization [4].

In order to comply with the development trend of the times and to improve the performance of the power grid and to enhance the level of the overall development of the power industry, countries around the world carried out benchmarking, and set the international “first-class level” grid as a guide to conduct benchmarking [5, 6]. However, the current standard management mostly selected only a few developed countries in Europe and America to make a comprehensive comparison, which means a few sample data and many indices cannot represent the internationally advanced level and benchmarking results cannot make a difference on the professional performance of the grid. Therefore, we first make the classification treatment based on the overall sample database after choosing internationally accepted grid key indices. And ‘world-class level’ range got by quantitative evaluation of key indices will be more representative and targeted. Doing diagnostic analysis on the indices around the various professional sectors and searching the method to enhance the indices will be more realistic.

Currently, the scope and outcomes of application data classification study mainly include the following two aspects. As one of the classification methods of orderly number of columns, optimal segmentation method proposed by Fisher in 1958. In 1967, MacQueen proposed K-means algorithm [7]. He summed up the researches of Cox [8], Fisher [6], and Sebestyen [9], and gave a detailed step of K-means algorithm and used mathematical methods to prove. In 1975, Hartigan systematically discussed on the clustering algorithms in his monograph ‘Clustering Algorithms’ [10].

On the basis of data classification theory and the combination of the characteristics the grid index, this paper researches the key indices “first-class” quantitative assessment. First, in accordance with internationally advanced grid evaluation system, this paper selected eight key indices of grid evaluation, and makes the basic indices classified into positive type, reverse type, and moderate type. Furthermore, this paper takes range transformation method for processing dimensionless. And then this paper chooses the optimal partition method, quintiles law, and K-means method for quantitative assessment. After the analysis of advantages and disadvantages of different methods to assess different types of indices, this paper determines ‘first-class level’ of each key index with the actual situation.

## 2 The Selection of Grid Evaluation Key Indices

Currently, there are many international power grid evaluation systems. After the sort and statistics of index construction hierarchy of the internationally advanced grid evaluation system, we find that the evaluation system mainly consists of three dimensions of ‘unlimited power, little power outage, good use of power’, while the

level of economic development, power generation capacity, and power structure of each country are different.

Among them, the “unlimited power” is a basic requirement of a first-class power grid supply, which means abundant power resources, strong network structure, and safe and stable operation. ‘Little power outage’ is the main goal of the first-class network reliability and economic operations, which requires optimizing network structure, scientific control, and operation and maintenance, improving power supply reliability. ‘Good use of power’ is the real social responsibility of the power company and the whole power industry, which need to support the development of new energy sources, the timely completion of project planning, and construction work of clean energy network, to enhance power grid capacity for clean energy accepted.

At the same time, according to index feature, eight key indices will be divided into positive type (the bigger index the better), moderate type (optimal index within a certain range), and reverse type (the smaller index the better). The eight indices are system average interruption time, system average interruption frequency, energy not supplied, the proportion of clean energy, electrical energy accounted for the proportion of final energy consumption, comprehensive line loss rate, and loss of load probability, power backup rate.

### 3 Assessment Methods Summary

In this paper quintile law, optimal segmentation method, and K-means clustering method were carried out on eight key indices of quantitative assessment.

#### 3.1 ‘First-Class’ Quantitative Assessment of Key Indices Based on Quintiles Law

First, we use range transformation to do dimension treatment on the indices. And then in the case of adequate index sample, if the indicators meet the normal distribution, we take the best segment rating value of the five classifications as “first-class” reference. Boundary point of five intervals range are as follows:  $\bar{x} + 1 * s$ ,  $\bar{x} + 0.33 * s$ ,  $\bar{x} - 0.33 * s$  and  $\bar{x} - 1 * s$  ( $\bar{x}$  is mean value of the indices,  $S$  is standard deviation of the indices) and then we do a normal distribution test. If the indicators do not follow a normal distribution we, respectively, provided four quantile by 16, 37, 63, and 84 % according to the standard normal distribution, and then we arrange the first value of 16 % of the sample as a “first-class level” reference.

### 3.2 *'First-Class' Quantitative Assessment of Key Indicators Based on the Optimal Partition Method*

The optimal segmentation has a reasonable division of the interval index as much as possible through minimization of error of indices which are in the same interval. First, we calculate Euclidean distance between each of the two national indices. Find the minimum value of the distance and returning the two countries associated with the minimum value as one level. Next, we make the combined level as a new 'country'. Continue finding the minimum value of the distance. After determining the different ranges with different centroid, the optimal segmentation method determines specific indicators division centroid through loss function graphs.

$$L[b(n, k)] = \sum_{t=1}^k D(i_t, i_{t+1} - 1) \quad (1)$$

where  $i_t$  represents the first index datum of the  $t$  interval;  $i_{t+1} - 1$  represents previous data of the first datum of the  $t + 1$  interval, that is the last datum of the  $t$  interval.  $D(i_t, i_{t+1} - 1)$  represents the loss within the same  $t$  interval;  $L[b(n, k)]$  represents the total loss within each interval after classifying  $n$  data into  $k$  intervals.  $L[b(n, k)]$  changes in trend with  $k$ . We draw trend graph, and then observe the corresponding inflection point. The inflection point is  $k$  value which makes  $L[b(n, k)]$  minimized in the case of the known  $n$ .

### 3.3 *'First-Class' Quantitative Assessment of Key Indicators Based on K-Means Clustering Method*

K-means clustering algorithm method is typically distance-based, and it uses the distance as the similarity evaluation index, namely that the closer the two objects, the greater the degree of similarity. We select the Euclidean distance to determine the distance between the each particle and indicator. Since the grid evaluation indices are one-dimensional, therefore, the absolute value of the difference between two indices is distance related which is defined as follows:

$$D(i, j) = |x_i - y_j| \quad i = 1, 2, \dots, N \quad j = 1, 2, \dots, K \quad (2)$$

where  $x_i$  is the first  $i$  index.  $y_j$  is the first  $j$  particle,  $N$  is the number of indices, and  $K$  is the number of particles. The data is divided into  $k$  level according to the shortest distance around each centroid. And then we calculate the average within each stage, a total of  $K$  times, and each average value as a new particle.

## 4 Case Analysis

### 4.1 Sample

According to the most recent year of data mining desirable principle, we choose 43 countries in all continents in the world based on 8 grid key indices, which is comprehensive and representative.

### 4.2 Case Results Show

When computing with quintile method, we determine division basis of the data after normal distribution test. Determining the optimal number of centroids should be according to loss function graphs during the process of calculating the optimal segmentation method. Thereby, we select first-class interval under the optimal number of centroid as the end result of the process. In order to facilitate comparison, the number of K-Means Classification method is defined as five.

### 4.3 Comparative Analysis

Through comparative analysis of three different quantitative results, we draw the following conclusions:

1. Due to the optimum partition method focus on the distance between the index intervals during the calculation, therefore, first-class range of quantifiable results will be interfered by those index which are far great than the mean value, which will result in very big 'first-class' interval, such as saidi and saifi. Quintiles law can be relatively better to avoid the above scenario.
2. Since the K-Means method clustered around centroid during the process of division of first-class intervals, which balances the impact of index value and index distribution to a certain degree while dealing with moderate type index. It follows that the "first-class" quantization intervals of K-Means method with respect to the other two methods are relatively more accurate.
3. For energy not supplied(ENS) index, the countries in the 'first-class' interval of quintiles law are Sweden, the Czech Republic, and Hungary, while the countries in the 'first-class' interval of K-Means method are Swedish, Czech, Hungarian, Portuguese, and Polish. But because the Euclidean distance between Portugal and the Czech Republic is big, we choose quintiles law as the quantitative evaluation method.

Considering the advantages and disadvantages of different methods to quantify the indices, numerical gap between different classification intervals and the actual

**Table 1** ‘First-class’ interval of key index and the major countries

Index	Index sample interval	‘First-class’ interval	The major countries in the ‘first-class’ interval
Saidi (min/year/household)	[0.44,2220]	[0.44,27.08]	Singapore, Luxembourg, South Korea, Denmark, Germany, Switzerland
Saifi (times/year/household)	[0.009,20.2]	[0.009,0.402]	Singapore, Luxembourg, Japan, South Korea, Netherlands, Switzerland
Energy not supplied (ENS) (%)	[0.00001,0.01075]	[0.00001,0.00002]	Czech, Hungary, Sweden
The proportion of clean energy (%)	[0.97,99.98]	[61.622,99.98]	Iceland, Norway, Brazil, Austria, New Zealand, Canada
Electrical energy accounted for the proportion of final energy consumption (%)	[14.4,45.15]	[31.335,45.15]	Israel, Norway, Sweden
Comprehensive line loss rate (%)	[2.97,16.47]	[2.97,3.49]	Finland, Netherlands
Loss of load probability (LOLP)(%)	[0.000228,0.002511]	[0.000228,0.00025]	United Kingdom, Israel
Power backup rate (%)	[-15.56,139.69]	[23.815,35.035]	Germany, Australia, United Kingdom

situation of countries, we finally determine international ‘first-class level’ interval of eight key grid rating indices and the corresponding countries, which are shown in Table 1.

## 5 Conclusions and Prospects

This paper selected eight key grid evaluation indicators and used quintiles law, optimal segmentation method, and K-Means method to do the ‘first-class’ level quantitative assessment. And then we identified relatively reasonable quantification methods for eight indices through a comparative analysis for the case of three methods. After comparison with the evaluation results and situation of states grid operation, quantitative assessment of ‘first-class’ interval are in-line with international realities, with a certain representative sense, which can be used as a basis for the relevant departments to reference. In addition, since there are many factors that affect the performance of many countries in grid operation, it is hard to objectively reflect the actual gap among countries through quantifying key index. So it needs to be further studied to propose specific evaluation and assessment methods for each index with the combination with the actual operation background of the power grid.

**Acknowledgements** Key Technology and Application of provincial company, “a world-class grid” construction evaluation and decision optimization (Project number: GHJS1500008).

## References

1. Dejjiao N, Tao C, Yongzhao Z (2012) Metadata hierarchical indexing algorithm in mass storage system. *Appl Res Comput* 29(2):510–513. doi:[10.3969/j.issn.1001-3695.2012.02.029](https://doi.org/10.3969/j.issn.1001-3695.2012.02.029)
2. Xu N (2010) Hierarchical data storage structure and algorithm research. Kunming University of Science and Technology
3. Haisheng L (2012) Data classification algorithm research in hierarchical storage system. *J Gansu Lianhe Univ (Nat Sci Edition)* 26(4):57–61. doi:[10.3969/j.issn.1672-691X.2012.04.016](https://doi.org/10.3969/j.issn.1672-691X.2012.04.016)
4. Sun J (2007) Thematic map data classification model research—the application of modern mathematics in the map data classification. The PLA Information Engineering University
5. Chang L, Liang H, Liu B (2010) Research on fuzzy hierarchical process model in the mapping data. *Geogr Geo-Inf Sci* 26(1):51–53
6. Fisher WD (1958) On grouping for maximum homogeneity. *J Am Stat Assoc* 53 (284):789–798
7. Macqueen JB (1967) Some methods for classification and analysis of multivariate observations. Berkeley. Fifth Berkeley Symp Math Stat Prob 281–297
8. Cox DR (1957) Note on grouping. *J Am Stat Assoc* 52(280):543–547
9. Sebestyen GS (1962) Decision-making processes in pattern recognition. ACM Monogr
10. Hartigan JA (1975) Clustering algorithms. Wiley, New York

# A Novel Polarimetric Marine Radar

Tao Jin, Huihui Xian, Xuebin Wang and Xiaohui Qi

**Abstract** Considering the poor anti-interference performance of the current marine radar, a novel marine radar based on polarization technology is proposed in this paper. Aiming at the structural characteristics of the floating targets on the sea, this paper analyses the polarization scattering characteristics of the marine radar targets, and based on the fact that marine radar targets are mainly slow-moving ones, and puts forward a general design of marine radar based on the timesharing polarization technology and also a mentality of design for the antenna in dual-polarimetric marine radar. The simulation result proves that the novel polarimetric marine radar is highly improved, compared to the current marine radar, both on its detection performance and anti-interference capability.

**Keywords** Marine radar · Polarization technology · TCR · DCR

## 1 Introduction

Marine radar, as the radar to ensure the safety of ship navigation, plays an important role in modern marine equipment. The main functions of modern marine radar include buoys detection, ships detection, islands detection, floating ice warning, targets ranging, and navigation. The marine radar ensures the safety of ship navigation in a complex environment, especially in low-visibility conditions. Therefore, the marine radar is essential to modern ships.

---

T. Jin · X. Wang · X. Qi

School of Information and Electrical Engineering, Harbin Institute of Technology, Weihai 264209, Shandong, China  
e-mail: jintao@hit.edu.cn

H. Xian (✉)

School of Translation and Interpretation, Shandong University, Weihai 264209, Shandong, China  
e-mail: xian\_huihui@sohu.com

© Springer-Verlag Berlin Heidelberg 2016

B. Huang and Y. Yao (eds.), *Proceedings of the 5th International Conference on Electrical Engineering and Automatic Control*, Lecture Notes in Electrical Engineering 367, DOI 10.1007/978-3-662-48768-6\_53



With the rapid development of technology, the modern radar technology has been updated rapidly. However, the marine radar has been developing at a comparatively slow speed. Its basic framework remains to be single-carrier-frequency monopulse non-coherent radar pattern, and the effective resolution is wanted for the deterioration of its working performance in bad weather (such as rain, snow, fog, wave, etc.).

Aiming at this problem, many researchers have constructed corresponding models and conducted analysis on the wave interference on the marine radar, suggesting the way to improve the performance of traditional marine radar by sea-clutter suppression regarding to its characteristic of fluctuation [1–3]. However, the effect of sea-clutter suppression in marine radar is restricted by varied factors and thus its stable performance is not expected.

The existing marine radar generally operates on single-polarization pattern which, in the process of detection, acquires the target characteristics mainly relying on target's scalars of range, frequency, phase, etc. Therefore, the existing marine radar is categorized into Scalar Radar. Take the attributes of electromagnetic wave into consideration. Polarization, the same as time domain, frequency domain, and airspace, is also one of the inherent attributes of the electromagnetic wave, but the existing marine radar is, from the perspective of polarization, not able to make the utmost of all of the information from target echo, and the vector information that reflect the target's inherent attributes is missed.

This paper proposes a marine radar design based on the polarization technology, aiming at improving the working performance of the existing marine radar by making full use of the advantages of the polarization technology in the detection of weak signals, the anti-interference, and target identification. The polarimetric marine radar, compared to the existing marine radar, will present salient advantages in its operating range, target detection, and target identification, and also exhibit the improved working performance in adverse weather.

## 2 Polarization Scattering Characteristics of Sea-Surface Targets

The detection targets of marine radar are mainly ships, islands, and floating ice. As large targets, ships and islands are easily detected by single-polarization marine radar. But other floating targets on the sea, like floating ice and small glaciers, pose great difficulty of detection for existing marine radar. The echo is too weak to be detected and fixed in the sea clutter. As for existing marine radar, this detection problem is in urgent need of resolution.

One of the salient characteristics of the floating object, like floating ice or small glacier, is that the object is floating on the sea or submerged under the sea surface. Its backscattering structure is formed by its own geometry structure and the sea surface, usually being plane reflector structure, dihedral corner reflector

**Table 1** Polarization scattering characteristics of typical scattering structures

Target type	Polarization scattering matrix (H-V)
Conductor plane	$S = A \begin{bmatrix} -1 & 0 \\ 0 & -1 \end{bmatrix}$
DCR	$S = A \begin{bmatrix} -\cos 2\psi & \sin 2\psi \\ \sin 2\psi & \cos 2\psi \end{bmatrix}$
TCR	$S = A \begin{bmatrix} -1 & 0 \\ 0 & -1 \end{bmatrix}$

(DCR) structure, or trihedral corner reflector (TCR) structure. According to target polarization decomposition theory, the floating target’s polarization scattering characteristics can be researched by means of analysis of typical reflector structures, which have already got results as shown in Table 1.

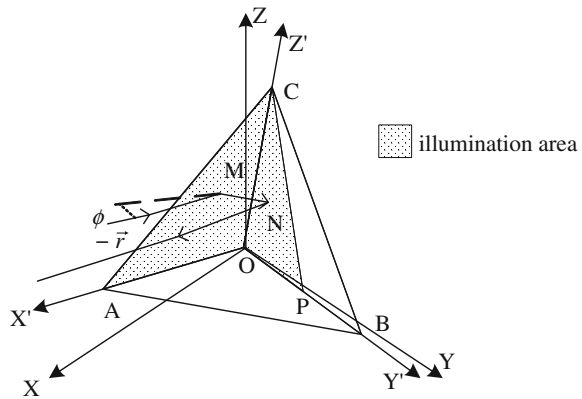
Gennarelli [4] has analyzed TCR backscattering characteristics based on physical optics (PO). For understanding polarization scattering characteristics of floating ice better, the depolarization scattering characteristics of TCR are analyzed with the PO model [5–8]. The vector expression of incidence ray is shown as Eq (1)

$$-\vec{r} = (-\cos\phi \sin\theta, -\sin\phi \sin\theta, -\cos\theta) \tag{1}$$

where  $\phi$  is the angle between +X axis and projection of incidence ray in the XOY plane,  $\theta$  is the angle between +Z axis and incidence ray. Keep XOY plane parallel to incidence ray and rotate TCR  $\gamma$  angle around incidence ray. After rotation, the axis of new rectangular coordinate are X', Y' and Z', the corresponding coordinate planes are 1', 2' and 3', and the TCR attitude is shown in Fig. 1.

As the X'OY' plane parallels to incidence ray, X'OY' plane is still dark. There is no change of illumination area. The coordinate transformation is shown as Eq (2).

**Fig. 1** Sketch map of rotating TCR twice-scatter



$$\begin{pmatrix} x' \\ y' \\ z' \end{pmatrix} = \begin{pmatrix} \cos^2 \phi + \sin^2 \phi \cos \gamma & \cos \phi \sin \phi (1 - \cos \gamma) & \sin \phi \sin \gamma \\ \cos \phi \sin \phi (1 - \cos \gamma) & \sin^2 \phi + \cos^2 \phi \cos \gamma & -\cos \phi \sin \gamma \\ -\sin \phi \sin \gamma & \cos \phi \sin \gamma & \cos \gamma \end{pmatrix} \begin{pmatrix} x \\ y \\ z \end{pmatrix} \quad (2)$$

Using PO model derivation, the electric-fields of twice-reflection wave are shown as Eq (3).

$$\begin{cases} E_{\perp 1'2'}^s = \frac{jk \exp(-jkR)E_0aa_1}{4\pi R} \cos 2\gamma \cos \phi \\ E_{// 1'2'}^s = \frac{jk \exp(-jkR)E_0aa_1}{4\pi R} \sin 2\gamma \cos \phi \\ E_{\perp 2'1'}^s = \frac{jk \exp(-jkR)E_0aa_2}{4\pi R} \cos 2\gamma \sin \phi \\ E_{// 2'1'}^s = \frac{jk \exp(-jkR)E_0aa_2}{4\pi R} \sin 2\gamma \sin \phi \end{cases} \quad (3)$$

Obviously, the echo has not only co-polarization component, but also cross-polarization component. The polarization-modulating intensity is related to its rotation angle. When the rotation angle is  $\gamma = \pi/4$ , the echo will fully be cross-polarization component which could not be received by the existing single-polarization marine radar. Therefore, the target will be stealth one to marine radar.

According to Pauli-basis, the TCR polarization scattering characteristics can be analyzed by Pauli-Basis decomposition. Therefore, Pauli-Basis decomposition simulations of TCR ( $\gamma = 5^\circ$ ) are carried out. The simulation result is shown in Fig. 2.

It is inferred from the simulation result that the existing single-polarization marine radar can only receive the co-polarization echo and the information in

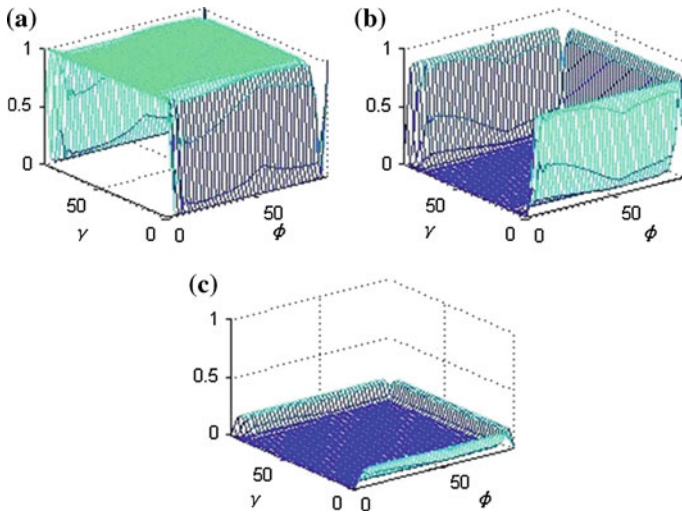


Fig. 2 Pauli-basis decomposition of TCR ( $\gamma = 5^\circ$ )

cross-polarization echo is missing. When the echo is primarily the cross-polarization one that could not be received by the existing marine radar due to its polarization mismatch, false dismissal probability will be highly increased and huge potential security problem is posed for the marine navigation. The polarimetric marine radar will effectively improve its detection performance and provide more security for the marine navigation.

### 3 Overall Design of Polarimetric Marine Radar

The marine radar is primarily detecting for the slow-moving targets like ships, floating ice and islands. Within several contiguous transmitting cycles the changes on the polarization scattering characteristics of the target as a result of its posture change could be ignored.

Therefore, with overall consideration of the target characteristics, radar cost and polarization measurement requirement, it is proposed that the polarimetric marine radar could operate on timesharing transmitting and timesharing receiving model. Based on the current single-polarization marine radar, the functions of dual-polarization marine radar will be realized by upgrading the original antenna to the dual-polarization antenna system and adding the isolator switches. The structural composition of the dual-polarization marine radar is illustrated in Fig. 3.

Within a transmitting cycle only one SPDT switch is turned on or off, and two SPDTs operate alternatively in contiguous cycle. As a result, the measurement of the polarization scattering matrix of the target will be completed within four transmitting cycles, shown in Table 2.

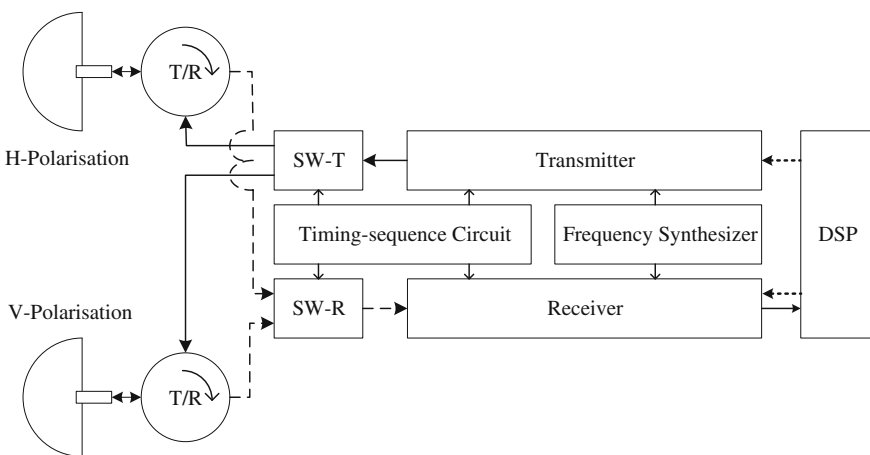


**Fig. 3** The composition block diagram of dual-polarization marine radar

**Table 2** Timing sequence of isolator switches

Transmitting period	SW-T	SW-R	Measure parameter
1	<i>H</i>	<i>H</i>	$S_{HH}$
2	<i>V</i>	<i>H</i>	$S_{HV}$
3	<i>V</i>	<i>V</i>	$S_{VV}$
4	<i>H</i>	<i>V</i>	$S_{VH}$

### 4 Dual-Polarization Antenna Design Approaches of Marine Radar

When ship sails on the sea, the swing of the hull could happen due to the tossing from the sea waves. Therefore, the stable working performance of the antenna under the swinging condition is required for the marine radar. With the full coverage on the pitch, it is also supposed to meet the requirement of high-precision azimuth orientation.

Therefore, the antenna of the marine radar needs to radiate a broad beam-width on the pitch for ensuring its effective coverage in the pitch plane while a beam-width as narrow as possible is needed on the azimuth plane. Taking the slow movement of the target into consideration, the current marine radar is generally adopting the mechanical scanning model of slot antenna, with the antenna positioned on the top of the ship which provides wide space for the antenna’s operation. Hence, it is proposed to add an orthogonal polarization antenna to the original slot antenna for the realization of the design of co-aperture dual-polarization antenna. The realization of dual-polarization antenna in marine radar could, on the one hand, maintains the indicators of working performance of the original antenna; on the other hand, performs the functions of the dual-polarization antenna. Its structural diagram is presented in Fig. 4.

Due to the demanding requirement from the polarization radar for the antenna in terms of the indicator of polarization isolation, the co-aperture antenna can hardly meet the demand. Thus, cylindrical wire grid, as a polarization filter, is suggested to be added to the antenna system for improving the polarization isolation.

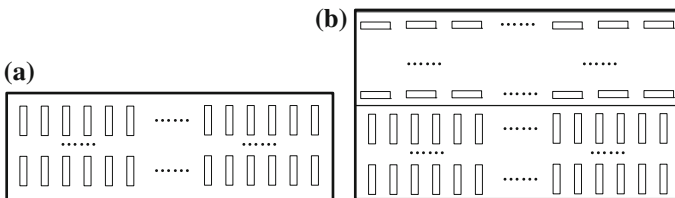


**Fig. 4** Sketch map of the dual-polarization antenna in marine radar. **a** Single-polarization antenna. **b** Dual-polarization antenna

## 5 Conclusions

A novel marine radar based on dual-polarization technique is proposed. With dual-polarization technology, the novel marine radar is superior to the existing marine radar and can work in severe weather. Besides, the novel radar provides the functions of polarization detection and polarization identification.

According to scattering characteristics of marine radar target, the overall design scheme of marine radar with *T/R* timesharing dual-polarization technology is proposed. The novel scheme just needs to upgrade the existing antenna to the dual-polarization antenna system and add the isolator switches based on existing marine radar with the advantages of low cost, easy implementation and good channel consistency.

Aiming at wide space for shipboard marine radar antenna, co-aperture dual-polarization shipboard antenna is proposed in the paper. The performances of the novel antenna are proven to be better than single-polarization ones.

**Acknowledgments** The research is supported by the Fundamental Research Funds for the Central Universities (Grant No. HIT. NSRIF. 2016103), Aerospace Support Fund (Grant No. 2014-HT-HGD14), and HIT (WH). Discipline Construction Guidance Fund (2015).

## References

1. Leonard T, Antipov I et al (2002) A comparison of radar sea clutter model. RADAR. doi:[10.1109/RADAR.2002.1174742](https://doi.org/10.1109/RADAR.2002.1174742)
2. Parthiban A et al (2004) Modelling and simulation of radar sea clutter using k-distribution. SPCOM. doi:[10.1109/SPCOM.2004.1458425](https://doi.org/10.1109/SPCOM.2004.1458425)
3. Bouvier C et al (1995) Simulation of radar sea clutter using autoregressive modelling and K-distribution. In: Radar conference. doi:[10.1109/RADAR.1995.522585](https://doi.org/10.1109/RADAR.1995.522585)
4. Gennarelli C, Pelosi G, Riccio G (1998) Physical optics analysis of the field backscattered by a depolarising trihedral corner reflector. *Microwaves Antennas Propag IEE Proc* 145(3):213–218
5. Pelosi G, Manara G, Fallai M (1997) PO expressions for the field scattered from anisotropic impedance flat plates. *Microwaves Opt Technol* 14(6):316–318
6. Gennarelli C, Pelosi G, Riccio G (1997) Explicit evaluation fo the field backscatterey bu an anisotropically loaded trihedral corner reflector. Report 97/1, DIIE, University of Salerno, Fisciano
7. Pelosi G, Manara G, Nepa P (1998) EM scattering from anisotropic impedance wedges illuminated at oblique incidence. *Electromagnetics* 18(2):117–133
8. Pelosi G, Manara G, Nepa P (1998) A UTD solution for the scattering by a wedge with anisotropic impedance faces: skew incidence case. *IEEE Trans Antennas Propag* 46(4):579–588

# Monitoring of the Performance of Excitation System Based on Measured PMU Data

Sai Wang, Xueping Gu, Wei Tang, Zhen Li and Yuanchao Huang

**Abstract** Traditional evaluation methods of performance of excitation system are often carried on offline or need special conditions. To realize monitoring and evaluation of performance of the excitation system in operation, this paper proposes practical arithmetic of monitoring the unit operation status based on PMU measured data. After data preprocessing, using valid data to identify field flashing, de-excitation, load rejection and terminal voltage drop. Then corresponding performance evaluation indexes of the excitation system, respectively under different conditions is calculated. The quantitative evaluation result of the performance of excitation can be obtained and it can provide some reference for the evaluation of the practical operation performance of excitation system.

**Keywords** Excitation system · Performance index · Status transfer · PMU

## 1 Introduction

The excitation system of generator has an important influence on the stability and stable operation of the generator and power system. At present, the performance of the unit excitation system is mainly tested by the way of the access network test or type test [1, 2], test conditions all have particular requirements and cannot be

---

S. Wang (✉) · X. Gu  
School of Electrical and Electronic Engineering,  
North China Electric Power University, Baoding 071003, Hebei, China  
e-mail: 972040116@qq.com

W. Tang  
State Grid Anhui Electric Power Company, Hefei 230061, China  
e-mail: tangw0016@ah.sgcc.com.cn

Z. Li · Y. Huang  
Beijing Monitoring Technology Center of NARI Group Corporation,  
Beijing 102200, China

© Springer-Verlag Berlin Heidelberg 2016

B. Huang and Y. Yao (eds.), *Proceedings of the 5th International Conference on Electrical Engineering and Automatic Control*, Lecture Notes in Electrical Engineering 367, DOI 10.1007/978-3-662-48768-6\_54

carried out often. Current testing results cannot comprehensively reflect the actual performance of the excitation systems in daily operation.

With the measured data from wide area measurement system (WAMS), this paper proposes a practical method to identify field flashing, de-excitation, load rejection, and terminal voltage drop of the generators and calculates the evaluation index of the excitation system. The evaluation method proposed is mainly applied to turbo generator with the capacity over 200 MW and self-shunt excitation system. It can provide a certain reference for improving the standard of online monitoring and evaluation of the performance of excitation system.

## **2 Acquisition and Preprocessing of the Measured Data of the Unit**

### ***2.1 Data Acquisition***

PMU substations send collected real-time data packets from units and their excitation systems to WAMS front system, front system receives and explains these packets and then put them into real-time high speed cache area for the use of functional application. In order to monitor the operation status of units and to analysis their performance, it is necessary to develop data interface to obtain real-time data of units from high speed cache area of WAMS system, which includes terminal voltage, terminal current, active power, reactive power, excitation voltage and excitation current etc.

### ***2.2 Data Preprocessing***

Before using and analyzing the obtained PMU real-time data, the correctness and reasonability of the data must be ensured. So it is necessary to conduct data preprocessing. The monitoring windows of the measured data is  $t_0$  ( $t_0$  can be set to 1 s), by monitoring remote measure data and remote sign data within  $t_0$  to judge whether abnormal conditions exist in the data within  $t_0$ , which include data invalidation, data deficiency, data with quality problems, etc. Concrete introduction is shown in Table 1.

In monitoring and the following index calculating, the terminal voltage described in this paper is the average of generator terminal three-phase voltage amplitude.

After recognizing and rejecting the data which is unable to meet analysis requirement, the further analysis is carried on using the data which is effective, complete, and with normal quality code. The flow of data acquisition and data preprocessing is shown in Fig. 1.



**Table 1** Abnormal types of data and introduction

No.	Abnormal type	Introduction
1	Recognition of abnormal working condition of PMU device	Detect normal, abnormal or faulty status of unit PMU or transmission channel
2	Judgment of data effectiveness	When terminal voltage is less than $-10\%U_N$ or bigger than $1.5U_N$ , the data is regarded as invalid
3	Judgment of data deficiency	Detect whether interruption exists in data
4	Shutdown detecting	Detect whether units stops
5	Data with abnormal quality	Detect whether the quality code of the data is abnormal

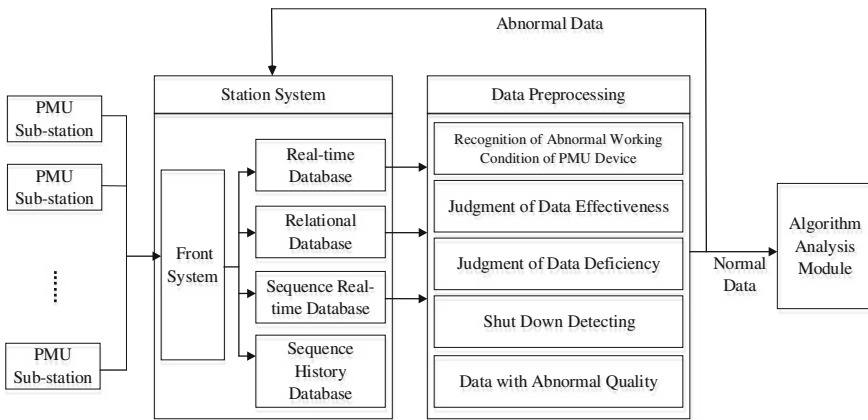


**Fig. 1** Flow of data acquisition and data preprocessing

### 3 Identification of Unit Operation Status Transfer

Field flashing, de-excitation, terminal voltage drop, and load rejection can reflect performance of excitation system. So this paper mainly pays attention to the above situations.

Considering that the above conditions, all happen during the terminal voltage or unit output active power transfers from one status to another status; therefore, this paper uses *unit operation status transfer* as the general term of field flashing, de-excitation, terminal voltage drop, load rejection, and so on. The transfer of unit operation status is shown in Fig. 2.

Changes of terminal voltage and unit output active power are mainly used to recognize the transfer conditions of unit operation status, the recognition judgment is shown in Table 2.

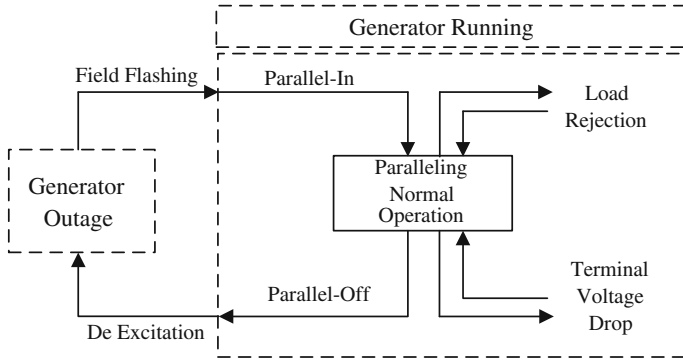


**Fig. 2** Transfer of unit operation status

**Table 2** Recognition of transfer of unit operation status

Types	Change of unit operation status
Field flashing	Terminal voltage increase: from $<50\%U_N$ to $>50\%U_N$
De-excitation	Terminal voltage decrease: from $>50\%U_N$ to $<50\%U_N$
Load rejection	Output active power sharp drop: from $>30\%P_N$ to $<5\%P_N$
Terminal voltage drop	Terminal voltage sharp drop

## 4 Evaluation of Excitation Performance Under Different Types of Unit Operation Status Transfer

Calculate the performance evaluation index, respectively, under four conditions including field flashing, the excitation, load rejection, and terminal voltage drop, then evaluate performance of the excitation.

The indexes described in this paper mainly refer to related national standard and industry standard [3, 4], but present evaluation standards of excitation performance are all under experimental conditions, therefore on the basis of above standards, considering the differences between online operation environment and experimental environment, appropriate changes, and engineering disposal are carried out according to situations possibly encountered in actual operation environment.

### 4.1 Field Flashing

Field flashing is an important part of generator paralleling. When the power grid runs well, there is no strict requirements for speed of field flashing; but when the generator is in emergency standby, in order to remove the power grid fault as quickly as possible, the generator in standby is hoped to be put into as quickly as

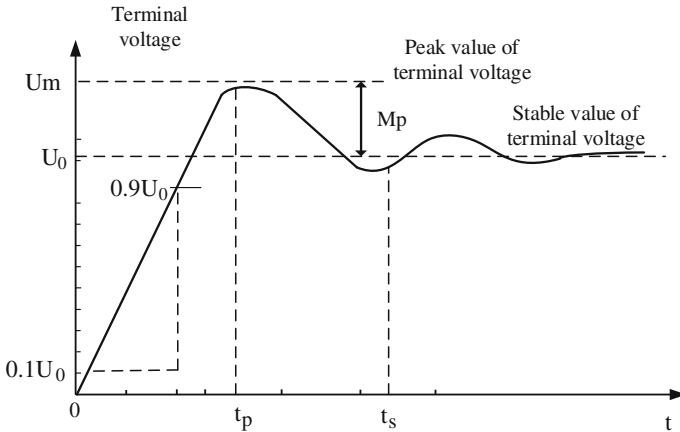


**Fig. 3** Curve of typical field flashing

possible, then it is necessary to reduce the time for field flashing. Curve of typical field flashing is shown in Fig. 3.

Performance evaluation index:

Overshoot:

$$\delta f = \frac{U_m - U_0}{U_0} \times 100 \% \tag{1}$$

In which:  $U_m$  is the maximum terminal voltage during field flashing,  $U_0$  is the stable value of terminal voltage.

Settling time  $t_s$ : time from the start of field flashing to stable status.

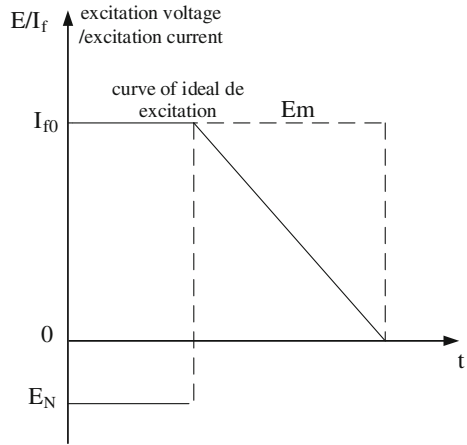
Number of oscillation  $n$ : the number of oscillation of terminal voltage during field flashing.

The literature [3, 4] specifies that when synchronous generator generates 100 % voltage field flashing, the automatic voltage regulator should guarantee the overshoot of terminal voltage is no more than 15 % (10 %) of the rated voltage, the oscillation number of terminal voltage should be no more than three, the regulating time should be no more than 10 s.

## 4.2 De-excitation

De-excitation of generator is divided into at normal shutdown and at fault, de-excitation at fault of modern generator is the only effective way to protect generator terminal fault, and it is the final defensive line of the protection of generator fault.

**Fig. 4** Curve of unit ideal de excitation



To satisfy the requirement of fast de-excitation, especially in de-excitation at fault, the de-excitation time should be as close as possible to the ideal de-excitation time  $0.167T_{d0}'$ . Curve of the ideal de-excitation is shown in Fig. 4.

Evaluation index of performance:

The actual de-excitation time: the time from the sending out of de-excitation order to the time when the excitation current decreases to 5% of the rated value.

The effective de-excitation time  $T_E$  [5]: according to the actual final effect of de-excitation which is the decay of generator terminal voltage to time to determine de-effective excitation time, influence of various kinds of factors on de-excitation performance can be taken into account comprehensively, and the actual effect of de-excitation can be reflected. The concrete calculation formula is as follows:

$$T_E = \frac{1}{U_0} \int_0^{t_{\text{end}}} u(t) dt \tag{2}$$

where  $u(t)$  is terminal voltage at time  $t$ ,  $U_0$  is the generator initial stable terminal voltage, and  $t_{\text{end}}$  is the time when the generator totally stops.

### 4.3 Load Rejection

Load rejection of steam turbines in operation not only produces certain negative influences on the stable operation of power grid, but also forms threaten to the secure operation of the units.

Evaluation index of performance:

Overshoot:

$$\delta l = \frac{U_m - U_0}{U_0} \times 100 \% \quad (3)$$

where  $U_m$  is the maximum terminal voltage during load rejection and  $U_0$  is the stable value of terminal voltage.

Number of oscillation  $n$ : the number of terminal voltage oscillation during load rejection.

Settling time  $t_s$ : time from the start of load rejection to stable status.

The literature [3, 4] specifies that after generator rejects rated load suddenly under rated power factor, the overshoot of terminal voltage should be not more than 15 % of the rated value, the oscillation number should be no more than three, the regulating time should be no more than 10 s.

#### **4.4 Terminal Voltage Drop Under Unit Normal Operation**

The typical curve of terminal voltage drop under unit normal operation status is shown in Fig. 5, such terminal voltage drop mainly arises from short circuit or other fault in somewhere in the power grid connected with the unit.

##### **4.4.1 Excitation Voltage Response Lag Time**

Excitation voltage response lag time is the time from terminal voltage changes abruptly to the time when excitation voltage starts to regulate correctly, it reflects the response speed of the excitation system. The concrete calculation formula is as follows:

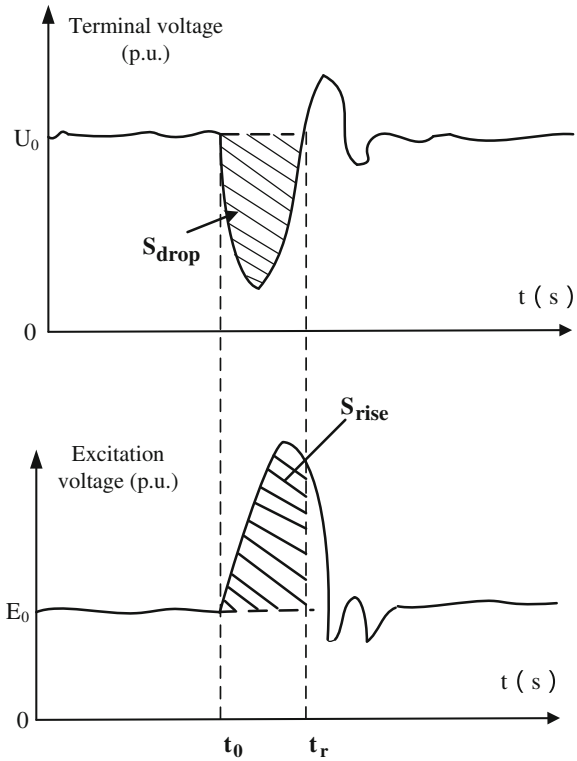
$$t_{lag} = t_{estart} - t_0 \quad (4)$$

In which,  $t_{lag}$  is response lag time,  $t_{estart}$  is the time excitation voltage starts to regulate, and  $t_0$  is the time terminal voltage starts to drop.

##### **4.4.2 Amplification-K**

$S_{drop}$  and  $S_{rise}$  are calculated, respectively, according to curve of terminal voltage and excitation voltage, as in Fig. 5. The ratio of the two subscribes the transient adjustment ability of the excitation system to terminal voltage deviation under disturbance, the bigger this value means the bigger the amplification of the

**Fig. 5** Curve of typical terminal voltage drop



excitation control system is, the stronger the transient adjustment ability is. The concrete calculation formula is as follows:

$$S_{\text{drop}} = \sum_{t_0}^{t_r} (u_0 - u(t)) \Delta t \tag{5}$$

$$S_{\text{rise}} = \sum_{t_0}^{t_r} (E(t) - E_0) \Delta t \tag{6}$$

$$K = \frac{S_{\text{rise}}}{S_{\text{drop}}} \tag{7}$$

In which,  $S_{\text{drop}}$ : terminal voltage drop area;  $S_{\text{rise}}$ : excitation voltage rise area;  $U_0$ : stable value of initial terminal voltage (in p.u.);  $U(t)$ : terminal voltage at time  $t$  (in p.u.);  $E_0$ : stable value of initial excitation voltage (in p.u.);  $E(t)$ : excitation voltage at time  $t$  (in p.u.);  $\Delta t$ : sampling interval, usually 0.02 s;  $t_r$ : time period from terminal voltage starts to drop to recover to the initial stable value the first time.

## 5 Conclusion

This paper proposes practical algorithm of acquisition and preprocessing of measured data of running generator unit. The normal data can realize the identification of field flashing, excitation, load rejection, and terminal voltage drop. Then calculating related indexes can realize performance evaluation of excitation system, which can provide some references for online evaluation of performance of unit excitation system.

## References

1. Liu Q (2007) Power system stability and generator excitation control. China Electric Power Press, Beijing
2. Fang SL, Su WM (2004) Analysis of relevant specifications for dynamic performance index of excitation system. *Electr Equip* 5(7):37–40
3. GB/T 7409.3-2007, Excitation system for synchronous electrical machines-technical requirements of excitation system for large and medium synchronous generators
4. DL/T 843-2010, Specification for excitation system for large turbine generators
5. Li JC (2011) Design and application of modern synchronous generator excitation system. China Electric Power Press, Beijing

# Comprehensive Evaluation on the Primary Frequency Regulation Performance of Generator Units Based on Data from a Wide Area Measurement System

Yan Zhang, Xuan Pan, Xinqiao Fan, Sai Wang, Zhen Li  
and Yuanchao Huang

**Abstract** On-line monitoring of the unit's primary frequency regulation performance can be realized on the basis of measured data from WAMS (Wide Area Measurement System). Based on measured data and according to the index importance, this paper establishes the unit primary frequency regulation performance evaluation index system, including the percentage of pass of the primary frequency regulation response lag time and stabilization time, the effect of primary frequency regulation, and percentage of pass of maximum regulation amplitude of load. Then, it employs close value methods to achieve the comprehensive performance evaluation of the primary frequency. The proposed method can provide some reference for comprehensive evaluations of the actual performance of a unit's primary frequency regulation.

**Keywords** Primary frequency regulation · Performance evaluation · Close value method · PMU

---

Y. Zhang  
State Grid Beijing Electric Power Research Institute,  
Beijing 100075, China  
e-mail: 39374260@qq.com

X. Pan  
State Grid Beijing Electric Power Company, Beijing 100031, China

X. Fan  
School of Automation, Beijing Information Science  
and Technology University, Beijing 100192, China

S. Wang (✉)  
School of Electrical and Electronic Engineering, North China Electric  
Power University, Baoding, Hebei Province 071003, China  
e-mail: 972040116@qq.com

Z. Li · Y. Huang  
Beijing Monitoring Technology Center of NARI Group Corporation,  
Beijing 102200, China



## 1 Introduction

The research on on-line monitoring of unit primary frequency regulation performance has great relevance for ensuring that the unit has a good performance for primary frequency regulation and the safe and stable operation of a power grid [1, 2].

WAMS, which is based on PMU, can realize the synchronous measurement of the parameter in each measuring point and real-time uploading [3], so it provides the data basis for primary frequency regulation performance evaluation.

The close value method is an optimization method of multi-objective optimized decision-making with a transparent process and visualization of the decision-making results. So it is suitable for comprehensive multi-objective evaluation, and this method has been applied in electric power assessment and other fields [4, 5].

This paper puts forward monitoring the primary frequency regulation performance based on WAMS data, firstly building the index system of primary frequency regulation performance, then calculating the unit primary frequency regulation indexes with on-line data, and afterwards using the close value method to realize comprehension evaluation of primary frequency regulation performance.

## 2 Index System of Primary Frequency Regulation Performance

### 2.1 *Percent of Pass of Response Lag Time and Stabilization Time of Primary Frequency Regulation*

When the power grid frequency jumps above the primary frequency regulation dead zone ( $\Delta fsq$ ) at  $T_0$ , then the knee-point time  $T_1$  can be calculated automatically by monitoring the variation of the generator output.  $T_1$  is the time when the unit actually operates.

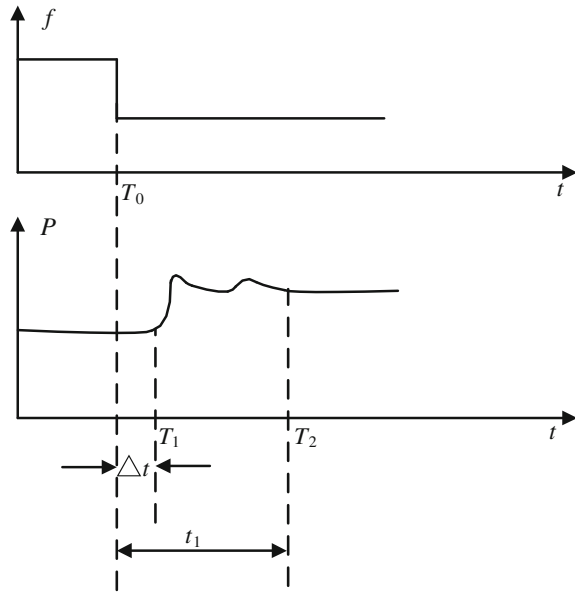
The response lag time of unit primary frequency regulation  $\Delta t$  can be calculated by the following formula:

$$\Delta t = T_1 - T_0 \quad (1)$$

During the primary frequency regulation, the time needed for the unit output to reach stability after the power grid frequency becomes stable refers to the stabilization time of the primary frequency regulation, and it should be shorter than one minute.

As is shown in Fig. 1, the stabilization time of the unit primary frequency regulation  $t_1$  can be obtained by the knee-point time  $T_2$  when the unit output tend to be stable. The concrete formula is as follows:

**Fig. 1** Schematic diagram of response lag time and stabilization time of primary frequency regulation



$$t_1 = T_2 - T_0 \tag{2}$$

The shorter is the response lag time of unit primary frequency regulation, the faster the unit reacts to frequency variation; the shorter is the stabilization time of unit primary frequency regulation, the faster the primary frequency regulation of unit performs.

The response lag time and stabilization time of primary frequency regulation reflect the lag characteristic and speed of regulation, and they can be calculated by the response status of units during a certain time; the concrete calculations are as follows:

$$OT1 = \frac{A}{ES} \tag{3}$$

$$OT2 = \frac{B}{ES} \tag{4}$$

In the formulas above,  $OT1$  refers to the percentage of pass of the response lag time of the primary frequency regulation;  $A$  is the number of times that the response lag time of the primary frequency regulation is shorter than 3 s;  $ES$  is the number of adjustment events of the primary frequency regulation;  $OT2$  refers to the percentage of pass of the stabilization time of the primary frequency regulation; and  $B$  is the number of times that the stabilization time of the primary frequency regulation is shorter than one minute.

## 2.2 Effect of Primary Frequency Regulation

### 2.2.1 Measured Contributing Electricity of Primary Frequency Regulation

Measured contributing electricity of the primary frequency regulation  $H_i$  refers to the integral value of electricity during a certain time when the frequency exceeds the dead zone of unit primary frequency regulation. Consider the actual unit output  $P_0$  when the frequency exceeds the dead zone of unit primary frequency regulation as the base point, integrate the electricity variation of the unit output, when the integral length is less than one or two minutes. If the frequency returns to normal within one or two minutes, the integral time will stop with it. The concrete calculation formula is as follows:

$$H_i = \int_{t_0}^{t_i} \text{sgn}(x)(P(t) - P_0)dt \quad (5)$$

In this formula,  $t_0$ : the time when power grid frequency exceeds dead zone of the primary frequency regulation;  $t_i$ : the time when frequency returns to the dead zone of the primary frequency regulation, wherein the total integral time should be less than one or two minutes;

$P(t)$ : actual active power of unit output at  $t$ ; and  $P_0$ : actual active power of unit output at  $t_0$ ;  $\text{sgn}(x)$ : sign function:

$$\text{sgn}(x) = \begin{cases} 1, & f < f_N - \Delta f_{sq} \\ 0, & f_N - \Delta f_{sq} \leq f \leq f_N + \Delta f_{sq} \\ -1, & f > f_N + \Delta f_{sq} \end{cases} \quad (6)$$

In this formula,  $f_N$  is rated at frequency 50 Hz and  $\Delta f_{sq}$  is the dead zone of the primary frequency regulation, for instance 0.033 Hz.

Regulation of the symbol of  $H_i$ : if generator output is less than the initial steady output when the frequency is higher, or if generator output is more than the initial steady output when the frequency is lower, the symbol of  $H_i$  is positive; if generator output is more than the initial steady output when the frequency is higher or if generator output is less than the initial steady output when the frequency is lower, the symbol of  $H_i$  is negative.

That is to say, when the integral electricity is positive, that means the changed direction of the unit output electricity helps the recovery of frequency. When the integral electricity is negative, the changed direction of the unit output electricity aggravates the out-of-limit status of the frequency and has a negative effect on the recovery of frequency.

### 2.2.2 Theoretical Contributing Electricity of the Primary Frequency Regulation

The theoretical contributing electricity of unit primary frequency regulation  $H_e$  is calculated by the following formula:

$$H_e = \int_{t_0}^{t_i} \Delta P(\Delta f, t) dt \quad (7)$$

$$\Delta P(\Delta f, t) = \Delta f(t) \times MCR/f_N \times K_c \quad (8)$$

In this formula,  $\Delta f(t) = |f(t) - f_N| - \Delta f_{sq}$  is the absolute value of the frequency difference when the frequency exceeds the dead zone;  $MCR$  is the rated active power of the unit;  $f(t)$  is the frequency at  $t$ ; and  $K_c$  is the unit speed variation rate.

### 2.2.3 Effect of Primary Frequency Regulation

When frequency goes beyond  $50 \text{ Hz} \pm \Delta f_{sq}$  and continues for more than twenty seconds, in this period (the maximum is 60 s) the ratio of measured contributing electricity to theoretical contributing electricity is called the primary frequency regulation effect ( $DX$ ), for which the concrete calculation is:

$$DX = \frac{H_i}{H_e} \quad (9)$$

In this formula,  $H_i$  and  $H_e$  are respectively the measured contributing electricity of the primary frequency regulation and the theoretical contributing electricity of primary frequency regulation. When  $DX < 0$ , then set  $DX=0$ .

If  $DX > 0$ , it means the direction of the primary frequency regulation is correct; if  $DX = 0$ , the direction of the primary frequency regulation is thought to be wrong, that is to say,  $H_i < 0$  means the direction of unit output variation aggravates the out-of-limit status of frequency, and it has negative effect on the recovery of frequency.

## 2.3 Percentage of Pass of the Maximum Regulation Amplitude of the Load

The percentage of pass of the maximum load regulation amplitude of the primary frequency regulation refers to the maximum regulation amplitude of the active power output from the point that the frequency exceeds the dead zone to recovery to the dead zone of primary frequency regulation.

Setting the maximum regulation amplitude of the load guarantees that, when the frequency has experienced a great change, the output of generator groups will not increase too violently to make the Main Fuel Trip (MFT) operate, and, if the value is too

small, the ability of the primary frequency regulation will be too weak. The amplitudes of a thermal power unit are limited to different values according to different capacities, while the amplitudes of a hydroelectric generating unit are not generally limited.

The calculation formula for percentage of pass of the maximum regulation amplitude of the load  $OV$  is as follows:

$$OV = \frac{C}{ES} \quad (10)$$

In this formula,  $C$  is the number of times that the regulation amplitude of the load is less than the maximum allowed regulation amplitude;  $ES$  is the number of primary frequency regulation events.

### 3 Evaluation Model of the Close Value Method

#### 3.1 Establishment of the Sample Index Matrix

Assuming that it has  $n$  units to evaluate, including  $z_1, z_2, z_3, \dots, z_n$ , and  $m$  evaluation indexes, including  $s_1, s_2, \dots, s_m$ , and the value of unit  $z_i$  in the index of  $s_j$  is  $c_{ij}$ , then  $m$  evaluation indexes of  $n$  units to evaluate make up the initial sample index matrix  $Y$ .

$$Y = (c_{ij})_{n \times m} \quad (11)$$

In this formula,  $i = 1, 2, \dots, n$ ;  $j = 1, 2, \dots, m$ .

#### 3.2 Standardization of the Sample Index Matrix

The percentage of pass of the response lag time, the percentage of pass of stabilization time, the effect index and the percentage of pass of the maximum regulation amplitude of the load are all positive indexes. The normalization calculation is as follows:

$$r_{ij} = \frac{c_{ij}}{\left(\sum_{i=1}^n c_{ij}^2\right)^{0.5}} \quad (12)$$

After normalization disposal, the normalized sample index matrix is obtained by:

$$Z = (r_{ij})_{n \times m} \quad (13)$$

In this formula,  $i = 1, 2, \dots$ , and  $n$ ;  $j = 1, 2, \dots, m$ .

Considering that the degree of importance of each index varies, the weight of each index can be determined by experts scoring:  $w$ {percentage of pass of the response lag time, percentage of pass of stability time, effect index, and percentage of pass of maximum regulation amplitude of load} = {0.2,0.2,0.5,0.1}.The weight matrix is

$$w = \begin{bmatrix} 0.2 \\ 0.2 \\ 0.5 \\ 0.1 \end{bmatrix} \tag{14}$$

The weighted data matrix  $Z'$  can be obtained by the following formula:

$$Z' = Z \times w = (r'_{ij})_{n \times m} \tag{15}$$

### 3.3 Calculation of the Visual Best and Worst Points of Each Index

Let:

$$r_j^+ = \max_{1 \leq i \leq n} \{r'_{ij}\} \tag{16}$$

$$r_j^- = \min_{1 \leq i \leq n} \{r'_{ij}\} \tag{17}$$

where,  $j = 1, 2, \dots, m$ .The collection of the visual best and worst points is composed of the maximum value and minimum value of each normalization index respectively, that is:

The collection of the visual best points is:

$$A^+ = (r_1^+, r_2^+, \dots, r_m^+) \tag{18}$$

The collection of the visual worst points is:

$$A^- = (r_1^-, r_2^-, \dots, r_m^-) \tag{19}$$

### 3.4 Calculation of “Close Value” of Each Sample Point

According to the calculation method of the distance in Euclid space, calculating the Euclid distance  $d_i^+$  from this point to the best point, and  $d_i^-$  from this point to the worst point, the calculation formulas are:

$$d_i^+ = \left[ \sum_{j=1}^m (r'_{ij} - r_j^+)^2 \right]^{0.5} \quad (20)$$

$$d_i^- = \left[ \sum_{j=1}^m (r'_{ij} - r_j^-)^2 \right]^{0.5} \quad (21)$$

where,  $i = 1, 2, \dots, n; j = 1, 2, \dots, m$ . Let:

$$d^+ = \min_{1 \leq i \leq n} \{d_i^+\}, d^- = \min_{1 \leq i \leq n} \{d_i^-\}.$$

Then the close value  $E_i$  of the  $i$ th unit to be evaluated is

$$E_i = \frac{d_i^+}{d^+} - \frac{d_i^-}{d^-} \quad (22)$$

where,  $i = 1, 2, \dots, n$ . According to the value of  $E_i$  of each unit to be evaluated, a comprehensive assortment of the primary frequency regulation performance of different units can be obtained.

## 4 Conclusion

This paper proposes the index evaluation system of the primary frequency regulation based on generator unit measured PMU data, which uses close value method to comprehensively evaluate the performance of unit primary frequency regulation. Using the obtained evaluation results can enable quantitative comparison between the different units.

The method proposed is conducive to promote power plants to put into use primary frequency regulation, which has a positive impact on raising the level of the power quality and power grid frequency control in electricity markets.

## References

1. Ma HJ, Su F, Shen CQ (2012) Online testing function development and implementation for generator primary frequency regulation performance. East China Electr Power 08:1420–1423
2. Gao L, Dai YP, Wang JF (2012) An online estimation method of primary frequency regulation parameters of generation units. Proc CSEE 16:62–69
3. Duan G, Yan YQ, Xie XD (2015) Development status quo and tendency of wide area phasor measuring technology. Autom Electr Power Syst 01:73–80
4. Huang J, Hong-zhong MA, Hui JI (2008) Application of intimate data method in synthetical evaluation about power quality. Relay 03:60–63+70

5. Liu JC, Wang W (2013) Distribution network assessment model based on entropy weight osculating value method. *East China Electr Power* 05:1047–1050
6. Zheng T, Gao F (2009) On-line monitoring and computing of unit PFR characteristic parameter based on PMU. *Autom Electr Power Syst* 11: 57–61



# A Novel PQ Control Strategy of Microgrid with Single-Phase Connected to Grid

Baoqun Zhang, Longfei Ma, Cheng Gong, Ran Jiao, Rui Shi  
and Zhongjun Chi

**Abstract** Based on the power hypothesis of feed-forward decoupling, PQ control is typical of the micro network control strategy, through the SPLL and  $d-q$  transformation module power and power factor control module and current control module to establish PQ control model, and in the original basis of ordinary phase lock loop to instantaneous reactive power phase lock loop. Finally using two half-bridge inverter dc micro-source to simulate practice single-phase parallel in MATLAB/Simulink simulation, it is concluded that using the control strategy of the micro-source in connection with power grid after a relatively short period of time, keeps the current in parallel and power grid voltage synchronization, output active power constant.

**Keywords** Microgrid · PQ control · Grid connected

---

B. Zhang (✉) · L. Ma · C. Gong · R. Jiao · R. Shi · Z. Chi  
State Grid Beijing Electric Power Research Institute, Beijing, China  
e-mail: davehilbert@163.com

L. Ma  
e-mail: malongfei1987@163.com

C. Gong  
e-mail: 123.gc@163.com

R. Jiao  
e-mail: jiaoran0418@sina.com

R. Shi  
e-mail: shirui\_56@163.com

Z. Chi  
e-mail: czjtsh@163.com

## 1 Introduction

Microgrid as important auxiliary systems of distribution network [1], has the advantage of flexible installation, green, efficient use of local resources and various forms of output, and its active and reactive power are adjustable and positive response. It is the developing tendency of distribution network power supply to access microgrid at the end of distribution network.

Feed-forward decoupling PQ control based on  $dq$  transformation is one of the mainstream micro network control strategy, particularly in photovoltaic and wind power. Renewable energy output power is greatly affected by the external environment and has been clearly intermittent. So energy storage devices with a larger capacity were needed to ensure constant power output, but high cost is required [2]. Therefore, the control target of this type of distributed generation (Distributed Generation, DG) is how to ensure maximum utilization of renewable energy, in the general PQ controller.

PQ design generally includes a phase-locked loop (Phase Locking Loop, PLL) and dq conversion module, power and power factor module and current control module, but built-in phase-locked loop are used in MATLAB/Simulink simulation usually. This paper presents a phase-locked loop based on instantaneous reactive power theory, and SPLL using PI regulator and negative feedback loop which can be quickly synchronized tracking grid phase, and current loop was designed by typical I system.

## 2 Establish PQ Control Model

Without considering system loss, the maximum distributed power given act as an inverter output reference power  $P_{ref}$ . Microgrid is often the expected output active power to the grid (i.e., inverter power factor is 1.0, and  $Q_{ref} = 0$ ), but grid-connected system can also output reactive power (i.e.  $Q_{ref} \neq 0$ ). Reactive and active power is contacted by power factor angle from  $Q_{ref} = P_{ref} * \tan \theta$  (where  $\theta$  is the power factor angle), so the reactive power control can be seen as the power factor control [3]. PQ control strategy was shown in Fig. 1.

## 3 The Parameters Design of PQ Control Strategy Model

### 3.1 PLL Design

1. General phase-locked loop (PLL) design

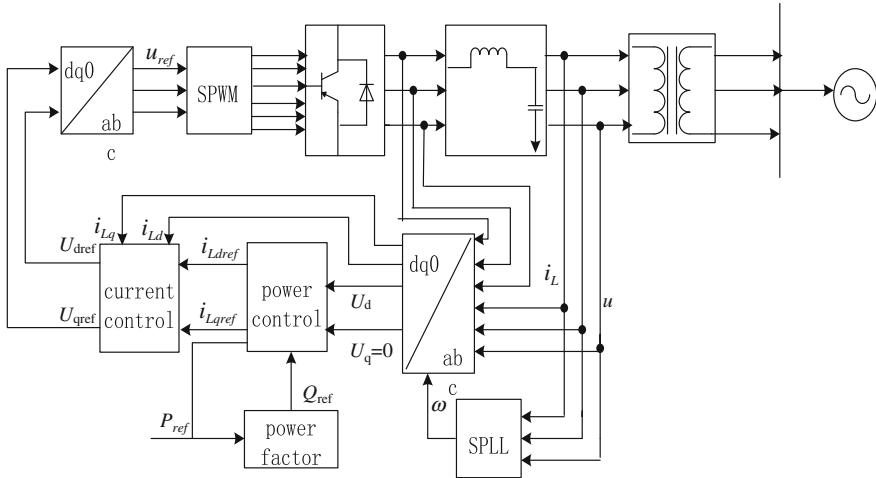


Fig. 1 The control strategy of PQ

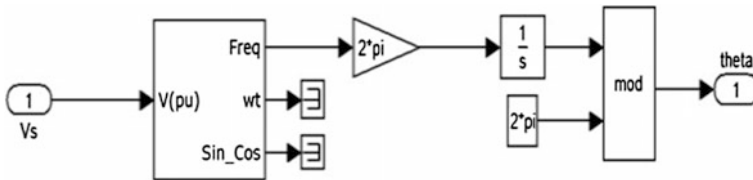


Fig. 2 The general control model of PLL

$V_s$  represent grid voltage in Fig. 2. Built-in virtual phase-locked loop of Simulink was used directly, and the output voltage phase can maintain synchronization with the grid after integral part (Fig. 2).

2. Phase-locked loop design based on instantaneous reactive power theory

SPLL adopted in this paper based on instantaneous reactive power theory [4] compared to PLL, which cannot only track the voltage when the voltage waveform distortion but also has good steady-state effects and fast dynamic response. Its control structure as shown in Fig. 3 and the specific principle is as follows: First, SPLL made three-phase grid voltage  $U_{abc}$  converted into  $U_d$  and  $U_q$ , through  $\alpha\beta$  transformation and  $dq$  transformation in turn. Where the reference angle of  $dq$  transformation is the PLL output  $\theta$ , and the difference between  $U_a$  and 0 is the difference of output voltage phase and the PLL output phase (When the PLL can be a completely tracking frequency, the difference value is 0). Error signal  $\omega$  was obtained by the value of  $U_a$  minus 0 through the PI controller, and  $w$  plus initial angular frequency  $w_0$  obtained angular frequency  $w$ , ( $w_0$  is generally the fundamental angular frequency value, so that even in the case of input power failure can

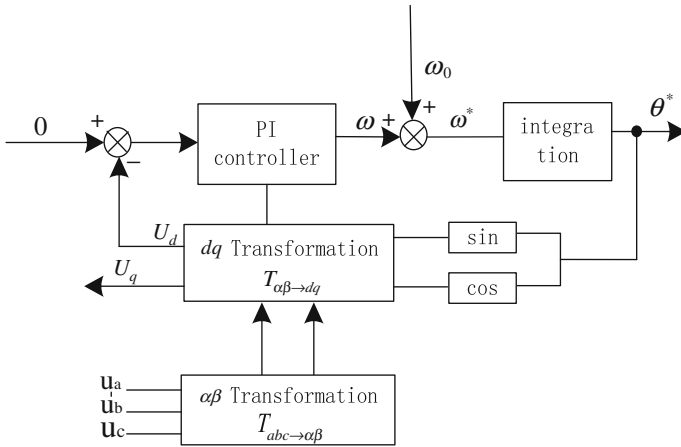


Fig. 3 The control structure of SPLL

still output sine wave of fundamental frequency), Then the final output of the phase angle  $\theta$  is obtained through integral part. In conclusion, SPLL can quickly synchronize the tracking phase grid by PI regulator and close-loop negative feedback.

It can be seen that,  $q$  axis voltage of the normal three-phase grid voltage after  $dq$  transformation is 0. Therefore, SPLL can track the grid frequency, when  $q$  axis voltage was controlled to 0.

### 3.2 Current Loop Control Model Parameter Design

#### 1. Current loop control model principle

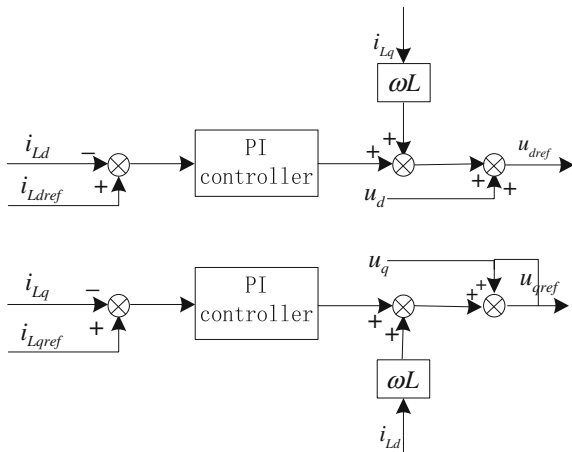
In the current loop control diagram shown in Fig. 8, the error is the difference between power control module output current reference value  $i_{Ldref}$  and practical feedback to the controller signals  $i_L$  through PI regulation.

If the current control error is 0, the inverter output current  $i_L$  can track no difference to the power control output  $i_{Lref}$ . Therefore, it is not only benefit to the active and reactive power control, but also the output voltage can track the grid voltage in time; output of the inverter reference was achieved by combination the current state feedback decoupling, power grid voltage feed-forward compensation and the output of the PI controller [5] (Fig. 4).

#### 2. Current loop decoupling principle

Inverter output is a strong coupling system under  $dq$  coordinate, which can be expressed as follows:

**Fig. 4** The control structure of the current loop



$$\begin{bmatrix} U_d \\ U_q \end{bmatrix} = \begin{bmatrix} Ls + r & \omega L \\ -\omega L & Ls + r \end{bmatrix} \begin{bmatrix} i_{Ld} \\ i_{Lq} \end{bmatrix} + \begin{bmatrix} U_{dref} \\ U_{qref} \end{bmatrix} \tag{1}$$

By the formula (1), the inductor current was affected not only by control element  $V_d$  and  $V_q$  but also by the disturbance of coupling voltage  $wLi_L$  and grid voltage  $U$ . So you can only eliminate the coupling term between them for independent control of the inductor current.

When the current loop used PI controller and the introduction of the current state feedback ( $wLi_{Ld}$ ,  $wLi_{Lq}$ ) is decoupled, the control equation was shown as follows:

$$\begin{bmatrix} V_d \\ V_q \end{bmatrix} = \begin{bmatrix} U_d \\ U_q \end{bmatrix} - (k_p + \frac{k_i}{s}) \begin{bmatrix} i_{Ldref} - i_{Ld} \\ i_{Lqref} - i_{Lq} \end{bmatrix} - \begin{bmatrix} -\omega L \\ \omega L \end{bmatrix} \begin{bmatrix} i_{Lq} \\ i_{Ld} \end{bmatrix} \tag{2}$$

The formula (1) was substituted into (2), we get:

$$Ls + r \begin{bmatrix} i_{Ld} \\ i_{Lq} \end{bmatrix} = (k_p + \frac{k_i}{s}) \begin{bmatrix} i_{Ldref} - i_{Ld} \\ i_{Lqref} - i_{Lq} \end{bmatrix} \tag{3}$$

It was known from the formula (2-3):  $d$  axis and  $q$  axis can be independently controlled, and increases voltage feed-forward compensation in the current loop can reduce the impact of the grid voltage for control system [6].

### 3. PI controller parameters design (Fig. 5).

A reasonable set of PI controller parameters can be no difference tracking the output current reference of power module, but also quickly dynamic response of the system. The  $d$  axis and  $q$  after current controller can be individually designed after the decoupling of the current state.

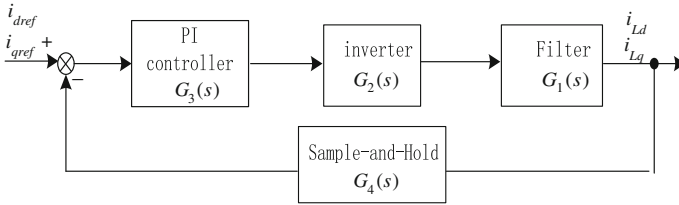


Fig. 5 The control structure of the system of current loop

Inductor current as the control variable, the transfer function of filter (Ignoring the influence of capacitance current) is:

$$G_1(s) = \frac{1}{Ls + r} = \frac{1/r}{1 + (L/r)s} \tag{4}$$

Because of the nonlinear characteristics of the inverter itself, and to avoid straight in Upper and lower bridge arm of the inverter, so it is necessary to introduce a delay for the drive signal of the inverter. Considering the above factors, the transfer function of the inverter with first-order inertia  $G_2(S)$  of small time constant and high gain is expressed as follows:

$$G_2(s) = \frac{k_{pwm}}{T_{pwm}s + 1} \tag{5}$$

where  $T_{pwm}$  is the time constant of the inverter and  $K_{Pwm}$  is the inverter magnification.

According to information found that, LPWM =  $V_{dc}/2$  generally when SPWM modulation adopted.

PI controller transfer function with pole-zero is

$$G_3(s) = k_p + \frac{k_i}{s} = \frac{k_p(\tau_i s + 1)}{\tau_i s}, k_i = \frac{k_p}{\tau_i} \tag{6}$$

Part of the sample and hold is equivalent to a first-order system, so transfer function  $G_4(S)$  is

$$G_4(s) = \frac{1}{T_s s + 1} \tag{7}$$

When PI controller system was not joined, open-loop functions are as follows:

$$W(s) = \frac{1}{T_s s + 1} \frac{T_{pwm}}{T_{pwm}s + 1} \frac{1/r}{1 + (L/r)s} \tag{8}$$

Do the following with sample and hold part:  $T_{\text{PWM}} = 0.5T_s$ ,  $T_K \approx T_s + T_{\text{PWM}} = 1.5T_s$ ; so open-loop transfer function of current loop is:

$$W(s) = \frac{k_{\text{pwm}}}{T_k s + 1} \frac{1/r}{1 + (L/r)s} \quad (9)$$

Current loop control system requires fast current follow characteristic, so only need to use PI zero offset current loop transfer function of the pole to be a typical type I system [7]. Make  $\tau_i = L/R$ , and the system transfer function after PI controller access system is as follows:

$$W_0(s) = \frac{k_p k_{\text{PWM}}}{r \tau_i s (T_k s + 1)} \quad (10)$$

Closed-loop transfer function of the current loop control system is

$$W'_0(s) = \frac{W_0(s)}{1 + W_0(s)} = \frac{k_p k_{\text{PWM}}}{T \tau_i T_K s + 1 + k_p k_{\text{PWM}}} = \frac{1}{\frac{r \tau_i T_k}{k_p k_{\text{PWM}}} s^2 + \frac{r \tau_i}{k_p k_{\text{PWM}}} s + 1} \quad (11)$$

If the second-order system in formula (11) has the ideal dynamic quality [8], the output current loop will be fast track to set value. According to the design method of typical type I system, taking that

$$\varepsilon^2 = \frac{T_k k_p k_{\text{PWM}}}{r \tau_i} = \frac{1}{2}; \begin{cases} k_i = \frac{k_p}{s} = \frac{r}{3T_s k_{\text{PWM}}} \\ k_p = \frac{r \tau_i}{2T_k k_{\text{PWM}}} = \frac{r \tau_i}{3T_s k_{\text{PWM}}} = \frac{L}{3T_s k_{\text{PWM}}} \end{cases}; W'_0(s) = \frac{1}{4.5T_s s^2 + 3T_s s + 1} \quad (12)$$

The ultimate goal of a typical Type I system design method is a second-order system reduced to be a first-order system [9].

Because the  $T_s$  magnitude in the formula (12) is general  $10^{-6}$ ,  $4.5T_s s^2 \ll 3T_s s$  [10]. So, the simplification of closed-loop transfer function by omitting the quadratic term is

$$W'_0(s) = \frac{1}{3T_s s + 1} \quad (13)$$

PI controller open-loop frequency response, closed-loop frequency response and step response were simulated in MATLAB, taking  $k_p = 0.0001$ ,  $k_i = 0.0006$ .

## 4 Simulation Analysis

### 4.1 Single-Phase Grid-Connected Based on PQ Control

In this paper, model was built in MATLAB/Simulink, and the simulation model of the main circuit shown in Fig. 6. The  $V_1$  and  $V_2$  equivalent represented two DC micro-source, respectively, which connected to main grid through the half-bridge voltage inverter, LC filter (added resistance to prevent resonance) and the line impedance in turn, where  $R_{LOAD}$  represents load.

According to the above analysis, the model of two nearby DC-source connected to grid was established in MATLAB/Simulink. And PQ controllers were used in the two DC sources micro, whose input were inverter output voltage, inductor current and the grid voltage of the  $q$  axis component. The output of PQ Control 1 and PQ Control 2 were half-bridge trigger pulse composed by  $T_1, T_2, T_3$  and  $T_4$ , both with SPWM modulation.

### 4.2 Simulation Result Analysis

The selection of simulation parameters are as follows.

Two LC filters parameters are

$$R_1 = 0.55 \Omega, L_{f1} = 1.5 \times 10^{-3} \text{H}, C_{f1} = 200 \mu\text{F}$$

$$R_2 = 0.55 \Omega, L_{f2} = 1.5 \times 10^{-3} \text{H}, C_{f2} = 200 \mu\text{F}$$

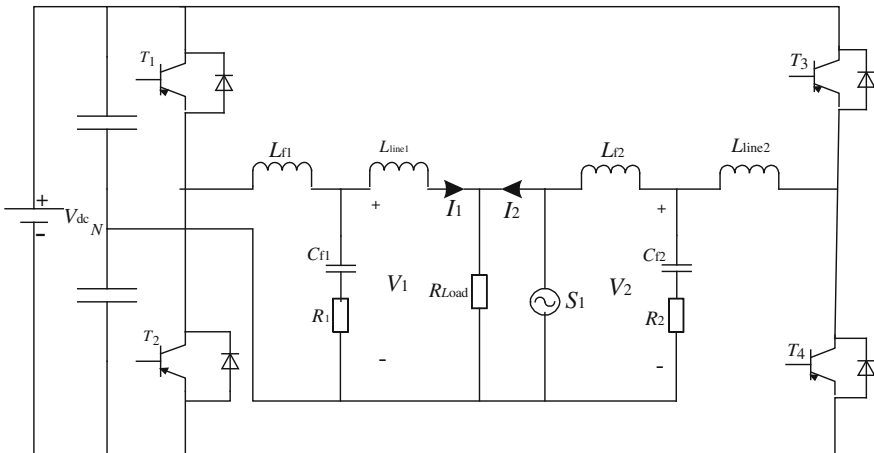


**Fig. 6** Two micro-sources single-phase connected to the grid based on the control of PQ. **a** DG1. **b** DG2



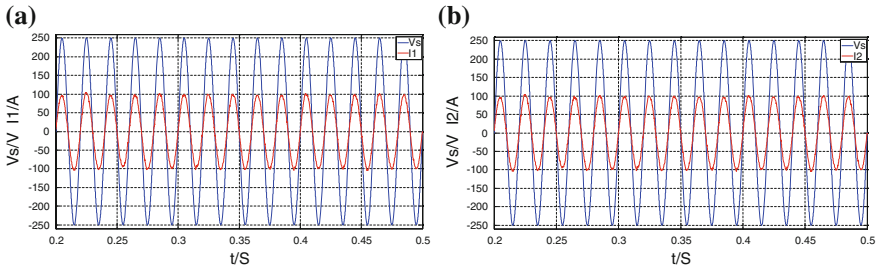


**Fig. 7** The curve of grid-connected current and network voltage

The output circuit parameters are

$$r_1 = 0.2 \Omega, L_{Line1} = 1.1 \times 10^{-3} H, r_2 = 0.2 \Omega, L_{Line2} = 1.1 \times 10^{-3} H$$

The system rated output are

$$U_n = 250 \text{ V}, f_n = 50 \text{ HZ}$$

PI controller parameters are

$$K_p = 0.0001, K_i = 0.0006$$

Finally the simulation diagram is as follows: (Fig. 7).

As can be seen from Fig. 6, two micro-sources after Grid connection did not affect each other. The respective grid-connection current keep stable state after 0.2 s, and grid-connection current phase was same with network voltage phase. This proved that the use of PQ control strategy can achieve good results of micro-source grid-connection in a short time.

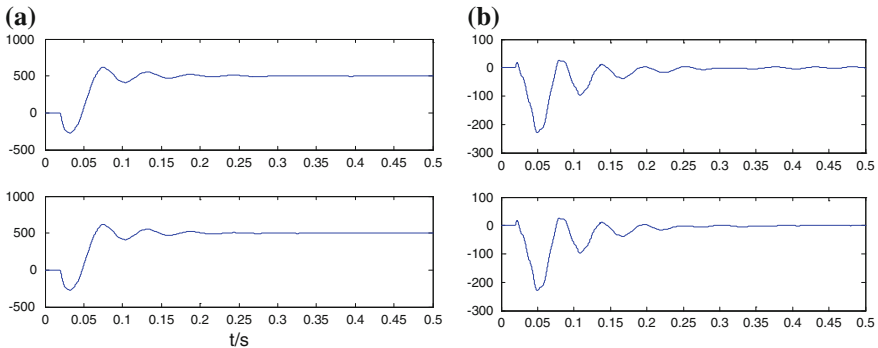


**Fig. 8** The curve of grid-connected active and reactive power **a** the curve of active power **b** the curve of reactive power

It can be seen from Fig. 8a that  $DG_1$  and  $DG_2$  can quickly reach the active power set point, and keep output active power stable at given value 500 W after 0.25 s. The reactive power output of  $DG_1$  and  $DG_2$  is 0 in Fig. 8b, so  $DG_1$  and  $DG_2$  is equal to the constant power load after 0.25 s. That is to say only active power was input to the grid under the condition of normal grid connected.

## 5 Conclusion

In this paper, single-phase grid-connected system with PQ control strategy was simulated. First, the principle and implementation method of PQ control strategy were analyzed, and then established SPLL and  $dq$  transformation model, power and power factor control module and current loop control model in MATLAB/Simulink. The SPLL which improved of PLL can more quickly and accurately track the phase of the grid and Typical I systems were selected for the design of the current loop parameters. Finally, with the simulation of two half-bridge inverter DC-source single-phase grid by PQ control strategy, it is concluded that PQ control strategy adopted by micro-source in power grid can keep the grid current and power grid voltage synchronization and output constant active power in a relatively short period of time. PQ control strategy established in this paper was versatile, can be applied to multiple micro-source occasions.

## References

1. Yu Y, Luan W (2009) Smart grid and its implementations. *Proc CSEE* 29(34):1–6
2. Zongxiang L, Caixia W, Yong M et al (2007) Overview on micro-grid research. *Autom Electr Power Syst* 31(19):101–102
3. Murakamia A, Yokoyama A, Tada Y (2006) Basic study on battery capacity evaluation for load frequency Control (LFC) in power system with a large penetration of wind power generation. *IEEE Trans Power Energy* 126(2):236–241
4. Sao CK, Lehn P W (2005) Autonomous load sharing of voltage source converters. *IEEE Trans Power Delivery* 20(2):1009–1016
5. Zhong QC, Weiss G (2009) Static synchronous generators for distributed generation and renewable energy. In: *IEEE/PES power systems conference and exposition*, pp 1–6
6. Katiraei F, Iravani MR, Lehn PW (2004) Micro-grid autonomous operation during and subsequent to islanding process. *IEEE Trans Power Delivery* 20(1):248–257
7. Brabandere K D, Bolsens B, Keybus JV et al (2007) A voltage and frequency droop control method for parallel inverters. *IEEE Trans Power Electron* 22(4):1107–1115
8. Dawei C, Guiping Z (2010) Power transmission characteristics of low voltage microgrids. *Trans China Electro Tech Soc* 25(7):117–122
9. Lu Z, Luo A, Rong F et al (2010) Micro-grid PQ control strategy analysis under utility voltage imbalance. *Power Electron* 44(6):71–74
10. Wang C, Li P (2012) Development of distributed energy resources and energy efficiency improvement on customer side. *Autom Electr Power Syst* 36(2):1–5

# Assessment of Civilian Demand Response Behavior Supporting Wind Power Digestion

Ran Jiao, Baoqun Zhang, Cheng Gong, Longfei Ma, Rui Shi, Zhongjun Chi, Bing Yang and Huizhen Liu

**Abstract** According to the time process characteristic and the economic efficiency characteristic of civilian active load system's interaction demand response behavior, this paper establishes the behavior analysis model of active load's interaction response. And we decouple the response behaviors between users' energy consuming load and electric load, and we extract out the target variables which can represent and identify the physical features of interactive response behavior from users' energy and electricity demand and the cooperation between distributed renewable energy and grid. Considering a power grid with wind and heavy air conditioning load, this paper designs a wind and cold storage air conditioner combined system, and through a case study of response behavior analysis on residential and commercial active load system, we verify the effectiveness of the behavior analysis model and the target variables.

**Keywords** Active load · Interaction response · Behavior characteristic analysis · Wind and cold storage air conditioner combined system

## 1 Introduction

To reduce the influence of the wind power and other random power sources on the power supply system, and effectively support the development of renewable energy, scholars conducted extensive research to digest wind power for grid-side energy storage technology. But the larger investment is needed, and large-scale electromagnetic energy storage and chemical storage technology is still at the exploratory stage of development.

Domestic and foreign research and practice has shown that cooperative development of smart grid technology and demand promotes the intellectualization of grid. To effectively digest distributed renewable energy (DRE), the use of smart power

---

R. Jiao (✉) · B. Zhang · C. Gong · L. Ma · R. Shi · Z. Chi · B. Yang · H. Liu  
State Grid Beijing Power Research Institut, Beijing, China  
e-mail: jiaoran0418@sina.com

two-way interactive operating mode and supporting technology, dynamic integration of user-side resources has become a core of research under the smart grid demand response mechanisms [1–4]. Literature [5] proposed three criteria for user-side demand response, namely, cost-effectiveness, potential applications and clipping capabilities. Literature [6] located user-side resources that can alleviate the problem of air conditioning load peak to three devices as air conditioning, refrigerators and freezers, and established a demand response model based on the priority of the wind power digestion.

Literature [7, 8] pointed out that, as the resident power load has been gradually diversifying, household appliances' automatic control continued to improve, as well as the development of new energy management system, in the case that electric power operators provide some economic stimulus, there would be a class of load; it can intelligently control a type of electrical equipment or device group, changing electricity using time and electricity power load size to match the operator's demand response strategies to obtain economic benefits. After equipping the appropriate storage device, this load can be completely out of the grid during certain hours, or even reverse transmission to the grid, this load can be called active load.

With the growing peak load and wind power, solar and other DRE sources high penetration access, the research for interactive response behavior of civil active load and system power load with storage capacity and renewable energy generation load has been becoming the focus of attention. For residents, active load response system including electric cars, Literature [8] established a joint initiative PV energy storage devices and residents load effective solar power digestion demand response model, and use user demand self-digestion factor to quantitatively measure response strength. Literature [6] represented response strength, different levels of incentives and punishment by introducing a user need ratio index to measure user load active transfer willingness. Literature [9] studied the effects of wind power penetration access on demand response strategies.

In summary, the study of demand response behavior analysis that has been carried out is focused on the behavior characteristics of demand response behavior; in order to further research and use demand response resources, we need to identify and quantitatively analyze its response behavior characteristics. This paper discussed the establishment of active load interactive response behavior analysis mode, extracted indicator variables that can characterize the behavior characteristics of interactive response, and took wind power combined with ice storage system as an example of the active load of the system, analyzed its response behavioral characteristics to verify the proposed response behavior analysis mode, and the effectiveness of characteristic variables.

## 2 Analysis Mode of Active Load Interactive Response Behavior

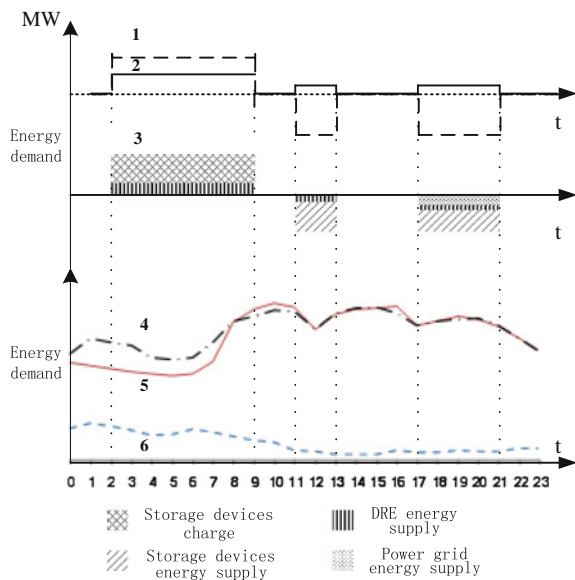
### 2.1 Time Distribution Characteristic of Response Behavior

In the active load system, the user energy needs can be supplied diversely; load system makes energy demand and electricity demand present new time distribution by interactive response, as shown in Fig. 1.

Under traditional load response mode, the user to adjust energy demand for electricity by adjusting their habits substantially, and transfer energy demand in time, reduce energy demand in peak, increase energy demand in valley, the energy demand curve is shown curve 1 (dashed line), where the horizontal axis represents the reference state, and the convex curve represents increasing energy demand, concave curve represents reduced energy requirements. Under active load interactive response mode, the user can avoid substantially adjusting their energy use habits, the time distribution characteristics of energy demand remains relatively stable as the curve 2 (solid line) shown in figure. At this point, the user's energy demand which is transferred from the original peak to valley can obtain a diverse supply, namely the grid, DRE, and energy storage equipment, as shown in curve 3 shadows. The curves 4, 5 in the figure represent electricity demand curve of load interactive response systems and unresponsive; curve 6 is distributed renewable power curve.

It is obvious that active load interactive response can less adjust energy demand time distribution, and even increase electricity consumption level, while using its

**Fig. 1** Time distribution characteristics of interaction response with active load



own demand response system, absorb DRE electricity, and in the meantime adjust energy demand time distribution to the maximum extent, meeting the power requirements of peak shaving.

### 2.2 Economic Efficiency Characteristic of Response Behavior

The goal of active load interactive response is to create a high level of economic efficiency to power users with energy, power system operation, and DRE operation. That is, within a user's wishes to use energy habits shift range, to satisfy user's needs of energy efficiently, while economically digest renewable energy, and meet the requirements of improving the grid load characteristics and reducing the distribution network capacity investment.

As Fig. 2 shows, active load system accepts the information input through its control management center, optimizes decisions response plan to achieve economic efficiency, including: (1) DRE system inputs intermittent and fluctuant generation contribute information, active load response coordinates with DRE absorption, improving the economical characteristics of renewable energy generation; (2) The user side energy use efficiency can be improved and the user's energy consumption expenditure can be reduced by according to the level of satisfaction, can be used to transfer the will; (3) the public system inputs grid demand of peak shaving, and the

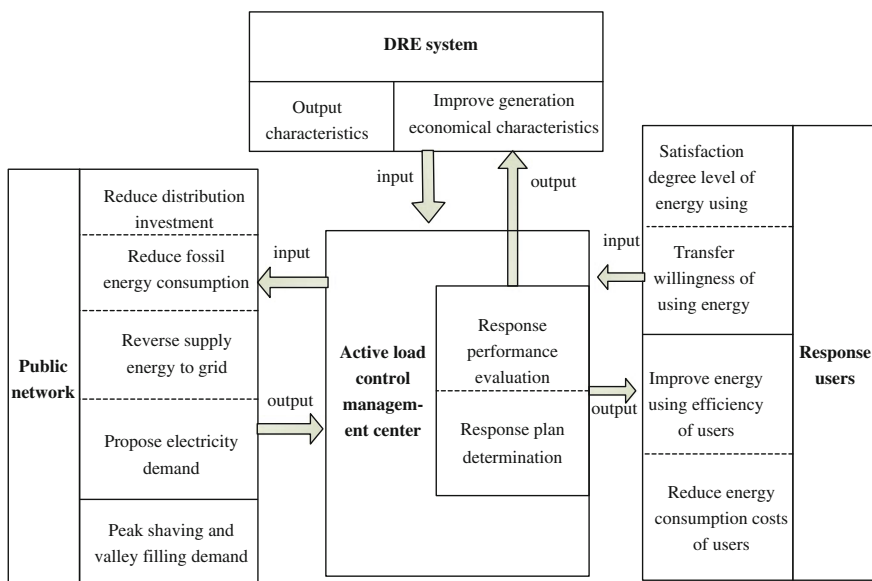


Fig. 2 Economic efficiency characteristics of interaction response with active load

active load system response timely storages energy, self-energizes, sends energy back to the grid, improving power grid load characteristics, reducing fossil energy consumption and distribution network investment, improve the economical characteristics of system operating.

### ***2.3 Physical Characteristics Analysis of Active Load Interactive Response Behavior***

It is obvious that time distribution characteristics feature the process characteristics of the response behavior, and the economic efficiency characteristics feature the result characteristics of the response behavior. The origin of the above process characteristics and result characteristics still comes from changes in the physical characteristics such as the energy demand and electricity demand implementation method, the absorbing method of DRE, and the coordinated operation condition of load system and the public network system. Therefore, this paper faced response behavior whole time process, establishing responsive behavior characteristics of indicators according to the difference of the physical characteristics in the following three areas of the response behavior.

1. The extent of active load systems energy demand, and adjustment, including the supply structure of energy demand;
2. The extent of electricity demand adjustment response of the active system when coordinating with the power grid peak shaving;
3. The ability and methods of the active load system supporting digesting DRE.

## **3 Applying Analysis**

### ***3.1 Example System Design***

Nowadays, active load system that has been much studied mainly include electric vehicle charging stations coordinating with solar photovoltaic generation, ice energy storage air conditioning coordinating with wind power and community load equipped with fuel cells and micro cogeneration plant (Micro CHP).

For the practical problem of obvious peak in summer, air conditioning electricity consumption while high level of wind power output in load valley at night causing difficulty in adjusting peak, this paper designed a wind and cold storage air conditioner combined active load system, as is shown in Fig. 3. The ice energy storage air conditioning can transfer excess energy generated by wind power to peak time with ice storage devices and release it in the form of cooling capacity, releasing

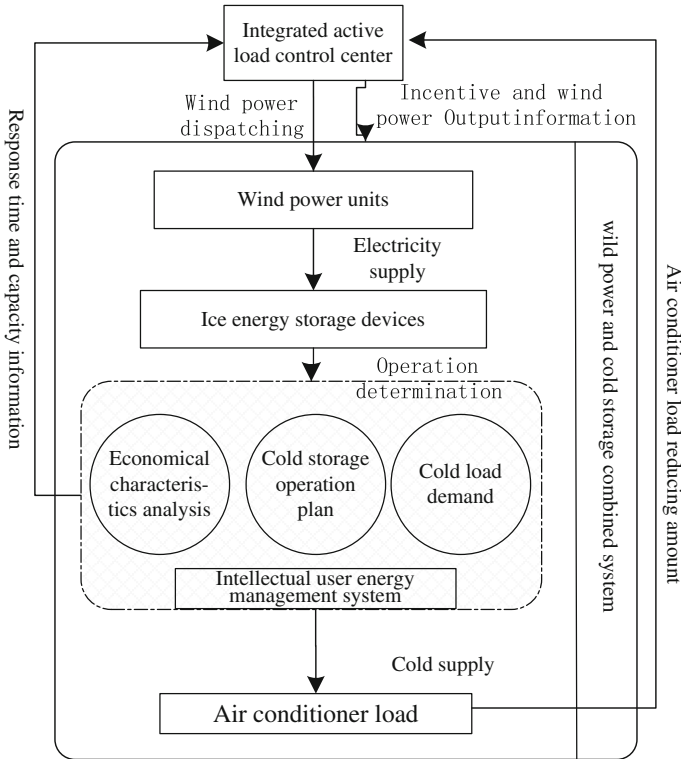


Fig. 3 Wind and cold storage air conditioner combined active load system

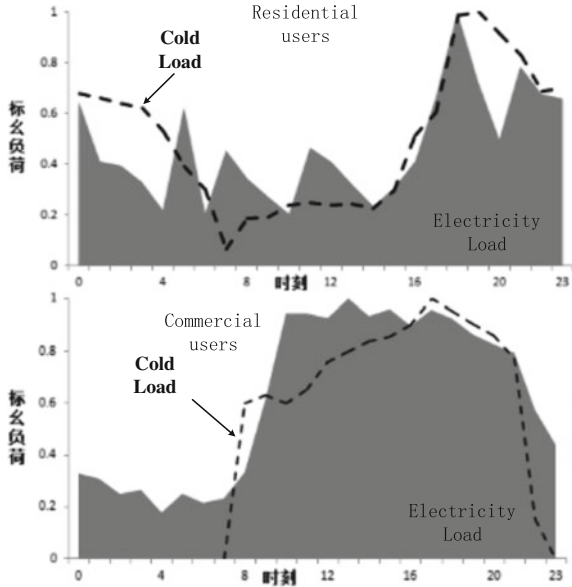
peak electricity load while ensuring cooling capacity demand of users and supporting economical wind power digestion.

### 3.2 Basic Parameters of Active Load System

1. In the analysis of the account case, consider two circumstances that wind and cold storage air conditioner combined active load system provides cooling services for residential and commercial (including large commercial buildings, office buildings, etc.) areas respectively, establishing residential active load system and commercial active load system. Among them, the electricity load curve and cold load curve of residential and commercial users before response is measured according to load of typical users, and the curve after normalization according to maximum value is shown in Fig. 4.
2. For the proportion of generation capacity of distributed wind power to cold storage air devices in the residential active load system and commercial active



**Fig. 4** Electric load and cooling load of different user category



- load system, consider two circumstances of 10 and 20 %, respectively. Choose the summer typical day wind power output curve of the power grid as wind power generation characteristics, as is shown in Fig. 5.
3. The partition of peak and valley of the grid is: peak time 10:00–12:00, 16:00–22:00; flat time: 7:00–10:00, 12:00–16:00, 22:00–23:00; valley time: 23:00–7:00 of the next day; the proportion of electricity prices at peak, flat and valley is 1.5:1:0.5.
  4. According to field study data for the local cold storage air conditioner operation characteristics, the operation efficiency of cold storage air units is 0.8824, and the attrition rate of the sending cold pipeline is 0.20, under the circumstances that ensuring whole cold demand without considering ice-melting speed and capacity limit of ice storage tank, we simulated the electricity demand of residential active load system and commercial active load system after response, and the curve after normalization is shown in Fig. 6.

**Fig. 5** Wind power output on typical day

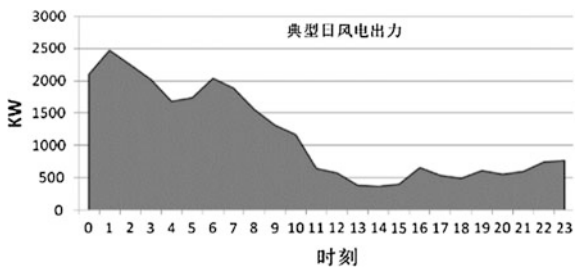
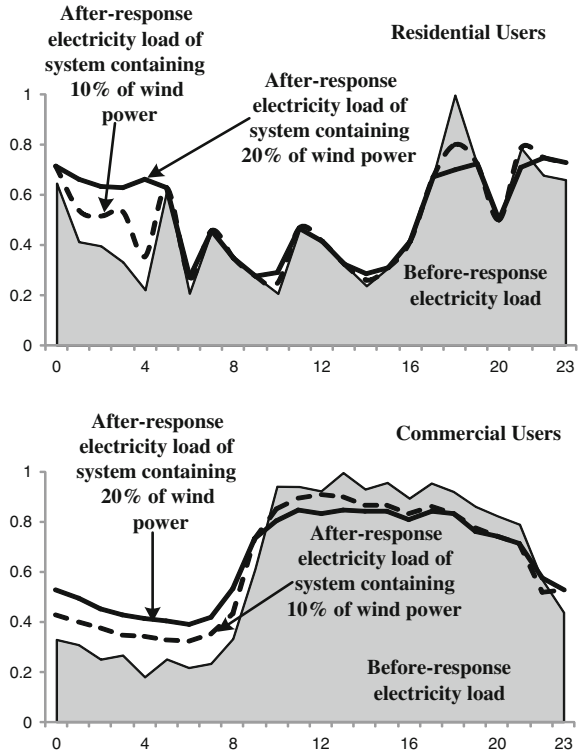


**Fig. 6** Electric load of residential and commercial active load systems after response



## 4 Conclusion

The demand response of active load can reduce newly installed capacity, improving system efficiency, and firmly supporting the economical digestion of distributed renewable resources. This paper established analysis mode of active load interactive response behavior base on characteristics analysis of active load interactive response behavior, and proposed characteristics analysis index of response behavior. Case analysis was conducted for response behavior of residential active load system and commercial active load system with combined wind power and ice energy storage respectively, verifying the effectiveness and characteristics of the proposed analysis mode and index, which mainly include

1. Decouple the relation between energy demand and electricity demand of response behavior, measuring the impact of response behavior on satisfaction degree of users.
2. Based on changes of time distribution characteristics of energy demand and electricity demand during the process of response behavior, extract analysis index, quantifying and measuring physical characteristics changes before and after response.

3. Merge response goals of effectively digesting distributed renewable resources, assessing and analyzing the physical characteristics of response behavior.

## References

1. Zhang Q, Wang X, Fu M (2009) Smart grid from the perspective of demand response. *Autom Electr Power Syst* 33(17):49–54
2. Wang B, Li Y, Gao C (2009) Demand side management outlook under smart grid infrastructure. *Autom Electr Power Syst* 33(17):49–54
3. Wang C, Li P (2012) Development of distributed energy resources and energy efficiency improvement on customer side. *Autom Electr Power Syst* 36(2):1–5
4. Li T (2012) Technical implications and development trends of flexible and interactive utilization of intelligent power. *Autom Electr Power Syst* 36(2):11–16
5. Hamidi F, Li F, Robinson F (2008) Responsive demand in networks with high penetration of wind power. In: *Transmission and distribution conference and exposition. T&D. IEEE/PES*
6. Moura PS, De Almeida AT (2010) The role of demand-side management in the grid integration of wind power. *Appl Energy* 87(8):2581–2588
7. Parsa M, Abdollahi A, Rashidinejad M (2011) Flexible demand response programs modeling in competitive electricity markets. *Appl Energy* 88(9):3257–3269
8. Castillo M, Caamano E, Matallanas E (2011) PV self-consumption optimization with storage and Active DSM for the residential sector. *Sol Energy* 85(9):2338–2348
9. Pina A, Silva C, Ferrão P (2012) The impact of demand side management strategies in the penetration of renewable electricity. *Energy* 41(1):128–137

# Research on CO<sub>2</sub> Laser Frequency Stabilization by Adjusting Grating Angle

Yanchao Zhang, Zhaoshuo Tian, Guang Dai, Chunlei Jin  
and Zhenghe Sun

**Abstract** A new frequency stabilization for CO<sub>2</sub> laser with frequency selection by grating is presented in this paper. A closed-loop control system was designed to stabilize the laser frequency at the gain curve center by measuring the changing laser power continuously and fine adjusting the grating angle of the laser cavity. In the experiment, the long-term laser power and frequency shift of the CO<sub>2</sub> laser 9P (10) line were measured to be less than  $\pm 0.035$  W and  $\pm 7$  MHz, respectively, when the frequency stabilization is in closed-loop operation. The CO<sub>2</sub> laser frequency stability is up to  $4.6 \times 10^{-8}$ . The frequency stabilization control system owns advantages of small volume, compact structure. It can be also used for other type of lasers.

**Keywords** Frequency stabilization · CO<sub>2</sub> laser · Grating · Angle adjusting

## 1 Introduction

Frequency-stabilized CO<sub>2</sub> lasers are widely used in the fields of optical metrology, laser detection, laser radar, and so on [1–4]. Optogalvanic effect, lamp-dip, saturated absorption effect, fluorescence method are common active frequency stabilization methods for CO<sub>2</sub> laser with high-frequency stability [5–7]. For example, the long-term stability and reproducibility was up to 10 kHz using fluorescence method [7]. The laser frequency can be stabilized by controlling the temperature of the laser tube. J. Qian et al. use this method to stabilize He–Ne laser. The frequency shift was less than 1.4 MHz in long term [8]. These frequency stabilization methods for CO<sub>2</sub> laser we mentioned usually need complex structure and large volume. In our previous work, a pulse build-up time method was used to stabilize pulsed CO<sub>2</sub> laser, with frequency stability up to  $10^{-8}$  [9–13].

---

Y. Zhang · Z. Tian · G. Dai · C. Jin · Z. Sun (✉)  
Information Optoelectronics Research Institute, Harbin Institute of Technology,  
Weihai 264209, China  
e-mail: szh641@163.com

In this paper, according to the laser theory and our studies for CO<sub>2</sub> laser [9–13], when the laser oscillating frequency is located at the centre of the gain curve the output laser power is the largest. For the CO<sub>2</sub> laser with frequency selected by grating, the subtle changes of the grating angle can result in significant changes in laser power and laser oscillating frequency. Grating angle is easily affected by temperature, vibration and other environmental factors in the experiment. A closed-loop stabilization circuit was designed in this paper, when the stabilization system worked, the laser frequency could be adjusted to near the centre of the gain curve by measuring and recording the laser power changing continuously and controlling the grating angle.

## 2 Experimental Setup

### 2.1 Laser Structure

Frequency-selected CO<sub>2</sub> laser by grating adopted semi-external cavity structure, as shown in Fig. 1. The laser consists of discharge tube and laser cavity. A total reflector and grating with a constant of 150 lines/mm constitute the laser cavity. The first-order reflectivity of grating is 85 % which is used for oscillation feedback in the cavity. The laser can be output from zero diffraction order of the grating. One end of the laser tube placed a gold-coated silicon-based total reflection mirror and the other end of the tube is placed with ZnSe window with 9–11 m broadband antireflection film coating, which sealed the vacuum chamber. The laser working gas was filled in the vacuum chamber. The tube is discharged by high voltage power supply and the gas discharge length is 1200 mm. A grating is placed near the ZnSe window. The grating is mounted on a stent which is composed of aluminum structure and PZT (piezoelectric ceramic), as shown in Fig. 1. During the piezoelectric ceramic stretching, the grating rotates at a slight angle to the axis O'. So the laser frequency and laser power can be adjusted by changing high voltage on the PZT. The grating and stent are mounted on a precision adjustable rotating plane. The CO<sub>2</sub> laser line can be selected by adjusting the grating angle. Laser beam

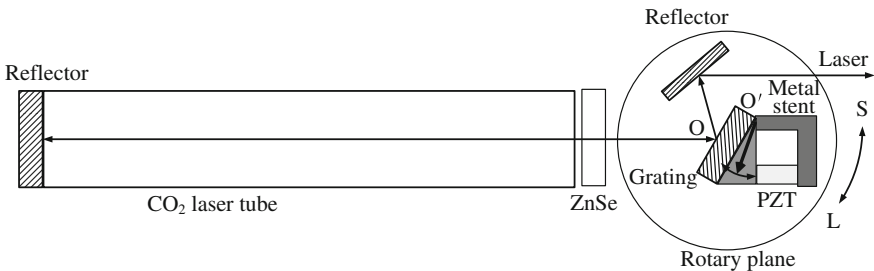


**Fig. 1** The optical path of the laser with line selected by grating

direction is shown in Fig. 1, the total reflector is used to change the beam direction. Grating and reflector were fixed in rotating plane, which can be rotated around the point O. The laser line moves to shorter or longer wavelength when the plane rotates along the S or L directions, respectively.

### 2.2 Laser Stabilization System

CO<sub>2</sub> laser frequency stabilization we designed was shown in Fig. 2. It mainly composed of A/D (analog digital) convertor, microprocessors, D/A (digital analog) converter and high voltage amplifier. The CO<sub>2</sub> laser output power was measured by laser power meter. The voltage from the laser power meter was amplified by preamplifier. Then, the signal was collected by analog digital convertor. The microcontroller is used to control and read the data from the ADC and analyze the laser power shift. Then the microcontroller gives error voltage signal which is converted into analog voltage by a DAC. The analog voltage is amplified by a HV amplifier and fed back to the PZT fixed on the grating to control the grating angle of the laser cavity. The laser power was stabilized to be around the maximum value, and the laser frequency was near around the gain curve center. Meanwhile, the laser power voltage from the detector can be recorded by a computer.

### 2.3 Control Algorithm

The stabilization system we designed finds the maximum values of the laser power. According to the laser principle, the laser output power is maximum when the laser frequency is oscillating at the center frequency of laser gain curve, so as to achieve the purpose of laser frequency stabilization. The relationship between laser power

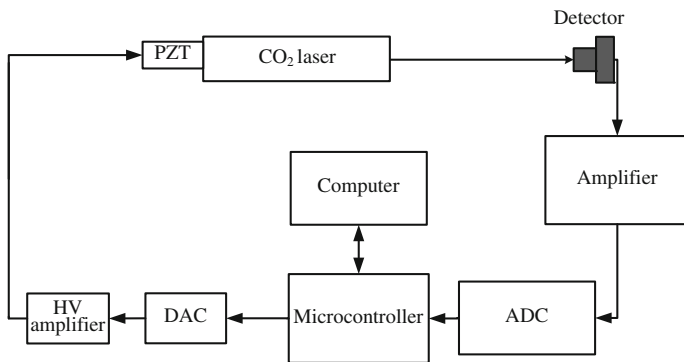
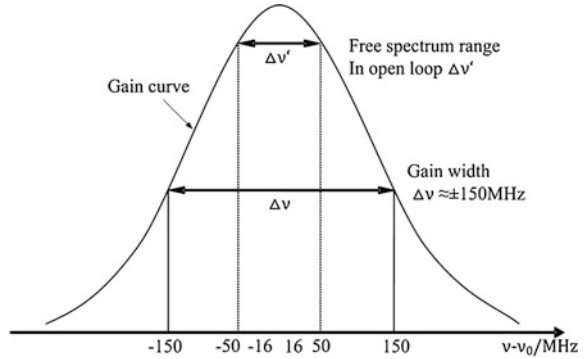


Fig. 2 The diagram of the stabilization system for CO<sub>2</sub> laser

**Fig. 3** The diagram of laser gain curve



and frequency is shown in Fig. 3.  $\Delta v$  is the gain width of the laser line.  $\Delta v'$  is the free spectrum range limited by the laser cavity length (about 1500 mm).

The principle of laser control algorithm can be described by the formula 1:

$$u_{n+1} = u_n + \mu \delta J_n \tag{1}$$

wherein  $u_{n+1}$  and  $u_n$  are  $n$  and  $n + 1$  times control voltage.  $\delta J_n$  is the  $n$  times laser power change value, and  $\mu$  is the step size. If the power level increases, the control voltage changes the direction of the same. If the power value decreases, the voltage change direction is reversed, which we named maximum method. In the experiment, in order to achieve a better stabilizing, a suitable iterative cycle and iterative step should be test.

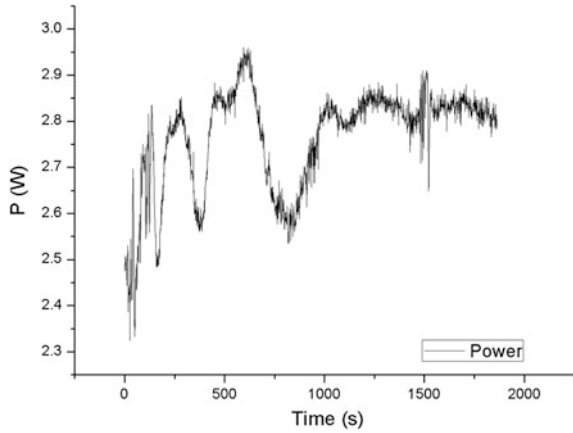
### 3 Experimental Results

In the experiment, the laser line 9P (10) branch, wavelength  $9.47 \mu\text{m}$  was selected by adjusting the rotary plane angle. The PZT voltage range is 0–150 V. The maximum stretch of the PZT is  $20 \mu\text{m}$ . The laser discharge current is 10 mA, the laser power was measured by power meter detector, which output voltage represent the laser power value.

#### 3.1 In Open-Loop Operation

In open loop, first, in the experiments, we measured the laser power in 30 min without active stabilization in free running mode. As shown in Fig. 4, the laser power value changes in the range 2.35–2.95 W, and the average power is 2.75 W. The long-term stability of the laser power is 0.145. Because of the long laser cavity, the laser frequency tuning range is mainly limited by the free spectral range which

**Fig. 4** The measurements of the laser power without active stabilization

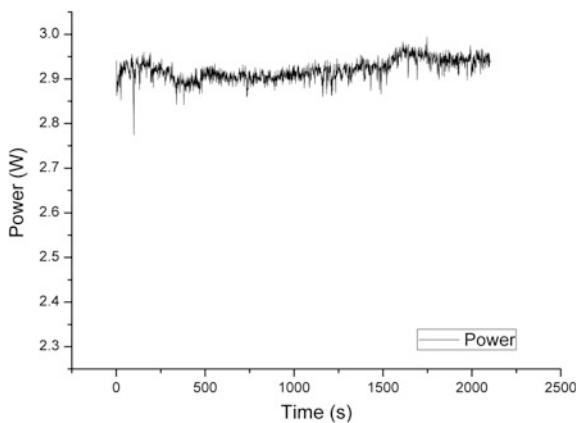


can be calculated to be about 100 MHz. So the laser frequency shift deviation from the center frequency is about  $\pm 50$  MHz. The frequency stability of the laser is about  $3.75 \times 10^{-7}$ .

### 3.2 In Closed-Loop Operation

Second, we measured the output laser power with active frequency stabilization in 30 min. The iterative cycle of the stabilization system is set to 1 s. The laser power variations with time are recorded in 30 min as shown in Fig. 5. It can be seen that the output power of CO<sub>2</sub> laser was kept near the maximum power value in a long period time. The laser power drift is about  $\pm 0.035$  W. The laser frequency shift is calculated to be  $\pm 7$  MHz. The frequency stability is up to  $4.6 \times 10^{-8}$ .

**Fig. 5** The measurements of the laser power with active stabilization





## 4 Conclusion

In this paper, a closed-loop stabilization system for branch selected by grating CO<sub>2</sub> laser was designed. The stabilization keeps the laser output power value to the maximum by adjusting grating angle. In the experiment, the method can effectively improve the output power stability of CO<sub>2</sub> lasers. In open-loop, laser power value change range is 2.35–2.95 W. The long-term stability of the laser power is 0.145. The frequency stability of the laser is about  $3.75 \times 10^{-7}$ . When the laser stabilization system is closed loop, the CO<sub>2</sub> laser power was kept near the maximum value 2.95 W. The power shift is about  $\pm 0.035$  W in a long time. The laser frequency shift calculated is about  $\pm 7$  MHz. The laser frequency stability is about  $4.6 \times 10^{-8}$ . The laser frequency stabilization has the advantages of compact structure, small volume, and low cost.

**Acknowledgment** This work was supported by Project HIT (WH) 201502 Supported by the Scientific Research Foundation of Harbin Institute of Technology at Weihai (Gran No. HIT (WH) 201502), Fundamental Research Funds for the Central Universities (Grant No. HIT. BRET. 2010014 and HIT.NSRIF.2013139), the Science and Technology Planning of Shandong Province, China (Grant No. 2011GHY11514).

## References

1. Lam TTY, Slagmolen BJJ, Chow JH et al (2010) Digital laser frequency stabilization using an optical cavity. *IEEE J Quantum Electron* 46(8):1178–1183
2. Willis LJ, Lim MJ (2008) Temperature-insensitive laser frequency stabilization with magnetic tuning. *Appl Opt* 47(13):2312–2316
3. Bian Z, Huang C, Chen D et al. (2012) Seed laser frequency stabilization for doppler wind lidar. *Chin Opt Lett* 10(9): 091405–091405
4. Kohlhaas R, Vanderbruggen T, Bernon S et al (2012) Robust laser frequency stabilization by serrodyne modulation. *Opt Lett* 37(6):1005–1007
5. Shy JT, Yen TC (1987) Optogalvanic lamb-dip frequency stabilization of a sequence-band CO<sub>2</sub> laser. *Opt Lett* 12:325–328
6. Ma Y, Liang D (2002) Tunable and frequency-stabilized CO<sub>2</sub> waveguide laser. *Opt Eng* 41(12):3319–3323
7. Tochitsky SY, Chou CC, Shy JT (1995) Frequency stabilization of the sequence-band CO<sub>2</sub> laser using the 4.3- $\mu$ m fluorescence method. *IEEE J Quantum Electron* 31(7):1223–1230
8. Qian J, Liu Z, Shi C et al (2012) Frequency stabilization of internal-mirror He–Ne lasers by air cooling. *Appl Opt* 51(25):6084–6088
9. Tian Z, Qu S, Sun Z (2005) Active and passive frequency stabilization for a Q-switched Z-fold radio-frequency-excited waveguide CO<sub>2</sub> laser with two channels. *Appl Opt* 44(29):6269–6273
10. Zhang YC, Tian ZS, Sun ZH, Fu SY, Sun JF, Wang Q (2013) High pulse repetition frequency RF excited waveguide CO<sub>2</sub> laser with mechanical Q-switching. *Infrared Phys Technol* 58:12–14
11. Zhang YC, Tian ZS, Sun ZH, Wang LL, Wang Q (2013) Study of frequency stabilization for electro-optical Q-switched radio frequency-excited waveguide CO<sub>2</sub> laser using build-up time method. *Appl Opt* 52(16):3732–3736

12. Zhang YC, Tian ZS, Sun ZH, Sun JH, Fu SY (2014) Study of offset frequency locking and active frequency stabilization for two RF-excited waveguide CO<sub>2</sub> laser with common ground electrode. *IEEE J Quantum Electron* 50(10):802–807
13. Tian ZS, Zhang YC, Sun ZH, Sun JF, Fu SY (2013) Study of stable laser cavity with hole-coupling output mirror. In: 2013 International Conference on Advanced Optoelectronics Lasers (CAOL). IEEE, pp 95–97

# Study on Shipborne Video Electro-optical Tracking System Based on FPGA

Zongjie Bi, Zhaoshuo Tian, Tao Luo and Shiyou Fu

**Abstract** Shipborne video electro-optical tracking system can be used for ocean target detection and recognition, marine rescue, etc. In this paper, an FPGA is selected as the core processor to realize the target detection and servo tracking. We propose a colour matching centroid tracking algorithm to solve the impact of complex water surface changes. Test results show that the system works normally and stably. In the  $640 \times 480$  video image resolution, the tracking accuracy of the azimuth motor is 80 pixels, and the maximum tracking angular velocity is  $30^\circ/\text{s}$ . The tracking accuracy of the pitch motor is 50 pixels, and the maximum tracking angular velocity is  $10^\circ/\text{s}$ . The minimum size of target recognition is  $16 \times 16$  pixels matrix.

**Keywords** Shipborne · Target detection · Colour matching · Electro-optical tracking

## 1 Introduction

With the rapid development of science and technology, mechanical manufacturing technology, computer technology, electrical automation technology, integrated circuit technology, optical technology, and other fields have made great progress. Photoelectric video tracking technology combines image processing, automatic control, machinery manufacturing, signal processing and other interdisciplinary technical knowledge, have been widely used in the fields of military, security, and civil, such as airborne electro-optical tracking and pointing system ship tracking platform, satellite reconnaissance and observation system, and so on [1].

---

Z. Bi · Z. Tian · T. Luo · S. Fu (✉)

Information Optoelectronics Research Institute, Harbin Institute  
of Technology at Weihai, Weihai 264209, China  
e-mail: fsytzs@126.com

© Springer-Verlag Berlin Heidelberg 2016

B. Huang and Y. Yao (eds.), *Proceedings of the 5th International Conference on Electrical Engineering and Automatic Control*, Lecture Notes in Electrical Engineering 367, DOI 10.1007/978-3-662-48768-6\_59

521

At present, there are many researches on target recognition and tracking algorithm, which are mainly used in the video optical tracking device in the machine vision system, such as robot vision system in real-time tracking for moving target [2, 3]. Gevers et al. proposed a new colour recognition model [4], which can deal with the influence of illumination change and object geometry change on target recognition. Ferrari et al. explored the image object recognition and image segmentation [5]. Bo et al. proposed the adaptive learning recognition algorithm based on the target RGB model [6], compared with the similar method, the experimental verification has a good recognition effect, high robustness. Rosin et al. proposed image segmentation and target detection based on different thresholds [7]. Wang Baoyun et al. researched on the target detection and tracking technology of sea surface moving target, including the establishment of the mathematical model of the marine environment, the characteristics of the target of the ship and the tracking algorithm [8].

In this paper, based on the application environment of complex water surface, the colour matching algorithm is proposed, which can increase the stability of the servo system, and achieves the ability of real-time detection and tracking using the hardware FPGA.

## 2 The Working Principle

The system is mainly used in the sea or the lake surface, which is used to detect, lock, and track the surface of the water or low altitude manoeuvring target. The complexity of the surface changes has a greater impact on the tracking system, so it needs higher tracking precision and better stability platform. In this paper, FPGA is used as the core control unit of the whole system, to achieve all the functional design, using the top-down design method to design the system. The system can be divided into two parts, including image processing and servo control, and the system's working principle is as follows:

With the operation of the system, the video capture module works in FPGA, and the colour video signal is displayed in real time on LCD, then in standby mode, waiting for selection. The motor of the azimuth and pitch axis is controlled by the control device, and then place the target in the centre of the screen, and then the target information is stored in the template. After starting the automatic tracking, the system switches to the tracking mode. After starting the auto tracking system, the target detection module will search the current frame based on the template information. After finding the matching target, the target will be automatically tagged in the position of the screen, and the target coordinate value of the current frame will be stored, and then it will be sent to the tracking module for tracking. If the target is unlocked, the system will automatically enter into the stable mode. If the target is re-emerging in the video screen, the system will automatically detect the target and then turn to the tracking mode. The structure of the system is shown in Fig. 1.

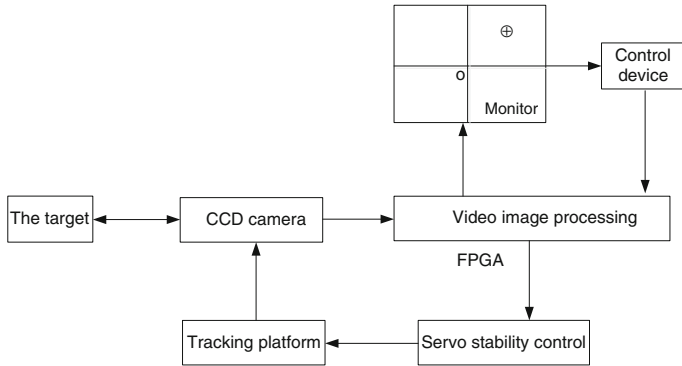


Fig. 1 System design block diagram

### 3 Research on Video Image Processing and Tracking System

In this part, several parts of the system will be described in detail.

#### 3.1 Video Capture Module Design

The system uses the CCD HD camera output mode for PAL standard, through the video decoder chip, the standard video data can be obtained, and then by cutting conversion,  $640 \times 480$  of the effective video data can be extract, which is stored in SDRAM. Then convert the format of the valid data to the video encoding chip, which will be displayed on the VGA LCD. The image processing in the later stage only needs to be analysed and processed.

#### 3.2 Video Image Preprocessing Design

Because in the process of transmission, transformation, and storage, the video image data may produce interference noise, as a result, error will exist in some data, which deviates from the essence of the image, so it is necessary to pre-process the image. Considering that FPGA is not suitable for complex numerical operations, this paper uses a fast median filtering algorithm suitable for FPGA. The traditional median filter is the median value of the set of points in the neighbourhood of the point, which needs more times, and the fast median filter reduces the number of operations and improves the efficiency.

### 3.3 Video Object Detection Module Design

According to different using conditions, the methods for objection and tracking algorithms include background cancellation method and frame difference method, which are suitable for a stable environment; as well as optical flow method and template correlation matching method, which are suitable for the actively changing background. The classical matching method based on template matching has the average absolute difference algorithm and the sum of absolute difference metric algorithm. The core ideas of these two algorithms are to compare the difference between the gray value of the target template and the search area in the search process. The sum of absolute difference metric algorithm is shown as follows:

$$R(p, q) = \sum_{x=0}^{m-1} \sum_{y=0}^{n-1} |S(p+x, q+y) - M(x, y)| \quad (x, y) \in (m, n) \quad (1)$$

$$R(p^*, q^*) = \min\{R(p, q)\}$$

When  $R(p^*, q^*)$  is obtained, the corresponding  $(p^*, q^*)$  is the position coordinates of the target.

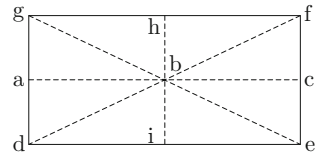
Template matching principle is relatively simple, only involves addition, subtraction, division, and it is relatively easy to achieve in the hardware, but the amount of computation is very large, and takes up a lot of computing time. Considering the real-time requirement of the system, the parallel processing of FPGA is very suitable for this algorithm.

The core idea of template matching is to find the most similar gray value information in the matrix of image pixels. Colour is the most obvious feature of the target object, the movement of the object can be reflected in the colour. This system is always applied a relatively simple background such as the sea and the sky, so using the colour information as the target feature is an effective method of identification.

Based on the principle of template matching algorithm and target colour recognition, the system improves the search strategy of the algorithm, which is matching target colour feature information in RGB colour model space. Algorithm's basic principle is that; First select an object in a frame image, then record the more bright position of the RGB information colour of the object, stored in the register, and then wait for the next frame of the image. Search image, find the template similar to the point, and ultimately calculate its centre of mass, so that complete the task of target detection. The specific process can be described as the following seven steps:

1. Select the target. Take the tracking box as the target information selection box, through the joystick control motor, camera focusing and other operations to make the target colour feature information clear. That is, the colour of the box is pure, and the target is stable in the tracking box.

Fig. 2 Sampling model



2. Sample target colour feature. There are lots of ways to select the sampling points, and the more the better, in theory. This system uses the type sampling model, which has 9 points (a–i), as shown in Fig. 2.
3. Store the information point. The RGB values of the selected sampling points are denoted as R, G, B. The maximum and minimum values for each component of RGB are sorted and stored separately.
4. Make matching strategy. In order to obtain high matching efficiency, low false recognition rate, the next sampling method for search is used. That is, in a full frame of video image data, the fixed position of the pixels is taken as the sample to be matched. Mark the position coordinates of the sample as  $S(x, y)$ .
5. Search matching. Search the next sampling as  $S(x, y)$ , and find a series of matching points. The matching condition is satisfied with the formula 2.

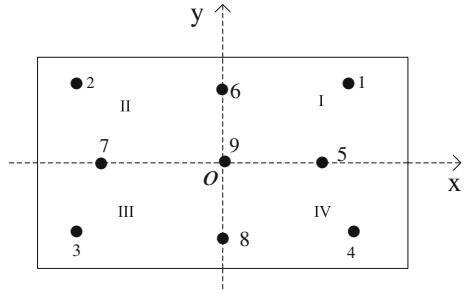
$$\begin{cases} r_{\min} \leq r_{(x,y)} \leq r_{\max} \\ g_{\min} \leq g_{(x,y)} \leq g_{\max} \\ b_{\min} \leq b_{(x,y)} \leq b_{\max} \end{cases} \quad (2)$$

6. Calculate target centroid position. Calculate the average value of the target position coordinates, which is regarded as the centre of the target.
7. Mark centroid position. The integer part is taken as the target position, so that the target’s recognition and positioning is accomplished and the red block identification is done in this position.

### 3.4 Servo Tracking Module Design

Video signal images are displayed in VGA in real time. In order to achieve the target tracking, the camera lens will be driven by the pitch motor and azimuth motor of the servo system to follow the object motion, which makes the target object in the centre of the screen. Image quadrant segmentation is shown in Fig. 3. Set the image centre  $O$  as the coordinate origin  $O(0, 0)$ , the image is divided into four quadrant: quadrant I, quadrant II, quadrant III, quadrant IV. Target detection module detects the target location in the screen in real-time, and the several cases are shown in Fig. 3. Set the object position  $T(x, y)$ , that is, the target miss distance in the X, Y axis direction. (Miss distance reflects in the image, which is the pixel number.) Through the real-time judgment of the relationship of the target miss

**Fig. 3** Image quadrant segmentation and target location



distance and the threshold to control the motor operate or not; Through the judgment of the target position to control the motor running direction; Through the judgment of the miss distance to control the motor running speed.

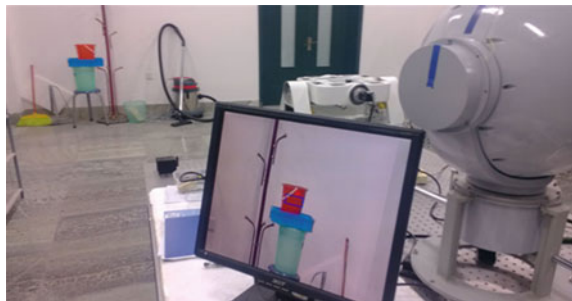
### 4 Experimental Results and Analysis

In order to verify the actual working conditions of the system, a large number of indoor and sea experiments are carried out.

#### 4.1 Target Tracking Experiment in the Lab

The indoor experimental scene is shown in Fig. 4. The distance between the photoelectric tracking platform to the target position is about 4 m, and the background is a single white walls, and the selection of test target is the red keg. After the target selection, press the lock button, and the colour information of the target is sampled and reserved. With the next frame, the search starts, and it will mark the target with a red box.

**Fig. 4** The indoor experimental scene





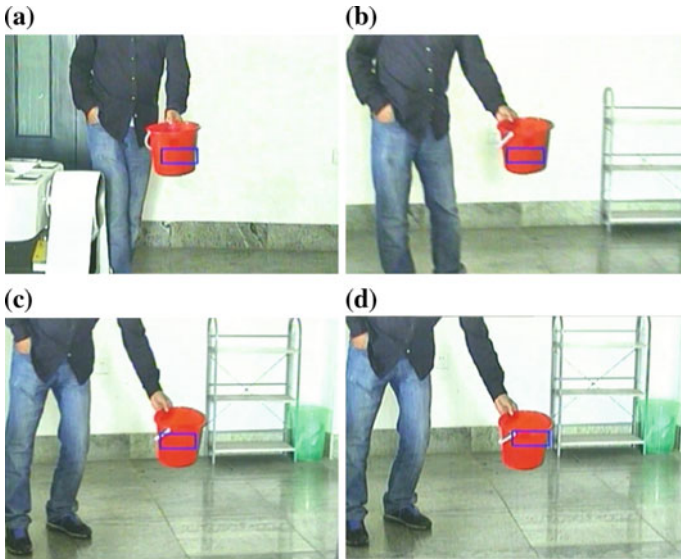


**Fig. 5** The process of the red keg tracking

From the experiment it can be found that the target recognition rate is very high, and relatively stable on the solid colour. The target recognition rate is related to the colour purity degree within the target lock frame. The higher the monochromaticity is, the higher the recognition rate will be. After repeated testing, the minimum size of the pixels in the screen will be  $16 \times 16$  at  $640 \times 480$  resolution.

After the target recognition and tracking test, hand the keg back and forth transmission. In order to obtain the complete frame of the screen video, the VGA image acquisition equipment is used, collecting the video images to the computer player software and record the whole process. The tracking results with a series of graphs, which is shown in Fig. 5. From the figure, it can be seen that the tracking frame is in the centre of the target, which is effective.

## 4.2 Target Experiment on the Sea

Due to the limited experimental conditions, the sea target experiment can only be done in small boat, and no large vessels could be used as test platform. The actual tracking condition at sea is shown in Fig. 6. The author keeps the boat close to the shallow water shore, and selects the fishing boat as the tracking target. The distance is about 300 m, and the test time is 8 min. The miss distance's change with time during the test is shown in Fig. 7, in which the red colour shows the pitch direction, and the blue colour shows the azimuth direction. From Fig. 7, it can be seen that the target is locked at 25 s, and then began to track. The miss distance maintained

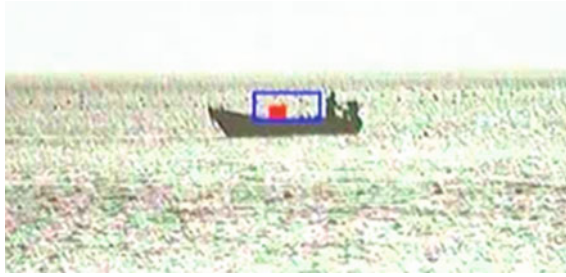


Fig. 6 The tracking effect of fishing vessels

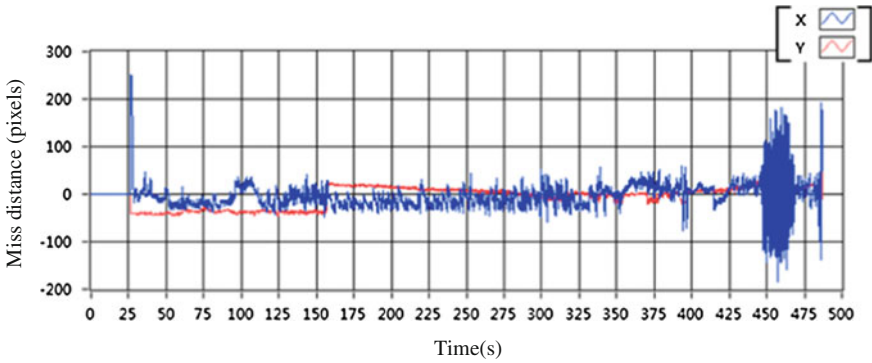


Fig. 7 The relationship between the miss distance changes with time

between +100 pixels and -100 pixels, showed that the target in the screen, tracking stability. The tracking failed at 450 s, and then the stable mode and tracking mode converse each other. At that time, the motor speed change is larger, and it turned to stable in 10 s approximately. The boat moved almost in the horizontal direction, and the pitch direction moved smaller. At 150 s, a mutation occurs due to the relative change in the fluctuation target. It can be seen that the system tracking is effective, and it can be applied in the sea.

### 5 Conclusion

In this paper, FPGA is the core controller, and the design for the shipborne video electro-optical tracking system is finished. In video image processing, this paper makes a theoretical analysis about the colour space and template matching algorithm. In order to solve the problem of complex searching process and the low efficiency in template matching algorithm, this paper improves the searching method, that is, searching in the next sample image data, and finally designing the

centroid tracking algorithm based on RGB colour feature matching, which is realized in FPGA. After the completion of the system design, several indoor and sea experiments were carried out. The experimental results show that the system has high recognition rate, good stability, and has certain anti-interference ability, which can overcome the influence of the small amplitude wave on the stability of the system. It can track the targets at low speed in real-time. The minimum pixel matrix size is  $16 \times 16$  in the  $640 \times 480$  resolution video. Azimuth tracking accuracy is about 80 pixels, and pitch tracking accuracy is about 50 pixels; Azimuth direction can be realized in  $n \times 360^\circ$  tracking, the maximum tracking angular velocity is  $30^\circ/\text{s}$ . Pitch direction can be realized in from  $-50^\circ$  to  $80^\circ$  tracking, the maximum tracking angular velocity of  $10^\circ/\text{s}$ . The CCD camera detection distance is farther than 10 km, with a certain ability to stabilize.

## References

1. Kang HJ, Kim SH, Lee SH et al (2012) Adaptive digital demodulation of encoder signal for positioning control of spiral servo track writing. *Microsys Technol Micro Nanosys Inf Storage Process Sys* 18(9):1247–1253
2. Jung B, Sukhatme GS (2010) Real-time motion tracking from a mobile robot. *Int J Soc Rob* 2 (1):63–78
3. Pinto AM, Moreira AP, Costa PG (2015) Streaming image sequences for vision-based mobile robots. *Lect Notes Electr Eng* 637–646
4. Gevers T, Smeulders AWM (1997) Colour based object recognition. *Lect Notes Comput Sci* 32 (98):453–464
5. Ferrari V, Tuytelaars T, Van L (2004) Simultaneous object recognition and segmentation by image exploration. *Eur Conf Comp Vis* 145–169
6. Bo L, Ren X, Fox D (2013) Unsupervised feature learning for RGB-D based object recognition. *Springer Tracts Adv Rob* 387–402
7. Rosin PL, Ellis TJ (1995) Image difference threshold strategies and shadow detection. *Proc Br Mach Vis Conf* 347–356
8. Wang B, Zhang R (2011) A new multilevel threshold segmentation method for ship targets detection in optical remote sensing images. *J Univ Sci Technol China* 41(4):293–298

# A Timing Synchronization Method with Peak Plateau for OFDM Systems

Yanping Li

**Abstract** Traditional timing synchronization methods require the identification of the peak value of the timing metric to realize the synchronization estimation. The proposed method in this paper requires only finding the peak plateau of the time metric and the terminal edge of the peak plateau. Consequently, the time metric of the novel method proposed in this paper could have no sharp peak value. A threshold to process the symbol timing metric in the proposed method must be established, after which it is easy to find the terminal end edge of the peak plateau, thus making the proposed method less complex.

**Keywords** OFDM · Timing synchronization · Peak plateau · Cyclic prefix

## 1 Introduction

Orthogonal frequency division multiplexing (OFDM) is a multi-carrier modulation technology that is a bandwidth-efficient signaling scheme for digital communications that was first proposed by Chang [1]. Now, OFDM technology is regarded as the core technology of mobile communications beyond 3G. So today people are researching the application of OFDM technology to low-voltage power line carrier communication. In recent years, the merger of MIMO and OFDM has become the focus of study.

But OFDM systems are very sensitive to timing synchronization errors, even more so than single carrier systems. So it is necessary to estimate timing synchronization errors for OFDM systems.

At present, there are many research projects on symbol timing estimation in OFDM systems [2–7]. These methods require the identification of the peak value of the timing metric, so the curve of the timing metric must have a sharp peak.

---

Y. Li (✉)

College of Electrical and Information Engineering, Heilongjiang Institute of Technology, Harbin 150050, China  
e-mail: ypl\_80@126.com

© Springer-Verlag Berlin Heidelberg 2016

B. Huang and Y. Yao (eds.), *Proceedings of the 5th International Conference on Electrical Engineering and Automatic Control*, Lecture Notes in Electrical Engineering 367, DOI 10.1007/978-3-662-48768-6\_60

531

In contrast, the timing synchronization method proposed in this paper is based on cyclic prefix. The timing metric of the proposed method does not have a sharp peak; rather it has a peak plateau. It is only required to find the terminal edge of the peak plateau. So the proposed method has low complexity and reduces the effect of a multipath channel.

## 2 The Details of the Proposed Method

The principal block diagram of the timing synchronization method with peak plateau for OFDM system is shown in Fig. 1.

There are three parts of the principal block diagram in Fig. 1. The first part is the energy part. The energy term of the received signal is shown in (1):

$$R_1(k) = \sum_{m=1}^M |r(k + (m - 1)(N + N_{cp}))|^2 \tag{1}$$

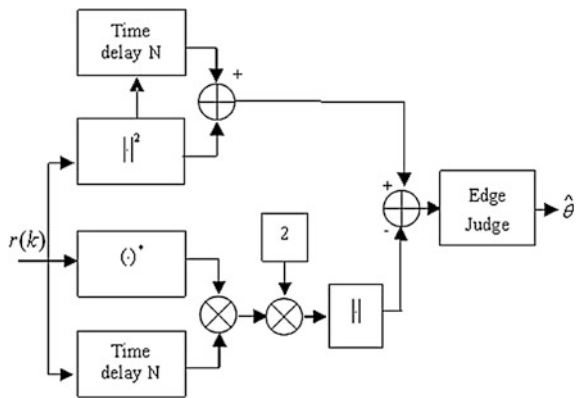
The energy term of the delay part of the received signal is shown in (2):

$$R_2(k) = \sum_{m=1}^M |r(k + (m - 1)(N + N_{cp}) + N)|^2 \tag{2}$$

The second part is the correlation function of the received signal and the received signal with delay  $N$ .

$$\phi(k) = \sum_{m=1}^M r^*(k + (m - 1)(N + N_{cp})) * r(k + (m - 1)(N + N_{cp}) + N) \tag{3}$$

**Fig. 1** Principal block diagram of timing synchronization method with peak plateau for OFDM systems



where,  $1 \leq k \leq N + N_{cp}$ ,  $M$  is the symbol number in per subcarrier.

The third part is the symbol timing estimation.

The novel symbol timing metric is presented in the difference timing synchronization method based on cyclic prefix for OFDM systems. The novel timing metric is shown in (4):

$$D(k) = R_1(k) + R_2(k) - |\phi(k)| * 2 \tag{4}$$

And a threshold is then set.

### 3 Set Threshold and Simulation Analysis

The symbol timing metric curves of the proposed method in an AWGN channel are shown in Figs. 2 and 3.

From Figs. 2 and 3, we can see that the length of the peak plateau is equal to the length of the cyclic prefix. And the edge at the end of the peak plateau is the tail of cyclic prefix. And so the edge can be found easily. If the edge is found, the time delay is also found.

The symbol timing metric curves of the proposed method in a multipath channel are shown in Figs. 4 and 5. From Figs. 4 and 5, we can see that the length of the peak plateau is shorter than the length of the peak plateau in an AWGN channel, because there is inter symbol interference in a multipath channel, which affects the front-end of cyclic prefix. The part which is affected by inter symbol interference is shown in Fig. 4.

From Figs. 4 and 5, we can see that the end of the peak plateau is also the tail of the cyclic prefix, so we can use the end edge of the peak plateau to find the time when the OFDM symbol start.

**Fig. 2** Timing metric of the novel algorithm in an AWGN channel (time delay = 50 samples)

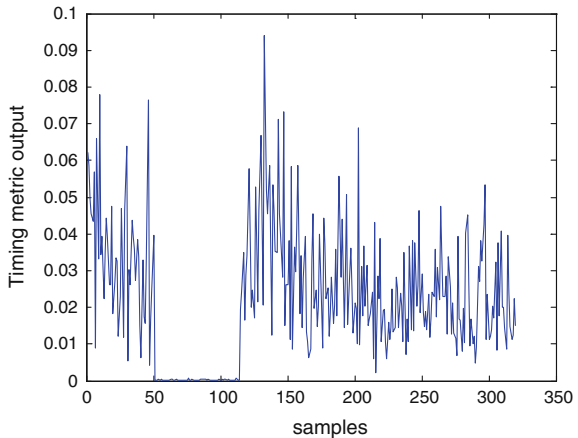


**Fig. 3** Timing metric of the novel algorithm in an AWGN channel (time delay = 50 samples)

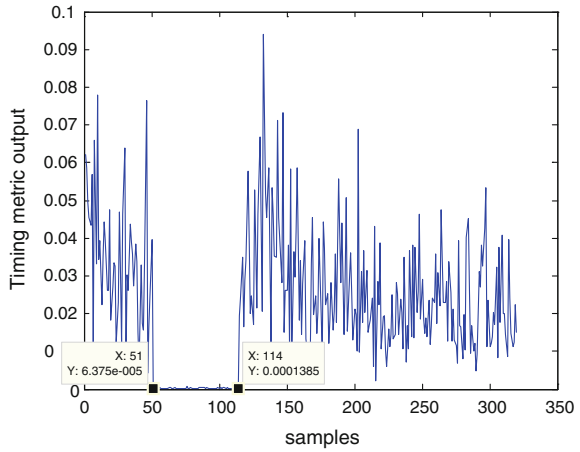


**Fig. 4** Timing metric of the novel algorithm in a multipath channel (time delay = 50 samples)

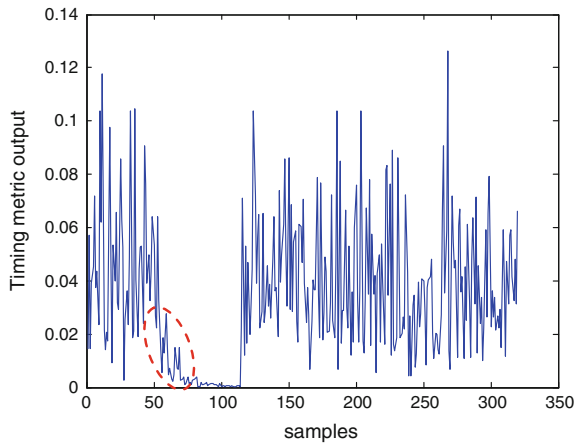
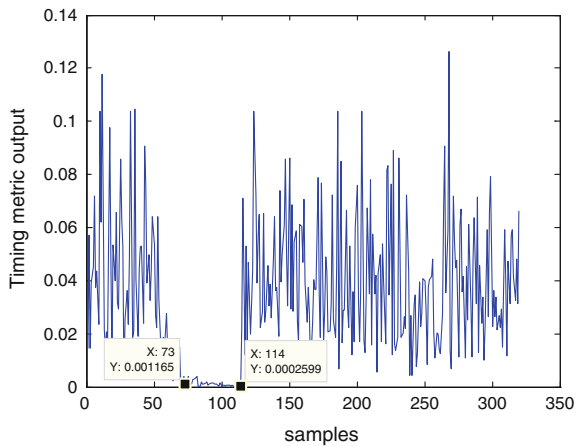


**Fig. 5** Timing metric of the novel algorithm in a multipath channel (time delay = 50 samples)



In order to reduce the effect of the useless values to the synchronization estimation, a threshold is set.

In order to find the edge easily, a threshold is set for the timing metric of the proposed method. The end edge of the peak plateau is found by judging the output of the timing metric which smaller than the threshold.

When the threshold is constant, the curves of the proposed timing metric have the conditions as shown below.

When SNR = 11 dB, the curve of the proposed timing metric is shown in Fig. 6.

The curve is a line not a peak plateau in Fig. 6, and when SNR < 11 dB, the curve is the same as the one in Fig. 6, which cannot yield the timing estimation.

When SNR = 12 dB, the curve has a peak shown in Fig. 7, but the peak value is not the end of the cyclic prefix.

**Fig. 6** Timing metric curve of the novel algorithm in a multipath channel after being processed (SNR = 11 dB)

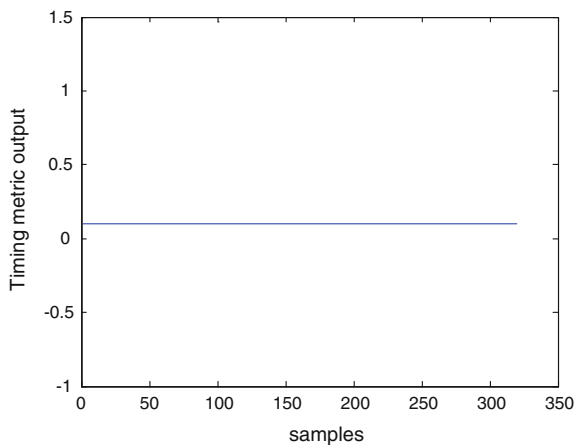


**Fig. 7** Timing metric curve of the novel algorithm in a multipath channel after being processed (SNR = 12 dB)

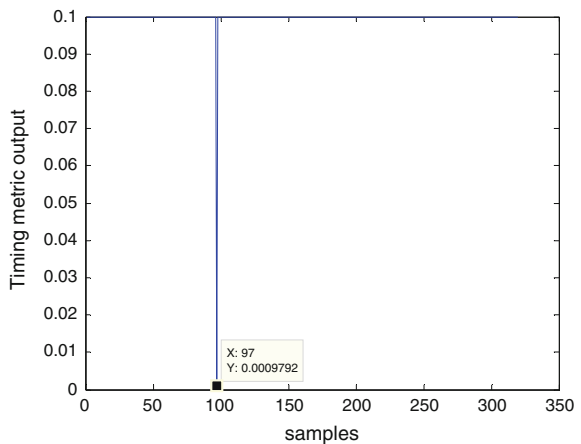
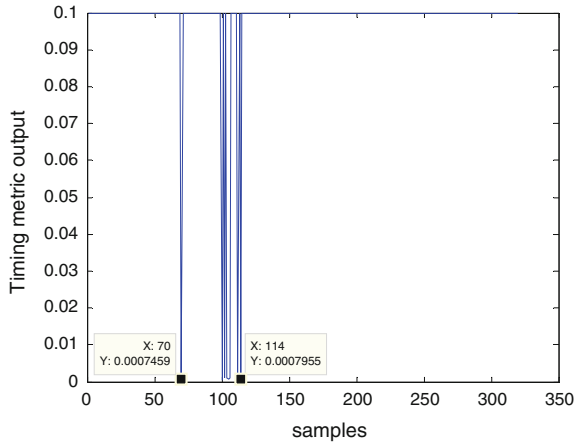




**Fig. 8** Timing metric curve of the novel algorithm in a multipath channel after being processed (SNR = 16 dB)



When SNR = 16 dB, the shape of the curve is the one we want, as shown in Fig. 8.

From the above analysis, when the threshold is constant, the proposed method has better symbol timing performance until SNR ≥ 16 dB. So the constant threshold is not suitable for the proposed method.

An adaptive threshold is proposed. The timing metric curve in AWGN channel after processing by the adaptive threshold is shown in Fig. 9.

From Fig. 9, we can see that the timing metric curve in an AWGN channel after processing is just a peak plateau, i.e., there are no other values. The length of the peak plateau is equal to the length of cyclic prefix. The edges of the peak plateau are very easy to find, and are vertical. So the timing synchronization estimation can be realized very easily. The sample after the cyclic prefix is the start of the OFDM symbol.

**Fig. 9** Timing metric of the novel algorithm in an AWGN channel after processing

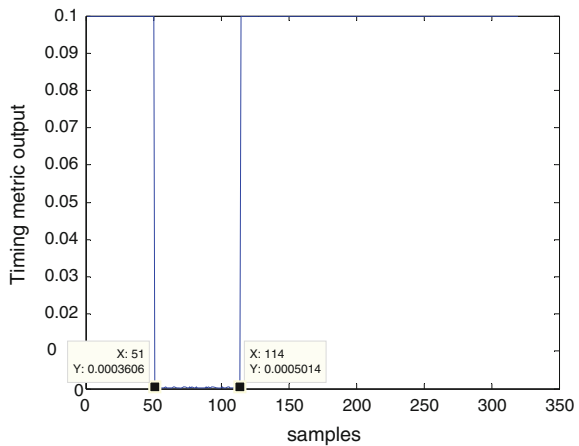
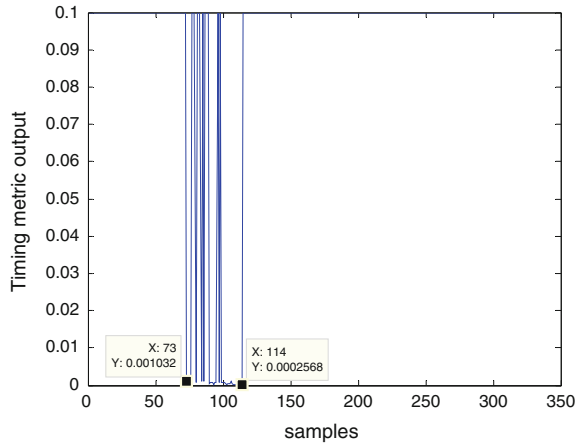


**Fig. 10** Timing metric of the novel algorithm in a multipath channel after processing



The timing metric curve in a multipath channel after processing by the threshold is shown in Fig. 10. From Fig. 10, we can see that the timing metric curve in a multipath channel after processing is also a peak plateau. There are no other values too. The length of the peak plateau is less than the length of the cyclic prefix. But the edges of the peak plateau are very easy to find, and are vertical. So the timing synchronization estimation can be realized very easily too. The sample after the cyclic prefix is the start of the OFDM symbol.

## 4 Conclusion

From the above analysis, the timing metric both in AWGN and in multipath channels has a peak plateau, and the end of the peak plateau is the tail of cyclic prefix. After processing by the threshold, the timing metric is just a peak plateau, and the edges are vertical, which can be found easily.

So the difference timing synchronization method based on cyclic prefix for OFDM systems is of low complexity and very easy to achieve.

**Acknowledgment** This study is supported by the National Nature Science Foundation of China (60372104).

## References

1. Chang RW (1996) Synthesis of band-limited orthogonal signals for multi-channel data transmission. *Bell Syst Tech J* 45:1775–1796
2. Moose PH (1994) A technique for OFDM frequency offset correction. *IEEE Trans Commun* 42 (10):2908–2914

3. Schmidl TM, Cox DC (1997) Robust frequency and timing synchronization for OFDM. *IEEE Trans Commun* 45(12):1613–1621
4. Minn H, Bhargava VK, Letaiefk KB (2006) A combined timing and frequency synchronization and channel estimation for OFDM. *IEEE Trans Commun* 54(3):416–422
5. Van de Beek JJ, Sandell M, Borjesson PO (1997) ML estimation of timing and frequency offset in OFDM systems. *IEEE Trans Sig Proc* 45(7):1800–1805
6. Jiang F, Mei S, Da G (2007) OFDM frame synchronization based on energy difference of the received preamble. *J China Univ Posts Telecommun* 14(1):96–99
7. Li CM, Sun WT, Wang PJ (2010) An overlap S&C method for OFDM synchronization. *IECE Electron Expr* 7(24):1773–1777

# GRNN Model for Fault Diagnosis of Unmanned Helicopter Rotor's Unbalance

Xi-hua Xie, Lei Xu, Liang Zhou and Yao Tan

**Abstract** In order to diagnose the unmanned helicopter rotor's unbalance fault accurately, a method based on particle swarm optimization algorithm and generalized regression neural network (PSO-GRNN) is proposed. The average mean square error got from cross-validation is used as the fitness function of particle swarm, then the optimal GRNN smooth factor is attained by using particle swarm optimization algorithm, and an optimal model for fault diagnosis is achieved finally. It can be concluded that, based on the PSO-GRNN model, the type and the grade of the helicopter rotor's unbalance can be diagnosed effectively, the diagnosis accurate rate of fault type is up to 94.29 % and the maximum error of fault grade is only 6.54 %, which is perfectly satisfied for the requirement of project.

**Keywords** Fault diagnosis · Unmanned helicopter · Rotor · Particle swarm optimization (PSO) · Generalized regression neural network (GRNN)

## 1 Introduction

As an important part of unmanned helicopter, the rotor can provide power not only for moving forward, but also for performing a variety of posture and motor transformation. As a single-channel load delivery system, the rotor system's work environment is complex, suffering a complex aero elastic load, especially the imbalance cycle alternating load when it moves forward, which can easily make the key components vibrate and fatigue, what is worse, it would lead to failure causing an accident. Therefore, the research on fault diagnosis of rotor unbalance is of great significance.

---

X. Xie · L. Xu (✉) · L. Zhou · Y. Tan

The State Key Laboratory of High Performance Complicated Manufacturing,  
Central South University, Changsha 410083, China  
e-mail: maxulei111@126.com

© Springer-Verlag Berlin Heidelberg 2016

B. Huang and Y. Yao (eds.), *Proceedings of the 5th International Conference on Electrical Engineering and Automatic Control*, Lecture Notes in Electrical Engineering 367, DOI 10.1007/978-3-662-48768-6\_61

539

In the study of rotor's fault diagnosis and recognition, many scholars have used BP neural network to achieve the diagnostic process [1–4]. Although the establishment of BP neural network can simulate that complex nonlinear systems of helicopter, but BP neural network training costs a long time. While GRNN has an advantage of fast convergence, and its influencing factors are much less than BP neural network.

Hereinafter, the GRNN network model was achieved for the rotor's unbalance fault diagnosis in this paper, and particle swarm algorithm was also introduced to optimize the GRNN model parameters. The problem that GRNN's topology is hard to determine was solved effectively, and the advantages of strong nonlinear mapping ability, high fault tolerance and robustness were retained. This method is proved to be applicative through the diagnosis of the concerned literature data.

## 2 The Establishment of PSO-GRNN Model

### 2.1 Generalized Regression Neural Network and Its Mathematical Basis

GRNN was proposed in 1991 by Donald Specht at The Lockheed Palo Alto Research Laboratory. As an improvement on RBF neural network, it is based on regression mathematical statistics. The GRNN neural network can approximate the implicit mapping relation from sample data [5]. Even with little sample data, it can also achieve a good prediction.

The theoretical basis of the GRNN is that by calculating the nonlinear regression of non-independent output variable  $Y$  with respect to the independent input variable  $X$ , the  $y$  of maximum probability was achieved. The random variable  $Y$  can be calculated by Eq. (1).

$$\bar{Y} = E(y/X) = \frac{\int_{-\infty}^{\infty} yf(x, y)dy}{\int_{-\infty}^{\infty} f(x, y)dy} \quad (1)$$

The GRNN model is composed of four network layers, including input layer, pattern layer, summation, and output layer. The topological structure of GRNN model is as shown in Fig. 1.

By applying the Parzen nonparametric estimation method, the output of the network  $\bar{Y}(X)$  can be known as Eq. (2):

$$\bar{Y}(X) = \frac{\sum_{i=1}^n Y_i \exp\left[-\frac{(X-X_i)^T(X-X_i)}{2\sigma^2}\right]}{\sum_{i=1}^n \exp\left[-\frac{(X-X_i)^T(X-X_i)}{2\sigma^2}\right]} \quad (2)$$

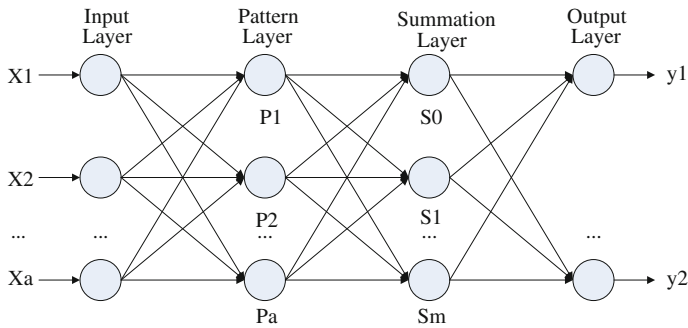


**Fig. 1** Topological structure of GRNN model

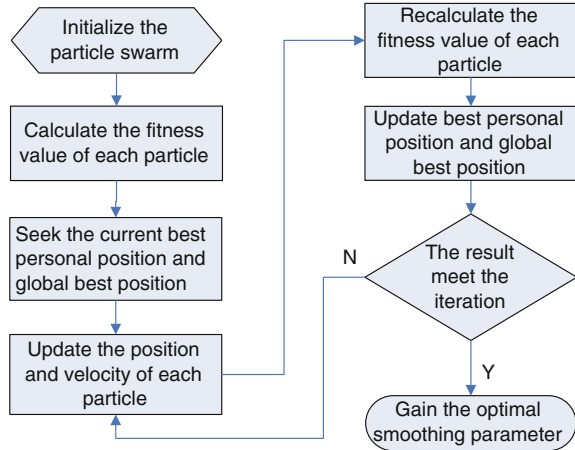
Obviously, the estimated value  $\bar{Y}(X)$  is a weighted average of all training samples  $Y_i$ , whose weighting factor corresponds to the index of the square of the Euclidean distance between independent variable  $X_i$  and the central value  $X$ . When smooth factor  $\sigma$  is large, the estimated value  $\bar{Y}(X)$  is approximated by the mean of all samples; and when  $\sigma$  is close to 0,  $\bar{Y}(X)$  will be close to the training samples. Only when  $\sigma$  is moderate, can  $\bar{Y}(X)$  take the dependent variable of all the training samples into account.

Therefore, it is necessary to carry on optimization design for smooth factor values. The choice of smooth factor is being manually adjusted at first, and most people have tried to use empirical values, which directly affect the accuracy and efficiency of GRNN network. As technology advances, Cross-validation has become a mainstream when searching a proper smooth factor, but considering that each step in the process is constant, it is usually required to change search scale and step to achieve optimization result, which will severely restrict the choice of smooth factor. To reduce the smooth factor optimization time and increase the accuracy and efficiency of GRNN network, the PSO algorithm combining the idea of cross-validation was proposed to solve the problem of optimizing smooth factor.

## 2.2 The GRNN Model Optimization Based on PSO Algorithm

Particle swarm optimization is an optimization algorithm based on swarm intelligence theory, which was proposed by Dr. Eberhart and Dr. Kennedy, stemming from the study of birds foraging behavior [6]. In the basic PSO algorithm, the process of each optimization problem is searching particles in space; the characteristic of a particle is expressed by the value of position, speed, and fitness. In every search process, a particle constantly adjusts its position and speed to be updated by tracking two optimal solutions. One is the optimal solution particle

**Fig. 2** Flow chart of PSO optimization



found itself, namely individual optimal solution; the other is the optimal solution that entire populations have found at present, namely the global optimal solution. Particle’s update process is as follows:

$$V_{ij}(t + 1) = wV_{ij}(t) + c_1r_1 [P_{ij}(t) - X_{ij}(t)] + c_2r_2 [P_{gj}(t) - X_{ij}(t)] \quad (3)$$

$$X_{ij}(t + 1) = X_{ij}(t) + \alpha V_{ij}(t + 1) \quad (4)$$

In that equation,  $X_{ij}(t + 1)$  and  $V_{ij}(t + 1)$  are the position and velocity of particle in some dimension for iteration of  $t + 1$  times;  $X_{ij}(t)$  and  $P_{ij}(t)$ ,  $P_{gj}(t)$  are the position of particle as well as individual optimal solution, global optimal solution for iteration of  $t$  times;  $w$  is inertia factor, indicating the particle’s ability to inherit the original velocity;  $c_1$ ,  $c_2$  are positive constants, called acceleration factor, indicating the weighted statistical accelerate items of particles’ pushing toward individual optimum and global optimum;  $r_1$ ,  $r_2$  are random numbers between  $[0, 1]$ ;  $\alpha$  is a constraint factor.

From the above description, it is needed to search optimal value for smooth factor of GRNN network, so the optimization problem turns into a one-dimensional particle swarm optimization problem. The algorithm flow is shown in Fig. 2.

### 3 The Application of PSO-GRNN Model in Fault Diagnosis on Helicopter Rotor’s Unbalance

Considering the special structure of helicopter rotor, it is difficult to install sensors to monitor the status of rotor directly. The relevant theoretical studies have shown [7–9], the feature vector that reflects the state of helicopter rotor which can be

extracted from helicopter airframe vibration signal directly, and a certain pattern recognition method is used to diagnose its status.

To achieve the rotor unbalance fault diagnosis, the method of two types GRNN network used to recognize fault type and fault grade is presented. First, the fault type is diagnosed through the first kind of GRNN network, and then the fault type diagnosis model is established. On this basis, the samples which have been classified correctly are selected. The corresponding second kind of GRNN network models for different fault grade identification is established, so the fault grade diagnosis model is also established. Finally the two-step diagnostic of rotor imbalance is achieved.

### 3.1 PSO-GRNN Diagnosis Model of Helicopter Rotor Unbalance Fault Type

There are various imbalance fault types of the helicopter rotor, in this paper three common types of them (pitch imbalance, mass imbalanced, and trim tab imbalance) are selected. Literature [10] has given a 105 group single unbalanced fault samples, the samples were all from the rotor unbalance experiments. By measuring the vibration signals of rotor test rig body, blind source separation technology is used to extract feature vectors which are relative to faults. In order to diagnose effectively, an independent component analysis method is chosen to extract a four-dimensional vector (X1, X2, X3, and X4) which is regarded as the network training input. The output value is discriminated according to the contour interval.

To establish experimental model, the first 35 samples for cross-training are selected, using PSO algorithm to optimize smooth factor and calculating the mean squared error under corresponding smooth factor each time, and then performing iterative refinement for smooth factor with average mean square error as fitness value, thus the optimal value of smooth factor is acquired and a PSO-GRNN fault type diagnosis model is achieved, and then established model is used to diagnose the fault types of remaining samples, the samples are shown in Table 1.

**Table 1** Samples of learning and testing data for fault type diagnosis

No.	X1	X2	X3	X4	The type of fault	Corresponding values
1	0.3292	3.9293	1.9923	0.3058	Fine	0.125
2	0.4369	4.4693	1.3207	0.3006	Pitch imbalance	0.375
3	0.2156	2.8401	1.7048	0.6975	Mass imbalance	0.625
4	0.8945	2.9024	3.5288	0.9418	Trim tab imbalance	0.875
...	...	...	...	...	...	...
102	0.3620	4.0108	1.9963	0.3000	Fine	0.125
103	0.4284	3.6397	1.2681	0.3357	Pitch imbalance	0.375
104	0.2994	2.7439	1.8341	1.2685	Mass imbalance	0.625
105	0.7544	2.8542	2.7800	0.7340	Trim tab imbalance	0.875



According to the literature [6] in recommended preferences, the PSO parameters are selected as follows, the number of particle population is 2, the interval of the particle position is [0.1, 2], speed interval is [-0.5, 0.5], the inertia factor  $w$  is a linear decreasing value which ranges from 0.9 to 0.4, and the acceleration factor  $c_1$ ,  $c_2$  are both set to 2, the maximum number of iterative times is set to 20, the constraint factor  $\alpha$  is 0.5. The specific iterative process is shown in Fig. 3.

After 16 generations optimization, a very good optimization effect can be achieved, the optimization result is  $\sigma = 0.2654$ , then the value of best fitness function is 0.0083. Using the optimization result  $\sigma = 0.2654$  to establish GRNN fault type diagnosis model, the remaining 70 groups of samples are diagnosed and predicted, then the diagnostic accuracy of various fault types and overall accuracy can be calculated. The fault type output is discriminated by interval divided between [0, 1] according to uniform distribution principle. At the same time a model with the smooth factor set to 1 by default is established, then a comparison with the BP neural network model in literature [10] is made, the result is shown in Table 2.

The result in Table 2 shows that the GRNN model with default setting  $\sigma = 1.0$  can identify a portion of the faults effectively, particularly the mass imbalanced fault, the recognition rate of which can reach 100 %. But for trim tab imbalance fault, the results are all mistaken for mass imbalance; it is difficult to meet the

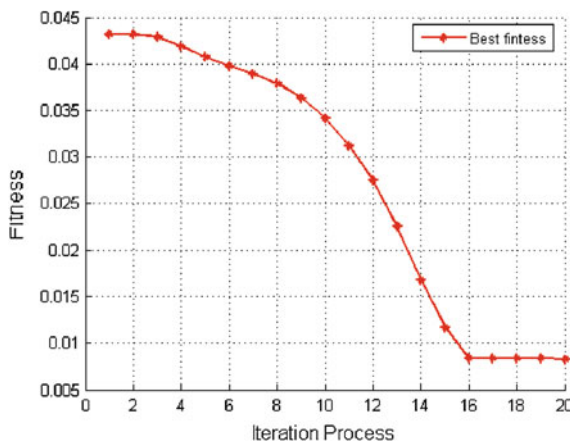


Fig. 3 Iterative optimization process of smoothing parameter

Table 2 Diagnosis accurate rate of fault types based on different model

	Fine	Pitch imbalance	Mass imbalance	Trim tab imbalance	Total (%)
PSO-GRNN	2/2	32/33	18/19	14/16	94.29
GRNN	1/2	26/33	19/19	0/16	65.71
BP [10]	1/2	9/10	8/10	4/5	77.5

requirement of the actual project. While the optimized PSO-GRNN fault type diagnose model can identify the fault types described above effectively, and it can improve the overall accuracy rate significantly, at the same time, the diagnosis accuracy of the PSO-GRNN model has also been improved to some extent that can be compared with the BP neural network in the literature [10].

### 3.2 PSO-GRNN Diagnosis Model of Helicopter Rotor Unbalance Fault Grade

According to different fault types, respective corresponding fault models are established. In this article, only fault grade diagnosis for the mass imbalance fault is performed, and the corresponding PSO-GRNN diagnosis model of fault grade is established. All samples are from the body vibration signal [10] with different counterweight, the four-dimensional characteristic signal (Y1, Y2, Y3, Y4) is attained after data processing. The samples are shown in Table 3.

While the PSO parameters are set according to chapter in front, the new established GRNN model of mass imbalance fault grade is optimized. In order to make full use of the data and prevent data from overfitting, average MSE obtained by cross-validation methods as PSO algorithm fitness function is used to search optimal smooth factor. As a result, the optimal smooth factor is  $\sigma = 0.5499$ . By using the first 24 samples to establish GRNN diagnosis model of fault grade, and performing predictive analysis for the 26-30 data group, the result of prediction based on PSO-GRNN model is obtained. The contraction with actual value is shown in Table 4.

It can be concluded from the results in Table 4, the maximum relative error of PSO-GRNN model's predictions is 6.54 %, and this method has a better accuracy and can meet project requirements.

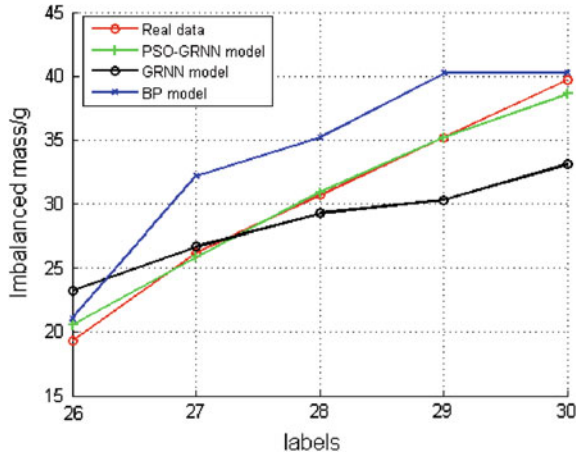
**Table 3** Samples of data for mass imbalance fault grade diagnosis

No.	Y1	Y2	Y3	Y4	Mass imbalance/g
1	0.5298	3.0906	2.2140	0.9180	19.3
2	0.3440	2.7885	1.6201	0.7407	30.7
3	0.1683	2.7861	1.5481	1.1601	39.7
...	...	...	...	...	...
26	0.6182	2.9932	2.2999	0.8539	19.3
27	0.3151	3.0603	1.6116	0.5304	26.2
28	0.2470	2.6171	1.5583	0.7013	30.7
29	0.2710	2.8630	1.4713	1.0942	35.2
30	0.2059	2.7811	1.5799	0.9664	39.7

**Table 4** The comparison of data and prediction based on PSO-GRNN model

No.	Real data/g	Predication/g	Absolute error/g	Relative error/%
26	19.3	20.5621	-1.2621	-6.54
27	26.2	25.8850	0.3150	1.20
28	30.7	30.9115	-0.2115	-0.69
29	35.2	35.1758	0.0242	0.07
30	39.7	38.6299	1.0701	2.70

**Fig. 4** The comparison chart of different models prediction



Based on the same samples that PSO-GRNN model was established, the corresponding ordinary GRNN model and BP model are built, and the fault grade for 26-30 data groups based on three different models, respectively, is predicted.

Figure 4 shows the contractions of the predicted results of three different models on latter five groups of samples, it is apparent to draw a conclusion that the superiority of PSO-GRNN model has a lower relative error rate.

## 4 Conclusions

Aimed at the current situation that smooth factor of generalized regression neural network is difficult to choose, PSO is used to optimize the smooth factor, which can effectively reduce the impact of human factors on the predicted results.

A two-step method diagnosis model of helicopter rotor's imbalance fault, using data from literature for model training and testing, is proposed and established. The result shows that the two-step PSO-GRNN model can diagnose the type and grade of the fault effectively.

The result of diagnostic and comparative analysis to literature data shows that, PSO-GRNN diagnostic model is obviously better than BP model and ordinary GRNN model. It is a new approach for similar fault diagnosis.

**Acknowledgements** This work was supported by the National Science and Technology Supporting Plan of China under Grant 2014BAD06B07, and supported by the Transformation and Industrialization of Scientific and Technological Achievements Program of Hunan Province, China, under Grant 2012CK1003.

## References

1. Pawar PM, Ganguli R (2007) Helicopter rotor health monitoring-a review. *Proc Inst Mech Eng Part G J Aerosp Eng* 221(5):631–647
2. Ganguli R, Chopra I, Haas DJ (1998) Helicopter rotor system fault detection using physics-based model and neural networks. *AIAA J* 36(6):1078–1086
3. Jianhang GYZZY (2002) Novel helicopter rotor imbalance fault diagnosis using only information from fuselage vibration. *J Vibr Eng* 4:004
4. Gao YD, Zhang ZC, Yu JH (2004) Novel method for diagnosis of helicopter rotor compound imbalance fault by using fuselage vibrations. *Acta Aeronaut Astronaut Sin Ser A B* 25(1):26–30 (in chinese)
5. Shi F, Wang XC et al (2010) MATLAB neural network analysis of 30 cases. University of Aeronautics and Astronautics Press, Beijing (in chinese)
6. Chen CY, Ye F (2004) Particle swarm optimization algorithm and its application to clustering analysis. In: 2004 IEEE international conference on networking, sensing and control, vol 2. IEEE, pp 789–794
7. Zengchang GYZ (2003) A theoretical basis for diagnosis of helicopter rotor imbalance fault using only information from fuselage vibrations. *J Vibr Meas Diagn* 4:010 (in chinese)
8. Zengchang GYZ (2009) Experimental study on unbalance fault diagnosis of helicopter rotor. *J Vibr Meas Diagn* 2:022 (in chinese)
9. Dun S-P (2010) Research on helicopter rotor imbalance fault experiment and diagnosis method. Nanjing University of Aeronautics and Astronautics, Nanjing (in chinese)
10. Yao F-H (2011) Research on helicopter rotor fault diagnosis based on blind source separation and artificial immune system. Nanjing University of Aeronautics and Astronautics, Nanjing (in chinese)

# A Double-Stage Strategy Based on DNA Computing to Search the Optimal Section of Active Splitting

Xiaoli Ye, Fei Tang, Jian Yang, Junru Xu, Yongle Zheng  
and Qiang Zhao

**Abstract** Splitting section searching is a non-polynomial problem (NP problem). However, DNA computing, a new type of computing model based on DNA molecules with its amazing parallel computing ability, powerful storage capacity, and the characteristics of low energy consumption can traverse through all the feasible solutions to solve the NP problem well. For the need of active splitting when the power grid goes instable after disturbance, this paper presents a double-stage strategy based on DNA computing to search the optimal section of active splitting successfully.

**Keywords** The optimal splitting section · Active splitting of power system · Non-polynomial problem · DNA computing

## 1 Introduction

The large-scale interconnected power grid enhances the electrical contact between the regional power grids also enlarges the risk of cascading failure. Power system splitting control is the key measure to keep power grid operating safely and stably. Different from the traditional passive splitting, active splitting control [1] is a kind of online, centralized, global, and active method, containing three techniques: when, where, and how to split. This paper only discusses the second one, namely the global searching of optimal splitting section.

Many researches try to search optimal splitting section of power grid alike the method based on intelligent algorithm, graph theory, the theory of slow homology, as well as, other methods. Articles [2] and [3] transform this problem into a single objective optimization, respectively, select simulated annealing (SA) and genetic

---

X. Ye (✉) · F. Tang · J. Yang · J. Xu · Y. Zheng  
School of Electrical Engineering, Wuhan University, Wuhan 430072, China  
e-mail: xlye@whu.edu.cn

Q. Zhao  
China Electric Power Research Institute, Beijing 100192, China

algorithm (GA) to search the best section. Even if the intelligent algorithm solves the problem, the solving process has strong randomness, thus unable to solve the non-polynomial problem (NP problem) thoroughly.

As a calculation method based on DNA molecular, DNA computing possesses high parallelism and low energy consuming features, making up the deadly short board of traditional electronic computers. DNA computing was first proposed in 1994 by Adleman [4], solved the Hamilton path problem of the directed graph with seven vertexes. Its strong practical application ability appeals the concern of many scholars. DNA computing made significant progress in various research areas so far: Braich successfully using DNA sticker model [5] to solve the satisfiability problem of 20 variables in 2002; In 2006, Shapiro states the advantages of DNA computer in daily life and its possibility of realization [6]; the closed circle DNA algorithm [7] to solve the shortest circuit problem is proposed by Zhou Kang et al. in 2008.

Under the power grid interconnection structure, the DNA computing can solve it through global search. A double-stage search strategy based on DNA computing is proposed to find the optimal splitting section successfully in this paper. The first stage based on the DNA model searches the shortest path connecting all the coherent generators in each subsystem. The second stage tries to find all paths connecting the virtual nodes in different subsystems through DNA computing.

## 2 The Mathematical Model of Searching the Optimal Active Splitting Section

There are two principles for building the objective function and constraint conditions, namely principle of coherent generators and power balance principle within subsystem [8].

### 2.1 Objective Function

At present there are two kinds of the most studied objective function for splitting, one is the minimum unbalanced power, as shown in Eq. (1), the other is minimum power flow impact, as shown in Eq. (2).

$$\min P_{\text{imbalance}} = \sum_{i \in I} (P_{Gi} - P_{Li} - \Delta P_{si}) \quad (1)$$

$$\min P_{\text{impact}} = \sum_{i \in I} |P_{Gi} - P_{Li} - \Delta P_{si}| \quad (2)$$

where  $P_{\text{imbalance}}$  denotes the unbalanced power,  $P_{\text{impact}}$  denotes the power flow impact;  $t$  denotes the number of the subsystems;  $P_{Gi}$ ,  $P_{Li}$ ,  $\Delta P_{si}$  respectively denote active power, load, loss of island  $i$ .

## 2.2 Constraint Conditions

### 2.2.1 Generator Coherent Constraint

When implementing the splitting, the coherent generators in one group must be assigned to the same subsystem, and generators in different coherent groups are not allowed in the same subsystem. Otherwise, the subsystem will need second split because the subsystem is still unstable. So, it is necessary to build the generator coherent constraint, as shown in Eq. (3).

$$\left\{ \begin{array}{l} \cup_{m=1}^t V_m^G = V^G \\ V_m^G \cap V_s^G = \emptyset, \quad \forall m \neq s \\ \forall n_{Gi}, n_{Gj} \in V_m^G (m \in t), \quad \exists L_{ij}, \prod_{l \in L_{ij}} b_l = 1 \\ n_{Gi} \in V_m^G, n_{Gj} \in V_s^G (\forall m \neq s), \quad \forall L_{ij}, \prod_{l \in L_{ij}} b_l = 0 \end{array} \right. \quad (3)$$

where  $V^G$  denotes the set of all generator nodes;  $V_m^G$  denotes the set of generator nodes in group  $m$ ;  $V_s^G$  denotes the set of generator nodes in group  $s$ ;  $n_{Gi}$ ,  $n_{Gj}$  denotes the generator node  $i$  and  $j$ , respectively.

### 2.2.2 Connectivity Constraints

Each subsystem must be connected and no isolated nodes survive, so the connectivity constraint is needed to meet. Connectivity constraint shows that any two nodes in each same subsystem lead at least one connecting path, as shown in Eq. (4).

$$\left\{ \begin{array}{l} \text{s.t.} \quad \forall n_i, n_j \in V_m, \quad \exists L_{ij}, \prod_{l \in L_{ij}} b_l = 1 \quad (i \neq j) \\ \forall n_i \in V_m, n_j \in V_s, \quad \forall L_{ij}, \prod_{l \in L_{ij}} b_l = 0 \quad (i \neq j, m \neq s) \\ \forall n_{Gi} \in V_G, n_{Lj} \in (V - V_G), \quad \exists L_{ij}, \prod_{l \in L_{ij}} b_l = 1 \quad (i \neq j) \end{array} \right. \quad (4)$$

where  $n_i$ ,  $n_{Gi}$ ,  $n_{Lj}$  represents node  $i$ , generator node  $i$ , load node  $j$ , respectively;  $L_{ij}$  denotes the path connecting node  $i$  and node  $j$  and is a set of many connected lines

denotes as  $l$ ;  $b_l$  shows the break status of line  $l$ , value 1 indicates in service, while 0 means out of service.

### 2.2.3 Power Flow Constraints

Power flow constraint contains equality and inequality constraint, as shown in Eq. (5). The equality constraint is in the characterization of supply and demand power balance in each subsystem after splitting with adjusting the output of generators and shedding load. Then the subsystems operate independently by achieving this constraint. The inequality constraint keeps the value of the electrical operation parameters in a certain stable range.

$$\begin{cases} k(P, Q, V, \theta) = 0 \\ g(P, Q, V, \theta) \leq 0 \end{cases} \quad (5)$$

where  $P$ ,  $Q$ ,  $V$  and  $\theta$  denote active power, reactive power, voltage magnitude and phase angle respectively.

## 3 DNA Computing

### 3.1 The Basis of DNA Computing

DNA computing is a new model established on the basis of the double helix model of DNA molecular presented by Watson and Crick. DNA molecule [9] is composed of the four deoxyribonucleic acids, as shown in Fig. 1. Nitrogenous base has four kinds: adenine (A), guanine (G), cytosine (C), thymine (T). And A is paired with T, G with C, only in this way can form effective hydrogen bond, as shown in Fig. 2. In addition, DNA has spatial double helix structure.

DNA computing is set up to solve practical problems. The DNA computing mainly contains double-stranded DNA computing model, DNA sticker computing model and closed-circle DNA computing model. The three models adopt different DNA fragment as raw material to encode and calculate, and all get well effect in application.

**Fig. 1** Structure of DNA molecular

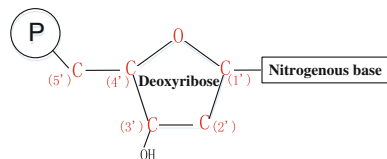
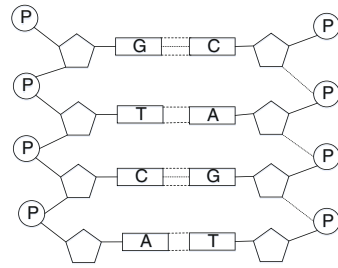




**Fig. 2** Model of double-stranded DNA



### 3.2 Methodology of DNA Computing

DNA computing uses the particular structure of DNA molecule to code the problem; after several biochemical reactions take place with biological enzyme in proper environment, DNA molecule would achieve stable state and generate the possible solution of the problem, from which optimum solution could be found with biological techniques. DNA calculation gradually forms a pattern that contains algorithm design, DNA calculation and solution, stated as below:

- (1) Algorithm design: determines the DNA model that describes the problem, corresponding coding, procedure of biological experiment and algorithm process.
- (2) DNA calculation: preparation and conduct of the biological experiment. The first stage is preparing the equipments and material for the experiment, calculating the DNA coding and composing the DNA sequence; the second stage is conducting biological experiment and checking the DNA sequence.
- (3) Solution: the last step of DNA computing, which is checking the DNA sequence and unscramble the information in the sequence.

## 4 The Double-Stage Strategy Based on DNA Computing to Search the Optimal Section of Active Splitting

### 4.1 Process of the Double-Stage Strategy

Power system is depicted as a directed graph  $G(V, E, c)$  whose edges with weight. In the graph,  $V$  denotes the set of all nodes, including generator nodes, load nodes and transmission nodes; The set  $E$ , collecting all edges represent transmission lines in the power system; as the weights of edges, set  $c$  shows the value of active power in the transmission lines, and the flow of each edge is the direction of the corresponding transmission line. Figure 3 shows a IEEE-39 bus system with information of coherent generator groups.

**Fig. 3** IEEE-39 bus system with group information

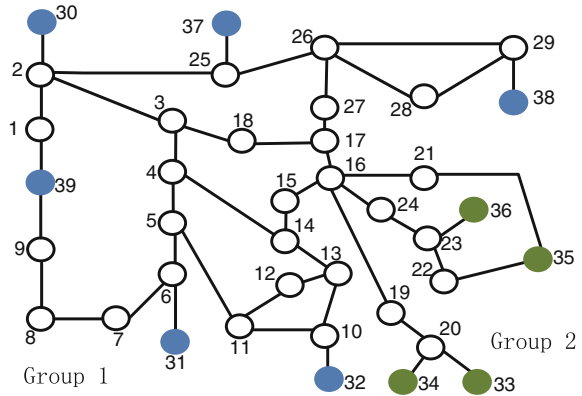
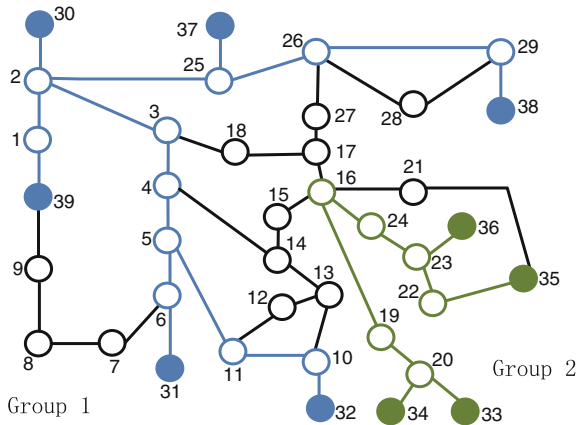


**Fig. 4** Shortest paths in coherent groups



First stage: search the shortest path which connects all generator nodes in each subsystem and condense the path into a virtual generator node. After encoding all nodes and edges, according to the group information of generators, DNA fragments of generator nodes are selected into corresponding biological reaction tube separately, and the raw material in each reaction tube contains all other nodes and edges. In each tube, by series of ordered ligation and screening operation experiments, the shortest path containing all generator nodes is traversed, show in Fig. 4, which is condensed into a virtual generator node. Then get a polymerized graph  $G'(V', E', c')$ , as shown in Fig. 5.

Second stage: search and analyze all paths that connect the two virtual generator nodes in corresponding subsystems, and then get optimal solution under two objective functions. This paper only considers two group splitting, and three and more groups is considered as several two group splitting. According to polymerized graph  $G'$ , all the nodes and edges are encoded, through the biochemical reactions, edge with minimum weight in each path connecting the two virtual generator nodes

**Fig. 5** The condensed graph

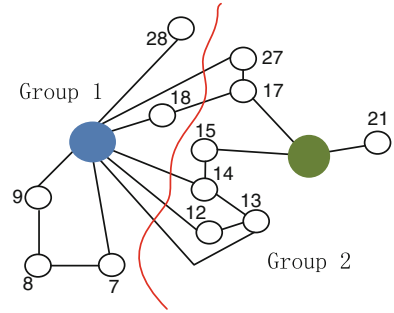
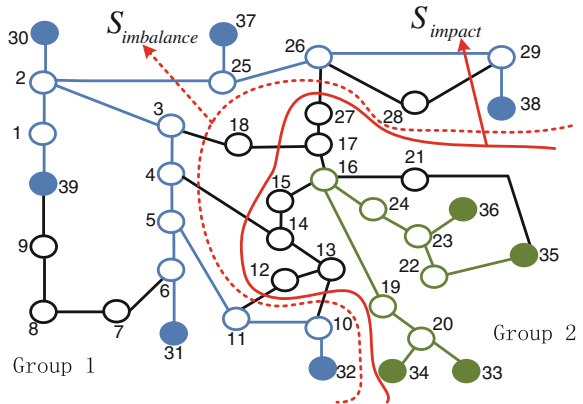


**Fig. 6** The optimal splitting sections



is selected and then the selected edges form a set  $S_{impact}$  as the optimal splitting section with minimum power flow impact. Near the former section, a optimal solution  $S_{imbalance}$  meets the objective function of minimum power imbalance, as shown in Fig. 6.

## 4.2 Process of the Double-Stage Strategy

According to the process of the double-stage strategy based on DNA computing optimal section of active splitting, the corresponding biochemical experiments of DNA computing steps are described as follow.

### 4.2.1 The First Stage

- (1) Code all the nodes in power system diagram  $G$ . All the generator nodes are represented by 20-mer DNA sequence  $p(i)q(i)$  with sticky ends, where  $i = 1,$

- 2, ...,  $n$ . Select two generator nodes randomly from each coherent group as the start and end point of the shortest path in this subsystem, and activate the hydroxyl (OH) at start point 3' and the phosphate group at the end point 5' to remove their chemical activity.
- (2) Code all the edges in diagram  $G$ , and the length of all edges are proportional to corresponding active power flow with double stranded DNA sequence. In accordance with the connection relation,  $q'(i)$  and  $p'(j)$  of 10-mer sticky ends are spared at both ends of a DNA duplex; ensure all the DNA codes are different.
  - (3) Conduct ligation reaction and fix them to the modified surface. Mix coherent generator nodes with all other nodes and DNA fragments of sides that contain complement sequence of a group in a test tube, and conduct ligation reaction. The reactant contains the DNA code of the shortest paths that traverse all nodes of this group. Conduct gel electrophoresis and collect the DNA fragments by the chain length. Fix the DNA fragments on the modified surface according to the order of gel electrophoresis and number them.
  - (4) Heat the surface of DNA fragments to unlock the duplexes, and flush out all fill chains on the surface. Mix the DNA single chain fragments with oligonucleotide  $p'(2)q'(2)$  that has fluorescein. After sufficiently reacted, the surface should be thoroughly cleaned to remove all the oligonucleotide fragments that are not hybridized. For the fluorescein in  $p'(2)q'(2)$ , select DNA fragment with one light spot in the scope of laser confocal microscopy, and abandon those with more than one light spot, because in one shortest path the climax could only appear once.
  - (5) Repeat step 4 to all the generator nodes except for the start and end point. Then add  $p'(1)$  and  $q'(n)$  to the reactant, and the paths that could form complete duplexes DNA are paths that start with point 1 and end with point  $n$ .
  - (6) Measure the length of the shortest DNA molecule and analyze the connection of the shortest path. Aggregating all shortest paths which are corresponding to each subsystem into a virtual generator node, and a coagulation diagram  $G'(V', E', c')$  can be constructed.

#### 4.2.2 The Second Stage

- (1) Conduct DNA coding to all the nodes and edges of the coagulation diagram  $G'(V', E', c')$  with the mentioned method. Set two virtual generator nodes as the start and end point of the search path, and activate them.
- (2) Construct ligation reaction and fix on the modified surface. Then a mixture that contains all paths that start and end with virtual generator nodes could be obtained.
- (3) Add  $p'(1)$  and  $q'(n)$  into the reactants in Step 2 and conduct ligation reaction, and a complete duplexes DNA which starts with 1 and ends with  $n$  could be

obtained. Fix the DNA fragments on the modified surface with the sequence of gel electrophoresis, and then decode the DNA fragments.

- (4) All the paths corresponding with the DNA chains could be obtained, as well as all the paths connecting any two virtual nodes. Pick the edge with the smallest weight in each path (minimum  $c_{ij}$ ) to form the splitting section, which is the optimum splitting section  $S_{\text{impact}}$  with minimum power flow impact. According to the power flow direction of power system coagulation diagram  $G'$ , search  $S_{\text{imbalance}}$  with minimum power imbalance near  $S_{\text{impact}}$ .

## 5 Conclusions

In this paper, a two-stage strategy based on DNA computing is proposed, which could solve the power system splitting with high performance. Conclusions are stated as below:

- (1) DNA calculation has been widely used in many regions to solve NP problems. A two-stage strategy based on DNA computing proposed in this paper, satisfying the constraints, solves the NP problem of power system optimal splitting section searching successfully.
- (2) The two-stage strategy could search the optimum section under the objective function of power flow impact and minimum power unbalance. Better splitting could be searched by balancing the objective functions.

**Acknowledgements** This work was financially supported by China Postdoctoral Science Foundation (2014M552080); the Fundamental Research Funds for the Central Universities; project of the 13th Five-year Plan of the State Grid Corporation, and Mid-long term strategy research on science and technology and technology forecasting (JSB51201402918).

## References

1. Shen C, Wu JY, Qiao Y et al (2006) Studies on active splitting control of power systems. Proc Chin Soc Electr Eng 26(13):1–6
2. Irving MR, Sterling MJH (1990) Optimal network tearing using simulated annealing. IEEE Proc C Gener Transm Distrib 137(1):69–72
3. Shazely S, Baraka H, Abdel-Wahab A (1998) Solving graph partitioning problem using genetic algorithm algorithms. In: Proceedings of the 1998 midwest symposium on systems and circuits, 1998. IEEE Circuits and Systems Society, Notre Dame, IN, USA, pp 302–305
4. Adleman LM (1994) Molecular computation of solutions to combinatorial problems. Science 266(5187):1021–1024
5. Braich RS, Chelyapov N, Johnson C et al (2002) Solution of a 20-variable 3-SAT problem on DNA computer. Science 296(5567):499–502
6. Shapiro E, Benenson Y (2006) Bringing DNA computers to life. Sci Am 294(5):44–51

7. Zhou K, Tong XJ et al (2008) A closed-loop DNA computing to solve the short problem circuit. *Syst Eng Electron* 30(3):556–560
8. Aghamohammadi MR, Shahmohammadi A (2012) Intentional islanding using a new algorithm based on ant search mechanism. *Int J Electr Power Energy Syst* 35(1):138–147
9. Zhang HY (2013) The research and application of graph clustering algorithm based on DNA computing. Shandong Normal University

# The Design and Realization of Motion Controller for Truss Robot

Peng Zheng, Wusheng Chou and Huaidong Zhou

**Abstract** Truss robot has been widely used in the field of industry. In consideration of the features of truss mechanism, and after deep analysis the characteristics of TMS320F28335 DSP chip of TI EP4CE10E22C8 FPGA chip of Altera, the paper presents a design and realization of motion control solution based on DSP and FPGA. This controller can meet the real-time response and precision as the system needs. The paper introduces the hardware structure of the control system, and also illustrates the functions of different modules. The control algorithm of DSP and FPGA is explained, respectively, including the flow chart and block diagram of the software system. The fine interpolation module, PI controller, encoder acquisition module which are implemented in FPGA are also introduced in the paper. Eventually, the simulation results and the hardware platform are presented.

**Keywords** Motion controller · DSP · FPGA · Interpolation

## 1 Introduction

Truss robot is a kind of right-angle coordinate robot, which is suitable for different kind of tasks. It has the advantage that the actuator can bear heavy load, move fast, and precisely. Nowadays it has been widely used in the area of manufacturing through combining with machine tools.

The motion control system of truss robot needs to have quick and precise response to instructions so as to meet the actual demands. Presently, the motion control systems are mainly built from the following: (1) system based on a FPGA

---

P. Zheng (✉) · W. Chou · H. Zhou  
Department of BeiHang University, Beijing 100191, China  
e-mail: zhengpeng2120@yeah.net

W. Chou  
e-mail: wschou@buaa.edu.cn

H. Zhou  
e-mail: zhouhuaidong869@126.com

only [1–3]; (2) system which include an ARM as the processor and a FPGA as the coprocessor [4, 5]; (3) system which include a DSP as the processor and a FPGA as the coprocessor [6, 7].

This paper presents a motion control system based on the third topology, that is to say, a solution with a floating-point DSP and a FPGA. DSP takes charge of executing more complex control algorithms, and FPGA is responsible for tasks that need repetitive acquisitions and massive computations. In consideration of the response speed and programming flexibility, the third topology is more suitable for the motion control system comparing to the previous two topologies.

The paper is organized as follows. In the next section, we introduce the hardware structure of the controller, and it also involves how they cooperate with each other. In Sect. 3, the control algorithm of DSP and FPGA is presented. Section 4 introduces the platform of the experiment and also presents the simulation results. Eventually, we conclude the paper in Sect. 5.

## 2 System Overview

The architecture of the motion control system is shown in Fig. 1, and it also presents how the processor and the coprocessor cooperate with each other. As the floating-point DSP has strong capacity in real arithmetic and flexible software programming, TMS320F28335 is adopted as the processor of the system. Nevertheless the DSP has a serious disadvantage because of its limited amount of integrated periphery; it cannot handle all the external signals as needed. Comparing with DSP, FPGA can provide higher performances in repetitive and massive computations, and it can also deal with the mass of external signals as long as the pins of chip are enough. So, the EP4CE10E22C8 is used as the coprocessor of the system to cooperate with DSP.

As shown in Fig. 1, the electronic system is mainly divided into the processor module and the coprocessor module. The processor module takes charge of the communication with the PC, which includes accepting instructions and feeding back real-time velocity and position information of the target. Due to the data

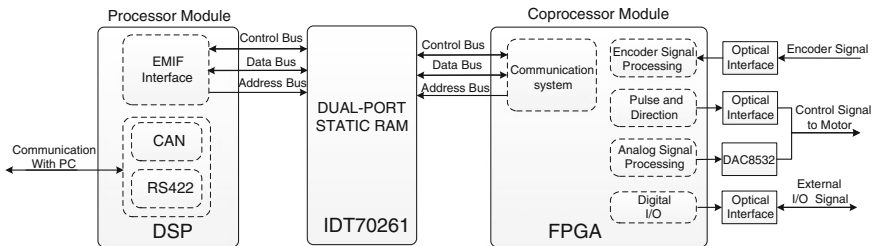


**Fig. 1** Block diagram of the control system



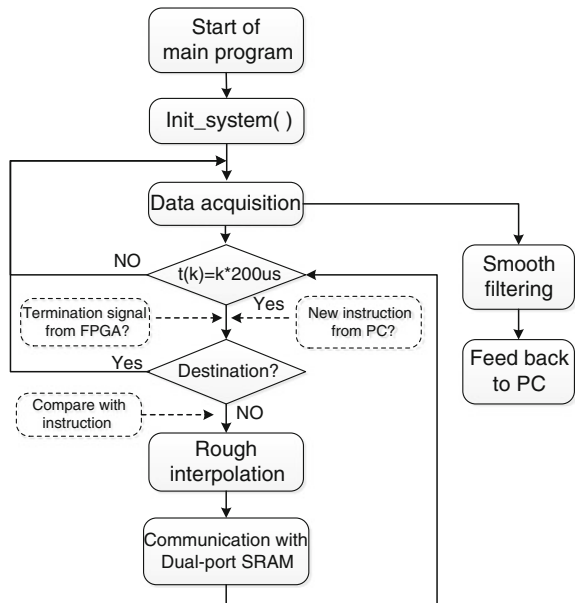
throughout between PC and DSP is not particularly high, this paper uses serial communication mode including CAN and RS422. However, the communication between DSP and FPGA needs large data throughout and high real-time response, so an IDT70261 which is a  $16K \times 16$  high-speed dual-port SRAM is adopted. It provides two independent ports with separate control, address, and I/O pins that permit independent, asynchronous access for reading or writing to any location in memory. Considering the sufficient storage and processing speed, IDT70261 is appropriate to be used to transfer data between DSP and FPGA. The coprocessor module plays the role of the assistance of DSP, which executes repetitive and massive computations. The FPGA accepts the interpolation data from DSP and performs the next fine interpolation; meanwhile it outputs the control instructions to the servo drivers by the way of analog voltage or pulse and direction. It also gathers the signals of the incremental encoders and some other sensors to ensure the rapidity and accuracy of the system.

### 3 Control Algorithm

#### 3.1 The Control Algorithm of DSP

Figure 2 shows the control algorithm of DSP, we can see, the system is initialized as soon as the main program is started.

Fig. 2 Flowchart of DSP control algorithm



Then the program performs data acquisition periodically while waiting for termination signals from FPGA or instructions from PC. During the period of data acquisition, DSP reads data from dual-port SRAM which is essential to execute the control algorithm and stored by FPGA. After DSP acquires the data, the program sends the featured data to PC after smooth filtering in order to display the real-time status of the system to operators. Once the termination signal from FPGA or new motion instruction from PC is detected, the program will judge whether the target is in position set by the PC. If the target is in position, the program will return to upper circulation. Or if not the program will perform the rough interpolation in the method of time splitting and store the interpolation points which will be instruction for FPGA to process the fine interpolation in dual-port SRAM.

### 3.2 The Control Algorithm of FPGA

The FPGA can be considered as the coprocessor of the control system. It is connected to DSP through a dual-port SRAM since the data throughput between them is fairly high. Figure 3 shows the block diagram of the design implemented in FPGA device which is explained in the following, such as the interface with IDT70261, encoder signals acquisition block, fine interpolation module, etc.

#### 1. Interface with Dual-port SRAM.

The function of the interface is to accept the data of rough interpolation and the control instructions of the fine interpolation, and also to feed back the real-time motion status of the mechanical system. These data are mainly stored and processed by the data buffer caches which contain a set of configuration and

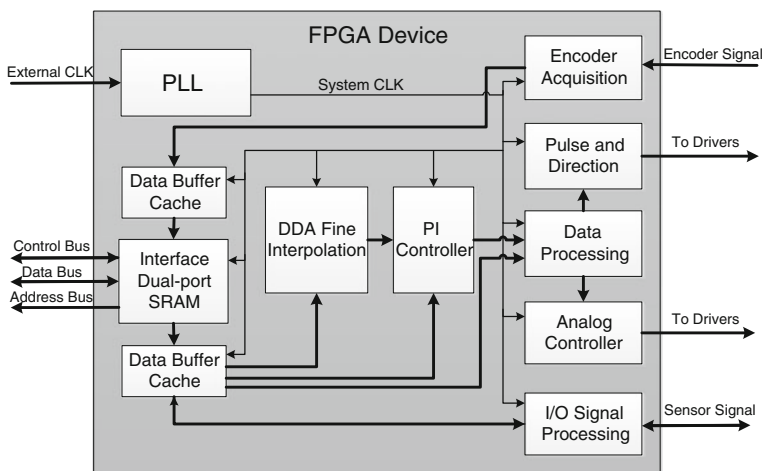


Fig. 3 Block diagram of design implemented in FPGA device

control registers with 16 bits. The other modules of FPGA device read and write the cache in order to control different ways of operation and to send the corresponding information to dual-port SRAM via the interface. For instance, the fine interpolation module reads the rough interpolation and control data, the PI controller reads the feedback data and the analog controller or the I/O processing module also needs the control instruction from the data buffer cache.

2. Fine interpolation module.

The primary advantages of digital differential analyzer are the high speed of calculation and the high uniformity of the pulses. It is convenient to realize multi-axis motion, or follow the trajectory of any functions.

In order to improve the precision of the trajectory, a method of half-preload to the integral accumulator is adopted, and the interpolation structure with half-preload is shown as Fig. 4. Interpolation with preload can make the overflow pulse more uniform, therefore, the actual motion trajectory is more close to theoretical trajectory.

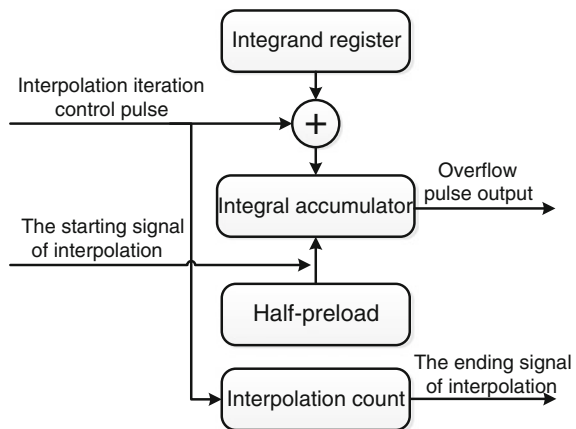
3. PI controller module.

The essence of achieving high-speed positioning in servo system is the quick response to the control instruction. While feedforward control can directly pass the instructions forward after processed, it can lead to the more quick response to the instructions. Figure 5 shows the schematic diagram of three-loop control with feedforward, which combines the classic three-loop position control with feedforward. The target acceleration, velocity, and position are computed by the interpolation module, and the actual status is provided to FPGA from motor drivers. In actual use, P algorithm is used in position loop control and PI algorithm is used in velocity loop and current loop. Finally the computed output instructions are sent to drivers after being processed.

4. Encoder acquisition block.

The signal of incremental photoelectric encoder consists of two pulse channels (CHA and CHB) and an index signal (CHI). The CHA and CHB pulses have

Fig. 4 DDA interpolation structure with half-preload



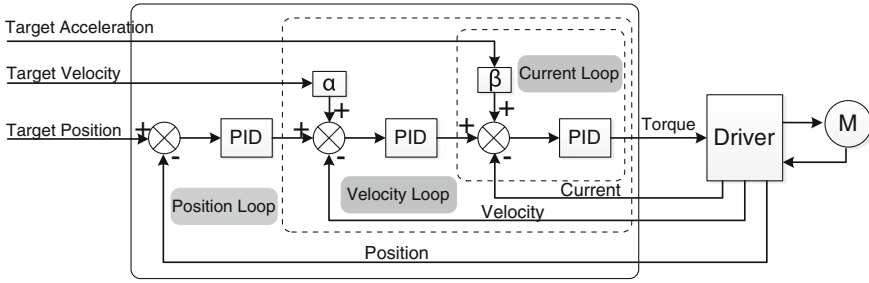


Fig. 5 Block diagram of three-loop control with feedforward

four state in a cycle (00, 01, 11, and 10), and the position of motor can be detected through a counter which operates when the state of CHA and CHB is changing. The rotation direction of motor can also be examined by the changing sequence of the state of CHA and CHB. The position value can be obtained directly by the counter of the pulse, whereas the velocity value needs to be calculated by an extra matched timer.

### 4 Simulation and Experimental Verification

Figure 6 shows a picture illustrating the view of the control electronic board assembly, where the main modules shown in Fig. 1 are indicated with red labels. The interfaces are connected to motor drivers, optical encoders, and PC.

The fine interpolation module is a critical control segment of the control system, which is performed in FPGA. Just as described before, the integral accumulator is

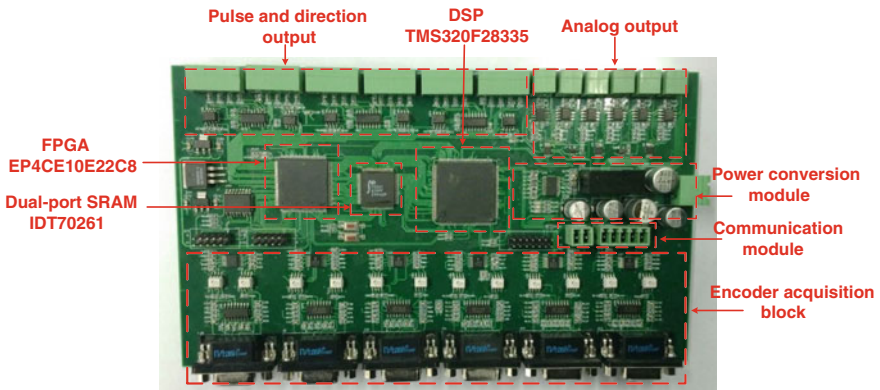


Fig. 6 Diagram of control electronic board

half-preloaded in order to improve the precision of the trajectory. The interpolation module compiled in Quartus II and the simulation wave carried out in Modelsim are shown in Fig. 7.

The encoder module accepts the CHA and CHB pulses of the encoder. It acquires the position of the motor through counting the number of pulses, and the velocity is calculated by the position counter and a matched timer. The rotation direction is output according to the changing sequence of the CHA and CHB. The packaged encoder module and simulation wave are shown as Fig. 8.

The function of the DAC module is to operate the output of DAC8532, which is a dual channel, 16-bit DAC offering a flexible serial host interface. The serial interface contains three signals, SCLK, SYNC, and DIN. SCLK is the serial input clock which is up to 30 MHz, SYNC is the frame synchronization which starts the conversion through accepting a falling edge and DIN is the serial data input. Figure 9 illustrates the packaged DAC module and the simulation wave.

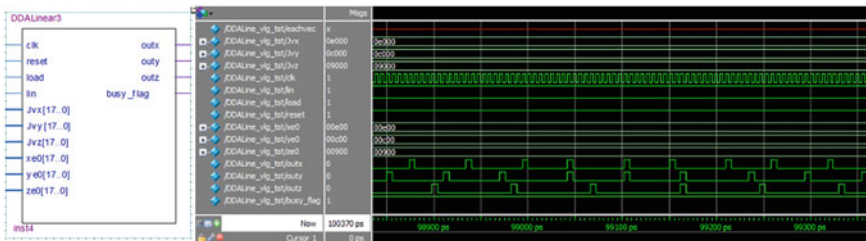


Fig. 7 Interpolation module and simulation wave in Modelsim

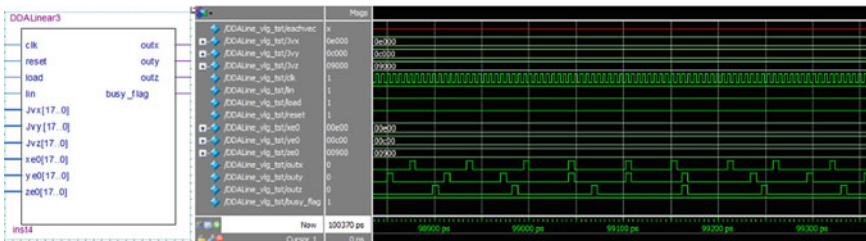


Fig. 8 Encoder acquisition module and simulation wave in Modelsim

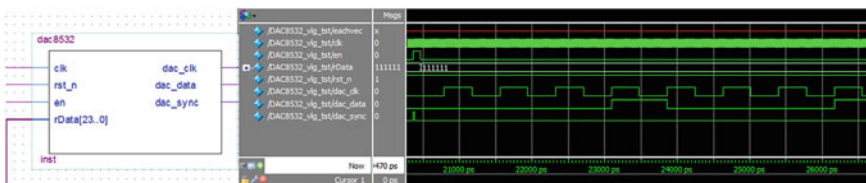


Fig. 9 DAC module and simulation wave in Modelsim

## 5 Conclusion

This paper presents a motion controller based on DSP and FPGA, and the design of hardware platform and the corresponding software programming have been finished preliminary. The simultaneous use of processor and coprocessor allows more flexibility on the development of the control system. The high-performance floating-point DSP ensures the response speed and calculation, meanwhile the FPGA meets the demand of the expansion of interfaces and its parallel processing method guarantees the speed as needed. In general, the controller can provide high processing speed and precise motion control, and it can meet the demand of the system.

**Acknowledgements** The authors are grateful for the support of China domestic research project for International Thermonuclear Experimental Reactor (ITER) Program under grant number 2012GB102006.

## References

1. Kung Y-S, Tseng K-H, Tai T-Y (2006) FPGA-based servo control IC for X-Y table, industrial technology. ICIT 2006
2. Oldknow KD, Yellowley I (2005) FPGA-based servo control and three-dimensional dynamic interpolation. *IEEE/ASME Trans Mechatron* 10(1):98–110
3. Shao X, Sun D (2005) A FPGA-based motion control IC design. In: Proceedings of the IEEE international conference on industrial technology, pp 131–136
4. Zhou M (2010) Design of embedded CNC device based on ARM and FPGA. In: The international conference on electrical engineering and automatic control (ICEEAC2010)
5. Tian J, Chen L, Kou X (2007) Design of embedded CNC system based on ARM and FPGA. *Mach Tool Hydraulics* 35(2)
6. Wu H, Pi Y (2011) The design and realization of motion controller based on DSP and FPGA. *Modular Mach Tool Autom Manuf Tech* 2
7. Li G, Ren D, Ge Y (2004) The development of the motion control board based on DSP and FPGA. *Mach Tool Hydraulics* 10

# Dynamic Characteristics of Wind Turbine Gearbox with the Chipping Fault

Xin Wang, Yuxiu Xu and Taotao Li

**Abstract** Studying on modulation characteristics of the transmission system to extract side frequency signals caused by the fault has important implications for planetary gearbox fault diagnosis. A torsion dynamics model of gearbox transmission system is established by lumped mass method with simulated planetary gear chipping fault through periodic pulse function. Using the Runge-Kutta method solved the equations to study the dynamic fault characteristics under the planetary chipping fault. Experimental results show: the planetary gear chipping fault can cause a large number side frequency around planetary mesh frequency, which also appears around first, second stage mesh frequency and its harmonic frequencies. The results of experimental signal analysis are the same with the theoretical analysis, so we can diagnose planetary chipping fault applying spectral analysis method.

**Keywords** Wind turbine · Planetary gearbox · Dynamics model · Chipping fault

---

X. Wang (✉) · Y. Xu  
School of Mechanical Engineering,  
Tianjin Polytechnic University, Tianjin 300387, China  
e-mail: 46607190@qq.com

Y. Xu  
e-mail: xuyu@tjpu.edu.cn

X. Wang · Y. Xu  
Key Laboratory of Advanced Mechatronics Equipment Technology,  
Tianjin 300387, China

T. Li  
Sany Heavy Energy Machinery Co., Ltd., Beijing 102206, China  
e-mail: litaotao124@163.cn

## 1 Introduction

Since the planetary gearbox signal is faintness, its fault signal is difficult to identify when coupling with the fixed-axis gearbox signal in the transmission system. Together with large noise signal interference, fault diagnosis for planetary gearbox is prone to make mistake judge. Therefore, it is necessary to study the coupled vibration characteristics of transmission systemic and find out the side frequency caused by planetary fault in coupling signal.

Feng et al. [1, 2] established a vibration signal model with planetary gearbox fault and derived Fourier spectrum expressions of the vibration signal. Datong et al. [3, 4] established a torsion dynamics model and a coupling dynamic model of gearbox transmission system. Mohanty [5] studied the dynamic signal characteristics of planetary chipping fault from the experimental point of view. Vicuña [6] analyze the spectral characteristics of in-phase and out-of-phase gear mesh processes through the vibration signal model. Most current researches are experimental simulations for the gearbox transmission system. It is rare to study the theory for wind turbine gearbox coupled transmission system, not to mention the research of planetary fault characteristics. There are huge difference between fault vibration signal characteristics of planetary gearbox and fixed-axis gearbox. Single pair gear dynamics model [7, 8] unable to describe the mix effect of dynamic signal and correctly extract the fault side frequency under coupling condition. Therefore, it needs to study the spectral characteristics of planetary gearboxes vibration signal, especially under fault conditions, so that to achieve the purpose of planetary gearbox fault diagnosis through the fault characteristics frequency components.

## 2 Nonlinear Dynamics Model of Gear Systems with Fault Parameters

The transmission system in this study is a wind turbine gearbox test rig with a two-stage fixed-axis gearbox and a one-stage planetary gearbox. The load is transmitted through the sun gear to the planets, which ride on a planetary carrier. The planetary carrier, in turn, transmits torque to the output shaft. Fixed-axis gears are all spur gears.



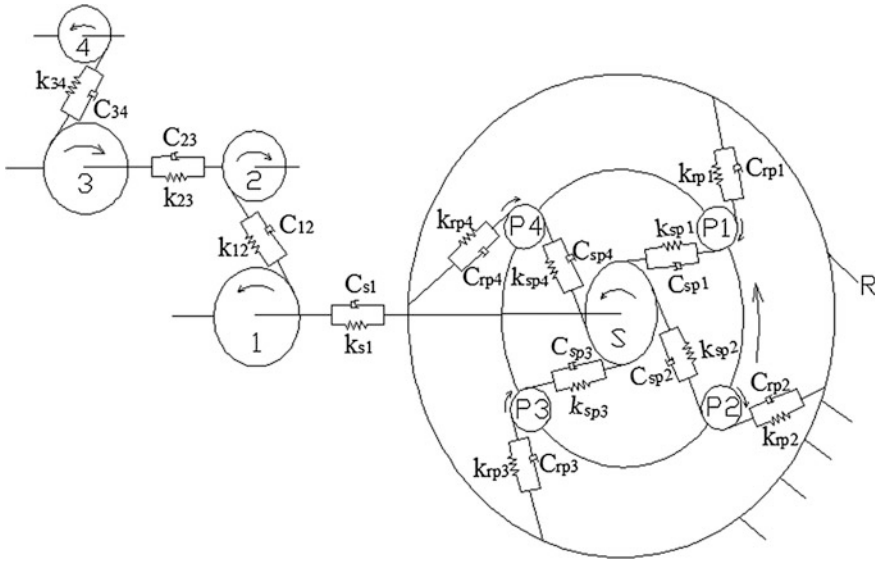


Fig. 1 A torsion dynamics model of gear transmission system

### 2.1 Lumped Mass Model

A torsion dynamics model of gear transmission system is established by lumped mass method with mesh parameters simulated by springs and dampers, which does not consider transverse vibration displacements, as show in Fig. 1.

According to the established model, the elastic deformation along the meshing line is:

$$\begin{cases} \delta_{spi} = u_c \cos \alpha_{sp} - u_{pi} - u_s \\ \delta_{rpi} = u_{pi} - u_r + u_c \cos \alpha_{rp} \\ \delta_{12} = u_1 - u_2 \\ \delta_{34} = u_3 - u_4 \end{cases} \quad (1)$$

where  $u_c, u_r, u_s, u_{pi}, u_1, u_2, u_3, u_4$  describe the displacement of planetary carrier, ring gear, sun gear, spur gear 1, 2, 3, 4.  $\delta_{spi}, \delta_{rpi}, \delta_{12},$  and  $\delta_{34}$  are the elasticity distortion in gear mesh direction between two gears.  $\alpha_{sp}, \alpha_{rp}$  are the pressure angle. According to Lagrange equation deduced the system vibration differential equations as formula (2):

$$\left\{ \begin{aligned}
 & (I_c/r_{bc}^2)\ddot{u}_c + \sum_{i=1}^4 C_{rpi} \cos \alpha_{rpi} \dot{\delta}_{rpi} + \sum_{i=1}^4 C_{spi} \cos \alpha_{spi} \dot{\delta}_{spi} + C_{uc}\dot{u}_c \\
 & + \sum_{i=1}^4 k_{rpi}(t) \cos \alpha_{rpi} \delta_{rpi} + \sum_{i=1}^4 k_{spi}(t) \cos \alpha_{spi} \delta_{spi} + k_{uc}u_c = F_{in} \\
 & (I_{pi}/r_{bpi}^2)\ddot{u}_{pi} - C_{spi}\dot{\delta}_{spi} + C_{rpi}\dot{\delta}_{rpi} - k_{spi}(t)\delta_{spi} + k_{rpi}(t)\delta_{rpi} = 0 \\
 & (I_s/r_{bs}^2)\ddot{u}_s - \sum_{i=1}^4 C_{spi}\dot{\delta}_{spi} + C_{s1}(\dot{u}_s/r_{bs}^2 - \dot{u}_1/r_{bs}r_{b1}) - \sum_{i=1}^4 k_{spi}(t)\delta_{spi} \\
 & + k_{s1}(u_s/r_{bs}^2 - u_1/r_{bs}r_{b1}) = F_s \\
 & (I_1/r_{b1}^2)\ddot{u}_1 + C_{12}\dot{\delta}_{12} + C_{s1}(\dot{u}_1/r_{b1}^2 - \dot{u}_s/r_{bs}r_{b1}) + k_{12}(t)\delta_{12} \\
 & + k_{s1}(u_1/r_{b1}^2 - u_s/r_{bs}r_{b1}) = F_1 \\
 & (I_2/r_{b2}^2)\ddot{u}_2 + C_{12}\dot{\delta}_{12} + C_{23}(\dot{u}_2/r_{b2}^2 - \dot{u}_3/r_{b2}r_{b3}) + k_{12}(t)\delta_{12} \\
 & + k_{23}(u_2/r_{b2}^2 - u_3/r_{b2}r_{b3}) = F_2 \\
 & (I_3/r_{b3}^2)\ddot{u}_3 + C_{34}\dot{\delta}_{34} + C_{23}(\dot{u}_3/r_{b3}^2 - \dot{u}_2/r_{b2}r_{b3}) + k_{34}(t)\delta_{34} \\
 & + k_{23}(u_3/r_{b3}^2 - u_2/r_{b2}r_{b3}) = F_3 \\
 & (I_4/r_{b4}^2)\ddot{u}_4 + C_{34}\dot{\delta}_{34} + k_{34}(t)\delta_{34} = F_{out}
 \end{aligned} \right. \tag{2}$$

$$F_{in} = T_{in}/r_{bc}, F_s = T_s/r_s, F_1 = T_1/r_1, F_2 = T_2/r_2, F_3 = T_3/r_3, F_4 = T_4/r_4.$$

where  $I_i$  ( $i = c, p, s, 1, 2, 3, 4$ ) are the rotational inertias of gears,  $r_{bi}$  ( $i = c, p, s, 1, 2, 3, 4$ ) are the radiuses of gears,  $k_{spi}(t)$ ,  $k_{rpi}(t)$ ,  $k_{12}(t)$ ,  $k_{34}(t)$  are the meshing stiffness coefficients of the gear mesh,  $k_{s1}$ ,  $k_{23}$ ,  $k_{uc}$  are the torsional stiffness coefficients of the gear mesh,  $C_{spi}$ ,  $C_{rpi}$ ,  $C_{12}$ ,  $C_{34}$ ,  $C_{s1}$ ,  $C_{23}$  are the damping coefficients of the gear mesh,  $T_{in}$ ,  $T_s$ ,  $T_1$ ,  $T_2$ ,  $T_3$ ,  $T_4$  are the torsions of gears.

### 2.2 Time-Varying Mesh Stiffness

When the gear system has a fault, the corresponding parameters must be changed along with the fault. When the gear exists chipping, the corresponding stiffness will be weakened at the single tooth, and the other teeth stiffness invariable. Therefore, periodic pulse function is used to represent a single tooth fault, which functions as

$$k_i(t) = 1 + \varepsilon \cos(\omega t + \varphi) - a\delta(t) \tag{3}$$

where the cycle of the periodic pulse  $a\delta(t)$  is once rotation time of gear, pulse width ratio is  $1:N$  ( $N$  is the tooth number), amplitude  $a$  represents the faulty degree of single tooth stiffness.

### 3 Example Simulation Calculation

According to the data of wind turbine gear transmission test rig, the simulation results are carried out, where the wind turbine gearbox transmission characteristic frequencies are in Table 1.

The Runge-Kutta method is used to calculate the time domain and frequency domain curves of displacement at the gear mesh point under the normal state. Taking  $a = 0.4$  simulate the planetary gear tooth fault, by substitution formula (3) into formula (2) to calculate the time domain and frequency domain curves of displacement on the gear mesh point under the fault state. The time domain and frequency domain diagram of the planetary gear under normal and fault condition are shown in Fig. 2.

Figure 2c shows the dominant peaks in the envelope spectrum corresponding exactly to the expected frequencies, i.e., the first stage mesh frequency  $f_1$ , the

**Table 1** The wind turbine gearbox transmission characteristic frequencies

Gear	Mesh frequency Hz
First stage fixed-axis gear $f_1$	1160
Secondnd stage fixed-axis gear $f_2$	417.6
Planetary gearbox $f_3$	101.5
Planetary fault frequency $f_r$	2.8

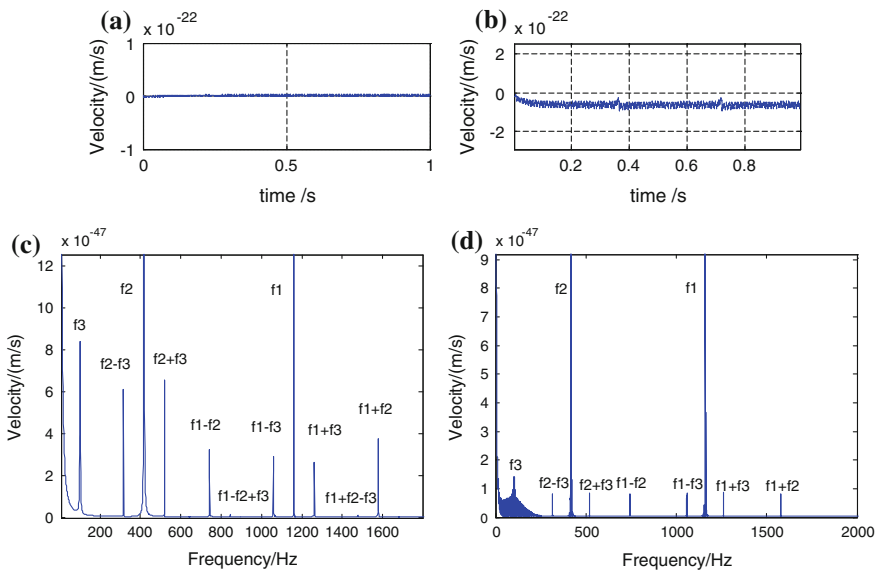


**Fig. 2** Simulated signal and analysis result: **a** normal, **b** a chipping tooth, **c** normal, **d** a chipping tooth

second stage mesh frequency  $f_2$ , the third stage (planetary) mesh frequency  $f_3$ . The main frequency are  $f_1, f_2, f_3$ . The secondary frequencies are their combinations  $f_1 \pm f_2, f_2 \pm f_3$ , and  $f_1 \pm f_3$ . While the amplitude of combinations  $f_1 \pm f_2 \pm f_3$  are too small, the peaks are not obvious. Meanwhile, there is no doubling frequency. The side frequency distribution of the secondary frequency  $f_1 \pm f_2$  is asymmetric and irregular, which is caused by the frequency superposition of AM and FM. From the whole view, the higher peaks are the first stage and second stage mesh frequency, the third stage planetary gear meshing frequency peak is minimum. This result is the same with the actual gearbox vibration signal where the planetary gearbox fault signal is the most difficult to identify.

From Fig. 2d can be seen as a large number of sidebands appeared around the planetary gear mesh frequency when the chipping fault occurs, with interval of planetary gear fault frequency  $f_r$ . There are also smaller sidebands around the first stage and second stage mesh frequency. Moreover, the chipping fault also caused the minor changes in the amplitude of the meshing frequency and its combinations.

#### 4 Experimental Signal Analysis

The test rig of the wind turbine gear transmission system is shown in Fig. 3, with 40 % faulty degree of the planetary gear in a single tooth.

Since the signal of experiments is often noisy, the useful information of spectra can be drowned in the noise, and the calculation of the chaos parameters is very sensitive to the noise. Therefore, the signal must reduce noise to enhance the accuracy of the spectrum analysis and chaotic parameters. Because the noise reduction by wavelet method is suitable for the nonlinear signal, the author adopts

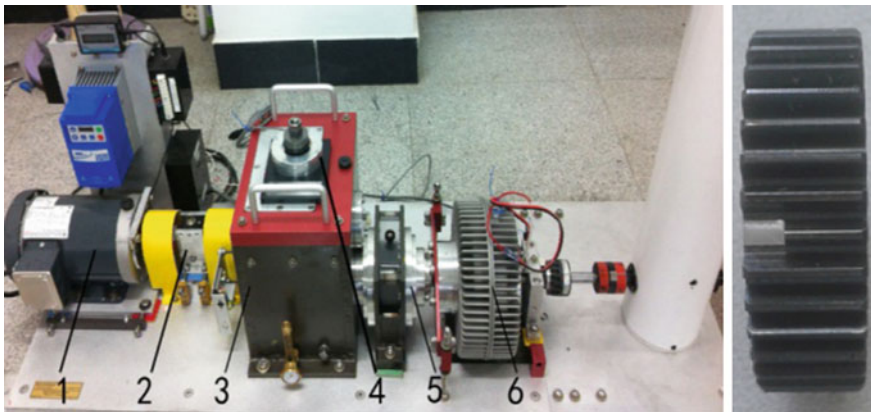


**Fig. 3** The transmission system of wind turbine and fault planetary gear. 1 Motor, 2 Torque sensor and encoder, 3 Two-stage fixed-axis gearbox, 4 Radial load of bearing, 5 Planetary gearbox stage 1, 6 Brake

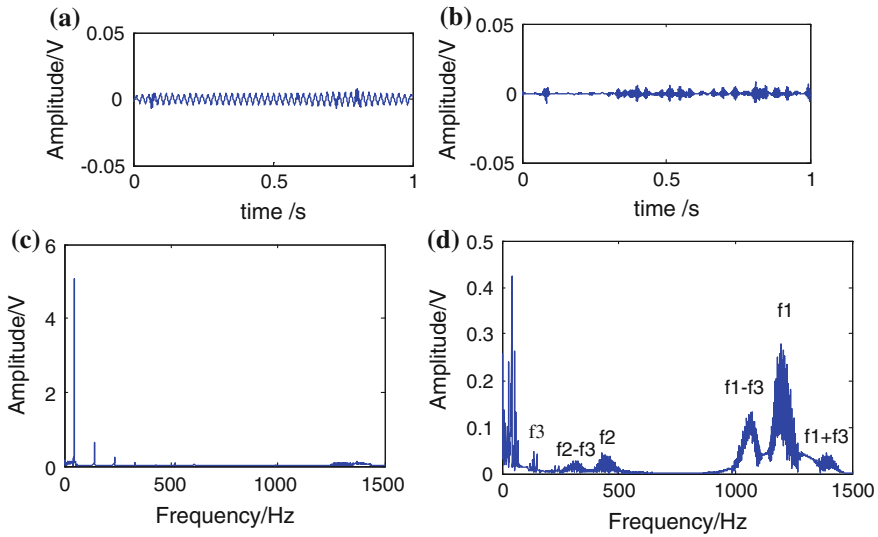


**Fig. 4** Test signal and analysis result: **a** normal, **b** a chipping tooth, **c** normal, **d** a chipping tooth

the wavelet method to improve the test data. Figure 4 is the time domain and frequency domain diagram of the planetary gearbox under the normal and chipping fault condition after noise reduction.

Figure 4d shows a large number of sidebands appeared around the planetary gear meshing frequency when the chipping fault occurs, with interval of planetary gear fault frequency  $f_r$ . There are also abundant sidebands around the first stage and second stage mesh frequency. Compared with the normal spectrum, the fault spectrum appears the peak frequency of  $f_2 \pm f_3$ ,  $f_1 \pm f_3$ , and their sidebands. The amplitude of meshing frequency and its sidebands have increased significantly. Those characteristics correspond with the simulation, and diagnose the planetary gear chipping fault.

## 5 Conclusions

Through the establishment of the gearbox torsional dynamics model, the coupling relationship between the gears is studied. The chipping fault of the planetary gear is simulated, and the signal characteristics of the planetary gear fault are summarized. Planetary gear chipping fault can cause a large number side frequency around planetary mesh frequency, which also appears around first and second stage mesh frequency and its harmonic frequencies. The results of the theoretical analysis are verified by analyzing the testing signal data of the planetary chipping fault. According to the side frequency of spectrum, the planetary chipping fault can be diagnosed.

**Acknowledgements** This work is supported by the major Fund Project for Transformation of Scientific and Technological Achievements from National (2060403), Natural Science Foundation of Tianjin (10JCZDJC23400, 13JCQNJC07000).

## References

1. Feng Z, Zuo MJ, Qu J et al (2013) Joint amplitude and frequency demodulation analysis based on local mean decomposition for fault diagnosis of planetary gearboxes. *Mech Syst Signal Process* 40:56–75
2. Feng Z, Zuo MJ (2013) Fault diagnosis of planetary gearboxes via torsional vibration signal analysis. *Mech Syst Signal Process* 36:401–421
3. Datong Q, Wei L, Jun Y et al (2012) Dynamic characteristics of wind turbine transmission system under varying wind speed and operation control conditions. *J Mech Eng* 48(7):1–8
4. Datong Q, Miaomiao T, Jun Y (2012) Study on dynamic characteristics of gear transmission system of wind generator under varying wind load. *Acta Energiæ Solaris Sinica* 33(2):190–196
5. Mohanty AR, Kar C (2006) Fault detection in a multistage gearbox by demodulation of motor current waveform. *IEEE Trans Industr Electron* 53(4):1285–1297
6. Vicuña CM (2014) Vibration characteristics of single-stage planetary gear transmissions. *Revista Chilena de Ingeniería* 22(1):88–98
7. Yangang W, Haiqi Z, Yang T et al (2010) Non-linear dynamic characteristics of gear system with single-tooth fault. *J Vib Meas Diagn* 30(6):654–656
8. Ma R, Chen Y, Cao Q (2012) Research on dynamics and fault mechanism of spur gear pair with spalling defect. *J Sound Vib* 331:2097–2109

# Demonstration for Low Cost Wireless Smart Sensor Networks Based on ARM for Structural Health Monitoring

Jian Xu, Wenhao Wan, Yuying Wu and Zhaoyu Sun

**Abstract** As a potential replacement of the traditional tethered system, wireless smart sensor networks (WSSNs) attract a lot of interests and have many applications, especially in civil engineering for structural health monitoring (SHM). However, many wireless sensor networks are based on some commercial wireless communication board and other sensor boards which need to be connected on it are expensive. Based on our previous research, this paper gives and demonstrates a proposal to make a low cost and low power wireless smart sensor using ARM Cortex™-M3 and some low cost and low power components. A new simple protocol is developed to realize reliable wireless communication between the gate way node (GWN) and the leaf node (LN) and an user interface on the PC client is also developed for displaying the measured results in real time.

**Keywords** Wireless smart sensor networks · Structural health monitoring · Low cost design · Gate way node · Leaf node

## 1 Introduction

Due to the aging civil infrastructures, the structural health monitoring (SHM) has attracted a lot of attention [1]. More and more researchers work on this area in order to develop approaches for continuously monitoring the health of essential infras-

---

J. Xu (✉) · W. Wan · Y. Wu · Z. Sun  
School of Electrical and Electronic Engineering, Wuhan Polytechnic Univeristy,  
Wuhan 430023, China  
e-mail: xujian01@gmail.com

W. Wan  
e-mail: wwh0518@qq.com

Y. Wu  
e-mail: wuyuying0913@gmail.com

Z. Sun  
e-mail: sunzhaoyu2012@gmail.com

tructures even the living facilities. The most attractive technology is using wireless smart sensor networks (WSSN) and there are many successful implementations of WSSN for full-scale and long-term SHM applications [2–6]. However, many WSSNs focus on the strain detection and use the commercial wireless hardware platform such as MEMSIC’s Mica2 or MEMSIC’s iMote2 [7–9], which leads the high cost of WSSNs and depends on the platform owner. Furthermore, the size and power consumption are fixed and cannot be changed according to specific applications. However, for the long-term SHM, low consumption sensor networks are very critical. This paper pays attention on the development of low cost platform of the WSSNs. Based on the power efficient and high performance ARM Cortex™-M3 chip, a low cost and low power design for WSSNs is presented and demonstrated with temperature sensor and humidity sensor.

## 2 Hardware Design

According to our previous research on wireless sensor networks [10], we use the similar design process on the ARM platform due to its widely use and potential to the future mobile applications for the WSSNs. Considering its low power consumption and high performance, ARM Cortex™-M3 is chosen for this study. Figure 1 shows the block diagram for the design. There are two parts of the

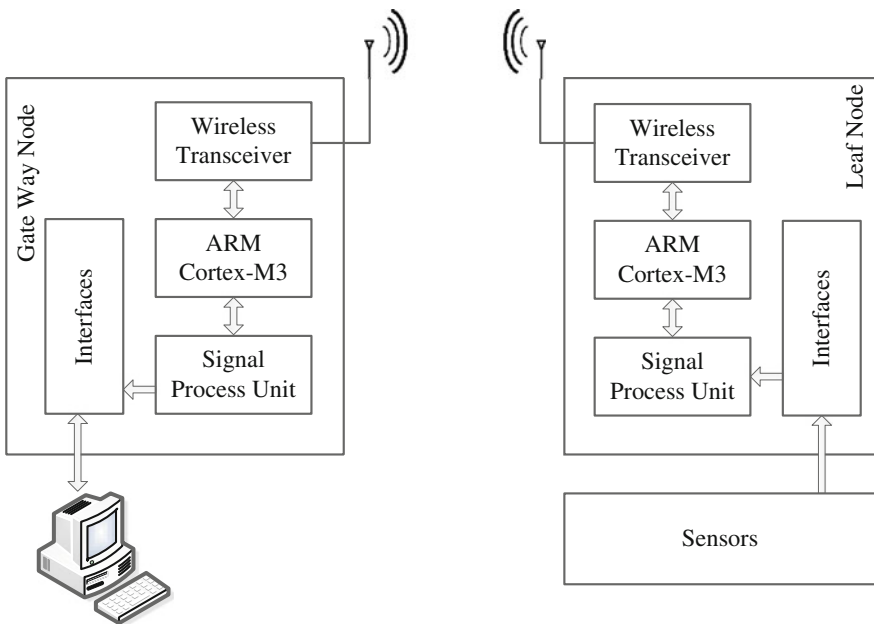


Fig. 1 Block diagram of hardware design



WSSNs. One is the gate way node (GWN) and the other is the leaf node (LN). Their configurations are similar but they have different functions.

For the LNs, the sensors will monitor the parameters related to the health of structures and then the detected signal will be transferred to the signal process unit (SPU) through the interface. Generally, the SPU on LNs consists of amplifiers and A/D converters which are used to amplify the detected signals and convert analog signals to digital signals to be processed by the CPU, and then, the digital signals, which are the data, will be sent to the wireless transceiver and are transmitted out through the antenna. On the LNs side, all the processes are controlled by the ARM Cortex™-M3.

On the GWN side, when the transceiver detects wireless signals from LNs (there is a protocol to identify this signal), the data will be received and processed by the CPU which is also ARM Cortex™-M3. Then the data will be sent to user's computer through SPU and the interface for postpone processing. Here, the SPUs are responsible for the communication between the GWNs and the user computer for the postpone processing.

In this design, the sensors part on the right side of Fig. 1, according to their characterizations, can be directly connected to the LNs with proper design for the SPU, or the LNs can be made general while the sensors should have their own SPUs. Actually, both of them can be implemented to the WSSNs system by changing the design of the interfaces.

For one WSSN, all the LNs will communicate with one GWN, and for many WSSNs, the GWNs will also communicate with each other and there is one GWN assigned as the top node to communicate with the terminal PC. This topology has been shown in our previous research in Ref. [10].

### 3 Hardware Configuration

In order to demonstrate this design, two evaluation boards (each one contains LM3S811—the ARM Cortex™-M3 CPU) are used to execute the data processing and control. Sensors used for this demonstration are temperature sensor DS18B20 and the humidity sensor HIH5030. Because the evaluation boards already have the interfaces connected to the CPU and there is no need to employ other SPUs, the sensors can be directly connected to the boards by wires.

As the evaluation boards have no transceivers, two small transceiver driver boards, on which there are just the transceiver chip and its necessary discrete components such as resistors and capacitors, are employed. In this demonstration, the transceiver chip is CC1100 due to its low cost, low power, and easy to use. And the maximum transceiving distance can be up to 500 m. Figure 2 shows the test field for the demonstration. Where, the left side is the GWN and the right side is the LN. Both of them use 433 MHz to communicate.

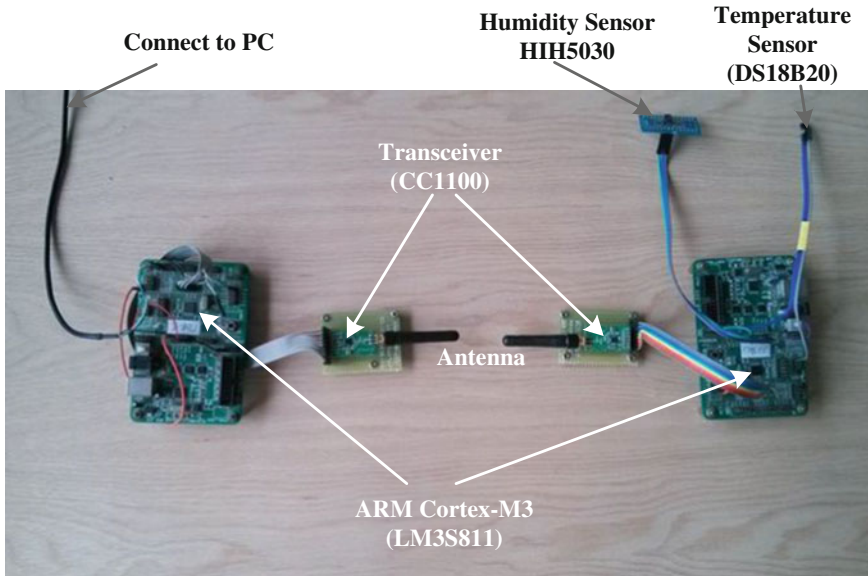


Fig. 2 Test field for the hardware design

## 4 Experiment

Under the hardware configuration shown in Fig. 2, a simple wireless communication protocol and a user interface on the PC client to drive the GWN and display the measurement results in real-time are developed. Because there are two sensors in this demonstration, wireless measurements are executed one by one. Whenever the LN wants to communicate with the GWN, there is an identification process to check if the communication is valid. Figures 3 and 4 show the wireless measurement results for temperature monitoring and humidity monitoring, respectively. Where, the red line is for the temperature by degree C with right axis and the green line is for the relative humidity (RH-%) with left axis and they are also shown digitally and simultaneously on the top of the figures. The other parameters for the communication between GWN and PC are shown on the right side of the figures.

In the experiment, for testing the temperature monitoring, some warm air is used to blow to the temperature sensor. The results display in the software on PC which is shown in Fig. 3. Where, the red line increases according to the temperature of the air. For testing the humidity monitoring, the humidity sensor is put on the top of a bottle of boiled water. Then on PC, the green line in the software increases which is shown in Fig. 4. However, because the two sensors are near each other and there is humidity for the air, when blowing the warm air to the temperature sensor, the humidity sensor is also affected a little bit. Then the humidity fluctuates which is as shown in Fig. 3.

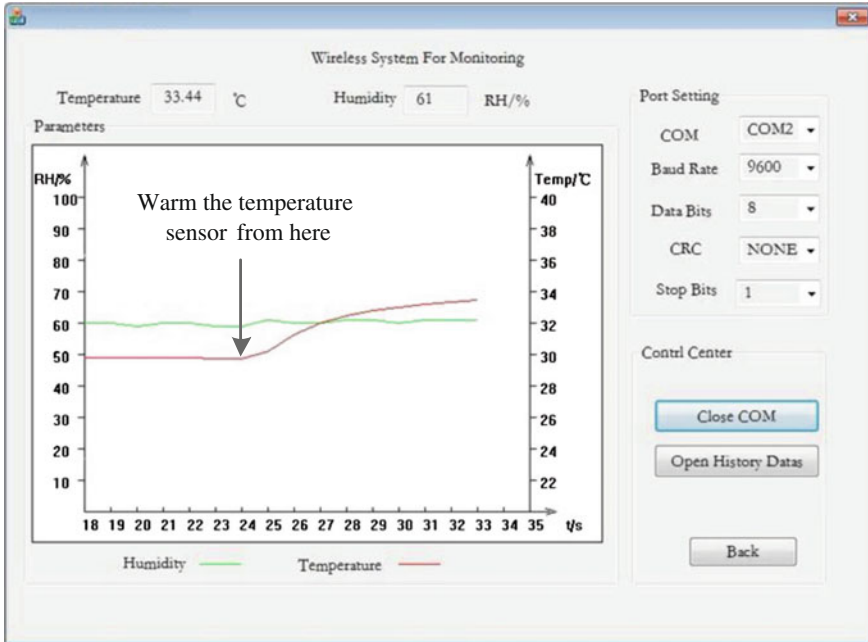


Fig. 3 Wireless measurement for temperature

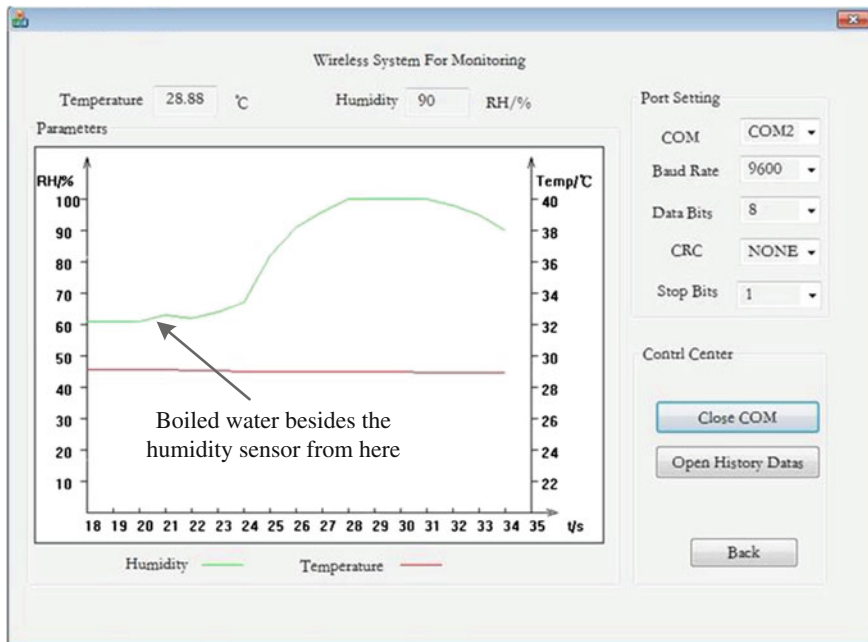


Fig. 4 Wireless measurement for humidity

In this demonstration of the proposal, the interval between the two measurements is set to 1 s to identify the reliability. Experimental results show that both the temperature and humidity can be displayed in real-time under indoor test. In addition, checking by browsing the original data verifies this conclusion.

## 5 Conclusions

Aimed on the low cost WSSNs for the SHM applications, a design based on ARM Cortex™-M3 is proposed. To demonstrate this design, some low cost and low power consumption components are used and a new simple protocol is created to realize the wireless communication between the GWN and the LN and a user interface on the PC client is also developed for displaying the measurement results for monitoring in real time. Wireless measurements by employing the temperature sensor and the humidity sensor are executed. All the test results demonstrate the design for the WSSNs and it can be practically implemented for the SHM applications. Furthermore, based on the widely using ARM core in smartphones, this design has the potential to work with smartphones via proper apps in the future.

**Acknowledgments** The author would like to thank the financial support of the National Natural Science Foundation of China (No. 61404095 and No. 11204223) and the Talent Scientific Research Foundation of Wuhan Polytechnic University (No. 2012424 and No. 2014728).

## References

1. Chang PC, Flatau A, Liu SC (2003) Health monitoring of civil infrastructure. *Struct Health Monit* 2(3):257–267
2. Cho S, Jo H, Jang SA, Park J, Jung HJ, Yun CB, Spencer BF Jr, Seo J (2010) Structural health monitoring of a cable-stayed bridge using smart sensor technology: data analyses. *Smart Struct Syst* 6(5–6):461–480
3. Jang SA, Jo H, Cho S, Mechtov KA, Rice JA, Sim SH, Jung HJ, Yun CB, Spencer BF Jr, Agha G (2010) Structural health monitoring of a cable stayed bridge using smart sensor technology: deployment and evaluation. *Smart Struct Syst* 6(5–6):439–459
4. Kurata M, Kim J, Zhang Y, Lynch JP, Linden GW, Jacob V, Thometz E, Hipley P, Sheng LH (2010) Long-term assessment of an autonomous wireless structural health monitoring system at the New Carquinez Suspension Bridge. In: *Proceedings of the SPIE, San Diego*
5. Whelan MJ, Gangone MV, Janoyan KD, Hoult NA, Middleton CR, Soga K (2010) Wireless operational modal analysis of a multi-span prestressed concrete bridge for structural identification. *Smart Struct Syst* 6(5–6):579–594
6. Zonta D, Wu H, Pozzi M, Zanon P, Ceriotti M, Mottola L, Picco GP, Murphy AL, Guna S, Corra M (2010) Wireless sensor networks for permanent health monitoring of historic buildings. *Smart Struct Syst* 6(5–6):595–618
7. Choi H, Choi S, Cha H (2008) Structural health monitoring system based on strain gauge enabled wireless sensor nodes. In: *Proceedings of the 5th international conference on networked sensing systems*

8. Meyer J, Bischoff R, Feltrin G, Motavalli M (2010) Wireless sensor networks for long-term structural health monitoring. *Smart Struct Syst* 6(3):263–275
9. Nagayama T, Ruiz-Sandoval M, Spencer BF, Mechtov KM, Agha G (2004) Wireless strain sensor development for civil infrastructure. In: *Proceedings of the 1st international workshop on networked sensing systems*, Tokyo, Japan
10. Xu J, Wan W, Zhang T (2014) Wireless sensor networks for structural health monitoring application—a design proposal. 511–512:130–133

# Risk Study on Long-Distance Oil and Gas Pipelines Engineering

Shujiao Tong, Zongzhi Wu, Rujun Wang and Yingquan Duo

**Abstract** Accidents such as leakage, fire, and explosion have happened occasionally in the long-distance oil and gas pipelines engineering in these years. Those accidents have caused large casualties, wealth loss, and environment pollution. So it is necessary to study the risk of the pipeline engineering in order to better avoid accidents and minimize losses of the long-distance oil and gas pipelines engineering. Based on the system safety theory, experts' advices, and survey data, a comprehensive risk analysis and assessment of oil and gas pipeline engineering was carried out in this paper. From humans, materials, environment, and management four aspects, 32 risk factors were identified and assessed by combining the possibility with the severity of those identified risks. The risk level of the oil and gas pipelines was divided into five degrades from low to high. The proposed method was then applied to a natural gas pipeline engineering to identify and assess the risk of each pipe of the selected long-distance natural gas pipeline engineering. As a result, the earthquakes, avalanches, tunnel construction, and third party liability were the higher risk factors, and the risk of the forth pipe was the highest and should strengthen the risk management. Finally, some suggestions were proposed to the safety and risk management of the oil and gas pipelines engineering. The risk assessment method was thus proved to be a powerful tool to the risk decision-making and management of the long-distance oil and gas pipelines.

**Keywords** Oil and gas pipelines · Risk identification · Risk assessment · Risk management

---

S. Tong (✉) · R. Wang · Y. Duo  
China Academy of Safety Science and Technology, Key Laboratory of Major Hazard Control and Accident Emergency Technology, State Administration of Work Safety, Beijing 100012, China  
e-mail: tongshujiao@mail.neu.edu.cn

Z. Wu  
State Administration of Work Safety, Beijing 100713, China

© Springer-Verlag Berlin Heidelberg 2016  
B. Huang and Y. Yao (eds.), *Proceedings of the 5th International Conference on Electrical Engineering and Automatic Control*, Lecture Notes in Electrical Engineering 367, DOI 10.1007/978-3-662-48768-6\_66

## 1 Introduction

With the rapid development of petrol industry and economy, China has become an exporter of energy from an energy input country. It is well-known that energy is a very important factor in the relationship between the national strategies. In order to ensure energy safety and avoid accidents, China has been vigorously carried out the strategic reserve and construction of oil and gas pipeline engineering in last decades [1, 2]. At present, most researches are focused on the oil and gas pipelines in-service, and less on the pipelines engineering [3–5]. Well, there are many risk factors such as the third party damage, corrosion, and mechanical damage, geological disaster, and so on in the process of the construction of oil and gas pipelines engineering. These risk factors are likely to lead to accidents, and even cause large numbers of casualties, property loss, and damage to the environment. Therefore, in order to avoid and minimize risks, prevent, and reduce construction accidents of the oil and gas pipelines, it is necessary to study the risk of oil and gas pipelines engineering.

Risk identification and assessment are the foundation of risk management. The risk decision of oil and gas pipelines can be obtained through qualitative analysis and quantitative calculation. The purpose of the risk assessment is to identify the risk by calculating the values of those identified risk during the process of the system. So the risk assessment result can provide the basis for the risk decision-making and management. Methods of risk assessment mainly include qualitative, semiquantitative, and quantitative methods [6]. At present, these methods have been applied extensively in the risk identification and assessment of the oil and gas pipelines. Representative qualitative assessment methods include safety check list (SCL), analogy analysis, fault mode, effect analysis (FMEA), and so on [7]. Typical semiquantitative methods include kent scoring, fault tree analysis (FTA), event tree analysis (ETA), etc [8, 9]. On comparing with the above methods, the quantitative risk assessment is the best accurate method that needs to consider the probability of and the consequences of the risk [10].

In order to improve the risk management, a comprehensive risk analysis can be made based on the system safety theory [11] from people, objects, environment, and management four aspects. On accounting of the qualitative analysis of all kinds of risk factors, the risk level of each pipe of pipeline can be quantitated from the likelihood and severity of each risk factor to analysis and assess the risk of the pipeline. In this paper, a natural gas pipeline engineering was studied as an example, the risk of each pipe of the selected gas pipeline was identified and assessed by applying the proposed method. The result of the study is helpful to the risk decision-making and management of the long-distance oil and gas pipelines engineering.

## 2 Risk Identification of Oil and Gas Pipeline Engineering

### 2.1 Risk Identification Method

There are many risks in the long-distance oil and gas pipelines engineering, such as third party damage, corrosion, overpressure, construction damage, equipment failure, pipe defects, disoperation, natural and geological disasters, etc. The risk factors of long-distance oil and gas pipelines in America are divided into 5 categories and 37 items. The risk factors in Canada are divided into 7 categories and 30 items. The risk factors in Europe are divided into 6 categories and 20 items [12]. But the above classifications are mainly according to the type of risk factors, which is less conducive to risk management in the long-distance oil and gas pipelines engineering practice.

It is well-known that the long-distance oil and gas pipeline engineering is a large and complex system, risks emerging in the construction process are various and different in different pipes. So people must adopt a comprehensive risk identification method to avoid missing some kind of risk. Based on the system safety theory, the risk factors of a system can be divided into four categories such as human factors, material factors, environmental factors, and management factors. Risk identification of the long-distance oil and gas pipelines engineering should be completed generally from the four factors of the system safety theory. The result of the risk identification is the base of the risk assessment and management of the long-distance oil and gas pipelines engineering.

### 2.2 Classification and Identification of Risk Factors

Based on the system safety theory and survey data, and combining the opinions of experts, the main potential risk factors of the pipeline engineering can be identified from the human factors, material factors, environmental factors, and management factors. As a result, there were 32 kinds of risks identified and listed in Tables 1, 2, 3, and 4.

In summary, the risk factors of long-distance oil and gas pipelines engineering in China can be divided into 4 categories and 31 items. There were 31 kinds of risks

**Table 1** Human factors

No.	Types of risk	Risk factors
1	Human factors	Technical ability of personnel
2		Third party damage
3		Loss of key personnel
4		Disoperation and illegal command
5		Personnel injury
6		Professional skill



**Table 2** Material factors

No.	Types of risk	Risk factors
1	Material factors	Mechanical defect
2		Motor vehicle
3		Electrical hazards
4		Earthwork piled
5		Material defects
6		Equipment failure
7		New materials or technologies
8		Corrosion
9		Tunnel construction
10		Running test of pipelines

**Table 3** Environmental factors

No.	Types of risk	Risk factors
1	Environmental factors	Covering reduction
2		Flood, water gully
3		Soil corrosion
4		Landslide, debris flow
5		Geological subsidence area
6		Geological fault zone
7		Lightning
8		Gale, storm
9		Destruction of ecological environment
10		Land requisition
11		Political, economic environment

**Table 4** Management factors

No.	Types of risk	Risk factors
1	Management factors	Subcontractor defaults
2		Poor management
3		Defects of contract
4		Third party liability
5		QHSE management defect

identified and listed in Tables 1–4. Among them, there were 6 human factors, 10 material factors, 11 environmental factors, and 5 management factors. It is mentioned that the risk factors may be different in different pipelines engineering.

### 3 Risk Evaluation of Long-Distance Oil and Gas Pipeline Engineering

#### 3.1 Risk Evaluation

According to the definition, risk is defined as a product of the likelihood of risk and the severity of the consequence caused by the risk. If the selected system includes some kinds of risks, then the total risk of the system is the comprehensive calculation of all the likelihoods and severity of each risk. Therefore, the risk value of the oil and gas pipeline can be calculated by the following equation:

$$R = \sum_{i=1}^{11} p_i \cdot c_i \tag{1}$$

where,  $R$  is the value of the total risk,  $i$  is the number of the risk,  $p_i$  is the possibility of the risk and  $c_i$  is the severity of the accident consequence caused by the risk. For a long-distance oil and gas pipeline, the total risk value is equal to the sum of all the pipes risk.

#### 3.2 Risk Levels

In the risk analysis practice, if a risk factor will not happen that the likelihood value of the risk  $f_i$  will be assigned to 0; if the risk happens exactly, then the value will be 10. The likelihood level classification of the risk can refer to Table 5.

If there is no loss caused by some risk factor, the severity value of risk  $c_i$  will be assigned to 0; if the risk brings large losses, then  $c_i$  will be assigned to 100. The severity level classification of the risk can be referred to Table 6.

According to the total risk value calculated by the Eq. (1), risk of pipeline can be divided into 5 levels. The risk level classification standards are listed in Table 7.

**Table 5** Level standards of the risk likelihood

$P$	Lowest	Lower	Middle	Higher	Highest
Values	0-2	2-4	4-6	6-8	8-10

**Table 6** Level standards of risk severity

$C$	Lowest	Lower	Middle	Higher	Highest
Values	0-20	20-40	40-60	60-80	80-100

**Table 7** Risk level standards

$R$	Lowest	Lower	Middle	Higher	Highest
Cents	0-400	400-800	800-1200	1200-1600	>1600

## 4 Application to a Case Study

In order to study the risk of the long-distance oil and gas pipelines engineering, a natural gas pipeline was selected to analysis the major risk factors and calculated the risk value. Based on the survey datum, the selected natural gas pipeline includes 10 pipes.

First of all, the selected pipeline construction engineering can be divided into 10 units. Taking the first pipe of the natural gas pipeline as an example, major risk factors can be identified through a preliminary qualitative risk analysis according to the above 32 identified risk. There were 11 risk factors including geological subsidence area, geological fault, new materials or technologies to use, corrosion, water gully, avalanches, tunnel construction, landslides, storm, third party liability, and poor engineering management. Five experts were invited to evaluate the severity of each risk factor. The weights of these experts were 0.25, 0.30, 0.20, 0.15, and 0.10. The analysis results of the severity of risk were shown in Table 8.

Similarly, the analysis results of the likelihood of each risk of the ten pipes were listed in Table 9.

And then the risk value factors of each pipe were identified and calculated in this paper. The risk value of each pipe was obtained and listed in the Table 10. According to Table 7, the risk level of each pipe can be calculated and the results are shown in Table 10. As observed from Table 10, the forth pipe was the most dangerous pipe and should be repaired immediately.

**Table 8** Results of the severity of each risk of the first pipe

No.	Risk factor	Expert 1 (0.25)	Expert 2 (0.30)	Expert 3 (0.20)	Expert 4 (0.15)	Expert 5 (0.10)	Severity score
1	Geological subsidence area	40	50	35	60	43	45.30
2	Geological fault	60	50	55	80	56	58.60
3	New materials/technologies	20	25	30	20	40	25.50
4	Corrosion	55	30	65	50	25	45.75
5	Water gully	40	50	27	20	38	37.20
6	Avalanche	70	65	55	40	56	59.60
7	Tunnel construction	60	50	40	40	64	50.40
8	Landslides	55	70	54	45	45	53.15
9	Storm	20	32	45	10	28	27.90
10	Third party liability	75	65	50	80	90	69.25
11	Poor engineering management	50	70	65	50	65	60.50

**Table 9** Results of the likelihood of each risk of the first pipe

No.	Risk factors	1	2	3	4	5	6	7	8	9	10
1	Geological subsidence area	1	2	0	3	2	0	1	0	0	2
2	Geological fault	0	0	5	4	0	0	0	5	0	0
3	New materials or technologies	2	2	2	2	2	2	2	2	2	2
4	Corrosion	4	3	4	4	3	2	2	4	2	2
5	Water gully	5	4	6	6	5	4	3	4	2	2
6	Avalanche	1	0	0	0	0	0	0	0	0	0
7	Tunnel construction	0	0	0	0	0	0	1	0	0	0
8	Landslides	0	0	0	2	1	0	3	0	0	0
9	Storm	2	3	3	5	6	7	6	6	6	5
10	Third party liability	4	5	5	5	3	4	3	5	4	3
11	Poor engineering management	3	4	3	3	4	4	3	3	3	4

**Table 10** Risk value and risk level of the selected pipeline

Pipe no.	Risk value	Risk level
1	993.90	Middle
2	1007.25	Middle
3	693.50	Lower
4	1647.55	Highest
5	995.40	Middle
6	762.50	Lower
7	862.65	Middle
8	1254.10	Higher
9	736.45	Lower
10	688.90	Lower

## 5 Conclusions and Suggestions

The following conclusions and suggestions can be inferred from the above risk study on the pipeline engineering through a detailed analysis and assessment.

- (1) There were 32 risk factors that have been identified in the oil and gas pipelines engineering from the human factors, material factors, environment factors, and management factors.
- (2) To the case study, the risk factors such as geological subsidence area, geological fault, avalanche, tunnel construction, landslides are less likely to occur, and they have occurred usually in the limited locations and should be avoided and controlled by the special risk management.

- (3) In accordance with pipes rating, the risk level of the fourth pipe is highest, and the first, third, and eighth pipes are the higher. These four pipes need to improve their risk management. The risk analysis and assessment should be carried out during the whole process of the oil and gas pipelines engineering.

**Acknowledgements** The research work was supported by National science and technology Foundation of China under Grant No. 2015BAK16B01.

## References

1. Wang JS, Chen M, Xiao ZH, Chao Y (2014) Study on social security risk of multinational oil and gas pipelines. *J Saf Sci Technol* 10(S2):83–86
2. Wu ZZ, Wang RJ (2014) Concern with the safety management of oil and gas pipelines—status. *Chin Saf News* 6:1–5
3. Jose L (2014) Challenges to the integrity of old pipelines buried in stable ground. *J Eng Fail Anal* 42:311–323
4. Anjuman S, Rehan S, Solomon T (2012) Risk analysis for oil and gas pipelines: a sustainability assessment approach using fuzzy based bow-tie analysis. *J Loss Prev Process Ind* 25(3):505–523
5. Spyros S, Fotis R (2006) Estimation of safety distances in the vicinity of fuel gas pipelines. *J Loss Prev Process Ind* 19(1):24–31
6. Wu ZZ, Gao JD, Wei LJ et al (2001) Risk assessment method and its application. Chemical Industry Press, Beijing
7. Zhang HB, Feng QS, Zheng HL, Bi YT (2008) QRA for the long distance oil and gas pipeline. *J China, Saf Sci* 8(9):161–165
8. Hu YH, He SH (2000) Comprehensive evaluation method. Science Press, Beijing
9. Zheng XB (2007) Long distance oil and gas pipeline engineering and its safety evaluation method. *J Oil Field Equip* 36(8):5–10
10. Zhang SZ, Wu ZZ, Zhang J, Duo YQ (2012) Oil and gas pipe line selection and risk evaluation of relevant laws and regulations and methods. *J Oil Gas Storage Transp* 31(9):64–668
11. Chen BZ (2011) System safety engineering, 2nd edn. Metallurgical Industry Press, Beijing
12. Dawotola AW, Van G et al (2009) Risk assessment of petroleum pipelines using a combined analytical hierarchy process-fault tree analysis (AHP-FTA). In: Proceedings of the 7th international probabilistic workshop, Delft, pp 491–501

# Optimization Method Based on Selection Strategy of Initial Point and Six Sigma Robust Design

Aimin Ji, Mengni Zhang, Pin Lv and Xu Yin

**Abstract** Usually, there are three problems in the traditional optimization methods: (1) the local optima arising from choosing an inappropriate initial point; (2) low efficiency and accuracy in solving the complex optimization problems; (3) the robustness of optimal solution is not considered. To solve these problems, a new optimization method, the six sigma robust optimal design based on a strategy of initial point selection, is proposed. Firstly, latin hypercube design (LHD) is chosen to determine the optimal initial point and nonlinear Programming by Quadratic Lagrange (NLPQL) is used to search for the optimal solution. Then, the six sigma robustness of the optimal solutions is analyzed. Finally, robust optimizations of the responses which do not meet the six sigma reliability are performed and the global optimal solutions are obtained. The optimization of the machine tool spindle is used in this paper to validate the performance of this method. The results show that the optimal solution obtained by using the proposed method can ensure the high reliability, and also has a high convergence speed.

**Keywords** Initial point · Six sigma · Robust design · Robust optimization

## 1 Introduction

Complex structures such as nonconvex and discontinuous function are usually the optimization objects of engineering practice. For nonconvex function in optimization problems, because there are several local optimums, it is easy to get the local optimal solution by choosing the wrong initial point when search the optimization results. In order to solve this problem, the intelligent optimization algorithm is widely adopted to get global optimization, such as particle swarm optimization, genetic algorithm, and simulated annealing algorithm. Kennedy and Eberhart [1]

---

A. Ji (✉) · M. Zhang · P. Lv · X. Yin  
College of Mechanical and Electrical Engineering, Hohai University,  
Changzhou 213022, China  
e-mail: jam@ustc.edu

balanced the searching ability of optimal solution dynamically by adjusting the inertia weight in particle swarm optimization. Clerc [2] improved the convergence performance of optimization algorithm by inserting shrinkage factors. Kitayama et al. [3] put forward the particle swarm optimization method in adaptive region, and achieved higher accuracy and efficiency. Foruie and Groenwold [4] compared particle swarm optimization with gradient and genetic algorithm. The results showed that particle swarm optimization is better than genetic algorithm and closed to gradient optimization. Oliveria and Petraglia [5] proposed an adaptive and fuzzy simulated annealing algorithm to solve the system problems composed by several nonlinear equations. Above all, these intelligent optimization methods are all global algorithms, though these methods can avoid falling into local optimal solution, it will lead to the excessive calculation. At same time, engineering reliability has not been considered for current optimization method. For machine parts, it will lead to the dimension out of constraint and it will affect the products performance, once there are manufactured errors or abrasion in working. Thus, robust design must be implemented on traditional optimal solution.

Robust design is an engineering design method that all the products designed by this method can always keep the product performance stably even if structural parameters change or the structure is aging and deterioration within its rated life [6]. From a statistical standpoint, the products quality for six sigma robust design must completely meet the all design requirements when fluctuating within the range of  $6\sigma$  ( $\sigma$  is the standard deviation of Statistics), which assures the product qualification rate up to 99.999998 %. Essentially, reliability design is merged into robust design based on tolerance model, which makes the average response away from the boundary constraints, decreases the response deviation, and promotes the reliability and robustness of the design results.

Based on the above two points, this paper puts forward an optimization method based on strategy of initial point selection and six sigma robust design. Firstly, the optimal initial point is determined by latin hypercube design (LHD) and the efficient global optimization solution is obtained by Nonlinear Programming by Quadratic Lagrange (NLPQL), then the reliability of every response is verified. Finally, the six sigma robust optimization analysis is made on those do not meet the reliability requirements, and global solutions that meet practical production requirements are obtained. The multi-objective optimization of machine tool spindle is taken as an engineering example for verification.

## 2 Strategy of the Initial Point Selection

In order to avoid the local optima arising from choosing an inappropriate initial point, this paper presents a strategy of the initial point selection that is selecting initial values of the design variables to optimize by using design of experiment (DOE), then using gradient optimization (GO) to achieve efficient global optimization solution. And LHD and NLPQL are chosen as design of experiments (DOE) and gradient

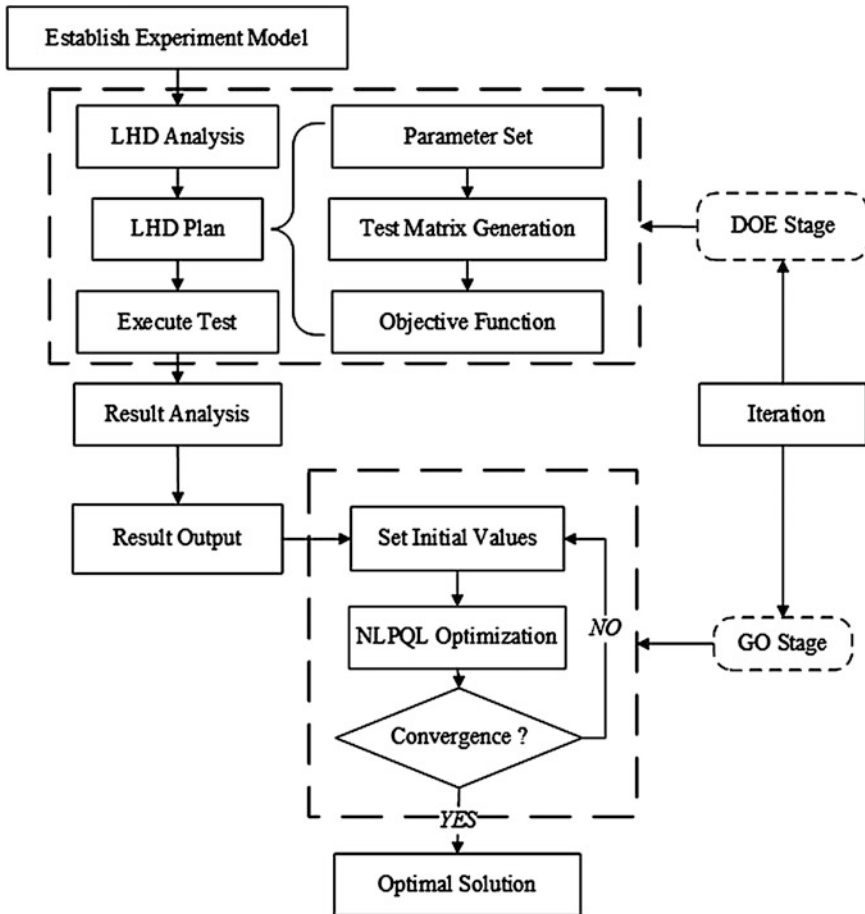


Fig. 1 The selection of the initial points

optimization (GO), respectively, to verify the feasibility of the strategy in the theory. Figure 1 describes the workflow of the selection of initial points.

### 3 Six Sigma Robust Optimization

#### 3.1 Six Sigma Robust Analysis

The purpose of the six sigma robust analysis is to evaluate the robust level of the optimal solution got from the selection strategy of initial point, and as the basis for whether the need continues to make the six sigma robust analysis. This paper firstly takes the method of two-order Taylor series expansion to obtain the average



value and standard deviation of the performance responses when design variables disturb randomly around the optimal solution. Then, the sigma level, reliability of optimal solution and performance response by statistical analysis are estimated. At last whether there is a need to continue to make six sigma robust optimal analysis is determined.

The secondary Taylor series expansion of performance response  $y(x)$  is:

$$y(x) = y + \frac{dy}{dx} \Delta x + \frac{1}{2} \Delta x^T \frac{d^2y}{dx^2} \Delta x \tag{1}$$

The mean expression of  $y(x)$  function can be acquired by get the expected value on both sides of Eq. (1):

$$\mu_y = y(\mu_x) + \frac{1}{2} \sum_{i=1}^n \frac{d^2y}{dx^2} \sigma_{x_i}^2 \tag{2}$$

The standard deviation expression of  $y(x)$ :

$$\sigma_y = \sqrt{\sum_{i=1}^n \left(\frac{\partial y}{\partial x_i}\right)^2 (\sigma_{x_i})^2 + \frac{1}{2} \sum_{i=1}^n \sum_{j=1}^n \left(\frac{\partial^2 y}{\partial x_i \partial x_j}\right)^2 (\sigma_{x_i})^2 (\sigma_{x_j})^2} \tag{3}$$

In the above formula,  $\sigma_{x_i}$  is the standard deviation of the  $i$ th parameters,  $\sigma_{x_j}$  is the standard deviation of the  $j$ th parameters [7].

### 3.2 Six Sigma Robust Optimization

If the optimal solution acquired by the strategy of initial point selection cannot meet the six sigma reliability standard by robust optimal analysis, then the six sigma robust optimal designs must be conducted by setting this optimal solution as the initial value. Therefore, six sigma robust optimization mathematical model Eq. (5) can be transformed by deterministic optimization model Eq. (4) [8].

$$\begin{cases} \text{Minimize } F(X) \\ \text{subject to } G_j(X) \leq 0 \\ X_{LSL} \leq X \leq X_{USL} \end{cases} \tag{4}$$

$$\begin{cases} \text{Minimize } F(\mu_y(X), \sigma_y(X)) \\ \text{subject to } G_j(\mu_y(X), \sigma_y(X)) \leq 0 \\ X_{LSL} + \Delta X \leq X \leq X_{USL} + \Delta X \end{cases} \tag{5}$$

In the Eqs. (4) and (5),  $X$  and  $Y$  are design variables and performance parameters, respectively.  $F$  and  $G$  are the objective function and the constraint function, respectively, in the optimization. In the robust optimization model, they are defined as the mean value  $\mu_y$  and standard deviation  $\sigma_y$ .  $\pm\Delta X$  is the change region of random design variable  $X$ , and this is  $\pm 6\sigma$  in six sigma robust optimization design. In this paper, the standard deviation is set as 1 % of mean, that is,  $\sigma = 1\% \mu$ .  $X_{LSL}$  and  $X_{USL}$  are the lower limit and upper limit of design variables, respectively.

## 4 Example of the Machine Spindle Optimization

### 4.1 Objective Function and Constraints

The machine spindle is a hollow stepped shaft. For ease of structural analysis, it is usually simplified as identical cross-section spindles represented by the equivalent diameter. Fig. 2 is the spindle bending deformation.  $d$  and  $D$  are assumed as the inner and outer diameters of the spindle respectively,  $l$  is the span,  $a$  is the length of overhanging end,  $y$  is the deflection, and  $F$  is the load at the overhanging end of the spindle.

For ease of comparison the optimization results with existing method results, the spindle related data are selected from Ref. [9]:  $d = 45$  mm,  $F = 15,000$  N, allowable deflection  $[y] = 0.125$  mm, allowable shear stress  $[\tau] = 220$  MPa, allowable torsion angle  $[\theta] = 0.02$  rad, material density  $\rho = 7800$  kg/m<sup>3</sup>, Elastic modulus  $E = 210$  GPa, Shear modulus  $G = 80$  GPa, spindle speed  $n = 80$  r/min, and input power  $P = 7.5$  KW.

The following mathematical model is been established according to the above parameters, design variables are set as:

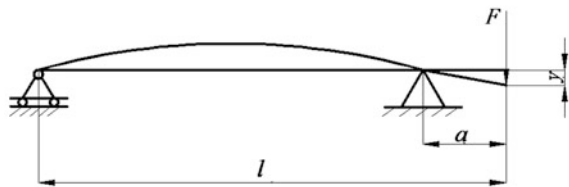
$$X = [x_1 \quad x_2 \quad x_3]^T = [D \quad l \quad a]^T \tag{6}$$

The objective of optimization minimizes the weight of spindle:

$$\min f(X) = \frac{1}{4 \times 10^9} \pi(D^2 - d^2)(l + a)\rho \tag{7}$$

Furthermore, the spindle optimization needs to meet the following constraints: Deflection constraint at the overhanging end:

Fig. 2 Machine spindle deformation



$$g_1(X) = \frac{64 Fa^2(l+a)}{3000 \pi E(D^4 - d^4)} - [y] \leq 0 \quad (8)$$

The torsional angle constraint at the overhanging end:

$$g_2(X) = \frac{32 T(l+a)}{G\pi(D^4 - d^4)} - [\theta] \leq 0 \quad (9)$$

Shear stress constraint:

$$g_3(X) = \frac{1,52,800 PD}{\pi(D^4 - d^4)n} - [\tau] \leq 0 \quad (10)$$

Boundary constraints:

$$50 \leq D \leq 150; \quad 210 \leq l \leq 600; \quad 90 \leq a \leq 150 \quad (11)$$

## 4.2 Optimization Results and Robust Design Process

On iSIGHT platform, we select the collaborative optimization algorithm in the spindle optimization model. First, the optimal solution [55.26, 271.58, 105.79] that obtained after 20 times DOE calculation is chosen as the initial point. After 64 times gradient iterative optimization, the optimal solution [60.68, 210.00, 90.00] is obtained. For comparison, the optimal solution based on the strategy of initial point selection and the results from Ref. [9] are presented in Table 1. From Table 1, the optimization results of the two methods are much closed. But the optimization iterations based on strategy of initial point selection reduce 25 times, the optimization efficiency improves by 22.94 %; it indicates that high precision and high

**Table 1** Comparison of optimization results

Parameter	Optimization results	
	Selection strategy of initial point	Ref. [9]
$D$ (mm)	60.68	60.69
$l$ (mm)	210.00	210.00
$a$ (mm)	90.00	90.00
Weight (kg)	3.046	3.05
Deflection at the overhanging end (mm)	0.1246	0.1246
Shear stress of the spindle (MPa)	29.25	29.26
Iterations	84	109

*Note* The optimization results in the table are not rounded because of comparison

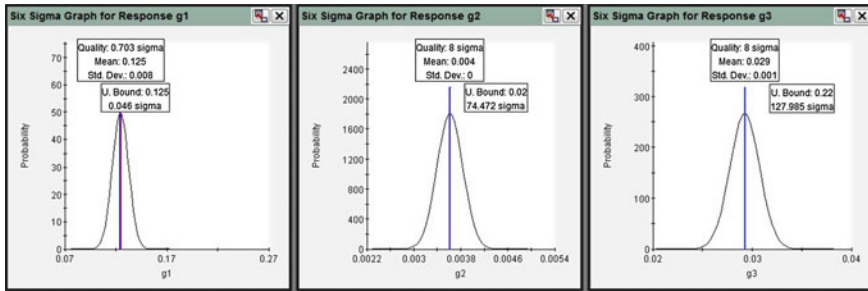


Fig. 3 Optimal solution response diagram of six sigma robust

Table 2 Result comparison about 6 sigma robust optimization strategy of initial point selection

Parameter	Before 6σ robust optimization	After 6σ robust optimization	The difference of results (%)
D (mm)	60.68	66.234	-9.15
l (mm)	210.00	223.136	-6.26
a (mm)	90.00	95.63	-6.26
Weight (kg)	3.046	4.6126	-51.23
Deflection at the overhanging end (mm)	0.1246	0.0934	25.04
Shear stress of the spindle (MPa)	29.25	19.94	31.85

Note The optimization results in the table are not rounded because of comparison

efficiency in solving multi-objective optimization problems by using the strategy of initial point selection can be obtained.

Considering the uncertainty of design variables, the robust analysis is made again on the above optimal solution. Figure 3 shows the six sigma robust analysis result for the optimal solution [60.68, 210.00, 90.00] obtained by this articles method and each constraint used as the response. According to the graph, the response level of the spindle strength constraints and the torsion angle constraints of spindle overhanging end both reach to 8σ level, but the response level of spindle rigidity constraints is only 0.7035σ. It can be seen that the reliability of rigidity constraint is only 51.824 % from Table 2. So the rigidity constraint will be easy to fail and the optimal solution become infeasible if the design variables deviate. Meanwhile, from Eq. (11), the optimized values of design variables  $x_2$  and  $x_3$  fall to lower limits, the sigma level is only 0.6745σ, the reliability is just 50 %, all values show that the optimal solution itself is also unreliable

So it is necessary to do six sigma robust optimization on the basis of robust analysis results, optimal solution [66.234, 223.136, 95.63] is acquired by establishing six sigma robust optimization model according to Eq. (5) on the former deterministic optimization model and searching optimization by NLPQL. Table 2

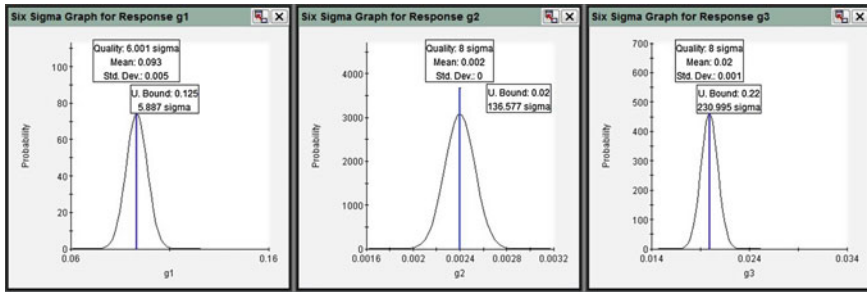


**Fig. 4** Response diagram of six sigma optimization solution

shows comparison of results before and after the six sigma robust optimization. Figure 4 is the analysis chart about six sigma optimization solutions.

From Table 2, after robust optimization the machine spindle's diameter increases 9.15 %, span and length of overhanging end both enlarge 6.26 %, quality objective improves nearly 51.23 %, but the optimal solution of design variables and the response level of rigidity constraint have reached to  $6\sigma$ , the reliability is closed to 100 %, the optimization solution robustness increases rapidly, the reliability of spindle optimization design hit 100 %. In addition, the deflection of spindle overhanging end and shear stress decrease significantly compared with the original robust optimization design, which, respectively, drops 25.04 and 31.85 %, so as to further improve the spindle performance.

## 5 Conclusions

The optimization method based on the strategy of initial point selection and six sigma robust designs was proposed in this paper. Firstly, LHD was chosen to determine the optimal initial point and NLPQL was used to achieve the efficient global optimization solution. Then, the six sigma robust analysis on the optimal solution obtained by strategy of initial point selection was analyzed. The six sigma robust optimization was proceeded on those responses which do not meet the six sigma reliability, and the optimal results were obtained. The optimization of machine spindle was taken as a validation example. The results show that the proposed method can not only increase the optimal efficiency and accuracy, but also ensure the reliability and robustness of the optimal solution.

**Acknowledgments** The authors wish to acknowledge the support provided by National Natural Science Foundation of China (Grant No. 51175146) and the Fundamental Research Funds for the Central Universities (Grant No. 2012B14014).

## References

1. Kennedy J, Eberhart R (1997) A discrete binary version of the particle swarm optimization algorithm. In: Proceedings of IEEE conference on systems. Orlando, United States, pp 4104–4109
2. Clerc M (1999) The swarm and queen: towards a deterministic and adaptive particle swarm optimization. In: Proceedings of the congress of evolutionary computation. Washington, DC, pp 1951–1957
3. Kitayama S, Yamazaki K, Arakawa K (2006) Adaptive range particle swarm optimization. In: Proceedings of 11th AIAA/ISSMO multidisciplinary analysis and optimization conference, Portsmouth, VA, vol 1, pp 129–138
4. Fourie PC, Groenwold AA (2002) The particle swarm optimization algorithm in size and shape optimization. *Struct Multidisc Optim* 23:259–267
5. Oliveria HA, Petraglia JA (2013) Solving nonlinear systems of functional equations with fuzzy adaptive simulated annealing. *App Soft Comput* 13:4349–4357
6. Chen LZ (2000) Robust design. China Machine Press, Beijing (in Chinese)
7. Hsieh CC, Oh KP (1992) MARS: a computer-based method for achieving robust systems. In: FISITA conference, the integration of design and manufacture, pp 115–120
8. Koch PN, Yang RJ, Gu L (2004) Design for six sigma through robust optimization. *Struct Multidisc Optim* 26:235–248
9. Chen JY, Jiao LM (2012) Optimization design of machine tool spindle based on collaborative algorithm. *J Zhengzhou Univ* 33:103–106 (in Chinese)

# Dynamic Flux and Torque Estimation of Single-Phase Induction Motors Based on the Vector Control Theory of Motors

Dandan Sun and Ding Wang

**Abstract** A method for flux and torque estimation for the single-phase induction motors is presented in this paper. This work is based on the vector control theory of electrical machines, and has realized an estimation of flux and torque and some intermediate variables like direct and quadrature values. Accordance with the algorithm, a basic experimental model is built in the Simulink of the Matlab and tested for sinusoidal waveforms feeding the single-phase motor. Simulation experiments show that the methods are correct and the estimation is effective to access to internal parameter of the single-phase induction motors in order to obtain AC drives with high performance.

**Keywords** Single-phase induction · Flux · Torque · Estimation

## 1 Introduction

The single-phase induction motors are used widely everywhere, because of its advantages of simple structure, low noise, and low cost. It is used in most household appliances that require motors, for example in refrigerators, washers, driers, fans, and blowers [1]. An interesting property of this type of motor is that the stator current alone does not create a revolving magnetic field a sinusoidal input will produce a pulsating magnetic field along a single axis. If the machine is at stand-still, this excitation will not provide any torque [2].

In the view of some information about the flux and torque observers, it is found that lots of the theories proposed are about the three-phase induction motors. There are few researches of the flux and torque estimation about single-phase induction

---

D. Sun · D. Wang (✉)

Provincial Key Disciplines for Control Science and Engineering,  
Heilongjiang University, Harbin, Heilongjiang, People's Republic of China  
e-mail: 782939172@qq.com

D. Sun

e-mail: 15124526043@163.com

© Springer-Verlag Berlin Heidelberg 2016

B. Huang and Y. Yao (eds.), *Proceedings of the 5th International Conference on Electrical Engineering and Automatic Control*, Lecture Notes in Electrical Engineering 367, DOI 10.1007/978-3-662-48768-6\_68

601

motors. In this paper, a method is proposed which is about the flux and torque estimation of single-phase induction motors.

Now, although direct torque control and vector control technology whose first work is to estimate the flux and torque has matured, however, some problems still exist in the flux and torque estimation. At the beginning, estimation schemes for AC motor drives were based on parameters like: speed, voltage, current, and frequency. How to reduce or even eliminate the impact of parameters on the flux estimates has been the research project which was studied by the scholars from various countries [3]. There are two basic methods of observation about flux estimate, which are the current model and the voltage model. The current models whose observation values are asymptotic and convergence has negative feature root, relate to the rotor time constant which is influenced easily by the motor operating conditions, the current model often requires real-time estimates. The voltage model exists accumulation of errors and drift problems which is caused by pure integral part of the system, so the result of estimate is unstable and the error is lager. After this, modified integrator algorithms, low pass filters and feedback techniques have been used. Various techniques have also been suggested for overcoming the above shortcomings, such as model reference adaptive system (MRAS), Luenberger and Kalman-filter observers, sliding mode observers, and artificial intelligence techniques [4].

These estimation schemes works good but they did not pay some attention to the internal motor structure. It is necessary to build estimators that allow access to internal parameters of the motor. This kind of estimators which is based on vector control theory of electric machines has a very important position. The trends in this field are conveying to realize feedback systems with estimated variables like flux and torque in order to obtain AC drives with high performance.

Based on the above theory, a method is proposed which is about the flux and torque estimation of single-phase induction motors. In this paper, the work is based on the vector control theory of electrical machines, which is named as a flux and torque estimator on a stationary frame with spinning rotor components. It is intended to realize an estimation of flux and torque and some intermediate variables like direct and quadrature values. A basic experimental model in SIMULINK is built and tested for sinusoidal waveforms feeding the motor.

## **2 Flux and Torque Estimation of the Single-Phase Induction Motors**

Around the vector control theory, there are different ways to represent motor behavior based on reference frames. One of them considers as a reference one of the feeding phases to the motor, in this case equations involved are simple. Another is a stationary reference of the stator, in this frame characteristic equations are quite complicated. The last reference is a synchronous frame spinning with the rotor, characteristic equations are as complex as second option [6, 7].



### 2.1 Estimation Scheme

Combination of synchronous frame spinning with the rotor as a stationary frame (including  $\theta_r$  angle in calculations) and the reference frame in which one of feeding phases is precisely the reference. Combination of two methods results in a simplified way to estimate variables. Finally, this result can be named as a flux and torque estimator on a stationary frame with spinning rotor components. Then we can get a result that: The estimator variables are in stator and are completely on stationary basics. The  $\theta_r$  angle is not necessary to be included in the calculations of direct and quadrature components of the voltage and current vectors. Flux is on the stationary frame but the component variables of the flux are totally referred to the synchronous rotor frame. Flux and torque components are referred to a spinning synchronous rotor frame but flux and torque estimated are referred to a stationary frame. The simulation model of the estimation system is shown in Fig. 1.

### 2.2 Characteristic Equations

Equations that describe flux and torque behavior are described as vector components [5]. The analysis starts from the description of the stator voltage and current space vectors.

$$V_s = V_s A(x) + a V_s B(x) \tag{1.1}$$

$$I_s = I_s A(x) + a I_s B(x) \tag{1.2}$$

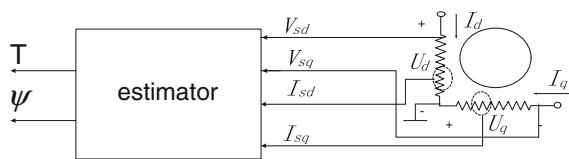
where:

$$a = e^{\pi j/2} \tag{1.3}$$

Voltage and current vectors are composed by a real part and an imaginary part described as follows:

$$V_{sd}(x) = \text{Re}(V_s(x)) \tag{1.4}$$

**Fig. 1** The simulation model of the estimation system



$$V_{sq}(x) = \text{Im} (V_s(x)) \quad (1.5)$$

$$V_s = V_{sd}(x) + jV_{sq}(x) \quad (1.6)$$

$$I_{sd}(x) = \text{Re}(I_s(x)) \quad (1.7)$$

$$I_{sq}(x) = \text{Im} (I_s(x)) \quad (1.8)$$

$$I_s = I_{sd}(x) + jI_{sq}(x) \quad (1.9)$$

where voltage vector of stator have real and imaginary components which are assumed to be in a reference frame spinning with the rotor, then its direct and quadrature components are described by next equations:

$$V_{sd} = V_s A(x) + 0.707B(x) \quad (1.10)$$

$$V_{sq} = 0.707V_s B(x) \quad (1.11)$$

Components of stator current vector are also referred to the synchronous spinning with the rotor reference frame.

$$I_{sd} = I_s A(x) + 0.707B(x) \quad (1.12)$$

$$I_{sq} = 0.707I_s B(x) \quad (1.13)$$

In order to find flux and torque signals it is necessary to obtain its direct and quadrature components referred to a stationary reference frame but in terms of the synchronous spinning rotor frame variables. For this calculations must be used stator resistance  $R_s$  as follows:

$$\psi_{sd}(x) = \int (V_{sd}(x) - I_{sd}(x)R_s) dx \quad (1.14)$$

$$\psi_{sq}(x) = \int (V_{sq}(x) - I_{sq}(x)R_s) dx \quad (1.15)$$

Magnitude of electromagnetic flux is determined by:

$$\psi(x) = \left( \psi_{sd}^2(x) + \psi_{sq}^2(x) \right)^{1/2} \quad (1.16)$$

Torque is calculated using also intermediate variables:

$$T(x) = 3P/4 \left( \psi_{sd}(x)I_{sq}(x) - \psi_{sq}(x)I_{sd}(x) \right) \quad (1.17)$$

### 2.3 Simulation Model

Experimental model is composed by an array of components that performs equations described above. Final decision about reference frame selected was taken based in the resources availability and the complexity of the characteristic equations.

Voltages and currents of stator are sensed directly at motor input leads and are electrically isolated in order to avoid an electrical short circuit between power stage and estimator low power circuit. The structure of the part of estimator is showed in the following Fig. 3.

### 3 Simulation Experiment and Analysis

According to the above structure of the estimator in Fig. 2, A simulation model is built in the Simulink.

There will be presented graphics of direct and quadrature flux components, estimated electromagnetic flux, and estimated developed torque. All mentioned above were obtained when motor is supplied with sinusoidal waveforms. The motor used is a single-phase 220 V, 50 Hz, 1/4 HP at rated load. Using utility power supply whose voltage is 220 V, whose phase is  $\pi/2$ , whose frequency is 50 H to feed the main winding of motor, using utility power supply whose voltage is 220 V, whose phase is  $0\pi$ , whose frequency is 50 H to feed the auxiliary winding of motor, We can obtain next simulation results. Figure 3a shows the flux simulation standard graphics of the auxiliary winding which is provided by the Matlab and Fig. 3b shows the flux graphics of the auxiliary winding estimated by the estimation formula. Figure 4a shows the torque simulation standard graphics which is provided

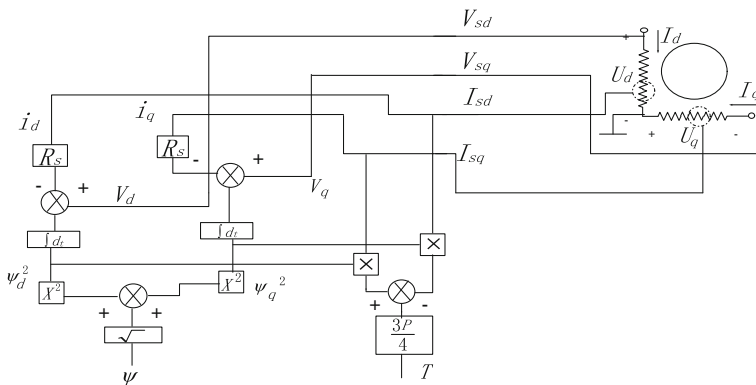
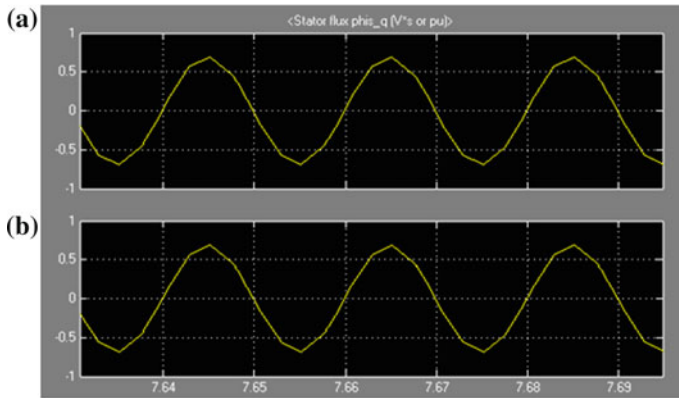


Fig. 2 The structure of the part of estimator



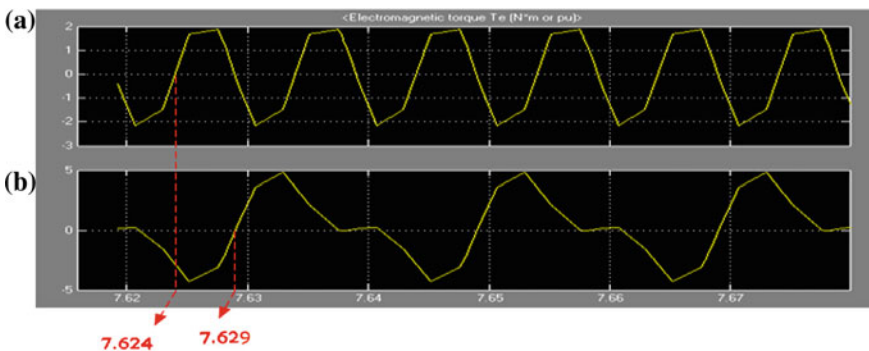
**Fig. 3** **a** The flux simulation standard graphics of the auxiliary winding which is provided by the Matlab. **b** The flux graphics of the auxiliary winding estimated by the estimation formula

by the Matlab and Fig. 4b shows the torque graphics estimated by the estimation formula. Figure 5 shows the behavior of flux estimated by the estimation formula.

Comparing Fig. 3a and b, it shows that the results are correct and the flux simulation standard graphics of the auxiliary winding which is provided by the Matlab is the same as the flux graphics of the auxiliary winding estimated by the estimation formula.

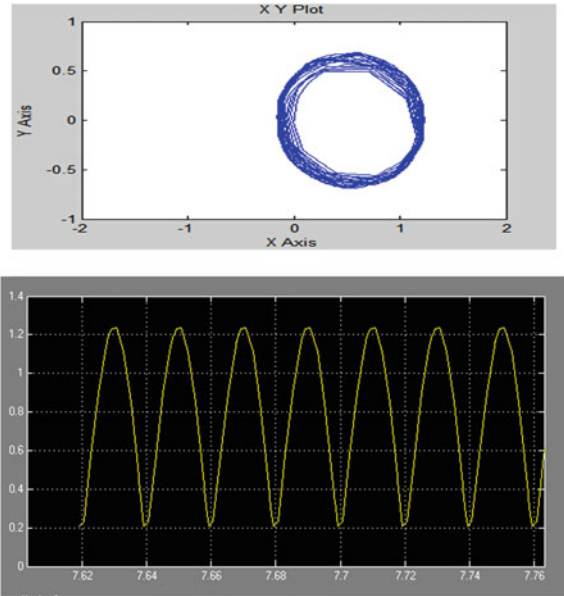
Comparing Fig. 4a and b, it shows that the results are correct and the torque estimated displays the problem of lagging. The delay time is about 0.005 s. At the same time, the value of torque estimated displays integral error, and the amplitude of torque estimated get bigger than the amplitude of standard torque.

Figure 5 shows the behavior of flux estimated by the estimation formula. By observing the graphics of the flux estimated, it is found that the flux estimated shows cyclical fluctuation problem.



**Fig. 4** **a** The torque simulation standard graphics which is provided by the Matlab. **b** The torque graphics estimated by the estimation formula

**Fig. 5** The behavior of flux estimated by the estimation formula



## 4 Conclusions

A method for flux and torque estimation for the single-phase induction motors is presented in this paper. The algorithm starts from the description of the stator voltage and current space vectors. Voltage and current vectors are composed by a real part and an imaginary part which are assumed to be in a reference frame spinning with the rotor. Stator resistance  $R_s$  is used to obtain the direct and quadrature components of flux and torque signals, which are referred to a stationary reference frame but in terms of the synchronous spinning rotor frame variables. Then, flux and torque are calculated using intermediate variables. Thus, experimental model is composed by an array of components that equations described flux and torque behavior, final decision about reference frame selected was taken based in the resources availability and the complexity of the characteristic equations.

A basic experimental model in SIMULINK is built and tested for sinusoidal waveforms feeding the single-phase induction motor. Simulation experiments show that the results are correct and the estimator is effective to access to internal parameter of the single-phase induction motors in order to obtain AC drives with high performance. This application idea is trying to show that the flux estimator can be applied to any vector control system. It requires flux as main feedback parameters in order to have a high performance system. But, the flux shows the delay problem and the amplitude of torque estimated that gets bigger than the amplitude of standard torque. It is necessary to overcome the delay problem in the later research. If controller is done by this algorithm, the controller also must overcome these problems.

**Acknowledgements** This work was supported by the Scientific and Technological Project of Education Bureau of Heilongjiang Province (Grant No: 12521419), P. R. China.

## References

1. Kenny BH, Lorenz RD (2001) Stator- and rotor-flux-based deadbeat direct torque control of induction machines. In: Industry applications conference 1:133–139
2. Rossiter Correa MB, Jacobina CB, da Silva ERC, Lima AMN (2004) Vector control strategies for single-phase induction motor drive systems. *IEEE Trans Industr Electron* 51(5):1073–1080
3. Young CM, Liu CC, Liu CH (1996) New inverter-driven design and control-method for two-phase induction motor drives. In: IEE proceedings electric power applications 143(6):458–466
4. Wells JR, Nee BM, Amrhein M, Krein PT, Chapman PL (2004) Low cost single-phase power induction machine drive for residential applications. In: IEEE applied power electronics conference and exposition, vol 3, pp 1579–1583
5. Jabbar MA, Khambadkone AM, Yanfe Z (2004) Space-vector modulation in a two-phase induction motor drive for constant-power operation. *IEEE Trans Ind Electr* 51(5):1081–1088
6. Ong CM (1988) Dynamic simulation of electric machinery using MATLAB Simulink. Prentice Hall, Upper Saddle River
7. Mir SA, Zinger DS, Elbuluk ME (1994) Fuzzy controller for inverter fed induction machines. *IEEE Trans Ind Appl* 30(1):78–84

# Performance Evaluation of Ballistic Missile Detection for the Skywave OTHR Based on the Preliminary and the Weighted Indexes

Shihua Liu, Defang Li and Bing Hu

**Abstract** Based on the ballistic missile detection characteristics of the skywave OTHR system, a ballistic missile detection performance method for the skywave OTHR is presented based on the preliminary index and the weighted index. The detection performance index is divided into the preliminary index and the weighted index. For the preliminary index, the performance quantization value is computed by a binary function. For the weighted index, a detection performance index system is constructed, and the performance quantization value of the index system is calculated according to the cloud gravity center theory. Based on the performance quantization values of the preliminary index and the weighted index, the ballistic missile detection performance is evaluated using the cloud remark assembly. Finally, the feasibility of this method is verified through a calculated example.

**Keywords** Skywave OTHR · Ballistic missile · Detection performance evaluation · Cloud gravity center · Preliminary index · Weighted index

## 1 Introduction

The skywave radar is a complicated and huge system, but its detection performance, which includes many factors and uncertainty, is an integrated index. It is also a complicated task but beneficial for national defense decision-making and scientific study to evaluate the detection performance of the skywave radar [1]. On the one hand, the current functional ability of skywave radar may be estimated objectively according to the evaluation; on the other hand, based on the evaluation, the development of the skywave radar may advance [2].

The appropriate detection performance evaluation model is the basis on which to evaluate the equipment. At present, both the evaluation model [3–5] for skywave radar combat effectiveness and the performance evaluation model [6–9] for skywave

---

S. Liu (✉) · D. Li · B. Hu  
Department 2, AFEWA, Wuhan 430019, China  
e-mail: kyoliu2010@sina.com

radar air target detection are widely studied, but the performance evaluation model for skywave radar ballistic missile detection is rarely reported. A ballistic missile is a special kind of object: it has the characteristics of long-distance flight, high flight speed, low RCS and echo coherence [10, 11]. Compared with the general air target detection, the ballistic missile detection not only has similitude, but also has its unique theoretic basis and method. In this paper, the performance evaluation model for skywave radar ballistic missile detection is studied based on the target characteristics of the ballistic missile and the existing evaluation model.

According to the ballistic missile detection theoretic basis of the skywave radar, the detection performance index is divided into the preliminary index and the weighted index. The different indexes are evaluated by the different evaluation methods, then the evaluation results are computed synthetically to finish the ballistic missile detection performance evaluation of the skywave radar.

## **2 Construction of the Ballistic Missile Detection Performance Index System**

The construction of the index system is the prerequisite for the ballistic missile detection performance evaluation [12]. The existing index system is constructed mainly according to the inherent ability of the skywave radar. This method may be used with the other radars, but not always be adaptable to the skywave radar. Skywave radar detection of the object is achieved by interaction with the ionosphere, that is, the ionosphere is a part of the skywave radar. Consequently, the effect of the ionosphere must be considered to evaluate the detection performance of the skywave radar.

### ***2.1 Selection of the Preliminary Index***

The preliminary index is the necessary condition of the detection performance evaluation, and the evaluation is continued after the preliminary index has been satisfied. The preliminary index includes channel usability, detection coverage and target altitude.

1. Channel usability. Sometimes, the working channel of the skywave radar is not usable because of the ionosphere effect, which limits the propagation of the HF electromagnetic waves. In these conditions, the skywave radar couldn't detect the target even if the radar's working status is otherwise good. Furthermore, the channel usability is determined by the natural environment: it can't be changed to improve the radar detection performance but must be used according to the actual conditions. Therefore, channel usability is a selected precondition of the preliminary index, i.e., the following evaluation is performed after the channel becomes usable.



2. Detection coverage. The detection coverage is the characterization of the radar detection ability; it is a tridimensional space in which the target could be detected. In this space, for normal radars, if the radar working parameters are unchanged, then the detection coverage does not change. But for the skywave radar, the detection coverage is restricted by the ionosphere (such as when it is blanketed by Es layer). The detection coverage is selected to the preliminary index for its uncertainty.
3. Target altitude. The target altitude is also a preliminary index when the detection object is a ballistic missile. The skywave radar detection of the ballistic missile is achieved mainly by detecting the plume. In order to detect the plume, the ballistic missile should fly into the ionosphere, that is, the ballistic missile should be above 60 km. Therefore, this target altitude actually means the altitude at the burnout point of the ballistic missile. For the uncertainty of the flight altitude at the ballistic missile burnout point, the target altitude is selected to the preliminary index.

## 2.2 *Ballistic Missile Detection Performance Index System Based on the Weighted Index*

Except for the performance index, the other indexes, which affect the ballistic missile detection performance of the skywave radar, need to be considered. A ballistic missile detection performance index system is constructed by a first grade index, three second grade indexes and twelve third grade indexes. The index system is shown as Table 1. The ballistic missile detection performance value of the skywave radar is based on the weighted index that is obtained by weighted computation of these indexes.

**Table 1** Ballistic missile detection performance index system based on the weighted index

First grade index	Second grade index	Third grade index
Ballistic missile detection performance of the skywave radar	Detection ability	Time usability
		Data rate
		Measurement precision
		Resolution
	Confrontation ability	Anti-jamming ability
		Counter-reconnaissance
		Anti-destruction ability
		Support ability
	Environment property	Phase disturbance
		Propagation path
		Propagation loss
		Environment noise

### 3 Ballistic Missile Detection Performance Evaluation of the Skywave Radar

The preliminary index and the weighted index are computed individually by different methods. According to the computed result, the ballistic missile detection performance of the skywave radar is evaluated based on the relative remark assembly.

#### 3.1 Detection Performance Computation Based on the Preliminary Index

Because the preliminary index is the necessary condition, hence, the performance quantitative value of the preliminary index is computed by the following binary function

$$E_1 = \begin{cases} 1 & \text{index satisfied} \\ 0 & \text{index unsatisfied} \end{cases} \quad (1)$$

where  $E_1$  is the quantitative value of the preliminary index?

#### 3.2 Detection Performance Computation Based on the Weighted Index and the Cloud Theory

The cloud is a transform model that represents the uncertainty between the qualitative concept and its quantitative expression by a linguistic label. The digital characteristics of the cloud include the expectation, the entropy and the excess entropy, its integrated ambiguity and random to form a mapping between qualitative and quantitative expressions [12].

1. The system status expression of the performance index

The  $N$  indexes can be abstracted by  $N$  cloud models, therefore, the system statue, which is expressed by  $N$  performance indexes, can be expressed by an  $N$ -dimension synthetic cloud. When the system statue is changed, the shape of the  $N$ -dimension synthetic cloud is simultaneously changed. The gravity center  $T$  of the  $N$ -dimension synthetic cloud can be expressed by a  $N$ -dimension vector, that is,

$$T = (T_1, T_2, \dots, T_N) \quad (2)$$

where  $T_1, T_2, \dots, T_N$  are the attribute values of the  $N$  performance indexes? When the system status is changed, its gravity center is changed to

$$T' = (T'_1, T'_2, \dots, T'_N) \quad (3)$$

## 2. Measurement of the deviation of the cloud gravity center

The cloud gravity center vector of the system under the ideal status is

$$T^0 = (T^0_1, T^0_2, \dots, T^0_N) \quad (4)$$

Then, the difference of the synthetic cloud gravity center between the ideal status and the given status can be scaled by the weighted deviation  $\theta$ . Firstly, the synthetic cloud gravity center vector under the given status is normalized to obtain a vector  $T^G = (T^G_1, T^G_2, \dots, T^G_N)$ , where

$$T^G_i = \begin{cases} (T_i - T^0_i)/T^0_i, & T_i < T^0_i \\ (T_i - T^0_i)/T_i, & T_i \geq T^0_i \end{cases} \quad i = 1, 2, \dots, N \quad (5)$$

Secondly, after the normalization, the synthetic cloud gravity center vector, which expresses the system status, is a dimensionless value. The weighted deviation is

$$\theta = \sum_{i=1}^N w_i T^G_i \quad (6)$$

where  $w_i$  is the weighted value of the  $i$ th index.

## 3. Computation of the system performance

Based on the cloud gravity center deviation, the performance quantization value of the whole system is

$$E_S = 1 - \theta \quad (7)$$

The system of the performance index system for ballistic missile detection based on the weighted index is shown as Table 1, the system indexes are the complete three grade indexes in the index system. Then, the performance quantization value of the ballistic missile detection performance index system based on the weighted index is computed by Eqs. (2)–(7).

**Table 2** Cloud remark assembly

Grade	None	Extreme bad	Very bad	Bad	Comparatively bad	Normal	Comparatively good	Good	Very good	Extreme good	Perfect
Attribute value	0	0.1	0.2	0.3	0.4	0.5	0.6	0.7	0.8	0.9	1

### 3.3 *Ballistic Missile Detection Performance Evaluation of the Skywave Radar Based on the Cloud Remark Assembly*

Provided that there are  $N$  preliminary indexes  $I_1, I_2, \dots, I_N$ , the ballistic missile detection performance quantization value of the skywave radar based on the preliminary index and the weighted index is computed by the following formula:

$$E_T = E_{I_1} \wedge E_{I_2} \wedge \dots \wedge E_{I_N} \wedge E_S \tag{8}$$

where  $E_T$  is the synthetic performance quantization value,  $E_{I_1}, E_{I_2}, \dots, E_{I_N}$  are the performance quantization values of the  $N$  preliminary indexes,  $E_S$  is the performance quantization values of the weighted index, and  $\wedge$  is the multiplicative operation.

After the computation of the performance quantization value, the ballistic missile detection performance of the skywave radar is evaluated using the cloud remark assembly. The cloud remark assembly is shown as Table 2 [12].

## 4 Example and Analysis

### 4.1 *Confirmation of the Index Weight*

The index weight is computed by the AHP method. The index weight computation result is  $w = (0.2216 \ 0.0464 \ 0.0464 \ 0.0464 \ 0.0877 \ 0.0464 \ 0.0877 \ 0.1485 \ 0.0877 \ 0.0877 \ 0.0464 \ 0.0471)$ .

### 4.2 *Confirmation of the Weighted Index Attribute Value*

The weighted index attribute value is obtained by the expert scoring and the mathematic model. The ballistic missile detection weighted index attribute value of the skywave radar under typical conditions is shown as Table 3 (ta value of 1 in the ideal condition).

**Table 3** Ballistic missile detection weighted index attribute value of the skywave radar in typical condition

Index	Attribute value	Index	Attribute value
Time usability	0.85	Anti-destruction ability	0.80
Data rate	0.50	Support ability	0.85
Measurement precision	0.50	Phase disturbance	0.75
Resolution	0.50	Propagation path	0.70
Anti-jamming ability	0.80	Propagation loss	0.60
Counter-reconnaissance	0.50	Environment noise	0.70

### 4.3 Computation of the Detection Performance Based on the Weighted Index and the Cloud Gravity Center Theory

The normalized cloud gravity center vector is computed by the weighted index attribute value and Eq. (5); the computation result is  $T^G = (0.15 \ 0.50 \ 0.50 \ 0.50 \ 0.20 \ 0.50 \ 0.20 \ 0.15 \ 0.25 \ 0.30 \ 0.40 \ 0.30)$ . Based on the cloud gravity center vector  $T^G$  and the expert weight  $w$ , the weighted deviation is computed and the result is  $\theta = 0.2643$ . Hence, the ballistic missile detection performance value based on the weighted index under typical conditions is  $E_S = 0.7357$ .

### 4.4 Ballistic Missile Detection Performance Evaluation Based on the Cloud Remark Assembly

As shown above, there are three preliminary indexes. Combined with the target and environment characteristics, the performance value is  $\{E_{I_1}, E_{I_2}, E_{I_3}\} = \{1, 1, 1\}$ .. The preliminary index performance value and the weighted index performance value are substituted into Eq. (8), and the whole performance value is  $E_T = 0.7357$ . Then, comparing the whole performance value to the cloud remark assembly (Table 2), the performance value belongs to good, which corresponds to the actual situation.

## 5 Conclusion

In order to evaluate the ballistic missile detection performance of the skywave radar, for the ballistic missile detection characteristic and the complicate electromagnetic environment, the ballistic missile detection performance evaluation index is divided into the preliminary index and the weighted index. For the preliminary

index, the performance quantization values are computed by a binary function. For the weighted indexes, a detection performance index system is constructed, and the performance quantization value of the index system is calculated according to the cloud gravity center theory. Based on the performance quantization values of the preliminary index and the weighted index, the ballistic missile detection performance is evaluated using the cloud remark assembly. Finally, the ballistic missile detection performance of the skywave radar under typical conditions is calculated. The feasibility of this method is verified through the calculated result.

## References

1. Yan DL, Li X, Cai WY et al (2010) Evaluation of operational effectiveness of sky wave OTHR. *J Air Force Radar Acad* 24:177–179
2. Zhou HJ, Hou YT, Liu Q (2010) A method of system effectiveness evaluation for phased array radar. *Space Electron Technol* 66–69
3. Jia J, Liu JZ, Sheng W (2013) A study on operational efficiency evaluation of sky-wave over-the-horizon radar. *Mod Radar* 35:10–14
4. Lu L, Xiao WJ, Yan SQ et al (2010) Combat efficiency evaluation of sky wave over-the-horizon radar. *Mod Defence Technol* 38:112–115
5. Zhu LY, Hu DN, Yin T et al (2013) An evaluation method of sky wave over-the-horizon radar operational effectiveness based on fuzzy neural network. *Mod Radar* 35:5–8
6. Liu SH, Sheng W, Zhang XH (2013) An evaluation scheme of skywave radar coverage based on GRG. In: *ICMTMA 2013*, pp 191–193
7. Liu SH, Sheng W, Zhang XH (2013) An evaluation scheme of skywave radar coverage of ship target based on GRG. *Appl Mech Mater* 427–429:888–891
8. Zhang XH, Sheng W, Liu SH (2013) An evaluation scheme of skywave radar coverage. *Mod Defence Technol* 41:133–137
9. Wang AY, Yang ZM (2012) Evaluation of detection effectiveness for sky wave OTHR at sea. *J Air Force Radar Acad* 26:199–201
10. Liang M (2013) Research on modeling technology for ballistic missile interception simulation. *J China Acad Electron Inf Technol* 8:56–59
11. Yang HM, Zhang JQ, Liu SH et al (2012) Simulation of ability of OTHR detecting ballistic missile impact factor. *Comput Simul* 29:63–66
12. Gu JC, Zhang HW, Qi L et al (2011) Evaluation of the efficiency of the phased array radar system based on the theory of center of gravity of cloud. *Electron Sci Technol* 24:73–75

# Personnel Surface Electric Field Research of Live Working on Insulation Bucket Arm Car of 500-kV Transmission Lines

Bing-ling Zhou and Dong-ze Xu

**Abstract** In order to improve the reliability and security of electricity supply and to increase the live working efficiency, a strong measure which improves the reliability of power supply is using insulated bucket arm car as work platform in live working of transmission line. With the purpose of assessing the security impact in which 500-kV transmission lines exert on a person who is using an insulated bucket arm car for live working, methods of electric field finite element calculation and electric field measurement are adopted to research the distribution law of person's surface electric field in different working conditions. This article aims at the characteristics of live line work mode of 500-kV transmission line and uses the method of finite element calculation to study on the surface electric field distribution law of worker who is developing live working on an insulation bucket arm vehicle. Considering with the characteristics of insulation bucket arm vehicle and electric transmission line operation, we systemically proposed live working safety protection method about using insulation bucket arm vehicle in 500-kV transmission line.

**Keywords** 500-kV transmission lines · Live working · Electric field calculation · Security protection

## 1 The Finite Element Theory

The basic idea of finite element theory is that: transform a partial differential equation of definite solution problem into a variational problem or weighted residual equation, by using the subdivision interpolation, discrete the variational problem into the extreme problem of multivariate function or a weighted margin

---

B. Zhou (✉)

Maintenance Branch of Jiangsu Electric Power Company, Nanjing 210024, China  
e-mail: horror321@yeah.net; 727482316@qq.com

D. Xu

School of Electrical Engineering, Wuhan University, Wuhan 430072, China

© Springer-Verlag Berlin Heidelberg 2016

B. Huang and Y. Yao (eds.), *Proceedings of the 5th International Conference on Electrical Engineering and Automatic Control*, Lecture Notes in Electrical Engineering 367, DOI 10.1007/978-3-662-48768-6\_70

equation directly, constitute algebraic equations, and then solving the approximation solution of boundary value problem for the system of equations.

### 1.1 The Energy Functional Extreme Solution of Electrostatic Field

When existing space charge  $\rho \neq 0$  in electrostatic field, electric field energy functional for field  $D$  is as follows:

$$W(\varphi) = \iint_D \frac{1}{2} \varepsilon E^2 dx dy = \iint_D \left\{ \frac{\varepsilon}{2} \left[ \left( \frac{\partial \varphi}{\partial x} \right)^2 + \left( \frac{\partial \varphi}{\partial y} \right)^2 \right] - \rho \varphi \right\} dx dy \quad (1)$$

Then, the energy functional variation is as follows:

$$\delta W(\varphi) = \frac{\partial}{\partial t} W(\varphi + t \delta \varphi) = \iint_D [\varepsilon \nabla \varphi \cdot \nabla (\delta \varphi) - \rho \delta \varphi] dx dy \quad (2)$$

By Green's formula:

$$\delta W(\varphi) = - \iint_D (\varepsilon \nabla^2 \varphi + \rho) \delta \varphi dx dy + \oint_C \varepsilon \frac{\partial \varphi}{\partial n} \delta \varphi |dl| \quad (3)$$

In the above formula,  $n$  is the boundary line of the unit normal vector, and  $D$  and  $C$ , respectively, for the field and its boundary.

1. The first kind of boundary processing is as follows:

Before solving algebraic equations, it is necessary to know Dirichlet boundary conditions, and suppose that  $i$  node  $U$  is known as  $U_{i0}$ , then:

$$\begin{aligned} b(i) &= U_{i0}, \quad K_{i,i} = 1, \quad K_{i,j} = 0 \quad \text{when } j \neq i \\ b_j &\leftarrow b_j - K_{j,i} U_{i0}, \quad K_{j,i} = 0 \quad \text{when } j \neq i \end{aligned}$$

Combined with boundary condition, then Dirichlet boundary degrees of freedom of nodes of the corresponding equations can be removed from the general equations, in order to reduce the algebraic equations on the number of equations.

2. The second boundary processing is as follows:

$$\alpha \frac{\partial u}{\partial n} + \gamma u = q \quad (4)$$



$a$ ,  $g$ , and  $q$  are known parameters, and  $a$  is the diffusion coefficient in the control equation. The second kind of boundary condition is a special case when  $g = 0$  for the formula (4). If  $g$  and  $q$  are zero at the same time, the finite element discrete process will automatically consider the boundary conditions, without special treatment.

### 1.2 The Discrete Solution of Variational Problem

First of all, divide the field  $D$  into  $e_0$  unit. Suppose  $n_0$  unit node corresponding potentials are, respectively  $\varphi_1, \varphi_2, \varphi_3 \cdots \varphi_{n_0}$ , then the energy functional  $W(\varphi)$  and  $W_C(\varphi)$  can be an approximate expression with  $W(\varphi_1, \varphi_2, \varphi_3 \cdots \varphi_{n_0})$  and  $W_C(\varphi_1, \varphi_2, \varphi_3 \cdots \varphi_{n_0})$ , and suppose that there are  $n$  nodes potential unknown, then:

$$d[W + W_c] = \frac{\partial(W + W_c)}{\partial\varphi_1}d\varphi_1 + \cdots + \frac{\partial(W + W_c)}{\partial\varphi_n}d\varphi_n = 0 \tag{5}$$

Considering the randomness of  $A$  selection  $d\varphi_i (i = 1, 2, \dots, n)$ , assuming that except  $d\varphi_i \neq 0$ , take the rest of the expression as zero, then:

$$\frac{\partial(W + W_c)}{\partial\varphi_i}d\varphi_i = 0 \tag{6}$$

By that analogy, we can get a  $n \times n$  linear algebraic equations, solving the equations to get each node potential value and then get the approximate solution of electric field.

### 1.3 The Calculation Steps of Methods of Electric Field Finite Element

The application of finite element method for solving boundary value problems of the electromagnetic field generally contains the following steps.

1. Subdivision: In order to build approximate function while using finite element method, we should divide field into lots of units, in which indicating the approximate function with the proper interpolation function.
2. Interpolation function: On account of the advantage of easy calculation and easy to meet the convergence requirements, the different order polynomial power function is used mostly in finite element method.

3. The formation of the unit matrix and the right-end item: The interpolation function has only in the value of a node that is connected with the unit, so the finite element matrix or the right side of the integral calculation can be performed in each unit and then superimposed to form the overall matrix and the right side.
4. The overall synthesis: The unit matrix and the right-end item should be added to the total matrix and previous right-end item. Assuming the unit number is  $M$ , the total stiffness matrix  $[K]$  and the right-end item  $b$  satisfy the following equations.

$$[K] = \sum_{e=1}^M [\bar{K}^e] \quad (7)$$

$$\{b\} = \sum_{e=1}^M \{\bar{b}^e\} \quad (8)$$

$[\bar{K}^e]$  is the augmented stiffness matrix, and  $[\bar{b}^e]$  is the extended right vector of the  $e$ th unit.

5. Solving finite element equations and calculating the node voltage. Then, get the remaining components in electric field.

## 2 The Establishment of Simulation Model

Chose the linear tower of which the serial number is 500 kV ZB to build simulation model (Fig. 1).

Simulate the electric field distribution under the power frequency electric field by using three-dimensional finite element method. Ignore the influence to the electric field distribution from insulator strings. The electric potentials of the tower, ground, and infinity are considered as zero (Fig. 2).

Use cylinder and sphere to simulate the operator. Insulation bucket arm vehicle model-specific dimensions are shown in Table 1. Model of the operator is shown in Fig. 3.

Chose points to calculate electric field strength based on the actual situation of the bucket arm insulated car.

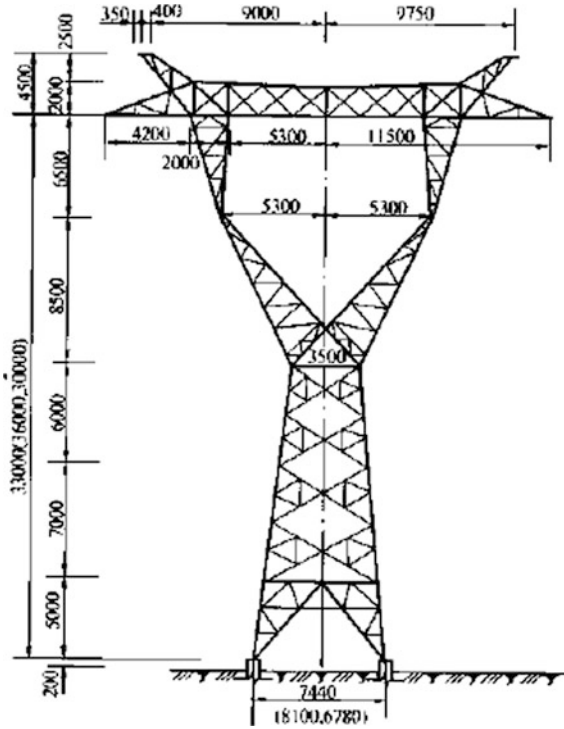


Fig. 1 Linear tower 500 kV ZB with the type of glass

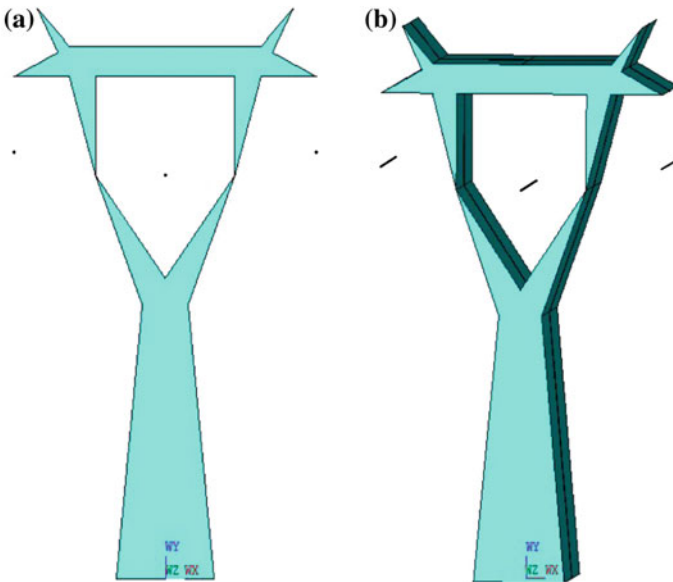
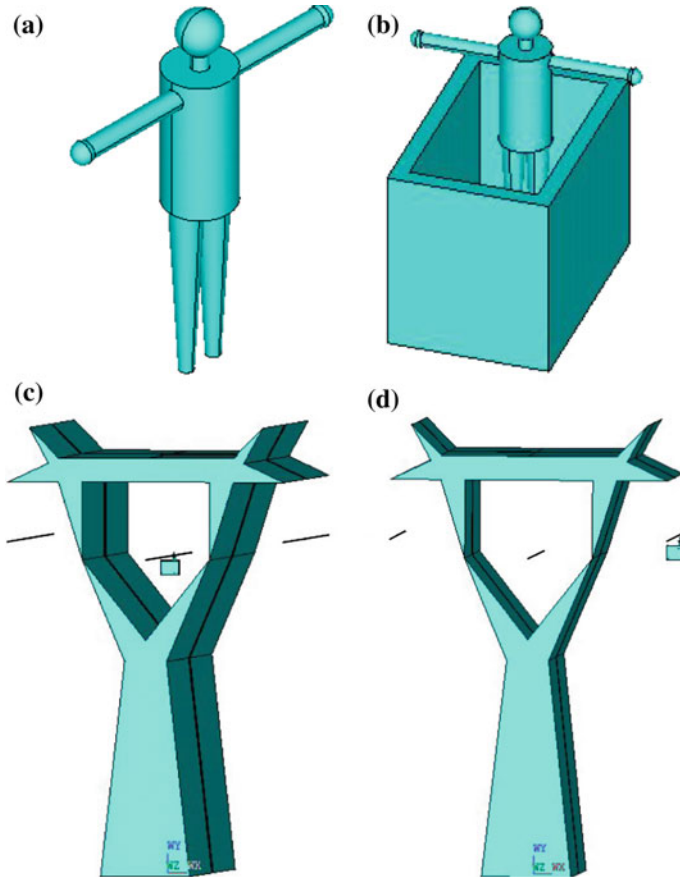


Fig. 2 Simulation model of 500 kV tower. a Front view. b Lateral view

**Table 1** Size of insulation bucket arm vehicle

The name of parameter	Parameter (m)
Length of vehicle	12.2
Width of vehicle	2.5
Height of vehicle	3.5
Maximum working height	37.5
Size of the platform	$1.016 \times 1.524 \times 1.067$

**Fig. 3** Model of the operator. **a** Arms stretched body model. **b** Model of the operator. **c** Operator at the middle phase. **d** Operator at side phase

### **3 500-kV Transmission Line Live Working Personnel Body Surface Electric Field on the Insulation Bucket Arm Vehicle**

According to the actual insulation bucket arm vehicle typical job position, and considering factors such as the activities scope of live working person and bucket arm vehicle, body position, the experience of bucket arm vehicle, and so on, and combing with the typical design of 500 kV tower, the safety assessment of different potential position has been analyzed.

In order to determine the safety path in which working bucket goes into, we simulated and computed worker surface electric field distribution of different job positions.

Because the structure of the body is only a little relative to the tower, it requires particularly big computer internal memory capacity if we want to solve just one time. So we adopted the subdomain method to establish a submodel and got an accurate calculation result.

#### ***3.1 Body Surface Electric Field Calculation of Live Working on 500-kV Transmission Line Bucket Arm Car***

Selecting the middle and edge phase conductor of 500-kV transmission lines as working location, respectively, calculate the working human body surface electric field distribution. The two typical load cases' calculation data are summarized in Table 2 (Fig. 4).

#### ***3.2 Actual Body Surface Electric Field Measurements of Live Working on 500-kV Transmission Line Bucket Arm Car***

On the 500-kV straight-line tower, select the edge phase and middle phase—two typical operating position—and the insulated bucket car into live working path interval position to measure the body surface electric field strength.

Technical measuring device is used to measure the electric field. At the specified measuring position, head, fingers, chest, and other parts nearby electric field strength are measured. Measure each part many times and then extract the average values as the final results, to reduce the measuring error.

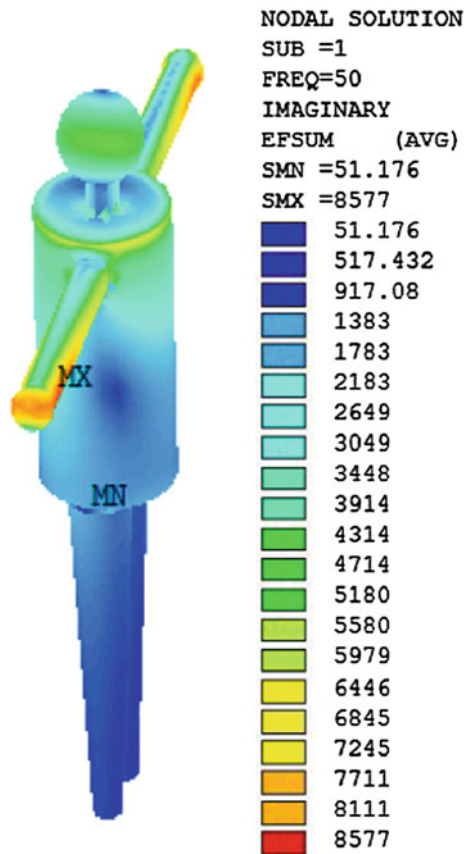
Figure 5 shows the selected position of measuring; the specific instructions of each location are shown in Table 3.

**Table 2** Working human body surface electric field calculation values

Human body parts	Human body location	
	Electric field intensity (kV/m)	
	Middle phase	Edge phase
Head	3.839	3.575
Chest	4.839	4.803
Hand (near the conductors)	8.577	6.788
Hand (away from the conductors)	6.705	6.056
Foot	0.051	0.015

*Note* The conductors are used as reverse phase sequence

**Fig. 4** Working human body surface electric field calculation chart



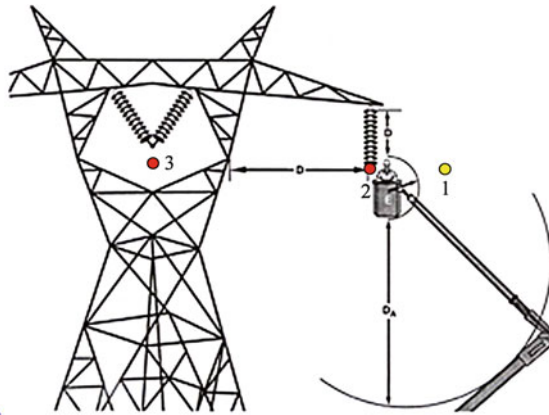


**Fig. 5** Diagram of the actual measuring location

**Table 3** The instructions of electric field measurement location on 500-kV transmission line bucket arm car

Calculation point	Instructions
Point 1	When bucket arm car enters the work process, 0.8 m away from the edge phase conductor
Point 2	Around the edge phase conductor of 500-kV lines
Point 3	Around the middle phase conductor of 500-kV lines

**Table 4** Measured values of the body surface electric field strength on 500-kV transmission line bucket arm car

Human body location	Human body parts		
	Electric field intensity (kV/m)		
	Hand	Head	Chest
1	5.7	2.1	2.8
2	6.3	2.5	3.1
3	7.1	2.8	3.3

Average the measured data through several measurements, and organize the final result to the Table 4.

Comprehensive the measured values and the simulation results of the working human body surface electric field, the following conclusions can be drawn:

1. When the working human body on the 500-kV transmission line bucket arm car is around or at the live working location, the maximum surface electric field strength appears in the hand, followed by the chest and head.
2. The data show that the simulation results are higher than the measured data. For instance, at the edge phase conductor of 500-kV transmission lines (location 3),

the maximum electric field strength of simulation results is 8.577 kV/m, which appears in the hand. The measuring device cannot accurately measure this electric field distortion, so the electric field strength of body surface calculation is quite strict and can be the security guard basis for judging of live working.

## 4 Conclusion

1. When the working human body on the 500-kV transmission line bucket arm car is around or at the live working location, the maximum surface electric field strength appears in the hand, followed by the chest and head.
2. When the worker perform live working on the 500-kV transmission line bucket arm car, the surface electric field strength does not exceed the GB6568.1-2000 standard safety limits, which is 15 kV and can ensure the safe operation.

## References

1. Guanrun J (1985) Overvoltage in electric power system. Hydraulic and Power Press, Beijing
2. Li H, Wen X (2000) The power frequency electric field intensity and distribution in workplace of 220 kV substation. *J Occup Health Damage* 15(4):246–247
3. Cui X (2003) International CIGRE series report in 2002 progress in research on electromagnetic compatibility of power system. *Power Syst Autom* 27(4):1–5
4. Liang Z, Dong X, Zheng L et al (2006) Measurement and analysis of power frequency electric field in 500 kV substations. *High Voltage Tech* 32(11):81–83, 122
5. Zhang Z, Cao P, Wan B et al (2008) Research on simulation test of the electric field in 1000 kV substation. *High Voltage Tech* 34(9):1807–1812
6. Hu Y, Hu J, Liu K (2010) The surface field strength of UHV AC and DC line live working personnel. *High Voltage Tech* 36(1)
7. Wang Y, Chen R, Yang T et al (2010) Calculated frequency electric field analysis of high-voltage substation. *Chongqing Univ Sci Technol: Nat Sci* 12(2):140–143
8. Zhang B, He J, Cui X et al (2006) Electric field calculation for HV insulators on the head of transmission tower by coupling CSM with BEM. *IEEE Trans Magn* 42(4):543–546



# Failure Mode Analysis on Machining Center Based on Possibility Theory

Hongzhou Li, Fei Chen, Zhaojun Yang, Liding Wang  
and Yingnan Kan

**Abstract** Aiming at the uncertainty of the expert judgment in the failure mode and effect analysis of machining centers, a failure mode analysis method for the machining centers based on the possibility theory is proposed. To express the uncertainty of the expert judgment, the possibility distribution of the attribute of the judgment is established and the information fusion of the possibility distribution is implemented using the comprehensive analysis method, obtaining the possibility distribution of the influence factor; The values are assigned to the weights using the subjective-objective combination weighting approach which combines the variation coefficient method and the subjective weighting method. And then the possibility values of the RPN are calculated and ranked. A machining center is taken as the example, and the proposed method is applied to analyze the criticality of its failure modes, and the design for reliability promotion is presented according to the ranking of criticality.

**Keywords** Possibility theory · Variation coefficient method · Failure mode · Machining center · Subjective and objective combination weighting approach

---

H. Li · F. Chen (✉) · Z. Yang · L. Wang · Y. Kan  
College of Mechanical Science and Engineering, Jilin University,  
Changchun 130025, China  
e-mail: yinshun\_9999@163.com

H. Li  
e-mail: 287505156@qq.com

Z. Yang  
e-mail: 2358584773@qq.com

L. Wang  
e-mail: 2644505863@qq.com

Y. Kan  
e-mail: 306219157@qq.com

H. Li  
College of Mechanical Engineering, Beihua University, Jilin 132011, China

## 1 Introduction

In order to improve the reliability of a product [1, 2], failure mode and effect analysis (FMEA) evaluates each failure mode's criticality rank by calculating RPN values and then ranking them.  $RPN = \text{severity } (S) \times \text{occurrence } (O) \times \text{detection } (D)$ . The main deficiencies of this method are as follows: (1) experts usually use qualitative language to present his grades when applying FMEA. However, the method is presented in the quantitative form. So it is difficult for the experts to make an accurate judgment; (2) in the calculation, the weights of three variables,  $S$ ,  $O$  and  $D$ , are equivalent, without considering the relative importance of  $S$ ,  $O$ ,  $D$ . In order to make up for these shortcomings and deficiencies, some scholars put forward TOPSIS method [3], which is based on the quantitative values, without reflecting the uncertainties of expert's grading; Some scholars [4] have better reflected the fuzziness of grading by applying fuzzy approach, but there are shortcomings in determining the weights. For example, the multi-objective fuzzy decision theory [5] ignores the weight of each factor; the fuzzy data envelopment analysis method [6] ignores the subjective information.

Aiming at the above shortcomings, the authors put forward a FMEA method, which establishes the possibility distribution of evaluation attribute space. And the possibility distributions of the influencing factors are obtained by implementing information fusion using comprehensive analysis method. The reasonable weights of the influencing factors are realized by variation coefficient method in combination with subjective weighting method, and further the possibility values of RPN of each failure mode of machining centres are obtained. Finally, the proposed FMEA method is applied to the machining centres as an example, and this method is verified.

## 2 The Possibility Distribution Model of the Failure Mode's Criticality

### 2.1 The Possibility Theory

Possibility theory is presented on the basis of fuzzy theory by Zadeh in 1978. It is a way to deal with uncertain information. Since the theory is particularly consistent with the human way of thinking, it is getting more and more applications [7].

**Definition 1** Suppose a mapping  $\pi : X \rightarrow [0, 1]$  satisfies  $\bigvee_{x \in X} \{\pi(x)\} = 1$ , then  $\pi$  is called the possibility distribution function (PDF) on  $X$ .

**Definition 2** Given PDF  $\pi$  on  $X$ , determines possibility degree  $\Pi : f(x) \rightarrow [0, 1]$  as shown in Eq. (1)

$$\forall A \in f(x), \prod(A) = \bigvee_{x \in A} \{\pi(x)\} \tag{1}$$

Then,  $\prod$  is possibility degree derived from  $\pi$ .

On the other hand, if the possibility degree  $\prod$  is given, then  $\prod$  can also determines possibility distribution function  $\pi$  on  $X$ , as shown in Eq. (2)

$$\forall x \in X, \pi(x) = \prod(\{x\}) \tag{2}$$

Possibility hypothesis: if  $A \in F(X)$ , then proposition “ $x$  is  $A$ ” induces a possibility distribution function  $\pi_x$  which is equal to  $A$ .

### 2.2 Determining the Possibility Distribution Function of Influence Factor

Suppose a domain of discourse  $V = \{v_1, v_2, \dots, v_n\}$  makes up a failure mode evaluation set of machining center, where  $v_n$  denotes the  $n$ th failure mode. Another domain of discourse  $U = \{u_1, u_2, \dots, u_m\}$  makes up an influence factor set, where  $u_m$  denotes the  $m$ th influence factor when evaluating the factors influencing the machining center’s failures. There are three influencing factors when evaluating on failure mode in this paper, namely Severity, Occurrence, and Detection. As there is fuzziness to some extent when experts evaluate the three influence factors, each influence factor’s influencing degree on a failure mode of the machining centers can be represented by a fuzzy set in the domain of discourse  $U$ . Suppose that some propositions  $P_{ij} (j = 1, 2, \dots, l)$  on the influence factor construct an evaluation attribute space  $P_i = \{P_{i1}, P_{i2}, \dots, P_{il}\}$ , and then each influence factor’s influencing degree on the failure mode can be expressed as the fuzzy set  $F_i (i = 1, 2, \dots, m)$ :

$$F_i = \sum_{j=1}^l \mu_{u_i}(P_{ij})/P_{ij} \quad (i = 1, 2, \dots, m) \tag{3}$$

where,  $\mu_{u_i}(P_{ij})$  denotes the relative grade of membership of proposition  $P_{ij}$  on  $u_i$  in the fuzzy set  $F_i$ .

Suppose  $u_i$  is a variable which takes values in the domain of discourse  $U$ . Based on the possibility theory, a possibility distribution  $\pi_{u_i}$  corresponding to  $P_{ij}$  can be induced by the proposition “ $u_i$  is  $P_{ij}$ ”. Also a possibility designation equation  $\pi_{u_i}(j) = \mu_{u_i}(P_{ij})$  can be obtained, which represents that the possibility that the influencing factor  $u_i$  is evaluated as  $P_{ij}$  is the relative membership degree of  $P_{ij}$  in the set  $F_i$ .

Then the possibility that the  $g$ th expert states “ $u_i$  as  $P_{ij}$ ” can be denoted as  $\pi_{u_i}^g(j) = \mu_{u_i}^g(P_{ij})$ . Thus, for the whole influence factor space, there is an influence factor possibility distribution:

$$\pi_{u_i}^g = \sum_{j=1}^l \mu_{u_i}^g(P_{ij})/P_{ij} \quad (\forall i \in [1, 2, \dots, m]) \tag{4}$$

Each component in the equation indicate that “ $u_i$  is  $P_{ij}$ ” induces the proposition that “the possibility of “ $u_i$  is  $F_j$ ” is  $\mu_{u_i}^g(P_{ij})$ ”

Mood operator (MO) used by experts are shown in Table 1.

In the process of evaluation, usually several experts are asked to assign a value to each influence factor. Since the information given by each expert can be all converted to possibility distribution via mood operators, the result obtained by fusing the information of factor  $u_i$  given by  $g$  experts is also the possibility distribution in the domain of discourse  $U$ , denoted by  $\prod_{u_i}$ , thus

$$\begin{aligned} \prod_{u_i} &= \sum_{j=1}^l \pi_{u_i}(P_{ij})/P_{ij} = \sum_{j=1}^l \pi_{u_i}^g(P_{ij})/P_{ij} \\ &= \sum_{k=1}^g a_k \mu_{u_i}^k(P_{ij})/P_{ij} \quad (\forall i \in [1, 2, \dots, m]) \end{aligned} \tag{5}$$

where  $\mu_{u_i}(P_{ij})$  represents the possibility degree that “ $u_i$  takes the value  $P_{ij}$ ” after fusing the information of evaluation given by  $g$  experts.  $a_k$  is weight,  $a_k \in [0, 1]$ ,  $\sum_{k=1}^g a_k = 1$ . Since we can’t completely assess the professional level of experts, we assign  $a_k = 1/g$ .

**Table 1** Mood operator of severity, occurrence mood, detection

Severity mood	MO	Occurrence mood	MO	Detection mood	MO
Minimum failure	0.1	Minimum failure rate	0.1	Unable to control	0.1
Very small failure	0.2	Very low failure rate	0.2	Minimum detectivity	0.2
Small failure	0.3	Low failure rate	0.3	Very low detectivity	0.3
Less small failure	0.4	Less low failure rate	0.4	Low detectivity	0.4
Medium failure	0.5	Medium failure rate	0.5	Less low detectivity	0.5
Less big failure	0.6	Less high failure rate	0.6	Medium detectivity	0.6
Big failure	0.7	High failure rate	0.7	Less high detectivity	0.7
Very big failure	0.8	Very high failure rate	0.8	High detectivity	0.8
Especially big failure	0.9	Maximum failure rate	0.9	Very high detectivity	0.9
Maximum failure	1	Complete failure	1	Maximum detectivity	1

### 2.3 Possibility Distribution of Criticality

Possibility distribution of influencing factors can be obtained by Eq. (5), and in the same way, the result by fusing every influencing factor is also the criticality’s possibility distribution of failure mode in the domain of discourse  $V$ , which is denoted by  $\prod_{v_i}$ .

$$\prod_{v_i} = \sum_{j=1}^m \pi_{v_i}(u_j)/u_j = \sum_{j=1}^m \mu_{v_i}(u_j)/u_j \tag{6}$$

where  $\mu_{v_i}(u_j)$  denotes possibility measure of “ $v_i$  is  $u_j$ ”, the value of which is  $\mu_{u_i}(P_{ij})$ .

### 2.4 Determining the Possibility Distribution Function of Occurrence of a Machining Center

The traditional FMEA obtains  $S, O, D$  by experts grading. Yet, this method ignores the useful data that objectively exists when FMEA is applied to particular machining center. In order to make full use of the objective useful data, this paper establishes membership degree of failure mode of machining center according to its historical operating data. The membership degree can be calculated by Eq. (7), which is numerically equal to the possibility degree [7, 8].

$$l_n(A)(x_i) = (\text{the time of } x_i \in A)/n \tag{7}$$

## 3 Sorting the Possibility Degree of Failure Mode’s Criticality

This paper applies the subjective-objective combination weighting method which combines the variation coefficient method [9] and the expert weighting method to determine weights of the possibility degree of failure mode’s criticality, the steps are as follows:

Step 1: determining objective weights:

Suppose a matrix  $A_{n \times m}$  which displays the possibility degrees of  $m$  influencing factors of  $n$  failure modes, namely

$$\mathbf{A}_{n \times m} = \begin{bmatrix} \mu_{v_1}(u_1) & \mu_{v_1}(u_2) & \dots & \mu_{v_1}(u_m) \\ \mu_{v_2}(u_1) & \mu_{v_2}(u_2) & \dots & \mu_{v_2}(u_m) \\ \dots & \dots & \dots & \dots \\ \mu_{v_n}(u_1) & \mu_{v_n}(u_2) & \dots & \mu_{v_n}(u_m) \end{bmatrix}$$

The objective weight of each index can be obtained based on variation coefficient method in Eq. (8).

$$w_{1j} = Q_j / \sum_{j=1}^m Q_j \tag{8}$$

where  $Q_j$  is influencing factor’s variation coefficient.

Step 2: Determining subjective weight  $w_{2j}$  by the experts assigning values.

Step 3: Subjective-objective combination weighting approach.

To apply linear weighting combination method, that is

$$\theta_j = \sum_{r=1}^m h_r w_{rj}, \quad r = 1, 2, 3, \dots \tag{9}$$

where  $\theta_j$  is the  $j$ th influencing factor’s combined weight.  $h_r$  is the coefficient of the  $r$ th weighting method,  $\sum h_r = 1, h_r > 0$ .  $w_{rj}$  is the weight of the  $j$ th index by the  $r$ th weighting method.

In this paper, that is

$$\theta_j = h_1 w_{1j} + h_2 w_{2j} \tag{10}$$

Suppose a matrix  $\mathbf{F}_{1 \times n}$  which is the possibility degree matrix of failure mode,  $f_{1j}$  is the possibility degree of the  $j$ th failure mode, then  $\theta$  denotes the weight vector  $\theta = [\theta_1, \theta_2, \dots, \theta_j, \dots, \theta_m]$ ,  $\mathbf{B}_{n \times m}$  denote the normalized possibility matrix  $\mathbf{A}_{n \times m}$  of failure modes’ influencing factors.

### 4 Real Case Analyses

A batch of machining center is presented as the research object. This paper determined 22 main failure modes and their frequencies are determined based on its historical operating data, then the possibility degree of occurrence of each failure mode is calculated by Eq. (7) and Definition 2, as shown in Table 2.

Four experts assign values to possibilities of  $O$ ,  $S$ , and  $D$  for the failure mode of machining center, according to Table 1, as shown in Table 3.

**Table 2** Possibility degree of occurrence of failure mode

Code	Failure modes	Frequency	Possibility degree
MD1	Moving component can't move	4	0.3
MD2	Leakage and breakdown of liquid, gas or oil	11	1
MD3	Can't return to zero	3	0.2
MD4	Clearance of moving component is too undersize	9	0.8
MD5	The sensing component is out of order	1	0.1
MD6	Transposition or shifting are over travel	6	0.5
MD7	Lock parts become less crowded	7	0.6
MD8	Protective sealing is bad	2	0.1
MD9	Motor can't start up	4	0.3
MD10	Vibrating or shaking	11	1
MD11	False alarm	3	0.2
MD12	Geometric accuracy exceeds standard	4	0.3
MD13	Moving parts speed maladjustment	3	0.2
MD14	Circuit are broken circuit	3	0.2
MD15	Electron component damaged	9	0.8
MD16	Guard or shield is damaged	2	0.1
MD17	liquid, gas or oil are closed	2	0.1
MD18	Controlling of Liquid or gas are failed	4	0.3
MD19	Moving parts have no action	6	0.5
MD20	Part fall off	1	0.1
MD21	Abnormal sound	6	0.5
MD22	Mechanical parts damaged	1	0.1

$\mu_{u_i}(p_j)$  is calculated by Eq. (5). Since historical data are introduced in calculating occurrence, its weights are:  $a_{11} = 0.4$ ,  $a_{1i} = 0.15$  ( $i = 2, 3, 4, 5$ ). And the weights of the severity and detection are,  $a_{2i} = 0.25$   $a_{3i} = 0.25$  ( $i = 1, 2, 3, 4$ ). The results are shown in Table 4.

Possibility degree matrix  $\mathbf{A}_{22 \times 3}$  can be obtained according to Table 4 and then normalized by extremum method, obtaining normalized matrix  $\mathbf{B}_{n \times m}$ .

Objective weight obtained by step 1 is  $w_{1j} = (0.40, 0.32, \text{ and } 0.28)$ . Subjective weights obtained by step 2 is:  $w_{2j} = (0.40, 0.3, 0.3)$ ,  $h_1 = 0.6$ ,  $h_2 = 0.4$ . Thus we can obtain the combined weight by step 3,  $\theta_j = (0.40, 0.31, \text{ and } 0.29)$ . We calculate the possibility degrees and then sort them. For comparison, we calculate and sort using traditional method and the proposed method which does not involve historical data, respectively, as shown in Table 5. For discussing conveniently, the proposed method is referred to method 1, the proposed method with no historical data is referred to method 2, and the traditional method is referred to method 3.

From Table 5, it is known that the sorting with the proposed method is different from traditional method, and some failure modes' orders are different obviously. For example, for failure mode MD2, its order is 9 with traditional method; the

**Table 3** Possibility degree assigned by experts

Code	Expert 1			Expert 2			Expert 3			Expert 4		
	<i>O</i>	<i>S</i>	<i>D</i>	<i>O</i>	<i>S</i>	<i>D</i>	<i>O</i>	<i>S</i>	<i>D</i>	<i>O</i>	<i>S</i>	<i>D</i>
MD1	0.7	0.8	0.6	0.6	0.7	0.6	0.7	0.8	0.5	0.6	0.7	0.5
MD2	0.6	0.5	0.3	0.5	0.6	0.4	0.5	0.5	0.3	0.6	0.6	0.4
MD3	0.5	0.5	0.8	0.5	0.6	0.7	0.3	0.4	0.7	0.6	0.5	0.8
MD4	0.6	0.4	0.5	0.4	0.4	0.6	0.4	0.5	0.6	0.6	0.6	0.6
MD5	0.5	0.7	0.4	0.3	0.8	0.3	0.5	0.7	0.3	0.4	0.8	0.4
MD6	0.3	0.8	0.5	0.5	0.7	0.6	0.3	0.8	0.6	0.4	0.6	0.4
MD7	0.5	0.9	0.2	0.4	0.7	0.3	0.4	0.8	0.2	0.4	0.8	0.4
MD8	0.4	0.4	0.2	0.4	0.3	0.3	0.6	0.4	0.2	0.4	0.5	0.4
MD9	0.2	0.6	0.4	0.4	0.5	0.5	0.5	0.6	0.5	0.4	0.5	0.4
MD10	0.6	0.6	0.9	0.8	0.5	0.8	0.5	0.4	0.8	0.4	0.7	0.9
MD11	0.3	0.2	0.6	0.3	0.1	0.6	0.5	0.3	0.4	0.5	0.2	0.5
MD12	0.2	0.4	0.5	0.5	0.5	0.6	0.4	0.4	0.5	0.3	0.6	0.6
MD13	0.3	0.5	0.4	0.4	0.6	0.4	0.5	0.5	0.5	0.3	0.4	0.6
MD14	0.2	0.3	0.3	0.3	0.4	0.2	0.4	0.2	0.2	0.4	0.2	0.4
MD15	0.9	0.3	0.4	0.7	0.4	0.9	0.5	0.5	0.4	0.7	0.3	0.3
MD16	0.5	0.1	0.1	0.3	0.2	0.1	0.5	0.2	0.2	0.4	0.2	0.2
MD17	0.1	0.2	0.2	0.3	0.3	0.3	0.4	0.2	0.3	0.3	0.3	0.3
MD18	0.3	0.4	0.5	0.4	0.4	0.5	0.1	0.5	0.5	0.3	0.6	0.4
MD19	0.4	0.7	0.5	0.3	0.6	0.6	0.2	0.8	0.6	0.2	0.8	0.7
MD20	0.2	0.2	0.2	0.4	0.3	0.2	0.3	0.4	0.2	0.4	0.2	0.3
MD21	0.6	0.3	0.3	0.7	0.4	0.5	0.5	0.2	0.6	0.4	0.3	0.6
MD22	0.5	0.2	0.1	0.3	0.3	0.1	0.4	0.2	0.1	0.5	0.4	0.2

**Table 4** Possibility degrees of *O*, *S*, *D*

Code	<i>O</i>	<i>S</i>	<i>D</i>	Code	<i>O</i>	<i>S</i>	<i>D</i>	Code	<i>O</i>	<i>S</i>	<i>D</i>
MD1	0.75	0.51	0.55	MD9	0.55	0.35	0.45	MD17	0.25	0.21	0.28
MD2	0.55	0.73	0.35	MD10	0.55	0.75	0.85	MD18	0.48	0.29	0.48
MD3	0.5	0.37	0.75	MD11	0.2	0.32	0.53	MD19	0.73	0.37	0.6
MD4	0.48	0.62	0.58	MD12	0.48	0.33	0.55	MD20	0.28	0.24	0.23
MD5	0.75	0.3	0.35	MD13	0.5	0.31	0.48	MD21	0.3	0.53	0.5
MD6	0.73	0.43	0.53	MD14	0.28	0.28	0.28	MD22	0.28	0.3	0.13
MD7	0.8	0.5	0.28	MD15	0.38	0.74	0.5				
MD8	0.4	0.31	0.28	MD16	0.18	0.3	0.15				

method 2 upgrades two levels of criticality compared with traditional method, method 1 upgrades six levels of criticality compared with method 3. These indicate that the criticality of failure mode MD2 is influences greatly on the failure modes of this batch of machining centers. So the improving redesign of the corresponding



**Table 5** Sorting comparison of the three methods

	Method 3		Method 2		Method 1	
	RPN	Code	Possibility degree	Code	Possibility degree	Code
1	269	MD10	0.79	MD1	0.86	MD10
2	268	MD1	0.74	MD10	0.67	MD1
3	178	MD3	0.63	MD15	0.65	MD2
4	143	MD6	0.59	MD3	0.64	MD15
5	137	MD4	0.53	MD4	0.63	MD4
6	131	MD15	0.52	MD6	0.58	MD6
7	120	MD19	0.52	MD2	0.57	MD7
8	112	MD5	0.51	MD5	0.57	MD19
9	106	MD2	0.5	MD7	0.52	MD3
10	94	MD7	0.46	MD19	0.44	MD21
11	93	MD9	0.45	MD21	0.43	MD5
12	91	MD12	0.4	MD9	0.41	MD9
13	89	MD13	0.39	MD13	0.4	MD12
14	83	MD21	0.38	MD12	0.36	MD13
15	62	MD18	0.32	MD8	0.34	MD18
16	50	MD8	0.28	MD18	0.25	MD11
17	42	MD11	0.28	MD11	0.24	MD8
18	25	MD14	0.18	MD22	0.15	MD14
19	20	MD20	0.15	MD14	0.11	MD22
20	19	MD17	0.14	MD16	0.1	MD20
21	15	MD22	0.13	MD20	0.09	MD17
22	11	MD16	0.09	MD17	0.07	MD16

parts is needed. For failure mode MD3, method 2 degrades one level compared with method 3; method 1 degrades six levels compared with method 3. This means that the criticality of MD3 is smaller. So there is no need to focus too much. There is the same trend in MD15 and MD7, etc. Thus, the proposed method to sort criticality is closer to real situation than traditional method.

**Acknowledgments** The author would like to thank the Science and Technology Development Program of Jilin province (No. 20130302009GX) and Project of Priority Funding for Basic Scientific Research Business of Jilin University (450060521026).

**References**

1. Yang Z, Chen C, Chen F (2013) Progress in the research of reliability technology of machine tools. *J Mech Eng* 49(20):130–139
2. Rui K, Rongde S (2006) *FMECA technology and its application*. National Defence Industrial Press, Beijing

3. Marcello B, Maro F, Roberto M (2003) Fuzzy TOPSIS approach for failure mode, effects and criticality analysis. *Qual Reliab Eng Int* 19:425–443
4. Yang Z, Xu B, Chen F (2010) A new failure mode and effects analysis model of CNC machine tool using fuzzy theory. In: *IEEE international conference on information and automation*. Harbin Engineering University, Harbin, pp 582–587
5. Li X, Shi MA, Li SC (2007) A study of application of theory of multi-objective fuzzy decision to failure modes and effects analysis. *J Xi'an Univ Technol* 23(3):331–333
6. Chen C, Yang ZJ (2013) Failure mode analysis of computer numerical control machine tools based on fuzzy-DEA. *J Jilin Univ* 43(06):1523–1528
7. Hu B (2010) *Fuzzy theory basis*. Wuhan University Press, Wuhan, p 6
8. Li H, Wang P (1994) *Fuzzy mathematics*. National Defence Industrial Press, Beijing
9. Huiqin X (2008) *The research on the methods of index's weight to be determined in the multiple attribute decision-making*. Northwest Normal University

# Microstructure and Tensile Properties of Squeeze Cast AZ91D Magnesium Alloy

Xizi Xiao, Yun Chen and Juan Du

**Abstract** Microstructure and tensile properties of squeeze cast AZ91D alloy in different heat treatment conditions are studied. The effect of wall thickness of specimens on tensile properties is also discussed. The results show that the microstructure of squeeze cast AZ91D alloy consists of primary  $\alpha$ -Mg matrix and  $\beta$ -Mg<sub>17</sub>Al<sub>12</sub> phase which is mainly present in the matrix and grain boundaries. Single phase  $\alpha$ -Mg solid solution is obtained after T4 treatment, and some granular precipitates are present in  $\alpha$ -Mg matrix. After T6 treatment, finer  $\beta$ -Mg<sub>17</sub>Al<sub>12</sub> phase precipitates within the  $\alpha$ -Mg matrix and along the grain boundaries again. The yield strength (YS) and ultimate tensile strength (UTS) of squeeze cast AZ91D alloy decrease, but the elongation increases with the increase of wall thickness. The SEM analysis of fracture surfaces shows that the squeeze cast AZ91D alloy displays different fracture modes in different heat treatment conditions.

**Keywords** Squeeze casting · Magnesium alloy · Microstructure · Tensile properties

## 1 Introduction

Magnesium alloy is very attractive in automobile industry, due to its low-density and high-specific strength, stiffness, and excellent castability and machinability [1, 2]. At present, most magnesium alloy castings are produced by high-pressure die

---

X. Xiao (✉)

School of Bioengineering, University of Pittsburgh, Pittsburgh 999039, USA  
e-mail: 1041128958@qq.com

Y. Chen

School of Logistic Engineering, Wuhan University of Technology,  
Wuhan 430063, China

J. Du

Department of Mechanical Electronic Engineering, Wuhan Technical College of  
Communications, Wuhan 430065, China

© Springer-Verlag Berlin Heidelberg 2016

B. Huang and Y. Yao (eds.), *Proceedings of the 5th International Conference on Electrical Engineering and Automatic Control*, Lecture Notes in Electrical Engineering 367, DOI 10.1007/978-3-662-48768-6\_72

casting process. However, the quality of high-pressure die castings cannot be improved by the subsequent heat treatment because of the gas porosities [3].

Squeeze casting, as an advanced forming technology with very wide application, is a process that involves slow laminar filling and the solidification of molten metal in a closed die under an imposed high pressure [4]. This process has the capability of producing pore-free near net-shape castings. This allows post-process solution and aging treatment to achieve excellent tensile properties [5]. However, limited information on microstructure and tensile properties of squeeze cast AZ91D alloy under different heat treatment states is available in the open literature.

This article presents the progress of an ongoing research work on squeeze cast of AZ91D magnesium alloy. The microstructure, tensile properties, and fracture behavior of squeeze cast AZ91D alloy under different heat treatment states are studied. The effect of wall thickness of specimens on tensile properties is also discussed. The aim of the present article is to provide foundation for the selection and performance improvement of magnesium alloy.

## 2 Experimental Procedures

The magnesium alloy selected for this study is the conventional magnesium alloy AZ91D, of which chemical composition is 8.99 % of Al, 0.772 % of Zn, 0.272 % of Mn, 0.052 % of Si, 0.0025 % of Cu, 0.0010 % of Ni, 0.0036 % of Fe, and the remaining of Mg. Tensile tests were derived from indirect squeeze cast tensile specimens having a rectangular cross section with gage length of 50 mm and width of 12.5 mm. The thicknesses of the various specimens were 1, 2, 3, 4, 6, and 8 mm, respectively. All the specimens were designed according to GB/T228-2002 standards, and they were radially and symmetrically around the downsprue [6], as shown in Fig. 1. Squeeze cast specimens are presented in Fig. 2. In order to ensure the filling of liquid magnesium alloy, the specimens were produced at pouring temperature of 740 °C, die temperature of 200 °C, squeeze velocity of 55 mm s<sup>-1</sup>, applied pressure of 120 MPa, initially pressurized time of less than 3 s, and dwell time of about 10 s.

**Fig. 1** D model of specimens



**Fig. 2** Squeeze cast specimens



T4(410 °C × 10 h) and T6(410 °C × 10 h + 200 °C × 10 h) treatments were applied to improve the tensile properties of several specimens of each thickness. These specimens were prepared by the standard metallographic technique of grinding and polishing followed by etching with oxalic acid. The microstructure of the specimens was examined using a light microscope. Fractured surfaces of tensile specimens were analyzed by the SEM to ascertain the nature of fracture mechanisms.

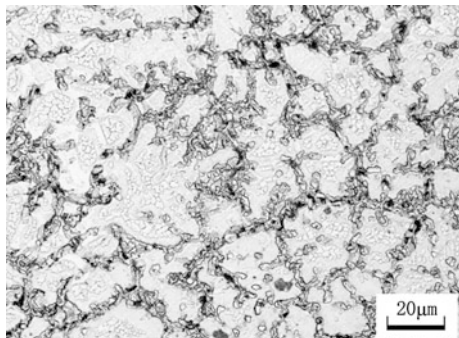
The tensile properties were performed at room temperature on an AG-IS100KN electronic universal tensile testing machine with a computer data acquisition system. The tensile properties, including yield strength (YS), ultimate tensile strength (UTS), and elongation of failure, were obtained based on the average of three tests.

### 3 Results and Discussion

#### 3.1 Microstructure

Figure 3 shows the microstructure of the squeeze cast AZ91D specimen with a section thickness of 8 mm revealed by optical microscopy. Its microstructure mainly consists of primary  $\alpha$ -Mg matrix and  $\beta$ -Mg<sub>17</sub>Al<sub>12</sub> phase which is mainly

**Fig. 3** Microstructure of squeeze cast AZ91D alloy (as-cast)



present in the matrix and grain boundaries. Due to non-equilibrium crystallization of magnesium alloy liquid during squeezing cast, discontinuous divorced eutectic microstructure ( $\alpha$ -Mg +  $\beta$ -Mg17Al12), which precipitates along the grain boundary, increases the brittleness of AZ91D alloy.

The solution treatment (T4) of AZ91D magnesium alloy includes the solution of  $\beta$ -Mg17Al12 phase and the redistribution and homogenization of alloy elements [7]. This is clearly illustrated in Fig. 4, showing single phase  $\alpha$ -Mg solid solution. After T4 treatment, grain boundary and coarse  $\beta$ -Mg17Al12 phase almost dissolve. Moreover, some granular precipitates, which are probably  $\beta$ -Mg17Al12 phase owing to Al precipitated from supersaturated  $\alpha$ -Mg matrix or undissolved intermetallic  $Al_6Mn$  phase, are present in  $\alpha$ -Mg matrix.

Figure 5a shows the microstructure of squeeze cast AZ91D specimen after 10 h solution heat treatment and then aging for 10 h. There is great difference between T6 temper treatment and as-cast structure. Coarse  $\beta$ -Mg17Al12 phase in as-cast structure becomes finer after T6 treatment. The  $\beta$ -Mg17Al12 phase morphology is

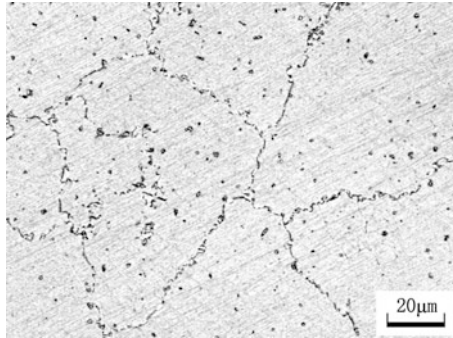


**Fig. 4** Microstructure of squeeze cast AZ91D alloy (T4)

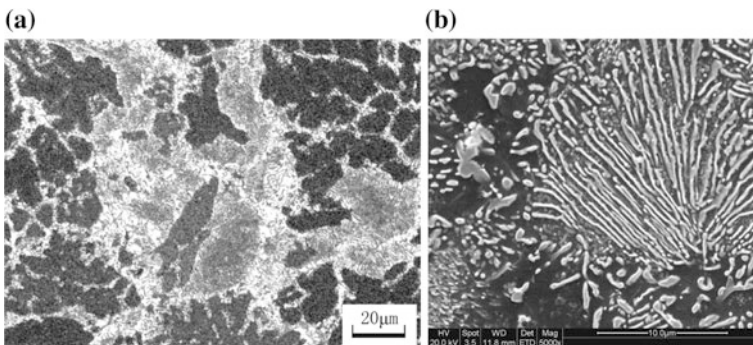


**Fig. 5** Microstructure of squeeze cast AZ91D alloy (T6). **a** Optical micrograph. **b** SEM micrograph

more clearly revealed in Fig. 5b by the SEM micrograph. Figure 5b shows the precipitation ways of  $\beta$ -Mg17Al12 phase including continuous and discontinuous precipitation. More granular  $\beta$ -Mg17Al12 phase presents evenly in  $\alpha$ -Mg matrix by continuous precipitation way. Fine lamellar, granular, and short-bar shape  $\beta$ -Mg17Al12 phase presents in grain boundary by discontinuous precipitation way. A significant improvement on tensile properties of the squeeze cast AZ91D alloy is mainly attributed to the fine lamellar  $\beta$ -Mg17Al12 phase, which prevents dislocation motion.

### 3.2 Tensile Behavior

Squeeze cast AZ91D alloy specimens with section thickness of 1 and 2 mm are hardly gained due to poor liquidity. Therefore, only tensile properties of specimens with section thickness of 3, 4, 6, and 8 mm were examined.

Figures 6, 7, and 8 illustrate the correlation between the tensile properties of squeeze cast AZ91D alloy under different heat treatment and wall thicknesses. This clearly demonstrates that the YS and the UTS decrease, but the elongation increases with the increase of wall thickness. The finer microstructure may be obtained due to the fast solidification rate of alloy liquid in a thin-wall specimen. According to the Hall–Petch equation, the strength of specimen reduces with grain size increasing [8]. The porosity of specimen is reduced as the wall thickness is increased due to the improvement of solidification conditions. Low porosity of specimen enhances the elongation.

The tensile properties of specimen with wall thickness of 8 mm under different heat treatment conditions are further discussed. The UTS and elongation of squeeze cast AZ91D alloy in T4 state are higher about 33 MPa and by 79.5 %, respectively, compared to as-cast state. The great improvement can be attributed to the dissolution

**Fig. 6** YS versus tensile specimen thickness for squeeze cast AZ91D alloy

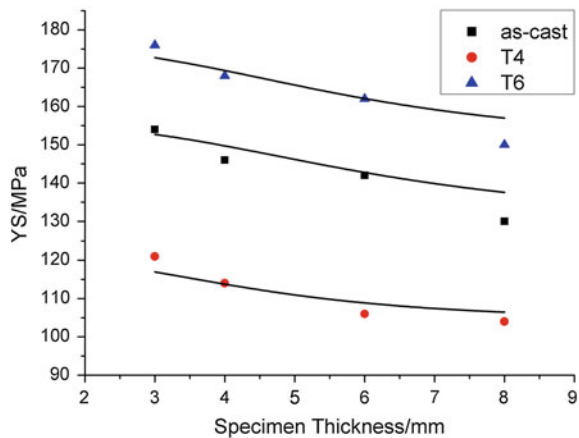


**Fig. 7** UTS versus tensile specimen thickness for squeeze cast AZ91D alloy

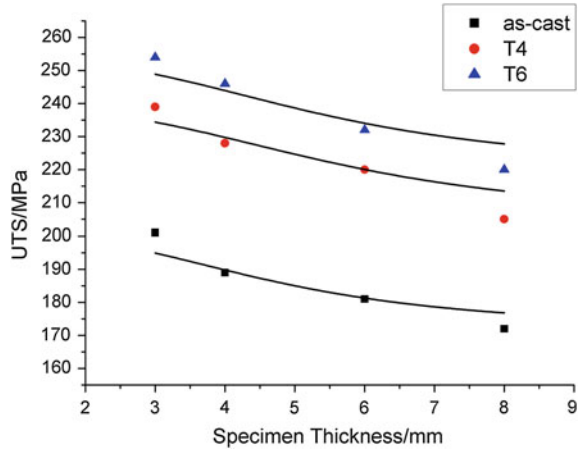
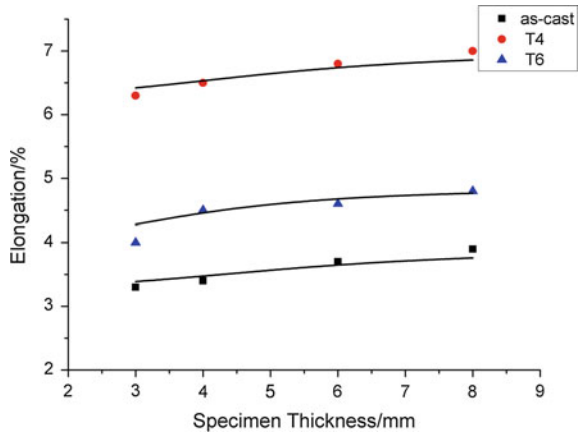


**Fig. 8** Elongation versus tensile specimen thickness



of brittle  $\beta$ -Mg<sub>17</sub>Al<sub>12</sub> phase which rends the metal matrix. After T6 heat treatment, the YS is about 44.2 % higher than in T4 state. It is mainly because fine lamellar, granular, and short-bar shape  $\beta$ -Mg<sub>17</sub>Al<sub>12</sub> phase presents in grain boundary and matrix.

### 3.3 Fracture Behavior

Figure 9 shows a typical fracture surface of the squeeze cast AZ91D specimens in as-cast conditions. Fracture surfaces are relatively smooth. A few tearing ridges and shallow dimples are observed on these fracture surfaces. Few tearing ridges are not enough to form cleavage rivers. Therefore, squeeze cast AZ91D magnesium alloy shows low room temperature ductility.



**Fig. 9** SEM fractograph of squeeze cast AZ91D alloy (as-cast)

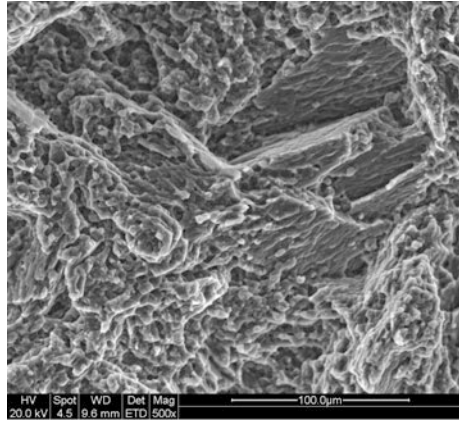
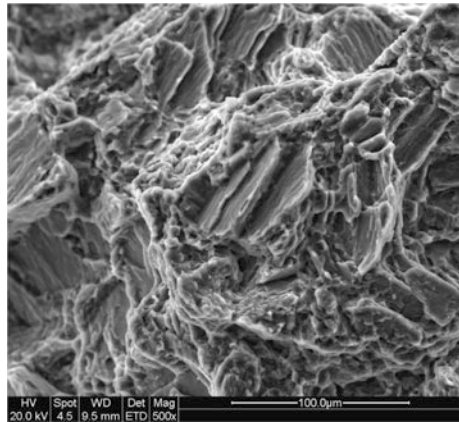


**Fig. 10** SEM fractograph of squeeze cast AZ91D alloy (T4)

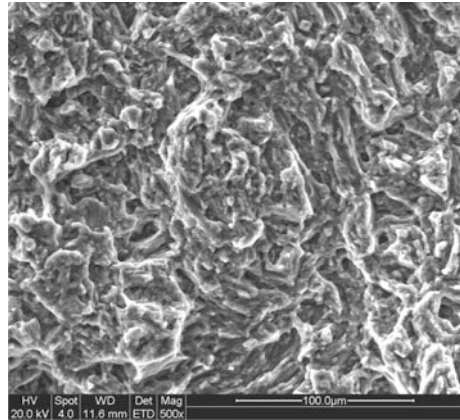


The tensile fracture surface of the squeeze cast AZ91D specimens after T4 treatment, as shown in Fig. 10, is obviously different with specimens in as-cast conditions. Fracture surface is covered by river markings and cleavage facets which are connected by tearing ridges. Some deep dimples are observed around tearing ridges. These features are the indication of the absorption of more energy and the larger plastic deformation prior to fracture of material [9]. Thus, squeeze cast AZ91D alloy after T4 treatment exhibits quasi-cleavage fracture modes. This also accounts for significant improvement in the elongation of squeeze cast AZ91D alloy after T4 treatment over as-cast one.

Figure 11 shows the fracture surface of the squeeze cast AZ91D specimens after T6 treatment.

After aging treatments for 10 h, fracture surface of specimen is also relatively smooth and characterized by fine river markings and a few shallow dimples. Squeeze cast AZ91D alloy in T6 conditions exhibits intergranular fracture modes.

**Fig. 11** SEM fractograph of squeeze cast AZ91D alloy (T6)



## 4 Conclusions

The present study concludes that the tensile properties of squeeze cast AZ91D vary significantly with section thickness and heat treatment states. The microstructure of squeeze cast AZ91D alloy consists of primary  $\alpha$ -Mg matrix and  $\beta$ -Mg<sub>17</sub>Al<sub>12</sub> phase which is mainly present in the matrix and grain boundaries. Single phase  $\alpha$ -Mg solid solution is obtained after T4 treatment, and some granular precipitates are present in  $\alpha$ -Mg matrix. After T6 treatment,  $\beta$ -Mg<sub>17</sub>Al<sub>12</sub> phase precipitates within the  $\alpha$ -Mg matrix and along the grain boundaries again. The YS and the UTS decrease, but the elongation increases with the increase of wall thickness. The tensile properties of squeeze cast AZ91D alloy have been improved significantly after heat treatment. The SEM analysis of fracture surfaces shows that the squeeze cast AZ91D alloy displays the characteristics of ductile fracture in as-cast conditions, quasi-cleavage fracture modes in T4 conditions, and intergranular fracture modes in T6 conditions.

**Acknowledgements** The work was supported by the Fundamental Research Funds for the Central Universities (WUT: 2014-IV-128)

## References

1. Mustafa KK (2008) Magnesium and its alloys applications in automotive industry. *Int J Adv Manuf Technol* 39:851–865
2. Aghion E, Moscovitch N, Arnon A (2009) Mechanical properties of die-cast magnesium alloy MRI 230D. *JMEPEG* 18:912–916
3. Gertsberg G, Aghion E, Kaya AA et al (2009) Advanced production process and properties of die cast magnesium composites based on AZ91D and SiC. *JMEPEG* 18:886–892
4. Luo JX, Li MH (2006) Synthetically control of the quality on squeezed castings. *Spec Cast Nonferrous Alloy* 26:715–718

5. Maleki A, Niroumand B, Shafyei A (2006) Effects of squeeze casting parameters on density, macrostructure and hardness of LM13 alloy. *Mater Sci Eng A* 428:135–140
6. Chen Y, Luo JX, Du J et al (2014) Study on fluidity of squeeze cast AZ91D magnesium alloy with different wall thicknesses. *Chin Foundry* 2:115–118
7. Zhang JM, Jiang BL, Wang ZH et al (2007) Effects of solid solution and ageing on fracture behavior of AZ80 magnesium alloy. *Spec Cast Nonferrous Alloy* 27:663–666
8. Chaudhri MM (2010) Indentation size effect and the Hall–Petch law. *Mater Sci Forum* 662:13–26
9. Zhou M, Henry H, Naiyi L et al (2005) microstructure and tensile properties of squeeze cast magnesium alloy AM50. *JMEPEG* 14:539–545

# Research and Design of Merging Unit of Electronic Transducer

Zheng Qiao, Bujuan Li, Yikang Zu and Yanqin Sun

**Abstract** Merging unit (MU) which is the core of digital substation is an important component of the interface between electronic transducer and protective device. In this paper, MU of traction substation is studied and designed according to IEC60044-8 and IEC61850-9-2, and the overall realization scheme of traction substation MU is given, which is characterized by using field programmable gate array (FPGA) as the hardware core of MU and divided into data acquisition module, data processing module and data transmission module, and the desired functionality of each module were described in detail and specific analysis.

**Keywords** Electronic transformer · Merging unit · IEC61850 · FPGA

## 1 Introduction

Electronic transformers have more advantages than electromagnetic transducer, such as small size, large dynamic ranges, without ferroresonance, good insulation. So it will be widely adopted in digital substation. But one of the key technical issues in digital substation implementation is how to interface between the electronic transformer and substation equipment. The Electronic transformer and substation equipment are connected by the merging unit (MU) researched in this paper is the device. Its main function is to receive samples which were export by electronic transformer synchronously, to validate and merge samples, and the digital combined sample value is then passed to substation spacer. To a certain extent, the digitization and sharing of process layer data are realized by application of MU. It has a great significance to simplify the secondary equipment and improve the accuracy and reliability of the system. So it will have a great significance to research on MU of electronic transformers.

---

Z. Qiao (✉) · B. Li · Y. Zu · Y. Sun  
Huanggang Normal University, Huanggang, Hubei, China  
e-mail: 373412838@qq.com

© Springer-Verlag Berlin Heidelberg 2016  
B. Huang and Y. Yao (eds.), *Proceedings of the 5th International Conference on Electrical Engineering and Automatic Control*, Lecture Notes in Electrical Engineering 367, DOI 10.1007/978-3-662-48768-6\_73

## 2 Needs Analysis and Hardware Design of MU

In this paper, the configuration of MU of 110-kV transformer substation is analyzed as an example, the high-pressure side is 110 kV, the low-pressure side of the feeder is 27.5 kV, AT power supply is used in the system, and V/X wiring is used in traction transformers. In the high-pressure side of 110-kV transformer, 9 signals, each protection and measuring current and voltage of A, B, C three phase need to be sample by MU. Commonly used electronic transformer includes two coils, it can gather protection and measuring current and voltage of A, B, C three phase at the same time and send them as a frame to MU. Thus, the MU needs to receive 6-way data from the high-pressure side of the transformer. Some GIS electronic transformer integrated three coils, and they can gather protection and measuring current and voltage of A, B, C three phase at the same time and send them as a frame to MU; thus, the MU needs to receive 3-way data from the high-pressure side of the transformer only.

In 27.5 kV feeder side and low side, 6-way data, measuring current, protection current and voltage of T line, F line need to be collected. Wherein the current signal can be obtained by the transformers of spacer layer, the voltage signal can be obtained by the bus merging unit, so MU need to receive two signals from the bus merging unit while conventional electromagnetic transformers or low-output electronic transformer is generally used for the low side (27.5 kV) considering the economy. If conventional electromagnetic transformer is used, protection and measuring current of each phase totally 4-way data need to be sample, respectively. If small-signal output electronic transformer is used, coils of each phase of protection current and measuring current are integrated in one transformer, the group of protection current, measuring current are sent out as a frame, then only 2-way data need to be sample.

The greatest demand should be considered in the design of MU. For the 220 kV side, 6-channel optical interface should be provided at least and receives 6-pressure side of the road from Gao electronic transformer's data. For 27.5 kV low-pressure side and feeder side, we should be able to provide two fiber optic interfaces for receiving voltage data from the bus merging unit, four cable interfaces, or two fiber optic interfaces for receiving the current data of low-pressure side.

The implementation of MU mainly uses FPGA and DSP, FPGA and ARM, and FPGA chip alone currently. Full use of field programmable gate array (FPGA) hardware, the use of rich I/O ports and user-customizable features for specific purposes, can take advantage of convenient development, fast, and efficient parallel processing of FPGA. Based on the analysis of configurations of traction substation, combined with communication features of MU, the implementation of FPGA chip alone is selected in this paper. The overall hardware implementation of MU is shown in Fig. 1.

Analog signals from conventional transformers and small-signal output by electronic transformer are connected to the MU through the AD converter after the

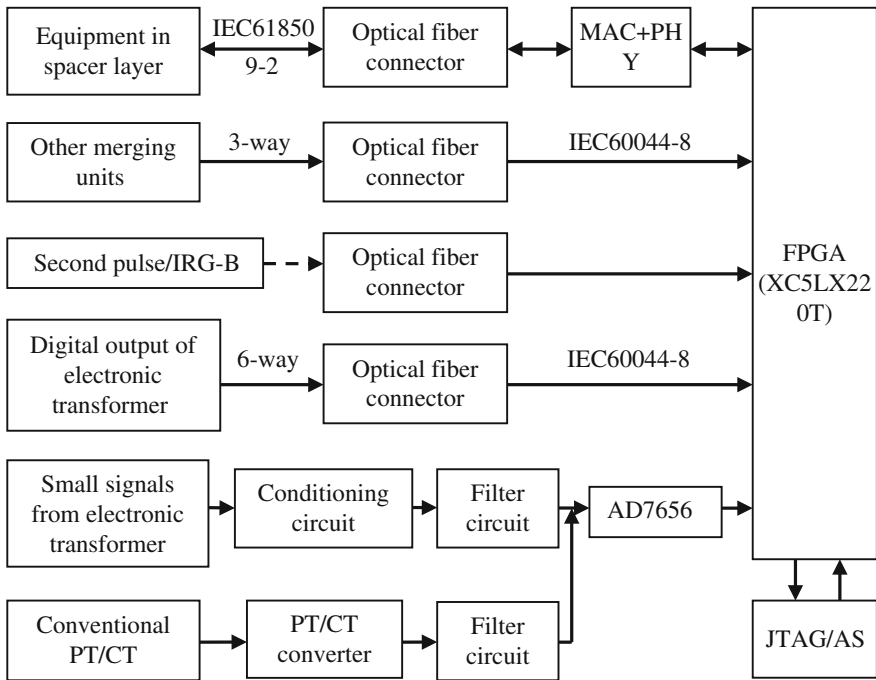


Fig. 1 Hardware implementation of MU

signal conditioning and filter circuit. The output signal FT3 data are connected to the MU through optical access which is from electronic transformers and the digital output from other MUs. The MU is also responsible for receiving the second pulse signal from the outside, and the data which is processed synchronously is sent to protection, monitoring, and control and fault recording and other devices in the spacer layer via Ethernet.

Considering the design demand and cost of MU, chip resources, processing speed, XC5LX220T of Xilinx company is selected as the main processor in this paper, making full use of more I/O ports, high-speed of parallel processing, and high precision. Chip AD7656 is selected to sample AD signals.

Data issued by the traditional transformers are processed by conditioning circuit and then changed into digital signals via A/D chip, packaged and sent to the secondary protection and control equipment.

Three CONVST control lines of AD7656 are connected together to sample 6-channel signal at the same time. The voltage and current data sampled are sent to the protection, monitoring and control, fault recorder, and other equipment in spacer layer via Ethernet by XC5LX220T. DM9000 which can achieve framing data in Ethernet format, address recognition, validation and sending functions is used to be the Ethernet controller.

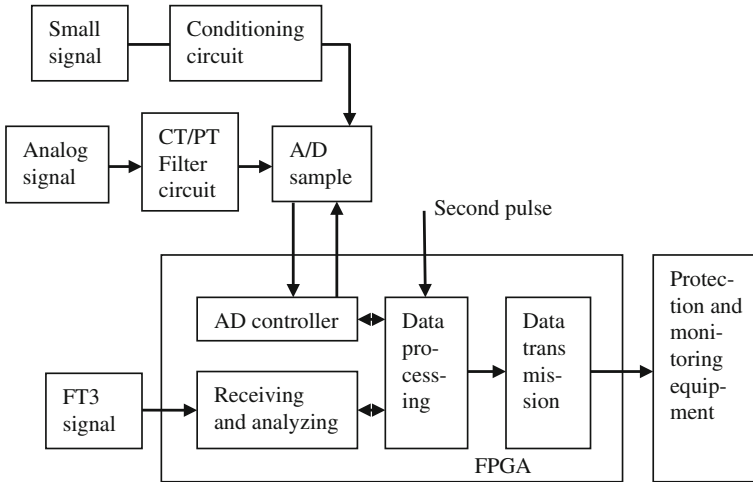


Fig. 2 The block diagram of software design of MU

### 3 Software Design of MU

In this paper, FPGA is used as the core of the hardware implementation; this implementation is divided into three modules, data acquisition, data processing, and data transmission, according to functional requirements. The block diagram of overall software design of MU is shown in Fig. 2.

#### 3.1 Data Acquisition Module

The MU designed in this paper can receive three input data: digital signals in FT3 format from electronic transformer and other MUs; small signal from electronic transformer; and analog signal from conventional transformers.

Data acquisition module, which is interface between the MU and the transformer, is responsible for collecting the data sent by the transformer. It consists of two parts: data receiving and analyzing module and AD sampling control module.

##### 3.1.1 Receiving and Analyzing Module

Data receiving and analyzing module is responsible for receiving FT3 signal from electronic transformers and other MUs, decoding the received data, verifying, and analyzing FT3 signal.

As shown in Fig. 3, receiving and analyzing process of data can be divided into Manchester-encoded data received by MU are decoded by decoding module,

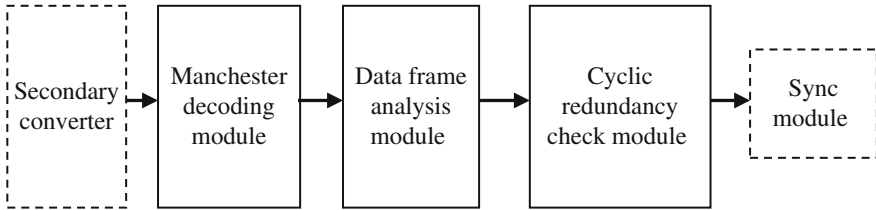


**Fig. 3** Data acquisition module

restored to original NRZ code, and then identifying the frame synchronization code, analyzing the signal, data cyclic redundancy check, and checking validity of the input data.

### 3.1.2 AD Sampling Control Module

AD sampling control module is responsible for controlling the AD chip to sample conventional analog signal from CT/PT and small signal from electronic transformer.

AD sampling module can be divided into three small modules: the second conversion, analog filtering, and AD sampling. Second conversion module is used to reduce 100 V, 5 A signal from the transformer to small voltage and low current; analog filter can avoid the impact of high harmonics when sampling; AD sampling module can be realized by AD7656. AD sampling control module in FPGA is mainly responsible for issuing control signals from AD7656 and controlling the AD converter for sampling.

## 3.2 Data Processing Module

Data processing module is divided into the following three sub-modules.

### 1. Integration module.

Integration algorithm is used to get original transformer data from electronic current transformer based on Rogowski coil and electronic voltage transformer based on RC voltage divider.

### 2. The resampling filter module.

The higher sampling rate is usually taken when sampling to ensure accuracy, reduce the power of quantization noise in effective band, improve signal-to-noise ratio for electronic transformer, 200 point/cycle, 10 kHz is used usually. However, such high sampling rate is not used in the existing protection device generally. Frequency of digital output of merged unit is switched to 80 fr uniformly in this



paper. The data sampling rate of 200 points/cycle is reduced to 80 points/cycle by resampling.

### 3. Synchronization module.

Brightest electrical quantities collected by MU need to be processed synchronously, the brightest sample data are imputed to the same sampling time and then be sent to the secondary protection and control equipment as one frame, we only consider the synchronization of various quarters in the same interval in this paper.

## 3.3 Data Transmission Module

Data transmission module is the interface between the MU and the secondary protection and control devices. It is responsible for framing the data which are processed by MU synchronously and sending it to protection monitoring and control, fault recording, and other equipment in standard format.

The IEC61850-9-1 and IEC61850-9-2 are both using Ethernet access, data encapsulation in frame format accordance to ISO/IEC8802.3 agreement, data transmission via TCP/IP protocol. Wherein the number of channels can be configured of the IEC61850-9-1 standard, packet transmission delay is determined and need the external clock to synchronize, but it is still point-to-point communication.

The number of channels can be flexibly configured of the IEC61850-9-2 standard, has network communication, and need the external clock to synchronize, but it has more complex to implement because of the packet transmission delay is uncertain and high degree dependence on the switch. Currently standard 9-2LE of 9-2 is generally used in engineering projects. Data transmission uses 9-2LE of IEC61850-9-2 in this paper. Packets of samples of IEC61850-9-2 LE is transmitted based on the Ethernet frame structure of ISO/IEC 8802-3 in the link layer.

## 4 Conclusion

The overall hardware and software implementations of MU of traction substation are given in this paper, combined with the analysis and design of actual needs of 110-kV traction substation. A feasible implementation of MU for digital traction substation is given in line with the requirements of communication standard of substation automation based on IEC61850, the data collecting, data processing, data transmitting modules designed in this paper can complete their respective functions better.

**Acknowledgment** This paper is supported by the university research of Huanggang Normal University, item number: 2014026203.

## References

1. Uzoamaka A, Haiyu L, Peter C et al (2011) Performance testing and assessment of merging units using IEC61850
2. Chen B, Wang X, Yan Z (2011) Design and implementation of data synchronous system for merging unit based on FPGA
3. Pang C, Vyatkin V, Fantuzzi C (2011) Time-complemented event-driven control framework for distributed motion control systems based on IEC 61499 and IEEE 1588
4. IEC 61850 9-2 (LE) (2004) Implementation guideline for digital interface to instrument transformers using IEC 61850-9-2
5. Wenjun MA, Longhua M, Pei A et al (2011) New type merging unit for digital substation
6. Moore R, Midence R, Goraj M (2010) Practical experience with IEEE 1588 high precision time synchronization in electrical substation based on IEC 61850 process bus
7. Tao R, Jianq B, Wang C (2011) Sampling rate conversion and data synchronization in big merging unit
8. Xiao X, Xu Y, Pan F et al (2009) Synchronization method based on FPGA for merging unit of the electronic transformers
9. Zhi-Liang Y, Zhen-Donq G, Ming C (2010) Implementation of the interface to electronic transducer in digital substation
10. Zhenyanq Z, Bin W, Enshu J et al (2011) The design of the merging unit of real-time and synchronicity based on Eplc3t144 chip

# Overall Iteration Design of a New Concept Wing Disk Solar-Powered Aircraft

Hong Da and Zhu Jihong

**Abstract** A new layout using wing disk solar aircraft concept with several wings around the disk fuselage is proposed in the research. The wings and fuselage can both provide lift during the overall rotation and forward flying. Propellers at the outer end of the wings are used to overcome the resisting moment, cyclical changes in the power forces, and deflection angle of ailerons to overcome the drag and roll torque in forward flight, which can also control the position and attitude. Aerodynamic analysis is developed based on rotor blade element theory and CFD method. The energy absorption and consumption and weight estimate of each subsystem are taken into account, and an optimization is laid out to meet the cruising flight requirement by iterative design.

**Keywords** Wing disk solar-powered aircraft · Aerodynamic analysis · Energy balance · Overall design

## 1 Introduction

Solar-powered aircraft takes solar radiation as the source of energy, compared with the conventional aircraft, and due to the special form of energy, the endurance is not affected by the fuel limit and has broad application prospects in military and civilian. Conventional solar-powered aircrafts generally have high aspect ratio wing, slender streamlined low-resistance body, or no body wing. Flying at night requires storage battery, but the size, weight, and location of the battery bring great burden to the overall design. At present, solar-powered aircrafts are generally made

---

H. Da (✉)  
School of Aerospace, Tsinghua University, Beijing, China  
e-mail: honda198829@126.com

H. Da  
Naval Academy of Armament, Beijing, China

Z. Jihong  
School of Computer Science and Technology, Tsinghua University, Beijing, China

of carbon fiber composite materials with frame structure to reduce the weight, so the high aspect ratio wings are flexible, which affects the distribution of aerodynamic load, and has an impact on the flight performance, even leads to security problems [1]. The “HELIOS” solar-powered aircraft took flight in 2003 and serious oscillation appeared and crashed in the atmospheric turbulence cases. The cause is the nonlinear stability and control problem of flexible high aspect ratio wing, and the coupling phenomenon appeared in some special dynamics [2]. Therefore, a new layout to improve the structure and aerodynamic efficiency and reduce the size is an important direction of the development of solar-powered aircraft.

Disk or flying saucer layout has compact structure and high stiffness, so the overall layout is a significance reference for the design of solar aircraft. The article proposes a wing disk solar-powered aircraft with 8 moderate aspect ratio wings arranged around the disk fuselage. The wings and fuselage can both provide lift during the overall rotation and forward flying. Propeller at the outer end of the wings are used to overcome the resisting moment, the forces given by propellers increase to make the lift greater, and the aircraft rise, on the contrary, the aircraft will drop. The drag during forward flight is offset by the difference of the propellers, which change periodically. The aircraft will face roll moment during forward flying, and there are ailerons on the wings, which can deflect differentially and periodically, and offset the roll moment, which can also control the attitude. A posture of lookup is chosen as the cruise flight mode, which can reduce the rotor downwash velocity and make full use of the lift provided by the disk fuselage. The available flight time hopes to cover from vernal equinox to autumnal equinox, and the flight area  $0^{\circ}\text{N}$ – $40^{\circ}\text{N}$ , while the flight high at 18 km, cruising speed at 15 m/s (Fig. 1).

The 8 wings are fixed at the outer edge of the fuselage. The main load-bearing wing and fuselage of the aircraft structure are made of carbon fiber composite materials and with frame structure form. The upper surface of the aircraft is covered with solar cell, which can provide power to the power system. There are avionics system, task system, energy management module and storage battery in the disk fuselage. During the day, the aircraft obtain solar radiation energy to satisfy the energy demand of flight and task, and use the excess energy to charge the storage battery, at night, the storage battery release energy to maintain the operation of the whole system.



**Fig. 1** The layout, structure, and flight mechanism of the aircraft

Overall design is developed for the configuration, and aerodynamic analysis is based on rotor blade element theory and CFD method. The energy absorption and consumption and weight estimate of each subsystem are taken into account, and an optimization is laid out to meet the cruising flight requirement by iterative design.

## 2 Overall Design

### 2.1 General Iterative Method

Set the initial size and flight status, get the lift, drag and torque, estimate the weight by means of aerodynamic analysis, then estimate the weight, and calculate the energy consumption requirement, finally test the weight balance and energy balance. Adjust the vehicle dimensions and flight state parameters to meet the design demand [3, 4] (Fig. 2).

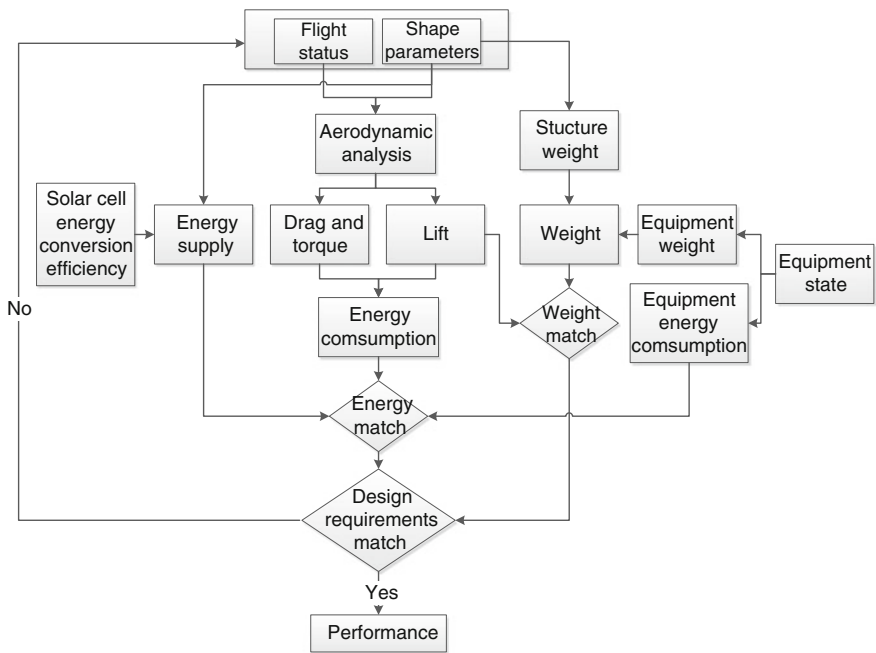


Fig. 2 The idea of overall design

## 2.2 Aerodynamics Analysis Based on Rotor Blade Element Theory

Assume wings of the aircraft have medium aspect ratio and good stiffness, and ignore the small deformation of wings in flight. Use simple straight wing with S1223 airfoil, which has good characteristics at low Reynolds number [5]. Set the temperature and viscosity coefficient value at the height of 18 km, and use Profili software to compute the lift and drag of airfoil, which increases linearly with the change of Reynolds number. Chose Re to be 478,000 and 327,700, calculate the corresponding airfoil characteristic, and use interpolation to obtain different Reynolds airfoil aerodynamic coefficients. The results are in good agreement with the wind tunnel test and numerical calculation (Fig. 3).

Set rotation angle of the aircraft is  $\psi \in (0, 2\pi)$ , wing root angle is  $\theta_0$ , rotate speed is  $n$ , the angular velocity is  $\Omega = 2\pi n$ , and the climb speed in the direction perpendicular to the plane of the disk is  $V_c$ . The velocity of blade element  $dx$  is

$$W_i(x) = \sqrt{(V_c + v_{in}(x))^2 + (\Omega x + V_{0i})^2} \tag{1.1}$$

where  $v_{in}$  is the downwash velocity,  $V_{0i}$  is the flow increment due to forward flying, and the air force of blade element is

$$\begin{aligned} dL_i &= \rho W_i^2 C_{li} c \cdot dx/2 \\ dD_i &= \rho W_i^2 C_{di} c \cdot dx/2 \end{aligned} \tag{1.2}$$

so the blade element contributes air force lift  $dU_i$ , drag  $dQ_i$ , and rotary torque  $dM_i$  to the whole aircraft

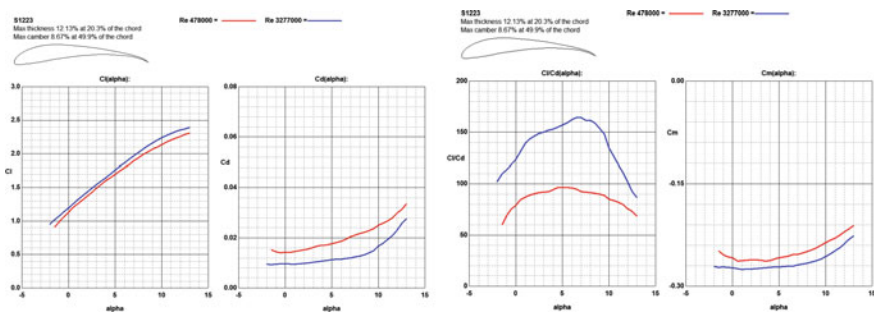


Fig. 3 The airfoil aerodynamic coefficients

$$\begin{aligned}
 dU_i &= dL_i \cos \varphi_0 - dD_i \sin \varphi_0 \\
 dQ_i &= dL_i \sin \varphi_0 + (dD_i + df_i) \cos \varphi_0 \\
 dM_i &= dQ_i \cdot x
 \end{aligned}
 \tag{1.3}$$

where  $\varphi_0$  is the flow angle of blade element  $dx$  and  $df_i = 0.072Re_i^{-1/5} \rho W_i^2 c \cdot dx/2$  is the turbulent boundary layer friction. The angle of attack of the whole aircraft is  $\alpha_D$ , and the blade element aerodynamic contribution in vertical direction is

$$dY_i = dU_i \cos \alpha_D - dQ_i \sin \alpha_D \tag{1.4}$$

So the whole lift and rotary moment can be determined by integral, and add the lift by the disk  $L_0$ .  $v_{in}$  can be calculated by combining the blade element method and momentum method, and iteration algorithm is as follows:

$$\begin{aligned}
 4\rho\pi x V' v_{in} &= \sum_{i=1}^8 \frac{1}{2} \rho b c W_i^2 \left[ a \left( \theta_0 - \frac{V_c + v_{in}}{\Omega x + V_{0i}} \right) + C_{l0} \right] \\
 V' &= \sqrt{V^2 \cos^2 \alpha_D + (V \sin \alpha_D - v_{in})^2}
 \end{aligned}
 \tag{1.5}$$

### 2.3 Aerodynamics Analysis Based on CFD Method

The aircraft geometry is based on CATIA, using the ANSYS software ICEM module, establishing the flow field. Use hexahedral/tetrahedral hybrid unstructured mesh, the surface of aircraft is treated with further encryption, and use the smoothing treatment to improve the mesh quality. The aircraft surface is provided with fixed wall boundary condition. Set a constant speed condition at the flow boundary, and the flow velocity magnitude and direction refer to the forward speed 15 m/s and angle of attack  $2^\circ$ . Air parameters chose the value at the height of 18 km. Use a revolving coordinate system to simulate the revolving flow field, and the rotate velocity is 2 rad/s. The calculation problem is simplified to a viscous incompressible flow problem, select the single equation Spalart–Allmaras turbulence model, and use low Reynolds number correction [6] (Fig. 4).

There are two typical flow states: In state 1, there is a wing in the flow direction, and in state 2, the angle bisector of two wings is in the flow direction. CFD method and blade element theory provide similar aerodynamic results, the lift, drag, rotary torque are compared in Table 1.

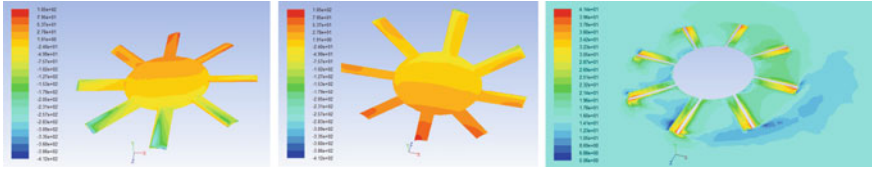


**Fig. 4** The results of surface pressure and flow velocity (the flow is in *X* direction, and the rotation is in *Y* direction)

**Table 1** Aerodynamic calculation results

State	Aerodynamic	Blade element theory	CFD rotor part	Deviation
State 1	Lift (N)	21,066.46	19,995.66	-0.05
	Drag (N)	4193.98	3436.75	-0.22
	Rotary torque (Nm)	-56,342.37	-73,884.06	0.24
State 2	Lift (N)	21,112.50	19,607.39	-0.08
	Drag (N)	4111.80	3654.94	-0.12
	Rotary torque (Nm)	-57,090.55	-73,569.43	0.22

### 2.4 Energy Balance Calculation

Based on the analysis of development of solar cell, GaAs thin film is most suitable as solar cell of the wing-type aircraft. The output power of solar cell has a direct relationship with light intensity and angle, affected by season, time, weather, and many other factors. Solar energy in unit area is available for

$$P_{solar} = S_{io} \tau \eta (\sin \lambda \sin \varepsilon - \cos \lambda \cos \varepsilon \cos(2\pi j / 23.935)) \tag{1.6}$$

where  $S_{io}$  is the solar radiation intensity,  $j$  is the time (in hours),  $\eta$  is the solar energy conversion efficiency, set to 0.33 according to the properties of GaAs films,  $\tau$  is the solar radiation attenuation factor in atmosphere, set to 0.7, and  $\lambda$  is the latitude, and  $\varepsilon$  is the inclination angle of rotation axis of the earth. The energy power output in different latitudes and time is shown in Fig. 5, where the straight lines show the average power available for the day [7].

The energy consumption of solar-powered aircraft must meet the minimum limits, which is 40° north latitude at autumnal equinox, that is,  $P_{solar} = 73 \text{ W/m}^2$ . Set disk radius  $R$ , number of wings is  $b$ , with length  $l$ , chord length is  $c$ , then area of solar cells is  $S$ . Energy available value can be expressed as  $P_{max} = P_{solar} S = P_{solar} (\pi R^2 + bcl)$ .

Referring to the power consumption of helicopter, the energy consumption of wing disk aircraft includes the flight  $P_{flight}$ , task system  $P_{task}$ , and avionics system  $P_{equ}$ . According to the aerodynamic calculation, considering the propulsion



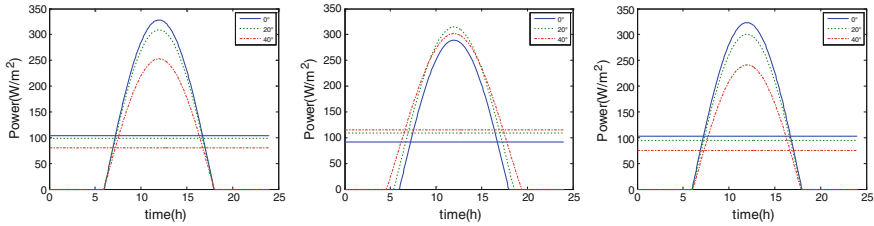


**Fig. 5** Solar radiation power changes in different latitudes and time (vernal equinox, summer solstice, and autumnal equinox)

efficiency  $\eta_{prop} = 65\%$ , set  $D_0$  as the drag by disk body, which is determined by CFD calculation, and the energy consumption can be given as

$$P_{need} = P_{flight} + P_{task} + P_{equ} = \frac{\sum_{i=1}^b dD_i \cdot W_i^T + D_0 \cdot V}{\eta_{prop}} + P_{task} + P_{equ} \quad (1.7)$$

### 2.5 Weight Estimate

The weight of the aircraft is  $m$ , according to the relationship between structural weight and the projection area of existing solar-powered aircrafts, give structure weight density of unit area of the fuselage and wings of wing disk aircraft, the reference also includes the weight of avionic, propulsion system, and takes storage battery technology development into account [8]. Weight of subsystems is shown in Table 2.

### 2.6 The Design Result

According to the design idea, carry out the overall design by adjusting aircraft parameters, and meet the weight and energy balance (Table 3).

**Table 2** Weight estimate

System	Weight
Fuselage structural weight density	2 kg/m <sup>2</sup>
Wing structural weight density	2.3 kg/m <sup>2</sup>
Solar cell weight density	0.25 kg/m <sup>2</sup>
Power management system	40 kg
Avionics	40 kg
Storage battery	600 Wh/kg
Cable	40 kg
A single propulsion system	10 kg
Task load	50 kg

**Table 3** Aircraft parameters

Parameter	Result
$R$	10 m
$l$	11 m
$c$	3.45 m
$\theta_0$	11°
$m$	2531 kg
Structure weight factor	0.52
$P_{\text{task}}$	500 W
$S$	617.76 m <sup>2</sup>

**Table 4** Cruise flight state parameters

Performance	Design status
$\alpha_D$	2°
$n$	0.3–0.4 r/s
$V_{\text{max}}$ (at cruise altitude)	20.7 m/s

The overall design can also be used for flight performance analysis. In order to avoid reverse flow region of rotor, the forward flight velocity should meet the following demand (Table 4)

$$\Omega R + V_{0i} = 2\pi n R + v \cdot \cos(-6\pi/4) - u \cdot \sin(-6\pi/4) \geq 0 \quad (1.8)$$

In cruise flight, lift is equal to the gravity, that is 24,803.8 N, and the power demand is 45,544 W, and in the scope of design conditions, solar cells can provide power of at least 45,714 W; the design can achieve to meet the demand of cruising flight.

### 3 Conclusions

This article puts forward a conceptual proposal with a new layout: wing disk solar-powered aircraft and proposed overall design. The blade element theory and CFD methods give similar results of aerodynamic performance. Take energy and weight balance estimate into account, lay out an optimization to meet the requirement, and give out basic flight performance.

### References

1. Gao G, Song B, Li Z, Ding X (2010) Key technologies of solar powered unmanned air vehicle. Flight Dyn 01:1–4 (in Chinese)
2. Noll TE, Brown JM, Marla E et al (2004) Investigation of the helios prototype aircraft mishap. NASA Report

3. Cao Q, Zhou Z, Chang M (2014) Design and research for conceptual parameters of solar-powered non-stop airplanes. *Flight Dyn* 02:132–136 (in Chinese)
4. Shiau J, Ma D, Chiu C et al (2012) Optimal sizing and cruise speed determination for a solar-powered airplane. *J Aircr* 47(2):622–629
5. Optimization design study of low-Reynolds-number high-lift airfoils for the high-efficiency propeller of low-dynamic vehicles in stratosphere. *Sci China (Technol Sci)* 10:2792–2807 (2010)
6. Zhang Q, Liu C (2013) Performance analyze of ducted fan unmanned aerial vehicle by fluent software. *Aircraft Des* 03:5–9
7. Noth A (2008) Design of solar powered airplanes for continuous flight. Suisse, Ecole Polytechnique Fédérale de Lausanne, ETH Zürich
8. New progress on Li/S batteries with high specific energy density in Dalian Institute of Chemical and Physics. *J Synth Crystale* 08:2097 (2014) (in Chinese)

# Research on an Automation Network for CSP Product Line

Tongbin Li, Bin Wang, Ning Zheng and Xin Kang

**Abstract** There are two developing technologies for automation networks designed by SMS Demag and applied to CSP in iron and steel plants, and currently a remote I/O topology for automation network via Internet can solve many of the problems of CSP's installation, debugging and maintenance on site. This informs us that hierarchical control theory of large scale systems is no longer adapted to the development of network technology. Therefore, the CSP automation network of caster and mill, system management, time synchronization, reflective memory, field bus, remote access, VPN gateway, single port, and security features are analyzed in this paper. Either by adding HMI and remote access to the traditional hierarchical control theory of large scale systems or treating it as an independent part without the traditional hierarchical control theory, this problem is solved in our work. We conclude that HMI and remote access in automation networks have independent and integrated functions and cannot be divided into L0-to-L4 for the metallurgical automation system.

**Keywords** CSP · Automation network · HMI · Field bus · Remote access

## 1 Introduction

CSP (Compact Strip Production [1]) production line for thin slab continuous casting and rolling is a new short flow process technology for the production of hot-rolled plate roll successfully developed in 1989 in the U.S. It is the most important of the revolutionary technologies in the world's iron and steel industry, also constituting the model for information technology and automation integrated applications so far.

---

T. Li · N. Zheng

School of Information Engineering, Putian University, Fujian 351100, China  
e-mail: tobelee@126.com

B. Wang · X. Kang (✉)

School of Mechanical and Electrical Engineering, Putian University, Fujian 351100, China  
e-mail: tokangxin@163.com

© Springer-Verlag Berlin Heidelberg 2016

B. Huang and Y. Yao (eds.), *Proceedings of the 5th International Conference on Electrical Engineering and Automatic Control*, Lecture Notes in Electrical Engineering 367, DOI 10.1007/978-3-662-48768-6\_75

China has established more than twenty CSP production lines by SMS Demag, Siemens/VAI, Danieli and other, with a current production capacity exceeding 18,000,000 tons per year.

In recent years, the research into CSP focused mainly on the problems of quality control and the development of new varieties. However, little research has been done on the automation and industrial control network in the CSP system. After many years' efforts, Baosteel has achieved an automation network for CSP engineering and technical achievements by introducing and absorbing an advanced CSP product line into the market abroad. This paper takes the CSP product line introduced by Baosteel as a case study to discuss the automation network.

### 1.1 Overview of CSP Automation Network

CSP made in SMS-DEMAG of Germany for Baosteel is the mainstream of the continuous casting and rolling production line in the world at present; the line model is shown as Fig. 1:

More than four iron and steel plants in China [2] owned SMS Demag because of its state-of-art [3, 4]. The automation network of CSP typically used in Baosteel and other plants have four different types when compared with a traditional network [5, 6]:

- (a) Plant wide automation network;
- (b) Reflective memory used as high speed process I/O bus of the level 1 (also known as L1, and so on L0, L2, L3, L4, all of them called L0-to-L4) process control systems as well as high speed interface of the Common HMI server;
- (c) High speed PDA network used by the Process Data Acquisition system for diagnosis and analysis;
- (d) Field bus used by the level 1 process control system for remote I/O access as well as interface with the drive systems.

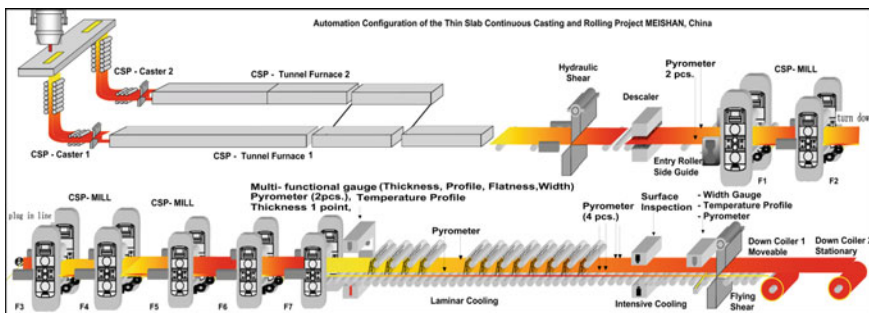


Fig. 1 CPS continuous casting and rolling production line

### 1.2 Fibre Optic Network for Caster

The network configuration is based on two separate hyper redundant rings, implemented on the basis of double core fibre optics and managed industrial ETHERNET rail-switches. This kind of network ensures fully redundant communication. In case the ring is interrupted, the communication runs with full functionality. The intelligent switches are permanently monitoring the communication backbones and, in case of a failure, the communication will be switched over to the redundant core as shown in Fig. 2.

The top of the figure is the corresponding system diagram for continue casting of parts. Especially the green lines connected between EDAS and Basic Automaton Systems are redundant for the system's reliability, and the bottom of the figure is continuous casting of parts such as the CSP cast platform, tunnel furnace, hydraulic device, pulpit caster and so on, as depicted in Fig. 1.

The configuration is based on two communication rings, namely, process and data bus. In this way, data and process variables are separated and, at the same time, the communication speed on each of the rings is increased:

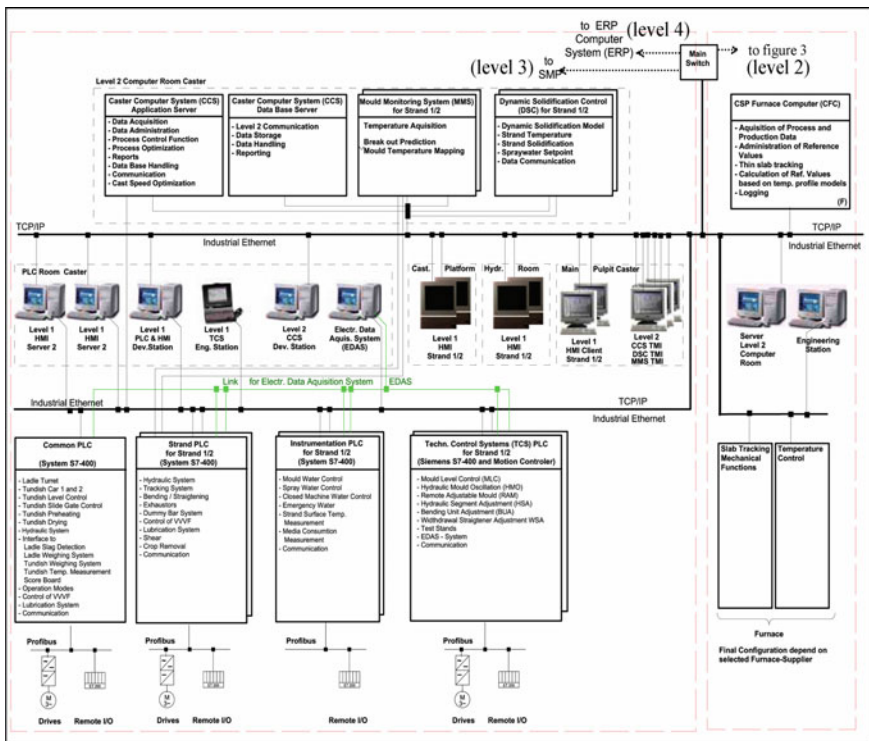


Fig. 2 Automation configuration of the thin slab continuous casting project in Baosteel

- (a) Process ring bus: Fibre Optical Ring Bus (Industrial Ethernet) for communication between PLC units and interface to Level 2;
- (b) Data ring bus: Fibre Optical Ring Bus (Ethernet) for HMI clients (operator work stations for Level 1 and Level 2) and interface to Level 2;
- (c) Network components: two core fibre optical segments (backbones) and managed industrial switches supporting the functionality of redundant rings, with each switch;
- (d) 2 × 2 fibre optical interfaces (BFOC) and up to four electrical ports (RJ45), rail-mounted in a cabinet.

*Remark* The Level 2 hardware is connected to a Layer 3 managed GIGABIT switch. Its technical data rate is 10/100BASE-TX or 100BASE-FX Multimode F/O. And the protocol is industrial ETHERNET TCP/IP, TCP/IP socket.

### 1.3 Fibre Optic Network for the Mill

An automation network is provided for the automation system of the hot strip mill (except the Level 2) to connect the subsequent systems, automation systems and peripheral devices as shown in Fig. 3.

The data exchange between these systems is carried out via a fibre optical link. For cable length shorter than 50 m, shielded twisted pair cables (CAT5/ULTRA5) are used. This fibre optic network based on the Ethernet technology is offered in order to connect the automation systems within the network. The data transfer rate

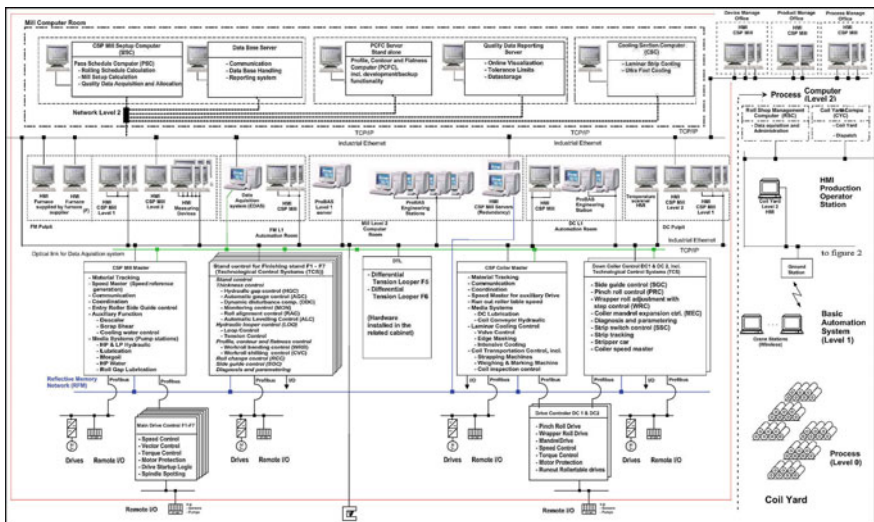


**Fig. 3** Automation configuration of the thin slab caster rolling project in Baosteel

on the backbone is 1000 Mbits/s. The transfer rate within the sub-segments up to the Client PCs is 100 Mbits/s.

In the relevant computer rooms located within the production area, a necessary Ethernet switch module is installed for the connection of the computer systems to the fibre optical network. Each switch module is linked to a HUB for connection to peripheral devices or is linked directly to the dedicated PCs. The configuration was determined during the design stage.

Standard Ethernet protocol TCP/IP or UDP is used for data communication.

The final LAN configuration and the necessary cable lengths can only be fixed during the engineering field 'Detail Specification', regarding the topology of the automation network in Figs. 2 and 3.

## **2 System Management**

### ***2.1 Systems and Network Management***

Most branded hardware vendors deliver their hardware with basic management software. With this software, the system administrator is able to monitor the hardware connected to the plant network. The management software consists of two parts: the management console to display the current status of hardware and components (storage, network interface, system board, etc.) and agent software that will collect the information on the node and send this information to the management console. The software supports SNMP and most of them support a Web interface. In normal operations, the customer has to work with several management applications. For example, in the case where HP PC hardware and CISCO components are used for the plant wide network, HP components will be monitored with the HP Insight Manager and the CISCO components with the CISCO Cluster Management Suite.

The management console is designed for the specific delivered hardware.

### ***2.2 Administrator Management of CSP Servers***

There is a server administrator tool designed to completely manage the server for CSP. It is a management software tool which belongs to the hardware vendor. A server administrator, without going to the continuous casting central console, can manage any individual server within the Plant network from virtually anywhere and anytime. The software tools have functions such as determining how much space is left on the server disks and whether to adopt the latest firmware, drivers, BIOS and drop drivers, operating system and the version. It also can diagnose whether the server made a modification and determine what's been installed most recently in the



server slots without shutting down. Of course, the tools can also monitor the health of a system, access asset and inventory information, analyze logs, update firmware and BIOS and diagnose problems. In addition, the software also supports the CSP system administrator via access using an Internet Explorer browser or Command Line Interface.

As a result, the engineers in a CSP site need not go to central console when they are notified that a server needs attention. Instead, they can use their Web browser to select the server and log in using their domain or Operating System password to perform the following actions:

- (a) Review automation network status about CSP product line;
- (b) Configure BIOS settings for the real-time local area network;
- (c) Configure server actions for a casting and rolling event;
- (d) Review server inventory and product information;
- (e) Review server configuration, including RAID;
- (f) Review hardware, alert, POST, and Server Administrator logs for CSP;
- (g) Run online diagnostics better to isolate problems, and not to cut-off the CSP product line;
- (h) Update BIOS or system firmware as the CSP requires.

### **3 Time Synchronisation, Reflective Memory and Field Bus**

#### ***3.1 Time Synchronisation***

Within the Windows Microsoft operating system, a time synchronisation protocol, the Simple Network Time Protocol (SNTP), is implemented. The SNTP is used for time synchronization of the PC servers and clients' applications within the plant network.

The time service works in a hierarchical structure. The PC servers and clients receive time from a domain controller (level 3). In the case that there are more than one domain controllers defined within the plant network, there will be defined a time master.

This master can receive the exact time from a user's external time source via NTP Protocol, which enables time accuracy within milliseconds or microseconds. Otherwise, the actual time of the master will be used for time synchronization.

For time synchronization of level 1 TCS applications, a time server tool will be installed into a PC client, which transmits a time stamp telegram to the TCS master. Within the TCS applications, this time stamp will be used by a special PROBAS time synchronisation service.

### 3.2 *Reflective Memory*

The Level 1 TCS automation systems as well as the HMI server are connected via a reflective memory network. The reflective memory concept provides a very fast and efficient way of sharing data across distributed computer systems. It is a high-speed, easy-to-use, daisy-chain fibre-optic network with a cycle time in the range of 1.5–2  $\mu$ s (transfer rate is approx. 13.4 Mb/s.).

Data are transferred by writing to the on-board global RAM. The data is automatically sent to the location in memory on all reflective memory boards on the network. Each participant has a local RAM which provides fast read access to stored data.

The basic automation system illustrated in Figs. 2 and 3 have the topology of the reflective memory network.

### 3.3 *Field Bus*

For the decentralized peripheral modules, a Profibus L2-DP is used. Via this data bus, the drives, the inputs/outputs of the switchgear and the decentralized peripheral modules in the field are connected to the control system.

The evaluation of the inputs/outputs in the field is performed with the decentralized modules ET 200. The ET 200 connection modules are latched onto a top-hat rail and can be pre-wired and checked without peripheral modules. Valves with a rated current of  $<2A$  can be directly activated with optical isolated outputs by the corresponding output modules of the ET 200.

The decentralized peripheral modules in the field are installed in local panels or terminal boxes. At these peripheral stations, the field devices and the local control elements are connected.

For cable length longer than 100 m, fibre optic cable will be used, and Fig. 2 gives the topology of the remote I/O network.

## 4 **Remote Access**

Further, a remote access from SELLER's office to the on-site system is required as a precondition for an optimal commissioning by using a VPN gateway. This remote access is also required for the warranty period after the acceptance of the system as shown in Fig. 4.

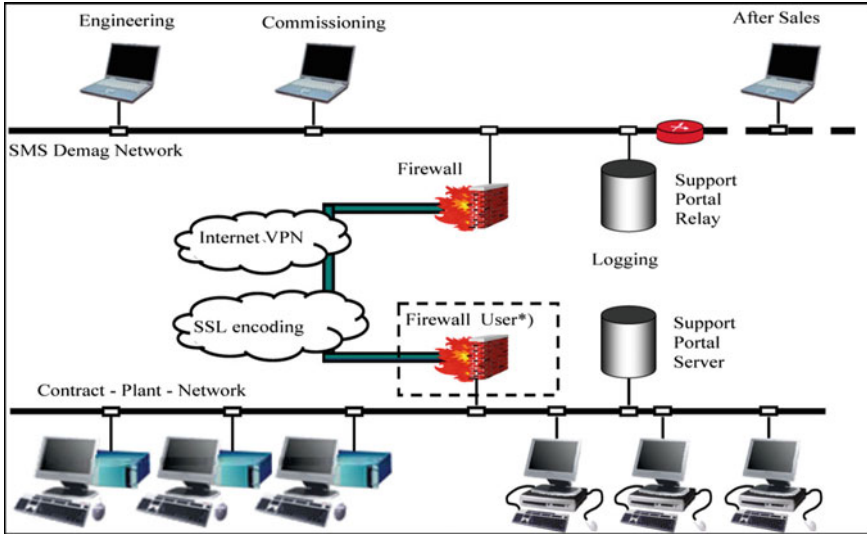


**Fig. 4** Internet/VPN access between SMS Demag and Baosteel

#### **4.1 Remote Access Portal**

The remote support portal is used for remote access by SMS Demag personnel during cold- and, hot-commissioning and the warranty period after FAT. This has been agreed between Baosteel and SMS Demag for after sales services, and is always at call.

#### **4.2 Support Portal Client/Server as Application**

The SMS Demag Support Portal is based on the *sym-media* SP/1 support communication platform. To be able to access the Support Portal, the SMS Demag Support Portal client and server on site must be installed. The server is managing the user access and logging all activities.

The client program is the actual user interface of the SP/1 system. It is via this interface that the various functions are operated:

- (a) The ability to access a customer's installation is subject to prior authorisation by SMS Demag on the SP/1 central system *and* having the suitable application software.
- (b) Access is never direct but always via the central gateway at SMS Demag.
- (c) Before a member of the SMS Demag staff may access the installation of a customer, this member of staff must be authorised in the customer's system.

- (d) The network access at the customer (firewall) can be configured such that no others accesses from the SMS Demag central system (IP) are admitted via a single port only.
- (e) Security gaps that open up with the use of standard browsers and technologies such as Java-Script or Active X are avoided by single-port technology.

When the connection is set up, the structure of the installation is transmitted to the client once the client and server authentication and the user identification via name and password have taken place. This enables the technician to attend to a great variety of plant configurations from a single client installation.

### **4.3 Security Features**

The client is completely developed in Java just like the entire system. The Java programming language features intelligent memory management.

Java excludes security gaps of the type which, for instance, occur in the case of direct memory access of the system. This rules out attacks such as those caused by provoking buffer overflows and hence overwriting program codes in the memory as early as in the language architecture. Gaps of this kind in other languages used to be and are still being exploited for illegal access to systems. The client-server communication is SSL coded.

### **4.4 Single-Port Technology**

The entire communication (text conference, document conference, file transfer, Win-HMI of TCS, telnet, etc.) is carried out by using a single port, i.e., communication is directed via this port only. It is therefore sufficient to open not more than one port for all functions in the firewall.

## **5 Conclusion**

*Overall conclusion and suggestion:* CSP automation network designed by SMS Demag has been used in Baosteel for a few years. More and more plants gradually adopt its use all of the world, and especially now in China. The operating CSP site of Baosteel and other plants can be supervisory and controlled by SMS Demag from Europe. SMS Demag has the remote capability, not limited by plants via the Internet, to analyze, debug, and maintain CSP for a more scientific and thoughtful after-sales service. This new method from development of CSP automation network and Internet results in the author's new thinking that the traditional L0-to-L4

hierarchical control theory of large scale systems [7, 8] for the metallurgical industry automation control system must undergo some changes. HMI for automation and the Internet for remote access can't be contained completely in the L0-to-L4 hierarchical control theory.

Today, the CSP automation network becomes more and more important in every level of L0-to-L4. It leads to the tendency that mixes L0-to-L4 together or all of HMI, and remote access is considered to be an important level (for example, it is stratified in the Figs. 2 and 3) in the automation network. If HMI and remote access are joined in the traditional hierarchical control theory of large scale systems for the metallurgical industry automation control system that divided automation network level into L0-to-L4 or not, this is a new important study especially in our metallurgical industry as it becomes more robust today [9, 10].

In conclusion, the author's opinion is that the traditional hierarchical control theory of large scale systems [8] for the metallurgical industry automation control system, which divides automation network level into L0-to-L4, is no longer adapted to the development of network technology. HMI and remote access in automation network have an independent and integrated functions in comparison to the L0-to-L4 and cannot divide the automation network level into L0-to-L4.

**Acknowledgments** We acknowledge the financial support provided by the National Natural Science Foundation of China (No: 11172138).

We acknowledge the financial support provided by Fujian province key scientific research project (Nos: 2015H6018 and 2015H0033).

## References

1. Gao ZF, Huang W, Chen FH et al (2014) Development of products by CSP technology and its trend. *J Angang Technol* 387(3):8–27
2. Wu Z, Wu R, Han B et al (2012) Characteristic point and progress on CSP thin slab casting and rolling process. *J Hot Working Technol* 41(15):36–40
3. Chen Y, Chen J, Long S (2012) The current state and development trend of thin slab casting and rolling technology. *J Anhui Metall* (3):24–27
4. Wang L, Deng C, Dong M et al (2012) Development of continuous casting technology of electrical steel and new products. *J Iron Steel Res Int* 19(2)
5. Cheng T, Jiao D (2013) Technical characteristics in engineering design and equipment of thin strip continuous casting and rolling. *J Gansu Metall* 35(1):36–38
6. Liu W, Fan J (2014) Development situation and prospect of continuous casting equipment at home and abroad. *J Mech Eng* 11:49–50
7. van de Kaa G, de Vries HJ, Rezaei J (2014) Platform selection for complex systems: building automation systems. *J Syst Sci Syst Eng* 23(4):415–438
8. Li T, Weng Y, Chen W et al (2014) Research on the configuration of the basic automation system for slab casters. *J Res Iron Steel* 42:58–61
9. Mao X, Gao J, Chai Y (2014) Development of thin slab casting and direct rolling process in China. *J Iron Steel* 49(7):49–60
10. He A, Song Y, Sun W et al (2014) Tunnel furnace optimization control of thin slab continuous casting and continuous rolling. *J Continuous Cast* 6:1–6

# An Improved BBO Algorithm and Its Application in PID Optimization of CFB Bed Temperature System

Hong Xue and Han Pu

**Abstract** In order to improve the performance of biogeography optimization (BBO) algorithm in PID controller parameter optimization of thermal systems and have superior convergence characteristics, the article gives an improved BBO algorithm. The improved BBO algorithm introduces the introducing convergence mechanism of particle swarm optimization on the basis of original migration strategy, so that the whole migration process has a certain direction. Also, the article uses phase-out strategy to remove poor parameters which are obtained after the migration and mutation processes. Thus, on the one hand, directional migration and elimination mechanism can ensure its fast convergence properties. On the other hand, mutational mechanisms can ensure the global characteristics of wide-area searching and avoid falling into local extrema. Using it in the PID optimization of CFB bed temperature system, the simulation results show that the improved BBO algorithm has a better performance than the standard BBO algorithm on convergence speed and precision. It is feasible and effective for PID controller parameter optimization in thermal system.

**Keywords** Improved BBO algorithm · PID parameter optimization · CFB bed temperature · Simulation research

## 1 Introduction

Biogeography-based optimization (BBO) is a new evolutionary algorithm based on the theory of biogeography, and it has been applied in optimization problems [1]. The algorithm has good convergence and stability, and many scholars have done

---

H. Xue (✉) · H. Pu (✉)

Department of Automation, North China Electric Power University,  
Baoding, China  
e-mail: xuehong1021@outlook.com

H. Pu

e-mail: hanpu102@263.net

© Springer-Verlag Berlin Heidelberg 2016

B. Huang and Y. Yao (eds.), *Proceedings of the 5th International Conference on Electrical Engineering and Automatic Control*, Lecture Notes in Electrical Engineering 367, DOI 10.1007/978-3-662-48768-6\_76

675

extensive research on this algorithm, greatly contributed to its application in engineering areas: The document [2] has combined differential mutation algorithm with biogeography algorithm and applied it to solving the economic load dispatch problem, and the effect is better than solving by basic BBO algorithm. The document [3] has combined the differential evolution with biogeography algorithm and used it to solve the problem of optimal power flow, and the effect proves that the hybrid algorithm is effective. The document [4] has combined the opposition-based learning (OBL) with BBO algorithm successfully and solved the problem of image segmentation. The document [5] uses logistic chaotic map to improve the original mutation mechanism, presents an improved BBO algorithm, and applies it to the design of the radar orthogonal waveforms. The document [6] combines the simulated annealing algorithm with BBO algorithm, proposes SA-BBO algorithm, and applies it to identify problems of early steam pressure in turbine optimal operation.

This article applies BBO algorithm to PID controller parameter optimization in bed temperature of circulating fluidized bed (CFB) and proposes an improved BBO optimization algorithm. This algorithm introduces convergence mechanism of the particle swarm algorithm to the migration strategy of BBO algorithm so that the whole migration process has a certain direction. Also, the article introduces elimination mechanism. The elimination mechanism compares the original parameters and the parameters obtained after iteration. The better of them is keep to the next iteration and the other is eliminated. So it can ensure that the group is not lost the excellent characteristics after the migration and mutation. On the one hand, directional migration and elimination mechanism ensure the algorithm rapid convergence properties, and on the other hand, mutational mechanisms ensure its wide global search feature and avoid falling into local optima in the optimization process. The simulation results show that this method achieved better control effects and the improved BBO algorithm has greater improvement in convergence and convergence rate than basic BBO algorithm.

## 2 Principle of Improved BBO Algorithm

BBO algorithm is a global optimized algorithm based on groups [7]. In BBO algorithm, each group has a number of feature vectors, described as a suitable index vector (SIV). SIV is corresponded to optimization solutions; habitat suitability index (HSI) is the measure of vector SIV, evaluating the group, corresponding to optimized value of objective function. The evolutionary process mainly consists of population migration and population mutation.

The immigration rate  $\lambda$  and emigration rate  $\mu$  can influence the population migration degree [8].  $\lambda$  and  $\mu$  of the population are the function of species  $K$ . According to the distribution of biogeography species, it can get different mobility model functions. In the migration operations, BBO algorithm selects the group  $H_i$  which needed to move in based on  $\lambda$  and selects the group  $H_j$  which

needed to move out based on  $\mu$ . Then, a randomly selected variable from the SIV of  $H_j$  replaces the corresponding variable of  $H_i$ . Finally, the suitability of the entire population is evaluated by calculating the HIS.

BBO algorithm uses mutation to simulate conditions that suitability of groups changes due to emergencies. According to the probability  $P_k$  under that the quantity of group  $i$  is  $k$ , the BBO algorithm mutates variable of group  $i$ .  $P_k$  is satisfied the following expression:

$$P'_k = \begin{cases} -(\lambda_k + u_k)P_k + u_{k+1}P_{k+1}, & k = 0 \\ -(\lambda_k + u_k)P_k + \lambda_{k-1}P_{k-1} + u_{k+1}P_{k+1}, & 1 \leq k \leq n - 1 \\ -(\lambda_k + u_k)P_k + \lambda_{k-1}P_{k-1}, & k = n \end{cases} \quad (1)$$

According to the basic principles of biogeography [11], the mutation rate is inversely proportional to the probability of species. The variation  $m_i$  was as follows:

$$m_i = m_{\max} \frac{1 - P_k}{P_{\max}} \quad (2)$$

where  $m_{\max}$  is the defined maximum variation rate of groups;  $P_{\max}$  is the maximum probability of all species. This mutation function allows low HSI group to a greater probability of a mutation, which makes the group to further improve.

In mutation operation, according to  $m_i$  to choose the group  $H_i$  need to modify, and then randomly generates a characteristic variable value to replace the corresponding characteristic variables in  $H_i$ , and then calculate the new HSI values.

### 3 Principle of Improved BBO Algorithm

The article applies the BBO algorithm to PID controller parameter optimization of CFB bed temperature. The parameters of PID controller are as BBO algorithm's feature vector. The migration strategy only replaced one parameter of the PID controller. It is difficult to guarantee PID parameters reasonably match each other. That will lead to the defects of slow convergence and poor convergence accuracy. Response to the problem, this paper introduces convergence mechanism of the particle swarm algorithm to the migration strategy of BBO algorithm. The improved migration strategy principle is that according to  $\lambda$ , we confirm the needed to be changed group  $H_i$ , and according to  $\mu$ , we confirm the needed to be moved-out group  $H_j$ . Finally combined with the current best fitness group  $H_{\max}$  in the iterative process, we can get the new group  $H_i$  as formula (3) shows:

$$H_i(m) = H_i(m) + c_1 \text{rand}(1)(H_j(m) - H_i(m)) + c_2 \text{rand}(1)(H_{\max}(m) - H_i(m)) \quad (3)$$

in which  $m = 1, 2, \dots, D$ .  $D$  is the number of SIV.



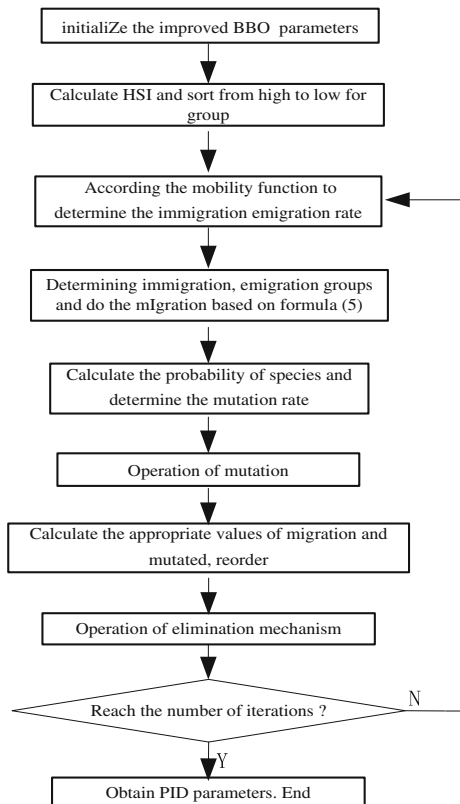
Migration and mutation strategies of BBO algorithm cannot guarantee that the PID parameters after iteration have better control effects than the PID parameters of previous iteration. To ensure each of the iterations makes PID parameters evolving toward the direction of optimal solution, the article introduces elimination mechanism to the BBO algorithm. The elimination mechanism is that we compare HSI of the  $SIV_1$  after migration, the  $SIV_2$  after mutation, and the  $SIV_3$  of the previous iteration. Then, we chose a SIV which has the best HSI as the group SIV in the  $SIV_1$ ,  $SIV_2$ , and  $SIV_3$ . Thus, it can ensure that the group is not lost the excellent characteristics after the migration and mutation and it can improve the convergence rate.

The article applies the improved algorithm BBO to the PID controller parameter optimization of CFB bed temperature and uses sum of error square IEAT index as HSI value to evaluate the merits of optimization. The IEAT index is as follows:

$$J = \int_0^t e^2(t)dt \tag{4}$$

When the value is smaller, the HSI is higher and the performance of optimization is better. The whole process of improved BBO algorithm is shown in Fig. 1:

**Fig. 1** The progress of improved BBO algorithm



## 4 PID Parameter Optimization of CFB Bed Temperature

CFB boiler bed temperature directly affects the furnace desulfurization and denitration. This article applies improved BBO algorithm to PID controller parameter optimization of CFB boiler temperature control system. This paper adopts a 310 t/h CFB boiler which is given in the literature [3]. When the fuel  $F = 210$  t/h, keeping the primary air, the secondary air, power load, and heating load unchanged, the bed temperature transfer function model is obtained under step disturbance of fuel. The formula is shown as below:

$$G(s) = \frac{3.43}{(148s + 1)^3} \quad (5)$$

This article initializes parameters according to the setting parameter principle of BBO algorithm. Article [2] has been proved that cosine function model has better performance in selecting the mobility function, so this paper selects cosine function as the mobility cosine function model. Also as for the formula (3), the values of  $c_1$  and  $c_2$  are based on the setting principles of particle swarm algorithm parameters. Finally, the improved BBO algorithm's main parameters are as follows:

In order to prove the effectiveness of the improved BBO algorithm, as a comparison, the article presents a general BBO algorithm to optimize PID controller parameters for the transfer function (5). The general BBO algorithm parameters is set according to Table 1 The experiment curve of error square sum under iteration times is shown in Fig. 2:

As is shown Fig. 2, in the optimization, compared to BBO algorithm, the improved BBO algorithm has faster convergence rate and the optimization results are better than traditional BBO algorithms. In addition, it can be seen from the data in Table 2 that the optimization results of BBO algorithm is unstable and fluctuate greatly in the 6 consecutive optimization simulation results. But in the improved BBO algorithm, the optimization results are always about 7 and the fluctuation is small. Directional convergence characteristic ensures the rapidity and stability of the convergence results and makes it possible to obtain satisfactory optimization results in shorter iteration cycle.

In addition, in order to verify the control effect of PID parameters obtained by optimization, the paper optimizes PID parameters again and controls the system

**Table 1** Parameters for improved BBO

$G$	$n$	$I$	$E$	$m_{\max}$	$c_1$	$c_2$
100	30	1	1	0.05	0.8	0.6

In which,  $G$  is the number of iterations

Fig. 2 Six experiment curves

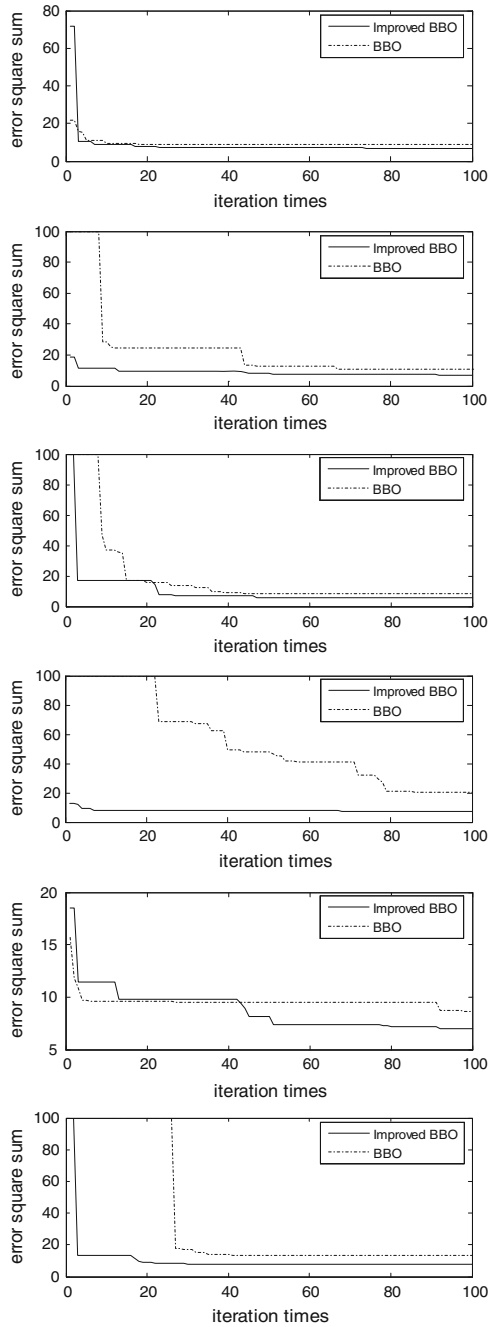


**Table 2** The final minimum sum of error square

Num	BBO	Improved BBO
1	9.1	6.7
2	11.0	7.0
3	8.6	6.1
4	20.4	7.1
5	8.7	7.0
6	13.4	7.5

shown in the formula (5). The controller parameters obtained by BBO and improved BBO algorithm are shown as follows:

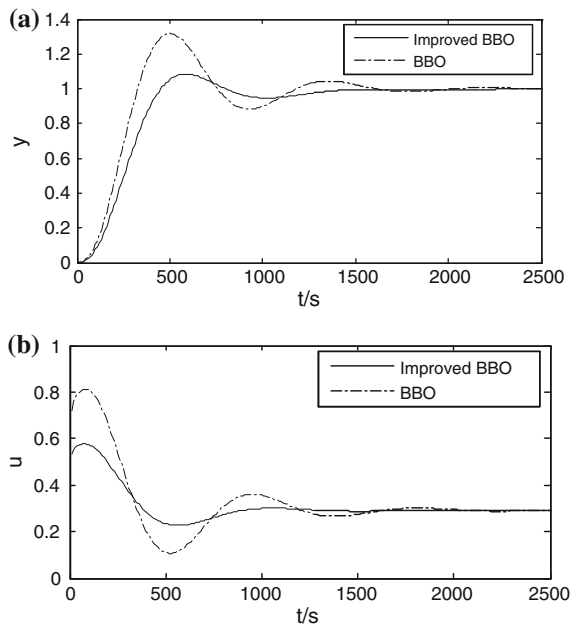
$$\text{BBO: } K(s) = 0.7212 + 0.002 \frac{1}{s} + 24.75s \tag{6}$$

$$\text{Improved BBO: } K(s) = 0.3766 + 0.0009 \frac{1}{s} + 24.98s \tag{7}$$

This article adopts MATLAB to do the simulation. The simulation time is 2500 s. The simulation result is shown in Fig. 3.

As is shown in Fig. 3 under control action of PID controller which is optimized by improved BBO algorithm, the system has a smaller overshoot and can set to a given value fast, showing a good dynamic performance and steady

**Fig. 3** The curve of step response **a** system output curve **b** the controller output curve



performance. In addition, from the controller output, the output amplitude and frequency of oscillation are smaller than the BBO algorithm. The control effect is satisfactory.

## 5 Conclusion

This paper presents an improved optimization BBO algorithm and successfully applies it to the PID controller parameter optimization of CFB temperature system. Improved BBO algorithm introduces convergence mechanism of particle swarm optimization to the original migration strategy so that the whole migration process has a certain direction and the use of elimination strategy eliminates the parameter which is worse after the migration. Compared with the original BBO algorithm, simulation results show that the improved BBO algorithm has greater improvement in convergence speed and the results are more stable in convergence. Also, the simulation results show that the optimized PID control parameters achieved satisfactory results.

## References

1. Wang CR, Wang NN, Duan XD (2010) Survey of biogeography-based optimization. *Comput Sci* 37(7):34–38
2. Bhattacharya A, Chattopadhyay PK (2010) Hybrid differential evolution with biogeography-based optimization for solution of economic load dispatch. *IEEE Trans on Power Syst* 25(4):1955–1964
3. Li JW, Zhao JQ, Zhang Y (2012) Optimal power flow on basis of combining improved differential evolution algorithm with biogeography-based optimization algorithm. *Power Syst Technol* 36(9):115–119
4. Zheng ZB (2011) Application of BBO in image segmentation. *Geomatics Inf Sci of Wuhan Univ* 36(8):932–935
5. Bi XJ, Wang J, Li B (2014) Orthogonal waveform design for radar based on biogeography-based optimization. *J Jilin Univ (Eng Technol Ed)* 44(3):867–873
6. Liu W, Ye YL, Si FQ (2013) Optimal operation pressure of steam turbine based on BP neural network and SA-BBO algorithm. *J Eng Therm Energy Power* 28(1):18–22
7. Ma HP, Li X, Lin SD (2009) Analysis of migration rate models for biogeography-based optimization. *J Southeast Univ* 39:16–21
8. Wang FL, Li P, Cao JT (2012) Improved biogeography-based optimization algorithm based on local search strategy. *J Jiang nan Univ* 11(4):467–473
9. Zhao WJ, Zhang WZ, Feng XL (2007) Bed temperature control characteristics of CFB boilers. *J Power Eng* 27(4):549–550

# Study on Joint Vibration Attenuation of the Satellite Attitude Control Actuator Using a Vibration Isolator and Vibration Absorbers

Peng Tian and Rui Zhong

**Abstract** The vibration isolator is the major solution to suppress the disturbance caused by high-frequency vibration of the satellite, but it is difficult to resolve the conflicts between the attenuation in the resonance region and the high-frequency attenuation in design. This paper studies the vibration attenuation of attitude control actuators. Control moment gyroscopes, chosen as the attitude control actuators, are installed on a vibration attenuation platform consisted of a vibration isolator and vibration absorbers. The motion of equations of the whole satellite including the vibration attenuation platform is established. Then, the dynamic characteristics of the vibration isolator are analyzed, and the optimization of vibration absorbers is conducted. Finally, a system of parameters design method of the vibration attenuation platform is proposed, which satisfies the requirement of vibration attenuation and guarantees the stability of the attitude control system.

**Keywords** Vibration isolator · Vibration absorber · Vibration control · Attitude control actuator

## 1 Introduction

Currently, flywheel and control moment gyroscopes (CMGs) are commonly used as satellite attitude control actuators. Because of the factors such as the static and dynamic imbalance of the rotor, the rotors of CMGs and flywheel can create high-frequency vibration, which can interfere satellite attitude control, and cause great decrease of the performance index of the precise optical sensing device. Therefore, the performance of the high-precision satellite needs to be improved by vibration attenuation technology [1–3].

---

P. Tian · R. Zhong (✉)  
Beihang University, 37 Xueyuan Road, Haidian District, Beijing, China  
e-mail: zhongruia@163.com

P. Tian  
e-mail: tpsx008@163.com

In 2010, solar dynamic detector launched by the USA conducted a large number of micro-vibration analyses. The flywheel vibrations caused significant influence to the scientific instruments. As for this kind of high-resolution spacecraft, it is necessary to take measures as flywheel vibration isolation [4]. Zhang Yao and others proposed the isolation platform of CMGs, where they considered the disturbance resource including the static and dynamic imbalance of the rotor, the disjoint of rotor shaft and framework axis, and the non-vertical dynamic model, and analyzed the dynamic characteristics of the vibration isolation platform [5, 6]; Ji-hoon Leea proposed that passive vibration isolator and dynamic vibration absorber could be applied to the precise equipment with repeated movement or waggle. Experiments show that the dynamic vibration absorber could reduce the peak of the vibration amplitude to about 60 % [7].

Although studies on joint vibration attenuation using vibration isolators and vibration absorbers are found in some fields [8], the analysis is limited, especially in the area vibration attenuation of satellite actuator. In view of this situation, this paper establishes a dynamic model of the whole spacecraft, including a vibration attenuation platform consisted of a vibration isolator, and supplemented by several vibration absorbers. The paper conducts a theoretical research on the system dynamics and accomplishes parameter optimization of the platform.

## 2 The Principle of Vibration Isolator and Absorber

### 2.1 The Principle of Vibration Isolator

Figure 1 shows the model of the vibration isolator, where  $F$  is disturbing force;  $F_T$  is the force passed to the installed base;  $K$  is the coefficient of spring stiffness;  $C$  is the damping coefficient;  $M$  is the device mass; and  $x$  is displacement. Suppose the base is determined, then the system dynamic equation can be described as:

$$\begin{cases} M\ddot{x} + C\dot{x} + Kx = F \\ C\dot{x} + Kx = F_T \end{cases} \quad (1)$$

So the force transfer function is as follows:

$$G(s) = \frac{F_T(s)}{F(s)} = \frac{(Cs + K)}{Ms^2 + Cs + K} \quad (2)$$

Substituting  $s = j\omega$  into the function, the transfer rate of the vibration isolation system can be described as:

$$T = \left| \frac{F_T}{F} \right| = |G(j\omega)| = \sqrt{\frac{1 + 4\xi^2 a^2}{(1 - a^2)^2 + 4\xi^2 a^2}} \quad (3)$$

Fig. 1 Model of isolator

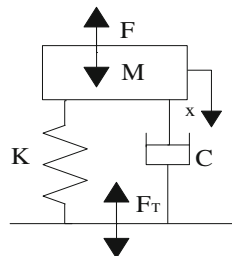
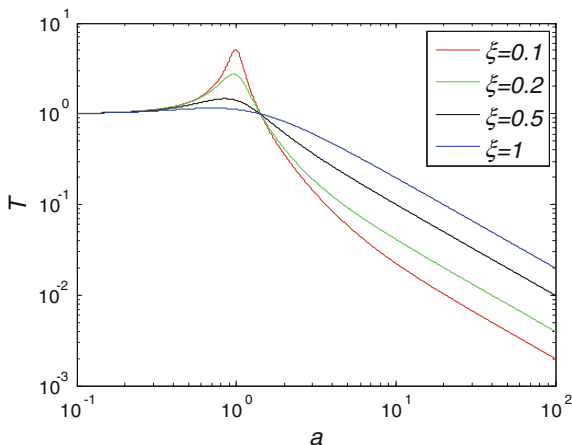


Fig. 2 The frequency response of the transfer rate



where  $\Omega_n = \sqrt{K/M}$  represents the inherent frequency,  $\xi = C/2M\Omega_n$  represents the damping ratio, and  $a = \omega/\Omega_n$  represents the frequency ratio.

With the transfer rate representing the vibration attenuation effect, MATLAB is used to draw the frequency response of the transfer rate, which is shown in Fig. 2.

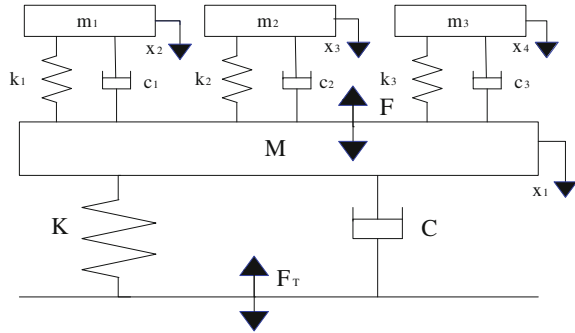
According to Fig. 2, there exists conflicts between the attenuation in the resonance region and that in the high-frequency region when the vibration isolator parameters change. With  $K$  determined, the greater the damping, the smaller the resonance peak, but lower the high-frequency attenuation. Using the active vibration isolator or the vibration absorber supplemented to restrain the resonance peak can both solve the conflict. As active vibration isolation consumes more energy and less stable, this paper combines vibration isolator and vibration absorbers, using vibration absorbers to improve the attenuation in resonance peak and vibration isolator to improve high-frequency attenuation.

### 2.2 The Principle of Vibration Absorber

This paper establishes a dynamic model of multiple vibration absorbers, and the dynamic equation is Eq. 4. Now, taking the example of a vibration isolator and



**Fig. 3** Model of the vibration isolator with three vibration absorbers



three vibration absorbers, Fig. 3 shows the illustration model and Eq. 5 shows the dynamic equation of the system.

$$M\ddot{x} + C\dot{x} + Kx = U \tag{4}$$

As shown in the equation,  $M$  is the mass matrix,  $C$  is the damping coefficient matrix,  $K$  is the stiffness coefficient matrix, and  $U$  is the external force vector.

$$\begin{bmatrix} M & 0 & 0 & 0 \\ 0 & m_1 & 0 & 0 \\ 0 & 0 & m_1 & 0 \\ 0 & 0 & 0 & m_1 \end{bmatrix} \begin{bmatrix} \ddot{x}_1 \\ \ddot{x}_2 \\ \ddot{x}_3 \\ \ddot{x}_4 \end{bmatrix} + \begin{bmatrix} c_1 + c_2 + c_3 + C & -c_1 & -c_2 & -c_3 \\ -c_1 & c_1 & 0 & 0 \\ -c_2 & 0 & c_2 & 0 \\ -c_3 & 0 & 0 & c_3 \end{bmatrix} \begin{bmatrix} \dot{x}_1 \\ \dot{x}_2 \\ \dot{x}_3 \\ \dot{x}_4 \end{bmatrix} + \begin{bmatrix} k_1 + k_2 + k_3 + K & -k_1 & -k_2 & -k_3 \\ -k_1 & k_1 & 0 & 0 \\ -k_2 & 0 & k_2 & 0 \\ -k_3 & 0 & 0 & k_3 \end{bmatrix} \begin{bmatrix} x_1 \\ x_2 \\ x_2 \\ x_2 \end{bmatrix} = \begin{bmatrix} F \\ 0 \\ 0 \\ 0 \end{bmatrix} \tag{5}$$

Transferring the force of installed base:

$$F_T = Kx_1 + C\dot{x}_1 \tag{6}$$

Let  $x = [x_1 \ x_2 \ x_3 \ x_4]^T$ ,  $\dot{X} = [\dot{x} \ \dot{x}]^T$ . Define the disturbance of the main system as input and the force transfer to the installed base as output, thus

$$\begin{cases} \dot{X} = AX + Bu \\ Y = C_yX + Du \end{cases} \tag{7}$$

where  $Y = F_T$ ,  $C_y = [K \ 0 \ 0 \ 0 \ C \ 0 \ 0 \ 0]$ ,  $u = F$ ,  $D = 0$ ,  $A = \begin{bmatrix} \mathbf{0}_4 & E_4 \\ -M^{-1}K & -M^{-1}C \end{bmatrix}$ ,  $B = [0 \ 0 \ 0 \ 0 \ 1/M \ 0 \ 0 \ 0]^T$

The force transfer function is as follows:

$$\mathbf{G}(s) = \mathbf{C}_y(s\mathbf{E} - \mathbf{A})^{-1}\mathbf{B} + \mathbf{D} \quad (8)$$

This system's transfer rate is as follows:

$$T = |F_T/F| = |\mathbf{G}(s)| = |\mathbf{G}(j\omega)| \quad (9)$$

Define the object function  $T_{\max}$  as maximum of  $G(j\omega)$  with given  $\zeta_h$  and  $f_h$  ( $h = 1, 2, 3$ ), so that

$$T_{\max} = \max |G(j\omega)| \Big|_{\zeta_1=\zeta'_1, \zeta_2=\zeta'_2, \zeta_3=\zeta'_3, f_1=f'_1, f_2=f'_2, f_3=f'_3}$$

where

$$f_h = \sqrt{k_h/m_h}/\sqrt{K/M}, \quad \zeta_h = 2c_h/\sqrt{k_h m_h}$$

$f_h$  and  $\zeta_h$  represent the damping ratio and the determined frequency ratio of the vibration absorber, respectively.

The target is to search the value for  $\zeta_h$  and  $f_h$ , which minimize  $T_{\max}$

$$\begin{aligned} \text{ming} &= \min T_{\max} \\ \text{subject to} & \zeta'' \leq \zeta_h \leq \zeta''', f'' \leq f_h \leq f''' \end{aligned} \quad (10)$$

$\zeta'', \zeta''', f'', f'''$  represent the upper and lower bounds of  $\zeta_h, f_h$ , respectively; then,  $c_h$  and  $k_h$  can be obtained by  $\zeta_h, f_h$ , respectively. This paper uses the optimization tool box in the MATLAB software to solve the optimal problem described in Eq. (10).

### 3 Dynamic Modeling

The satellite is equipped with satellite attitude control actuators (four CMGs) and a platform of vibration attenuation. The coordinate system can be defined as follows: inertial coordinate system  $f_e(o_e x_e y_e z_e)$ ; top platform coordinate system in the platform of vibration attenuation  $f_u(o_u x_u y_u z_u)$ , mass center being  $o_u$ ; frame coordinate system  $f_{ci}(\vec{c}_{gi}, \vec{c}_{si}, \vec{c}_{ii})$ , from which unit vectors  $\vec{c}_{gi}, \vec{c}_{si}$  represent the direction of the gimbal angular velocity and the rotor angular velocity in the top platform coordinate system of the number  $i$  gyro, respectively, and the two are perpendicular,  $\vec{c}_{ii} = \vec{c}_{gi} \times \vec{c}_{si}$ ; bottom platform coordinate system of vibration attenuation  $f_d(o_d x_d y_d z_d)$ , mass center being  $o_d$ ; and satellite body coordinate system  $f_s(o_s x_s y_s z_s)$ , mass center being  $o_s$ . Define  $\mathbf{A}_{ab}$  as the transformation matrix from  $b$  coordinate system to  $a$  coordinate system.

### 3.1 The Strut Kinematic Modeling of Vibration Isolator

The top and bottom strut coordinates system of the strut  $i$  are  $\mathbf{f}_{rp_i}(o_{rp_i}, x_{rp_i}, y_{rp_i}, z_{rp_i})$  and  $\mathbf{f}_{rq_i}(o_{rq_i}, x_{rq_i}, y_{rq_i}, z_{rq_i})$ ;  $o_{rp_i}$  and  $o_{rq_i}$  are the connection points between the top or bottom strut and the platform, respectively.

The equations of motion of the top and bottom strut are Eqs. (11) and (12):

$$\mathbf{r}_{p_i} = \mathbf{t} + \mathbf{A}_{eu}\mathbf{p}_i, \mathbf{v}_{p_i} = \dot{\mathbf{t}} + \mathbf{A}_{eu}\boldsymbol{\omega}_p^\times \mathbf{p}_i, \mathbf{a}_{p_i} = \ddot{\mathbf{t}} + \mathbf{A}_{eu}\dot{\boldsymbol{\omega}}_p^\times \mathbf{p}_i + \mathbf{A}_{eu}\boldsymbol{\omega}_p^\times \boldsymbol{\omega}_p^\times \mathbf{p}_i \quad (11)$$

$$\mathbf{r}_{q_i} = \mathbf{d} + \mathbf{A}_{ed}\mathbf{q}_i, \mathbf{v}_{q_i} = \dot{\mathbf{d}} + \mathbf{A}_{ed}\boldsymbol{\omega}_q^\times \mathbf{q}_i, \mathbf{a}_{q_i} = \ddot{\mathbf{d}} + \mathbf{A}_{ed}\dot{\boldsymbol{\omega}}_q^\times \mathbf{q}_i + \mathbf{A}_{ed}\boldsymbol{\omega}_q^\times \boldsymbol{\omega}_q^\times \mathbf{q}_i \quad (12)$$

where  $\mathbf{t}$  and  $\mathbf{d}$  represent the vector from  $o_e$  to  $o_u$  or  $o_d$ , respectively;  $\mathbf{p}_i$  and  $\mathbf{q}_i$  represent the vector from  $o_u$  or  $o_d$  to the connection point of top and bottom platform, respectively; and  $\boldsymbol{\omega}_p$  and  $\boldsymbol{\omega}_q$  represent the angular velocity of the top platform and bottom platform relative to the inertial system, respectively.  $()^\times$  represents the skew symmetric matrix for vector cross.

The strut vector, the strut length, the axial unit vector along the strut, the vector of the strut velocity, and the acceleration vector can be described as follows:

$$\mathbf{R}_i = \mathbf{r}_{p_i} - \mathbf{r}_{q_i}, l_i = \|\mathbf{R}_i\|, \mathbf{r}_{ui} = \mathbf{R}_i/l_i, \mathbf{v}_{R_i} = \mathbf{v}_{p_i} - \mathbf{v}_{q_i}, \mathbf{a}_{R_i} = \mathbf{a}_{p_i} - \mathbf{a}_{q_i} \quad (13)$$

The top strut and the top platform are connected by spherical hinge, while the bottom strut and the bottom platform are connected by universal hinge. As shown in Eq. (14),  $\bar{\mathbf{y}}_i$  is the unit vector of the moving axis of the hinge and  $\bar{\mathbf{k}}_i$  is the unit vector of the determined axis of the hinge:

$$\bar{\mathbf{h}}_i = \bar{\mathbf{y}}_i \times \bar{\mathbf{k}}_i, \mathbf{y}_i = (\mathbf{k}_i^\times \mathbf{r}_{ui}) / \|\mathbf{k}_i^\times \mathbf{r}_{ui}\| \quad (14)$$

The angular velocity of the strut is as follows:

$$\boldsymbol{\omega}_i = \boldsymbol{\omega}_i + \omega_{ri}\mathbf{r}_{ui} \quad (15)$$

where  $\boldsymbol{\omega}_i = \mathbf{r}_{ui}^\times \mathbf{v}_{R_i} / l_i$ ,  $\omega_{ri} = -(\boldsymbol{\omega}_i^T \mathbf{h}_i) / (\mathbf{r}_{ui}^T \mathbf{h}_i)$

The angular acceleration of the strut  $\boldsymbol{\varepsilon}_i$  can be acquired by the derivation to Eq. (15).

The velocity and the acceleration of the strut, respectively, are as follows:

$$\dot{l}_i = \mathbf{r}_{ui}^T \mathbf{v}_{R_i}, \ddot{l}_i = \mathbf{r}_{ui}^T \mathbf{a}_{R_i} - \mathbf{r}_{ui}^T [\boldsymbol{\omega}_i^\times \boldsymbol{\omega}_i^\times \mathbf{R}_i] = \mathbf{r}_{ui}^T \mathbf{a}_{R_i} + l_i \boldsymbol{\omega}_i^T \boldsymbol{\omega}_i - l_i \omega_{ri}^2 \quad (16)$$

The acceleration in the mass centers of the top and bottom struts is as follows:

$$\mathbf{a}_{ui} = \mathbf{a}_{q_i} + \boldsymbol{\varepsilon}_{li}^\times \mathbf{r}_{rpi} + \boldsymbol{\omega}_{li}^\times \boldsymbol{\omega}_{li}^\times \mathbf{r}_{rpi} + \ddot{l}_i \mathbf{r}_{ui} + 2\dot{l}_i \boldsymbol{\omega}_{li}^\times \mathbf{r}_{ui}, \mathbf{a}_{di} = \mathbf{a}_{q_i} + \boldsymbol{\varepsilon}_{li}^\times \mathbf{r}_{rqi} + \boldsymbol{\omega}_{li}^\times \boldsymbol{\omega}_{li}^\times \mathbf{r}_{rqi} \quad (17)$$

where  $\mathbf{r}_{rpi}$  and  $\mathbf{r}_{rqi}$  represent the vector from  $o_{rp_i}$  and  $o_{rq_i}$  to the mass centers place.

### 3.2 The Strut Dynamic Modeling of Vibration Isolator

The translational and rotational dynamic equations of the whole strut are as follows:

$$m_{ri}\mathbf{a}_{ui} + m_{si}\mathbf{a}_{di} = \mathbf{F}_{ri} + \mathbf{F}_{si} \quad (18)$$

$$\begin{aligned} (\mathbf{I}_{ri} + \mathbf{I}_{si})\boldsymbol{\varepsilon}_{li} + \boldsymbol{\omega}_{li}^{\times}(\mathbf{I}_{ri} + \mathbf{I}_{si})\boldsymbol{\omega}_{li} = & \mathbf{R}_i^{\times}\mathbf{F}_{ri} + M_{ui}\mathbf{h}_{ui} - c_{ri}(\boldsymbol{\omega}_{li} - \mathbf{A}_{eu}\boldsymbol{\omega}_p) - c_{ui}(\boldsymbol{\omega}_{li} \\ & - \mathbf{A}_{ed}\boldsymbol{\omega}_q) \\ & - (m_{ri}\mathbf{r}_{rpi} + m_{si}\mathbf{r}_{rqi})^{\times}\mathbf{a}_{qi}(\mathbf{I}_{ri} + \mathbf{I}_{si})\boldsymbol{\varepsilon}_{li} + \boldsymbol{\omega}_{li}^{\times}(\mathbf{I}_{ri} + \mathbf{I}_{si}) \end{aligned} \quad (19)$$

where  $m_{ri}$  and  $m_{si}$  represent the top and bottom mass;  $\mathbf{I}_{ri}$  and  $\mathbf{I}_{si}$  represent the top and bottom strut inertia in the inertial system;  $\mathbf{F}_{ri}$  is the force of the spherical hinge on the top strut;  $\mathbf{F}_{si}$  is the force of the universal hinge on the bottom strut;  $M_{ui}\mathbf{h}_{ui}$  is the torque of the universal hinge on the bottom strut;  $c_{ri}$  and  $c_{ui}$  are the damping coefficient of the spherical hinge and universal hinge, respectively.

Multiplying function (19) by  $\mathbf{r}_{ui}^{\times}$ , then the function of  $\mathbf{F}_{ri}$  can be obtained as follows:

$$\begin{aligned} \mathbf{F}_{ri} = & (\mathbf{r}_{ui}^T\mathbf{F}_{ri})\mathbf{r}_{ui} - \{\mathbf{r}_{ui}^{\times}(\mathbf{I}_{ri} + \mathbf{I}_{si})\boldsymbol{\varepsilon}_{li} + \mathbf{r}_{ui}^{\times}[\boldsymbol{\omega}_{li}^{\times}(\mathbf{I}_{ri} + \mathbf{I}_{si})\boldsymbol{\omega}_{li}] + c_{si}\mathbf{r}_{ui}^{\times}(\boldsymbol{\omega}_{li} - \boldsymbol{\omega}_p) \\ & + c_{ui}\mathbf{r}_{ui}^{\times}(\boldsymbol{\omega}_{li} - \boldsymbol{\omega}_q) + \mathbf{r}_{ui}^{\times}[(m_{ri}\mathbf{r}_{rpi} + m_{si}\mathbf{r}_{rqi})^{\times}\mathbf{a}_{qi} - \mathbf{r}_{ui}^{\times}M_{ui}\mathbf{h}_{ui}]\}/l_i \end{aligned} \quad (20)$$

$$\mathbf{r}_{ui}^T\mathbf{F}_{ri} = m_{ui}\mathbf{r}_{ui}^T\mathbf{a}_{ui} + k_i(l_i - l_{0i}) + c_i\dot{l}_i \quad (21)$$

where  $k_i$  is the stiffness coefficient of the strut,  $c_i$  is the damping coefficient of the strut, and  $l_{0i}$  is the nominal length of the strut; then,  $M_{ui}$  can be acquired by multiplying  $\mathbf{r}_{ui}^T$  by Eq. (19)

The force  $\mathbf{F}_{si}$  is as follows:

$$\mathbf{F}_{si} = m_{ui}\mathbf{a}_{ui} + m_{di}\mathbf{a}_{di} - \mathbf{F}_{ri} \quad (22)$$

### 3.3 The Dynamic Modeling of Vibration Absorber

Define the coordinate system of the vibration absorber as  $\mathbf{f}_{tk}(O_{tk}x_{tk}y_{tk}z_{tk})$ , mass center being  $O_{tk}$ . In the coordinate system of the top platform, the translational and rotational dynamic equations of the vibration absorbers are as follows:

$$\begin{cases} m_k\mathbf{A}_{ue}\ddot{\mathbf{f}}_{tk} + \mathbf{C}_{kt}\mathbf{A}_{ue}\dot{\Delta}\mathbf{t} + \mathbf{K}_{kt}\mathbf{A}_{ue}\Delta\mathbf{t}_k = 0 \\ \mathbf{A}_{utk}(\mathbf{I}_k\dot{\boldsymbol{\omega}}_{tk} + \boldsymbol{\omega}_{tk}^{\times}\mathbf{I}_k\boldsymbol{\omega}_{tk}) = -\mathbf{K}_{kr}\Delta\boldsymbol{\theta}_{tk} - \mathbf{C}_{kr}(\mathbf{A}_{utk}\boldsymbol{\omega}_{tk} - \boldsymbol{\omega}_p) \end{cases} \quad (23)$$

where  $m_k$  and  $I_k$  represent the mass and inertia of the number  $k$  vibration absorber;  $r_{tk}$  is the vector of the vibration absorber in  $f_e$ ;  $\Delta t_k$ , equals to  $r_{tk} - t - A_{eu}t_k$ , is the displacement of the vibration absorber relative to the top platform;  $t_k$  is the position of connection point of the vibration absorber and the top platform in  $f_u$ ;  $\Delta \theta_{tk}$  is the Euler angles of  $f_{tk}$  relative to  $f_u$ ;  $C_{kt}$ ,  $K_{kt}$ ,  $C_{kr}$ , and  $K_{kr}$  are translational damping matrix, translational stiffness matrix, rotational damping matrix, and rotational stiffness matrix of the vibration absorbers, respectively.

So the force and torque of the vibration absorbers are as follows:

$$F_{tk} = C_{kt}A_{ue}(\dot{r}_{tk} - \dot{t} - A_{eu}\omega_p^\times t_k) + K_{kt}A_{ue}(r_{tk} - t - A_{eu}t_k) \tag{24}$$

$$T_{tk} = K_{kr}\Delta\theta_{tk} + C_{kr}(A_{utk}\omega_{tk} - \omega_p) + t_k^\times F_{tk} \tag{25}$$

### 3.4 The Dynamic Modeling of the Whole Satellite

Using Newton–Euler method, the translational and rotational dynamic equations of the top platform system are as follows:

$$\begin{cases} (m_p + \sum_{j=1}^4 m_j)\dot{v}_p + \sum_{j=1}^4 m_j\omega_p^\times(v_p + \omega_p^\times r_{guj}) + \sum_{j=1}^4 m_j\dot{\omega}_p^\times r_{guj} + \omega_p^\times m_p v_p = -A_{ue} \sum_{i=1}^6 F_{ri} + \sum_{k=1}^N F_{tk} + F_e \\ I_u \dot{\omega}_p + \omega_p^\times (I_u \omega_p + h_c) = -\sum_{i=1}^6 p_i^\times A_{ue} F_{ri} + \sum_{i=1}^6 f_{pi} + T_c + T_e + \sum_{k=1}^N T_{tk} \end{cases} \tag{26}$$

were  $m_p$  is the mass of the top platform;  $m_j$  is the mass of each CMG;  $v_p$  is the velocity of the top platform;  $r_{guj}$  represents the radius vector from  $o_u$  to the number  $j$   $o_g$ ;  $I_u$  is the inertia matrix of the top platform system and CMGs;  $h_c$  is the angular momentum of CMGs relative to satellite;  $f_{pi}$  is the damping torque of the spherical hinge connected by the top platform;  $T_c$  is the torque generated by CMGs; and  $F_e$  and  $T_e$  are generated by the static and dynamic imbalance of the rotors.

The dynamic equation of the bottom platform system is as follows:

$$\begin{cases} m_s(\dot{v}_s + \omega_s^\times v_s) = -A_{se} \sum_{i=1}^6 F_{si} + F_{ext} \\ I_s \dot{\omega}_s + \omega_s^\times I_s \omega_s = -\sum_{i=1}^6 (A_{sd} q_i + r_{ds})^\times (A_{se} F_{si}) + \sum_{i=1}^6 f_{qi} + T_{ext} - A_{se} \sum_{i=1}^6 M_{ui} h_i \end{cases} \tag{27}$$

where  $m_s$  and  $I_s$  are the mass and inertia matrix of the bottom platform system;  $F_{ext}$  and  $T_{ext}$  are the disturbing force and torque of the external environment;

$f_{qi} = c_{ui}(A_{be}\omega_i - \omega_b)$  is the damping torque of universal hinge connected by the bottom platform;  $r_{ds}$  represents the vector form  $o_s$  to  $o_d$ ; and  $\omega_b = \omega_q \cdot v_p$  is the velocity of the satellite.

Equations (26) and (27) are the dynamic equations of the whole satellite. The top platform system includes the top platform, CMGs, and vibration absorbers; the bottom platform system includes the bottom platform and satellite body.

## 4 The Joint Vibration Attenuation Design

In this paper, the vibration attenuation is designed to improve high-frequency attenuation by vibration isolator while resolving the attenuation in the resonance region by the vibration absorber. The parameters of vibration absorbers are designed after the parameters of vibration isolator; finally, the stability of the attitude control system of the parameters is verified.

### 4.1 The Derivation and Parameter Design of the Transfer Function of Vibration Isolator

When calculating the inherent characteristics of the vibration isolation platform and the actuators, suppose the base is determined, platform configuration remains the same, Euler angles and Euler angular velocities are small, and the mass and inertia of the strut can be ignored.

According to the derivation of the force transfer function from Eq. (9), the disturbing transfer function of vibration isolator can be obtained. This transfer function is  $6 \times 6$  matrix, the vibration isolator is equal to Stewart platform, and its main parameters are as follows:

$$I_u = \begin{bmatrix} 9 & 0 & 0 \\ 0 & 9 & 0 \\ 0 & 0 & 16 \end{bmatrix} \text{kg} \cdot \text{m}^2, \mathbf{p} = \begin{bmatrix} 0.5 & -0.25 & -0.25 & 0.5 & -0.25 & -0.25 \\ 0 & 0.25\sqrt{3} & -0.25\sqrt{3} & 0 & -0.25\sqrt{3} & 0.25\sqrt{3} \\ 0 & 0 & 0 & 0 & 0 & 0 \end{bmatrix} m,$$

$$\mathbf{q} = \begin{bmatrix} 0.25 & -0.5 & 0.25 & 0.25 & -0.5 & 0.25 \\ 0.25\sqrt{3} & 0 & -0.25\sqrt{3} & -0.25\sqrt{3} & 0 & 0.25\sqrt{3} \\ 0 & 0 & 0 & 0 & 0 & 0 \end{bmatrix} m, m_u = m_p + \sum m_j = 90 \text{ kg}$$

The transfer functions of each channel are described in Eq. (28):  $x$ -axis translation,  $y$ -axis translation,  $z$ -axis translation,  $x$ -axis rotation,  $y$ -axis rotation, and  $z$ -axis rotation, respectively.

$$\begin{aligned}
 & \frac{cs^3 + (k + 0.021c^2)s^2 + 0.042kcs + 0.021k^2}{45s^4 + 2.26cs^3 + (2.26k + 0.021c^2)s^2 + 0.042kcs + 0.021k^2} \\
 & \frac{cs^3 + (k + 0.021c^2)s^2 + 0.042kcs + 0.021k^2}{45s^4 + 2.26cs^3 + (2.26k + 0.021c^2)s^2 + 0.042kcs + 0.021k^2} \\
 & \frac{cs + k}{45s^2 + cs + k} \\
 & \frac{cs^3 + (k + 0.033c^2)s^2 + 0.066kcs + 0.033k^2}{72s^4 + 3.6cs^3 + (3.6k + 0.033c^2)s^2 + 0.066kcs + 0.033k^2} \\
 & \frac{cs^3 + (k + 0.033c^2)s^2 + 0.066kcs + 0.033k^2}{72s^4 + 3.6cs^3 + (3.6k + 0.033c^2)s^2 + 0.066kcs + 0.033k^2} \\
 & \frac{cs + k}{21.33s^2 + cs + k}
 \end{aligned} \tag{28}$$

Because of the symmetry of the vibration isolator, the transfer function of  $x$ -axis translation and rotation is the same as that of  $y$ -axis translation and rotation, while  $z$ -axis is independently decoupled.

The parameter design of vibration isolator mainly is the design of stiffness  $K$  and damping  $C$ . To guarantee the fast response character of the system, the bandwidth of control system is approximately 1 Hz, and the system is fully stable when the frequency of vibration isolator is 7.5 times of the bandwidth control system, get  $\Omega_n = 7.5$  HZ; the vibration isolator frequency of  $z$ -axis translation is less than that of  $z$ -axis rotation, get  $M = 45$  kg.  $\Omega_n = \sqrt{K/M}$ , then get  $K = 87000$  N/m. The magnification multiples of the resonance area are described as  $n = 1 / (2\xi\sqrt{1 - \xi^2})$ , where  $n$  should be between 3 and 6, then get  $C = 600$  N/(m/s), and the design parameters of the vibration isolator are finished.

Suppose the amplitude of the input force (torque) of the platform is 1, the frequency of it is 80 Hz and the output force (torque) of the platform is the transfer rate of the channel. Figure 4 shows  $x(y)$  direction output force,  $x(y)$  direction output torque,  $z$  direction output force, and  $z$  direction output torque.

As shown in Fig. 4, the vibration isolation performance of  $z$ -axis rotation is poor, and the frequency response of torque transfer function of  $z$ -axis can be described as shown in Fig. 5. As shown in the Fig. 5, when the frequency is 80 Hz, the amplitude is -24.6 dB and transfer rate is  $10^{-24.6/20} = 0.0589$ , which indicates that time domain analysis is in line with frequency domain analysis.

### 4.2 The Parameters Design of Vibration Absorbers

Take the direction of  $z$ -axis rotation as an example to conduct the parameters design of the vibration absorbers, and the parameters design of the other channels is alike.

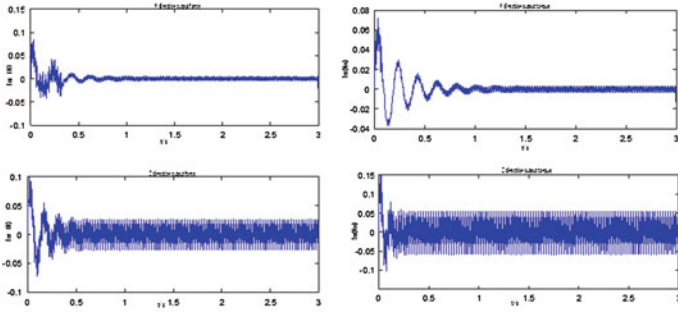


Fig. 4 The output force (torque) of the each direction

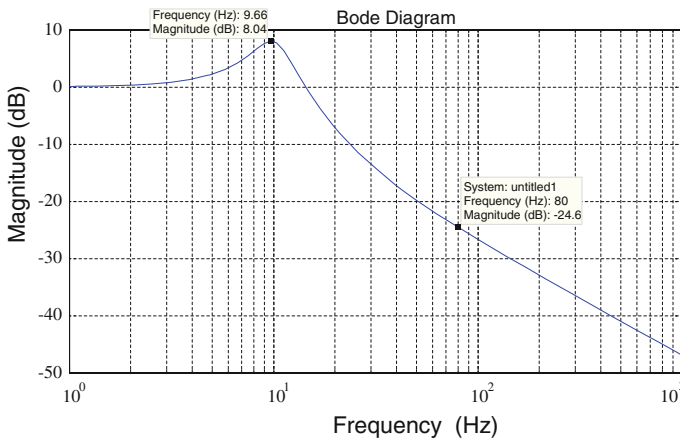


Fig. 5 The frequency response of torque transfer function of z-axis

Optimize the parameters of the vibration absorbers using the method in function 10, and the optimized parameters such as  $\mu = 0.1$  can be described as follows:

$$f'_1 = 0.95, \quad \zeta'_1 = 0.173, \quad f'_2 = 0.73, \quad \zeta'_2 = 0.163, \quad f'_3 = 0.59, \quad \zeta'_3 = 0.1244$$

Figure 6 shows the frequency response of the added three vibration absorbers after the parameters are optimized. In the original resonant frequency, 9.66 Hz, the amplitude decreases to 5.2 from 8.04 dB. Although the newly generated peak is 5.71 dB, it is smaller than the original one 8.04 dB, which shows that it is effective to the attenuation in resonance region.

To get greater high-frequency attenuation, the damping coefficient of the vibration isolator has been reduced and the vibration absorbers has been used to restrain the enlargement of the attenuation in resonance region caused by the damping reduction of the vibration isolator. Change  $C$  to 400 N/(m/s), and optimize the parameters of the vibration absorbers; then, the frequency response can be



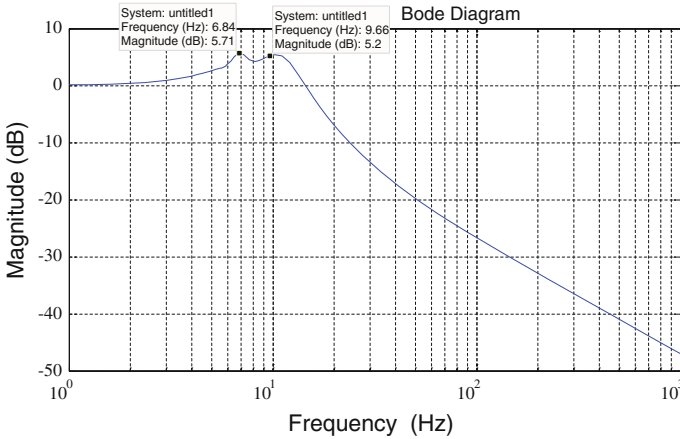


Fig. 6 The frequency response of the optimized vibration absorbers ( $C = 600$ )

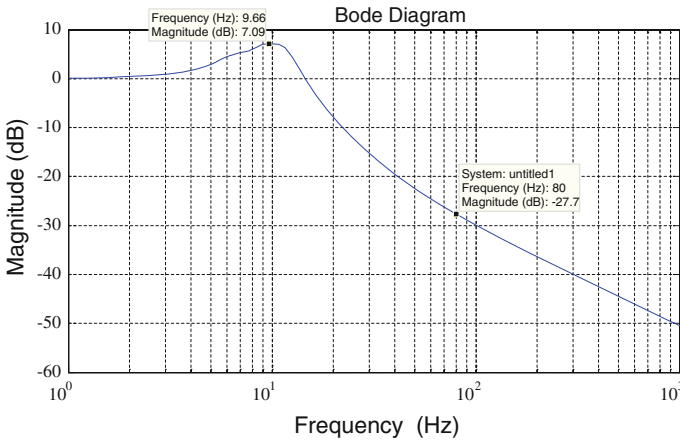


Fig. 7 The frequency response of the optimized vibration absorbers ( $C = 400$ )

described as shown in Fig. 7. The amplitude shown in Fig. 7 is smaller than that shown in Fig. 5, which indicates that the attenuation in resonance region complies with the design requirement. When the attenuation in 80 Hz decreases to  $-27.7$  dB from original  $-24.6$  dB, the desired effect has been achieved by the improvement of high-frequency attenuation.

### 4.3 The Stability Analysis of Attitude Control System

Simplify the attitude control system, neglect the vibration attenuation platform- and satellite-coupled characteristics, and take PID controller commonly used in

engineering as the attitude controller. Take  $z$ -axial rotation (the yaw channel) as an example to analyze the stability of the attitude control system.

In circumstances that attitude stabilization controls, suppose that the Euler angles and the Euler angular velocities are small, and neglect the coupled terms, then the transfer function of the satellite dynamic and kinematic can be written as (29):

$$\theta(s) = 1/I_z s^2 \tag{29}$$

PID controller is as follows:

$$PID(s) = K' \frac{(s + \tau_p)(s + \tau_q)}{s} \tag{30}$$

where  $\tau_p = 0.08$ ,  $\tau_q = 0.0005$ , and  $I_z = 800 \text{ kg} \cdot \text{m}^2$ .

When  $C = 400$ , the transfer function of the  $z$ -axial rotation of the three vibration absorbers with parameters optimized is as follows:

$$G_z(s) = \frac{129s^7 + 3.4 \times 10^4 s^6 + 2.31 \times 10^6 s^5 + 2.51 \times 10^8 s^4 + 8.26 \times 10^9 s^3 + 5.29 \times 10^{11} s^2 + 7.68 \times 10^{12} s + 3.22 \times 10^{14}}{6.88s^8 + 456s^7 + 9.12 \times 10^4 s^6 + 3.89 \times 10^6 s^5 + 3.84 \times 10^8 s^4 + 9.96 \times 10^9 s^3 + 6.17 \times 10^{11} s^2 + 7.68 \times 10^{12} s + 3.22 \times 10^{14}}$$

The transfer function of the open-loop system below the yaw channel is as follows:

$$G(s) = PID(s)G_z(s)\theta(s) \tag{31}$$

The root locus is shown in Fig. 8. According to Fig. 8, the system changed into conditional stability, so the stable condition of the system is  $0.295 < K' < 26300$ . Suppose  $K' = 6000$ , then  $k_p = 483$ ,  $k_i = 0.24$ ,  $k_d = 6000$  can be obtained.

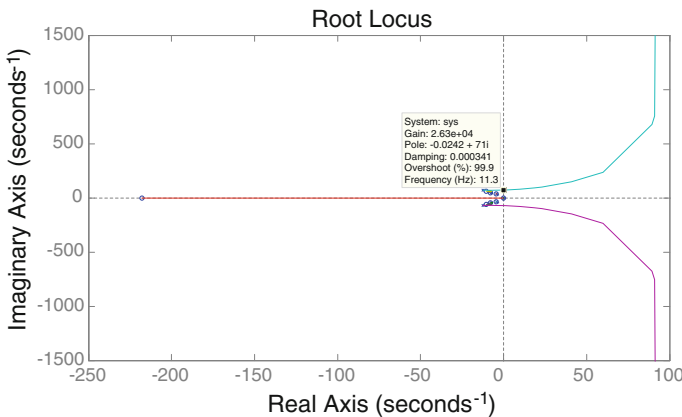


Fig. 8 The root locus of the yaw channel

### 5 The Simulation Analysis

Using the satellite dynamic model established in this paper simulated the attitude stability task of the attitude control, and this paper analyzes the influence of disturbance caused by the static and dynamic imbalance on the accuracy and stability of whole satellite attitude. Conduct the attitude stability control setting that all the initial Euler angles are  $1.5^\circ$  (Figs. 9, 10, and 11).

Thus, the satellite attitude stability (angular velocity of attitude) can be improved from  $6 \times 10^{-6}$  to  $3.8 \times 10^{-7}$  rad/s with vibration isolator, while the satellite attitude stability improves to  $1.6 \times 10^{-7}$  rad/s with vibration attenuation platform consisted of a vibration isolator and vibration absorbers.

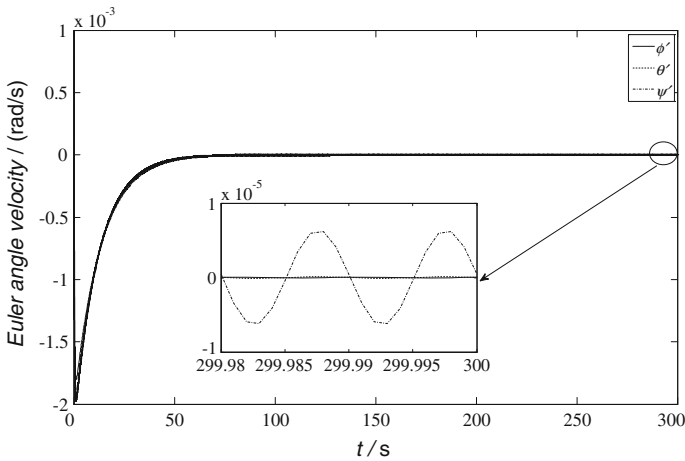


Fig. 9 The attitude angular velocity of attitude without vibration control

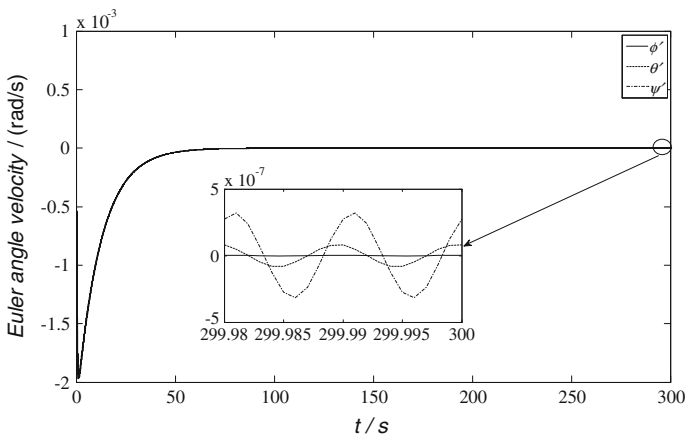


Fig. 10 The angular velocity of attitude with vibration isolator (Stewart platform)

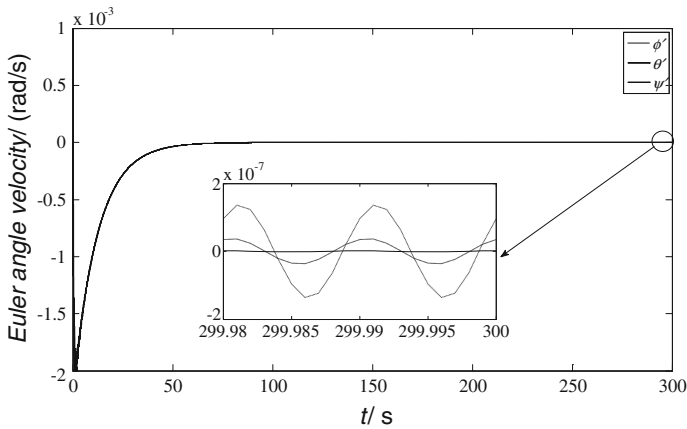


Fig. 11 The angular velocity of attitude with vibration attenuation platform

## 6 Conclusions

This paper studies the vibration attenuation of attitude control actuator on satellites. The paper proposes a method of joint vibration attenuation using vibration isolator and absorbers. First the principle of vibration isolation and absorption is analyzed, and then, the dynamic equations of whole satellite are established. Analysis of the system transfer function suggests that greater high-frequency attenuation can be achieved by decreasing the damping of the vibration isolator, while the enlargement of the attenuation in resonance region can be suppressed by vibration absorbers. Therefore, optimization of the parameters of vibration absorbers is conducted. Simulation results validate that the satellite attitude stability can improve by an order of magnitude after adopting the vibration isolator, while the attitude stable amplitude can further be cut off by 60 % while adopting joint vibration attenuation platform.

**Acknowledgement** Authors would like to acknowledge the funding of the National Natural Science Foundation of China (Grant No. 11402009)

## References

1. Blaurock C, Liu A, Dewell L et al (2005) Passive isolator design for jitter reduction in the terrestrial planet finder coronagraph. In: Optical modeling and performance precisions II, SPIE, San Diego, pp 1–12
2. Wilson GW (1975) Double gimbal control moment gyroscope gimbal control loop synthesis. AIAA, USA, pp 1–8
3. Seltzer SM., Schweitzer G, Bernard AJ (1972) Attitude control of a spinning skylab. In: AIAA guidance and control conference, AIAA, USA, pp 1–9

4. Liu KC, Blaurok CA (2011) Solar dynamics observatory on-orbit jitter testing analysis and mitigation plans. In: Proceedings of AIAA guidance navigation and control conference, AIAA, Portland, pp 1–28
5. Yao Z, Shijie X (2012) Parameters design of Stewart platform for control moment gyroscopes vibration isolation. *ACTA Astronautica* 645–659
6. Yao Z, Shijie X (2010) High frequency vibration isolation of control moment gyroscope on satellites. In: 61st international astronomical congress, Prague, 10:8444–8452
7. Lee JH, Dong Y, Lee MG (2011) Passive vibration reduction with silicone springs and dynamic absorber. *Int Conf Opt Precis Eng Nanotechnol* 19:431–435
8. Xu Z, Gong X (2010) An active-damping-compensated magnet or rheological elastomer adaptive tuned vibration absorber. *J Intell Mater Syst Struct* 1039–1047

# Weight Calculation of Oil and Gas Pipelines Risk Factors Based on Improved AHP

Tianyu Wang, Deyu Xu, Rujun Wang and Shujiao Tong

**Abstract** Oil and gas pipelines have many risk factors, such as third party damage, corrosion, design, and maloperation, which possess many specific risk factors, the least buried depth, ground operations, ground equipment, public education, line status, patrol frequency, and many others. How to determine the weight of each factor accurately is a widespread concern. In this study, the improved three-scale AHP method is introduced to determine risk index weight of pipelines. This method has the advantages of being concise and practical, as well as having a small workload, strong pertinence, and easy-to-compare factor significance, all of which make it more accurate and objective to determine the indexes weights and to conform better to the actual situation. The method proceeds in three steps: first, using improved AHP to determine weight of the two-level index; then, similarly, determining the weight of the three-level index successively; and finally, calculating the weight values of all risk factors.

**Keywords** Pipelines · Risk factors · Weight · Three-scale AHP

## 1 Introduction

Pipeline transportation has many advantages, such as safety, high efficiency, reliability, strong continuity, large capacity, low cost advantages, and so on, and is the most economic and reasonable way to transport oil and gas. However, with the

---

T. Wang (✉) · D. Xu

Faculty of Resource and Safety Engineering, China University of Mining and Technology, Beijing 100083, China  
e-mail: 522843975@qq.com

R. Wang · S. Tong

China Academy of Safety Science and Technology, Beijing 100012, China

R. Wang · S. Tong

Key Laboratory of Major Hazard Control and Accident Emergency Technology, State Administration of Work Safety, Beijing 100012, China

© Springer-Verlag Berlin Heidelberg 2016

B. Huang and Y. Yao (eds.), *Proceedings of the 5th International Conference on Electrical Engineering and Automatic Control*, Lecture Notes in Electrical Engineering 367, DOI 10.1007/978-3-662-48768-6\_78

increasing pipeline service life of pipelines, pipeline accidents happen frequently [1–3]. According to incomplete statistics, since 1995, there have been more than 1000 accidents of all kinds involving oil and gas pipelines, which strongly threatens the safe and reliable operation of pipeline systems [3–7]. Therefore, it's a serious threat to national economic development as well as people's lives and property safety.

There are many risk factors for oil and gas pipelines accidents, including from large ones such as third party damage, corrosion, design, and maloperation, which itself contains many specific risk factors as well [1–3]. However, among pipeline risk factors, the influences of these factors on pipelines risk can be primary or secondary, so how to determine the weight of each factor has been of widespread concern, and the method plays an important role in formulating targeted safety protection measures for the pipeline's company.

Currently, the commonly used methods for determining the weights of pipeline risk factors are: the AHP, the expert evaluation method, and others. While these methods have played an important role in engineering practice, however, these methods are either too subjective, or too complex, and, in practical application, they also have certain limitations. For example, the traditional AHP method, which has nine scales and is the most commonly used method in actual application. It is a system analysis method which combines qualitative analysis and quantitative calculation, which is specially suitable for index weight determination of multi-level and multi-structuring, and which can make the complicated problem hierarchical, qualitative, and quantified [7–9]. However, for the nine-scale method, there are many evaluation indexes which makes the scale workload too great and easily produces antipathy and poor decisions even among experts. Meanwhile, the concept of scale is fuzzy, and, when actually applied, its defects include significant subjectivity, confused participants, so that it is difficult to reach accurate judgments as well.

To solve the above problems, the improved three- scale AHP method is introduced to determine the risk index weight of pipelines, which has the advantages of being concise and practical, having a small workload, strong pertinence, and easily compares the significance of factors. All this makes it more a more accurate and objective way to determine the indexes weights as it also conforms better to the actual situation.

## **2 Improved AHP Method to Determine Indexes' Weights**

To apply the improved three-scale method to determine indexes' weights, follow the specific steps as described next.

### 2.1 Construct Judgment Matrix A

According to the scale theory, three-scale comparative judgment matrix is constructed as follows, which is named

$$A = \begin{bmatrix} a_{11} & a_{12} & \cdots & a_{1n} \\ a_{21} & a_{22} & \cdots & a_{2n} \\ \vdots & \vdots & \vdots & \vdots \\ a_{n1} & a_{n2} & \cdots & a_{nn} \end{bmatrix} \tag{1}$$

and

$$a_{ij} = \begin{cases} 1, & \text{which represents } i \text{ is more important than } j \\ 0, & \text{which represents } i \text{ is equally important than } j \\ -1, & \text{which represents } i \text{ is less important than } j \end{cases} \tag{2}$$

### 2.2 Construct the Optimal Transfer Matrix D of Matrix A

The optimal transfer matrix  $D$  can be expressed as

$$D = \begin{bmatrix} d_{11} & d_{12} & \cdots & d_{1n} \\ d_{21} & d_{22} & \cdots & d_{2n} \\ \vdots & \vdots & \vdots & \vdots \\ d_{n1} & d_{n2} & \cdots & d_{nn} \end{bmatrix} \tag{3}$$

and  $d_{ij} = \sum_{k=1}^n (a_{ik} + a_{kj})$ , transform the optimal transfer matrix  $D$  into judgment matrix  $E$ .

$$E = \begin{bmatrix} e_{11} & e_{12} & \cdots & e_{1n} \\ e_{21} & e_{22} & \cdots & e_{2n} \\ \vdots & \vdots & \vdots & \vdots \\ e_{n1} & e_{n2} & \cdots & e_{nn} \end{bmatrix} \tag{4}$$

and  $e_{ik} = \exp(d_{ik})$ , the transformed matrix  $E$  has good consistency.



### 2.3 Calculate the Indexes' Weights

The product root method was applied to solve the index weight, namely

$$w_i = \frac{(\prod_{k=1}^n e_{ik})^{1/n}}{\sum_{k=1}^n (\prod_{k=1}^n e_{ik})^{1/n}} \tag{5}$$

## 3 Determine Weights of Pipeline Risk Factors

### 3.1 Pipeline Risk Evaluation Index System

While there are many risk factors underlying oil and gas pipeline accidents, generally speaking, they can be attributed to the third party damage, corrosion, design, and maloperation, which itself contains many specific risk factors as well, such as the least buried depth of pipeline, ground operations, public education, outer coating of the pipeline, soil corrosivity [1–6], and others. See Fig. 1 for a comparative diagram that systematizes the importance degree of each index to establish three-level index system of oil and gas pipelines.

### 3.2 Determine Weights of Pipeline Risk Factors

#### 1. Two-level index judgment matrix and weight calculation

The references [1–6] contain supporting material on the pipeline risk assessment guideline, KENT scoring method, and relevant research findings on pipelines at home and abroad. Having asked expert for advice and considering the contribution rate of buried pipeline risk factors  $U_1, U_2, U_3, U_4$ , one can determine the judgment matrix  $A$ , the optimal transfer matrix  $R$ , and consistency matrix  $D$  as follows.

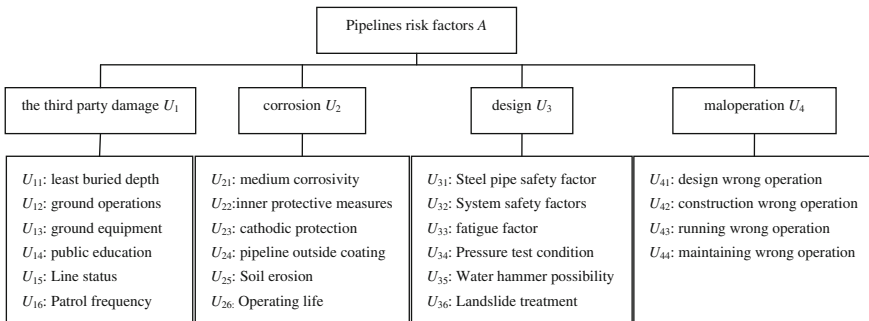


Fig. 1 Index system of the evaluation for pipeline risks

$$A = \begin{bmatrix} 0 & 1 & 1 & 1 \\ -1 & 0 & 1 & 1 \\ -1 & -1 & 0 & -1 \\ -1 & -1 & 1 & 0 \end{bmatrix};$$

$$R = \begin{bmatrix} 0 & 0.5 & 1.5 & 1 \\ -0.5 & 0 & 1 & 0.5 \\ -1.5 & -1 & 0 & -0.5 \\ -1 & -0.5 & 0.5 & 0 \end{bmatrix}$$

$$D = \begin{bmatrix} 1 & 1.65 & 4.48 & 2.72 \\ 0.61 & 1 & 2.72 & 1.65 \\ 0.22 & 0.37 & 1 & 0.61 \\ 0.37 & 0.61 & 1.65 & 1 \end{bmatrix}$$

According to formula (5), the two-level index weight values of pipelines risk factors are such,  $w = (0.455, 0.276, 0.102, 0.167)$

2. Weight calculation for third party damage

Similarly, comparing the contribution rate of each index and ascertaining the comparison matrix to determine each index weight of the third party damage,  $A_{U_1}, R_{U_1}, D_{U_1}$  are as follows.

$$A_{U_1} = \begin{bmatrix} 0 & 0 & 1 & -1 & 1 & 1 \\ 0 & 0 & 1 & -1 & 1 & 1 \\ -1 & -1 & 0 & -1 & 1 & -1 \\ 1 & 1 & 1 & 0 & 1 & 1 \\ -1 & -1 & -1 & -1 & -1 & 0 \\ -1 & -1 & 1 & -1 & 1 & 0 \end{bmatrix};$$

$$R_{U_1} = \begin{bmatrix} 0 & 0 & \frac{5}{6} & -\frac{1}{2} & \frac{7}{6} & \frac{1}{2} \\ 0 & 0 & \frac{5}{6} & -\frac{1}{2} & \frac{7}{6} & \frac{1}{2} \\ -\frac{5}{6} & -\frac{5}{6} & 0 & -\frac{4}{3} & \frac{1}{3} & -\frac{1}{3} \\ \frac{1}{2} & \frac{1}{2} & \frac{4}{3} & 0 & \frac{5}{3} & 1 \\ -\frac{7}{6} & -\frac{7}{6} & -\frac{1}{3} & -\frac{5}{3} & 0 & -\frac{2}{3} \\ -\frac{1}{2} & -\frac{1}{2} & \frac{1}{3} & -1 & \frac{2}{3} & 0 \end{bmatrix}$$

$$D_{U_1} = \begin{bmatrix} 1.00 & 1.00 & 2.30 & 0.61 & 3.21 & 1.65 \\ 1.00 & 1.00 & 2.30 & 0.61 & 3.21 & 1.65 \\ 0.43 & 0.43 & 1.00 & 0.26 & 1.40 & 0.72 \\ 0.65 & 0.65 & 3.79 & 1.00 & 5.29 & 2.72 \\ 0.31 & 0.31 & 0.72 & 0.19 & 1.00 & 0.51 \\ 0.61 & 0.61 & 1.40 & 0.37 & 1.95 & 1.00 \end{bmatrix}$$

According to formula (5), the two-level index weight values of third party damage are such,  $W_{U_1} = (0.200, 0.200, 0.087, 0.330, 0.062, 0.121)$

### 3. Weight calculation of corrosion

Similarly, comparing the contribution rate of each index, and ascertaining the comparison matrix to determine each index weight of corrosion,  $A_{U_2}, R_{U_2}, D_{U_2}$  are as follows.

$$\begin{aligned}
 A_{U_2} &= \begin{bmatrix} 0 & 0 & -1 & -1 & 1 & 1 \\ 0 & 0 & -1 & -1 & 1 & 1 \\ 1 & 1 & 0 & -1 & 1 & 1 \\ 1 & 1 & 1 & 0 & 1 & 1 \\ -1 & -1 & -1 & -1 & 0 & 1 \\ -1 & -1 & -1 & -1 & -1 & 0 \end{bmatrix}; \\
 R_{U_2} &= \begin{bmatrix} 0 & 0 & -\frac{1}{2} & -\frac{5}{6} & \frac{1}{2} & \frac{5}{6} \\ 0 & 0 & -\frac{1}{2} & -\frac{5}{6} & \frac{1}{2} & \frac{5}{6} \\ \frac{1}{2} & \frac{1}{2} & 0 & -\frac{1}{3} & 1 & \frac{4}{3} \\ \frac{5}{6} & \frac{5}{6} & \frac{1}{3} & 0 & \frac{4}{3} & \frac{5}{3} \\ -\frac{1}{2} & -\frac{1}{2} & -1 & -\frac{4}{3} & 0 & \frac{1}{3} \\ -\frac{5}{6} & -\frac{5}{6} & -\frac{4}{3} & -\frac{5}{3} & -\frac{1}{3} & 0 \end{bmatrix} \\
 D_{U_2} &= \begin{bmatrix} 1.00 & 1.00 & 0.61 & 0.43 & 1.65 & 2.30 \\ 1.00 & 1.00 & 0.61 & 0.43 & 1.65 & 2.30 \\ 1.65 & 1.65 & 1.00 & 0.72 & 2.72 & 3.79 \\ 2.30 & 2.30 & 1.40 & 1.00 & 3.79 & 5.29 \\ 0.61 & 0.61 & 0.37 & 0.26 & 1.00 & 1.40 \\ 0.43 & 0.43 & 0.26 & 0.19 & 1.72 & 1.00 \end{bmatrix}
 \end{aligned}$$

According to formula (5), the two-level index weight values of corrosion are such,  $W_{U_2} = (0.143, 0.143, 0.236, 0.329, 0.087, 0.062)$

### 4. Three-level index judgment matrix and weight calculation for design

Similarly, comparing contribution rate of each index and ascertaining the comparison matrix to determine each index weight of design,  $A_{U_3}, R_{U_3}, D_{U_3}$  are as follows.

$$\begin{aligned}
 A_{U_3} &= \begin{bmatrix} 0 & 1 & 1 & 0 & 1 & 1 \\ -1 & 0 & 1 & -1 & 1 & 1 \\ -1 & -1 & 0 & -1 & 1 & 1 \\ 0 & 1 & 1 & 0 & 1 & 1 \\ -1 & -1 & -1 & -1 & 0 & 1 \\ -1 & -1 & -1 & -1 & -1 & 0 \end{bmatrix}; \\
 R_{U_3} &= \begin{bmatrix} 0 & \frac{1}{2} & \frac{5}{6} & 0 & \frac{7}{6} & \frac{3}{2} \\ -\frac{1}{2} & 0 & \frac{1}{3} & -\frac{1}{2} & \frac{2}{3} & 1 \\ -\frac{5}{6} & -\frac{1}{3} & 0 & -\frac{5}{6} & \frac{1}{3} & \frac{2}{3} \\ 0 & \frac{1}{2} & \frac{5}{6} & 0 & \frac{7}{6} & \frac{3}{2} \\ -\frac{7}{6} & -\frac{2}{3} & -\frac{1}{3} & -\frac{7}{6} & 0 & \frac{1}{3} \\ -\frac{3}{2} & -1 & -\frac{2}{3} & -\frac{3}{2} & -\frac{1}{3} & 0 \end{bmatrix} \\
 D_{U_3} &= \begin{bmatrix} 1.00 & 1.65 & 2.30 & 1.00 & 3.21 & 4.48 \\ 0.61 & 1.00 & 1.40 & 0.61 & 1.95 & 2.72 \\ 0.43 & 0.72 & 1.00 & 0.43 & 1.40 & 1.95 \\ 1.00 & 1.65 & 2.30 & 1.00 & 3.21 & 4.48 \\ 0.31 & 0.51 & 0.72 & 0.31 & 1.00 & 1.40 \\ 0.22 & 0.37 & 0.51 & 0.22 & 0.72 & 1.00 \end{bmatrix}
 \end{aligned}$$

According to formula (5), the two-level index weight values of design are such,  $W_{U_3} = (0.280, 0.170, 0.122, 0.280, 0.087, 0.062)$

5. Three-level index judgment matrix and weight calculation for maloperation

Similarly, comparing contribution rate of each index and ascertaining the comparison matrix to determine each index weight of maloperation,  $A_{U_4}, R_{U_4}, D_{U_4}$  are as follows.

$$\begin{aligned}
 A_{U_4} &= \begin{bmatrix} 0 & 1 & -1 & 1 \\ -1 & 0 & -1 & 1 \\ 1 & 1 & 0 & 1 \\ -1 & -1 & -1 & 0 \end{bmatrix}; \\
 R_{U_4} &= \begin{bmatrix} 0 & 0.5 & -0.5 & 1 \\ -0.5 & 0 & -1 & 0.5 \\ 0.5 & 1 & 0 & 1.5 \\ -1 & -0.5 & -1.5 & 0 \end{bmatrix} \\
 D_{U_4} &= \begin{bmatrix} 1.00 & 1.65 & 0.61 & 2.72 \\ 0.61 & 1.00 & 0.37 & 1.65 \\ 1.65 & 2.72 & 1.00 & 4.48 \\ 0.37 & 0.61 & 0.22 & 1.00 \end{bmatrix}
 \end{aligned}$$

**Table 1** Weight values of pipeline risk factors

Two-level index	$U_1$						$U_2$					
Three-level index	$U_{11}$	$U_{12}$	$U_{13}$	$U_{14}$	$U_{15}$	$U_{16}$	$U_{21}$	$U_{22}$	$U_{23}$	$U_{24}$	$U_{25}$	$U_{26}$
Weight	0.091	0.091	0.040	0.150	0.028	0.055	0.039	0.039	0.065	0.091	0.024	0.017
Two-level index	$U_3$						$U_4$					
Three-level index	$U_{31}$	$U_{32}$	$U_{33}$	$U_{34}$	$U_{35}$	$U_{36}$	$U_{41}$	$U_{42}$	$U_{43}$	$U_{44}$		
Weight	0.028	0.017	0.012	0.028	0.009	0.006	0.046	0.028	0.076	0.017		

According to formula (5), the two-level index weight values of maloperation are such,  $W_{U_4} = (0.276, 0.167, 0.455, 0.102)$

4. Weight values of pipeline risk factors

According to the above calculation, the weight values of each three-level index can be obtained and the results enumerated in Table 1.

From Table 1, we can see that, of all risk factors of pipelines, public education is the most important factor, and the least buried depth, ground operations, pipeline outside coating are the second most important factors. Also, maloperation, cathodic protection, patrol frequency, poor operating design, ground equipment, medium corrosivity, inner protective measures, steel pipe safety factor, pressure test condition, line status and poor construction procedure play an important role successively, in decreasing importance, while other factors have even less effect.

The results can be used for formulating targeted protective measures and for strengthening risk management as well, which has major significance.

## 4 Conclusions

1. The improved three-scale AHP method has the advantages of a clear concept, simple scale, small workload, and avoidance of the shortcomings of the nine-scale method, which generates vagueness, and confusion, and is also strongly subjective in application. The improved AHP is used to determine weight indexes for oil and gas pipelines, with results that are more accurate and objective.
2. The results of the improved AHP method can provide the theoretical foundation for formulating targeted protective measures and strengthening risk management as well, which has major significance.

## References

1. Yu L (2014) A method for long-distance oil and gas transmission pipeline route selection based on potential loss of life. *China Safety Sci J* 24(02):71–76
2. Zhang S (2012) Accident risk analysis and route selection method of long-distance oil and gas transportation pipeline. China University of Mining and Technology (Beijing), Beijing
3. Zhang S, Wu Z (2014) Risk-based optimization method for long-distance oil and gas transmission pipeline route. *Acta Petrolei Sinica* 35(03):570–576
4. Huang L, Yao A, Xian T et al (2014) Research on risk assessment method of oil & gas pipeline with consideration of vulnerability. *China Safety Sci J* 24(07):93–99
5. Wang K, Wang X, Chu A et al (2010) Study on the risk assessment technology of oil and gas pipeline. *Liaoning Chem Ind* 39(01):35–42
6. Q/SY 1180.3-2009 Pipeline integrity management specification, part 3: Guideline of pipeline risk assessment
7. Liu C (2007) Evaluation technology of corrosion protection for buried steel pipeline. Beijing University of Technology, Beijing
8. Zhan J (2005) The research on scale in AHP. Guangxi University, Guangxi
9. Wu D, Li D (2004) Shortcomings of analytical hierarchy process and the path to improve the method. *J Beijing Normal Univ (Natural Science)* 40(02):264–268

# Optimization for the Structure of Front Transmission Gearbox

Zhenqi Yu

**Abstract** By applying finite element method and static analysis, the front transmission gearbox model of a tracked vehicle is simplified and the boundary conditions treatment and finite element mesh generation techniques were used to ensure the correctness of the analysis. Then, based on the analysis and computation, the displacement and stress distribution of the gearbox are calculated. Then, dynamic modal analysis is conducted for the gearbox to obtain the natural frequencies of various orders and the corresponding vibration modes in constraint mode, which provided basis for subsequent structure optimization. According to the results of finite element computation, the strength and the stiffness of each part of the gearbox are analyzed and the weak link is obtained. After extending the design space, the structure is redesigned through topology optimization to improve the strength and stiffness.

**Keywords** Finite element method · Gearbox case · Free modal analysis · Topology optimization

## 1 Introduction

Front transmission gearbox, as an important component of transmission system, bears large load, deforms significantly, and produces great stress in the gear transmission. Owing to the complex stress and shape of the gearbox, cracks are likely to occur in the whole gearbox and local regions due to insufficient static compressive strength [1]. In the paper, the front transmission gearbox of a tracked vehicle was studied using large finite element software ABAQUS. To reduce the weight and improve the stiffness and strength of the gearbox, topology optimization design was performed for the original gearbox structure by adopting structural

---

Z. Yu (✉)

School of Mechanical and Vehicular Engineering, Beijing Institute of Technology, Beijing 100081, China  
e-mail: xy6203\_yzq@sina.com

© Springer-Verlag Berlin Heidelberg 2016

B. Huang and Y. Yao (eds.), *Proceedings of the 5th International Conference on Electrical Engineering and Automatic Control*, Lecture Notes in Electrical Engineering 367, DOI 10.1007/978-3-662-48768-6\_79

709

optimization technique. The method provides feasible approach for the optimization design of complex structural parts with multiple loads, thus presenting great theoretical and practical significance.

Great progress with remarkable achievements has been made in China and other countries concerning the statics and dynamic analysis of gearbox. By using NASTRAN software, Lianjin et al. [2] calculated the natural frequency of two-stage cylindrical gear reducer. Takatsu et al. [3] analyzed the transfer function of single-speed gearbox through structural synthesis method and obtained the dynamic characteristics of gearbox. For single-speed gearbox, Zeguang et al. [4] performed modal analysis for the gear system using finite element method and acquired the vibration modes of various orders of the whole gearbox. Chengyun and Tengjiao [5] established a finite element-based static–dynamic computation model for the gearbox of reducer with center transmission.

As structural optimization has been widely applied in engineering field, the optimization design of gearbox structure has also been studied. By employing an impact rammer case as the research object, Wei et al. [6] analyzed the status of design of gearbox structure in China and put forth an optimization design method for impact rammer case. By utilizing the optimization design module and the parametric programming language APDL of Ansys, Zhao Lijuan and Liu Hongmei designed the optimal structure of the box body [7]. Yang [8] reduced the weight of the comprehensive transmission gearbox of tracked vehicle by using HyperWorks software.

## 2 Basis Principle of Topology Optimization

On the basis of OptiStruct, interpolation model with variable density is used. Thereby, the design variable is the relative material distribution of discrete element. The objective function and constraint conditions are associated with the type of optimization. So, various objective functions and constraint conditions can be selected according to different optimization objectives.

In the precondition that the strength and stiffness of the structure are not changed, lightest structure is sought by using the topology optimization model. The design variable is still the relative density of the elements.

The objective function in the following formula is the minimum weight, while the constraint conditions are stress constraint and displacement constraint, or other constraints such as the frequency of the structure.

$$\begin{cases} \text{design variable } x = (x_1, \dots, x_n)^T \\ \text{objective function } \min W = \sum_{e=1}^n x_e v_e \\ \text{constraint conditions} \end{cases} \quad (1)$$



After building the mathematical model of the structure, the model needs to be solved through optimization algorithms. There are three optimize methods in OptiStruct, namely optimality criteria method, duality method, and feasible direction method.

### 3 Construction of Finite Element Model

#### 3.1 Mesh Convergence and Actual Mesh Generation

The computation accuracy of finite element software is closely related to the mesh generation: the higher, the accuracy of mesh generation. However, the more the meshes, the higher the requirement of computation for hardware is, and the longer the computation takes. As nonlinear computation takes long time for contact model, the approach for selecting suitable mesh accuracy is significant for ensuring computation accuracy and saving computation resource. So, mesh convergence analysis needs to be conducted for the model.

In the research, the mesh amount was changed through single-factor experiments and optimal element size is obtained for mesh generation by comparing the results acquired with different mesh amounts. So, secondary tetrahedral element (C3D10) was applied with constant load and boundary conditions. The size of driver element was set to be 30, 24, 20, and 14 mm, respectively.

The comparison of data in Table 1 indicates that favorable accuracy of simulation computation can be obtained when the element size is 20 mm. Considering computation accuracy and efficiency at the same time, the elements of the whole model are set to 20 mm.

#### 3.2 Mesh Generation Loading of Boundary Conditions

Through mesh convergence analysis, tetrahedral four-node quadratic elements (C3D10) of 20 mm were applied for mesh generation of the front transmission gearbox model, as illustrated in Fig. 1. There are total 384,509 of the elements.

**Table 1** Calculation results of mesh convergence

Element size/mm	Mises/Mpa
30	26.3545
24	26.3544
20	25.3543
14	25.3543

**Fig. 1** Mesh generation and finite element model for the new front transmission case



### 3.3 Loading of Boundary Conditions

Cast iron was used as the material of the gearbox case in the simulation experiments. The basic parameters are given in Table 2.

The joint surfaces of different parts in the finite element model of combination solid are difficult to be processed. Based on previous experience, binding constraints are utilized to simulate the contact state of two joining parts.

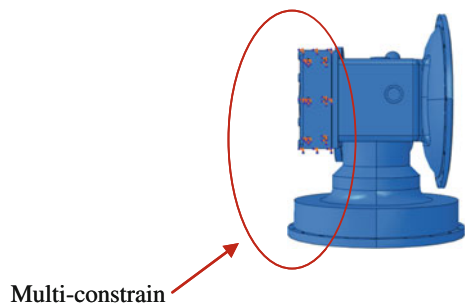
The bearing location of displacement boundary condition is demonstrated in Fig. 2. Multi-constrain is exerted on the bottom of the gearbox.

To exert load boundary condition to the bearing hole, two uniformly distributed loads in axial and tangential directions are acted in the area within 120° of radial

**Table 2** Parameters of material characteristics

E/GPa	$\rho$ (kg/m <sup>3</sup> )	$\mu$
120	$7 \times 103$	0.30

**Fig. 2** Displacement boundary condition of the new model of front transmission gearbox



direction and an impulsive cosine load of 120° in radial direction. The impulsive cosine load is calculated using

$$q_{x\theta} = \frac{Q}{4RL} \cos\left(\frac{3}{2}\theta\right) \tag{2}$$

where  $Q$  is the radial resultant force and  $R$  is the axis radius.

### 4 Postprocessing and Results Analysis

Finite element model was built and then the material characteristics are input. After loading boundary conditions, finite element computation is performed for the gearbox. The cloud pictures of equivalent von Mises stress and displacement of the whole gearbox and different parts of the gearbox were obtained, as shown in Fig. 3.

Table 3 shows the location and value of the maximum equivalent Mises stress of the front transmission gearbox model. The maximum equivalent Mises stress (588 Mpa) is found on the bottom of the gearbox. The maximum equivalent Mises stresses of different parts of the model are within the yield strength of the material, while there is also probability of fatigue failure for some parts.

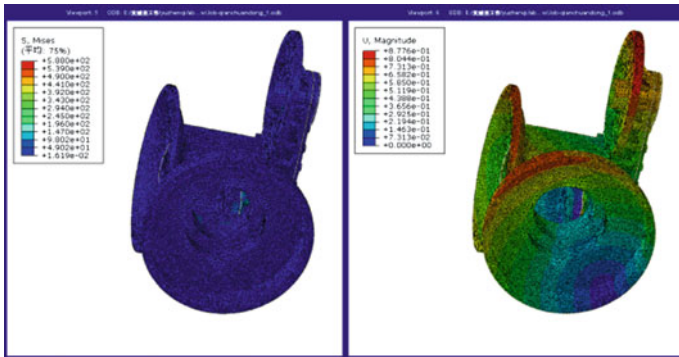


**Fig. 3** Cloud pictures of equivalent von Mises stress and displacement of the whole front transmission gearbox

**Table 3** Locations and values of maximum equivalent Mises stresses of different parts of the gearbox model

Part	Value of maximum equivalent Mises stress/Mpa	Location of maximum equivalent Mises stress
Whole front transmission system	588	Same location bottom of the gearbox
End cover	76.71	Bottom edge of the end cover
Counter shaft	406.4	Edge of the contact position of counter shaft and gearbox

**Table 4** 7–20 orders of free modals and their natural frequencies (Hz)

Order	Natural frequency/Hz
7	401.645
8	417.8415
9	457.225
10	513.3018
11	588.9016
12	613.7741
13	637.8201
14	644.2532
15	681.417

#### 4.1 Results of Free Modal Analysis of the Gearbox

Practice has proved that by analyzing the modal of gearbox, the structural stiffness and natural mode of vibration can be learned in the initial design, corresponding design defects can be avoided, and the design can be modified and optimized in time. In the research, the natural frequencies and corresponding vibration modes of the first 15 orders of the gearbox were calculated. Among which, there were 6 orders of rigid modals and 14 orders of non-rigid ones. The first 6 orders were not considered as their natural frequencies of the rigid modals are zero, and the natural frequencies of the 14 orders of non-rigid modals are listed in Table 4.

## 5 Topology Optimization and Comparison of the Gearbox Structure

The end covers in the left and the right of the transmission gearbox and the front end cover are commonly 10–15 mm in thickness and the gearbox shows simple structure. So topology optimization is conducted for the upper and lower cases according to the following scheme:

1. Design variable. Multiple locations including the stiffeners of the upper and lower cases, the external edges of the bearing seats in the left and the right ends of the case, the boss in the connecting position of the hydraulic motor, etc., are adopted as the optimization design space in the scheme. The topology density of the elements in the design space is utilized as the design variable.
2. Constraint conditions. According to the results of static finite element analysis, the displacements of several points with large displacement in the analysis are applied as the constraints. In addition, the upper limits of the maximum displacements of these points are considered as the constraint conditions of scheme 1, as illustrated in Table 5.

**Table 5** Constraint conditions

Constraint	Node id	Upper limit of displacement/mm
Disp1	628722	0.525
Disp2	640254	0.510
Disp3	640351	0.480

- Objective function. The research is to reduce the weight of the structure in the precondition of maintaining the original strength and stiffness of the gearbox. So, mass minimization is set as the objective function.
- Optimization result. Final optimization result is obtained through four times of iteration.
- Comparison analysis. Constraint modal analysis is conducted for the optimized gearbox model with same constraint conditions of the original finite element model. The left end cover and deputy case are fixed to restraint 6 degrees of freedom. The natural frequencies obtained in the modal analysis of the optimized gearbox model and the original one are compared in Table 6, and the comparison of maximum equivalent Mises stresses acquired in the stiffness analysis of the optimized gearbox model and the original one is shown in Table 7.

**Table 6** Optimization results

Order	Natural frequency/Hz	
	Original design	Optimal design
7	401.645	479.645
8	417.8415	426.855
9	457.225	465.28
10	513.3018	536.7380
11	588.9016	595.6934
12	613.7741	621.534
13	637.8201	648.9031
14	644.2532	654.532
15	681.417	685.331

**Table 7** maximum equivalent Mises stresses

Part	Value of maximum equivalent Mises stress/Mpa		Location of maximum equivalent Mises stress
	Original	Optimal	
Whole front transmission system	588	581	Bottom of the gearbox
End cover	76.71	75.65	Bottom edge of the end cover
Counter shaft	406.4	405.3	Edge of the contact position of counter shaft and gearbox

## 6 Conclusion

By using finite element software, a three-dimensional finite element model was constructed for the gearbox to analyze the load and the structural characteristics and perform equivalent processing. Cloud pictures of equivalent displacement and equivalent von Mises stress are obtained through finite element computation, so as to acquire the distribution and value of displacement and stress and find the weak links of the original design. The method provides basis for the modification of the structure of transmission gearbox of tracked vehicle. According to the optimization results, the gearbox is reconstructed and thereby the topological structure of the new gearbox was obtained. Afterward, static and free modal analysis was carried out for the new gearbox model. The comparison showed that the weights of the original and optimized gearbox were 385.1 and 373.3 kg; the later was 11.8 kg less than the former. The comprehensive stress of the optimized gearbox reduced by 6–10 MPa while the strength increased significantly comparing with those of the original one. Moreover, the stress distribution of the optimized gearbox, which was consistent with the actual loading situation, differed slightly with that of the original one. Furthermore, the natural frequencies of each order of the free modal of the optimized gearbox and the original one were basically the same, which indicated that the change of topological structure of the gearbox in the optimization did not influence the dynamic characteristics of the gearbox in low orders of free modal.

## References

1. Yang F et al (2008) Analysis on structure strength of tanks' gear box based on virtual prototyping technology. *J Acad Armored Force Eng* (2)
2. Lianjin L, Weiping Z (1989) An approach to noise suppression of gear boxes. *J Northeast Univ Technol* 10(4)
3. Takatsu et al (1991) Analysis and experiment on the vibration transmission in a single stage gearbox. In: *JSME international conference on motion and power transmission*, vol 10, pp 104–109
4. Zeguang T, Runfang L, Tengjiao L (2000) Finite element modal analysis for gear system. *Mech Des Res* (3)
5. Chengyun Y, Tengjiao L (2001) Finite element analysis and structural optimization for gearbox with central transmission. *Heavy Mach* (2)
6. Wei W, Xianyi M, Liantong D (2008) Research on the structural optimization design for vibration-impact rammer case. *J Beijing Univ Civil Eng Archit* 24(4):55–60
7. Lijuan Z, Hongmei L (2007) Optimal design of case of reducer in mine field based on ANSYS. *J Mech Transm* 31(4):49–57
8. Yang Y (2007) Structural topology optimization of integrated transmission gearbox. Beijing Institute of Technology, Beijing

# Study on the Hydrostatic Slide Film Temperature Field and Bearing Capacity of Precision Grinding Machine

ChuanShe Guo and Yi Cui

**Abstract** In order to improve the machining precision of precision surface grinding machine, the static performance and thermal performance of the machine hydrostatic guide are analyzed, and the static characteristics and temperature distribution of the oil pad under an inlet oil pressure of 2.8–3.4 MPa and an oil film thickness of 38–44  $\mu\text{m}$  were researched. The simulation results show that the initial temperature of the oil chamber area is 20 °C, and the temperature gradually decreases from the inlet. When the oil film thickness is 40  $\mu\text{m}$ , the inlet oil pressure increases from 2.8 to 3.4 MPa; accordingly, the each pair of oil film bearing capacities increases from 7510 to 8240 N. The research results can provide the basis for the optimization design of guide.

**Keywords** Precision grinding machine · Hydrostatic slide · Temperature field · Bearing capacity

## 1 Introduction

For the material that has the characteristics of high hardness and brittle, precision machine tool is the best way to achieve smooth surface [1–3]. Guide as one of the key components of precision machine tool, its precision has a large influence on the accuracy of machine tool. The hydrostatic slide has many good performances, such as small friction coefficient, long service life, good precision retention, and not crawling at a low speed, and it is widely applied to precision machine tool.

The oil film temperature of hydrostatic slide has an influence on the precision of the slide. It will make the guide heat and produce thermal deformation which is

---

C. Guo (✉) · Y. Cui (✉)  
School of Mechanical Engineering, University of Shanghai  
for Science & Technology, 200093 Shanghai, China  
e-mail: gcs819@163.com

Y. Cui  
e-mail: cuiyi@usst.edu.cn

extremely unfavorable to the machining precision of precision machine tool. So the oil film temperature should be reasonably controlled. The oil film thickness and inlet oil pressure of the liquid hydrostatic guide are the important parameters that affect the oil film temperature and static characteristic; thereby, it can affect the guide accuracy and reduce the machine tool performance. Many scientists have carried out research in this area. Harigaya used the unsteady state thermal hydrodynamic lubrication theory to analyze the influence of the lubricating oil viscosity on the oil film thickness and oil film thickness on the diesel engine piston ring [4]. Xia studied the effect of oil film thickness on the temperature field to hydrostatic thrust bearing of aspheric precision machine tool as the object [5]. Jiang Yun thought that oil film of hydrostatic guide heating is the main heat source when compared with the heating of motor, and he calculated the effect of oil film heat on guide precision [6]. Jeon and Kim analyzed the hydrostatic slide between oil films and obtained the overall structural deformation and oil film properties in change of hydrostatic slide [7]. Eiji Shamoto created a new model and proposed a new algorithm to improve the precision of motion errors of hydrostatic guide, and the relationship between the film reaction and the rail contour error is discussed through finite element analysis method, which is represented by transfer function [8].

From the above introduction, the current research on oil film is mainly about hydrostatic thrust bearings and small stroke guide. But there are only a few investigations in large stroke and linear guide oil film temperature field. The hydrostatic slide oil film of high-precision surface grinding machine is taken as the research object in this paper, combining the finite element numerical simulation with experiment; the influence of oil film thickness on the temperature field and the static characteristic is studied.

## 2 Hydrostatic Slide Introduction

### 2.1 *Closed Hydrostatic Slide System*

Oil film stiffness and load capacity are the two most important performances of hydrostatic guides, mainly related to the oil film thickness of guide. The opposed oil pad is used in this study. Closed hydrostatic slide system is shown in Fig. 1, which consisted of opposed oil chamber, throttle, hydraulic pump, relief valve, crude filter, fine filter, and oil tank.

The hydrostatic guide restrictors of precision machine tool are capillary restrictor. The hydrostatic guide has 16 oil chambers, 6 pairs of horizontal oil chamber, and 2 pairs of side oil chamber, in which side oil chambers is served as a guide.

Oil pad is composed of seal oil, oil chamber, and oil inlet holes, as it is shown in Fig. 2.



**Fig. 1** Closed hydrostatic guide system diagram

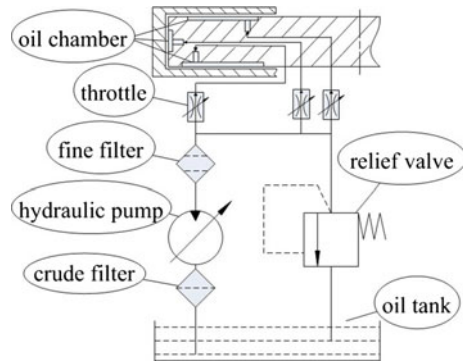
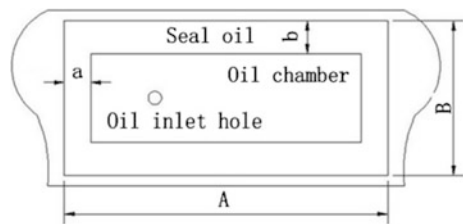


**Fig. 2** Oil pad schematic



## 2.2 Static Characteristic

Guide performance has important influence on machining accuracy of high-precision machine; it is necessary to ensure guide has good dynamic and static characteristics. The static performance includes rail stiffness and bearing capacity.

### 1. Effective bearing area of oil pad:

Effective bearing area of an oil chamber is the oil chamber with pressure  $P_r$ , evenly acts on this area, and it produces a total thrust that is equal to actual total thrust  $P$ , which is generated by the oil chamber and its surrounding sealing surface.

The oil pad of actual pressure distribution and imaginary equivalent stress distribution is shown in Figs. 3 and 4, respectively.

The effective bearing area of the oil chamber (dashed line range in Fig. 4) is as follows:

$$A_e = \frac{P}{p_r} = \frac{1}{6} [5A(B - b) - 4a(B - b)] \approx (A - a)(B - b) \quad (1)$$

where  $A$ ,  $B$ ,  $a$ , and  $b$  are shown in Fig. 2;  $P$  is the total thrust of an oil chamber and its surrounding sealing surface;  $p_r$  is the oil chamber pressure.

### 2. Bearing capacity is an external load that oil film can withstand under a certain film thickness. The oil pad and the surface of the supports must be separated by oil film. The carrying capacity of each pair of oil chambers is as follows:

**Fig. 3** Actual pressure distribution

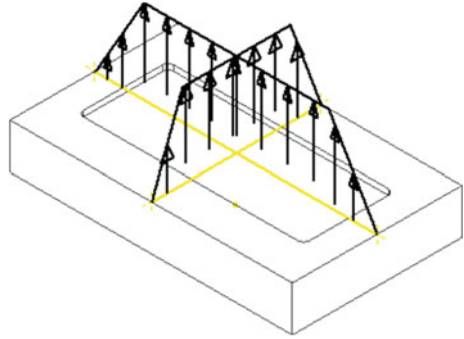
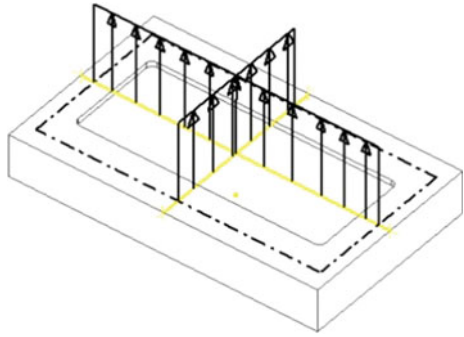


**Fig. 4** Imaginary equivalent stress distribution



$$W = p_1 A_{e1} - p_2 A_{e2} = \frac{\mu q}{h_1^3 B_1} A_{e1} - \frac{\mu q}{h_2^3 B_2} A_{e2} \tag{2}$$

where  $\bar{B}_i = \frac{1}{6} \left( \frac{A_i + a_i}{B_i - b_i} - \frac{B_i + b_i}{A_i - a_i} \right) i = 1, 2; h = h_1 + h_2$ .

where  $q$  is the oil pad flow;  $\bar{B}_i$  is the lower and upper oil pad flow coefficient;  $p_i$  is the lower and upper oil pad oil chamber pressure;  $h_1$  and  $h_2$  are the lower and upper oil pad oil film thickness, respectively;  $h$  is the oil film total thickness of each pair of oil pads; and  $\mu$  is the dynamic viscosity.

### 3 Numerical Simulation

#### 3.1 Establishment of Finite Element Model and Boundary Condition Setting

Because oil pad geometric shape is simple, its model can be built directly on the pretreatment of CFX. The three-dimensional model of oil pad on different film

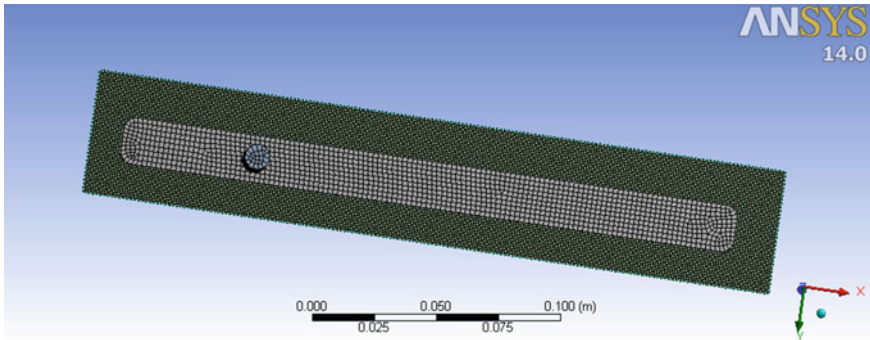


**Fig. 5** Finite element model of oil pad

thicknesses (19–22  $\mu\text{m}$ ) is established, and finite element meshing is performed, as shown in Fig. 5. The size of oil film is extremely small, and the hexahedral mesh is selected to improve the accuracy of calculation. In addition, considering the size of oil pad is much larger than that of the oil film thickness, the oil chamber and oil slick are separated to improve the accuracy of calculations while reduce the amount of calculation, and meshing is performed separately. The setting of oil film mesh size is smaller than that of the oil chamber.

The inlet pressure is arranged between 2.8 and 3.4 MPa, the initial temperature is set to 20  $^{\circ}\text{C}$ , and lubricating oil VG46 is applied; at the same time, due to the hydraulic oil return back to the tank, the outlet pressure is 0 Pa. Bearing surface is set to a fixed surface, and the condition between the fixed wall and the fluid is no-slip boundary; other surfaces are the default boundary condition. The convergence tolerance level is set to  $10^{-5}$ . The model is solved after setting the boundary conditions, and the results after iteration calculation are convergent.

### 3.2 *Temperature Field Distribution*

By calculating, the contours and distribution of hydrostatic guide internal fluid temperature field under different film thickness are obtained. When the oil film thickness is 19  $\mu\text{m}$ , temperature distribution as it is shown in Fig. 6.

As shown in Fig. 6, the initial temperature of the oil lumen area is 20  $^{\circ}\text{C}$ , and the temperature gradually decreases from the inlet. The highest temperature is 26.2 or 24.7 $^{\circ}\text{C}$  with a lubricant film thickness of 19  $\mu\text{m}$  or 22  $\mu\text{m}$ , respectively, and the smaller the oil film thickness is, the higher the temperature is. Figure 7 shows the relationship between the different film thickness and film temperature. It can be seen that the lower the temperature of oil film, the greater the film thickness.

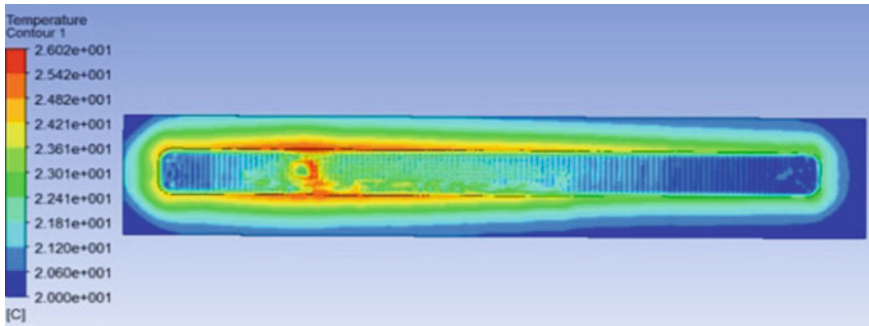
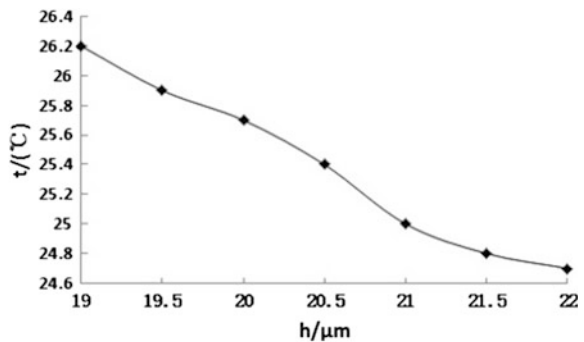


Fig. 6 Oil film temperature field contours

Fig. 7 Relationship of thickness and temperature of oil film



### 3.3 Static Characteristics of Guide Rails

By using the finite element model of the oil film, the oil film pressure is simulated. The pressure distribution on the film surface can be obtained when the inlet oil pressure is 3.2 MPa and the film thickness is 19 μm, as shown in Fig. 8. As shown in the figure, the pressure reduces within oil chamber to the surrounding area, and the maximum pressure is about 1.9 MPa. The bearing capacity  $F$  of underside oil film is obtained as 17,210 N by integrating the pressure on the entire area.

The relationship between the inlet oil pressure and oil film bearing capacity is studied in the paper. The relation curve about the bearing capacity and thickness of oil film at a different oil inlet pressure is shown in Fig. 9. It can be seen from the picture that at the same inlet oil pressure, the smaller the oil film thickness is, the greater the oil film bearing capacity is. Also, under the same oil film thickness, the higher the inlet oil pressure is, the larger the bearing capacity is. When the input pressure is 2.8 MPa, oil film thickness is 38, 41, and 44 μm corresponding to the  $F$  as 8050, 7340, and 6690 N. When the pressure increases to 3 MPa, the  $F$  increased to 6.8, 5.6, and 5.4% correspondingly. When the pressure increases to 3.4 MPa,  $F$  increased to 10.5, 8.9, and 7.8 %, respectively.

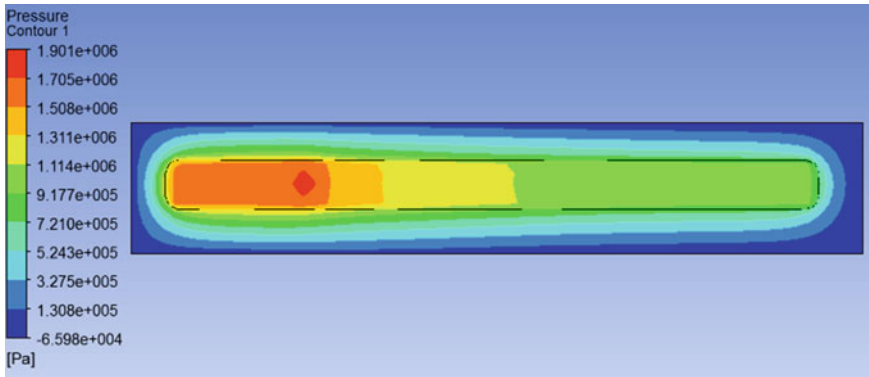
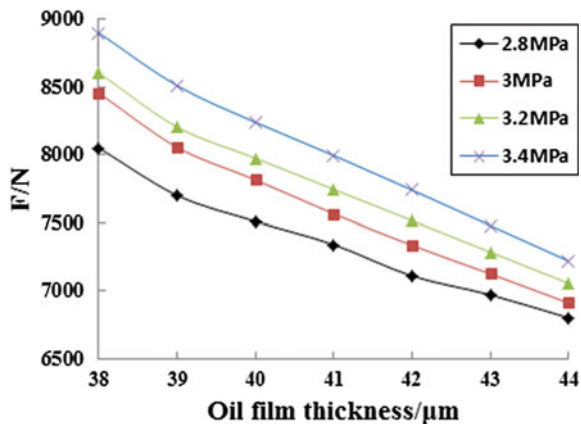


Fig. 8 Film surface pressure distribution

Fig. 9 The relationship between film thickness and bearing capacity under different pressures



### 4 Summary

By using the ANSYS CFX software, the simulation models of hydrostatic slide oil pad under different thickness are established, and then, the temperature fields and pressure fields can be obtained. The simulation results show the respective highest temperature is 26.2 or 24.7°C with a lubricant film thickness of 19 or 22  $\mu\text{m}$ , and the higher the oil film is, the thinner the temperature is. At the same inlet oil pressure, the smaller the oil film thickness is, the greater the oil film bearing capacity is. Under the same oil film thickness, the higher the inlet oil pressure is, the larger the bearing capacity is. When the oil film thickness is 40  $\mu\text{m}$ , the inlet oil pressure is increased from 2.8 to 3.4 MPa and the oil bearing capacity increased from 7510 to 8240 N accordingly. The research results can provide the basis for the optimization design of guide.

**Acknowledgements** The authors gratefully acknowledge the financial support provided by National Science and Technology Major Project of China (Grant No. 2011ZX04004-051).

## References

1. Luca A, Mario P (2006) Hydrostatic journal bearing with coaxial floating sleeve. *Mech Res Commun* 33(3):394–400
2. Luo SB, Zhang JM (2003) Precision machining equipment and technology of aspheric optics. *Opt Precis Eng* 11(1):75–78 (in Chinese)
3. Zhang XY (2004) Research on DHM-500 precision CNC non-spherical lens grinding machine. *Nanotechnol Precis Eng* 2(1):54–58 (in Chinese)
4. Harigaya Y, Suzuki M, Toda F et al (2006) Analysis of oil film thickness and heat transfer on a piston ring of a diesel. *Eng Gas Turbines Power* 128(3):685–693
5. Xia YM, Zhang GQ, Luo SB et al (2012) Temperature field distribution of non-spherical hydrostatic bearings for precision machine tools. *Opt Precis Eng* 20(8):1759–1764 (in Chinese)
6. Jiang Y, Hu GA, Sun T (2011) Thermal finite element analysis of hydrostatic guide. *Aviat Precis Manuf Technol* 47(5):23–25 (in Chinese)
7. Jeon SY, Kim KH (2004) A fluid film model for finite element analysis of structures with linear hydrostatic bearings. *Mech Eng Sci* 218:309–316
8. Shamoto E, Park C-H, Moriwaki T (2001) Analysis and improvement of motion accuracy of hydrostatic feed table. *CIRP Annals-Manuf Technol* 50:285–290

# Study on Fuzzy Classifier Based on Genetic Algorithm Optimization

Qian Gao and Nai-bao He

**Abstract** Most of the fuzzy classifiers are created by fuzzy rules based on transcendent knowledge or expert's knowledge. In mountains of the existing data, it is difficult to obtain transcendent knowledge and then more difficult to obtain fuzzy rules. To solve this problem, a new way for creating fuzzy classifier based on GA for a classification problem of quantitative attribute is proposed in this paper, which consists of a set of fuzzy rules generated according to the attribute of the classified objects, then choosing the optimal fuzzy rules subset forming the classifier by the genetic algorithm to reduce the number of rules and improve the classification accuracy. The result of data simulation was applied to the iris with better effects.

**Keywords** Fuzzy classifier · Genetic algorithm · Optimization · Pattern classification

## 1 Introduction

The use of fuzzy systems for pattern classification is an alternative to other traditional recognition techniques. A fuzzy classifier is capable of accounting uncertainties and as such has the potential of performing well for classification applications. The genetic algorithm has many successful applications in the data mining, but the most typical one is the classifier which is proposed by Holland based on the bucket algorithm [1–5]. In the understanding accuracy and speediness,

---

Q. Gao (✉)

School of Computer Engineering, Jiangsu University of Technology,  
Changzhou 213001, China  
e-mail: gaoqian@jsut.edu.cn

N. He

School of Electrical Engineering, Jiangsu University of Technology,  
Changzhou, China

© Springer-Verlag Berlin Heidelberg 2016

B. Huang and Y. Yao (eds.), *Proceedings of the 5th International Conference on Electrical Engineering and Automatic Control*, Lecture Notes in Electrical Engineering 367, DOI 10.1007/978-3-662-48768-6\_81

the classifier performs very well. Many people put forward the hybrid classifier by combining the genetic algorithm and the other machine-learning techniques after Holland. Usually in the classification problem, the genetic algorithm is used to extract and choose the important attribute and give up the secondary and extra attribute. For classification problems, the size of the attribute collection belonging to the classified objects will affect the secondary and extra attribute. For classification problems, because the size of the attribute collection belonging to the classified objects will affect the accuracy and the processing time of the classification, it will also affect the size of required sample set in constructing classifier [6–10]. Choosing the important attribute can improve the quality of the classification results. Avoiding the other secondary attributes may cause some unnecessary negative effects. But it is nearly impossible to construct the completely accurate classifier, where an important reason is that it is always unavoidable to contain the uncertainty and fuzziness in the data of the objects to be classified and the training sample data constructing the classifier are usually insufficient. In order to deal with this kind of the problem better, introducing fuzzy set theory in the classifier is naturally thought of, and that can achieve easier knowledge expression and better comprehension.

In this paper, a fuzzy classifier design using GAs is proposed that enables the extraction and optimization of all the necessary fuzzy classifier parameters from the training set. On the one hand, the combination of fuzzy set theory and genetic algorithm can be defined the new individual encoding way and the new genetic operators, and it can control the parameters of the evolutionary process; on the other hand, it can learn and adjust the parameters of the fuzzy set to improve the structure of the fuzzy rules and to improve the capability of the control systems. The Madanny-type fuzzy rule is decomposed into a set of fuzzy rules sets. In the each rule, the antecedent constituted only by a attribute and the consequent constituted by the belonging class, assigning some effectiveness factors for the rule according to the training sample data at the same time; then optimizing the rule sets constituted by fuzzy rules above with the genetic algorithm, to get a favorable classifier having less rules, involving less attributes and having better comprehensibility.

The rest of this paper is organized as follows. In Sect. 1, we briefly review basic concepts of fuzzy system structure. In Sect. 2, we present a method of knowledge acquisition. In Sect. 3, we propose optimizing the fuzzy rule set with the genetic algorithm. The conclusions are discussed in Sect. 4.

## 2 Fuzzy System Structure

Fuzzy set theory originally proposed by Zadeh provides a general way to cast knowledge about a process in the form of linguistic IF–THEN rules. Fuzzy logic is composed of fuzzy sets and fuzzy rules. For the classification problem of numerical attributes, first performing the normalization process to each attribute and defining 7 fuzzy rule subsets in the interval  $[0, 1]$  correspond to the language value positive



big (PB), positive middle (PM), positive small (PS), zero (O), negative small (NS), negative middle (NM), and negative big (NB). The each fuzzy subset is described with the triangular membership functions in Figs. 1 and 2. To be able to deal with the predefined class represented by a symbol, the class will be represented with the corresponding integer value. The membership function of  $e$  and  $ec$  is given as follows:

In this work, a type of fuzzy model known as Mamdani model is used. In this model, both fuzzy premise part and consequence part are represented in linguistic terms. A typical fuzzy rule used under this scheme has the following structure:

$$\text{IF } x_1 \text{ is } A_1 \text{ AND } x_2 \text{ is } A_2. \dots \text{AND } x_n \text{ is } A_n \text{ THEN } y \text{ is } B_j$$

where the input variable  $x_i$  and output variable  $y$  have fuzzy sets  $A_i$  and  $B_j$ , respectively.

If a fuzzy system has  $M$  rules, then the output  $\hat{y}$  is the sum of weighted rule consequences.

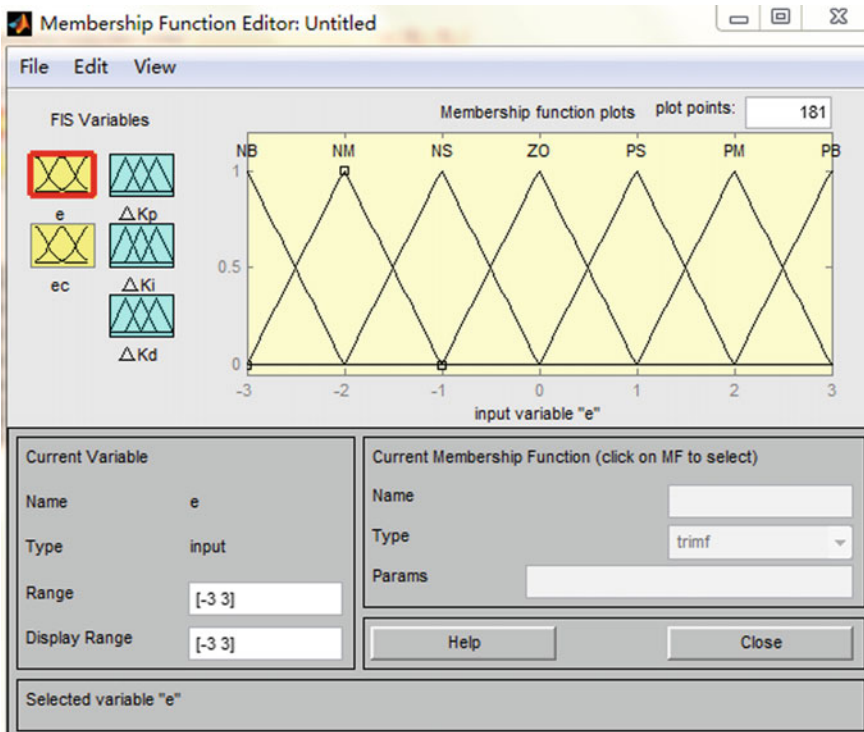


Fig. 1 The membership function of the parameter  $e$

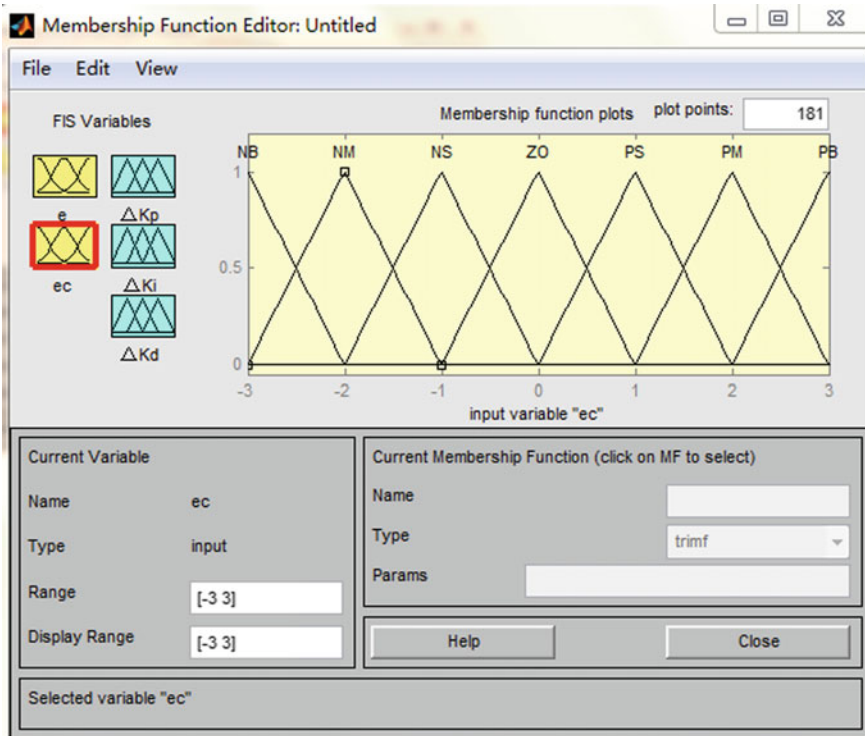


Fig. 2 The membership function of the parameter  $ec$

$$\hat{y} = \frac{\sum_{i=1}^M \sigma_i \alpha_i y_i}{\sum_{i=1}^M \sigma_i \alpha_i} \tag{1}$$

where  $\sigma_i$  is the weight of rule  $i$ ,  $\alpha_i$  is the firing strength of input pattern  $x$  on the premise of rule  $i$ ,  $y_i$  is the contribution of rule  $i$ , and  $M$  is the number of rules.

### 3 Knowledge Acquisition Method

The training sample is  $\mathbf{x}^m = (x_1^m, x_2^m, \dots, x_m^m)$  and the class is  $\mathbf{y}^m \in \{1, 2, \dots, W\}$ . The structure of fuzzy rules is as follows:

$$\text{Rule } R_{ij}^k : \text{if } x_i \text{ is } X_{ij} \text{ then class} = W \text{ with influence } \varpi_{ij}^w = \varphi_{ij}^w$$

where  $w = 1, 2, \dots, W$ ;  $W$  is the number of the predefined classes;  $j = 1, 2, \dots, 7$ , which have affected the definition of  $\varphi_{ij}^w$  as the following.

$$\varphi_{ij}^w = \frac{\sum_{m=1}^M \mu_{x_{ij}}(x_i^m) y^m}{\sum_{m=1}^M y^m} = \frac{1}{M} \sum_{m=1}^M \mu_{x_{ij}}(x_i^m) \tag{2}$$

where  $n$  represents the class determined by the attribute  $i$  and the language value  $j$  and there is the  $y^m = n$ , where  $M$  is the number of the records belonging to the class  $n$  in the training sample data set.

Above all, a data set with  $n$  attributes and  $w$  predefined classes can generate an initial rule set consisting of seven rules after the process above.

The class of a new object  $(x_1, x_2, \dots, x_n)$  is classified according to the following steps:

1. Examining each rule of the fuzzy rule sets generating from the section above, calculating the membership degree of the samples to be classified to its antecedent fuzzy subsets, and merging the impact factors of the fuzzy rule corresponding to the same class with the following formula:

$$\varpi_i^w = \frac{\sum_{m=1}^M \mu_{x_{ij}}(x_i) \varphi_{ij}^w}{\sum_{j=1}^7 \mu_{x_{ij}}(x_i)} \tag{3}$$

To each class,  $\varpi_i^w$  can be achieved by merging the above formula with the following formula:

$$\varpi^w = \min\{\varpi_i^w | i = 1, 2, \dots, n\} \tag{4}$$

2. Making  $\varpi^w$  taking the peaked  $w$ , that is the class the sample belonging to
3. Genetic operators.

Due to integer-encoding and use of the representation schemes discussed earlier, these operators are different from their counterparts used in general binary-encoded fuzzy approaches.

A genetic algorithm is a well-known method to optimize an objective function with linear or nonlinear constraints. It is a stochastic global search technique, in which the derivative evaluation of the error function is not required. There are four GA operators which is mutation, crossover, reproduction, and survival of the fittest. Due to integer-encoding and use of the representation schemes discussed earlier, these operators are different from their counterparts used in general binary-encoded fuzzy approaches.

The parameter setting of the genetic algorithm

```

begin
  initialize Q(0);
  t=0;
  while(t<T)do
    for K=1 to N do
      evaluate fitness of Q(t);
    end for
    for K=1 to N do
      select operation to Q(t);
    end for
    for K=1 to N/2 do
      crossover operation to Q(t);
    end for
    for K=1 to N do
      mutation operation to Q(t);
    end for
    for K=1 to N do
      Q(t+1)=Q(t);
    end for
    t=t+1;
  end while
end

```

where  $Q(t)$  is the population,  $N$  is the population size, and  $t$  is the times.

## 4 Optimizing the Fuzzy Rule Set with the Genetic Algorithm

Genetic fuzzy system involves learning and tuning process. It is difficult to distinguish between the two.

GA can be employed to generate fuzzy rules and adjust membership functions of fuzzy sets. There are many attributes describing the objects in the actual problems, and it is not appropriate to use the all the rules of the initial rule set achieved from above to a new object to be classified. The reasons are as follows:

1. Too many attributes inevitably causing larger initial fuzzy rule set, and that will add the unnecessary processing time in the classification.
2. If some attributes are secondary, then they will have lower impact factors and may cause the negative impacts to the classification.

So it is necessary to optimize the initial fuzzy rule set achieved above and choose the optimal or suboptimal fuzzy rule set. Using the genetic algorithm to choose the fuzzy rule set with higher classification accuracy and smaller fuzzy rule set is very important.

## 5 Conclusion

In this work, a classifier consisting of the fuzzy rules and optimizing the initial fuzzy rule set with the genetic algorithm to get the streamlined fuzzy rule set has proposed. The genetic rule-based learning from predefined rule base and adaptive evolutionary algorithm with simplistic binary coding scheme managed to exploit the potential of optimization with ease of understanding that facilitated the rules optimization for semi-expert judgment automation in software project management.

**Acknowledgements** This work is partially supported by JSUT Research Funding (Granted Numbers: KYY130017, KYY13001) and Innovation Team Funding (Granted Number: TDZD13003).

## References

1. Hsua CC, Choa HJ (2015) A genetic algorithm for the maximum edge-disjoint paths problem. *Neurocomputing* 148:17–26
2. Mousavi BS, Fazlollah S, Navid R (2014) Semantic image classification by genetic algorithm using optimised fuzzy system based on Zernike moments. *SIViP* 8:831–840
3. Trawinski KC, Quirin A (2012) A study on the use of multiobjective genetic algorithms for classifier selection in FURIA-based fuzzy multiclassifiers. *Int J Comput Intell Sys* 5:231–241
4. Chang LZ (2013) Study on the manufacturing resource classify based on features. *Appl Mech Mater* 411–414:1880–1891
5. Du YT, Yongbum L et al (2004) Medical image classification using genetic-algorithm based fuzzy-logic approach. *J Electron Imaging* 13:780–793
6. Cerdón O (2011) A historical review of evolutionary learning methods for Mamdani-type fuzzy rule-based systems: designing interpretable genetic fuzzy systems. *Int J Approx Reason* 52(6):894–913
7. Nguyen CH, Pedrycz W, Duong TL et al (2013) A genetic design of linguistic terms for fuzzy rule based classifiers. *Int J Approx Reason* 54(1):1–21
8. Alcalá R, Nojima Y, Herrera F et al (2011) Multiobjective genetic fuzzy rule selection of single granularity-based fuzzy classification rules and its interaction with the lateral tuning of membership functions. *Soft Comput* 15(12):2303–2318
9. Stavroudis DG, Galidaki GN, Gitas IZ et al (2012) A genetic fuzzy-rule-based classifier for land cover classification from hyperspectral imagery. *IEEE Trans Geosci Remote Sens* 50(1):130–148
10. Zhou QF, Yang J (2015) Design of fuzzy classification system applying expertise based on genetic algorithms[C]. *Appl Mech Mater* 738:377–381

# Research on Automatic Identification of Color and Classification Applied to Electric Online Monitoring

Yi Zhang, Feng Zhang, Bin-quan Zhu and Lv Tang

**Abstract** Rapid development of unattended substation requires that computer image recognition technology should be applied to power system more imminently. This paper analyzes the advantages of applying fuzzy pattern recognition technique to electric online monitoring image color identification and classification, and proposes a new method. Firstly, the algorithm acquires all kinds of identification color center based on sample learning sets given by experts; then, it introduces fuzzy  $c$ -means (FCM) clustering method and connected graph traversal technique. Based on the identification of color membership of pixel's corresponding color pattern and color's no-mutation rules, this paper comprehensively analyzes the whole image to form each color pattern and obtain the color identification results of each area. This method is prevalently instructional to similar color automatic identification.

**Keywords** Electric power · Online monitoring · Color · Fuzzy mode identification · Connected graph traversal

## 1 Introduction

With the expansion of grid size and increase of work efficiency, unattended substation, as an advanced substation management mode, is applied more widely [1, 2]. Based on traditional remote sensing, remote communication, remote control, and remote regulating, remote viewing is utilized in unattended substation to monitor inside place, main equipment, operation status, and important parameters. Remote viewing is directly visual and easy to handle. However, monitoring with manpower for straight 24 h is very unscientific; in particular, unattended substations use

---

Y. Zhang (✉)

Zhejiang University of Water Resources and Electric Power, Hangzhou 310014, China  
e-mail: eezhangf@yeah.net

F. Zhang · B. Zhu · L. Tang

State Grid Zhejiang Electric Power Company, Hangzhou, China

© Springer-Verlag Berlin Heidelberg 2016

B. Huang and Y. Yao (eds.), *Proceedings of the 5th International Conference on Electrical Engineering and Automatic Control*, Lecture Notes in Electrical Engineering 367, DOI 10.1007/978-3-662-48768-6\_82

733

centralized monitor technology that several monitors have to supervise ten or even more than one hundred substations [3]. In this operation mode, it cannot satisfy modern grid development if remote viewing system only adapts and transfers substations' image signal. If remote viewing system can utilize computer image identification technology to fully adapt color, texture, shape, and change of images and online intelligence compare by criterion of experts knowledge base, according to actual work environment of substations. Hence, it can dynamically capture abnormal operation conditions of substations, send warning signals, and help monitors with accident treatment. This not only saves human sources but also lays the foundation of finding out abnormal conditions of substations. In recent years, online monitor system based on image processing has been applied successfully in many areas [4]. Compared with other businesses, it is a little lagging because the research on image analysis and abnormal discriminant method of substations with complicated background is not systematic or mature enough. Automatic color identification is a very important application of image processing in power system [5]. This paper proposes an innovative clustering method which realizes color identification and classification of monitor image based on connected graph traversal. Meanwhile, considering that substation image fuzzy treatment because of distortion and noise in industrial environment matches fuzzy theory spirit, therefore, fuzzy *c*-means (FCM) clustering method is introduced to increase applicability and robustness. Examples illustrate that this method is not only flexible in treatment but also accurate in identification.

## 2 Overall Framework System

Substation real-time monitor system based on automatic image identification increases automatic monitor level. This design adds image analysis and identification functions to background monitor computer based on present video monitor system, while present industrial CCD camera, monitor system, and communication mode do not need to be changed. The overall structure of power equipment online monitor system based on automatic image identification is shown in Fig. 1.

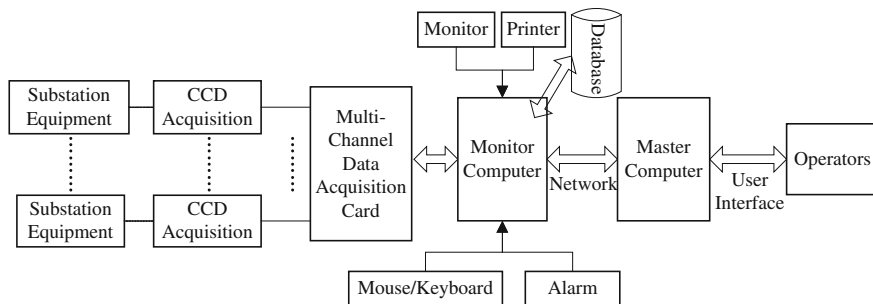


Fig. 1 The overall structure of the substation remote video monitor and analysis system

As acquisition device of image online monitor, industrial CCD image sensors are installed in appropriate places near power device in substations. They transform substations' operation conditions to optical signals and input to monitor computers as static images after digital cameras treatment. When monitor computers find abnormal condition changes occur in substations, the system realizes constant image acquisitions by calling instructions. Then, it sends alert and uploads the abnormal images to the master computer by communication network and reminds monitors to view and analyze the images. The system core is monitor computer which is in charge of the whole process of image acquisition, pretreatment, automatic identification, intelligent analysis, and transform. To save resources, only when substations operate abnormally, monitor computers send images to master computers, otherwise do not.

### 3 System Disposal Process

The concrete process of computer automatic image identification and treatment is as follows: remove interruptions and increase image quality with substation image pretreatment. Based on substation operation image feature algorithm, compare and identify characteristics to estimate the operation conditions of power device. Computers and database exchange data information constantly in image identification. Compare benchmark image in database and historical images to conform present image changes and estimate operation conditions of substations. If substations are normally operating, monitor computers switch channels at regular time to monitor, identify, and analyze substations and store normal images in database. If substations are abnormally operating, monitor computers identify hidden troubles and send warning signals. Meanwhile, monitor computers switch display channels to abnormal device images automatically and constantly sample abnormal images. The abnormal images will be stored in database to be viewed and analyzed by professionals, and the concrete process is shown in Fig. 2.

From Fig. 2, the core of image processing is identifying all image characteristics and comparing them with expert database to estimate substation operation conditions. The main characteristics of images include color, shape, and texture. Undoubtedly,

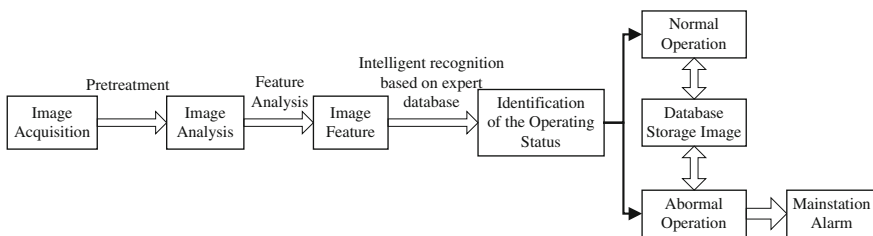


Fig. 2 The flow diagram of the substation remote video monitor and analysis system



color is very important in automatic identification and processing. In substation online monitoring, devices' phase, type, and class of workers (by identifying the color of safety helmet) are distinguished by color. Based on the online monitor characteristics of power images, this paper proposes an automatic color identification and classification algorithm, the starting point of which is that substation typical colors have RGB color center and range, respectively, and these color centers can be obtained by expert classification and statistics. In real-time monitoring, to realize color mode identification and automatic classification, making color class center as constraint and making single pixel as operation unit, every typical color class center's membership of this pixel color mode is calculated. Traditional classification utilizes "biggest membership," that is, classify pixel points to biggest membership color, without considering this point's membership to other color class, which cannot fully take advantage of clustering results. This paper improves it by introducing FCM clustering method and taking advantage of connected graph traversal algorithm to design multilayer for fuzzy processing, according to image color no-mutation and mutual connection. It classifies substation monitor image color mode and meanwhile obtains color distribution which utilizes fuzzy membership's rich information and increases algorithm's noise resistance and robustness.

#### 4 The Learning of Typical Device Color Class Center

With several examples of substation images from hardware acquisition device, pick all the device color class learning set of typical area under experts' guidance. The class center is calculated by statistics. Average the sum of  $R$ ,  $G$ , and  $B$  component values' corresponding  $R$ ,  $G$ , and  $B$  component values of learning set, and Eq. 1 is obtained [6–8].

$$\text{mean}(R) = \frac{\sum_{i=1}^N R_i}{N}; \quad \text{mean}(G) = \frac{\sum_{i=1}^N G_i}{N}; \quad \text{mean}(B) = \frac{\sum_{i=1}^N B_i}{N}. \quad (1)$$

The standard deviation is as follows:

$$\begin{aligned} \text{std}(R) &= \sqrt{\sum_{i=1}^N [R_i - \text{mean}(R)]^2}; & \text{std}(G) &= \sqrt{\sum_{i=1}^N [G_i - \text{mean}(G)]^2}; \\ \text{std}(B) &= \sqrt{\sum_{i=1}^N [B_i - \text{mean}(B)]^2} \end{aligned} \quad (2)$$

where  $N$  is the number of color class learning sample set and  $\text{mean}(R)$ ,  $\text{mean}(G)$ , and  $\text{mean}(B)$  are class center  $R$ ,  $G$ , and  $B$  component values. Several typical device color class centers are obtained, such as close-to-red mutual inductor, gray transformer, yellow (A phase), green (B phase), red (C phase), white safety helmet

(leaders), blue safety helmet (managers), yellow helmet (builders), and red safety helmet (outsiders). The next step of these color class centers will be used to instruct monitor images' color identification.

### 5 Calculation of Pixel Membership

To obtain the corresponding typical color class center's membership of any monitor image pixel, FCM clustering is utilized for the base of pixel color classification and full image color pattern.

Fuzzy *c*-means (FCM) clustering method adopts clustering criterion function as error quadratic sum function. Set

$X = \{x_1, x_2, \dots, x_k, \dots, x_n\}$  is a limited sample set, and FCM minimizes clustering criterion function (Eq. 3).

$$J_m = \sum_{i=1}^C \sum_{j=1}^N (u_{ji})^m \|x_j - w_i\|^2 \tag{3}$$

$W = \{w_1, w_2, \dots, w_i, \dots, w_c\}$  means there are *C* clustering center sets,  $\|\cdot\|$  is Euclidean Distance, *m* is fuzzy index ( $1 \leq m < \infty$ ), and membership matrix  $U = \{u_{ji}\}$  satisfies.

Traditional FCM is completed by iterative optimization to objective function  $J_m$ ; take a derivative of  $w_j$  and  $u_{ji}$  by  $J_m$ , make it 0, and substitute into  $\sum_{i=1}^C u_{ji} = 1$ .

$$u_{ji} = \frac{\left(\frac{1}{\|x_j - w_i\|^2}\right)^{\frac{1}{m-1}}}{\sum_{i=1}^C \left(\frac{1}{\|x_j - w_i\|^2}\right)^{\frac{1}{m-1}}} \tag{4}$$

$$w_i = \frac{\sum_{j=1}^N (u_{ji})^m x_j}{\sum_{j=1}^N (u_{ji})^m} \tag{5}$$

Hence, the specific steps are as follows:

1. Given category number is *C*, parameter *m*, allowable error  $E_{max}$ ,  $t = 1$ ;
2. Calculate  $W(t) = \{w_1, w_2, \dots, w_i, \dots, w_c\}$  by Eq. 5;
3. Calculate new membership matrix  $U(t + 1) = \{u_{ji}\}$ ;
4. Calculate error  $\Delta = \max\|U(t + 1) - U(t)\|$ ;

If  $\Delta > E_{max}$ , return to step 2 or go to the end.

According to the characteristics of substation image identification, all kinds of color class centers are obtained based on sample learning set from experts in advance. When optimizing FCM objective function, all the fuzzy classification results can be acquired better by introducing fixed class center. Because when class center is fixed, Eq. 4 is the optimal solution of objective function  $J_m$ . Therefore, the fixed FCM algorithm of class center can be simplified as follows:

1. According to the characteristics of learning sample set, calculate class centers by Eq. 1;
2. Calculate membership matrix by Eq. 4 to get membership;
3. Remove fuzziness from membership matrix and get classification results.

Fixed FCM algorithm of class center does not need iteration, and the optimal solution can be obtained directly in constraint. In traditional FCM algorithm, class center is obtained by iteration step by step and the attribute needs to be explained more to meet people's habits. While in this paper, the FCM algorithm learns experts' sample set to obtain clear manpower classification and the results do not have to be explained anymore. Because when device experts classify typical image colors, they have the impressions of typical device colors. Identification process is comparing all the typical colors of monitor images and picking a best-match one. This process matches fixed FCM algorithm of class center so it is better than the traditional one.

## 6 Pixel Classification and Analysis of Monitor Image

After previous FCM classification, the result is unknown monitor image about all typical color class membership matrix  $U = \{u_{ji}\}$  which includes every pixel point's membership of monitor image. To make sure every pixel point classification and every area classification of whole image, fuzzy treatment is necessary. The common way is determining object's classification by maximum membership. This way is simple and convenient but cannot fully take advantage of FCM results for more optimal classification.

To solve this problem, according to fuzzy math idea, this paper proposes that define a pixel as fuzzy point, if its maximum membership value is not 20 % bigger than the second maximum one. Experiments indicate that the noise in images is usually a fuzzy point, and the result might be wrong if the classified by the combination of point operation (classification only depends on FCM result) and maximum membership. The method in this paper significantly removes noise effect and increases the accuracy of noise classification results by introducing neighborhood calculation.

In the acquisition process of unit pixel classification, neighborhood attribute and the characteristic of image color will not mutate and the pixel points belong to same color class will connect as an area with same color.

To make connected graph traversal correct, the pixel points have three statuses in calculation: (1) process completion—this point has clear color mode classification; (2) processing—this point has been traversed, but no clear classification; and (3) to be processed—this point has not been traversed, and classification still unknown.

The algorithm defines a present color process stack which divides and isolates the same color area. The first element in stack is the clear non-fuzzy point of color class.

Based on these three pixel statuses, stack processing function and connected graph traversal remove fuzziness treatment by neighborhood operation, and whole device image information calculation method is designed as below:

- Step 1: The original status of pixel point is unprocessed. Make the upper left corner pixel point the first to be processed which determines whether it is an unprocessed non-fuzzy point. If it is, set this point status unprocessed and the color mode belong to its maximum membership class. Press the present process class and jump to step 2, otherwise continue to search unprocessed non-fuzzy points from up to down and left to right. If no non-fuzzy points are found when scan is over, then scan from the beginning again. Classify the unclassified fuzzy points by step 3 until all pixel points are classified and whole image color information is obtained.
- Step 2: If stack is empty, the areas belong to present color class have all been traversed and then return to the last scan position of step 1 to go on searching non-fuzzy points, otherwise pull out of stack. If this point is fuzzy, jump to step 3, otherwise determine whether this non-fuzzy point belongs to present class. If it does, set this point status process completed. This point belongs to its membership's maximum class. Starting from this point, scan unprocessed pixel point (marked as unprocessed) in around  $3 \times 3$  area from up to down and left to right. Press those points in stack and continue step 2.
- Step 3: When the present point is fuzzy, determine whether there are unprocessed points around its  $3 \times 3$  area. If there is, set the present point unprocessed and press it and other unprocessed points around in stack again to execute step 2. Otherwise combine its neighborhood color class certain pixels (pixels still in processing are not considered) to decide the category. Specific judgment collects all pixel color class information (this point is counted with its biggest membership color class) in  $3 \times 3$  area around from the beginning of this point. The color class has the most pixels is this fuzzy point's category. If two classes have the same numbers of pixels, then this fuzzy point's biggest membership class will be its category. Set this pixel unprocessed and go to step 2.
- Step 4: Count the number of pixels in all color classes in all areas and define the color class with the most pixels as the typical color class for further analysis and judgment.

**Table 1** The comparison between results of expert's judgment and computer automatic recognition

Expert's judgment	Computer automatic recognition		Match rate (%)
	Match	Not match	
317	293	24	92.4

From the algorithm above, it is found that introducing fuzzy point neighborhood judgment and connected graph traversal classifies pixel color mode class of monitor images better and meanwhile obtain all color class area information rapidly.

To test the effectiveness of this method, we send 317 typical monitor images of test substation in the program based on C++. The comparison between results of expert's judgment and computer automatic recognition is shown in Table 1, which indicates this method has better recognition to online monitor image automatic classification of substations.

## 7 Conclusions

Applying computer image process and intelligent identification technologies to online monitor image identification and analysis is a new method to remote monitor substation operation status. This paper innovatively proposes a color automatic identification and classification method applied to power online monitoring by the research on the characteristics of power online monitor image color identification. This method introduces fuzzy pixel neighborhood judgment and connected graph traversal based on calculating monitor image pixels' membership to every typical color with improved FCM algorithm. Single pixel's class and the whole image area color information can be obtained more accurately and rapidly with this method which is prevalently instructional to similar color automatic identification. The research will concentrate on solving the problems of low quality of image, missed or false report due to camera focus inaccuracy. With the development of computer and monitor technology, improvement of image processing, and identification algorithm, image processing and identification technologies will be researched and applied further in power online monitoring which will influence future power monitor and control technology profoundly.

## References

1. Hong X (2001) Telecontrol system tending towards networks. *Autom Electr Power Sys* 25 (6):1–3
2. Zhenhua L (2002) Design and operation of remote visual system for Substation. *Autom Electr Power Sys* 26(14):73–75
3. Zhu D, Sun C, Chen F (2009) Centralized remote monitoring system of 500 kV substation. *Electr Power Autom Equip* 29(5):126–129

4. Han P, Zhang X, Wang B et al (2008) Interactive method of furnace flame image recognition based on neural networks. Proc CSEE 28(20):22–26
5. Li Z, Li W, Yao J et al (2010) On-site detection of pollution level of insulators based on infrared-thermal-image processing. Proc CSEE 30(4):132–138
6. Bczdek JC, Hathaway RJ (1988) Recent convergence results for the fuzzy c-means clustering algorithm. Classification (02):237–247
7. Ji Z, Chen Q, Sun Q et al (2009) Image segmentation with anisotropic weighted fuzzy c-means clustering. J Comput Aided Des Comput Graph 10:1451–1459
8. Liu G, Liang X, Zhang J (2011) Contourlet transform and improved fuzzy c-means clustering based infrared image segmentation. Sys Eng Electr 33(02):443–448

# Design of Control System for an Intelligent Closestool

Shuyun Zhu, Yan Chen, Hanhan Wang and Fangjuan Xie

**Abstract** In order to relieve the burden of nursing care for the patients or the elderly, a control system for intelligent closestool is designed for a wheelchair-bed. The hardware and software of the control system are implemented on atmega128. This developed control system has been applied in a class of closestool products. It has functions of autoup and down, auto flip, auto-induction for urine and stool, cleaning and drying, antifouling and ozone deodorization, silencing, and LCD display indication of the clearing process displayed and with voice prompt. Also, the temperature and water and wind pressure can be adjusted. The system is intelligent, humane, easy-to-use, and healthy and hygienic in use.

**Keywords** Intelligent closestool · Atmega128 · PWM control · Step-motor

## 1 Introduction

Intelligent closestools are used for medical care and elderly care. The function is unitary. Parallel with the high-tech development of microcomputer digital processing systems, nanomaterials, and lasers, etc., intelligent closestools, featuring not only intelligence, consistent with humane conditions, but also health, comfort, and environmental protection, are appearing on the market. In addition, this device t has functions such as of cover heating dry, warm water wash, warm wind, antifouling

---

S. Zhu (✉) · Y. Chen · H. Wang · F. Xie  
Department of Automation, College of Science and Technology, Nanchang University,  
Nanchang 330029, Jiangxi, China  
e-mail: 2008zhushuyun@163.com

Y. Chen  
e-mail: 290311310@qq.com

H. Wang  
e-mail: whh\_luck@163.com

F. Xie  
e-mail: 181274256@qq.com

deodorization, sterilization and so on. It conforms to the development trend for toilets to meet future human conditions.

Although there will be a large market space, at present, mainly imported products have appeared on the market. They are expensive and rarely offer mobility. The closestool designed in this paper is primarily connected to the nursing bed. It delivers a great convenience to patients and especially to the elderly.

## **2 Functions of the Closestool Control System**

The closestool designed in this paper can provide a comprehensive nursing care to manage processing of the patient's stools and urine in bed. The design includes functions such as auto-up and -down cover, auto flip, auto cleaning, warm water washing, warm air drying, anti-fouling deodorization, and, during washing, the water pressure and temperature can be adjusted, as well as the water temperature, air temperature, overheating protection, voice prompt, etc [1–6].

## **3 System Working Process**

The system can detect the patient's defecation by sensor. The closestool can immediately shatter and extract feces and urine stored in sludge storage box; then, valves of various kinds are opened in turn, to clean private parts, hips, and the closestool interior; finally, the nozzle also functions to dry the hips and private parts, using warm air drying in real-time. Spanning induction, suction, cleaning, and drying, the whole process has been realized through automatic intelligence, so that the user can keep dry and clean. Thus, the related nursing problems are solved easily. In addition, the intelligent closestool also has the functions of double deodorization and sound attenuation, which maintains a therapeutic environment in bed.

## **4 Overall Design for the Control System**

The Atmega128 is used in the system as the core control chip. This employs an eight series single chip microcomputer produced by the ATMEL company. It is a product of the highest configuration of single-chip microcomputer. It realizes control of the peripheral equipment, such as solenoid valves, the motor, heating device, liquid crystal display and the voice prompt [2, 3], by cooperating with the corresponding peripheral driving circuit and gathering all kinds of sensor signals in real-time through the input signal of sensor, buttons, etc. The control system's overall design block diagram is shown in Fig. 1.



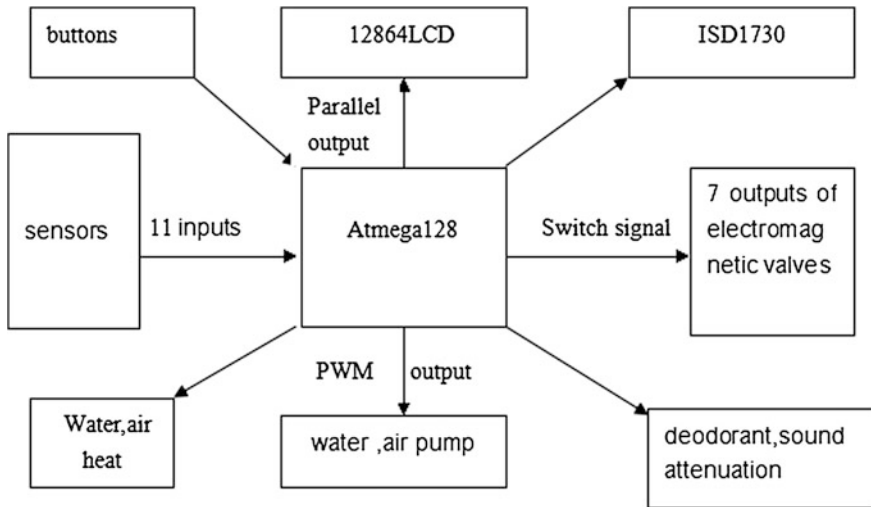


Fig. 1 Structure of the control system

## 5 The Main Module Design for the Control System

### 5.1 Master Control Module

Considering the requirements of the actual functionality and performance, Atmega128 is used as the control chip, which is a high-performance, low-power CMOS 8-bit microcontroller based on the AVR enhanced RISC architecture, non-volatile program and data memories. Also, it is rich in peripherals, e.g., two 8-bit PWM channels, six PWM channels with programmable resolution from 1 to 16 bits, 8-channel, 10-bit ADC, 53 programmable I/O lines, etc. Consequently, it can fully accomplish control for multiple input and multiple output systems.

### 5.2 Sensor and Detection Module

There are many sensors used in the system. According to the signal types, they can be classified into four categories: high-low level electrical signals, square wave signals, digital signals and analog signals. There are six high-low electrical level signals: the sensors for water tank high and low liquid levels, a leak sensor, the sensor assembly, a dirt sensor, and the closestool liquid level sensor.

There are three square wave outputs, namely, the high and low liquid level sensor of the water tank and the urine sensor. Also, there is one digital signal output, for water temperature in water tank, and there is one analog signal for the air-pressure sensor in air box.

The high-low level electrical output sensor (high and low liquid level sensor of the water tank, etc.) employs an isolation liquid level sensor for all functions. They are non-contact, have high-low electrical levels of output and can directly connect with MCU. The peripheral circuit is simple. In addition, dirt detection is done with an infrared sensor.

Square wave detection is used by the square wave signal sensor (the urine sensor, et al.). It has good electrical conductivity in these locations. One can use only anti-corrosive materials as electrodes, which can directly detect on and off conditions. To prevent false detection, square wave excitation and detection can be used.

The water-temperature sensor for the water supply tank uses the 18B20, which is an integrated digital output sensor.

The air-pressure sensor for the air box uses a common negative-pressure sensor, which accesses the PF0 (ADC0) of the Atmega128.

### ***5.3 The Control of the Water Pump, Air Pump and Seven Outputs in the Electromagnetic Valve Module***

A brushless DC motor with 24 V/120 W is used for water pump, uses CMOS tube drive mode, on both ends and a 0.1  $\mu\text{F}$  capacitance, which can prevent the water pump from suddenly stopping to work on the CMOS high voltage pulse. The input of the pump connects to the PB5 port of the single-chip microcomputer, which forms the PWM wave to control the pump. The pulse width is adjusted.

An AC motor with 220 V is used for the air pump, employing an optical coupler and a bidirectional thyristor drive. The supporting pressure of the bidirectional thyristor should be greater than 600 V. The input of the pump connects with the PB6 port of the single-chip microcomputer, which forms the PWM wave to control the pump. The pulse width can be adjusted.

There are seven outputs of electromagnetic valves for the system, including three water valves and four air valves. According to different quantities of water, electromagnetic valves with different power were used. So, there are two driving circuits: a high-power CMOS tube drive mode and low-power triode drive mode, which connects in turn to the MCU pin PA1–PA7.

## **6 Control System Software Design**

In order to make the system's software feature portability, maintainability, and extendibility, the programs are written with the C language. Based on the modular design method, the programs include primarily the main program, a stool flushing subroutine, a urine washing subroutine, etc. This system can realize the two functions

of being either automatic or manual. In order to simplify the length of this paper, only the automatic process is introduced only. Information on the other, manual process can be consulted. According to the functional classification, the automatic washing process can be divided into two parts: stools cleaning and urine cleaning.

### 6.1 Main Program Design

The function of the main program is to complete the initialization work of SCM, and to realize the control function of the system by calling up the subroutine. Automatic button will be detected when pressed. If pressed, the machine goes into the automatic cleaning process. The software flow diagram is shown in Fig. 2, including the processing of stools and urine, cleaning, and drying, and then it returns to the ready state to continue detecting.

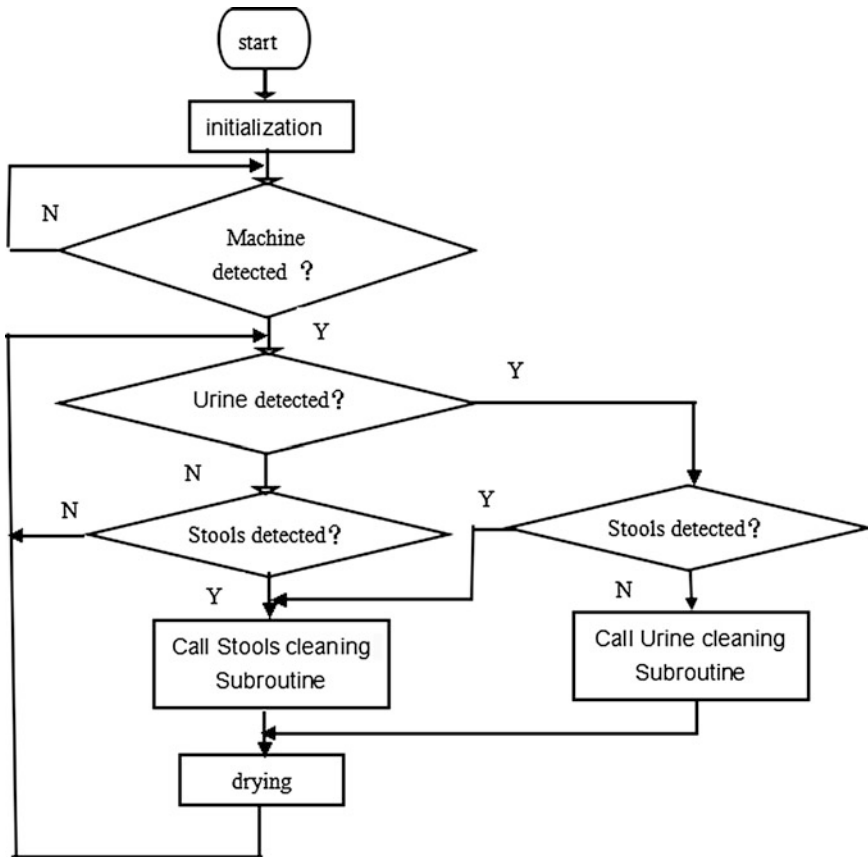


Fig. 2 Diagram of the main program for automatic mode

## 6.2 *Subroutine Design for Stool Cleaning*

The stool flushing process is divided into several stages: induction defecate, stool cleaning for the first time and a second time, (with a one-minute pause in between), cleaning the anus, the private parts and buttocks for the first time, and then, a second time, cleaning the urinals, drying the private parts and buttocks, and drying the back.

## 6.3 *Subroutine Design for Urine Cleaning*

The urine cleaning process entails: pouring of salt water, strong suction, cleaning the anus, private parts and buttocks, cleaning the closetool, drying the private parts and buttocks, and dry the back. The whole process is similar to stool cleaning.

# 7 **Experimental Results**

SPI is be used to communicate with atmega128 and the ISD1730 voice prompt.

An operation scheme, which is stable and reliable, was developed after many experiments. The key design of the control system is embodied in the following schematic aspects: (1) strict logic sequence for the control system; (2) multi-channel sensor signal acquisition and processing; and (3) complex design for power management system.

In the design of hardware system, the large-current driver modules are separated from the control board. For example, since the water pumps and air-pump drive circuit is complex, the current of the drive circuit for water heating, air heating current and electromagnetic valve, etc., is too high. So, it requires a reasonable allocation of power management and a reasonable design that is convenient for commissioning; The sensor signals requires sharp classification and processing circuit also must be clear, especially in regard to the stool and urine detection, as well as the liquid level and leak-detection signal sampling, in order to provide timely warning.

In software design, reasonable allocation for the MCU resources and requests strictly for the control-system logic sequential when programming are mandatory. Especially for control of the water valve and air valves, one must pay attention to “open the valve, and then drive pump; first close pump, then close the valve”, otherwise it’s easy to cause serious pipeline failures.

## 8 Conclusion

The functions of the intelligent toilet designed in this paper are reasonable and have been already basically realized. Some individual functions will be improved and the entire system also needs to be improved. Due to the necessary parallel advances in social acceptance and public information along with networked and intelligent implementation, these devices will enter market gradually, including for use in hospitals, nursing homes, and people homes: Undoubtedly, they are a great help to people with disabilities and to bed-ridden patients to achieve a better life.

## References

1. Bai J, Zhang H, Liu J (2010) Design of intelligent toilet for wheelchair-bed. *Mach Des Res* 26:121–124
2. Zhou Z, Zhang H, Liu X, Peng X (2012) Design and research on intelligent urine and stool processor. *Manuf Autom* 34:100–103
3. Yang J, Fu L (2008) Design of electrical control system of full-automatic urinal. *Mod Electr Technol* 16:55–58
4. Gu D, Yang D, Xu Y et al (2008) Design and implementation of control system for intelligent closestool. *Comput Eng Appl* 44:98–101
5. Wang W, Liu Q, Gu D (2009) Design and implementation of control system for intelligent closestool based on AVR. *Comput Meas Control* 17:1301–1304
6. Wang H, Wang R, Gu G (2005) Measure system of pH value of urine in intelligent closestool system. *Instrum Tech Sens* 10:22–24

# Research on Damage Assessment of Corroded Oil and Gas Pipelines Based on Fracture Mechanics

Rujun Wang and Shujiao Tong

**Abstract** Generally, oil and gas pipeline is made of carbon steel, alloy steel and other metal materials. The biggest threat to the integrity of the oil and gas pipeline is the presence of corrosion. Corrosion will happen when the metal pipeline is affected by chemical or electrochemical attack, or microbial reaction with its environment. With the increasing of the service time, the corrosion of the oil and gas pipelines has become more and more serious. The wall thickness of the corroded pipeline will be lessened and that may lead the decrease of the strength of the pressurized pipeline. Thus, a leak may be happened at the corrosion area if the actual operation pressure of the pipeline is larger than the maximum safe pressure. So it is significant to study and assess the damage condition of the corroded oil and gas pipelines. Based on the theoretical foundations of fracture mechanics, the mathematical model for the failure pressure of corroded oil and gas pipelines was built in this paper firstly. And then, the corrosion damage level of the pipeline was divided into 3 grades according to the ability of the corroded pipeline. Furthermore, 20 corroded pipes were selected to study the damage assessment. The maximum safety operating pressure and damage level of each corroded pipe were carried out by applying the proposed mathematical model in the paper. As a result, the computational data were closed to the experimental data. The corrosion damage level and repair plan of the twenty pipes were discussed, and there were three pipes need to repair immediately. The results show that the proposed method can well assess the corrosion degree of the oil and gas pipelines with defects and can provide a scientific basis for the safe operation and emergency management of the oil and gas pipelines enterprise.

---

R. Wang

China Academy of Safety Science and Technology, Beijing 100012, China

S. Tong (✉)

Key Laboratory of Major Hazard Control and Accident Emergency Technology,  
State Administration of Work Safety, China Academy of Safety Science and Technology,  
Beijing 100012, China

e-mail: tongshujiao@mail.neu.edu.cn

© Springer-Verlag Berlin Heidelberg 2016

B. Huang and Y. Yao (eds.), *Proceedings of the 5th International Conference on Electrical Engineering and Automatic Control*, Lecture Notes in Electrical Engineering 367, DOI 10.1007/978-3-662-48768-6\_84

751

**Keywords** Damage assessment · Failure pressure · Oil and gas pipelines · Corrosion

## 1 Introduction

Pipeline has become one of the most safe and effective way for the transportation of oil and gas. Generally, oil and gas pipeline is made of carbon steel, alloy steel and other metal materials. With the increasing of the service time, the corrosion of the oil and gas pipelines has become more and more seriously for the surrounding environment and the materials conveyed in them. The oil and gas pipeline will be corroded and become more and more thinning, that will reduce the bearing capacity of the oil and gas pipeline. The corroded pipeline may be prone to leak or rupture if its corrosion defect expands to a certain extent. Once leaked, the oil and gas may be spilled out and caused the accidents causing heavy casualties and property damage such as fire, explosion and pollution unfortunately [1]. According to statistics, many oil and gas pipeline accidents were happened since 2000 in China [2]. Therefore, it is significant for the oil and gas pipeline enterprise to detect the corrosion of the pipeline, predict the residual strength and assess the damage level of the servicing pipelines. Enterprise can make the correct risk strategy for the pipeline enterprise. The research on the corroded pipeline is important for the safety operation and emergency management of oil and gas pipeline enterprise.

At present, many researches have been done to predict the failure pressure of the corroded pipelines. B31G, DNV RP-F101, PCORRC, and finite element method are widely used in the assessment of the residual strength of corroded pipeline [3–6]. Because the failure mechanism of corroded pipeline is the burst failure, the failure pressure analysis is the basis of the assessment of the residual strength of the pipeline with defects. So based on the theoretical foundations of fracture mechanics, the mathematical model for the failure pressure of the corroded oil and gas pipelines was built in this paper firstly. And then, 20 corroded pipes were selected as a case study to calculate the maximum safety operating pressure and assess the damage level by applying the proposed mathematical model. Furthermore, the corrosion degree and repair plan of the selected gas pipes were discussed too. The results show that the proposed method can well evaluate the corrosion degree of the defect oil and gas pipeline and can provide the scientific basis for the safe operation and emergency management of the oil and gas pipeline enterprise.

## 2 Method of Failure Pressure for Corroded Pipelines Based on Fracture Mechanics

Pipeline corrosion defects will be influenced by many uncertain factors, including defect size, pressure, corrosion rate of growth, yield stress and geometry dimensions. A corrosion defect of the pipeline is shown in Fig. 1. Here,  $t$  is the wall thickness of the pipeline,  $d$  is the depth of the corrosion defect and  $L$  is the length of the corrosion region, projected onto the longitudinal axis of the pipeline.

Usually, the pipeline will be under hoop stress. The presence of the defect will interrupt the normal hoop stress trajectories at the defect and affect the stress trajectories in neighbouring regions. Hence, there is both stress redistribution and stress concentration around the defect. This may due to the failure of the oil and gas pipelines. Based on fracture mechanics, the hoop stress of the corroded pipeline can be predicted by the following equation [7, 8].

$$S_F = S_{flow} \left[ \frac{1 - A/A_0}{1 - (A/A_0)/M} \right] \tag{1}$$

where  $S_{flow}$  is the flow stress of a material, MPa;  $A$  is the projection area of the defect,  $m^2$ ;  $A_0$  is the wall area at the defect,  $m^2$ ;  $M$  is the Folias coefficient; and  $D$  is the diameter of the pipeline.

The parameter  $A$  is a key parameter to determine the hoop stress. From the parabolic area, rectangular area to the effective area, some methods have been proposed by researchers. In addition, the flow stress  $S_{flow}$  is related to the yield stress of the materials made for the pipelines. It is related to the mechanical characteristics and operating conditions of the different materials. There are at least three relationships for its description in the existing literature.

For the common carbon steel, the  $S_{flow}$  can be expressed as follows [9]:

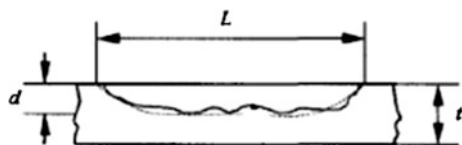
$$S_{flow} = 1.1 \times SMYS \tag{2}$$

where  $SMYS$  is the minimum yield stress of the pipe material.

For the common carbon steel and low-alloy steels whose minimum yield strength is less than 483 Mpa, the  $S_{flow}$  can be expressed as follows [10]:

$$S_{flow} = SMYS + 68.95 \tag{3}$$

**Fig. 1** A corrosion defect of the pipeline





For the common carbon steel and low-alloy steels whose minimum yield strength is less than 551 Mpa, the  $S_{\text{flow}}$  can be expressed as follows:

$$S_{\text{flow}} = (\text{SYT} + \text{SUT})/2 \quad (4)$$

where SYT is the yield stress of materials under specified temperature and SUT is the ultimate tensile stress of the materials under specified temperature.

For pressurized pipeline, if the wall thickness of the pipeline is smaller than the pipe diameter, and the density of the fluid is low relative to the fluid pressure, then the failure pressure of the corroded pipeline can be given as follows:

$$P_F = S_F \cdot \frac{2t}{D} \quad (5)$$

Hence, (5) can be transformed into (6):

$$P_F = \frac{2t}{D} \cdot S_{\text{flow}} \cdot \left[ \frac{1 - 0.85(d/t)}{1 - 0.85(d/t)/M} \right] \quad (6)$$

The failure pressure of the corroded pipeline is the maximum safe operating pressure of the oil and gas pipeline. In order to ensure the safety of the corroded oil and gas pipelines, it is necessary to control the pipeline operating pressure less than the failure pressure of the pipelines.

### 3 Damage Assessment Criteria for Corroded Pipeline

According to the ability of the corroded pipeline, the corrosion damage level of the pipeline is divided into 3 grades, as shown in Table 1.

When the maximum safe working pressure (failure pressure) is greater than MAOP, the corrosion damage level of the pipelines is 3; when the ratio of the maximum safe working pressure and MAOP is larger than the pipeline design

**Table 1** List of the damage assessment criteria for corroded pipeline

Corrosion damage level	Repair plan	Assessment conclusion
1	Repair immediately	The corrosion of the pipeline is very serious and should be repaired immediately
2	Repair within a limited term	The corrosion of the pipeline is serious; the repair plan should be formulated or reduced the operating pressure to the safe operation pressure
3	Monitor	The corrosion of the pipeline is not serious; the pipeline can be used normally. But the pipeline should be monitored

coefficient and smaller than 1, the damage level is 2; when the ratio of the maximum safe working pressure and MAOP is not larger than the pipeline design coefficient, the damage level of the corroded pipeline is 1.

## **4 Prediction of Failure Pressure for Selected Corroded Pipelines**

### ***4.1 Parameters of the Selected Corroded Pipelines***

In order to study the failure pressure of different steel oil and gas pipelines, twenty typical pipes with defects are selected to assess the damage degree. The main parameters of the selected pipeline are shown in Table 2.

### ***4.2 Prediction of the Failure Pressure***

According to the above formula and data in Table 2, the failure pressure of each pipe was forecasted and analysed. The failure pressure and the test results are shown in Fig. 2.

As shown in Fig. 2, the computational data were close to the experimental data. The results show that the proposed method can well evaluate the corrosion degree of the defect oil and gas pipeline and can provide the scientific basis for the safe operation and emergency management of the oil and gas pipeline enterprise.

### ***4.3 Damage Assessment of the Corroded Pipelines***

By comparing the maximum safe working pressure (failure pressure) with the maximum allowable working pressure, we can make sure of the damage level of the corroded oil and gas pipelines. The pipeline design coefficient was taken as 0.8. And then, the damage degree of corroded pipelines can be obtained according to the damage criteria (see Table 1). The results were shown in Table 3.

As shown in Table 3, there are three pipes with the corrosion damage level 1 needs to be repaired immediately, there is one pipe with the corrosion damage level 2 needs to be repaired in a limited terms, and other sixteen pipes with corrosion damage level 3 should be monitored to make sure of the safety of the pipeline. The result of the damage assessment of the corroded pipeline is helpful to the maintenance and management of the oil and gas pipeline.

Table 2 Parameters of the selected pipes with defects

No.	Diameter/mm	Thickness/mm	Defect length/mm	Defect depth/mm	SUT/MPa	SYT/MPa	Test burst pressure/MPa
1	304.8	6.35	26.00	4.95	543.0	351.0	15.36
2	304.8	6.35	33.00	4.25	570.0	382.0	16.29
3	304.8	6.35	37.00	4.64	463.0	351.0	14.29
4	323.1	8.64	63.5	2.16	469	356	24.4
5	323.6	8.61	144.8	3.30	469	356	23.9
6	323.6	8.64	127.0	2.67	469	356	21.7
7	324.0	6.01	19.35	3.60	570.0	382.0	16.22
8	324.0	10.30	243.00	5.15	514.0	380.0	23.20
9	324.0	10.30	243.00	5.15	514.0	380.0	22.00
10	508.0	6.60	381.00	2.62	598.9	443.4	11.25
11	508.0	6.35	900.00	3.43	672.5	429.6	8.00
12	508.0	6.35	1000.00	3.18	672.5	434.8	8.40
13	508.0	6.70	1016.00	2.66	601.0	430.0	11.56
14	508.3	5.61	596.9	3.35	587	462	8.0
15	611.4	6.55	901.7	3.30	535	403	9.4
16	611.5	6.40	1371.6	2.57	535	403	9.8
17	612.5	6.43	1432.6	3.56	535	403	7.9
18	863.6	9.63	213.4	3.63	508	400	10.8
19	863.6	9.47	185.4	3.00	508	400	10.6
20	863.6	9.37	91.4	4.62	508	400	9.2

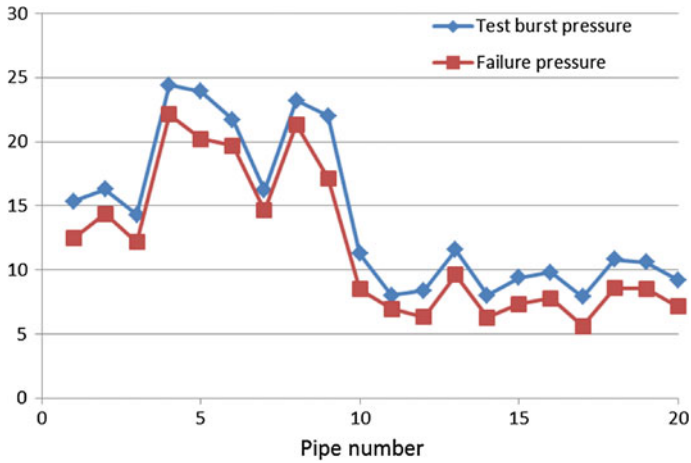


Fig. 2 Comparison of computational values with experimental values

Table 3 Assessment result of the selected corroded pipes

No.	Corrosion damage level	Corrosion degree	Repair plan
1	3	Not serious	Monitor
2	3	Not serious	Monitor
3	3	Not serious	Monitor
4	3	Not serious	Monitor
5	3	Not serious	Monitor
6	3	Not serious	Monitor
7	3	Not serious	Monitor
8	3	Not serious	Monitor
9	3	Not serious	Monitor
10	3	Not serious	Monitor
11	1	Very serious	Repair immediately
12	1	Very serious	Repair immediately
13	1	Very serious	Repair immediately
14	3	Not serious	Monitor
15	2	Serious	Repair within a limited term
16	1	Not serious	Monitor
17	3	Not serious	Monitor
18	3	Not serious	Monitor
19	3	Not serious	Monitor
20	3	Not serious	Monitor

## 5 Conclusions

1. A mathematical model has been built to predict the failure pressure of the corroded oil and gas pipelines based on the theoretical foundations of fracture mechanics. It is verified that the proposed method can well evaluate the corrosion degree of the defect oil and gas pipeline and can provide the scientific basis for the safe operation and emergency management of the oil and gas pipeline enterprise.
2. The corrosion damage level of the No. 11, No. 12 and No. 13 pipes is the first level; they need to be repaired immediately; the fifteen pipes need to be repaired in the limited terms, and the corrosion damage level of other pipelines are all 3, they can be monitored to make sure of the safety.
3. In order to ensure the safety, the operating pressure must be controlled less than the failure pressure if the corroded oil and gas pipelines are not repaired. Detection and maintenance of the corrosion defects should be carried out regularly, and the failure pressure of pipeline corrosion should be predicted according to the investigation of the corrosion defect.

**Acknowledgements** The research work was supported by National science and technology Foundation of China under Grant No. 2015BAK16B01.

## References

1. Ma B, Shuai J, Liu DX, Xu K (2013) Assessment on failure pressure of high strength pipeline with corrosion defects. *J Eng Fail Anal* 32(1):209–219
2. Wu ZZ, Wang RJ (2014) Concern with the safety management of oil and gas pipelines—Status. *Chin Saf News* 6:1–5
3. He DS, Guo J, Zhang P (2007) Assessment method for remaining strength of corroded pipeline and its application. *J Acta Petrolei Sinica* 28(6):125–128
4. Shuai J, Xu K (2003) Assessment method for failure probability of corroded pipeline. *J Acta Petrolei Sinica* 24(4):86–89
5. Wang X, Zhao DF (2013) Safety assessment of oil gas pipelines corrosion based on ASME B31G standard. *J Indus Saf Environ Prot* 39(1):57–59
6. American society of mechanical engineers (2009). ASME B31G-2009. Manual for determining the remaining strength of corroded pipelines. American national standard:5–6
7. Huang J, Hou WW, Chen J (2013) Corrosion and protection of pipeline. *J Liao Ning Chem Indus* 11(1):1327–1330
8. Choi JB, Goo BK (2003) Development of limit load solutions for corroded gas pipelines. *J Press Vessels Pip* 80:121–128
9. Kiefner JF, Vieth PH (1989) A Modified criterion for evaluation the remaining strength of corroded pipe. Final report on project PR 3-805 to the pipeline research committee of the American Gas Association
10. Keith E (2006) *Piping and pipelines assessment guide*. Elsevier, Boston

# The Research on Capacity Rise Phenomenon of the Cable Line Under AC Voltage Withstand Test

Geqing Qi, Wenfeng Song, Dan Yuan, Zhuang Qi, Jianing Guo,  
Wei Zhang and Lulu Wang

**Abstract** Capacity rise phenomenon is comparatively prevalent, which induces abroad attention. But under the tests with alternating voltage, especially to the long cable line tests, there has not enough recognition. The capacity rise phenomenon is dismissal, under the tests with alternating voltage to the short line. But to the long line, the condition is serious. Capacity rise reaches the times of impressed voltage in the extreme situation, which is unacceptable. The paper analyzes the equivalent circuit of distribution parameters, to draw the analog simulation conclusion of the correlative parts voltage response, in connection with ‘long’ and ‘short’ cable under different frequencies and sheath grounding modes. There are some suggestions at last.

**Keywords** Cable line · Distribution parameters · Alternating voltage test · Capacity rise

## 1 Introduction

In the commissioning test of high-voltage electric equipment, to aim at testing leave factory, transportation, field installation, etc., field AC voltage withstand test on trials is one of the most immediate and effective methods. To make AC voltage withstand test on capacity trials is at large. Such as doing induced over voltage withstand tests on transformers and electromagnetic voltage transformers. Also impressing AC voltage withstand test on current transformers, GIS (contain HGIS, PASS, GIL), high-voltage power cable, etc. Generally, impressed voltage withstand tests ignore the influence of capacity rise. Due to the function of distribution parameters, the phenomenon of capacity rise is valued between the long cable and

---

G. Qi (✉) · W. Song · D. Yuan · Z. Qi · J. Guo · W. Zhang · L. Wang (✉)  
State Grid Dalian Electric Power Supply Company, Dalian, Liaoning, China  
e-mail: qqqing777@163.com

L. Wang  
e-mail: wlulu@163.com

GIL transmission electricity line. If we continue to use the accustomed thought mode, there will be a problem. Even the hell and gone effect will be man-made. This paper is in connection with ‘long’ and ‘short’ cable under AC voltage withstand test, drawing the analog simulation of the capacity rise. The conclusion has been made.

## 2 Capacity Rise Phenomenon in the Power Grid

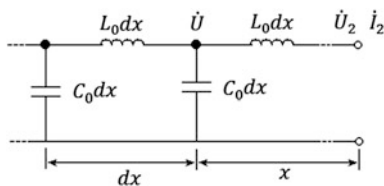
In the high-voltage power grid, capacity rise phenomenon is common. Capacity rise is known as capacity effect. Also called a phenomenon, which the voltage drop  $UL$  drives up the capacitive reactance voltage drop  $UC$  under the capacity current in the loop. The loop in which the inductance and capacitance are in series is under the power supply electromotive force, and the capacitive reactance is greater than the inductive reactance [1, 2]. In the high-voltage test, test transformer makes AC voltage withstand test on large capacitive trials. Because of the test transformer leakage reactance [3], they will bring obvious capacity rise phenomenon to the test trials. The high-pressure side will have capacity rise, when the electromagnetic voltage transformer has the induced overvoltage withstand test. The long high-voltage line with no load can be regarded as a chain loop, which has infinite inductance–capacitance in series. Capacity effect makes the voltage of the line higher than the power supply. The voltage is greater, when the point of line is close to the terminal. If the inductive reactance and capacitive reactance are similar, there will be a resonance. The voltage of the inductive reactance and capacitive reactance will rapidly rise [4–8], which is applied well in the series resonance withstand voltage test.

For the long lossless high-voltage electric transmission line with no load, the equivalent circuit of distribution parameters is as shown in Fig. 1. In Fig. 1,  $L_0$  and  $C_0$  are the inductance and capacitance of the per unit length of the line.

As shown in Fig. 1, we can list the voltage and current matrix expression of  $x$ , which is the distance between the point and the line terminal:

$$\begin{bmatrix} \dot{U}_x \\ \dot{I}_x \end{bmatrix} = \begin{bmatrix} \cos \alpha x & jZ_c \sin \alpha x \\ j\frac{\sin \alpha x}{Z_c} & \cos \alpha x \end{bmatrix} \begin{bmatrix} \dot{U}_2 \\ \dot{I}_2 \end{bmatrix} \tag{1}$$

**Fig. 1** The equivalent circuit of long-distance electric transmission line



If the length of the line is  $l$ , the voltage of the line head end is  $\dot{U}_1$  and the current of the line head end is  $\dot{I}_1$ . The expression is as follows:

$$\begin{bmatrix} \dot{U}_1 \\ \dot{I}_1 \end{bmatrix} = \begin{bmatrix} \cos \alpha l & jZ_c \sin \alpha l \\ j\frac{\sin \alpha l}{Z_c} & \cos \alpha l \end{bmatrix} \begin{bmatrix} \dot{U}_2 \\ \dot{I}_2 \end{bmatrix} \quad (2)$$

Due to the open circuit of line terminal with no load, the current  $\dot{I}_2 = 0$ . By the Eq. (2), the expression of the line head end and terminal voltage is as follows:

$$\dot{U}_1 = \dot{U}_2 \cos \alpha l \quad (3)$$

or

$$\frac{\dot{U}_2}{\dot{U}_1} = \frac{1}{\cos \alpha l} = \varepsilon_{12} \quad (4)$$

In the Eqs. (1) and (4),  $Z_c = \sqrt{L_0/C_0}$ ,  $\alpha = \omega\sqrt{L_0C_0}$ , and  $\varepsilon_{12}$  is the transfer coefficient of the line terminal. Under normal conditions,  $\alpha l$  is far less than 90°,  $\varepsilon_{12}$  is a little bigger than 1, namely, the rise of capacity is less. But when the line is long, the situation is worse, and it will be treated seriously.

When the accomplished high-voltage cross-linked polyethylene cable is made AC voltage withstand test on, the instance is the same as the power supply which charges for line with no load. When the cable is rather long, the capacity rise phenomenon of the cable terminal is obvious, the value relates to the length, the thickness of insulation and the section, etc. (namely, relating to the distribution parameters). Underside, to make the analog simulation of the ‘short’ cable (the length is less than 10 km) and the ‘long’ cable (the length is greater than 80 km) on the AC voltage withstand test. To realize the change of the capacity rise between the different lengths cable with no load under the alternating voltage.

## 2.1 The Simulation of Cable Capacity Rise

Using the EWB software to make the analog simulation of the cable capacity rise, the following condition is assumed: Short, long cable core and outer sheath will be considered by the distribution parameters. The outgoing lines of any part of cable outer sheath (if every phase cable is made up of many sections) just join together. The pressured voltage value of head end cable is constant, and the frequency is alterable.



### 2.2 The Analog Simulation of Short Cable

*The equivalent circuit* Under 110 kV voltage grade, take the cable whose cross section is 800 mm<sup>2</sup> and the length is 10 km, for example. The distribution parameters are discount parameters of field measurement (for convenience, unit parameter chooses 2 km) [9], the voltage application of analog power supply is 1 kV (rms), and the equivalent circuit is shown in Fig. 2.

*The voltage of the short cable core terminal follows the frequency variation* Use the three conditions which are cable metal sheath head end grounding, two-terminal grounding, and terminal grounding. The situation of short cable core terminal is shown in Fig. 3 by the frequency variation.

In Fig. 3, within 10–400 Hz, the voltage of the cable core terminal is consistent under the three conditions. The capacity rise is 1 % below fewer than 200 Hz; the capacity rise is 5 % below fewer than 400 Hz. Over 500 Hz, the voltage of the cable core terminal is different. With the frequency increase, the capacity rise increases sharply. When the frequency is 1000 Hz, the capacity rise reaches 48.3 %.

*The influence of the supply frequency on the short cable core head end and terminal phases* The simulation result shows that the short cable core head end and terminal

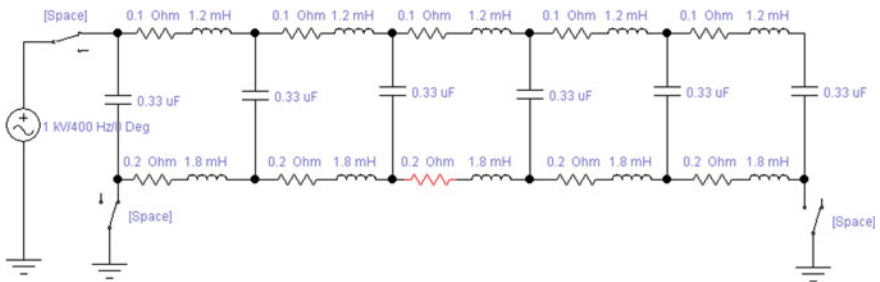


Fig. 2 The analog simulation circuit of short cable

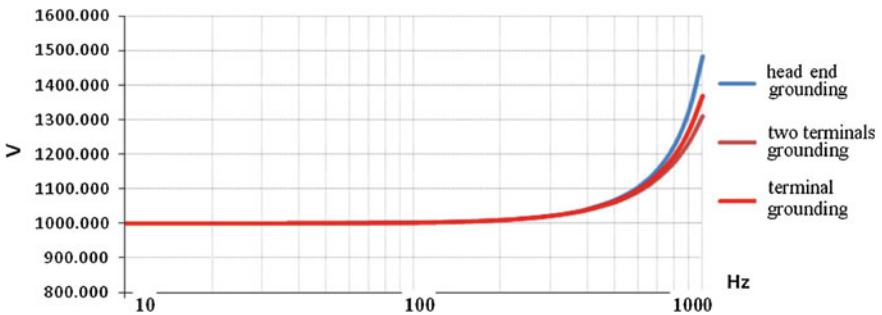
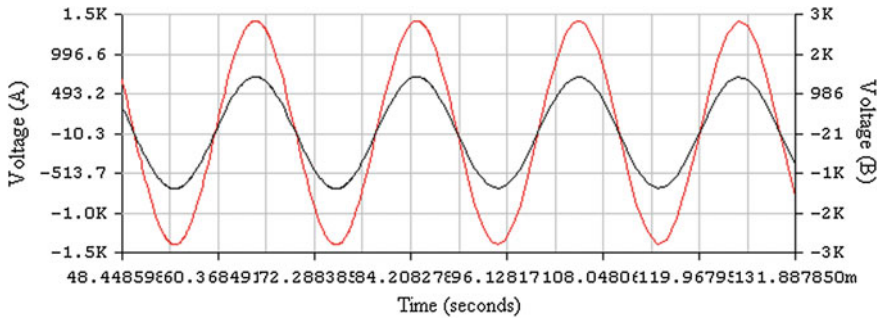
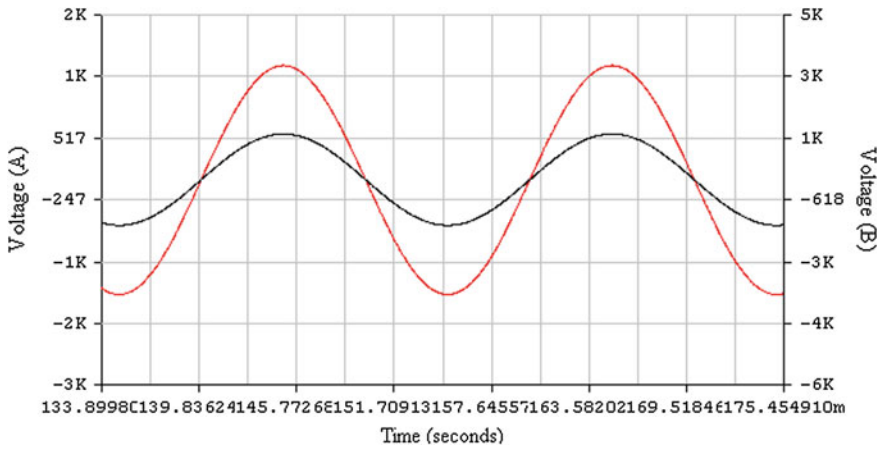


Fig. 3 The situation of short cable core terminal by the frequency variation



**Fig. 4** The voltage phase comparison of the ground lead core head end and terminal by the sheath terminal grounding



**Fig. 5** The voltage phase comparison of the head end and terminal under the sheath two-terminal grounding

voltage phases are consistent under the different sheath grounding modes within 10–1000 Hz. When the frequency is 50 Hz, Fig. 4 shows the cable core head end voltage phase oscillograph under the two modes of sheath groundings, and Fig. 5 shows the cable core terminal voltage phase oscillograph under the two modes of sheath groundings. (The A passageway is head end voltage, and the B passageway is terminal voltage.)

Figures 4 and 5 show that the voltage phases are consistent, when the frequency is 50 Hz under the cable sheath terminal or two-terminal grounding.

*The influence of the supply frequency on sheath voltage distribution* The simulation supply frequencies are 50, 100, 150, 200, and 250 Hz. The voltage distribution conditions of cable metal sheath are shown in Figs. 6 and 7 under the head end grounding and two-terminal grounding.

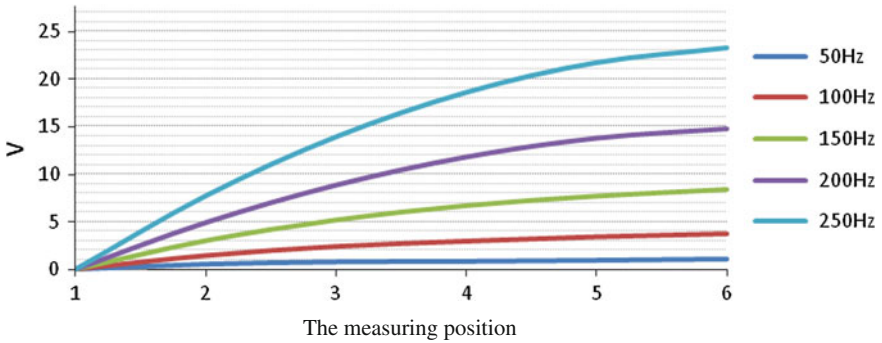


Fig. 6 The voltage distribution condition of cable metal sheath head end grounding following the frequency variation

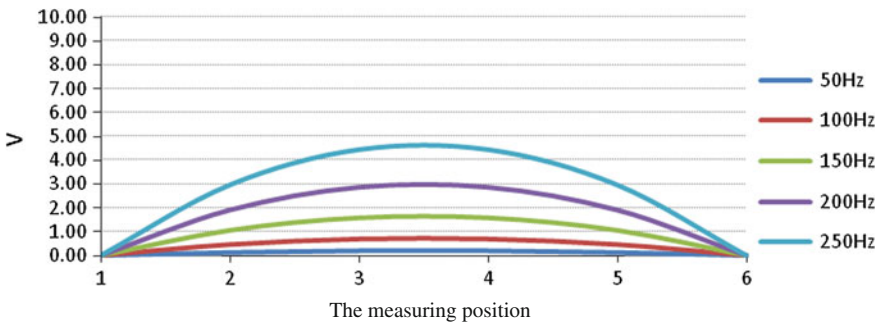


Fig. 7 The voltage distribution condition of cable metal sheath two-terminal grounding following the frequency variation

In Figs. 6 and 7, ‘1’ refers to the head end of the sheath, and ‘6’ refers to the terminal of sheath. From the figure, the sheath voltage distribution features are different under the two groundings. When one end of the sheath is grounding, the terminal voltage of the sheath rises. When two ends of the sheath are grounded, the highest voltage value appears in the middle part of the cable, and the value decreases by degrees to zero at the end of the cable. The figure also shows that the sheath voltage distribution increase follows the frequency variation increase (in the given frequency limits).

### 2.3 The Analog Simulation of Long Cable

The equivalent circuit Under 110 kV voltage grade, take the cable whose cross section is 800 mm<sup>2</sup> and the length is 10 km, for example. The power supply is idem; the simulation circuit is shown in Fig. 8.

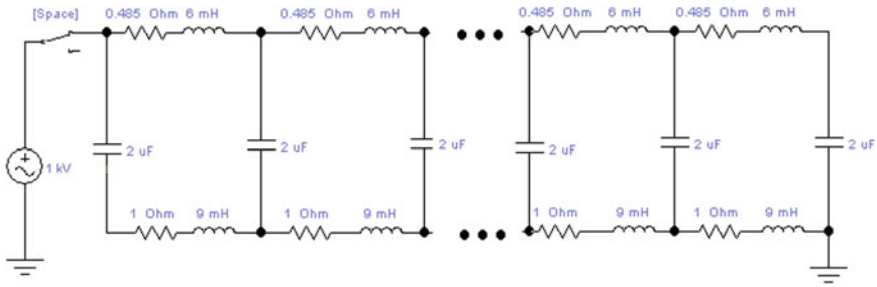


Fig. 8 The distribution parameter simulation circuit of long cable

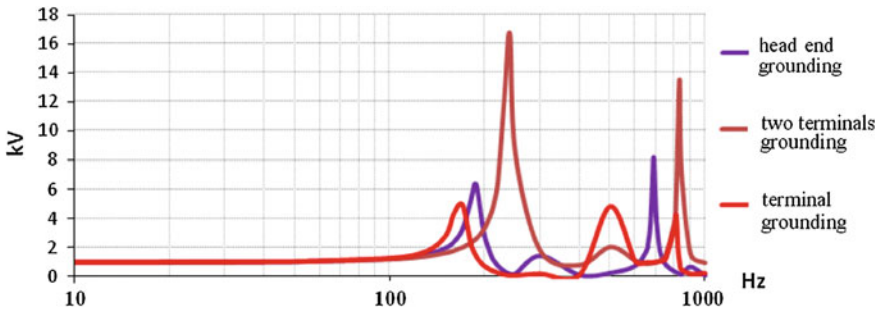
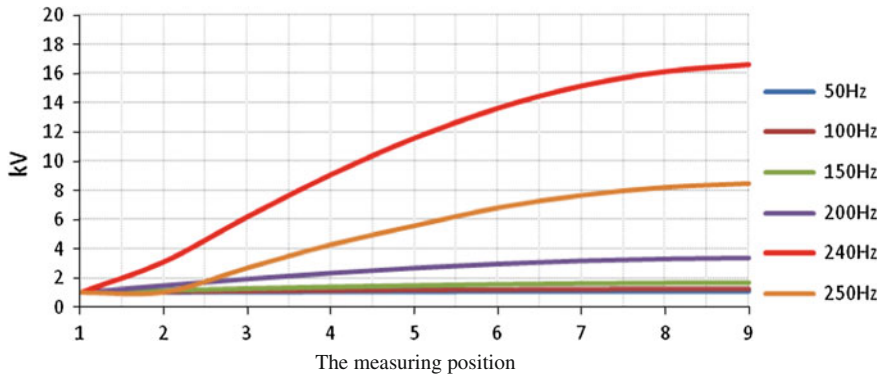


Fig. 9 The voltage distribution condition of the long cable core terminal following the frequency variation

*The voltage of the long cable core terminal follows the frequency variation* Use the three conditions which are cable metal sheath head end grounding, two-terminal grounding, and terminal grounding. The situation of short cable core terminal is shown in Fig. 9 by the frequency variation, and the simulation supply frequency limit is within 10–1000 Hz.

From Fig. 9, within 10–1000 Hz, the cable core terminal voltage features are complicated under the different grounding modes. When the cable metal sheath head end is grounding, there are three core terminal voltage extreme points within 170, 500, and 810 Hz. The voltage effective value of the maximum extreme point is 4.96 kV, which is 4.96 times of the applied voltage value. When the cable metal sheath terminal is grounding, there are two effective values within 186 and 686 Hz. The voltage effective value of the maximum extreme point is 8.16 kV, which is 8.16 times of the applied voltage value. When the cable metal sheath head end and terminal are grounded, there are two extreme points within 240 and 830 Hz. The voltage effective value of the maximum extreme point is 16.71 kV, which is 16.71 times of the applied voltage value.

*The voltage distribution of long cable core within the identical frequency* The simulation result indicates that the voltage distribution conditions of the different



**Fig. 10** The voltage distribution of the cable core along the axis direction within different frequencies

sheath groundings following the frequency variation are generally identical, but there are diversities within the given frequency (resonant frequency). Taking two terminals of the sheath grounding for example, the frequencies are 50, 100, 150, 200, 240, and 250 Hz. The voltage distribution of the cable core is shown in Fig. 10.

In Fig. 10, ‘1’ refers to the core head end, and ‘9’ refers to the core terminal by abscissa. In the selected frequency limits, the core voltage distribution is in direct proportion to the frequency. But within resonant frequency which is 240 Hz, the voltage is highest, and the maximum value is 16.7 times of the head end voltage value.

*The influence of the supply frequency on long cable core head end and terminal voltage phase* The simulation result shows that the change of long cable core head end and terminal voltage phase are ample within 10–1000 Hz. When the frequency is less than 100 Hz, the cable core head end and terminal voltage phase are basically consistent; the sheath grounding modes have little influence on the voltage phase. Following the increase of the frequency, the complex changes appear in the voltage phase, and the sheath grounding modes have influence on the voltage phase. In Figs. 11 and 12, at 186 Hz, the voltage phase changes of the sheath head end and terminal are shown under different grounding modes. (A passageway and B passageway are the same as above.)

From Figs. 11 and 12, when the cable sheath terminal is grounding, the phase difference of the core head end and terminal voltage phase is 71.50. When the sheath two terminals are grounded, the phase difference of the core head end and terminal voltage phase is 8.40. By this token, the sheath grounding mode has important influence on the phase difference.

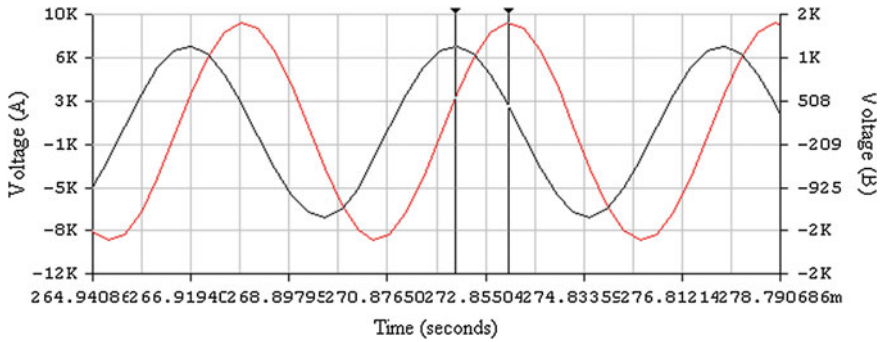


**Fig. 11** The voltage phase comparison of the ground lead core head end and terminal by the sheath terminal grounding within 186 Hz

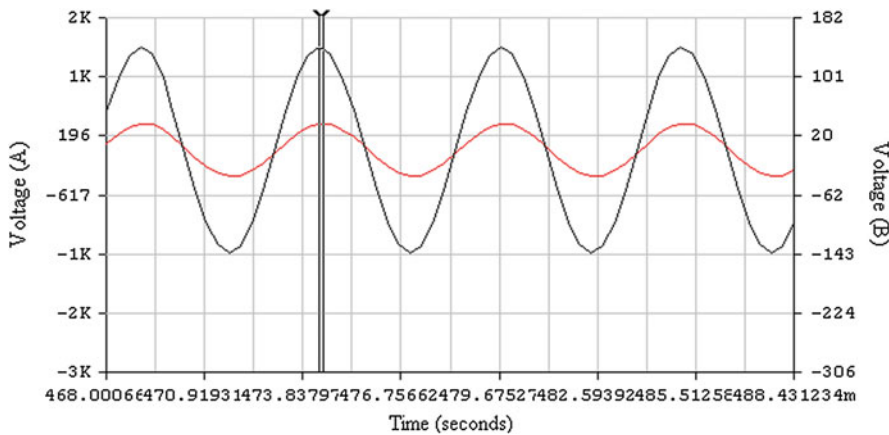


**Fig. 12** The voltage phase comparison of the ground lead core head end and terminal by the sheath two-terminal grounding within 186 Hz

The diversification of the sheath voltage distribution by the supply frequency changes. The simulation supply frequencies are 50, 100, 150, 200, and 250 Hz. The voltage distribution conditions of cable sheath are shown in Figs. 13 and 14 under the head end grounding and two-terminal grounding.

As Figs. 13 and 14 show, the sheath voltage regularities of distribution are similar to those of the short cables under the two grounding modes. The voltage amplitude has the quite rise. The maximum voltage value of the middle part of the sheath is 5.183 kV by the two-terminal grounding. The maximum voltage value of the head end part of the sheath is 6.616 kV by the terminal grounding.

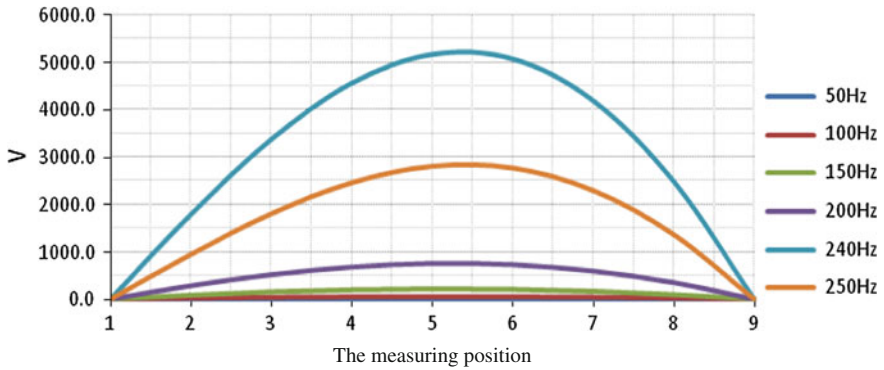


**Fig. 13** The voltage distribution of the cable core along the axis direction within different frequencies by the cable sheath two-terminal grounding

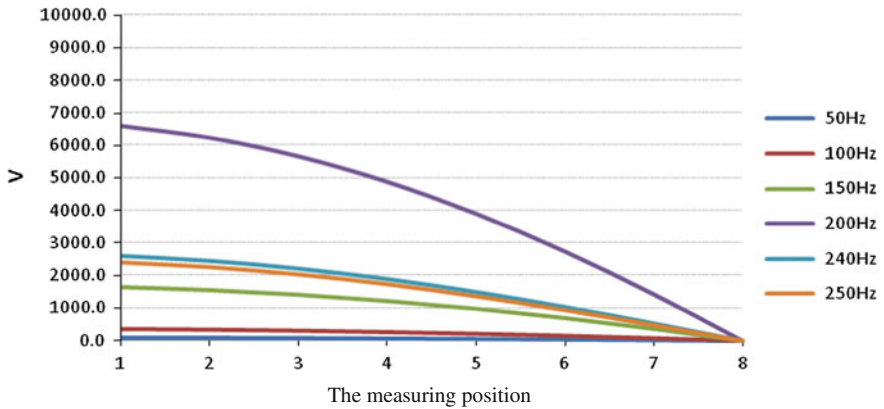


**Fig. 14** The voltage distribution of the cable core along the axis direction within different frequencies by the cable sheath terminal grounding

### 2.4 The Correlation Analysis

The simulation result above indicates that the cable head end has pressured the certain voltage, the voltage diversifications of the cable cores which are short or long and sheath are different by the changing of the frequency.

### 2.5 The Voltage Diversification Analysis of Cable Core

In the voltage amplitude diversification of the cable core terminal, the short cable core terminal voltage value is monotonously increasing within 10–1000 Hz. The

voltage wave shape is smooth within 10–200 Hz. But the shape rises at 200 Hz. The amplitude reaches the maximum at 1000 Hz. The sheath grounding modes have little influence on the cable core terminal voltage. In frequency limits of regulation allowed (20–300 Hz) [10–13], the most capacity rise makes up 2.2 % of capacity rise at 300 Hz. The curve of the long cable changes abundantly within 10–1000 Hz. During the 10–100 Hz, the curve is smooth. The curve fluctuates severely, and when the frequency is greater than 150 Hz, the sheath grounding modes begin to affect the cable core terminal voltage. Beginning with little influence (10–100 Hz) rises to the prominent influence (greater than 150 Hz). In frequency limits of regulation allowed, the maximum capacity rises are 396, 538, and 1571 % by the sheath head end grounding, terminal grounding, and two-terminal grounding. If the same capacity rises appear in the test, it is unacceptable.

In the voltage distribution of the long cable core, the distribution is consistent under the different sheath grounding modes. The voltage of the head end is low; the voltage of the terminal is high. The voltage amplitude has increased following the frequency changing, especially in the certain frequency, and the amplitude rises obviously. In addition, the capacity rise of the short cable core terminal is little in the frequency limits of regulation allowed, so no simulation is there.

In the aspect of the voltage phase of the short cable core head end and terminal, the voltage phase is consistent under the different sheath groundings. There is no relation to the frequency. When the supply power frequency is less than 100 Hz, the head end and terminal voltage phase of the short cable core have no change by the different sheath grounding modes and the affect of frequency is a little. When the power supply frequency is greater than 150 Hz, the head end and terminal voltage phase of the short cable core change much under the different sheath grounding modes. And there are relations to the phase. The phase difference of the core head end and terminal reaches 71.50 at 186 Hz by two-terminal grounding.

## ***2.6 The Voltage Distribution Analysis Along Cable Sheathing***

When one end of the cable sheathing is grounded, the long and short cables have similar voltage distribution. The voltage magnitude increases as frequency increases. Under given frequency, the maximum sheath terminal voltage of the short cable is 23.36 V (250 Hz) and 6616 V (200 Hz) of the long cable; when both terminals of the cable sheathing are grounded, the voltage distribution is also similar: 4.47 V (250 Hz) of the short cable and 5183 V (240 Hz) of the long cable under given frequency.



## 2.7 Discussion

In view of the analysis above, the voltage response of the cores, terminal, and sheath is different when placing the same voltage to the head of the long and short cables. The voltage response is more distinguished on the long cable.

Certain generalizations can be derived from the simulation data. In the short cable circumstances, the frequency change between 10 and 150 Hz has little influence on the core terminal voltage and can be ruled out. When two terminals are grounded, the cable midpoint has the maximum sheathing voltage and the frequency influence can be approximately ruled out, too. But if only one terminal of the sheath is grounded, a small voltage can be expected on the other terminal. In this situation, make sure both terminals are grounded.

The long cable situation is different. Though the frequency (under 100 Hz) influence is little, the capacity rise is 25 % at 100 Hz and the maximum voltages are 365.6 V when one sheathing end is grounded and 71.4 when both terminals are grounded. The maximum voltages are unacceptable when converted to the test voltage condition. It is worth noting that frequency change between 10 and 50 Hz has limited influence on the core terminal voltage, and the capacity rise is 5 % (longer cable needs to be recalculated) at 50 Hz. This is practically acceptable, the midpoint voltage can reach 16.1 V when both terminals are grounded, and the voltage of ungrounded terminal can reach 72.9 V and nearly 1 kV (converted to test voltage) when one terminal is grounded. So for the sake of the insulation sheath safety, special measures need to be taken to lower the partial voltage when conducting AC voltage withstand test [14–16].

Given all that, the choice of the test frequency is critical, especially for the long cable. By satisfying the rule requirements, about 50 Hz or little less than 50 Hz is better for the AC voltage withstand test and also can prevent man-made damage of the insulation.

## References

1. Chen C (2002) Theory and operation technique of the over-voltage protection. China Electric Power Publishing House, Beijing
2. Xie G (1985) Hyper-voltage of power systems. Water Resources and Electric Power Press, Beijing
3. Zhang R, Chen C, Wang C (2002) High-voltage testing technology, 2nd edn. Tsinghua University Press, Beijing
4. Jiang R (1997) XLPE power cable lines. China Electric Power Publishing House, Beijing
5. Zhang M, Zhang L, Wang H (2011) Suppression characteristics of ferranti effect for extra-high voltage transmission line. Eng J Wuhan Univ 44(4):500–502
6. Yao Y, Chen B, Tian C (2008) Application of magnetically controlled reactor in 500 Kv transmission line from Sanyou to Jiangling. High Volt Eng 34(5):984–988
7. Tang B, Chao Q, Chang X, Lai G, Yao X (2011) Reflection on the voltage rise at the long line end. Heilongjiang Power 4:271–273

8. Gao Y, Du B, Zhang Y, Shi W, Liu W, Xu Q (2004) Study on the overvoltage for 110 kV power supply system with a long line. *High Volt Appar* 1:14–16
9. Yang F, Liu W, Gan J (2008) The comparative analysis on parameter measure of the high voltage power cable line. *Sichuan Electr Power Technol* 8:87–89
10. DL/T5221-2005 (2005) Technical rules for design of urban power cable lines
11. DL/T401-2002 (2002) The guide for choice high voltage cable
12. GB Z18890.1-2002 (2002) The test method and require of 220 kV XLPE power cable
13. IEC60840-2004 (2004) Power cables with extruded insulation and their accessories for rated voltages above 30 kV( $U_m = 36$  kV) up to 150 kV( $U_m = 170$  kV)—test methods and requirements
14. Wang J, Liu J, Wu H (2004) Countermeasures to prevent the troubles with the outer sheaths of high voltage single-core cable. *High Volt Eng* 1:97–98
15. Wang X, Lin J, Chen G, Huang Q, Chen Z, Zuo Z, Li F (2008) Electromagnetic transient analysis of 500 kV submarine cable transmission system from Guangdong to Hainan 12:6–11
16. Yao J (2004) Discussion on the grounding mode of able sheath based on a power able fault. *High Volt Eng* 4:48–49

# Lyapunov-Based Control Strategy for Grid-Connected Inverter with Improved Transient Response

Jinhao Wang, Chaoying Yang and Yulong Wu

**Abstract** Repetitive control is commonly known as good steady-state tracking but slow transient response. This paper presents a hybrid control scheme with Lyapunov energy function embedded in conventional repetitive control for the purpose of fast transient response with system disturbance. Convergence of control is guaranteed by Lyapunov energy function. The proposed method is applied for single phase grid-connected inverters, which are commonly used in distributed generation interfacing to utility. Under load disturbance, the proposed method is compared with PI + Repetitive control scheme by computer simulation via MATLAB/Simulink. It is shown that the proposed hybrid control strategy has an improved dynamic response and good capacity of steady-state tracking.

**Keywords** Lyapunov functions · Repetitive control · Steady-state tracking · Transient response · Grid-connected inverters

## 1 Introduction

With the increasingly serious environmental pollution, renewable energy and stored energy have been applied more and more widely. This energy source is generally connected to the power grid via interfacing DC/AC inverter. When the distributed energy source is less than tens of KW, single phase inverter is commonly used and plays an important role in grid stability based on its performance. The stability of

---

J. Wang (✉)

State Grid Shanxi Electric Power Research Institute, Taiyuan 030000, Shanxi, China  
e-mail: 7wjh@163.com

C. Yang (✉)

Shanxi State Grid Corporation of China, Taiyuan 030000, Shanxi, China  
e-mail: ycy629@126.com

Y. Wu (✉)

Shanxi Shijizhongshi Electrical Technology Company, Taiyuan 030000, Shanxi, China  
e-mail: mark32167@126.com

© Springer-Verlag Berlin Heidelberg 2016

B. Huang and Y. Yao (eds.), *Proceedings of the 5th International Conference on Electrical Engineering and Automatic Control*, Lecture Notes in Electrical Engineering 367, DOI 10.1007/978-3-662-48768-6\_86

control strategy, dynamic response, and steady-state tracking ability are critical to maintain good state of the power grid, which consists of several types of inverters [1–3].

Traditional single phase inverter control contains proportional-integral (PI) control, proportional resonant (PR) control, repetitive control, and hysteresis control [4–12]. As a classical control method, PI control is simple and has fast dynamic response, but due to lack of ability of suppressing sub-harmonic, it will produce higher steady-state tracking error. Different harmonics need different controllers and the control structure is also complex. As a typical nonlinear control method, hysteresis control is simple with good stability, but due to the uncertainty of switching frequency, it will produce a lot higher order harmonic for the system. Repetitive control only needs one controller to suppress each sub-harmonic, it is widely used because the structure of this system is very simple, but the greatest disadvantage of repetitive control is that the delay time of dynamic control is long while dynamic response is slow. Many domestic and overseas scholars are trying to improve the repetitive control: Literature [5, 6] raised the method of combining H-infinity with repetitive control which improved the current tracking ability of internal model; unfortunately, it still could not improve the transient response rate of the system. Literature [7, 8] combined repetitive control with PT control and obtained a good dynamic performance, but PT control weakened repetitive control's ability of suppressing each sub-harmonic; due to the coupling relationship between the two controls, several disturbances of power grid will aggravate the current distorting of inverter. Literature [9, 10] added the repetitive control to the state feedback in the state of pole placement, which effectively suppresses the late cycle of instruction signal within closed-loop control system; however, the control variable of the state feedback in the state of pole placement is complex and has higher demands on the feedback parameter accuracy.

Lyapunov method is often applied to the linear and nonlinear control to judge the stability of the control under the condition of disturbance. In the inverter grid-connected system, this method has been applied to the stability analysis of inverter controller [11, 12]. Among these applications, Lyapunov function for the nonlinear system is complex and cannot be effectively simplified; furthermore, the controlling conditions are not easy to realize, so it is hard to apply in engineering. In [11, 12], although Lyapunov improved the dynamic response rate of the system, it still cannot suppress the harmonic distortion of the system.

This paper examines the control strategy of single phase grid-connected inverter, and Lyapunov energy function is constructed to maintain system stability and improve the dynamic response of system. The proposed strategy in this paper can effectively improve anti-disturbance ability of the single phase grid-connected inverter and at the same time reduce the steady-state tracking error of the inverter. At the end of this paper, experiment results are provided to demonstrate the correctness and validity of the above control policy.

**Fig. 1** Single phase grid-connected inverter structure diagram

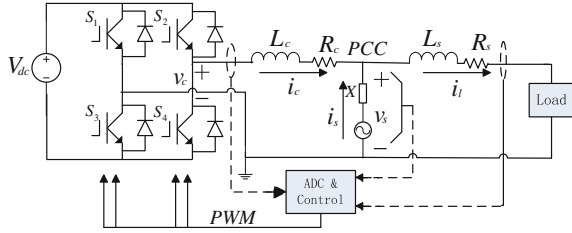
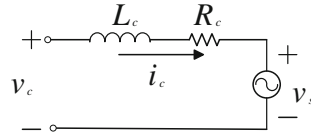


**Fig. 2** Simplified single phase grid-connected inverter structure diagram



## 2 System Structure and Control Strategy

Figure 1 shows the structural diagram of single phase grid-connected inverter, including PV plant array, L-shaped inverter filter, load, and control system. The control system generates reference current of the inverter by collecting the grid voltage  $v_s$  and load current  $i_t$ . It is a simplified structure of single phase inverter,  $v_c$  is the output voltage of the inverter, imagine  $v_c = v_{dc} \times u$ , and  $u$  is the control signal of the input inverter. Figure 2 is the simple form of Fig. 1.

In Fig. 2, according to the KVL equation

$$L \frac{di_c}{dt} + Ri_c + v_c = v_s \tag{1}$$

The reference current  $i_c^*$  output by the inverter is the tracking reference of  $i_c$ , so the dynamic tracking error is given below

$$e = i_c^* - i_c. \tag{2}$$

## 3 Hybrid Control of Lyapunov and Repetitive Strategy

### 3.1 Lyapunov Stability Theory

Imagine the system state equation is  $\dot{X} = f(X, t)$ , if the scalar function  $\tilde{V}$  of continuous first derivatives exists and satisfies the following conditions [13]

$$\begin{cases} f(0, t) = 0(t \geq t_0) \\ V(X, t) > 0 \\ \tilde{V}(X, t) < 0 \end{cases} \tag{3}$$

The equilibrium state which is at the origin is asymptotic stability. With  $x \rightarrow \infty$  and  $V(X, t) \rightarrow \infty$ , the global linear and nonlinear system is asymptotic stability.

According to the tracking error of inverter current, based on Eq. (2), the Lyapunov energy function is constructed as follows:

$$V = \frac{1}{2}e^2 \tag{4}$$

In Eq. (4),  $V > 0$

The derivative of time is given as:

$$\frac{dV}{dt} = e \frac{de}{dt} = e \frac{dV}{dt} \left( \frac{di_c^*}{dt} - \frac{di_c}{dt} \right) \tag{5}$$

Take Eq. (1) into Eq. (5)

$$\frac{dV}{dt} = e \frac{de}{dt} = e \left[ \frac{di_c^*}{dt} - \frac{v_s - uV_{dc} - Ri_c}{L} \right] \tag{6}$$

In order to make  $dV/dt < 0$

$$\alpha e = \frac{di_c^*}{dt} - \frac{v_s - uV_{dc} - Ri_c}{L} \tag{7}$$

Take Eq. (7) into Eq. (6)

$$u = \frac{L}{V_{dc}} \times \left( \alpha e - \frac{di_c^*}{dt} - \frac{R}{L} i_c \right) + \frac{v_s}{V_{dc}} \tag{8}$$

where  $u$  is the control signal of the input inverter. If the given power grid is disturbed, then the control signal  $u$  can be expressed as follows:

$$u = \frac{L}{V_{dc}} \times \left( \alpha e - \frac{di_c^*}{dt} - \frac{R}{L} i_c \right) + d \tag{9}$$

where  $d$  can be described as the disturbance received by the entire control system.

### 3.2 Repetitive Control

Repetitive control is a kind of internal model control, and it can better suppress each sub-harmonic, when periodical signal exists in the internal model; it can be tracked with zero steady-state error by the closed-loop system. The traditional repetitive control is shown in Fig. 3.

For the inverter system, internal model transfer function is given below.

$$G(s) = \frac{e^{-sT}}{1 - Qe^{-sT}} \tag{10}$$

To combine the Lyapunov function and the repetitive control and ensure the overall stability of the system, this paper adds Lyapunov equivalent transfer function  $G_c(s)$  modules into traditional repetitive control, and this design adopted repetitive controller as shown in Fig. 4.

$G_p(s)$  is the transfer function of inverter under the mode of repetitive control,  $G_c(s)$  is the equivalent transfer function of Lyapunov,  $Q(s)e^{-sT}$  and  $G_f(s)$  are the improved repetitive controller parameters,  $I_g(s)$  is the output current of inverter, and  $d$  is the disturbance received by the power grid.

Excluding the repetitive control and Lyapunov, the tracking error of the inverter is given as:

$$E_0(s) = \frac{u - d}{1 + G_c(s)G_p(s)} \tag{11}$$

When adding the repetitive control into inverter model, the tracking error of the system is given as follows:

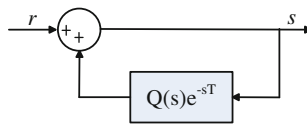


Fig. 3 Traditional repetitive control block diagram

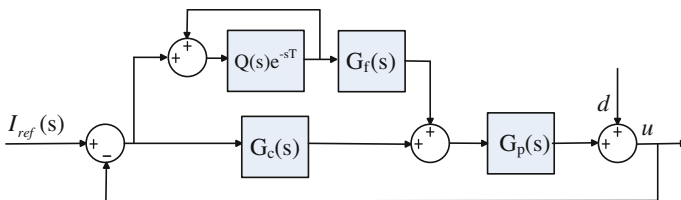


Fig. 4 Improved repetitive control block diagram

$$E(s) = E_0(s) \times \frac{1 - Q(s)e^{-sT}}{1 - [1 - G_f(s)H(s)]Q(s)e^{-sT}} \tag{12}$$

where

$$H(s) = G_p(s)/(1 + G_c(s)G_p(s)) \tag{13}$$

In order to keep the balance of the system

$$[1 - G_f(s)H(s)] < 1 \tag{14}$$

Equation (14) constructed one of the conditions of system’s stable running condition.

### 3.3 The Selection of Stable Parameters

Figure 5 shows the overall system block diagram, where  $u_{Lyapunov} = \frac{L}{V_{dc}} \times (\alpha e - \frac{di_c^*}{dt} - \frac{R}{L} i_c)$  is the voltage controlled by Lyapunov. The following part analyzes the selection of stable parameters of the overall system block diagram.

It is often been ignored that the uncertainty of parameters selection, the steady state drawn by Lyapunov energy function, is only the stable condition under ideal condition. In this paper, Lyapunov control section simultaneously satisfies Eqs. (14) and (19); because of the uncertainty during the process of parameters selection, this paper only considers the uncertainty existed in the process of filter parameter selection. This paper takes  $R^*$  and  $L^*$  for the estimation value of the filter parameter, and then one can get

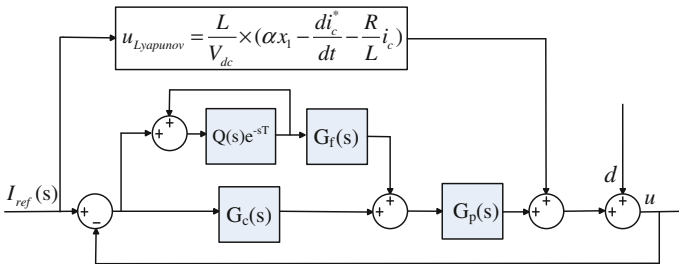


Fig. 5 Improved repetitive control block diagram



$$u_2 = \frac{L^*}{V_{dc}} \times \left( \alpha e - \frac{di_c^*}{dt} - \frac{R^*}{L^*} i_c \right) + \frac{v_s}{V_{dc}} \quad (15)$$

Add Eq. (14) into Eq. (10)

$$\frac{dV}{dt} = e \left[ \frac{di_c^*}{dt} \left( 1 - \frac{L^*}{L} \right) + \frac{\alpha e L^* - v_s - R^* i_c + R i_c}{L} \right] \quad (16)$$

According to the Lyapunov stability theorem

$$\frac{dV}{dt} = e \frac{de}{dt} = \alpha e^2 < 0 \quad (17)$$

Simplify the Eq. (15)

$$\left| \frac{L^*}{L} \times \alpha e^2 \right| > \left| e \left[ \frac{di_c^*}{dt} \left( \frac{L^*}{L} - 1 \right) - \left( \frac{R}{L} i_c - \frac{L^*}{L} \times \frac{R^*}{L} i_c + d \right) \right] \right| \quad (18)$$

In the process of the inverter parameter selection, the influence of inductance error on control system is greater than the influence of filter resistance error on the system, so Eq. (18) can be presented as:

$$\alpha > \frac{\left| \frac{di_c^*}{dt} \left( \frac{L^*}{L} - 1 \right) - \frac{R-R^*}{L} i_c + d \right|_{\max}}{\left| \frac{L^*}{L} \times e \right|_{\min}} \quad (19)$$

According to Eqs. (14) and (19),  $u_{Lyapunov}$  automatically adjusts its size to guarantee the two stability condition hold true, which not only ensure the dynamic response rate of the system, but also improve its steady-state tracking ability.

## 4 Simulation and Experiment Results

In order to validate the proposed control strategy, a simulation model was established on the basis of Fig. 1. In the process of improving repetitive control,  $Q(s)$  equals 0.96, and circuit parameters are shown in Table 1.

In Eq. (18),  $\alpha$  is  $3 \times 10^5$ . The proposed hybrid control strategy is compared with PI and repetitive control to validate its effectiveness.

Figures 6 and 7 show PCC simulation current waveform under sudden load change. It can be observed that when the load shifts from R1 to R2, the control current of “Lyapunov control and repetitive control” is basically returned in smoothed state under the sudden load change; the current controlled by “PI and

**Table 1** System Parameters

Parameter name	Parameter value
DC side voltage $V_{dc}/V$	400
Power grid side voltage effective value $v_s/V$	220
Grid frequency $f/Hz$	50
Filter inductance $L_s/mH$	6
Filter resistance $R/\Omega$	0.3
Switching frequency $f/kHz$	10
Sampling frequency $f_s/kHz$	10
Load $R_1/\Omega$	10
Load $R_2/\Omega$	20

**Fig. 6** PCC current transient when load shifts from R1 to R2

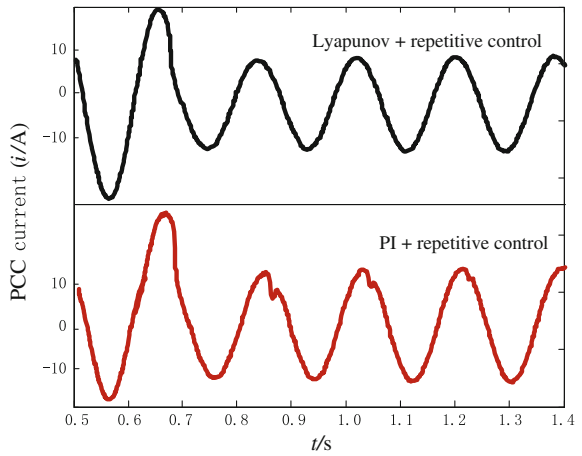


**Fig. 7** PCC current transient when load shifts from R2 to R1

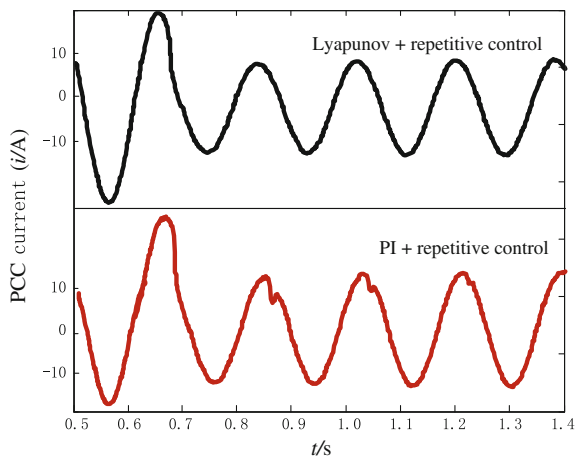
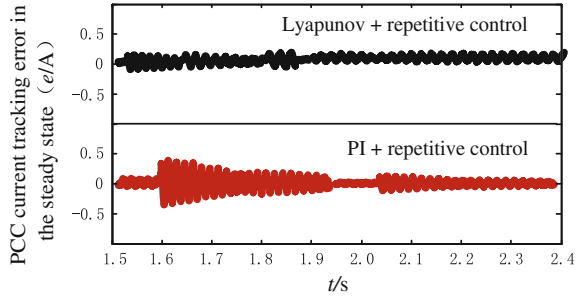


**Fig. 8** PCC current tracking error in the steady state



repetitive control” only restores stability after the forth cycle. Figure 7 shows the current that used the method of this paper restores stability after the second cycle. The current of “PI and repetitive control” restores stability after the third cycle. From Figs. 6 and 7, in the process of dynamic adjustment, the overshoot of PCC current waveform under “Lyapunov + repetitive control” is obviously smaller than “PI + repetitive control.” Moreover, waveform distortion of latter is obviously bigger than former. It can be concluded that the dynamic response has been improved a lot.

By comparing “Lyapunov + repetitive control” and “PI + repetitive control,” one can draw Fig. 8, and the stable state error of the “Lyapunov + repetitive control” is much smaller than other methods and improve the stable precision of the control. Under the method of this paper, the stable tracking ability of the system and anti-disturbance are better, and it can benefit to stable operation of the system.

## 5 Conclusions

As a large number of renewable energy and new energy-storing device adopts single phase grid-connected inverter, its good performance is crucial to maintain the safe run of the system. This paper raised the compound control strategy that combine Lyapunov and repetitive control and guarantee the stability of control system through making variable function of the two sides of the inverter negative all the time. Lyapunov method can make up for the disadvantage of suppressing the late cycle of instruction signal within closed-loop control system and the slow dynamic response, and it can fully guarantee the dynamic performance of the control system. To simplify the repetitive controller design, reducing the steady-state tracking error of the inverter output current is benefit to the stable operation of the system. Compared with the traditional “PI + repetitive control,” the method raised in this paper verifies the correctness and effectiveness of this control strategy.

## References

1. Khadkikar V, Chandra A, Singh BN (2009) Generalised. Single-phase p–q theory for active power filtering: simulation and DSP-based experimental investigation. *IET Trans Power Electron* 2:67–78
2. Huang ZX, Zou XD, Li T (2012) Research on current control mode single-phase dynamic voltage regulator based on pole-assignment and repetitive control. *Trans China Electrotech Soc* 27:252–260 (In Chinese)
3. Radu IB, Leonardo RL, Daniel R et al (2011) IEEE enhanced power quality control strategy for single-phase inverters in distributed generation systems. *IEEE Trans Power Electron* 26:798–806
4. Gao JL, Huang XJ, Lin F (2010) Deadbeat control strategy for PWM rectifiers based on repetitive observer. *Trans China Electrotech Soc* 25:47–54 (In Chinese)
5. Geng YW, Wu XJ, Xu LH (2013) Three-phase four-wire PV-AF system based on  $H_{\infty}$  and repetitive control. *Proc CSEE* 33:90–96 (In Chinese)
6. Yan SJ, Leng B, Du H (2012) Research on the three-phase four-leg inverter based on  $H_{\infty}$  repetitive control. *Electric Mach Control* 16:39–47 (In Chinese)
7. Zhang X, Wang YJ, Yu C (2014) An improved repetitive control strategy for grid-connected inverters with LCL filter. *Autom Electr Power Syst* 38:101–107 (In Chinese)
8. Song JC, Liu GR, Li YX (2011) Research on the inverter based on improved repetitive control combined with dual loop PI control. *J China Coal Soc* 36:1768–1772 (In Chinese)
9. Liu XM, Zou XD, Kang Y (2007) An inverter based on state-feedback integral control and repetitive control technology with state-observer. *Trans China Electrotech Soc* 22:91–95 (In Chinese)
10. Jia YQ, Zhu ML, Feng Y (2014) State feedback based repetitive control for single-phase inverter. *Trans China Electrotech Soc* 29:57–63 (In Chinese)
11. Kwak SS, Yoo SJ, Park JC (2014) Finite control set predictive control based on Lyapunov function for three-phase voltage source inverters. *Inst Eng Technol* 7:2726–2732
12. Lu WG, Li AX, Zhao NK (2014) Control of single-phase Buck inverter by improved Lyapunov direct method. *Electric Mach Control* 18:18–23 (In Chinese)
13. Yu CG (1997) *Modern control theory*. Harbin Institute of Technology Press, Harbin

# The Simulation of STATCOM for Distribution Systems Using a Mathematical Model Approach

Wei Xie and Jian-Min Duan

**Abstract** In this paper, the necessity and merits of STATCOM, as a reactive power compensator, are firstly analyzed. Secondly, the principle of STATCOM is introduced. And combining with the mathematical model of STATCOM, the direct current control method is introduced. At last, the model of STATCOM is built. Then through the figure contrast, the feasibility and effectiveness of this method is verified.

**Keywords** STATCOM · Mathematical model · Direct current control · PWM · PI regulator · Decoupling control

## 1 Introduction

STATCOM is an important part of modern flexible AC transmission systems (FACTS), and it is mainly based on GTO, IGBT, and the DC capacitor [1]. Comparing the other conventional non-reactive compensation devices, it has the following advantages:

- Using of digital control technology, high reliability, low maintenance costs; at same time, achieving optimal reactive power flow and voltage control through the dispatch center is the constructing component of the digital power system;
- Stationary operation, security and stability, no large rotating equipment, no mechanical noise, which greatly improve the life of the device;
- The storage capacitor of DC side of the STATCOM, not only regulates the reactive power system, but also be a part of the active power control system, which is beneficial to the grid;

---

W. Xie (✉) · J.-M. Duan  
Beijing University of Technology, Beijing 100124, China  
e-mail: xiew\_bj@hotmail.com

W. Xie · J.-M. Duan  
Beijing Polytechnic, Beijing 100176, China

- Compensating the instantaneous system voltage, even if the system voltage is reduced, it can still maintain the maximum reactive current [2]; reactive current generated from the STATCOM is basically not influenced by the system voltage;
- Terminal voltage of the STATCOM is not sensitive to the external system. When the external system capacity and the capacity of the compensation device capacity change, SVC will become unstable and STATCOM can still output the stable voltage.

Because of these advantages, STATCOM, as a novel device of dynamic reactive power, has become a modern reactive power compensation direction of development [3].

## 2 The Construction of the Mathematical Model of STATCOM

Figure 1 is a schematic wiring diagram of STATCOM, and the approach of input-output model can be used to build the model. Before modeling, there are some assumptions: All losses in the STATCOM and resistive devices, including the resistance of switching devices (such as IGBT and diode), are represented by equivalent resistance- $R$  [4]. Leakage inductance of the transformer and the circuit inductance are represented by equivalent inductance- $L$ , only considering the fundamental component of the output voltage and the non-periodic component and ignoring the other harmonic components [5].

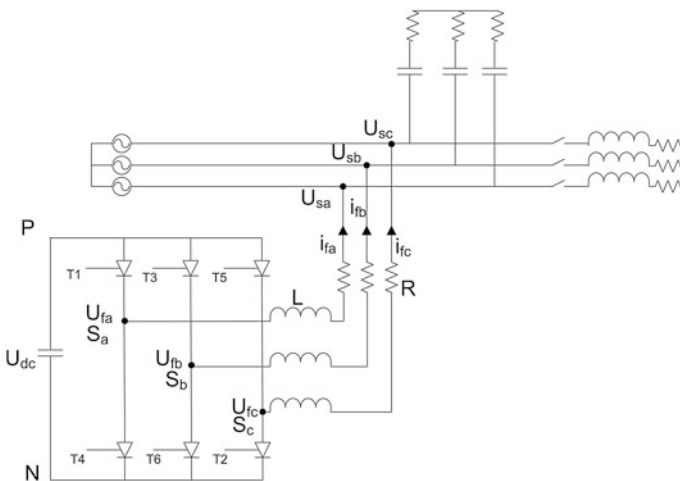


Fig. 1 STATCOM circuit diagram

Control variables: Switching function  $S_k$

$$S_k = \begin{cases} 1 & \text{on} \\ 0 & \text{off} \end{cases}$$

Control object: DC voltage  $U_{dc}$ , output current  $i_{fa}$ ,  $i_{fb}$ ,  $i_{fc}$ ;

Disturbance variable:  $U_{sa}$ ,  $U_{sb}$ ,  $U_{sc}$ ;

By controlling the switches,  $U_{dc}$  remains constant, while the STATCOM output current can track the instruction of current immediately, according to Kirchhoff's voltage and current law; the following equations can be written as [6]:

$$\begin{cases} C \frac{dU_c}{dt} = S_a i_{fa} + S_b i_{fb} + S_c i_{fc} \\ L \frac{di_{fa}}{dt} = U_{sa} - U_{fa} = U_{sa} - S_a U_{dc} - U_{N0} \\ L \frac{di_{fb}}{dt} = U_{sb} - U_{fb} = U_{sb} - S_b U_{dc} - U_{N0} \\ L \frac{di_{fc}}{dt} = U_{sc} - U_{fc} = U_{sc} - S_c U_{dc} - U_{N0} \end{cases} \quad (1)$$

Using the  $abc$ - $dq$  coordinate system and its inverse transform to transform Eqs. (1).

$$\begin{aligned} C \frac{dU_c}{dt} &= [S_a, S_b, S_c] \begin{bmatrix} i_{fa} \\ i_{fb} \\ i_{fc} \end{bmatrix} = [S_d, S_q] \begin{bmatrix} \cos(\omega t), \cos(\omega t - 2\pi/3), \cos(\omega t + 2\pi/3) \\ -\sin(\omega t), -\sin(\omega t - 2\pi/3), -\sin(\omega t + 2\pi/3) \end{bmatrix} \\ &= \begin{bmatrix} \cos(\omega t), -\sin(\omega t) \\ \cos(\omega t - 2\pi/3), -\sin(\omega t - 2\pi/3) \\ \cos(\omega t + 2\pi/3), -\sin(\omega t + 2\pi/3) \end{bmatrix} \begin{bmatrix} i_{fd} \\ i_{fq} \end{bmatrix} \\ &= [S_d, S_q] \begin{bmatrix} \frac{3}{2}, & 0 \\ 0, & \frac{3}{2} \end{bmatrix} \begin{bmatrix} i_{fd} \\ i_{fq} \end{bmatrix} = \frac{3}{2} (S_d i_{fd} + S_q i_{fq}) \end{aligned} \quad (2)$$

$$\begin{aligned} \begin{bmatrix} i_{fa} \\ i_{fb} \\ i_{fc} \end{bmatrix} &= \begin{bmatrix} i_{fd} \cos(\omega t) - i_{fq} \sin(\omega t) \\ i_{fd} \cos(\omega t - \frac{2}{3}\pi) - i_{fq} \sin(\omega t - \frac{2}{3}\pi) \\ i_{fd} \cos(\omega t + \frac{2}{3}\pi) - i_{fq} \sin(\omega t + \frac{2}{3}\pi) \end{bmatrix} \\ L \frac{di_{fa}}{dt} &= L \begin{bmatrix} \frac{di_{fd}}{dt} \cos(\omega t) - i_{fd} \omega \sin(\omega t) - \frac{di_{fq}}{dt} \sin(\omega t) - i_{fq} \omega \cos(\omega t) \\ \frac{di_{fd}}{dt} \cos(\omega t - \frac{2}{3}\pi) - i_{fd} \omega \sin(\omega t - \frac{2}{3}\pi) - \frac{di_{fq}}{dt} \sin(\omega t - \frac{2}{3}\pi) - i_{fq} \omega \cos(\omega t - \frac{2}{3}\pi) \\ \frac{di_{fd}}{dt} \cos(\omega t + \frac{2}{3}\pi) - i_{fd} \omega \sin(\omega t + \frac{2}{3}\pi) - \frac{di_{fq}}{dt} \sin(\omega t + \frac{2}{3}\pi) - i_{fq} \omega \cos(\omega t + \frac{2}{3}\pi) \end{bmatrix} \\ &= LT_{dq-abc} \begin{bmatrix} \frac{di_{fd}}{dt} \\ \frac{di_{fq}}{dt} \end{bmatrix} - \omega LT_{dq-abc} \begin{bmatrix} i_{fq} \\ -i_{fd} \end{bmatrix} = \begin{bmatrix} U_{sa}, & S_a, & 1 \\ U_{sb}, & S_b, & 1 \\ U_{sc}, & S_c, & 1 \end{bmatrix} \begin{bmatrix} 1 \\ -U_{dc} \\ -U_{N0} \end{bmatrix} \end{aligned} \quad (3)$$

$$\begin{aligned}
 L \begin{bmatrix} \frac{di_{fd}}{dt} \\ \frac{di_{fq}}{dt} \end{bmatrix} &= \omega L \begin{bmatrix} i_{fq} \\ -i_{fd} \end{bmatrix} + T_{dq-abc}^{-1} \begin{bmatrix} U_{sa}, & S_a, & 1 \\ U_{sb}, & S_b, & 1 \\ U_{sc}, & S_c, & 1 \end{bmatrix} \begin{bmatrix} 1 \\ -U_{dc} \\ -U_{N0} \end{bmatrix} \\
 &= \omega L \begin{bmatrix} i_{fq} \\ -i_{fd} \end{bmatrix} + T_{dq-abc}^T \begin{bmatrix} U_{sa}, & S_a, & 1 \\ U_{sb}, & S_b, & 1 \\ U_{sc}, & S_c, & 1 \end{bmatrix} \begin{bmatrix} 1 \\ -U_{dc} \\ -U_{N0} \end{bmatrix} \\
 &= \omega L \begin{bmatrix} i_{fq} \\ -i_{fd} \end{bmatrix} + \begin{bmatrix} U_{sd}, & S_d, & 0 \\ U_{sq}, & S_q, & 0 \end{bmatrix} \begin{bmatrix} 1 \\ -U_{dc} \\ -U_{N0} \end{bmatrix}
 \end{aligned} \tag{4}$$

In summary,

$$\begin{cases} L \frac{di_{fd}}{dt} = U_{sd} - S_d U_{dc} + \omega L i_{fq} \\ L \frac{di_{fq}}{dt} = U_{sq} - S_q U_{dc} - \omega L i_{fd} \end{cases} \tag{5}$$

$$C \frac{dU_c}{dt} = \frac{3}{2} (S_d i_{fd} + S_q i_{fq})$$

### 3 STATCOM Control

STATCOM control methods can be distributed into indirect current control or direct current control. The indirect control method, by the contrast of the direct control method, is simpler. However, the response speed of it is slower. Moreover, the control accuracy of it is not satisfactory. Direct control is a PWM control strategy which uses the appropriate track and controlling the instantaneous reactive current of STATCOM, and obtains the PWM pulse signal to drive IGBT [7]. This method has fast transient response and steady performance. The principle of the control is shown in Fig. 2.

In this method, since the introduction of dq0 coordinate system, the command current and the feedback current of STATCOM Id, Iq are DC signals in steady state,

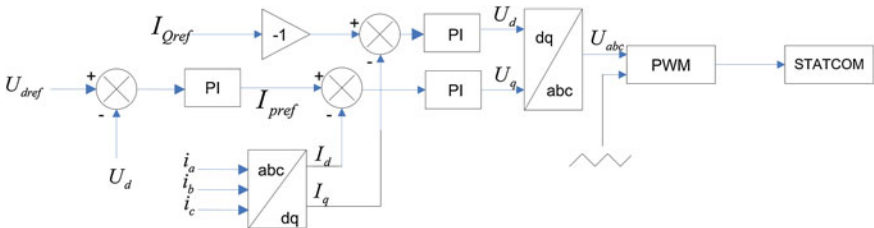


Fig. 2 PWM control method for direct current



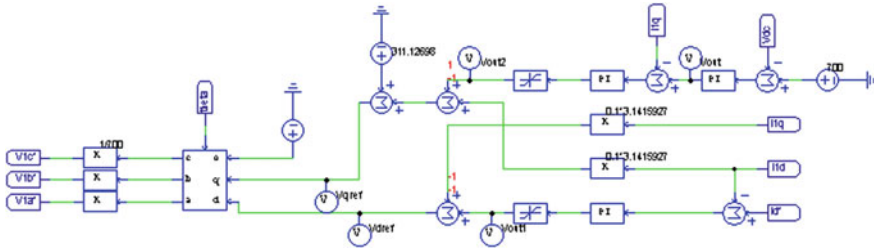


Fig. 3 Decoupling control circuit model diagram

so the steady state without error can be achieved by PI regulator [8]. In this mode, the characteristics of STATCOM are more like a controlled current source. In this simulation, the capacity of the STATCOM is 15 MVar, voltage rating is 10 kV, the frequency of switches are 15 kHz, Rms line current is 866 A, DC capacitor voltage is 17,000 V, the capacity of capacitor is 3505  $\mu$ F, and the value of inductance is 1.37 mH. The load:  $R = 1.55 \Omega$ ,  $L = 20$  mH:  $C = 0.5$  mF. According to the mathematical model, a control block diagram is shown in Fig. 3:

### 4 Analysis of Simulation Results

As shown in Figs. 4 and 5, the simulation model is structured in PSIM and simulates the model in different types of loads. In this design, the power system is connected inductive load and capacitive load at  $t = 0$  s and  $t = 0.2$  s, respectively, to verify the performance of the STATCOM.

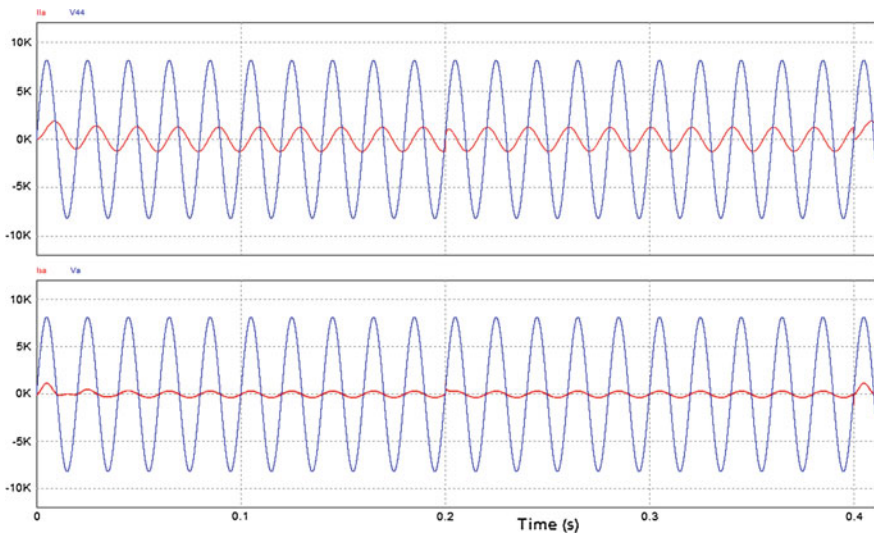


Fig. 4 The phase relationship of voltage and current before and after STATCOM

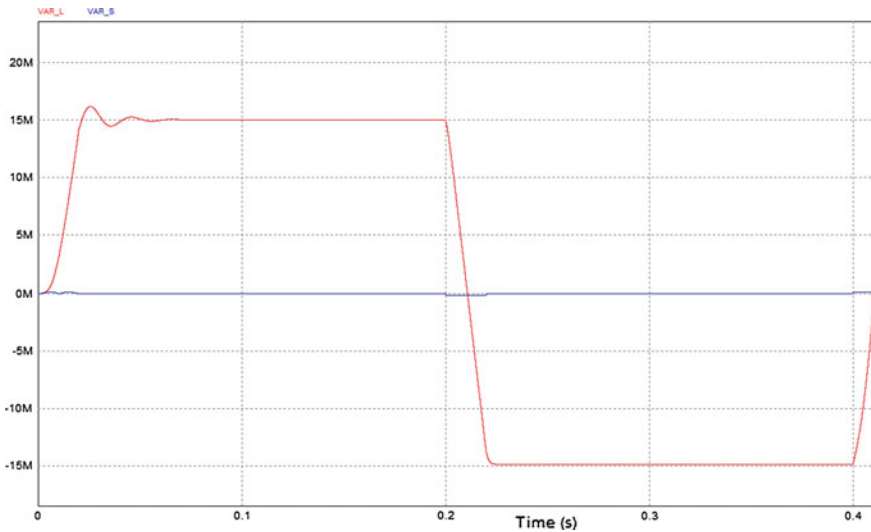


Fig. 5 The changes of the reactive power

## 5 Conclusions

This chapter describes the mathematical model of STATCOM. By using the PSIM software to create a direct current control model, from the analysis above, we can see the good compensation effects. STATCOM can effectively maintain the system voltage and reactive power compensation with good performance.

**Acknowledgments** The research work was supported by general program of science and technology development project of Beijing Municipal Education Commission under grant KM201510858004 and key program of Beijing Polytechnic under grant YZKB2014008.

## References

1. Chen W, Liang W, Gau H (2010) Design of a mode decoupling STATCOM for voltage control of wind-driven induction generator systems. *IEEE Trans Power Deliv* 3:1758–1767
2. Xiang Z, Xie D, Gong JX et al (2008) Dynamic characteristics analysis of STATCOM for reactive compensation in wind farm. *Autom Electr Power Syst* 32(9):92–95
3. Zhang CP, Jiang QR, Tong LY (2008) A decoupling-controlled STATCOM for power quality improvement of impact loads. In: *IEEE Asia Pacific conference*, pp 109–112
4. Wen XL, Yin XG, Cheng HX (2007) The general mathematical model and performance analysis of multi-pulse three-level STATCOM. In: *Electric machines & drives conference*, pp 760–765
5. Pelletier C, Goossenaerts J, Szirbik N (2001) A centralized translation interface based on the PSIM ontology. In: *International conference*, pp 653–656

6. Hochgraf C, Lasseter RH (1998) Statcom controls for operation with unbalanced voltages. *IEEE Trans Power Deliv* 13(2):538–544
7. Lu YM, Zhang B, Yin LY (2008) The switched affine linear system model and control of DC-DC converter. *CSEE* 28(15):16–22
8. Song ZZ, Ma XP, Wang Y (2012) D-STATCOM mathematical modelling and system simulation based on direct current control. *Electr Measur Instrum* 49(6):57–60

# The Design of Linear Three-Dimensional Calibration

Dequan Guo, Xinrui Zhang, Hui Ju, Hong Liu and Jin Chen

**Abstract** This paper introduces the concept of calibration techniques and a kind of commonly used calibration method for three-dimensional (3D) target feature points. In the experiment, firstly, to improve the accuracy of the information corner, we selected optimizing and preprocessing method appropriately, and SUSAN algorithm is used to extract corner information. As a reference or approximation, linear model is utilized to get the linear model parameters, and then, different points are selected in the iteration method for more accuracy. The experimental results demonstrate this designed method can obtain the camera calibration parameters accurately.

**Keywords** Three-dimensional calibration · Corner detection · Calibration parameters · Linear

---

D. Guo · X. Zhang · H. Ju  
Department of Automatic Control Engineering, Chengdu University  
of Information and Technology, Chengdu 610225, Sichuan, China  
e-mail: gdq20103@sohu.com

X. Zhang  
e-mail: 476611054@qq.com

H. Ju  
e-mail: juhui@cuit.edu.cn

H. Liu (✉)  
Sichuan University, Chengdu 610041, Sichuan, China  
e-mail: liuhong@scu.edu.cn

J. Chen  
Neijiang Vocational and Technical College, Neijiang 641100, Sichuan, China  
e-mail: 99241569@qq.com

## 1 Introduction

An important problem in machine vision is the vision system calibration [1–4]. Three-dimensional image information is collected by computer vision system, to establish characteristic relationship between objects in real 3D environment, such as size, color, position, shape, and the relationships among the geometry information, and these are used to identify the objects. The points in space objects, on the surface of the reflected light intensity which is through the brightness of the points from image, and the relationship between the geometric model of the camera position can be used to determine the location of points in the image and the geometric relationship of the corresponding points on surfaces, the geometric model used in the parameter, these are called the camera parameters. The relationship between the parameters is generally expressed by matrix form, which can be obtained through the experiment and calculation, and the process of experiment and calculation is camera calibration [2, 3]. In process of creating the relationship among the field sites, from the camera image pixel locations, the general method is employed for the known feature points of image coordinate and world coordinate model to calculate the camera parameters. The internal parameters refer to the scene in the Cartesian space points and image points, and the relationship between the objects and images is related to the image center, lens distortion, focal length, and so on. The external parameters are the scenery outside the coordinate system in the camera coordinate system [4].

For the camera calibration, the domestic and foreign scholars have proposed many methods, and some of these methods have been widely used in different environments. A three-dimensional target is placed at the front of the specified camera in the traditional camera calibration method, there are series of predictable target points, which are used as feature points, and these points are utilized to establish equation from the image coordinates and three-dimensional space coordinates. Solving the equation of inside and outside, the camera parameters can be obtained. In the Faugeras camera calibration method, four parameter model is adopted, and the known  $N$  points are used to solve  $2N$  orthogonal matrix equation [4].

## 2 Camera Model

For the purpose of obtaining the position of  $P$  in the image, it can be used the model in the ideal environment. This method is simple and efficient, which can be used to express the projection  $P'$  from the point  $P$ ; when the ligature from the center of light  $O$  to point  $P$  is associated with the image plane, this relationship is called perspective projection, or center projection; then, we can obtain the following:

$$x = f \frac{X_c}{Z_c} \quad y = f \frac{Y_c}{Z_c} \tag{1}$$

The point  $P$  in the space is corresponded to the coordinate  $(x, y)$  from the image and with the coordinate  $(X_c, Y_c, Z_c)$  in the camera system. The relationship is in matrix format and it can be changed to homogeneous coordinate:

$$Z_c \begin{bmatrix} x \\ y \\ 1 \end{bmatrix} = \begin{bmatrix} f & 0 & 0 & 0 \\ 0 & f & 0 & 0 \\ 0 & 0 & 1 & 0 \end{bmatrix} \begin{bmatrix} X_c \\ Y_c \\ Z_c \\ 1 \end{bmatrix} \tag{2}$$

It can be easy to obtain Eq. (3), and we can know that  $\alpha_x = f/dx$ ,  $\alpha_y = f/dy$ ,  $\alpha_x$  is scale factor on  $u$  axis,  $\alpha_y$  is scale factor on  $v$  axis,  $\mathbf{M}_1$  is camera inner parameter matrix,  $\mathbf{M}_2$  is the outside parameter matrix, and  $\mathbf{M}$  is a projection matrix with  $3 \times 4$ . Through the matrix relationship, the world coordinates of  $P$  can be determined and the relationship between the points  $P'$  in the camera imaging and the pixel coordinates can obtained.

### 3 Camera Calibration

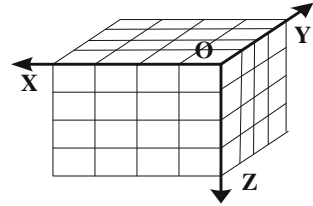
#### 3.1 Calibration Based on 3D Targets

Put the target in the front of the camera, as shown in Fig. 1, and select each corner from the target, and these are described as their feature points [2, 3].

$$\begin{aligned} Z_c \begin{bmatrix} u \\ v \\ 1 \end{bmatrix} &= \begin{bmatrix} \frac{1}{dx} & 0 & u_0 \\ 0 & \frac{1}{dy} & v_0 \\ 0 & 0 & 1 \end{bmatrix} \begin{bmatrix} f & 0 & 0 & 0 \\ 0 & f & 0 & 0 \\ 0 & 0 & 1 & 0 \end{bmatrix} \begin{bmatrix} \mathbf{R} & \mathbf{t} \\ \mathbf{0}^T & 1 \end{bmatrix} \begin{bmatrix} X_w \\ Y_w \\ Z_w \\ 1 \end{bmatrix} \\ &= \begin{bmatrix} \frac{f}{dx} & 0 & u_0 & 0 \\ 0 & \frac{f}{dy} & v_0 & 0 \\ 0 & 0 & 1 & 0 \end{bmatrix} \begin{bmatrix} \mathbf{R} & \mathbf{t} \\ \mathbf{0}^T & 1 \end{bmatrix} \begin{bmatrix} X_w \\ Y_w \\ Z_w \\ 1 \end{bmatrix} = \mathbf{M}_1 \mathbf{M}_2 \begin{bmatrix} X_w \\ Y_w \\ Z_w \\ 1 \end{bmatrix} \\ &= \mathbf{M} \begin{bmatrix} X_w \\ Y_w \\ Z_w \\ 1 \end{bmatrix} = \begin{bmatrix} m_{11} & m_{12} & m_{13} & m_{14} \\ m_{21} & m_{22} & m_{23} & m_{24} \\ m_{31} & m_{32} & m_{33} & m_{34} \end{bmatrix} \begin{bmatrix} X_w \\ Y_w \\ Z_w \\ 1 \end{bmatrix} = M_1 M_2 X_w = M X_w \end{aligned} \tag{3}$$

The more the accuracy in measurement, the more the precision in calculating angular point position. Accurate measurements of its position relative to the world

**Fig. 1** 3D target (calibration reference)



coordinate system can be made and then use these relationships from the feature point on the target image coordinate and world coordinate, and it is easy to determine the internal and external parameters of camera.

### 3.2 Model Calibration

The linear model of camera can be expressed as follows:

$$s_i \begin{bmatrix} u_i \\ v_i \\ 1 \end{bmatrix} = \begin{bmatrix} m_{11} & m_{12} & m_{13} & m_{14} \\ m_{21} & m_{22} & m_{23} & m_{24} \\ m_{31} & m_{32} & m_{33} & m_{34} \end{bmatrix} \begin{bmatrix} X_{wi} \\ Y_{wi} \\ Z_{wi} \\ 1 \end{bmatrix} \tag{4}$$

In the equation,  $(X_{wi}, Y_{wi}, Z_{wi}, 1)$ , the point I is the world coordinate in 3D target,  $(u_i, v_i, 1)$  is the corresponding image coordinate [2, 3], and this can be changed to three equations:

$$\begin{cases} s_i u_i = m_{11}X_{wi} + m_{12}Y_{wi} + m_{13}Z_{wi} + m_{14} \\ s_i v_i = m_{21}X_{wi} + m_{22}Y_{wi} + m_{23}Z_{wi} + m_{24} \\ v_i = m_{31}X_{wi} + m_{32}Y_{wi} + m_{33}Z_{wi} + m_{34} \end{cases} \tag{5}$$

To eliminate the  $s_i$  in Eq. (5), we can obtain Eq. (6):

$$\begin{cases} m_{11}X_{wi} + m_{12}Y_{wi} + m_{13}Z_{wi} + m_{14} - u_i m_{31} - u_i Y_{wi} m_{32} - u_i Z_{wi} m_{33} = u_i m_{34} \\ m_{21}X_{wi} + m_{22}Y_{wi} + m_{23}Z_{wi} + m_{24} - v_i m_{31} - v_i Y_{wi} m_{32} - v_i Z_{wi} m_{33} = v_i m_{34} \end{cases} \tag{6}$$

If N points are selected, there are 2N linear Eq. (7):

$$\begin{cases} m_{11}X_{wi} + m_{12}Y_{wi} + m_{13}Z_{wi} + m_{14} - u_i m_{31} - u_i Y_{wi} m_{32} - u_i Z_{wi} m_{33} = u_i m_{34} \\ m_{21}X_{wi} + m_{22}Y_{wi} + m_{23}Z_{wi} + m_{24} - v_i m_{31} - v_i Y_{wi} m_{32} - v_i Z_{wi} m_{33} = v_i m_{34} \\ \dots \\ m_{11}X_{wn} + m_{12}Y_{wn} + m_{13}Z_{wn} + m_{14} - u_n m_{31} - u_n Y_{wn} m_{32} - u_n Z_{wn} m_{33} = u_n m_{34} \\ m_{21}X_{wn} + m_{22}Y_{wn} + m_{23}Z_{wn} + m_{24} - v_n m_{31} - v_n Y_{wn} m_{32} - v_n Z_{wn} m_{33} = v_n m_{34} \end{cases} \tag{7}$$

and Eq. (7) can be simplified as:

$$\mathbf{KM} = \mathbf{U} \tag{8}$$

There,  $\mathbf{K}$ ,  $\mathbf{M}$ , and  $\mathbf{U}$ , respectively, define the parameters and matrix in Eq. (7), and then, we calculate the solution of the linear equations by least square, as follows:

$$\mathbf{M} = (\mathbf{K}^T \mathbf{K})^{-1} \mathbf{K}^T \mathbf{U} \tag{9}$$

From the above Eq. (9),  $m_{34}$  cannot affect the relationship between  $(X_w, Y_w, Z_w)$  and  $(u, v)$ ; for convenient operation, it can be assumed  $m_{34} = 1$ , and then, the unknown quantity is reduced to 11. Six known points are obtained, these 12 linear equations as Eq. (6) can be solved, and at last, the linear equations of the conventional method can solve the matrix  $\mathbf{M}$ .

If the selected points are located in one plane,  $(X_w, Y_w, Z_w)$  is linear correlation, and then, the rank of  $\mathbf{K}^T \mathbf{K}$  will be less than 11; it will not be able to obtain certain solutions of  $\mathbf{M}$ . And this situation requires that points are located in different plane, and the number is not less than 6 points, due to errors in the process of extracting angular point inevitably; in order to improve the accuracy, there are more fixed points.

Based on camera parameter matrix  $\mathbf{M}$ , it can further solve Eq. (3), intrinsic matrix parameters, and external parameter matrix of camera. Through the matrix, it can be determined the space point coordinates and its corresponding image point coordinate. In the matrix of the camera, the relationships between external parameters are listed as the following:

$$m_{34} \begin{bmatrix} m_1^T & m_{14} \\ m_2^T & m_{24} \\ m_3^T & 1 \end{bmatrix} = \begin{bmatrix} \alpha_x & 0 & u_0 & 0 \\ 0 & \alpha_y & v_0 & 0 \\ 0 & 0 & 1 & 0 \end{bmatrix} \begin{bmatrix} r_1^T & t_x \\ r_2^T & t_y \\ r_3^T & t_z \\ \mathbf{0}^T & 1 \end{bmatrix} \tag{10}$$

$$m_{34} \begin{bmatrix} m_1^T & m_{14} \\ m_2^T & m_{24} \\ m_3^T & 1 \end{bmatrix} = \begin{bmatrix} \alpha_x r_1^T + u_0 r_3^T & \alpha_x t_x + u_0 t_z \\ \alpha_y r_2^T + v_0 r_3^T & \alpha_y t_y + v_0 t_z \\ r_3^T & t_z \end{bmatrix} \tag{11}$$

Among them,  $m_i^T (i = 1, 2, 3)$  is expressed as the first three elements of row vector in the matrix,  $m_{i4} (i = 1, 2, 3)$  depicts matrix element of the first line of the fourth column,  $r_i^T (i = 1, 2, 3)$  depicts the first line of the rotation matrix, respectively, and  $t_x, t_y,$  and  $t_z$  are, respectively, the three components of translation vector  $\mathbf{t}$  [2, 3].

It can be obtained from Eq. (11); according to the equal relationship, compare both sides of Eq. (11) corresponding elements, and because the third row of the matrix is the unit orthogonal  $|r_3| = 1$ , and thereby  $m_{34} = 1/|m_3|$ , this numerical



value is not necessary from the front assumption; it can be obtained by calculation. The available internal and external parameters are listed as the following:

$$\text{Parameter 1: } \begin{cases} r_3 = m_{34}m_3 \\ u_0 = (\alpha_x r_1^T + u_0 r_3^T)r_3 = m_{34}^2 m_1^T m_3 \\ v_0 = (\alpha_x r_1^T + u_0 r_3^T)r_3 = m_{34}^2 m_2^T m_3 \\ \alpha_x = m_{34}^2 |m_1 \times m_3| \\ \alpha_y = m_{34}^2 |m_2 \times m_3| \end{cases} \quad (12)$$

$$\text{Parameter 2 : } \begin{cases} r_1 = \frac{m_{34}}{\alpha_x} (m_1 - u_0 m_3) \\ r_2 = \frac{m_{34}}{\alpha_y} (m_2 - v_0 m_3) \\ t_z = m_{34} \\ t_y = \frac{m_{34}}{\alpha_y} (m_{24} - v_0) \\ t_x = \frac{m_{34}}{\alpha_x} (m_{14} - u_0) \end{cases} \quad (13)$$

In Eq. (12),  $x$  is the vector product operators; usually the first five variables are calculated firstly, and then, obtained variables are used to solve the behind variables.

### 4 SUSAN Corner Detection

Minimum nuclear value similar area algorithm (SUSAN) [5] is a common typical corner detection algorithm. This algorithm is based on the change of the gray level to the defined point (corner). Figure 2 shows a black rectangle on a white background of the image, with a template center in the positions of the five graphics. In this algorithm, firstly define the value of a nuclear similar USAN. USAN area is constituted by the defined round area (the center called the “nuclear,” and its size is determined by the template boundary) with size of  $3 * 3$ ,  $5 * 5$  or  $7 * 7$ , the gray values of each pixel area are compared with the regional center pixel gray value, pixels and the center pixel gray value around looking for the same (or similar) of all pixels, in order to gain such an area (or template), the “cross-shaped” symbols for template center position, these relations are shown in Fig. 2a. Use this template to traverse the whole image, and the position relations are shown in Fig. 2b–e.

From USAN, the center of mass and the size of the second-order differential good 2nd image feature detection and edge information; it is shown in Fig. 2; when half part of the template is identical with USAN, the points are located at the margins; when testing the pixel points for possible angle, minimum USAN area, and combining the maximum inhibition method, it is easy to obtain the final prayer corners.

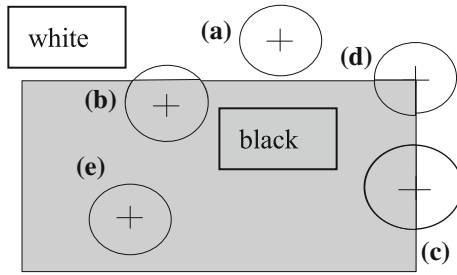


Fig. 2 Round templates are in the different place in the image

### 5 Experiment Results

Camera calibration:

Figure 4 shows the result of the corner extraction from Fig. 3, in the preprocessing, to get more clear images and reduce redundant points and lines, and dilate processing is used to achieve better result. In view of the image characteristics, to build a tilt to the lower right of the template, the method of plus and subtract is used to remove line between pixels, and then, the required feature points are more obvious.

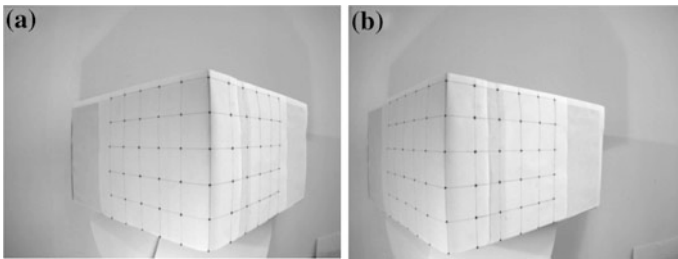


Fig. 3 a Left image. b Right image

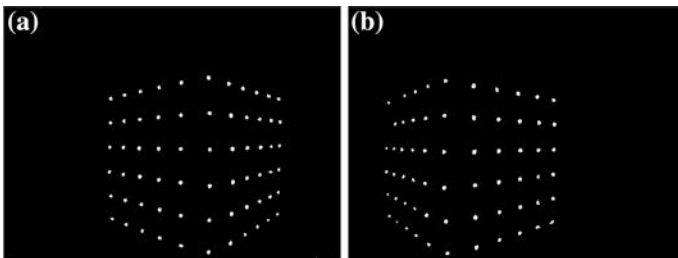
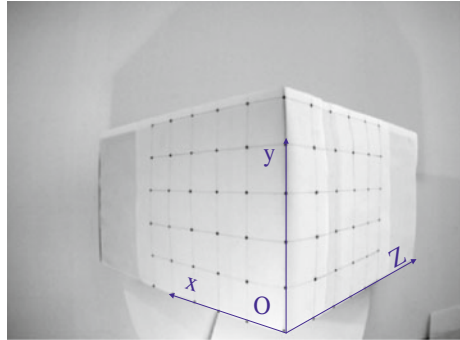


Fig. 4 a Left preprocess image. b Right preprocess image

Fig. 5 Calibration coordinate



In Fig. 5, there are last two points in the top-left on the plane  $XOY$ , and there are some work to compensate for the lack of points. The unit is mm in world coordinates, and the unit is pixel in image pixel coordinates. According to the calibration method, all the selected points on the target are 66 and 50. It can obtain the left and right camera parameter for  $M$  matrix, respectively. To improve the accuracy of the above two values and have the data normalized (the next digit by the processing of rounding), then:

The left the camera parameters,  $M$  matrix is

$$\begin{bmatrix} -0.2609 & -0.0058 & 1.5598 & 147.3060; \\ 0.6146 & -1.3761 & 0.4955 & 384.1811; \\ 0.0030 & -0.0001 & 0.0024 & 263.1118 \end{bmatrix}$$

$$u_0 = 200.9742, v_0 = 211.1091, \alpha_x = 363.9121, \alpha_y = 359.7801$$

$$t_x = -38.7434, t_y = 126.2439, t_z = 263.1180$$

$$r_1 = [-0.6213 \quad -0.0016 \quad 0.7836]$$

$$r_2 = [-0.0239 \quad -0.9995 \quad 0.0188]$$

$$r_3 = [0.7832 \quad 0.0096 \quad 0.6210]$$

The right parameter,  $M$  matrix is:

$$\begin{bmatrix} -0.4183 & -0.0855 & 1.6569 & 308.8876; \\ 0.3289 & -1.3673 & 0.5143 & 376.2924; \\ 0.0019 & -0.0003 & 0.0027 & 308.4201 \end{bmatrix}$$

$$u_0 = 346.6006, v_0 = 222.4963, \alpha_x = 397.8617, \alpha_y = 404.6844$$

$$t_x = 29.2764, t_y = 117.2057, t_z = 308.4201$$

$$r_1 = [-0.8201 \quad 0.0050 \quad 0.5720]$$

$$r_2 = [-0.0627 \quad -0.9964 \quad -0.0575]$$

$$r_3 = [0.5696 \quad -0.0830 \quad 0.8176]$$

There are some deviations in calibration parameters: (1) The accuracy of the calibration is not high; (2) the process of extraction control points may cause a certain error, because the pixels in the processing of obtaining may have some deviation to the real value. The second row is obvious instance in the right eye diagram, and there is missing a point, which can be roughly estimated by up and down points. To reduce the error, we can choose more points to validate matrix. The next step is to imitate planar reference calibration method to improve it.

## 6 Summary

This paper analyzes the common calibration methods and has done the calibration experiment with general linear calibration model. Through 3D targets to establish a three-dimensional coordinate system, it extracts the corner in the calibration graph information, according to the linear model, to calculate the calibration parameters and then determines the internal and external parameters of the camera.

There are some works to improve it, and Newton–Raphson (NP) algorithm or Levenberg–Marquardt (LM) optimization algorithm will help to optimize and then calculate the solution of nonlinear model. By choosing linear model, the calibration error is difficult to avoid, because select all points to solve the equations, and then select the removed edges of the intermediate point calculation, an average of two parts; therefore, the error data are reduced less. To further improve the effect, we will combine nonlinear model method to explore it.

**Acknowledgments** The work is supported by the Scientific Research Foundation of CUIT, Project (KYTZ201417, KYTZ201320), and also supported in part by the National High Technology Research and Development Program of China (863 Program, Grant No. 2013AA013802) and Foundation of China and Natural Science Foundation of Sichuan Province (Grant No. 2013GZX0147-3). The authors also gratefully acknowledge the helpful comments and suggestions of the reviewers, which have improved the presentation.

## References

1. Zhang G (2005) Machine vision [M], vol 6. Beijing: Science Press, pp 5–11
2. Zhang G (2008) Visual measurement, vol 5. Beijing: Science Press, pp 9–15. 10-36102-128, 134-36102
3. Ma S, Zhang Z (2003) Computer vision—calculating theory and algorithm, vol 9(1). Beijing: Science Press, pp 5–8, 52–67
4. Xu D, Tan M, Li Y (2008) Robot vision measurement and control, vol 2. Beijing: National Defense Industry Press, pp 23–25, 39–66, 120–139
5. Smith SM, Brady JM (1995) SUSAN—a new approach to low level image processing, technical report TR95SMS1c, pp 1–53

# Design and Development of LED Dimming System Based on Wireless Remote and Bluetooth Control Technologies

Yiwang Wang, Bo Zhang, Sikui Wu, Xiang Cang and Xiaoxiao Li

**Abstract** LED illumination has good dimming characteristics, aiming at the application requirements of intelligent lighting and other application fields, and a novel LED lighting dimming control system based on wireless remote and Bluetooth control technologies was designed. The system can simultaneously achieve control by remote or Bluetooth wireless terminal devices (such as smart-phone), and the system also has open- and closed-loop control optional modes to meet different needs. The system composition was described and presented in detail, and the system hardware and software design principles were given. Finally, the experimental results show that the system can achieve good dimming control functions, with good usability.

**Keywords** LED illumination · Wireless remote control · Intelligent dimming · Bluetooth technology

---

Y. Wang (✉) · B. Zhang · S. Wu · X. Cang · X. Li  
School of Electronics and Information Engineering,  
Suzhou Vocational University, Suzhou 215104, China  
e-mail: wyiwang@163.com

B. Zhang  
e-mail: 76163186@qq.com

S. Wu  
e-mail: 874358487@qq.com

X. Cang  
e-mail: 951253606@qq.com

X. Li  
e-mail: 834707939@qq.com

## 1 Introduction

With the development of LED technologies and improvement efficiency of LED luminous efficiency. The LED luminous with high efficiency, long life, energy saving, and environmental pollution has become a new generation of energy-efficient lighting, widely used in lighting and other fields [1–3]. Due to LED operating characteristics, LED is a current-type device, which has relatively high requirements of the magnitude and stability of operating current.

Thus, one of the key technologies of LED lighting is that the power supply or the drive circuit is adaptable to the LED's characteristics [4]. Currently, LED's drive power supply has constant voltage and two types of constant current, among of them the constant current drive is a common way. The constant current drive can eliminate temperature and process variations and other factors caused the current or voltage variations, and then guarantee a constant LED brightness [5]. Brightness adjustment and LED lighting control are achieved by adjusting the constant current value of drive power supply.

The LED lighting has good control characteristics, which can develop LED lighting products with different dimming performance. With the rapid development of the short-range wireless communication technologies, using the wireless control can achieve the LED intelligent remote dimming control. But a single-wireless remote control means which need to configure a special remote control device. Bluetooth technology is a low-power, low-cost, and high-speed bidirectional wireless communication, which use decentralized network architecture and fast frequency hopping and short packet technology [6]. Meanwhile, with the popularity and development of smartphones, Bluetooth technology is also increasing rapidly [7].

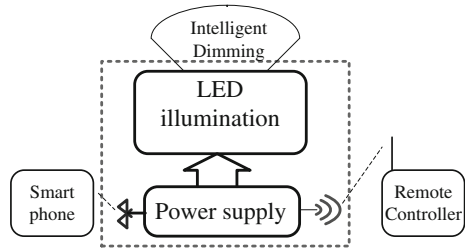
In this paper, combining both advantages of wireless remote control and Bluetooth technologies, LED intelligent dimming illumination system based on wireless remote and Bluetooth technologies was designed. The system can provide different control dimming modes depending on the users' needs. The designed system has advantages of flexible and convenient. The system components, hardware development, and software design were introduced, and the system was validated.

## 2 System Structure and Operation Principle

### 2.1 System Structure

The designed system structure shown in Fig. 1 includes driver power supply, remote controller, and smartphone Bluetooth control devices. The intelligent LED system can receive control commands from the remote controller and also receive control commands from the smartphone Bluetooth control devices.

**Fig. 1** System structure



## 2.2 Operation Principle

LED illumination is a semiconductor electroluminescent device with unidirectional conductivity, and its equivalent model is shown in Fig. 2 [8–10].

When using constant current driver, through regulating the value of LED drive current  $I_{led}$  can change the brightness of LED lighting. Designed dimming system control diagram is shown in Fig. 3. In order to improve the control precision, increase the current/light intensity feedback as closed-loop control. But in the case of general dimming less precision, which can be directly used open-loop control method. The remote control instructions through control system are converted into a duty cycle control signal of LED drive current and then regulated the output current to achieve dimming control.

**Fig. 2** LED illumination equivalent circuit

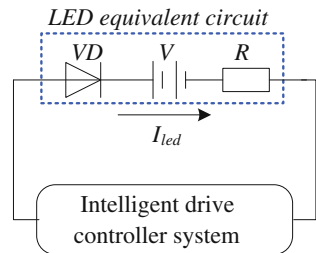
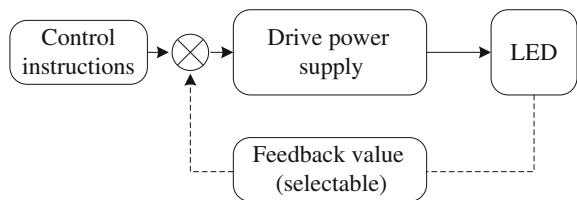


**Fig. 3** Lighting control system block diagram



### 3 System Design and Implementation

#### 3.1 System Hardware Design

The system uses a high-performance MCU as the main control chip architecture; system hardware includes MCU module, wireless remote communication module, Bluetooth communication module, LED constant current driver module, and other circuit modules. The hardware system block diagram is shown in Fig. 4.

MCU module selected STC15W408AS [11], which is a high-performance MCU chip, containing UART, SPI, and PWM functions, and the MCU can meet the design requirements. Wireless remote control receiver module circuit used SYN480R module, and the SYN480R module is mainly used in wireless RF remote fields, with higher sensitivity; and it can be applied to LED dimming remote control needs, and its output port is connected with the MCU. The Bluetooth wireless communication module used the SPI port connected with the MCU. The wireless communication connected circuits as shown in Fig. 5.

LED constant current driver power supply used a constant current driver control chip and PWM dimming circuit [12, 13]. Through the MCU microcontroller output, PWM control signals adjust its current value, enabling LED dimming control. In this design, the systems have a three-way dimming control output signals. The control circuit diagram is shown in Fig. 6.

For more high-precision control application fields, the design also provides closed-loop illumination control. Through digital optical sensor lighting TSL2561T collect information, then complete the online real-time closed-loop control functions.

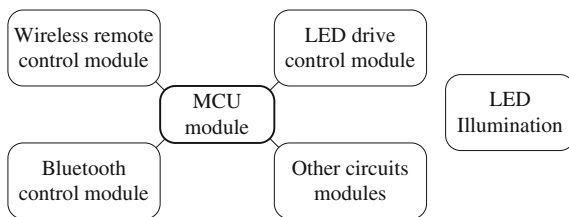


Fig. 4 The hardware system block diagram



Fig. 5 Wireless remote communication circuit connection diagram



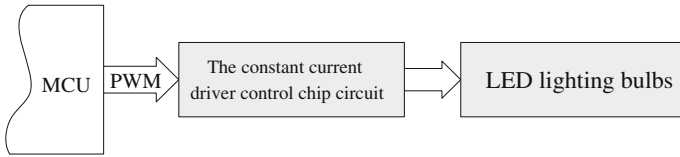


Fig. 6 LED dimming circuit diagram

The selected high-precision digital light sensor as capture illumination devices is collected by the MCU AD channel. Information is collected through the MCU AD channel.

### 4 System Software Design

System software includes two parts: remote control software and dimming control software, and the remote control software is divided into wireless remote software and Bluetooth control terminal software. The MCU receives dimming control software instruction through the wireless remote control or Bluetooth control terminal software, according to the instruction, and achieves the appropriate dimming control. Remote commands include command buttons, and dimming and switching commands, which is controlled by a preset protocol and control protocol that includes a start code, function code, instructions, check code, and other components.

Bluetooth intelligent terminal control software, using wireless control APP software, is based on Android system. The software includes two parts a communication process and dimming control. Through smartphone software, LED lighting dimming control can be achieved. The entire system software is shown in Fig. 7.

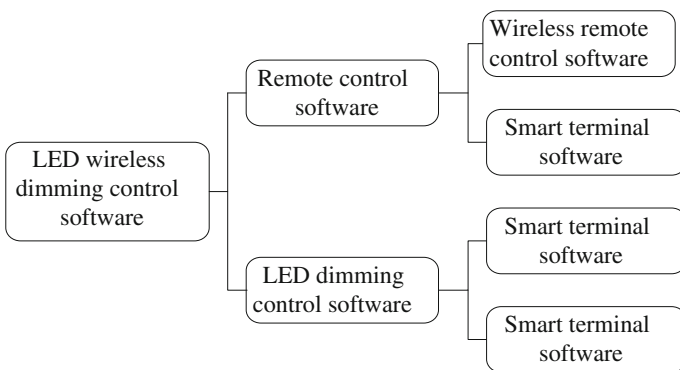
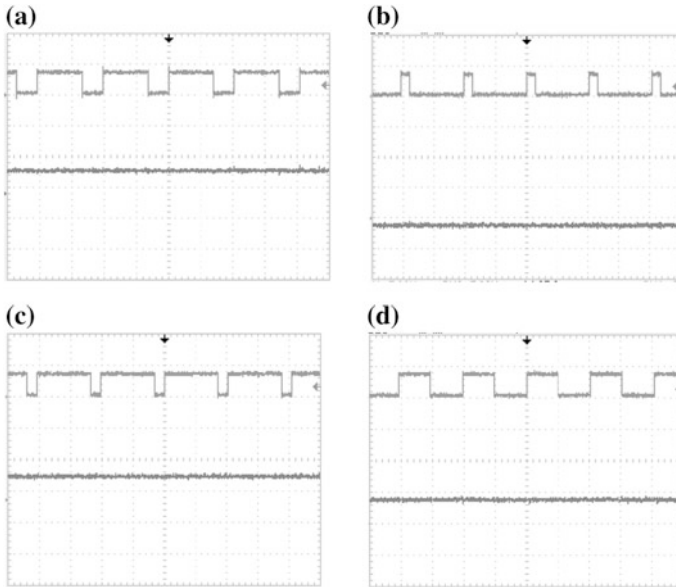


Fig. 7 System software composition structure diagram



**Fig. 8** Experimental test waveforms. **a** 70 % dimming. **b** 28 % dimming. **c** 83 % dimming. **d** 50 % dimming

## 5 System Testing and Verification

The experimental tests on designed prototype control system were carried out. The test load is LED lighting bulbs. Using the remote control and Bluetooth, different dimming modes were tested, and some of the test experimental waveforms are shown in Fig. 8, the waveforms results compared with the control instructions, and analysis results of the designed control system can be accurately controlled in accordance with the remote control dimming commands, and achieve the desired control effect and indicators.

## 6 Conclusions

In this paper, a novel LED intelligent dimming illumination system based on wireless remote and Bluetooth technologies was designed, and the system combined with wireless remote control and Bluetooth two technologies has good versatility and flexibility advantages. Simultaneously, the system has two optional modes, open- and closed-loop control, to meet different application needs. Hardware and software systems were developed and implemented, and verified by experimental prototype test system. The designed system will provide a new way for LED dimming control technology and has theoretical and practical values.

**Acknowledgments** The research work was partly supported by the 2014 Senior Talent Culture Project of Suzhou, Scientific Research Achievement Innovation Foundation of Suzhou Vocational University, and Jiangsu Qing Lan Project.

## References

1. Kai Y, Xinbo R, Beibei W et al (2008) The 4th generation of light source LED. The world of power supply 3:21–26
2. Zhu B, Luo Q, Wang Y, Zhou L (2013) High step-down constant current LED driver with multiple-output. *Trans China Electrotech Soc* 28(6):178–183
3. Zhang X, Yan L, Xia W, Yang Z (2009) HB-LED drive strategy summarization. *China Light Lighting* 12:17–19
4. Yang Y, Zhao M, Lu J, Li F, Wu X (2010) Controller IC design for high-brightness white LED driver. *J Zhejiang Univ (Eng Sci)* 44(1):111–117
5. Chen Y, Feng Q (2010) Hysteresis current control in the constant current driving for LED. *Microelectron Comput* 27(6):193–196
6. Tu Z, Feng Y (2014) Study of digitalized control system for welding power source based on bluetooth communication. *Electr Weld Mach* 44(7):17–22
7. Wang H (2013) Appliance control system based on bluetooth network. *Chin J Electron Devices* 36(4):523–526
8. Marques LS, Sá Jr. EM, Antunes FLM, Perin AJ (2005) Step down current controlled dc-dc converter to drive a high power led matrix employed in an automotive headlight. In: COBEP 05-8° Brazilian power electronics conference, pp 474–478
9. Sá Jr. EM, Antunes FLM, Perin AJ (2007) Junction temperature estimation for high power light-emitting diodes. In: IEEE-International symposium on industrial electronics—ISIE, pp 3030–3035
10. Sá Jr. EM, Antunes FLM, Perin AJ (2008) Low cost self-oscillating ZVS-CV driver for power LEDs. In: IEEE Power electronic, specialists conference, pp 4196–4201
11. [www.stcmcu.com](http://www.stcmcu.com)
12. [www.silan.com.cn](http://www.silan.com.cn)
13. Zhang Q, Yang X, Zhang Z, Lu Q (2012) Design and realization of serial communication in bluetooth module. *Res Explor Lab* 31(3):79–82

# Open PID-Type Iterative Learning Control for Linear Time-Invariant System

Xuelian Zhou and Qiang He

**Abstract** Open PID-type Iterative learning control (ILC) is an effective and simple approach for the control of linear time-invariant system which performs the same task repetitively. In this paper, the open PID-type ILC is studied for linear time-invariant (LTI) systems, which uses the proportional, derivative and integral parameter of the tracking error to update the input variables iteratively. The paper analyzes the convergence of the open PID-type. According to the PID parameters, its convergence condition is got. By selecting appropriate gains parameters of the open PID-type ILC system, the output of the open PID-type iterative learning control system converges to desired output monotonically. The absolute error between the desired output and the actual output converges to zero faster. The simulation results show that the open PID-type ILC system in the paper is stable, effective and has high performance.

**Keywords** Iterative learning control (ILC) · Open PID-type ILC · Convergence · Simulation

## 1 Introduction

It is well known that iterative learning control (ILC) has been able to determine a control input iteratively. The output of control system can track the desired trajectory over a fixed time interval very well [1]. The ILC algorithm has been offered by Arimoto in 1984 [2]. ILC is a new control algorithm, which is mainly applied in the repetitive motion control. It can realize completely tracking task over a fixed time interval. The applications of ILC have been widely utilized in many fields,

---

X. Zhou · Q. He (✉)  
College of Computer and Information Science, Southwest University,  
Chongqing 400715, China  
e-mail: heq@swu.edu.cn

X. Zhou  
e-mail: xlz@swu.edu.cn

such as system identification [3], robotic assembly [4], electromechanical systems [5], motion control system [6], and industrial processes [7]. In the design phase of controller, the requirement of knowledge about control system can be minimized, i.e., one of the attractive features of ILC.

Despite the continual advanced control theory, PID controller is still widely applied in many industry fields [8]. This is due to its effectiveness, simple structure, and robustness. Consequently, the design of iterative learning control schemes usually utilizes PID strategy.

## 2 Principle of Iterative Learning Control

The principle of ILC is demonstrated in Fig. 1. All signals illustrated are assumed to be defined on a finite interval. The subscript  $j$  denotes the number of operation cycle. The principle of the scheme is as follows: An input  $u_j(t)$  is used to the system during the  $j$ th trial. Then, it generates the output  $y_j(t)$ . The error between the desired trajectory and the actual trajectory expresses as Eq. 1. The ILC algorithm calculates a modified control input  $u_{j+1}(t)$  which will be stored in memory units until the next trial, at which time the new control input is used to the control system. The new control input should be designed to generate a smaller error than the previous control input [9]. The control task of ILC is to find an appropriate control input sequences which will cause the output trajectory to track the desired trajectory very well as the iteration  $j$  increases.

$$e_j(t) = y_d(t) - y_j(t) \tag{1}$$

A linear time-invariant system expresses as Eq. 2

$$\begin{aligned} \dot{x}(t) &= Ax(t) + Bu(t) \\ y(t) &= Cx(t) \end{aligned} \tag{2}$$

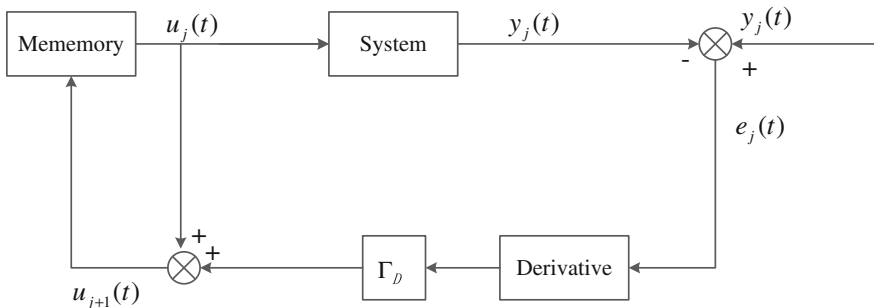


Fig. 1 Open D-type ILC scheme

where  $t \in [0, T]$  and  $y(t)$ ,  $x(t)$  and  $u(t)$  are output, state, and control variables, respectively. Output  $y(t)$  is able to measure.

In 1984, the ILC learning control algorithms expressed as Eq. 3 by Arimoto, which is called open D-type ILC algorithm. Its principle is demonstrated in Fig. 2.

$$u_{j+1}(t) = u_j(t) + \Gamma_D \dot{e}_j(t) \tag{3}$$

The desired output of the linear time-invariant system is described as Eq. 4:

$$x_d(t) = e^{At}x_d(0) + \int_0^t e^{A(t-x)}Bu_d(x)dx \tag{4}$$

$$y_d(t) = Cx_d(t)$$

where  $x_d(t)$ ,  $u_d(x)$ , and  $x_d(0)$  are desired state variables, desired control input sequences, and desired initial state, respectively.

According to Eq. 3,  $\Delta u_{j+1}(t)$  can be expressed as Eq. 5

$$\Delta u_{j+1}(t) = \Delta u_j(t) - \Gamma_D \dot{e}_j(t) = \Delta u_j(t) - \Gamma_D C \frac{d}{dt} \int_0^t e^{A(t-x)}B\Delta u_j(x)dx \tag{5}$$

Simplifying Eqs. 5 and 6 can be obtained as

$$\Delta u_{j+1}(t) = (I - \Gamma_D C B)\Delta u_j(t) - \int_0^t \Gamma_D C A e^{A(t-x)}B\Delta u_j(x)dx \tag{6}$$

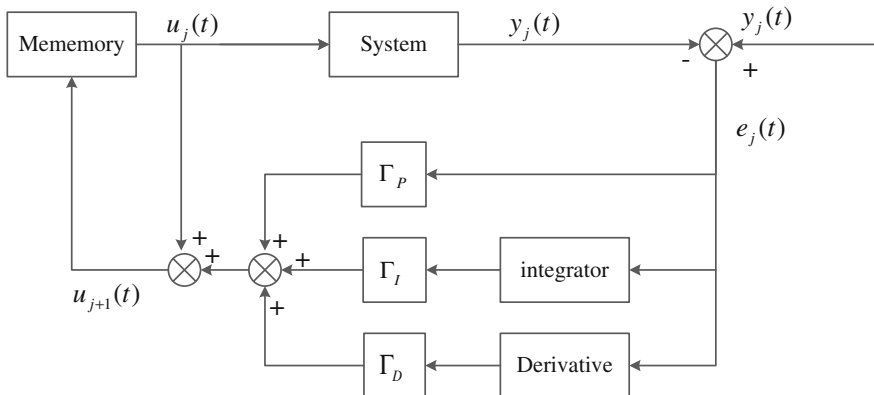


Fig. 2 Open PID-type ILC scheme

where  $\Delta u_j(t) = u_d(t) - u_j(t)$

The norm of Eq. 6 is got described as Eq. 7:

$$\|\Delta u_{j+1}(t)\| \leq \|I - \Gamma_D CB\| \|\Delta u_j(t)\| + \int_0^t \|\Gamma_D CA e^{A(t-x)} B\| \|\Delta u_j(x)\| dx \quad (7)$$

In Eq. 7,  $\|\cdot\|$  is the matrix norm [10].

Multiplied by  $e^{-\lambda t}$ , Eq. 8 is expressed as follows:

$$e^{-\lambda t} \|\Delta u_{j+1}(t)\| \leq \|I - \Gamma_D CB\| e^{-\lambda t} \|\Delta u_j(t)\| + b_1 \int_0^t e^{-\lambda(t-x)} e^{-\lambda x} \|\Delta u_j(x)\| dx \quad (8)$$

where  $b_1 = \sup_{t \in [0, t_f]} \|I - \Gamma_D CA e^{At} B\|$

The definition of  $\lambda$  norm is described as Eq. 9:

$$\|\Delta u_{j+1}(t)\|_\lambda \leq (\|I - \Gamma_D CB\| + b_1 \frac{1 - e^{-\lambda t}}{\lambda}) \|\Delta u_j(t)\|_\lambda \quad (9)$$

If  $\|I - \Gamma_D CB\| + b_1 \frac{1 - e^{-\lambda t}}{\lambda} < 1$ , the  $\lambda$  norm of  $\Delta u_j(t)$  will converges to 0. When  $\lambda$  is large enough,  $\|I - \Gamma_D CB\| < 1$ , and the  $\lambda$  norm of  $\Delta u_j(t)$  will converges to 0.

The error between output and desired output is described as Eq. 10.

$$e_j(t) = \int_0^T C e^{A(t-x)} B \Delta u_j(x) dx \quad (10)$$

The  $\lambda$  norm of  $e_k(t)$  is described as Eq. 11:

$$\|e_j(t)\|_\lambda \leq \|C\| \|B\| \frac{1 - e^{(\|A\| - \lambda)t_f}}{\lambda - \|A\|} \|\Delta u_j\|_\lambda \quad (11)$$

where  $\lambda > \|A\|$

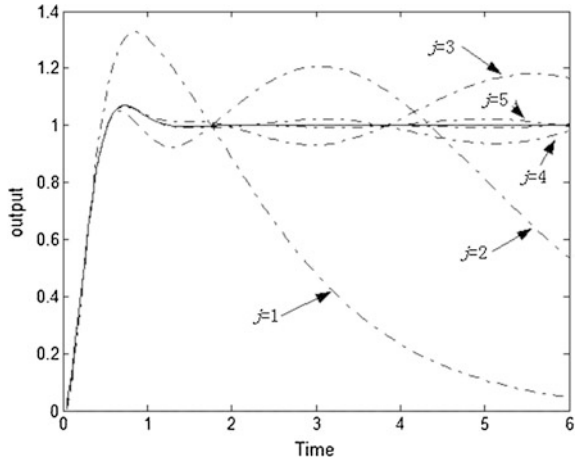
According to Eqs. 10, 11 and 12 can be expressed:

$$\lim_{j \rightarrow \infty} \sup_{t \in [0, T]} \|e_j(t)\| = 0 \quad (12)$$

If  $\|I - CB\Gamma_D\| < 1$ , then the error converges to zero. In other words,  $\lim_{j \rightarrow \infty} e_j(t) = 0$ .

The open PID-type ILC algorithm is expressed as Eq. 13. Its scheme is shown in Fig. 3.

**Fig. 3** Tracking performance of the open PID-type ILC system outputs at different iteration numbers



$$u_{j+1}(t) = u_j(t) + \Gamma_P e_j(t) + \Gamma_D \dot{e}_j(t) + \Gamma_I \int_0^t e_j(x) dx \tag{13}$$

$\Gamma_P$ ,  $\Gamma_D$ , and  $\Gamma_I$  are real constant coefficients, which are called as proportional, derivative, and integration learning coefficients, respectively.

Convergence conditions are expressed as Eq. 14:

$$\left. \begin{aligned} \|I - CB\Gamma_P\| < 1 \\ \|I - CB\Gamma_D\| < 1 \\ \|I - CB\Gamma_I\| < 1 \end{aligned} \right\} \tag{14}$$

where  $I$  is a unit matrix.

### 3 Simulation Experiment

The closed-loop transfer function of typical second-order control system of reference model is given as follows:

$$\Phi(s) = \frac{\omega_n^2}{s^2 + 2\zeta\omega_n s + \omega_n^2} \tag{15}$$

The time-domain specifications of second-order control system are given as follows:



- Overshoot  $\sigma_p$  is no less than 7 %.
- Settling time  $t_s$  is no less than 1.5 s.
- Stable error is no greater than 0.02.

The damping ratio is determined by Eq. 16.

$$\zeta = \frac{\ln(1/\sigma_p)}{\sqrt{\pi^2 + (\ln(1/\sigma_p))^2}} = 0.646 \quad (16)$$

The value of settling time  $t_s$  is 1.2. The undamped natural frequency is determined by Eq. 17.

$$\omega_n = 4.4/\zeta t_s = 5.675 \quad (17)$$

The damped oscillatory frequency is determined by Eq. 18:

$$\omega_d = \omega_n \sqrt{1 - \zeta^2} = 4.33 \quad (18)$$

The desired output is described as Eq. 19:

$$y_d(t) = 1 - \frac{1}{\sqrt{1 - \zeta^2}} e^{-\zeta \omega_n t} (\sqrt{1 - \zeta^2} \cos(\omega_d t) + \zeta \sin(\omega_d t)) \quad (19)$$

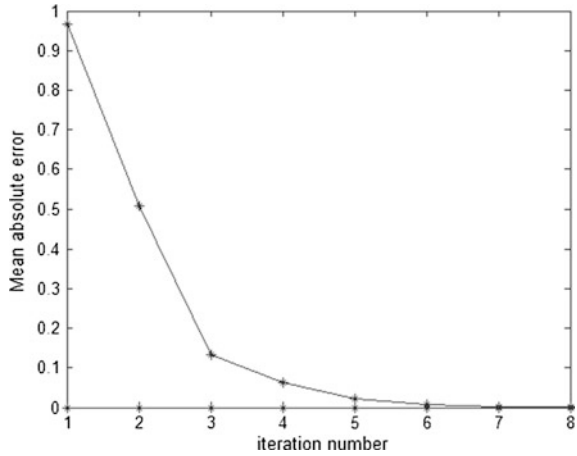
The linear time-invariant system model is described as Eq. 20:

$$A = \begin{bmatrix} 0 & 1 \\ -1 & -2 \end{bmatrix}, B = \begin{bmatrix} 0 \\ 1 \end{bmatrix}, C = [0 \quad 1] \quad (20)$$

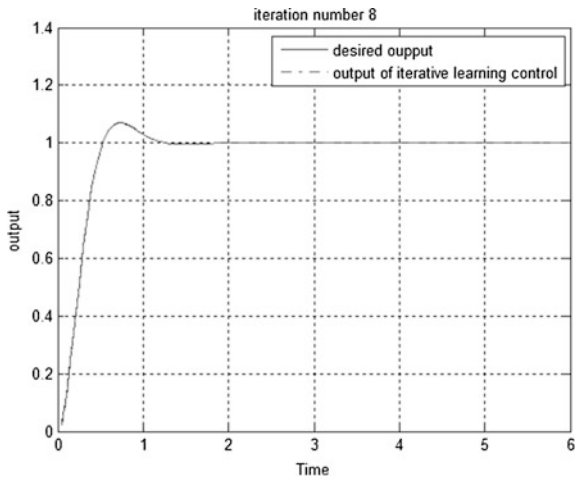
According to Eq. 14,  $\Gamma_P = 2.8, \Gamma_I = 5.7, \Gamma_D = 0.77$  are the gains parameters selected in the open PID-type ILC system.

Figure 3 shows the desired output  $y_d(t)$  (solid curve) and the actual output  $y_j(t)$  (other curves) for  $k = 1, 2, 3, 4,$  and  $5$ . As Fig. 3 indicates, by increasing the iteration number, the output of open PID-type iterative learning control system can converge to the desired output faster. Figure 4 demonstrates that the average absolute error between the desired output and the actual output changes as iteration  $j$  increases. It can be seen that with the increase of the iteration times, the average absolute value of errors of the output trajectory is quickly converging to 0. It indicates that the convergence in the open PID-type iterative learning control system is monotonic. Figure 5 shows output of open PID-type iterative learning control system tracks the desired output very well at 8th iteration number. These models are simulated by using MATLAB R2012b.

**Fig. 4** The average absolute values of the tracking error versus the number of iteration



**Fig. 5** The trajectory tracking curve of the 8th iteration



### 4 Conclusions

The paper analyzes the convergence of the open PID-type. According to the PID parameters, its convergence condition is obtained. The gain parameters in open PID-type ILC system are very important, which would affect notably the tracking performance and convergence of ILC system. By selecting appropriate gain parameters of the open PID-type ILC, the output of this system tracks the desired output very well after 8th iteration number. It causes the monotonic convergence. The speed of monotonic convergence is very fast. The absolute error between the desired output and the actual output converges uniformly to zero. The simulation results illustrate that the open PID-type iterative learning control system in this paper is effective and stable and has high performance.

**Acknowledgements** This work was supported in part by the Research Programs for the standardization administration of the People's Republic of China under Grant No. 20150009-T-604. This work was also supported in part by Chongqing Engineering Research Center for Instrument and Control Equipment.

## References

1. Dai H, Lu YM (2011) Iterative learning control for linear time-variant continuous systems with iteration-varying initial conditions and reference trajectories. *J Grad Sch Chin Acad Sci* 28:366–367
2. Ruan X, Li ZZ (2014) Convergence characteristics of PD-type iterative learning control indiscrete frequency domain. *J Process Control* 24:86–90
3. Kim TA, Sugie T (2013) An iterative learning control based identification for a class of MIMO continue-time systems in the presence of fixed input disturbance and measurement noises. *Int J Syst Sci* 9:737–748
4. Sun M, Wang D, Wang Y (2010) Varying-order iterative learning control against perturbed initial condition. *J Frankl Inst* 247:1526–1540
5. Li XD, Chow TWS (2014) Iterative learning control or a class of nonlinear discrete-time systems with multiple input delays. *Int J Syst Sci* 39:361–364
6. Lin MT, Yen CL, Tsai MS (2013) Application of robust iterative learning algorithm in motion control system. *Mechatronics* 23:530–533
7. Ruan X, Bien Z, Park KH (2012) Iterative learning controllers for discrete-time large-scale systems to track trajectories with distinct magnitudes. *Int J Syst Sci* 36:221–226
8. Wei YS, Li XD (2014) PID and EPID types of iterative learning control based on evolutionary algorithm. In: *Proceedings of the 33rd Chinese control conference*, vol 1, pp 443–446
9. Ahn HS, Moore KL, Chen YQ (2007) *Iterative learning control robustness and monotonic convergence for interval systems*, 1st edn. Springer, London
10. Yu SJ, Qi XD (2012) *Iterative learning control theory application*, 1st edn. China machine press, Beijing

# Development of an Integrative Pointing Gimbal Mechanism for Space Application

Bo Pan, Shuyang Zhang, Lin Li, Fanxin Sun and Yongqiang He

**Abstract** This paper summarizes the development of an integrative pointing gimbal mechanism (IPGM) for space application, such as the directional antenna, the space manipulator, the mobile camera, and other pointing mechanisms. Different from the traditional gimbal mechanisms, the two drive units of this pointing gimbal mechanism are integrated into a compact package, so the mass, the inertia, and the volume can be much smaller. And without the connecting part between the two axes, the stiffness of this IPGM is bigger under the same output ability, which offers better dynamic performance and control law. The key part of the IPGM is also analyzed by numerical calculation, so as to ensure the reliable running of the shafting under the space environments. To assess its capabilities, the qualification environment testing including the thermal cycling testing and the sinusoidal vibration were carried out. The testing results show that the performance of the IPGM is almost the same between the former and the end of each testing.

**Keywords** Space mechanism · Pointing gimbal mechanism · Integrative · Temperature

## 1 Introduction

The pointing gimbal mechanism is one of the most important mechanisms for space application. It is always seen in the directional antenna [1], the space manipulator, the mobile camera, and other pointing mechanisms. Because the mass and the outer envelope of spacecraft are limited on most occasions, lightweight and compact size is always one of the most important themes for space mechanism design [2]. In order to reduce the mass and the volume, a lightweight and compact pointing gimbal mechanism will be introduced.

---

B. Pan (✉) · S. Zhang · L. Li · F. Sun · Y. He  
Beijing Institute of Spacecraft System Engineering,  
China Academy of Space Technology, 100094 Beijing, People's Republic of China  
e-mail: panbojob@126.com

© Springer-Verlag Berlin Heidelberg 2016  
B. Huang and Y. Yao (eds.), *Proceedings of the 5th International Conference on Electrical Engineering and Automatic Control*, Lecture Notes in Electrical Engineering 367, DOI 10.1007/978-3-662-48768-6\_91

## 2 Design Description

The housing of the axis B is directly mounted in the output shaft of axis A, as shown in Fig. 1. The inner races of bearings are mounted in the “U” housing structure in the drive unit of axis A, through some connecting part. And the outer races of bearings are directly mounted in the “large” output shaft of axis A. Seen from the static coordinates, the inner races of bearings are static and the outer races of bearings are running, when the axis A of the IPGM is working. As a result, the two drive units are integrated into a compact package. The mass, the inertia, and the volume can be much smaller than the traditional ones (Fig. 1b). And without additional connecting part between the two axes, the stiffness of this IPGM is bigger under the same output ability, which offers better dynamic performance and control law. Figure 1a shows several rotational positions of the IPGM. The axis A can rotate from  $-110$  to  $+110$  °C, and the axis B can rotate from  $-360$  to  $+360$  °C. So the pointing space can reach more than a ball surface. In each drive unit, the motor, the gear reducer, and the angle sensor are totally the same.

The ultrasonic motor has many advantages, for example, high torque with low speed, compactness in size, absence of electromagnetic interference, a fast response characteristic, and a large holding torque at switch-off power [3]. Recently, many prototypes of the ultrasonic motor have been developed successfully, and some have already been used in space. Figure 2 shows a type-40 ultrasonic motor, which is used in the IPGM. The combination of low mass, small volume, and high drive ratio makes harmonic gear one of the most important moving parts in space mechanisms since its coming out [4]. In the IPGM, a type-50 short-cup harmonic gear is applied, with the gear ratio 160:1, as shown in Fig. 3. This type of harmonic gear can offer the same output capability with less mass and volume compared with the traditional one. Lubrication is a critical aspect for proper, effective performance. The harmonic drive gears in the IPGM were lubricated with PFPE grease [5]. The inner and outer races of bearings were lubricated with MoS<sub>2</sub> film, and bearing cages were made of PTFE-based self-lubricating polymers.

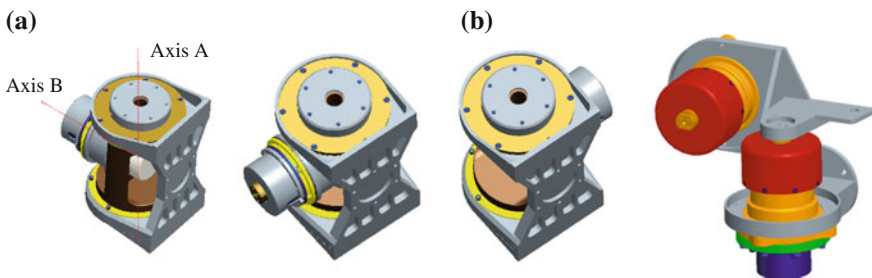


**Fig. 1** Comparison between the IPGM and other traditional gimbal mechanism. **a** IPGM. **b** The traditional gimbal mechanism

**Fig. 2** The ultrasonic motor in the IPGM



**Fig. 3** The harmonic gear in the IPGM



To achieve high precision of position control in the IPGM, the angle position of output rotor is needed. Optical encoder and resolver are widely used in shaft angle measure. Although optical encoder has high performance with the same mass, its reliability and its survival capabilities in extreme environment are not as good as resolver. Thus, a single-channel resolver is used for angle sensor, as shown in Fig. 4. Its precision is better than  $\pm 0.1^\circ$ . For high-precision application, a resolver with higher precision could be selected, such as a double-channel resolver.

**Fig. 4** The single-channel resolver in the IPGM



**Fig. 5** The prototype of the IPGM



**Table 1** Performance parameters of the IPGM

Specification	IPGM data
Rated output torque	$\geq 8$ Nm
Maximum output torque	$\geq 14$ Nm
Angle measure accuracy	$0.1^\circ$
Rotate speed	$0\text{--}2.25^\circ/\text{s}$
Weight	$< 2$ kg
Life span	8 years

Figure 5 depicts the prototype of the IPGM and shows its mass as 1979 g. Because the primal objective is to design a prototype, the structure of the IPGM is not fully optimized. In the latter application, the structure can be optimized again, and the mass, the inertia, and the volume will be much smaller. Table 1 shows the performance parameters of the IPGM prototype. And with the optimization of system design, some of the parameters could be better.

### 3 Critical Part Analysis

In order to give a good performance in space temperature environment, the key point of the compact configuration of IPGM is the shafting design, especially the shafting design of axis A. Figure 6 shows the shafting design of axis A that is different from the general design. The output shaft and the outer race of bearing are fitted, and the shell and the inner race of bearing are fitted.

As usual, the output shaft and the shell are made of aluminum alloy (LY12) or titanium alloy (TC4). The SiCp/Al [6], as a new composite material, has the similar density to aluminum alloy (LY12) and has the similar elastic modulus and the coefficient of linear expansion to titanium alloy (TC4). With regard to the variation of bearing clearance with the temperature cycling, the mechanical analysis of the shaft and the shell with the different combination of the three materials (Table 2) was conducted below, to select the best material combination and the optimum range of the diametrical dimension.

**Fig. 6** The schematic shafting design of axis A

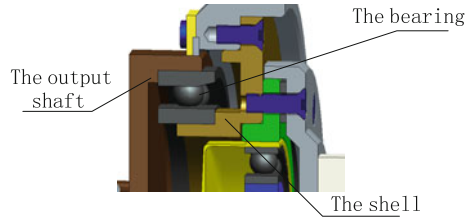


**Table 2** The combinations of three materials

Combination	Shell	Shaft
1	TC4	LY12
2	TC4	TC4
3	LY12	TC4
4	LY12	LY12
5	SiCp/Al	TC4
6	TC4	SiCp/Al
7	SiCp/Al	SiCp/Al

With the temperature cycling (such as from  $-60$  to  $80$  °C), the magnitude of interference between the inner race of bearing and the shell is changing which leads to the variational deformation of inner race of bearing. The deformation  $\Delta_s$  of inner race was derived as follows [7, 8]:

$$\Delta_s = \frac{2(I_i + \Delta I_{iT}) \left(\frac{d_i}{d_s}\right)}{\left[\left(\frac{d_i}{d_s}\right)^2 - 1\right] \left\{ \left[ \frac{\left(\frac{d_i}{d_s}\right)^2 + 1}{\left(\frac{d_i}{d_s}\right)^2 - 1} + \mu_b \right] + \frac{E_b}{E_s} [1 - \mu_s] \right\}} \tag{1}$$

where  $I_i$  is the original magnitude of interference and  $\Delta I_{iT}$  is the changing magnitude of interference with the temperature cycling.

Similarly, the deformation  $\Delta_h$  of outer race was derived as follows [7, 8]:

$$\Delta_h = \frac{2(I_o + \Delta I_{oT}) \left(\frac{d_h}{d_o}\right)}{\left[\left(\frac{d_h}{d_o}\right)^2 - 1\right] \left\{ \left[ \frac{\left(\frac{d_h}{d_o}\right)^2 + 1}{\left(\frac{d_h}{d_o}\right)^2 - 1} - \mu_b \right] + \frac{E_b}{E_s} \left[ \frac{\left(\frac{D_h}{d_h}\right)^2 + 1}{\left(\frac{D_h}{d_h}\right)^2 - 1} + \mu_h \right] \right\}} \tag{2}$$

where  $I_o$  is the original magnitude of interference and  $\Delta I_{oT}$  is the changing magnitude of interference with the temperature cycling.

The actual radial clearance of bearing is defined as follows:



$$\Delta P_d = \Delta_T - \Delta_s - \Delta_h \tag{3}$$

where  $\Delta_T$  is the variational radial clearance of bearing with the temperature cycling.

The actual radial clearance of bearing is defined as follows:

$$U_a = U_r - U_g + \Delta P_d \tag{4}$$

where  $U_r$  is the original clearance of bearing and  $U_r - U_g$  is the clearance of bearing after the preload.

Based on Hertz contact theory and Palmgren simplified calculation, the relation between the actual radial clearance of bearing and the contact load between balls and races of bearing can be written as follows:

$$U_a = e^3 \sqrt{(\Sigma\rho)Q^2} \tag{5}$$

where  $Q$  is the contact load between balls and races of bearing.

With the temperature cycling, the thermal deformation of inner and outer races of bearing, the thermal deformation of bearing balls, and the magnitude of interference due to thermal deformation would lead to the change of bearing clearance. When the bearing clearance is minus, the contact force will appear between ball and race of bearing. This will introduce the extra thermal load beside the working load. Figure 7 shows the influence from temperature on the bearing clearance, considering of the variational magnitude of the interference in the shafting. Figure 8 shows the variational contact load between ball and race of bearing with the temperature cycling. The radial clearance of bearing was considered to be 0  $\mu\text{m}$  after the preload.

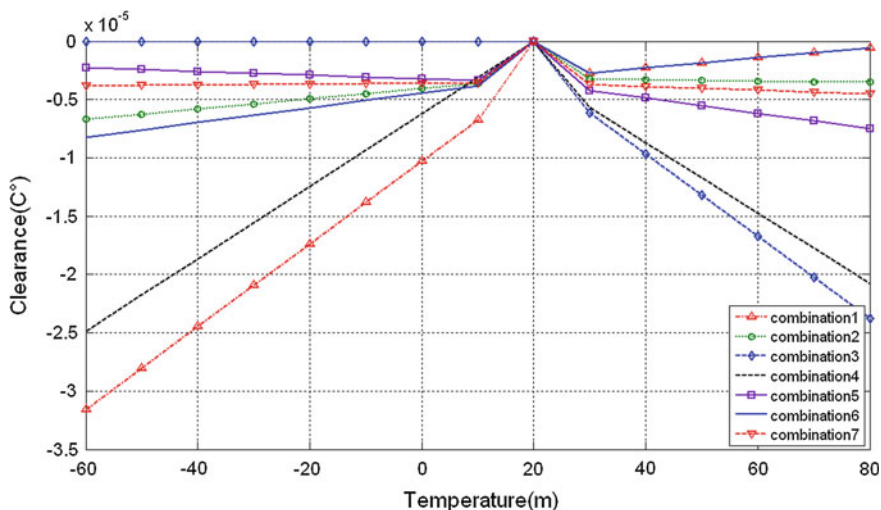


Fig. 7 The clearance of bearing

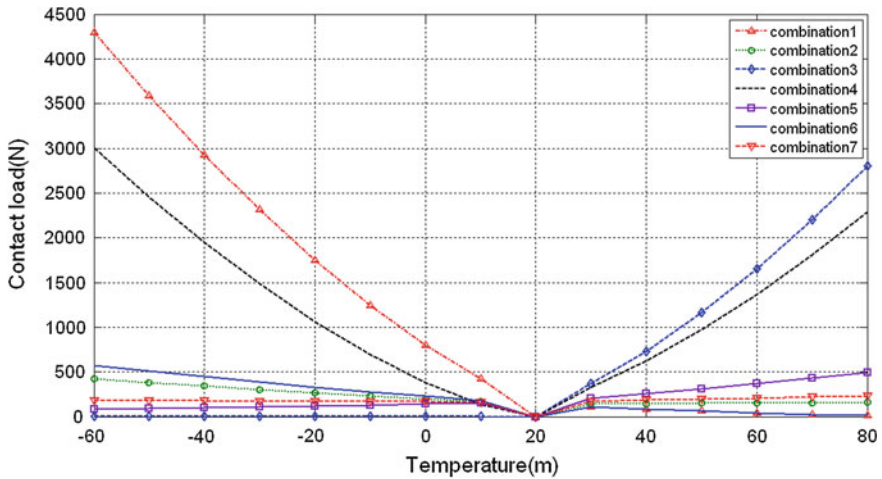


Fig. 8 The contact load between ball and race of bearing

In Combination 1, the radial clearance of bearing decreases with the temperature reducing (from  $-60$  to  $0$  °C), which will lead to the increasing of the contact load between ball and race of bearing (the load could be 1 kN level). And such a load would lead to the increase of the friction moment in bearing, and the wear in the bearing would also increase. As a result, the Combination 1 is not a good choice because of the bad performance at low temperature.

In Combination 3 and Combination 4, the radial clearance of bearing between the shell and the inner race of bearing would arrive at  $50 \mu\text{m}$  at the most. It is unacceptable for high-precision shafting which will induce a large radial run-out of the shafting.

In Combination 2 and Combination 7, both of the shell and the shaft are made of the same material. They have the similar performance at low and high temperature. The radial clearance of bearing and the contact load between balls and races are all acceptable. Combination 7 makes a balance between the performance at low and high temperature, and Combination 2 performs worse at low temperature.

Combination 5 and Combination 6 have different characteristics. Combination 5 has the better performance at low temperature, while Combination 6 has better performance at high temperature.

Considering the material cost, machining cost, weight, and so on, the Combination 7 is the best choice. Moreover, the machining and assembling dimension preference can also be concluded. Table 3 shows the result of preferences.

**Table 3** The control of dimension

	Item to control	Control range
1	The fit value between the outer race of bearing and the output shaft	Assure the magnitude of interference from 3 to 5 $\mu\text{m}$
2	The fit value between the inner race of bearing and the shell	Assure the magnitude of interference from 1 to 2 $\mu\text{m}$

## 4 Qualification Testing

The qualification environments included variations in temperature and sinusoidal vibration to assess its capabilities in environments of space and launch.

### 4.1 Thermal Cycling

The qualification thermal environment was  $-30$  to  $+50$   $^{\circ}\text{C}$  in normal air condition in a controlled thermal cycling test box, as shown in Fig. 9. The IPGM was working well between and after the thermal cycling testing.

### 4.2 Sinusoidal Vibration

The qualification units were exposed to a maximum 12 g sinusoidal vibration with a sweep rate of 4 octaves/min from 5 to 100 Hz in the vertical orthogonal axis and a maximum 4 g sinusoidal vibration with a sweep rate of 4 octaves/min from 5 to 100 Hz in the other orthogonal axes, as shown in Fig. 10.

The low-level sine vibration curves of the IPGM are almost the same, before and after the full-level sinusoidal vibration testing, as shown in Fig. 11. The frequencies

**Fig. 9** Thermal cycling testing for the IPGM

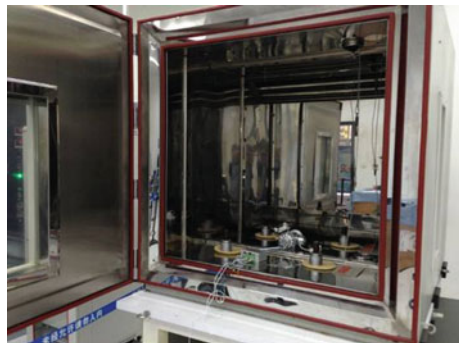


**Fig. 10** Sine vibration testing for IPGM

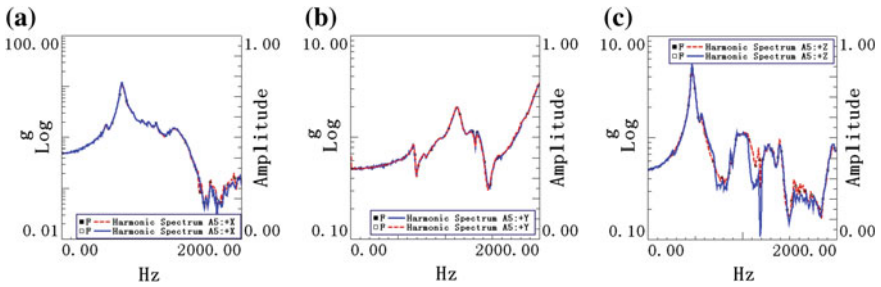


**Fig. 11** Comparison between the low-level vibration curves of the IPGM before and after the full-level sinusoidal vibration testing of all three axes. **a** x direction. **b** y direction. **c** z direction

of the curve peak in each direction are 665.27 Hz(X), 1132.4 Hz(Y), and 464.52 Hz(Z). And the IPGM was working well after each sinusoidal vibration testing.

## 5 Conclusion and Prospect

To meet the requirement of lightweight and compact size for space application, an integrative pointing gimbal mechanism prototype is developed. Though the drive unit of the second stage is integrated in the output shaft of the drive unit in the first stage, the mass, the rotational inertia, and the volume are effectively reduced. And the thermomechanic analysis of the “U” structure and the application of some special metal matrix composites ensures the steady running of the IPGM going through the environments of launch and space. Some primary qualification testing is completed to assess its capabilities. The testing results are satisfactory.

The improved IPGM will be developed by the third quarter of 2015 and will complete its qualification and life testing by the end of 2015. This qualification testing will include high-level sine vibration and thermal vacuum environment from  $-60$  to  $+80$  °C.

**Acknowledgment** This research is funded by the National Basic Research Program of China (Grant No. 2013CB733000) and the Chinese Advanced Armament Research Project of 12th Five-year Plan (Grant No. 51320030201).

## References

1. Pan B, Zhang D, Shi W et al (2011) Modeling and analysis on pointing accuracy of the antenna oriented mechanism in satellite. *Spacecraft Eng* 20(5):75–80
2. Ma X, Yu D, Sun J et al (2006) The researching evolvement of spacecraft deployment and driving mechanism. *J Astronaut* 27(6):1123–1131
3. Zhao X, Chen B, Zhao C (2003) Nonlinearly frictional interface model of rotated traveling wave type ultra-sonic motor. *J Nanjing Univ Aeronaut Astronaut* 35(6):629–633
4. Zhou H, Sun J, Wen Q et al (2009) Lubrication and performance of harmonic drive used in spacecraft. *J Astronaut* 30(1):378–381
5. Wan Z, Hao H, Zhou H et al (2013) Performance and testing of harmonic drive gears lubricated with two types of lubrication: liquid-lubricated H-DLC-coating and solid MoS<sub>2</sub>. In: *Proceedings of 15th European space mechanisms & tribology symposium*
6. Zhang Q, Wu G, Jiang L et al (2005) Thermal properties of a high volume fraction SiC particle-reinforced pure aluminium composite. *Phys Status Solid A-Appl Mater Sci* 202(6):1033–1040
7. Fei Y (2009) *Theory and application of mechanical thermal deformation*. National Defense Industry Press, Beijing
8. Harris T, Kotzalas M (2009) *Essential concepts of bearing technology*. China Machine Press, Beijing

# Multiuser Scheduling on Dual-Hop Relay Networks and Effect of Feedback Delay

Jiyao Wei and Xianyi Rui

**Abstract** In cooperative communication, the evaluation of the system performance and its degree of fairness mainly depend on the choice scheduling made on channel. However, in real system, feedback delay between channel estimation time and the real transmit information time cannot be ignored. And the delay effects on both the performance of the cooperative communication system and the scheduling of information transmission. In this paper, we focus on studying multiuser scheduling on dual-hop relay networks and the effect of feedback delay. Simulation advocates the performance of a multiuser relay network equipped with a single amplify-and-forward (AF) relay over Rayleigh fading environments. The results show that the channel capacity and the degree of fairness effected by feedback delay decrease obviously.

**Keywords** Multiuser scheduling · Feedback delay · Channel capacity · Degree of fairness

## 1 Introduction

In point-to-multipoint multiuser cooperative communication, for example, the case of a cellular system, the base station can select the mobile user with the strongest channel in a time/frequency bin to schedule data transmission. This strategy, which has come to be known as opportunistic scheduling, and the opportunistic scheduling make impact on the dual-hop relay networks [1–3]. Among the proposed cooperative strategies [4], amplify and forward (AF) attracts considerable attention due to its ease of implementation and low power consumption. The author in [5–7] studied the multiple relays scheduling for amplify-and-forward cooperative

---

J. Wei (✉) · X. Rui (✉)

College of Electronic and Information Engineering, Soochow University, Suzhou, China  
e-mail: weijiyao0331@163.com

X. Rui

e-mail: xyruis@suda.edu.cn

© Springer-Verlag Berlin Heidelberg 2016

B. Huang and Y. Yao (eds.), *Proceedings of the 5th International Conference on Electrical Engineering and Automatic Control*, Lecture Notes in Electrical Engineering 367, DOI 10.1007/978-3-662-48768-6\_92

827

networks. In real environment, feedback delay cannot be ignored. In [6, 7], the performance of outdated channel state information of amplify-and-forward (AF) cooperative communication was investigated. Above literature only considers the impact of the opportunistic schedule or feedback delay on performance of system. This paper studies scheduling algorithm as well as feedback delay. Besides, the effect that feedback delay has on scheduling performance will also be discussed.

## 2 System Model

One example of this is point-to-multipoint dual-hop links where a source (S) communicates with  $L$  scattered destinations  $D_k, k \in 1, 2, 3, \dots, L$  via a single relay (R), as shown in Fig. 1. Assuming that each node is configured, single antenna and all nodes operate in half-duplex mode, and there is no direct link between S and  $D_k$ .

The whole process can be divided into three parts: the first data transmission, user's selection, and the second data transmission. Considering the constraints of half-duplex mode, data transmission is divided into two time slots. During the first time slot, S transmits information to R. During the second time slot, by amplify and forward (AF), R retransmits information to  $D_k$ .

In the first slot, the received signal at the relay can be written as follows:

$$y_{sr}(n) = \sqrt{P_S}h_{sr}(n)x_s(n) + n_{sr}(n) \quad (1)$$

where  $P_S$  is the transmit power at S,  $h_{sr}$  denotes the channel gain of S-R,  $x_s(n)$  is the  $n$ th transmission symbol of source node, and  $n_{sr}(n)$  is corresponding additive white noise whose average is 0 and variance is 1.

In the second slot, the relay employs AF to simply amplify the received signal from the source and retransmits a scaled copy of the signal to the destination.  $\beta$ , amplification coefficient of AF, can be written as follows

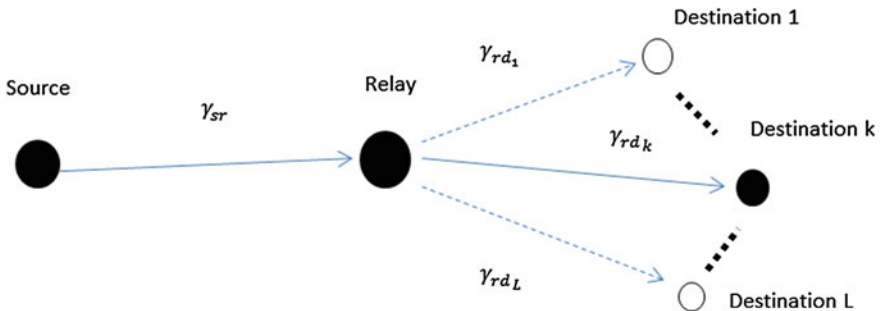


Fig. 1 Illustrative system model for point-to-multipoint dual-hop links

$$\beta = \frac{1}{\sqrt{P_s|h_{sr}|^2 + \sigma_{sr}^2}} \quad (2)$$

so  $x_r(n)$ , the data retransmitted by relay node can be written as follows:

$$\begin{aligned} x_r(n) &= \beta y_{sr}(n) \\ &= \frac{\sqrt{P_s}}{\sqrt{P_s|h_{sr}|^2 + \sigma_{sr}^2}} h_{sr} x_s(n) + \frac{1}{\sqrt{P_s|h_{sr}|^2 + \sigma_{sr}^2}} n_{sr}(n) \end{aligned} \quad (3)$$

The signal destination node  $D_k$  receives is as follows:

$$\begin{aligned} y_{rd_k}(n) &= \sqrt{P_r} h_{rd_k} x_r(n) + n_{rd_k}(n) \\ &= \frac{\sqrt{P_s P_r}}{\sqrt{P_s|h_{sr}|^2 + \sigma_{sr}^2}} h_{sr} h_{rd_k} x_s(n) + \frac{\sqrt{P_r}}{\sqrt{P_s|h_{sr}|^2 + \sigma_{sr}^2}} h_{rd_k} n_{sr}(n) + n_{rd_k}(n) \\ &= \frac{\sqrt{P_s P_r}}{\sqrt{P_s|h_{sr}|^2 + \sigma_{sr}^2}} h_{sr} h_{rd_k} x_s(n) + \tilde{n}_{rd_k}(n) \end{aligned} \quad (4)$$

In this formula,  $\tilde{n}_{rd_k}(n) = \frac{\sqrt{P_r}}{\sqrt{P_s|h_{sr}|^2 + \sigma_{sr}^2}} h_{rd_k} n_{sr}(n) + n_{rd_k}(n)$ ,  $P_r$  is the relay retransmit power.

In this paper, the state information of cooperative transmission is outdated; thus, it effects the gain of links between nodes. According to Jake's fading correlation model, the channel with a feedback delay can be modeled as follows:

$$\tilde{h}_{sr}(n) = \rho_{sr} h_{sr} + \sqrt{1 - \rho_{sr}^2} \omega_{sr} \quad (5)$$

$$\tilde{h}_{rd_k}(n) = \rho_{rd_k} h_{rd_k} + \sqrt{1 - \rho_{rd_k}^2} \omega_{rd_k} \quad (6)$$

In the formula,  $\tilde{h}_{sr}(n)$  and  $\tilde{h}_{rd_k}(n)$  representatively denote outdated channel coefficients of the S-R and R- $D_k$ .  $\rho_{sr}$  is the correlation coefficient between the real channel and the estimation channel in the first time slot, while  $\rho_{rd_k}$  denotes the correlation coefficient between the real channel and the estimation channel in the second one. According to Ref. [4],  $\rho = J_0(2\pi\tau f_D)$ ,  $J_0(\cdot)$  stands for the zeroth Bessel function of the first kind and  $f_D$  represents the maximum Doppler frequency on the S-R link. In simulation, we assume that  $\rho = \rho_{sr} = \rho_{rd_k}$ ,  $h_{sr}$ ,  $\omega_{sr}$ ,  $h_{rd_k}$ , and  $\omega_{rd_k}$  denote a circularly symmetric complex Gaussian random variable.



Relatively, the instantaneous SNRs of the first and the second time slot can be representatively denoted as follows:

$$\tilde{\gamma}_{sr} = \left| \tilde{h}_{rdk} \right|^2 \frac{P_s}{N_0} \quad (7)$$

$$\tilde{\gamma}_{rdk} = \left| \tilde{h}_{rdk} \right|^2 \frac{P_r}{N_0} \quad (8)$$

where  $N_0$  represents noisy power spectral density.

### 3 Scheduling Algorithm

As the resource of system is limited, when multiusers are using the limited resource, scheduling balances the system performance and the degree of fairness. This paper studies the following scheduling algorithms.

#### 3.1 Round Robin (RR)

RR is a distributed algorithm, as it does not require external signaling. Each node periodically changes its role slot by slot. In Ref. [5], scheduling priority of every user is equal and probability is the same. Each user is scheduled periodically; thus, round robin (RR) seeks the highest level of fairness. This algorithm ignores users' channel performance and makes sure every user get the same resource; thus, there is no "starvation." But in real multiuser communication service, RR is not ideal which leads to the low throughput of users.

#### 3.2 Absolute SNR-Based Scheduling

Absolute SNR-based scheduling ignores the fairness of users; the scheduler selects and sequences the users according to their channel transient performance. Then, scheduler distributes resource to the best user.  $k$  stands for the user that is scheduled. The algorithm can be written as follows:

$$k = \operatorname{argmax}(\gamma_{rdk}) \quad (9)$$

$\gamma_{rdk}$  represents  $k$ 's SNR. The chosen of the user that has good channel performance makes sure that the system performance is maximized, and the utilization ratio of

resource is highest. But this also makes the users that have bad channel performance get little or no resource, which leads to the “starvation” of the users.

### 3.3 Normalized SNR-Based Scheduling

Proportional fair (PF) is the compromise of round robin (RR) and greedy scheduling algorithm (MAX). RR ensures the fairness of users, while MAX focuses on the maximum of system performance. PF reconciles both fairness and system performance which eliminates the starvation and avoids the lowest system performance. Assume that the scheduled user is  $k$ , so the PF can be written as follows:

$$k = \operatorname{argmax} \frac{R_k(t)}{\overline{R}_k(t)} \quad (10)$$

$R_k(t)$  stands for  $k$ 's speed at  $t$  time, and  $\overline{R}_k(t)$  represents  $k$ 's average speed during  $t$ . When system schedules, some good-performing user,  $\overline{R}_k(t)$ , will gradually increase and the priority decreases. If some user's channel quality is bad and gets little resource for long, then its average speed will decrease and priority will increase. And then the user will get the opportunity to be scheduled.

According to Shannon theory,  $C = B \log_2(1 + \gamma)$ , where  $C$  is rate of transmission,  $B$  is bandwidth, and  $\gamma$  is SNR. Assuming that bandwidths are the same, so that the bigger the SNR is, the faster the transmission rate is. In what follows, we refer to the proportional fair one based on SNR as the “normalized SNR-based scheduling” [8].

$$k = \operatorname{argmax} \frac{\gamma_k(t)}{\overline{\gamma}_k(t)} \quad (11)$$

## 4 Fairness Index

Fairness index is standard used to measure whether the resource distribution between users is equal or not. This paper adapts max–min index, that is

$$I_{\min-\max} = \frac{\min\{x_j\}}{\max\{x_i\}} \quad (12)$$

$x_i, x_j$  representatively stands for the total resources distributed to user  $i$  and user  $j$ ,  $i, j \in \{1, 2, 3, \dots, L\}$ .

### 5 Simulation Result

This section will simulate round robin (RR), absolute SNR-based scheduling (MAX), and normalized SNR-based scheduling (PF) in both ideal channel and delay channel, respectively. We observe the impact that delay channel effects on scheduling algorithm according to channel capacity and fairness index. The simulation is as the following: Each channel between any two random nodes is a flat Rayleigh channel. And every channel is independent. Assuming that the transmitted powers of source (S) and relay (R) are equal, that is,  $P_S = P_r$ . Ignoring the direct link, source signal is BPSK and is based on AF. The signal of sent  $N = 10,000$ .

Figure 2 clearly shows that MAX guarantees the best system performance. PF is better than RR in channel capacity (Fig. 3).

“MAX, PF, and RR” represent the simulation in ideal channel. “LateMAX, LatePF, and LateRR” represent the simulation in feedback delay. Because of the

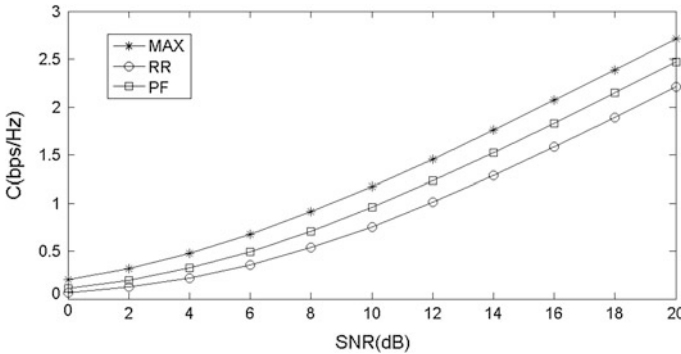


Fig. 2 Comparison of capacity for 3 scheduling algorithms in ideal channel

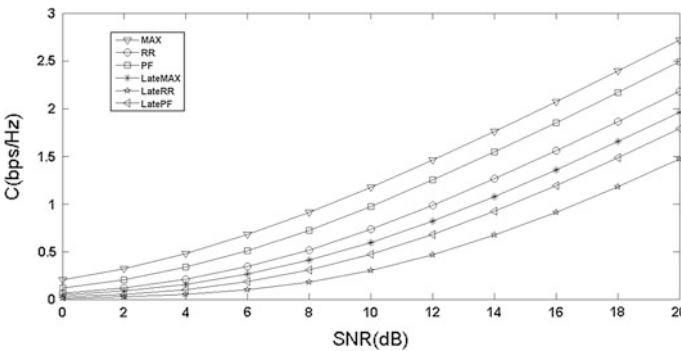
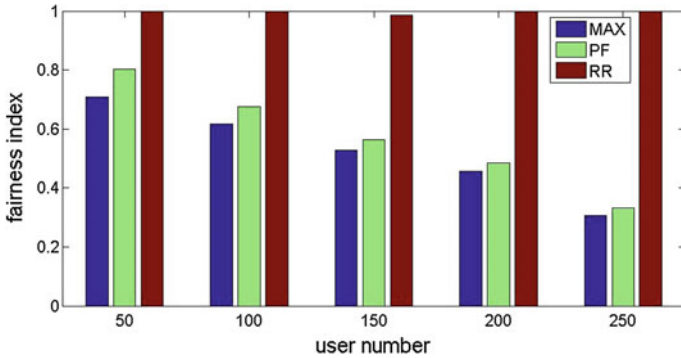


Fig. 3 Comparison of capacity for 3 scheduling algorithms in ideal channel and feedback delay. User number is 100,  $\rho = 0.6$



**Fig. 4** Simulation of the fairness in 3 scheduling algorithms in ideal channel. User number: 50–250

impact of the feedback delay, system performance in all the scheduling algorithms becomes bad (Fig. 4).

When there are 150 users, the fairness index of RR is below 1. It is because that the user number is not divided by  $N$  with no remainder. As the user number grows larger, the impact that weight effects have on the fairness of system is stronger, which leads to the decrease of the fairness index of the MAX and PF.

Figure 5 clearly shows that the impact that feedback delay effects have on fairness makes the fairness index of MAX and PF decrease. RR is not affected by feedback delay because it is an absolute fair algorithm and ignores the system performance.

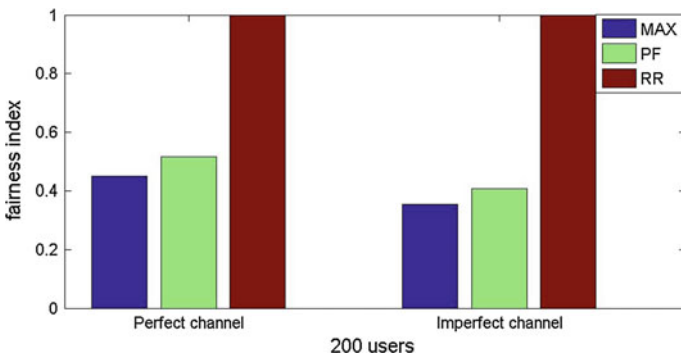


**Fig. 5** Comparison of fairness for 3 scheduling algorithms in ideal channel and feedback delay. User number: 200

## 6 Conclusion

This paper studies round robin (RR), absolute SNR-based scheduling (MAX), and normalized SNR-based scheduling (PF) in ideal channel and feedback delay. By comparing channel capacity and fairness, we can conclude that PF is the compromise of RR and MAX. It not only ensures fairness, but also improves the system performance. Simulations in different channels demonstrate that feedback delay impacts on scheduling performance and fairness and make them worse.

## References

1. Yang N, Elkashlan M, Yuan J (2011) Impact of opportunistic scheduling on cooperative dual-hop relay networks. *IEEE Trans Commun* 59:689–694
2. Oyman Ö, Win MZ (2008) Power-bandwidth tradeoff in multiuser relay channels with opportunistic scheduling. In: Proceedings of 46th annual Allerton conference on communication, control, and computing. Monticello, IL, pp 72–78
3. Wang N, Gulliver TA (2015) Queue-aware transmission scheduling for cooperative wireless communications. *IEEE Trans Commun* 63:1149–1161
4. Kramer G, Gastpar M, Gupta P (2005) Cooperative strategies and capacity theorems for relay networks. *IEEE Trans Inf Theory* 51:3037–3063
5. Krikidis I, Belfiore JC (2007) Scheduling for amplify-and-forward cooperative networks. *IEEE Trans Veh Technol* 56:3780–3790
6. Zhong B, Zhang X, Li Y, Zhang Z, Long K (2013) Impact of partial relay selection on the capacity of communications systems with outdated CSI and adaptive transmission techniques. In: 2013 IEEE wireless communications and networking conference (WCNC), pp 3720–3725
7. Zhong B, Zhang Z, Long K (2013) Performance analysis for amplify-and-forward relay selection with outdated channel state information. *IEEE Commun Lett* 10:100–110
8. Yang L, Alouini MS (2006) Performance analysis of multiuser selection diversity. *IEEE Trans Veh Technol* 55(6):1848–1861

# Research on System Modeling and Starting Strategy of Inverter for Medium-Frequency Induction Heating

Sen-lin Cheng, Hu Xu, Chuan Wang and Qiang-zhi He

**Abstract** Aiming at the puzzle of being low in starting success rate and poor in starting performance of the current source medium-frequency induction heating power supply, the paper presented a novel starting control strategy based on energy pre-charge starting system. In the paper, it made the anatomy and study comprehensively on a variety of energy pre-charge starting methods, constructed the system model of energy pre-charge starting control, and put forward to the starting strategy based on the load capacitor pre-charged. The results of the starting control strategy simulation demonstrated that the constructed system model and the presented starting strategy are reasonable and feasible. The research results provide a novel reference method for solving the starting control of medium-frequency induction heating power supply.

**Keywords** Induction heating · Current source inverter · Control model · Energy pre-charge starting · Starting strategy

## 1 Introduction

The SCR current source induction heating power supply (SCR-CS-IHPS) is widely used induction heating equipment in forging industry. The starting of current source inverter has always been a major puzzle in the induction heating field [1–4]. Since the SCR inverter belongs to the load commutated inverter, it becomes more complicated to start in SCR-CS-IHPS. Engineering experience shows that the most effective starting method of SCR-CS-IHPS is the energy pre-charge starting. The function of pre-charged energy is that it identifies the load resonant frequency conveniently based on the zero-input response of the load circuit and provides the commutation voltage for the SCR converter. But in the starting process, because the energy feeding speed cannot catch up the energy decaying speed in the inverter, it will result in

---

S. Cheng (✉) · H. Xu · C. Wang · Q. He  
College of Automation, Chongqing University, Chongqing 400044, China  
e-mail: csl@cqu.edu.cn

starting failure of SCR inverter because of the commutation failure. Many scholars have studied on this puzzle, and there are multiple starting methods proposed, such as the frequency sweeping starting [5], DC inductance pre-magnetized starting [5], load-magnetized starting [5], double-auxiliary-bridge starting [6], and load capacitor pre-charged starting [5]. Among them, the load capacitor pre-charged starting owns the maximum pre-charged energy. When it works in unloaded or light load, all the 5 kinds of methods above can complete the starting normally, but when the inductor is full of cold material, it would result in starting failure because of the extremely fast decay speed in energy pre-charged. Obviously, if the pre-charged energy is more enough, then the starting ability will be stronger. Based on the identification of load circuit parameter, the paper builds the control system model of starting process [7–9] and presents a load capacitor pre-charged starting strategy with a stronger starting performance. The simulation experiment shows that even if it is the most complicated starting situations, it is still has good starting performance.

## 2 Pre-charge Starting Analysis

As shown in Fig. 1, the implementation of inverter commutation depends on the load voltage  $u_H$ ; thus, there must be pre-charged energy on load circuit before starting. In Fig. 1, the energy storage devices  $L_d, L, C$  can store energy in advance, which can guarantee the inverter to start with enough initial energy.

Assuming the load magnetization pre-charge current for inductor branch is  $I_{L0}$ , which is equal to the current on  $L_d$ , and  $I_{L0}$  can be converted to the voltage  $U_m$  on the capacitor shown in formula (1).

$$U_m = QR I_{L0} \tag{1}$$

In formula (1),  $Q$  is the quality factor, and  $Q = \sqrt{L/R^2C}$ . When capacitor pre-charged starting, the voltage on compensation capacitor  $C$  is  $U_{c0}$ , which is related to the load status, and it can be close to the limit value. Suppose the energy is converted as magnetic energy, then it will need to meet formula (2).

$$U_{c0} \geq Q^2 R I_{L0} \tag{2}$$

**Fig. 1** Energy pre-charge storage circuit

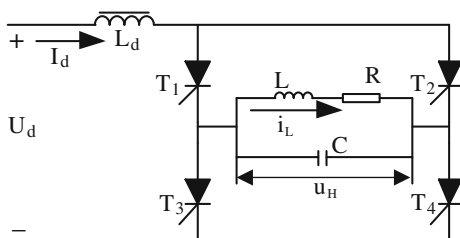
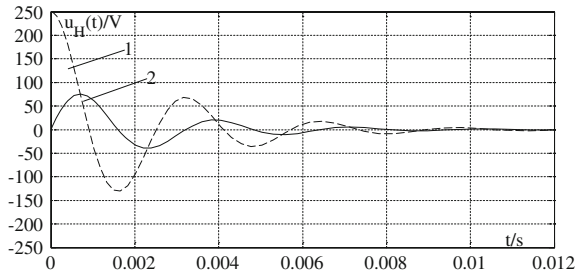


**Fig. 2** Zero-input response of capacitor and load magnetization pre-charge methods



Accordinging formula (1) and (2), it can get formula (3).

$$U_{c0}/U_m \geq Q \tag{3}$$

In formula (3),  $Q$  is not less than 1. It shows the energy pre-charged result that the capacitor pre-charge method can get more initial energy than load magnetization pre-charge method, which means the capacitor pre-charge has a longer decay process under the same load situations. It also can be seen from its zero-input response in Fig. 2 when the parameter of the circuit is, respectively,  $R = 0.4 \Omega$ ,  $L = 0.5 \text{ mH}$ ,  $C = 500 \mu\text{F}$ ,  $I_{L0} = 100 \text{ A}$  and  $U_{c0} = 250 \text{ V}$  from formula (2). In Fig. 2, the curve 1 is the response by capacitor pre-charge method and curve 2 is the response by load magnetization pre-charge method. In addition, the resonant frequency of load circuit is  $\omega_0 = \sqrt{1/LC - R^2/L^2}$ .

Based on the changing of load circuit, it is as shown in Fig. 3 to the load circuit of auxiliary bridge starting presented with a series capacitor.

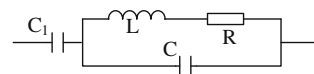
$$Z_b(j\omega_b) = \frac{1 - L(C + C_1)\omega_b^2 + j\omega_b R(C + C_1)}{-RCC_1\omega_b^2 + j\omega_b C_1(1 - LC\omega_b^2)} \tag{4}$$

The circuit impedance of the load is shown as formula (4) under the frequency  $\omega_b$

$$L^2 C(C + C_1)\omega_b^4 - [L(C + C_1) + R^2 C(C + C_1) + LC]\omega_b^2 + 1 = 0 \tag{5}$$

Substituting  $R = 0.4 \Omega$ ,  $L = 0.5 \text{ mH}$ ,  $C_1 = C = 500 \mu\text{F}$  into the formula (5), the equation does not exist real solution. It means that when auxiliary bridge exists, the load circuit belongs to forced oscillation, it has a sharp impact to devices when commutation. At the same time, when the auxiliary bridge is out work, the load circuit recovers its resonant performance, but the resonant frequency is different greatly with switching frequency of inverter, and thus, the starting effect is imperfect.

**Fig. 3** Load circuit of auxiliary bridge starting





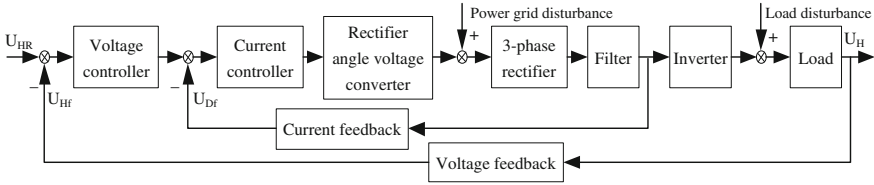


Fig. 4 Double closed-loop control system structure

### 3 Double Closed-Loop Control System of Voltage and Current

Because it contains the multiple starting situations, the successful starting should satisfy the condition that the system response speed must meet the real-time control requirement, and the system response must meet the control accuracy requirement. In engineering, the most starting control depends on auxiliary circuits and is the control of limited current and voltage in open-loop. Although it has a strict starting sequence, it is hard to ensure the control accuracy and stability. In addition, the load current is used as the feedback variable in existing closed-loop control, but it is more suitable for the temperature and power control in steady state. Because of the particularity of starting process, the both must be satisfied in requirement of the energy supply speed and the voltage amplitude on the load. Thus, the system structure is designed as the double closed-loop control system of voltage and current in the paper, the inner is current feedback, and the outer is load voltage feedback. The control system structure is shown in Fig. 4.

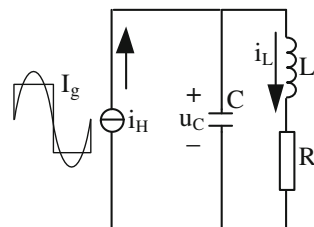
### 4 Starting Process Modeling

The equivalent load circuit with input current is shown in Fig. 5.

It can get the formulas (6) and (7) according to Kirchhoff's current and voltage law.

$$i_H = Cdu_C/dt + i_L \tag{6}$$

Fig. 5 The equivalent load circuit with input current



$$u_C = i_L R + L di_L / dt \tag{7}$$

Then, the transfer function of load shows as formula (8).

$$G_O(s) = \frac{Ls + R}{LCs^2 + RCs + 1} \tag{8}$$

The transfer function of rectifier is shown as formula (9).

$$G_R(s) = K_R / (T_R s + 1) \tag{9}$$

In Fig. 1, the filter consists of inductor  $L_d$ , and its transfer function shows as formula (10).

$$G_{FL}(s) = L_d s \tag{10}$$

In Fig. 5, the load input signal  $i_H$  is the output of inverter, and the primary harmonic is taken, which shows as formula (11).

$$i_H(t) = 4I_g \sin(\omega_s t) / \pi \tag{11}$$

Its Laplace transformation form is shown as formula (12).

$$I_H(s) = \frac{4I_g \omega_s}{\pi(s^2 + \omega_s^2)} \tag{12}$$

where  $I_g$  is the amplitude of the input current  $i_H$  and  $\omega_s$  is the switching frequency of inverter.

The Laplace transformation form of inverter input  $I_{d1}$  shows as formula (13),  $I_{d1}$  is the output of the filter, and its amplitude is  $I_g$ .

$$I_{d1}(s) = I_g / s \tag{13}$$

Thus, the transfer function of the inverter is shown as formula (14).

$$G_{inv}(s) = \frac{I_H(s)}{I_{d1}(s)} = \frac{4\omega_s s}{\pi(s^2 + \omega_s^2)} \tag{14}$$

For convenience of verification, the power grid and load disturbance are ignored, the controller only adopts the proportional control, and all the outer and inner feedback of loop circuit are taken as the unit feedback.

$$H_{FC}(s) = H_{FV}(s) = 1 \tag{15}$$

Assuming that after filtering, the maximum amplitude of load voltage, the control voltage of rectifier angle and the DC current is, respectively,  $U_{HM}$ ,  $U_{\alpha M}$  and

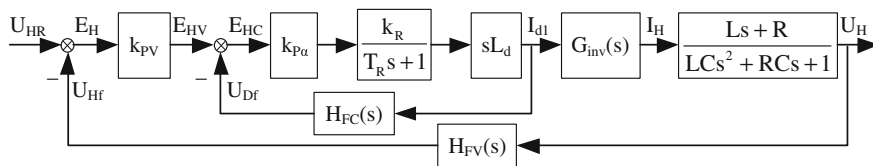


Fig. 6 Control system structure diagram of transfer function

$I_{d1M}$ . Then, the parameter  $k_{PV}$  and  $k_{P\alpha}$  of the controller, respectively, shows as the following. And the system structure diagram of transfer function is shown as Fig. 6.

$$k_{PV} = I_{d1M} / U_{HM} \tag{16}$$

$$k_{P\alpha} = U_{zM} / I_{d1M} \tag{17}$$

### 5 Research on Starting Control Strategy

The analysis of starting process includes the load characteristic identification, the system energy pre-charge, and the starting control. Load characteristic identification is to obtain the load resonant frequency, and the equivalent parameter of load inductor depends on a cycle of charge and discharge to the load circuit. The system energy pre-charge means that the magnetization pre-charge to the inductor  $L_d$  and the load capacitor energy pre-charge, which makes their initial energy to reach the required level. The starting control is to connect the load to inverter, and it can fast and accurately control the output of rectifier after the starting condition met. The control model is shown as Fig. 6.

- Load characteristic identification

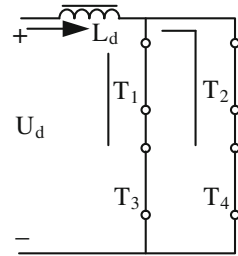
The load characteristic is determined by the load parameters. The identification of the load characteristics depends on its zero-input response. In the parallel resonant circuit, capacitance of  $C$  is the known, and the inductance of the inductor can be estimated by the expression (18).

$$L = N\mu_r\mu_0n\pi r^2 \tag{18}$$

In the equation,  $n = N/l$ ,  $l$ ,  $r$ ,  $\mu_0$  and  $\mu_r$  is, respectively, the turn number of coil in unit length, coil length, bar radius, permeability of vacuum and the differential permeability of iron bar.

The resonant frequency can be obtained by detecting the period  $T$  of the response of zero input, and the equivalent resistance  $R$  of inductor can be estimated as formula (19).

**Fig. 7** Magnetizing pre-charge path of  $L_d$



$$R = L\sqrt{1/LC - (2\pi/T)^2} \tag{19}$$

- System energy pre-charge

The pre-charged voltage of  $C$  is limited to its rated voltage, which is charged by another auxiliary capacitor, and the initial current on inductor  $L_d$  must meet the inequality (20).

$$I_{d0} \geq U_0/R_1 \tag{20}$$

where  $U_0$  is the threshold voltage of inverter commutation,  $R_1$  is the impedance of load, and also  $R_1 = L/RC$ .

The magnetizing pre-charge path of  $L_d$  is shown as Fig. 7, and the initial current can control to be increased to  $I_{d0}$  gradually.

- Starting control

When connecting the load to inverter, SCR  $T_1$  and  $T_4$  are turned off because of its inverse voltage, which realizes the conducting from 4-bridge-arm on convert to only  $T_2$  and  $T_3$  working. At the first commutation process, it only needs a turn off time of SCR  $t_q$  to be able completing the process (do not have to be wait until the natural zero-crossing to commute). Usually,  $t_q$  is in the microsecond level, but the natural zero-crossing time is in millisecond level. The less the time of the first commutation is, the greater the opportunity of starting successfully is when working on a hard situation to start. The first commutation process is shown as Fig. 8.

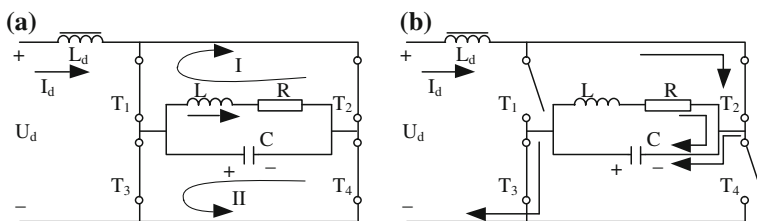


**Fig. 8** The first commutation process. **a, b**  $U_d$  is the rectifier output voltage,  $L_d$  is the filter inductor,  $I_d$  is the current on  $L_d$ ,  $R$ ,  $L$  and  $C$  respectively is equivalent resistor, equivalent inductor and the load compensating capacitor.  $T_1$ – $T_4$  are all SCR. I and II are two current loop

After completing the energy pre-charge, the initial energy of load circuit reaches the maximum. Then, it is connected the load to inverter and gets ready for the first commutation, and the process is shown as Fig. 8a. The capacitor  $C$  discharges through the loop I and II, SCR  $T_1$  and  $T_4$  turn off, and the path of  $I_d$  becomes the cathode of  $U_d \rightarrow L_d \rightarrow T_2 \rightarrow \text{RLC} \rightarrow T_3 \rightarrow$  the negative of  $U_d$ . Therefore, the completing the first commutation only needs a turn off time of SCR, which shows in Fig. 8b. The following control is based on the load voltage oscillation so as to control inverter-state switching, its principle is similar to the above, and there is no longer to repeat.

## 6 Experiment Result and Its Analysis

When the parameters are selected for  $R = 0.4 \Omega$ ,  $L = 0.5 \text{ mH}$ ,  $C = 500 \mu\text{F}$ ,  $U_{c0} = 500 \text{ V}$ , it made the simulation with the help of MATLAB/Simulink toolbox, and the Fig. 9 is the step response of control system shown as in Fig. 6. The comparison result of the simulation starting between the presented starting strategy and the general pre-charge strategy is shown as in Fig. 10.

From Fig. 9, the correctness of the model is verified by step response of the control system constructed by authors. The starting response of two different strategies is shown in Fig. 10. Under the same initial starting and load conditions, the response curve 1 and response curve 2 in Fig. 10 is, respectively, the response curve by presented starting strategy and general pre-charge strategy, the time of the first zero-crossing in curve 1 is shorter than in curve 2, and which means that it has indeed improved the system starting quality.

**Fig. 9** Step response of control system model

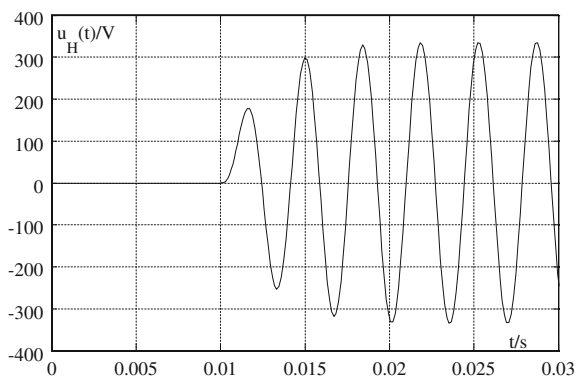
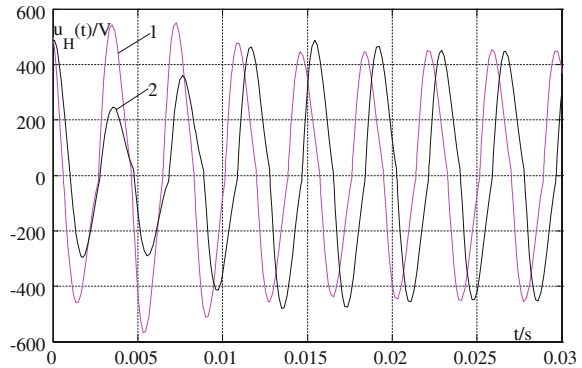


**Fig. 10** Response in different starting strategies



## 7 Conclusions

Based on the load capacitor pre-charge model, the paper presented a starting control strategy that can effectively improve the starting performance of SCR-CS-IHPS. Load capacitor pre-charge starting is a classical and actual method, and by means of deep analysis and comparative research, the experiment shows that the presented starting strategy is much shorter in first zero-crossing time based on the load capacitor pre-charge model. The research result provides a new thinking for start and control of the current source inverter.

## References

1. Alaa M, Egon O, Danny M et al (2010) Review of control techniques for inverters parallel operation. *Electr Power Syst Res* 80(12):1477–1487
2. Fisk M (2011) Validation of induction heating model for alloy 718 components. *Int J Comput Meth Eng Sci Mech* 12(4):161–167
3. Vadim C, Boris A, Arieh LS (1997) Approximate analysis of a starting process of a current source parallel inverted with a high-Q induction heating load. *IEEE Trans Power Electron* 12(2):294–301
4. Aiguo PH, Grant AC, John TB (2006) Direct ZVS start-up of a current-fed resonant inverter. *IEEE Trans Power Electron* 21(3):809–812
5. Fuentes R et al (2010) Comparative analysis of three starting methods for parallel resonant current. In: 5th IET international conference on power electronics, machines and drives, vol 2010, Brighton, April 2010. IET Conference Publications, Institution of Engineering and Technology
6. Qiang F, Ma L (2008) Technique of starting parallel inverter intermediate-frequency power supply on heavy load. *Beijing Ligong Daxue Xuebao* 28(3):241–244
7. Tibor S, Eva HD (2013) Adaptive control in series load PWM induction heating inverters. *Int J Electron* 100(12):1714–1723
8. Pham HN et al (2013) Dynamic analysis and control for resonant currents in a zone-control induction heating system. *IEEE Trans Power Electron* 28(3):1297–1307
9. Arash K et al (2008) Closed loop power control of an induction furnace. In: ICEM'08. 2008 international conference on electrical machines, Algarve, September 2008. Proceedings of the 2008 international conference on electrical machines. Institute of Electrical and Electronics Engineers Computer Society

# Optimal Configuration of Bypass Diodes for a High-Concentration Photovoltaic System

Ting-Chung Yu, Yao Ti Hung, Yih-Bin Lin, Chih-Hao Chen  
and Yan-Cheng Liou

**Abstract** The high-concentration photovoltaic (HCPV) system uses high-magnification condenser lens to focus sunlight on the surfaces of group III–V photovoltaic (PV) cells. The PV cells can convert sunlight to electricity effectively. However, since the HCPV system includes PV cells and concentrating equipment, its components are more than those of general photovoltaic systems and are more prone to high cost and malfunctions. Bypass diodes are installed in the HCPV modules to prevent power consumption when they are shaded or damaged. The main purpose of this paper is to investigate the influence of bypass diodes on the HCPV modules and look for an optimal bypass diode configuration. In this research, the authors cooperated with Arima EcoEnergy Technologies Corp. whose HCPV products were used as references for modeling the simulation system. MATLAB/Simulink was used as the modeling tool to establish a HCPV simulation system using the built-in PV cell model. Simulations were implemented under different shaded conditions and investigated the effects of power generations under different bypass diode configurations. According to the simulation results, the configuration of 1 bypass diode per 2 PV cells is the best in general and random shaded conditions; however, the configuration of 1 bypass diode per 3 and 6 PV cells are better for some special conditions. The simulation results in this paper can be provided to HCPV companies as references, while designing products in the future, and should be helpful for improving performance and cost of the products.

**Keywords** High-concentration photovoltaic system · Sunlight irradiance · Optimal configuration · Bypass diode

---

T.-C. Yu (✉) · Y.-B. Lin · C.-H. Chen · Y.-C. Liou  
Department of Electrical Engineering, Lunghwa University of Science and Technology,  
Taoyuan 33306, Taiwan  
e-mail: tingyu@mail.lhu.edu.tw

Y.T. Hung  
Arima EcoEnergy Technologies Corp, New Taipei City 23943, Taiwan  
e-mail: Eric.Hung@arimaeco.com

# 1 Introduction

The HCPV system has become a new focus of attention of the global photovoltaic (PV) industry. It has the advantages of high conversion efficiency, low average cost of electricity (LCOE), and others. Its great value and development potential has attracted the attention of PV industry and research institutes in USA, Europe, Japan, and China who devote their efforts to related research. It has become a rising star in PV industry.

Partial shading on PV modules can cause large reverse voltages and reduce the generated output power. Bypass diodes are frequently used to minimize the effects of shading on PV module power generation. In theory, it is better to connect each PV cell of a PV module in parallel with a bypass diode. PV modules can generate more output power than those without bypass diodes. However, the power dissipated by all the bypass diodes can be comparable with the power produced by PV modules in lower power conditions such as low-irradiance climate. This can be happened especially in the case of HCPV modules, whose amount of PV cells is much more than those of general PV modules. Therefore, how to get a balance point between shaded effects of PV modules and power dissipation by bypass diodes has become an important issue.

In recent years, many literatures concerning PV modules, bypass diodes, and shaded effects have been published [1–6]. In the study of [1], Ding et al. used Simscape solar cell to be the simulation element in the MATLAB platform to show the I–V and P–V characteristics of PV cells. The related parameters of PV cells such as open-circuit voltage, short-circuit current, irradiance can easily be set in the Simscape solar cell model. Diaz-Dorado et al. examined the performance of a photovoltaic array in [2] with an overlapped bypass diodes configuration. They found a different way to balance the PV power generation and power dissipation by all the diodes. In the research of [4], Barreiro et al. proposed a testing of various module types with and without bypass diodes. The results of the experimentation showed that the performance efficiency and functionality of bypass diodes is highly dependent on the orientation of the PV modules. Vemuru et al. [5] used a non-overlapping bypass diode configuration in a randomly shaded solar module and compared with modules devoid of bypass diodes to find the impact of using bypass diodes on the PV cell performance under shading. This paper investigates the influence of bypass diodes in HCPV modules under different shaded conditions. The optimal configuration of bypass diodes in PV modules is discussed and suggested in later sections.

This paper is organized as follows. Section 2 introduces the structure of the HCPV cell, module, and bypass diode. Modeling of the HCPV cell and module with bypass diodes are described in Sect. 3. Section 4 shows the simulation results with different bypass diode configurations under a fully shaded condition, while Sect. 5 is the conclusion of this paper.



## 2 Structures of HCPV Cell, Module, and Bypass Diode

### 2.1 HCPV Cell and Module

The basic structure of a HCPV cell is shown in Fig. 1. It uses a Fresnel lens device [7] to collect and concentrate incident sunlight to the surface of the group III–V PV cell. A HCPV module consists of many HCPV cells mutually connected with circuits in series or in parallel. The HCPV module used as an example in this paper is composed of totally 144 GaAs PV cells in series. Each solar tracker consists of 8-HCPV modules in parallel. Two trackers are connected in series to the inverter of the HCPV system (Fig. 2). Owing to the design of condenser for the HCPV cell,

Fig. 1 Basic structure of a HCPV cell

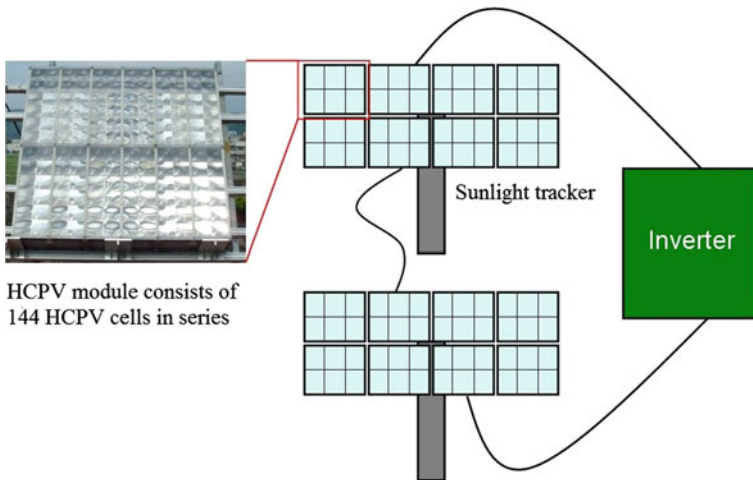
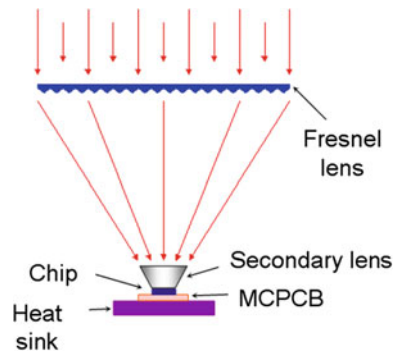


Fig. 2 Electrical connection diagram of a HCPV system

incident sunlight is gathered in a small range. It not only greatly reduces the use of HCPV cell area, but also substantial increases energy density of the light-receiving area.

## 2.2 HCPV Cell and Module

Most of the PV modules are composed of PV cells in series. When one or more PV cells malfunctioned or are shaded for some reasons, it results in significantly reduced current, even no current or large voltage drop under a totally shaded condition. This would cause a lot of power losses. However, if the PV cell is connected with a bypass diode in parallel, the current of series circuit can go through the bypass diode under malfunctioned or shaded conditions. Therefore, the whole PV module will not cause serious consequences due to one malfunctioned or shaded PV cell. Working schematic diagram of bypass diodes is shown in Fig. 3.

For example, a 3-MW HCPV system needs about one million bypass diodes due to the common configuration of 1 bypass diode per 1 PV cell. In the circuit, each bypass diode is an electronic component which must be packaged and protected. There are totally two million electronic components needed to be packaged and protected in a 3-MW HCPV system. Therefore, if the configuration of one bypass diode per several PV cells is chosen, in addition to reducing costs and power dissipation of bypass diodes, the risk of packaging failure for bypass diodes is also reduced.

Currently the design of crystalline PV modules [8, 9] commonly chooses the configuration of one bypass diode per several PV cells (Fig. 4). The result of this design provides reference and feasibility for developing the configuration of bypass diodes used in HCPV modules. The design of sharing bypass diodes can effectively

**Fig. 3** Working schematic of bypass diodes

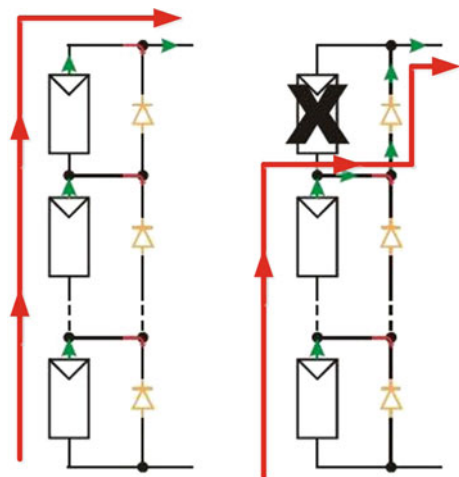
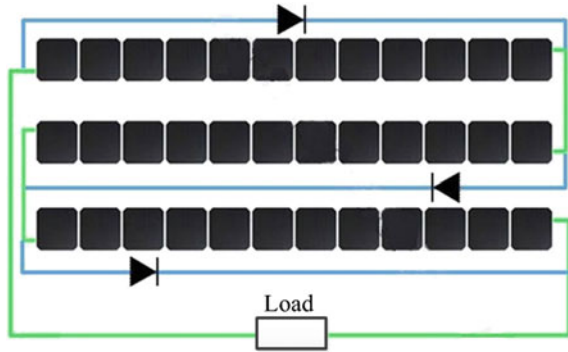


**Fig. 4** Configuration of sharing bypass diodes



reduce the amount of bypass diodes used. Therefore, finding a way or trend to reduce the number of bypass diodes and get an optimal configuration of bypass diodes is the main topic of this paper.

### 3 Modeling of HCPV Module with Bypass Diodes

The research topic of this paper focuses on the generation behavior of HCPV modules. Before establishing the model of HCPV module, a single GaAs PV cell model has to be determined first. A physical PV cell model included in MATLAB/Simscap toolbox is chosen as the GaAs PV cell model in this paper. Although the built-in physical PV cell model is standardized, it is more intuitive when building connections between PV cells and other components to set up the HCPV system. Table 1 is the electrical specification sheet for the GaAs PV cell used in this paper.

Figure 5 shows the configuration diagram of a HCPV module used in this paper. Each HCPV module includes 6 series connected receivers. Each receiver is composed of 24 HCPV cells in series. Therefore, there are 144 GaAs PV cells in one HCPV module. A HCPV module simulation system established by MATLAB/Simulink is shown in Fig. 6. Figure 7 shows an internal component wiring in each receiver. It is easy to modify the wiring of bypass diodes in order to change the configuration of bypass diodes.

**Table 1** The electrical specification sheet for the GaAs PV cell

Items	Value	Items	Value
Series resistance (W)	0.18671	Fill factor F.F. (%)	86.54
Short-circuit current $I_{SC}$ (mA)	2137.4	Maximum working current $I_{mp}$ (mA)	2102.7
Open-circuit voltage $V_{OC}$ (V)	3.185	Maximum working voltage $V_{mp}$ (V)	2.802
Maximum power $P_{max}$ (mW)	5891.2		

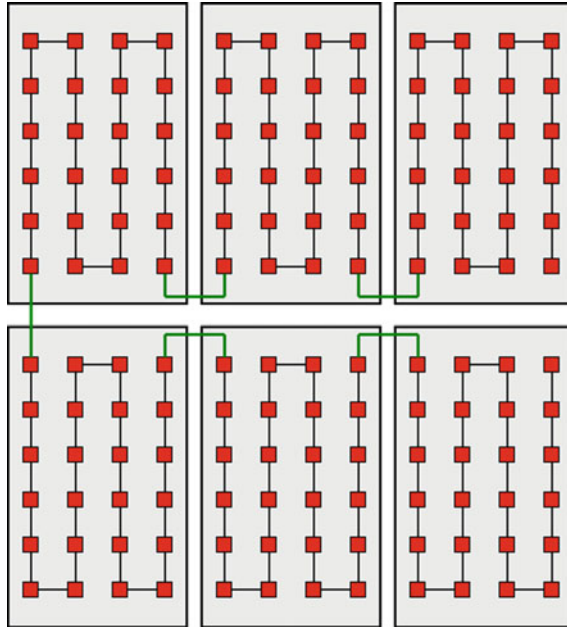


Fig. 5 Configuration diagram of a HCPV module

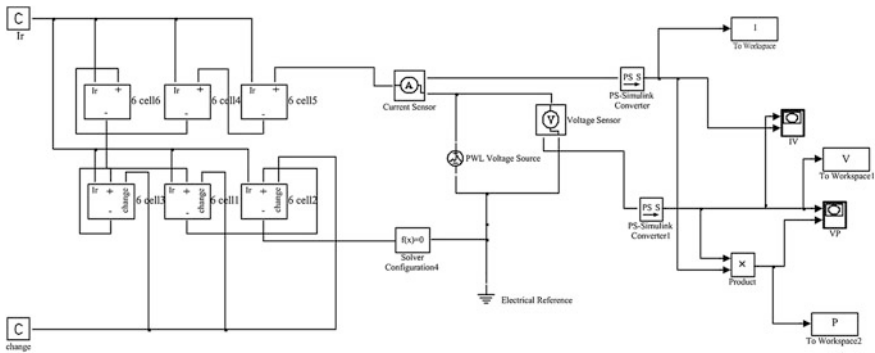


Fig. 6 A HCPV module simulation system by MATLAB/Simulink

### 4 Analyses of Simulation Results

In order to get close to the actual operation of HCPV modules, five different shaded modes [Fig. 8(1–5)] are chosen in this paper. It includes row shading, column shading, and random shading. The irradiance used in the simulations is set to be  $1000 \text{ W/m}^2$  under normal circumstances and set to be  $0 \text{ W/m}^2$  under shaded conditions. Next, different configurations of one bypass diode per several PV cells are

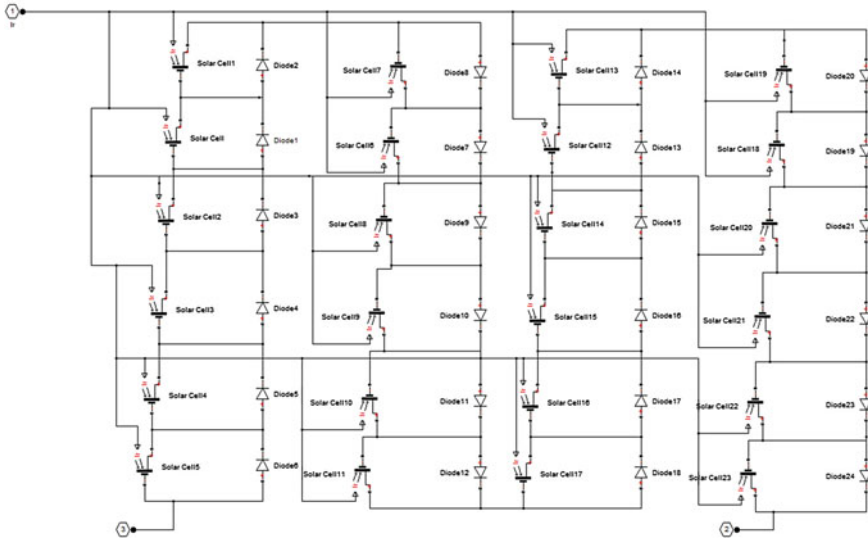


Fig. 7 Internal component wiring in each HCPV receiver

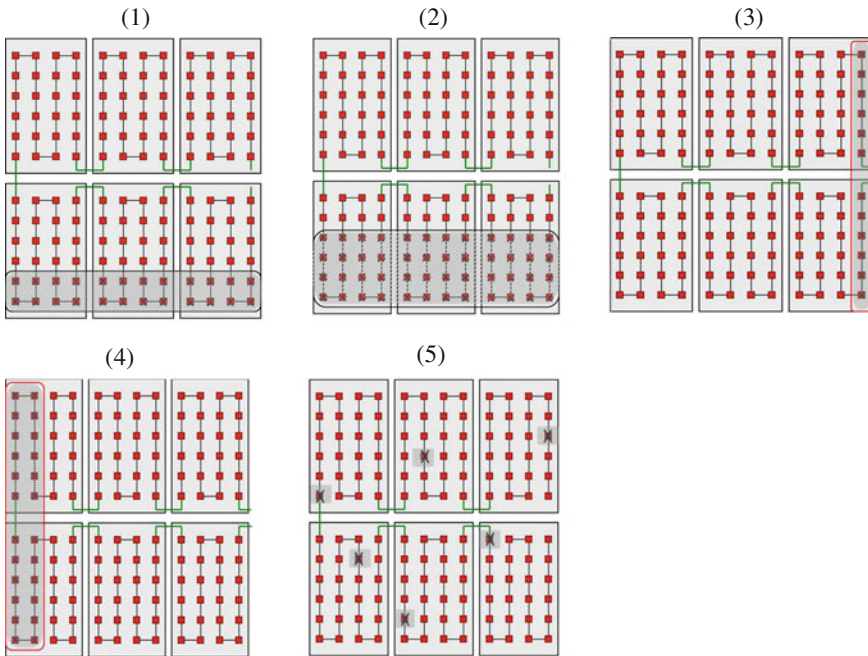


Fig. 8 Five different shaded modes of a HCPV module

**Table 2** The electrical specification sheet for the bypass diode

Items	Value	Items	Value
Average rectified output current	2.0 A	Continuous reverse voltage	40 V
Maximum forward voltage	0.5 V	Operating temperature range	-55 to 125 °C
Forward surge current	50 A	Storage temperature range	-65 to 175 °C
Repetitive peak reverse voltage	40 V		

used in the established HCPV module simulation system in order to find an optimal configuration after analyzing the simulation results.

Since the HCPV module consists of 6 receivers, each receiver contains 24-HCPV cells in series. Therefore, eight different configurations of one bypass diode per 1 cell, 2 cells, 3 cells, 4 cells, 6 cells, 8 cells, 12 cells, and 24 cells are chosen to use in the simulation system. Table 2 is the electrical specification sheet for the bypass diode used in this paper.

In order to highlight the effects of the configurations of bypass diodes on HCPV power generation, the sunlight irradiance of all the shaded areas is set to be 0 W/m<sup>2</sup> in the following simulations. The simulation results of the P-V curves of the HCPV module with 8 different bypass diode configurations under 5 different shaded modes are shown in Figs. 9, 10, 11, 12, and 13. The values of maximum power of the HCPV module for each bypass diode configuration under different shaded modes are listed in Table 3.

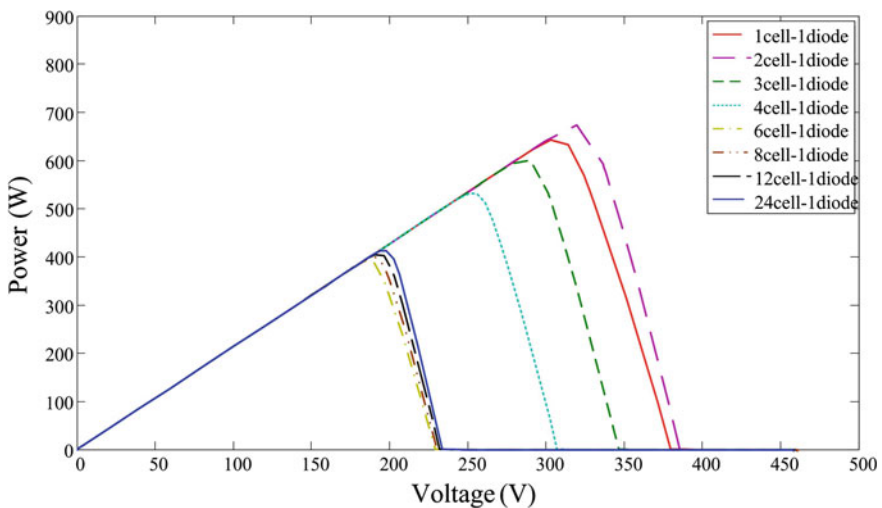


**Fig. 9** P-V curves of the HCPV module in shaded mode 1

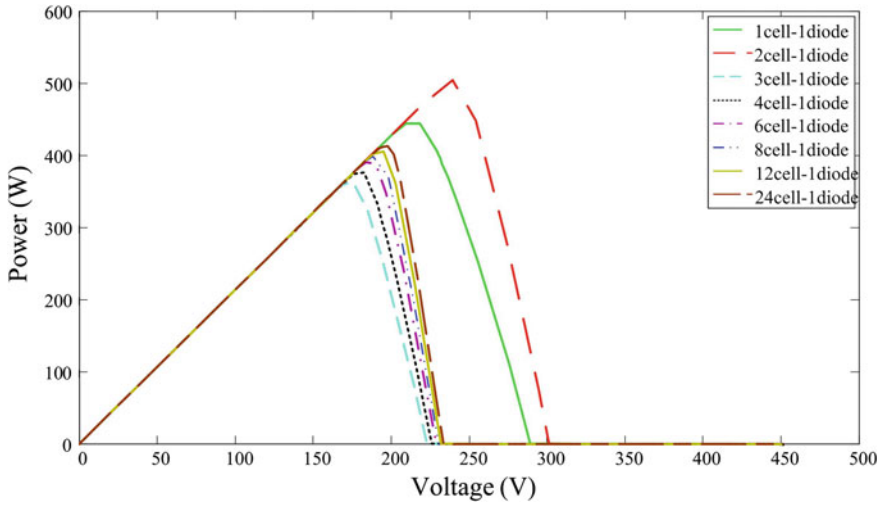


Fig. 10 P-V curves of the HCPV module in shaded mode 2

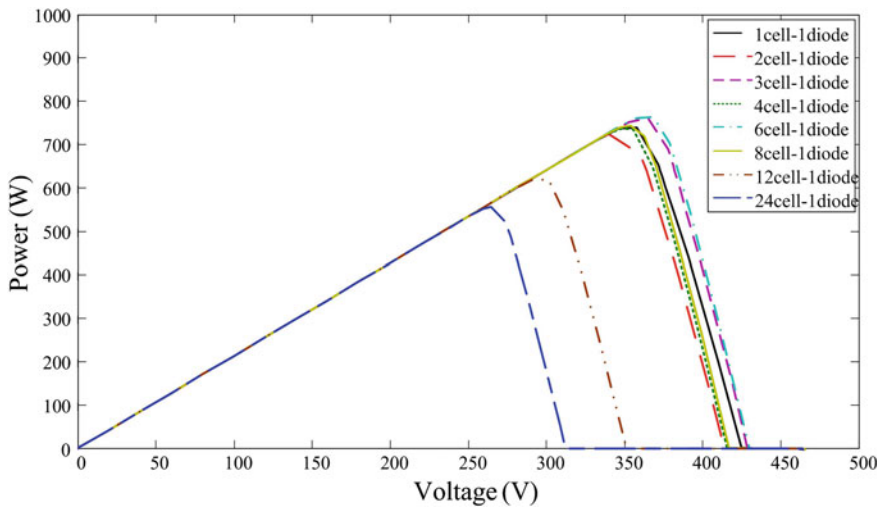


Fig. 11 P-V curves of the HCPV module in shaded mode 3

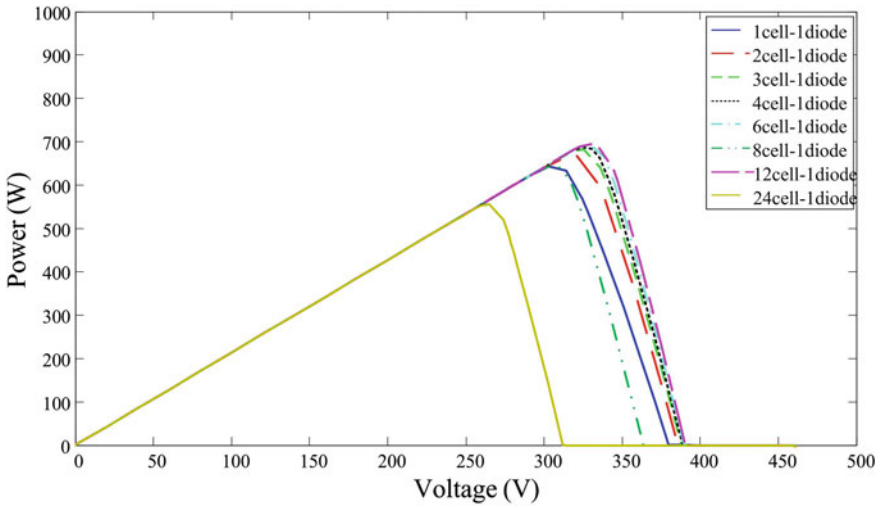


Fig. 12 P-V curves of the HCPV module in shaded mode 4

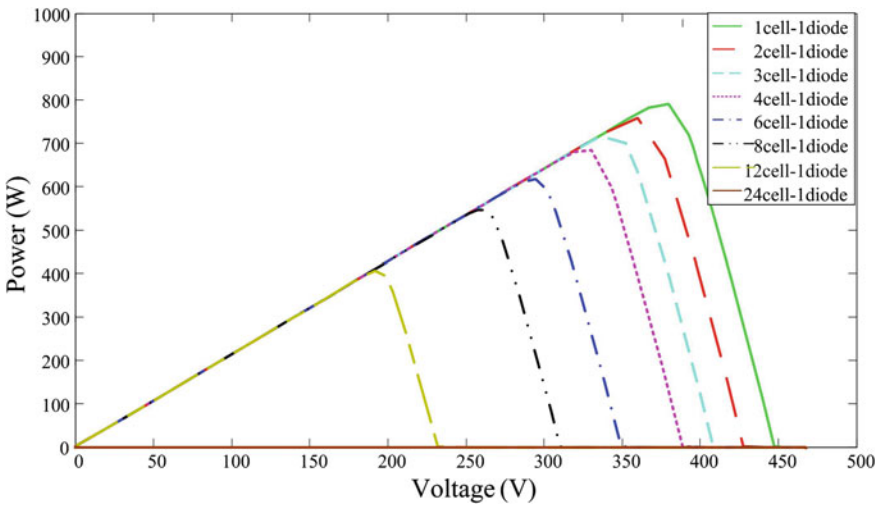


Fig. 13 P-V curves of the HCPV module in shaded mode 5



**Table 3** Values of maximum power of the HCPV module for each bypass diode configuration under different shaded modes

Configuration	1 diode per 1 cell (W)	1 diode per 2 cells (W)	1 diode per 3 cells (W)	1 diode per 4 cells (W)	1 diode per 6 cells (W)	1 diode per 8 cells (W)	1 diode per 12 cells (W)	1 diode per 24 cells (W)
Mode 1	642.7	673.2	600.9	532.2	388.4	399	405.3	413.3
Mode 2	444.3	504.2	363.3	377.2	390.4	399	405.3	413.5
Mode 3	739	723.6	760.6	734.7	763.3	743.7	697	556.6
Mode 4	739	723.6	760.6	738.8	767.1	743	696.7	556.5
Mode 5	791	757.6	715.6	683.9	617	545.7	406.3	0

## 5 Conclusion

The main purpose of this paper is to explore the optimal configuration of bypass diodes for a HCPV system. It is expected to effectively reduce the costs of HCPV modules and minimize the effects on power generation. According to simulation results from previous section, the configuration of 1 diode per 2 HCPV cells possesses a better output power than the others under shaded modes 1 and 2. By contrast, under shaded modes 3 and 4, the configurations of 1 diode per 3 and 6 cells have better results due to one side deviation of the shaded area. Under shaded mode 5, since the shaded condition is more uncertain and severe, it can be observed from simulation results that the configuration of 1 diode per 2 cells has the best result with only 5 % power loss and the configuration of 1 diode per 3 cells had 10 % power loss. The less the bypass diodes used, the more the power losses dissipated. The HCPV module is useless when the configuration of 1 diode per 24 cells is used under the random shaded condition.

Based on the above results, the configuration of 1 diode per 2 cells is a more conservative approach. It not only can save half of the bypass diode costs, but also has better output power than the others under general shaded (mode 1 and 2) and random shaded (mode 5) conditions. However, the configurations of 1 diode per 3 and 6 cells should have better results in exceptional circumstances of shade (mode 3 and 4). The simulation results shown in this paper can provide HCPV product manufacturers for future reference in terms of design and performance improvements.

## References

1. Khanna V, Das BK, Bisht D (2013) Matlab/SimElectronics models based study of solar cells. *Int J Renew Energy Res* 3(1):30–34
2. Diaz-Dorado E, Suarez-Garcia A, Carrillo C, Cidras J (2010) Influence of the shadows in photovoltaic systems with different configurations of bypass diodes. In: *International*

- symposium on power electronics electrical drives automation and motion, Italy, 14–16 June 2010, pp 134–139
3. Pandiarajan N, Muthu R (2011) Mathematical modeling of photovoltaic module with simulink. In: International conference on electrical energy systems, India, 3–5 Jan 2011, pp 258–263
  4. Barreiro C, Jansson PM, Thompson A, Schmalzel JL (2011) PV by-pass diode performance in landscape and portrait modalities. In: 37th IEEE photovoltaic specialists conference (PVSC), USA, 19–24 June 2011, pp 3097–3102
  5. Vemuru S, Singh P, Niamat M (2012) Modelling impact of bypass diodes on photovoltaic cell performance under partial shading. In: IEEE international conference on electro/information technology, Indianapolis, 6–8 May 2012, pp 1–5
  6. Mori I, Kubota M, Mita Y (2014) A test structure of bypass diodes for on-chip high-voltage silicon photovoltaic cell array. In: International conference on microelectronic test structures, Udine, 24–27 Mar 2014, pp 157–160
  7. Willeke G (2003) High concentration photovoltaics-state-of-the-art and novel concepts. In: 3rd world conference on photovoltaic energy conversion, Japan, 18 May 2003, pp 2841–2844
  8. Ziar H, Afjei E, Siadatan A, Arjhangmehr A (2011) Different diode configurations evaluation in photovoltaic arrays using binary coding method. In: International Aegean conference on electrical machines and power electronics, Istanbul, 8–10 Sept 2011, pp 682–686
  9. Ziar H, Mansourpour S, Afjei E, Kazemi M (2012) Bypass diode characteristic effect on the behavior of solar PV array at shadow condition. In: 3rd power electronics and drive systems technology, Tehran, 15–16 Feb 2012, pp 229–233

# Optimal Design and Analysis of a 3.3-MW Wind Turbine Gear Train

Jianxin Zhang and Zhange Zhang

**Abstract** In this paper, we design a type of 3.3-MW wind gear train based on genetic algorithm and finite element analysis method. We first construct the basic wind gear train by using two standards NWG structure and a pair of parallel shaft gears, respectively, as the low-, middle-, and high-speed stages. Then, genetic algorithm is applied to achieve optimal parameter for the basic wind gear train. Finally, ANSYS as finite element analysis tool is employed to verify the optimized gear train. We compare the deformation and stress of the every stage original and optimized gear chain under maximum operating conditions. The analysis results show that optimized parameters can well meet the requirements of 3.3-MW wind turbine.

**Keywords** Wind turbine gear train · Structure design · Optimal design · Finite element analysis

## 1 Introduction

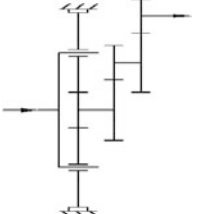
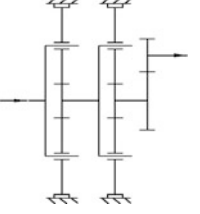
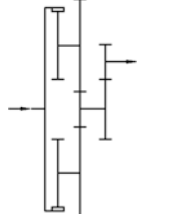
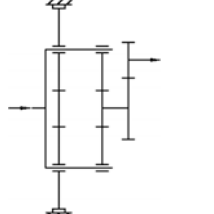
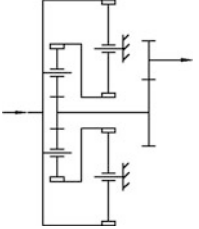
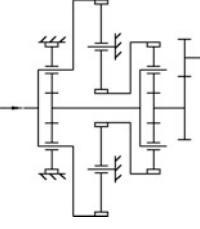
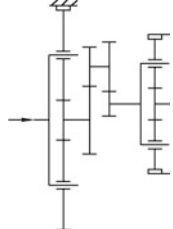
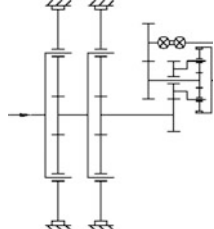
The wind turbine generator set is one of the most important mechanical systems which can transform the wind power into electric energy. The performance of wind turbine generator set is directly determined by the performance characteristics of driven train. The wind turbine-driven train is generally composed by impeller, the gearbox, and generator. The gearbox is an important subsystem of wind turbine-driven train, and it locates between the impeller and the generator. The main purpose of gearbox is to transfer power from the low-speed impeller to the high-speed generator, and it can convert large torque into low torque. To achieve

---

J. Zhang (✉) · Z. Zhang  
Key Lab of Advanced Design and Intelligent Computing, Ministry of Education,  
Dalian University, Dalian 116622, China  
e-mail: zjx99326@163.com

Z. Zhang  
e-mail: nicege@163.com

**Table 1** Common megawatt-class wind turbine gear train

One planetary gear stage; two spur wheel stages	Two planetary gear stages; one spur wheel stage	Planetary gear-stage fixed planet	Planetary gear-stage fixed ring wheel
			
Planetary coupled gearbox	Differential gearbox	Hydraulic torque limiting	Hydrostatic differential gearbox
			

the transformation requirement, a large ratio between impeller and generator need considered for the design of driven train. To get the high transmission ratio, the megawatt-class wind turbine gear trains are commonly configured with multistages [1]. The specific structures of the wind turbine gear trains are given in Table 1. Generally, planetary gear train outperforms the parallel gear train under the similar operation condition, and it also has the advantages of high drive efficiency, small size, light weight, larger transfer ratio, steady, strong shock, vibration resistance, and so on.

Wind turbine gearbox connects to the impeller directly, and it works at the situation of various loads, which makes the gears be easily damaged. The main types of gear failures include insufficient flexural strength, tooth surface gluing, tooth surface pitting and broken [2]. Meantime, the wind turbine gearbox is installed at tens of meters high or even more than one hundred meters high from the ground in a narrow space of the turbine tower, which makes it be difficultly maintained and repaired. Furthermore, the gear train system faults account for almost 60 % total faults of the gearbox [3]. Those situations require gear train with high reliability of 20 years of service life. As one of the most expensive components of the wind turbine system, the failures ratio exceeds the expectation. In order to meet the requirements of use and reduce the weight, the structure of gear train should be moderate.

## 2 A 3.3-MW Wind Turbine Gear Train Design

### 2.1 Structural Form of the 3.3-MW Wind Gear Train

The wind turbine gear chain consists with three stages, and, respectively, is low-, middle-, and high-speed stages. The low-speed stage adopts a standard NWG structure composed by four planetary gears and a sun gear with modulus being 14 mm. The number of gear teeth are 29, 37, and 103, respectively. The middle-speed stage adopts a standard NWG structure which composed with three planetary gears and a sun gear. The modulus is 11 mm. The number of gear teeth is 20, 37, and 94, respectively. The high-speed stage uses a pair of parallel shaft gears, and the modulus are 13 mm. The number of gear teeth are 25 and 88. The detailed structure of the designed gear train is given in Fig. 1.

### 2.2 Optimization Design of the Drive Train

The traditional design has a complex process, and it requires a lot of parameter selection and verification checking which makes a lot time-consuming and laborious. Furthermore, the selected parameters are not the best.

Therefore, we use a smart method that the optimization of parameters adopts the genetic algorithm [4]. The algorithm is based on the computer to select parameters and check performance in a smart way, where, the optimization goal is the minimal volume of the gear train. There are eight mutually uncorrelated parameters of the gear train used as the optimization parameters which include modulus, teeth, tooth width, and there are twelve constraint conditions which include the design requirements, performance requirements, installation requirements [5].

New gear train parameters are obtained by optimization calculation. The new modulus of the first stage is 14 mm and the number of gear teeth are 28, 36 and 100, respectively. The new modulus of the middle stage is 12 mm and the number of gear teeth are 18, 33, and 84, respectively. The new modulus of the high-speed stage is 17 mm, and the number of gear teeth are 17 and 60. The volume of the original gear train is larger than the volume of the optimal. So there is some redundancy in the original designing by comparing the original gear parameters and the optimal parameters.

**Fig. 1** Structural form of a 3.3-MW wind gear train



### 3 Finite Element Analysis

Finite element analysis technique is a kind of effective way to verify the design results. To verify the feasibility of the optimized wind power gear train, we compare the stress and strain performance of the optimized gears and original gears with ANSYS in the same situation. The models of gears are built by PRO/E with parametric design method [6], then importing the model into ANSYS for analysis. The specific analysis process is give as follows:

#### Step 1: Solid Modeling.

The accurate model of gears can be built by PRO/E, which is the important software to establish 3-D models in the parametric method. However, these models cannot be directly used to the finite element analysis tool. The chamfer, fillet, and little details must be removed [7] because they always made the meshing perish or complex. On the other side, the complex meshes have a negative impact on the calculation efficiency.

#### Step 2: Finite Element Modeling and Meshing.

Import the established model into ANSYS, and then set the material properties, element types, and so on. Solid bricks 8 nodes 185 adopt as the cell type, and the material properties are the same to actual. To reduce the computational complexity and ensure the authenticity, linear density adopts 5 and the meshing can get the smart size.

#### Step 3: Static Analysis.

In this process, the constraints and loads are imposed on the finite element model. To ensure all analysis consistency, all gears' inner surface is imposed with full restraint and their two sides have the axial constraints. The forces determined by the input power and the structure of the gearbox are loaded tangential to the addendum circle [8]. The setting ensures that analysis condition are hard than the actual. If the gears can work in such extreme circumstances, the gears can work well in the other conditions.

#### Step 4: Results Analysis.

We select pinion gears of each stage for stress analysis as they are easier to destroy than the others. On the other hand, they have a brief computing process. We get some results including stress and deformation diagram for original and optimal gears. By comparing the deformation and stress size of the optimal gears and the original gears under the same loads, we can see clearly whether the optimal results meet the requirements.

The deformation results of original and optimized (optimal) gears are given in Fig. 2. There are six diagrams in Fig. 2. Figure 2a, b is the deformation of original and optimized low-speed-stage sun gear, respectively. Figure 2c, d are the deformation of original and optimized intermediate-speed-stage sun gear, respectively.

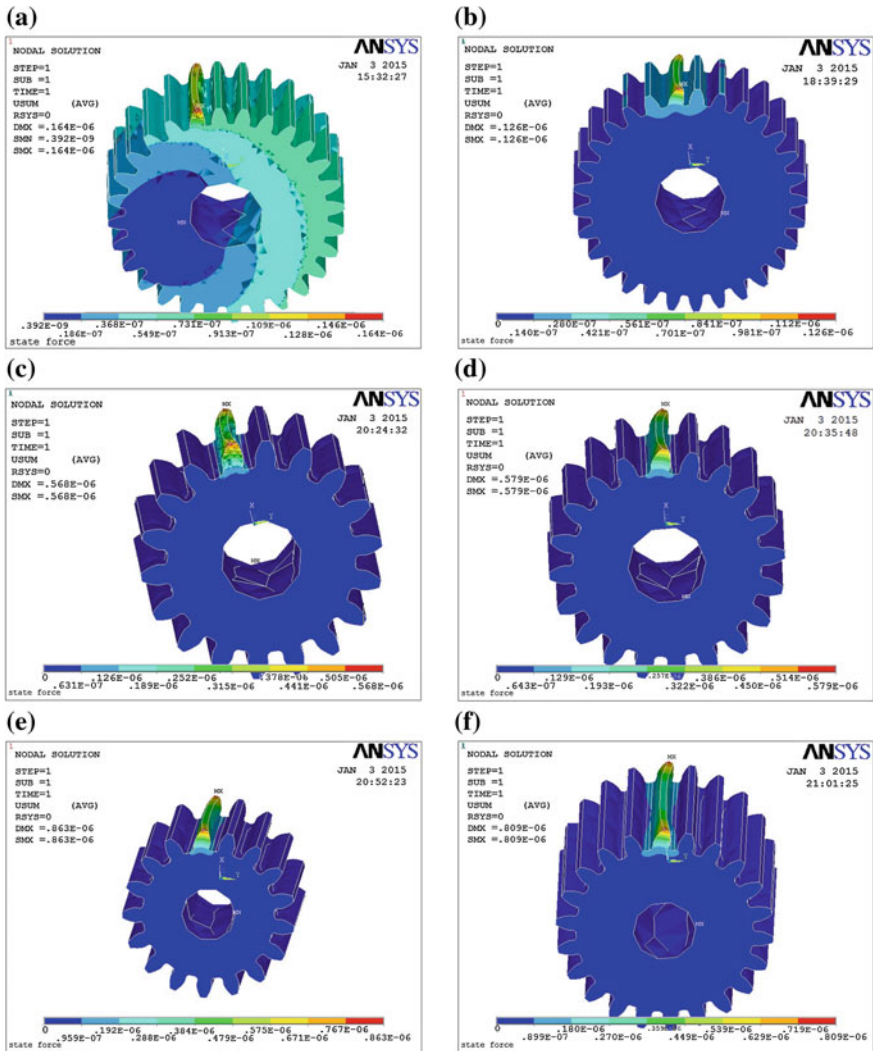


**Fig. 2** The deformation of original and optimized gears. **a** Deformation of original low-stage sun gear. **b** Deformation of optimal low-stage sun gear. **c, d** Deformation of original mid-stage sun gear. **e, f** Deformation of original high-stage sun gear

Figure 2e, f are the deformation of original and optimized high-speed-stage pinion gear, respectively. There are not only one pairs of teeth keep in touch with each other in actual conditions. We chose one extreme condition that the force loads at one tooth so that all of the deformations for the gears are similar. The deformation is changed larger from root to roof in the radial direction and is reduced from two sides to the middle in the axial direction. The largest shift parts are on the tip of the both sides.

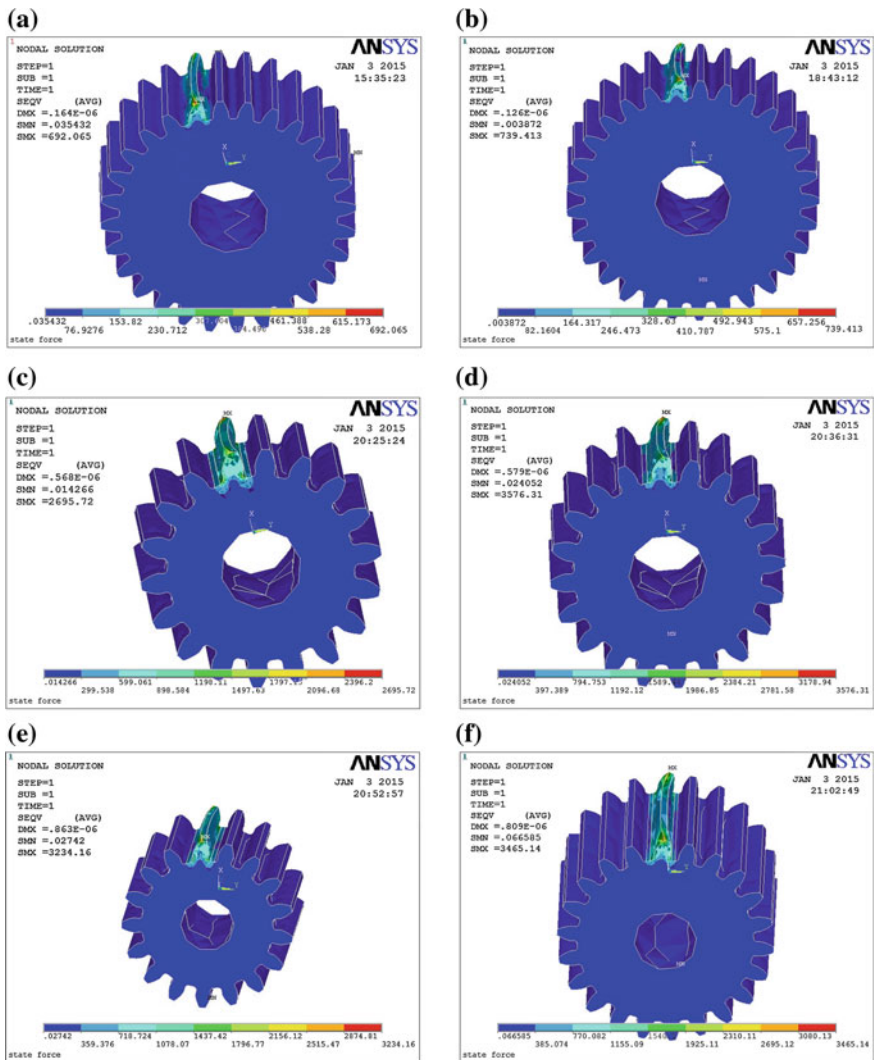


**Fig. 3** The stress of original and optimized gears. **a** Stress of original low-stage sun gear. **b** Stress of optimal low-stage sun gear. **c, d** Stress of original mid-stage sun gear. **e, f** Stress of original high-stage sun gear

The stress analysis results of original and optimized gears are given in Fig. 3. There are also six diagrams in Fig. 3, where (a) and (b) are the stress of original and optimized low-speed-stage sun gear, respectively; (c) and (d) are the stress of original and optimized intermediate-speed-stage sun gear, respectively; and (e) and (f) are the stress of original and optimized high-speed-stage pinion gear, respectively. The stress of the gears are similar in the graphs, the stress is changed larger



**Table 2** The stress and deformation of the every stages pinion gears

Content	Gear train	Low-speed-stage sun gear	Intermediate-speed-stage sun gear	High-speed-stage pinion gear
Largest deformation (m)	Original	$0.164 \times 10^{-6}$	$0.568 \times 10^{-6}$	$0.863 \times 10^{-6}$
	Optimal	$0.126 \times 10^{-6}$	$0.579 \times 10^{-6}$	$0.809 \times 10^{-6}$
Normal deformation (m)	Original	$0.913 \times 10^{-7}$	$0.315 \times 10^{-6}$	$0.479 \times 10^{-6}$
	Optimal	$0.703 \times 10^{-7}$	$0.322 \times 10^{-6}$	$0.449 \times 10^{-6}$
Largest stress (MPa)	Original	692.065	2695.72	3234.16
	Optimal	739.413	3576.31	3465.14
Normal stress (MPa)	Original	230–400	900–1497	1078–1437
	Optimal	246–410	1192–1589	1155–1540

from middle to roof and boot in the radial direction and reduced from two sides to the middle in the axial direction. The largest stress is on the tip of the both sides.

The main stress and deformation of the every stages pinion gears are shown in the following Table 2. There are two kinds of deformations in Table 2. The largest deformation is the effect of local force and they are easy to destroy, so the largest deformation of the gear must be less than the maximum allowable value. The maximum deformation of each optimized gear is smaller than that of the original except the middle stage, but its value is less than the allowable. The middle part of the gear is the main area of work, so the middle deformation is used as a basis, and they all reduced by comparing the optimized gears and the original ones. There are two kinds of stresses in Table 2. These place work under much stress and are easily destroyed. So, we must do some heat treatment, chamfer and fillet in these weak place to improve the strength of the gears [9]. The largest stress of the optimized gears is bigger than that of the original but less than the allowable; in order to ensure the gears work well, we can do some partial structural change to bear the increasing stress. The root stresses are increased by comparing the optimized gears and the original ones, but they are less than the maximum allowable value.

## 4 Conclusion

We design a type of 3.3-MW wind gear train based on genetic algorithm and finite element analysis method in this paper. The basic wind gear train is composed by two standards: NWG structure and a pair of parallel shaft gears, which are, respectively, as the low-, middle-, and high-speed stages. The genetic algorithm is applied to achieve optimal parameter for the basic wind gear train. ANSYS as finite element analysis tool is employed to verify the optimized gear train by comparing the deformation and stress of the every stages original and optimized gears under the maximum operating conditions. The results show that the optimal design of the gear train based on genetic algorithm is more effective, and the designed wind gear train can well meet the real requirement of 3.3-MW wind turbine.

**Acknowledgements** This work is supported by the National Natural Science Foundation of China (No. 61202251), and the Program for Liaoning Excellent Talents in University (No. LJQ2013133).

## References

1. Pang ZF, Zhang CL, Yang JX, Zhao ZQ (2011) Innovative development of gear body formand transmission structure. *J Mech Transm* 35(01):1–4
2. Wang H, Li XL, Wang G, Xiang D, Rong YM (2013) Research on failure of wind turbine gearbox and recent development of its design and manufacturing technologies. *Chin Mech Eng* 24(11):1542–1549
3. Xie Y, Qiang JX (2009) Condition monitoring of large-scale megawatt wind turbines. *J Shanghai Dianji Univ* 12(4):271–275
4. Buiga O, Tudose L (2014) Optimal mass minimization design of a two-stage coaxial helical speed reducer with Genetic Algorithms. *Adv Eng Softw* 68:25–32
5. Mendi F, Baskal T, Boran K, Boran FE (2010) Optimization of module, shaft diameter and rolling bearing for spur gear through genetic algorithm. *Expert Syst Appl* 37:8058–8064
6. Li Z, Chen Y (2013) The computer simulation on wind turbine gearbox design. In: *The international conference on technological advances in electrical, electronics and computer engineering*, pp 454–458
7. Tian W, Fu SX, Li CY (2008) Reasonable analysis of root stresses and teeth compliances based on ANSYS. *J Changsha Aeronaut Vocat Tech Coll* 8(4):48–51, 63
8. Yang SH, Li GG (2013) 3D simulation on root stresses and tooth deformations of whole gear. *Comput Aided Eng* 22(2):36–40
9. Bao JH, He WD, Li LX (2010) Finite element analysis of locomotive traction gear. In: *International conference on mechanic automation and control engineering*, pp 649–652

# The Analysis of Battery Cooling Modes of EV

Yue Yang, Pengyu Wang, Guangming Lu, Hang Dong, Feng Li and Yanru Suo

**Abstract** In this paper, the lithium battery for electric vehicles is used. The working principle and the heating principle of the battery are analyzed. Based on the battery heating principle, the performance of the existing battery cooling mode is qualitatively analyzed. Battery heating model is established on the basis of which different battery cooling models are established, including air cooling mode, indirect water cooling mode, and direct liquid cooling mode. Compared with the air cooling mode, the cooling effect of the liquid cooling mode is more obvious, and the range of temperature of the battery cell in battery packs is much smaller in the liquid cooling mode.

**Keywords** Battery · Cooling system · Cooling modes · Simulation

---

Y. Yang (✉) · P. Wang · G. Lu · H. Dong · F. Li · Y. Suo  
State Key Laboratory of Automotive Simulation and Control, Jilin University, Nanling Campus, 5988 Renmin Street, Changchun 130000, Jilin, People's Republic of China  
e-mail: 694878487@qq.com

P. Wang  
e-mail: WangPY@jlu.edu.cn

G. Lu  
e-mail: 1104712727@qq.com

H. Dong  
e-mail: 792334867@qq.com

F. Li  
e-mail: 492200836@qq.com

Y. Suo  
e-mail: 940820154@qq.com

## 1 Introduction

The development of electric vehicles (EVs) has received wide attention from the society and strong support from the government and has become an important product in the field of new energy vehicles. The electric vehicle is powered by the battery pack, and the performance of the battery pack directly affects the performance of the electric vehicle. The performance of the battery pack is strongly influenced by temperature. The battery capacity, life, and efficiency will decline and even cause an accident, if the temperature is too high. Therefore, it is necessary to control the temperature of the battery in a reasonable temperature range. In this paper, a battery pack model is built based on AMESim, and different forms of cooling system in the model are simulated, in order to contrast the control effect of different cooling forms of the battery temperature.

## 2 Battery Heating Principle

### 2.1 Working Principle of Lithium Battery

The working process of lithium ion battery is actually that lithium ion intercalates and deintercalates in negative and positive electrodes through electrolyte and diaphragm [1–4]. The working principle is shown in Fig. 1.

While the battery is charged, the electrons run from the positive electrode to the negative through the external circuit. At the same time, lithium ions deintercalate from the positive electrode and move to the negative through the diaphragm, combining with the electron and intercalating into carbon materials. The more the lithium ion is intercalated, the higher the charging capacity is. In contrast, when discharging, the electrons run from the negative electrode to the positive electrode through the external circuit. Simultaneously, lithium ions deintercalate from the

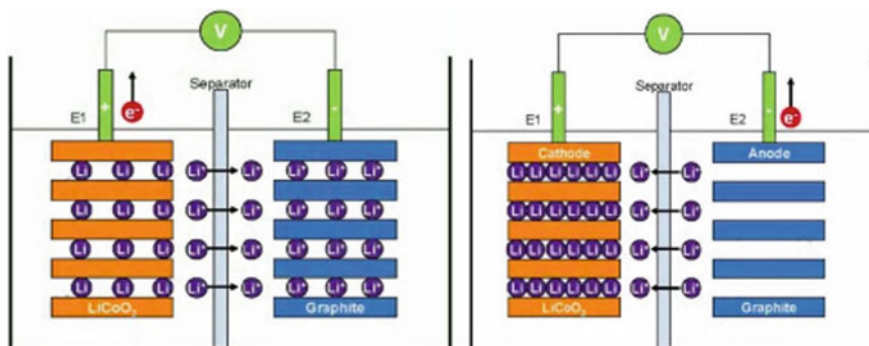


Fig. 1 Working principle of lithium ion battery

negative electrode and move back to the positive electrode. The more the lithium ions move back to the positive electrode, the higher the discharging capacity is. As the process of charging and discharging is going on, lithium ions intercalate in and deintercalate from the positive and negative electrodes repeatedly.

## 2.2 Lithium Ion Battery Heating Model

In 2001, Sato et al. in Honda Automotive Co., Ltd [5] verified a model for calculating the thermal power of a battery by experiments, and applied it in Ni-MH batteries and Li-ion batteries. They thought that the internal heat of the battery is divided into four parts, that is, the electrochemical reaction heat, the side reaction heat, the ohmic heat, and the polarization heat. Among them, the electrochemical reaction heat is generated from the internal chemical reactions when batteries are working, and it is a negative value when charging and a positive one when discharging. The polarization heat, a positive value, is the energy loss caused by electrode potential deviating from equilibrium electromotive force. The Joule heat is the heat that is generated by the internal resistance of the battery, which is always positive. The side reaction heat, which is generally very small and almost negligible for lithium batteries, is mainly generated by the self-discharge, electrolyte decomposition, and other factors. The calculation model of electrochemical reaction heat  $Q_r$  is shown in formulas (1)–(4).

$$Q_r = -T \left( \frac{\delta(\Delta G)}{\delta T} \right) \quad (1)$$

$$\Delta G = -nFE \quad (2)$$

$$Q_r = nFT \left( \frac{\delta E}{\delta T} \right) \quad (3)$$

$$Q_r = \frac{Q_1}{F/3600} I_c = -0.0337 Q_1 I_c \quad (4)$$

In the formula,  $n$  is the amount of substance of the electrons participated in the reaction, and the unit is mol.  $I_c$  is the charging current, and the unit is A.  $E$  is equilibrium electromotive force, and the unit is V.  $F$  is the Faraday's constant, and the value is 96,484.5 C/mol.  $Q_1$  is the total heat generated by the charging of the positive and negative electrodes, and the unit is KJ/h.

The calculation models of the polarization heat  $Q_p$  and the ohmic heat are shown in formulae (5)–(6).

$$Q_p = I^2 R_p (W) = 3.6 I^2 R_p (\text{KJ/h}) \quad (5)$$

$$Q_e = I^2 R_e (W) = 3.6 I^2 R_e (\text{KJ/h}) \quad (6)$$

$R_p$  and  $R_e$  are, respectively, polarization resistance and ohmic resistance, and the unit is  $\Omega$ .

### 3 The Analysis of Battery Cooling Mode

Battery thermal management type is classified according to the heat-transfer medium [6–9], and is generally divided into air cooling, liquid cooling, and phase-change material cooling.

#### 3.1 Air Cooling System

Without using any external auxiliary power, the air cooling system directly uses the natural wind to take away the heat of the battery. The system is simple, and the cost is low. At present, there are two kinds of air cooling ventilation modes, serial and parallel. As for serial ventilation mode, as shown in Fig. 2, cold air blows in from the left and blows out from the right. The air is gradually heated by the battery, so the air temperature gets higher and higher and the cooling effect becomes worse and worse from the left to the right. The battery temperature increases from left to right in the battery box, resulting in the inconsistency of the distribution of the battery module temperature, which affects the cooling effect of the battery.

Parallel ventilation makes the airflow more evenly distributed among the battery modules, which ensures the consistent distribution of battery pack temperature field. The parallel ventilation mode is shown in Fig. 3.

It can be seen that the main advantages of the air cooling mode are as follows:

(1) The structure is simple, and the weight is relatively small; (2) there is no possibility of liquid leakage; (3) there is effective ventilation when harmful gas is produced; and (4) it is of low cost.

Fig. 2 Serial air cooling

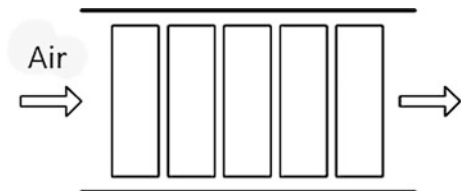
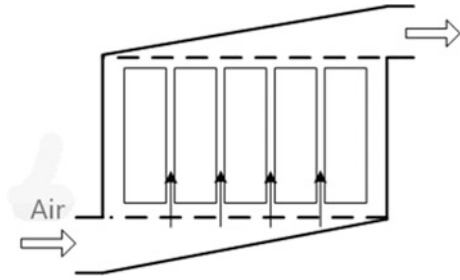


**Fig. 3** Parallel air cooling



The disadvantage is as follows: The heat-transfer coefficient between the air and the cell surface is low, so the cooling and heating rates are slow.

### 3.2 Liquid Cooling System

Compared with air, liquid has a relatively high heat-transfer coefficient. Therefore, the heat generated by batteries can be quickly taken away and the battery temperature can be effectively reduced.

Liquid cooling is mainly divided into direct-contact mode and indirect-contact mode.

Indirect-contact liquid cooling system must integrate the sleeve and other heat-transfer facilities with the battery pack in order to achieve the cooling effect, which, in some way, reduces the efficiency of heat transfer and increases the complexity of the design and maintenance of the thermal management system.

Direct-contact liquid cooling systems usually use non-conduction heat-transfer materials with high heat-transfer coefficient, such as mineral oil and ethylene glycol. As for indirect-contact liquid cooling system, water and antifreeze fluid are usually used as heat-transfer material.

Performance comparison of different cooling modes is shown in Table 1.

**Table 1** Performance comparison of different cooling modes

Item	Cooling modes		
	Air cooling	Indirect water cooling	Direct liquid cooling
Ease of use	Easy	Medium	Medium
Ease of integration	Easy	Difficult	Difficult
Cooling ability	General	Medium	High
Refrigeration consistency	Low	Medium	High
Easy maintenance	Easy	Medium	Difficult
Initial cost of system	Low	High	High

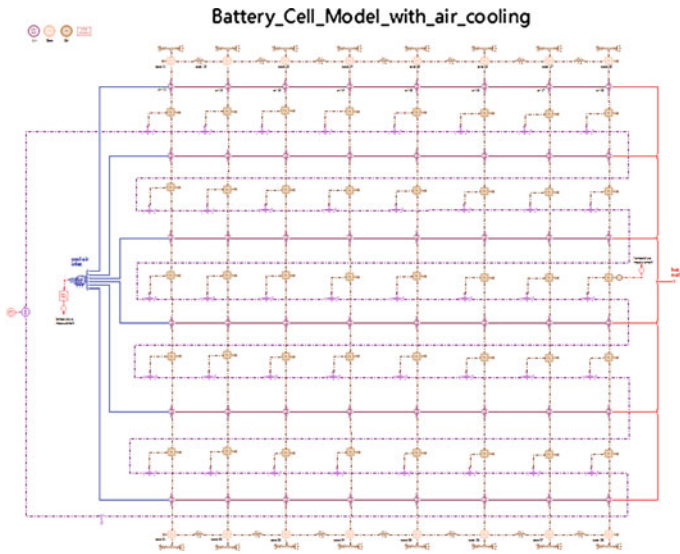


Fig. 4 Air cooling battery pack model

### 4 Build the AMESim Model of Power Battery Pack and Its Cooling System

According to the analysis above, the battery pack model is built using AMESim in this paper. The ambient temperature is 30 °C. In the battery pack, there are 40 series of battery monomers. The battery pack takes the power consumed by an EV in 4 consecutive EPA-US06 cycles as its current source. The model builds the heat capacity of a single cell and that of the battery shell. In this paper, the heat capacity of one side of the battery shell is divided averagely into 8 parts to replace the single heat capacity. The model also builds the heat-exchange interface between each cell of the battery, the heat-exchange interface between the battery and the battery shell, and the heat-exchange interface between the battery shells. The model is shown in Figs. 4 and 5. Figure 4 shows the air cooling battery pack model. The liquid cooling battery pack model is shown in Fig. 5. Both direct and non-direct liquid cooling systems can be achieved in the same liquid cooling battery pack model.

### 5 Simulation Result Analysis

Conducting the simulation analysis in AMESim, the average temperature rise curves of the 40 battery cells in the battery pack in three cooling modes are obtained, as shown in Fig. 6. It can be seen that the temperature raises 25.14 °C



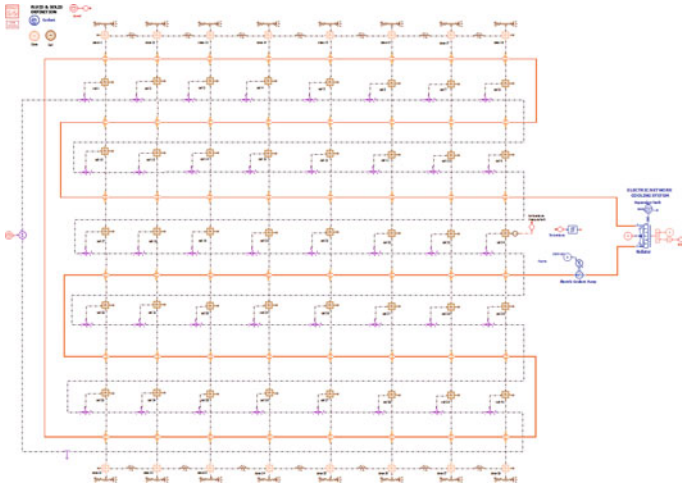


Fig. 5 Liquid cooling battery pack model

Fig. 6 Average temperature rise curves of the 40 battery monomers in the battery pack



under the air cooling mode, 14.2 °C under non-direct liquid cooling mode, and 9.85 °C under direct liquid cooling mode. When the initial ambient temperature is 30 °C, the battery temperature rises to 55.14 °C under air cooling mode, 44.2 °C under non-direct liquid cooling mode, and 39.85 °C under direct liquid cooling mode. Figure 7 shows the average heat-exchange ratio under 3 modes. It is shown in Fig. 7 that the battery heat-exchange ratio under direct liquid cooling mode is significantly higher than that under air cooling mode.

Take the final temperature of the 40 battery monomers under 3 cooling modes as one set of data. The mean square deviation is shown in formula.

**Fig. 7** Battery monomer average heat-exchange ratio curves

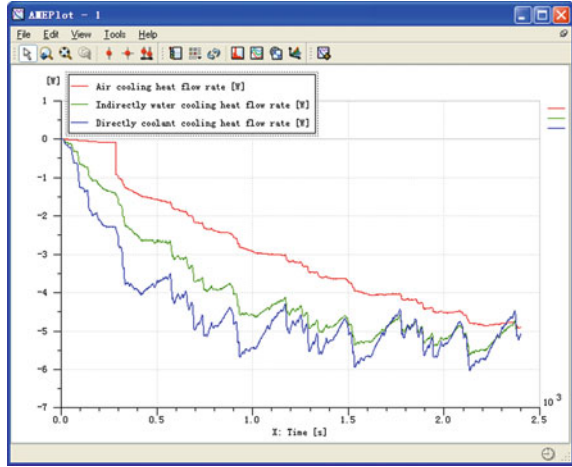


**Table 2** Comparison of simulation results of different cooling modes

Contrasting parameter	Cooling modes		
	Air cooling	Indirect water cooling	Direct liquid cooling
Final temperature at the end of simulation (°C)	55.14	44.2	39.85
Elevated temperature (°C)	25.14	14.2	9.85
Mean square deviation of the final temperature of all monomers	0.9392	0.0289	0.0162

$$\sigma = \sqrt{\frac{1}{N} \sum_{i=1}^N (x_i - \mu)^2} \tag{7}$$

$$\mu = \frac{\sum_{i=1}^N x_i}{N} \tag{8}$$

The comparison of simulation results of different cooling modes is shown in Table 2.

## 6 Analysis of the Characteristic of Battery Temperature

In this paper, the charging or discharging process of a lithium ion battery with a nominal capacity of 180 A h is tested, and the battery charging or discharging efficiency is calculated. Charging or discharging efficiency is defined as follows:

**Fig. 8** Charging efficiency curve

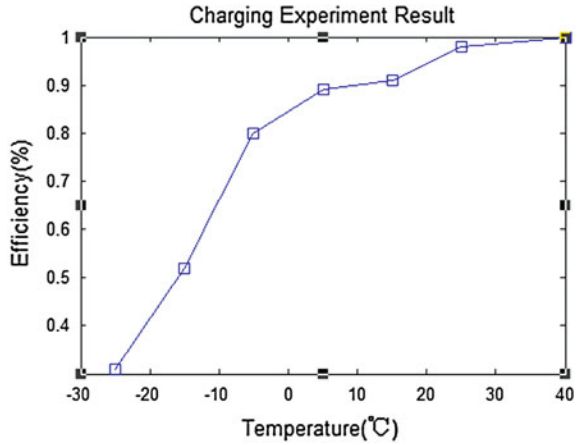
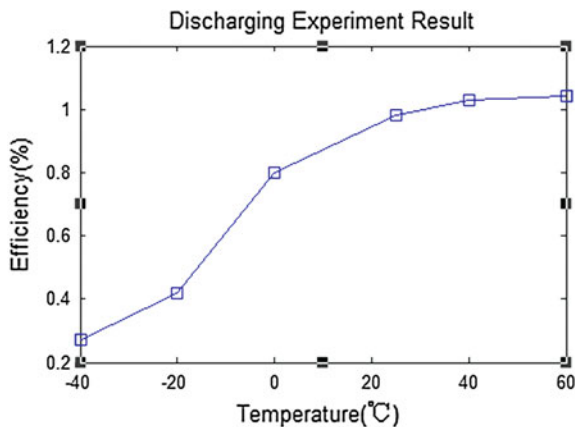


**Fig. 9** Discharging efficiency curve



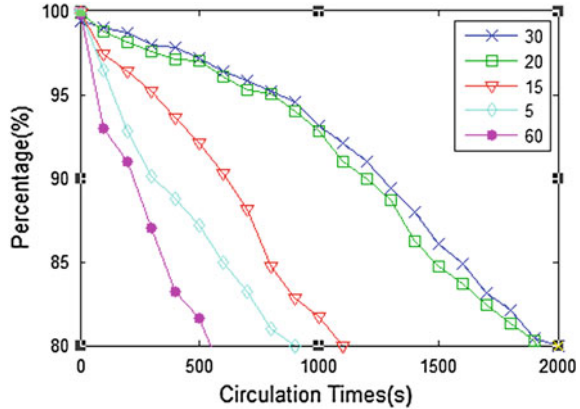
$$\text{Charging/discharging efficiency} = \frac{\text{Actual Charging/Discharging Capacity}}{\text{Nominal Capacity}}$$

Charging efficiency curve is shown in Fig. 8. Discharging efficiency curve is shown in Fig. 9.

When the circulating capacity reduces to 80 % of the nominal capacity, take that 80 % nominal capacity as the end of the battery’s life. The cycling life curve of the battery at different temperatures is shown in Fig. 10.

For charging, when the temperature is above 5 °C, a high efficiency can be guaranteed and can reach more than 90 %, as shown in Figs. 8 and 9. For discharging, the temperatures need to reach 20 °C to guarantee more than 90 % efficiency, as shown in Figs. 8 and 9. When the temperature is between 30 and 40 °C, both charging and discharging efficiency can reach 95 % or more. The battery life is the maximum when the temperature is 30 °C and is obviously decreased at a

**Fig. 10** Relationship of battery life with temperature



relatively high temperature 60 °C and a relatively low temperature 15 °C, as shown in Fig. 10. So it can be obtained that when the temperature is between 30 and 40 °C, the battery life reaches to its maximum.

It is seen from the simulation results of the model that when the initial temperature is 30 °C, both direct liquid cooling and indirect water cooling modes are able to control the battery temperature within 40 °C, but the effect of air cooling is not ideal. Therefore, liquid cooling can satisfy the requirements, and in the actual use, we can choose indirect water cooling or direct liquid cooling according to the situation.

## 7 Conclusion

The operating temperature of a battery is an important parameter for charging and discharging, and the working efficiency and service life of the battery will be limited if the temperature is too high. The heating principle of lithium ion battery, followed by an analysis of three battery cooling modes, is first analyzed in this paper, and the characteristics of them are compared. A lithium ion battery pack model was built in the AMESim software, and the model of the three cooling modes was established, respectively. Under the same environment temperature and working cycle, the cooling capacity of the three cooling modes and the temperature difference between each two battery monomers in the battery pack were compared and analyzed. Based on the experiment, the conclusion is drawn that the charging or discharging efficiency and the service life of the battery will be kept at a higher level when the battery temperature is between 30 and 40 °C. The simulation results show that compared with the air cooling mode, under water cooling mode, the battery can get enough cooling, so that the battery can work within an appropriate operating temperature range and the battery temperature differences between each two monomers are relatively small. The cooling effects of indirect water cooling

and direct cooling are not much different, and the difference between each two battery monomers is also small. Therefore, indirect water cooling is a suitable battery cooling mode.

## References

1. Gu WB, Wang CY (1998) The use of computer simulation in the evaluation of electric vehicle batteries. *Power Sources* 75(1):151–161
2. Mills A, Al-Hallaj S et al (2005) Simulation of passive thermal management system for lithium-ion battery packs. *J Power Sources* 141:307–315
3. O’Keefe MP, Markel T (2006) Dynamic programming applied to investigate energy management strategies for a plug-in HEV. In: EVS-22. Yokohama, Japan, pp 1035–1046
4. Tian S (2007) The research of the thermal characteristics of the lithium battery. Tianjin University, Tianjin
5. Sato N (2001) Thermal behavior analysis of lithium-ion batteries for electric and hybrid vehicles. *J Power Sources* 99:70–77
6. Yang S, Tao W (2006) Heat transfer. Higher Education Press, Beijing
7. Xin N (2012) The thermal characteristics analysis and simulation of EV’s lithium battery pack. Jilin University, Changchun
8. Makino M, Ogawa N (2003) Automotive air-conditioning electrically driven compressor. SAE (1)
9. Johnson VH (2002) Heat-generated cooling opportunities in vehicles. SAE (1)

# The Research of Aviation Dangerous Weather Forecast for Fog and Haze Based on BP Neural Network

Yanfen Cheng and Rui Wu

**Abstract** The fog-haze, as one of the dangerous aviation weather, influences the pilot to see the runway in the air. It is very dangerous to flight for safe landing. Because of the existence of fog-haze, the phenomenon of plane's taking off or delaying is not uncommon. In this paper, analyze the main physical factors of fog-haze and establish model based on BP neural network; in addition, the forecasting performance of the model was tested; at last, the short-term forecasting operational system of fog-haze which can be used for aviation meteorological services is built based on software development techniques.

**Keywords** BP neural network · Fog-haze · Single-station forecasting

## 1 Introduction

In the aviation meteorological security, fog-haze with low visibility often affects flight activity, and it is one of the direct factor to flight safety. Although modern airport navigation and ILS facilities are perfect, the new generation of planes is growing, and this results in a more serious requirement on visibility of weather. So the question of fog-haze forecast in accuracy, which have been closely linked to aviation security, flight mission of fine scheduling, etc.

In fact, droplets or ice crystals are the main components of the fog [1]. Although both the particles, water vapor content and appearance, have significant differences, fog-haze still have similar weather conditions in the formation process [2]. In the

---

Y. Cheng · R. Wu (✉)

School of Computer Science and Technology, Wuhan University of Technology,  
Wuhan 430063, China  
e-mail: nanjing2004921@126.com

Y. Cheng

e-mail: nanjing163@126.com

© Springer-Verlag Berlin Heidelberg 2016

B. Huang and Y. Yao (eds.), *Proceedings of the 5th International Conference on Electrical Engineering and Automatic Control*, Lecture Notes in Electrical Engineering 367, DOI 10.1007/978-3-662-48768-6\_97

877

stagnant weather, it is easy to make fog–haze. In other words, fog–haze is more likely to happen if the air circulation or air diffusion is shut down or if the cold air or wind speed is weak [3]. Therefore, it is feasible to the forecast of fog–haze weather which is based on BP neural network.

## 2 Related Work

### 2.1 Fog–Haze Sample Data

The subjects of this study is an airport in central china, part of the surface meteorological observation data in autumn and winter between 2010 and 2013(data source come from weather shared of Web site, artificial observation, and revision). Each group of sample data is observed at the day before the 20:00 to the next day 20:00, 24 h. Select 30 sets of data as the training sample of neural network model, and after model completes its training, 10 sets will be as test samples.

The forecast factors are selected, and its main factors are the day-to-day humidity, atmospheric stability, wind speed, and so on, which is often used to describe the forecast area.

The forecast factors should effectively provide much information as possible to neural network model; however, more is not necessarily better. The large and complex factors will not only bring enormous computation to model, but also reduce its stability [4]. The model should get rid of redundant factors after analyzing and researching, including precipitation from 20 pm to next day 20 pm, evaporation, wind speed, and large maximum and minimum relative humidity, which could make up input as main information for fog–haze forecast model.

Output factors of the model can be classified according to the degree of objective harms of flight safety into several categories:

No fog–haze—a spacious view: The visibility is more than 2000 m, and there is no obvious cumulonimbus. Flight conditions is excellent, and the quantitative value can be used as 0.2.

Mist and weak haze—a clear view: The visibility is more than 1600 m less than 2000 m. Flight conditions are good, and the quantitative value can be used as 0.4.

Fog: The visibility is less than 1600 m. As the sun came up, fog will dissipate after 2–3 h. Flight conditions are poor and proposed that airport should postpone the flight. The quantitative value can be used as 0.6.

Haze: The visibility is less than 1200 m. A large number of aerosols in the air is not easy to dissipate. The plane cannot meet flying conditions in a short time. Our suggestion is to shut down the airport temporarily. The quantitative value can be used as 0.8.

## 2.2 Construction of BP Neural Network Model

### 2.2.1 Building the Model

Three-layer BP structure can approach any rational function, and the application is maturely utilized in neural network [5]. In fog-haze forecasting model, the number of input/output layer neuron is designed to be one. The number of hidden layer neurons should be between three and ten based on empirical formula and the actual situation of the model. It is ideal to obtain the number of neurons in hidden layer through MATLAB by comparative analysis methods.

In forecast model, output values must be between 0.0 and 1.0. The original data of meteorological observation should be a normalization to deal with this question, to be used as input parameters of the input layer [6]. Input layer and hidden layer, hidden layer and output layer that their weights and thresholds can use default value of system. Considering transfer functions, tansig function (the hyperbolic tangent S-type transfer function) can be used for neurons in hidden layer and logsig function (S-type transfer function, the output value is between 0 and 1) can be used for neuron in output layer. Training function is traingdx (gradient descent w/momentum vector and adaptive training function) [7]. Their errors will be shown in chart 1 after running this code on the MATLAB (Table 1).

Viewing the experience result, the performance of network does not to get better and will gradually stabilize when the amount of neurons in hidden layer expands to a unique number. It is often ineffective to approximation effect for function. In this case, when the number of neurons increased to 8, predicting error of the neural network has stagnated without any significant change. Select the number of neurons which spend less time, so the number of neurons will be eight.

### 2.2.2 The Choice of Training Function

As setting network parameters for forecast model, to choose two typical training functions from the MATLAB toolbox, a better one will be as a training function for weights and thresholds in neural network trains better performance.

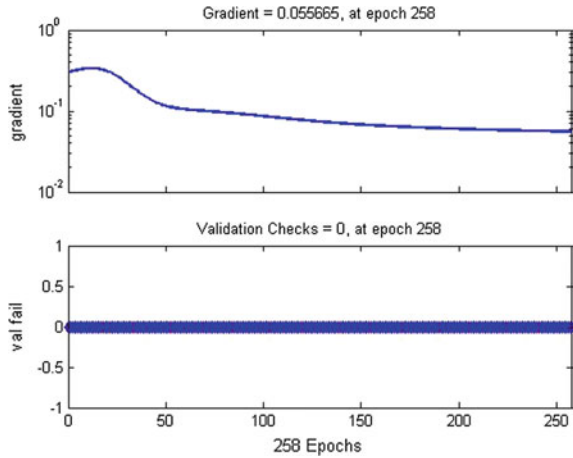
Trainda: This function can be capable of altering learning rate of progression through training. It changes the size of learning rate in the process of training by itself, and the rest of usage is similar to traingdx function with omitting the momentum factor parameters of MC.

**Table 1** After running this code on the MATLAB

No.	Res	4	5	6	7	8	9	10
1	Error	0.0280	0.0235	0.0200	0.0172	0.0145	0.0145	0.0145



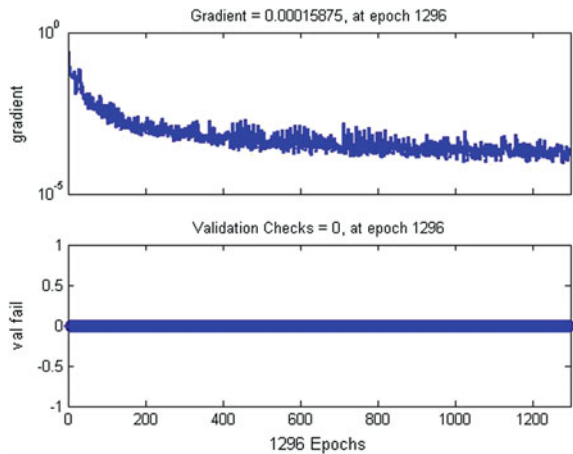
**Fig. 1** Trainгда's decline curve error in the graph



Trainrp: It determines the change of weights and thresholds by using error gradient's direction, and the size of error gradient does nothing to the change of weights and thresholds which will be determined by `delt_inc` and `delt_dec`.

Using `trainгда` function, the number of hidden layer neurons is set up to be eight, and then it should have the result as shown in Fig. 1. Using `trainrp` function will train on weights and thresholds for forecast model, and then it should have the result shown in Fig. 2. By comparison and analysis, the latter is no doubt better than the former from the point of sample error, convergence, and stability for the network model. Consequently, `trainrp` function is chosen as the training function of the model.

**Fig. 2** Trainrp's decline curve error in the graph



## 2.3 Results

### 2.3.1 Forecast Model Test

Ten new data groups will be as test samples of BP neural network. The test code is as follows:

$$Y = \text{sim}(\text{net}, \text{Ptest})$$

Test results are as follows:

$$Y = \begin{matrix} 0.7956 & 0.8100 & 0.8050 & 0.3994 & 0.8100 \\ 0.8151 & 0.2210 & 0.2150 & 0.5700 & 0.2210 \end{matrix}$$

The targets are as follows:

$$T = \begin{matrix} 0.8000 & 0.8000 & 0.8000 & 0.4000 & 0.8000 \\ 0.8000 & 0.2000 & 0.2000 & 0.6000 & 0.2000 \end{matrix}$$

Results from model tests have shown that the SSE is 0.0021 and MSE is 2.1072e-04. These results suggest that model’s error is very small, and neural network model with selecting trainrp function can be satisfied for the fog-haze weather forecasting.

### 2.3.2 Contrast Between Forecast Model and Actual Forecast Operation

In the day-to-day business, there is no professional automation system for fog-haze weather forecast, and various forecasting results got more analysis from numerical data and artificial experience. From say on the whole, to BP neural network, the research of the fog-haze forecast just still is in an abecedarian phase, so contrast test will compare this model with business level which have for now. Randomly select 10 sets of forecast data that come from artificial forecast’s data about airport in the autumn and winter of 2012-2013; and it will compare the results of BP network’s simulation in contrast experiment, and the last results are shown in Table 2.

Certain generalizations can be derived from the data in Table 2, with results based on less than 0.03 of absolute error as a reference; the model prediction’s accuracy is 80 %; and artificial forecast’s accuracy is 60 %. Thus, it can be seen that the forecast results of a BP network model which compare the manual forecast have a remarkable elevation. The results, in simulating the formation and occurrence time of the fog-haze, are coincident with the actual situation. The forecast of BP network model is an increase of 20 % accurate compared with professional skill

**Table 2** BP network's simulation in contrast experiment

No.	Date	The forecast results of BP model	The forecast results of artificial	Actual weather
1	121025	0.2166	0.2	0.2
2	121027	0.3301	0.2	0.4
3	121102	0.2150	0.2	0.2
4	121105	0.5754	0.4	0.6
5	121107	0.8170	0.4	0.8
6	121206	0.8135	0.8	0.8
7	130101	0.3745	0.8	0.4
8	130110	0.2335	0.2	0.2
9	130121	0.2250	0.2	0.2
10	130127	0.7951	0.6	0.8

by artificial work, which can get the expected result. The findings can be used as reference in forecasting operation, can let the forecasters more effectively to know about how fog-haze is formed and developed.

## 2.4 Conclusion

Fog-haze is a low probability event in weather phenomenon. The traditional forecast method apt to be influenced by human factor and local factors, and it makes the model of forecast that we want to promote is limited. In this paper, the results from forecast model of fog-haze are based on BP neural network which will be realized by computer simulations. The system avoids artificial intervention which brings more stable, impersonal, and reliable results to forecast. At the same time, introducing local meteorological factors in this model is more suited to actual work for a single station.

## References

1. Wang Y, Cao B, Huang B (2010) Fog forecast experiment of single station. *J Appl Meteorol Sci* 21(1):110–113
2. Ceng SL (2012) Studies on forecasting technology and operational system for three typical dangerous weather affecting aviation. Lanzhou: Lanzhou University
3. He D (2012) Based on artificial neural network algorithm Chengdu Fog forecast. *China Sci Technol Inf* 3:89–91
4. Liu DY, Yang J, Niu SJ, Li ZH (2011) On the evolution and structure of a radiation fog event in Nanjing. *Adv Atmos Sci* 28(1):223–237

5. Zhu D, Xu C (2013) The recognition of handwritten digits based on BP neural network and the implementation on Android IEEE 1498–1501
6. Xingfeng CAO (2012) A BP neural network meteorological prediction. Bull Sci Technol 28 (8):55–57
7. Yuan Z, Zhang R, Zhou S (2002) Model recognition and forecast of fog over the airport based on ANN. J PLA Univ Sci Technol 3(4):82–86

# Small Power Sine Wave Inverter Design

Xuefeng Bai, Yongjian Ma, Hanqing Li and Pei Li

**Abstract** How to turn the DC power supply (24 V) into AC power (220 V, 50 Hz) and load feedback power supply based on single-phase full-bridge inverter circuit has been discussed, and it is converted to a stable frequency power supply for a number of electrical appliances such as lights and computer requirement use. SG3525 chip fixed-frequency pulse width modulation circuit and field effect transistor (N channel MOSFET) whose switch speed quick, nothing secondary break down and good hot stability have been applied sufficiently. Inverter main part has been composed of DC/DC circuit, input protection circuit, output protection circuit, overheat protection circuit, DC/AC conversion circuit, and full-bridge circuit. The overcurrent and overheat circuit as well as the normal work light have also been designed. Practice has proven that the system is stable, has good utility, low-cost, and strong practicability. It can be used as a variety of portable electrical general power supply.

**Keywords** Inverter circuit · MOSFET · SG2535 · PWM · SPWM

## 1 Research Background and Effects

With the shortage of fossil fuels and serious environment problems, people try to exploit renewable energy resources continuously. For its clean and practical, solar power has been one of the most important forms of developing and utilizing the renewable energy resources. It plays an important role to reduce environmental pollution and alleviate the energy to be short. With its characteristics of low-carbon, environmental protection and being used in situation, photovoltaic (pv) power generation has been rapidly developed and has higher application value in the distributed generation in recent years [1]. The use of solar energy will depend on conversion equipment and auxiliary equipment. Due to the high cost of solar power

---

X. Bai (✉) · Y. Ma · H. Li · P. Li  
Beijing Information Science and Technology University, Beijing, China  
e-mail: welcomebj\_2008@163.com

generation, main research work will be focused on high-performance, low-cost, and simple processing technology of pv materials and devices. Inverter is the main equipment of the grid system; its conversion efficiency and cost will directly influence the efficiency of the whole system. Therefore, there is an utmost urgency to improve the inverter technology.

Inverter is also called the inverter power supply. It is a kind of power conversion device that can convert direct current (DC) to alternating current (AC). Its outputs can be used for all kinds of equipment to meet user's need for AC power in mobile power supply or the areas without electricity. AC transformer can be used to increase AC voltage levels and stable voltage and frequency can be got. Because of DC higher bus voltage, generally, a step-up transformer is not needed in large capacity inverter system. In small- and medium-sized inverter system, DC lower bus voltage such as 12 and 24 V for booster circuit will be applied to increase voltage.

Main circuit of inverter needs control circuit. Two kinds of control mode usually have been applied: square wave and sine wave. The square wave output circuit has lots of advantages such as simple, low cost, and so on, but this mode also has the disadvantages of low-efficiency and big harmonic component. In recent years, sine wave output inverter technology has become more mature and become a new trend of inverter development. For now, microelectronics with PWM function has come out and improved dramatically. A major problem that we have to face is harmonic in the field of pv grid power generation at present. The effects of grid current harmonics have become increasingly serious, so it is necessary to study control method that combines current instantaneous value control and PID control to make the system have good dynamic performance and high tracking precision. On this basis, in order to make solar cells work on the maximum power output point, a set of MTPP algorithm is needed to be designed that makes the power generation system have fast tracking to adapt all kind of situation of electricity work [2].

## 2 Design Project Selection

Task results show form: Inverter can transform 24 V direct current (DC) produced by the battery plate to sine wave power with frequency 50 Hz, 220 V alternating current (AC). Prestage driving circuit, booster circuit, inverter circuit, and protection circuit will be designed at all levels. Driving circuit adopts two pieces of independent circuit module to generate the waveform. The design block diagram of the system is shown in Fig. 1.

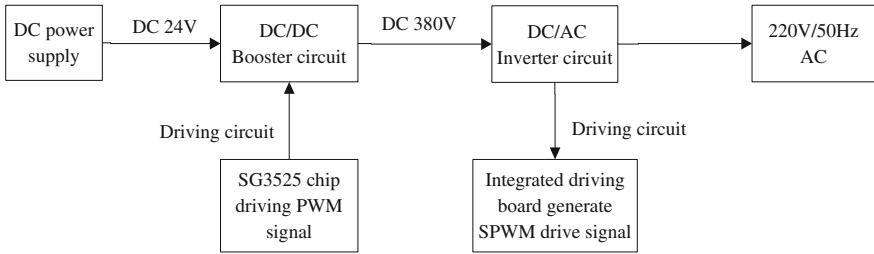


Fig. 1 The design block diagram of the system

The advantages of the scheme:

1. The cost is low, SG3525 chip and integrated SPWM driving plate is low cost, and price of two pieces of driving plate is not more than 50 yuan, respectively, after mass production.
2. Building protection circuit is very convenient and flexibly, and the driving chip is very easy to be designed and simple to apply.
3. The driving circuit has been divided into two independent blocks; circuit debugging will become very simply and also can quickly find out the mistakes to improve reliability of circuit.
4. Small size. Driving circuit chip encapsulation will adopt patch type to reduce the volume of whole circuit greatly.

The disadvantages of the scheme:

1. The loss is higher, because the two pieces of driving circuit will require power supply and to a certain extent cause the loss of power.
2. Accuracy is not higher. The control accuracy and speed will be lower than the ARM development board.
3. The flexibility is not higher. The chip has fixed waveforms; software will be unable to be used to adjust different functions in the later use.

This topic is requested to design small power inverter. Firstly, the low cost can make small power inverter have practical significance and the possibility of mass production. Secondly, convenient maintenance and detection should be considered, and two pieces of driving circuit and a piece of power main circuit will be designed independent. When one piece is damaged, it can be detected quickly and carried on the independent maintenance. Finally, considering the problem of portability and volume, scheme can control three high circuit volume in 15 cm × 10 cm × 5 cm size range. Some analysis is done to decide to adopt this scheme. In conclusion, it will meet the requirements of the topic.

### 3 Inverter Circuit Structure Design

#### 3.1 Inverter Overall Design

The inverter circuit has been composed of main circuit and driving circuit. The inverter circuit has been composed of main circuit and driving circuit. Main circuit includes booster link, rectifier link, inverter, and filtering link; driving circuit includes booster driving circuit (generally referred to as the former driving circuit) and the inverter driving circuit (generally referred to as the latter driving circuit). The sine wave inverter circuit principle diagram is shown in Fig. 2. Single-phase full-bridge circuit has been used in sine wave inverter circuit. MOSFET has been used as power devices in inverter circuit. MOSFET is a voltage-type control device with simple driving circuit, large capacity voltage and current, high operating frequency, lower switching loss, and also high working reliability. Inverter converts DC voltage to 50 Hz frequency SPWM wave, and it will be converted to 220 V standard sine wave through filtering inductance and power frequency transformer. Using this method, the system structure is simple and the higher harmonic waveform component can be inhibited effectively. SPWM control mode will be adopted in inverter circuit. Switch mode signal is generated by comparing sine wave reference signal and a triangular carrier signal, generally. There are two forms: polar and bipolar. Under the same switching frequency, for the sine wave, its harmonic content and switching loss generated in the dual polarity SPWM control are greater than the single polarity. So, single polarity SPWM control will be applied in this design.

In the former driving circuit, as the core, the SG3525 chip has been used to build the peripheral circuit to generate PWM driving level needed by the booster section. In the latter driving circuit, integrated SPWM circuit has been implemented to provide SPWM inverter driving level. Power main circuit has been made up of push-pull topology booster circuit and single-phase full-bridge inverter circuit. The design main tasks are as followed:

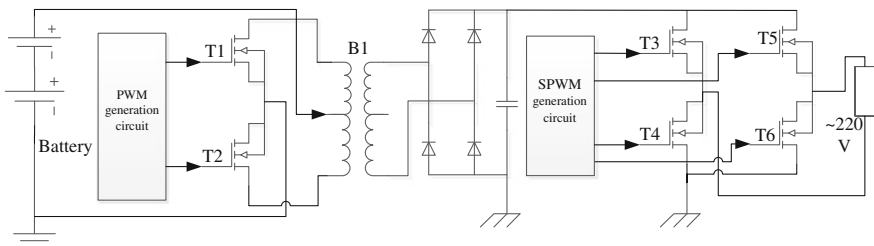


Fig. 2 Sine wave inverter circuit principle diagram



1. The power main circuit design.
2. The former driving circuit design.
3. The protection circuit design.

The goal of design:

1. Input: DC 24 V (battery or adjustable DC power supply).
2. Output: AC 220 V, 50 Hz frequency (sine wave).
3. The output power: 300 W.
4. Input overvoltage protection; output overvoltage protection; current protection; and overheating protection function.
5. Can be used as general power supply of a variety of electric equipment.
6. Contains work lamp.

Driving circuit design will decide whether the whole inverter circuit can work properly; a high quality of the driving circuit will improve the stability of the whole circuit board greatly. If wanted to get a good performance of driving circuit, we must fully understand the whole circuit power supply situation. In addition to the main loop of the power, inverter also contains a lot of power supply for small signal, such as 15 V power supply of pulse width modulation of signal SG3525 chip, other power supply for operational amplifier chip, and 15 V power supply for integrated driving chip. It also has a key role to provide a stable power supply for the above circuit [4].

### ***3.2 The PWM Driving Part***

PWM duty cycle changes to 50 %, mainly to protect MOS driven by the signal that will not work in a larger duty ratio state as soon as it is turned on to reduce the boot instantaneous MOS shock pressure. PWM output is from 11 to 14 ft, two feet output waveform phase complement and reversed phase each other. High-level voltage is from 3.8 V to 5.6 V. Low-level voltage is between 0 and 0.5 V. In motherboard precursors, respectively, there are two 10 k resistor to pull PWM signal to the ground, and this pull-down resistor is to add a dummy load to SG3525 PWM signal to make signal stability [5].

In this part of the circuit, SG3525 adopted closed-loop modulation; its 2 ft is given to a 5 V fixed benchmark (produced by SG3525 16 ft); 1 foot connects high-voltage component of the former stage booster; when the output voltage is greater than 2 ft fixed value, the error amplifier of SG3525 will vary it as the error to enlarge modulate duty ratio of PWM modulation; and there is a small static current when inverter is under non-load operation. The principle of this feature is that the PWM duty cycle is smallest under non-load operation, at the time of loading to pull duty ratio to the largest immediately to make the circuit work at peak efficiency.

### 3.3 The Latter Driving Circuit

Integrated single polarity SPWM chip has been used in the latter driving circuit. IR2110S has been adopted as driving chip. On this driving board, the common and often used functions are integrated such as voltage, current, temperature protection function, LED alarm display function, and fan control function and can be set up to 50/60 Hz output and the size of the dead zone. Its driving level locking function will enhance the anti-interference ability of the board greatly. External 12-MHz crystal oscillator is used. Chip has adopted the CMOS process, SPWM sine generator, dead band time control circuit, amplitude factor multiplier, soft start circuit, and protection circuit; RS232 serial communication interface and 12832 serial LCD driver modules have been integrated in the internal.

### 3.4 Sine Wave Inverter LC Filter Parameters

Calculation of sine wave inverter LC filter parameters is an extremely complex thing. Here, a kind of simple approximate calculation method will be introduced. It has been proved to be feasible in the actual inspection. SPWM filter inductor and normal shock of switch power supply output filter inductance are similar, and only SPWM pulse width is changed; after filtering, the voltage is sine wave instead of DC voltage. Within half a cycle of sine, according to the inductor ripple current, maximum point to calculate is feasible. Here, a few physical quantities will be introduced.

$$L = \frac{(U_{dc} - U_o)T_{on}}{1.4I_o} = \frac{(U_{dc} - U_o)\frac{U_o}{U_{dc}f_{sw}}}{1.4\frac{U_o}{R}} = \frac{R(1 - U_o/U_{dc})}{1.4f_{sw}} \quad (1)$$

- $U_{dc}$  input voltage of H-bridge inverter, the range is about 320–420 V;
- $U_o$  output voltage, 0–311 V, effective value is 220 V;
- $D$  the duty ratio of SPWM carrier, varying in sine law;
- $f_{sw}$  SPWM switching frequency, the frequency of this subject is 20 kHz;
- $I_o$  output current, the peak current of the inductor is about  $1.4I_o$ ;
- $T_{on}$  switch tube conduction time, varying in sine law;
- $L$  LC filter inductance as needed;
- $R$  inverter load resistance.

Load resistance  $R$  is an uncertain value, and according to the experience, we can determine that the inductance  $L$  is about 2 mH, and it should use the high-frequency filtering inductance dedicated by inverter. After the filter inductance is determined, the filter capacitance  $C$  numerical can be calculated; calculating filter capacitance  $C$  is relatively easier. Basically, filter cutoff frequency is 1/10–1/2 of SPWM carrier frequency computation. Its formula is as follows:

$$f = \frac{1}{2\pi\sqrt{LC}} \quad (2)$$

where the SPMW carrier frequency is 20 kHz. In the formula,  $f$  takes 2.4 kHz and  $C$  has been calculated to take 2.2  $\mu\text{F}$ .

## 4 Design Summary

The design of the sine wave inverter based on full-bridge inverter circuit, SG3525 chip, and integrated SPWM chip has been used as control core. The design includes the inverter former driving circuit, power circuit, main circuit, and protection circuit. Finally, the design of the sine wave inverter is completed successfully. Current protection, voltage protection, and dead band time settings have used in the design of circuit. The circuit can get stable sine wave AC single-phase 220 V power supply, and inverter circuit part mainly uses integrated SPWM control chip. When the battery voltage is too high or too low, inverter power supply will stop work to protect the inverter power supply and battery. When the battery voltage fluctuates within the normal range, output voltage is unaltered. When the output current is too large, system will start the current protection to protect device load to normal operation of the power supply.

**Acknowledgement** This work was supported by city board of education “PXM2015\_014224\_000050” undergraduate education-college students’ research training (municipal); Beijing municipal education commission science and technology project (No. KM201511232023); and Beijing Higher Education Young Elite Teacher Project, 2015, (No. 71A1511136).

## References

1. Xue J (2013) A single-phase unfenced photovoltaic (pv) grid inverter control design. *J Low Voltage Apparatus* 8(1):25–30
2. Franquelo LG, Rodriguez J, Leon JI, Kouro S, Portillo R, Prats MM (2008) The age of multilevel converters arrives. *IEEE Ind Electron Mag* 2(2):28–39
3. Zhou H (2010) Single-phase photovoltaic (pv) grid inverter control system of the study. *Power Electron Technol* 44(12):130–131
4. Liu L, Lou Y (2012) Single-phase photovoltaic (pv) grid inverter control strategy research and design. *J Commun Power supply Technol* 29(1):14–16
5. Guo K, Xiao N (2012) Single-phase photovoltaic (pv) grid inverter system research. *J Electron Technol* 35(12):179–185

# Uncertainty Quantification Using Random Set Based on IODM

Zhao Liang

**Abstract** This paper focuses on the mechanical model uncertainty quantification when the system parameters are in the form of probability box; for example, when the probability distribution of the system variable is specified by interval parameters, the variable is in the form of probability box. We develop an improved outer discretization method (IODM) for constructing random sets which provides a convenient mechanism for representing probability box. The method can increase the fineness of the random set's approximation to the bounds of the probability box with a limited focal element. It is shown that the method is helpful for the uncertainty quantification when the model is computationally expensive.

**Keywords** Uncertainty quantification · Probability box · Improved outer discretization method · Random set

## 1 Introduction

When dealing with reliability estimation or risk analyses in mechanical engineering, it is important to take account of the uncertainties of the system itself [1]. The assigned information on the parameters controlling the system response is usually affected by imprecision. Here, the imprecision means 'the variety of alternatives that in a given situation are left unspecified.' The cumulative distribution function (CDF) of the system parameters affected by imprecision is not unique, but is bounded between an upper and a lower bound. Sometimes the envelope characterized by the bounds is called probability box [2]. Random set theory provides a general mechanism for handling various uncertainties [3–5]. Using the extension principle [6], the uncertainty of the system response can be quantified from the random set of the system's parameters. This paper focuses on the representation of the probability box using random set. There is a close relationship between random

---

Z. Liang (✉)

Institute of Electronic Engineering, CAEP, Mianyang 621900, China  
e-mail: swjtu\_zhaoliang@126.com

© Springer-Verlag Berlin Heidelberg 2016

B. Huang and Y. Yao (eds.), *Proceedings of the 5th International Conference on Electrical Engineering and Automatic Control*, Lecture Notes in Electrical Engineering 367, DOI 10.1007/978-3-662-48768-6\_99

893

set and probability box. A probability box can always be discretized to obtain a random set. The discretization is not unique, and the existing outer discretization method (ODM) usually discretizes the probability box in a uniform way. The fineness of the discretization is based on the number of focal elements. But the increasing focal elements call for more calculation of system response. So an improved outer discretization method (IODM) is presented in this paper, and it can increase the fineness of the approximation to the bounds of the probability box with a same discretization degree.

This paper is organized as follows: Sect. 2 introduces the basic definitions of random set theory; Sect. 3 describes the method proposed to approximate the probability box using random set; and in Sect. 4, a mechanical example is provided to illustrate the method.

## 2 Random Set Theory

Suppose  $N$  observations were made of a system parameter  $u \in U$ , each of which resulted in an imprecise measurement given by a set  $A_i (A_i \subseteq U)$ . Let  $n_i$  denotes the number of occurrences of the  $A_i$ , and let  $\zeta(U)$  denotes the power set of  $U$ . A frequency function  $M$  can be defined as:

$$\begin{cases} M : \zeta(U) \rightarrow [0, 1] \\ M(\phi) = 0 \\ \sum_{A \in \zeta(U)} M(A) = 1 \end{cases} \tag{2.1}$$

$M(A_i)$  is also called as the basic probability assignment. Let  $Z$  denotes the set of observations, consider a probability measure  $P(z)$  defined on  $Z$  related to  $U$  through a multivalued mapping  $\Gamma: Z \rightarrow \zeta(U)$ . The basic probability assignment can be obtained as:

$$\begin{cases} M(A_i) = P(z_i) = n_i/N \\ z_i = \Gamma^{-1}(A_i) \end{cases}, \quad (z_i \in Z) \tag{2.2}$$

The multivalued mapping expresses the imprecision of each measurement. For each set  $A \in \zeta(U)$ ,  $M(A_i)$  expresses the probability of  $z_i = \Gamma^{-1}(A_i) (z_i \in Z)$  and it does not exclude that the subsets of  $A_i$  can get additional probability deriving from other subsets  $B$  of  $U$  such that  $A_i \cap B \neq \emptyset$ .  $A_i$  is called focal element when  $M(A_i) > 0$ , and let  $\zeta$  denotes the family of all focal elements, then the pair  $(\zeta, M)$  is called a random set. For the reason of imprecision, only the lower and upper bounds on the probability of a parameter  $u \in U$  or of a subset  $E \subseteq U$  can be calculated. They satisfy the relationship as  $\text{Bel}(E) \leq \text{Pro}(E) \leq \text{Pl}(E)$ , where  $\text{Bel}(E)$  denotes the belief measure and  $\text{Pl}(E)$  denotes the plausibility measure.

Let  $y = f(u)$ ,  $f$  is a mapping  $U \rightarrow Y$ . The random set  $(R, \rho)$ , which is the image of  $(\zeta, M)$  through  $f$ , can be obtained by the extension principle [3] as:

$$\begin{cases} R = \{R_j = f(A_i) : A_i \in \zeta\} \\ \rho(R_j) = \sum_{A_i:R_j=f(A_i)} M(A_i) \end{cases} \tag{2.3}$$

where  $R_j$  denotes the focal elements of  $R$ , and it can be represented by the interval:

$$R_j = \left[ \inf_{\forall u \in A_i} f(u), \sup_{\forall u \in A_i} f(u) \right] \tag{2.4}$$

Equation (2.4) implies twice global optimizations when calculating each focal element  $R_j$ . Vertex method [7] and Lipschitzian Optimization [8] can be used to solve these approximations under certain conditions. After getting  $\rho(R_j)$ , the limit cumulative probability distribution functions of  $y$  can be obtained as:

$$\begin{cases} F_{\text{lower}}(y) = \text{Bel}(\{y' \in Y : y' \leq y\}) = \sum_{R_j: y \geq \sup(R_j)} \rho(R_j) \\ F_{\text{upper}}(y) = \text{Pl}(\{y' \in Y : y' \leq y\}) = \sum_{R_j: y \geq \inf(R_j)} \rho(R_j) \end{cases} \tag{2.5}$$

### 3 Improved Outer Discretization Method

Consider the PDF of the system parameter  $u$  is  $\text{PDF}(u, \theta)$ , where  $\theta$  is the PDF uncertain parameter vector. The bounds of CDF specified in Eq. (3.1) indicate a probability box for  $u$ ,

$$\begin{cases} \overline{\text{CDF}}(u) = \sup_{\theta \in Q} \int_{-\infty}^u \text{PDF}(u, \theta) du \\ \underline{\text{CDF}}(u) = \inf_{\theta \in Q} \int_{-\infty}^u \text{PDF}(u, \theta) du \end{cases} \tag{3.1}$$

The ODM is a widely proposed method for discretizing the probability box to a random set. According to ODM, the  $[0, 1]$  ordinate interval of  $\text{CDF}(u)$  is discretized into  $n$  subintervals of length  $m_j > 0$  ( $j = 1, \dots, n$ ) first, and then the  $j$ th focal element of  $u$  is specified as below:

$$A_j = \left[ \overline{\text{CDF}}^{-1} \left( \sum_{s=0}^{j-1} m_s \right), \underline{\text{CDF}}^{-1} \left( \sum_{s=0}^{j-1} m_s \right) \right] \tag{3.2}$$

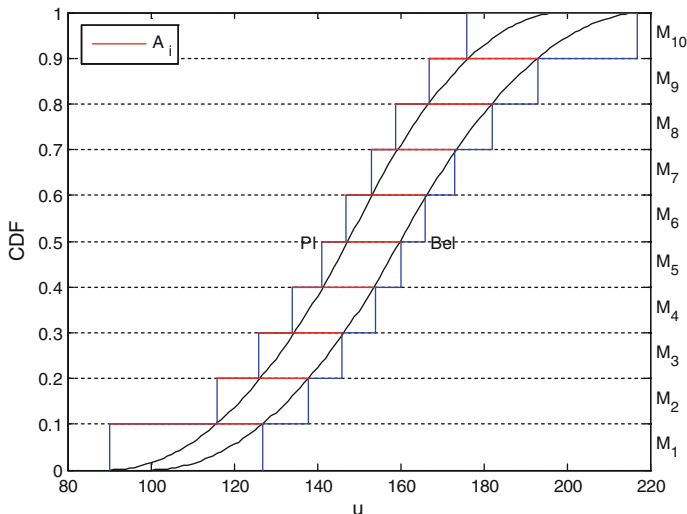


Fig. 1 Discretization of probability box by ODM with ten focal elements

And the basic probability assignment for  $A_j$  is  $M(A_j) = m_j$ . The uniform discretization is usually used in ODM, and it implies subintervals of equal length  $1/n$ . Figure 1 illustrates the discretization of probability box by ODM with ten focal elements  $A_j$ .

The discretization error of ODM can be represented by a  $L_1$  distance as

$$L_1 = \int_{-\infty}^{+\infty} |\text{Pl}((-\infty, u]) - \overline{\text{CDF}}(u)| du + \int_{-\infty}^{+\infty} |\text{Bel}((-\infty, u]) - \underline{\text{CDF}}(u)| du \quad (3.3)$$

Obviously, smaller discretization error can be obtained by increasing the subintervals of  $A$ , but it leads to an expensive calculation for random set of system response. So the IODM proposed here is to reduce the discretization error with no more subintervals. Given the number of focal elements, the IODM uses an optimization method to divide the ordinate interval of CDF into unequal subintervals which provide a minimum  $L_1$  distance. The optimization problem can be specified as:

$$\begin{aligned} &\min(L_1), \\ &\text{s.t. } \text{Pl}((-\infty, u]) \geq \overline{\text{CDF}}(u), \text{ Bel}((-\infty, u]) \leq \underline{\text{CDF}}(u) \end{aligned} \quad (3.4)$$

Intelligence optimization algorithms such as genetic algorithm can be used to solve the optimization problem. After the division of ordinate interval, the focal elements of system parameter can also be obtained by Eq. (3.2). Then, we can use the extension principle to get the image of random set  $(\zeta, M)$  through the system model  $f$ .

### 4 Numerical Example

A linear mass spring damper system is subjected to a harmonic external force, and the steady-state magnification factor  $D_s$  is defined as the ratio of the amplitude of the steady-state response of the system to the static displacement of the system as:

$$D_s = \frac{k}{\sqrt{(k - m\omega)^2 + (c\omega)^2}} \tag{4.1}$$

where  $m$  denotes the mass,  $c$  denotes the damper viscosity,  $\omega$  denotes the circular frequency of the applied force, and they are all controllable model parameters. Precise values are assigned to these parameters as follows:  $m = 11$ ,  $c = 20$ , and  $\omega = 2.5$ . While the spring stiffness  $k$  is an uncertain parameter, the information of  $k$  is given by a triangular distribution, and closed intervals are specified for possible minimum, mode, and maximum value of  $k$  as:  $k_{\min} = [90,100]$ ,  $k_{\text{mode}} = [150,160]$ ,  $k_{\max} = [200,220]$ . Here, the objective is to quantify the uncertainty in the steady-state magnification factor  $D_s$  based on the stated information.

The probability box for spring stiffness  $k$  can be obtained from a nested sampling method, as shown in Fig. 1. An ODM with nine focal elements of equal length and an IODM with nine focal elements of unequal length are both used to discretize the probability box of  $k$ . Table 1 gives the focal elements and basic probability assignments for IODM.

After the random sets for  $k$  are obtained by ODM and IODM, respectively, the extension principle stated by Eq. (2.3) is used to map the  $(\zeta, M)$  to the mechanical system response through function  $D_s$ . Then, the upper and lower CDFs of  $D_s$  can be

**Table 1**  $(\zeta, M)$  of spring stiffness  $k$  for IODM

$j$	$A_j$	$M(A_j)$
1	[90,122]	0.065
2	[111,134]	0.097
3	[123,146]	0.129
4	[134,155]	0.129
5	[143,165]	0.161
6	[152,174]	0.129
7	[160,186]	0.129
8	[170,198]	0.096
9	[181,216]	0.065



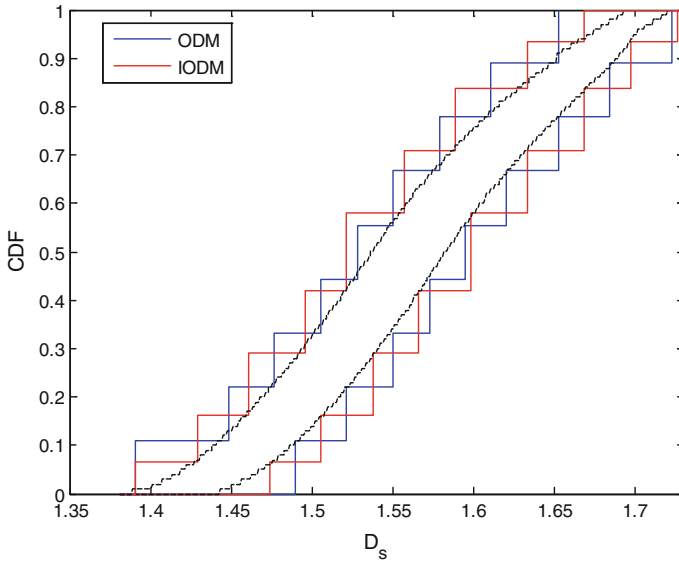


**Fig. 2** Upper and lower CDFs of the mechanical system response  $D_s$  from ODM and IODM

calculated with the image  $(\mathbf{R}, \rho)$  of  $(\zeta, M)$ , as Eq. (2.5) stated above. The resulting CDF bounds of  $D_s$  are displayed in Fig. 2.

The dashed lines in Fig. 2 define the precise quantification for the model uncertainty, and they are obtained from a second-order probability method with adequate sampling. The  $L_1$  distance between the ODM lines and the dashed lines is 0.031, while the distance between the IODM lines and the dashed is 0.029. It indicates that the IODM leads to more accurate uncertainty quantification.

## 5 Summary

This paper presents an IODM for discretizing the probability box to a random set, and the numerical example shows that the method provides a smaller discretization error with the same number of focal elements for random set. It can be used for the improvement of the uncertainty quantification when the computation of the mechanical model is expensive. Future work will include the theoretical demonstration of the relationship between IODM and uncertainty quantification through a system mapping.

## References

1. Oberkampf WL, Helton JC, Joslyn CA et al (2004) Challenge problems: uncertainty in system response given uncertain parameters. *Reliab Engng Syst Safety* 85:11–19
2. Ferson S, Tucker WT (2013) Probability boxes as info-gap models. In: Annual conference of the north American fuzzy information processing society. Institute of Electrical and Electronics Engineers, Piscataway
3. Tonon F (2004) Using random set theory to propagate epistemic uncertainty through a mechanical system. *Reliab Engng Syst Safety* 85:169–181
4. Tonon F, Bernardini A, Mammino A (2000) Determination of parameters range in rock engineering by means of random set theory. *Reliab Engng Syst Safety* 70:241–261
5. Oberguggenberger M, Fellin W (2008) Reliability bounds through random sets: nonparametric methods and geotechnical applications. *Comput Struct* 86(10):1093–1101
6. Dubois D, Prade H (1991) Random sets and fuzzy interval analysis. *Fuzzy Sets Syst* 42:87–101
7. Dong WM, Shah HC (1987) Vertex method for computing functions of fuzzy variables. *Fuzzy Sets Syst* 24(1):65–78
8. Jones DR, Pertuncun CD, Stuckman BE (1993) Lipschitzian optimization without Lipschitz constant. *J Optimiz Theory App* 73(1):157–181

# Coordinated Control Method of AGC and AVC in Power Grid

Shiguang Li, Zian Wang, Xinjing Wu and Jiatong Du

**Abstract** With the coupling relationship between active power and reactive power in power system becoming stronger, the control mode that automatic generation control (AGC) and automatic voltage control (AVC) operate separately may influence the control effect. Considering the different control period of AGC and AVC, this paper proposes a coordinated control method of AGC and AVC with a connection on the timescale of minute level and second level. On the minute level, an optimal power flow model of active power and reactive power associated together is established, and a AGC and AVC associated optimization control method are proposed. On the second level, the paper improved the respective control strategies of AGC and AVC, also proposed a coordinated correction control method of both of them. Simulations are made to verify that the method proposed in this paper meets the respective control objective of AGC and AVC. At the same time, it can realize the economical operation of power system, restrain the mutual influence of AGC and AVC, while promote the mutual support between AGC and AVC.

**Keywords** Automatic generation control (AGC) · Automatic voltage control (AVC) · Associated optimization · Coordinated correction

## 1 Introduction

As two key applications of the power grid dispatching automation system, the automatic generation control (AGC) and automatic voltage control (AVC) are usually considered decoupled and controlled independently. This decoupling control mode is more effective at the initial stage of the power grid construction. But with the contact of power grid being close and the increase of load, the independent control mode has been exposed to some problems. For example, with the contact of

---

S. Li (✉) · Z. Wang · X. Wu · J. Du  
China Electric Power Research Institute, Beijing 100192, China  
e-mail: lishiguang@epri.sgcc.com.cn

power grid being close and the increasing transmission power level of tie line, when the tie line power and the plan deviation are large, AGC for tracking plan value will cause the tie line power fluctuations, which will cause the voltage fluctuation of tie line node and area of power grid nearby, thus affecting the quality control for AVC. On the other hand, with the growth of load level, the power flow of some lines is fairly heavy, and the AVC regulation to their end node voltage may cause change even the violation of the line power flow limits, thus affecting the control quality of AGC. Visibly, grid active power control and reactive power control cannot be completely decoupled, independent control may cause the repeat adjustments of AGC and AVC, which will influence the control effects [1–4].

In recent years, academics have conducted active explorations for the coordinated control of AGC and AVC in grid. The literature [5, 6] intended to improve the voltage stability and suppress the low-frequency oscillation as the goals of control, researched the coordinated strategy of AGC and AVC after the load growth or fault. The literature [7, 8] researched on AGC and AVC coordinated control strategy of different levels put forward the control algorithm of optimization level and prediction level, verified the coordination effect. The literature [9, 10] based on event-driven mechanism proposed the AGC and AVC, alternating iterative coordination control strategy, reduced the mutual influence between them.

This paper considers the different control cycles of AGC and AVC, and according to the timescale, it puts forward the AGC and AVC coordinated control method with the cohesion of minute and second levels. It realizes the joint optimization control of active power and reactive power on the minute level and the coordinated corrective control of active power and reactive power on the second level. The two levels interact with each other, improving the safe and economic operation level of the power system.

## 2 Architecture of the Coordinated Control System

According to the provisions in the standard series of State Grid Corp of China Technology of smart grid dispatching support system, the period of AGC is no longer than 20 s, and AVC period is no more than 5 min. Obviously, although AGC and AVC are both in real-time control category, the control cycles are not at the same timescale. Therefore, the implementation of AGC and AVC coordinated control needs to be carried out in the minute- and second-level hierarchy, respectively, and keeps the mutual connection between the two levels. Therefore, in full use of the existing implementation to the AGC and AVC, this paper improves the model and strategy, and bases on the timescale of minute and second levels, puts forward two-level control architecture. As shown in Fig. 1.

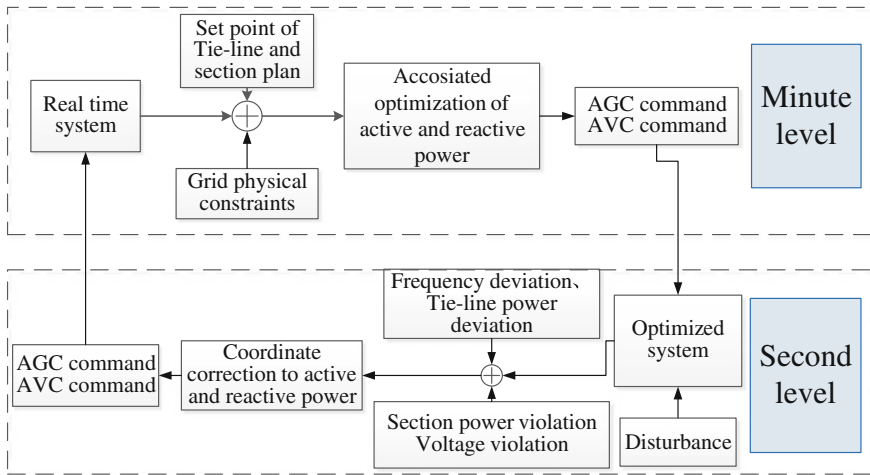


Fig. 1 Structure of coordinated control

The general idea of coordinated control architecture is to build the unified model of active and reactive power in the minute level, calculate active power and reactive power of joint optimization periodically, and give the control command of AGC and AVC uniformly. And it improves the control strategy of AGC and AVC, respectively, in the second level, establishes a coordination mechanism between them, and periodically monitors the operational status of power grid optimization. When it is found that the state variables are beyond the allowable operating range, the system will give the control commands of AGC and AVC, respectively, in terms of the active power and reactive power correction coordination. The implementation mode of two levels is shown as follows.

### 3 The Minute Level of Hierarchical Optimization Model

The main task of minute level is to adjust the active and reactive power output, tracking the load trend, make the gird operating near the optimal power flow state in a relatively long timescale. The mathematical model can be the AVC non-model-based reactive power optimization, controlling objectives and constraints into the AGC, and the establishment of active and reactive power optimal power flow model can be combined.

The usual mathematical model of AVC is based on the minimum network loss as objective and the security for the nonlinear constrained optimization problem [11], as shown below:

$$\min P_{\text{loss}} = \sum_{i=1}^N V_i \sum_{j=1}^N V_j G_{ij} \cos \theta_{ij}$$

$$\text{st} \begin{cases} P_{G,i} - P_{D,i} - V_i \sum V_j (G_{ij} \cos \theta_{ij} + B_{ij} \sin \theta_{ij}) = 0 & i \in N \\ Q_{G,i} - Q_{D,i} - V_i \sum V_j (G_{ij} \sin \theta_{ij} - B_{ij} \cos \theta_{ij}) = 0 & i \in N \\ V_{i,\min} \leq V_i \leq V_{i,\max} & i \in N \\ Q_{G i,\min} \leq Q_{G,i} \leq Q_{G i,\max} & i \in S_G \\ T_{i,\min} \leq T_i \leq T_{i,\max} & i \in S_T \\ B_{i,\min} \leq B_i \leq B_{i,\max} & i \in S_B \end{cases} \quad (1)$$

Parameter  $N$  is the total number of nodes;  $S_G$ ,  $S_T$ , and  $S_B$ , respectively, represent generator node set, OLTC node set, reactive power compensation node set;  $P_{\text{loss}}$  means loss;  $V$ , node voltage magnitude and phase angle;  $G_{ij}$ ,  $B_{ij}$  for the real and imaginary part of the node admittance matrix elements;  $P_G$ ,  $Q_G$  as the generator active and reactive power;  $P_D$ ,  $Q_D$  as the load active power and reactive power;  $T$  for OLTC types;  $B$  reactive power compensation capacity; subscript max, min, respectively, represent the maximum and minimum limits.

The main goal of AGC is to control the frequency values near, control the tie line power tracking plan value, and control the important line power flow security at rated. For the frequency control, type (1) with equality constraints in the constraint conditions is to ensure the active power balance, so as to realize the balance of supply and demand of the whole system, and to keep the frequency near the rated value. But because of each node in the solving process, there will be a certain generation and load unbalance, which may increase the frequency and the rated value deviation in the whole system of the accumulated frequency control, in order to ensure the quality of frequency fluctuation constraint that should be introduced, as shown below:

$$\left| \sum_{i \in S_G} P_{G,i} - \sum_{j \in S_D} P_{D,j} \right| \leq 10B\epsilon \quad (2)$$

$B$  for the system frequency deviation coefficient (MW/0.1 Hz); Epsilon allows for frequency fluctuations, usually not more than 0.5 Hz;  $S_D$  for load node collection.

When modeling for tie line power control, the link can be equivalent to generating set, tie line power is the power generating set, sending power grid of the equivalent generator power is negative, and by the end, the power grid is positive. The equivalent units fixed reactive power and active power tracking plan value. Set  $L$  for link node and then the equivalent unit constraint conditions for:

$$|P_{G,L} - P_{T,0}| \leq \eta \quad (3)$$

$P_{T,0}$  for the tie line power plan and  $\eta$  for tie line power deviation dead time, usually no more than 5 MW.

To control the important section, usually the line power flow control, the basic requirement is to avoid overload. Without loss of generality, we can constrain the system of the line power, as shown below:

$$P_{ij,\min} \leq P_{ij} \leq P_{ij,\max} \quad (4)$$

Parameter  $P_{ij}$  means power transmitted on line  $L_{i,j}$ .

The active power of AGC units are adjustable, and the formula (2)–(4) can be added to the constraint conditions of type (1), and the minimum network loss is the objective.

Based on the type of reliable solution of application of primal dual interior point method, unified calculation of minute-level AGC and AVC strategy can be followed.

## 4 The Second Level of Correction Strategy

The main task of second level is periodically monitoring the change of power network state quantity in a relatively short timescale, to keep the amount of state in the reasonable operation interval.

### 4.1 Interactive Effects Between AGC and AVC

AGC usually adopts fixed tie line bias control (TBC) mode. Through the calculation of area control error (ACE), systems determine whether AGC acts or not. ACE calculation formula is as follows:

$$ACE = 10B\Delta f + \Delta P_T \quad (5)$$

$\Delta f$  and  $\Delta P_T$  are the deviations of frequency and tie line power.

In addition, according to the expression of the power flow in the transmission:

$$P_{ij} = V_i V_j (G_{ij} \cos \theta_{ij} + B_{ij} \sin \theta_{ij}) - V_i^2 G_{ij} \quad (6)$$

In the second level, the interaction of AGC and AVC mainly exists between the line power flow and voltages of end nodes. So the path of coordination between AGC and AVC correction control strategy is to avoid the interaction worsening the system state, while achieving mutual support regulating with this interaction when necessary.

## 4.2 The Coordinated Tie Line Correction Control

In order to guarantee the control effect of tie line power, the sensitivity of the generators to the tie line power flow shall be considered in the regulation of AGC unit distribution. The method is as follows:

$$\frac{\partial P_{ij}}{\partial P_G} = \frac{\partial P_{ij}}{\partial \theta_i} \cdot \frac{\partial \theta_i}{\partial P_G} + \frac{\partial P_{ij}}{\partial \theta_j} \cdot \frac{\partial \theta_j}{\partial P_G} + \frac{\partial P_{ij}}{\partial V_i} \cdot \frac{\partial V_i}{\partial P_G} + \frac{\partial P_{ij}}{\partial V_j} \cdot \frac{\partial V_j}{\partial P_G} \quad (7)$$

When the ACE is mainly caused by the tie line power deviation, the unit with high sensitivity can be chosen for the tie line power regulation. While the ACE is mainly caused by the deviation of frequency, the main choice will be the unit with low sensitivity, in order to ensure the elimination of frequency deviation and the less impact on the tie line power.

Meanwhile, we have to calculate the variation of the node voltage resulting from the AGC regulation according to the sensitivity of the tie line to the node voltage. Sensitivity is calculated as follows:

$$\frac{\partial P_T}{\partial V_i} = V_j(G_{ij} \cos \theta_{ij} + B_{ij} \sin \theta_{ij}) - 2V_i G_{ij} \quad (8)$$

According to the sensitivity calculated with the formula above and tie line power deviation, we can calculate the voltage after AGC regulation, launch the AVC regulation according to the voltage and reactive power sensitivity correction algorithm [12] when necessary, to avoid the node voltage violation.

## 4.3 Coordinated Correction to Heavily Loaded Lines

For the correction of the heavily loaded lines, we need to find units with high sensitivities, which is calculated according to the formula (8), combined with the ACE adjust direction. The units that not only can effectively reduce the load of the line, but also can reduce the ACE shall be the priority options.

But in some cases, such as AGC correction would deteriorate the power grid ACE. We should regulate the line flow by adjusting the end node voltages, instead of the AGC. Essentially, it is to adjust the active power by adjusting the reactive power. It needs the sensitivity of active reactive power source (such as generators) to activate power of the line, and its expression is as follows:

$$\frac{\partial P_{ij}}{\partial Q_G} = \frac{\partial P_{ij}}{\partial \theta_i} \cdot \frac{\partial \theta_i}{\partial Q_G} + \frac{\partial P_{ij}}{\partial \theta_j} \cdot \frac{\partial \theta_j}{\partial Q_G} + \frac{\partial P_{ij}}{\partial V_i} \cdot \frac{\partial V_i}{\partial Q_G} + \frac{\partial P_{ij}}{\partial V_j} \cdot \frac{\partial V_j}{\partial Q_G} \quad (9)$$



According to the equation above, the reactive power source with high sensitivity to line power should be found out, to limit the line power flow. What needs to be pointed out is that the amount changed on line power by reactive power regulation is usually very little, so this method is only suitable for trimming, as an auxiliary method for AGC regulation under special circumstances.

Node voltage coordination control correction. AVC on the contact line or heavy load line near zone grid node voltage correction may cause contact line or heavy haul railway power change. Considering that during normal operation of the network, although the node voltage is limited, is slightly offset voltage limit. So under normal circumstances, AVC regulating winding or poetic couplet line power change quantity is not big. But in order to ensure the correction control AVC alone does not worsen tie line or line power, it can use its power and can be adjusted in the range of voltage regulation margin constraints, as shown below:

$$\Delta V \leq \left| \Delta P_{ij} \cdot \frac{\partial Q}{\partial P_{ij}} \cdot \frac{\partial V}{\partial Q} \right| \tag{10}$$

$\Delta V$  is the voltage amplitude and can be adjusted, and  $\Delta P_{ij}$  is adjustable power margin.

## 5 Example Verification

In order to verify the proposed effect of coordinated control of AGC and AVC, we select the new England 10 generator 39 node system [13] set the load of node 20 for the tie line power of sending power grid, and set the line between nodes 21 and 22 for the heavy load lines. Firstly, if we verify the minute-level control strategy, increase the load of odd load nodes by 10 %, and reduce the even load nodes by 10 %, then the total load of the system increases to 123.2 MW, frequency decreases to 0.55 Hz, and node voltage increases by 10 beyond the upper limit (voltage limits 0.94–1.06 pu). Set the tie line power plan value 800 MW, and the overloaded line power limits 583 MW. The control effect of AGC and AVC combined optimization is shown in Table 1.

**Table 1** Optimization control effect of minute level

Control variables	Before	After
Node 10 voltage (pu)	1.062	1.057
Line 22-21 power (MW)	599.78	573.39
Tie line power (MW)	680.0	796.8
Frequency (Hz)	49.45	49.99
Net loss (MW)	31.72	32.63
Net loss rate (%)	0.51	0.50

It is clear that, after the AGC and AVC coordinated optimization, the system frequency, tie line and heavily loaded line power, and node voltage are maintained in the acceptable range. But the system loss is increased, and this is mainly due to power generation increase significantly after optimization result. But in the optimization process, the minimum network loss is the object, and thus, the net loss rate remains at a relatively low level.

Based on grid section of minute-level optimization, we verify the second-level AGC and AVC coordinated correction control strategy. To the tie line control, set a moment of interconnecting line power plan value 787 MW. According to the relationship between the sensitivity of tie line power and generator power, adjust the generators 33 and 34 and distribute the regulation of power about 10 MW according to spare capacity. But only adjusting AGC may lead to node 20 voltage lower than limited, changes from 0.943 to 0.939. So it needs synchronous adjustment of AVC and AGC. According to the relationship between the sensitivity of voltage and reactive power, we still choose generator 33 and 34 by adjusting the AVC. Without causing other node voltage violations, two generators share at least 9 Mvar reactive power. The control effect of AGC and AVC coordinated correction is shown in Table 2.

Obviously, after the coordination correction of the AGC and AVC, the tie line flow is kept in a reasonable range, and the tie line end node voltage is prevented from violation.

For the overloaded line control, if ACE is qualified and line 22-21 power limit is reduced from 583 to 573 MW, the line power is slightly over limited. Using AVC-aided AGC regulation, according to the sensitivity of line power and reactive power of the generators, select generator 35 and 36 to be involved in AVC regulation; when the other node voltages are qualified at the same time, make two generators share at least 36 Mvar reactive power, and the regulating effects are shown in Table 3.

Thus, it can be seen that when line power is slightly over limit, using AVC regulation of voltage across the line instead of the AGC correction to the heavily loaded line flow will not affect the power grid ACE, also will make the line power controlled in the reasonable range, and improve the node voltage level.

**Table 2** Coordinated correction effect of tie line at second level

Control variables	Before	After
Interconnecting line power (MW)	796.8	786.9
Node 20 voltage (pu.)	0.943	0.944

**Table 3** Coordinated correction effect of heavy load line at second level

Control variables	Before	After
ACE (MW)	5.46	5.46
Line 22-21 power (MW)	573.39	572.87
Node 21 voltage (pu.)	1.039	1.034
Node 22 voltage (pu.)	1.057	1.052

**Table 4** Node voltage regulation range of heavy load line

Node	Current voltage (pu.)	Lower voltage limit (pu.)	Upper voltage limit (pu.)
21	1.034	0.94	1.035
22	1.052	0.94	1.053

For the node voltage control, when adjusting the voltage of overloaded line end node, due to line 22-21 power (572.87 MW) is close to the rated limit (573 MW). The AVC regulation to the voltage of node 21 and 22 may cause the line power violation, and it needs to define a node voltage regulating range according to the formula (10), as shown in Table 4.

Obviously, because the line power flow is close to the limit, not to make it worse, the rise space of line end node voltage is limited.

## 6 Conclusion

In this paper, the coordinated control method of AGC and AVC in the grid is based on the existing methods of AGC and AVC. Through the improvement of the mathematical model and control strategy, it implements the AGC and AVC on different timescales of joint optimization and coordination correction. It shows that the method is correct and effective by the example analysis. At the same time, control effect shows that the method is also in the satisfaction of the AGC and AVC of respective control target, optimizes the economic operation level of the power grid, inhibits the interaction between the AGC and AVC, and promotes the auxiliary support to adjust between the AGC and AVC.

**Acknowledgments** This paper got the support of innovation fund project of China Electrical Power Research Institute “The coordinated control of Automatic Generation Control and Automatic Voltage Control in the Same Time-Scale” (DZ83-14-008), which we herewith acknowledge with best thanks.

## References

1. Yu T, Wei W (2011) Coordinated scheme for automatic voltage control of Hunan power grid. *Power Syst Technol* 35(4):82–86 (in Chinese)
2. Yu T, Guo R (2012) Control scheme for voltage reactive power of regional power grid based on load forecast. *Power Syst Prot Control* 40(12):121–124 (in Chinese)
3. Qinglai G, Hongbin S, Boming Z et al (2006) Extension of common information model for automatic voltage control system. *Power Syst Technol* 30(S2):66–70 (in Chinese)
4. Yu T, Wei W, Tianjiao P et al (2014) Study of medium-term and long-term time-scale system frequency fluctuations simulation under high penetration of wind power. *Power Syst Clean Energy* 30(1):87–93 (in Chinese)

5. Fang Y, Yuanzhang S, Cheng L (2010) Coordinated control of AGC redispatching and AVC to enhance voltage security. *Autom Electr Power Syst* 34(4):7–11 (in Chinese)
6. Haowei Y, Wei H, Fei X et al (2011) Research on damping control system of optimization coordination of AGC and AVC. In: *The international conference on advanced power system automation and protection*. IEEE: Beijing, China, pp 1931–1937
7. Miao L, Jianbo S, Xiaoping L et al (2011) Optimal coordinated control strategy of AGC and AVC based on hierarchical control. In: *The international conference on advanced power system automation and protection*. IEEE, Beijing, China, pp 1890–1895
8. Wei H, Shuying W, Fei X et al (2011) An optimal coordinated control strategy of AGC and AVC based on hierarchical control. *Autom Elect Power Syst* 25(15):40–45 (in Chinese)
9. Hu W, Lu Q, Xu F et al (2011) The hierarchical coordinated optimizing control of AGC and AVC system based on event-driven system. In: *The 46th international universities power engineering conference*. UPEC, Soest, Germany, pp 1086–1090
10. Lianjie L, Ying W, Xianyong X et al (2012) An coordinated optimal control strategy of AGC and AVC based on alternating iterative method. *Sichuan Elect Power Technol* 35(3):30–35 (in Chinese)
11. Wei X (2010) Study on large-scale power networks real-time reactive power optimal control method. Zhejiang University, Hangzhou, China (in Chinese)
12. Fulong Y, Zhiming W, Weichun G et al (2013) Voltage and reactive power automatic control of power system. Beijing, China (in Chinese)
13. Yu T, Hu L, Jiang Z (2010) Impacts of connection and control modes of multi-terminal DC power transmission system on transient stability. *Power Syst Technol* 34(2):87–91 (in Chinese)

# Research into Key Points and Application Ideas of Reliability Assessment for Medium-Voltage Distribution Networks

Lingyun Wan, Tingting Wei, Jin Fu, Gaolin Wu, Qunying Yang and Wei Song

**Abstract** Firstly, some commonly used terms of medium-voltage distribution networks' reliability assessment are briefly introduced. Then, some normative suggestions about key points of reliability assessment, such as assessment indexes, parameters, and methods, are systematically put forward. In addition, some key issues of models, parameters, and methods for reliability evaluation are analyzed, and corresponding reasonable disposal methods are given. As for distribution network models, the establishing idea is given, where an organic connection is established between the reliability assessment and reliability statistics. Moreover, some ideas of applying reliability assessment in the phases of network planning, renovation, operation, and maintenance are proposed, improving the power supply reliability fundamentally and bringing more benefits for the power supply enterprises. The reliability assessment of 5 cases is conducted, which can test the effects of load switches, load curves, equipment capacity constraint, and load shedding on the reliability indexes, and the results indicate that the presented normative suggestions are practical.

**Keywords** Medium distribution networks · Reliability assessment · Normative suggestions · Engineering application

---

L. Wan · J. Fu · G. Wu · W. Song  
Electric Power Research Institute of State Grid Chongqing Electric Power Company,  
Yubei District, Chongqing 401123, China

T. Wei (✉)  
State Key Laboratory of Power Transmission Equipment and System Security  
and New Technology, Chongqing University, Shapingba District,  
Chongqing 400044, China  
e-mail: wtt\_address@126.com

Q. Yang  
Chongqing Electric Power Company, Yuzhong District, Chongqing 400014, China

## 1 Introduction

In recent years, with the development of China's economy and society, customers' demand for power supply reliability is higher and higher. The assessment and analysis through only the statistics of outage accidents is hard to adapt to the high demand for power supply reliability. Since the power supply reliability assessment can effectively guide the power system planning, design, construction, reconstruction, operation, and management, and can improve the power supply reliability fundamentally and increase the investment profits of power grids, more and more power supply enterprises are carrying out or are planning to carry out this work.

At present, due to the lack of a general technical standard for the reliability assessment of medium-voltage distribution systems, some related institutions, such as power supply enterprises, colleges, research institutions, and companies, use different models, methods [1–5], and indexes as well as assumptions and simplified processing methods during the assessment process. These factors all bring a big obstacle to the promotion and application of power supply system reliability assessment. Given all that, Electric Reliability Management Centre of China's State Electricity Regulatory Commission authorized China's State Grid to compile a technical standard for the reliability assessment of medium-voltage distribution networks.

In this paper, based on the existing research achievements, some normative suggestions about assessment indexes, models, parameters, and methods are put forward systematically, with the status of distribution networks and reliability management being considered as well as the real demands for reliability assessment of power supply enterprises, thus providing the reference for the development of technical standards for the reliability assessment of medium-voltage distribution systems. At last, some ideas of applying reliability assessment in the phases of network planning, renovation, operation, and maintenance are proposed.

## 2 Related Terms and Definitions

- Fault localization and isolation time: the time from fault occurrence and fault isolation, unit: h.
- Fault repairing time: the time from the outage caused by the device fault to the power restoration through device repairing or change, unit: h.
- Fault outage-interconnection switch switching time: the time from the isolation of the fault point to the completion of the load transfer, unit: h.
- Fault outage-load transfer time: the time from the occurrence of fault outage to the completion of load transfer, including the fault location and isolation time and the fault outage-interconnection switch switching time, unit: h.

- Power restoration operation time at the upstream of the fault point: the time from the isolation of the fault point to the restoration of power supply after the re-connection of the switching devices on the upstream, unit: h.
- Power restoration time on the upstream of the fault point: the time from fault occurrence to power restoration on the upstream of the fault point, including fault location and isolation time and the time of power restoration on the upstream of the fault point, unit: h.
- Scheduled outage-isolation time: the time from the occurrence of the scheduled outage to the isolation of the scheduled feeder, unit: h.
- Scheduled outage-interconnection switch switching time: the time from the isolation of the scheduled outage feeder to the completion of load transfer, unit: h.
- Scheduled outage-load transfer time: from the occurrence of scheduled outage to the completion of load transfer, including the isolation of the scheduled outage to the scheduled outage-interconnection switch switching time, unit: h.
- Power restoration operation time on the upstream of the scheduled outage feeder section: from the isolation of scheduled outage feeder to power restoration on the upstream after the re-connection of the switch devices on the upstream of the section, unit: h.
- Power restoration time on the upstream of the scheduled outage feeder: from the occurrence of scheduled outage to power restoration on the upstream of the scheduled outage wire section, including scheduled outage-isolation time and power restoration operation time on the upstream of the scheduled outage wire section, unit: h.
- Rate of component failure: the times of internal fault outage (cannot perform the required function) in the facility unit running time.
- Rate of component planned outage: the times of the planned outage in the unit running time.
- Rate of system planned interruption: during the period of statistics, the planned outage times of 100 km lines in power supply system (excluding the planning outage caused by the superior power grid), unit: times/(100 km year).

### **3 Assessment Models, Parameters, Indexes, and Methods**

#### ***3.1 Distribution Network Models***

Single electrical equipment such as distribution transformer, line, switch, bus is basic unit of the distribution network reliability evaluation. For the establishment of distribution network model, the influence of all kinds of equipment should be considered, and some equipment should be merged or neglected to simplify the practical complex distribution network structure, making it suitable for the reliability evaluation.

In order to make full use of reliability statistic data, the establishment of a distribution network model should be combined with the research achievements of reliability statistics. According to Electric Reliability Management Code issued by the reliability center of China Federation of Electric Power Enterprises, China's power distribution devices related to the customer service reliability can be divided into 9 categories and each category can be further divided into several smaller classes [6]. Based on the Table of Distribution Devices' Influence on Equipment Failure Rates from Work Guidance of Customer Power Supply Reliability [7], the models of main distribution devices can be established, so as to construct a distribution network model. For example, an overhead line and its accessories may be merged into the overhead line model because they all affect the failure rate of the overhead line.

## 3.2 *Assessment Parameters, Indexes, and Methods*

### 3.2.1 **Assessment Parameters**

Parameter plays an important role in calculation model, mainly used to describe the model. It can be divided into basic parameter and reliability parameter.

Basic parameter includes network topology, basic parameter of distribution lines, transformers, and load points. Basic parameter of lines and transformers mainly includes physical and electrical parameter. Load point parameter should contain not only capacity and customer numbers, but also "important level" to adapt to different requirements for power supply reliability of different customers.

Reliability parameters can be divided into failure outage and scheduled interruption parameter.

#### 1. Failure parameters

- Substation 10/6/20 kV bus: (equivalent) average failure rate, (equivalent) average repair time.
- Overhead line, cable line: average failure rate, average repair time.
- Sectionalizer: average failure rate, average repair time, average failure localization, and isolation time.
- Circuit breaker, fuse: average failure rate, average repair time, failure outage-operation time at the upstream of the upstream circuit breaker.
- Load switch, transformers: average failure rate, average repair time.
- Tie switch: failure outage-switching time of tie switch.

#### 2. Scheduled outage parameter

- Substation 10/6/20 kV bus: (equivalent) average scheduled interruption rate, (equivalent) average scheduled interruption duration.
- Overhead line, cable line: average scheduled interruption rate, average scheduled interruption time.



- Sectionalizer: average isolation time of scheduled interruption.
- Circuit breaker, load switch, and fuse: scheduled interruption–operation time of upstream circuit breaker.
- Tie switch: scheduled interruption—switching time of tie switch.

### 3.2.2 Assessment Indexes

The reliability assessment indexes can be categorized as load point indexes and system ones. The commonly used load point indexes [8] include the average failure rate ( $\lambda_{LP}$ , times per year), the annual outage duration ( $U_{LP}$ , h per year), the average outage duration ( $r_{LP}$ , h per time), the average service availability index of a load point (ASAI-LP, %), and the energy not supplied of a load point (ENS-LP, kWh per year). System reliability indices include the system average interruption frequency index (SAIFI, times per household per year), the system average interruption duration index (SAIDI, h per household per year), the average service availability index (ASAI, %), and the energy not supplied (ENS, kWh).

### 3.2.3 Assessment Methods

Traditional assessment methods of a medium-voltage distribution network can be roughly categorized as the simulation methods and analytical ones [8]. Due to their accurate models, simple principles, and flexible analyses to the influence of elements with different functions, the analytical methods have been more and more popular for the distribution network reliability assessment. For the networks with distribution generators or microgrids, assessment methods should be improved to solve some special problems. The methods used for a technical standard should be practical and can quickly evaluate the general large-scale medium-voltage distribution networks that include weak links, tie switches, and capacity constrained equipment.

## 4 Some Considerations of Models, Parameters, and Methods

1. The three-state model of operation, failure, and scheduled interruption is employed to describe the facility outage model [1].
2. The failure rate of a substation 10/6/20 kV bus should contain the failure rate caused by its higher voltage level power grids (including the substation), and some other reliability parameters of the substation 10/6/20 kV bus as well.
3. The fuse function of opening and closing with load should be taken into account.

4. The effect of a load switch to reduce the outage range should be taken into consideration because it can break a normal loading current for a scheduled interruption.
5. Normally opened tie switches only operate in the case of load transferring. Due to the neglecting of second-order faults, tie switches are considered completely reliable.
6. The scheduled interruption of higher voltage level power grids should be considered and related reliability parameters should be merged into the corresponding substation 10/6/20 kV busses.
7. Generally, one or two sectionalizers will be installed where a circuit breaker or load switch is placed to mark breaking points. This kind of sectionalizer is considered completely reliable to simplify the calculation.
8. Maximum load, minimum load, average load, a particular load, or a load curve can be used for the reliability assessment according to different purposes and applications.
9. Equipment capacity constraints should be considered during the assessment because the transferred load will increase if an equipment capacity is unrestricted.
10. In practice, load shedding is conducted according to load priorities, which should be abided by the calculation model.
11. Because distribution automation can reduce the failure locating and isolating time, tie switch switching time, etc., the influence of distribution automation can be reflected by the corresponding parameters.

## **5 The Application of Reliability Assessment**

### ***5.1 Purpose and Significance***

Applying reliability assessment in the phases of network planning, renovation, operation, and maintenance can guide each section effectively and improve the power supply reliability fundamentally, thus bring more benefits.

1. In the planning section, the reliability of planning networks which is obtained by reliability assessment can be used to optimize network structure and conduct scheme comparison to determine the optimal planning scheme.
2. In the renovation section, the results of reliability assessment can be applied to search the bottle necks and find measures to improve the reliability.
3. In the operation section, the reliability assessment results can be applied to find the operation risk the optimal operation, and the defensive measures.
4. In the maintenance section, the reliability assessment results can be used to select the optimal maintenance scheme which has minimal impact on the reliability, and realizing the reliability-centered maintenance gradually.

## 5.2 *The Application Ideas*

The application ideas of reliability assessment in each section are as follows:

### 1. Planning section

- Give the alternative planning schemes of optimizing network structure.
- Evaluate the reliability of selected alternative. Besides the commonly used frequency, time, and unavailability indexes, it is generally preferable to use the expected energy not supplied (EENS), which is a combination of probability and consequence.
- Conduct an economic analysis of the planning investment and the economic and social benefits brought from the reliability improvement.
- Conduct the scheme comparison to determine the optimal design scheme.

### 2. Renovation section

- Identify the system's and important loads' weak parts based on the reliability assessment results,
- Present the reliability improving measures in networks, equipment, managements, and technologies based on the analyses of weak parts.
- Conduct the benefit and cost analyses of measures to select the optimal construction and renovation project.

### 3. Operation section

The significance of reliability assessment application to this section is identifying the operation risks, determining the optimal operation mode, and evaluating the effects of risk defensive measures. The operation measures include load transfers, temporary network reconfigurations, and so on.

- Determine several operation modes using the offline power flow and contingency analysis, which may be associated with load transfers and temporary network reconfigurations.
- Select the load curve representing a time period (weekly, monthly, or seasonal).
- Calculate the system reliability using a specific load curve for each operation mode.
- Conduct an economic analysis.
- Compare the economic analyses results to determine the optimal operation mode.

### 4. Maintenance section

The application of reliability assessment to maintenance section can be called reliability-centered maintenance. The basic tasks of reliability-centered maintenance conclude comparison between maintenance alternative, lowest-risk maintenance scheduling, predictive maintenance versus corrective maintenance, and ranking importance of components.

## 6 Test Example

In the distribution network shown in Fig. 1, load points are ranked according to their importance grades, resulting in the list of *e, d, c, d, a*; the rest parameters are shown in Tables 1 and 2. During the reliability assessment, we have the following simplifications: neglecting the influence of higher voltage power grids and the sectionalizers on both sides of a circuit breaker (or a load switch). The rated capacities of load point *a, b, c, d,* and *e* are 800, 200, 50, 100, and 315 W, respectively.

Based on the failure mode effect analysis method, the reliability indexes can be obtained, which are shown in Table 3. The 5 cases related to these tables are as follows.

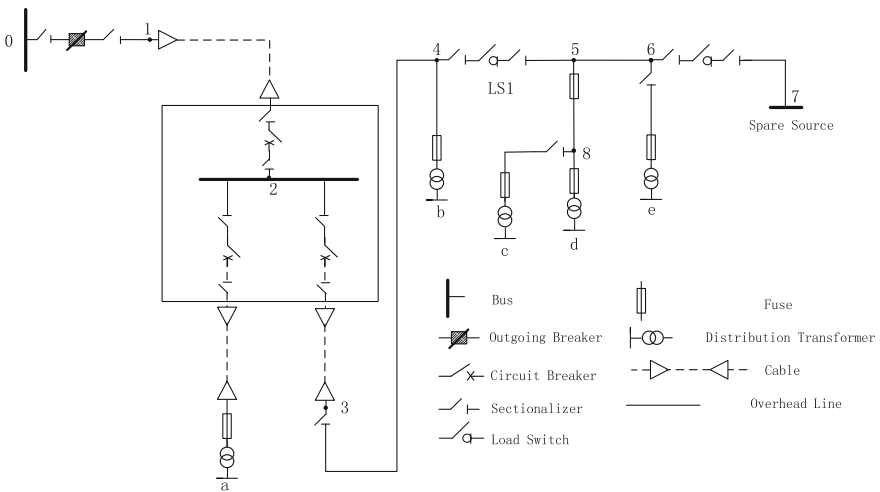


**Fig. 1** A reliability test example

**Table 1** Data 1 of the test example

Outage time/rate	Failure outage	Scheduled interruption
Location and isolation time (h)	1	0.1
Switching time of tie switch (h)	0.5	0.1
Average power restoration time of the upstream switch (h)	0.3	0.1
Outage rate of overhead (cable) line (times per 100 km per year)	6	7

**Table 2** Data 2 of the test example

Equipment		$L$ (km)	$\lambda$ (times per 100 km per year)	$T$ (h)
Main line	0-1	0.5	0.3	2
	1-2	2	0.1	5
	2-3	3	0.1	5
	3-4	3	0.3	2
	4-5	1	0.3	2
	5-6	2	0.3	2
	6-7	2	0.3	2
	5-8	1	0.3	2
Branch line	2-a	1	0.1	5
	4-b	1.5	0.3	2
	8-c	1.5	0.3	2
	8-d	0.5	0.3	2
	6-e	1	0.3	2
Circuit breaker		–	0.25	3
Load switch		–	0.2	2.5
Sectionalizer		–	0.25	2.5
Fuse		–	0.2	2
Transformer		–	0.35	4

**Table 3** System reliability indexes

System indexes	Case 1	Case 2	Case 3	Case 4	Case 5
SAIDI (h per household per year)	5.0186	5.0282	1.8838	2.5455	2.3182
ASAI (%)	99.9427	99.9426	99.9785	99.9709	99.9735
SAIFI (times per household per year)	0.795	0.843	0.795	0.795	0.795
ENS (kWh)	4965	4974	1765	3048	2172

Case 1: There is no tie switch or the spare capacity is 0 kVA.

Case 2: In addition to the conditions of case 1, load switch 1 (LS1) in Fig. 1 is replaced by a sectionalizer.

Case 3: In addition to the conditions of case 1, the spare capacity is unlimited.

Case 4: In addition to the conditions of case 1, the spare capacity is limited to 500 kVA and priority load shedding measures will be taken under capacity off-limits.

Case 5: In addition to the conditions of case 4, a load curve is used. For the used curve, the actual load capacity is half of the rated value for half of the study period and the other period is the rated capacity.

Note that  $L$  denotes the length of lines,  $\lambda$  denotes the outage rate of equipment,  $T$  denotes average repair time,  $N$  denotes the numbers of household, and  $W$  denotes the load-rated capacity.

Table 3 shows that the SAIFI of case 2 is the largest because of the absence of load switches, and the spare capacity can greatly improve the system reliability.

## 7 Conclusion

Based on the status of China's distribution networks and reliability management, some normative suggestions are systematically put forward for technical standards of medium-voltage distribution network reliability assessment with the common assessment problems being considered. In addition, some ideas of applying reliability assessment in the phases of network planning, renovation, operation, and maintenance are proposed, improving the power supply reliability fundamentally and bringing more benefits for the power supply enterprises. Through several test examples, it is shown that the proposed suggestions are practical and operable.

## References

1. Li W (2006) Risk Assessment of power systems: models, methods and applications
2. Allan RN, Billinton R, Sjarief I et al (1991) A reliability test system for educational purposes-basic distribution system data and results. *IEEE Trans Power Delivery* 6(2):813–820
3. Wang Z, Qiu J (2002) An efficient algorithm for assessing reliability indexes of general distribution system. *IEEE Trans Power Syst* 17(3):608–614
4. Chen W (1998) Fundamentals of distribution system reliability. China Electrical Power Press, Beijing
5. Xie K, Yang Q, Wan L (2012) Theoretical foundation of power reliability. China Electrical Power Press, Beijing
6. Power Reliability Management Center of China Electricity Council (2013) Power reliability management code. China Electrical Power Press, Beijing
7. State Grid Corporation of China (2012) Working guide for power supply reliability for customer service in power supply system. China Electrical Power Press, Beijing
8. Hua Z, Wang Z, Xie K, Li W (2013) A comparison study of reliability assessment methods for medium voltage distribution networks. *Power Syst Technol* 11:3295–3302

# Heat Transfer-Based Fault Diagnosis for Heat Exchanger of Aircraft Environmental Control System

H. Zhuohuan, W. Lulu and Y. Mo

**Abstract** In this project, combined with the process of heat transfer for plate-fin heat exchangers in aircraft environmental control system, we attempt to establish mathematical model based on inputs and outputs of heat exchangers. Then, the relative observer is given to generate residuals by the comparison of the outputs between heat exchangers and observers. Furthermore, fault information is obtained from the evaluation of residuals. Finally, simulation results show that the proposed scheme for heat exchanger failure detection is effective; it can be regarded as the theoretical basis of relevant engineering technology.

**Keywords** Environmental control systems · Heat exchangers · Fault diagnosis · Heat transfer · Aircraft

## 1 Introduction

Over the past decades, with the rapid development of the aviation industry, there has been a growing research interest in the reliability of aircraft environmental control systems. It is conceivable that heat exchanger plays an important role in environmental control system of aircraft cabin. The performances of heat exchanger deserve our more concern recently. Plate-fin heat exchangers are featured by compact construction and high heat changing efficiency of unit volume, which widely used in aircraft environmental control system. At the same time, fault diagnosis has a lot of research reports [1–4] for decades in other areas such as mathematics, biology, and control theory. Authors also have the relevant works focus on linear matrix inequality-based fault diagnosis of nonlinear systems [5–7]. However, the research of engineering thermodynamics based on the theory of fault diagnosis is few. Applicants are informed based on the application and research of fault diagnosis technology in this field. Xiaoyuan and Jixian [8] and Zhihong and

---

H. Zhuohuan · W. Lulu (✉) · Y. Mo  
University of Shanghai for Science and Technology, Shanghai 200093, China  
e-mail: huzhuohuan@hotmail.com

Tiejun [9] have researched the application of fault diagnosis of power station boiler based on neural network; Li and Wenguo [10] has presented the knowledge expression of boiler fault diagnosis expert system; Puyan and Ningsheng [11] have reported the application of fault diagnosis in thermal power plant thermal system and the existing problems; Haichao and Yingjun [12] and Xiaohui et al. [13] put infrared hot imaging technology into fault diagnosis of transformer; and Junru [14] and He et al. [15] have researched soft fault diagnosis problem of heat exchanger by the method of Parameter estimation which has the limitations on fault diagnosis caused by abrupt faults and structural changes.

In this project, based on the analysis of heat transfer of plate-fin heat exchangers, we establish their mathematical model based on inputs and outputs. The observer is constructed from mathematical model. Then, residuals are obtained by comparing the outputs between actual systems and their model. Finally, heat exchanger failure information is given by evaluating residuals.

## 2 Mathematical Model

It is well known that the work of the plate-fin heat exchanger is extremely complicated. Heat transfer process of them is abstracted and simplified following in [14]. Considering the cold side of the heat exchanger, gas flow cross-sectional area is  $A_1$ , cold gas flow rate  $V_1$ , density  $\rho_1$  and enthalpy  $H_1$ , heat  $C_1$ , pressure  $p_1$ , temperature  $T_1$ , heat transfer coefficient of wall surface and working substance  $\alpha_1$ , and heat transfer area of wall shell  $S_1$ , surface temperatures  $T_w$ , and it is apparently that  $T_w > T_1$ .

Ignoring heat transfer of the refrigerant in the flow of normal, the heat transfer quantity from the surface to the cold gas side is as follows:

$$dQ_1 = \alpha_1(T_w - T_1)S_1dl_xdt \quad (1.1)$$

where  $dl_x$  is the length infinitesimal in the direction of refrigerant flow. Then, the state of the incompressible refrigerant after the absorbing heat changes into

$$dQ_1 = A_1\rho_1C_1dl_xdT_1 \quad (1.2)$$

From (1.1) and (1.2), we have

$$A_1\rho_1C_1dldT_1 = \alpha_1(T_w - T_1)S_1dl_xdt \quad (1.3)$$

It can be rewritten as follows:

$$\frac{dT_1}{dt} = \frac{\alpha_1S_1(T_w - T_1)}{A_1\rho_1C_1} \quad (1.4)$$



That is,

$$\frac{\partial T_1}{\partial t} + V_1 \frac{\partial T_1}{\partial l} = \frac{\alpha_1 S_1 (T_w - T_1)}{A_1 \rho_1 C_1} \quad (1.5)$$

Similarly, heat transfer equation of the hot side is as follows:

$$\frac{\partial T_2}{\partial t} + V_2 \frac{\partial T_2}{\partial l_y} = \frac{\alpha_2 S_2 (T_w - T_2)}{A_2 \rho_2 C_2} \quad (1.6)$$

where the related parameter defines refer to the cold side.

Then, let specific heat of heat exchanger plates be  $C_w$ , quality be  $M_w$ , and we have

$$\frac{\partial T_w}{\partial t} = \frac{\alpha_1 S_1 (T_1 - T_w)}{M_w C_w} + \frac{\alpha_2 S_2 (T_2 - T_w)}{M_w C_w} \quad (1.7)$$

where heat release of the hot-side refrigerant is  $Q_2$ , and as  $Q_1$  in (2), we have

$$\frac{\partial T_w}{\partial t} = \frac{\alpha_1 S_1 (T_1 - T_w)}{M_w C_w} + \frac{\alpha_2 S_2 (T_2 - T_w)}{M_w C_w} \quad (1.8)$$

From (1.1), (1.2), and (1.3), following lumped parameter method, we can gain

$$\frac{dT_1}{dt} + V_1 (T_{1o} - T_{1i}) = \frac{\alpha_1 S_1 (T_w - T_{1i})}{A_1 \rho_1 C_1} \quad (1.9)$$

$$\frac{dT_2}{dt} + V_1 (T_{2o} - T_{2i}) = \frac{\alpha_2 S_2 (T_w - T_{2i})}{A_2 \rho_2 C_2} \quad (1.10)$$

$$\frac{\partial T_w}{\partial t} = \frac{\alpha_1 S_1 (T_{1o} - T_w)}{M_w C_w} + \frac{\alpha_2 S_2 (T_{2o} - T_w)}{M_w C_w} \quad (1.11)$$

where  $T_{1i}$  and  $T_{1o}$  are the inlet temperature of the hot and cold sides of the heat exchanger, and they can be considered as input parameters of heat exchanger;  $T_{1\sigma}$  and  $T_{2\sigma}$  are the outlet temperatures of the hot and cold sides of the heat exchanger, and they can be combined with  $T_w$  as the output parameter of the heat exchanger.

Let vector  $x = [T_{1o}, T_{2o}, T_w]^T$ ,  $u = [T_{1i}, T_{2i}]^T$ , form (1.9), (1.10), and (1.11), we have

$$\begin{cases} \dot{x} = Ax + Bu \\ y = Cx \end{cases} \quad (1.12)$$

is the state-space mathematical model of the heat exchanger, where

$$A = \begin{bmatrix} -\frac{\alpha_1 S_1}{A_1 \rho_1 C_1} - V_1 & 0 & \frac{\alpha_1 S_1}{A_1 \rho_1 C_1} \\ 0 & -\frac{\alpha_2 S_2}{A_2 \rho_2 C_2} - V_2 & \frac{\alpha_2 S_2}{A_2 \rho_2 C_2} \\ \frac{\alpha_1 S_1}{M_w C_w} & \frac{\alpha_2 S_2}{M_w C_w} & -\frac{\alpha_1 S_1}{M_w C_w} - \frac{\alpha_2 S_2}{M_w C_w} \end{bmatrix}, B = \begin{bmatrix} V_1 & 0 \\ 0 & V_2 \\ 0 & 0 \end{bmatrix},$$

$C$  is a row of full-rank matrix which is optional, and  $(A, C)$  is considerable.

### 3 Fault Detection

Fault types of the heat exchanger described by system include leakage, fouled, and clogged. These faults can cause the changes of the refrigerant flow rate ( $V_1$  or  $V_2$ ) or the heat transfer coefficient ( $\alpha_1$  or  $\alpha_2$ ). Change matrices  $A$  and matrices  $B$  into  $A'$  and  $B'$ , respectively, and let  $Ef = (A' - A)x + (B' - B)u$ . Then, the system can be rewritten as follows:

$$\begin{cases} \dot{x} = Ax + Bu + Ef \\ y = Cx + D\Delta \end{cases} \tag{1.13}$$

without loss of generality, we consider the white noise  $\Delta$  at the output of the system, let  $f$  with its differential and  $\Delta$  norm as bounded, that is  $\|f\| \leq f_1, \|\dot{f}\| \leq f_2, \|\Delta\| \leq \varepsilon$ , and  $f_1 > 0, f_2 > 0, \varepsilon > 0$ .  $D$  is full-rank matrix.

For system fault detection, observer is constructed as follows:

$$\begin{cases} \dot{\hat{x}} = A\hat{x} + Bu + L(\hat{y} - y) \\ \hat{y} = C\hat{x} \end{cases} \tag{1.14}$$

where  $L$  is a row of the optional full-rank matrix and makes the observer asymptotic stability, and all eigenvalues of  $(A + LC)$  have negative real parts.

Let us denote

$$e = \hat{x} - x, \quad \varsigma = \hat{y} - y \tag{1.15}$$

The residual system is as follows:

$$\begin{cases} \dot{e} = (A + LC)e - Ef \\ \varsigma = Ce - D\Delta \end{cases} \tag{1.16}$$

Because  $(A + LC)$  is stable, consequently, when fault free or  $f = 0$ , we have  $\left\| \lim_{t \rightarrow \infty} \varsigma \right\| \leq |D|\varepsilon$ . When fault or  $f \neq 0$ , we have  $\left\| \lim_{t \rightarrow \infty} \varsigma \right\| > |D|\varepsilon$ . Thus, evaluation of residuals for system failure detection strategy is as follows:

$$\begin{cases} \left\| \lim_{t \rightarrow \infty} \zeta \right\| \leq |D|\varepsilon, & \text{Fault free} \\ \left\| \lim_{t \rightarrow \infty} \zeta \right\| > |D|\varepsilon, & \text{Fault} \end{cases} \tag{1.17}$$

It is obviously that observer is the system fault detection observer.

### 4 Mathematical Model

In this section, numerical example is provided to demonstrate the validity of the proposed method. For the system, we denote

$$V_1 = 1, V_2 = 1.7, \frac{\alpha_1 S_1}{A_1 \rho_1 C_1} = 0.3, \frac{\alpha_2 S_2}{A_2 \rho_2 C_2} = 0.6, \frac{\alpha_1 S_1}{M_w C_w} = 0.6, \frac{\alpha_2 S_2}{M_w C_w} = 0.8.$$

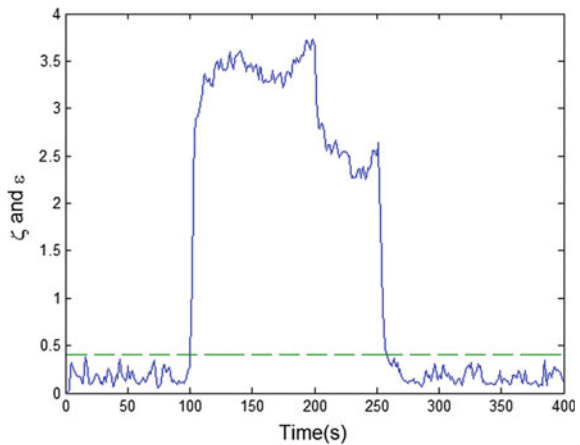
Substitute the formulas given above in the system and then solve it for  $A$  and  $B$ , and let  $C = E = D = I$ . Let  $u = [\sin(0.1t), \cos(0.1t)]^T$ , denote  $t$  as simulation time, and assume the number of steps is 400. The fault condition simulated is shown as the following,

$$f = \begin{cases} [0, 0.1, 0]^T & 100s < t \leq 150s \\ [0.1, 0.15, 0]^T & 150s < t \leq 200s \\ [0.15, 0, 0]^T & 200s < t \leq 250s \\ [0, 0, 0]^T & \text{others} \end{cases} \tag{1.18}$$

We can know  $(A, C)$  is observable and  $(A + LC)$  is stable, and let  $\Delta$  be white noise and  $\|\Delta\| = 0.4$ . The trend chart of  $\zeta$  and  $\varepsilon$  is given as follows.

From Fig. 1, it shows that when the failure occurs,  $\zeta$  is greater than  $\varepsilon$ , otherwise  $\zeta$  is not more than  $\varepsilon$ . The proposed failure detection for the state-space mathematical model of heat exchanger is valid, especially for abrupt faults.

Fig. 1  $\zeta$  and  $\varepsilon$  trend chart



## 5 Conclusions

In this project, based on the analysis of heat transfer of plate-fin heat exchangers, we established its state-space mathematical model from inputs and outputs. The observer is constructed based on mathematical models. Then, we obtained system residuals by comparing the outputs between actual systems and their model. Finally, evaluation of residuals obtained heat exchanger failure information. Simulation results show that the proposed state-space model for heat exchanger failure detection is effective and provides theoretical guidance for relevant engineering practice.

**Acknowledgement** This work is supported in part by National Science Foundation of China (51276118) and (51129602).

## References

1. Frank PM, Köppen-Seliger B (1995) New developments using AI in fault diagnosis. In: Proceedings of the IFAC artificial intelligence in real-time control, Beld, Slovenia, pp 3–14
2. Patton RJ, Frank PM, Clark RN (1989) Fault diagnosis in dynamic systems theory and application. Prentice Hall, Hertfordshire
3. Zhu FL, Feng C (2010) Full-order observer-based actuator fault detection and reduced-order observer-based fault reconstruction for a class of uncertain nonlinear systems. *J Process Control* 20(10):1141–1149
4. Alkan A, İlyas E (2011) Variance sensitive adaptive threshold-based PCA method for fault detection with experimental application. *ISA Trans* 50(2):287–302
5. Zhuohuan H, Zhengzhi H, Zuohua T (2009) Fault detection and diagnosis for singular stochastic systems via B-spline expansions. *ISA Trans* 48(4):519–524
6. Zhuohuan H, Zhengzhi H, Zuohua T (2008) Fault detection of singular stochastic systems via observers. In: International symposium on intelligent information technology application workshops, Shanghai, China, pp 209–212
7. Zhuohuan H, Zhengzhi H, Zuohua T (2011) Fault diagnosis for singular stochastic systems. *J Shanghai Jiaotong Univ (Sci)* 16(4):497–501
8. Xiaoyuan L, Jixian G (2005) Application of neural network expert system for fault diagnosis of boiler in thermal power plant. *Micro-Comput Inf* 21(3):24–25
9. Zhihong Y, Tiejun C (1997) Production process fault diagnosis expert system of neural network for thermal power plants. *Control Decision-Making* 12(3):252–255
10. Li L, Wenguo X (2003) Knowledge representation of expert system for fault diagnosis of boiler. *Res Utilization Energy* 26(1):26–28
11. Puyan Z, Ningsheng C (2001) Application to fault diagnosis in the thermal system and problems in China. *Turbine Technol* 12(6):321–323
12. Haichao R, Yingjun G (2007) Based on thermography thermal fault diagnosis method of power transformer. *Fire Sci* 16(1):52–54
13. Xiaohui T, Quan G et al (2010) Application of infrared imaging technique in diagnosis of transformer hot fault. *Baotou Steel Technol* 36(6):18–20
14. Junru Z (2005) Research of fault diagnosis of aircraft environmental control system. Northwestern Polytechnical University, Fremont
15. He J, Zhu L, Zhao J, Guo Y (2011) Fault diagnosis of aircraft heat exchangers based on RELS method. In: Intelligent control and information processing (ICICIP), Dalian, China, pp 499–503

# Direct Torque Control of Permanent Magnet Synchronous Motor at Low Speed Using a Variable PI Feedback Flux Observer

Suying Zhang, Wenshuai Cui, Yankai Shen and Huixian Liu

**Abstract** In the study of direct torque control (DTC) of permanent magnet synchronous motor (PMSM), the stator resistance is easily affected by temperature variation and its value varies from time to time. What is more, it will lead to flux ripple. In order to solve the problem of error existing between the set value of the stator flux and the reality, an improved method based on variable parameter PI is proposed to compensate the stator resistance. By constructing the stator flux observer mathematical model of DTC of PMSM and analyzing the stator resistance variation influenced by the stator flux observation, it can be found that the stator resistance is compensated by adjusting PI parameters with time, the flux error will be reduced, and this new method will be testified by MATLAB software. The simulation result shows that the improved stator resistance compensation algorithm has effectively solved the flux ripple problem, decreased the flux error, and achieved the expected control effect.

**Keywords** PMSM · DTC · Stator resistance compensator · Torque ripple reduction

---

S. Zhang · W. Cui (✉) · Y. Shen · H. Liu  
School of Electrical Engineering, Hebei University of Science  
and Technology, Shijiazhuang 050000, China  
e-mail: cuiwenshuai555@sina.com

S. Zhang  
e-mail: zhsy8985@sina.com

Y. Shen  
e-mail: shenyankai1989@163.com

H. Liu  
e-mail: 2006guanyue@163.com

## 1 Introduction

Direct torque control (DTC) was firstly proposed by Depenbrock Takahashi and Naguchi in 1980s. Its main idea is to control the stator flux space vector and electromagnetic torque, simplify the calculation, and reduce the influence of motor parameters. However, DTC is an unsophisticated control method which has lots of advantages such as quick response of torque, excellent dynamic performance, and less parameter dependence [1, 2]. But this method also has the disadvantages of increasing torque ripple and narrow speed range which are caused by drift in stator flux linkage estimation. What is more, the stator resistance variation, the test accuracy of rotor's initial position, and stator flux offset error in measurement are the reasons for why there is change in stator flux linkage estimation [3].

In recent years, an improved method based on PI controller to compensate stator resistance has been proposed [4]. However, the parameters of the traditional PI method are not adjustable. This paper introduces a modified method that the parameters are determined by the scope of the stator flux error, which has a better time-varying performance and a smaller computational complexity [5].

## 2 Mathematical Model Based on PMSM

DTC system is composed of inverter, permanent magnet synchronous motor (PMSM), the estimation of flux model, torque model, and rotor position model, the switching table model, and so on. The torque signal is the output of the regulator that takes the error between the given and actual rotating speeds as inputs. The flux value and torque value can be calculated by the flux linkage model and torque model. In addition, the motor rotor position, the flux error, and torque error between the estimated signal and the actual signal also can be known. The purpose of regulating speed can be achieved by selecting the appropriate switching vectors of the inverter and adjusting the output torque.

The stator voltages  $\alpha - \beta$  are expressed as follows:

$$u_\alpha = R_s i_\alpha + \frac{d}{dt} \Psi_\alpha \quad (2.1)$$

$$u_\beta = R_s i_\beta + \frac{d}{dt} \Psi_\beta \quad (2.2)$$

$$\theta = \arctan \frac{\Psi_\alpha}{\Psi_\beta} \quad (2.3)$$

where  $u_\alpha$  and  $u_\beta$  represent the  $\alpha - \beta$  axis components of voltage, respectively;  $i_\alpha$  and  $i_\beta$  stand for the  $\alpha - \beta$  current components;  $\Psi_\alpha$  and  $\Psi_\beta$  are for the stator flux;  $\theta$

for flux angle; and  $R_s$  for the stator resistance. Torque equation is expressed as follows:

$$T_e = \frac{3}{2} n_p (\Psi_\alpha i_\beta - \Psi_\beta i_\alpha) \quad (2.4)$$

where  $n_p$  is the number of pole pairs.

### 3 Stator Flux Algorithm

In this system, the stator flux of AC motor is observed by the flux model. In static coordinate  $\alpha - \beta$ , the stator flux of PMSM are expressed as follows:

$$\begin{cases} \Psi_\alpha = \int e_\alpha dt = \int (u_\alpha - R_s i_\alpha) dt \\ \Psi_\beta = \int e_\beta dt = \int (u_\beta - R_s i_\beta) dt \\ \Psi_s = \sqrt{\Psi_\alpha^2 + \Psi_\beta^2} \end{cases} \quad (3.1)$$

where  $e_\alpha$  and  $e_\beta$  mean the components of counter-electromotive force on  $\alpha - \beta$  axis, respectively;  $\Psi_s$  is for the flux amplitude.

The accuracy of the flux observer will be affected by the variation of stator resistance when the motor is in low-speed running, and at that time, the pressure drop of the stator resistance and the power supply voltage will be at the same level which makes the running environment worse. At the same time, there are many factors that affect the resistance value, such as temperature and voltage. The value will vary with temperature seriously. However, the change of temperature is the main reason causing the flux linkage error.

Not only does the value change of stator resistance influence the accuracy of flux values, but also it leads to the torque variation [6]. When the motor speed is low, the errors of sector judgment and voltage space vector judgment will make the motor unstable.

In the process of analyzing the flux and torque equations, it can be noticed that the accuracy of flux observation can be affected by the variation of stator resistance. The influence caused by the stator resistance change is more serious especially if the power supply voltage drop on the stator resistance is at the same order when the motor is in low-speed running. In addition, there are many factors that affect the stator resistance, such as the change of the temperature and voltage frequency. After all, the temperature is the main reason, because the resistance value varies with temperature seriously during operation.

Assume that the changes of stator resistance and stator current are, respectively,  $\Delta R_s$ ,  $\Delta i_s$ , and then, the actual relationship between the flux and torque can be expressed as follows [7]:

$$\Psi_{\alpha} = \int (u_{\alpha} - (R_s + \Delta R_s)(i_{\alpha} + \Delta i_{\alpha})) dt \quad (3.2)$$

$$\Psi_{\beta} = \int (u_{\beta} - (R_s + \Delta R_s)(i_{\beta} + \Delta i_{\beta})) dt \quad (3.3)$$

$$\Psi_s = \int (u_s - (R_s + \Delta R_s)(i_s + \Delta i_s)) dt \quad (3.4)$$

$$T_e = \frac{3n_p}{2} [\Psi_{\alpha}(i_{\beta} + \Delta i_{\beta}) - \Psi_{\beta}(i_{\alpha} + \Delta i_{\alpha})] \quad (3.5)$$

Considering that the change of stator resistance cannot be detected directly, the equations with no change in stator resistance are expressed as follows:

$$\hat{\Psi}_{\alpha} = \int (u_{\alpha} - R_s(i_{\alpha} + \Delta i_{\alpha})) dt \quad (3.6)$$

$$\hat{\Psi}_{\beta} = \int (u_{\beta} - R_s(i_{\beta} + \Delta i_{\beta})) dt \quad (3.7)$$

$$\hat{\Psi}_s = \int (u_s - R_s(i_s + \Delta i_s)) dt \quad (3.8)$$

$$\hat{T}_e = \frac{3n_p}{2} [\hat{\Psi}_{\alpha}(i_{\beta} + \Delta i_{\beta}) - \hat{\Psi}_{\beta}(i_{\alpha} + \Delta i_{\alpha})] \quad (3.9)$$

The errors between the actual value and the observed value of the stator flux and electromagnetic torque are expressed as follows [8, 9]:

$$\Delta \Psi_{\alpha} = \Psi_{\alpha} - \hat{\Psi}_{\alpha} = \int -\Delta R_s(i_{\alpha} + \Delta i_{\alpha}) dt \quad (3.10)$$

$$\Delta \Psi_{\beta} = \Psi_{\beta} - \hat{\Psi}_{\beta} = \int -\Delta R_s(i_{\beta} + \Delta i_{\beta}) dt \quad (3.11)$$

$$\Delta \Psi_s = \Psi_s - \hat{\Psi}_s = \int -\Delta R_s(i_s + \Delta i_s) dt \quad (3.12)$$

$$\Delta T_e = T_e - \hat{T}_e = \frac{3n_p}{2} [\Delta \Psi_{\alpha}(i_{\beta} + \Delta i_{\beta}) - \Delta \Psi_{\beta}(i_{\alpha} + \Delta i_{\alpha})] \quad (3.13)$$

From (3.12) and (3.13), it is obvious that the change of stator resistance not only affects the accuracy of flux values, but also leads to the torque variation. When the motor is in low-speed running, the change of resistance will lead to the errors of



sector judgment and errors of voltage space vector judgment which causes the motor to run unstably [10]. Equation (3.14) can be calculated according to (3.12):

$$\frac{d\Psi_s}{dt} = (i_s + \Delta i_s)dR_s \tag{3.14}$$

$$\frac{d\Psi_s}{dt(i_s + \Delta i_s)} = dR_s \tag{3.15}$$

PI stator resistance compensator can be designed as follows (3.16):

$$dR_s = \left( k_p + \frac{k_i}{s} \right) d\Psi_s \tag{3.16}$$

where  $k_p, k_i$  stand for the proportional gain and integral of the PI compensator, respectively. The structure diagram is shown in Fig. 1.

When analyzing the PI controller parameters, the  $k_p$  can decrease the response time and reduce the static error. In addition, it will lead to excessive overshoot and system oscillation if the value is too big. The change of  $k_i$  mainly affects the static error, and it will prolong regulating time if the value is too big. Based on the above problems, an improved method to adjust the parameters  $k_p$  and  $k_i$  is proposed. The change trends of  $k_p$  and  $k_i$  are shown in Fig. 2, and the parameter change law can be summarized as follows:

- (1)  $k_p$  changes appropriately with the same trend of the input signal error.
- (2)  $k_i$  changes appropriately with the contrary trend of the input signal error.

**Fig. 1** Compensation of stator resistance

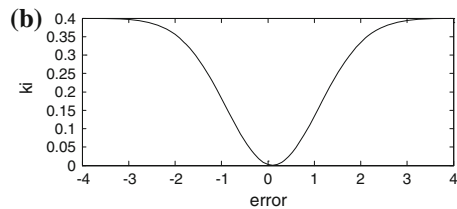
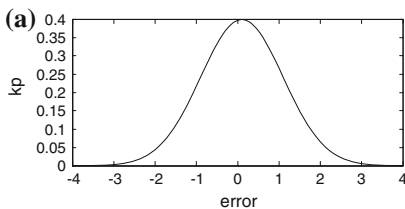
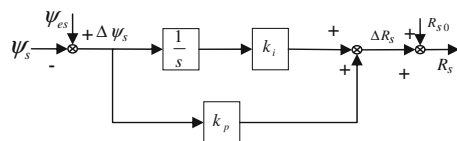


**Fig. 2** The rules of  $k_p$  and  $k_i$  with the different signal deviation

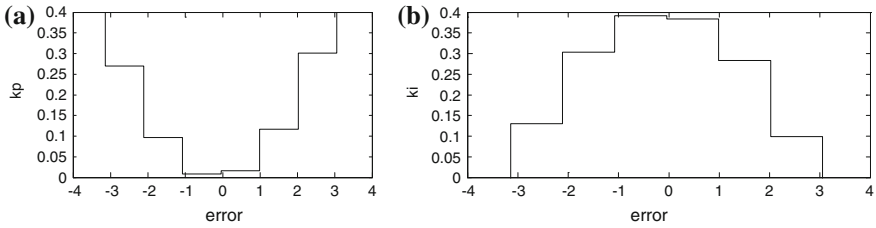


Fig. 3 The simplified rules of  $k_p$  and  $k_i$  with the different signal deviation

$$\begin{cases} k_p = k_1 \frac{1}{\sqrt{2\pi}\sigma_1} \left( 1 - \exp\left(-\frac{e^2}{2\sigma_1^2}\right) \right) \\ k_i = k_2 \frac{1}{\sqrt{2\pi}\sigma_1} \left( 1 - \exp\left(-\frac{e^2}{2\sigma_1^2}\right) \right) \end{cases} \quad (3.17)$$

In order to get the precise values of  $k_p, k_i$ , the normal function forms of the parameters are expressed as follows.

But the computation procedure based on normal distribution function is complexity and will affect the system response rate, and a simple change trend of  $k_p$  and  $k_i$  is shown in Fig. 3.

### 4 Simulation

This part mainly introduces the simulation based on MATLAB software, and an improved method of the flux observer with resistance compensation is proposed. The motor parameters set as follows:  $n_p = 4$ ;  $R_s = 2.875\Omega$ ;  $\Psi_s = 1\text{Wb}$  motor speed  $\omega_m = 80\text{rad/s}$ ; inductance on axis  $d L_d = 42.44\text{mH}$ ; inductance on axis

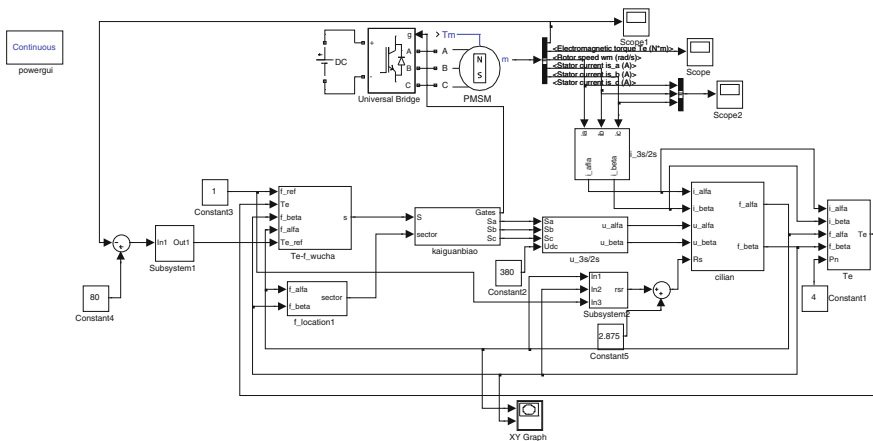


Fig. 4 The improved block diagram of the PMSM DTC

$q L_q = 79.57 \text{ mH}$ ; moment of inertia  $J = 0.003 \text{ kg} \cdot \text{m}^2$ ; dc voltage  $U_{dc} = 400 \text{ V}$ , and the Simulink diagram is shown in Fig. 4.

This paper intercepted a waveform when the value of resistance is divorced from the estimated value and keeps for a period of time, and the advantage of the improved method can be proved in Fig. 4.

Figures 5 and 6 show the traditional flux observer waveform of flux linkage and the improved flux observer waveform of flux linkage. It is obvious that the flux is closer to the estimated value in Fig. 6, and the waveform is smoother.

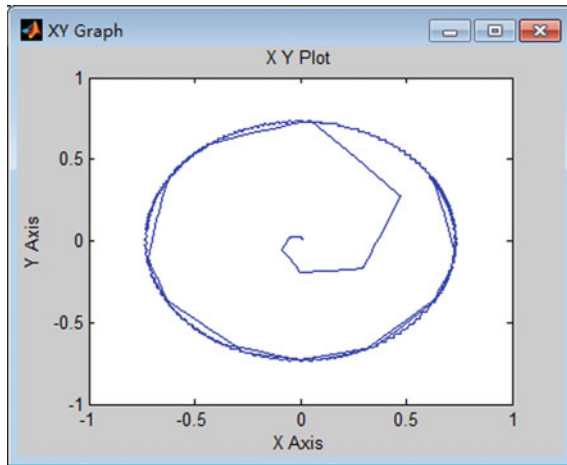


Fig. 5 The traditional flux observer waveform of flux linkage

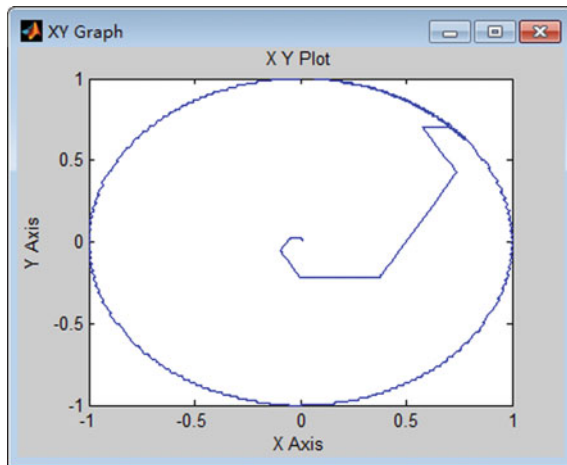


Fig. 6 The improved flux observer waveform of flux linkage

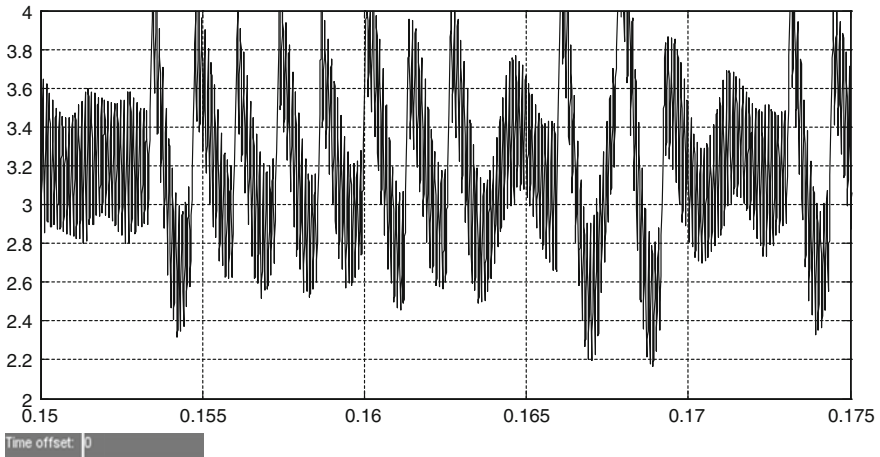


Fig. 7 The traditional flux observer waveform of torque

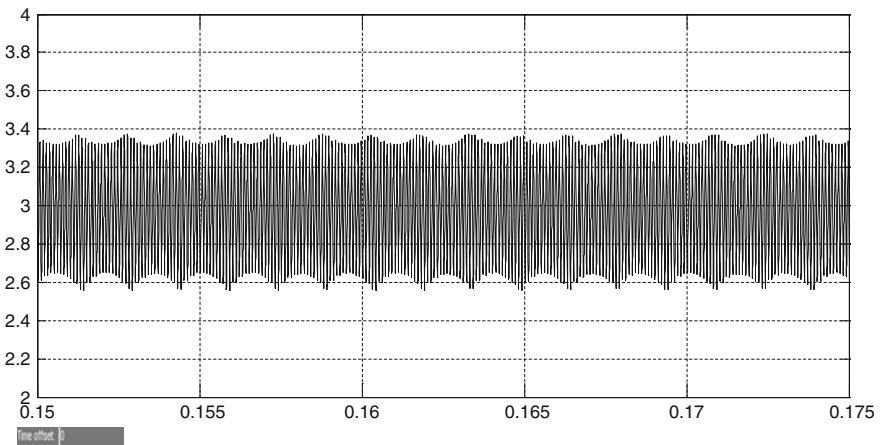


Fig. 8 The improved flux observer waveform of torque

Figures 7 and 8 show the traditional flux observer waveform of torque and the improved flux observer waveform of torque. It is obvious that with the feedback compensation, the torque ripple reduced, and the error of stator resistance is compensated.

The results prove that when compared with the original system, the improved system reduces torque ripple and performs more stable. Besides, the stator flux is closer to the value than before, and the torque and speed have better tracking characteristics. In addition, the error of stator flux between the actual value and the estimated in the improved system will be less than before. In general, the experiment verifies the feasibility and effectiveness of this method.

## 5 Conclusion

In this paper, a modified algorithm to deal with the problems of increasing torque ripple is proposed, and the stator resistance compensation algorithm based on variable parameter PI has improved the control accuracy. The simulation results prove that not only does the adaptive PI control method compensate the stator resistance, but also it gets a good speed–torque performance and achieves the desired control effect.

**Acknowledgements** This study was made possible through a project grant the Technology Foundation for Selected Overseas Chinese Scholar which is supported by Hebei Provincial Department of Human Resources and Social Security No. C201400114 and Hebei Natural Science Foundation under Grant No. F2014208148.

## References

1. Rahman MF, Zhong L, Hu WY, Lim KW, Rahman MA (1997) A direct torque controller for permanent magnet synchronous motor drives. *IEEE Trans Energy Convers* 14:637–642
2. Rahman MF, Zhong L, Lim KW (1998) A direct torque controller interior magnet synchronous motor drive incorporating field weakening. *IEEE Trans Ind Applicant* 34:1246–1253
3. Rahman MF, Haque ME, Tang L, Zhong L (2004) Problems associated with the direct torque control of an interior permanent-magnet synchronous motor drive and their remedies. *IEEE Trans Ind Electron* 51(4):799–809
4. Shyu K-K, Lin J-K, Pham V-T, Yang M-J, Wang T-W (2010) Global minimum torque ripple design for direct torque control of induction motor drives. *IEEE Trans Ind Electron* 57(9):3148–3156
5. Zhang Y, Zhu J (2011) Direct torque control of permanent magnet synchronous motor with reduced torque ripple and commutation frequency. *IEEE Trans Power Electron* 26(1):235–248
6. Haque ME, Rahman MF (2001) Influence of stator resistance variation on direct torque controlled interior permanent magnet synchronous motor drive performance and its compensation. In: School of electrical engineering and telecommunications the University of New South Wales Sydney NSW 2052, Australia
7. Shyu KK, Shang LJ, Chen HZ (2004) Flux compensated direct torque control of induction motor drives for low speed operation. *IEEE Trans Power Elect* 19(6):1608–1613
8. Haque ME, Rahman MF (2001) Influence of stator resistance variation on direct torque controlled interior permanent magnet synchronous motor drive performance and its compensation. In: IEEE industry applications conference on record of the, pp 2563–2569
9. Haque ME, Rahman MF (2000) A PI stator resistance compensator for a direct torque controlled interior permanent magnet synchronous motor drive. In: 3rd international power electronics and motion control conference, pp 175–179
10. Tang L, Rahman MF, Haque ME (2004) Low speed performance improvement of a direct torque controlled interior permanent magnet synchronous machine drive. In: Proceedings of 19th annual IEEE APEC, vol 1, pp 558–564

# Research on the Speed Synchronization Control Method of Double-HST Motor

Qian Ming Yang, Jian Li and Ling Qi Kong

**Abstract** Embedded spilled oil recovery machine is one of the important mechanical equipment of oil spill emergency response and the speed synchronization of sweep arm end (float) and oil boom reel is the key technology of that. The problem of that line-speed synchronization of float and oil boom reel of embedded spilled oil recovery machine has been studied and the joint synchronization control scheme which adopt PID and equal control been also put forward in order to realize the speed coordination control of dual motor driven by HST with the PLC as the core of controller in this paper. The scheme of hardware design for the speed synchronization control system has been given and the software of the key technologies also been design and ran. The system speed has been simulated and analysis by MATLAB simulation software and the evaluation methods of the linear velocity errors been also put forward. Study in this paper provides reference for the follow-up projects and similar technical design. The stages of research results provide a reference for design work of the follow-up and similar technologies.

**Keywords** Oil spill recovery · Proportional valve-controlled motor · PID · Equal control · Synchronization control

## 1 Introduction

Oil boom-mechanized retractable device is an important part of the embedded-type oil spill recovery system, which is mainly composed of sweep arm and oil boom reel components, for the realization of the oil boom-mechanized release and rolling operation. Sweep arm movement coordination simulation analysis and body mechanics analysis of HST driving scheme were given in the reference [1, 2]. With the sea to random loads, its operation condition, considering its low speed, high

---

Q.M. Yang (✉) · J. Li · L.Q. Kong  
Economic and Technical Development Zone, 579 Qianwangang Road,  
Qingdao 266510, Shandong Province, People's Republic of China  
e-mail: yqm8396@163.com

© Springer-Verlag Berlin Heidelberg 2016  
B. Huang and Y. Yao (eds.), *Proceedings of the 5th International Conference on Electrical Engineering and Automatic Control*, Lecture Notes in Electrical Engineering 367, DOI 10.1007/978-3-662-48768-6\_104

937

torque when working with motion and load characteristics, the line speed of oil boom release (rolling) and the end of sweep arm synchronization, is one of the key performance indexes of the dynamic quality of the work.

Electro-hydraulic valve-controlled motor drive is one of the most commonly used methods of low-speed and high-torque drive system, applied widely in industrial mechanical equipment. According to the actual requirement of control accuracy, commonly used control methods mainly include open-loop or closed-loop hydraulic synchronous control, closed-loop control is mainly to “equal control” and “the master-slave mode” [3, 4]. With the development of modern control theory and its successful application in industrial control, synchronous closed-loop control adopted adaptive control theory and intelligent control theory to design control strategies and the corresponding controller, such as PI and PID optimal regulator, adaptive model following controller (AMFC), a model reference adaptive controller (MRAC), neural network adaptive synchronization control algorithm, and the neural network learning algorithm of synchronization [5–9]. The starting point of control measures choosing mainly includes technical, cost-effective, and the convenience and reliability in the use of the process. In this paper, according to the technology requirements of the actual design, on the basis of comprehensive analysis, present a method of dual proportional valve-controlled motor speed controlling based on PLC and “equal control” and provide design reference for solving this kind of engineering design.

## 2 Composition and Control Requirements of System

### 2.1 The System Composition and Working Principle

The system composition of oil boom release and rolling device is shown in Fig. 1, which mainly composes of sweep arm body 6, oil boom reel 1, and their drive

Fig. 1 Booms release and rolling device

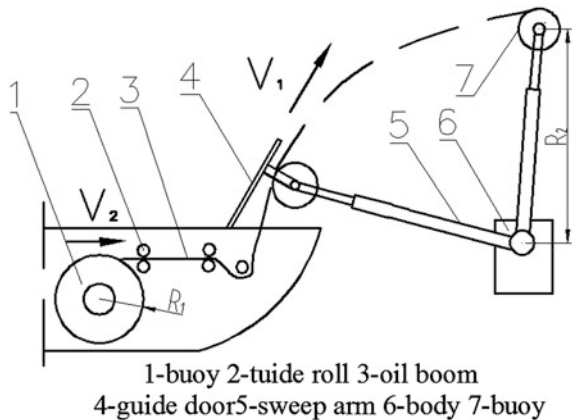


Fig. 2 Sweep arm body HST

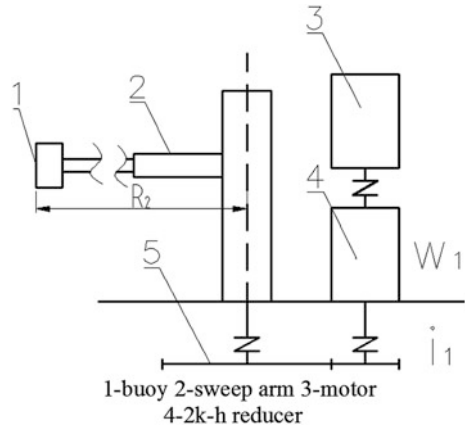
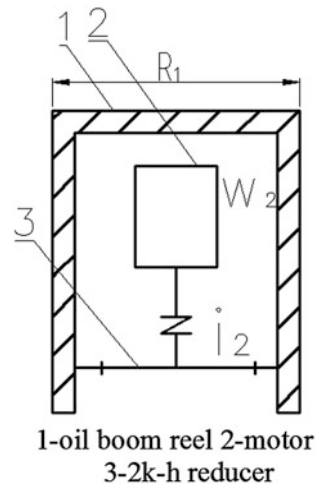


Fig. 3 Oil boom reel HST



system. Figures 2 and 3 show the composition of sweep arm body and oil boom reel drive system. One end of the oil boom is fixed on the oil boom buoy; the other end is wound on the oil boom reel. The both sides of oil boom are floating clamped by the guide roll of oil recovery machine to assist its release and rolling. Sweep arm body and the oil boom reel are driven by two HST electric hydraulic valve-controlled motors, to realize the rotary movement of them. In the stage of oil recovery preparation, the front manipulator of sweep arm grasps the oil boom buoy and the HST drive system drives the sweep arm and the oil boom reel to rotate in different angular velocity at the same time to release and draw the oil boom. After the oil recovering stage, two HST systems rotate in the opposite direction with different angular velocity to roll the oil boom.



## 2.2 The Requirements for System Control

Because of the different motion rotating geometric radius, deceleration ratio and driving load, the control of linear velocity of sweep arm rotary motion is hard to exactly synchronous with oil boom reel which were driven by HST, so make the rage of linear velocity synchronization error in  $\pm 15$  mm/s in the actual operating process. This paper adopts double-closed-loop equal control, combined with the existing synchronous control circuit, puts forward a new control strategy method to make it meet the requirements of speed control accuracy.

Figure 2 shows the sweeping arm body transmission system, and Fig. 3 shows the oil boom reel transmission system. Assuming the linear velocity of sweep arm front is  $V_1$  and that of oil boom reel outside is  $V_2$ , then:

$$V_1 = \omega_1 \cdot R_1 = 2\pi \cdot n_1 R_1 i_1 \quad (2.1)$$

$$V_2 = \omega_2 \cdot R_2 = 2\pi \cdot n_2 R_2 i_2 \quad (2.2)$$

where  $n_1$  = sweeping arm drive motor speed, r/s;  $R_1$  = sweeping arm length, m;  $i_1$  = sweeping arm reduction ratio;  $w_1$  = sweeping arm angular velocity, rad/s;  $n_2$  = oil boom reel motor speed, r/s;  $R_2$  = oil boom reel diameter, m;  $i_2$  = oil boom reel reduction ratio;  $w_2$  = oil boom reel angular velocity, rad/s.

Oil spill recovery equipment is affected by all kinds of random load from the sea when it is operating, let us assume, for the sake of analysis that:

1. Ignore the elastic expansion amount of oil boom when it is releasing or rolling.
2. The winding outside diameter of oil boom reel is constant; that is, ignore the oil boom negligible thickness.

Therefore, double-HST system control requirements can be summarized as follows:

1. When the system is coordinated operation, sweep arm end and oil boom reel outside need to keep the same linear velocity, that is  $V_1 = V_2$ .
2. After the oil boom released, the linear displacement of sweep arm end and oil boom reel outside should be the same that is equal to  $L$ , which is the release length of oil boom.
3. The speed of motion coordination can be adjusted when the system is running.

To make the linear velocity of the sweep arm end (buoy) and oil boom reel outside is the same as the target speed there should have:  $V_1 = V_2 = V$ .

By Eqs. (2.1) and (2.2), there should have:

$$\frac{R_2 i_2}{R_1 i_1} = \frac{n_1}{n_2} \quad (2.3)$$

$$n_1 = \frac{V}{2\pi \cdot R_1 i_1} \tag{2.4}$$

$$n_2 = \frac{V}{2\pi \cdot R_2 i_2} \tag{2.5}$$

Equation (2.3) is the speed ratio of the two motors when they are in coordination running, which is related with its rotating radius ( $R$ ) and reduction ratio ( $I$ ). Equations (2.4) and (2.5) are the numerical relationship between the target speed and the tow motors.

Thus, it can be seen that although the linear speed of the two executive elements is same, but the motor rotation speed is not same. So, accurately realize the speed control of the two motors is the premise and key to realize the linear velocity coordinated control of the two ends of the oil boom. In addition, in order to make the linear displacement of the two actors is same after the system running, the speed ratio should be coordinated and the start-stopping times of the two motors should be kept synchronization.

### 3 Methods to Realize the Synchronization of Double HST

#### 3.1 Synchronous Control by PID Associated with “Equal Control”

Speed “equal control” means that actuators independently, respectively, tracking the target output to achieve synchronous drive when more than one actuators need synchronization control have.

Figure 4 shows the principle diagram of the equal control with independent feedback.

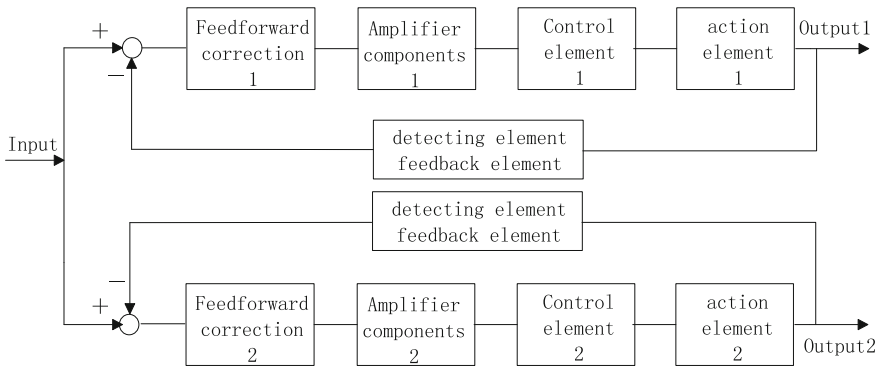
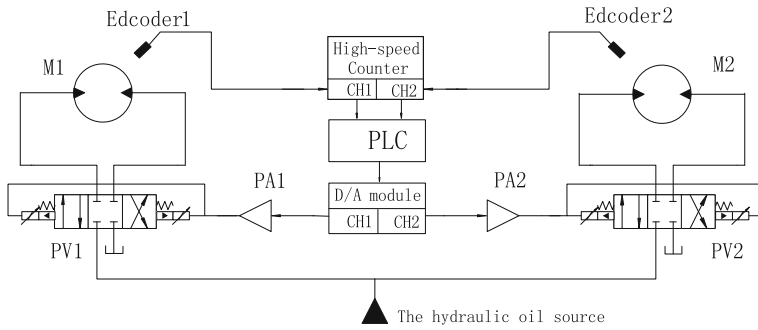


Fig. 4 Principle diagram of equal control with independent feedback



**Fig. 5** Principle diagram of closed-loop double-HST motor speed system

movement parameter with independent feedback; to guarantee the two outputs have good speed following characteristics, realizing synchronous control of velocity.

Figure 5 shows the principle diagram of closed-loop double-HST proportional valve-controlled motor speed system. The system consists of oil boom reel motor  $M_1$ , sweep arm body motor  $M_2$ , proportional directional valve  $PV_1$  and  $PV_2$ , proportional amplifier  $PA_1$  and  $PA_2$ , edcoder<sub>1</sub> and edcoder<sub>2</sub>, PLC and D/A module.

The control process of Fig. 5 is as follows: first, set speed control command signal to PLC; second, convert the two motor speed value to the corresponding digital quantity through Eqs. (2.4) and (2.5) and send them to the D/A modal; finally, D/A module converts digital signals into analog signal and transmit them to the proportional amplifier to adjust the opening volume of proportional valve so that can realize the control of motor speed and direction. The motor output speed can be feedback through the speed sensor]. PLC compares it with the set speed to form closed-loop control circuit until the motor speed meets the design accuracy.

To make the control system for better control effect, use the PLC built-in PID modal in practical control. So that can combine the PID and “equal control” to realize double closed-loop motor speed synchronous control. Figure 6 shows the principle diagram of the equal control system.

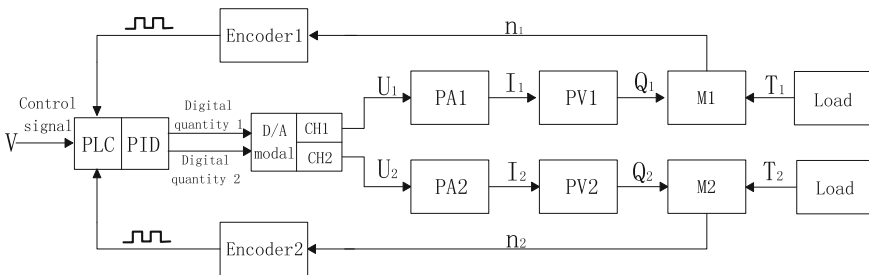


**Fig. 6** Principle diagram of equal control system

### 3.2 Hardware and Software Design of the Control System

Hydraulic control system consists of LEDUC-MSI 63CC quantitative hydraulic motor which bring speed sensor, Huade 4wra10, and 4wra6 proportional valve and its proportional amplifier, DVP-20EH00T3 PLC and D/A module of Delta.

High-speed counter and the joint application of PID control strategy is the core technology of PLC control program. The high-speed counter in Delta is not limited by the scan cycle, so that it can accept the highest 20 kHz frequency of high-speed pulse, and the measured number of pulses will be stored to register for the use of computing through the instructions program.

The PID control can be easily embedded through the built-in PID function of PLC, which format is PID S1 S2 S3 D. Among them, the S1 as target, S2 is current value, S3 as the starting address of the operation parameters, D for the output value. In this system, through the result of calculation from Eqs. (2.4) and (2.5) are set to the target motor speed of sweep arm and oil boom reel first. Second, the pulse number from high-speed counter is turned into the current speed through Eq. (3.1) and feedback to the PLC as the current value. Finally, the output of PID control will be sent to the D/A module through the instruction to be turned to analog which will control proportional amplifier.

$$n = \frac{60D}{Nt} (\text{rpm}) \quad (3.1)$$

where  $D$  = the number of pulses;  $t$  = acquisition cycle;  $N$  = the number of pulses encoder produced each lap.

#### 1. Speed detection

In double-HST proportional valve-controlled motor control system, the speed detection is accomplished by the hall speed sensor (speed gear and hall element) brought by motor itself through send the motor speed pulse signal (39 pure turn) to built-in high-speed counter HHSC0 of PLC. Figure 7 shows the PLC control program for sweep arm body motor speed detection.

Through setting, the parameters of high-speed counter HHSC0 complete the pulse count and calculate the motor current speed through Eq. (3.1). Then, store the result in D130 register.

#### 2. PID control

Figure 8 shows the PLC program of sweep arm body motor PID control.

Through setting, the parameters such as sampling time, proportional gain, integral gain, differential gain and target value, start the PID control and its operation result is stored in the D230 register. Among them, if the PID control parameter is reasonable directly determines the performance of the control system.

**Fig. 7** PLC control program for sweep arm body motor speed detection

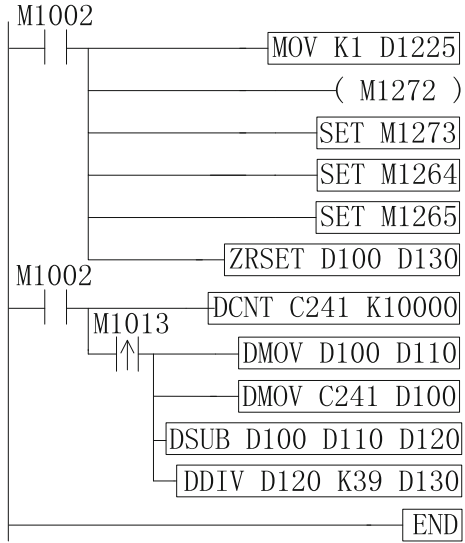
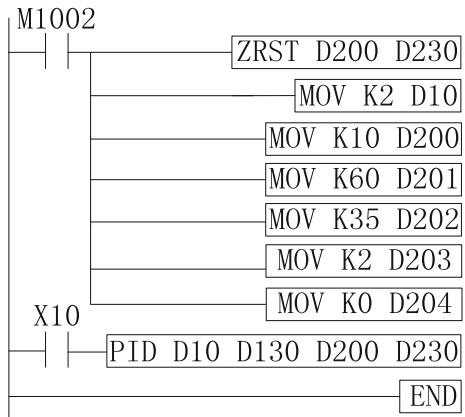


**Fig. 8** PLC program of sweep arm body motor PID control



### 3. Proportional control

Figure 9 shows the proportional-controlled valve control program of sweep arm body motor.

The PID calculation results are multiplied by the corresponding gain coefficient which is in register D230 and send the results to corresponding D/A module through the TO instruction. The D/A module output current signal controls the opening of the proportional-directional valve to realize accurately adjustable speed of the motor.

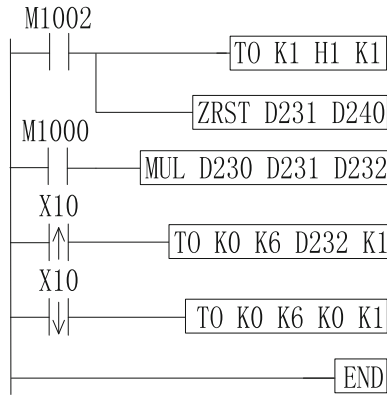


Fig. 9 Proportional-controlled valve control program

### 4 Synchronization Error Calculation

In practical control system, the current speeds of sweep arm and oil boom reel are calculated by PLC control program and the results are stored in the PLC register. The linear velocity of the two actuators is calculated by Eqs. (2.1) and (2.2). The linear velocity error between the two actuators and the linear velocity error between actuators and target speed are calculated by Eqs. (4.1), (4.2) and (4.3). In the man-machine interface, the results are displayed by the configuration software.

$$\Delta V = V_1 - V_2 \tag{4.1}$$

$$\delta_1 = V - V_1 \tag{4.2}$$

$$\delta_2 = V - V_2 \tag{4.3}$$

where  $\Delta V$  = the linear velocity error between the buoy and boom reel, m/s;  $\delta_1$  = the linear velocity error between buoy and the target speed, m/s; and  $\delta_2$  = the linear velocity error between the boom reel and the target speed.

Figure 10 shows the simulation curve of the system by using MATLAB simulation software.

Figure 10 shows that two motor speed stability after started about 6 s, the steady velocity error  $\Delta n$  less than 0.1 r/s and the linear velocity error between the two actuators  $\Delta V$  less than 7 mm/s. So, the PID and “equal control” system with PLC as the control core can well meet the design accuracy requirements of synchronous control system.

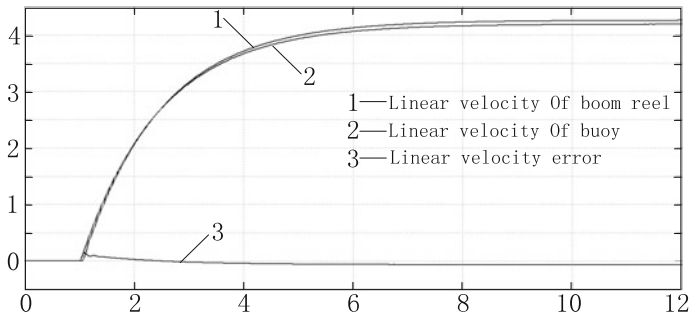


**Fig. 10** Simulation curve of the system

## 5 Conclusion

The problem of that line-speed synchronization of float and oil fence reel of embedded spilled oil recovery machine has been studied and the joint synchronization control scheme which adopt PID and equal control been also put forward in order to realize the speed coordination control of dual motor driven by HST with the PLC as the core of controller in this paper. On the basis of the selection of hardware design of control system, the key technology of PLC control program is given. To test the synchronous control accuracy of the control system, the system control error is calculated and analyzed. The results show that this scheme can realize synchronous linear velocity error  $\Delta V$  less than 7 mm/s which less than system design requirements. This paper solves the problem of two hydraulic motor speed synchronization control which have different motion radii and reduction ratios, this can provides a reference for the follow-up work of this project and similar technology.

## References

1. Yang QM et al (2014) Kinematic modeling for telescopic jib arm of oil spill recovery system based on D-H displacement matrix method. *J Shandong Univ Sci Technol (Nat Sci)* 01:92–97
2. Yang QM et al (2014) The design of HST driven technology and mechanical analysis for the sweep oil arm of the ship borne skimmer. *Mod Manufact Technol Equip* 02:1–3
3. Shi GL et al (1997) Hydraulic synchronous closed-loop control and its application. *Mach Tool Hydraulics* 04:3–7
4. Li JF et al (2012) The Research on control type and control strategy of synchronous hydraulic closed-loop control system. *IERI Proc* 3:220–225
5. Aly AA (2012) Model reference PID control of an electro-hydraulic drive. *Int J Intell Syst Appl (IJISA)* 4(11):24–32 (MECS)
6. Liu XF et al (2011) Speed synchronization control of dual-motor in large crawler crane based on fuzzy PID control. *J Jilin Univ (Eng Technol Ed)* 03:659–664

7. Zhu XB et al (2008) Research for method of adaptive model following control in electro hydraulic servo systems. *Hydraulics Pneumatics Seals* 04:57–60
8. Hu SS et al (2000) Model-following robust adaptive control based on neural networks. *Acta Autom Sinica* 05:623–629
9. Chen HZ (2012) Research of the electro-hydraulic servo system based on RBF fuzzy neural network controller. *J Softw* 7(9):1960–1967 (Academy)



# Design and Development of an In Situ Radioactivity Measuring System in the Marine Environment

Yingying Zhang, Bingwei Wu, Ying Zhang, Guoxing Ren,  
Dongyan Liu and Lu Cao

**Abstract** It is significant to develop the in situ radioactivity measuring system in the marine environment for the autonomous and continuous monitoring in the long term and even for the pollution early warning. The design of a set of a marine radioactivity measuring system was presented in the paper using the underwater spectrometer as the sensor. A data acquisition and control device was developed to collect and process the gamma ray spectra measured by the sensor, and also to be responsible for the monitoring system control and power supply. The bulk monitoring data were transferred to the server in the laboratory through the Beidou satellite. The gamma ray spectra measured and the analysis results of the radioactivity in the seawater were provided for the users. This research work and measured data have great importance to the more particular knowledge of the radioactivity in the marine environment and to the development of the marine radioactive monitoring and pollution early warning.

**Keywords** Marine radioactivity monitoring · Buoy system · Underwater spectrometer · Remote communication · Gamma ray spectra

## 1 Introduction

The marine radioactive pollution is a very serious problem caused by the explosions of Fukushima Daiichi Nuclear Power Plant. To understand the influence of the accident and continuous discharge of the radioactive wastewater on the Western

---

Y. Zhang (✉) · B. Wu · Y. Zhang · D. Liu · L. Cao  
Shandong Provincial Key Laboratory of Ocean Environment Monitoring Technology,  
Institute of Oceanographic Instrumentation, Shandong Academy of Sciences,  
No 37 Miaoling Road, 266001 Qingdao, China  
e-mail: triciayyz@163.com

G. Ren  
College of Information Science and Engineering, Ocean University of China,  
No 238 Songling Road, Qingdao 266100, China

© Springer-Verlag Berlin Heidelberg 2016  
B. Huang and Y. Yao (eds.), *Proceedings of the 5th International Conference on Electrical Engineering and Automatic Control*, Lecture Notes in Electrical Engineering 367, DOI 10.1007/978-3-662-48768-6\_105

Pacific, it is necessary to carry out a continuous radioactivity monitoring in the marine environment. Using the traditional laboratory method, a large amount of seawater samples must be collected in many designated positions and then taken back for the further processes and analysis. This kind of monitoring method is cumbersome and time-consuming. To measure the radioactivity in the marine environment in a timelier and effectively mode and even to provide the pollution warning, an autonomous buoy system was developed for the in situ, continuous, and long-term monitoring of radioactivity in the seawater.

According to the principle of modular design, the radioactive monitoring buoy system is made up of a marine radioactivity sensor, a data acquisition and control device, a power supply part, a set of remote communication equipment, and monitoring software except the buoy platform. To give some guidance for the further research and development of marine radioactive monitoring, the used sensor and some modules design in the radioactive monitoring buoy system were presented in this paper. The energy spectrum measured in the seawater was also provided.

## 2 System Structure

### 2.1 Marine Radioactivity

The radioactive monitoring buoy system used an underwater gamma spectrometer named KATERINA, made in Hellenic Centre for Marine Research, as the marine radioactivity sensor [1, 4]. It consists of a 3" × 3" NaI detection crystal, connected with a photomultiplier tube, a preamplifier, and power supply, together with the electronics for signal amplification, data acquisition, and storage (Fig. 1). The gamma rays in the seawater shine on the NaI(Tl) crystal and then emit fluorescence, which make the photoelectrons out in the photocathode of the photomultiplier tube. The voltage pulse signals are formed on the output load of the photomultiplier tube after the stepwise multiplication of the photoelectrons, whose amplitude is proportional to the energy of the gamma ray. Then, the gamma ray spectrum is acquired through amplification and pulse-amplitude analysis. All the technical specifications of the underwater gamma spectrometer KATERINA are given synoptically in Table 1.

The KATERINA sensor was calibrated in the laboratory (energy, energy resolution, and efficiency) from energy threshold ( $\sim 50$  keV) to 3000 keV. First, calibration was performed in laboratory with seven specific point sources of  $\gamma$ -radiation,

**Fig. 1** Function diagram of the underwater gamma spectrometer KATERINA

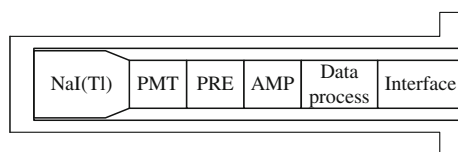


**Table 1** Technical specifications of the underwater gamma spectrometer KATERINA

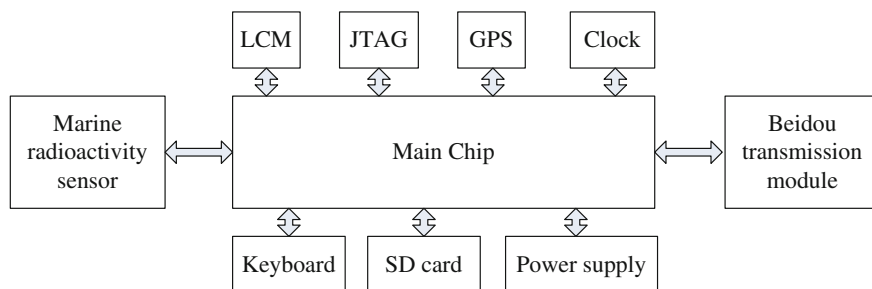
Energy range	Variable up to 4000 keV
Detection limit for $^{137}\text{Cs}$	0.02 Bq/L (24 h integration)
Resolution	6 % ( $^{137}\text{Cs}$ )
Spectroscopy	256, 512, 1024, 2048 channels
Operating temperature	-10 °C to +50 °C
Maximum depth	400 m
Power autonomy with currently sued battery packs (upgradable)	Up to 100 days (extended)
Energy and efficiency calibration	Yes
Computer autonomy	Yes
PC terminal connection	Yes
Attachable to buoys and sea platforms (independent of operating system)	Yes

which were placed in fixed geometry and the distance between source and detector. Then, the marine detector efficiency and absolute calibration was performed using a calibration tank filled with water.

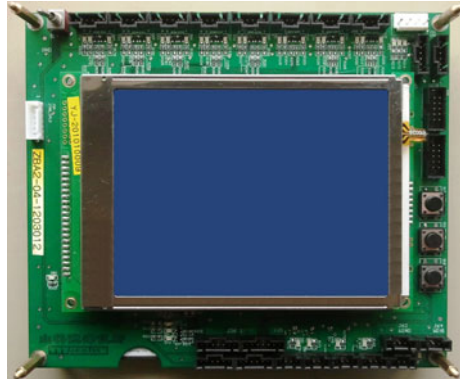
## 2.2 Data Acquisition and System Control

The data acquisition and system control is the key component of the marine radioactive monitoring buoy. Because GPS works in the continuous mode with the power always on, the data acquisition and system control used a kind of double-microprocessor design. One microprocessor, C8051F021, is responsible for receiving GPS signals. Another microprocessor using C8051F120, embedded operating system RTX51, is responsible for the sensor control, data process, data storage, data query, data transmission, and command response.

As shown in Fig. 2, it includes nine functional modules. The modules of receiving, storing, and transmitting are combined to collect, store, analyze, and

**Fig. 2** Function diagram of the data acquisition and system control

**Fig. 3** Main control circuit board developed for the buoy system



transmit the data from the sensor and at the same time to receive the command from the laboratory and to control the sensor. The GPS module is responsible for the GPS positioning. The clock module is designed for the clock calibration. The modules of LCM, JTAG, and keyboard are combined for the in situ data presentation, parameters setting, and system debugging. The power supply of the sensor, Beidou transmission module, and some others are all controlled by this part.

The high-integrated SOC mainboard was used in the master control system, which was made up of the power source, the clock circuit, CPU mainboard, the interface circuit, and the relay control circuit. The master control system developed for the marine radioactive monitoring buoy was shown in Fig. 3. A LCD touch screen supports in situ system debugging, device programming, signal test, and field service. A CF card adapter supports the online data storage in the large volume for the long-term and continuous monitoring task.

### 2.3 Remote Communication

Same as the underwater monitoring networks developed by some other countries [2, 3, 6], the gamma ray spectra measured need to be transmitted by the satellite. A pair of Beidou receivers is used to achieve data and command transmission in the marine radioactive monitoring buoy system. The bidirectional communication mode is designed to transmit the operation status and measured data from the buoy to the laboratory and to transmit the feedback and command from the laboratory to the buoy. The users can ask the data for the buoy and also modify the parameters of the buoy remotely. The data volume of the gamma ray spectrum in once measurement is large, but the data able to be transmitted by the Beidou receiver in one transmission process is limited. So the reasonable data transmission mechanism of the subpackage and response was designed to ensure no data missing. This is important for the system design and development.

The XDP200YX BD-I ordinary receiver was used and programmed for the marine radioactive monitoring buoy system. It can receive from three Beidou satellites at the same time. It has the characteristics of the small volume, low power consumption, and convenient installation.

## 2.4 Monitoring and Early Warning Software in the Laboratory

The monitoring and early warning software of the marine radioactive monitoring buoy system is developed in the Visual C++ programming environment based on the Window<sup>TM</sup> operating system. The software is designed to have several functions: the data receiving, storing, displaying, processing, analyzing and warning service, system control, and parameters setting in the remote operation mode. The gamma ray spectrum measured by the system is shown in Fig. 4.

Many researches on the automated analysis of gamma ray spectra have been made in the last years [5, 7]. It also was researched and developed for the buoy system. The nuclides are identified through a given database after the automated energy calibration. The photopeak determination and net area calculation is executed automatically based on the smoothed spectrum. Then, the quantitative results of the activities  $A$  ( $\text{Bq m}^{-3}$ ) can be derived by appropriate calculation.

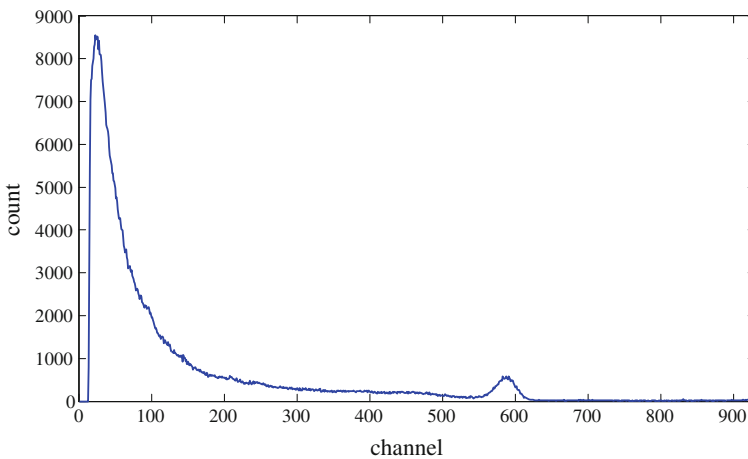


Fig. 4 The gamma ray spectrum measured by the system

$$A = \frac{\text{CPS}}{I_r \Delta t \varepsilon_m} \quad (1.1)$$

where CPS is the counts,  $I_r$  is the intensity of the gamma ray,  $\Delta t$  is the measuring period in second, and  $\varepsilon_m$  is the marine efficiency in  $\text{m}^3$  [8].

### 3 Conclusion

The radioactive monitoring buoy system developed is able to be used to measure the radionuclide inventory in the seawater continuously, to identify nuclides and compute their activities, and transmit data to the laboratory remotely. The data receiving and processing software provides the spectra curve measured in real time and also some radionuclide's activities. It has many modules of the historical data query, trend analysis, report generation, parameter, and alarm setting. This system developed and its data measured are very important for the researches on the radioactivity in the marine environment.

**Acknowledgments** We acknowledge the financial support from International Science & Technology Cooperation Program of China (No. 2013DFR90220), Key Research Program of Shandong Province (No.2015GSF115001), Science and Technology Plan of Shandong Province (No. 2014GGX103003). The discussion with Dr. Christos Tsabaris in Hellenic Centre for Marine Research is greatly appreciated. The authors are sincerely grateful for the comments and suggestions of the anonymous reviewers.

### References

1. Eleftheriou G, Tsabaris C, Androulakis EG et al (2013) Radioactivity measurements in the aquatic environment using in-situ and laboratory gamma-ray spectrometry. *Appl Radiat Isot* 82 (7):268–278
2. Osvath I, Povinec PP, Livingston HD et al (2005) Monitoring of radioactivity in NW Irish Sea water using a stationary underwater gamma-ray spectrometer with satellite data transmission. *J Radioanal Nucl Chem* 263(2):438–440
3. Tsabaris C (2008) Monitoring natural and artificial radioactivity enhancement in the Aegean Sea using floating measuring systems. *Appl Radiat Isot* 66(11):1599–1603
4. Tsabaris C, Bagatelas C, Dakladas T et al (2008) An autonomous in situ detection system for radioactivity measurements in the marine environment. *Appl Radiat Isot* 66(10):1419–1426
5. Tsabaris C, Prospathopoulos A (2011) Automated quantitative analysis of in-situ NaI measured spectra in the marine environment using a wavelet-based smoothing technique. *Appl Radiat Isot* 69(10):1546–1553
6. Wedekind C, Schilling G, Grutmuller M et al (1999) Gamma-radiation monitoring network at sea. *Appl Radiat Isot* 50(4):733–741
7. Zhang Q, Aliaga-Rossel R, Choi P (2006) Denoising of gamma-ray signals by interval-dependent thresholds of wavelet analysis. *Meas Sci Technol* 17(4):731–735
8. Zhang YY, Li CK, Liu DY et al (2015) Monte Carlo simulation of a NaI(Tl) detector for in situ radioactivity measurements in the marine environment. *Appl Radiat Isot* 82(7):44–48

# The Design of Shield Posture's Monitoring and Control System Based on Configuration Software

Yiping Shi and Yungen Wang

**Abstract** In municipal engineering construction, the shield construction method is usually adopted. How to effectively control shield posture in the shield construction directly relates to the construction quality. Based on the research of shield posture's monitoring and control system, this paper presents a design scheme of shield posture's monitoring and control system. It introduces the design of hardware structure: PLC monitoring and control network are based on field bus and the design and implementation of the monitoring computer and control software by using configuration software in detail. This research has been applied in the actual engineering project. It has important significance to improve the quality of shield construction and improve the level of the shield construction.

**Keywords** Shield posture · Monitoring and control system · Configuration software · PLC network

## 1 Introduction

With the continuous development of city, the urban construction is becoming more diverse and complex. In particular, the city traffic has been from plain surface traffic to vertical transportation. The tunnel has become an important approach of urban traffic. Shield construction method is usually adopted in tunnel excavation. How to effectively control shield posture in the shield construction directly relates to the quality of tunnel and construction success or failure. Thus, achieving high-level

---

Y. Shi (✉)

College of Electrical and Electronic Engineering, Shanghai University of Engineering Science, 333 Long Teng Rd., Shanghai 201620, China  
e-mail: syp@sues.edu.cn

Y. Wang (✉)

Saida (Shanghai) Transmission Engineering LTD,  
Room 1402 Number 6 Long 313, Ning Guo Rd., Shanghai 200090, China  
e-mail: wang2007@sh163.com

© Springer-Verlag Berlin Heidelberg 2016

B. Huang and Y. Yao (eds.), *Proceedings of the 5th International Conference on Electrical Engineering and Automatic Control*, Lecture Notes in Electrical Engineering 367, DOI 10.1007/978-3-662-48768-6\_106

955

real-time monitoring and control of shield posture is always a difficult engineering problem concerned by shield construction personnel. It is also a research topic in this field. This paper researches the shield posture's monitoring and control system. It mainly includes PLC monitoring and control network based on field bus and the monitoring and control software by using configuration software WinCC. This paper is divided into five parts: introduction; introduction to configuration software; monitoring and control system of shield posture; the design of shield posture monitoring and control software based on WinCC; and conclusion.

## 2 Introduction to Configuration Software [1]

Monitoring configuration software is evolved along with the development of the computer technology and industrial control technology, such as DCS and PLC. The monitor configuration software is growing stronger in the field of industrial control. It has been widely used in areas such as industry, agriculture, building, and office automation system.

Monitoring configuration software is a software platform tool of supervisory control and data acquisition. It is referred to as "SCADA." It is an integral part of industrial application software. Monitoring configuration software not only has the function of supervisory control and data acquisition, but also has the configuration, development, and opening features. It has rich setting function, the use of flexible and powerful. With the development of configuration software and control system, monitoring configuration software has separated from the hardware partly and provided the stage for the automation software development. The rapid development of OPC, Ethernet, and field bus have greatly simplified the interconnection between heterogeneous devices and reduced the development workload of I/O device driver software.

Real-time database is the core technology of SCADA system. It is essentially a data structure model of supporting real-time computing, a unified management, and supporting variable structure. It has supported for industry standards (such as OPC specification), distributed computing, and real-time database system redundancy and so on.

Now the configuration software running on Windows platform is a window structure similar to the resource browser. It has the following features:

- Configuring and editing all kinds of resources in industrial control system;
- Processing data alarm and alarm system;
- Providing a wide range of data driver;
- Generating and printing all kinds of report;
- Using a script language provides the function of secondary development;
- Storing the historical data and supporting the query of history data.



### 3 Monitoring and Control System of Shield Posture [2-4]

Real-time monitoring and control system of shield posture mainly include the automatic monitoring of the posture deviation and automatic control. The domestic monitoring system is usually used from foreign products. It includes SLS-T system from German VMT company, ZED system from Britain, and TMG-32 B(gyro-scope) system from Japan TOKIMEC. Many places still use artificial measurement. Most of the monitoring and control system used in domestic is selected from the complete sets of shield products abroad. The monitoring and control system consists of PLC programmable controller's control code and the upper control computer control program. It has close relationship between the specific control devices and the power equipment. Therefore, it has a certain technical and nonstandard content.

#### 3.1 Hardware Structure

The shield posture's monitoring and control system uses PLC monitoring network based on field bus [5, 6] (as shown in Fig. 1). The monitoring and control system is divided into two parts based on fluctuation. The upper part of the system is a remote computer connected to a monitoring computer through the network. It can remote monitor shield posture through the way of communicating with each other.

The lower part of the system includes monitoring computer and several sets of PLC to hang on the bus. One of them is as the main control PLC. In profibus-dp, network uses the master-slave structure. Host station has a DPM1 (master PLC) and DPM2 (monitoring computer). DPM1 host station mainly completes the control

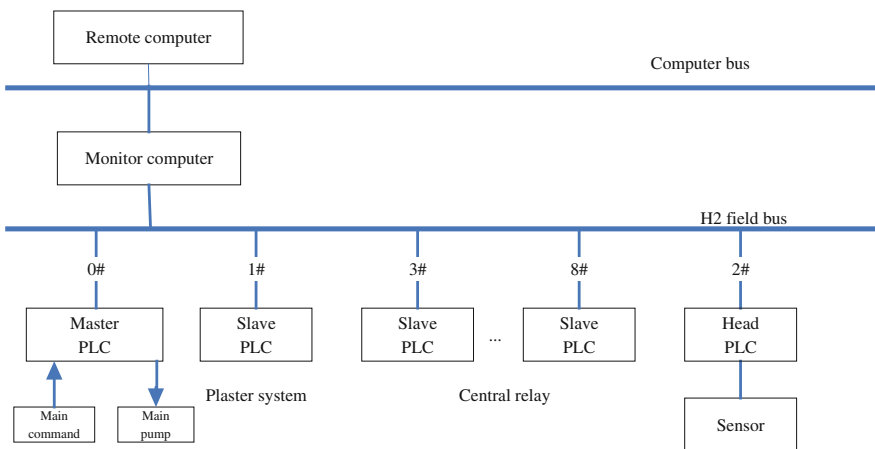


Fig. 1 System hardware structure

process. It exchanges data with DPM2 master station through the token. DPM2 realizes the remote control through communicating with remote computers in remote control. The entire network segment includes two master stations and eight slave stations. 1# slave station (mud system PLC) completes the control of water pump motor and electric valve. 2# slave station (head PLC) rectifies control of motor, valve, and correction. Sensor data include corrective quantity, head jacking force, incision, mud valve, and head tilt. 3#–8# slave stations (relay loop PLC) which hang on the bus control the relay pump connected to more than one PLC.

## **3.2 Software System**

### **3.2.1 PLC Control Software**

All PLC control logic programs are solidified in CPU units of the master PLC. PLC software is mainly responsible for logical and practical work such as position counting of shield construction, output performing conditional logic, action processing manual button, and alarm signal processing. It can use configuration tool. It can set communication rate of each site on the field bus, the site object number, and address mapping in the main control PLC in each site.

### **3.2.2 Monitoring and Control Software**

Monitoring and control software is based on real-time database. It provides the human–computer interaction interface. It is responsible for data acquisition, analysis, and automatic control posture. The software monitors the shield posture and the automatic control is done by monitoring computer. The overall module structure of software includes system parameter setting, measure data input, posture deviation calculation and automatic control, monitoring data automatic display, and result data statistics and analysis.

## **4 The Design of Shield Posture’s Monitoring and Control Software Based on WinCC [7, 8]**

WinCC developed by Siemens is a rising star in HMI/SCADA software and enters into the World Market of industrial control configuration software in 1996. That year it was called the best HMI software by Control Engineering magazine. In the shortest time, it has developed into the third worldwide success of SCADA system. In Europe, it became the first undisputed.

WinCC was designed according to the system used worldwide. So from the beginning it is suitable for the control system produced by the world's major manufacturers. The types of communication driver are also in constant increase. Through the way of OPC, WinCC can also communicate with the third-party controller. As an important part of Siemens-integrated automation system, WinCC ensures the convenient connection and efficient communication with SIMATIC S5, S7, 505 series PLC. WinCC combines with the STEP7 programming software closely and shortens the development cycle. In addition, WinCC takes system diagnosis to SIMATIC PLC and gives hardware maintenance conveniently.

This design mainly uses WinCC configuration software programming to realize the real-time monitoring and control of the shield posture. It was used in Windows XP or Windows 2000 operating system platforms.

In the shield posture's monitoring and control software system, it first enters the system of the splash screen. This system is mainly divided into five modules: the setting parameters, monitoring posture, deviation display, control posture, and data statistics. Screen has five buttons. In the screen of setting parameters, it can set some of the basic parameters and the original path coordinates of shield. The parameter includes the shield tunnel segment assembling restriction, history posture characteristics, environmental parameters, and push the total force and date.

Monitoring and controlling posture images are relatively important in the system. It includes the monitoring data show, the calculation of deviation and display and the part of the attitude control. Images of the upper four buttons, it is respectively for the suspension system, system operation, automatic adjustment and manual correction.

Click on the "System pause" button, the program will send out a stop signal to control the work of shield. Then, the shield is in the standby state. Monitoring system still monitors the position of shield machine, just in front of the monitoring data for standby state. "System running" button is the first time into the system to be effective with suspension system condition. The system will send out a signal operation to make the shield begin or continue to push forward. When the deviation data are more, the system will set automatic suspended signal. The system is in standby state. Then, the staff chooses whether to let the system to automatically rectify or to set up manually. If you select manual correction, the system will be transferred to another picture.

In the right foot of images, there are two buttons. They are "show incision coordinates" and "show the shield tail coordinates." By selecting different coordinates, it can show or hide the coordinate data. At the same time, it can display real-time coordinates and time.

When in monitoring control picture, click the "manual correction" button to enter the control picture. It will display the deviation of the data more detailed in the control screen. It has a graphic image to set the correct deviation in order to endure the position of shield machine enables shield to the right ahead.

To be sure, if the system enters the manual correction, shield will not do anything to push forward. That is, the shield is in the standby state. When the deviation

is set up, the system will return to monitor screen and click operation button. The shield system is in working condition.

Images are divided into three parts. They are deviation value, correction value, and image area. Deviation value is the deviation display in which the monitoring data are calculated. When the deviation value reaches a certain value, it will display a different color. Normal area is black. The micro-partial area is gray and partial area is white. Strong partial area is yellow and alarm area is red. Correction value is set by the staff. It used to change the angle of the shield and shield-driving power so as to shield can return to the original lines. The image area is the role of image display in the main deviation. The image on the left shows the horizontal and vertical deviations of incision and shield tail center. White dot represents the center of incision. Black dot represents the center of shield tail. The vertical axis is perpendicular to the axis and the horizontal axis is the horizontal axis. The origin is as the reference point. Namely, three points are in one point without deviation.

The function of statistical analysis is corresponding in the splash screen “statistics” button. In the WinCC configuration software, the monitoring data can be automatically archived. So there need not to separate when the design process. So, as long as you return to the splash screen click “statistics” button, you can print of the filed data. It includes incision center, shield tail center coordinates, incision horizontal, incision vertical, shield tail levels, shield tail vertical, incision mileage, horizontal deviation angle, and vertical deviation angle.

## 5 Conclusion

In municipal engineering construction, shield posture’s monitoring and control system is widely used in shield construction. This paper researches the shield position monitoring and control system and designs PLC monitoring and control network based on field bus and monitoring and control software using configuration software WinCC. This research has been applied in the actual engineering project. It has important significance to improve the quality of shield construction and improve the level of the shield construction.

## References

1. Meng Q (2012) The Design and development of monitoring configuration software. China Electric Power Press, Beijing
2. Shen B (2005) Shield posture real-time monitoring principle and method. Shanghai Trenchless Technol (2)
3. Qi H (2003) The introduction of measurement method of shield posture and segment position. J Shanghai Tunn (3)
4. Shi Y et al (2010) The Design and implementation of the measurement and control system of shields posture. ICIECS 2010

5. Yang X (1999) The fieldbus technology and its application. Tsinghua University Press, Beijing
6. Shi Y et al (2005) The design of shield control system based on fieldbus. J Comput Appl Softw 22(3)
7. Liu H (2009) WINCC configuration software and its application. Mechanical Industry Press, Beijing
8. Siemens (2004) Introduction of siemens WinCC V6. University of Aeronautics and Astronautics Press, Beijing

# Application Research of SuperCapacitance on Fuel Consumption Wheel Crane

Chao Li, Lu Niu and Aihong Tang

**Abstract** Through a series of experiments among the super capacitor, the battery and the traditional electric capacity, the preponderances of super capacitor in specific power density, specific energy and service life have carried out. The result states that the use of super capacitance as energy storage component can make great contributions to energy saving and environment protection and it has a bright future in application of hybrid system on fuel consumption wheel crane.

**Keywords** Supercapacitance · Hybrid system · Wheel crane · Environment

## 1 Introduction

The rapidly developing hybrid power technology is being generalized and applied in more and more fields in recent years. The main advantage of hybrid power system lies in the fact that it can render the engine an optimum working condition to effectively reduce the exhaust emission and oil consumption [1].

Meanwhile, it can regenerate braking energy to convert mechanical energy into electric energy and reserve it to be used again to drive the working mechanism and further reduce fuel consumption.

In this study of hybrid power technology, we successfully conducted the hybrid power system transformation for a wheel crane (25T) with an engine of 120 kW, taking the supercapacitor as the energy storage device. The transformed system has a remarkable energy saving effect. The test result shows that it saves over 30 % fuel amount under the same working condition and reduces over 25 % environmentally harmful exhaust emission.

---

C. Li (✉) · A. Tang  
School of Automation, Wuhan University of Technology, Wuhan, China  
e-mail: curiolichao@gmail.com

L. Niu  
School of Art and Design, Wuhan University of Technology, Wuhan, China  
e-mail: niulu\_520@aliyun.com

## 2 Working Condition and the Way of Energy Transformation of Traditional Wheel Cranes

As the most common loading and unloading machine in harbour docks and various construction sites, wheel crane can work for long distance running with great motility. It can lift, bring down, start, and brake the loads in a frequently periodic interval working mode. As the working place varies, its power system setting is commonly the combination of engine and generator. The fuel in wheel crane engine is transformed into mechanical energy after burning and then converted into electric energy by the generator. The electric energy can drive the motors in various parts to complete corresponding mechanical operations.

### 2.1 Heavy Load Lifting Stage

In the process of lifting heavy loads, the crane’s system absorbs electric energy from the generator set, overcoming the system’s frictional force and the gravity to doing work on the loads. Part of the electric energy absorbed is converted into thermal energy and the remaining into load potential energy (Fig. 1).

$E_\varepsilon$  is the total energy that the generator set absorbs;  $E_C$  is the energy consumed by the chopper;  $E_M$  is the energy the motor consumes;  $E_J$  is the energy the machine driven system consumes; and  $E_L$  is the work that the system has applied to the loads.

After the lifting is completed, the remaining energy in the system will be reserved as load potential energy. Apart from the part, the system consumes, and according to the efficiency analysis of every part, the energy value of this part is counted within the range of  $0.59 E_\varepsilon$  to  $0.86 E_\varepsilon$ .

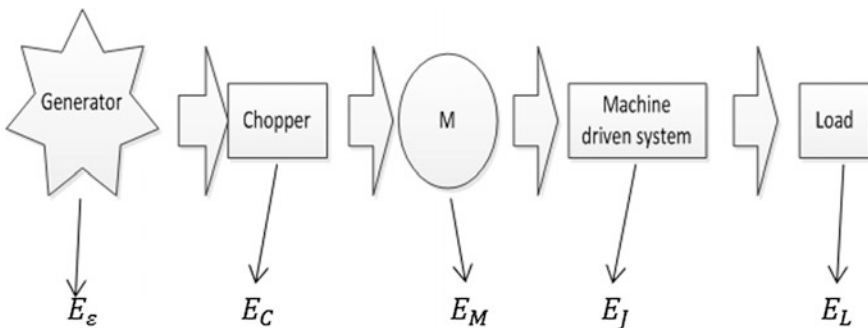


Fig. 1 The flowchart of the energy during heavy load lifting stage

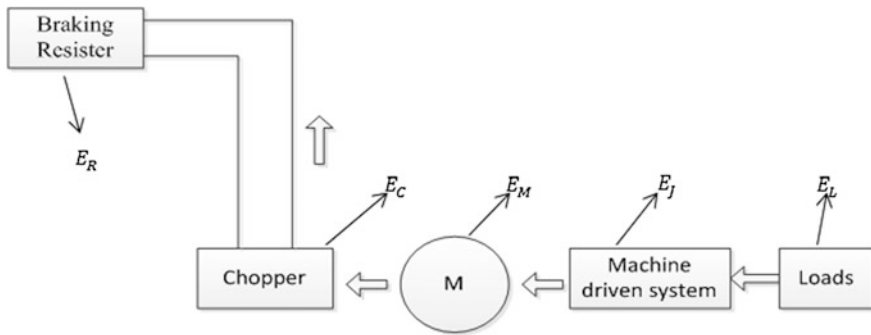


Fig. 2 The flowchart of the energy during lowering stage

## 2.2 Lowering Stage

In the lowering stage, the motor is in the condition of power generation. The potential energy loaded is converted into direct current through the motor and the frequency transformer, which is then consumed by the braking resister. The flowchart of the energy is shown in Fig. 2.

$E_R$  is the energy that is consumed by the braking resister, and the other attributes are the same with the above. The estimation of the  $E_R$  value is within 37 % $E_c$ –63 % $E_c$ , which is a considerable amount of energy.

## 3 The Hybrid System

### 3.1 The Transformation Method of Energy Saving

From the perspective of the working characteristics and energy consumption conditions during work of the traditional wheel crane, a great deal of energy is wasted by the generator motor in the lifting and lowering processes [2]. Therefore, we can conduct energy saving transformation to the traditional wheel crane from the following aspects:

1. Set up energy saving devices to recycle regenerated potential energy

When the loads are being brought down, the wheel crane’s motor transforms the potential energy of the loads into electric energy. As there is no energy saving device on traditional wheel crane, this part of electric energy is wasted on the braking resister and converted into thermal energy. The conclusion drawn from the previous section is that the energy consumed on the braking resister takes up 37–63 % of the total energy consumption of the lifting mechanism. This not only wastes energy but increases the thermal pollution of the entire machine. Thus,



through setting up appropriate energy saving system during the lowering process, this part of regenerated energy can be absorbed and reserved. With the optimization control strategy, recycling the regenerated braking energy of the system can be maximally achieved.

## 2. Improve the efficiency of the generator set

In order to realize various dynamic performance requirements, usually large generator set is selected for traditional wheel crane. But in most cases, the engine works under light load, thus lowering the economical and emission efficiency. However, the intervention of the energy saving system equipped with energy saving devices can act to adjust the loading of the engine in the effect of cutting the peak and filling the valley. This enables the engine to work within a relatively high-efficiency range, thus greatly improving the average efficiency of the engine.

## 3. Reduce the emission capacity of the engine

As the dynamic system of the crane must be equipped with a high-capacity and superpower engine, the total capacity of the entire crane has been made heavier. Once started, the throttle of the diesel engine must be accelerated to increase the diesel provision amount, which leads to incomplete burning of the fuel, black smoke emission, and fuel consumption increase that give rise to environment pollution.

But it is not necessary for the engine to provide maximal power in the operation of the wheel crane. If the wheel crane is equipped with energy saving devices, the energy saver will provide power assistance to the system, which will not affect the dynamic performance of the crane in reducing the displacement of the engine. The reduction of the motor's power can reduce power loss and improve engine's rate of work; at the same time, smaller displacement engine has relatively less friction and thermal loss, which correspondingly reduce the oil consumption.

## ***3.2 Working Principles of Hybrid Power System***

In this hybrid power system, the driving force exported from the generator is transformed into electric power entirely by the generator. Part of the electric energy drives the working motor through the electric motor. The superfluous electric energy is saved in the energy saver. When the electric energy provided by the generator cannot meet the system's needs, the electric energy saved in the energy saver will be released, together with the generator set to drive the working motor. Besides, during the process of heavy load lowering or braking operation, the working motor will be pushed forward to generate electric energy and the electric energy will be reserved in the energy saver.

Energy controller is a device that can transform direct current power supply into a DC power supply of different voltages or currents. The filter capacitor is used to

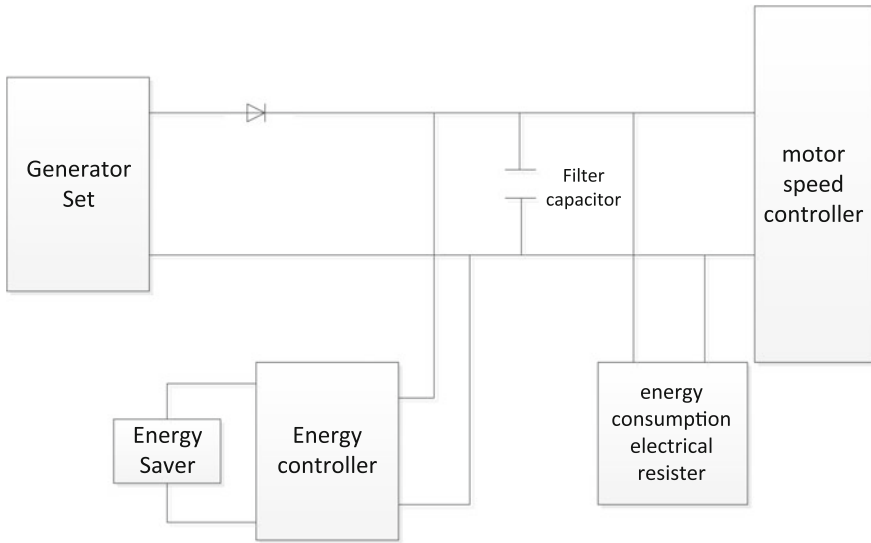


**Fig. 3** The principle diagram of the hybrid system

stabilize the DC busbar voltage. The energy consumption electrical resister, as the energy saver, absorbs the redundant elements of the recovered energy. When the energy saver fails to work, the energy consumption electrical resister still works to ensure the reliability of the system when the motor is under regenerative braking (Fig. 3).

## 4 SuperCapacitance

### 4.1 Working Principle

Supercapacitance’s charge and discharge process is a physical change, which is different from the chemical changes of storage battery and will not pollute the environment, and in theory, it has extremely long life, up to hundreds of thousands of times.

When the applied voltage is applied on the capacitor, two electric layer formed on the surface of two electrodes, i.e. the capacitor. This polarization effect can be used to store electrical energy, and this is because it is related to the electrical energy stored in the capacitor’s capacitance and the applied voltage:

$$C = \frac{\epsilon A}{d} \tag{4.1}$$

$$E = \frac{CV^2}{2} \tag{4.2}$$

In the formulas,  $\epsilon$  is the effective electrolyte constant;  $d$  is the spacing distance of the electrode surface and adsorbed ions;  $A$  is the electrode surface area;  $C$  is the capacitance;  $V$  is the applied voltage; and  $E$  is the electric energy stored.

### 4.2 The Difference Between SuperCapacitance and Batteries and Traditional Capacitor

Batteries, supercapacitors, and capacitor can store electrical energy, but their principles of store electrical energy are different. As shown in Table 1, supercapacitance is between the batteries and traditional capacitors in the two performance parameters: specific energy and specific power; the cycle life and charge and discharge efficiency are much higher than the battery, and its service life is usually more than the life of the device; therefore, the supercapacitance requires no maintenance in life, in addition to easing environmental requirements and pollution free, which is also called green energy. Supercapacitance to adapt to the high current charge and discharge generally can be done in 10–30 min charged and discharged. Another advantage of the supercapacitor is a wide operating temperature range and can work in  $-40\text{ }^\circ\text{C}$ ; this point is that a battery cannot match.

These characteristics of the supercapacitance determine its broad application prospects. The main purpose is focused on two aspects: first, as the temporary standby power of electrical equipment, it has been achieved in hybrid electric vehicles and shows the energy saving and environmental protection role; second, in the application of the hybrid field bridge and shore bridge [3], the main role is the supply of peak and pulse power. As a secondary energy, it is able to meet a short period of high-power input/output, in which the lifting power requirements of rising and falling, at the same time, spreader action process is an iterative process, and each cycle has a certain potential feedback, and thus, the supercapacitor forms a periodic charged and discharged process; therefore, the application of supercapacitance technology will be more meaningful in port machinery than in the automotive industry.

**Table 1** Comparison of the three kinds of energy storage components

Properties	Lead acid battery	Super	Ordinary
Charging time/h	1–5	0.3–30	$10^{-3}$ – $10^{-6}$
Discharge time/h	0.3–3	0.3–30	$10^{-3}$ – $10^{-6}$
Specific energy/(Wh · kg <sup>-1</sup> )	10–100	1–10	<0.1
Charge and discharge efficiency	0.5–0.85	0.85–0.98	>0.95

## 5 Result Analysis

The application experiments of supercapacitance on RTG have achieved gratifying results.

When falling, the supercapacitance can play the role of the “reservoir” when it is incorporated into the electrical system. It can be charged by the potential energy produced by the falling of the load (discharged when the load rises). So it can be energy saving. According to statistics, the hybrid power systems save about 50 % energy than the traditional power system, which can transform the RTG into a energy saving type.

Both the energy consumption of the engine and the fuel consumption has been greatly reduced. Furthermore, the black smoke, which used to be discharged from exhaust pipe at the moment when the RTG lifts up cargo, now is gone. And so is the noise to be reduced. Then, the “green RTG” (environment-friendly RTG) is achieved.

RTG cannot transform energy back to the grid. Since the super capacitance can quickly release a large current, it can ease the impact to the diesel engine and the disturbance on the grid when incorporated into the electrical system.

## 6 Conclusion and Prospect

In theory, there is potential energy feedback in RTG’s every working cycle (the falling of lifting mechanism), and from this point of view, the energy saving effect of supercapacitance technology application on RTG is much more obvious than that on automobile.

The application research of supercapacitance technology in port machinery industry is now hot spot, because the supercapacitance can be applied to not only the fixed port machinery, but also the mobile machinery, which will reduce the impact to the internal combustion engine and the disturbance to the entire grid when the machine brakes under heavy load. The technology also has a large application value in other construction machinery.

## References

1. Guan T (2003) The technical progress of the container handling machinery in 21st century. *Hoisting Conveying Mach* 4:7–9
2. Xiong Q, Tang D (2003) Research progress on super capacitor in hybrid electric vehicle. *Acta Scientiarum Naturalium Universitatis Sunyatseni* (s1):130–133
3. Dunjian Fu (2003) Development and application of advanced tech on the container handling machinery. *China Ports* 4(10):14–15

# Research on Elastic Characteristic of Interconnected Oil Gas Suspension

Y.J. Chen, L. Wang, Y.F. Zhang, G.H. Zheng and X. Zhang

**Abstract** Regarding as rollover problem for multi-axis heavy vehicles when no transverse stability rod attached, lateral stiffness calculation and experiment were researched. Gas pressure, vertical stiffness formula, and lateral stiffness formula were deduced through real gas state equation. By program analysis, it was concluded that the vertical stiffness of interconnected structure was equivalent to that of independent suspension, but the lateral stiffness was multiplied when turning. Through real vehicle test, vehicle body lateral angles of two suspension forms were compared. It was verified that vehicle handling and stability performances are improved when suspension system is interconnected.

**Keywords** Oil gas suspension · Interconnection · Lateral stiffness · Handling and stability · Real gas state equation

## 1 Introduction

Parameters of a suspension system play important roles in vehicle handling stability and safety. Multi-axle heavy-duty vehicles usually use interconnected oil gas suspension to enhance lateral stiffness when there is not a transverse stability rod. At

---

Y.J. Chen (✉) · L. Wang · Y.F. Zhang · G.H. Zheng · X. Zhang  
China North Vehicle Research Institute, Beijing, China  
e-mail: chenyjie1206@163.com

L. Wang  
e-mail: wanglu@163.com

Y.F. Zhang  
e-mail: zhangyafeng@163.com

G.H. Zheng  
e-mail: zhengguanhui@163.com

X. Zhang  
e-mail: zhangxu@163.com

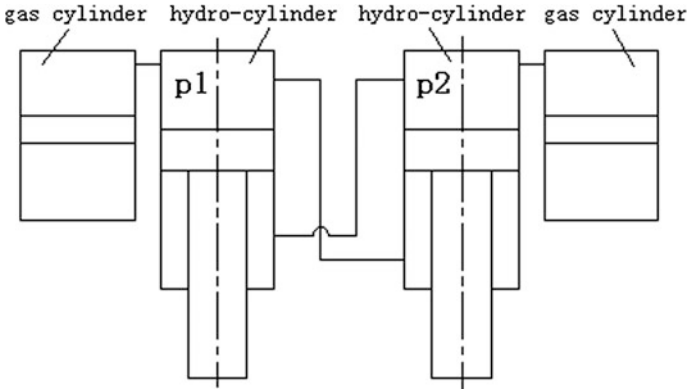


**Fig. 1** Structure of interconnected suspension

the same time, it can meet technical requirements of vehicle handling and stability and has become the development direction of intelligent suspension system [1, 2].

## 2 Structure of Interconnected Suspension

The structure of interconnected oil gas suspension is shown in Fig. 1. It is not difficult to see that a main oil cavity and an annular oil cavity can be used as anti-pressure cavity of the other side oil gas spring, so as to effectively alleviate the lateral angle of a vehicle body when the vehicle turns.

## 3 Characteristic Calculation

### 3.1 Force of Oil Gas Spring

Force of a left oil gas spring is as follows:

$$F_{s1} = p_1A_c - p_2A_h \tag{1}$$

Force of a right oil gas spring is as follows:

$$F_{s2} = p_2A_c - p_1A_h \tag{2}$$

in which  $p_1$  is the pressure of a left cylinder,  $p_2$  is the pressure of a right cylinder, the piston area is  $A_c = \frac{\pi}{4}D_c^2$ , the annular cavity area is  $A_h = \frac{\pi}{4}(D_c^2 - D_g^2)$ , the piston diameter is  $D_c$ , and the piston rod diameter is  $D_g$ .

Real gas state equation is [3, 4] as follows:

$$p = \frac{RgTm_q}{V_q - m_q b} - \frac{am_q^2}{V_q^2} \tag{3}$$

in which,  $T$  is thermodynamic temperature, and nitrogen gas constants are as follows:

$$a = 456.37 \text{ m}^6 \text{ Pa/kg}^2, \quad b = 0.00361 \text{ m}^3/\text{kg}, \quad Rg = 296.77 \text{ J/(kg K)}$$

Gas quality expression is as follows:

$$m_q = V_q \left[ \frac{0.17}{ab} D - 0.67 \frac{(3b \cdot Rg \cdot T_0 + 3p_{1j} b^2 - a)/b}{D} + 0.33/b \right]$$

$$D = \left( \left( C + 20.78((M + N)/a)^{0.5} b \right) a^2 \right)^{1/3}$$

$$C = -36b \cdot Rg \cdot T_0 + 72p_{1j} b^2 - 8a$$

$$M = Rg^2 \cdot T_0^2 (4b \cdot Rg \cdot T_0 + 12p_{1j} b^2 - a)$$

$$N = 4p_{1j} (3p_{1j} b^3 \cdot Rg \cdot T_0 - 5abRg \cdot T_0 + b^4 p_{1j}^2 + 2ab^2 p_{1j} + a^2)$$

### 3.2 Vertical Stiffness of Oil Gas Suspension

If both sidewheels have same excitation, displacements of them are as follows:

$$s_1 = s_2 = s \tag{4}$$

in which,  $s_1$  and  $s_2$  are, respectively, piston displacement of left and right oil gas spring.

Accumulator displacement is as follows:

$$(A_c - A_h)s = A_x s_x \Rightarrow s_x = \frac{(A_c - A_h)s}{A_x} \tag{5}$$

$A_x$  is the work area of the accumulator.

Gas chamber volume is as follows:

$$V_q = A_x L_g = A_x \left( L_{gi} - \frac{(A_c - A_h)s}{A_x} \right) \tag{6}$$

in which,  $L_{gi}$  is the gas chamber height of a static equilibrium position.

Pressure of oil gas spring is as follows:

$$p = \frac{RgTm_q}{A_x \left( L_{gj} - \frac{(A_c - A_h)s}{A_x} \right) - m_q b} - \frac{am_q^2}{\left[ A_x \left( L_{gj} - \frac{(A_c - A_h)s}{A_x} \right) \right]^2} \tag{7}$$

Vertical stiffness of the spring is as follows:

$$\frac{dF_t}{ds} = (A_c - A_h)^2 \left\{ RgTm_q \left[ A_x \left( L_{gj} - \frac{(A_c - A_h)s}{A_x} \right) - m_q b \right]^{-2} - 2am_q^2 \left[ A_x \left( L_{gj} - \frac{(A_c - A_h)s}{A_x} \right) \right]^{-3} \right\} \tag{8}$$

### 3.3 Lateral Stiffness of Oil Gas Suspension

According to the left oil gas spring, the volume of the main oil cavity is as follows:

$$V_1 = A_c s_1 = A_h s_2 \tag{9}$$

Accumulator displacement is as follows:

$$s_{x1} = \frac{A_c s_1 - A_h s_2}{A_x} \tag{10}$$

The expression of the left gas chamber height with the displacement is as follows:

$$L_{g1} = L_{gj} - s_{x1} = L_{gj} - \frac{A_c s_1 - A_h s_2}{A_x} \tag{11}$$

Gas chamber volume is as follows:

$$V_{g1} = A_x L_{g1} = A_x \left( L_{gj} - \frac{A_c s_1 - A_h s_2}{A_x} \right) \tag{12}$$

Through formulas (3) and (12), the main oil cavity pressure of the left spring can be deduced:

$$p_1 = \frac{RgTm_q}{A_x \left( L_{gj} - \frac{A_c s_1 - A_h s_2}{A_x} \right) - m_q b} - \frac{am_q^2}{\left[ A_x \left( L_{gj} - \frac{A_c s_1 - A_h s_2}{A_x} \right) \right]^2} \tag{13}$$



According to same principle, the main oil cavity pressure of the right spring is as follows:

$$p_2 = \frac{RgTm_q}{A_x \left( L_{gj} - \frac{A_c s_2 - A_h s_1}{A_x} \right) - m_q b} - \frac{am_q^2}{\left[ A_x \left( L_{gj} - \frac{A_c s_2 - A_h s_1}{A_x} \right) \right]^2} \tag{14}$$

Through formulas (1), (13), and (14), the left and right spring force can be expressed as follows:

$$F_{s1} = \left[ \frac{RgTm_q}{A_x \left( L_{gj} - \frac{A_c s_1 - A_h s_2}{A_x} \right) - m_q b} - \frac{am_q^2}{\left[ A_x \left( L_{gj} - \frac{A_c s_1 - A_h s_2}{A_x} \right) \right]^2} \right] A_c - \left[ \frac{RgTm_q}{A_x \left( L_{gj} - \frac{A_c s_2 - A_h s_1}{A_x} \right) - m_q b} - \frac{am_q^2}{\left[ A_x \left( L_{gj} - \frac{A_c s_2 - A_h s_1}{A_x} \right) \right]^2} \right] A_h \tag{15}$$

Differentiating  $s_1$  in formula (10), the lateral stiffness of the gas spring is as follows:

$$\frac{dF_{s1}}{ds_1} = A_c^2 \left[ RgTm_q \left[ A_x \left( L_{gj} - \frac{A_c s_1 - A_h s_2}{A_x} \right) - m_q b \right]^{-2} - 2am_q^2 \left[ A_x \left( L_{gj} - \frac{A_c s_1 - A_h s_2}{A_x} \right) \right]^{-3} \right] - A_h^2 \left[ -RgTm_q \left[ A_x \left( L_{gj} - \frac{A_c s_2 - A_h s_1}{A_x} \right) - m_q b \right]^{-2} + 2am_q^2 \left[ A_x \left( L_{gj} - \frac{A_c s_2 - A_h s_1}{A_x} \right) \right]^{-3} \right] \tag{16}$$

According to formula (16), suspension stiffness is [5, 6] as follows:

$$K_s = \frac{1}{i^2} \frac{dF_{s1}}{ds_1} \tag{17}$$

in which  $i$  is lever ratio of suspension.

Torque of carriage when vehicle turns is as follows:

$$dT = \frac{1}{2} K_s B^2 d\phi \tag{18}$$

in which  $d\phi$  is the lateral angle of carriage, and  $B$  is distance of wheel.

Finally, lateral suspension stiffness can be deduced [7]:

$$K_\phi = \frac{dT}{d\phi} = \frac{1}{2} K_s B^2 \tag{19}$$

### 4 Test and Simulation

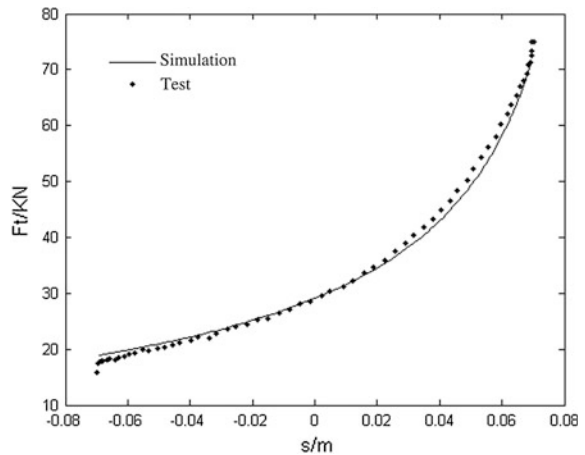
Static characteristics of oil gas spring are tested as shown in Fig. 2. Taking a sine function in which excited frequency is as follows:

$f_z = 0.02$  Hz, and amplitude is  $A_z = 70$  mm, simulation and test results of elastic force are shown in Fig. 3. It is not difficult to see that simulation curves of elastic force and test data are basically consistent through real gas state equation, which prove the correctness of the deduction process.

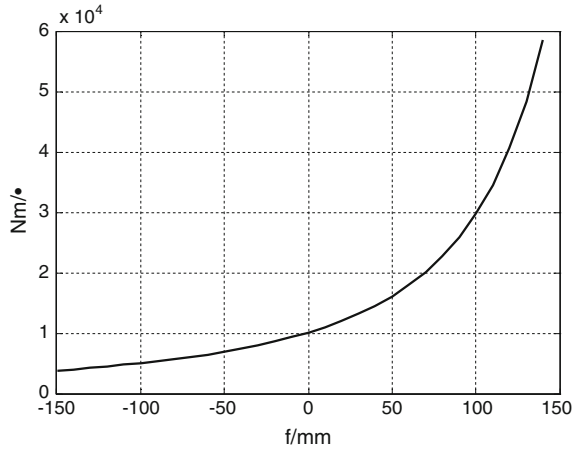
Fig. 2 Test of characteristics of oil gas spring



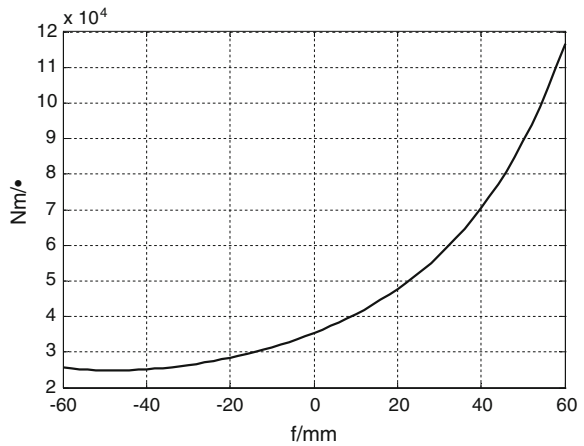
Fig. 3 Simulation and test of elastic force



**Fig. 4** Lateral stiffness of independent suspension



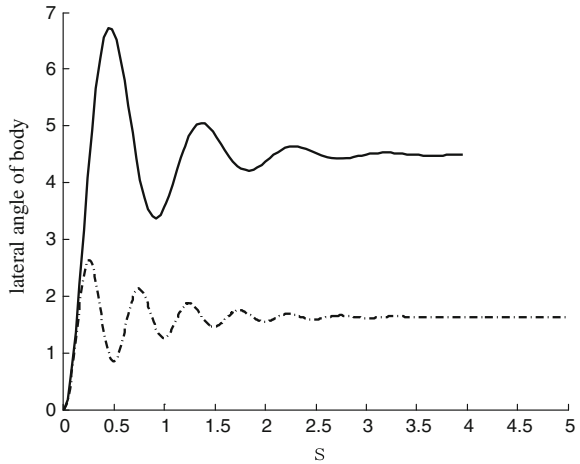
**Fig. 5** Lateral stiffness of interconnected suspension



Lateral stiffness curves of an independent suspension and an interconnected oil gas suspension are shown in Figs. 4 and 5, and the maximum lateral stiffness is multiplied when the interconnected oil gas suspension is used.

In order to proof the effect on vehicle handling and stability performance of the interconnected suspension, the prototype was installed on the multi-axle heavy vehicle. The body lateral angle test was completed under 0.4 g lateral acceleration, and the result is shown in Fig. 6. When the independent suspension is used in the vehicle, the maximum lateral angle of the body is 6.8°. Otherwise, the maximum lateral angle is 2.6° when the interconnected suspension is used. It is verified that the interconnected suspension has a superior handling performance and a good application prospect.

**Fig. 6** Lateral stiffness of interconnected suspension



**Acknowledgment** Sponsored by the Ministerial Level Advanced Research Foundation (623010202.4)

## References

1. Chen YJ, Ning D (2010) The research for the deflection of throttle slice under the local distribution of variable load. *Mech Eng* 4:51–55
2. Chen YJ, GU L, Guan JF (2008) Research on the mathematical model and analysis the throttle aperture of hydro-pneumatic spring. *Beijing Inst Technol* 5:388–391
3. Chen YJ, Meng Q (2009) Vibration test of semi-active hydro-pneumatic suspension of a  $8 \times 8$  wheel-type vehicle. *J Vib Shock* 9:25–27
4. Chen YJ, Gu L (2010) Heat balance and influence factor of semi-active hydro-pneumatic spring. *J Jilin Univ* 40(4):1034–1038
5. Chen YJ, Gu L (2009) Experiment and analysis of large deflection of throttle slice of hydro-pneumatic spring. *J Jilin Univ*, vol 2
6. Wang Z (2005) Simulation analysis and experimentation study on hydro-pneumatic suspensions system for drill rig with automobile chassis. Jilin University, Jilin
7. Deprez K, Moshou D, Ramon H (2005) Comfort improvement of a nonlinear suspension using global optimization and in situ measurements. *J Sound Vib*, pp 1004–1014

# Impact of Switching Three-Phase Breaker at Different Period on Inter-turn Protection for High-Voltage Shunt Reactor

Sheng-Hong Lin, Shu-Yan Pan and Hua-Ren Wu

**Abstract** In this paper, the simulation of inter-turn protection for high-voltage (HV) shunt reactors is studied by using Simulink. Expound that when the closing angles of the three-phase circuit breaker are different, the zero-sequence current and zero-sequence voltage will occur in the system. Demonstrated that during such time, the protection criterion of inter-turn protection will be satisfied in some cases, and thus, the false tripping will occur possibly. Finally, some suggestions are given to avoid the false tripping in the inter-turn protection.

**Keywords** HV shunt reactor · Three-phase inconformity of circuit breaker · Inter-turn protection · False tripping

## 1 Introduction

As the key equipments of the transmission line, the HV shunt reactors are generally used to compensate the capacitance effect in the unload line, prevent the self-excitation, eliminate the coupling current, be against resonance overvoltage, and reduce the power loss [1–3]. In the process of system running, the inter-turn short-circuit fault is one of the most common faults of HV shunt reactors. In the 500-kV transmission line with HV shunt reactors, the principle of the zero-sequence directional power protection with compensation is often applied to determine whether the inter-turn short-circuit fault occurs. Although it can improve the sensitivity of the inter-turn protection, false tripping in some transient process will also happen [4].

---

S.-H. Lin (✉) · H.-R. Wu  
School of Electrical and Automation Engineering, Nanjing Normal University,  
Nanjing 210042 China  
e-mail: linshenghong5061@163.com

S.-Y. Pan  
Nari Technology Co., Ltd., Nanjing 210042 China

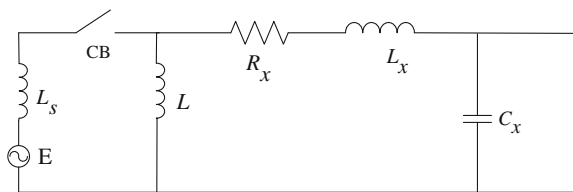
Up to now, some work has been done to study the switching overvoltage in the shunt reactors. As shown in the literature, in the transient process of switching off shunt reactors, the multi-occurrence restriking overvoltage and the overvoltage resulted in switching the three-phase breaker at the same time have a strong impact on the insulation coordination in power systems [5–8]. Moreover, the breakers with closing resistors and the resistance–capacitance absorbing devices can limit the maximum switching overvoltage in the shunt reactors [9–11]. However, in some transient processes, the impacts of the asymmetric flow on the inter-turn protection have hardly any discussion. When the three phases of breaker are not closing at the same time, the zero-sequence current and the zero-sequence voltage will be appeared. Once the zero-sequence current and the zero-sequence voltage satisfy the inter-turn protection criterion of the zero-sequence directional power, the false tripping of inter-turn protection of shunt reactor will occur.

This paper focuses on the inter-turn protection of HV shunt reactor and analyzes the principle of the inter-turn short-circuit protection in the HV shunt reactor. When the discrepancy of three phases of breaker closing occurs, the zero-sequence current and the zero-sequence voltage are simulated. Moreover, action situation of the protection in two cases is shown. Finally, some measures are proposed to avoid the false tripping in the inter-turn protection.

## 2 System Model

Consider a 500-kV power transmission system. The length of the power line is  $l$ . The HV shunt reactor  $L$  is installed in the head of the line. The shunt compensation degree of the line is set to be  $K_{SR}$ . To facilitate the analysis, the common circuit breaker (CB) is used, which does not furnish closing resistors. In addition,  $R_x$ ,  $C_x$ , and  $L_x$  are the impedance, capacitance, and reactance of the transmission line, respectively. Figure 1 shows the equivalent simplified connecting diagram between the shunt reactor and the other components.

**Fig. 1** The equivalent simplified connecting diagram



### 3 Principle of the Inter-turn Protection in 500-kV HV Shunt Reactor

At present, HV shunt reactors often have the single-phase structure. Therefore, the faults include single-phase grounding fault and inter-turn short-circuit fault in general case. When the inter-turn short circuit occurs in the reactor, no matter how many turns are short-circuited, the differential protection cannot carry on the effective protection. Therefore, it is meaningful to determine the high-sensitivity and high-reliability inter-turn short-circuit protection methods. In the following, the principle of the zero-sequence directional power protection is briefly analyzed.

Figure 2 shows the equivalent zero-sequence circuit when the inter-turn short-circuit fault occurs. In the figure,  $X_{L1}$  and  $X_{L2}$  are the zero-sequence reactance on each side of the point of failure,  $X_{S0}$  is the zero-sequence reactance of the system, and  $I_0$  and  $U_0$  are the zero-sequence current and zero-sequence voltage on the side of transmission line. Assume that the forward direction of the zero-sequence current is the direction from the neutral point of the HV shunt reactor to high-handed lead-out line. Moreover, the zero-sequence voltage  $U_0$  and the zero-sequence current  $I_0$  are collected from the head end. Figure 3 shows the vector diagram of the voltage and current, and  $U_{oc}$  is the compensation voltage.

It can be seen from the figure that, when inter-turn short-circuit fault occurs, the zero-sequence current  $I_0$  lags behind the zero-sequence voltage  $U_0$ . By the similar methods,  $I_0$   $90^\circ$  also lags behind  $U_0$   $90^\circ$ , in the internal grounding short-circuit fault. However, when the external grounding short-circuit fault occurs,  $I_0$  pulls

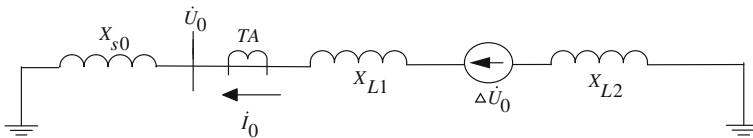
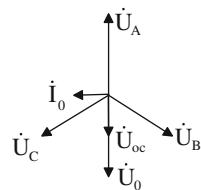


Fig. 2 The equivalent zero-sequence circuit when the inter-turn short-circuit fault occurs

Fig. 3 The vector diagram of voltage and current in the inter-turn protection



ahead  $U_0$   $90^\circ$  inversely [12]. Based on the phase relationship between  $I_0$  and  $U_0$ , the inter-turn short-circuit fault, internal grounding short-circuit fault, and external grounding short-circuit fault can be distinguished, which is the principle of the zero-sequence power directional protection.

Moreover, to improve the sensitivity of the inter-turn protection of the reactor, the compensation voltage  $\dot{U}_{oc} = j\dot{I}_0 X_{oc}$  is introduced, where  $X_{oc}$  is the fixed compensation reactance of the zero-sequence power directional protection with impedance angle for  $90^\circ$ . Therefore,  $U_{oc}$  always pulls ahead  $I_0$   $90^\circ$ . Furthermore, when the inter-turn short circuit in the reactor happens, the action equation of the relay can be written as follows:

$$0^\circ < \arg \frac{\dot{U}_0 + j\dot{I}_0 X_{oc}}{\dot{I}_0} < 180^\circ \tag{1}$$

## 4 Simulation Results

To investigate the impacts of switching three-phase breaker at different periods on the inter-turn protection for high-voltage shunt reactor, the simulation model is established according to Fig. 2.

### 4.1 Parameter Setup

The parameters of the HV shunt reactor and the neutral point reactor are given in Table 1. The setup of the other simulation parameters is shown in Table 2.

**Table 1** Parameters of the HV shunt reactor and the neutral point reactor

	Normal voltage (kV)	Reactance (H)
HV shunt reactor	$550/\sqrt{3}$	3.095
Neutral point reactor	100	0.453

**Table 2** Simulation parameter setup

Parameter	Symbol	Value
Length of the transmission line	$l$	400 km
Compensation degree	$K_{SR}$	0.95
Simulation time	$t$	0.5 s
compensating impedance	$X_{oc}$	$978.6 \Omega$



### 5 Results

In this system, the voltage and current in the protection device are provided by the voltage and current transformers, respectively. To facilitate, investigate the action of inter-turn protection and assume that the transformers in this paper are in the linear unsaturated state.

In this simulation, the impact of transmission line is not taken into account. In the initial state of the simulation, all three phases of the CB are open. During the process of simulation, when the CB is closed as the closing time shown in Table 3, the waveforms of the current and the voltage in the HV shunt reactor are given in Figs. 4 and 5. In Table 3,  $T_{1cl}$ ,  $T_{2cl}$ , and  $T_{3cl}$  are the closing time of phases A, B, and C, respectively. In Fig. 4,  $I_{ra1}$ ,  $I_{rb1}$ , and  $I_{rc1}$  are the currents of phases A, B, and C, respectively. In Figure 5,  $U_{ra1}$ ,  $U_{rb1}$ , and  $U_{rc1}$  are the voltages of phases A, B, and C, respectively. It is shown in Figs. 4 and 5 that, when the switching angles are different, zero-sequence current and zero-sequence voltage will be produced in the system.

According to the experience of the operation and test, when the CB closes in the HV transmission line, a large direct current will occur. When the three-phase switches are not closed at the same time, the zero-sequence current and the zero-sequence voltage will be generated.

Figure 6 shows the waveforms of the amplitude and angle of zero-sequence current, the amplitude and angle of zero-sequence voltage, the angle of protect

**Table 3** The closing time of the CB

Simulation	$T_{1cl}$ s	$T_{2cl}$ s	$T_{3cl}$ s
1	0.10	0.102	0.104
2	0.10	0.11	0.12

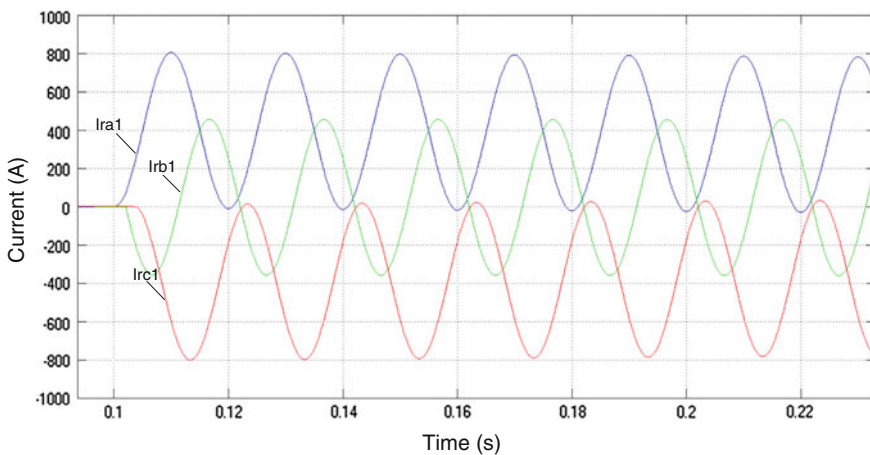


**Fig. 4** The waveforms of the current in HV shunt reactor

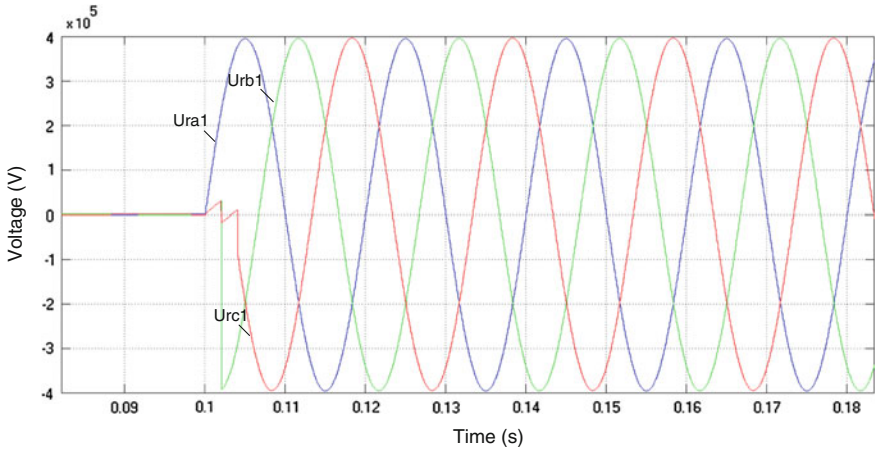


Fig. 5 The waveforms of the voltage in HV shunt reactor

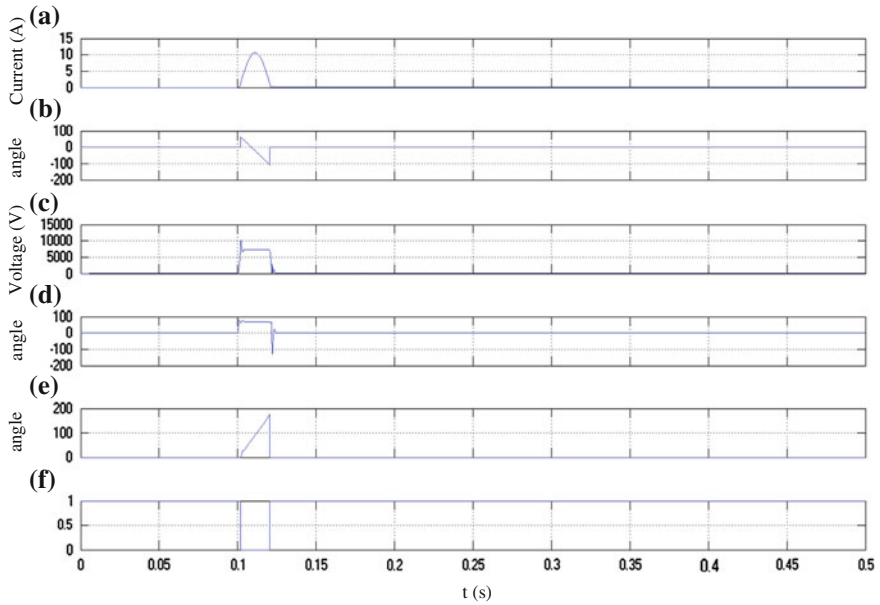
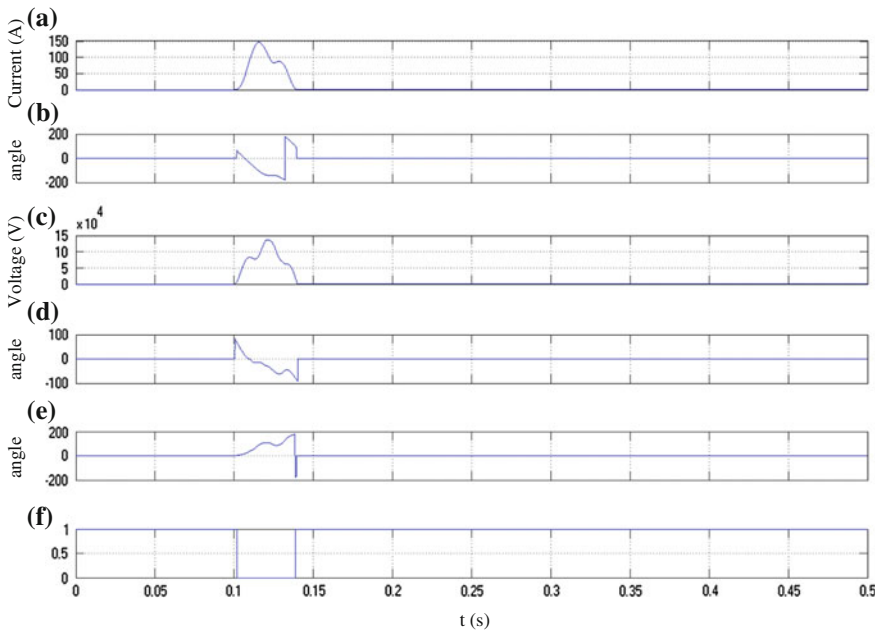


Fig. 6 The inter-turn protection action state of simulation 1. **a** The amplitude of zero sequence current. **b** The angle of zero sequence current. **c** The amplitude of zero sequence voltage. **d** The angle of zero sequence voltage. **e** The angle of protection criterion. **f** The action state (0:trip 1:block)

criterion, and the action state of inter-turn protection after closing the three phases of CB according to simulation 1 in Table 3. If the amplitude of the zero-sequence current or the zero-sequence voltage is very small, the angle of it is regarded as zero. It can be seen that when the closing times of the three phases in the CB are different, the zero-sequence current in the HV shunt reactor will be generated. During the time from 0.1 to 0.123 s, the action of Eq. (1) is satisfied. But the amplitude of the generated zero-sequence current is very small. In this case, increasing the starting value of zero-sequence current can be used to avoid false tripping. Moreover, if the sampling values of the current and the voltage after closing all phases of the CB are used to calculate the zero-sequence current and the zero-sequence voltage, the false tripping will not happen.

When the CB is running for a very long time, the closing time lag of the three phases maybe enlarged. Closing the three phases of CB according to simulation 2 in Table 3, Fig. 7 shows that the amplitude of the zero-sequence current is large; other blocking measures should be added to avoid false tripping. Moreover, in practical system, the closing time lag of the three phases is not so large.

In addition, if the compensating impedance is decreased and the three phases of CB are closed according to simulation 2 in Table 3, Figs. 7 and 8 show that the false tripping does not happen. It can be seen that, although the principle of the zero-sequence directional power protection with compensation can improve the sensitivity of the inter-turn protection, false tripping in some transient process will also occur.



**Fig. 7** The inter-turn protection action state of simulation 2. **a** The amplitude of zero sequence current. **b** The angle of zero sequence current. **c** The amplitude of zero sequence voltage. **d** The angle of zero sequence voltage. **e** The angle of protection criterion. **f** The action state (0:trip 1:block)

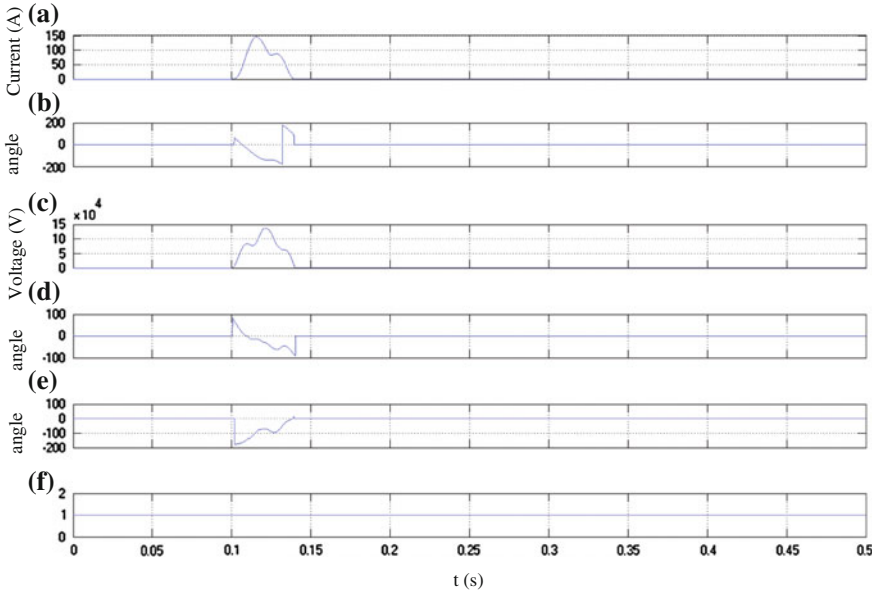


**Fig. 8** The inter-turn protection action state after decreasing the compensating impedance. **a** The amplitude of zero sequence current. **b** The angle of zero sequence current. **c** The amplitude of zero sequence voltage. **d** The angle of zero sequence voltage. **e** The angle of protection criterion. **f** The action state (0:trip 1:block)

### 5.1 Conclusions

In this paper, the following conclusions are derived:

In the neutral-grounded system, the three-phase switches may close at different time, which will satisfy the inter-turn action equation.

When the closing time lag of the three phases is very small, the zero-sequence current is also very small. In this case, increasing the starting value of zero-sequence current can be used to avoid false tripping. However, when the closing time lag of the three phases is large, the zero-sequence current is large. In this case, other blocking measures should be added to avoid false tripping.

In addition, for the tests of the CB, it should be strictly checked whether the closing time of the three switches is at the same time. Moreover, switching three-phase breaker at different periods caused by man-made operation should also be avoided.

**Acknowledgements** This work was financially supported by the National Natural Science Foundation of China (51177074).

## References

1. Dvorak LL, Chalrman DC, Dawson RW, Dempsey H, Disante CM, Gadsden JD, Huddleston III, Schulze LJ (1991) Summary of the 'Guide for the protection of shunt reactors' ANSI C37.109. *IEEE Trans Power Deliv* 6(1):116–118
2. He J, Li Y, Guo Z, Li B, Dong X (2002) Relay protection for UHV transmission lines. *Autom Electric Power Syst* 26(2):1–6
3. Ban G, Prikler L, Banfai G (2003) 750 kV reactive power control automatic reclosing and overvoltage protection. *IEEE Power Tech Conference, IEEE, Bologna, Italy*
4. Chen S, Wang Z (2003) Research and development of a new digital shunt reactor protection. *Autom Electric Power Syst* 27(24):70–73
5. Sun Q, Li Q, Wang G (2010) Characteristic analysis of shunt reactor switching over-voltages interrupted by SF6 circuit breaker with chopping current. *Trans China Electrotech Soc* 25 (2):170–176
6. Chang W, Huang M (2002) Modeling SF6 circuit breaker for characterizing shunt reactor switching transients. *IEEE Trans Power Deliv* 11(3):1533–1540
7. Prikler L, Ban G, Banfai G (1997) EMTP models for simulation of shunt reactor switching transients. *Electr Power Energy Syst* 19(4):235–240
8. Yang D (1992) Test and research on disconnecting shunt reactors with SF6 breakers. *High Volt Eng* 22(2):50–55
9. Pan X, Wang X, Wang B (2000) Analysis and criterion of eliminating the need for closing resistors in 500 kV line circuit breaker. *Electr Switch* 4:24–30
10. An Y, Wen X (2013) Overvoltage of shunt reactor by prebreakdown of SF6 breaker and protection measures. *High Volt Eng* 39(1):75–80
11. Hu N (2011) Investigations on controlled switching of shunt reactor. *Dalian University of Technology, Dalian*
12. Wang W, Huang R (1995) Operation analysis of the zero sequence directional power protection in 500 kV shunt reactor. *Relay* 4:3–6

# The Application Software Framework About Distributed Intelligent Alarm Information in Intelligent Substation

Xin Xu, Zhiqiang Yao, RenHui Dou, Hao Ren, Mingzhi Geng and Hui Ren

**Abstract** With rapid development of the power grid construction and the new energy, power grid operating characteristic has major changes. The intelligent alarm processing function in the existing dispatching automation system cannot meet the requirements of the power grid operation. Distributed application has become a new application requirement for power grid dispatching automation system. In recent years, the distributed application research on distributed state estimation, distributed intelligent alarm, and distributed SCADA has been reported. Base on the status and application of the intelligent power network dispatch and control system, the intelligent alarm function analyzes the difference between the traditional alarm system and the distributed intelligent alarm system. And the paper studies the architecture and specification of the two-level distributed intelligent alarm system and analyzes the value and its future application prospect of distributed intelligent alarm for dispatching operation.

**Keywords** Two-level distributed · Intelligent alarm · Distributed · IEC 61850

## 1 Introduction

Since the twenty-first century, the large area blackout events have broken out in North America, Western Europe, and Asia that results in a huge loss of social production and people's life. Power system exposed many problems in equipment management and the condition monitoring. With loose regulatory system and incompatible monitoring system, power system cannot achieve the alarm message unified management and sharing.

Our country power industry has accumulated a lot of valuable power equipment historical data. On the one hand, these very large data provide valuable experience for fault diagnosis and prediction of equipment; on the other hand, these data

---

X. Xu (✉) · Z. Yao · R. Dou · H. Ren · M. Geng · H. Ren  
China Electric Power Research Institute, Nanjing 210009, China  
e-mail: symbol1000@126.com

dispersedly store up in different condition monitoring and diagnosis system, data complexity, difficult calculation, and high storage cost, so its potential value is also difficult to be fully utilized [1].

## **2 Research Status of Power System Distributed Application**

In traditional centralized architecture, plant stand side does not maintain grid model information. All the equipment modeling work is completed in the dispatch master station with the RTU system upload telemetry [2], remote raw data to the dispatch master station system. Based on the power network equipment parameters and static topology information and combined telemetry remote information from plant stand side upload [3], we can complete advanced application functions such as the topological analysis and state estimation. With the size of the grid increased, information dimension raised, and distributed application has become a new application requirement for power network dispatch automation system. In recent years, the distributed application research on distributed state estimation, distributed intelligent alarm, and distributed SCADA has been reported.

## **3 Status of Distributed Intelligent Alarm**

The current research and application about intelligent alarm are mainly dispatch center centralized diagnosis and substation local diagnosis. The problems can be entrusted to solve alarm problems of substation-dispatch center two levels about lack of coordination and distributed fault diagnosis [4].

The dispatch center centralized fault diagnosis establishes a fault diagnosis model of the entire network to accomplish fault diagnosis in the dispatch center for entire network alarm information. In order to reduce the amount of information transmission, a large number of closely related alarm relay protection signals in substation fault recording signals and equipment online monitoring signals do not real time transfer to dispatch center [5, 6]. Dispatch center usually only uses SOE records main protection and circuit breaker active events in SCADA system to do judgment, and in alarm information may be false positives and absence. These have become one of the difficult problems in dispatch center for many years [7–10].

The researchers have made algorithm research on centralized fault diagnosis in the dispatch center, many literatures, but the practicality of function has not been ideal. Representative methods are as follows: expert system and 0–1 optimization method. These methods are aimed at the time sequence of alarm information [11, 12].

Intelligent alarm method based on expert system uses reasoning style to make intelligent alarm. Expert system judges whether produces the alarm according to the predetermined expert and comparison rule, set alarm generation mode. Intelligent alarm generation method based on expert system is only applicable to simple mode and poor maintainability; tense relationship is also an important content, and the tense relationship in system mainly exists as a descriptive knowledge of fault process.

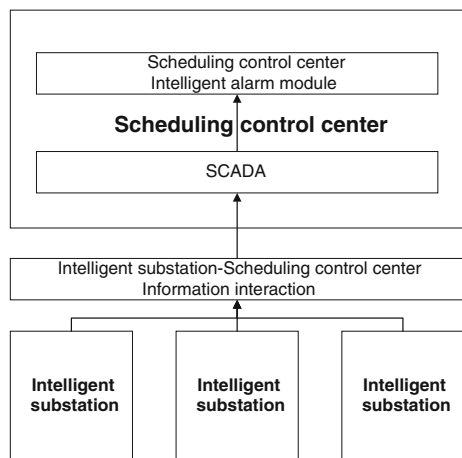
Intelligent alarm method based on 0–1 optimization method expresses alarm information to the action state of protection and switch. Using an optimization model to represent, cause of the alarm is judged by finding optimization. 0–1 optimization method has difficulty in multiprotection modeling [13]. When a complex chain failure occurs, it is easy to have multiple solutions or loss of the optimal solution. In addition, the diagnosis of the time relationship of the general alarm information is also existed, but the problem is that judgment is too simple.

### 4 Intelligent Alarm Model in the Traditional Architecture

The control center centralized SCADA system collects equipment measurement raw data information from each substation RTU (remote terminal unit); alarm information is generated by SACDA data processing module and sends to the main station intelligent alarm module in the form of message. Figure 1 shows traditional centralized intelligent alarm system [14–20].

As shown in the traditional centralized system structure, plant stand side dose not maintain grid model information, but upload telemetry and remote raw data to dispatch center by the RTU system [21]. All the equipment modeling work is

**Fig. 1** The traditional centralized intelligent alarm system





completed in the dispatch center. Switch accident judgment is achieved by switch trip defluxion information and protection action information. The tests have bore out corresponding protection signal and fault signal action. If signal is detected, switch is determined as fault trip, starting fault recall, and conducting alarm function about text, graph, or voice.

## **5 Distributed Intelligent Alarm System Architecture Design**

### ***5.1 General***

Distributed application system is based on the information in the substation and master station at all levels, defining functional requirements and targets of the slave station and master station at all levels. All level master stations laterally integrate and comprehensively analyze upload information from subordinate master stations or son stations, and then, master stations form comprehensive information to upload upper master station, thus establishing the distributed application collaborative mechanism between all level master stations and master-son stations [22]. This section mainly summarizes the system overall architecture design, system information interactive workflow, the key technology, and difficulty.

### ***5.2 Intelligent Alarm Under Distributed Architecture***

Adopting the “distribution and autonomy” overall technical idea, distributed intelligent alarm changes “centralized control station intelligent alarm” to “substation-control station two-level distributed intelligent alarm.” It takes advantage of real-time information highly redundant in the substation to make diagnostic information preprocessing, protection refusal operation, unwanted operation identification, and false alarm processing, so accurate, concise alarm information can be sent to control center. This technology can avoid receiving lots of original alarm information and improve the power grid fault processing speed.

### ***5.3 Two-Level Distributed Intelligent Alarm System Architecture***

The purpose of substation-control station distributed intelligent alarm is preprocess alarm information in the substation which will avoid master station to receive lots of original alarm information. It is good for reducing the communication pressure of

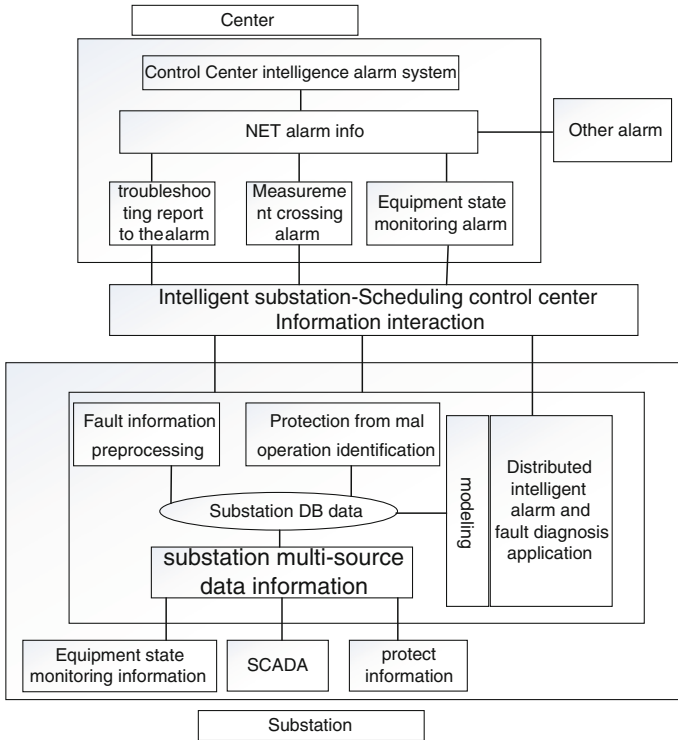


**Fig. 2** Two-level distributed intelligent alarm between intelligent substation and scheduling control center

control station. Figure 2 shows substation–control station two-level distributed intelligent alarm system.

Substation intelligent alarm application real-time function extracts and analyzes information about alarm from monitoring system relay the protection and equipment online monitoring signal. For the time sequence of alarm information and using the time constraint relationship between equipment failure protection and breaker action, intelligent alarm application function can extract the fault event link which can visually reflect the fault evolution process, at the same time, and identify breakpoint alarm, fault alarm, and missing alarm. Substation equipment model based on SCD file needs modeling one time when building or rebuilding substation. The analysis results and output information of substation intelligent alarm have transmitted to the control station by real-time data network. After joining the intelligent alarm information of each substation, the control station gives the cause of the accident and the comprehensive alarm information, which provides dispatcher to analyze.

### 5.4 Substation Intelligent Alarm

The correct rate of intelligent alarm has important relationship with the reliability and integrity of data source. Previous centralized intelligent alarm has many disadvantages in data access and repeated maintenance workload. With the expansion of the grid scale and promotion of regulation and control, the above problem is particularly prominent, so we carry out research on distributed intelligent alarm technology.

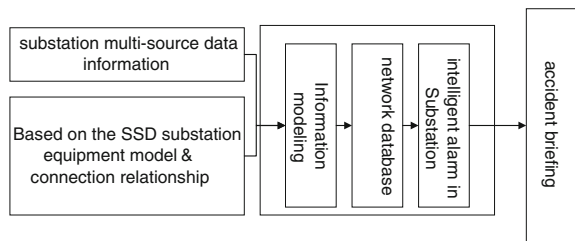
#### 1. General idea

Figure 3 shows substation intelligent alarm architecture. Substation intelligent alarm uses normalized data information content of substation stage data planning, combines IEC61850 first equipment and second equipment unified model, and establishes blurry alarm technology based on association rule and case in the complete substation. Through online identifying fault disturbance reason of input information, false signal and lost signal, substation intelligent alarm classifies substation alarm events, completes intelligent alarm reasoning function, and concludes the accident reason. The controllers are easy to judge substation equipment operation status and fault reasons, so they can provide an alert briefing which is in accord with the dispatch terminal requirements.

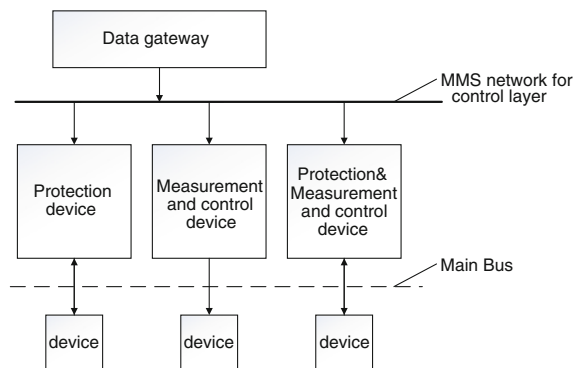
#### 2. Multisource information fusion in the substation

Figure 4 shows diagram of multisource information fusion in the substation. The substation intelligent alarm software deploys on the graph gateway machine. The

**Fig. 3** Two-stage distributed intelligent alarm between intelligent substation and scheduling control center



**Fig. 4** Multisource information fusion in the substation



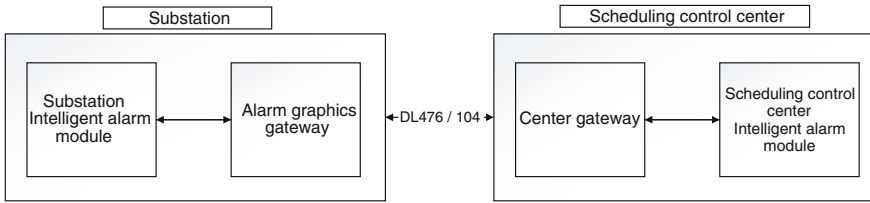


Fig. 5 Information interaction diagram between substation and center

graph gateway machine connects to substation station control layer network, receives MMS message from substation IED device, and forms distributed intelligent alarm data interface file. Distributed intelligent alarm processing module analyzes and handles file, forms important warning or accident brief, and uploads to control master station through 476 standard specification transmission function module.

### 3. Substation fault information preprocessing

Substation intelligent alarm is based on logic and inference model of intelligent substation fault information, realizes classification and filtering of alarm information through online real-time analysis and inference, and provides classified alarm bulletin for the control station. The intelligent alarm event shows intelligent alarm typical event set. The typical fault of the power network is mostly single fault. The diagnostic method based on switching value information can make an accurate judgment.

### 4. The master station alarm information processing analysis

Substation and control station can exchange information through the DL476/104 protocol to realize many functions such as substation end alarm direct transmission, the master station to son station remote viewing, and call of information. In order to realize alarm information exchange and remote viewing, it needs to deploy special “alarm graphics gateway” server in the substation. The alarm graph gateway which uses DL476/104 string data block transmits the alarm information with the substation monitoring system and the dispatch terminal, respectively. Figure 5 shows the information exchange between master station and substation.

## 6 Advantage of the Distributed Intelligent Alarm

The substation monitoring system and the alarm graph gateway are established alarm information transmission by establishing the TCP connection. Alarm graphics gateway deploys alarm forwarding program; at the same time, it establishes TCP connection with the substation monitoring system and the dispatching terminal and transmits alarm information. Alarm graphics gateway directly forwards alert information which receives from the substation monitoring system to the dispatch terminal. The dispatch terminal front gateway establishes the TCP

connection with alarm graphics gateway, receives alarm information, and sends it to the main station intelligent alarm in the form of message. The substation alarm direct transmission has the ability of sending multi-level control. If link be interrupted in the substation and the control center, after the link recovery, the alert information can be recovered during the interruption. The principle of master station intelligent alarm processing alarm messages is as follows: alarm information does not enter into the database; alarm information stores file; and alarm information is displayed in the alarm window and sends to the integrated intelligent alarm module processing.

## References

1. Juste KA, Kita H, Tanaka E et al (1999) An evolutionary programming solution to the unit commitment problem. *IEEE Trans Power Syst* 14(4):1452–1459
2. Xu S, Xie X, Xin Y (2005) Present application situation and development tendency of synchronous phasor measurement technology based wide area measurement system. *Power Syst Technol* 29(2):44–49
3. Xue Y, Wei W, Dong Z et al (2007) A review of wide area measurement system and wide area control system. *Autom Electric Power Syst* 31(15):1–5
4. Xue Y, Li H (2008) A review of CIGRE 2008 on power system operation and control. *High Volt Eng* 34(11):2253–2258
5. He J, Zhou J, Wang M (2009) Application of wide area phasor measurement technology in smart grid. *Power Syst Technol* 33(15):16–19
6. Jiang D, Lu X, Yang G (2008) A novel phasor measurement unit with free scaled synchronized time-mark. *Autom Electr Power Syst* 32(3):56–60
7. Zhu X, Pei J (2010) The research of family alert system based on MCU. *Manuf Autom* 32(7):211–215
8. Ying C (2007) The design of automatic fire warning control system based on C8051. Dalian Maritime University, Dalian
9. Ongsakul W, Petcharaks N (2004) Unit commitment by enhanced adaptive Lagrangian relaxation. *IEEE Trans Power Syst* 19(1):620–628
10. Gao X, Zhang P (2005) Application technology of power fault information system. *Electric Power Autom Equip* 25(4): 11–15
11. Li Y (2008) Application of intelligent warning expert system to Nantong power system. *Jiangsu Electr Eng* 27(5):48–50
12. Li Q, Zhou J, Yu E et al (2005) A hybrid algorithm for power system state estimation based on PMU measurement and SCADA measurement. *Autom Electr Power Syst* 29(19):31–35
13. Li D, Cao Y (2007) Wide-area real-time dynamic state estimation method based on hybrid SCADA/PMU measurements. *Power Syst Technol* 31(6):72–78
14. Li D, Li R, Sun Y et al (2010) Data compatibility analysis of WAMS/SCADA hybrid measurements state estimation. *Proc CSEE* 30(16):60–66
15. Li Q, Yu E, Lu S et al (2005) An improved optimal PMU placement algorithm [J]. *Power System Technology* 29(12):57–61
16. Zhang J, Xie Y, Yang X et al (2008) Studies on placement of PMUs and its effect on state estimation's precision. *Electr Power* 41(6):23–27
17. Chen G, Tang Y, Zhang J et al (2010) Optimal PMU placement based on Taguchi method considering N-1 condition. *Autom Electr Power Syst* 34(1):25–27
18. Liu X, Jiang Q, Cao Y (2009) Optimal PMU placement to guarantee observability under N-1 condition. *Proc CSEE* 29(10):47–51

19. Chen X, Tao J, Jiang Q et al (2008) An algorithm for PMU configuration considering high risk cascading failure. *Autom Electr Power Syst* 32(4):11–14
20. Liu Da, Xie X, Mu G et al (2005) An on-line voltage stability index of power system based on synchronized phasor measurement. *Proc CSEE* 25(1):13–17
21. Gu W, Wan Q (2010) Linearized voltage stability index for wide-area voltage monitoring and control. *Trans China Electro Tech Soc* 25(6):110–115
22. Liu M, Zhang B, Yao L et al (2009) On-line voltage stability monitoring based on PMU and improved Thevenin equivalent model. *Autom Electr Power Syst* 33(10):6–10

# The Design and Implementation of Substation Graphic Gateway System Based on IEC61850 Technology

Mingzhi Geng, Renhui Dou, Yanping Wu, Zhiqiang Yao,  
Hao Ren and Xin Xu

**Abstract** As the application of IEC61850, the condition monitoring systems and auxiliary systems have been used in substation, and the amount of substation data becomes more and more large. In order to solve the management problems generated by large amounts of substation data, the National Dispatching Center has proposed the Direct alarm and Remote browsing techniques based on traditional remote communication device. This paper uses an embedded platform graphic gateway and uses IEC61850 to get real-time data and graphics of substation. It sends the data to D5000 system of dispatch center via DL/476, and the real-time data transmission and monitoring data refresh have reached the requirements of engineering applications and achieved good applied effect.

**Keywords** Smart substation · Direct alarm · Remote graphics browsing · IEC61850 · CIM/G

## 1 Introduction

The development of smart grid has become a global consensus recently. As one part of low-carbon electricity, smart grid technology has developed rapidly in China and has become a new trend for the future development of the power grid. Smart substation is an important foundation for the strong smart grid. It plays an important role in smart grid “six major areas,” which support dispatch automation system as a smart grid node. As a data source, a good status of substation is related to the stable operation of power system. The national electric power dispatching and control center of china has proposed “Direct alarm and Remote browsing” technology according to the different business needs of dispatch centers [1–10].

---

M. Geng (✉) · R. Dou · Y. Wu · Z. Yao · H. Ren · X. Xu  
China Electric Power Research Institute, No. 8, NARI Road, Gulou District,  
Nanjing, Jiangsu Province, People’s Republic of China  
e-mail: 363559227@qq.com

© Springer-Verlag Berlin Heidelberg 2016  
B. Huang and Y. Yao (eds.), *Proceedings of the 5th International Conference on Electrical Engineering and Automatic Control*, Lecture Notes in Electrical Engineering 367, DOI 10.1007/978-3-662-48768-6\_111

999

The so-called Direct alarm refers to the substation real-time alarm information which has been filtered, handled, and optimized sent directly to the alarm window of master station through proprietary channels, and operators of master station may be the first time to monitor substation equipment, secondary equipment fault condition by alarm window. "Remote viewing" that refers to the dispatch center can browse picture of substation monitoring system at any time; it can get the performance status of substation system, power flow information, and the status of devices as well; and it would give some good suggestion for operators.

Compared with traditional substation remote control systems, only substation needs to draw mainline diagrams and maintain database and its data, and dispatch centers can get the files and data from substation directly. The graphic gateway described in this paper can get substation real-time data by IEC61850 and transmit the picture files to dispatch centers through DL/476 protocol.

## 2 System Architecture

### 2.1 System Functional Framework

The system functional framework with "Direct alarm and Remote browsing" involves two soft modules: one in substation and the other in master station. Function module in master station is divided into three parts: front-end module, picture browsing module, and alarm window module. Front-end module can receive graphic browsing and data refresh request command from picture browsing module, and also can send the request to the gateway of substation to obtain the graphic file, SCADA data, and alarm information from substation. The main function of the graphic gateway includes data collection, data transmission services, and substation wiring diagram generation.

The operator in master station browses mainline diagrams and monitors the substation status from alarm window. The gateway system draws mainline diagrams, parses the substation SCD file, generates real-time database, processes the alarm information, and transmits all the data to dispatch centers according to the commands sent by the operator in the dispatch center. System frame graphic gateway is shown in Fig. 1.

### 2.2 IEC61850 Data Acquisition

IEC61850 standard is the latest international communication standard in substation automation area approved by the International Electrotechnical Commission, which defines 30 kinds of public data categories, nearly 400 kinds of data objects and



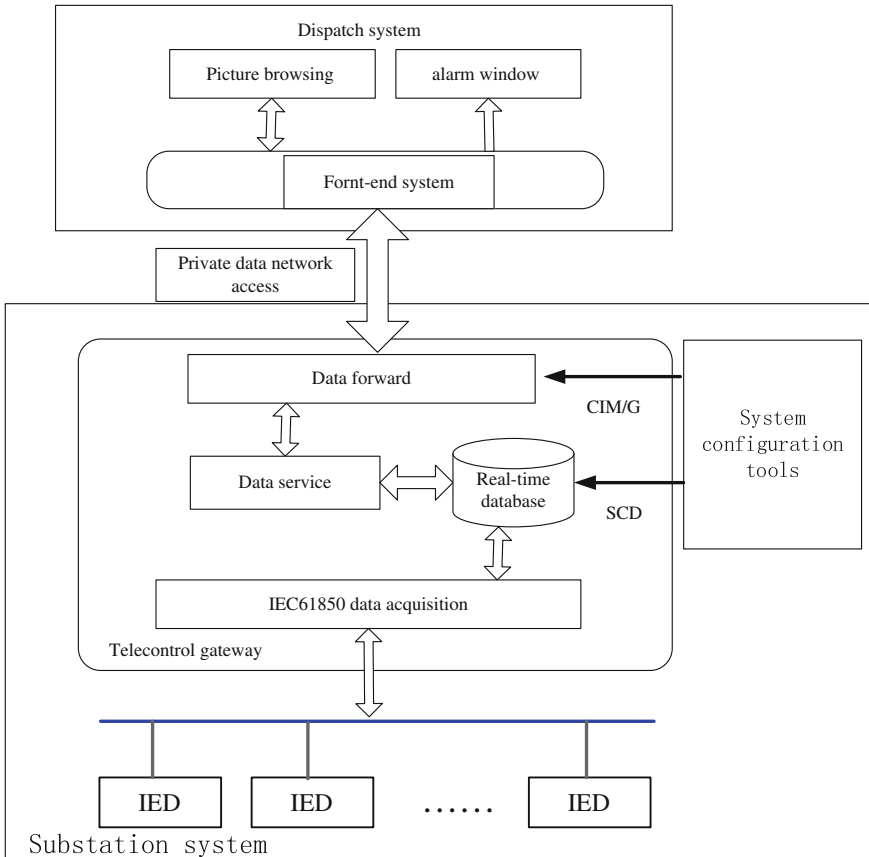


Fig. 1 Substation graphic gateway system frames

more than 80 kinds of logical nodes, and it can describe the vast majority devices of the substation. This standard uses the client/server model to establish communication framework and uses a set of object-oriented abstract communication service interface (ACSI) for data exchange.

Firstly, taking advantage of chart-module integration tools of substation to draw wiring diagrams, establish Substation Configuration Description Model (SCD model) and achieve the association between primary device and secondary equipment in the SCD model. Secondly, exported graphic files automatically establish data mapping from the measured point of graphic files to the measurement index (reference) of SCD. Use IEC61850 index (reference) to get data from IED by ACSI and write to real-time database. Finally, transmit the data and graphic files to dispatch center.

**Table 1** CIM/G basic structure

---

```

<?xml version="1.0" encoding="GBK"?>
<G w="2000" h="1050" bgc="0,0,0">
  <Layer name="The Third Main-line Diagrams of Power Systems"
type="0" show="1" >
    <Text id="1" fs="26" x="617" y="345" ts="Bay status " ... />
    <line id="2" x1="476" y1="498" x2="1300" y2="498"... />
    <Bus id="31" x1="98" y1="231" x2="498" y2="231" ... />
    <CBreaker id="40" x="236" y="610" devref="... " ... />
    <GroundDisconnector id="41" x="188" y="926" devref="... " />
    <DText id="73" wm="1" app="100000"... />
    <ConnectLine fm="0" id="275"...link="0,0,225;1,0,276;1,1,277"/>
    .....
  </Layer>
</G>

```

---

### 2.3 CIM/G Graphic Generation

CIM/G, a graphic depiction specification of the power system, is a plain text language that uses XML standard, its basic graphic format is compatible with SVG, and it can express power system equipment and models directly. Currently, the monitoring graphics in substation automation system of main secondary equipment manufacturers can support CIM/G standard. This paper generates CIM/G substation monitoring graphics by chart-module integration tools, and Table 1 shows the basic structure of CIM/G.

## 3 Data Exchange Process

### 3.1 Graphic Information Indexing

In CIM/G graphic files, each grid graphic elements, such as measurement (DText), has a unique identification. As it established the data mapping between the measurement and the IEC61850 reference of SCD by chart-module integration tools [16]. The data displayed in wiring diagrams have its unique ID in CIM/G graphic files. Substation gateway uses IEC61850 index to get data value from real-time database and then transmits the CIM/G graphic file and its data to master station, and the data includes data ID and date value. Master displays the data values according to the data ID (Fig. 2).

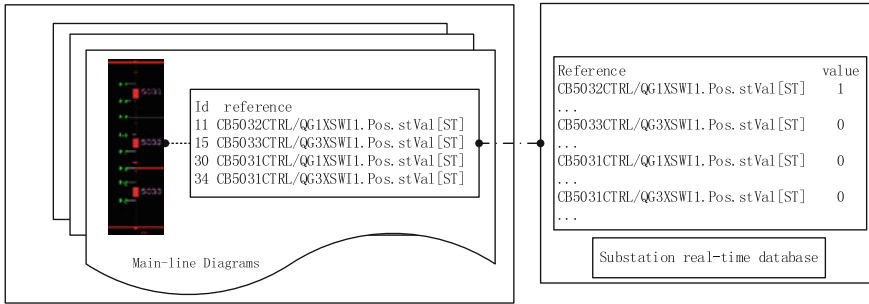


Fig. 2 Substation graphic index graph

### 3.2 Remote Viewing of Processing

After the front-end module of master station establishes a socket connection to substation as a client, it will send the browsing graphic request to the substation gateway. When receiving the command, including the file name, the gateway opens the file transfer threads to transfer the graphic file. Firstly, the substation sends the file size and modification time to the master station. After obtaining the master confirmation, it will send graphic files to the master station until the last frame of the file.

When browsing graphic files already exist in the master station system, it will send the request to obtain real-time data. When receiving the data command, the data request message will be sent to the data service module and the data service module will get data from real-time database and returned telemetry data. The gateway organize data packet in the DL/T 476 message format and send it to the master station until it receives a release message from the master station.

There is a root graphic in the master station, which has all the graphic index. The substation soft module goes into the soft processing flow after receiving master station request, and its processing is shown in Fig. 3.

### 3.3 Direct Alarm Processing

Similar to remote viewing of processing, the substation gateway can send the single event or a comprehensive analysis result to the master station via “direct function.” Its processing flows are shown in Fig. 4.

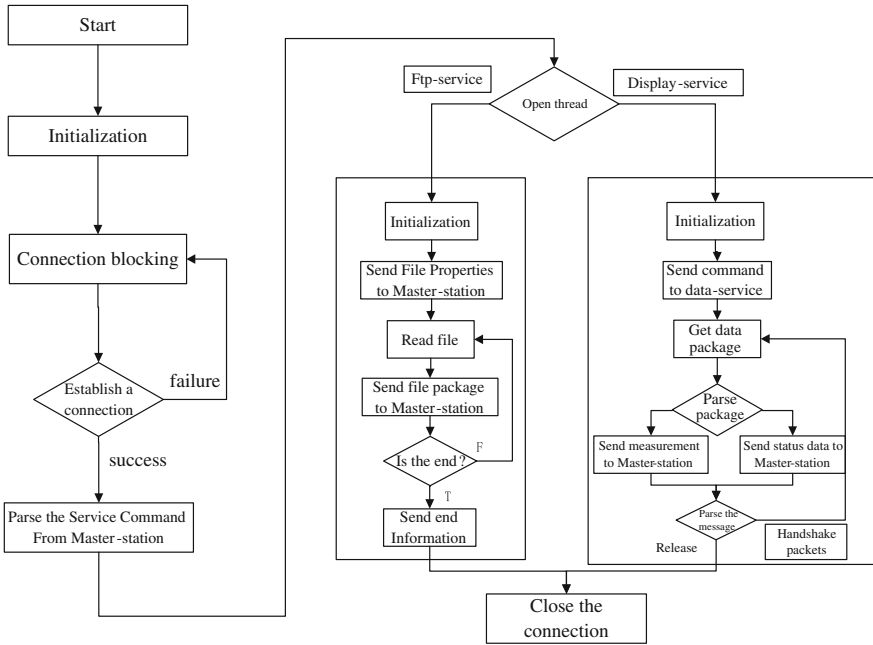


Fig. 3 Substation master graphic information exchange procedure

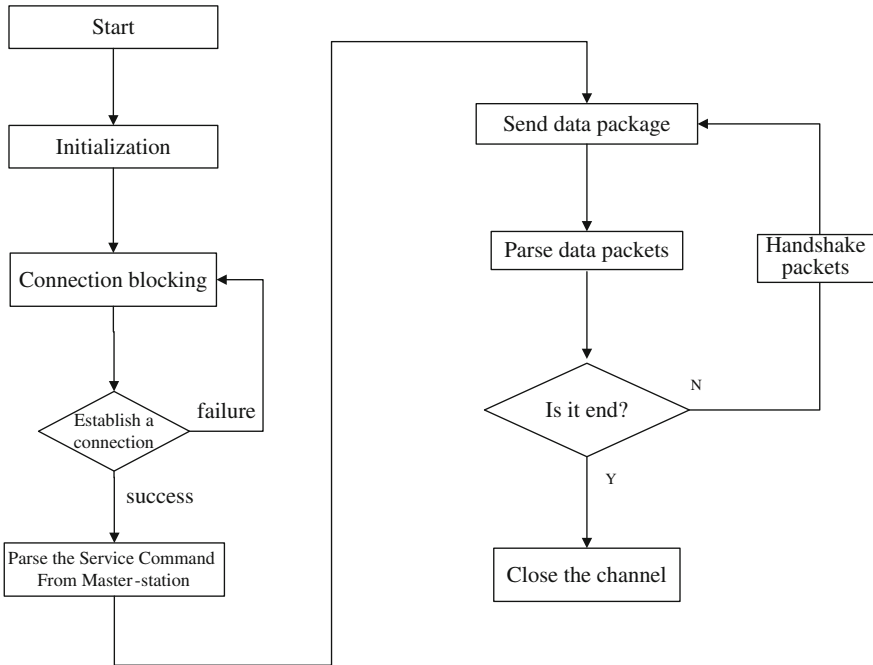


Fig. 4 Information exchange procedure of "Direct Alarm"

## 4 Conclusion

“Direct alarm and remote viewing” proposed by the national electric power dispatching and control center of china is one kind of new information interaction between substation and master station. It can transmit large amounts of data from substation to master station in the form of text and graphics. The alarm graphic gateway described in this paper can achieve the “direct alarm and remote viewing” function deploying on the embedded device. It can reduce the construction cost of substation. At present, the system has been applied in Changshu 500 kV substation, in Suzhou City, and achieved good project results.

## References

1. Wang Z, Zhu S, Zhou S (2004) Controller design for inverter based distributed generation. *Autom Electr Power Syst* 28(24):61–66
2. He L (2012) An introduction to IEC61850 application. China Electric Power Press, Beijing
3. IEC61850 (2009) Communication networks and systems in substations, 2.0 edn
4. Hu DX, Wo JD (2010) Virtual circuit system of smart substation based on IEC61850. *Autom Electric Power Syst* 34(17):78–82
5. Li R, Li Y, Zhou F et al (2010) The functional frame and design principles of smart substation. *Power Syst Protect Control* 34(7):1–4
6. Sun YM, Qiu YT, Yang QW et al (2013) Study on the technology integration of project design and configuration for smart substation. *Autom Electric Power Syst* 37(14):70–74
7. Hoga C, Skare P (2006) IEC61850 projects in Germany and Switzerland. In: Transmission and distribution conference and exhibition, 2005/2006 IEEE PES, Siemens AG, Nuremberg, May 2006
8. Crispino F, Villacorta CA, Oliveira PRP, Jardini JA, Magrini LC (2004) An experiment using an object-oriented standard IEC61850 to integrate IEDs systems in substations. In: Proceedings of the 2004 IEEE, transmission and distribution conference and exposition, Latin America, Nov 2004, pp 22–27
9. Song X, Shen J, Li J, Xiao Z et al (2013) Design of new generation smart substation. *Electric Power Constr* 34(6):11–15
10. Ni Y, Yang Y, Fan C et al (2014) Discussion on integration of secondary devices in smart substations. *Autom Electr Power Syst* 38(3):194–199
16. Gao X, Jiang JN, Qiu YT, Yang YJ, Wu ZJ (2013) The research of SCD application based on IEC 61850. In: 2013 international conference on electrical, control and automation engineering, pp 20–24

# An Improved Particle Swarm Optimization and Application

Dongsheng Zhou, Lin Wang and Jiang Wei

**Abstract** Particle swarm optimization (PSO) is prone to fall into the premature convergence, and convergence precision is low and other shortcomings in solving complex problems. This paper presents an algorithm based on the adaptive inertia weight of the second-order oscillation particle swarm optimization (SOPSO); the algorithm combines SOPSO and adaptive inertia weight advantages, and it is good solution to the above-mentioned problem. Finally, the simulation on four test functions and the application on the key frame extraction from human motion capture data show that the algorithm not only has a strong search capability, and the convergence precision and stability have been effectively improved.

**Keywords** SOPSO · Adaptive inertia weight · Key frame extraction

## 1 Introduction

In addition to the ant colony algorithm and a kind of fish algorithm in computer intelligence field, particle swarm optimization (PSO) is a swarm intelligence optimization algorithm, and the algorithm was first proposed by Kennedy and Eberhart through stochastic optimization algorithm simulates the foraging behavior of birds in 1995. The idea mainly comes from artificial life and evolutionary computation theory [1]. Compared with other evolutionary algorithms, PSO is simple and versatile and has been widely used in recent years in the fields of function optimization, neural networks, fuzzy system control, and applications of GA [2].

However, the PSO, in dealing with complicated peak, is easy to fall into local optimal solution and is slow convergence speed late evolution. Therefore, many

---

D. Zhou (✉) · L. Wang (✉) · J. Wei  
Key Laboratory of Advanced Design and Intelligent Computing,  
Ministry of Education, Dalian University, Dalian 116622, China  
e-mail: donyson@126.com

L. Wang  
e-mail: wangl26@126.com

scholars proposed and used PSO to improve the solution and the performance of the algorithm. For example, Yang et al. [3] proposed the PSO with inertial factor, Ouyang et al. [4] proposed the PSO with compression factor, Shi and Eberhart [5] proposed a fuzzy adaptive PSO, Yan and Luo [6] proposed the PSO based on simulated annealing, Zhang et al. [7] proposed the Multilevel Thresholding Based on Exponential Cross Entropy and Niche Chaotic PSO, and Li et al. [8] proposed the improved PSO algorithm based on genetic crossover factor. These algorithms improved the PSO in different aspects and different levels, but there are insufficient algorithm itself.

To overcome the premature convergence and the poor local search capability in late evolution, this paper mainly does the following work: Choosing the second-order oscillating PSO algorithm to improve the global optimization ability. Taking the adaptive weighting to avoid the premature algorithms, and enhance the local search ability of the algorithm. Simulating on the basic test functions and applying on key frame extraction.

## 2 Our Algorithms

In this paper, to overcome the premature convergence and the poor local search capability in late evolution, we combine SOPSO with adaptive inertia weight. The outline of the AWSOPSO (an adaptive weight of second-order oscillation particle swarm optimization) is as follows:

1. Randomly generate the initial position and velocity of each of the particles;
2. Evaluate the fitness of each particle, put the current position and fitness of each particle in pbest, then select the best fitness in pbest, and store the corresponding position and fitness in gbest;
3. Update the velocity vector and position as the formula (1)

$$\begin{cases} v_{i,j}(t+1) = \omega v_{i,j}(t) + c_1 r_1 [p_{i,j} - (1 + \xi_1)x_{i,j}(t) + \xi_1 x_{i,j}(t-1)] \\ \quad + c_2 r_2 [p_{p,j} - (1 + \xi_2)x_{i,j}(t) + \xi_2 x_{i,j}(t-1)] \\ x_{i,j}(t+1) = x_{i,j}(t) + v_{i,j}(t+1), \quad j = 1, 2, \dots, d \end{cases} \quad (1)$$

4. Update the  $\omega$  as the formula (1);
5. For each particle, compare its fitness with its experienced best location; if better, take it as the current best location;
6. Compare with all current pbest and gbest and update gbest;
7. If it meets the iterations, stop search, output the result, or go to the third step.

### 3 Test Functions

In order to verify the effectiveness of the proposed algorithm in this paper, we adopt four commonly used four test functions for testing [11, 12].

Function name	Expression	Global optimization
$f_1$ : Sphere function	$f_1(x) = \sum_{i=1}^{30} x_i^2$	$f_1(x) = 0$
$f_2$ : Rastrigr function	$f_2(x) = \sum_{i=1}^n [x_i^2 - 10 \cos(2\pi x_i) + 10]$	$f_2(x) = 0$
$f_3$ : Griewank function	$f_3(x) = \frac{1}{4000} \sum_{i=1}^n x_i^2 - \prod_{i=1}^n \cos(\frac{x_i}{\sqrt{i}}) + 1$	$f_3(x) = 0$
$f_4$ : Schwefel problem function	$f_4(x) = \sum_{i=1}^n  x_i  + \prod_{i=1}^n  x_i $	$f_4(x) = 0$

#### 3.1 Experimental Results

The algorithm presented in this paper is compared with PSO, AWPSO (the PSO with an adaptive inertia weight), and SOPS algorithm.

The parameters are set as the following. The total quantity of particles is  $N = 100$ , the largest iteration time is  $M = 5000$ , each experiment was set up to run 1000 times, in the all algorithm, the accelerating factor is  $c_1 = c_2 = 1$ , the inertia weight is  $\omega = 0.8$ , and our algorithm takes the adaptive inertia weight from 0 to 1. We use four methods for four test functions to calculate and find maximum, minimum, standard deviation, and the mean in the optimal solution resulting. The experiment result is as shown in Table 1.

From Table 1, it can be seen:

1. For simple unimodal function sphere, the algorithm presented in this paper is the best performance in solving accuracy (average best fitness value) and robustness (standard deviation).
2. The Rastrigr function, Schwefel problem function, and the Griewank function are typical multimodal function, with a large number of local minima, which can effectively test the performance of global search algorithms. In Table 1, most of the worst values of our algorithm are better than the optimal values of other three algorithms, it means the performance of global search of our algorithm is better than other algorithms.
3. Compared with the results of the four functions, from a single peak function to multimodal function, it clearly can be seen that our algorithm has a better performance in solving accuracy, robustness, and the ability of global search, and for some relatively complex issues, it also has stronger practicability and effectiveness.



**Table 1** The results of each optimization algorithm for each test function

Algorithm		Test function			
		$f_1$	$f_2$	$f_3$	$f_4$
PSO	Optimal value	7.3616E-06	7.2264E+00	2.1145E-05	1.5269E-02
	Worst value	1.5412E-02	6.5094E+01	2.9669E-03	1.1804E+00
	Average value	1.2366E-03	2.7052E+01	5.2685E-04	1.6290E-01
	Standard deviation	1.4870E-03	9.2602E+00	4.1354E-04	1.2251E-01
AWPSO	Optimal value	1.9486E-01	3.1567E+01	9.8945E-03	1.4485E+00
	Worst value	1.3720E+00	1.5750E+02	9.1100E-02	5.6631E+00
	Average value	6.1988E-01	8.5286E+01	3.3272E-02	3.1711E+00
	Standard deviation	1.9442E-01	1.8690E+01	1.0290E-02	6.4253E-01
SOPSO	Optimal value	1.5631E-07	5.7316E-05	4.4895E-09	2.3072E-03
	Worst value	3.7582E-04	6.4154E-02	1.8319E-05	6.8604E-02
	Average value	2.9651E-05	6.2379E-03	1.7631E-06	2.1643E-02
	Standard deviation	3.1540E-05	6.3987E-03	1.8144E-06	1.0301E-02
AWSOPSO (our algorithm)	Optimal value	5.7904E-10	1.6792E-07	3.9844E-11	9.5341E-04
	Worst value	4.7228E-07	7.7323E-05	2.3600E-08	4.5451E-02
	Average value	6.9843E-08	1.4238E-05	4.0529E-09	1.2593E-02
	Standard deviation	5.3386E-08	1.0904E-05	3.2046E-09	6.3101E-03

## 4 Key Frame Extraction

### 4.1 The Fitness Function

The key frame extraction motion capture data technology is to get a representative gesture frame from motion data and that could be on behalf of the entire movement sequence. We define a fitness function to assess the reasonableness of key frame extraction results, and it aims to have the optimal number of key frames and minimize the reconstruction error, namely the optimal compression ratio. Because the reconstruction error is smaller, the more the number of key frames is, we need to balance the reconstruction error and the compression ratio, and we define the fitness function as Formula (2):

$$\begin{cases} f(\text{key}) = pE(\text{key}) + (1 - p)R(\text{key}) \\ (\text{key}) = \frac{\text{length}(\text{key})}{\text{total}(\text{key})} \end{cases} \quad (2)$$

where  $p$  is inertia weight ranging from 0 to 1,  $E(\text{key})$  is the compression ratio,  $\text{length}(\text{key})$  is the number of key frame extraction, and  $\text{total}(\text{key})$  is the motion sequence of frames.

In order to unify the dimensionless of the reconstruction error and the compression ratio, it needs standardization process for the reconstruction error. The standardization process is according to the formula (3)

$$E(\text{key}) = \frac{E_{\text{key}}}{E_{\text{max}}} \tag{3}$$

where  $E(\text{key})$  is the reconstruction error when the key frame is key, and  $E_{\text{max}}$  is the reconstruction error when the key frame is the first frame or the last frame.

### 4.2 Experiment and Result Analysis

We use data from the CMU Database; in the experiment, the population size is 30, the number of the population is 30, and the iteration is 5000. We chose the walking, jumping, kicking the ball, dancing, and walk–jump–walk, five different types of motion data, using our algorithm to extract the key frame from them, comparing with another four methods, for the extraction of the same number of key frames. We compare the error rate, and the result is as shown in Table 2.

*Remarks* In Table 2, when the type of motion data is dancing, using the distance curve method to extract the key frames cannot get 29 key frames. The data of 838.0436 are the reconstruction error when the key frames are 30.

In Fig. 1, the length of the five rectangular cylinders represents the reconstruction error of five different algorithms on the same type of motion data. The numbers in figure, respectively, denote the reconstruction error of our algorithm in the five types.

In Fig. 2, the length of the five rectangular cylinders represents the reconstruction error of the five types of motion data on the same algorithm.

In Fig. 1, for the type of walking, the four algorithms except the curve saliency have similar reconstruction errors. The distance curve algorithm is a bit better. For

**Table 2** The compression ratio and reconstruction error of different algorithm

Motion type		Walking	Jumping	Kicking the ball	Dancing	Walk–jump–walk
Total frames		343	439	801	1033	1199
Number of key frames		18	14	21	29	41
Compression ratio (%)		5.25	3.1891	2.6217	2.8074	3.4195
The reconstruction error	Curve saliency [16]	468.0795	780.5908	1721.1	1246.9	884.779
	Uniform sampling	191.7637	722.1363	1477.3	1018.1	731
	Quaternion	208.2598	533.6983	699.7185	1011.1	1234
	Distance curve [15]	187.1955	676.9474	735.9441	838.0436 (30)	745.6044
	Our algorithm	191.6959	206.8784	279.36	389.1399	483.5058

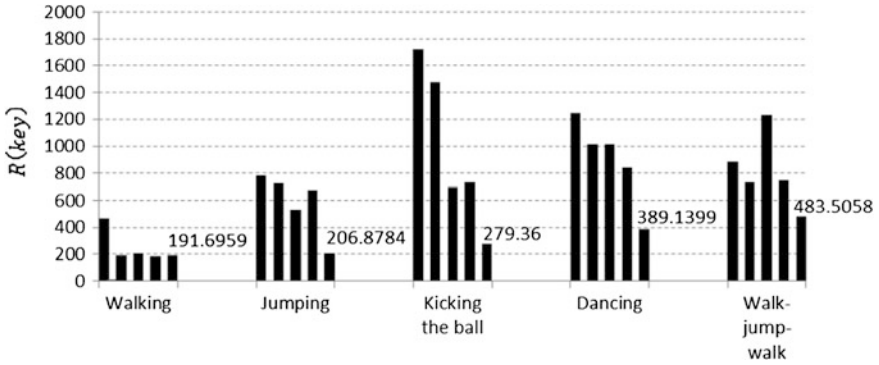


Fig. 1 The reconstruction error of five different types of motion data

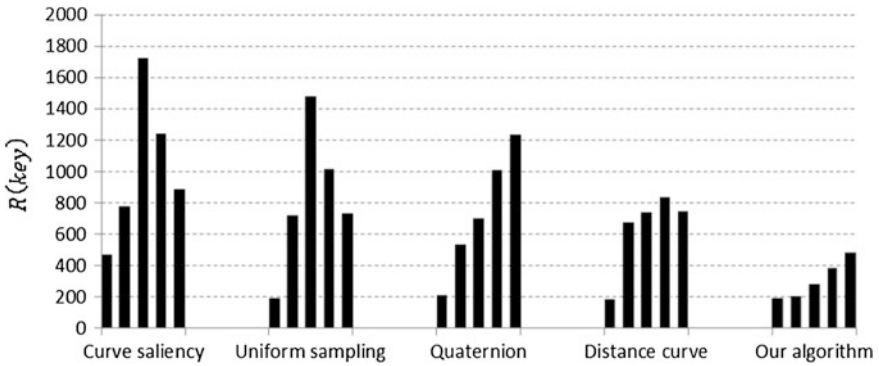


Fig. 2 The reconstruction error of five different algorithms

the rest of the types of the motion data, on the condition of the same compression ratio, the reconstruction error of our algorithm is obvious less than the other four algorithms. It reflects the superiority of the algorithm.

In Fig. 2, on the condition of the same compression ratio, our algorithm performs better than other four algorithms. The reconstruction is lower than others.

From the above conclusions, we can know it is feasible to apply our algorithm to the key frame extraction from human motion capture data. Furthermore, our algorithm cannot only maintain the minimum error rate and can achieve a very good compression ratio. It is an effective algorithm for key frame extraction.

## 5 Conclusions

In this paper, we analyze the principle of PSO algorithm; due to its prone to premature convergence, convergence accuracy is not high and it is easy to fall into local optimum characteristics, and we combine with the second-order vibration particle swarm optimization and the adaptive weight advantage. Through the four standard test function simulations and compared with other typical algorithms, the experimental results show that this algorithm has a better convergence performance and effectively improve the global search ability and stability. Furthermore, on the application of the key frame extraction from human motion capture data, it demonstrates the feasibility and superiority of the algorithm. However, there are still some areas that need improvement for the too complex multimodal function, it costs too much time, and the next step is to combine with other intelligent algorithms to put forward more efficient algorithm to adapt to the complex problems. The other question is when applying it to the key frame extraction, this algorithm does not accurately get the preset number of key frames, and we will do the further research in this area.

## References

1. Kennedy J (2010) Particle swarm optimization. In: Encyclopedia of machine learning. Springer, US, pp 760–766
2. Leung SYS, Tang Y, Wong WK (2012) A hybrid particle swarm optimization and its application in neural networks. *Expert Syst Appl* 39(1):395–405
3. Yang X, Yuan J, Yuan J, Mao H (2007) A modified particle swarm optimizer with dynamic adaptation. *Appl Math Comput* 189(2):1205–1213
4. Ouyang C, Li X, Wang N (2010) A best wavelet packet basis image compression algorithm based on PSO. In: 2010 fourth international conference on genetic and evolutionary computing. IEEE, pp 11–13
5. Shi Y, Eberhart RC (2001) Fuzzy adaptive particle swarm optimization. In: Proceedings of the 2001 congress on evolutionary computation, vol 1. IEEE, pp 101–106
6. Yan ZC, Luo YS (2014) A particle swarm optimization algorithm based on simulated annealing. In: Advanced materials research, vol 989. pp 2301–2305
7. Zhang Y, Wu Y, Wu S, Song Y (2012) Multilevel thresholding based on exponential cross entropy and niche chaotic particle swarm optimization. In: Advances in computer, communication, control and automation. Springer, Berlin, pp 617–624
8. Li J, Sun XX, Li SB, Li R (2008) Improved particle swarm optimization based on genetic hybrid genes. *Comput Eng* 2:1021–1025
9. Dorigo M, de Oca MAM, Engelbrecht A (2008) Particle swarm optimization. *Scholarpedia* 3 (11):1486
10. Bratton D, Kennedy J (2007) Defining a standard for particle swarm optimization. In: Swarm intelligence symposium, 2007. SIS 2007. IEEE, pp 120–127
11. Hu JX, Zeng JC (2007) Two-order oscillating particle swarm optimization. *J Syst Simul* 19 (5):997–999
12. Qin Z, Yu F, Shi Z, Wang Y (2006) Adaptive inertia weight particle swarm optimization. In: Artificial intelligence and soft computing–ICAISC 2006. Springer, Berlin, pp 450–459

13. Zhao H, Feng L (2014) An improved adaptive dynamic particle swarm optimization algorithm. *J Netw* 9(2):488–494
14. Pohlheim H (2010) Geatbx: example functions (single and multi-objective functions) 2 parametric optimization. GEATbx Database
15. Zhang Q, Xue X, Zhou D, Wei X (2014) Motion Key-frames extraction based on amplitude of distance characteristic curve. *Int J Comput Intell Syst* 7(3):506–514
16. Bulut E, Capin T (2007) Key frame extraction from motion capture data by curve saliency. In: *Computer animation and social agents*, p 119

# Quantitative Analysis of Air Injection for Compressor Active Control

Zhanheng Sun, Sanmai Su, Junjie Liu and Gao Rao

**Abstract** Aimed at analysing compressor stability with continual air injection quantitatively, the effect of injection air flow coefficient was investigated based on the Moore–Greitzer model with air injection. By changing the jet velocity for changing the quasi-steady state of the compressor, the influence of constant flow coefficient on the stability of the compressor was analysed theoretically. The results show that the compressor characteristic variation is the stability mechanism of compression system with air injection. Increasing the jet speed makes the compressor characteristic lineup, and the critical stall point shifts to left. There exists a corresponding minimum injection velocity for different throttle coefficients and the stability margin can be determined theoretically.

**Keywords** Aeroengine · Compressor active control · Stall · Air injection · Flow coefficient · Stability analysis

## 1 Introduction

Compressor is one of the important components in aeroengine, which limits the performance of engine as it enters stall and surges status. Active stability control has been the current research focus of compressor stability control field for the purpose of high efficiency and performance achieving [1, 2]. Air injection was proved to be one of the most promising methods for stall control [3].

Most researches on air injection mostly focus on the stability mechanism. Theory analysis indicates that the physical mechanism for eliminating rotating stall is prohibiting the back flow [4] or changing the movement of the vortex trajectory [5] through the tip clearance. Researchers investigated the stability mechanism experimentally in low-speed compression systems, which proved the positive

---

Z. Sun · S. Su (✉) · J. Liu · G. Rao  
School of Power and Energy, Northwestern Polytechnical University,  
Xi'an 710072, China  
e-mail: microeng@nwpu.edu.cn

© Springer-Verlag Berlin Heidelberg 2016  
B. Huang and Y. Yao (eds.), *Proceedings of the 5th International Conference on Electrical Engineering and Automatic Control*, Lecture Notes in Electrical Engineering 367, DOI 10.1007/978-3-662-48768-6\_113

1015

influence of air injection for compression systems' stability [6, 7], and concluded that air injection inhibits the development of modal wave perturbation [8].

However, the issue that smaller injected flow coefficient just postpones the inception of stall [7], but larger flow stabilizes the compressor [6, 8], which some researchers may meet in experiments, has not been fully discussed. And literatures on quantitative analysis about the critical parameter, namely injected flow coefficient, are rare.

This paper analysed the stability mechanism in quasi-steady-state compressor characteristic shift aspect based on Moore–Greitzer model with air injection, and the effective injected air flow coefficient which prohibits rotating stall is analysed theoretically.

## 2 Compression System Model

Figure 1 shows the simplified structural model of the compression system, which includes upstream duct, injectors, compressor, downstream duct, plenum and throttle valve, where the plenum was considered as the combustion chamber in aeroengine for volume effect and the throttle valve simulated the turbine for pressure drop and throttle characteristics.

The classic model which uses flow and pressure rise coefficient to capture both stall and surge dynamic characteristics of the compression system shown in Fig. 1 was established by Moore and Greitzer [9] as follows:

$$\begin{cases} \frac{d\Psi}{d\xi} = \frac{1}{4l_c B^2} (\Phi - \gamma\sqrt{\Psi}) \\ \frac{\partial\Phi}{\partial\xi} = \frac{1}{l_c} \left( \Psi_c(\Phi) - \Psi + \frac{J_1}{4} \frac{\partial^2\Psi_c}{\partial\Phi^2} \right) \\ \frac{dJ_1}{d\xi} = \frac{1}{2+\mu} J_1 \left( \frac{\partial\Psi_c}{\partial\Phi} + \frac{J_1^2}{8} \frac{\partial^3\Psi_c}{\partial\Phi^3} \right) \end{cases} \quad (1)$$

where  $J_1$  stands for the first Fourier mode squared,  $\Psi$  stands for the compressor pressure rise coefficient,  $\Phi$  stands for the mass flow coefficient,  $\xi$  stands for the nondimensional time,  $\gamma$  stands for the throttle coefficient, and  $\Psi_c(\Phi)$  stands for the quasi-steady-state compressor characteristic, and for the other parameters, see Ref. [8].

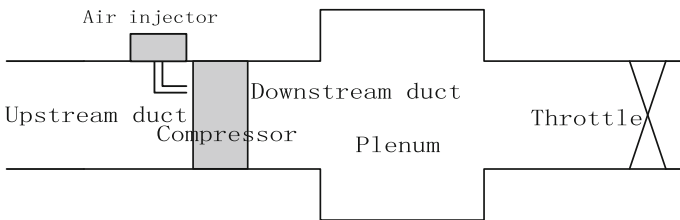


Fig. 1 Sketch and the section definition of compressor system with air injector

The quasi-steady-state compressor characteristic  $\Psi_c(\Phi)$  differs from specific compressor, and the stable region was obtained from experiments and the unstable section was estimated. Typical characteristics describe compressor pressure rise changing with flow. There are many expressions of this feature, but in control has been widely recognized in the literature indicating that the feature is the cubic function. In F.K. Moore and E.M. Greitzer’s study,  $\Psi_c(\Phi)$  could be approximated by a cubic polynomial given by:

$$\Psi_c(\Phi) = \Psi_0 + H \left( 1 + \frac{3}{2} \left( \frac{\Phi}{W} - 1 \right) - \frac{1}{2} \left( \frac{\Phi}{W} - 1 \right)^3 \right) \tag{2}$$

The relevant parameter definition is shown in Fig. 2, where  $\Psi_t(\Phi) = \Phi/\gamma^2$  defined as the throttle characteristic.

When compressor is working in stable region, namely  $J_1 = 0$ , the derivatives of each variable on the left of Eq. 1 equal 0, and the flow coefficient through compressor and pressure rise coefficient satisfies the following:

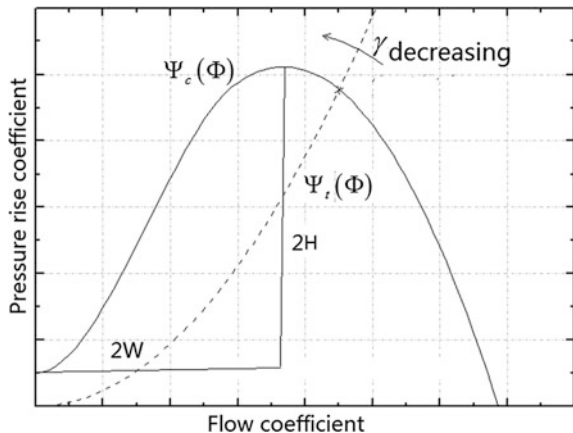
$$\Psi_c(\Phi) - \frac{1}{\gamma^2} \Phi = 0 \tag{3}$$

Steady-state operating point of the compressor system is the compressor and the throttle valve characteristic intersection, and the image shown in Fig. 2 corresponds to the solution of Eq. 3.

The compression system model with continual air injection was studied by Behnken et al. [2–10], and the model with continual air injection operating in stable state is given by:

$$\Psi_{cu}(\Phi) - \frac{1}{\gamma^2} \Phi^2 = 0 \tag{4}$$

**Fig. 2** Compressor and throttle characteristics





$$\Psi_{cu}(\Phi) = \Psi_c(\Phi) + \Psi_j(\Phi) \tag{5}$$

where  $\Psi_j(\Phi) = \left(\frac{h_a + h_j}{h_a} \Phi_j - \Phi\right) \frac{h_j}{h_a} \Phi_j - \frac{1}{2} \left(\frac{h_j}{h_a} \Phi_j\right)^2$  indicates a shift in the steady-state characteristic of the compressor because of introducing the momentum.

Addition effects,  $h_a$  and  $h_j$  are compressor inlet area and the opening of the air injector;  $\Phi_j$  is the injected flow coefficient.

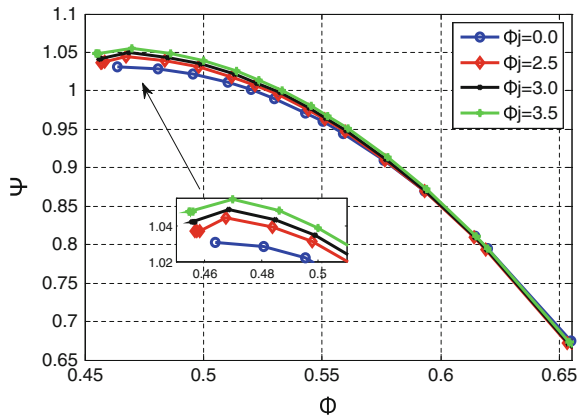
### 3 Effect of Continual Air Injection

The effect of continual air injection was verified theoretically and experimentally [6–8]. Figure 3 shows the general result in compressor characteristic. The legend and coordinate calibration on the figure shows the relative size and has nothing to do with the real quantity in experiments.

We conclude the effect as two aspects: the pressure rise enhancement and the flow coefficient decrement in critical stall point. The higher the injected flow coefficient is, the better it works.

And an implicit fact we learn from Fig. 3 is that there is a limitation for certain injected flow coefficient functioned. A corresponding minimum flow through compressor exists for specific injected flow and the compressor enters stall if the main flow decreases over the minimum flow. It is in agreement with the observation in the experiment [7], and the operation failure of injected air is highly related to the compressor working state.

**Fig. 3** Compressor and throttle characteristics



### 4 The Stability Analysis of Compressor with Continual Air Injection and Injected Flow Coefficient Determination

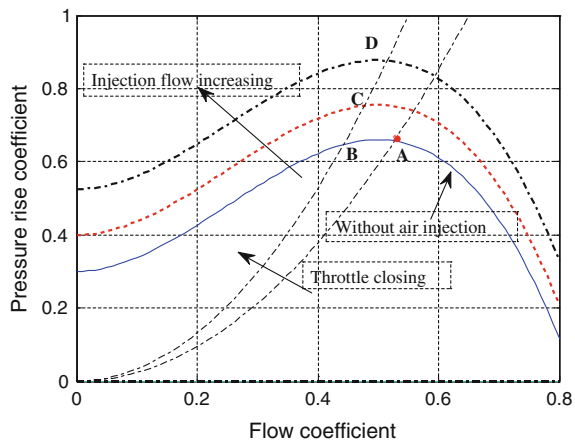
$\Psi_{cu}(\Phi)$  in Eq. 5 is the quasi-steady-state characteristic of the compressor with continual air injection. And the characteristic changes as the injected flow coefficient increases, which is the principle of eliminating instability using continual air injection.

Figure 4 shows the compressor characteristics with different air injection. It is obvious that the steady-state compressor characteristic moves upward and the critical stall point moves leftward, and different injected flow coefficient corresponds to different characteristic.

The compressor operates stably at the critical stall point A at beginning, with the corresponding throttle coefficient  $\gamma_1$ . When the operating state changes, i.e. the throttle coefficient decreases to  $\gamma_2$  from the beginning  $\gamma_1$ , the equilibrium point crosses the critical point A and reaches the point B, the intersection point of throttle and compressor characteristic curve, which implies the stall state occurring in this compression system, the mean pressure rise and the flow coefficient dropping followed. Eliminating instability, continual air injection is used. The system still remains stall while the injected air flow coefficient  $\Phi_j$  is small, i.e. the intersection point C. The intersection point moves as  $\Phi_j$  increases, until the new critical stall point D, where the compressor operates stable. If the compressor quits stall, it must satisfy the following:

$$\Psi_{cu}(\Phi_1) - \frac{1}{\gamma_2^2} \Phi_1 \geq 0,$$

**Fig. 4** Compressor characteristic with different flow coefficients



namely

$$\Psi_0 + H \cdot \left(1 + \frac{3\alpha}{2W} - \frac{\alpha^3}{2W^3}\right) - \frac{h_j}{h_a} \Phi_j (W + \alpha) + \frac{h_j}{h_a} \Phi_j^2 + \frac{h_j^2 \cdot \Phi_j^2}{2h_a^2} - \frac{1}{\gamma_2^2} (W + \alpha)^2 \geq 0 \quad (6)$$

$\Phi_{j0}$  is the minimum injected flow coefficient for stability purpose which holds the equality.

For a specific compressor state, that is certain  $\gamma_2$ , the compression system stays unstable if the injected flow coefficient is less than  $\Phi_{j0}$ . This theory can explain the limitation in Fig. 2 and the failure in experiment [7].

Intersection point moves rightward while increasing injected flow coefficient, as shown in Fig. 4. For achieving stability margin, namely  $\text{Exp} \geq 0$ , it must satisfy the following:

$$\Psi_{\text{cu}}(\Phi_0) - \frac{1}{\gamma_2^2} \Phi_0 \geq 0 \quad (7)$$

$\Phi_{j1}$  is the maximum injected flow coefficient for stability purpose which holds the equality. By solving the inequality, we have the following:

$$\Phi_{j1} = \left[ -k + \sqrt{k^2 - 2 \left(\frac{h_j}{h_a}\right)^2 \left(2H + \Psi_0 - \frac{4W^2}{\gamma_2^2}\right)} \right] / \left(\frac{h_j}{h_a}\right)^2$$

From the above analysis, for the fixed injector opening, we concluded that in the specific unstable state, i.e. the throttle coefficient  $\gamma_2$ , stall will be eliminated and the stability margin will be expanded, while  $\Phi_j$  satisfies the following:

$$\Phi_{j0} \leq \Phi_j \leq \Phi_{j1} \quad (8)$$

## 5 The Effects of Continual Air Injection on Stability Margin

For the purpose of quantifying the stability margin [8]  $\text{Exp}$ , we have the following:

$$\text{Exp} = \left(1 - \frac{m_{\text{with}}}{m_{\text{without}}}\right) \times 100\% \quad (9)$$

where  $m_{\text{with}}$  and  $m_{\text{without}}$  are the flow of critical stall point with and without air injection, respectively.

Without considering the effects of viscosity, the critical stall point locates the top point of the characteristic, and the curve slope of the characteristic is 0 [10]. According to bifurcation theory, the critical point is at the left of the peak considering viscosity.

Ignoring the viscosity, having  $\Phi_0, \Phi_1$  being the critical stall point with and without air injection, respectively, we get the following:

$$\Phi_0=2 W, \Phi_1= W + \alpha$$

where  $\alpha^2 = W^2 - \frac{2W^3}{3H} \cdot \frac{h_j}{h_a} \cdot \Phi_j$ , The corresponding pressure rise coefficient are given as:

$$\Psi_0 = \Psi_0 + 2H$$

$$\Psi_1 = \Psi_0 + H \cdot \left(1 + \frac{3\alpha}{2W} - \frac{\alpha^3}{2W^3}\right) - \frac{h_j}{h_a} \Phi_j(W + \alpha) + \frac{h_j}{h_a} \Phi_j^2 + \frac{h_j^2 \cdot \Phi_j^2}{2h_a^2}$$

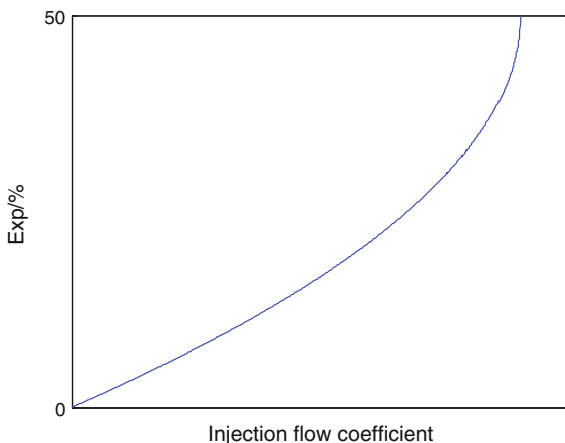
Using Eq. 9, we have the stability margin as:

$$\text{Exp} = (0.5 - \alpha/2 W) \times 100 \% \tag{10}$$

which indicates that the stability margin is related merely to injected flow coefficient, i.e. the injected mass flow, for the given compressor.

Figure 5 shows the tendency of the stability margin with the injected flow coefficient incensement. From the figure, we concluded that the stability margin increases with the injected flow coefficient, and the maximum value is 50 % theoretical, with the corresponding injected flow coefficient  $\Phi_j = 3H/2 W \cdot h_a/h_j$ . But due to the limitation of physical condition virtually, the theoretical value of the injected flow coefficient is much greater than the actual value, and the effective part is the left portion in Fig. 5 merely. For a specific injected flow and injector opening, the stability margin is a certainty.

**Fig. 5** Stability margin evolution over injected flow coefficient



## 6 Conclusions

The mechanism of eliminating stall behaviour by using continual air injection was analysed from compressor characteristic shift perspective, based on the Moore–Greitzer model with air injector. We concluded that the compressor characteristic shift induced by continual injection, that is critical stall point moving leftward, is one of the explanations of stabilizing rotating stall by using air injection. There is a certain range of air injection flow coefficient, which has the compressor quit stall and achieves some stability margin under specific unstable operation. The stability margin have exact theoretical value for a given injected air flow coefficient.

**Acknowledgements** Grateful acknowledgement is made of the Aeronautical Science Foundation of China (2013ZB53019) for this work.

## References

1. Sanmai S, Lv Y, Huang S (2014) Analysis of aircraft engine active stability control method. *Adv Aeronaut Sci Eng* 5(1):7–11
2. LV Y (2014). Research on modeling method of aero-engine compressor active stabilization control. Northwestern Polytechnical University, Xian
3. Hendricks GJ, Gysling DL (1994) Theoretical study of sensor-actuator schemes for rotating stall control. *J Propul Power*. doi:[10.2514/3.23717](https://doi.org/10.2514/3.23717)
4. Zhang H, Chu W, Lu X et al (2006) Numerical investigation of tip injection effect on a high speed axial compressor flow field and performance. *J Aerosp Power*. doi:[10.13675/j.cnki.tjjs.2006.06.006](https://doi.org/10.13675/j.cnki.tjjs.2006.06.006)
5. Lu X, Chu W (2007) Exploring mechanism of stall margin enhancement of subsonic axial flow compressor through steady micro tip injection. *J Northwest Polytechnical Univ* 25(1):17–21
6. Tong Z, Nie C, Zhu J (2006) Investigation on micro tip injection improving the stability of an axial compressor. *J Eng Thermophys* 27(1):121–124
7. Nie C, Xu G, Cheng X et al (2002) Micro air injection and its unsteady response in a low speed axial compressor. *J Turbomach*. doi:[10.1115/1.1508383](https://doi.org/10.1115/1.1508383)
8. Li L, Hu J, Wang Z et al (2006) Experiment of effect of micro injection on compressor stability. *J Propul Technol*. doi:[10.13224/j.cnki.jasp.2014.01.021](https://doi.org/10.13224/j.cnki.jasp.2014.01.021)
9. Moore FK, Greitzer EM (1986) A theory of post-stall transients in a axial compressor systems: part I: development of equations. *J Eng Gas Turbines Power* 10(1115/1):3239887
10. Behnken RL (1996) Nonlinear control and modeling of rotating stall in an axial flow compressor. California Institute of Technology Pasadena, California

# Thermocapillary Flows in Half-zone Liquid Bridges Under Axial Magnetic Fields

Ruquan Liang, Linyang Zhu, Limin Kong, Fuqiang Yan  
and Shuo Yang

**Abstract** The physical and mathematical model of the liquid bridge in half-floating zone method which is exposed to static magnetic field is built and numerically simulated without the effects of gravity. The governing equations are N-S equations combined with the conservation equation of energy which is calculated by the SIMPLE algorithm. On a staggered grid, the level set function and the continuum surface force (CSF) model is adopted to capture the free surface. The result indicates that under certain strength of static magnetic field, different temperature differences between the two disks and different aspect ratios of the liquid bridge have influence both on the free surface deformation and inner velocity field in different degrees.

**Keywords** Two-phase flow · Liquid bridge · Microgravity · Magnetic field

## 1 Introduction

The floating zone method has been developed and widely used on the ground, which is considered as one of the most promising methods in space material product [1]. In this method, thermocapillary convection is the vital factor of controlling the

---

R. Liang (✉) · L. Zhu · L. Kong · F. Yan · S. Yang  
Key Laboratory of National Education Ministry for Electromagnetic Processes  
of Materials, Northeastern University, 3-11, Shenyang 110819, China  
e-mail: liang@epm.neu.edu.cn

L. Zhu  
e-mail: zhu\_linyang@126.com

L. Kong  
e-mail: klmkdt@163.com

F. Yan  
e-mail: yanffqq@163.com

S. Yang  
e-mail: 812886674@qq.com

quality of crystal growth under microgravity which is driven by surface tension gradient. Experiments have proven that the striations in crystals grown in space may be caused by oscillatory thermocapillary flow in floating zone configurations [2]. Temperature gradient plays a vital role in thermocapillary convection and thus influences the crystal growth. With the development of space technique, the crystal growth technique has been an important research subject.

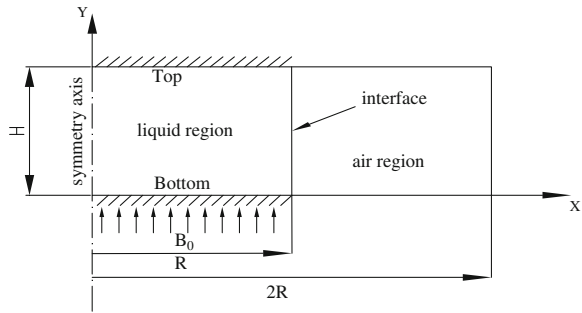
In 1978, C.H. Chun and Wuest carried out an experiment of the thermocapillary oscillatory convection at reduced gravity effect for the first time [3]. Studies of Ruquan Liang, Shuo Yang and Jizhao Li showed that the axial magnetic fields which generate the Lorentz force affect the velocity level both inside the liquid bridge and on the free surface and hindered the fluid motion [4]. Silicon floating zone experiments under static axial magnetic fields, employing P- and Sb-doped crystals of 8 mm diameter and zones of 10–12 mm length, showed that the magnetic field has an effect on the formation of dopant striations [5]. Herrmann et al. (1992) and Cröll et al. (1994) have experimentally proven that steady magnetic fields can suppress the unsteady thermocapillary convection and enhance the character of floating zone [6]. Many studies have focused the attention on the effects of temperature difference and aspect ratios on the stability of liquid bridge. But the effect of these factors under magnetic field on stability of low Prandtl number ( $Pr = 0.09$ ) liquid bridge is rarely reported in the literature. Therefore, it is studied in the present paper.

## 2 Physical and Mathematical Models

The liquid bridge is taken as the study model to simulate the industrial floating zone technique [7]. The liquid region is defined between two flat coaxial disks which are horizontal and differently heated. The radius of liquid bridge with height  $H$  and coaxial cylindrical tube used to control gas stream are  $R$  and  $2R$ , respectively. Correspondingly, the aspect ratio is signed by  $H/R$ . The diameter of the model considered is  $d = 2R = 5.0$  mm and the aspect ratio is 1. The temperatures of upper and lower rods are  $T_u$  and  $T_l$ , respectively. Hereafter, the temperature difference is  $\Delta T = T_u - T_l$ . In this investigation, when dealing with the effect of aspect ratio on thermocapillary, we define  $T_u = 730$  K and  $T_l = 705$  K as the default value. The liquid bridge is surrounded by a concentric annular gas channel under axial magnetic field with strength  $B = 0.01$  T, see Fig. 1.

Let be the velocity field,  $\rho$  the density and the dynamic viscosity. Besides,  $\mathbf{g}$  and  $p$  are denoted as the gravity vector and the pressure, respectively. Then,  $U$  is taken as the characteristic velocity, as the dimensionless temperature and  $L = 2R$  as the characteristic length. Therefore, through a series of simplifying calculations, the dimensionless governing equations for this model are expressed as follows:

**Fig. 1** Model of the half-floating zone liquid bridge under axial magnetic fields



$$\frac{\partial u}{\partial x} + \frac{\partial v}{\partial y} = 0 \tag{1}$$

$$\frac{\partial \mathbf{u}}{\partial t} + \nabla \cdot (\mathbf{u}\mathbf{u}) = -\frac{\nabla P}{\rho} + \frac{1}{\rho Re} \nabla \cdot (2\mu \mathbf{D}) + \left( \frac{1 - Ca\Theta}{We} \right) \frac{\kappa \delta(d)\mathbf{n}}{\rho} + \frac{Ha^2}{\rho Re} (\mathbf{u} \times B_0 \mathbf{e}_y \times B_0 \mathbf{e}_y) \tag{2}$$

$$\frac{\partial \Theta}{\partial t} + u \frac{\partial \Theta}{\partial x} + v \frac{\partial \Theta}{\partial y} = \frac{1}{RePr} \Delta \Theta \tag{3}$$

$$\frac{\partial \Phi}{\partial t} + u \frac{\partial \Phi}{\partial x} + v \frac{\partial \Phi}{\partial y} = 0 \tag{4}$$

where  $\kappa$  is the curvature,  $\delta$  is the Dirac delta function,  $d$  is the level set function,  $\mathbf{n}$  is the unit normal vector directing to the air region and  $\mathbf{D}$  is the viscous stress tensor. The surface tension varies linearly with the liquid temperature which is measured by the temperature coefficient. Therefore, the surface tension can be formulated by, where  $\sigma_0$  is the surface tension value which is set at reference temperature  $T_1$ . The kinematic viscosity is denoted as  $\nu$  where  $\mu$  is the dynamic viscosity. The related dimensionless parameters are expressed as follows:  $Ca$  is the capillary number;  $We$  is the Weber number;  $Re$  is the Reynolds number;  $Pr$  is the Prandtl number;  $Ma$  is the Marangoni number; and  $Ha$  is the Hartmann number. Under the static magnetic field, the Lorentz force is formulated by  $\mathbf{J} \times \mathbf{B}_0$  where  $\mathbf{J}$  is the current density vector and  $\Phi$  is the induced electric potential. Considering no electric potential, the Lorentz force is simplified as [8]. Apart from that, this paper supposes that the liquid motion is laminar and buoyancy effects are not considered.

In this paper, a uniform mesh is adopted to discretize the axisymmetric liquid bridge, and the determination of time step not only meets the CFL condition but also ensure the convergence of calculation. Moreover, the SIMPLE algorithm is used to solve the governing equation and a staggered grid is adopted for the velocity



and distance function. The parts of the boundary conditions are implemented by using the user-defined functions (user-defined function, UDF). The continuum surface force (CSF) model is taken to solve the difficulties in modeling topologically complex interfaces which have surface tension [9]. Finally, the numerical simulation under the axial uniform magnetic fields is completed.

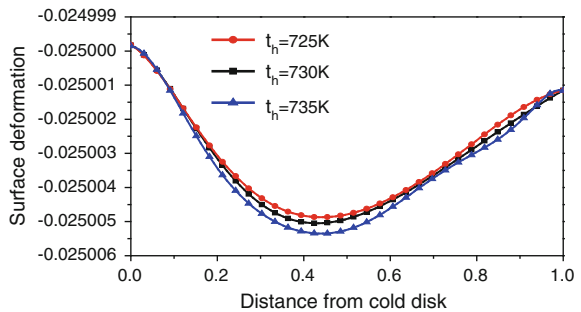
### 3 Results and Discussion

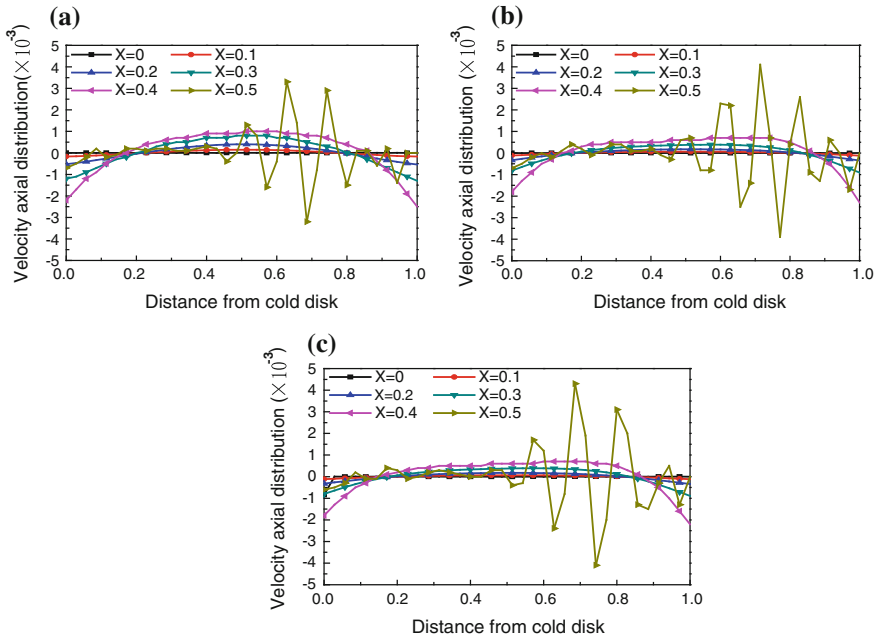
Figure 2 characterizes the deformation on the free surface at different temperature differences. It is found that the maximum value of surface deformation is reached when the distance from cold disk is around 0.43. The magnitude of surface deformation increases with the larger temperature difference. Besides, the effect of temperature difference on the middle part is larger than that on both sides to some extent.

Figure 3 shows the axial velocity distribution at different temperature differences and radius, where  $x = 0$  and  $x = 0.5$  represent the central axis and the free surface, respectively. By comparing Fig. 3a, b, it is found that with the temperature difference increasing, the axial velocity from  $x = 0$  to  $x = 0.4$  becomes a bit smaller, but larger for free surface, see Fig. 3. In Fig. 3a, the maximum value of axial velocity on the free surface is  $3.5 \times 10^{-3}$  or so, while in Fig. 3b is  $4.5 \times 10^{-3}$  or so. The starting point of oscillation on the free surface moves about 0.1 unit distance toward the hot disk. The increase of temperature difference has an enhancing effect on the instability on the free surface.

Figure 4 shows the axial velocity distribution at different radial places at different aspect ratios. The velocity distribution is almost the same when the aspect ratios are  $H/R = 0.8$  and  $H/R = 1.2$ , see Fig. 4a, c. For  $H/R = 1$ , oscillation and variation ranges on the free surface is a bit smaller comparing with the value when the aspect ratios are  $H/R = 0.8$  and  $H/R = 1.2$ , see Fig. 4b, which means that the axial uniform magnetic field can have a better suppressing effect on the thermo-capillary convection of the liquid bridge when the aspect ratio is  $H/R = 1$ .

**Fig. 2** Deformation on the free surface at different temperature difference





**Fig. 3** Axial velocity distribution under different temperature difference. **a**  $\Delta T = 20$  K, **b**  $\Delta T = 25$  K, **c**  $\Delta T = 30$  K

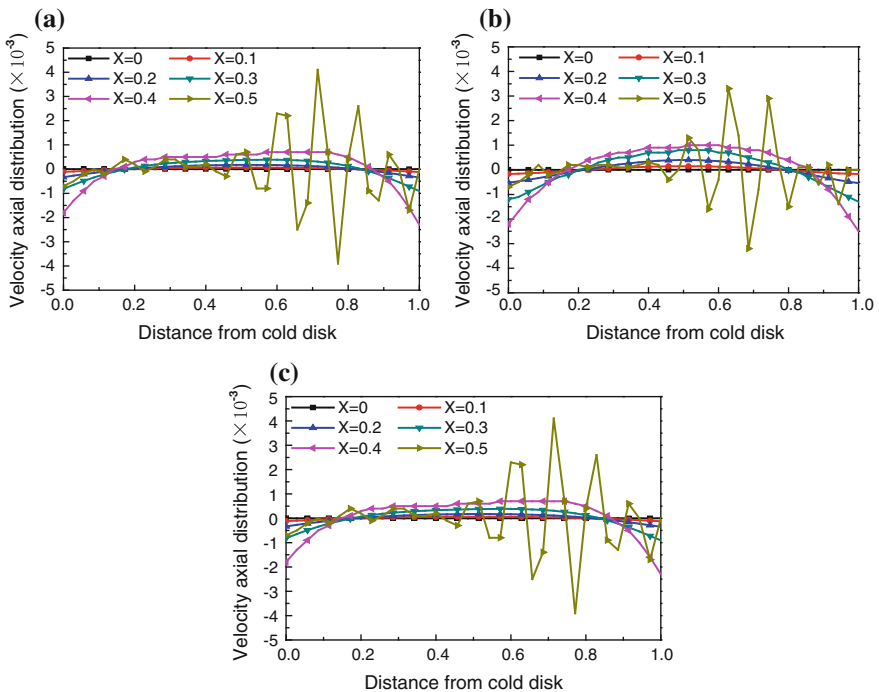


**Fig. 4** Axial velocity distribution by different radial places. **a**  $H/R = 0.8$ , **b**  $H/R = 1$ , **c**  $H/R = 1.2$

## 4 Conclusions

In this paper, it is found that under a certain axial magnetic field, the increasing of temperature difference increases the magnitude of surface deformation and enhances the oscillation on the free surface but has little effect on inside motion. On the other hand, the oscillatory onset of thermocapillary flow is also slightly delayed. The aspect ratio  $H/R = 1$  has a suppressing influence on the fluid motion of the liquid bridge, but this effect is only shown on the free surface rather than the inside.

**Acknowledgements** The present work is supported financially by the National Natural Science Foundation of China under the grant of 51376040 and 11072057.

## References

1. Hu WR, Xu SC (1994) Microgravity fluid mechanics. Science Press, Beijing
2. Li K, Xun B, Imaishi N, Yoda S, Hu WR (2008) Thermocapillary flows in liquid bridges of molten tin with small aspect ratios. *Int J Heat Fluid Flow* 29:1190–1196
3. Chun CH, Wuest W (1978) A micro-gravity simulation of the marangoni convection. *Acta Astronaut* 5:681–686
4. Liang RQ, Yang S, Li JZ (2014) Thermocapillary convection in floating zone with axial magnetic fields. *Microgravity Sci Technol*. doi:10.1007/s12217-013-9353-x
5. Dold P, Cröll A, Benz KW (1998) Floating-zone growth of silicon in magnetic fields. I. Weak static axial fields. *J Crystal Growth* 183:545–553
6. Prange M, Wanschura M, Kuhlmann HC, Rath HJ (1999) Linear stability of thermocapillary convection in cylindrical liquid bridges under axial magnetic fields. *J Fluid Mech* 394:281–302
7. Gaponenko Y, Glockner S, Mialdun A, Shevtsova V (2011) Study of a liquid bridge subjected to interface shear stresses. *Acta Astronaut* 69:119–126
8. Liang RQ, Bei D, Yan FS, Geng DQ (2014) Thermocapillary convection of low prandtl number fluids under uniform magnetic fields. *Appl Mech Mater* 580–583:2970–2973
9. Brackbill JU, Kothe DB, Zemach C (1992) A continuum method for modeling surface tension. *J Comput Phys* 100:335–354

# A Dual-Redundancy Thermal Backup Control Method for the Two-Wheeled Self-balancing Robot

Yong Tao, Tianmiao Wang, Ye Wang, Jianhong Liang  
and Zhongyuan Chen

**Abstract** Aiming at the static instability and vehicle body reliability of the two-wheeled self-balancing robot, this paper puts forward a dual-redundancy thermal backup control method of self-balancing robot based on robot steering sensor and gyroscope robot body attitude sensor. It presents the effective dual-redundancy control scheme, its fault detection and switching method on power supply system, master control logic, driver control, power circuit, and actuator.

**Keywords** Dual-redundancy thermal backup · Self-balancing robot · Gyroscope attitude sensor

## 1 Introduction

A variety of personal vehicles used in the narrow space shuttle, the exhibition inspection, and other special occasions are being developed. Relative to the conventional four-wheeled vehicle, the two-wheeled self-balancing electric robot has the advantages such as energy saving and environmental protection. Through the detection and analysis of the system posture, the self-balance system keeps the state variables in a preset band and keeps the system balance. With the characteristics of flexible movement, intelligent control, and environment friendly, the self-balancing electric robot is a typical unstable, nonlinear, and strong coupling system.

The two-wheeled self-balancing robot has been investigated for a long time and a lot of design and control mechanism have been proposed. The design, analysis, modeling, and control of a two-wheeled balancing mobile robot is discussed for

---

Y. Tao (✉) · T. Wang · J. Liang  
School of Mechanical Engineering and Automation, Beihang University,  
Beijing 100191, People's Republic of China  
e-mail: taoy@buaa.edu.cn

Y. Wang · Z. Chen  
Ninebot Inc., Beijing 100192, People's Republic of China

enhancing lateral stability [1]. A novel narrow vehicle based on a mobile-wheeled inverted pendulum and a movable seat, called UW-Car, is investigated in [2]. A simple Mamdani-like fuzzy controller is presented for a self-balancing vehicle control [3]. An If-Then fuzzy rule-base is given to cooperate with the parallel distributed compensation control of the self-balancing transporter [4]. A novel adaptive output recurrent cerebellar model articulation controller is utilized [5]. In [6], a radial basis-function neural network is proposed for a self-balancing scooter.

Based on the online estimation of the self-balance vehicle's attitude angles, an attitude solution algorithm based on quaternion is given [7]. An active disturbance rejection control method is proposed [8]. A self-balancing human transportation vehicle is proposed for the teaching [9]. An electric drive system for self-balanced vehicles is presented in [10]. The modelings, system design, control and implementation of two-wheeled self-balanced vehicle are introduced in [11–13]. The analysis and design of a passive steering mechanism for a self-balanced vehicle is proposed in [14]. The mechanics principle of two-wheeled electrical motorcycle is analyzed and the system mathematical mode is established [15].

The safe and reliable operation of the two-wheeled self-balancing robot is a key technology under different motion states such as no-load, manned, forward, backward, rotating, and braking. A dual-redundancy thermal backup control method is proposed based on the robot steering sensor and gyroscope body attitude sensor. The failure detection and switching method are presented. The experimental results verify the effectiveness of the proposed method.

## 2 System Description

The dual-redundancy thermal backup method is presented to improve the self-balancing robot safety of two kinds of components. One is the component with higher failure rate and another one is the component whose failure will affect the safety of the components such as the robot actuator, the control and drive circuit, the battery, the gyroscope attitude and steering sensor, and the signal conditioning circuit.

According to the dual-redundancy backup design, the two sets of the working system and the backup system are running at the same time. The working system and backup system monitor the working state through the digital communication mode. Once the backup system detects the system's working fault, it immediately deprives the control of the system and upgrades to the working system. At the same time, it sends out alarm types to notify the user. The body structure layout of the two-wheeled self-balancing robot is shown in Fig. 1.

The dual-redundancy thermal backup control method is used in the actuators, gyroscope attitude sensor, main control logic circuit, actuator control and power amplifier circuit, steering sensor, energy module and monitoring circuit, and the pedal sensors. The structure of the control method is shown in Fig. 2.



Fig. 1 Two-wheeled self-balancing robot

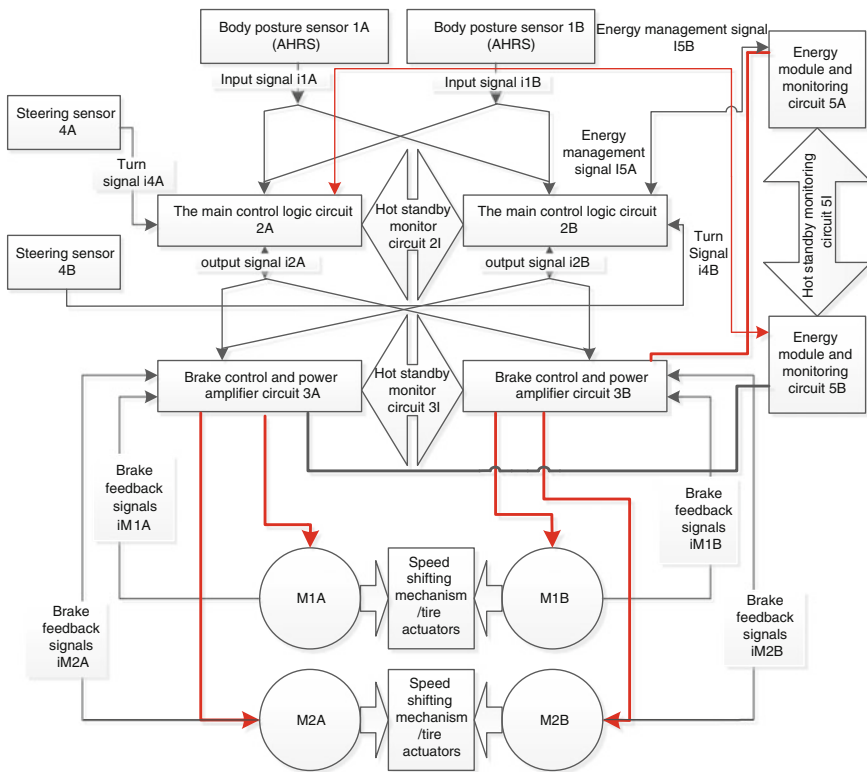


Fig. 2 Structure of the dual-redundancy thermal backup control method

### 3 Dual-Redundancy Thermal Backup Mechanism

#### 3.1 The Mutual Backup of the Gyroscope Attitude Sensor and Steering Sensor to Judge the Validity of the Data and the Fault

There are angular rate gyroscope and accelerometer in the self-balancing robot. The six real-time attitude data are calculated, which are the steering angle  $D_t$ , the pitch angle  $D_p$ , the rolling angle  $D_y$ , the steering angular rate  $R_t$ , the pitch angular rate  $R_p$ , and the roll rotation rate  $R_y$ . According to the limitation of robot inertia, robot movement restrictions, and driver reaction speed, the attitude data rate is set to the upper limit of the threshold. By comparing the predicted values with the actual values, the sensor is judged whether it is in the normal operation.

There is a typical experiment. The steering angle data  $D_t$  is predicted by Kalman filtering, and the upper and lower limits of the prediction value are obtained. As shown in Fig. 3, the horizontal axis denotes time and the vertical axis denotes  $D_t$ . If the actual value of  $D_t$  of the gyroscope attitude sensor 1A is lower than the limit of the predicted value, and the actual value of the  $D_t$  of the gyroscope attitude sensor 1B is still within the range of the predicted values, then the  $D_t$  of sensor 1A is not correct and the output value of the sensor 1B should be used.

The main control logic circuit will give up all the data from sensor 1A and only use the data from the sensor 1B to ensure that the robot continues to work and not to lose its balance. At the same time, the sound and light are activated to remind drivers of existing internal component failure, the speed are reduced, and the self-balancing robot is parked slowly.

The steering sensor is installed in the self-balancing robot. The driver's output value should be equal to the steering of the robot by a mechanical device. There is an upper limit of the sensor signal output change rate according to the driver's operation. The change rate can be properly predicted by the control method. By comparing the predicted values with the actual values, the sensor is judged whether to be faulty or not.

**Fig. 3** The validity of the output data of the two sets of sensors is predicted by the control method and threshold prediction

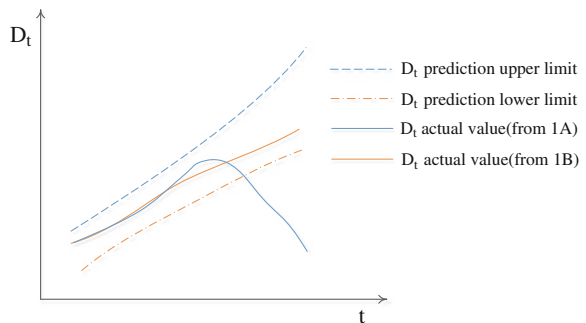
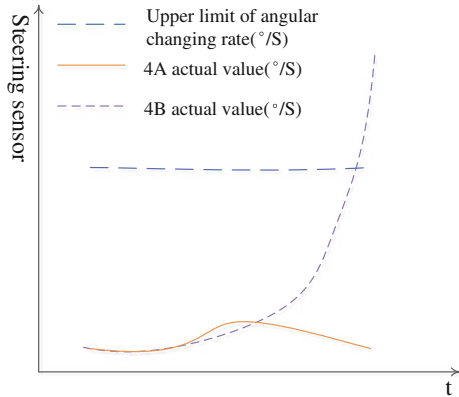


**Fig. 4** Judge the effectiveness of the output data of the two sets of sensors by the threshold of the changing rate



In a typical example, the change rate of the steering sensor is set as  $100^{\circ}/s$ , due to the restriction of the mechanical structure and the control of the manipulator. As shown in Fig. 4, when the actual value of the steering sensor 4A exceeds the threshold value and the steering sensor 4B is still in the range of the threshold value, the steering sensor 4A is not correct and the steering sensor 4B should be taken as a valid value.

### 3.2 *The Interactive Backup, Fault Judgement, and Switching of Two Sets of Control Logic*

Master controller of the robot provides driving signal excitation to drive circuit via sensor input and appropriate solution. The fault of this unit will cause the robot lose balance. The two master controllers with exactly same functions are connected via the data line and then send the query signal to each other regularly with the frequency of 1000 Hz, which is the mutual-check heartbeat mechanism. Then, the other part returns the signal value received from the self-sensing device, the output value after resolving, and other data.

In a typical example, these data include the single value received from the self-sensing device and the output value after resolving. If a certain master controller 2B is under fault, then it will not response to the inquiry of the master controller 2A. At this time, the master controller 2A will know that the master controller 2B is under fault, and then initiatively acquires the control right and then emerges the alarm signal (Fig. 5).



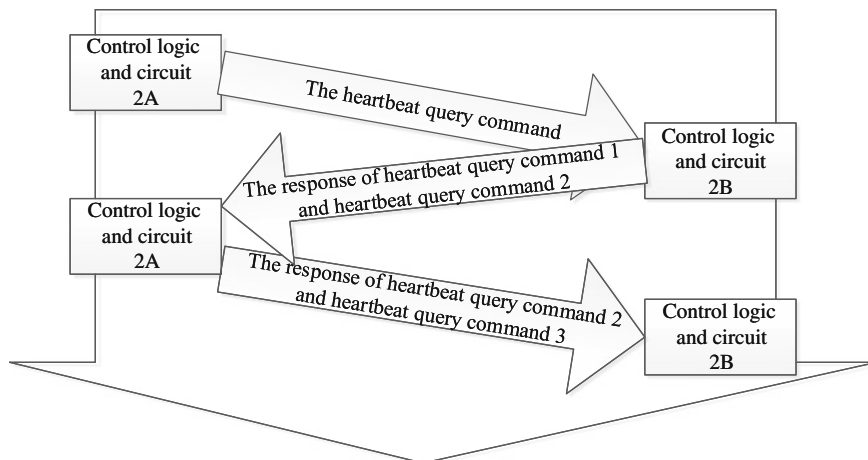


Fig. 5 Principle schematic diagram of mutual-check heartbeat mechanism

### 3.3 *Judgement of Actuator Fault and Thermal Backup Process Method*

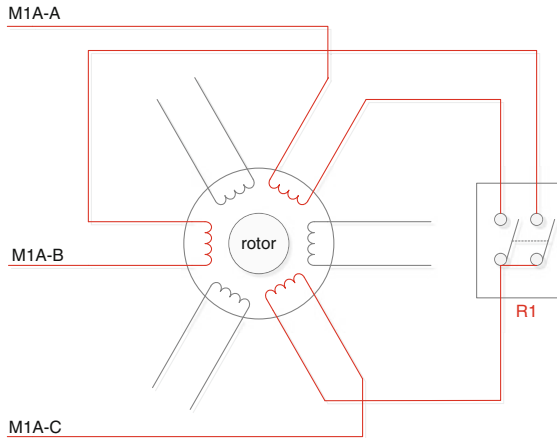
The robot is judged whether it is invalid through the sensor on actuator, winding resistance, inductance value, and other electrical characteristics of the actuator itself. Then, the two actuators are connected to the tire in the same side. When any actuator works normally, the whole system can work normally.

If any actuator is under fault, then the arrester brake control and driving circuit can judge which actuator is under fault. Then, it can cut off the electrical connection of that fault actuator through the breaker circuit and emerge the alarm signal.

In a typical example, the DC brushless motor is applied to the actuator. If output of this motor speed measured sensor is not correct or has no output, then the duty ration of drive current and output PWM will be obviously abnormal. For example, the change rate exceeds the specific threshold value and absolute values exceed the preset security threshold value. This situation can be detected via current sensor, so as to judge its fault.

In a typical example, the two DC brushless motors with 2 sets of independent stator winding are applied to the actuator. There are two double-winding DC brushless motors in the system, which drive the tires in the left side and right side. Each DC brushless motor integrates 2 motor rotors, 2 sets of winding, and 2 sets of speed and rotor position sensor on its spin axis. It is equivalent to that two motors share one case and rotor. M1 is divided into 2 independent stator windings through the specific winding mode: The motor M1A and motor M1B windings share the same axis, the same rotor, and same case in physics. But they are isolated in logical and electrical aspects. Therefore, M1 can be handled as the two motors of M1A and

**Fig. 6** Double-winding motor

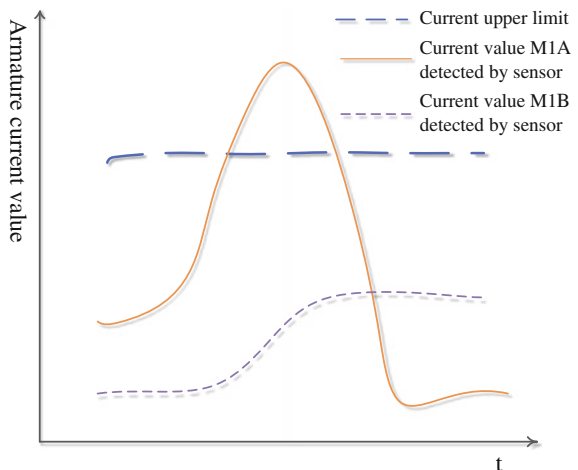


M1B, and then M2 can also be handled as the two motors of M2A and M2B, as shown in Fig. 6.

The M1A-A, M1A-B, and M1A-C are the three armature terminals of winding M1A. The R1 is the normal open relay, which is applied to cut off the electrical connection between the motor M1A winding and driving circuit under abnormal situation.

The armature inner resistance of motor M1A and M1B determines that their maximum current values are no more than 100 A. If the winding part of M1A is burned, then the drive current will rise to more than 100 A. The situation can be detected by the current sensor installed in driver circuit 3A, as shown in Fig. 7. The abscissa axis displays the time and the vertical axis displays armature current value.

**Fig. 7** The related current variation when one winding in double-winding motor emerges fault



In a certain moment, the M1A raises to exceeding the current up-limit value, so as to judge the winding fault of motor M1A. At this time, the driving circuit 3A cuts off the output of M1A winding and then notifies the driving circuit 3B through the thermal backup monitoring line 3I.

When 3B receives the single, it immediately opens M1B winding to replace the work of M1A. Because the work frequency of monitoring line 3I can reach to 10 kHz, the time consumption during 1 ms and winding switching process is not more than 1 s. Therefore, the user cannot feel this switching process. In this way, it can effectively pretend the incidents caused by losing balance of the whole robot because of motor winding burning.

### ***3.4 Judgement on Driving Circuit Fault and Thermal Backup Process Method***

Assume the driving circuit 3A has the control right at present and it is controlling the motor M1A and motor M2A. The motors M1B and M2B are under open-circuit state. If at a certain moment, the driving circuit 3A emerges fault, it is usually shown in the following form:

- The abnormal change of current and PWM;
- The abnormal change of temperature on circuit board;
- It does not make the correct answer on the mutual-check heartbeat query issued to the driving circuit 3B.

The driving circuit 3B can immediately cut off the electrical connection between winding M1A, M2A, and 3A through the thermal backup monitoring line, so as to make it under the open-circuit state, and then immediately starts to drive winding M1B and M2B. It will apply the self-replacement of 3B for 3A, apply M1B to replace M1A, and M2B to replace M2A, so as to ensure that the robot does not lose momentum and balance. The 3B immediately notifies the situation to master control logic 2A/2B through communication data line; the later one can emerge sound light alarm to the driver and then control the robot to slow down and stop voluntarily, in order to ensure the safety of driver.

### ***3.5 Judgement on Pedal Detection Sensor Fault and Thermal Backup Process Method***

In order to improve the safety under the unexpected situation, it designs 4 pedal detection sensors to detect whether there is driver driving the two-wheeled self-balancing robot. If there is driver on the robot, in general, his left and right feet are standing on the pedal; at this time, apply micro-switch and photoelectric to

approach the sensor or resistance strain gage, and others that can be served as the pedal detection sensor to detect whether there are feet standing on. In order to ensure safety, there are 2 sensors set up on the left and right feet treading position. These sensors are simply connected to 2A or 2B, and then apply the parallel mode to judge its state. When any sensor detects the treading state, the master control logic 2A or 2B sets that there is someone driving on the robot.

During the driving process, if the driver drops due to the accident, the pedal detection sensor can immediately detect that there is nobody treading on the robot. Then the master control logic will change to the quickly reduce the control quantity of actuator control and power amplifier circuit output. The vehicle immediately reduces the response sensitivity and output power, and then automatically cut off power when the vehicle body inclination, output current, and temperature exceed a certain threshold. This function also makes the power to be restricted within the safety scale when the two-wheeled self-balancing vehicle starts and stops. In this way, the reaction speed is slower, which can avoid the driver emerge accidents because of miss-operation when getting on or off the vehicle.

The output single in each pedal detection sensor is individually connected to the main control logic circuit, so that the main control logic circuit can apply majority method to detect whether the sensor is invalid when the driver opens. If it defects that a certain sensor is invalid, the main control logic circuit will apply sound and light alarm to prompt the driver and stop the work.

The output single of pedal detection sensor is filtered through Schmidt trigger software; its output single can still keep a short time 0.6 s after the disappearing of intention. Therefore, even the jitters, physical activity of driver during the driving process that one foot leaves the pedal or double feet leave the pedal will not lead to error judgment of robot that the driver has gone off the robot. In this way, it can not only ensure the effective detection whether the driver is on the robot, but also ensure the interference in short time will not affect the normal work of foot pedal detection mechanism.

## 4 Conclusion

Through the analysis on the working condition and actual application environment of two-wheeled self-balancing robot, it puts forward the dual-redundancy control method for power supply system, steering sensor, vehicle body attitude sensor, master control logic, driver control, power circuit, and actuator. It proposes the fault detection and switching method, which can continue to work reliably under the situation that one of the thermal backup components is invalid, so as to avoid that the robot immediately goes out of control and loses balance. The test result shows that the dual-redundancy thermal backup method can effectively prevent the losing control of robot caused by key components fault.

## References

1. Kwon SJ, Kim S, Yu J (2015) Tilting-type balancing mobile robot platform for enhancing lateral stability. *IEEE/ASME Trans Mechatron* 20:1470–1481
2. Huang J, Ding F, Fukuda T et al (2013) Modeling and velocity control for a novel narrow vehicle based on mobile wheeled inverted pendulum. *IEEE Trans Control Syst Technol* 21(5):1607–1617
3. Chiu CH, Chang CC (2012) Design and development of Mamdani-Like Fuzzy control algorithm for a wheeled human-conveyance vehicle control. *IEEE Trans Industr Electron* 59(12):4774–4783
4. Huang C-H, Wang W-J, Chiu C-H (2011) Velocity control realisation for a self-balancing transporter. *IET Control Theory Applications*. 5(13):1551–1560
5. Chiu CH (2010) The design and implementation of a wheeled inverted pendulum using an adaptive output recurrent cerebellar model articulation controller. *IEEE Trans Ind Electron* 57(5):1814–1822
6. Tsai CC, Huang HC, Lin SC (2010) Adaptive neural network control of a self-balancing two-wheeled scooter. *IEEE Trans Ind Electron* 57(4):868–873
7. Zengfeng YE, Feng E (2012) Attitude stabilization based on quaternion and Kalman filter for two-wheeled vehicle. *Chin J Sen Actuators Pap* 25(4):524–528
8. Jian HU, Yan GF (2014) Analysis of two-wheeled self-balancing mobile robots based on ADRC. *J Mech Electr Eng* 31(2):159–164
9. Lin SC, Tsai CC (2009) Development of a self-balancing human transportation vehicle for the teaching of feedback control. *IEEE Trans Educ* 52(1):157–168
10. Hofer K (2010) Electric drive system for self-balanced vehicles. In: *Proceedings of INDUSCON*, pp 1–4
11. Rumi SMI et al (2014) System design of two wheeler self-balanced vehicle. In: *Proceedings of mechatronics*, pp 331–336
12. Huang CF, Yeh TJ (2011) Modeling, control and implementation of a pedaled, self-balanced unicycle. In: *Proceedings of SII*, pp 1323–1328
13. Huang, CF, Yeh TJ (2012) Modeling and control of a pedaled, self-balanced unicycle. In: *Proceedings of AIM*, pp 965–970
14. Hong JH et al (2013) Analysis and design of a passive steering mechanism for a pedaled, self-balanced, personal mobility vehicle. In: *Proceedings of SII*, pp 179–184
15. Yun-Wu TU et al (2004) Model and simulation of self-balance control system. *Acta Simulata Systematica Sinica* 16(4):839–841

# The Influence of Surface Roughness on the Aerodynamic Characteristics of Overhead Wire

Zhangqi Wang and Lizhong Qi

**Abstract** The aerodynamic characteristic parameters are the foundation of vibration analysis of the overhead conductors. In this paper, a typical overhead conductor is studied using computational fluid dynamics (CFD) method. The smooth wire model and rough wire model are established, respectively, and the experimental analysis is carried out in the numerical wind tunnel. The aerodynamic parameters are obtained, and the influence of roughness of the wire surface is investigated.

**Keywords** Overhead wire · Surface roughness · Aerodynamic characteristics · CFD

## 1 Introduction

The overhead conductor breeze vibration and galloping and subspan oscillation are all wind-induced vibration [1–3]. In the studies of wire vibration problems, the accurate and reasonable expression of wind forces acting on overhead line is very important. Therefore, the study of wire aerodynamic characteristics of wire is the basis of vibration analysis.

In the wind-induced vibration analysis of overhead conductors, the unsteady aerodynamic force acting on the wire is directly related to the flow separation and vortex formation, which has strong nonlinear characteristics, so it is difficult to simplify potential flow theory or some analytic formulas to describe the unsteady aerodynamic force. In the early stage of the research, the wind tunnel experiment is the foundation, and the air dynamic parameters of the wire are obtained through the experiment. However, wind tunnel test cannot meet the variety of needs of the actual engineering, due to the presence of high cost, long period, measuring accuracy, limited means, model test, and practical problems of the equivalence

---

Z. Wang (✉) · L. Qi

Department of Mechanical Engineering,

North China Electric Power University Baoding, Beijing, China

e-mail: wzq2146@163.com

© Springer-Verlag Berlin Heidelberg 2016

B. Huang and Y. Yao (eds.), *Proceedings of the 5th International*

*Conference on Electrical Engineering and Automatic Control*, Lecture Notes

in Electrical Engineering 367, DOI 10.1007/978-3-662-48768-6\_116

1039

problem. Therefore, the development and progress of the numerical wind tunnel technology based on computational fluid mechanics (computational fluid dynamics (CFD)) provides a new way for the calculation of the fluid dynamic parameters [4–7].

In this paper, the numerical simulation method is used to calculate the aerodynamic parameters of smooth wire model and rough wire model to study the influence of surface roughness. The calculated results and the existing wind tunnel test results were compared, to explore the conductor surface roughness on the gas dynamic parameters.

## 2 Finite Element Model of Overhead Conductor

The surface roughness of the wire will have an effect on the aerodynamic characteristics of the wire. This paper analyzes the influence of the surface roughness on the aerodynamic characteristics of a high-voltage engineering that uses the JL1/G3A-1250/70-76/7-type overhead wires. Here, the wire roughness  $R$  is defined as follows:

$$R = \frac{d}{D} \quad (1)$$

in which,  $D$  is the strand wire diameter, and  $d$  is the diameter of wire.

The aerodynamic characteristics of the wire mainly depend on its cross section shape as power transmission conductor is slender structure, so the simplified two-dimensional model can be used. In this paper, the numerical simulation of the two-dimensional turbulent flow in the wire is carried out using the fluid mechanics analysis software. The flow field is more than 10 times of the diameter of the wire during the establishment of the flow field model. The fluid analysis model and the dividing grid are shown in Fig. 1a, b respectively. Figure 2a, b shows the local enlargement of the rough lead model and the smooth lead model.

During the calculation, the left side of the area is set as the velocity inlet boundary, the right side is set as the outflow boundary, and the conductor is set as the solid boundary. Air density is  $1.205 \text{ kg/m}^3$ , air movement viscosity is  $1.48 \times 10^{-5} \text{ m}^2/\text{s}$ , and turbulent viscosity ratio is 10. In order to solve the problem of velocity and pressure coupling in the momentum equation, the SIMPLE algorithm is adopted. In order to overcome the numerical simulation of numerical instability at high Reynolds number, use the QUICK windward format, the convection term for the third-order accuracy, and the remaining items such as diffusion term for the second-order accuracy.

In this paper, the aerodynamic parameters of a smooth overhead wire model and a rough lead model are calculated by calculating the wind speed 5–30 m/s (interval 1 m/s).

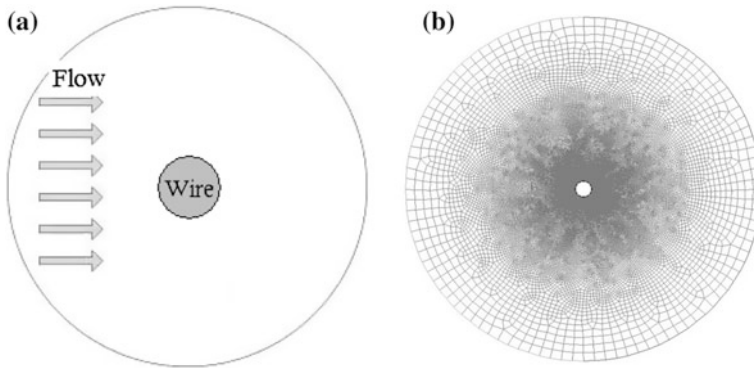


**Fig. 1** Geometry model of external flow field of conductors. **a** Geometry model. **b** Subdivision model

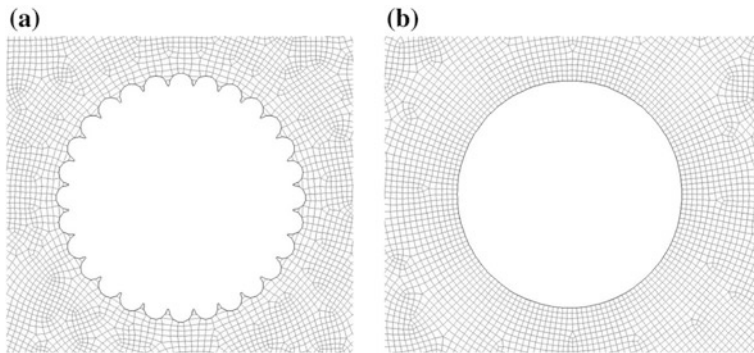


**Fig. 2** Local enlarged image of wire boundary model. **a** Rough model. **b** Smooth model

### 3 Calculation Results and Analysis

Figures 3, 4, and 5 show the lift coefficients, the drag coefficients, and the moment coefficients during the iterative at the flow speed of 5 m/s.

Lift force is the force perpendicular to the direction of flow, which is induced by the periodic vortex shedding appear at the edge of wire induced wire in the. As shown in Fig. 3, the time-averaged lift of the vortex shedding is generally zero as the wire is a symmetrical structure, so the lift coefficient is always around 0, and the fluctuation frequency is the frequency of vortex shedding  $f_s$ .

Drag force is mainly caused by the pressure difference between the surface of the airflow through the wire and the surface friction before and after wire. The generation and disappear of vortex will produce a flow of resistance to the wire. It is also a periodic force, in which the maximum and minimum values of the two resistance are corresponding to the lift cycle; that is, the change frequency of



**Fig. 3** The lift coefficients iterative

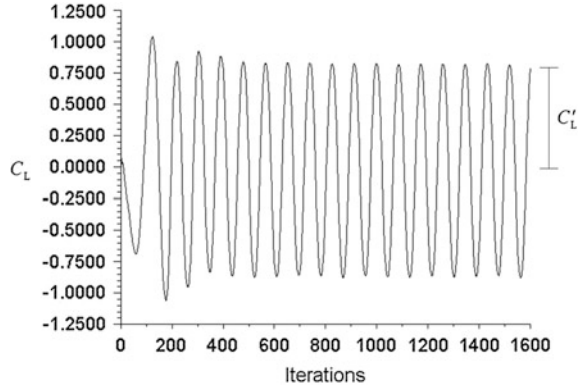


**Fig. 4** The drag coefficients iterative

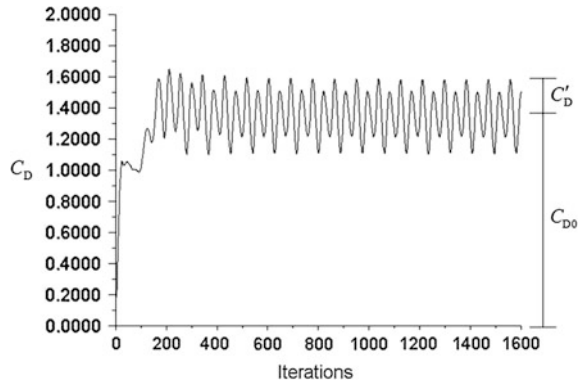
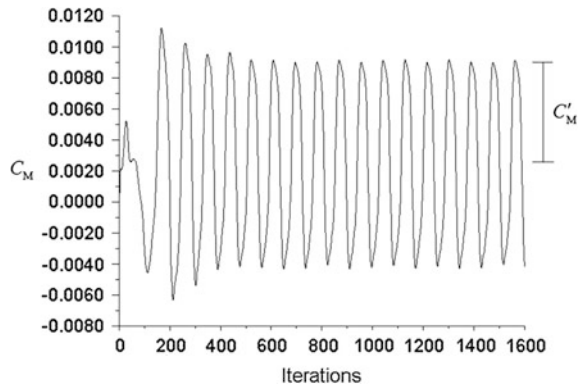


**Fig. 5** The moment coefficients iterative



resistance coefficient is two times of the frequency of vortex shedding, and due to the asymmetry of the grid, the two pulse amplitude in the resistance of a lift cycle is not identical, and here, we take the amplitude of the larger, as shown in Fig. 4.

The torque is the composition force of the shear force acting on each place on the wire, and the periodic variation of the frequency of the lift is  $f_s$ , which is also a periodic change of  $f_s$ . For wires of circular cross section, due to the symmetry of the structure, each point of the same arm, so the torque coefficient is very small, as shown in Fig. 5 shows.

Figure 6 shows the flow line diagram corresponding to the change of the lift coefficient. From the streamlines can be seen when the lift coefficient develop from below to the top, the underside of the wire produced a vortex, with the lift coefficient is more and more big, below the scroll slowly away from the above gradually formed a small vortex. However, when the lift coefficient developed from above downward, the top of the scroll slowly away from below gradually formed a small vortex, and forming a cycle.

Figure 7 shows a schematic of the velocity field around the large section conductor under the condition of the wind speed and 5 m/s. As can be seen from the diagram, the wind speed of the upwind side of the wire is small, and the speed of the upper and lower sides is relatively large.

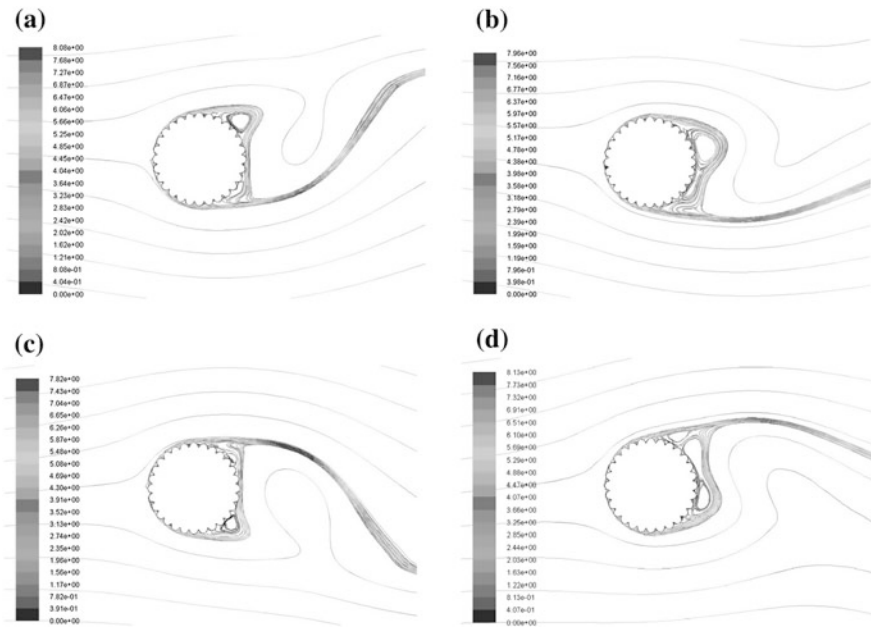


**Fig. 6** The streamlines diagram of the conductor during a circle period. **a, d** Negative lift coefficient. **b, c** Positive lift coefficient

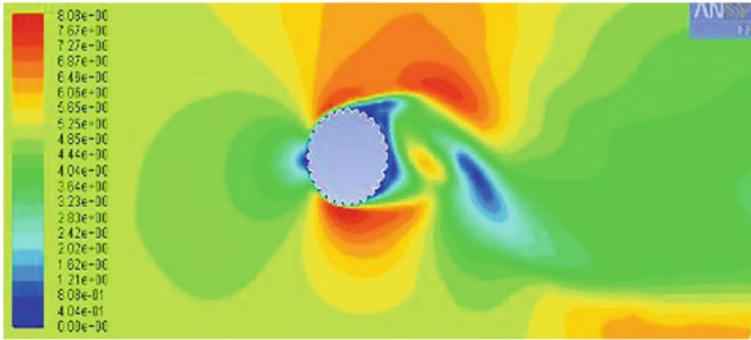


Fig. 7 Velocity profiles of 5 m/s

### 4 Steady Drag Coefficient

Figure 8 shows the comparison of the steady flow resistance coefficient, obtained from numerical simulation results and the wind tunnel test results. In the numerical model, the rough wire model and smooth wire model are studied, respectively.

As shown in Fig. 8, the numerical simulation results are in good agreement with the test results, except some differences in the local characteristics. In the wind tunnel test, the steady-state drag coefficient has a significant decrease if the Reynolds number between 20,000–40,000, and the Reynolds number is 40,000–60,000, there is a rebound in the Reynolds number 40,000–60,000, and gradually stabilized after the Reynolds number 60,000. The steady drag coefficient of the rough boundary model has a significant decrease in the Reynolds number 20,000–40,000, gradually stabilized after the Reynolds number 40,000. The steady drag coefficient of the smooth boundary model has a significant decrease in the Reynolds number 20,000–60,000, which is gradually stabilized at the Reynolds number 60,000. And the decrease amplitude of the wind tunnel test results in the Reynolds number 20,000–40,000 is larger than the simulation results, and the steady drag coefficient is slightly

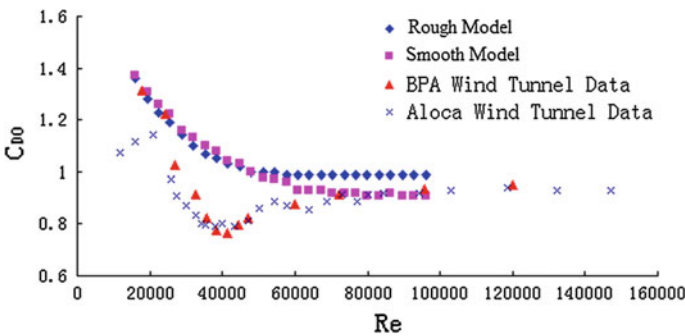


Fig. 8 The comparison of numerical results and test results

larger than the experimental results. In the Reynolds number 20,000–40,000, the steady drag coefficient of smooth boundary model is higher than that of rough boundary model, but just a little difference. After Reynolds number 60,000, rough boundary model steady-state drag coefficient of stability around 0.99, wind tunnel test stable results in about 0.94, smooth boundary model is stable in about 0.91, visible roughness  $R$  is more, stable steady-state drag coefficient is smaller.

### 5 Pulse Dynamic Coefficient

Figures 9 and 10 show the fluctuating life and drag coefficient of rough wire model and smooth wire model, respectively.

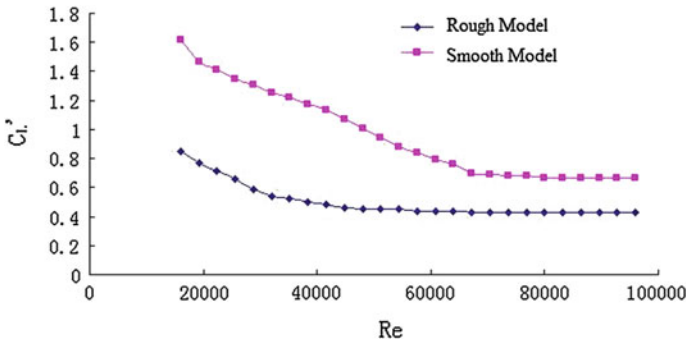


Fig. 9 The comparison of fluctuating lift coefficients

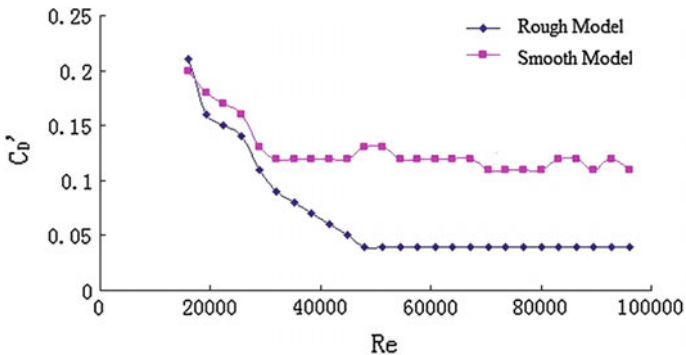


Fig. 10 The comparison of fluctuating drag coefficients

As shown in Figs. 9 and 10, both the fluctuating lift coefficient and the fluctuating drag coefficient of smooth wire model and rough wire model firstly decreased and then gradually stable, and the rough boundary model becomes stable much earlier compared with the smooth boundary model. The fluctuating coefficient of the smooth model is larger than that of the rough model, whether it is the drop or the steady. This shows that the smooth boundary model is more prone to the breeze vibration than the rough boundary model. Smooth boundary model and rough boundary model are also shown to decrease gradually after a steady trend, and smooth boundary model is more stable than the rough boundary model. The coefficient of fluctuating drag is much smaller than the coefficient of fluctuating lift, so the variation of lift will influence the wire much more big.

## 6 Conclusion

In this paper, a numerical simulation method is adopted to calculate the aerodynamic parameters of the rough boundary wire model and the smooth boundary wire model. The calculation results are compared with the wind tunnel test results, and the influence of the roughness of the surface of the large cross section on the aerodynamic parameters is discussed. The conclusions are listed as follows:

- (1) When stable airflow blowing transmission wire, the lift coefficient of the wire is always around 0 of the sine wave of  $f_s$ . The drag coefficient is also unstable, and changing rate is twice of the lift coefficient.
- (2) When the wind speed increases, the steady-state resistance coefficient of the wire in the Reynolds number 20,000–40,000 is decreased. The reason is that with the increase of wind speed, the end of the wire is getting more and more turbulent, the tail flow becomes narrow, and the drag coefficient is small.
- (3) The roughness of the wire will effect the aerodynamic characteristics of the wind load: (1) In the Reynolds number range of 20,000–40,000, the steady-state resistance coefficient of the large cross section lead is higher than that of the rough boundary model; After the Reynolds number 60,000, the steady-state resistance coefficient of smooth boundary model and rough boundary model tend to be a stable value, and the larger the lead roughness is, the smaller the resistance coefficient is. (2) With the increase of Reynolds number, the fluctuating coefficient of the wire firstly decreased and then gradually becomes steady. The fluctuating drag coefficient is much smaller than the fluctuating lift coefficient. The fluctuation coefficient of the smooth boundary model is always larger than that of the rough boundary model, which indicated that the wind vibration is more prone to the smooth conductor than the rough conductor.

## References

1. Fleming JF, Athins RS, Mozer JD (1978) A program for longitudinal load analysis of electric transmission lines. *Comput Struct* 9(3):237–253
2. Siddiqui FMA, Fleming JF (1984) Broken wire analysis of transmission line systems. *Comput Struct* 18(6):1077–1085
3. Peyrot AH, Kluge RO, Lee JW (1980) Longitudinal loads from broken conductors and broken insulators and their effect on transmission lines. *IEEE Trans Power Appar Syst* 99(1):222–234
4. Jamaledin A, McClure G, Rousselet J, Beauchemin R (1993) Simulation of ice-shedding on electrical transmission lines using ADINA. *Comput Struct* 47(4/5):523–536
5. Roshan FM, McClure G (1998) Numerical modeling of the dynamic response of ice-shedding on electrical transmission lines. *Atmos Res* 46:1–11
6. Kalman T, Farzaneh M, McClure G (2003) Numerical analysis of the dynamic effects of shock-load-induced ice shedding on overhead ground wires. *Comput Struct* 2007(85):375–384
7. McClure G, Lapointe M (2003) Modeling the structural dynamic response of overhead transmission lines. *Comput Struct* 81(8–11):825–834

# Multi-objective Optimization Algorithm in Mission Planning of On-Orbit Servicing Spacecraft

Qing Zhang, Jianxin Zhang, Qiang Zhang and Xiaopeng Wei

**Abstract** On-orbit servicing (OOS) spacecrafts can provide a variety of services, so it is necessary to make reasonable mission planning between spacecrafts to improve the efficiency of collaborative works. In this paper, a multiple spacecraft mission planning based on multi-objective optimization algorithm is proposed according to the specific characteristics of mission planning in order to complete the optimization target, such as task completion time, fuel consumption, and service priorities. In this algorithm, the model of mission planning problem is established by designing decision variables and formal constraints, and Pareto optimal sets and multiple sets of solutions of that problem are the results of the improved NSGA-II. In particular, ideal solution can be chosen as necessary. From the results of two simulation examples, we can see that our method can solve the multi-spacecrafts mission planning problem under multiple constraints efficiently. It is expressive, flexible, extensible, and feasible easily.

**Keywords** On-orbit servicing (OOS) · Spacecraft mission planning · Improved NSGA-II algorithm

## 1 Introduction

On-orbit servicing (OOS) was originally proposed for traditional spacecraft one-time design and closed system. However, with the development of space technology, OOS also involves physical assessment as well as changes the current status of the spacecraft, including on-orbit testing, on-orbit filling, system upgrading, and on-orbit maintenance [1–3]. And OOS has a strong military background and great application value to increase the space combat capability.

---

Q. Zhang · J. Zhang · Q. Zhang (✉) · X. Wei  
Key Lab of Advanced Design and Intelligent Computing, Ministry of Education,  
Dalian University, Dalian, People's Republic of China  
e-mail: Zhangq26@126.com

© Springer-Verlag Berlin Heidelberg 2016  
B. Huang and Y. Yao (eds.), *Proceedings of the 5th International Conference on Electrical Engineering and Automatic Control*, Lecture Notes in Electrical Engineering 367, DOI 10.1007/978-3-662-48768-6\_117

1049

We obtain the task execution plan which has obvious time attribute, spatial attribute, subject attribute, object attribute, and target attribute under the common constraints of space resources and space mission environment in the mission planning of spacecraft [4].

As a complicated multi-objective constraint problem, the main research purpose of on-orbit service mission planning is selecting an optimal assignment scheme under the condition that all the constraint conditions of optimization solution have been met such as the requirements of the task, environmental conditions, and optimizing the element in which a certain number of service spacecrafts and target spacecrafts are provided [5]. At present, a lot of algorithms for on-orbit service mission planning have been presented. Alfriend et al. made a research about the optimal service strategy of an in-service spacecraft performing multiple tasks in synchronous orbit [6]. Shen et al. proposed one-to-many on-orbit service of spacecraft on circular orbit [7]. However, they did not consider the service time and collaboration work of spacecraft. Zhang et al. proposed a coordinated target assignment method for multi-service spacecraft based on discrete particle swarm algorithm [8], in which they designed some new update formulas about position and speed of discrete particle swarm according to the characters of spacecraft co-allocation.

In this paper, we build a mathematical model of mission planning problem of on-orbit spacecraft in the basics of the properties of OOS spacecraft mission planning and the research in the task assignment problem of uninhabited combat air vehicle (UCAV) [9, 10] and the problem of imaging satellites scheduling [11]. In this method, we use improved NSGA-II algorithm to get Pareto optimal collection of solutions for this problem and make a specific numerical example and a comparative analysis of the results.

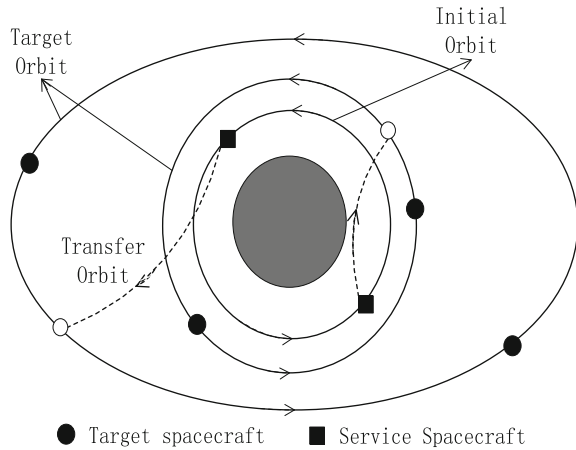
## 2 Problem Description

### 2.1 Detailed Description of the Problem

The mission scenarios and transfer process of OOS spacecrafts which run on the predefined tracks separately are shown in Fig. 1. Meanwhile, the priorities of target spacecraft's tasks are different. When the service spacecraft receive the OOS order, the service spacecraft moves from preparation orbit to target orbit after Lambert double pulse orbit maneuver [12], and the transfer process can be simply described as the following figure. The target of mission planning is to choose service goals for each spacecraft and to make sure that the task has a high efficiency and lower power consumption according to the planning rule of "one-to-one" and the service principles that the high-priority target spacecraft gets prior service.



**Fig. 1** On-orbit servicing spacecraft mission scenarios and transfer process



## 2.2 Multi-objective Optimization Model

### 2.2.1 Decision Variables

Assuming that the number of the service spacecrafts is  $N$ , and the service spacecrafts provide services to the target spacecrafts whose number is  $M$  with different priorities after receiving the service order. In other words, the formation which was composed of  $N$  service spacecrafts serves  $M$  different targets. According to the characteristics of the planning issues, the decision variables can be defined as Eq. (1):

$$x_i = \begin{cases} j, & i \text{ serves } j \\ 0, & i \text{ doesn't serve } j \end{cases} \quad (1)$$

where  $i = 0, 1, \dots, n, j = 0, 1, \dots, m$ .

### 2.2.2 Objective Function

#### 1. Task Priority

Spacecrafts have different priorities because of the different values of them, which results in the on-orbit spacecraft should firstly serve the target spacecraft with high priority. We define  $P$  to represent target spacecraft's priority, and the higher value means the higher priority, and  $P_j$  represents the priority of the  $j$ th target spacecraft. Then, the priorities of each spacecraft to finish their tasks can be expressed as Eq (2):

$$J_1 = \max \sum x_i P_j \quad (2)$$

where  $i = 0, 1, \dots, n$ ,  $j = 0, 1, \dots, m$ . Taking the maximum of the objective function can guarantee that the spacecraft complete tasks with maximum value.

## 2. Task Completion Time

When spacecraft is in service, the objective function is the function of the consumed time in the last time owing to the limitation of fuel or some tasks are urgent which require the shortest task completion time. This can be expressed as Eq (3):

$$\Delta T = \max \{x_i \Delta t_{ij}\} \quad (3)$$

where  $\Delta t_{ij}$  is the time of the  $i$ th service spacecraft serves the  $j$ th target spacecraft. Then, the objective function can be expressed as Eq (4):

$$J_2 = \min \Delta T \quad (4)$$

## 3. Fuel Consumption

In this paper, we only consider the fuel consumption of orbit's maneuvering because the fuel consumption of spacecraft running on the original orbit is much less than that of orbit's maneuvering, and fuel consumption can be measured by the speed of orbital maneuvering. Then, the fuel consumption of the  $i$ th service spacecraft serves the  $j$ th target spacecraft can be expressed as Eq (5):

$$J_3 = \min \sum x_j \Delta v_{ij} \quad (5)$$

where  $\Delta v$  is the velocity increment of completing the task, and  $\Delta v_{ij}$  is the velocity increment of the  $i$ th service spacecraft serves the  $j$ th target spacecraft.

This is a multi-objective optimization problem because all the above objective functions should reach its optimum.

### 2.2.3 Constraints

#### 1. Time constraints on mission

Since the objective function is the mission completion time in this paper, therefore, it is necessary to limit the maximum value of mission completion time in order to avoid the longtime of orbital maneuvering in accordance with the reality.

$$t_f \leq T \quad (6)$$

where  $T$  is the allowing maximum time, and two pulses can be defined as  $t_{i2}$  and  $t_{i2} = t_f$ .

## 2. Transfer constraints on orbital

Considering the preparation need of the actual pulse motorization, it is required that any two pulses time intervals should be greater than the permissible minimum time interval. The constraint is described as follows:

$$t_{i2} - t_{i1} \geq \Delta t_{\min} \quad (7)$$

where  $i = 1, 2, \dots, n$ , and  $\Delta t_{\min}$  is the minimum time interval.

## 3. The maximum velocity increment constraints

The velocity increment of spacecraft performing the tasks must be less than the maximum speed increment which can be offered. The constraint is described as follows:

$$\Delta v_{ij} \leq \Delta v_{\max} \quad (8)$$

where  $\Delta v_{\max}$  represents the maximum speed increment that the spacecraft can offer, and  $\Delta v_{ij}$  represents the needed speed increment when the  $i$ th serves  $j$ th.

# 3 Multi-objective Algorithm

## 3.1 NSGA-II

Mission planning issue within the scope of multi-objective is a problem about optimization. The following part will be considered the priority, fuel consumption, and completion time of a task, using the optimized mathematical model to get optimal Pareto solution collection.

NSGA-II [13] is a multi-objective algorithm on the basis of NSGA [14], improved by Deb and other people. Its most prominent feature is the use of a fast non-dominated sorting and crowding mechanism, which considerably corrects the shortcomings of NSGA. Experiments show that NSGA-II is a multi-objective optimization algorithm with better overall performance, which has been applied to a lot of planning and production activities [15].

## 3.2 Improved NSGA-II

### 3.2.1 Coding

The key of mission planning about service spacecraft is to determine which service spacecraft serves the target spacecraft. In Ref [5], the best plan was achieved by

building the model of 0–1 integer programming and taking the NSGA-II algorithm with the constraint of time and fuel consumption. For example, the number of service spacecraft is 2 and the number of target spacecraft is 4, if we use the binary coding, then the feasible region is a matrix that has two rows and four columns. That is to say, the size of the feasible region is 28. If the project is that the service spacecraft 1 serves the target spacecraft 2 and the service spacecraft 2 serves the target spacecraft 1, then the corresponding matrix is  $\begin{vmatrix} 0 & 1 & 0 & 0 \\ 1 & 0 & 0 & 0 \end{vmatrix}$ . But in this paper, on-orbit service needs a service of “one-to-one.” So under the assigned mode,  $\begin{vmatrix} 0 & 1 & 0 & 1 \\ 1 & 0 & 0 & 0 \end{vmatrix}$  and  $\begin{vmatrix} 0 & 1 & 0 & 0 \\ 1 & 1 & 0 & 0 \end{vmatrix}$  are infeasible solutions. Thus, it makes search efficiency of the algorithm discount.

So in this paper, the natural number coding mode is used. The length of each particle is equal to the total number of target spacecrafts. The particle consists of number assigned by servicing spacecraft which are arranged according to the numbering sequence of the target, which is regarded as a possible distribution plan. For example, the number of the service spacecraft  $N$  is 4; the number of the target spacecraft  $M$  is 8, so a particle is represented as: 1 2 4 3 2 1 4 3.

It shows that service spacecraft 2 is assigned to targets 2 and 5, while service spacecraft 3 is assigned to targets 3 and 6. So the size of feasible region is 32. In other words, it replaces the original matrix with two integers.

However, considering that the paper requires “one-to-one” service in on-orbit servicing, if with a real coding, each generation is likely to search the individuals, with the same target but not consistent with practical problems in the target space. These infeasible points are bound to affect the algorithm efficiency.

So the feasible region will be greatly reduced to integer coding. And if penalty function is mostly used for constrains in the NSGA-II, then this paper will fix infeasible solution into a feasible one during the objective function calculation. For example, [3,3] refers to service spacecraft. If 1 and 2 both serve for the target spacecraft 3, it does not conform to the “one-to-one” service principle. Then by revising it to [3,4], the operation also ensures the diversity of the population.

### 3.2.2 Crossover Operator

NSGA-II algorithm uses SBX crossover [16], which is the process of simulating binary crossover. The operation is carried out on the parent individuals which are real coded. That is, for a given random intersection, exchange the sections on either intersection of two parent individuals.

This paper is to introduce the arithmetic crossover operator [16] into NSGA-II, respectively; set  $X_{it}$  and  $X_{jt}$  as the real coding of corresponding decision variables with two individual intersections in  $t$ -generation. After crossover, the decision variable values of two individuals are given as follows:

$$\begin{aligned} X_i^{t+1} &= X_i^t + rand * ratio(X_j^t - X_i^t) \\ X_j^{t+1} &= X_j^t - rand * ratio(X_j^t - X_i^t) \end{aligned} \quad (9)$$

Ratio is the random number of [0,1], which is distributed uniformly. It can ensure that the searching region of crossover operator covers all the neighborhood of  $X_{i_t}$  and  $X_{j_t}$  and are more likely to be searched between the two areas. Arithmetic crossover operator has better global search capability, can maintain the diversity of the population better, and has a good convergence rate.

### 3.2.3 Gauss Mutation Operator

In this paper, Gaussian mutation [16] is introduced into the NSGA-II Gaussian distribution, known as the Galton distribution, is also called the normal distribution. After Gaussian mutation, the  $i$ th decision variable values of individuals are given as:

$$X_i^t = X_i + \mu(X_{\max} - X_{\min}) \quad (10)$$

$X_{\max}$  and  $X_{\min}$  are the upper and lower limits of the variable, respectively.  $\mu$  is the random number in accordance with Gaussian distribution. Gauss mutation operator has a good local escape and search capabilities.

## 4 Simulation Results

In order to demonstrate feasibility of this algorithm, several experiments were carried out. For this purpose, a MATLAB computer simulation program was developed. Assume that there are two service spacecrafts (SS) with different service capabilities on the same orbit, waiting for service order to serve the target spacecraft (TS). Also there are 4 target spacecrafts on different orbits, and the requirement is service spacecraft finish on-orbit service for target spacecraft in the limited time period and get the best result. Optimal configuration of sample 1 and sample 2 are set as follows. We calculated that the allowing maximum time is  $T = 5000$  s, the initial time is  $t_0 = 100$ , the maximum speed increment that the spacecraft can offer is  $\Delta v_{\max} = 3$  km/s, and the minimum time interval is  $\Delta t_{\min} = 100$  s.

The parameter values of the improved NSGA-II are set as follows:

- (1) Group = 200;
- (2) Evolution algebra = 200;
- (3) Crossover probability = 0.9;
- (4) Mutation rate = 0.1.

### 4.1 Sample 1: Comparison with Divided Weighted Optimization Method

In order to analyze the effect of multi-objective optimization, set the initial parameters of the spacecraft’s orbit, refer to Table 1 as Reference [5].

We choose three groups of Pareto optimal solution calculated by Improved NSGA-II (I-NSGA-II), and compare the results calculated by divided weighting method (DWM) under the same configuration. The comparative results are given in Table 2.

The result comparison shows when multiple objectives simplify to single objective, we can select only one group of solution, and this result is in the search area near improved NSGA-II optimization Pareto optimal outcome, while three compromise proposals can be selected from the improved NSGA-II multi-objective optimization Pareto optimal solution set according to the actual situation.

### 4.2 Sample 2: Comparison with NSGA-II Algorithm Optimization

In order to analyze the effect of multi-objective optimization, we set the initial parameters of the spacecraft’s orbit referred in Table 3 of Reference [5]. The comparison between same assignment plans is given in Table 4.

**Table 1** Initial orbital parameters of the spacecraft [5]

Spacecraft	$a$ (m)	$e$	$i$ (°)	$\Omega$ (°)	$\omega$ (°)	$f$ (°)	Priority
SS1	7150000	0.01	98	220	30	230	
SS2	7150000	0.01	98	220	30	50	
TS1	7300000	0.02	103	220	0	130	0.7
TS2	7250000	0.02	104	222	25	230	0.9
TS3	7300000	0.01	95	215	20	50	0.6
TS4	7250000	0.03	94	218	10	15	0.7

Note We set the same initial parameters as in reference [5] to compare the two results

**Table 2** Comparison between simulation results

Algorithm	Optimal assignment solution	Priority level	Fuel consumption (m/s)
DWM	SS1 → TS2 SS2 → TS1	1.6	2183.4
I-NSGA-II	SS1 → TS2 SS2 → TS4	1.6	1659.1
	SS1 → TS2 SS2 → TS4	1.6	2166.9
	SS1 → TS2 SS2 → TS3	1.5	2011.7
	SS1 → TS2 SS2 → TS3	1.5	3812.6

**Table 3** Initial orbital parameters of the spacecraft [5]

Spacecraft	$a$ (m)	$e$	$i$ (°)	$\Omega$ (°)	$\omega$ (°)	$f$ (°)	Priority
SS1	7078561	0.01	50	30	10	0	
SS2	7078561	0.01	50	30	10	10	
TS1	7378561	0.02	50	30	10	20	0.7
TS2	7278561	0.02	50	30	10	30	0.9
TS3	7278561	0.01	50	30	10	30	0.6
TS4	7278561	0.03	50	30	10	25	0.8

**Table 4** Comparison between same assignment plans

Assignment plan	Mission completion time (s)	Fuel consumption (m/s)
SS1 → TS2 SS2 → TS4	3650.4	1659.1
SS1 → TS2 SS2 → TS4	1932.9	3422.6

From samples above, we can conclude that:

1. Under the same mission assignment plan, there are different completion time and fuel consumption.
2. Three goals cannot be optimal simultaneously. There will be a corresponding reduction in fuel consumption while fuel consumption is increasing, and the priority is worthy improving at the cost of fuel consumption.
3. Running the program shows that improved NSGA-II algorithm has a faster convergence, and it can be also applied in larger models. Figures 2 and 3 show the fitness change of the Pareto optimal front in 5th and 70th generations.

**Fig. 2** Pareto optimal front of 5th generation

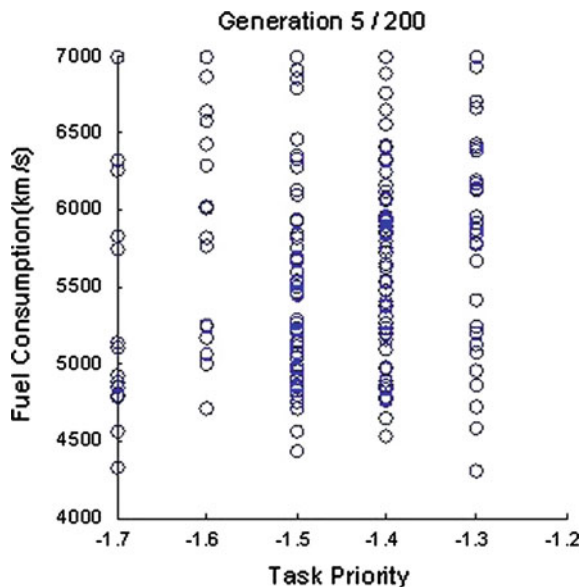


**Fig. 3** Pareto optimal front of 70th generation

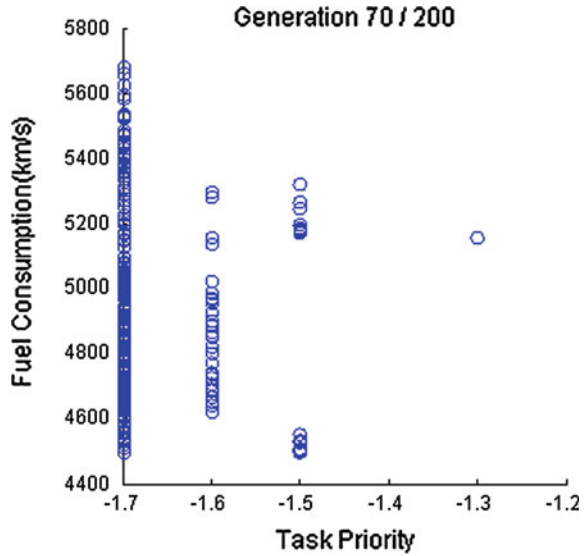


**Table 5** Two algorithms result in different priorities

Priority	Corresponding number	
	NSGA-II	I-NSGA-II
1.5	38	28
1.6	92	85
1.7	70	87

(4) There are 200 sets of optimization results totally that used two algorithms result in different priority levels. The corresponding number contrast is as shown in Table 5:

## 5 Conclusion

In allusion to the research on mission assignment of on-orbit servicing spacecraft, in this paper, we present a project based on improved NSGA-II algorithm. In this algorithm, the model of mission planning problem is established by designing decision variables and formal constraints, and Pareto optimal sets and multiple sets of solutions of that problem are the results of the improved NSGA-II (R-NSGA-II). We make some improvements on the NSGA-II algorithm are as follows: We replace binary coding with integer coding; in this way, we reduce the infeasible solutions and overlapping individuals of the target space, so as to achieve the target of reducing the feasible region and improving the search efficiency. In addition, we



also introduce the arithmetic crossover operator and Gaussian mutation. In particular, ideal solution can be chosen as necessary. From the results of two simulation examples, we can see that our method can solve the multi-spacecrafts mission planning problem under multiple constraints efficiently. It is expressive, flexible, extensible, and feasible easily.

**Acknowledgements** This work is supported by the National Natural Science Foundation of China (No. 61202251, 60875046), the Program for Liaoning Excellent Talents in University (No. LJQ2013133), and Program for Changjiang Scholars and Innovative Research Team in University (No. IRT\_15R07), the Program for Liaoning Innovative Research Team in University (No.LT2015002), and by the Natural Science Foundation of Liaoning Province (201102008).

## References

1. Yao W, Chen XQ, Huang YY, Tooren MV (2013) On-orbit servicing system assessment and optimization methods based on lifecycle simulation under mixed aleatory and epistemic uncertainties. *Acta Astronaut* 87:107–126
2. Richards MG (2006) On-orbit serviceability of space system architectures. Dissertation, Massachusetts Institute of Technology
3. Krolikowski A, David E (2013) Commercial on-orbit satellite servicing: national and international policy considerations raised by industry proposals. *New Space* 1(1):29–41
4. Cao YH, Feng SX, Zhang YL, Shu L (2007) Design and implementation of military space mission planning system in a web environment. *J Acad Equip Command Technol* 18(3):47–51
5. Liang YG, Wang WL (2013) Research on mission assignment of on-orbit servicing spacecraft. *J Nat Univ Defense Technol* 35(5):26–30
6. Alfriend KT, Lee DJ, Creamer NG (2006) Optimal servicing of geosynchronous satellites. *J Guidance Control and Dyn (Impact Factor: 1.15)* 29(1):203–206
7. Shen HJ (2003) Optimal scheduling for satellite refuelling in circular orbits. Georgia Inst Technol, Alexander
8. Zhang QX, Sun FC, Xu B, Liu HP (2012) Multiple spacecrafts on-orbit service task allocation based on DPSO. *Chin Space Sci and Technol* 32(2):68–76
9. Ye YY, Min CP, Zhu HY, Shen LC (2005) Multiple UCAV mission assignment based on integer programming. *Inf Control* 34(5):549–552
10. Dai J, Cheng J, Song M (2009) Cooperative task assignment for heterogeneous multi-UAVs based on differential evolution algorithm. *IEEE Int Conf Intell Comput Intell Syst* 163–167
11. Frank J, Jonsson A, Morris R, Smith DE (2007) Planning and scheduling for fleets of earth observing satellites. In: *Proceedings of 2007 IEEE Aerospace Conference*, 1–8
12. Howard C (2009) *Orbital mechanics for engineering students*. Elsevier, London
13. Kalyanmoy D, Amrit P, Meyarivan T (2002) A fast and elitist multi-objective genetic algorithm: NSGA-II. *IEEE Trans Evol Comput* 6(2):182–197
14. Kalyanmoy D (2001) *Multi-objective optimization using evolutionary algorithms*. Wiley, New York, pp 210–302
15. Srinivas N, Deb K (1995) Multi-objective function optimization using nondominated sorting genetic algorithms. *Evol Comput* 2(3):221–248
16. Fu L, Dou MG, Zhu JK, Song ZM (2011) Improvement of Non-dominated Sorting Genetic Algorithm. *Comput Digital Eng* 39(2):11–15

# Product Conceptual Design Based on Polychromatic Sets Theory and Axiomatic Design

Jianxin Zhang, Yangjie Zhou, Qiang Zhang and Xiaopeng Wei

**Abstract** We propose a function–parameter model based on polychromatic sets theory in the paper. The proposed model aims to resolve the weaknesses of function–means tree which is difficult to convey the complex mechanical system and constraints among them and to deal with the disadvantages of axiomatic design in the product conceptual design process that does not provide the realization methodologies of specific mapping from the function requirements to the design parameters. The function–parameter model can present complex mechanical system and constraints among them and illustrate the realization methodologies of specific mapping, and five possible constraints between function requirements and design parameters are also presented. Exemplified by the main module design of snow-removing car, the function–parameter model based on polychromatic sets theory is further elaborated.

**Keywords** Conceptual design · Function–means tree · Polychromatic sets theory · Axiomatic design · Constraints

## 1 Introduction

Conceptual design is the early stage of product design. Although conceptual design occupies a small part of the product design process, it accounts for over 70 % of the total life cycle of cost of a product [1]. So far, many theories and methodologies that support the conceptual design have been proposed by many scholars, among which the function–means tree (FMT) module [2] and axiomatic design (AD) module [3] are widely used. However, these two methods have some disadvantages. The tra-

---

J. Zhang (✉) · Y. Zhou · Q. Zhang (✉) · X. Wei  
Key Lab of Advanced Design and Intelligent Computing, Ministry of Education,  
Dalian University, Dalian, People's Republic of China  
e-mail: zjx99326@163.com

Q. Zhang  
e-mail: zhangq26@126.com

ditional FMT has not taken the constraints between functions and means into consideration and is difficult to convey the complex mechanical system and constraints among them. The AD cannot provide the realization methodology of specific mapping from the function requirements (FRs) to the design parameter (DPs) and does not support experience design. Zhang et al. [4] modified the FMT. The automatic candy packing machine based on the modified FMT and AD was designed. The modified FMT can overcome the disadvantages of AD, but it still cannot convey the constraints between FRs and DPs. In order to overcome the disadvantages of FMT, the function–parameter model based on polychromatic sets theory that can not only present complex mechanical system and constraints among them but also illustrate the specific mapping means is proposed.

## 2 Function–Means Tree and Polychromatic Sets Theory

### 2.1 *The Function–Means Tree*

Pahl defined “function” in the product conceptual design as “the average and desired relationships that arise in input and output of the system” [5]. It is the description of product’s task realization. The total function describes the total task, and it can be divided into a number of sub-functions. The decomposition process cannot stop until the meta-functions appear. The function is the essential properties of the product. The value of products is granted by the function of products. Products are the carriers of the function. According to Hubka’s law [6], there are causal relationships between functions and means of the mechanical system. The functions are implemented by the means. The methods correspond to a series of entities. The active result of the entity is the solution of the function. Thus, the mechanical system can be represented by the combination model of functions and means. FMT is a powerful tool to decompose product function and can display the model of mechanical system.

The schematic diagram of FMT is showed in Fig. 1 [7]. The FMT adopted a top-down layered modeling method. The total function of a system lies in the top. A function is followed by a method, and the method is followed by the function. By such analogy, until the most basic method arise. However, traditional FMT is difficult to convey the complex system. The more complex the system is, the more the branches of a tree are. A function can be implemented by several means. The tree will become far bigger. It is not convenient to express model information. Johan et al. [8] extended the FMT. They thought that the FMT should include more information. In addition to the functions and means, constraints and objectives were involved in the FMT. It was known as the extended function–means tree (EFMT). The EFMT defined the specific mapping rules between

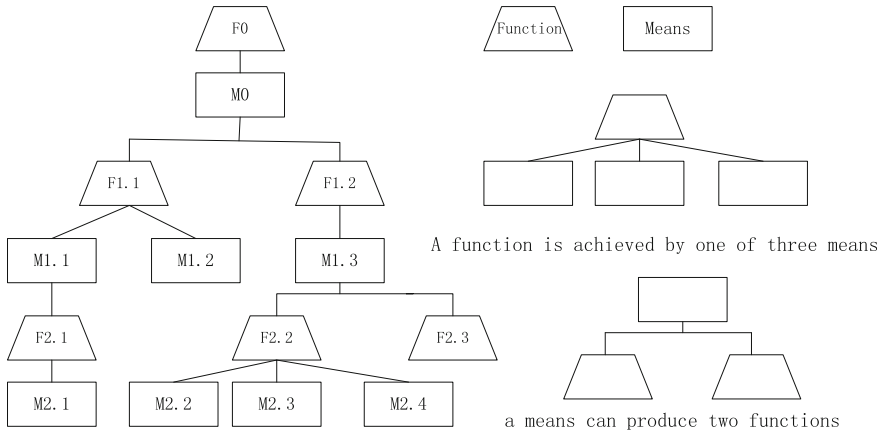


**Fig. 1** Traditional function–means tree

functions and means. Every layer has the corresponding constraints and objectives, and the EFMT can better express the design process of mechanical products. However, the EFMT cannot still describe the complex constraints of products.

### 2.2 The Polychromatic Sets Theory

The PST is convenient for the computer programming and plays an important part in the complex mechanical system modeling. The PST was first put forward by Professor Palov from Russia in 1995. Palov further improved the basic PST and represented the PST system in 2002. The PST has been widely used in the Russian aerospace companies [9].

In polychromatic sets, the elements of the general set are the ones of the polychromatic sets. The colors of the elements are divided into individual color and unification color. Given a set  $A$  as  $A = \{a_1, \dots, a_i, \dots, a_n\}$ , where “ $a_i$ ” is an element of set  $A$  and “ $n$ ” is the number of elements. The individual color set is shown in [10, 11]:

$$F(a_i) = \{f_1, \dots, f_j, \dots, f_m\} \tag{1}$$

where “ $m$ ” is the total number of properties of the element “ $a_i$ ,” and the rank of “ $f_j$ ” is “ $j$ ” in the property of the element “ $a_i$ .”

Similarly, the unification color of polychromatic set “A” is expressed as:

$$F(A) = (F_1, \dots, F_l, \dots, F_r) \tag{2}$$

where “r” is the property number of the set “A,” and the “F<sub>r</sub>” is the rth property of set “A.” The set “F(a<sub>i</sub>)” and the element of the set “F(A)” could have the same or different name.

The polychromatic sets consist of six parts [12]. The six parts are shown in the following form:

$$PS = \{A, F(a), F(A), [A \times F(a)], [A \times F(A)], [A \times A(F)]\} \tag{3}$$

The “F(a<sub>i</sub>)” is the individual color of element “a<sub>i</sub>.” The set “F(a)” consists of the individual color of all elements. It can be represented by the Boolean matrix “[A × F(a)]” as follows:

$$\|a_{ij}\|_{A,F(a)} = [A \times F(a)] = \begin{matrix} & f_1 & \dots & f_j & \dots & f_m \\ \begin{bmatrix} a_{11} & \dots & a_{1j} & \dots & a_{1m} \\ \dots & \dots & \dots & \dots & \dots \\ a_{i1} & \dots & a_{ij} & \dots & a_{im} \\ \dots & \dots & \dots & \dots & \dots \\ a_{n1} & \dots & a_{nj} & \dots & a_{nm} \end{bmatrix} & a_1 \\ & \dots \\ & a_i \\ & \dots \\ & a_n \end{matrix} \tag{4}$$

The rows of the matrix show the individual colors of the elements. The columns represent all the elements painted by a certain individual color. If the element “a<sub>i</sub>” has the property of “f<sub>j</sub>,” then the coefficient “a<sub>ij</sub>” equals “1.” Otherwise, it is “0.”

In polychromatic sets, the mutual relations exist in the unification color of elements. Then, individual color can be signified by the matrix “[a<sub>ij</sub>]<sub>A,F(A)</sub> = [A × F(A)].” There are also mutual relations between the individual color and the unification color. The correlations can be described by the matrix “[c<sub>ij</sub>]<sub>F(a),F(A)</sub> = [F(a) × F(A)].” The more detail of polychromatic sets is given in reference [12]. In response to the practical problems, there is no need to consider every part of six parts. A matter should be dealt with according to its specific circumstances.

### 3 The Function–Parameter Model Based on Polychromatic Sets Theory

#### 3.1 The Combination of Polychromatic Sets Theory and Axiomatic Design

Johannesson proposed the idea that the FMT could support the axiomatic design [13]. It laid the foundation of combination of PST and AD. According to the study of PST that Tang and Jiang et al. made [14, 15], the paper puts forward a new model of product: concept—function—parameter model-based PST (Fig. 2). In the conceptual design process, mechanical products are divided into several layers that consist of function requirements and design parameters. Every design parameter is considered as the element of PST. The elements include individual color and unification color. The unification color of elements is the function implemented by a certain design parameter. The individual color is the property of a certain design parameter.

In the function–parameter model mentioned above, five different relations,  $R_1, R_2, R_3, R_4, R_5$ , are used to relate the FRs, DPs, and C-objects to each other. The relations are, when they are shown, represented graphically by different lines and arrows between objects. The five relations are defined as follows:

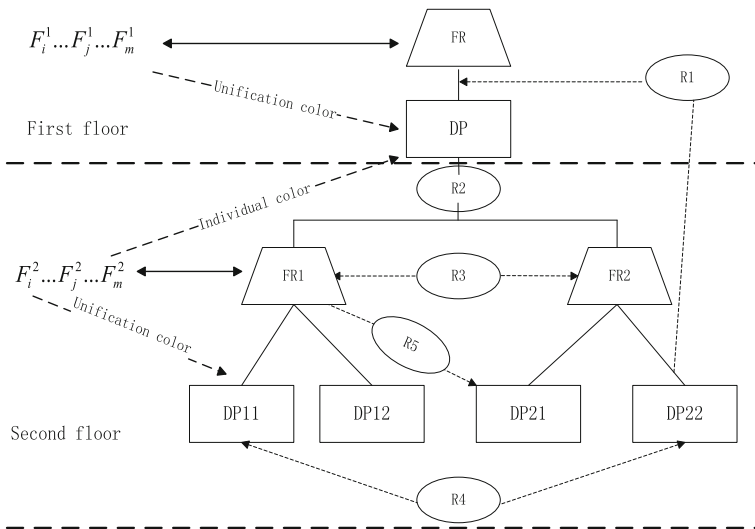


Fig. 2 Function–parameter model based on PST

1. An FR is achieved by a DP ( $R_1$ );
2. ADP is constrained by a FR decomposed by the DP ( $R_2$ );
3. Parallel FRs may interact with other ( $R_3$ );
4. Parallel solution DPs with different “parents” may interact with each other ( $R_4$ );
5. An FR is constrained by other DP with the same layer ( $R_5$ ).

Analyzing the five constraint relationships  $R_1, R_2, R_3, R_4,$  and  $R_5,$  they can be divided into three classes:  $F_{1c}$ —the constraint relationships of direct reasoning  $R_1$  and  $R_2$ ;  $F_{2c}$ —the constraint relationships in the same level  $R_3$  and  $R_4$ ; and  $F_{3c}$ —other constraint relationships. The set of constraints of sides is shown as follow:  $F(c) = \{F_{1c}, F_{2c}, F_{3c}\}.$  It can be expressed by the “formula (5).”

$$[R \times F(C)] = \begin{matrix} & F_{1c} & F_{2c} & F_{3c} \\ \begin{bmatrix} 1 & 0 & 0 \\ 1 & 0 & 0 \\ 0 & 1 & 0 \\ 0 & 1 & 0 \\ 0 & 0 & 1 \end{bmatrix} & R_1 \\ & R_2 \\ & R_3 \\ & R_4 \\ & R_5 \end{matrix} \tag{5}$$

### 3.2 PST Represents the Reasoning Constraints

In the polychromatic graphic  $G = \{A, C\},$  the node “A” signifies the FRs and DPs in the decomposition process. The set “C” expresses three classes of constraints between FRs and DPs. Two nodes are connected by a side in function–parameter model-based PST. Different sides show different constraint. The set of unification color “ $F(c) = \{F_{1c}, F_{2c}, F_{3c}\}$ ” [11] is shown as follows:

1. If the element “ $F_{1c}$ ” equals “1,” then the constraint relationship of direct reasoning “ $R_1$ ” or “ $R_2$ ” exists in top-down nodes. The constraint can be described by the matrix “[ $F(a) \times F(A)$ ]”.
2. If the element “ $F_{2c}$ ” equals “1,” then the constraint relationship in the same level “ $R_3$ ” or “ $R_4$ ” exists in two nodes. The constraint can be expressed by the matrix “[ $F(A) \times F(A)$ ]” or “[ $F(a) \times F(a)$ ]”.
3. If the element “ $F_{3c}$ ” equals “1,” then the other constraint relationship “ $R_5$ ” exists in two nodes. The constraint can be shown by the matrix “[ $F(a) \times F(A)$ ]”.

If the hierarchical structure has been broken down to the lowest level of the model, there is no need for defining the individual color of elements. The constraint relationship can be expressed by the matrix “[ $A \times F(A)$ ]”.

### 4 Case Study

The snow-removing machine consists of main module and auxiliary module. The function of the main module is removing snow. The functions of the auxiliary module are loading and steering [16, 17]. As the selection of auxiliary module depends on the main module, the main module plays the decisive role. The paper mainly represents the selection process of the main module. The constraints that the auxiliary module generates are ignored. The ways of removing snow have been mature, such as spraying snow-dissolving agents, high-pressure snow-blowing machine, turbojet engine, snow plough machine, snow blower machine, and artificial snow-removing [16]. These snow-removing ways could be directly considered as the scheme elements. The function-parameter model based on PST is shown in Fig. 3.

The individual colors of snow-removing function are the types of snow, snow-removing efficiency, environmental temperature, environmental impact, the effect of snow-removing, road conditions, snow thickness, the speed of removing snow, and the degree of mechanical complexity. The individual colors of snow-removing function are specifically described in the Table 1. The scheme elements are shown in Table 2.

As shown in Fig. 3, the “R<sub>1</sub>” is the only constraint relationship. It means that “F<sub>1c</sub>” equals “1.” As the individual color lies in the lowest level of the main module, it can be considered as the scheme element. The constraint between FRs and DPs can be described by the matrix “[A × F(A)]” as follows:

$$[A \times F(A)] = \begin{matrix} & F_1^1 & F_2^1 & F_3^1 & F_4^1 & F_5^1 & F_6^1 & F_7^1 & F_8^1 & F_9^1 & F_{10}^1 & F_{11}^1 & F_{12}^1 & F_{13}^1 & F_{14}^1 & \\ \begin{matrix} \left[ \begin{array}{cccccccccccccc} 1 & 0 & 0 & 1 & 0 & 0 & 0 & 1 & 1 & 0 & 1 & 1 & 0 & 1 \\ 1 & 0 & 0 & 1 & 0 & 1 & 1 & 1 & 1 & 0 & 1 & 0 & 1 & 1 \\ 1 & 1 & 1 & 1 & 0 & 1 & 1 & 1 & 1 & 0 & 1 & 0 & 1 & 1 \\ 1 & 0 & 0 & 1 & 0 & 1 & 1 & 1 & 0 & 1 & 1 & 0 & 1 & 1 \\ 1 & 1 & 1 & 1 & 0 & 1 & 1 & 1 & 1 & 0 & 1 & 0 & 1 & 1 \end{array} \right] & a_1 \\ & & & & & & & & & & & & & & & a_2 \\ & & & & & & & & & & & & & & & a_3 \\ & & & & & & & & & & & & & & & a_4 \\ & & & & & & & & & & & & & & & a_5 \end{matrix} \end{matrix} \quad (6)$$

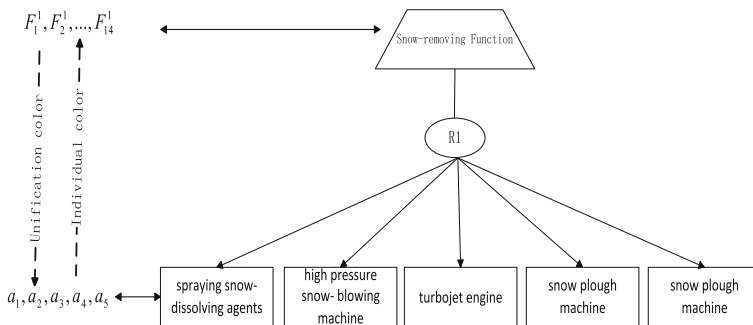


Fig. 3 Function-parameter model of the main module



**Table 1** The meaning of different functions

Function symbol	Meaning	Function symbol	Meaning
$F_1^1$	Removing natural snow	$F_2^1$	Removing compressed snow
$F_3^1$	Removing frozen snow	$F_4^1$	High efficiency
$F_5^1$	Low efficiency	$F_6^1$	Environmental protection
$F_7^1$	Environmental temperature $t < -10\text{ }^\circ\text{C}$	$F_8^1$	Environmental temperature $t > -10\text{ }^\circ\text{C}$
$F_9^1$	Good effect of removing snow	$F_{10}^1$	General effect of removing snow
$F_{11}^1$	Complex road conditions	$F_{12}^1$	Flat road conditions
$F_{13}^1$	Thick snow	$F_{14}^1$	Thin snow

**Table 2** The meaning of different scheme elements

Scheme element symbol	Meaning
$a_1$	Spraying snow-dissolving agents
$a_2$	High-pressure snow-blowing machine
$a_3$	Turbojet engine
$a_4$	Snow plow machine
$a_5$	Snow blower machine

According to the design demand, the snow-removing machine that can fast-clean the thick snow near an airport, and be low effect of environment should be designed. The snow is the mixture of natural snow, compressed snow, and frozen snow. The set of individual colors of the snow-removing machine is shown as follows:

$$F(A) = \{F_1^1, F_2^1, F_3^1, F_4^1, F_5^1, F_6^1, F_{13}^1\} =$$

$F_1^1$	$F_2^1$	$F_3^1$	$F_4^1$	$F_5^1$	$F_6^1$	$F_7^1$	$F_8^1$	$F_9^1$	$F_{10}^1$	$F_{11}^1$	$F_{12}^1$	$F_{13}^1$	$F_{14}^1$	
•	•	•	•	•	•							•		

$$\begin{bmatrix}
 1 & 0 & 0 & 1 & 0 & 0 & 0 & 1 & 1 & 0 & 1 & 1 & 0 & 1 \\
 1 & 0 & 0 & 1 & 0 & 1 & 1 & 1 & 1 & 0 & 1 & 0 & 1 & 1 \\
 1 & 1 & 1 & 1 & 0 & 1 & 1 & 1 & 1 & 0 & 1 & 0 & 1 & 1 \\
 1 & 0 & 0 & 1 & 0 & 1 & 1 & 1 & 0 & 1 & 1 & 0 & 1 & 1 \\
 1 & 1 & 1 & 1 & 0 & 1 & 1 & 1 & 1 & 0 & 1 & 0 & 1 & 1
 \end{bmatrix}
 \begin{matrix}
 a_1 \\
 a_2 \\
 a_3 \\
 a_4 \\
 a_5
 \end{matrix}
 \tag{7}$$

As shown in the above matrix, the scheme element “ $a_3$ ”and “ $a_5$ ” can meet the design demand. In view of the economic, the “ $a_3$ ” could choose the retired turbojet engine. The “ $a_3$ ” is cost-effective through turning waste into treasure.

## 5 Conclusion

The paper proposes a new modeling method of product conceptual design. This new method synthesizes the polychromatic sets theory and AD and makes up for some flaws of FMT and AD. It can not only present complex mechanical system and constraints among them but also illustrate the realization methodologies of specific mapping from FRs to DPs and provide a brand-new train of thought for the product design. Exemplified by the main module design of snow-removing car, the efficiency and feasibility of this proposed approach is validated, and the evaluation mechanism of the new method is worth for further studying.

**Acknowledgements** This work is supported by the Program for Changjiang Scholars and Innovative Research Team in University (No.IRT1109), the Natural Science Foundation of Liaoning Province (201102008), and by the Program for Liaoning Excellent Talents in University (LJQ2013133).

## References

1. Asiedu Y, Gu P (1998) Product life cycle cost analysis: state of the art review. *Int J Prod Res* 36(4):883–908
2. Suh NP (2001) *Axiomatic design, advances and application*. Oxford University Press, London
3. Robotham AJ (2002) The use of function-means trees for modeling technical, semantic and business functions. *J Eng Des* 13(3):243–251
4. Zhang G, Tang D (2009) Axiomatic design based on improved function-means tree. *J Eng Des* 16(1):1–6
5. Pahl G (1992) *Engineering design*. China Machine Press, Beijing
6. Hubka V et al (1988) *Theory of technical systems*. Springer, New York
7. Tan R, Yuan C, Sun L et al (2000) Function-means tree method in conceptual design. *Mech Sci Technol* 19(4):563–565
8. Malmqvist J (1997) Improved function-means Tree by inclusion of design history information-Johan. *J Eng Des* 8(2):107–117
9. Pavlov V (2000) *Polychromatic sets and graphs for CALS technology*. Stank Press, Moscow, pp 10–25
10. Wang X, Li S (2013) Scalable routing modeling for wireless AD hoc networks by using polychromatic sets. *IEEE Syst J* 7(1):50–58
11. Li Z, Gao X, Zhao L (2010) *Information modelling and optimization based polychromatic sets theory*. Science Press, Beijing
12. Li Z, Song C, Li T (2001) Manufacturing simulation of product based on polychromatic sets and polychromatic graphs. *Comput Integr Manufact Syst*. 7(7):67–71
13. Johannesson H, Soderberg R (2000) Structure and matrix models for tolerance analysis from configuration to detail design. *Res Eng* 12:112–125
14. Tang F, Li Z (2003) A new approach to conceptual design of mechanical product using polychromatic sets. *J Comput Aided Des Comput Graph* 15(2):150–155
15. Jiang L, Li D, Zhou X et al (2013) Concept design of connecting rod cleiner fixture based on polychromatic sets. *Mach Tool Hydraulics* 41(7):131–134
16. Chen Y, Teng H (2012) Comprehensive dependency matrix for heterogeneous modular combination coupling analysis. *J Mech Eng* 48(11):21–28
17. Li Y, Wu W, Wang J et al (2014) Study on parameter optimization of concave disc copying icebreaking snow sweeper. *Int J Smart Home* 8(3):197–206

# Study on Dynamic Balance PID Control Algorithm and Its Application on the Quadrotor

Hongwei Yan, Hongbin Li and Shaohua Song

**Abstract** This paper aims to present a dynamic balance PID control algorithm for the quadrotor, and the control algorithm combines the dynamic balance algorithm and the regular PID control algorithm. The proposed control algorithm used an angle as the set point of the PID controller. The selected angle is oriented opposite the sampling value of the inclination angle of the quadrotor, and its absolute value is smaller than the sampling value of the inclination angle. By using Newton–Euler equation approach, the mathematical model of the quadrotor is derived. And the simulation model is built based on the mathematical model in MATLAB. A simulation control system for the quadrotor which is based on the dynamic balance PID control algorithm is built. Simulation results show that by using the dynamic balance PID control algorithm, the inclination angle of the quadrotor can be controlled to a set error range, which validate the proposed control algorithm.

**Keywords** Dynamic balance · PID control · Quadrotor · Inclination angle

## 1 Introduction

Dynamic balance is macro-balance which is in constant motion and constant change. Balance is a dynamic process, and absolute static balance does not exist. Dynamic balance has been a hot topic in robot research. Kim [1] and Zhong et al. [2] proposed dynamic balance control algorithm for six-legged walking robot and suspended wheeled mobile manipulator. Zhou and Meng [3] presented a general fuzzy reinforcement learning method for biped dynamic balance control. Baek and Jun [4] improved the stabilization of a hopping humanoid robot by using a linearization method. On the other hand, PID control is a mature control method. Combination of the PID control algorithm and modern control theory can be more effective to solve the problem of the quadrotor's control. In [5], the control system

---

H. Yan (✉) · H. Li · S. Song  
Ludong University, NO. 186, Middle Hongqi Rd, Yantai 264025, China  
e-mail: yanhongwei@hitwh.edu.cn

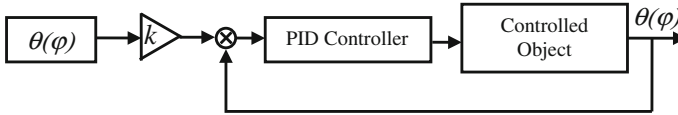


**Fig. 1** Diagram of the dynamic balance PID controller

of the quadrotor was divided into two parts: the active disturbance rejection control loop and the classical PID control loop. Similarly, the controller which was proposed in [6] consists of a linear PID feedback and a compensation of inertia torques. In [7] and [8], the decentralized PID neural network control scheme and fuzzy PID control were, respectively, used in quadrotor. As stated above, combination of dynamic balance control algorithm and PID control has not been addressed in the control of the quadrotor.

In this paper, a dynamic balance PID controller for the quadrotor is proposed. Based on the control algorithm, the set point of the PID controller is not zero which is different to the regular PID controller. Instead, the set point of the PID controller is an angle, as shown in Fig. 1. The angle is oriented opposite the sampling value of the inclination angle of the quadrotor, and its absolute value is smaller than the sampling value of the inclination angle. By and large, the quadrotor moves toward balance, but never be absolute balance.

In Fig. 1,  $-1 < k < 0$ .  $\theta$  and  $\varphi$  are inclination angles of the quadrotor relative to  $X$ -axis and  $Y$ -axis and the feedback values of the PID controller. As shown in Fig. 1, because the set point of the PID controller is not zero, the quadrotor keeps on oscillating. But by the gain  $k$ , the amplitude of the oscillation is decreased. In other words, for a long time, the quadrotor is tending to balance, namely dynamic balance. When the amplitude of the oscillation is within a value of range, we can consider the quadrotor is hover stabilization. The dynamic control algorithm can also be applied to the control of unstable robot such as one-legged robot and unicycle robot. This paper is organized as follows. In Sect. 2, we developed the mathematical model of the quadrotor. The simulation results are shown in Sect. 3. Finally, in Sect. 4, we draw some conclusions of this work.

## 2 Mathematical Model

### 2.1 Coordinate System

In order to analyze the mechanism theoretically, the coordinate system has to be built. To facilitate the theoretical analyses, we set up two coordinate systems. In order to describe the position of the quadrotor according to the ground, the fixed earth coordinate system  $\{E\}$  is constructed. And the body coordinate system  $\{B\}$  is used to describe the attitude of the quadrotor. We consider that the attitude of the

{B} is obtained by rotating  $\phi$  around  $X_E$ , rotating  $\theta$  around  $Y_E$ , and rotating  $\psi$  around  $Z_E$ . So, the rotation matrix between coordinates {B} and {E} is

$$\begin{aligned}
 R(\phi, \theta, \psi) &= \begin{bmatrix} c\psi & -s\psi & 0 \\ s\psi & c\psi & 0 \\ 0 & 0 & 1 \end{bmatrix} \cdot \begin{bmatrix} c\theta & 0 & s\theta \\ 0 & 1 & 0 \\ -s\theta & 0 & c\theta \end{bmatrix} \cdot \begin{bmatrix} 1 & 0 & 0 \\ 0 & c\phi & -s\phi \\ 0 & s\phi & c\phi \end{bmatrix} \\
 &= \begin{bmatrix} c\theta c\psi & -s\psi c\phi + c\psi s\theta s\phi & s\psi s\phi + c\psi s\theta c\phi \\ c\theta s\psi & c\psi c\phi + s\psi s\theta s\phi & -c\psi s\phi + s\psi s\theta c\phi \\ -s\theta & c\theta s\phi & c\theta c\phi \end{bmatrix} \tag{1}
 \end{aligned}$$

where

$$c\psi = \cos(\psi), s\psi = \sin(\psi), c\theta = \cos(\theta), s\theta = \sin(\theta), c\phi = \cos(\phi), s\phi = \sin(\phi).$$

### 2.2 Mathematical Model

For further analysis, some assumptions are made as follows: (a) The quadrotor is homogenously symmetric rigid body. (b) The origin of the coordinate {E} is the geometrical center and the center of the mass. (c) Both the aerodynamic resistance and the gravity are irrelevant to the height of the quadrotor. (d) The lift force of the quadrotor is proportional to the motor speed. (e) The influence of the air flow is ignored.

The motion of the quadrotor can be considered as rigid body of six degrees of freedom: rotation around the three axes (pitch, roll, and yaw) and linear motion along the three axes. According to Newton second law and moment and momentum theorem, the forces and moment can be calculated by the following formula:

$$\Sigma \vec{F} = m \cdot \frac{d\vec{v}}{dt}, \Sigma \vec{M} = \frac{d\vec{H}}{dt} \tag{2}$$

where  $\vec{F}$  is the external force.  $m$  is the mass of the quadrotor.  $\vec{v}$  is the absolute velocity of the quadrotor in the earth coordinate system.  $\vec{M}$  represents the external moment.  $\vec{H}$  is the absolute moment of momentum of the quadrotor in the earth coordinate system.

In the body coordinate {B}, according to the theoretical mechanics, the following equations can be deduced.

$$\frac{d\vec{v}}{dt} = \vec{I}_v \frac{\tilde{d}\vec{v}}{dt} + \vec{\omega} \times \vec{v}, \quad \frac{d\vec{H}}{dt} = \vec{I}_H \frac{\tilde{d}\vec{H}}{dt} + \vec{\omega} \times \vec{H} \tag{3}$$

where  $\vec{I}_v$  is the unit vector along  $\vec{v}$ .  $\vec{\omega}$  is the total angular velocity vector of the body coordinate system relative to the earth coordinate system.  $\vec{I}_H$  is the unit vector along  $\vec{H}$ .  $\frac{\tilde{d}\vec{H}}{dt}$  represents the relative derivation of the quadrotor in the {B}.

In the body coordinate  $\{B\}$ ,  $\vec{v}$  and  $\vec{\omega}$  can be described as follows:

$$\vec{v} = u\vec{i} + v\vec{j} + w\vec{k}, \quad \vec{\omega} = p\vec{i} + q\vec{j} + r\vec{k}$$

Linear velocity and angular velocity can be calculated by the following equations:

$$\begin{cases} m(\dot{u} + wq - vr) = \sum F_{xB} \\ m(\dot{v} + ur - wp) = \sum F_{yB} \\ m(\dot{w} + vp - uq) = \sum F_{zB} \end{cases}, \quad \begin{cases} I_x \dot{p} - (I_y - I_z)qr = \sum M_{xB} \\ I_y \dot{q} - (I_z - I_x)rp = \sum M_{yB} \\ I_z \dot{r} - (I_x - I_y)pq = \sum M_{zB} \end{cases} \quad (4)$$

where  $I_x$ ,  $I_y$ , and  $I_z$  represent the moment inertia of the quadrotor relative to the  $x_B$ ,  $y_B$ , and  $z_B$  in  $\{B\}$ .

Given the projection of the gravity of the quadrotor is  $[G_x, G_y, G_z]^T$ , the following relation can be deduced:

$$\begin{bmatrix} 0 \\ 0 \\ -mg \end{bmatrix} = R \cdot \begin{bmatrix} G_x \\ G_y \\ G_z \end{bmatrix}$$

Then, the force and moment can be calculated by the following equations:

$$\begin{cases} \sum F_{xB} = G_x = mg \cdot \sin(\theta) \\ \sum F_{yB} = G_y = -mg \cdot \sin(\phi) \cos(\theta) \\ \sum F_{zB} = T_1 + T_2 + T_3 + T_4 - mg \cdot \cos(\theta) \cos(\phi) \end{cases} \quad (5)$$

$$\begin{cases} \sum M_{xB} = (T_4 - T_2) \cdot d \\ \sum M_{yB} = (T_1 - T_3) \cdot d \\ \sum M_{zB} = (M_1 - M_2 + M_3 - M_4) = L(T_1 - T_2 + T_3 - T_4) \end{cases} \quad (6)$$

where  $d$  represents the distance from the geometric center to the axis of the motor. And  $L$  is the ratio of the couple force to the lift force provided by the rotors.  $T_i$  ( $i = 1-4$ ) represent the four rotors' lift forces.

According to the Euler equations, relations between  $[\dot{\phi}, \dot{\theta}, \dot{\psi}]^T$  and  $[p, q, r]^T$  can be described as follows:

$$\begin{bmatrix} p \\ q \\ r \end{bmatrix} = \begin{bmatrix} c\theta c\psi & -s\psi & 0 \\ c\theta s\psi & c\psi & 0 \\ -s\theta & 0 & 1 \end{bmatrix} \cdot \begin{bmatrix} \dot{\phi} \\ \dot{\theta} \\ \dot{\psi} \end{bmatrix} \quad (7)$$

Suppose the projection of the  $T_1, T_2, T_3, T_4$  is  $T_{EX}, T_{EY}, T_{EZ}$ , then we can deduce the following equation:

$$\begin{bmatrix} T_{EX} \\ T_{EY} \\ T_{EZ} \end{bmatrix} = R \cdot \begin{bmatrix} 0 \\ 0 \\ \sum T_i \end{bmatrix}$$

We assume that the expression of  $\vec{v}$  in the earth coordinate system is

$$\vec{v} = v_x \vec{i} + v_y \vec{j} + v_z \vec{k}$$

Then, the linear velocity equations can be deduced.

$$T_{EX} = m \cdot \frac{dv_x}{dt}, \quad T_{EY} = m \cdot \frac{dv_y}{dt}, \quad T_{EZ} - mg = m \cdot \frac{dv_z}{dt} \quad (8)$$

The input value of the PID controller can be defined as follows:

$$\Delta\theta = \theta \cdot k - \theta = \theta(k - 1), \quad \Delta\varphi = \varphi \cdot k - \varphi = \varphi(k - 1) \quad (9)$$

The steady values of the lift forces of the four rotors are as follows:

$$T_{is} = \frac{G}{4 \cos \theta \cos \varphi} \quad (i = 1, 2, 3 \text{ and } 4) \quad (10)$$

where  $i$  represents the  $i$ th rotor of the quadrotors.

And the control law can be expressed as follows:

$$T_i = \begin{cases} T_{is} + K_p \cdot \Delta\theta + K_D \cdot \frac{d(\Delta\theta)}{dt} + K_I \cdot \int \Delta\theta dt & i = 1, 3. \\ T_{is} + K_p \cdot \Delta\varphi + K_D \cdot \frac{d(\Delta\varphi)}{dt} + K_I \cdot \int \Delta\varphi dt & i = 2, 4. \end{cases} \quad (11)$$

In order to obtain the moment inertia of the three coordinate axes of the quadrotors, we mapped out the quadrotors in Solidworks. In Solidworks software,  $I_x = 0.019198 \text{ kg m}^2$ ,  $I_y = 0.019198 \text{ kg m}^2$ , and  $I_z = 0.037468 \text{ kg m}^2$ .

### 3 Simulations

Main simulation modules are shown in Fig. 2.

As shown in Fig. 2, there are eight main modules in the simulation model. In the assignment module, the mass of the components of the quadrotor and the moment of inertia of each axis are assigned. The linear velocity module and the angular

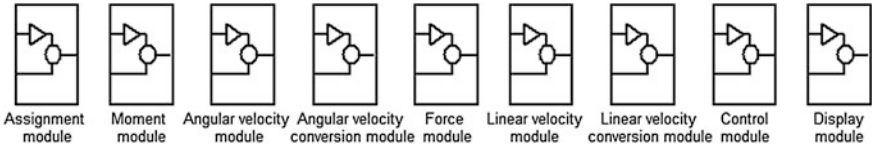


Fig. 2 Main simulation modules

velocity module are built based on Eq. (4). The moment module and the force module are built based on Eqs. (5) and (6), respectively. Based on Eqs. (1), (7), and (8), the angular velocity and linear velocity of the quadrotor are converted from the body coordinate system  $\{B\}$  to the earth coordinate system  $\{E\}$  by the angular velocity conversion module and the linear velocity conversion module. In the control module, the output lift forces of the rotors are calculated based on Eqs. (9)–(11). And finally, the display module is used to display the values and curves of the parameters of the quadrotors. To facilitate the simulation, both the initial values of  $\theta$  and  $\varphi$  are 0.7 rad, the gravity of the quadrotor is 1 kg,  $L = 1$ ,  $d = 0.3$  m,  $K_P = 0.05$ ,  $K_I = 0.013$ , and  $K_D = 0.01$ . Figures 3 and 4 show the relationships between variation trends of the inclinations and the gain  $k$ .

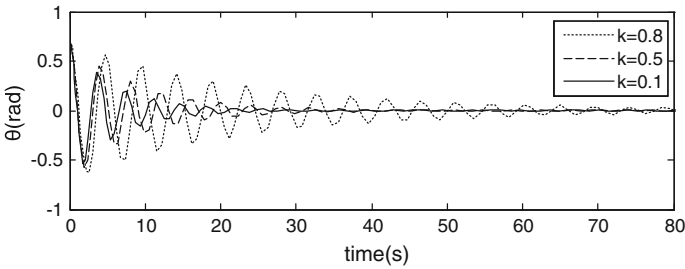


Fig. 3  $\theta$  versus  $k$

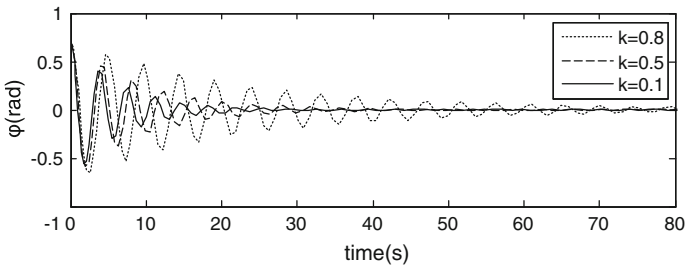
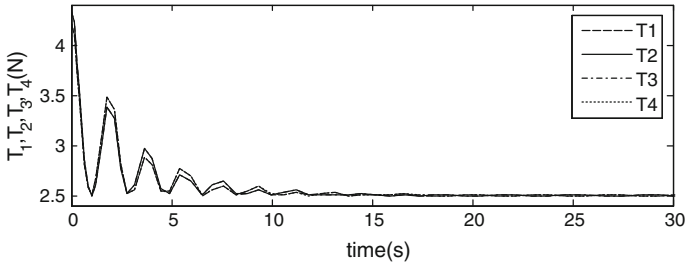


Fig. 4  $\varphi$  versus  $k$





**Fig. 5** Lift forces versus time

As is shown in Figs. 3 and 4, the value of  $k$  produces an effect on the motion process of the quadrotor. When  $k = 0.8$ , variation of the inclinations from 0.7 to 0.1 rad takes 47 s. When  $k = 0.5$  and 0.1, the adjustment time is then cut to 18 and 13 s, respectively. We can find that the adjustment time is affected by the gain  $k$ . The smaller the  $k$  is, the sooner the quadrotor becomes stable. Figure 5 gives the lift forces of the four rotors.

As shown in Fig. 5, under the control of the dynamic balance PID controller, the lift forces of the four rotors are oscillatorily damped to the steady values (2.5 N). Consequently, the resultant force of the steady values of the four rotors is close to 10 N, which is equal to the weight of the quadrotors.

## 4 Conclusions

In this paper, a dynamic balance PID controller was proposed and was applied to controlling the stability of the quadrotors. The simulation results show that both the inclination angles and the lift forces of the four rotors show damping oscillation behavior, which validate the feasibility and effectiveness of the proposed control algorithm. The main contribution of this paper is that it has found a control algorithm which not only can be used to control the quadrotor but also can be applied to the control of the unstable robot such as one-legged robot and unicycle robot.

## References

1. Kim JY (2015) Dynamic balance control algorithm of a six-legged walking robot, little crabster. *J Intell Rob Syst* 78:47–64
2. Zhong G, Deng H, Kobayashi Y, Wang H (2014) Theoretical and experimental study on remote dynamic balance control for a suspended wheeled mobile manipulator. *Nonlinear Dyn* 79 (2):851–864
3. Zhou C, Meng Q (2003) Dynamic balance of a biped robot using fuzzy reinforcement learning agents. *Fuzzy Sets Syst* 134(2):169–187

4. Baek K, Jun H (2012) Dynamic balance of a hopping humanoid robot using a linearization method. *Int J Humanoid Rob* 09(3):6–8
5. Liu G, Wang B, Cao YF (2014) Combined PID/ADRC flight control for a quadrotor unmanned helicopter. *J Yunnan Univ Natl* 23(2):151–156
6. Su J (2011) Attitude control of quadrotor aircraft via nonlinear PID. *J Beijing Univ Aeronaut Astronaut* 37(9):1054–1058
7. Chen YM, Yong-Ling HE, Kong LB, Zhou MF (2014) Decentralized PID neural network control for a quadrotor helicopter. *J Chin Inert Technol* 22(2):185–190
8. Zhang J, Zhang H, Liu H, Huo J (2014) Fuzzy-PID control for macro-quadrotor UAV. *Ordnance Ind Autom* 33(6):58–62

# The Electronic, Magnetic, and Vibrational Properties of $\text{Ce}_3\text{Co}_{29}\text{Ge}_4\text{B}_{10}$

Liu-Tao Zhao, Xiao-Xu Wang, Jin-Rong Huo, Hai-Xia Cheng,  
Jian-Qiao Xie, Lu Li and Ying Liu

**Abstract** We have studied the electronic and vibrational properties of  $\text{Ce}_3\text{Co}_{29}\text{Ge}_4\text{B}_{10}$  compounds using the first-principles GGA + U method. The calculation finds that the magnetic moment of Ce and Co atoms has a good agreement with experimental value when  $U = 3.8$  eV. Also, the calculated lattice constants and atomic positions are corresponding to the experimental results. By using the interatomic pair potential obtained with the lattice inversion method, the phonon density of states of  $\text{Ce}_3\text{Co}_{29}\text{Ge}_4\text{B}_{10}$  compounds is also studied.

**Keywords** Electronic properties · Magnetic properties · Interatomic potentials · Lattice vibration

## 1 Introduction

The cerium intermetallic compounds have been investigated by a number of researchers because of their unusual and interesting physical properties [1–4]. These properties arise from the strongly correlated nature of the  $4f$  electrons and their hybridization with the conduction electrons. In this work, the structural, electronic, and magnetic properties of  $\text{Ce}_3\text{Co}_{29}\text{Ge}_4\text{B}_{10}$  are calculated by first-principles calculations GGA + U method. In addition, the phonon densities of states of  $\text{Ce}_3\text{Co}_{29}\text{Ge}_4\text{B}_{10}$  are evaluated by atomistic simulation which makes it possible to predict some properties related to lattice vibration.

---

L.-T. Zhao · X.-X. Wang (✉) · J.-Q. Xie  
Beijing Computing Center, Beijing 100094 China  
e-mail: wangxx@bcc.ac.cn

J.-R. Huo · H.-X. Cheng · L. Li  
Institute of Applied Physics, Beijing University of Science and Technology,  
Beijing 100083, China

Y. Liu  
Hebei Advanced Thin Film Laboratory, Department of Physics, Hebei Normal University,  
Shijiazhuang 050024 Hebei, China

## 2 Methodology

### 2.1 Method of First Principles

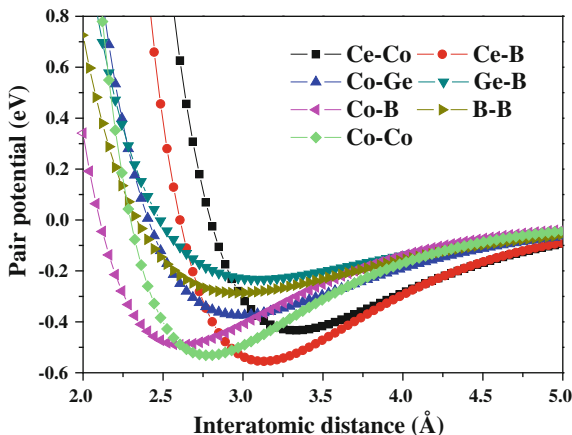
For electronic structure, cohesive energy, and magnetic moments on  $\text{Ce}_3\text{Co}_{29}\text{Ge}_4\text{B}_{10}$  calculations, we use Vienna ab initio simulation package (VASP) [5, 6] with the projector-augmented wave (PAW) [7] construction for the pseudo-potential. The package is based on the density functional theory (DFT) [8, 9]. The exchange-correlation energy and potential were treated with the generalized gradient approximation (GGA) using the functional of Perdew, Burke, and Ernzerhof (PBE) [10]. GGA could describe the complex system precisely. However, it has been proved that there will be a matter when dealing with the localized  $4f$  and  $3d$  electron. Therefore, we adopt the GGA + U method, namely applying the Hubbard parameter U correction on Ce  $4f$  electrons, to perform the calculation. In Monkhorst–Pack [11],  $k$ -point meshes with a density of at least  $(4 \times 4 \times 5)$  points in the Brillouin zone of the compound are chosen. The convergence thresholds between optimization cycles for energy change and maximum force are set as  $1 \times 10^{-7}$  eV/atom and  $1 \times 10^{-6}$  eV/Å, respectively. We carry out the calculation with the default of plane wave cut-off energy when we set PREC = high. The total density of states (DOS) and the site-projected DOS are given (states/eV/cell).

### 2.2 Method of Pair Potentials

According to Chen’s lattice inversion method, the pair potentials can be inverted strictly from the cohesive energy curves [12, 13]. An introduction to the lattice inversion method is given in these previous works [14–17]. Here, the pair potentials can be fitted simply by the Morse function

$$\Phi(x) = D_0 \left( e^{[-\gamma(x/R_0-1)]} - 2e^{[-(\gamma/2)(x/R_0-1)]} \right) \quad (1)$$

where  $D_0$ ,  $R_0$ , and  $\gamma$  are potential’s parameters. Several important inverted pair potential curves are shown in Fig. 1.

**Fig. 1** Some important potential curves

### 3 Discuss and Results

#### 3.1 Electronic and Magnetic Properties

We built the quaternary phase compound  $\text{Ce}_3\text{Co}_{29}\text{Ge}_4\text{B}_{10}$  type structure with the  $P4/nmm$  space group. We first optimize the structure, yielding the following lattice parameters:  $a = 11.2084 \text{ \AA}$  and  $c = 7.86360 \text{ \AA}$ . These lattice parameters are in very good agreement with the experiment results [18]:  $a = 11.206 \text{ \AA}$  and  $c = 7.8641 \text{ \AA}$ . The crystal structure and refinement parameter are listed in Table 1. There will be an influence for interatomic interaction if we take into account the distance between atoms. Furthermore, the distances of different sites are displayed in Table 2. Generally, the exchange interaction of bonds longer than  $3.2 \text{ \AA}$  can be ignored. For the sake of brevity, we only list the interatomic distances in the range of  $0\text{--}3.2 \text{ \AA}$ .

Our calculation indicates that magnetic moment of  $\text{Ce}_3\text{Co}_{29}\text{Ge}_4\text{B}_{10}$ ,  $0.573 \mu\text{B}/\text{Ce}$ , and  $0.526 \mu\text{B}/\text{Co}$  matches very well with the experimental data  $0.58 \mu\text{B}/\text{Ce}$  and  $0.36 \mu\text{B}/\text{Co}$  in [19] when  $U = 3.8 \text{ eV}$ . The magnetic moment of Co and Ce atoms at different sites is described in Fig. 2. For accuracy, we select  $U = 3.8 \text{ eV}$  to calculate magnetic moment and site-projected DOS of  $\text{Ce}_3\text{Co}_{29}\text{Ge}_4\text{B}_{10}$ .

In Fig. 2, we can find that the magnetic moment of Ce-4d atoms has a pronounced change with increasing  $U$  value. Thus, we plot the DOS of Ce-4d  $f$  electron (Fig. 3) at different  $U$  parameters. It reveals that Ce-4d atoms  $f$  electron provide large magnetic moment as the peak of spin down appears an obvious split. From Fig. 2, we can observe that the major contribution of magnetic moment for Co atoms comes from 2c site. In order to have a farther understanding, the occupancy of electrons both upon and below the Fermi level of Ce atoms is given in Table 3. According to Table 3, the asymmetrical DOS between the majority and minority spin channels near the Fermi level could be observed visibly.

**Table 1** Calculated and experimental [3] crystal parameter (Å) for the  $Ce_3Co_{29}Ge_4B_{10}$  structure

Calculated					Experimental				
Atom	Site	$x/a$	$y/b$	$z/c$	Atom	Site	$x/a$	$y/c$	$z/c$
Ce1	2b	0.25	0.75	0.5	Ce1	2b	0.25	0.75	0.5
Ce2	4d	0	0	0	Ce2	4d	0	0	0
Co1	2c	0.25	0.25	0.4665	Co1	2c	0.25	0.25	0.466(5)
Co2	8i1	0.25	0.6420	0.8891	Co2	8i1	0.25	0.642(1)	0.889(2)
Co3	8i2	0.25	0.0262	0.4732	Co3	8i2	0.25	0.026(2)	0.473(2)
Co4	8i3	0.25	0.0902	0.9818	Co4	8i3	0.25	0.090(2)	-0.018(2)
Co5	8j1	0.1321	0.1321	0.2412	Co5	8j1	0.132(1)	0.132(1)	0.241(2)
Co6	8j2	0.1351	0.1351	0.6942	Co6	8j2	0.135(1)	0.135(1)	0.694(2)
Co7	16k	0.0781	0.5883	0.3350	Co7	16k	0.078(1)	0.588(1)	0.335(1)
Si	8i	0.25	0.5612	0.1594	Si	8i	0.25	0.561(2)	0.159(4)
B1	2c1	0.25	0.25	0.2430	B1	2c1	0.25	0.25	0.24(3)
B2	2c2	0.25	0.25	0.9010	B2	2c2	0.25	0.25	0.90(1)
B3	8i	0.25	0.0110	0.7520	B3	8i	0.25	0.01(1)	0.75(2)
B4	8j	0.0515	0.0515	0.4854	B4	8j	0.051(5)	0.051(5)	0.485(4)
$a = 11.2084$					$a^* = 11.206(1)$		0.02140 % (Err.)		
$c = 7.86360$					$c^* = 7.8641(9)$		0.00636 % (Err.)		
$v = 987.890$					$v^* = 987.5(2)$		0.03950 % (Err.)		

**Table 2** Interatomic distances (Å) for the crystallographic sites of the  $Ce_3Co_{29}Ge_4B_{10}$  structure

	Ce	Co	Ge	B
Ce-2b	–	Co-16k(2.9085)	Ge-8i(3.2052)	–
Ce-4d	–	Co-8j1(2.9365)	Ge-8i(3.1629)	–
Co-2c	–	Co-8j2(2.4752)	–	B-2c1(2.7752)
Co-8i1	–	Co-8i1(2.3699)	Ge-8i(2.2640)	B-8i(1.9862)
Co-8i2	Ce-2b(3.0082)	Co-8j2(2.4338)	Ge-8i(2.6019)	B-8j(2.1552)
Co-8i3	Ce-4d(2.9166)	Co-8j1(2.4259)	Ge-8i(2.1536)	B-2c2(1.8621)
Co-8j1	Ce-4d(2.7685)	Co-8i3(2.4259)	Ge-8i(2.5652)	B-2c1(1.8311)
Co-8j2	Ce-4d(3.1555)	Co-16 k(2.4082)	–	B-8i(1.9100)
Co-16k	Ce-2b(2.8879)	Co-8j2(2.4082)	Ge-8i(2.3419)	B-8j(1.9436)

\*The blanks filled with dash indicate that the distance between them greater than 3.2 Å

Then, site-projected DOS are plotted in Fig. 4 since it has a consequence which is accordant with experimental data on magnetic moment and lattice parameter. In Fig. 4, the most important contribution to the values of the Ce DOS above Fermi level comes from 4*f* state. And the DOS of 4*f* state at Ce-4*d* site has an obvious asymmetry different from Ce-2*b* site which is well symmetric. Next, comparing the DOS of Co-8*i* 3*d* electron with Co-2*c* site, it can be indicated that the 3*d* electron of Co-2*c* site is asymmetry near the Fermi level, whereas it is symmetrical at Co-8*i* site.

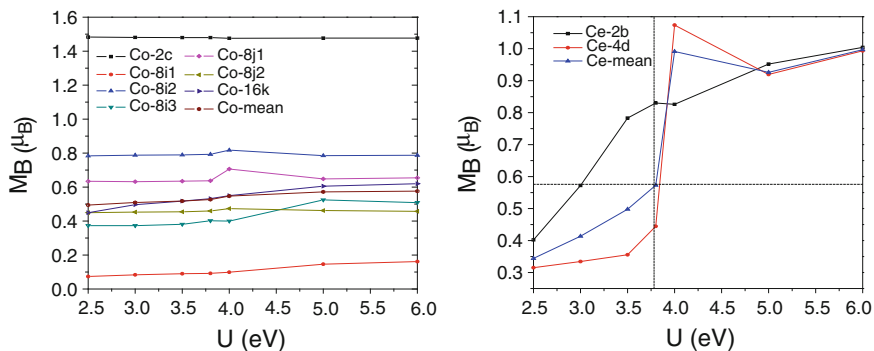


**Fig. 2** The magnetic moment per Ce and Co atom at different sites in compound with respect to the  $U$  parameter

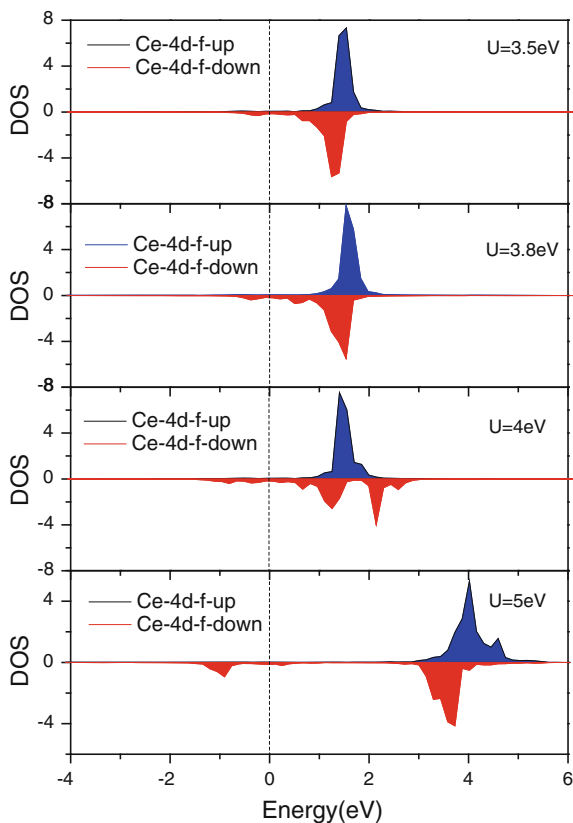


**Fig. 3** The DOS of Ce-4d site f electron at variational  $U$  values

**Table 3** The density of states of Ce-2b and Ce-4d

Site		$U$ value (eV)	Energy level (eV)	3.0	3.5	3.8	4.0	5.0
		Electron						
Ce	2b	f-up	<0	0.0545	0.0454	0.0408	0.0545	0.0300
			>0	2.8414	2.8386	2.8345	2.8414	2.7966
		f-down	<0	0.0694	0.0550	0.0842	0.0447	0.0353
			>0	2.8302	2.8364	2.8363	2.8208	2.8162
	4d	f-up	<0	0.1048	0.0959	0.0868	0.0918	0.0344
			>0	2.7970	2.8049	2.8123	2.8081	2.7359
		f-down	<0	0.1904	0.1904	0.2224	0.3548	0.4401
			>0	2.7062	2.7034	2.6659	2.5316	2.4080

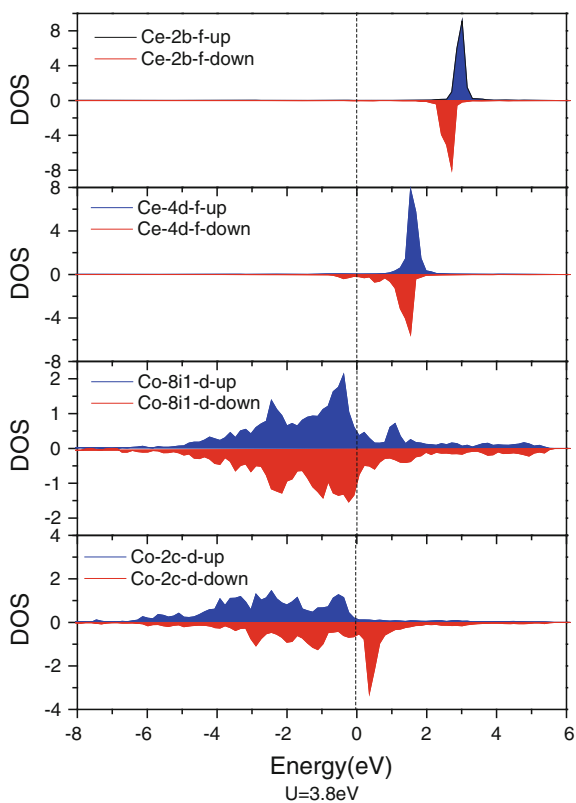


**Fig. 4** Site-projected DOS of Ce-2b, Ce-4d, Co-2c, and Co-8i1 when  $U = 3.8$  eV



### 3.2 Lattice Dynamic Simulations

Since the potentials are inverted from the virtual structures, it is necessary to test the reliability for the complex structures. So the structure parameters of  $\text{Ce}_3\text{Co}_{29}\text{Ge}_4\text{B}_{10}$  are calculated. The structure of  $\text{Ce}_3\text{Co}_{29}\text{Ge}_4\text{B}_{10}$  is simulated by the energy minimization process which is realized by conjugate gradient methods. The results are  $a = 11.212 \text{ \AA}$  and  $c = 7.873 \text{ \AA}$  which are very close to those obtained from the experiments  $a = 11.206 \text{ \AA}$  and  $c = 7.864 \text{ \AA}$  [18]. It furnishes convincing evidence that the potentials are reliable. Therefore, these potentials can be applied to calculate the lattice dynamic properties of  $\text{Ce}_3\text{Co}_{29}\text{Ge}_4\text{B}_{10}$ .

The calculated phonon density of states (PDOS) of  $\text{Ce}_3\text{Co}_{29}\text{Ge}_4\text{B}_{10}$  is shown in Fig. 5. It is shown that the highest frequency for  $\text{Ce}_3\text{Co}_{29}\text{Ge}_4\text{B}_{10}$  is 18.02 THz. The PDOS is extended due to the relatively low symmetry and various interatomic distances. The vibrational modes are mostly excited by B atoms contribute a major part to the local modes with high-frequency. Ce contributes to the modes below 5.00 THz only. Co and Ge contribute mainly on low frequencies part of PDOS.

In addition to the DOS, the dependences of the specific heat, vibrational entropy, and Debye temperature on the temperature for  $\text{Ce}_3\text{Co}_{29}\text{Ge}_4\text{B}_{10}$  are derived from the calculated PDOS as shown in Fig. 6. The figure clearly shows that the variation of specific heat and entropy with temperature for the ternary systems does not show any anomaly. The Debye temperature reflects the property of the materials at lower temperature and lower frequency. The calculated Debye temperature near 0 K is 437 K. Unfortunately, in the existing literature, there are no experimental data on the PDOS and Debye temperature of the compounds. Therefore, the above calculation results have not been verified by experiments.

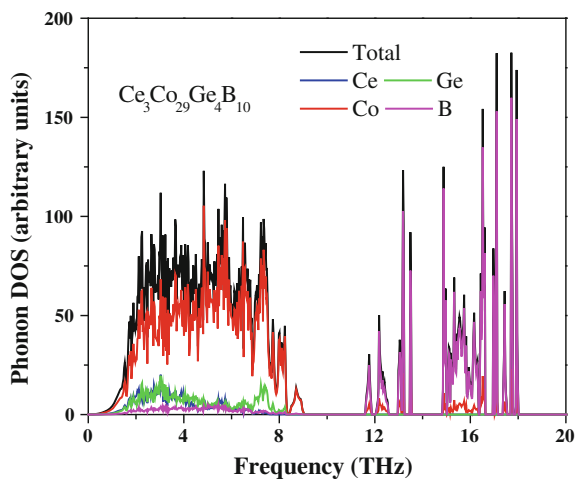


Fig. 5 Calculated phonon densities of states

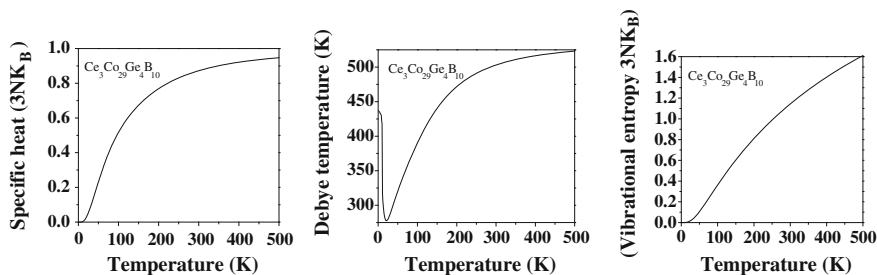


Fig. 6 Calculated specific heat, vibrational entropy, and Debye temperature

## 4 Conclusions

In summary, we show in this paper that the magnetic moment and electronic density of states of  $\text{Ce}_3\text{Co}_{29}\text{Ge}_4\text{B}_{10}$  are calculated by the first-principles calculations based on DFT. The calculated results are in good agreement with observed results from the literatures. We have also calculated the lattice vibrational properties of  $\text{Ce}_3\text{Co}_{29}\text{Ge}_4\text{B}_{10}$  compounds.

**Acknowledgments** The work was supported by the National Natural Science Foundation of China (Grant No. 11272048 and Grant No. 50971024) and the 973 Project in China (No. 2011CB606401).

## References

1. Custers J, Lorenzer K-A, Müller M, Prokofiev A, Sidorenko A, Winkler H, Strydom AM, Shimura Y, Sakakibara T, Yu R, Si Q, Paschen S (2012) Destruction of the Kondo effect in the cubic heavy-fermion compound  $\text{Ce}_3\text{Pd}_{20}\text{Si}_6$ . *Nat Mater* 11:189–194
2. Deen PP, Strydom AM, Paschen S, Adroja DT, Kockelmann W, Rols S (2010) Quantum fluctuations and the magnetic ground state of  $\text{Ce}_3\text{Pd}_{20}\text{Si}_6$ . *Phys Rev B* 81:064427-1-8
3. Goto T, Watanabe T, Tsuduku S, Kobayashi H, Nemoto Y, Yanagisawa T, Akatsu M, Ano G, Suzuki O, Takeda N, Dönni A, Kitazawa H (2009) Quadrupole ordering in clathrate compound  $\text{Ce}_3\text{Pd}_{20}\text{Si}_6$ . *J Phys Soc Jpn* 78:024716–024724
4. Nemoto Y, Yamaguchi T, Horino T, Akatsu M, Yanagisawa T, Goto T (2003) Ferroquadrupole ordering and Gamma\_5 rattling motion in clathrate compound  $\text{Ce}_3\text{Pd}_{20}\text{Si}_6$ . *Phys Rev B* 68:184109-1-10
5. Kresse G, Hafner J (1993) Ab initio molecular dynamics for liquid metals. *Phys Rev B* 47:558–561
6. Kresse G, Furthmüller J (1996) Efficiency of ab-initio total energy calculations for metals and semiconductors using a plane-wave basis set. *Comput Mater Sci* 6:15–50
7. Blöchl PE (1994) Projector augmented-wave method. *Phys Rev B* 50:17953–17979
8. Hohenberg P, Kohn W (1964) Inhomogeneous electron gas. *Phys Rev* 136:B864–B871
9. Kohn W, Sham LJ (1965) Density function theory. *Phys Rev* 140:A1133–A1138
10. Perdew JP, Burke K, Ernzerhof M (1996) Generalized gradient approximation made simple. *Phys Rev Lett* 77:3865–3868

11. Monkhorst Hendrik J, Pack James D (1976) Special points for Brillouin-zone integrations. *Phys Rev B* 13:5188–5192
12. Chen NX, Ren GB (1992) Carlsson-Gelatt-Ehrenreich technique and the Möbius inversion theorem. *Phys Rev B* 45:8177–8180
13. Chen NX, Ge XJ, Zhang WQ, Zhu FW (1998) Atomistic analysis of the field-ion microscopy image of  $\text{Fe}_3\text{Al}$ . *Phys Rev B* 57:14203–14207
14. Cheng HX, Wang XX, Hu YW, Zhang GH, Shen J, Qian P, Chen NX (2015) Atomistic study on the site preference and lattice vibration of  $\text{Gd}_{3-x}\text{Y}_x\text{Co}_{29}\text{T}_4\text{B}_{10}$  ( $T = \text{Al}$  and  $\text{Ge}$ ). *J Solid State Chem* 224:7–13
15. Wang XX, Qian P, Zhang ZF, Liu Y, Shen J, Chen NX (2013) Site preference, magnetism and lattice vibrations of intermetallics  $\text{M}_{7-x}\text{T}_x\text{B}_3$  ( $M = \text{Rh}, \text{Ru}$ ;  $T = \text{Fe}, \text{Co}$ ). *Intermetallics* 42:112–119
16. Li JC, Qian P, Zhang ZF, Yuan XJ, Wang YW, Shen J, Chen NX (2013) Site preference, magnetism and lattice vibrations of intermetallics  $\text{Lu}_2\text{Fe}_{17-x}\text{T}_x$  ( $T = \text{Cr}, \text{Mn}, \text{Ru}$ ). *J Solid State Chem* 201:250–255
17. Qian P, Hu QY, Shen J, Feng Y, Pan HY, Hu P (2010) An atomistic simulation of the structural and vibrational properties of  $\text{A}_4\text{Fe}_3\text{Al}_{32}$  ( $A = \text{Th}, \text{U}$ ). *Model Simul Mater Sci Eng* 18, 045002 (8 pp) 1–8
18. Zhang H, Campbell SJ, Edge AVJ (2000) Formation and structure of rare-earth intermetallic compounds  $\text{R}_3\text{Co}_{29}\text{M}_4\text{B}_{10}$ . *J Phys Condens Matter* 12, L159–L166
19. Özdemir A et al (2012) Magnetic properties of  $\text{R}_3\text{Co}_{29}\text{Si}_4\text{B}_{10}$  ( $R = \text{La}, \text{Ce}, \text{Pr}, \text{Nd}, \text{Sm}, \text{Gd}$  and  $\text{Dy}$ ) borides. *J Magn Magn Mater* 324:1258–1261

# Effects of Activation Treatment on Interfacial Bonding in A356-10 wt% B<sub>4</sub>C Composite Sheets Prepared by Rheo-Rolling

Zhan Yong Zhao, Yang Zhang, Zhou Yang Zhao, Ren Guo Guan, Yuan Dong Li and Ben Chao Chen

**Abstract** A novel semisolid stirring and rheo-rolling process for preparing aluminum–boron carbide composite sheets was proposed. The microstructure and interfacial bonding of A356-10 wt% B<sub>4</sub>C composites were investigated. The activated B<sub>4</sub>C particles had no impurities on the surface. Furthermore, no particles with an acute angle were observed, which contribute to improved wettability between the B<sub>4</sub>C particles and the aluminum matrix. The strengthening phases Al<sub>3</sub>BC and Al<sub>2</sub>O<sub>3</sub> are formed on the interface between particles and matrix, resulting in chemical bonding. A356-10 wt% B<sub>4</sub>C composite sheets with good mechanical properties were fabricated via the combination of semisolid stirring and rheological rolling. The Vickers hardness of the composite sheet with activated B<sub>4</sub>C particles reached 109 HV, and the tensile strength reached 197 MPa.

**Keywords** Activation · B<sub>4</sub>C · Sloping · Vibration · Semisolid · Rolling

## 1 Introduction

B<sub>4</sub>C-reinforced aluminum-based composites are ideal candidates for the nuclear industry due to excellent neutron absorption and mechanical properties [1]. The poor wettability of B<sub>4</sub>C with aluminum is the main problem when preparing

---

Z.Y. Zhao · Y. Zhang · Z.Y. Zhao · R.G. Guan (✉) · B.C. Chen  
School of Materials and Metallurgy, Northeastern University,  
Shenyang 110819, China  
e-mail: guanrg@smm.neu.edu.cn

R.G. Guan · Y.D. Li  
State Key Laboratory of Advanced Processing of Non-ferrous  
Metals and Reutilization, Lanzhou University of Technology,  
Lanzhou 730050, China

R.G. Guan  
JiangSu Province Binxin Special Steel Material Co., Ltd,  
Lianyungang 222113, China

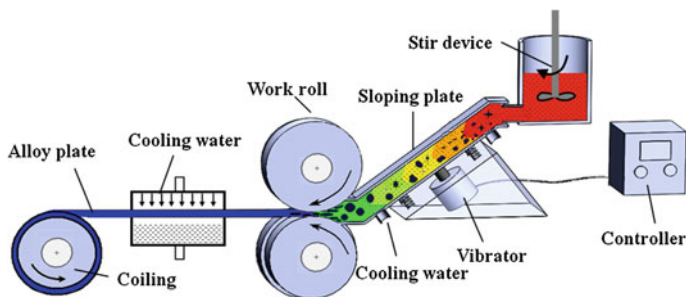


**Fig. 1** Schematic diagram of the experimental setup

Al-B<sub>4</sub>C composites [2]. Therefore, a novel semisolid stirring and rheo-rolling process for preparing Al-B<sub>4</sub>C composite was proposed, as shown in Fig. 1. The activated B<sub>4</sub>C was added to semisolid matrix slurry that was stirred, such that the agitation assisted the diffusion of reinforcement particles. The slurry was poured onto a vibratory inclined plate [3]. The primary solid phase was refined, and the reinforcement was dispersed under strong shearing and vibration. Finally, sheets of the A356-10 wt% B<sub>4</sub>C composites were prepared by rheological rolling. The sheets of the A356-10 wt% B<sub>4</sub>C composites prepared by the process are used in the bulletproof vests, armor tanks, containment of nuclear waste, neutron absorber in nuclear power plant, and transportation applications. Although an extensive amount of information is available on Al-B<sub>4</sub>C composites, there are less reports about the activation treatment and its effect on interfacial bonding. Therefore, in this study, the surface variation of B<sub>4</sub>C and interfacial bonding property of A356 with activated B<sub>4</sub>C were investigated. The corresponding materials with non-activated B<sub>4</sub>C are also studied as reference.

## 2 Materials and Methods

The B<sub>4</sub>C particles were cleaned with a 4 vol% HCl solution for 5 h and then washed with alcohol. Stirring was used to make sure that the B<sub>4</sub>C particles were in full contact with the liquid. After the cleaning process, the B<sub>4</sub>C particles were heat-treated at 400–500 °C, for different times. First, the A356 alloy was heated to 720 °C, and the melt was stirred at 500 rpm for 25 min using an impeller driven by an ac motor. When the temperature of the melt decreased to 580 °C, the B<sub>4</sub>C was added under continued stirring. To manufacture contrasting composites, both activated and non-activated B<sub>4</sub>C particles were used. The following process parameters are relevant: Rolling speed is 0.2 m s<sup>-1</sup>, cooling water flow rate is 2.5 × 10<sup>-4</sup> m<sup>3</sup> s<sup>-1</sup>, and the frequency of the sloping plate is 80 Hz. The A356-10 wt% B<sub>4</sub>C sheet with a cross-sectional size of 4 × 160 mm was obtained by rheo-rolling under conditions of combined shear and vibration. The specimens

were analyzed using a scanning electron microscope (SEM). The precipitate phase was analyzed by X-ray diffractometry (XRD). The Vickers hardness of the A356-10 wt% B<sub>4</sub>C composite sheet was analyzed by the microhardness tester. The mechanical property of the A356-10 wt% B<sub>4</sub>C composite sheet was investigated using a tensile testing machine.

### 3 Results and Discussion

#### 3.1 Surface Characterization of B<sub>4</sub>C Particles

SEM micrographs and energy-dispersive spectrometer (EDS) analysis results for B<sub>4</sub>C are shown in Fig. 2. There are many acute angles on the surface of B<sub>4</sub>C particles without pickling, as shown in Fig. 2a. The presence of such acute-angled particulate surfaces inside the composites results in a decrease in the strength of interfacial bonding [4]. During the pickling process with mechanical stirring, the B<sub>4</sub>C particles collided and rubbed against each other. The acute angle of the B<sub>4</sub>C particles was passivated, and acid-soluble impurities such as Fe elements were cleared after pickling, as shown in Fig. 2b–d.

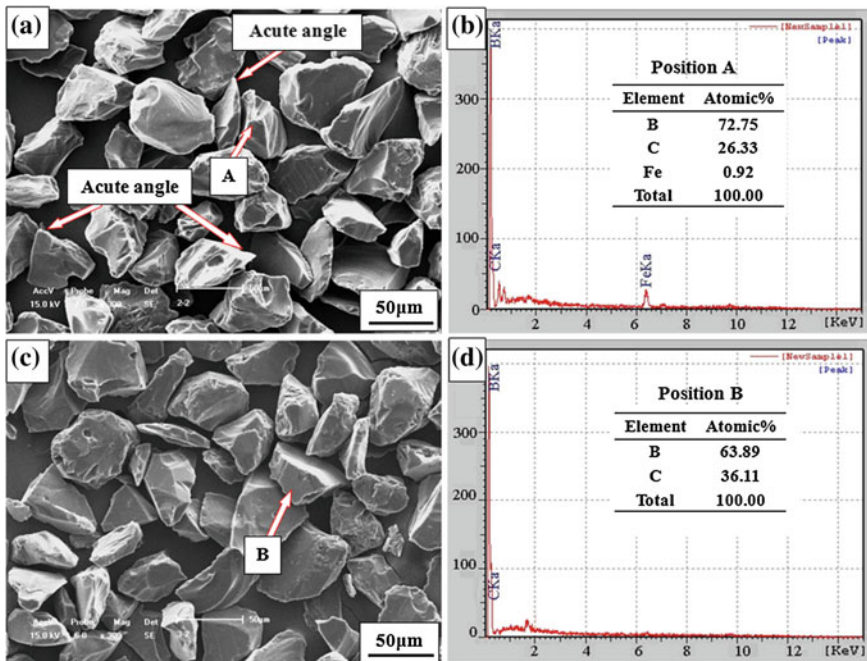
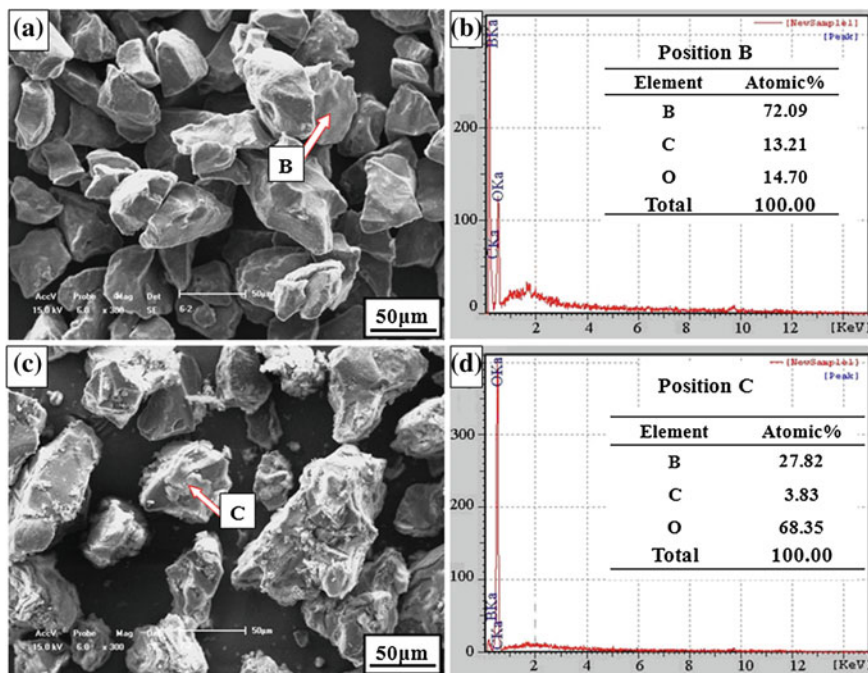
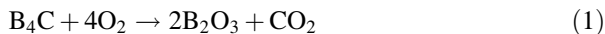


Fig. 2 SEM micrographs and EDS analyses of the B<sub>4</sub>C particles: **a, b** without pickling, **c, d** after pickling



**Fig. 3** SEM micrographs and EDS analyses of the oxidic B<sub>4</sub>C particles: **a, b** 450 °C, **c, d** 500 °C

The oxygen content of B<sub>4</sub>C particles increases with the increase in the oxidation temperature, as shown in Fig. 3. The oxygen content increased to 14.70 at.% at 450 °C, as shown in Fig. 3a, b; however, some B<sub>4</sub>C particles show the evidence of sintering (Fig. 3a). The oxygen content increased to 68.35 at.% when the temperature of oxidation treatment increased to 500 °C, as shown in Fig. 3c, d. However, the B<sub>4</sub>C particles are now seriously sintered, as shown in Fig. 3c. After the oxidation treatment, the surface of the B<sub>4</sub>C particles became white. The reactions that occurred on the surface of B<sub>4</sub>C are as follows [5]:



B<sub>2</sub>O<sub>3</sub> is a white, glassy solid that adheres to the surface of B<sub>4</sub>C particles, causing the surface color to turn white. Due to its low melting point, B<sub>2</sub>O<sub>3</sub> exists as a liquid on the surface of B<sub>4</sub>C when the temperature is higher than 450 °C. Wettability is enhanced when the B<sub>2</sub>O<sub>3</sub> makes contact with aluminum liquid, and B<sub>2</sub>O<sub>3</sub>-Al<sub>2</sub>O<sub>3</sub> is formed by a liquid-liquid reaction [6]. To an extent, the more the amount of B<sub>2</sub>O<sub>3</sub> generated through the oxidation treatment, the better the interfacial bonding, and therefore, the better the composite's mechanical performance. However, B<sub>2</sub>O<sub>3</sub> became liquid when the oxidation temperature is higher than 450 °C, which is bad from the perspective of attaining an optimal distribution of particles in the composite.

### 3.2 Interfacial Compounds

There are two compounds in the composites, indicated by a dark gray zone B and a shallow black zone C, as shown in Fig. 4a. It was determined that the composition corresponding to position B contained the elements Al and O and that in position C contained the elements Al and Mg, as shown in Fig. 4c, d. Figure 5 shows the XRD

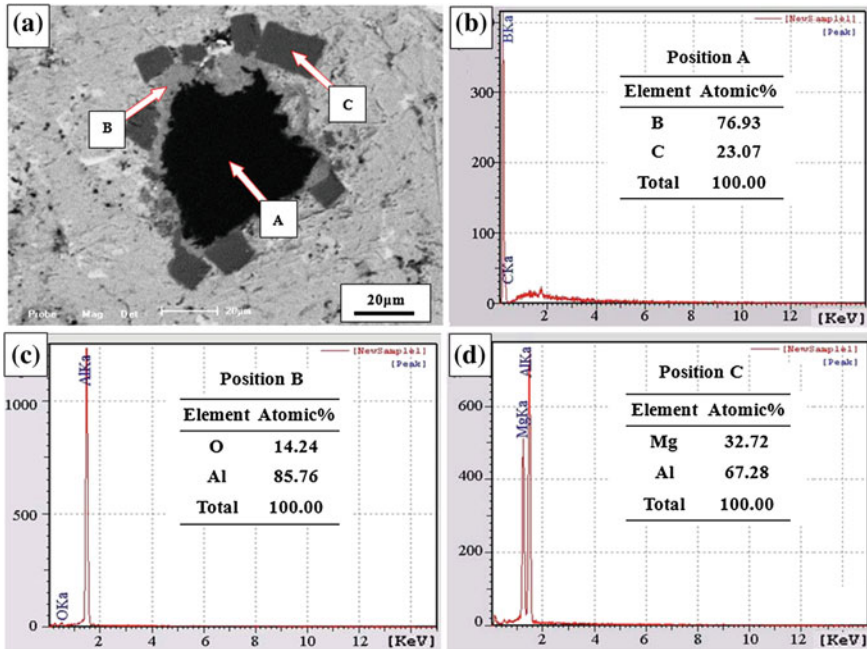
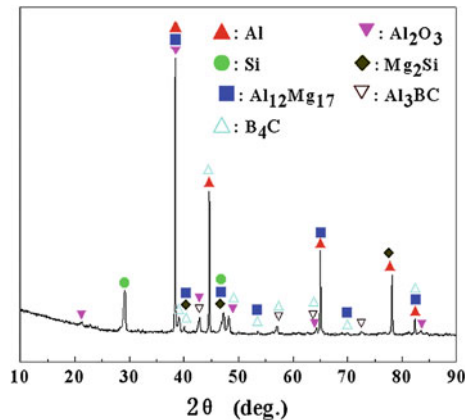


Fig. 4 SEM micrographs of a B<sub>4</sub>C particles in alloys and EDS analyses: b–d selected point in (a)

Fig. 5 XRD pattern of the composites with activated B<sub>4</sub>C





analysis of the composites. The results from the XRD and EDS analyses showed that the dark gray zone B contained  $\text{Al}_2\text{O}_3$ , while the shallow black zone C contained  $\text{Al}_{12}\text{Mg}_{17}$ .

### 3.3 Effect of Activation Treatment on the Composite Microstructure

Figure 6a, b depicts the optical micrographs of the composites with  $\text{B}_4\text{C}$  particles. The non-activated  $\text{B}_4\text{C}$  particles were found to be distributed unevenly and showed different levels of agglomeration, as shown in Fig. 6a. In contrast, the activated  $\text{B}_4\text{C}$  particles were distributed evenly in the matrix, as shown in Fig. 6b. Non-activated  $\text{B}_4\text{C}$  particles have poor wettability with aluminum and exhibit a wetting angle of greater than  $90^\circ$ . Thus, it is difficult for non-activated  $\text{B}_4\text{C}$  particles to combine with the aluminum matrix, and the distribution of  $\text{B}_4\text{C}$  particles was not homogeneous. In the case of the activated  $\text{B}_4\text{C}$ , the  $\text{B}_2\text{O}_3$  on the surface of  $\text{B}_4\text{C}$  becomes a liquid and attaches to the particles at high temperatures, facilitating a reaction between Al and  $\text{B}_2\text{O}_3$  and resulting in a new kind of compound  $\text{B}_2\text{O}_3\cdot\text{Al}_2\text{O}_3$ . The new compound  $\text{B}_2\text{O}_3\cdot\text{Al}_2\text{O}_3$  enhances good interfacial bonding and good wettability of the  $\text{B}_4\text{C}$  particles and contributes to a uniform distribution of  $\text{B}_4\text{C}$  particles.

### 3.4 Interfacial Bonding Characteristics

A previous study has shown that the tensile strength and hardness of as-cast (non-heat-treated) A356-10 wt%  $\text{B}_4\text{C}$  reach 180 MPa and 90 HV, respectively [7, 8]. In the present study, A356-10 wt%  $\text{B}_4\text{C}$  alloyed sheets exhibited good

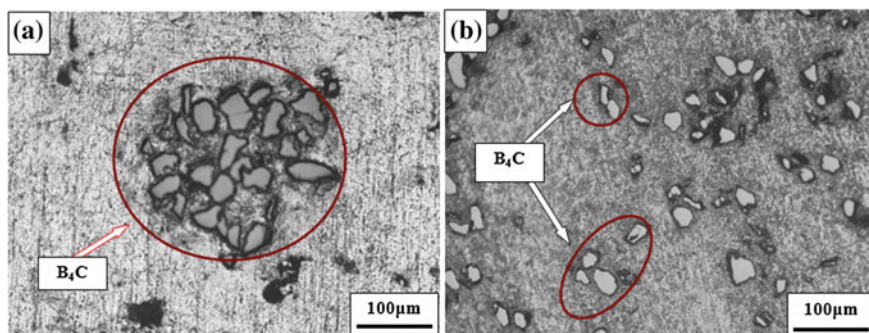


**Fig. 6** Optical microscope micrograph of **a** alloy with non-activated  $\text{B}_4\text{C}$  and **b** alloy with activated  $\text{B}_4\text{C}$

properties when activated  $B_4C$  was used. The tensile strength and hardness values in the composite samples with the activated  $B_4C$  were 197 MPa and 109 HV, respectively, i.e., an increase of 9.4 and 21.1 %, respectively.

## 4 Conclusions

1. The results show that activated  $B_4C$  particles had no impurities on the surface. Furthermore, no particles with an acute angle were observed, which contributes to improved wettability between the  $B_4C$  particles and the aluminum matrix. The strengthening phases  $Al_3BC$  and  $Al_2O_3$  are formed on the interface between the particles and the matrix, resulting in chemical bonding.
2. A356-10 wt%  $B_4C$  composite sheets with good mechanical properties (tensile strength and Vickers microhardness) were fabricated via the combination of semisolid stirring and rheological rolling. The Vickers hardness of the composite sheet with activated  $B_4C$  particles reached 109 HV, and the tensile strength reached 197 MPa.

**Acknowledgements** This work was supported by the National Natural Science Foundation for Outstanding Young Scholars of China under Grant No. 51222405 and National Natural Science Foundation of China under Grant No. 51474063.

## References

1. Lai J, Zhang Z, Chen XG (2012) The thermal stability of mechanical properties of Al- $B_4C$  composites alloyed with Sc and Zr at elevated temperatures. *Mater Sci Eng A* 532:462–470
2. Aizenshtein M, Froumin N, Dariel MP, Frage N (2008) Wetting and interface interactions in the  $B_4C/Al$ -Me (MeCu, Sn) systems. *Mater Sci Eng A* 474:214–217
3. Mao WM, Zheng Q, Zhu DP (2010) Rheo-squeeze casting of semi-solid A356 aluminum alloy slurry. *Trans Nonferrous Metals Soc Chin* 20:1769–1773
4. Tuncer N, Tasdelen B, Arslan G (2011) Effect of passivation and precipitation hardening on processing and mechanical properties of  $B_4C$ -Al composites. *Ceram Int* 37:2861–2867
5. Nie C, Gu J, Liu J, Zhang D (2008) Investigation on microstructures and interface character of  $B_4C$  particles reinforced 2024Al matrix composites fabricated by mechanical alloying. *J Alloy Compd* 454:118–122
6. Wang H, Feng L, Lee SH, Chen JB, Fan BB, Chen DL, Lu HX, Xu HL, Zhang R (2013)  $ZrB_2$ - $Al_3BC_3$  composites prepared using Al- $B_4C$ -C additives and spark plasma sintering. *Ceram Int* 39:897–901
7. Shorowordi KM, Laoui T, Haseeb ASMA, Celis JP, Froyen L (2003) Microstructure and interface characteristics of  $B_4C$ , SiC and  $Al_2O_3$  reinforced Al matrix composites: a comparative study. *J Mater Process Technol* 142:738–743
8. Lashgari HR, Zangeneh S, Shahmir H, Saghafi M, Emamy M (2010) Heat treatment effect on the microstructure, tensile properties and dry sliding wear behavior of A356-10 %  $B_4C$  cast composites. *Mater Des* 31:4414–4422

# LQR Optimal Control on the Positioning Accuracy and Rigidity for the Pneumatic Actuator

Hongwei Yan, Hongbin Li and Shengjun Zhou

**Abstract** This paper aims to present a linear quadratic regulator optimal controller (LQR optimal controller) for a vertical hopping pneumatic actuator. In order to achieve stable hopping, both the piston positioning accuracy and positioning rigidity have to be controlled to the desired values during the flight phase. Because the duration of the flight phase is limited, the settling time of the system should be controlled as short as possible. The proposed LQR optimal control scheme is essential to control the piston position and the chamber pressure simultaneously and satisfy the real-time requirement of the pneumatic actuator. A pneumatic position servo model is developed by Simulink tools in the form of system function (S-function). In simulation, the piston positioning and chamber pressure error are within 0.2 mm and 0.001 MPa, respectively. The settling time is about 120 ms, which can meet the real-time requirement of the pneumatic actuator.

**Keywords** LQR optimal control · Pneumatic actuator · Positioning accuracy · Positioning rigidity

## 1 Introduction

Because of gas's character of compression, low rigidity, and viscosity, the positioning accuracy and rigidity are unsatisfactory. Wang et al. [1] proposed a pneumatic hydraulic combination control servo system and realized compliant force control for the pneumatic hydraulic combination-controlled mechanical arms.

---

H. Yan (✉) · H. Li  
Ludong University, NO. 186, Middle Hongqi Road, Yantai 264025, China  
e-mail: yanhongwei@hitwh.edu.cn

H. Li  
e-mail: lhbm@126.com

S. Zhou  
Wuhan Second Ship Design and Research Institute, Wuhan 430064, China  
e-mail: zsjhitzone@163.com

In [2], a PD controller was built for a pneumatic actuator, which used the gas internal energy of the cylinder's two chambers as the set point of the PD controller. And the control scheme can control the piston position and the chamber pressure simultaneously. In order to overcome the influence of time-varying and nonlinear characteristic of the pneumatic system, in [3], the online identification, Kalman filter, and a LQG optimum self-tuning controller were used. In [4], the position plus velocity plus derivative of the pressure feedback control method was proposed to improve the control performance of the pneumatic system. In [5], displacement, velocity, and acceleration were used as variables for the state feedback controller, which improved the real feature and accuracy of the system. Through local linearization, the LQR can be used to solve the issue of designing the controller for multi-input and multioutput (MIMO) system. To improve the control of the two-wheeled self-balancing robot system, [6] used the LQR algorithm to make the system stable. It should be noted that the LQR algorithm can only be used in the linear system. Based on feedback linearization, [7, 8] built the pseudo-linear system of the pneumatic system. As stated above, the synchronous control of the positioning rigidity and accuracy of the pneumatic system based on the LQR optimal feedback control method has not yet been published. In this paper, the LQR control method is used to control the dual-valve-controlled cylinder system. First of all, mathematical model of the pneumatic actuator is developed. Then, LQR optimal feedback controller is designed. Finally, simulation results are shown and we draw some conclusions of this work.

## 2 Mathematical Model

In this section, a mathematical model is proposed for the pneumatic actuator. For further analysis, some assumptions are made as the following. The charge and exhaust of the cylinder is in quasi-static process and follows the ideal gas law; the leakages between the system and the outside and between the drive cavity and back-pressure chamber are negligible; there is no heat exchange between the system and the outside, and the thermodynamic process is an adiabatic process.

The structure of the vertical hopping pneumatic actuator is shown in Fig. 1. The pneumatic actuator consists of a double-acting air cylinder with a padded foot attached to the lower end of the cylinder rod. Under the constraint of the slide, the guide rod and the pneumatic actuator as a whole can move in the vertical direction.

The moving coordinate system OZ is used to describe the movement of the rod relative to the pneumatic actuator. The origin O is located on the intersection of the axis of the piston rod and the surface of the lower cylinder head.

The dynamics of the piston rod relative to the cylinder can be described by the following equation:

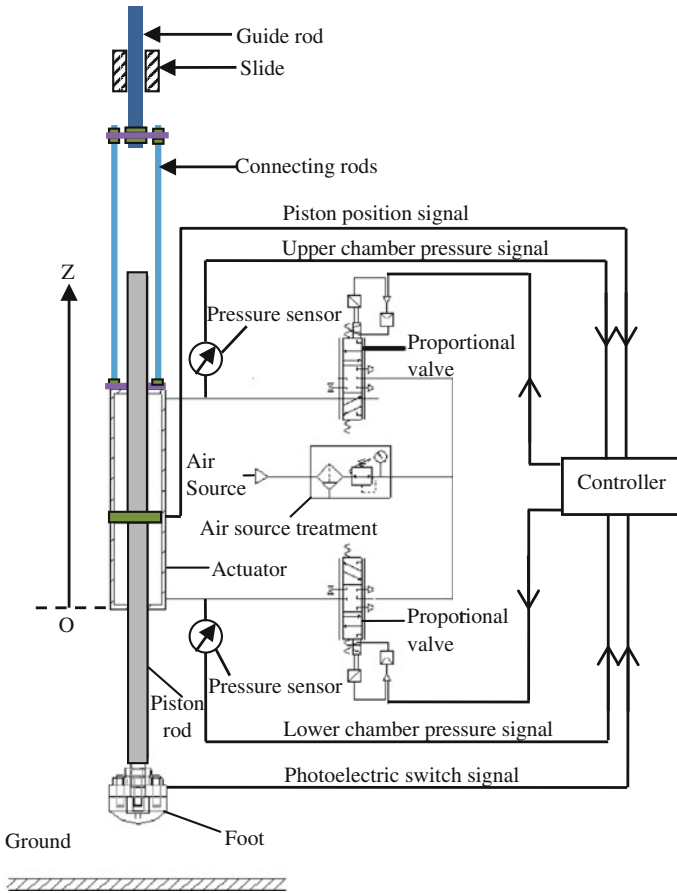


Fig. 1 Schematic diagram of the vertical constrained pneumatic actuator

$$\frac{d^2z}{dt^2} = \frac{1}{m} (p_2A - p_1A - F_f - mg) \tag{1}$$

where  $m$  and  $z$  represent the piston rod's mass and the piston position,  $p_1$  and  $p_2$  represent the relative pressure of the upper and lower chambers, respectively,  $A$  represents the effective area of the piston, and  $F_f$  is the friction force.

A gas pressure equation of upper chamber of the cylinder is derived as:

$$\frac{dp_{1t}}{dt} = \begin{cases} \frac{kRT_2 q_{m1in}}{A(s-z+z_{10})} - \frac{kp_{1t}}{z+z_{10}} \frac{dz}{dt} & A_{e1} \geq 0 \\ \frac{kp_{1t}}{s-z+z_{10}} \frac{dz}{dt} - \frac{kRT_1}{A(s-z+z_{10})} q_{m1out} \left(\frac{p_{1t}}{p_{st}}\right)^{\frac{k-1}{k}} & A_{e1} < 0 \end{cases} \tag{2}$$

where  $k$ ,  $R$ ,  $q_{m1in}$ ,  $q_{m1out}$ ,  $s$ ,  $z_{10}$ ,  $z_{20}$ ,  $p_{1t}$ , and  $p_{2t}$  represent the specific heat constant, the universal gas constant, the cylinder air temperature, the input mass flow of the proportional valve, the output mass flow of the proportional valve, the stroke of the cylinder, the converted piston displacement of the upper closed dead volume, the converted piston displacement of the lower closed dead volume, and the absolute pressure of the upper and lower chambers, respectively. In case the airflow through the valve is considered as a sonic one, mass flow  $q_m$  can be expressed as:

$$q_m = \begin{cases} A_{ei} p_{st} \left\{ \frac{2k}{RT_s(k-1)} \left[ \left( \frac{p_{ii}}{p_{st}} \right)^{\frac{2}{k}} - \left( \frac{p_{ii}}{p_{st}} \right)^{\frac{k+1}{k}} \right] \right\}^{\frac{1}{2}} & (0.528 \leq \frac{p_{ii}}{p_{st}} < 1) \\ A_{ei} p_{st} \left[ \frac{k}{RT_s} \left( \frac{2}{k-1} \right)^{\frac{k+1}{k-1}} \right]^{\frac{1}{2}} & (0 < \frac{p_{ii}}{p_{st}} < 0.528) \end{cases} \quad (3)$$

where  $i = 1$  and  $i = 2$  represent the parameters of the lower chamber and upper chamber, respectively. The parameters of the model above are as follows:  $m = 1.277$  kg,  $A = 1649.34$  mm<sup>2</sup>,  $s = 0.25$  m,  $z_{10} = z_{20} = 0.004$  m,  $T_s = 293.15$  K,  $p_{st} = 0.52$  MPa,  $R = 287.1$  J/kg·K, and  $k = 1.4$ .

### 3 Design of Controller

#### 3.1 Establishment of the State Space Expression

Figure 2 shows the schematic diagram of the system.

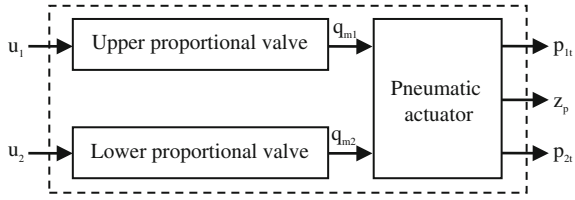
In Fig. 2,  $u_1$  and  $u_2$  represent the control voltages of the upper and lower proportional valves. It is apparent that the dual-valve-controlled cylinder system is two-input, three-output system. The input values are control voltages of the two proportional valves; the output values are the pressure of the chambers and the piston position of the pneumatic actuator. For the dual-valve-controlled cylinder system, the state variables can be chosen as:

$$x_1 = z_{1p}, \quad x_2 = \dot{x}_1 = \dot{z}_p, \quad x_3 = p_{1t}, \quad x_4 = p_{2t}$$

Model of the state space expression is derived as:

$$\begin{aligned} \dot{x}_1 = \dot{y} = x_2, \quad \dot{x}_2 = \ddot{y} &= \frac{m_b + m_l}{m_b m_l} [(p_{2t} - p_{1t}) A_p - F_f] = \frac{m_b + m_l}{m_b m_l} A_p x_4 - \frac{m_b + m_l}{m_b m_l} A_p x_3 - \frac{m_b + m_l}{m_b m_l} F_f \\ \dot{x}_3 = \dot{p}_{1t} &= \frac{kRT_1}{A_p(L_s - x_1 + z_{10})} q_{m1} + \frac{kx_3}{L_s - x_1 + z_{10}} x_2, \quad \dot{x}_4 = \dot{p}_{2t} = \frac{kRT_1}{A_p(x_1 + z_{20})} q_{m2} + \frac{kx_4}{x_1 + z_{20}} x_2 \end{aligned}$$

**Fig. 2** Diagram of the dual-valve-controlled cylinder system



Forms of vectors and matrix are as follows:

$$\begin{bmatrix} \dot{x}_1 \\ \dot{x}_2 \\ \dot{x}_3 \\ \dot{x}_4 \end{bmatrix} = A \begin{bmatrix} x_1 \\ x_2 \\ x_3 \\ x_4 \end{bmatrix} + B \begin{bmatrix} u_1 \\ u_2 \end{bmatrix} + E, \quad y = \begin{bmatrix} z_{1p} \\ p_{1t} \\ p_{2t} \end{bmatrix} = C \begin{bmatrix} x_1 \\ x_2 \\ x_3 \\ x_4 \end{bmatrix} \tag{4}$$

where

$$A = \begin{bmatrix} 0 & 1 & 0 & 0 \\ 0 & 0 & -\frac{m_b + m_l}{m_b m_l} A_p & \frac{m_b + m_l}{m_b m_l} A_p \\ 0 & \frac{kx_3}{L_s - x_1 + z_{10}} & 0 & 0 \\ 0 & \frac{kx_4}{x_1 + z_{20}} & 0 & 0 \end{bmatrix},$$

$$E = \begin{bmatrix} 0 \\ -\frac{m_b + m_l}{m_b m_l} F_f \\ \frac{kRT_1 C_d \omega k_v}{A_p (L_s - x_1 + z_{10}) \sqrt{T_u}} \Phi(p_{1t}, p_{2t}) (1 - e^{-\frac{t}{\tau}}) u_0 \\ \frac{kRT_1 C_d \omega k_v}{A_p (L_s - x_1 + z_{10}) \sqrt{T_u}} \Phi(p_{1t}, p_{2t}) (1 - e^{-\frac{t}{\tau}}) u_0 \end{bmatrix}$$

$$B = \begin{bmatrix} 0 & 0 \\ 0 & 0 \\ \frac{kRT_1 C_d \omega k_v}{A_p (L_s - x_1 + z_{10}) \sqrt{T_u}} \Phi(p_{1t}, p_{2t}) (1 - e^{-\frac{t}{\tau}}) & 0 \\ 0 & \frac{kRT_1 C_d \omega k_v}{A_p (L_s - x_1 + z_{10}) \sqrt{T_u}} \Phi(p_{1t}, p_{2t}) (1 - e^{-\frac{t}{\tau}}) \end{bmatrix},$$

$$C = \begin{bmatrix} 1 & 0 & 0 & 0 \\ 0 & 0 & 1 & 0 \\ 0 & 0 & 0 & 1 \end{bmatrix}$$

The state space expression of the dual-valve-controlled cylinder system can be derived through local linearization.

$$\begin{aligned}
 A &= \begin{bmatrix} 0 & 1 & 0 & 0 \\ 0 & -55 & -907.5 & 907.5 \\ 0 & 1.875 & 0 & 0 \\ 0 & -12.3529 & 0 & 0 \end{bmatrix}, B = \begin{bmatrix} 0 & 0 \\ 0 & 0 \\ 0.5226 & 0 \\ 0 & 6.971 \end{bmatrix}, C \\
 &= \begin{bmatrix} 1 & 0 & 0 & 0 \\ 0 & 0 & 1 & 0 \\ 0 & 0 & 0 & 1 \end{bmatrix}, E = \begin{bmatrix} 0 \\ 0 \\ -2.6132 \\ -34.8534 \end{bmatrix}
 \end{aligned}$$

Based on the above state space expression, the controllability and observability of the system are proved by matrix calculation.

### 3.2 Choice of the Weighting Matrix

For the dual-valve-controlled cylinder system which is described by matrix  $\{A, B\}$ , the linear quadratic optimal control index is introduced by citing the performance index functional:

$$J = \int_0^{\infty} [x^T(t)Qx(t) + u^T(t)Ru(t)] dt \tag{5}$$

Final purpose of the research is hopping of the pneumatic actuated one-legged robot. Consequently, the real-time performance of the controller is the highlight. With this in mind, the LQR weighting matrix has to consider the dynamic response first. Then, the value of  $Q$  is increased, and the value of  $R$  is set to 1.

The weighting matrix of the state variables  $Q$  and the control inputs  $R$  are as follows:

$$Q = \begin{bmatrix} 2000000 & 0 & 0 & 0 \\ 0 & 0 & 0 & 0 \\ 0 & 0 & 2000000 & 0 \\ 0 & 0 & 0 & 2000000 \end{bmatrix}, R = \begin{bmatrix} 1 & 0 \\ 0 & 1 \end{bmatrix}$$

The optimal of the solutions is calculated by citing the sufficient and necessary condition equation:

$$u = -Kx, \quad K = R^{-1}B^T P \tag{6}$$



where  $P$  represents the result of the ARE equation:

$$PA + A^T P - PBR^{-1}B^T P = -Q \tag{7}$$

$$P = (1.0e + 005) \cdot \begin{bmatrix} 1.1802 & 0.00158 & -0.0189 & 0.0014 \\ 0.0158 & 0.0002 & -0.0002 & 0.0000 \\ -0.0189 & -0.0002 & 0.0273 & -0.0000 \\ 0.0014 & 0.0000 & -0.0000 & 0.0020 \end{bmatrix} \tag{8}$$

$$K = \begin{bmatrix} k_{11} & k_{12} & k_{13} & k_{14} \\ k_{21} & k_{22} & k_{23} & k_{24} \end{bmatrix} = \begin{bmatrix} -990.3 & -12.1 & 1429 & -1.1 \\ 1009.6 & 13.8 & -15 & 1415.5 \end{bmatrix} \tag{9}$$

The schematic diagram of the optimal feedback controller is shown in Fig. 3.

## 4 Results and Discussion

### 4.1 Simulation

Based on the mathematical model of the pneumatic actuator and the control diagram (see Fig. 3), the simulation model of the pneumatic servo system is built in MATLAB. In the simulation model, the desired values of the chambers' pressure and piston position are 0.3 MPa and 0.09 m, respectively. As shown in Fig. 4, the system is stable and has a good dynamic performance. The settling time is about 0.12 s, and the steady error of the piston position and the chambers' pressure are 0.2 mm and 0.001 MPa, respectively.

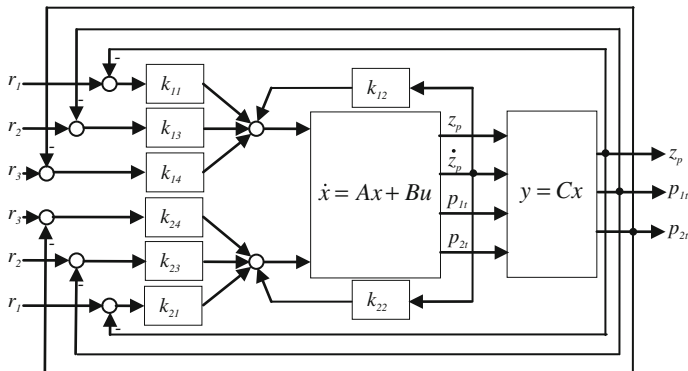


Fig. 3 Schematic diagram of the LQR optimal feedback controller

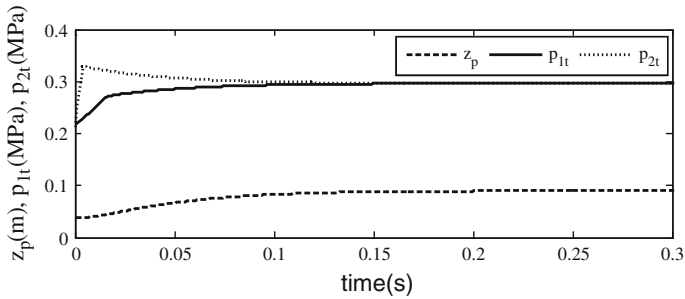


Fig. 4 Curves of the dynamic parameters

## 4.2 Conclusion

Because of the influence of the gas compressibility and pneumatic system's inherent strong non-line feature, it is difficult to control the positioning accuracy and rigidity simultaneously. In this paper, a LQR optimal feedback controller was proposed and was applied to controlling the positioning accuracy and rigidity. Simulation results show that by using the proposed LQR optimal controller, the settling time of the system is about 0.12 s, and the steady error of the piston position and chambers' pressure are 0.2 mm and 0.001 MPa, respectively, which meet the requirement of the one-legged robot. The main contribution of this paper is that it has found a control scheme for the pneumatic actuator which can control the piston position and chambers' pressure simultaneously, precisely and rapidly.

## References

1. Wang HY, Zhao KD, Liu CC (2007) Design and simulation of compliant force control for pneumatic hydraulic combination control servo system. *Chin Hydraulics Pneumatics* 7:12–16
2. Li Z, Yan HW, Su XW, Sun ZC, Zhao SM, Ji J (2013) Precise control of the piston position and the pressure of cylinder chambers for the pneumatic actuator. *The Mediterr J Measur Control* 9 (4):153–158
3. Wang XY (2001) Research on LQG self-tuning control of pneumatic position servo-system. *Power Eng* 21(4):1372–1375
4. Bai YH, Li XN (2009) Improvement of the state feedback control for pneumatic position servo system. *J Mech Eng* 45(8):101–105
5. Sun MJ, Qu YB, Zhang Y (2008) Design and research on DSP control with multivariable state feedback for pneumatic position servo system. *Chin Hydraulics Pneumatics* 3:17–19
6. Wu JF, Zhang JD (2012) Improved control based on two-wheeled self-balancing robot LQR controller. *J Harbin Univ Sci Technol* 17(6):1–5
7. Wang SB, Bao G, Yang QJ (2002) Feedback linearization control for pneumatic servo systems controlled by proportional flow valve. *Mach Tool Hydraulics* 3:39–40
8. Du JM, Xiao HJ, Gao LL, Li BR (2014) Spool position servo control based on feedback linearization for the high-pressure and large-flow-rate pneumatic valve. *Chin Hydraulics Pneumatics* 5:66–70

# A Study of Visual Servo System Based on Binocular Camera

Lei Hu and Chen Shen

**Abstract** In robot-assisted orthopedic surgery, instruments attached to end-effector may collide with patient in the process of drilling. To solve this problem, a robot visual servo control system based on binocular cameras is built. Visual information is used by improved PID algorithm to control the surgical robot to track the movement of the patient. In addition, the model of the control system is established by MATLAB. At last, a model experiment is performed to verify the feasibility of the system.

**Keywords** Robot · Visual servo · Simulation · PID controller

## 1 Introduction

In the field of medicine, visual servo technology can assist the surgeon in complex surgery by utilizing the relative position between patient and surgical instruments [1, 2]. For instance, if a patient's limbs are not fastened or fastened not firmly during the robot-assisted orthopedic operation, they may collide with surgical tools and cause harm to healthy sites when the patient suddenly moves. In order to avoid this situation and improve surgical safety, this paper constructs a visual servo system based on binocular camera.

---

L. Hu · C. Shen (✉)

School of Mechanical Engineering and Automation, Beihang University,  
Beijing, China

e-mail: 947313933@qq.com

© Springer-Verlag Berlin Heidelberg 2016

B. Huang and Y. Yao (eds.), *Proceedings of the 5th International Conference on Electrical Engineering and Automatic Control*, Lecture Notes in Electrical Engineering 367, DOI 10.1007/978-3-662-48768-6\_123

1105

## 2 Architecture of the System

The visual servo control system consists of three parts: visual inspection subsystem, motion control subsystem, and visual controller, whose structure is shown in Fig. 1. The main function of the system is to control the robot tracking the target motion rapidly and accurately based on visual feedback.

### 2.1 Visual Inspection Subsystem

Visual inspection subsystem is the feedback link of visual servo control system. Based on the visual feedback information, robot can operate in dynamic and uncertain occasion. This work adopt Micron Tracker H40 binocular camera as the vision sensor, which is shown in Fig. 2. Micron Tracker H40 can be used in a

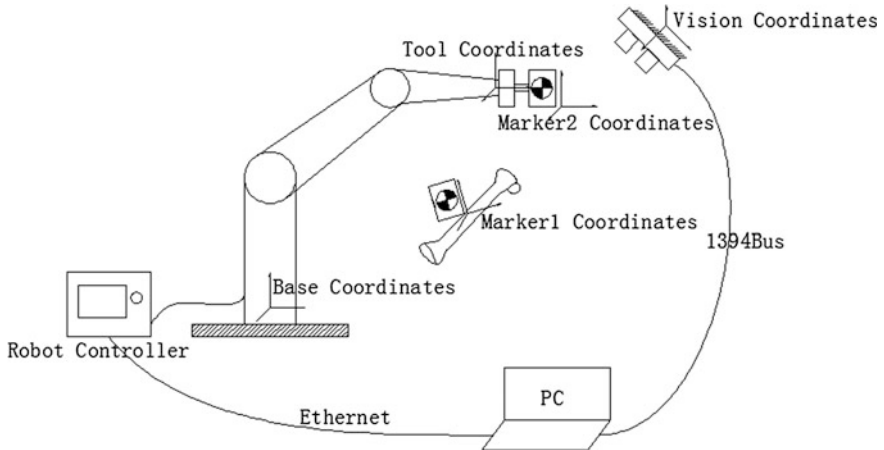
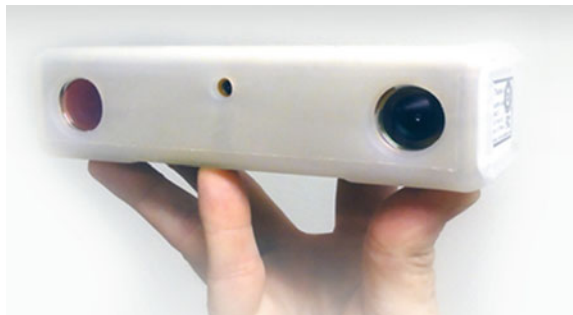


Fig. 1 Structure diagram of visual servo control system

Fig. 2 Micron Tracker H40 binocular camera



variety of clinical guided procedures. And it uses stereoscopic vision in real time to detect and track Markers (specially marked objects) and computes the position and orientation of the Markers at a certain frequency.

In visual inspection subsystem, the surface of Marker1 and Marker2 is printed with high contrast black-and-white images according to the certain mode. Marker2 is fixed on the end-effector of the robot, whose position and orientation in tool coordinates can be acquired by measurement. Marker1 is fixed on the moving target (such as tibia or femur of the patient) and moves along with it. Micron Tracker H40 is fixed in a proper position of the surgery room so that the images of Marker1 and Marker2 can fall within the field of vision. Then, at a certain frequency, consecutive images of left and right cameras are gathered to calculate the position and orientation of Markers which is described in vision coordinates according to the difference between the two images, camera model, and the projection relationship. At last, the position and orientation information of Markers is sent to visual controller in real time through IEEE 1394.

## 2.2 *Motion Control Subsystem*

The function of motion control subsystem is to control the robot to carry out actions according to instructions sent by the visual controller. UR5, a six degrees of freedom articulated robot made by the Universal Robots company, is adopted in the solution owing to its small, lightweight, and easy to use design. The highlight of UR5 is its ability to realize the security cooperation between human and machine without barriers. The robot controller of UR5 is connected with industrial PC through Ethernet interface. Based on TCP/IP protocol, the control program run in PC communicates with the robot controller in order to send instructions or receive robot status information.

## 2.3 *Visual Controller*

Visual controller lies in an essential position of the whole system; it adopts proper algorithms to work out the controlled quantity and controls the movement of robot based on position error obtained by visual feedback link. Because the position and orientation is acquired directly by binocular cameras, the system put forward is a position-based visual servo control system [3], whose functional block diagram is illustrated in Fig. 3. Visual controller provides an entrance point for robot controller; therefore, the movement of robot is indirectly controlled by visual information.

The calculation process of the position error in visual controller is as follows:

1. At the beginning,  $M_{2V}$ , the homogeneous matrix of Marker2 which contains position and orientation information described in vision coordinates, can be acquired by binocular cameras;  $M_{2T}$ , the homogeneous matrix of Marker2

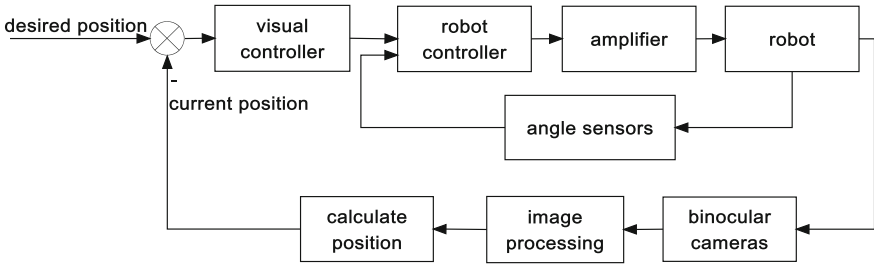


Fig. 3 Principle block diagram of position-based visual servo control system

described in tool coordinates, can be precisely obtained by measuring. With the information of six joint angles,  $M_{TB}$ , the homogeneous matrix of end-effector which described in base frame, can be calculated by forward kinematics of the robot.

2. In order to control the movement of robot according to the relative position between surgical instruments and patients, all homogeneous matrix described in different coordinates must be unified in a global coordinates. Therefore, a mapping matrix which describes the relationship between vision coordinates and base coordinates must be determined. According to the principle of coordinate transformation,  $M_{2B}$ , the homogeneous matrix of Marker2 under the base coordinates, can be summarized as  $M_{2B} = M_{TB} \cdot M_{2T}$ . Based on previous results, the mapping matrix can be computed as follows:

$$M_{\text{map}} = M_{2B} \cdot M_{2V}^{-1} \tag{1}$$

3. At the beginning, the end-effector and target object may not be in accordance with each other. This offset is depicted by the homogeneous matrix  $M_{\text{bind}}$ . In order to keep this offset during the following process,  $M_{\text{bind}}$  must be obtained. After  $M_{2V}$  and  $M_{1V}$  are obtained,  $M_{\text{bind}}$  can be calculated as follows:

$$M_{\text{bind}} = M_{2V}^{-1} \cdot M_{1V} \tag{2}$$

4. During the tracking process, program calculates  $M_{1V}$  and  $M_{2V}$  at a certain frequency by visual information. Hence, the homogeneous matrix  $M_{\text{errV}}$  which contains position error described in vision coordinates is computed as follows:

$$M_{\text{errV}} = M_{1V} - M_{2V} \cdot M_{\text{bind}} \tag{3}$$

5. Map the error described in vision coordinates to error in base coordinates:

$$M_{\text{errB}} = M_{\text{map}} \cdot M_{\text{errV}} \tag{4}$$

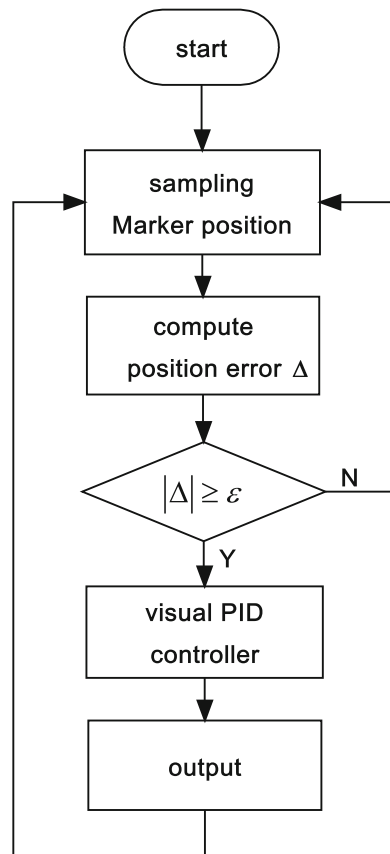
The fourth column of homogeneous matrix  $M_{\text{errB}}$  consists of position errors in base frame such as  $\Delta_X, \Delta_Y, \Delta_Z$ .

### 3 PID Controller and System Simulation

Visual controller uses a combination of integral separation, incomplete derivative, and dead zone PID control algorithm [4]. It takes advantage of doing without the precise mathematical model of the object. Because of adopting computer-controlled mode and a fairly short sampling period, integral operation is replaced by sum and differential operation is replaced by backward-difference [5].

Instructions which the robot controller accepts can be classified into position control mode and speed control mode. For position control mode, it is obvious that when error occurs the robot cannot rapidly track the uncertain movement of the target. Moreover, when the speed of the target is too fast or jerky, the tracking may lag, vibrate, or even lead to safety shutdown of the robot. Hence, the ideal tracking process is to change the speed of robot in real time according to the state of target motion. Therefore, the controlled quantity of PID controller should be the speed of end-effector. The working flow chart of the visual servo control system is shown in Fig. 4.

Fig. 4 Work flowchart of the visual servo control system



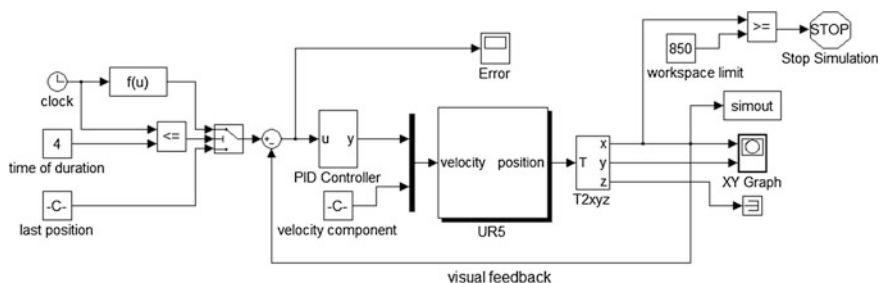


**Fig. 5** Visual control system with PID controller

In order to simplify the system simulation model, only consider the movement along  $x$ -axis of base frame during the tracking process. Uniform linear motion is chosen as a typical motion of the target [6]. The simulation time is symbolized by  $u$ , and the equation of uniform linear motion is  $f(u) = ku + d_0$ , where  $d_0$  is the initial position in  $x$ -axis. The speed of target can be adjusted by modifying the slope  $k$  in this equation.

By using MATLAB/Simulink, a dynamic system modeling and simulation tool, the model of visual servo control system is established [7, 8], which is shown in Fig. 5. The system mainly includes target motion module, visual PID controller, robot motion control subsystem, visual feedback link, and information output link.

In simulation process, make  $k = 10, 20, 50$ , respectively, i.e., target moves at different speed. The uniform linear movement lasts for 4 s and simulation time is set to 10 s. The results are shown in Fig. 6. As shown in the diagram, the faster the target moves, the greater the overshoot of dynamic tracking will be. When target stops, error cannot decrease to zero immediately because of the existence of inertia and time delay. Instead, it increases in the opposite direction first, then gradually decreased to zero. When target moves at 20 mm/s, the maximum overshoot of

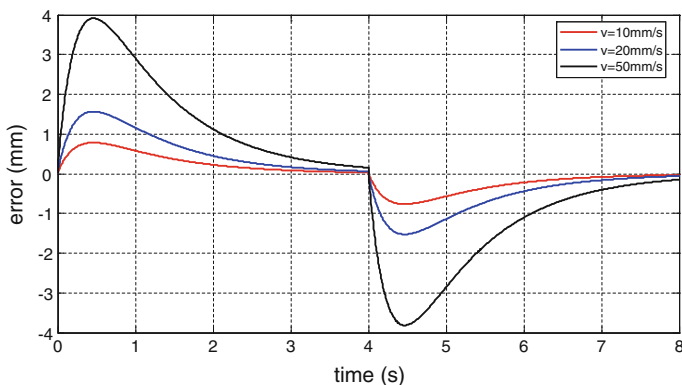


**Fig. 6** Tracking error curve of the uniform linear motion



dynamic process is less than 2 mm and the peak time is about 0.4 s. The simulation result indicates that the accuracy and speed of the visual servo control system meet the clinical requirements.

### 4 Visual Tracking Experiment

Experiment platform, which is shown in Fig. 7 is set up with UR5 robot, linear motion unit, control computer, Micron Tracker H40, and Markers attached to end-effector or target.

Marker1 fixed on linear motion unit moves at the speed of 10 and 20 mm/s, respectively. The sampling frequency of Micron Tracker H40 is 15 Hz. And for every 0.1 s, the position of Marker1 and Marker2 is recorded to compute the tracking error. Connecting the points of error value every period, the dynamic visual tracking error curve can be obtained, which is shown in Fig. 8.

Subjected to environmental noise and mechanical vibration, the dynamic tracking error curve fluctuates slightly. As shown in the picture mentioned above, the experimental result is similar with the simulation result. At the beginning, error

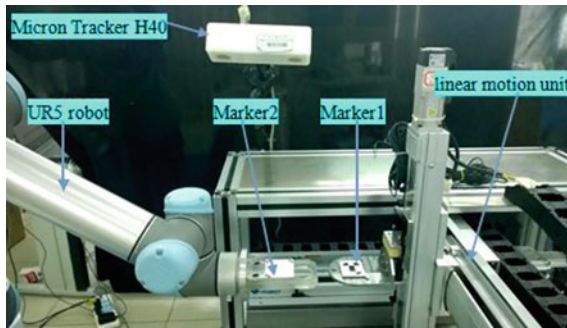


Fig. 7 Experiment platform of visual tracking

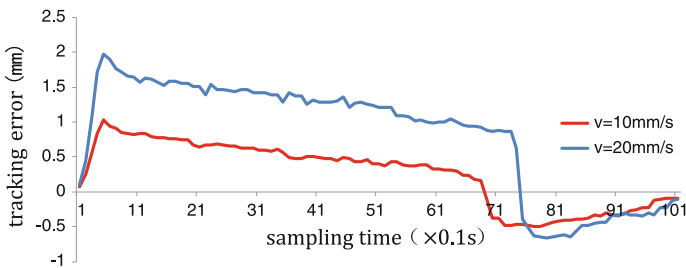


Fig. 8 Dynamic visual tracking error curve

increases rapidly and then decreases gradually under the control of visual controller. When target comes to a halt, error increases in the opposite direction because of the existence of inertia and decreased to zero eventually. When target moves at 20 mm/s, the maximum overshoot of dynamic process is about 2 mm and when the velocity is 10 mm/s, the maximum overshoot is about 1 mm. The experimental result shows that the accuracy and speed of the visual servo control system meet the clinical requirements.

## 5 Conclusion

Aiming at the problem those surgical instruments may collide with human body during robot-assisted orthopedic surgery; this paper presents a visual servo control system based on binocular camera and illustrates the function, structure, and work flow of the system. Then, a system model is established to simulate by MATLAB. At last, an experiment is conducted to verify the feasibility of the system. From a long-term point of view, visual servo technology in robot-assisted surgery is a future direction; it can effectively improve the accuracy and safety of operation and reduce the risk of surgery.

**Acknowledgments** This work was supported by the National Hi-Tech Research and Development Program of China (“863” Project) (Grant No. 2015AA043204).

## References

1. Riviere CN, Gangloff J, de Mathelin M (2006) Robotic compensation of biological motion to enhance surgical accuracy. *Proc IEEE* 94(9):1705–1714
2. Krupa A, Gangloff J, Doignon C (2003) Autonomous 3-D positioning of surgical instruments in robotized laparoscopic surgery using visual servoing. *IEEE Trans Robot Autom* 19(5):842–851
3. Yang Z (2008) Research on robot control with position-based visual servoing and target recognition methods. Taiyuan University of Science & Technology, Taiyuan
4. Fang Y (2008) A surevy of robot visual servoing. *CAAI Trans Intell Syst* 3(2):109–112
5. Hutchinson Seth (2006) Visual servo control. *IEEE Robot Autom Mag* 2:82–90
6. Diang J (2013) The design and research of control method on robot visual servoing. Zhejiang University of technology, Hangzhou
7. Yang N (2013) Design of visual servo system on PUMA560 manipulator. Harbin Institute of Technology, Harbin
8. Zhao X, Du X, Gong J (2012) Simulation of image-based robot visual servo system for dynamic object. *Mach Tool Hydraulics* 40(11):116–119

# Exploration of the Gas–Liquid Separation Effect of Vortex Tool in Downhole

Zhijian Wang, YanBob Jia and Kai Liu

**Abstract** The increasing water rate of gas well has seriously threatened gas production, and it gets more and more people’s concern and attention. Therefore, vortex tool is developed for downhole gas–liquid separation to improve gas production. We used UG software to establish the vortex tool model and conduct simulation calculation by fluent software. Then, analyze the influence of the separation effect of gas flow rate, downhole gas–liquid ratio, and vortex tool structure. The analysis results show that gas flow rate, gas–liquid ratio, and vortex tool spiral angle are main factors influencing the effect of vortex tool drainage. The higher the gas flow rate and the greater the gas–liquid ratio, the effect of gas–liquid separation of vortex tool is better. When spiral angle of the vortex tool is 50°, separation effect is better.

**Keywords** Vortex tool · Gas–liquid separation · Spiral angle · Velocity of the gas · Gas–liquid ratio fluent · Numerical simulation

## 1 Introduction

The problem of gas well with liquid seriously affected the efficient development of gas field, and the eventual recovery of gas reservoirs severely reduced [1]. Attention has been paid to the liquid of the seriousness of the problem in our country, the development of the gas lift, pumping machine and bubble discharge and so on a series of drainage technology, and achieved some results [2, 3]. But the traditional process of drainage gas recovery in the process of lifting, handling, and injection consumes a lot of energy and greatly increases the extraction cost of gas and at the same time caused serious pollution to the environment. Therefore, we need to develop new and efficient drainage technology. Abroad have long noted the problems that exist in the

---

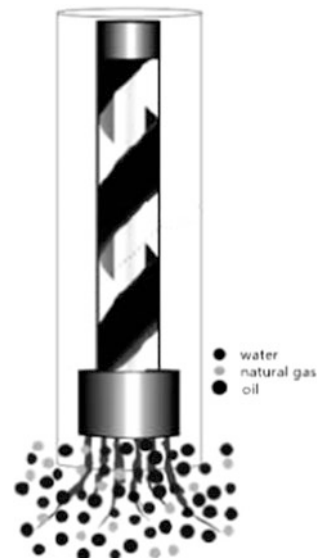
Z. Wang · Y. Jia · K. Liu (✉)  
Shenyang Aerospace University, Moral South Street,  
Number 37, Shenbei Area, Shenyang 110136, Liaoning, China  
e-mail: tadesuosi@163.com

traditional drainage technology, and many companies are devoted to the type of drainage gas recovery tool. Vortex tool is developed by the US department of energy on high and new technology products, and it is a kind of simple structure and has small volume and high efficiency of drainage tool. Most of the fluid due to centrifugal force effect is high-speed spin to tube wall and along the wall movement, and gas is in the middle of the casing pipe flow at a high speed. The efficient transmission of spiral form will last long distances [4]. Over the past few years, the success of the application shows that scientific and rational use of vortex tool can effectively solve the problem of hole liquid in USA. Fluent software was used to conduct a numerical simulation of vortex tool, research the working status of the vortex tool in the wellbore, and analyze the flow rules and characteristics of the vortex flow.

## 2 The Principle of Drainage Gas Recovery of Vortex Tool

Mixture of gas and liquid at a certain axial velocity into the vortex tool, on both sides of the entrance, can make the gas and liquid mixed fully, and along the spiral baffle movement, fast to rotate, the mixture will produce larger tangential velocity. Under the same tangential velocity, due to liquid density that is much larger than gas, liquid will obtain the greater centrifugal force, and under the action of centrifugal force, the heavier liquid will be left on the wall, the liquid film is formed on the wall, and the gas will be formed in the center column (Fig. 1). By the principle of conservation of energy, when the mixture has a larger tangential velocity, axial velocity can decrease, the velocity gradient between the fluid and the pipe is reduced, friction resistance tubing wall on the fluid is reduced, and thus, the

**Fig. 1** Simulation movement forms after mixture flows through vortex tool



pressure drop decreases on the tubing axial. The second point is that the slip of fluid droplet and airflow will be reduced. Lifting the same amount of liquid, compared with no vortex tool, the desired gas velocity is relatively low. Reduction of the sliding force can reduce the total tubing pressure drop.

### 3 Model Establishment and Model Validation

#### 3.1 Selection of Multiphase Flow Model

Euler model is chosen as the model of multiphase flow [5] and makes the following assumptions:

1. The flow is dominated by the mist flow of droplets;
2. In the flow, natural gas volume fraction (0.90) is far greater than the liquid phase (0.10);
3. In the process of gas–liquid, two-phase flow distribution is very uneven, and the flow field has both droplet and liquid membrane [5].

#### 3.2 The Control Equations

From the perspective of numerical calculation, when the liquid in the form of droplets joins gas fluid, the fluid not only by the internal force of fluid, also by droplets of gas fluid force [5].

The volume fraction equation

$$\hat{\rho}_q = \alpha_q \rho_q, \sum \alpha_q = 1, \quad v_q = \int_V \alpha_q dV$$

The continuity equation

$$\frac{\partial}{\partial t} (\alpha_q \rho_q) + \nabla (\alpha_q \rho_q v_q) = \sum_{k=1}^n m_{pq}$$

The kinetic energy conservation equation

$$\frac{\partial}{\partial t} (\alpha_q \rho_q) + \nabla (\alpha_q \rho_q v_q) = -\alpha_q \nabla p + \nabla \bar{\tau}_q + \sum_{p=1}^n (R_{pq} + m_{pq} v_{pq}) + \alpha_q \rho_q (F_q + f_{lif,q} + F_{vm,q})$$

$$\frac{\partial}{\partial t} (\alpha_q \rho_q \bar{v}_q) + \nabla (\alpha_q \rho_q \bar{v}_q) = -\alpha_q \nabla p + \nabla \bar{\tau}_q + \sum_{p=1}^n (\bar{R}_{pq} + m_{pq} \bar{v}_{pq}) + \alpha_q \rho_q (F_q + f_{lif,q} + F_{vm,q})$$

in the formula,  $\rho$  is the density,  $\text{kg/m}^3$ ;  $v$  is the speed,  $\text{m/s}$ ;  $\tau$  is the shear force,  $\text{N}$ ;  $m$  is quality,  $\text{kg}$ ;  $\alpha$  is a phase of moisture content,  $\%$ ;  $R$  is the interaction force,  $\text{N}$ ; and the subscript  $p, q$  represent separately the gas phase and water phase.

## 4 Building the Vortex Tool Model and Setting Flow Conditions

Using UG software, respectively, establish model of vortex tooling in which spiral angle is  $55^\circ$ . The casing model is established with inner diameter 62 mm and length of 1000 mm in the vortex tool model outside, imports the Gambit software, and extracts fluid domain and meshing. Using Fluent software to conduct numerical simulation. Assumes that the gas–liquid two-phase flow under the action of vortex tool, and do bottom-up three-dimensional unsteady turbulent flow in a vertical pipeline. Choose standard k-epsilon turbulence model, and enable the multiphase model; entrance boundary is the speed of entrance. Setting the inlet velocity is 6.5 m/s. For the liquid phase, at the entrance, the droplet diameter is 10  $\mu\text{m}$ , and volume fraction is 10 %. Outlet is pressure outlet boundary. Exit boundary is full flow boundary, and the wall boundary layer flow field is treated with the selection of standard wall function. So, according to the similarity of movement, under the condition of same movement time, set the length of 1000 mm of gas and liquid flow. Because computing speed of the software is limited by the number of grid nodes and computer memory, unable to simulate 1000 m of gas and liquid flow. So, according to the similarity of the movement, under the condition of same movement time, set the length of 1000 mm of gas and liquid flow, and then, according to actual output, calculate the simulation of 1000 mm flow rat.

## 5 Calculation Results and Analysis

### 5.1 Volume Ratio of Water Varies Regularly

In Fig. 2, water volume fraction cloud can be seen from model inlet to model outlet. From the picture, we can see that the volume of the water phase is 10 % at the entrance of the tool ( $z = 0$  mm). At the exit of the tool ( $z = 173$ ), two-phase flow due to centrifugal force, the liquid left behind on the wall. With the two-phase flow rotary flow upward along the column, the liquid phase is formed at  $z = 723$  stable film, and in the center of the pipe, volume rate of water is reduced, to form the air column. So far the liquid in the pipe wall forms the spiral state of liquid membrane, and the gas phase formed gas column in the center of the tube.

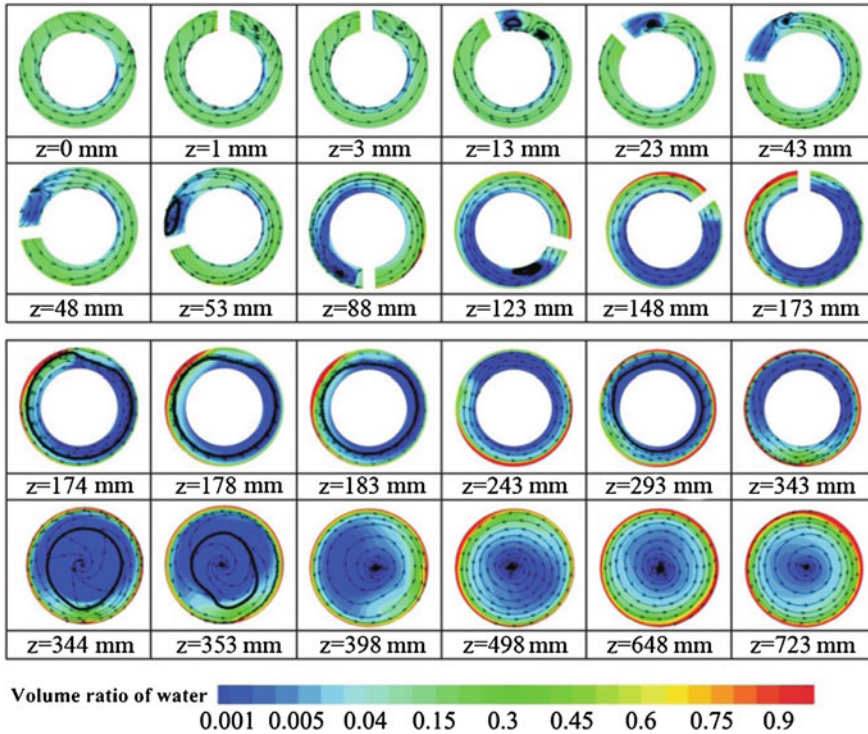


Fig. 2 Water volume fraction distribution

### 5.2 The Variation of Pressure Distribution

In Fig. 3, with the increase of the distance, a layer of larger pressure is formed on the inner wall of the tube, and the pressure of the gas column in the middle is smaller. Analyzing pressure distribution cloud also proves that the above chart shows spiral regular patterns of the volume rate of the liquid phase.

### 5.3 The Variation of Velocity Distribution

Intercept model respectively 443, 533, 623, 713 mm four interface axial distribution cloud and graph analysis velocity variation. In Fig. 4, we can see that the gas column in the middle of the tube is gradually stabilized with the increase of distance [6]. Figure 5 shows a different cross-sectional axial velocity curve; the horizontal axis is the ratio of a distance from a point of the interface to the origin point and the diameter of the interface, vertical axis is the ratio of the velocity of the point and the inlet velocity, and it is obvious that the gas velocity in the central section of the  $z = 623\text{ mm}$  is the largest.

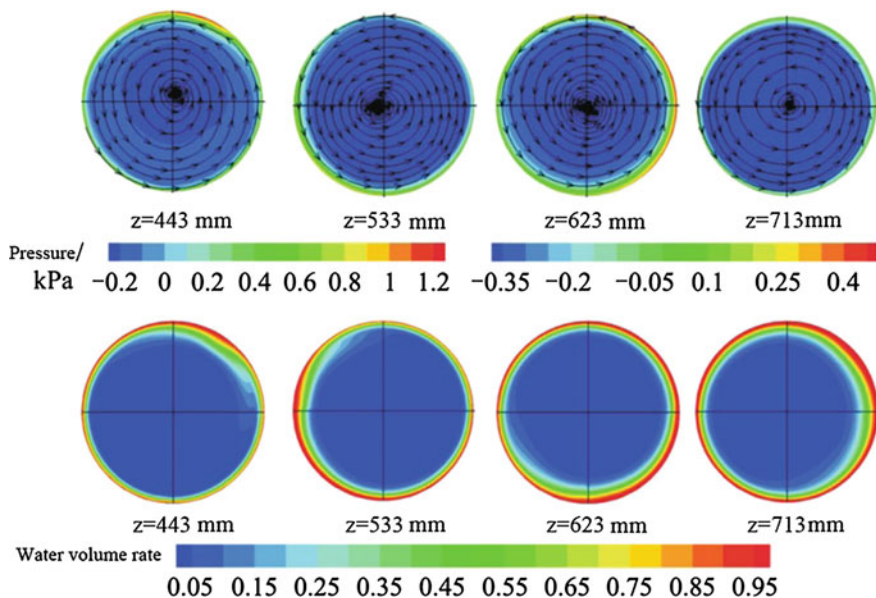


Fig. 3 Water volume fraction distribution cloud

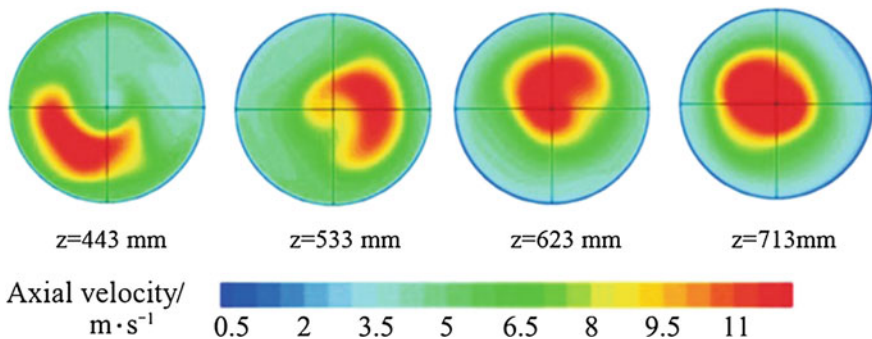


Fig. 4 Different cross-sectional axial velocity cloud

### 5.4 The Variation of Pressure Drop

According to Fig. 6, vortex tools can obviously reduce the pressure drop. Although the vortex tool section will have obvious pressure drop, and after the tool section pressure drop obviously reduced, in general, the pressure drop of gas well is reduced.



**Fig. 5** Different cross-sectional axial velocity curve

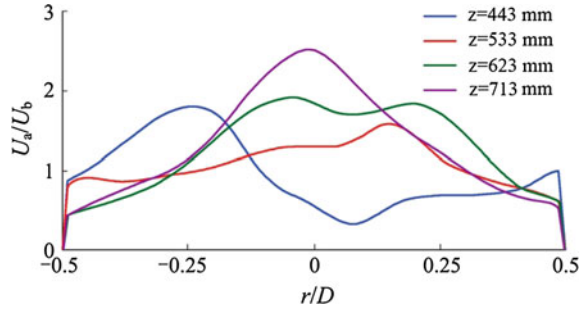
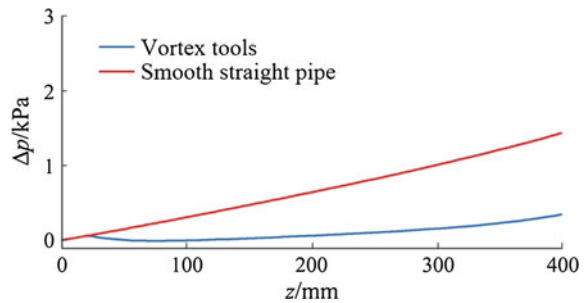


**Fig. 6** The variable curves of pressure drop



## 6 The Work Mechanism of Vortex Tools

Figure 7 shows the flow path lines and clearly shows the spiral movement that after two-phase flow passes through the vortex tools. Through the above simulation results, we can know that when the gas-liquid two-phase flow passes through the vortex tool, it will produce a very strong swirling flow. The flow pattern of the two-phase flow in a very short distance is changed from the flow pattern of mist flow dominated by liquid drop to flow pattern of the liquid film flow, and the

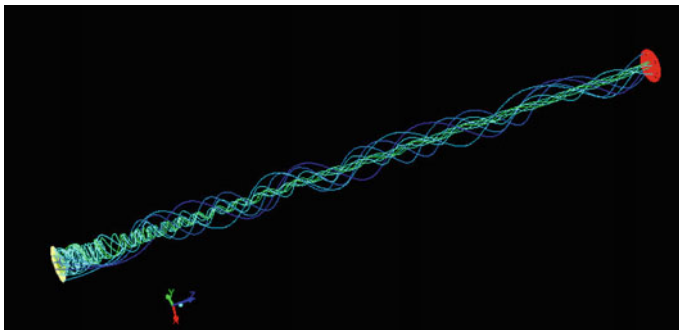


**Fig. 7** The model path lines

pressure drop and the critical gas flow velocity are decreased. Two-phase flow formed two areas after tool: The center gas column area with small swirl flow and high flow velocity and swirling flow is stronger and forming upward spiral flow area of the liquid film on the wall.

## 7 Conclusion

1. The gas–liquid two-phase flow is changed into a circular flow through the vortex tool, which is expressed as a continuous gas column in the center of the wellbore, and the liquid is carried out in the form of liquid film near the wall. The flow structure makes the flow pressure drop far lower than that of the smooth tube, and the velocity of the central column is much higher than that of the smooth pipe, which can improve the carrying liquid capacity of gas.
2. The process of vortex drainage about downhole tools placed in the wellbore is studied. The vortex tool transforms the droplet mist flow into the annular flow, which reduces the friction resistance of the tubing, thereby reducing the critical flow rate of gas wells.
3. It is suggested that the indoor experimental work of eddy current tools is recommended, and the results of numerical simulation and experiment are compared and analyzed, further validation study, in order to better guide the on-site construction.

## References

1. Qiming Y (2001) An analysis of present situation of studying new gas recovery technique by downhole gas liquid separation abroad. *Nat Gas Ind* 21(2):85–88
2. Xiaohong B, Xuri L, Kaiwen L (2011) The application and improvement of the drainage and gas production technology by velocity string. *China Petrol Mach* 39(12):60–62
3. Chun L, Wei W (2004) Status quo of water displacement gas recovery process at home and abroad. *Tuha Oil Gas* 9(3):255–261
4. Wang Z, Cui H, Li S (2010) Numerical study of down-hole spiral gas liquid separators. *Sci Technol Eng* 10(6):1358–1361
5. Zhao Y (2010) FLUENT technology and application examples. Tsinghua University Press, Beijing
6. Du J, Zhou J (2004) Water-moving and gas-recovering method of deep wells with low pressure and bottom water. *Nat Gas Ind* 24(6):86–88

# Study on Hopping Height Control and Detection for the Pneumatic Actuator

Hongwei Yan, Hongbin Li and Shengjun Zhou

**Abstract** The research objective of this paper is to study control algorithm and detection method for the pneumatic actuator's hopping height. Mathematical model of the pneumatic actuator is developed based on the Newton equations and thermodynamic equations, and the simulation model is built in MATLAB. At the acceleration stage of the hopping process, acceleration time and opening of the proportional valves are controlled to adjust the hopping height of the pneumatic actuator. Vertical hopping test rig is built, and an ultrasonic ranging system is mounted beside the foot to detect the hopping height of the pneumatic actuator. Both simulation and experimental results show that the hopping height can be controlled effectively by changing the acceleration time and the opening of the proportional valves.

**Keywords** Hopping height • Pneumatic actuator • Acceleration time • Opening of the proportional valves • Ultrasonic sensor

## 1 Introduction

Control of hopping height for the hopping robot has been a hot topic. In [1], an explicit model of the pneumatic spring was built, and a model-based height controller was proposed. Taking account of torque limits of motors, a method of

---

H. Yan (✉) · H. Li  
Ludong University, NO. 186, Middle Hongqi Road,  
Yantai City 264025, China  
e-mail: yanhongwei@hitwh.edu.cn

H. Li  
e-mail: lhbm@126.com

S. Zhou  
Wuhan Second Ship Design and Research Institute,  
Wuhan City 430064, China  
e-mail: zsjhitzone@163.com

controlling the hopping height was proposed in [2]. In [3], a hybrid controller which includes the near-inverse controller and the recursive least squares parameter estimator was introduced to improve the hopping performance. In [4], the correlations between the posture and movement of the trunk and lower limbs and hopping height in the ground contact phase of two-legged hopping in the place were revealed. In [5], a control algorithm to control the hopping height and the horizontal velocity simultaneously was proposed. Based on the spring-loaded inverted pendulum model, a control of hopping robots was widely investigated in [6], and a more accurate representation of the hopping robot is proposed using a two mass model and inelastic impact with the ground. In [7], the authors investigated the control of a four-link hopper by using the complete dynamics of the system and used partial feedback linearization to control the configuration in continuous time, and discrete parameter variations of the control object of apex height adjustment were realized. In [8], a hopping mechanism with stiffness switching was proposed to achieve a meaningful hopping height. For the purpose of obtaining the model to adjust the hopping height, in [9], a built-in learning system based on reinforcement learning for generalization was introduced. In our preceding study [10], the influential factors on the hopping height of the pneumatic actuator were studied systemically. But the hopping height was obtained by theoretical calculation, and the hopping height has not been adjusted during the continuous hopping. In this paper, an ultrasonic ranging sensor is mounted beside the foot of the pneumatic actuator in this paper, and the hopping height can be measured directly by the sensor. The movement stability is studied as the hopping height changes. This paper is organized as following. In Sect. 2, we developed the mathematical model of the pneumatic actuator. Control methods of the acceleration stage are studied on simulation in Sect. 3. The experimental results are shown in Sect. 4. Finally, in Sect. 5, we draw some conclusions of this work.

## 2 Mathematical Model

To facilitate the theoretical analysis, mathematical models of the pneumatic actuator have to be developed based on some assumptions. As shown in Fig. 1, the vertically constrained pneumatic actuator system mainly includes a double-rod and double-acting cylinder, two proportional valves, and the mechanism. Motion equation of the pneumatic actuator relative to the ground can be described as follows:

$$\frac{d^2z_b}{dt^2} = \frac{1}{M} (p_2A_2 - p_1A_1 + F_f + F_{fs} - Mg), \quad \frac{d^2z_f}{dt^2} = \frac{1}{m} [(p_2 - p_1)A_p - F_{f2} - mg] \quad (1)$$

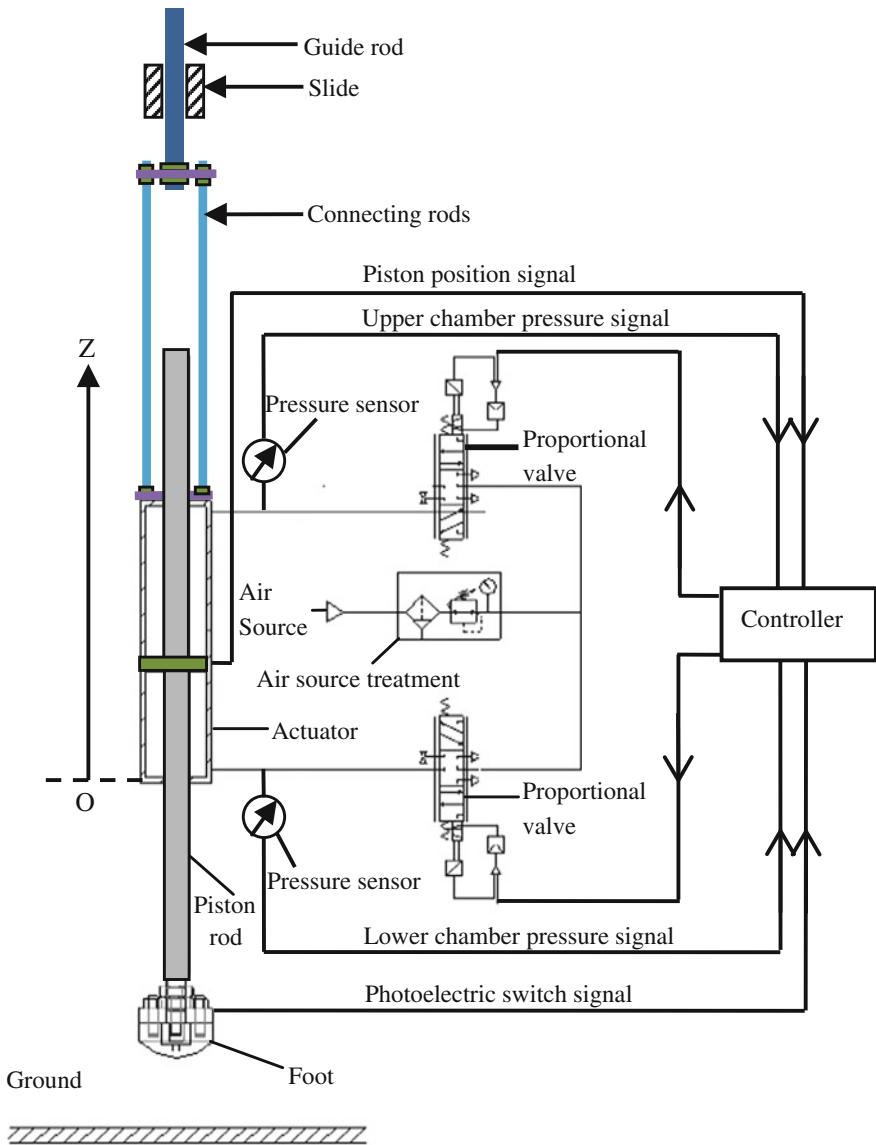


**Fig. 1** Schematic diagram of the vertically constrained pneumatic actuator

where  $M$ ,  $m$ ,  $F_{fs}$ , and  $F_{f2}$  represent the mass of the pneumatic actuator, the mass of the piston rod, the friction force between the guide rod and the slide, and the friction force between the piston and the cylinder tube, respectively.

The upper and the lower chamber's pressure equations of charging and discharging can be deduced at the ideal gas condition as follows:

$$\begin{aligned} \frac{dp_{1t}}{dt} &= \begin{cases} \frac{kRT_s q_{m1in}}{A_1(z_{rb} + z_{10})} - \frac{kp_{1t}}{z_{rb} + z_{10}} \frac{dz_{rb}}{dt} & A_{e1} \geq 0 \\ \frac{kp_{1t}}{z_{rb} + z_{10}} \frac{dz_{rb}}{dt} - \frac{kRT_s}{A_1(z_{rb} + z_{10})} q_{m1out} \left(\frac{p_{1t}}{p_{st}}\right)^{\frac{k-1}{k}} & A_{e1} < 0 \end{cases} \\ \frac{dp_{2t}}{dt} &= \begin{cases} \frac{kRT_s q_{m2in}}{A_2(s - z_{rb} + z_{20})} - \frac{kp_{2t}}{s - z_{rb} + z_{20}} \frac{dz_{rb}}{dt} & A_{e2} \geq 0 \\ \frac{kp_{2t}}{s - z_{rb} + z_{20}} \frac{dz_{rb}}{dt} - \frac{kRT_s}{A_2(s - z_{rb} + z_{20})} q_{m2out} \left(\frac{p_{2t}}{p_{st}}\right)^{\frac{k-1}{k}} & A_{e2} < 0 \end{cases} \end{aligned} \quad (2)$$

where  $A_e$  represents the effective area of the throttle orifice;  $A_e > 0$  and  $A_e < 0$  represent charging and discharging process, respectively;  $q_{m1in}$ ,  $q_{m2in}$ ,  $q_{1out}$ ,  $q_{2out}$ , and  $k$  represent the input and output mass flow of the lower and upper chamber, and the specific heat constant, respectively.

In case the air flow through the valve is considered as a sonic one, mass flow  $q_m$  is given as:

$$\begin{aligned} q_{miin} &= \begin{cases} A_{ei} p_{st} \left\{ \frac{2k}{RT_s(k-1)} \left[ \left(\frac{p_{it}}{p_{st}}\right)^{\frac{2}{k}} - \left(\frac{p_{it}}{p_{st}}\right)^{\frac{k+1}{k}} \right] \right\}^{\frac{1}{2}} & (0.528 \leq \frac{p_{it}}{p_{st}} < 1) \\ A_{ei} p_{st} \left[ \frac{k}{RT_s} \left(\frac{2}{k+1}\right)^{\frac{k+1}{k-1}} \right]^{\frac{1}{2}} & (0 < \frac{p_{it}}{p_{st}} < 0.528) \end{cases} \\ q_{miout} &= \begin{cases} A_{ei} p_{it} \left\{ \frac{2k}{RT_i(k-1)} \left[ \left(\frac{p_{at}}{p_{it}}\right)^{\frac{2}{k}} - \left(\frac{p_{at}}{p_{it}}\right)^{\frac{k+1}{k}} \right] \right\}^{\frac{1}{2}} & (0.528 \leq \frac{p_{at}}{p_{it}} < 1) \\ A_{ei} p_{it} \left[ \frac{k}{RT_i} \left(\frac{2}{k+1}\right)^{\frac{k+1}{k-1}} \right]^{\frac{1}{2}} & (0 < \frac{p_{at}}{p_{it}} < 0.528) \end{cases} \end{aligned} \quad (3)$$

where  $i = 1$  and  $i = 2$  represent the parameters of the lower chamber and upper chamber, respectively. Beside Eqs. (1)–(3), there are friction force equations and temperature equations, which are not given here.

### 3 Simulation

Based on the mathematical model in Sect. 2, the simulation model of the pneumatic actuator is built by Simulink tools in the form of S-function. The main modules are shown in Fig. 2.

As shown in Fig. 2, there are seven main modules in the simulation model. Constant values of the model are given in the assignment module. The thermodynamic module, buffering module, acceleration module, and flight phase module are used for real-time calculation of the thermodynamic and motion parameters of the pneumatic actuator. In the control module, the control voltages of the upper and

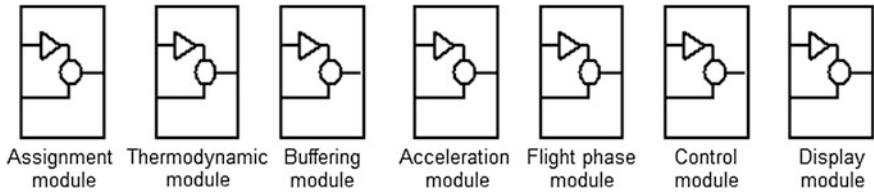


Fig. 2 Main simulation modules

lower proportional valves are calculated. And the display module is used to show the values and the curves of the parameters.

At the acceleration stage, the main control objective is to replenish energy for the pneumatic actuator. Hopping height will vary according to how much energy is injected into the pneumatic actuator. The controllable variables include the acceleration time and the opening of the proportional valves. In order to study the control method of the hopping height and the movement stability while the hopping height changes, the values of the controllable variables are changed every 30 hopping cycles. The simulation results are shown in Figs. 3 and 4.

As shown in Fig. 3, when the acceleration time switches between 50 and 70 ms, the pneumatic actuator can keep continuous hopping. The hopping height switches between 30 and 55 mm, and the hopping height can be stable within 5 hopping periods. When the control voltages of the two proportional valves switch between 7.4 V/2.6 V (7.4 V/2.6 V means the control voltages for the upper and lower proportional valves are 7.4 and 2.6 V, respectively.) and 8 V/2 V, the pneumatic actuator can keep continuous hopping (see Fig. 4). The hopping height switches between 42 and 56 mm, and the hopping height can be stable within 5 hopping periods.

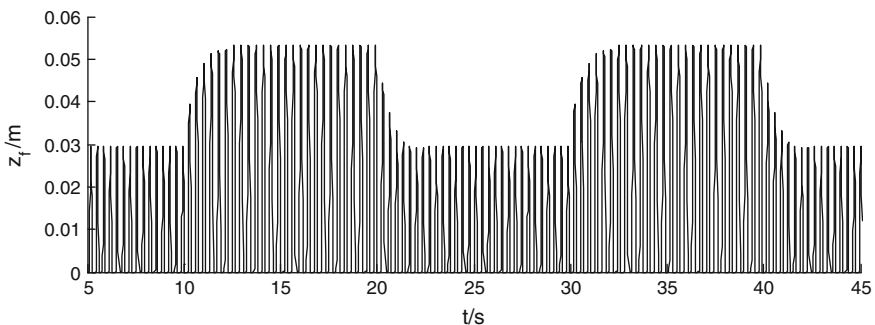
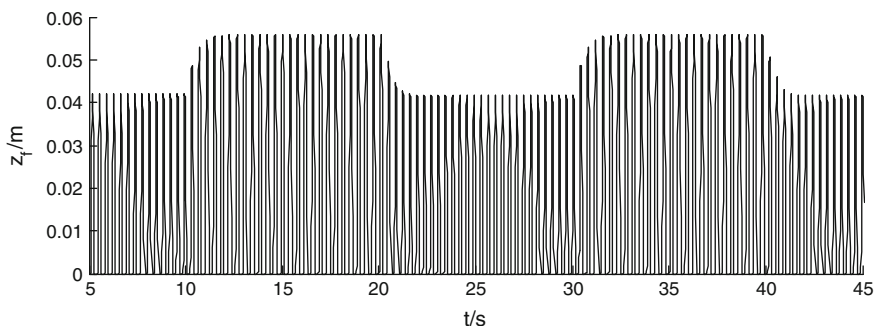


Fig. 3 Simulation results of hopping height versus the acceleration time



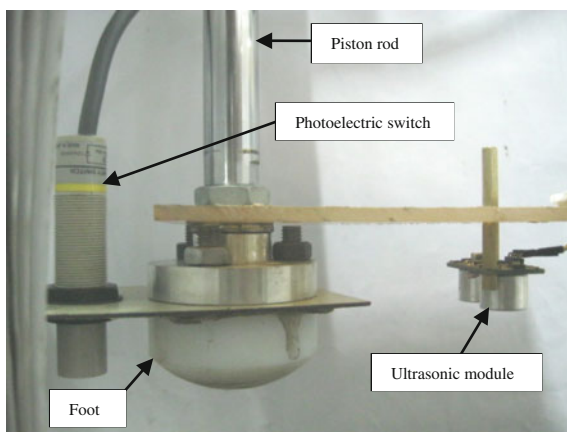
**Fig. 4** Simulation results of hopping height versus the opening of the proportional valves

## 4 Experiments

To verify the above-mentioned simulation results, experimental study is carried out in this section. As shown in Fig. 5, in the test rig, the ultrasonic ranging module is mounted beside the foot of the pneumatic actuator. During hopping, the distance between the foot and the ground is sampled with the ultrasonic ranging module.

As shown in Fig. 5, the photoelectric switch is used to distinguish between the stance phase and the flight phase of the pneumatic actuator. An ultrasonic ranging module (KS103) is mounted beside the foot. During the hopping progress, the ultrasonic module can measure the distance between the foot and the ground, and then, the hopping height of the pneumatic actuator is obtained. In order to ensure the detection precision, the detect range should be limited in 40–180 mm. Consequently, the ultrasonic module is mounted at the position as shown in Fig. 5. For the mounting location, the detected distance is about 43 mm when the pneumatic actuator is on the ground. Influenced by the sampling period, the measurement results of the hopping height are discrete points.

**Fig. 5** Photograph of structure of the foot





When experiments are to be made, the control parameters (the acceleration time and the opening of the proportional valves) switch every 20 hopping periods. The experimental results are shown in Figs. 6 and 7. When the acceleration time switches between 50 and 70 ms, the hopping height switches between about 22 and 38 mm. When the control voltages switch between 7.4 V/2.6 V and 8 V/2 V, the hopping height switches between about 31 and 42 mm. The experimental results are lower than the simulation results. This is caused by the leakages and the supply pressure fluctuation in the experimental process. Moreover, there are individual points lower than 43 mm as shown in Figs. 6 and 7, which is the result of vibration when the foot touches the ground.

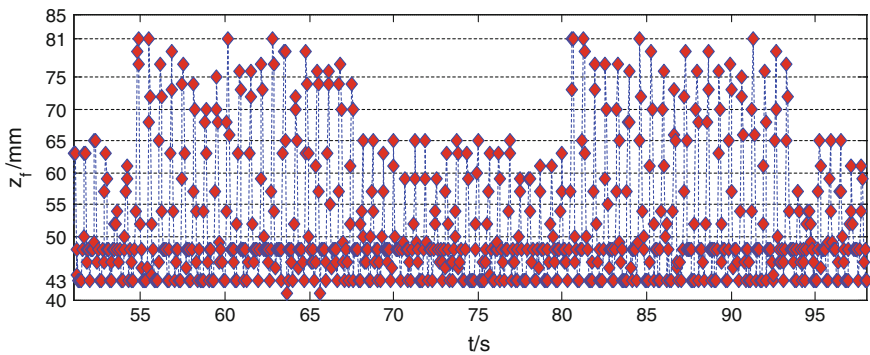


**Fig. 6** Experimental curves of hopping height versus the acceleration time

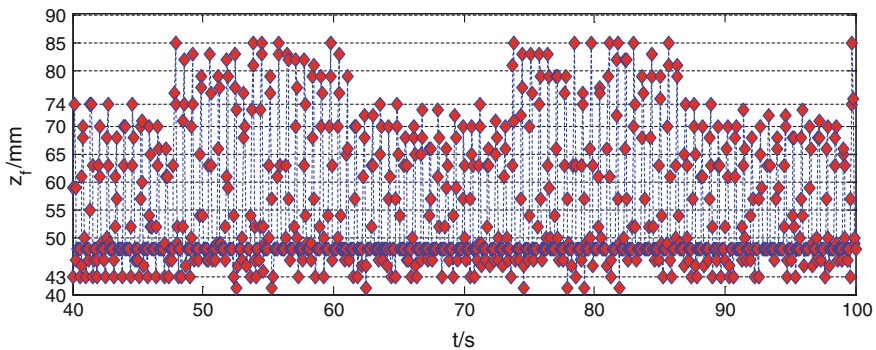


**Fig. 7** Experimental curves of hopping height versus the opening of the proportional valves

## 5 Conclusion

Through simulations and experiments, we draw the following conclusions: Ultrasonic ranging module can be used to measure the hopping height of the pneumatic actuator. By adjusting the acceleration time and opening of the proportional valves, hopping height of the pneumatic actuator can achieve real-time control in the process of continuous hopping. The transient process is smooth, and the transient period is within five. The control method has good practicability and maneuverability.

## References

1. Harbick K, Sukhatme G (2002) Controlling hopping height of a pneumatic monopod. In: Proceeding of ICRA, pp 3998–4003
2. Ohashi E, Ohnishi K (2006) Hopping height control for hopping robots. *Electr Eng Jpn* 155 (1):64–71
3. Prosser AJ, Kam M (1992) Control of hopping height for a one-legged hopping machine. In: Proceeding of mobile robots VII, pp 604–612
4. Nakamata O, Nitta O, Furukawa Y (2014) Analysis of the factors influencing the hopping height during two-legged hopping in the place in healthy subjects: with special reference to the posture and movement of the trunk and lower limb. *J Jpn Phys Ther Assoc* 41:290–300
5. Cherouvim N, Papadopoulos E (2009) Control of hopping speed and height over unknown rough terrain using a single actuator. In: Proceeding of ICRA, pp 2743–2748
6. Mathis FB, Mukherjee R (2013) Apex height control of a two-mass hopping robot. In: Proceeding of ICRA, pp 4785–4790
7. Mathis FB, Mukherjee R (2013) Apex height control of a four-link hopping robot. In: Proceeding of IROS, pp 5121–5126
8. Sugawara Y, Mizuguchi K, Kobayashi N (2010) A hopping mechanism through the use of resonance. *J Sys Des Dyn* 4(1):129–141
9. Kusano Y, Tsutsumi K (2002) Hopping height control of an active suspension type leg module based on reinforcement learning and a neural network. In: Proceeding of intelligent robots and systems, pp 2672–2677
10. Li Z, Yan HW, Ji J, Lin XS (2015) Study on dynamic characteristics of the vertical hopping of the one-legged robot. *Robot* 37(4):467–477

# An Interval-Reduced-Basis Approach for Predicting Acoustic Response of Coupled Structural-Acoustic System

Zheng Lv, Zhiping Qiu and Qi Li

**Abstract** To predict and improve the acoustic behavior, an interval-reduced-basis approach is presented for acoustic response of coupled structural-acoustic system. In the present approach, the acoustic response is approximated by using a linear combination of interval-basis vectors with undetermined coefficients. The reduced-order equations are derived based on Galerkin scheme to compute the undetermined coefficients. In addition, the determination of the acoustic response range is transformed into a sequence of quadratic programming problems subject to box constraints, which are computed using the DC algorithm effectively. Numerical example is presented to demonstrate the implementation of the present approach and show that the new approach has a good accuracy and efficiency.

**Keywords** Interval-reduced-basis approach · Acoustic response · Coupled structural-acoustic system · Quadratic programming problem · DC algorithm

## 1 Introduction

The increase of customer expectations makes designer pay more attentions to the noise level of products, especially for vehicle passenger compartment and aircraft cabin. From the viewpoint of both commercial interests and legislations for noise, predicting acoustic behavior has a very important significance at the design stage.

Traditionally, a structural-acoustic problem is solved on the basis of deterministic model with well-defined parameters. However, latest engineering advances

---

Z. Lv (✉) · Z. Qiu · Q. Li  
School of Aeronautic Science and Engineering, Beihang University,  
Beijing 100191, China  
e-mail: lvbaolvzheng@126.com

Z. Qiu  
e-mail: zpqiu@buaa.edu.cn

Q. Li  
e-mail: lq12131010@163.com

have started to recognize the need for defining multiple types of uncertainty. Probabilistic models [1–3] cannot treat situations with incomplete information on which to evaluate a probability, or when that information is ambiguous [4]. Many interval-based uncertainty models have been developed to handle such situations, such as the Taylor series-based interval analysis method (TIAM) [5, 6], the interval perturbation method [7, 8], and equivalent transformation method [9, 10]. Qiu etc. and Chen have focused on a series of researches on the application of interval analysis method for various analysis models, such as static problem [11], dynamic problem [12], and eigenvalue problem [6, 13]. Xia etc. [14, 15] extended the method for the response ranges of acoustic fields. However, the traditional interval analysis method has two drawbacks [11, 16]: First, accurate results can be obtained only for small variation coefficient of interval parameters; and second, the second-order analysis method based on interval arithmetic may result in an over-estimation of the response due to interval extension.

In this paper, an interval-reduced-basis approach is presented for the acoustic response of coupled structural-acoustic system. Compared with the traditional interval analysis methods, the present approach has its own advantages as follows: (1) The original structural-acoustic problem is reduced into a sequence of reduced-order equations, which need less calculation amount; (2) the explicit expression of acoustic response with respect to interval parameters can be obtained after calculating the undetermined coefficients; (3) both the efficiency and accuracy can be controlled by considering additional basis vectors.

## 2 Interval FEM Formulation of Structural-Acoustic System

The dynamic equilibrium equations of the structural-acoustic system are given in the following form of tensors.

$$\sigma_{ij} + f_i = \rho_s \ddot{u}_i, \quad p_{ii} - \ddot{p}/c_0^2 = 0 \quad i, j = 1, 2, 3 \quad (1)$$

where  $\sigma_{ij}$ ,  $u_i$ ,  $f_i$ , and  $\rho_s$  are the stress, displacement, body force, and mass density in the structure domain, respectively,  $p$  and  $c_0$  are the sound pressure and acoustic velocity in the fluid domain, respectively.

Applying Galerkin scheme to the equilibrium equation and the boundary conditions of the coupled system, and integrating by parts, and substituting the discretized structure and fluid domain representation into Eq. (1), we obtain

$$\mathbf{M}_s \ddot{\mathbf{a}} + \mathbf{K}_s \mathbf{a} - (\mathbf{Q}_{sf})^T \mathbf{p} / \rho_f = \mathbf{F}_s \quad (2)$$

$$\mathbf{Q}_{sf} \ddot{\mathbf{a}} + \mathbf{M}_f \ddot{\mathbf{p}} + \mathbf{K}_f \mathbf{p} = 0 \quad (3)$$

where  $\mathbf{K}_s$ ,  $\mathbf{M}_s$ , and  $\mathbf{Q}_{sf}$  are the structural stiffness matrix, the structural mass matrix, and spatial coupled matrix, respectively;  $\mathbf{a}$  and  $\mathbf{p}$  are the node displacement vector and the node sound pressure vector, respectively;  $\mathbf{F}_s$  is the force vector;  $\mathbf{K}_f$ , and  $\mathbf{M}_f$  are the acoustic stiffness matrix and the acoustic mass matrix, respectively.

By combining Eqs. (2) and (3), and assuming that the external excitation is time harmonic, the coupled system can be described by the FEM formulation

$$\begin{pmatrix} \mathbf{K}_s - \omega^2 \mathbf{M}_s & -(\mathbf{Q}_{sf})^T / \rho_f \\ -\omega^2 \mathbf{Q}_{sf} & \mathbf{K}_f - \omega^2 \mathbf{M}_f \end{pmatrix} \begin{pmatrix} \mathbf{a} \\ \mathbf{p} \end{pmatrix} = \begin{pmatrix} \mathbf{F}_s \\ \mathbf{0} \end{pmatrix} \quad (4)$$

where  $\omega$  is the angle frequency.

The above equation can be rewritten in a more compact fashion as

$$\mathbf{A} \mathbf{x} = \mathbf{b} \quad (5)$$

where

$$\mathbf{A} = \begin{pmatrix} \mathbf{K}_s - \omega^2 \mathbf{M}_s & -(\mathbf{Q}_{sf})^T / \rho_f \\ -\omega^2 \mathbf{Q}_{sf} & \mathbf{K}_f - \omega^2 \mathbf{M}_f \end{pmatrix}, \quad \mathbf{x} = \{\mathbf{a} \ \mathbf{p}\}^T, \quad \mathbf{b} = \{\mathbf{F}_s \ \mathbf{0}\}^T. \quad (6)$$

We assume that the uncertainties in the coupled system are caused by the interval parameter vector

$$\boldsymbol{\alpha} = (\alpha_s) \in \boldsymbol{\alpha}^I = (\alpha_s^I) = [\underline{\boldsymbol{\alpha}}, \bar{\boldsymbol{\alpha}}] = [(\underline{\alpha}_s), (\bar{\alpha}_s)], \quad s = 1, 2, \dots, N \quad (7)$$

where  $\boldsymbol{\alpha} = (\alpha_s)$  are the interval parameter vectors of the system,  $\underline{\boldsymbol{\alpha}} = (\underline{\alpha}_s)$  and  $\bar{\boldsymbol{\alpha}} = (\bar{\alpha}_s)$  are the lower and upper bounds of  $\boldsymbol{\alpha} = (\alpha_s)$ , respectively; then, the dynamic equilibrium equations of the structural-acoustic system with uncertain parameters can be rewritten as follows:

$$\mathbf{A}(\boldsymbol{\alpha}) \mathbf{x}(\boldsymbol{\alpha}) = \mathbf{b} \quad (8)$$

The solution set of Eq. (8) is given by

$$\mathbf{x}(\boldsymbol{\alpha}) \in \mathbf{x}^I(\boldsymbol{\alpha}) = [\underline{\mathbf{x}}(\boldsymbol{\alpha}), \bar{\mathbf{x}}(\boldsymbol{\alpha})] \quad (9)$$

where

$$\bar{\mathbf{x}}(\underline{\mathbf{x}})(\boldsymbol{\alpha}) = \max_{\boldsymbol{\alpha} \in \boldsymbol{\alpha}^I}(\min)\{\mathbf{x}(\boldsymbol{\alpha}) : \mathbf{x}(\boldsymbol{\alpha}) \in R^n, \mathbf{A}(\boldsymbol{\alpha}) \mathbf{x}(\boldsymbol{\alpha}) = \mathbf{b}\}. \quad (10)$$

### 3 Interval-Reduced-Basis Approach

#### 3.1 Selection of Interval-Reduced-Basis Vectors

The novel idea in this paper is to approximate the acoustic response using a linear combination of interval-basis vectors with undetermined coefficients. Without any loss of generality, the approximation of the acoustic response can be expressed as

$$\mathbf{x}(\boldsymbol{\alpha}) = \sum_{k=0}^{m-1} \zeta_k \boldsymbol{\varphi}_k(\boldsymbol{\alpha}) = \zeta_0 \boldsymbol{\varphi}_0(\boldsymbol{\alpha}) + \zeta_1 \boldsymbol{\varphi}_1(\boldsymbol{\alpha}) + \cdots + \zeta_{m-1} \boldsymbol{\varphi}_{m-1}(\boldsymbol{\alpha}) = \boldsymbol{\Psi}(\boldsymbol{\alpha}) \boldsymbol{\xi} \quad (11)$$

where  $\boldsymbol{\Psi}(\boldsymbol{\alpha})$  is a matrix of  $m$  interval-basis vectors,  $\boldsymbol{\xi}$  is the vector of undetermined coefficients in the interval basis.

Expanding the matrix  $\mathbf{A}(\boldsymbol{\alpha})$  at the midpoint of the interval parameter and neglecting the higher-order terms, the dynamic equilibrium equations of structural-acoustic system can be rewritten as follows:

$$\left( \mathbf{A}_c + \sum_{s=1}^N \mathbf{A}_s \delta_s \right) \mathbf{x}(\boldsymbol{\alpha}) = \mathbf{b} \quad (12)$$

where  $\mathbf{A}_c$  and  $\mathbf{A}_s$  are the nominal value and uncertainty of interval matrix  $\mathbf{A}(\boldsymbol{\alpha})$ , respectively,  $\delta_s$  is interval parameters and belongs to  $[-1, 1]$ .

Both sides of Eq. (12), being multiplied by  $\mathbf{A}_c^{-1}$ , give

$$\left( \mathbf{I} + \sum_{s=1}^N \mathbf{A}_c^{-1} \mathbf{A}_s \delta_s \right) \mathbf{x}(\boldsymbol{\alpha}) = \mathbf{A}_c^{-1} \mathbf{b}. \quad (13)$$

If the condition  $\left\| \sum_{s=1}^N \mathbf{A}_c^{-1} \mathbf{A}_s \delta_s \right\| < 1$  is satisfied, the inverse of coefficient matrix of Eq. (13) can be expanded by the Neumann series

$$\left( \mathbf{I} + \sum_{s=1}^N \mathbf{A}_c^{-1} \mathbf{A}_s \delta_s \right)^{-1} = \mathbf{I} + \sum_{k=1}^{\infty} \left( - \sum_{s=1}^N \mathbf{A}_c^{-1} \mathbf{A}_s \delta_s \right)^k = \mathbf{I} - \mathbf{P} + \mathbf{P}^2 - \mathbf{P}^3 + \cdots \quad (14)$$

where

$$\mathbf{P} = \sum_{s=1}^N \mathbf{A}_c^{-1} \mathbf{A}_s \delta_s. \quad (15)$$

Both sides of Eq. (13), being multiplied by Eq. (14), give

$$\mathbf{x}(\boldsymbol{\alpha}) = (\mathbf{I} - \mathbf{P} + \mathbf{P}^2 - \mathbf{P}^3 + \dots)\mathbf{A}_c^{-1}\mathbf{b}. \quad (16)$$

Taking the product terms  $\mathbf{P}^k\mathbf{A}_c^{-1}\mathbf{b}$ ,  $k = 0, 1, \dots, m-1$  as the interval-basis vectors, the first  $m$ th-order interval-basis vectors can be expressed as

$$\begin{aligned} \boldsymbol{\varphi}_0(\boldsymbol{\alpha}) &= \mathbf{A}_c^{-1}\mathbf{b} = \mathbf{e}_0, & \boldsymbol{\varphi}_1(\boldsymbol{\alpha}) &= \sum_{s=1}^N \mathbf{A}_c^{-1}\mathbf{A}_s\delta_s\boldsymbol{\varphi}_0(\boldsymbol{\alpha}) = \delta_s\mathbf{e}_s \\ \boldsymbol{\varphi}_{m-1}(\boldsymbol{\alpha}) &= \sum_{s=1}^N \mathbf{A}_c^{-1}\mathbf{A}_s\delta_s\boldsymbol{\varphi}_{m-2}(\boldsymbol{\alpha}) = \delta_{s_1}\delta_{s_2}\dots\delta_{s_{m-1}}\mathbf{e}_{s_1s_2\dots s_{m-1}} \end{aligned} \quad (17)$$

where  $\mathbf{e}_0 = \mathbf{A}_c^{-1}\mathbf{b}$ ,  $\mathbf{e}_s = \mathbf{A}_c^{-1}\mathbf{A}_s\mathbf{A}_c^{-1}\mathbf{b}$ , and  $\mathbf{e}_{s_1s_2\dots s_{m-1}} = \mathbf{A}_c^{-1}\mathbf{A}_{s_1}\dots\mathbf{A}_c^{-1}\mathbf{A}_{s_{m-1}}\mathbf{A}_c^{-1}\mathbf{b}$  are deterministic vectors.

### 3.2 Derivation of Reduced-Order Equations Based on IRBA

Based on the novel idea of interval-reduced-basis approach, substituting Eq. (11) into Eq. (12) gives

$$\left(\mathbf{A}_c + \sum_{s=1}^N \mathbf{A}_s\delta_s\right) \sum_{k=0}^{m-1} \zeta_k\boldsymbol{\varphi}_k(\boldsymbol{\alpha}) \approx \mathbf{b}. \quad (18)$$

To obtain the interval-reduced-order equation of the structural-acoustic system, the variant of the Galerkin scheme is applied in this section. The Galerkin scheme is an orthogonal projection technique, which enforces the condition that the weight function is equal to the basis function.

Considering Eq. (18) and applying the Galerkin scheme give

$$\left(\mathbf{A}_c + \sum_{s=1}^N \mathbf{A}_s\delta_s\right) \sum_{k=0}^{m-1} \zeta_k\boldsymbol{\varphi}_k(\boldsymbol{\alpha}) - \mathbf{b} \perp \boldsymbol{\Psi}(\boldsymbol{\alpha}). \quad (19)$$

Both sides of Eq. (18), being multiplied by the interval-basis vectors, give

$$\boldsymbol{\varphi}_l^T(\boldsymbol{\alpha}) \left(\mathbf{A}_c + \sum_{s=1}^N \mathbf{A}_s\delta_s\right) \sum_{k=0}^{m-1} \zeta_k\boldsymbol{\varphi}_k(\boldsymbol{\alpha}) = \boldsymbol{\varphi}_l^T(\boldsymbol{\alpha})\mathbf{b}, \quad l = 0, 1, \dots, m-1. \quad (20)$$

Taking the inner product of interval vectors  $\boldsymbol{\varphi}_l(\boldsymbol{\alpha}), \boldsymbol{\varphi}_k(\boldsymbol{\alpha})$  gives

$$\sum_{k=0}^{m-1} \langle \boldsymbol{\varphi}_l^T(\boldsymbol{\alpha}) \mathbf{A}_c \boldsymbol{\varphi}_k(\boldsymbol{\alpha}) \rangle \zeta_k + \sum_{k=0}^{m-1} \sum_{s=1}^N \langle \delta_s \boldsymbol{\varphi}_l^T(\boldsymbol{\alpha}) \mathbf{A}_s \boldsymbol{\varphi}_k(\boldsymbol{\alpha}) \rangle \zeta_k = \langle \boldsymbol{\varphi}_l^T(\boldsymbol{\alpha}) \mathbf{b} \rangle. \quad (21)$$

The above equation can be rewritten in a more compact fashion as

$$\mathbf{R} \boldsymbol{\xi} = \mathbf{P} \quad (22)$$

where

$$r_{l,k} = \langle \boldsymbol{\varphi}_l^T(\boldsymbol{\alpha}) \mathbf{A}_c \boldsymbol{\varphi}_k(\boldsymbol{\alpha}) \rangle + \sum_{s=1}^N \langle \delta_s \boldsymbol{\varphi}_l^T(\boldsymbol{\alpha}) \mathbf{A}_s \boldsymbol{\varphi}_k(\boldsymbol{\alpha}) \rangle \quad (23)$$

$$p_l = \langle \boldsymbol{\varphi}_l^T(\boldsymbol{\alpha}) \mathbf{b} \rangle, \quad k, l = 0, 1, \dots, m - 1. \quad (24)$$

Up to now, the reduced-order equations of the coupling system are derived based on the interval-reduced-basis approach. Obviously, the number of algebraic operations in reduced-order equations is much smaller than that required to solve the original equations given in Eq. (8) directly.

### 3.3 Determination of Acoustic Response Range via the DC Algorithm

Substituting the deterministic coefficients obtained in Eq. (22) into Eq. (11), and ignoring the order greater than two, the explicit expression of the acoustic response is obtained as

$$\mathbf{x}(\boldsymbol{\alpha}) = \zeta_0^* \mathbf{e}_0 + \delta_s \zeta_1^* \mathbf{e}_s + \delta_{s_1} \delta_{s_2} \zeta_2^* \mathbf{e}_{s_1 s_2} \quad (25)$$

where  $\boldsymbol{\xi}^* = \{\zeta_0^*, \zeta_1^*, \dots, \zeta_{m-1}^*\}^T$  is the solution of the reduced-order equations.

According to the optimization form given in Eq. (10), the acoustic response range can be determined as

$$\bar{x}_i(\underline{\mathbf{x}}_i)(\boldsymbol{\alpha}, \boldsymbol{\kappa}) = \zeta_0^* e_0^i + \begin{cases} \max(\min) \left[ \delta_s \zeta_1^* e_s^i + \delta_{s_1} \delta_{s_2} \zeta_2^* e_{s_1 s_2}^i \right] \\ \text{s.t. } -1 \leq \delta_s \leq 1 \end{cases} \quad (26)$$



Introducing the notation

$$\mathbf{E} = \begin{bmatrix} e_{11}^i & e_{12}^i & \cdots & e_{1N}^i \\ e_{21}^i & e_{22}^i & \cdots & e_{2N}^i \\ \vdots & \vdots & e_{s_1 s_2}^i & \vdots \\ e_{N1}^i & e_{N2}^i & \cdots & e_{NN}^i \end{bmatrix} \quad \begin{aligned} \mathbf{D} &= \zeta_2^* (\mathbf{E} + \mathbf{E}^T) \\ \mathbf{d} &= \{\zeta_1^* (e_1^i, e_2^i, \dots, e_N^i)\}^T \\ \mathbf{Y} &= \{\delta_1, \delta_2, \dots, \delta_N\}^T \end{aligned} \quad (27)$$

The optimization problem mentioned above can be transformed into the quadratic problems subject to box constrains as follows:

$$\begin{cases} \max(\min) g(\mathbf{Y}) = \frac{1}{2} \mathbf{Y}^T \mathbf{D} \mathbf{Y} + \mathbf{d}^T \mathbf{Y} \\ \text{s.t. } -1 \leq y_i \leq 1, \quad i = 1, 2, \dots, N \end{cases} \quad (28)$$

Due to the difficulty in checking the positive semi-definiteness of matrix  $\mathbf{D}$ , the optimization problem is non-convex quadratic programming subject to box constraints [17]. One of the highlights in this paper is to determine the acoustic response range via the DC algorithm combined the branch and bound scheme instead of interval arithmetic. The advantage of this algorithm is to converge to the global optimal solution for the quadratic programming problem [18, 19].

After having calculated the solution of Eq. (28), the acoustic response range can be given as

$$\bar{x}_i(\boldsymbol{\alpha}, \boldsymbol{\kappa}) = \zeta_0^* e_0^i + \max g(\mathbf{Y}) \quad \underline{x}_i(\boldsymbol{\alpha}, \boldsymbol{\kappa}) = \zeta_0^* e_0^i + \min g(\mathbf{Y}) \quad (29)$$

where  $\max g(\mathbf{Y})$  and  $\min g(\mathbf{Y})$  are the maximum value and the minimum value of the optimization problem given in Eq. (28), respectively.

## 4 Numerical Example

A structural-acoustic system of car model is shown in Fig. 1. Considering the realistic complex environment, the acoustic velocity  $c_0$  and the density  $\rho_f$  of air surrounding the acoustic cavity are modeled as interval parameters, and the interval numbers of [330, 350] m/s and [1.125, 1.325] kg/m<sup>3</sup> are assigned for  $c_0$  and  $\rho_f$ , respectively. The properties of structural materials listed in Table 1 are also assumed to be interval parameters.

The acoustic responses of the coupled system are, respectively, computed via VM, TIAM, and IRBA including two and three interval-basis vectors shown in Fig. 2. We refer to the first- and second-order IRBA by IRBAI and IRBAII. For the sake of comparison, the bounds of the amplitude of sound pressure for the four selected frequencies are listed in Table 2, and the total wall-clock time taken by each method is also listed in the table. As expected, IRBA gives better results

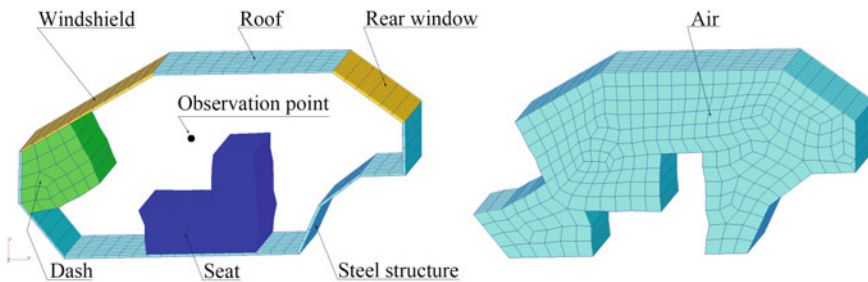


**Fig. 1** The structural-acoustic system of car model

**Table 1** Properties of structural materials

Assembly	Material	Young's modulus		Density (kg/m <sup>3</sup> )	
		LB	UB	LB	UB
Dash/seat	Foam	0.0048	0.0052	0.95	1.05
Window	Glass	61.75	68.25	2660	2940
Roof/steel	Steel	199.5	220.5	7315	8085

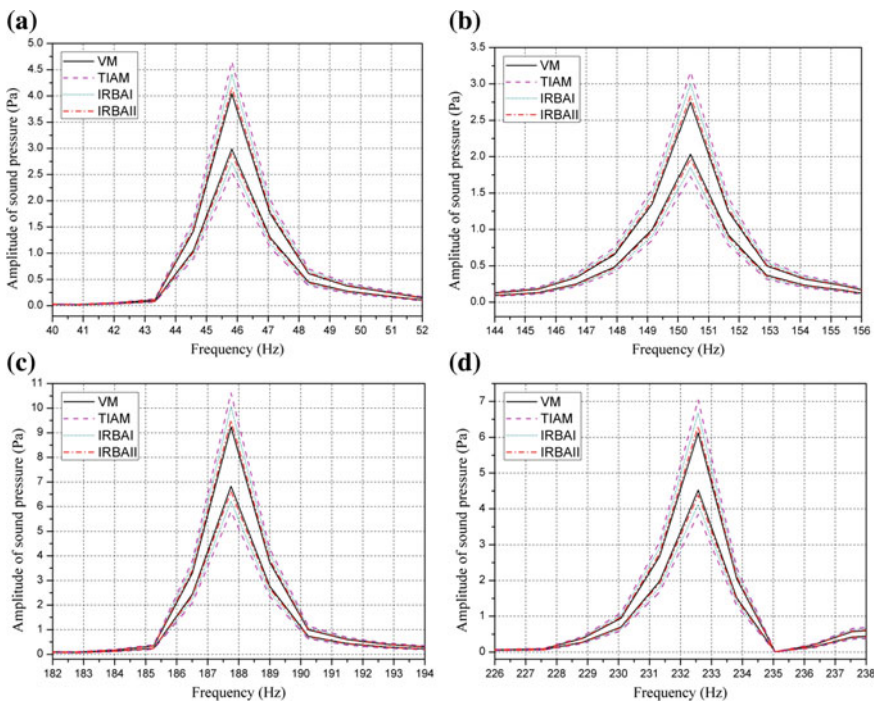


**Fig. 2** The acoustic response range in partial frequency bands. **a**  $\omega = 40\text{--}52$  Hz, **b**  $\omega = 144\text{--}156$  Hz, **c**  $\omega = 182\text{--}194$  Hz, **d**  $\omega = 226\text{--}238$  Hz

**Table 2** Comparisons between the results for various methods

Frequency (Hz)	Bounds	VM (3390.08 s)	TIAM (131.22 s)	IRBAI (126.45 s)	IRBAII (156.49 s)
45.82	LB	2.9887	2.5496	2.7298	2.8983
	UB	4.0432	4.6502	4.4075	4.1789
150.40	LB	2.0334	1.7298	1.8714	1.9797
	UB	2.7511	3.1657	2.9982	2.8674
187.75	LB	6.8261	5.8262	6.3118	6.6203
	UB	9.2353	10.5041	9.8995	9.5022
232.57	LB	4.5257	3.8369	4.1084	4.3081
	UB	6.1231	7.0445	6.6771	6.4068

compared with TIAM, which indicates that the proposed method has high accuracy. Furthermore, the accuracy of IRBAII is higher than that of IRBAI. The good accuracy of IRBAII can be attributed to the speedy convergence and the application of the DC algorithm. According to the relative errors, we also draw a conclusion that three interval-basis vectors considered are sufficient to achieve high accuracy, even though the accuracy of the solution depends on the number of interval-basis vectors.

From the total wall-clock time, it can be found that the computational cost of IRBAI is comparable to that of TIAM, and the total wall-clock time of IRBAII is much shorter than that of VM but is a little longer than that of TIAM. The exceeded time is mainly implemented to calculate the interval-reduced-basis vectors and the reduced matrix. Some measures such as parallel algorithm can be taken to further improve the computational efficiency.

## 5 Summary

In this paper, we present a new interval-reduced-basis approach for acoustic response of coupled structural-acoustic system. The present approach reduces the original structural-acoustic problem into a sequence of reduced-order equations and allows to obtain the explicit expression of acoustic response with respect to interval parameters. In addition, the accurate acoustic response range is determined via the DC algorithm. With the help of numerical example, we conclude that the present approach has significant improvement over the results obtained by the traditional interval analysis methods, and both the efficiency and accuracy can be controlled by considering additional interval-basis vectors.

**Acknowledgements** The project is supported by ‘111’ Project (No. B07009), National Nature Science Foundation of the P.R. China (No. 11372025, No. 11432002), Aeronautical Science Foundation of China (No. 2012ZA51010).

## References

1. Allen MJ, Vlahopoulos N (2000) Integration of finite element and boundary element methods for calculating the radiated sound from a randomly excited structure. *Comput Struct* 77:155–169
2. Chen G, Zhao GZ, Chen BS (2009) Sensitivity analysis of coupled structural-acoustic systems subjected to stochastic excitation. *Struct Multidiscip Optim* 39:105–113
3. Novick J, Finette S (2011) Stochastic basis expansions applied to acoustic propagation in an uncertain, range, and depth-dependent, multi-layered waveguide. *J Acoust Soc Amer* 129:2600
4. Ferson S, Ginzburg LR (1996) Different methods are needed to propagate ignorance and variability. *Reliab Eng Syst Saf* 54:133–144
5. Sim JS, Qiu ZP, Wang XJ (2007) Modal analysis of structures with uncertain-but-bounded parameters via interval analysis. *J Sound Vib* 303:29–45
6. Chen SH, Lian HD, Yang XW (2003) Interval eigenvalue analysis for structures with interval parameters. *Finite Elem Anal Des* 39:419–431
7. Qiu ZP, Elishakoff I (1998) Antioptimization of structures with large uncertain-but-non-random parameters via interval analysis. *Comput Methods Appl Mech Eng* 152(3–4):361–372
8. Qiu ZP (2003) Comparison of static response of structures using convex models and interval analysis method. *Int J Numer Methods Eng* 56:1735–1753
9. Guo SX, Lu ZZ (2001) Interval arithmetic and static interval finite element method. *Appl Math Mech* 22:1390–1396
10. Wang C, Qiu ZP (2013) Equivalent method for accurate solution to linear interval equations. *Appl Math Mech* 34:1031–1042
11. Chen SH, Lian HD, Yang XW (2002) Interval static displacement analysis for structures with interval parameters. *Int J Numer Methods Eng* 53:393–407
12. Chen SH, Song M, Chen YD (2007) Robustness analysis of responses of vibration control structures with uncertain parameters using interval algorithm. *Struct Saf* 29:94–111
13. Qiu ZP, Chen SH, Elishakoff I (1996) Bounds of eigenvalues for structures with an interval description of uncertain-but-non-random parameters. *Chaos, Solitons Fractals* 7:425–434
14. Xia B, Yu D, Liu J (2013) Interval and subinterval perturbation methods for a structural-acoustic system with interval parameters. *J Fluids Struct* 38:146–163
15. Xia B, Yu D (2012) Interval analysis of acoustic field with uncertain-but-bounded parameters. *Comput Struct* 112–113:235–244
16. Chen SH, Yang XW (2000) Interval finite element method for beam structures. *Finite Elem Anal Des* 34:75–88
17. Moore RE, Kearfott RB, Cloud MJ (2009) Introduction to interval analysis. Society for Industrial and Applied Mathematics, Philadelphia
18. Tao PD, Souad EB (1988) Duality in d.c. (difference of convex functions) optimization: subgradient methods, trends in mathematical optimization. *Int Ser Numer Math* 84:277–293
19. An LT, Tao PD (1998) A branch and bound method via d.c. optimization algorithms and ellipsoidal technique for box constrained nonconvex quadratic problems. *J Global Optim* 13:171–206

# FE Research on Influence of Pouring Temperature on Thermal Fatigue Depth for Aluminum Alloy Die Casting Die

Chenggang Pan, Huqun Yang, Wenchao Ma, Qin Xiao  
and Qingming Chang

**Abstract** A three-dimensional finite element model of the aluminum alloy front cover die casting die was established by PRO/E and PROCAST software. Thermal balance forming of die casting die and the influence of pouring temperature on thermal fatigue depth of die cavity surface were analyzed. The results showed that the temperature amplitude increased with the decrease of distance from die cavity surface. The higher the pouring temperature is, the bigger the thermal fatigue depth will be.

**Keywords** Aluminum alloy · Die casting die · Thermal fatigue depth · FEM · Pouring temperature

## 1 Introduction

Aluminum alloy die casting is a kind of very important net-forming methods of mass production. The main failure mechanism of aluminum alloy die casting is the thermal fatigue [1, 2]. Aluminum alloy melting temperature is 600–760 °C, cavity surface temperature of the casting die is up to 600 °C above [3, 4], and thermal

---

C. Pan (✉) · H. Yang · W. Ma · Q. Xiao · Q. Chang

Key Laboratory for Ferrous Metallurgy and Resources Utilization of Ministry of Education, Wuhan University of Science and Technology, Wuhan 430081, China  
e-mail: pcg2000@163.com

H. Yang  
e-mail: yanghuqun2009@163.com

W. Ma  
e-mail: 819089266@qq.com

Q. Xiao  
e-mail: 370219757@qq.com

Q. Chang  
e-mail: qmchang@163.com

© Springer-Verlag Berlin Heidelberg 2016

B. Huang and Y. Yao (eds.), *Proceedings of the 5th International Conference on Electrical Engineering and Automatic Control*, Lecture Notes in Electrical Engineering 367, DOI 10.1007/978-3-662-48768-6\_127

1139

fatigue failure accounts for about 70 % [5]. When the thermal stress is greater than the thermal fatigue limit in the die casting cycle, thermal fatigue will happen. Moreover, the thermal stress is caused by temperature fluctuations of die casting die. So it becomes more and more important that understanding the evolution of surface temperature changes rules, the formation of the heat balance, and depth of thermal fatigue. Zhao Xinyi, Hsieh, and other researchers studied the effects of cooling process, cooling water temperature and cooling pipe diameter, die pre-heating temperature, pouring temperature, and other factors on die temperature filed [6–9]. But rare researches of thermal fatigue depth of aluminum alloy die casting die was reported.

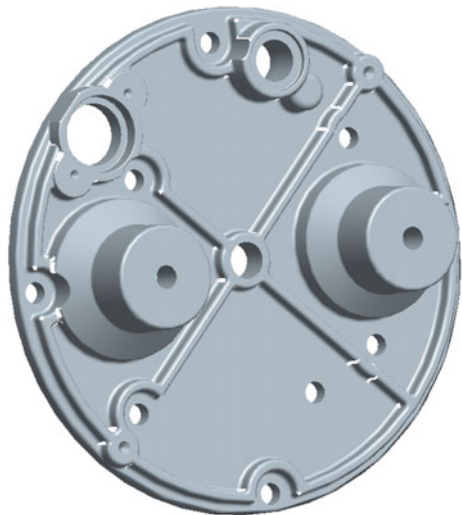
In this paper, the 3D geometrical model and FEM of aluminum alloy front cover die casting were established using the PRO/E and PROCAST software, respectively. Thermal equilibrium formation rules of aluminum alloy die casting die were obtained by analyzing temperature versus die casting time curves of a few points with different distances from die surface, and the thermal fatigue depth of die with different pouring temperature was determined.

## 2 Numerical Simulation

### 2.1 Establishment of Model

Figure 1 shows the part drawing of front cover made of aluminum alloy A390. Figure 2 shows simplified model for fixed half and moving half of die casting die.

**Fig. 1** Part drawing of front cover die casting



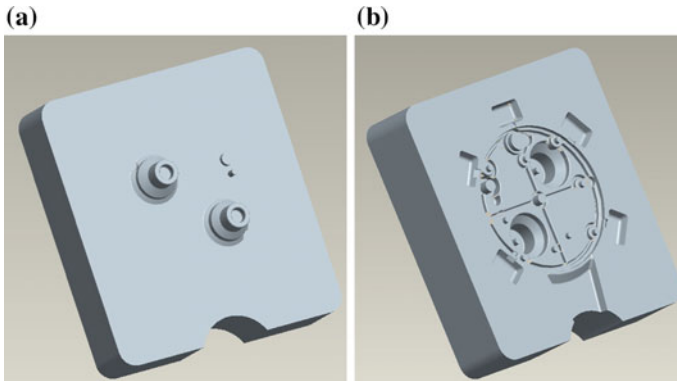


**Fig. 2** Simplified model of die casting die. **a** Fixed half, **b** moving half

## 2.2 Parameter Settings

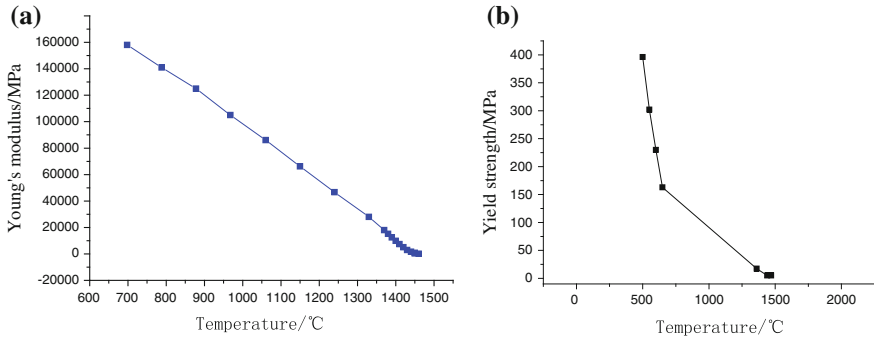
Preheating temperature of die casting die was 200 °C, and pouring temperature were 700, 800, 900, 1000, and 1100 °C, respectively. Heat transfer coefficients of casting part–die, die–die, die–air, and die–release agents were 1500, 1000, 5, and 500 W/(m<sup>2</sup> °C), respectively. Because die cavity is quickly filled with liquid metal in several milliseconds, at the same time, the simulation is focused on the die, and the filling process did not take into account. Cycle time of die casting is 30 s, start filling at 0 s, open die at 15 s, push-off die casting at 20 s, injection release agent at 23 s, end of spraying at 25 s, and clamping die at 29 s.

## 2.3 Physical Parameters

A hot-work tool steel H13 was selected as die material, and the nominal Young's modulus and yield strength of H13 at different temperatures are shown in Fig. 3.

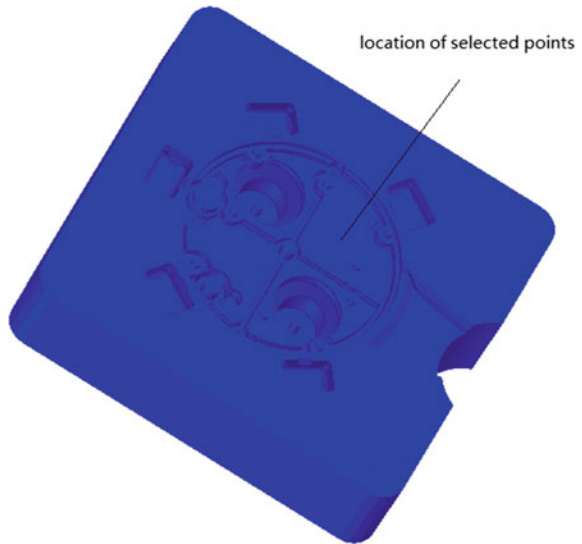
## 3 Results and Discussions

Figure 4 shows the location of selected points at different distances from die surface. Figure 5 shows temperature–time curves of selected 11 points on die casting die surface with pouring temperature of 800 °C. The 11 curves, line 1, 2, 3, 4, 5, 6, 7, 8, 9, 10, 11, represent 11 temperature–time curves of 11 selected points whose distances from die surface were 0, 1, 2, 3, 5, 10, 20, 30, 40, 50, 55.98 mm, respectively. As shown in Fig. 5, die casting die temperature gradually becomes



**Fig. 3** **a** Nominal Young's modulus and **b** yield strength versus temperature for H13

**Fig. 4** Location of selected points



stable and comes into thermal steady state from the preheat temperature 200 °C after about 80 die casting cycle. Figure 6 shows temperature–time curves of point 1 with different pouring temperatures. As shown in Fig. 6, the higher the pouring temperature is, the higher the thermal equilibrium temperature will be. Figure 7 shows the temperature amplitudes of 11 points with different pouring temperatures after thermal steady state. From Figs. 5, 6, and 7, the nearer the distance from the surface is, the greater the temperature fluctuation will be. The higher the pouring temperature is, the bigger the temperature fluctuation will be. Despite the different pouring temperatures, there is no temperature fluctuation beyond 20 mm distance from die surface. It demonstrates that hot and cold cycle of die casting regardless of



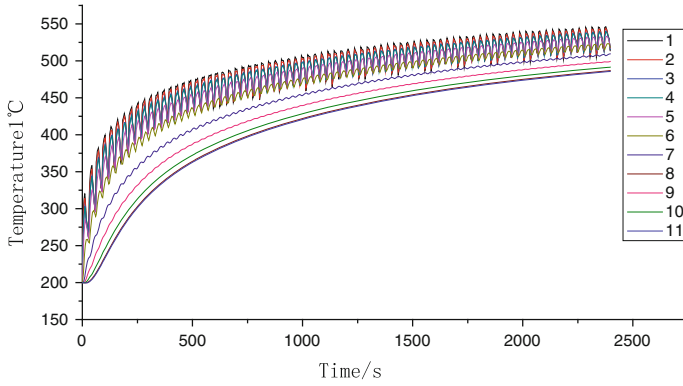


Fig. 5 Temperature–time curves of 11 selected points

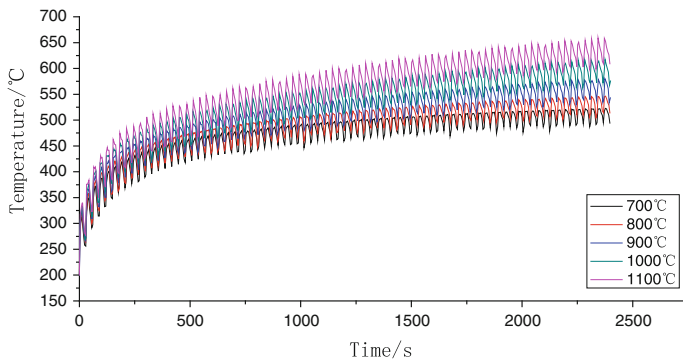
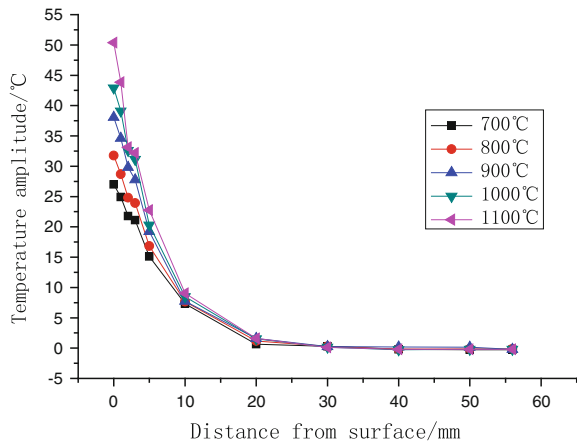


Fig. 6 Temperature–time curves of point 1 with different pouring temperatures

Fig. 7 Temperature amplitudes of 11 selected points with different pouring temperatures



pouring temperature only affects 20 mm distance from die surface which is the thermal fatigue section.

Malm and Norström [10] proposed a material-related model for thermal fatigue of tool steels in hot-work applications. Equation (1.1) formulated the material-related model of thermal fatigue for tool steels. This model was built based on the elastic and plastic strain theory of tool steels during the thermal cycling. The tool steels suffered from repeated thermal cycling are assumed to be elastic-ideal-plastic and isotropic. When tool steel reaches thermal equilibrium state, strain and stress of tool steels also reach thermal equilibrium condition at the lowest temperature and highest temperature, respectively.

$$T_2 \leq T_1 + \frac{(1 - \nu_2)\sigma_2}{\alpha E_2} \tag{1.1}$$

$T_2$  is the critical temperature without plastic deformation taken place;  $T_1$  is the lowest equilibrium temperature; and  $\nu_2$ ,  $\sigma_2$ ,  $\alpha$ , and  $E_2$  are the Poisson’s ratio, yield strength, thermal expansion coefficient, and elastic modulus of tool steels at temperature  $T_2$ , respectively.

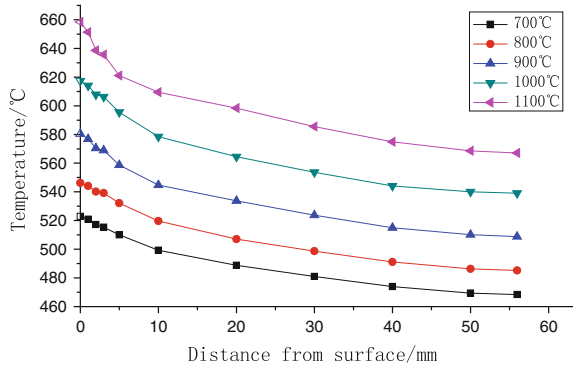
By substitution of the data,  $\alpha = 12 \times 10^{-6}$ ,  $\nu_2 = 0.3$ ,  $T_1$  of different pouring temperatures, and  $\sigma_2(T)$  and  $E_2(T)$  of Fig. 3, into the Eq. (1.1), critical temperature  $T_2$  and thermal fatigue depth with different pouring temperatures were obtained. Table 1 shows the  $T_1$ ,  $T_2$ , and thermal fatigue depth.

Figure 8 shows the highest surface temperature–distance curves of die casting die with different pouring temperatures in thermal equilibrium state. As shown in Fig. 8, the highest surface temperature of the die casting die in thermal equilibrium state increases with the rise of pouring temperature and decrease of distance from the die surface. The section whose temperature below critical temperature  $T_2$  is full elastic and secure [11], while the section whose temperature above critical temperature  $T_2$  is full plastic and insecure. Finding out the critical points of temperature  $T_2$  of different pouring temperatures in the highest surface temperature–distance curves of die casting die of Fig. 8, the distance value corresponding to critical temperature  $T_2$  is the maximum thermal fatigue crack depth. From Table 1 and Fig. 8, thermal fatigue depth of die casting die is very thin and increases with the increase of pouring temperature.

**Table 1**  $T_1$ ,  $T_2$ , and thermal fatigue depth with different pouring temperatures

Pouring temperature (°C)	$T_1$ (°C)	$T_2$ (°C)	Thermal fatigue depth (mm)
700	410	521	0.9
800	435	543	1.3
900	458	556	6
1000	489	578	10
1100	527	602	18

**Fig. 8** The highest surface temperature–distance curves of die casting die in thermal equilibrium state



## 4 Conclusions

1. The three-dimensional finite element model of aluminum alloy front cover part was established using PRO/E and PROCAST software.
2. The temperature curves of different distances of 11 points from the cavity surface with different pouring temperatures were analyzed. The nearer the cavity surface is, the larger the temperature fluctuation will be.
3. The temperature fluctuation range in thermal balance condition decreases from the casting die surface and inwards. The thermal fatigue depth of die casting die is very small. The higher the pouring temperature is, the bigger the thermal fatigue depth will be.

**Acknowledgements** This work was financially supported by the National Natural Science Foundation of China (No. 51375353), Open Fund of the State Key Laboratory of Refractories and Metallurgy of WUST(No. 2014QN03), and Open Fund of the Key Laboratory for Metallurgical Equipment and Control of Ministry of Education of WUST(No. 2013A17).

## References

1. Yu XH, Dong QY, Qi HJ (1998) Crack failure of die casting die. *Die Mould Technol* 2:84–89
2. Han XW, Wu W, Leng ZL, Yang JF (2009) Numerical simulation of temperature field and thermal stress field of Al alloy die-casting dies and its service life forecast. *Hot Work Technol* 38(19):60–63
3. Hu XP, Zhao GQ, Wu BY (2008) Temperature change and stress distribution analysis of die surface in Al-alloy die casting process and experimental study on die heat check. *China Foundry* 5(1):47–53
4. Klobčar D, Tušek J (2008) Thermal stresses in aluminium alloy die casting dies. *Comput Mater Sci* 43(4):1147–1154
5. Zhou YH, Wu W, Zhou HB, Zhang GM (2005) Use life of dies and optimizing process control of die casting. *Res Stud Foundry Equip* 6:43–45

6. Zhao XY, Xu JH, Pan MY, Ning ZL (2014) Cycle simulation for the temperature field of crankcase mold and thermal balance analysis. *Foundry* 63(6):571–574
7. Li ZX, Liu WH, Xiong SM, Liu BC (2003) Study on temperature field of dies in die casting process of magnesium alloys. *Foundry* 52(6):400–404
8. Zhang GM, Zhang J, Wu W (2004) Study on temperature field of dies casting process of magnesium alloys based on CAE. *Foundry* 53(7):559–562
9. Hsieh SS (1989) Transient thermal analysis of the waterlines effect in the die casting dies. *Appl Math Model* 13(5):282–290
10. Maim S, Norström LÅ (1979) Material-related model for thermal fatigue applied to tool steels in hot-work applications. *Metal Sci* 13(9):544–550
11. Persson A, Hogmark S, Bergström J (2004) Temperature profiles and conditions for thermal fatigue cracking in brass die casting dies. *J Mater Process Technol* 152(2):228–236

# Analysis of the Protection of a Simplified Surge Protective Device for Low-Voltage AC Power System

Huiping Liu, Xiaoqing Zhang and Kejie Huang

**Abstract** Surge protective devices (SPDs) are applied in the low-voltage AC power system to limit lightning transient overvoltage so as to protect the low-voltage electronic devices. However, traditional SPDs have some shortcomings such as too many components that are big in size. Aiming to overcome these shortcomings, a simplified circuit is proposed when the circuit of traditional SPD is analyzed in this paper. Simulation analysis of the lightning transient response of traditional and simplified circuit is performed with PSCAD/EMTDC, and furthermore, the simulation results of two circuits are compared. It shows that the simplified circuit has a qualified protective performance and can be applied to lightning overvoltage protection of electronic devices in low-voltage AC power system by comparison.

**Keywords** Surge protective device · Low-voltage AC power system · Lightning transient overvoltage · PSCAD/EMTDC · Lightning transient response

## 1 Introduction

With the development of science and technology, electronic devices have been widely used. Since the insulation strength and withstand voltage of electronic devices applied in low-voltage AC power system are low, these electronic devices are vulnerable to transient overvoltage. The destruction can cause failures and losses, so overvoltage protection of low-voltage AC power system has been widely concerned. According to the studies [1–3], most of the damages were caused by lightning surges along the power lines. In order to prevent the electronic devices in

---

H. Liu (✉) · X. Zhang · K. Huang  
Beijing Jiaotong University, Haidian District, Beijing 100044, China  
e-mail: 14125972@bjtu.edu.cn

X. Zhang  
e-mail: zxqiong@hotmail.com

K. Huang  
e-mail: 13117380@bjtu.edu.cn

the low-voltage power system from being damaged, it is necessary to install SPDs in low-voltage power system to restrain the lightning transient overvoltage.

This paper analyzes the circuit of traditional SPD, but which has the shortcomings of too many components and bigger size. Aiming at these shortcomings, a simplified circuit is proposed. Moreover, PSCAD/EMTDC software is used to perform a simulation analysis for the lightning transient response of traditional and simplified SPD. Through comparing the protective performance of two circuits, the simulation results also prove that the simplified SPD can accord with the SPD design standard [4] and has a better applicability in low-voltage AC power system to limit lightning transient overvoltage.

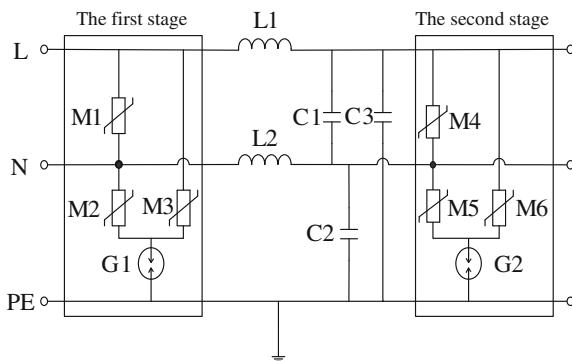
## 2 The Circuits of SPD

### 2.1 The Traditional SPD Circuit

According to IEC standards, the SPD used in low-voltage power system usually includes two protective modes, namely common and differential protective modes [5, 6]. A traditional SPD circuit is shown in Fig. 1, which has both protective modes. The circuit includes two stage protections, which consisted of metal oxide varistors (MOVs) and gas discharge tubes (GDTs). Therefore, the MOVs can be separated from power system, which slows down the aging phenomenon of the MOVs due to the long-term leakage current. The first stage mainly takes part in bleeding off lightning current, and the second stage is used to limit transient overvoltage. The LC low-pass filter in circuit can filter the high-frequency part of surges, which makes protection effect better.

This circuit model is often used in single-phase AC power supply system, and L, N, and PE line mean, respectively, live, neutral, and protective earth wire. In the first stage of traditional SPD circuit, M1 can limit differential-mode overvoltages appearing between L and N, while M2–G1 and M3–G1 can limit common-mode overvoltages appearing between L–PE and N–PE. A similar overvoltage limiting

**Fig. 1** Traditional SPD circuit



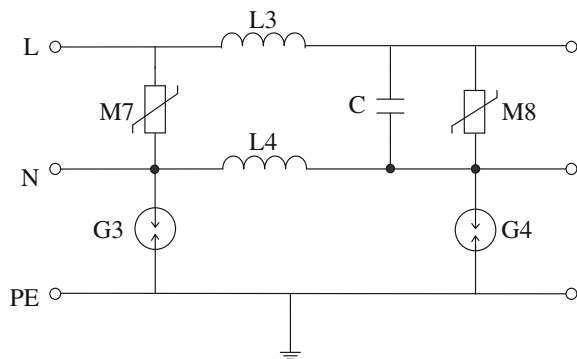
situation holds for M4, M5–G2, and M6–G2 in the second stage [7]. The decoupling inductances L1 and L2 in circuit take role in coordinating the protective characteristic between the two stages and can restrain the high-frequency part of surges [7]. L1-C3 and L2-C2 attenuate the high-frequency surges for common mode. The values of inductances and capacitances should be equal separately, which can prevent common-mode overvoltages transforming to differential-mode overvoltages.

### 2.2 The Simplified SPD Circuit

The traditional SPD is usually used in low-voltage single-phase AC power system. However, it contains quite many protective components, which causes a higher cost and a bigger size. In order to overcome these disadvantages, a simplified SPD circuit is proposed, as shown in Fig. 2. In comparison with the traditional SPD, the simplified SPD reduces the number of MOVs from 6 to 2 and the number of capacitances from 3 to 1. Then, the size of SPD is decreased and the cost is reduced.

In simplified SPD circuit, M7–G3 and M8–G4 can limit the common-mode overvoltages appearing between L and PE, and G3 and G4 can limit that appearing between N and PE. Besides, M7 and M8 can limit the differential-mode overvoltages appearing between. On account of the asymmetry between L and PE and N and PE in this simplified circuit, differential-mode overvoltages can appear between L and N when the common-mode overvoltages are limited. In this case, M7 and M8 can also restrain this kind of resultant differential-mode overvoltages. The high-frequency surges coming from live wire are released through L3–C–G4 and those from neutral wire are released through L4-G4 directly, since the residual voltage on GDT is very low when GDT is breakover. The differential-mode high-frequency surges resulted in circuit asymmetry are bled off through C, L3, and L4, so the power-follow current will not appear after the overvoltage is limited.

Fig. 2 Simplified SPD circuit



### 3 Simulation Analysis of SPD

The voltage fluctuation margin is considered when choosing MOVs and GDTs. According to the experience [8], the voltage  $U_{1mA}$  of MOV in the first stage is taken as 620 V and that in the second stage as 510 V. The nominal DC breakover voltage  $U_{DC}$  of GDTs is 600 V. The values of inductances and capacitances in LC low-pass filter should be determined by the filter principle [9]. According to this principle, the outputting voltage will be not over only if the period  $T_f$  of filter is larger than the period  $T$  of outputting voltage 6 times. Besides, the period  $T_f$  of filter can be regulated by changing the values of inductances and capacitances. The decoupling effect appears when the value of inductance is up to  $40\mu\text{H}$ . However, further increasing the value of inductances has no effect on the residual voltage, so the value of inductances can be determined as  $40\mu\text{H}$ . The values of capacitances vary from  $0.1\mu\text{F}$  to  $100\mu\text{F}$ .

The MOVs and GDTs are core components in a SPD, so it is important to simulate dynamic characteristic of them. The model of MOV is given, but that of GDT is not defined in the electromagnetic transient simulation software PSCAD/EMTDC. Therefore, it is crucial to build the model of GDT. When the voltage on GDT is greater than  $U_{DC}$ , GDT is breakover; on the contrary, it stays in a high-impedance condition. According to its characteristic, the model of GDT is built as shown in Fig. 3. In this model, the switch K controlled by voltage and nonlinear resistance R is in series used to simulate the characteristic of GDT; namely, switch K and nonlinear resistance R, respectively, indicates the on-off characteristic and the resistance characteristic when GDT is breakover.

After components of two circuits are determined, the lightning transient responses of the traditional and simplified SPD are simulated by PSCAD and comparison is made. According to IEC61643-22 and GB18802.1-2002, the  $1.2/50\ \mu\text{s}$  to  $8/20\ \mu\text{s}$  20 kV/10 kA combination wave is injected into SPD in order to test the protective performance. Concrete method is as follows. For common mode, current impulse is injected into L, N, and PE lines, and then, the residual voltage between L and PE is measured. As for differential mode, the current

**Fig. 3** Schematic of GDT model

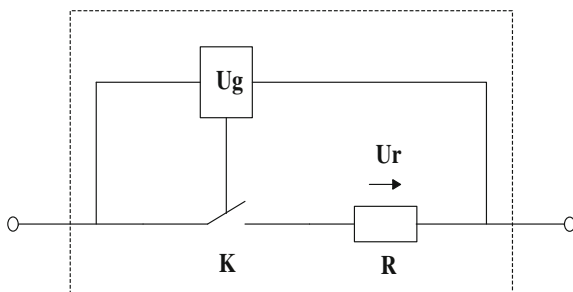
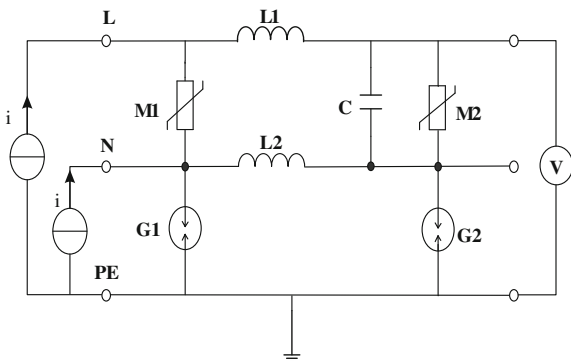




**Fig. 4** Schematic of simulation on common mode



impulse is injected into L and N lines, and then, the residual voltage between the two lines is measured; at the same time, PE line hangs in the air. Figure 4 shows a simulation schematic of the simplified circuit on common mode.

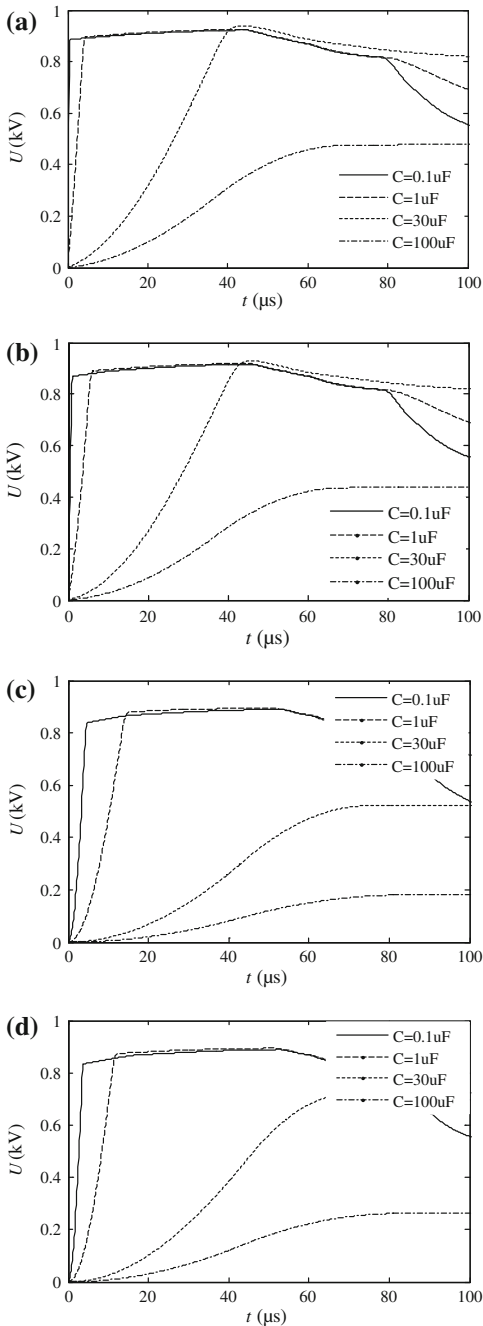
### 4 Protective Performance of Two Circuits

The traditional and simplified circuits are simulated on different modes when changing the values of capacitances. The results are shown in Table 1. The typical residual voltage waveform is shown in Fig. 5 when the values of capacitances are equal and taken as 0.1, 1, 30, and 100  $\mu\text{F}$ , respectively. The simulation values of residual voltages shown in Fig. 5 correspond to Table 1. In Table 1 and Fig. 5, it

**Table 1** The residual voltages of traditional and simplified circuits on different protective modes when the values of capacitances are different

Capacitance C-C3 ( $\mu\text{F}$ )	Common-mode L-PE (kV)		Differential-mode L-N (kV)	
	Traditional circuit	Simplified circuit	Traditional circuit	Simplified circuit
0.1	0.91	0.89	0.89	0.89
1	0.92	0.91	0.89	0.89
10	0.94	0.94	0.91	0.91
20	0.94	0.94	0.72	0.89
30	0.92	0.92	0.52	0.73
40	0.84	0.84	0.41	0.58
45	0.78	0.78	0.37	0.52
60	0.62	0.62	0.29	0.41
100	0.40	0.40	0.18	0.26

**Fig. 5** Simulation results of circuits on different modes. **a** Simulation results of traditional circuit on common-mode. **b** Simulation results of simplified circuit on common-mode. **c** Simulation results of traditional circuit on differential-mode. **d** Simulation results of simplified circuit on differential-mode



can be found that the protective performance is perfect when the values of capacitances are within appropriate range. Besides, the residual voltages of two circuits are equal roughly on common mode when the values of capacitances are equal, while that are unequal on differential mode. It can be also concluded from Table 1 that the residual voltages on differential mode are equal between the two circuits when the values of capacitances in traditional circuit are taken as 20, 30, and 40  $\mu\text{F}$  and that as 30, 45, and 60  $\mu\text{F}$  in simplified circuit, respectively. The reason is that the equivalent values of capacitances are 30, 45, and 60  $\mu\text{F}$ , respectively, when the values are taken as 20, 30, and 40  $\mu\text{F}$ . The equivalent value  $C_{\text{eq}}$  is calculated as

$$C_{\text{eq}} = \frac{C1 \times C2}{C1 + C2} + C3 \quad (1)$$

Since the values of  $C1$ ,  $C2$ , and  $C3$  are equal in Eq. (1), they are defined as  $C0$ . Therefore, Eq. (1) can be expressed as

$$C_{\text{eq}} = \frac{3}{2} C0 \quad (2)$$

It can be found from Eq. (2) that the residual voltages of two circuits on differential mode are equal when the values of capacitances in simplified circuit are 3/2 times as much as that in traditional circuit. Hence, on the basis of decreasing the number of components, the protective performance on differential mode can be improved by increasing the values of capacitances in simplified circuit. By this way, the residual voltages on common mode also can be decreased and the protective performance of simplified circuit is better than that of traditional circuit.

## 5 Conclusion

This paper analyzed the circuit of traditional SPD suppressing lightning transient overvoltage, and further more proposed a simplified circuit of SPD, which made up for some shortcomings such as too many components that are big in size.

On the basis of decreasing the number of components, it is concluded that the protective performance of simplified SPD can be improved even exceed that of traditional SPD. Therefore, the simplified SPD can meet the requirements and replace the traditional SPD in low-voltage power system.

**Acknowledgment** The work is partly supported by National Natural Science Foundation of China under Award no. 51420105011.

## References

1. Hasse P (2005) Overvoltage protection of low voltage systems. China Electric Power Press, Beijing
2. Peter H (2000) Overvoltage protection of low voltage systems. IEE, Power Engineering Series, No. 33
3. Durham MO, Durham KD, Durham RA (2002) TVSS designs. IEEE Ind Appl Mag 8:31–36
4. Chinese National Standard, GB 50057-94 (2000) Design code for protection of structure against lightning. Standard Press, Beijing, China
5. IEC 61643-1 Low-voltage surge protective devices—Part 1 (2005) Surge protective devices connected to low-voltage power distribution systems—requirements and tests. IEC Publication, Geneva, Swiss
6. IEC 61643-2 Low-voltage surge protective devices—Part 2 (2005) Surge protective devices connected to low-voltage power distribution systems -Selection and application principles. IEC Publication, Geneva, Swiss
7. Sheng C, Zhang X (2014) A circuit simplification for AC power supply. J Circ Syst Comput 23 (5)
8. Zhang X (2000) Lightning protection of electronic systems inside buildings. Publishing House of Electronics Industry, Beijing, China
9. Qiu G (2006) Circuit. Higher Education Press, Beijing

# Investigation of Load Distribution Among Teeth of an Aero-engine Spline Coupling

Xiangzhen Xue, Sanmin Wang, Jian He and Hui Wu

**Abstract** Involute spline coupling is a significant part in power transmission system, and the research on the rules of the load distribution among the teeth of it is extremely important for the working reliability. The work reported here calculated the actual meshing teeth, using the method loaded step by step considering the backlash, calculated the deformation and load distribution of spline coupling by the method, established the finite element model, simulated it for the deformation of teeth, and validated against the deformation calculated using the method loaded step by step. The results show that due to the large backlash under the working conditions given in this paper, the actual meshing teeth of spline is less, deformation obtained by finite element method is consistent with the deformation obtained by the method loaded step by step, and the first meshed tooth is out of shape seriously, whereas the second tooth will most likely to fail. It is concluded that increasing the actual meshing teeth and then reducing fretting wear can improve stability and reliability of spline coupling as well as reduce the failure.

**Keywords** Stiffness of single tooth · Backlash · Finite element · Deformation · Load distribution

## 1 Introduction

Because of its capacity of high-specific torque transmission and the ability of getting different sides fit easily, the spline coupling has been widely used in the transmission system, such as aviation and ship. During the spline coupling process,

---

X. Xue (✉) · S. Wang  
School of Mechanical Engineering, Northwestern Polytechnical University,  
Xi'an 710072, China  
e-mail: a\_zheny@163.com

J. He · H. Wu  
Institute of Mechanical Engineering,  
Xi'an Applied Optics Institute, Xi'an 71006, China

the entire teeth engage simultaneously and the load is divided uniformly. However, due to the tooth clearance and tooth deformation and other factors, only a part of the tooth participates in the engagement, and the load of each pair of tooth is not same. In the traditional design process of spline coupling, it cannot accurately estimate the bearing capacity of it considering only 30 or 50 % teeth are in engagement, and it often make the size of the spline coupling too large [1]. As aviation parts, in order to improve the design precision, the weight of spline coupling is limited to a certain range to avoid fretting wear caused and the research on the laws of the load distribution among tooth is very important.

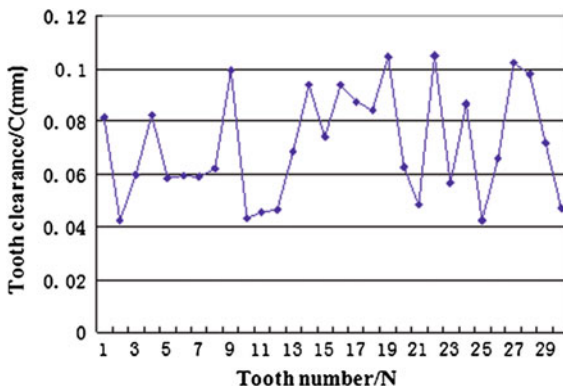
At present, the domestic and foreign experts had a lot of studies on the wear, strength, parameters, and other aspects of the spline coupling [2–5]. At the same time, in recent years, the research on the load distribution of the spline coupling is more and more because the load distribution is the basis of the calculation of wear and strength. Tjernberg [6, 7] used finite element method, calculated the stress concentration coefficient of a pair of spline coupling and compared with the results of numerical calculation results, and set up the analytical model of axial load distribution and torque transmission. Adrien et al. [8] have researched on the torque transmission of spline coupling and concluded that the main factor which is influencing the wear of spline coupling is the distribution of the axial torque without changing the root stress concentration coefficient of tooth. Chase et al. established tooth engaging model based on statistics to predict the order of engagement which is determined by the tooth clearance, and studied the load and stress distribution of spline coupling. It is concluded that only part of tooth loaded and the load carrying capacity of the first engagement is the largest [9, 10]. The stress distribution of the spline coupling is studied by using the numerical analysis model and the experimental method, and they were verified by the finite element simulation [11]. And based on the finite element method, Francesca et al. [12] established and formed a theoretical method which is developed to study the actual engaging tooth number and load distribution of the spline coupling with offset. These above researches have not considered the tooth clearance which is not consistent with the actual situation. In this paper, the actual engaging tooth number of spline coupling was calculated with considering tooth clearance using stepwise loading method and calculated the deformation and load distribution according to this method; the entity model of the spline coupling was established in PROE, finite element model was established in ANSYS, and then, the two results of deformation were verified. It provides an accurate numerical basis for optimizing the structure, studying the wear and predicting the life of spline coupling.

## 2 Analysis on the Deformation and Load Distribution of Spline Coupling

### 2.1 Calculation and Analysis of the Actual Engaging Tooth Number of the Spline Coupling

There is tooth clearance in the actual work because of the manufacturing error and assembly error.  $c_j$  is the clearance on both sides of the internal spline coupling, and  $c'_j$  is the clearance on both sides of the external spline coupling. Here,  $c_j$  equals to  $c'_j$  without regard to the center offset of the axes. Then, a set of initial clearance of the spline coupling is obtained as shown in Fig. 2. Because of the existence of the tooth clearance, the tooth with a small clearance is first engaged, the clearance is then followed, and it is finished until all the loads are divided. The actual engagement number of tooth of the spline coupling  $N_a$  is less than the number of design tooth  $N$ . The total force acting on the spline coupling is  $F = \frac{T}{r}$ . First, we make the smallest clearance of tooth with the initial clearance  $C_1$  that eliminates minimum clearance  $c_{\min 1}$  and contact with each other. Then, it should calculate the second group clearance with  $C_2 = C_1 - c_{\min 1}$ , after eliminating the minimum clearance, and find out the minimum value of  $c_{\min 2}$  in  $C_2$ . In particular,  $c_{\min 2}$  cannot be zero.  $c_{\min 2}$  is clearance of the second-smallest clearance in spline coupling. In order to eliminate this clearance, the force must be  $F_2 = 0.001 \times k \times c_{\min 2}$ , but the force that has been assigned to the spline coupling is  $F_{a1} = 0$  before removing the clearance  $c_{\min 2}$ , and the rest of load is  $F_{n1} = \frac{T}{r} - F_{a1}$ . If  $F_2 < F_{n1}$ , then  $c_{\min 2}$  can be eliminated. After eliminating the smallest clearance  $c_{\min 1}$  and the second-smallest clearance  $c_{\min 2}$ , the third-smallest clearance  $C_3 = C_2 - c_{\min 2}$  should be calculated, and the force eliminating the third-smallest clearance is  $F_3 = 0.001 \times (3 - 1) \times k \times c_{\min 3}$ . Before removing the clearance  $c_{\min 3}$ , the force that has been assigned to the spline coupling is  $F_{a2} = F_{a1} + 0.001 \times c_{\min 2} \times k$ , and the rest of the load is  $F_{n2} = \frac{T}{r} - F_{a2}$ ,  $F_{i=1} < F_{n(i-2)}$ ,  $i = 2 \dots N_a$ . It is necessary to calculate the clearance of  $C_i = C_{i-1} - c_{\min(i-1)}$  after the smallest clearance  $c_{\min 1}$ , second-smallest clearance  $c_{\min 2}$ , and the clearance  $c_{\min(i-1)}$  eliminated. Then, the force eliminating this clearance is  $F_i = 0.001 \times (i - 1) \times k \times c_{\min i}$ . Before removing the clearance  $c_{\min i}$ , the force that has been assigned to the spline coupling is  $F_{a(i-1)} = F_{a(i-2)} + 0.001 \times (i - 2) \times c_{\min(i-1)} \times k$ , and the rest of the load is  $F_{n(i-1)} = \frac{T}{r} - F_{a(i-1)}$ , step by step in this way until  $i = N_a$ . When  $F_i \geq F_{n(i-1)}$ , the actual engaging tooth number of the spline coupling under the torque  $T$  is  $N_a$ . Where  $k$  is the stiffness of single tooth, the value here is  $2.0765 \times 10^6$  N/mm. And the initial clearance is shown in Fig. 1.

**Fig. 1** The initial clearance of spline couplings



### 2.2 Calculation of Deformation and Load Distribution of Spline Coupling in Meshing

It can be known from Sect. 2.1, that the actual meshing tooth number is  $N_a$  under the torque  $T$ . When the number of tooth involved in meshing to  $v$ , the rigid body movement of the spline coupling has eliminated the minimum gap from  $c_{\min 1}$  to  $c_{\min N_a}$ . At this time, the force  $F_i$  to eliminate  $c_{\min N_a}$  is less than the unallocated load  $F_{n(N_a-1)} = \frac{T}{r} - F_{a(N_a-1)}$ . Therefore, it still produces a small deformation  $\delta_{N_a+1}$  after the first  $N_a$  of the tooth engaging.

$$\delta_{N_a+1} = \frac{\frac{T}{r} - F_{a N_a}}{0.001 \times k \times N_a} \tag{1}$$

where  $F_{a N_a}$  is the total load of all the tooth when  $c_{\min N_a}$  is eliminated:

$$F_{a N_a} = F_{a(N_a-1)} + 0.001 \times (N_a - 1) \times c_{\min N_a} \times k \tag{2}$$

In the elimination of the smallest tooth clearance, all the tooth participated in engagement do not deform, so the deformation of each tooth from the first engagement of the spline coupling to the last engagement is as follows:

$$\begin{aligned} \delta_1 &= c_{\min 2} + c_{\min 3} + \dots + c_{\min N_a} + \delta_{N_a+1} \\ \delta_2 &= c_{\min 3} + \dots + c_{\min N_a} + \delta_{N_a+1} \\ &\vdots \\ \delta_{N_a-1} &= c_{\min N_a} + \delta_{N_a+1} \\ \delta_{N_a} &= \delta_{N_a+1} \end{aligned} \tag{3}$$



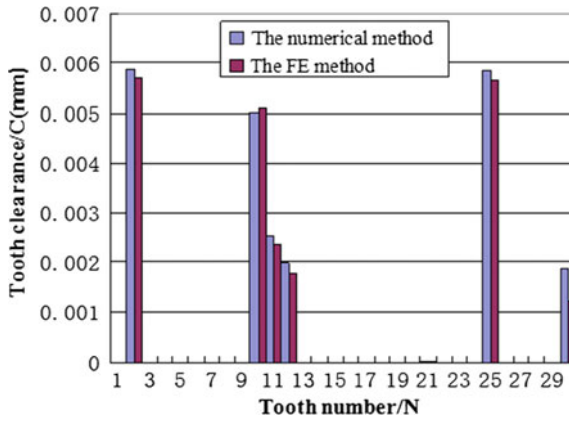


Fig. 2 The deformation of spline couplings

And the load of each tooth from the first engagement of the spline coupling to the last engagement is as follows:

$$\begin{aligned}
 F_1 &= 0.001 \times k \times \delta_1 \\
 F_2 &= 0.001 \times k \times \delta_2 \\
 &\vdots \\
 F_{N_a} &= 0.001 \times k \times \delta_{N_a}
 \end{aligned}
 \tag{4}$$

The results of spline deformation and load distribution are shown in Figs. 2 and 3, respectively.

As shown in Fig. 2, the deformation calculated using the finite element method and the numerical method is basically same; the maximum deformation of

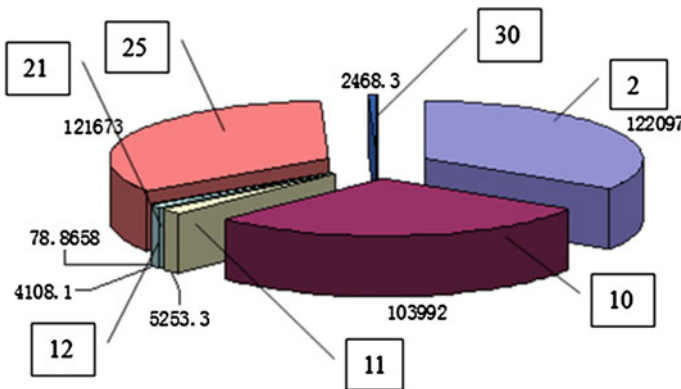


Fig. 3 The load distribution of teeth loaded

numerical method is  $5.7897\ \mu\text{m}$ , the minimum is  $0.308\ \mu\text{m}$ , the deformation of the pair No. 2 of tooth is maximum, and the deformation of the pair No. 30 of tooth is minimum. As shown in Fig. 3, the load of the pair No. 2 of tooth which is  $122097\ \text{N}$  is the largest and the load of no meshing is  $0\ \text{N}$ .

### 3 Finite Element Model Simulations Verification

Importing the spline entity model with backlash established in PROE to ANSYS. Assuming that unit type is SOLID186, elastic modulus is  $210\ \text{GPa}$ , Poisson's ratio is  $0.28$ , the density is  $7800\ \text{kg/m}^3$ , and the friction coefficient of COF is  $0.3$  [13], and then, the finite element is established. Finally, we set up the contact model of 30 pairs, impose constraints, and solve, and the results are shown in Figs. 4 and 5.

As shown in Fig. 4, the FEM stress result shows that the tooth number which actually participates in mesh is 7 under the given load and geometric parameters in this paper. It is consistent with the following numerical results: Those tooth numbers are No. 2, 10, 11, 12, 21, 25, and 30, respectively. It meets the design condition of spline coupling. And the stress of the second pair of tooth is maximum which is  $0.134 \times 10^9\ \text{Pa}$ .

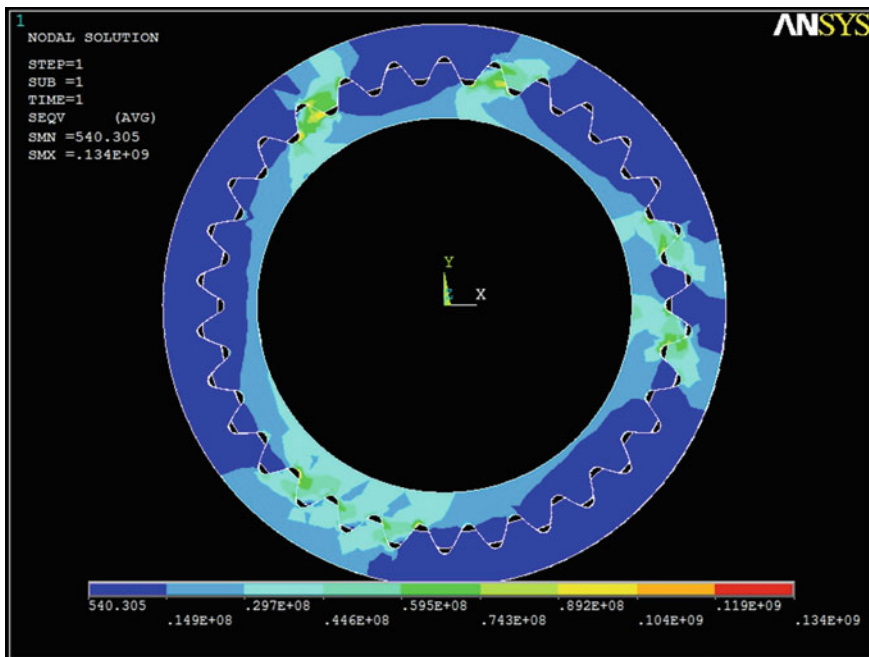


Fig. 4 The von Mises stress of spline couplings

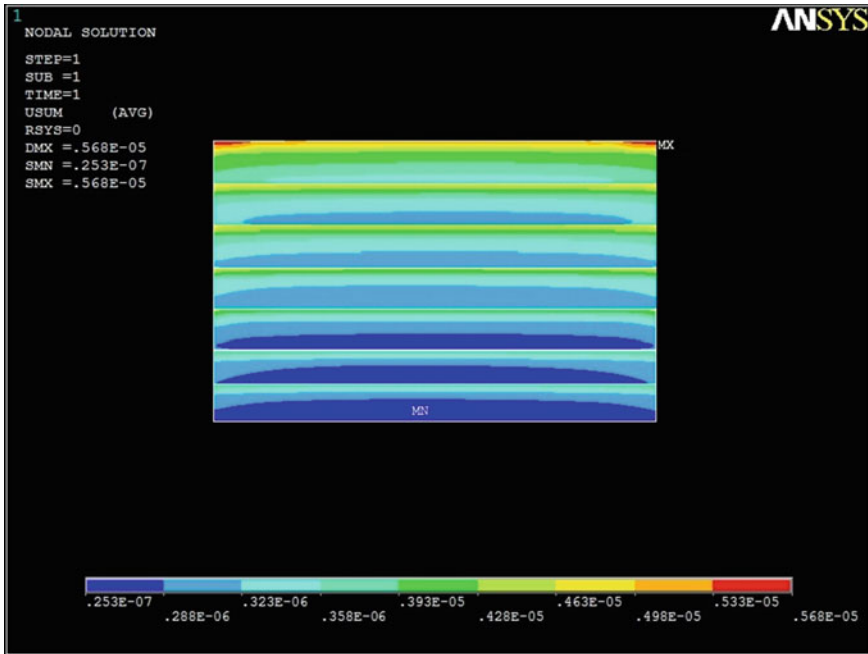


Fig. 5 The deformation of spline couplings

From Fig. 5, the maximum deformation calculated by FEM is 5.68  $\mu\text{m}$  and the minimum is 0.253  $\mu\text{m}$ .

#### 4 Conclusion

1. Due to the large tooth clearance, actual tooth number of participation meshing is 7, which is less than the number of designing. It is harmful to long-term stability work.
2. By the calculation, the load of the second tooth for which the tooth clearance is least reaches 122097 N and this tooth is most likely to fail.
3. The maximum amount of deformation calculating by FEM is 5.6800  $\mu\text{m}$ , the minimum is 0.253  $\mu\text{m}$ ; the maximum deformation calculated by progressive loading increasing is 5.8797  $\mu\text{m}$ , and the minimum amount of deformation is 0.308  $\mu\text{m}$ ; the two methods are basically the same, and the calculation results show that the deformation of the first engagement tooth is maximum.

## References

1. Robins RR (2008) Tooth engagement evaluation of involute spline couplings. Department of Mechanical Engineering Brigham Young University, America
2. Ratsimba CHH, McColl IR, Williams EJ et al (2004) Measurement, analysis and prediction of fretting wear damage in a representative aero-engine spline coupling. *Wear* 257(23):1193–1206
3. Leen SB, Richardson IJ, McColl IR et al (2001) Macroscopic fretting variables in a splined coupling under combined torque and axial load. *J Strain Anal Eng Des* 36(5):481–497
4. Ding J, Sum WS, Sabesan R et al (2007) Fretting fatigue predictions in a complex coupling. *Int J Fatigue* 29(3):1229–1244
5. Ding J, McColl IR, Leen SB (2007) The application of fretting wear modelling to a spline coupling. *Wear* 262(26):1205–1216
6. Tjernberg A (2001) Load distribution in the axial direction in a spline coupling. *Eng Fail Anal* 8:557–570
7. Tjernberg A (2001) Load distribution and pitch errors in a spline coupling. *Mater Des* 22(3):259–266
8. Adrien B, Manuel P, Marc S (2009) Extended equations of load distribution in the axial direction in a spline coupling. *Eng Fail Anal* 16(2):200–211
9. Chase KW, Sorensen CD, Sorensen BD et al (2010) Variation analysis of tooth engagement and load sharing in involute splines. *Am Gear Manuf Asso* 9(2):54–62
10. Chase KW, Sorensen CD, Brian JK (2010) Variation analysis of tooth engagement and loads in involute splines. *Trans Autom Sci Eng* 7(4):746–754
11. Vincenzo C, Francesca C, Andrea M (2012) Analysis of the pressure distribution in spline couplings. *Mech Eng Sci* 226(12):2852–2859
12. Francesca C, Andrea M, Michele G (2012) Load distribution in spline coupling teeth with parallel offset misalignment. *Mech Eng Sci* 0(0):1–11
13. Hu Z, Zhu R, Jin G, Ni D (2013) Analysis of fretting frictional contact parameters of aviation involute spline couplings. *J Central South Univ (Sci Technol)* 44(5):1822–1828 (in Chinese)

# Dynamics Analysis of Linear Array Deployable Structure Based on Symmetrical Scissor-Like Element

Bo Li, San-Min Wang, Ru Yuan, Chang-jian Zhi and Xiang-zhen Xue

**Abstract** Based on the Cartesian frame, the dynamic model of the linear array deployable structures was established, the motion constraint equations were completed by the constraint conditions of the scissor-like element (SLE). The numerical calculation was carried out using multi-step Runge–Kutta method, the law of velocity and acceleration during the motion process were obtained, and the constraint default stabilization method was also utilized to avoid the divergence of the results. The results show that the velocity, acceleration, and reaction force of the scissor mechanism along  $y$ -axis presents better symmetry properties because the horizontal constant force is in  $x$  direction. Meanwhile, at the side of the mechanism withstanding the external force, the dynamic properties of each node along  $x$  direction change more obviously; however, the changing amplitude of the velocity, acceleration, and other physical quantities are very small along  $x$ -axis on the non-force side.

**Keywords** Scissor-like element (SLE) · Linear array · Symmetrical features · Stability constraint default · Dynamic

## 1 Introduction

Deployable structure has the characteristics of small size, large space, which can be expanded into a preset contracted state and maintain a steady configuration. Therefore, it has a broad application prospects in the fields of aviation, aerospace, and construction. The scissor deployable structure in the paper is a kind of bar deployable structures, the scissor unit is the basic unit consisting of scissor deployable structures, which is connected by two links to form “X”-type structure through the hinge with the movement contraction function. The scissor hinge units

---

B. Li (✉) · S.-M. Wang · R. Yuan · C. Zhi · X. Xue  
School of Mechanical Engineering, Northwestern Polytechnical University,  
Xi'an 710072, China  
e-mail: yunfenglibo@126.com

© Springer-Verlag Berlin Heidelberg 2016  
B. Huang and Y. Yao (eds.), *Proceedings of the 5th International Conference on Electrical Engineering and Automatic Control*, Lecture Notes in Electrical Engineering 367, DOI 10.1007/978-3-662-48768-6\_130

1163

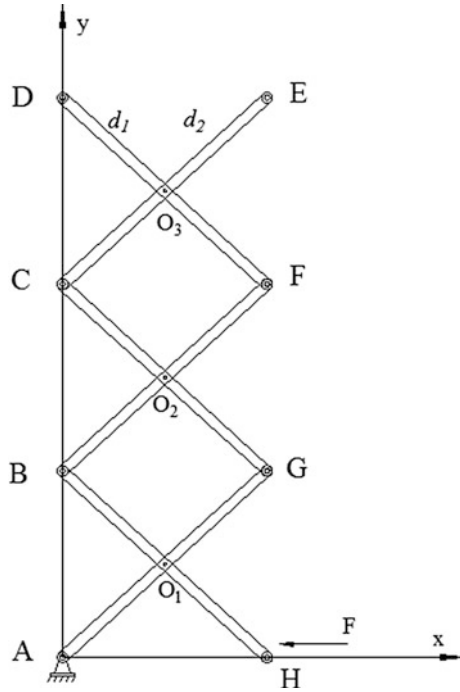
can be composed of a variety of specific deployable forms using different ways, such as flat stretch arm, spherical grid system, and quadrilateral cross-sectional stretching arms.

In recent years, with the increasing of the competition of the international aerospace engineering, the demanding for dynamic behavior of deployable structures [1–3] in the motion process becomes more intense, the need to accurately predict the dynamics of deployable structures grows more urgent. Cambridge University Professor Pellegrino [4] together with the European Space Agency carried out the design and structure optimization of the two-dimensional and three-dimensional scissor structure as the basic unit consisting of deployable structure; Gantes [5, 6] completed the geometric design of the hemispherical deployable structures through symbols operation method and made sure the advantage of symbolic operation method in the geometric design of deployable structures; Langbecker [7] made an in-depth research on the motion characteristics and expanding conditions of deployable scissor-type mechanism and established a folding equations to analyze translation, cylindrical and the expanding process of ball deputy agencies; Oxford University Chen et al. [8] and Gan and Pellegrino [9] studied the bifurcation phenomenon in the kinematic analysis of deployable structures and thus may explain the emergence of mutations of hexagonal ring. Huang et al. [10, 11] carried out the simulation analysis of dynamics of the deployable structures with clearance after the expansion lock structure through clearance collision hinge model; Chen et al. [12] carried out structure design study for six prism unit deployable antenna; Ji et al. [13] analyzed and simulated the expanding process of the asymmetrical planar deployable structure, the expanding conditions of asymmetrical bodies were discussed, and the dynamics acceleration, velocity, and other physical quantities were carried out using the numerical simulation, but the impact of reaction force on institutions was not made a full discussion. In the engineering field, symmetry deployable structures can be applied to a broader field [14]; the symmetrical array deployable institutions were regarded as objects in the paper; Lagrange multipliers were used to build a dynamic model; the Baumgarte stabilization method was used to avoid numerical divergence; the dynamic characteristics of the reaction force, acceleration, and other physical dynamics during the expanding process of the deployable structures were made a thorough study, as opposed to asymmetrical bodies, which shows a specificity of symmetrical institutions during motion process.

## 2 Dynamics Model and Equations of Symmetrical Deployable Structures

The scissor unit was arrayed along a straight line, and the adjacent units were connected by joints, the linear array combination deployable structures can be obtained, shown in Fig. 1. Scissor unit consists of two bars ( $d_1$ ,  $d_2$ ), which was connected by joint  $o_3$ . A unit was made up with five nodes, including a hinge point and four endpoints which were equaled by hinged point.

**Fig. 1** Linear array deployable mechanism-based SLE



### 2.1 Constraint Equation of Scissor Mechanism

Constraint equation is a prerequisite for dynamics analysis. Due to the symmetry of scissor mechanism, a detailed analysis of constraint equations for unit mechanism was in favor of considering the overall organization of the constraint equations. Figure 2 shows the plane mathematical model of any scissor unit. The bar  $ij$  and bar  $kl$  rely on hinge  $o$  to connect and transmit motion, achieving scalability. Due to the design needs, the distance between the endpoint of each rod and the hinge  $o$  can be changed.

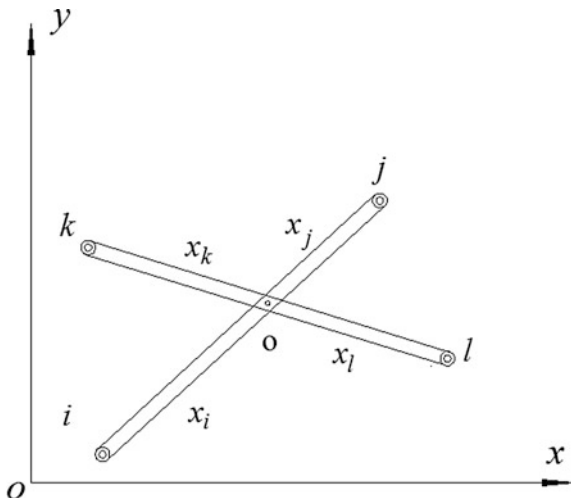
According to the basic constraint equations between the rigid bodies, the constraint equation of any plane scissor unit can be established as follows:

$$\Phi_q = \frac{b}{a+b}x_i + \frac{a}{a+b}x_j - \frac{d}{c+d}x_k - \frac{c}{c+d}x_l = 0 \tag{1}$$

where  $a, b, c, d$  refer to the distance from endpoints  $i, j, k, l$  to the pin  $o$ .

The constraint equations of scissor units obtained can be assembled; then, the whole constraint equations of the mechanism can be obtained. For the unit symmetry deployable mechanism shown in Fig. 1, its constraint equation can be written as follows:

**Fig. 2** Unit scissor hinge constraints



$$\Phi = \begin{bmatrix} x_a \\ y_a \\ y_h \\ x_a + x_g - x_b - x_h \\ y_a + y_g - y_b - y_h \\ x_c + x_g - x_b - x_f \\ y_c + y_g - y_b - y_f \\ x_c + x_e - x_d - x_f \\ y_c + y_e - y_d - y_f \\ (x_a - x_g)^2 + (y_a - y_g)^2 - l_{ag}^2 \\ (x_b - x_h)^2 + (y_b - y_h)^2 - l_{bh}^2 \\ (x_b - x_f)^2 + (y_b - y_f)^2 - l_{bf}^2 \\ (x_c - x_g)^2 + (y_c - y_g)^2 - l_{cg}^2 \\ (x_c - x_e)^2 + (y_c - y_e)^2 - l_{ce}^2 \\ (x_d - x_f)^2 + (y_d - y_f)^2 - l_{df}^2 \end{bmatrix} = 0 \tag{2}$$

the constraint Eq. (2) can be represented as a matrix form.

$$\Phi(\mathbf{q}, t) = [\Phi_1(\mathbf{q}, t) \quad \Phi_2(\mathbf{q}, t) \quad \cdots \quad \Phi_i(\mathbf{q}, t)]^T = 0 \quad i = 15 \tag{3}$$



### 2.2 Dynamic Equation of Scissor Mechanism

The speed and acceleration equation of the system can be obtained after the constraint equations were calculated first- and second-order derivative:

$$\dot{\phi}(q, \dot{q}, t) = \phi_q(q, t)\dot{q} + \phi_t(q, t) = 0 \tag{4}$$

$$\ddot{\phi}(q, \dot{q}, \ddot{q}, t) = \phi_q(q, t)\ddot{q} + (\phi_q\dot{q})_q\dot{q} + 2\phi_{qt}\dot{q} + \phi_{tt} = 0 \tag{5}$$

where  $\Phi_q(q, t)$  is the Jacobian matrix order:

$$\eta = -(\phi_q\dot{q})_q - 2\phi_{qt}\dot{q} - \phi_{tt} \tag{6}$$

Then, Eq. (5) can be converted to

$$\ddot{\phi}(q, \dot{q}, \ddot{q}, t) = \phi_q(q, t)\ddot{q} - \eta = 0 \tag{7}$$

Mass matrix of the scissor mechanism in Fig. 1 can be assembled as follows:

$$\mathbf{M} = \frac{\rho Al}{6} \begin{bmatrix} 2\mathbf{I}_2 & \mathbf{I}_2 \\ \mathbf{I}_2 & 2\mathbf{I}_2 \end{bmatrix} \tag{8}$$

where  $\rho, A, l$ , respectively, represent rod density, cross-sectional area and unit rod length,  $\mathbf{I}_2$  is the  $2 \times 2$  unit matrix.

The scissor mechanism variation equation can be obtained according to Newton's law:

$$\delta q^T (M\ddot{q} - Q) = 0 \tag{9}$$

where  $\mathbf{M}, \mathbf{Q}$  stand mass matrix and generalized force matrix respectively.

The variation equations can be obtained from constraint equations:

$$\Phi_q \delta q = 0 \tag{10}$$

The Lagrange motion differential equations can be obtained through arranging formula (9) and (10):

$$M\ddot{q} + \phi_Q^T \lambda = Q \tag{11}$$

where  $\lambda$  is the Lagrange multiplier.

The Lagrange augmented matrix can be combined with motion differential equations and acceleration constraint equations:

$$\begin{bmatrix} M & \phi_Q^T \\ \phi_q & 0 \end{bmatrix} \begin{bmatrix} \ddot{q} \\ \lambda \end{bmatrix} = \begin{bmatrix} Q \\ \eta \end{bmatrix} \tag{12}$$

Formula (12) only introduced an acceleration constraint equation, the velocity, and position obtained will not necessarily meet the position constraint equations and velocity constraint equations; the constraint violation phenomenon would occur during the solving process. To avoid the constraint violation problem, this paper used a constraint violation stabilization method Baumgarte [15] proposed, namely the correction factors were introduced to correct the system

$$\phi \ddot{q} - \eta - 2\alpha \dot{\phi} - \beta^2 \phi = 0 \tag{13}$$

where  $\eta$  is acceleration right item which includes velocity, displacement, time.  $\alpha$  and  $\beta$  are the correction coefficient greater than 0, usually it would have a good stability when  $\alpha$  and  $\beta$  equal each other.  $\alpha$  and  $\beta$  are taken as 5 in the paper during the process of simulation and calculation.

Stable dynamics equation can be obtained after constraint correction:

$$\begin{bmatrix} M & \phi_Q^T \\ \phi_q & 0 \end{bmatrix} \begin{bmatrix} \ddot{q} \\ \lambda \end{bmatrix} = \begin{bmatrix} Q \\ \eta - 2\alpha \dot{\phi} - \beta^2 \phi \end{bmatrix} \tag{14}$$

Although the correction coefficient introduced which destroyed the initial dynamics equation of the system has some influence on acceleration time history, it has small impact on coordinate time history and avoiding the divergence of the results in a large part. Meanwhile, the stability of the equation even can reach about 75 % when  $\alpha$  and  $\beta$  are equal.

### 3 Numerical Simulation of Scissor Array Symmetrical Deployable Mechanisms

According to the geometric model shown in Fig. 1, each bar is in uniform quality, density  $\rho = 2840 \text{ kg/m}^3$ , each bar length is  $l = 2 \text{ m}$ , the expansion rod cross section is rectangular, the cross-sectional width is  $b = 0.02 \text{ m}$ , height is  $h = 0.05 \text{ m}$ , the axial force  $F = -50 \text{ N}$  was applied to point  $H$ . The initial values  $\dot{q}(t_0)$  and  $q(t_0)$  have been known at the initial time, the integration step is taken as  $0.02 \text{ s}$ , and the constraint force of the scissor deployable mechanism can be obtained according to  $R = -\Phi_q^T \lambda$ . Also, the multi-step Runge-Kutta method was used to solve the kinetic equation, the changing curve of displacement, velocity, acceleration, and reaction forces of endpoint of each rod for the scissor array

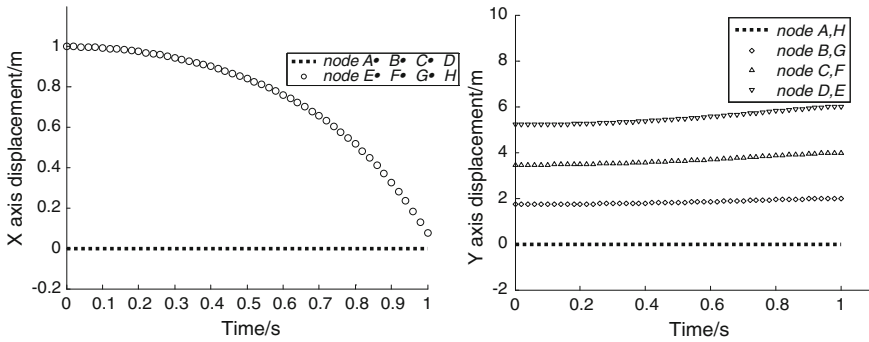


Fig. 3 Changing curve of the node displacement with time

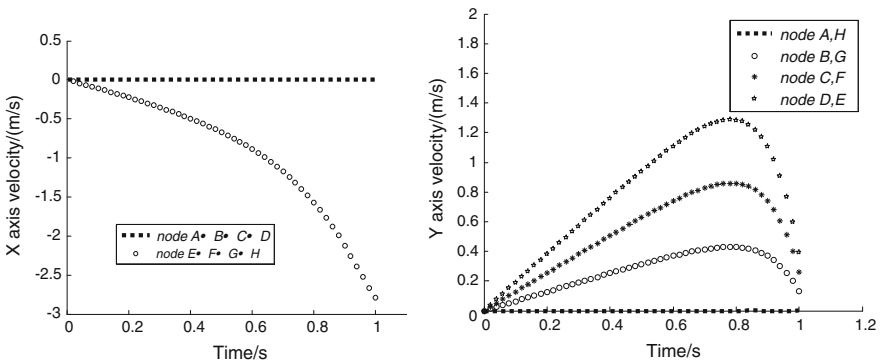
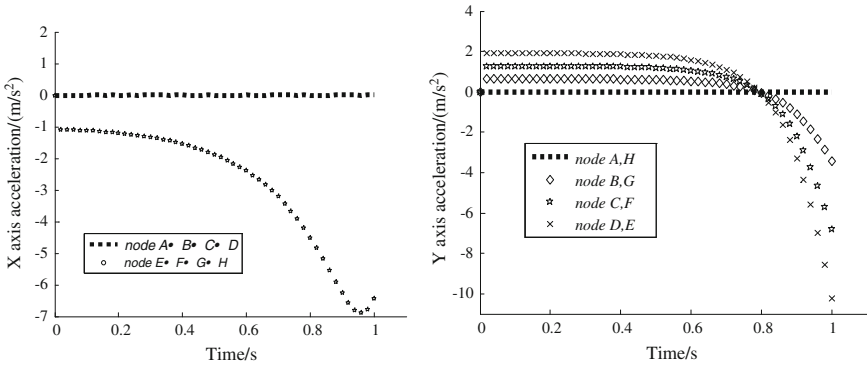


Fig. 4 Changing curve of the node velocity with time

deployable structures with time can be obtained during deploying process, which is shown in Figs. 3, 4, 5, and 6.

It can be concluded from all the figures shown above that the movement of each node is very complex, but which presents the unique symmetry properties that the array structure owns during the expansion process that the freedom of  $y$  direction of endpoint  $H$  is constrained and the node  $H$  suffers the reverse force of  $x$ -axis. As shown in Figs. 3, 4, and 5 that the displacement, velocity, and acceleration of node  $A, B, C, D$  converge to 0 in the  $x$  direction during the kinematic process. The acceleration and velocity of node  $E, F, G, H$  along  $x$  direction are gradually increasing, the displacement of node approaches zero simultaneously. The displacement, velocity, and acceleration of node  $A, H$ , node  $B, G$ , node  $C, F$ , node  $D, E$  along the  $y$ -axis show the symmetry property. It is shown in three figures, when  $t = 0.8$  s, the mechanism reached a critical state; after more than 0.8 s, the geometry properties of the scissor mechanism will be damaged. During the process of 0–0.8 s, velocity and displacement gradually increased with the changing of acceleration. The similar situation is shown in Fig. 6, and the movement of the



**Fig. 5** Changing curve of the node acceleration with time

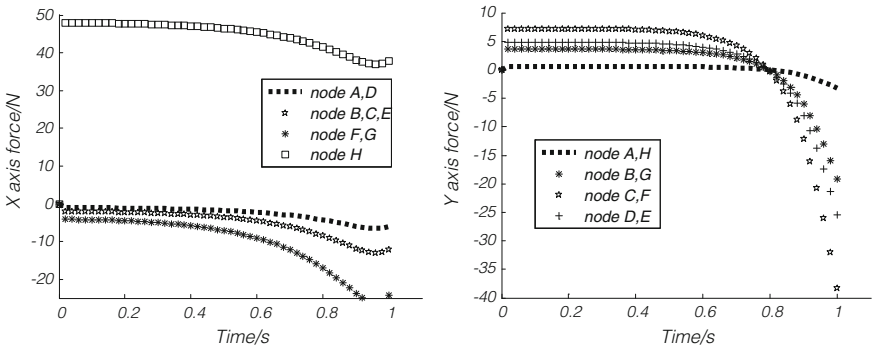


**Fig. 6** Changing curve of the node constraint force with time

mechanism will be damaged after the time beyond 0.8 s. At this moment, the constraint force of the corresponding node along the y-axis still maintained symmetry. Meanwhile, the symmetrical characteristic of each node in the x direction was not obvious since the force was along the x-axis.

### 4 Conclusions

1. As shown in Fig. 5, the change of the acceleration of node in x direction is relatively stable before 0.4 s and the acceleration increased rapidly after 0.4 s. In order to ensure the mechanism can slowly deploy, a reasonable strategy can be made according to Figs. 5 and 6;
2. During the deployment process of the scissor array deployable mechanism, the dynamics of the each node along x direction on the force side changed more

obviously. However, the dynamics of  $x$  direction of the each node on the non-force side changed slightly, which was caused by constraints, and symmetry properties of the scissor mechanism;

3. It can be seen from the figures above that the scissor mechanism along  $y$ -axis has a uniform variation in displacement, velocity, acceleration, and force, which shows the symmetry of the scissor linear array deployable structure along  $y$ -axis is more obvious. Due to the impact of the external force in  $x$ -axis, the symmetry properties of the constraint force for the node in  $x$  direction do not turn out.

**Acknowledgments** The authors acknowledge the financial support provided through Grant No. 51175422, from National Natural Science Foundation of China.

## References

1. Bo Li, Wang S, Yuan R (2014) Stability of linear array deployable structures based on structure of scissor-like element. *J Harbin Inst Technol* 46(9):50–54
2. Miedema B, Mansour WM (1976) Mechanical joints with clearance: a three-mode model. *J Eng Ind* 98(4):1319–1323
3. Bai Z, Zhao Y (2011) Dynamics simulation of deployment for solar panels with hinge clearance. *J Harbin Inst Technol* 41(3):11–14
4. Pellegrino S (2001) Deployable structures. Springer, New York
5. Gantes CJ (2001) Deployable structures: analysis and design. Wit Press, UK
6. Gantes C, Giakoumakis A, Vouvounis P (1997) Symbolic manipulation as a tool for design of deployable domes. *Comput Struct* 64(1):865–878
7. Langbecker T (1999) Kinematic analysis of deployable scissor structures. *Int J Space Struct* 14(1):1–15
8. Chen Y, You Z, Tarnai T (2005) Three fold-symmetric Bricard linkages for deployable structures. *Int J Solids Struct* 42:2287–2301
9. Gan WW, Pellegrino S (2006) Numerical approach to the kinematic analysis of deployable structures forming a closed LOOP. *Mech Eng Sci* 220 Part C:1045–1056
10. Huang T, Wu D, Yan S (1999) Nonlinear dynamic modeling of deployable truss structures with clearances. *Chin Space Sci Technol* 19(1):7–12
11. Huang T, Wu D, Yan S (1999) Dynamic simulation of a deployable truss structure with clearances. *Chin Space Sci Technol* 19(3):16–22
12. Chen X, Guan F (2001) A large deployable hexapod paraboloid antenna. *Chin J Space Sci* 21(1):68–72
13. Ji B, Wang H, Jin D (2013) Analysis and simulation of the deployment process for asymmetric planar scissor structures. *Eng Mech* 30(7):7–13
14. Raskin I (2000) Stiffness and stability of deployable pantographic columns. University of Waterloo, Waterloo
15. Baumgarte J (1972) Stabilization of constraints and integrals of motion in dynamical systems. *Comput Methods Appl Mech Eng* 1:1–16

# Research and Development Analysis of Information Security in Smart Grid Construction

Yixin Ding, Ming Li, Li Yan and Junwei Ma

**Abstract** Information and communication technology, which is accelerating the integration, has been already widely used in smart grid construction, so information security risk has become increasingly prominent. In this paper, a brief description of information security in the electric power system was introduced, information security risks were analyzed in detail, and then, the solution suggestions were given, in order to build information security protection architecture of the power system and to ensure safe and stable operation of the smart grid.

**Keywords** Smart grid · Information security · Operation security · Active defense · Protection system

## 1 Introduction

In the ‘Twelfth Five-Year’ period, State Grid Corporation will speed up the construction of smart grid with characteristics of ‘informatization, automation, and interaction.’ And cloud computing, Internet of Things (IOT), and big data tech-

---

Y. Ding

Information and Telecommunication Company, State Grid Jiangsu Electric Power Corporation, No. 215 Shanghai Road, Nanjing 210029, China

e-mail: koch@zib.de

M. Li

Information and Telecommunication Company, State Grid Anhui Electric Power Corporation, No. 9 Huangshan Road, Hefei 230009, China

L. Yan

Information and Telecommunication Company, State Grid Shandong Electric Power Corporation, No. 150 Jinger Road, Jinan 250021, China

J. Ma (✉)

Information and Telecommunication Company, State Grid Shanxi Electric Power Corporation, No. 169 Fudong Road, Taiyuan 030001, China

e-mail: junweima@foxmail.com

© Springer-Verlag Berlin Heidelberg 2016

B. Huang and Y. Yao (eds.), *Proceedings of the 5th International Conference on Electrical Engineering and Automatic Control*, Lecture Notes in Electrical Engineering 367, DOI 10.1007/978-3-662-48768-6\_131

1173

nology will be widely used in the smart grid construction, so information security risks will become more prominent. With the Iran's nuclear power plant event as an example, due to invasion of data transmission in a crucial moment, related important data were lost and the whole plan was forced to be shelved. Similar major accidents were occurred in the domestic power industry. Therefore, as the basis of national energy, it is of great practical significance to study and solve the problem of information security in the construction of the smart grid [1].

## **2 Information Security Summary**

According to the definition of information security of the National Institute of Standards and Technology (NIST) of USA, information security refers to the protection of information systems in order to ensure the integrity, availability, and confidentiality of information resources.

Information security technology development has been gone through three major stages: The first stage is communication confidential stage, which takes focus on the refusal of non-authorized users' access to information in the process of remote communication and ensures the authenticity of communication [2]; the second is computer security and information security stage, ensuring the confidentiality of hardware resource, software resource, information processing, information storage, and information transmission in the computer system; and the third is information security protection phase, which pays more attention to the protection and defense of information by itself and information system, in order to ensure the integrity, availability, confidentiality, and non-repudiation.

## **3 Current Situation of Information Security in the Power System**

State Grid Corporation has been focused on strengthening the construction and management of information security for years. For example, the company compiled the information security emergency plans, conducted regular anti-accident exercises, and established the information security management approach, work standards, and regulations [3].

The network and information system of State Grid Corporation is composed of the production control district, management information district, and three defense lines. According to the fifth file of the State Electricity Regulatory Commission Region, the production control district follows the 'safe partition, private network, horizontal segregation, and longitudinal certification' of the security protection principles. The management information region is divided into enterprise intranet and extranet, with implementation of the 'two networks and two computers,

partition and hierarchy, grade protection, and multilayered defense.’ Three defense lines are established in the outlet of the enterprise extranet, boundary of the enterprise intranet and extranet, and boundary of the production control district and management information district, in order to build comprehensively the rank protection system of information security [4].

### 4 Information Security Problems in Smart Grid Construction

With the continuous development of information and communication technology, informatization application fields have been expanding in the smart grid construction, so information security is facing greater risk. Every little accident of

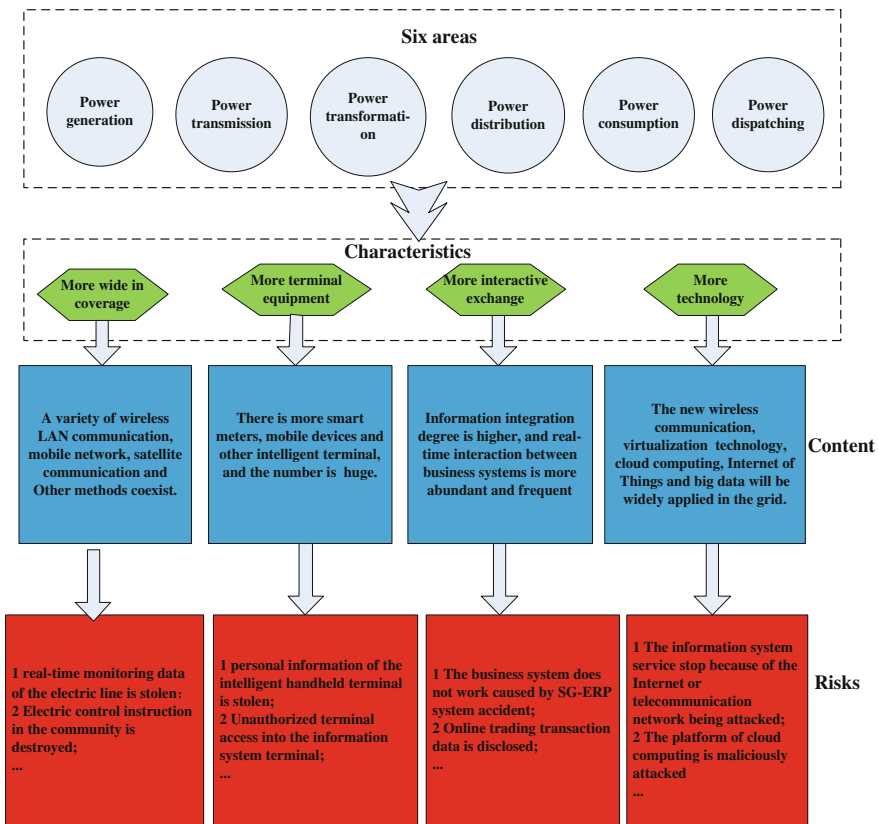


Fig. 1 Risk of the six areas in smart grid construction



information security is likely to lead to overall security accident. Therefore, State Grid Corporation must organize the staff of all regions and departments to coordinate each other and prevent in advance [5].

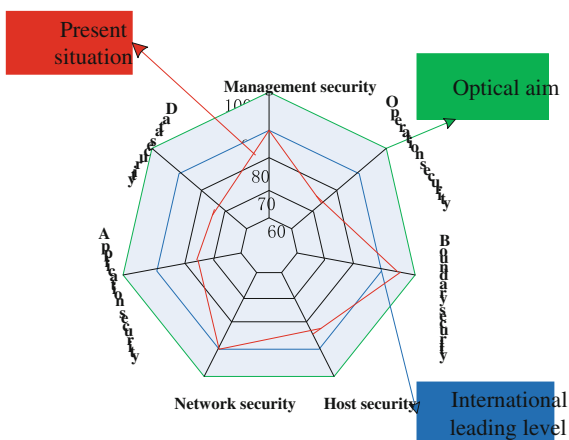
Specifically, the smart grid construction generally covers the power generation, transmission, transformation, distribution, consumption, and dispatching of the six areas, which includes the UHV grid as the backbone, the coordinated development of power grid at all levels, with characteristics of ‘informatization, automation, and interaction.’ Facing with the information security risks and challenges of the smart grid construction, all aspects of business system security should be given full consideration. The risk is shown in Fig. 1.

### 5 Main Work of Information Security in Smart Grid Construction

Based on the analysis of information security of large enterprises at home and abroad, combined with the maturity model from the famous international consulting firm, the information security architecture is evaluated in management, operation, boundary, host, network, application, and data security of seven aspects [6]. The results show that State Grid Corporation is relatively good at the management, boundary, host, and network security, not at the operation, application, and data security which need to be further strengthened, as shown in Fig. 2.

According to the analysis above, the following work should be paid more attention.

Fig. 2 Present situation analysis of information security



### ***5.1 Taking Information Security Technology as the Center***

The technology is the key of solving information security. Only adopting reasonable and efficient technology means can we eliminate information security risks to a great extent. Therefore, application and data security can be improved. According to the power system characteristics, the next work is as follows [7]:

1. Business-oriented strategy. Guided by the smart grid construction, the use of advanced and mature technology in the grid is to enhance the overall information security protection ability and to achieve the strong support and safeguard of the company's strategic development.
2. Active defense. Starting from the information security system architecture, with the technology as the breakthrough point, passive defense of event-driven is being gradually turned into active defense of message driven, through using the 'partition and hierarchy, security access, dynamic perception, and comprehensive protection' principle.
3. Continuous tracking. We should track continuously the development trend of international informatization and information security work, and try to apply them in the information security protection of State Grid Corporation.

### ***5.2 Building Longitudinal-Depth Protection System***

One of the keys to the smart grid is strong, which is not only the security and stability of the backbone grid, but also the same strict requirement on the entire information environment of smart grid operation. Therefore, it is the basis to establish a set of longitudinal-depth protection system covering from the physical layer to the application layer for strong smart grid construction [8].

### ***5.3 Information Security Team Construction***

Team construction is effective implementation of the information security. State Grid Corporation should take the technical support team of China Electric Power Research Institute and State Grid Electric Power Research Institute as the foundation, to strengthen the effort in personnel training, build a national information security laboratory, and finally improve the quality performance of information security in the seven aspects.

## 6 Conclusion

With the wide application of information and communication technologies in the construction of smart grid, the information security is facing greater threat and risk. The emphasis on information security work cannot be overstated any time, any place. In 2003, for example, large portions of the northeastern USA and Canada experienced an electric power blackout. The outage affected more than 50 million people and caused economic losses of about 6 billion dollars. The cause was the loopholes in information system and the primary server crashed, resulting in early warning failure. Therefore, the State Grid Corporation must employ the means of the mature high-tech, modern management and security team to build the protection system of power information security, in order to guarantee the safe and stable operation of smart grid.

## References

1. Liu XY, Zhang Q, Li ZM (2014) A survey on information security for smart grid. *Electr Power Inf Commun Technol* 4
2. Chen LJ, Mei SW, Chen Y (2012) Smart grid information security and its influence on power system survivability. *Control Theory Appl* 2
3. Yu Y, Lin WM (2010) Study on information secure evaluation framework of smart grid application system. 12th annual meetings of china association for science and technology on information and communication technology and smart grid, pp 497–500
4. Wang HK, Gu ZW (2012) Information security risk assessment of smart grid. *Electr Power Inf Technol* 11
5. Yuan YQ, Ge XY, Lu LL (2012) A new information security model in smart grid. *Inf Bus Intell Commun Comput Inf Sci* 267:39–44
6. Ma JW, Yan L, Zhao M, Zhu LZ (2014) Study on precautionary measure of information security in electric power systems. *Inf Secur Technol* 5(8):85–87
7. Chen T, Wang X (2012) Smart grid information security risk analysis and reflection. *Electr Power Inf Technol* 12
8. Jiang CZ, Zhang T, Yu Y (2012) Research on information security protection model for smart grid based on classified protection. *Comput Modernization* 4

# The Multiobjective Optimization Model of Open Mill Mastication Parameters

Zhang Liang, Wang Qidong, Zhu Lihong and Zhao Han

**Abstract** Through the analysis of the efficiency and energy consumption of the mastication process of open mill, the time and carbon emission objective function of the process is established. Considering the actual constraint in the process of open mill performance and mastication parameters, a multiobjective optimization model is established, which takes the open mill linear speed of roller, roller spacing, and roller ratio as the variables and the minimum processing time and the lowest carbon emission as the optimization objectives. An improved genetic algorithm is utilized to solve the optimization model. The validity of the proposed model is verified by an example, and the sensitivity of the optimization results and the optimization variables are analyzed.

**Keywords** Open mill · Mastication parameters · Carbon emissions · Multiobjective optimization model

## 1 Introduction

Mastication is an essential process of rubber production [1]. In rubber processing, emissions are mainly from mastication and vulcanization process, 90 % of total emissions [2]. Therefore, in order to improve the production efficiency and reduce carbon emissions in the production process, many rubber enterprises need to solve the engineering problems of reasonable selection of production equipment and processing parameters.

At present, there are numerous scholars at home and abroad for the optimization of process parameters. Li et al. [3] classified and analyzed the optimization of cutting parameters in the domestic and international research status of production efficiency, cost profit target, and energy consumption target. Using genetic algorithm, neural network method and fuzzy rough set theory in the literatures [4–10],

---

Z. Liang · W. Qidong · Z. Lihong (✉) · Z. Han  
Hefei University of Technology, Hefei, China  
e-mail: zhllong2002@163.com

the optimization problem of high speed machining parameters was studied, and the relationship between cutting parameters and energy consumption and energy efficiency was found. Through the analysis of the above results, we find that most of these studies use a single-objective optimization method, a lot of the study of the efficiency, the cost for the optimization objectives of the use of multiobjective optimization. However, there is little research on the environmental impact as the optimization goal. Finally, these studies have almost all of the optimization of the parameters of the process parameters and the optimization of the parameters in the process of rubber production.

Therefore, in this paper, the production efficiency and environmental impact as a comprehensive optimization objective, the optimization of process parameters in the process of refining machine is studied. The mathematical model of the process parameters is created. The model is based on the assumption of ensuring the maximum production efficiency. The minimum carbon emissions as the optimization objective and the actual situation of the equipment and the process of the plastic chain are constrained.

## 2 The Establishment of the Optimization Model

### 2.1 Optimization Variables

In open mill for production, the front line of roller speed  $v_2$ , and distance  $e$  (the minimum distance between the front and rear roller and roller speed ratio  $f$  (before and after the two line of roller speed ratio) is plastic compounding process important operating variables. The values of these three variables are closely linked to the processing ability, the processing efficiency, and the energy consumption of the mill. Therefore, the linear speed of roller  $v_2$ , roller distance  $e$ , and roller speed ratio  $f$  are considered as the optimization variables.

### 2.2 Optimization Objective Function

The refining process and carbon emissions [3] of plastics are the optimization objectives in the paper.

#### 2.2.1 The Time Function of Plastic Refining Process

In the process of using the thin—pass method, a full—time work includes the time and the auxiliary time. The mathematical model of the time function of the process of plastic refining can be expressed as follows:

$$T_0 = \frac{2 \times 10^3 KD}{ev_2(f+1)} + T_f \tag{1}$$

In this formula,  $D$  is the roller diameter,  $K$  the empirical coefficient and generally  $K = 0.007$ , and  $L$  the roller length. In this formula,  $T_s$  for the time of plastic refining,  $T_f$  for the auxiliary time.

### 2.2.2 Carbon Emission Function of Plastic Chain

Plastic mixing process of carbon emissions mainly includes energy consumption  $C_d$  caused by carbon emissions and carbon emissions caused by the process of producing waste gas and wastewater in the process of plastic refining  $C_q$  and  $C_w$ .

$$C_a = C_d + C_q + C_w \tag{2}$$

1. Carbon emissions  $C_d$  caused by electricity

In the process of plastic refining, a large amount of energy is needed. The calculation of carbon emissions caused by the electric energy consumption is as follows:

$$C_d = F_d E_d \tag{3}$$

In this formula,  $F_d$  is the carbon emission factor (kgCO<sub>2</sub>/kWh) generated by electricity and  $E_d$  is the electric energy consumption of plastic chain. In this paper, the average 0.5412 (kgCO<sub>2</sub>/kWh)<sup>3</sup> is used as the electric energy carbon emission factor.

According to the method provided by the literature [11, 12], we can get the plastic refining energy consumption:

$$E_d = \left[ P_{kd} + a_1 \left( \frac{50v_2}{3\pi D} \right) + a_2 \left( \frac{50v_2}{3\pi D} \right)^2 \right] T_0 + 1.2 \times \frac{v_2 DLK_p}{2 \times 10^9 e} (f^2 - 1) T_s \tag{4}$$

In this formula,  $P_{kd}$  is the mills' minimum no load power and  $a_1$  and  $a_2$  are speed coefficients of the roller.  $K_p$  is the shear coefficient; according to the experience,  $K_p = 200$ .

2. Carbon emissions from waste gas treatment

In the process of plastic refining, the waste gas emitted by the rubber material mainly consists of dust particles, CS<sub>2</sub>, and non-methane hydrocarbons [13]. In general, it will deal with the waste gas discharged into the atmosphere through the fan. Carbon emissions from this process are mainly derived from the energy consumption of fans. Therefore, we can get the formula of carbon emissions from waste gas treatment.  $P_{ff}$  is the power rating of wind turbine.

$$C_q = F_d P_{fj} T_0 \tag{5}$$

3. Carbon emissions from wastewater treatment

The wastewater from rubber product enterprises is mainly used for cooling the circulating water, the water quality is less, and the main component is water. According to the research of the literature [14, 15], carbon emission factor for wastewater treatment is 0.2 kg CO<sub>2</sub>/L.

$$C_w = 0.2 \text{ KDLT}_0 \tag{6}$$

From the above analysis, the carbon emission function in the process of plastic operation is obtained:

$$C_a = 0.5412 \left[ P_{kd} + a_1 \left( \frac{50v_2}{3\pi D} \right) + a_2 \left( \frac{50v_2}{3\pi D} \right)^2 \right] T_0 + 0.5412 \left[ 1.2 \times \frac{v_2 DLK_p}{2 \times 10^9 e} (f^2 - 1) T_s + P_{fj} T_0 \right] + 0.2 \text{ KDLT}_0$$

In open smelting machine in practical work, plastic mixing parameter value must be limited to selecting open smelting machine’s roller line speed, speed ratio range, maximum, and distance conditions. The machine must be in the range of the limit conditions. The mathematical model of multiobjective optimization of the process of the opening of the machine is as follows:

$$\min F(v_2, e, f) = (\min T_0, \min C_a) \tag{8}$$

$$s.t. \quad v_{\min} \leq v_2 \leq v_{\max}; \quad f_{\min} \leq f \leq f_{\max}; \quad e_{\min} \leq e \leq e_{\max}; \tag{9}$$

$$\frac{v_2 DLK_p}{2 \times 10^9 e \eta} (f^2 - 1) \leq P_{\max}$$

### 3 Optimization Algorithm

In this paper, a modified genetic algorithm is used to optimize the parameters of the plastic chain of the mill. This algorithm is based on the combination of Pareto [16] and genetic algorithm, which is based on the genetic algorithm, which adds the technology of population sorting, niche, adaptive value sharing mechanism, and so on. The algorithm program is shown in Fig. 1.

Among them, the maximum algebra is 100, the population size is 100, using 10 binary code, the probability is 0.7, the probability of mutation is 0.05.

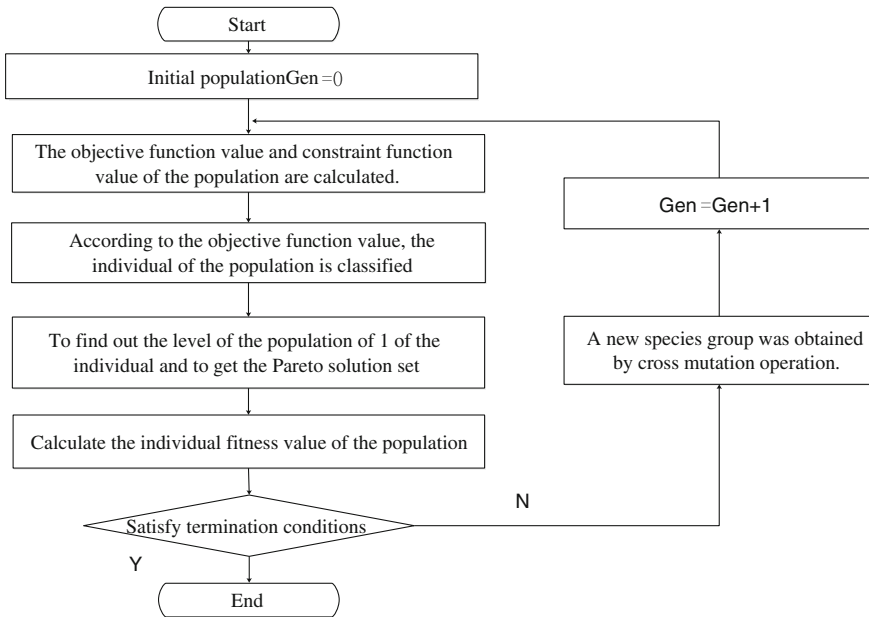


Fig. 1 Optimization algorithm flowchart

## 4 Optimization Examples

In the case of a certain type of air spring, the model is verified to verify the validity of the optimization model.

### 4.1 Test Conditions

The basic parameters of the test are shown in Table 1.

The quality of the air spring used in the experiment is 12 kg. Other relevant parameters and coefficients are shown in Table 2.

### 4.2 Optimization Results and Analysis

Optimization calculation is done by using MATLAB toolbox. Examples of the optimization results are shown in Table 3.

From the optimization results of Table 3, we can know that the optimization effect is more obvious for the time and carbon emissions, and the optimization of



**Table 1** Specification parameter of the mill

Roller size $D \times L$ (mm $\times$ mm)	The minimum roller line speed $v_{2\min}$ (mm s <sup>-1</sup> )	The roller of the line speed $v_{2\max}$ (mm s <sup>-1</sup> )	Minimum speed ratio $f_{\min}$	Maximum speed ratio $f_{\max}$	Minimum roll distance $e_{\min}$ (mm)	Maximum roll distance $e_{\max}$ (mm)	Maximum effective plastic refining power $P_{\max}$ (kW)	Effective power factor of the mill
250 $\times$ 620	50	200	1.1	1.3	0.1	1	22	0.85

**Table 2** Parameters used in calculation

Auxiliary time $T_f$ (S)	Blower rated power $P_{\bar{f}}$ (kW)	Minimum idle power $P_{kd}$ (kW)	Speed coefficient of roller $a_1$	Speed coefficient of roller $a_2$
100	20	9.88	0.126	$1.32 \times 10^{-6}$

**Table 3** Optimization results

Optimization results	The highest production efficiency as the target	Minimum carbon emissions as the target	Comprehensive optimization objective	Relative optimization rate (%)
Carbon emissions $C_d$ (g)	1690	1190	1423	35.1
Plastic refining time $T_0$ (s)	157	219	186	-33.3
Roller line speed $v_{2min}$ ( $\text{mm s}^{-1}$ )	184.637	168.443	176.185	9.2
Roll pitch $e$ (mm)	0.838	0.796	0.816	5.1
Speed ratio $f$	1.293	1.102	1.109	17.2

the single-objective optimization is more than 30 %; in total carbon emissions, the carbon emissions of wastewater and waste gas are small, and the carbon emissions are mainly derived from the energy consumption of the mill; both single optimization goal is integrated optimization, linear velocity of roller and roller spacing value are close to their maximum value, the change was less than 10 %, and the ratio of the value choice changes greatly. The cause of this result is to carbon emission minimum as the optimization objective, ratio value is smaller, and roller material on the force of the shear is small. Thus, the energy consumption of the machine is less, so the carbon emission is less. To attain the highest production efficiency, the ratio is higher; the shear strength of the material is higher. Therefore, the energy consumption of the mill is more, so the carbon emission is relatively more. When the production efficiency and carbon emissions are integrated to optimize the target, the time and the carbon emissions of the carbon chain are between the above two.

### 4.3 Sensitivity Analysis

In this paper, we analyze the sensitivity of the target function and the carbon emissions of the three optimization variables by the method of factorial design. The selected variable data were 27 groups, and the specific data are shown in Table 4.

**Table 4** Variable values for sensitivity analysis

No.	Front line of roller speed $v_2/(\text{mm s}^{-1})$	Roll pitch $e/\text{mm}$	Speed ratio $f$
1	50	0.1	1.1
2	50	0.1	1.2
3	50	0.1	1.3
4	50	0.2	1.1
5	50	0.2	1.2
6	50	0.2	1.3
7	50	0.3	1.1
8	50	0.3	1.2
9	50	0.3	1.3
10	100	0.1	1.1
11	100	0.1	1.2
12	100	0.1	1.3
13	100	0.2	1.1
14	100	0.2	1.2
15	100	0.2	1.3
16	100	0.3	1.1
17	100	0.3	1.2
18	100	0.3	1.3
19	150	0.1	1.1
20	150	0.1	1.2
21	150	0.1	1.3
22	150	0.2	1.1
23	150	0.2	1.2
24	150	0.2	1.3
25	150	0.3	1.1
26	150	0.3	1.2
27	150	0.3	1.3

1. Sensitivity analysis of the influence of optimization variables on time objective function.

Based on partial derivative of time objective function calculation roller line speed and the speed ratio and distance, we can get time objective function on line of roller speed, speed ratio and distance sensitivity (absolute value). Results are shown in Figs. 2, 3, and 4.

Comparison Fig 2, 3 and 4, we can see maximum distance sensitivity of time objective function, and minimum sensitivity of roller speed ratio. From Fig 2 it can be seen that when the roll and pitch line of roller speed while maintaining unchanged, the ratio is increased, the ratio of the sensitivity shows a decreasing trend; From Fig 3 it can be seen that when the roll and pitch ratio while maintaining unchanged, line of roller speed is increased, the sensitivity of the linear speed of roller is decreased; From Fig 4, it can be seen that when the line

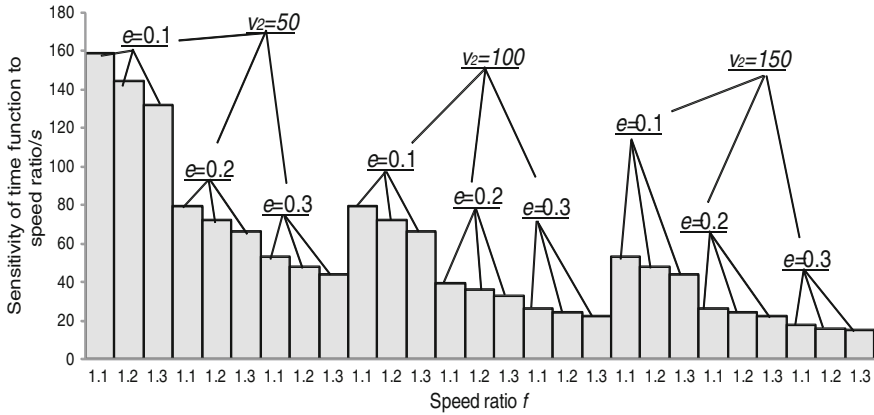


Fig. 2 Sensitivity analysis of time function to speed ratio

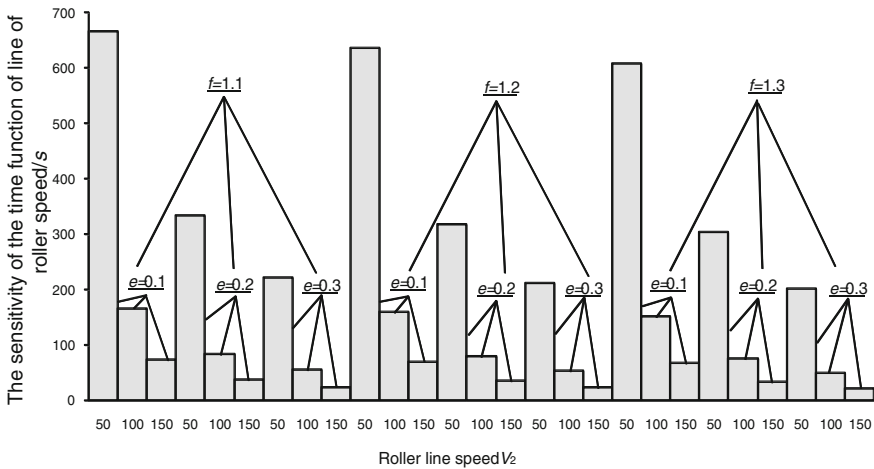


Fig. 3 Sensitivity analysis of time function of line of roller speed

of roller speed ratio and also remained unchanged, and distance is increased, the sensitivity of shows a obvious decreasing trends.

- The sensitivity analyses of optimization variables on the impact of the target function on carbon emissions.

This paper is on carbon emissions in the objective function, roller distance and roller line speed of roller speed ratio calculation of partial derivative. We can get the carbon emissions of sensitivity function and distance and roller line speed of roller speed ratio (absolute value). Results are shown in Figs. 5, 6, and 7.

Comparison Fig 5, 6 and 7 can be found, the line speed of roller on carbon emissions objective function of maximum sensitivity, roller speed ratio of

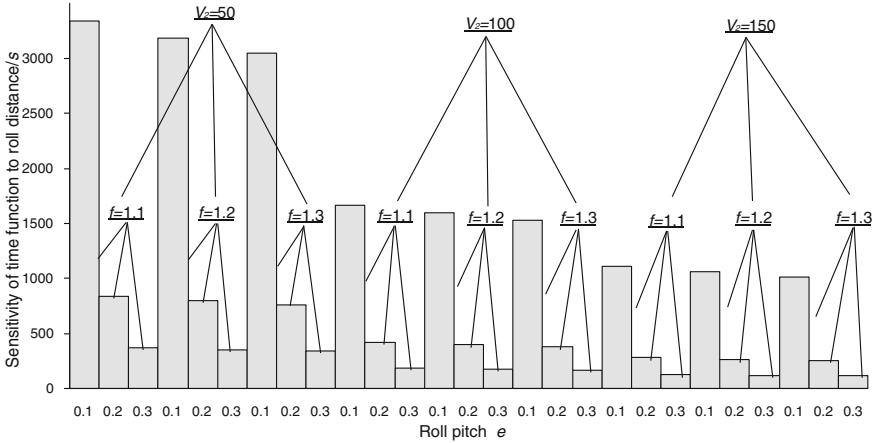


Fig. 4 Sensitivity analysis of time function to roll distance

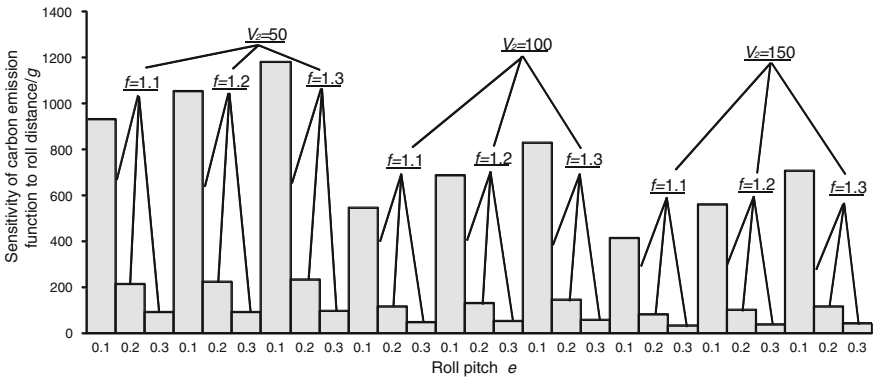


Fig. 5 Sensitivity analysis of carbon emission function to roll distance

minimum sensitivity. From Fig 5, we can see that when the roller line speed and the speed ratio also remains unchanged, the distance and the sensitivity of the present trend with distance and decreases; from Fig 6, we can see that when the roll and pitch ratio also remains unchanged, the sensitivity of the linear speed of roller showing the trend and increase with the increase of the line speed of roller; from Fig 7 it can be seen, when the constant line speed of roller, speed sensitivity showing with increase of speed and distance and increase first and then decrease, and increase the fluctuating trend.

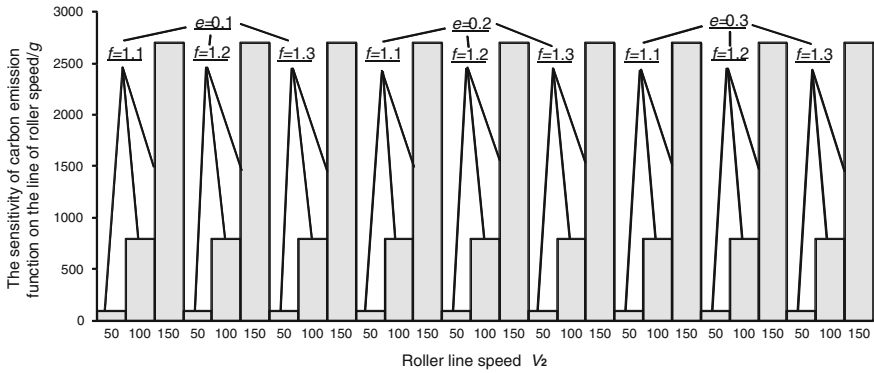


Fig. 6 Sensitivity analysis of carbon emission function on the line of roller speed

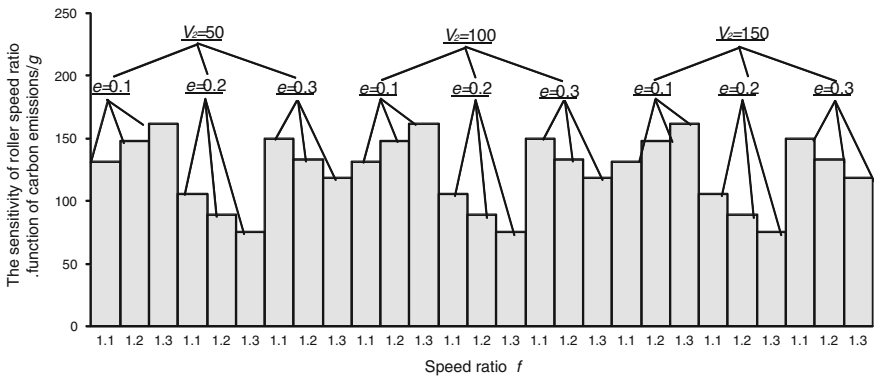


Fig. 7 Sensitivity analysis of carbon emission function to speed ratio

### 5 Summary

This paper based mill during mastication in the analysis, select the linear speed of roller, roller distance and roller speed ratio as the optimization variables; the multiobjective optimization model was constructed to maximum production efficiency and the lowest carbon emissions, the linear speed of roller, roller distance, roller speed ratio and the maximum power are constraint conditions. Pareto genetic algorithm is used to solve the optimization model. The model is validated by the specific examples, and the sensitivity analysis is carried out on the plastic chain parameters. The results show that this method has a certain value in engineering application for improving production efficiency and reducing carbon emissions. Plastic chain is only a link in the process of rubber products. The work will focus on the multiobjective optimization model of the whole process.

**Acknowledgement** This study is supported by National Key Technology Support Program (2013BAG 08B01).

## References

1. Lu P (2010) Practical rubber handbook. Chemical Industry Press, Beijing
2. Xuefeng D, Zhang H, Cao R (2013) Study on the waste gas emission factors of rubber products industry-taking the tire enterprise as an example. *Sichuan Environ* 32(6):83–86
3. Li C, Cui L, Liu F, Li L (2013) Multi-objective NC machining parameters optimization model for high efficiency and low carbon. *J Mech Eng* 49(9):87–96
4. Zhitong C, Baoguo Z (2009) Mathematic model on cutting parameter optimization for unit cutting process. *J Mech Eng* 45(5):230–236
5. Xie ST, Guo YB (2011) Optimization approach of cutting parameters for minimizing production cost in CNC turnings. *Comput Integr Manuf Syst* 17(10):2144–2149
6. Li J, Yao Y, Liu C, Li S (2006) Cutting parameters optimization in turning based on genetic algorithm. *Comput Integr Manuf Syst* 12(10):1651–1656
7. Saravanan R, Asokan P, Vijayakuman K (2003) Machining parameters optimization for turning cylindrical stock into a continuous finished profile using genetic algorithm(GA) and simulated annealing(SA). *Int J Adv Manuf Technol* 21(1):1–9
8. Wu MP, Liao WH (2005) Internet-based machining parameter optimization and management system for high-speed machining. *Trans Nanjing Univ Aeronaut Astronaut* 22(1):42–46
9. Rajemi MF, Mativenga PT, Aramcharoen A (2010) Sustainable machining: selection of optimum turning conditions based on minimum energy considerations. *J Clean Prod* 18:1059–1065
10. Mori M, Fujishima M, Inamasu Y et al (2011) A study on energy efficiency improvement for machine tools. *Manuf Technol* 60(1):145–148
11. Jingan Wu, Musong Li (2006) Rubber processing machinery. Chemical Industry Press, Beijing
12. Shi J, Liu F, Xu D, Chen G (2009) Decision model and practical method of energy-saving in NC machine tool. *China Mech Eng* 20(11):1344–1346
13. Ding X, Yang S, Zhang H, Cao R (2014) Analysis and evaluation of sulfur malodor in rubber products industry. *Environ Sci Surv* 33(3):70–72
14. Intergovernmental Panel on climate change (2006) IPCC national greenhouse gas emissions inventory Guide (Chinese version). IPCC national greenhouse gas inventory plan, Beijing
15. National Standardization Committee (2012) GB27632-2011 Rubber products industrial pollutant discharge standard. China Environmental Science Press, Beijing
16. Wang H, Qin X, Ren C (2012) Optimization of cutting parameters in helical milling process based on pareto genetic algorithm. *China Mech Eng* 23(17):2058–2061

# Precision Compensation Analysis of Spacecraft Assembly Parallel Mechanism

Guangtong Liu, Guotao, Yanlei Zhang and Laiying Tang

**Abstract** The pose of spacecraft can be adjusted automatically, intellectualized, high-precisioned by 6 DOF parallel spacecraft assembly platform, resolved the problem of high-precision spacecraft assembly. In digital assembly process, spacecraft assembly platform is used as the positioning mechanism for spacecraft, but it occurs structure deformation caused by spacecraft, which can affect the precision of assembly. This work focuses on the research about the deformation error and proposes a corresponding error compensation method in order to satisfy high-precision requirement in the procession of assembly. To take account of deformation of all parts in the assembly platform, finite element method is applied. Firstly, this paper verifies the feasibility of deformation analysis based on finite element comparing with the stiffness matrix method. Secondly, it establishes a posture error model for the platform. Finally, it proposes an error compensation method based on finite element analysis results and tests the compensation method.

**Keywords** Precision compensation · Spacecraft · Parallel mechanism

## 1 Introduction

When spacecraft is assembled, one cabin is fixed by crane, the other one installed on the assembly platform. By adjusting position of the platform, the cabin assembly can be achieved. Due to the gravity of cabin, the assembly platform occurs material deformation, which makes the platform position exist positioning error. Although assembly platform is subjected to the same load, the varying stress of parts under different postures makes the error change. In this paper, the assembly platform which is a 6-UPS parallel mechanism has six degrees of freedom. The more the degree of freedom is, the more complex the error is. So the compensation is getting more difficult.

---

G. Liu (✉) · Guotao · Y. Zhang · L. Tang

Beijing Institute of Spacecraft Environment Engineering, China Academy of Space Technology, 104#You Yi Road Haidian District, Beijing, China  
e-mail: liugt2007@qq.com

© Springer-Verlag Berlin Heidelberg 2016

B. Huang and Y. Yao (eds.), *Proceedings of the 5th International Conference on Electrical Engineering and Automatic Control*, Lecture Notes in Electrical Engineering 367, DOI 10.1007/978-3-662-48768-6\_133

1191



Traditionally the problem of mechanical deformation is studied by using the theory of stiffness matrix, but this method ignores the influence of joint despite considering the deformation of branched chain [1]. With the development of computer technology, finite element method is an important method to analysis mechanical strength and stiffness. Zhu [2, 3] analyzed static stiffness of 3-TPT parallel machine by finite element method using ANSYS software and obtained static stiffness and static characteristics of the machine under different attitudes. In this paper, it simulates mechanical stress and deformation of the actual situation using ABAQUS software, which is of great significance for the error research of spacecraft assembly platform.

## 2 Spacecraft Assembly Parallel Mechanism

As shown in Fig. 1, the spacecraft assembly platform is a 6-UPS parallel mechanism. Figure 2 is schematic diagram of this parallel mechanism. The 6-UPS parallel mechanism is made up of a fixed platform, a movable plate, and six variable branched chains. One end of each chain is connected to the movable plate through a ball joint, while the other end is attached to the fixed platform by a U-joint. This design is to overcome a local degree of freedom that the link rotates itself around its own axis. By adjusting the length of six branched links, the position of the movable plate relative to the fixed one can be controlled.

During the assembly process of spacecraft cabins, it can adjust posture of the cabin installed on the movable plate by controlling the length of six chains. So the assembly is subjected to the constant gravity. In order to assemble the cabin installed on the movable plate to the fixed cabin successfully, the positioning precision of assembly platform must meet actual requirements. Therefore, it is necessary to eliminate positioning error caused by the material deformation under heavy load.

**Fig. 1** The assembly platform

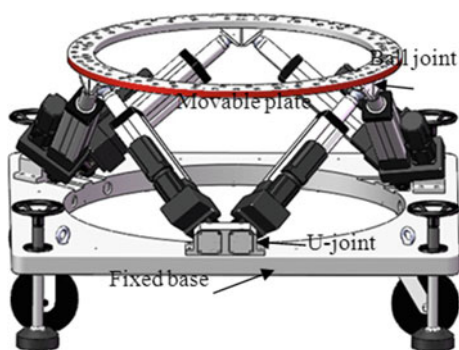
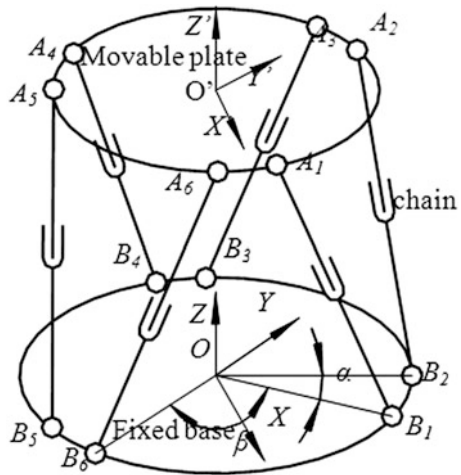


**Fig. 2** Diagram of the assembly platform



### 3 Finite Element Analysis Method

The accuracy of finite element analysis is influenced by the factors such as the way of meshing, cell size, and cell type. And the precision of the data is limited in most cases. However, error of the assembly platform is small. Therefore, it is necessary to examine whether the error of finite element analysis can achieve the demanded accuracy or not. Based on the stiffness matrix, this paper studies the influence of the chain length error on the output error and gets the theoretical value of output error. In order to verify reliability of the finite element analysis, the theoretical value is compared with the result of finite element calculation.

#### 3.1 Stiffness Matrix Method

Broadly speaking, there is a displacement at the end of a mechanism when a force is exerted on it. So the ratio of its force and the displacement is defined as stiffness, namely  $K = F/X$ . According to the principle of virtual work, in 1990 Gosselin firstly found a way to map from operating force of spatial mechanism to deformation at the end under the assumption of only considering the deformation of chains. The mapping relation is described as a matrix, namely the stiffness matrix [4]. The stiffness matrix formula for parallel mechanism is described as below:

$$Kc = J^T [k_i] J \tag{1}$$

where J is the Jacobi matrix of parallel mechanism,  $[k_i]$  is the stiffness matrix of chains which is a  $6 \times 6$  diagonal matrix.

Therefore, according to  $[F; M] = Kc \cdot [\Delta x \ \Delta y \ \Delta z \ \Delta \alpha \ \Delta \beta \ \Delta \gamma]^T$ , the positioning error of the assembly platform is calculated under the action of force and torque based on the stiffness matrix.

### 3.2 Finite Element Method

Stiffness matrix theory only considers the chain length error and not positioning error of the joint. For the sake of analysis, the influence of joint locating error is eliminated by removing the fixed platform and fixing the bearing directly on the ground. The mechanism is assembled by its components. And then according to the actual constraint relations, set up sliding pair, revolute pair, and spherical pair, and set the boundary condition to fixing the three bearing (see Fig. 3).

As seen from the result from ABAQUS, the coordinates of the points before and after the deformation are read. So we can take three target points on the movable plate and record the three coordinates of the points before and after the deformation. SVD method is a kind of position fitting algorithm, and its essence is getting the pose of the rigid body coordinate system relative to the fixed coordinate using three points on the rigid body in its own coordinate system and static coordinate [5]. Therefore, through the SVD method, calculate the actual pose of the mobile platform according to the coordinates of the three target points before and after the deformation, and the actual pose subtracts the target pose and gets the positioning error.

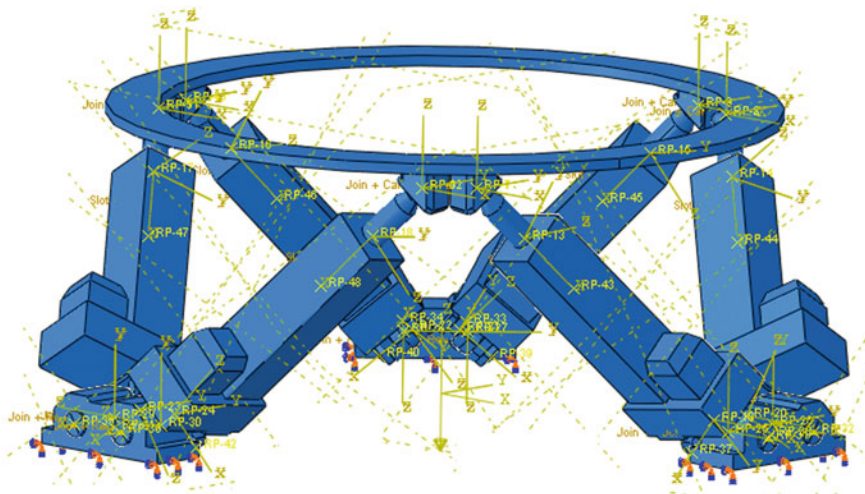


**Fig. 3** The model of finite element analysis

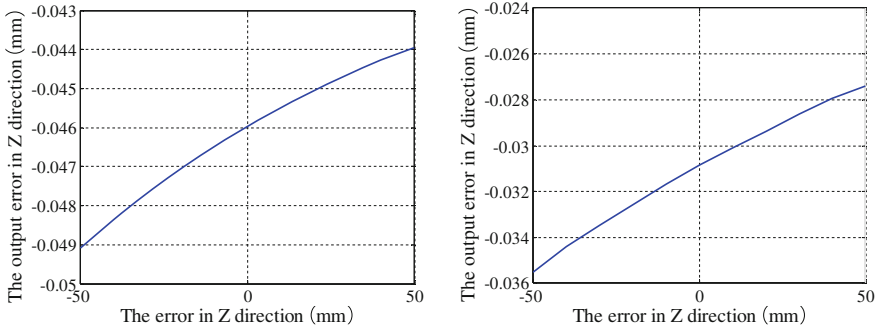


Fig. 4 The error in  $z$  direction when moving along  $z$ -axis

### 3.3 Models Comparison

Here is moving along  $z$  direction, for example, and we calculate the pose error in each direction. The following Fig. 1 describes the output error in  $z$  direction calculated by the two methods above (see Fig. 4).

In general, the values of the error calculated by two methods are different, but the difference is not big. And the tendency of curve is basically the same. Therefore, it is available to calculate the error of the assembly platform using FEA method.

## 4 Precision Analysis and Compensation

### 4.1 Error Model

As shown in Fig. 1, the coordinate system  $O-XYZ$  and  $O'-X'Y'Z'$  is set up, respectively, in the center of the fixed base and movable plate. The end position of the assembly platform can be described as the vector  $X = [D^T M^T]^T$ , where  $D = [xyz]^T$  is position vector of the movable coordinate system origin and  $M = [\alpha \beta \gamma]^T$  is attitude angles of the movable coordinate system.

The assembly platform mainly includes position error of the joint point and length error of the branched chain. The error of joint point is expressed as follows:

$$\delta p = [\delta A_1^T \quad \delta B_1^T \quad \delta A_2^T \quad \delta B_2^T \quad \dots \quad \delta A_6^T \quad \delta B_6^T]^T \tag{2}$$

where,  $\delta A_i = [\delta A_{ix} \quad \delta A_{iy} \quad \delta A_{iz}]^T$ ,  $\delta B_i = [\delta B_{ix} \quad \delta B_{iy} \quad \delta B_{iz}]^T$ .

The relationship between output error at the end and error sources can be described as follows:

$$\delta X = J_p^{-1}(\delta l - J_s \delta p) \tag{3}$$

where  $\delta l = [\delta l_1 \quad \delta l_2 \quad \dots \quad \delta l_6]^T$ ,

$$J_p = \begin{bmatrix} \vec{l}_1^T & (s_6 \times \vec{l}_6)^T \\ \dots & \dots \\ \vec{l}_6^T & (s_6 \times \vec{l}_6)^T \end{bmatrix}_{6 \times 6}, \quad J_s = \begin{bmatrix} \vec{l}_i^T R & -\vec{l}_i^T & \dots & 0 \\ 0 & \dots & \vec{l}_i^T R & -\vec{l}_i^T \end{bmatrix}_{6 \times 36}$$

### 4.2 The Values of Error Resource

Although the load on the assembly platform is the same under different pose, the output error at the end is different. And the length error of branched chain has the certain regularity along with the change of the pose, so it can be compensated with the results calculated by stiffness matrix. The position error of ball points in movable platform is small enough to be ignored. But the corners of fixed platform have bigger deformation. So the position error of U-joint in the fixed plate is the main error source. However, the position error of U-joint has a certain relation to the shape of fixed platform, the position of supporting legs, and the structure of bearings, and so on. Therefore, the error is complex and has non-fixed changing rule.

The hinge point position error is solved by using the following method:

According to the static analysis of parallel mechanism, the maximum and the minimum forces of the branched chains in the parallel structure can be obtained in the whole workspace. By finite element analysis, exerting the max force to the six branched chain at the same time, we can get the static platform six hinge point coordinates Bimax. While exerting the min force to the six branched chain at the same time, we can get the static platform six hinge point coordinates Bimin. So the hinge point coordinate error range is obtained as shown in the Table 1. Take the average of the hinge point error as the coordinate point error source  $\delta p$ .

**Table 1** The error value of coordinate point

No.	Axis x error $\delta x_i$ (mm)		Axis y error $\delta y_i$ (mm)		Axis z error $\delta z_i$ (mm)	
	Range	Average	Range	Average	Range	Average
1	-0.012 to -0.049	-0.031	0.002 to -0.044	-0.021	-0.052 to -1.29	-0.67
2	-0.012 to -0.042	-0.027	0.002 to -0.082	-0.04	-0.047 to -1.17	-0.61
3	0.001 to 0.15	0.075	-0.001 to -0.17	-0.084	-0.057 to -1.09	-0.57
4	0.001 to 0.17	0.085	-0.001 to -0.15	-0.073	-0.057 to -1.09	-0.57
5	-0.002 to 0.082	0.040	0.012 to 0.042	0.027	-0.047 to -1.17	-0.61
6	-0.002 to 0.043	0.021	0.012 to 0.049	0.031	-0.052 to -1.29	-0.67

### 4.3 Error Compensation

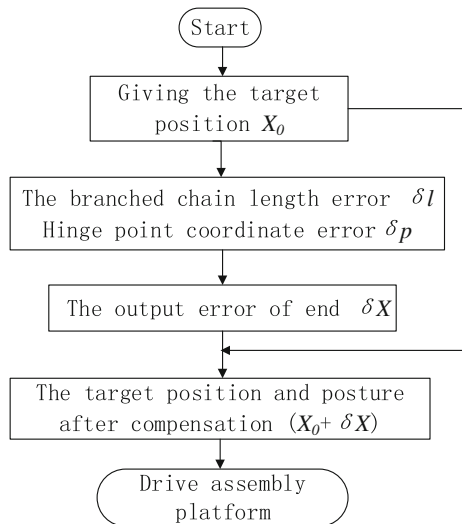
Due to the assembly platform by the spacecraft's only gravity, the load vertically downward and its direction remains the same. And the pose space of the institution is relatively small, so you can think that the main error is along the  $z$ -axis error and errors of the other degrees of freedom are lesser that can be ignored. The key of compensation process is that considering the position error of the hinge point and the branched chain length error at the same time. According to the positive solution's error model, we can obtain the output error of the end along the  $z$  and take the error value as the next step of the error compensation.

Assume in order to realize the target position for  $X_0$ , error compensation process is as follows: According to the error model, we can solve the output error value of the end  $\delta X = J_p^{-1}(\delta l - j_z \delta p)$  by the error source  $\delta l$  and  $\delta p$ . Therefore, branched chain length error can be obtained from the formula (3); The error of hinge point coordinates  $\delta p$  can be taken as  $[\delta \bar{x}_i \ \delta \bar{y}_i \ \delta \bar{z}_i]$ , because terminal error value  $\delta X$  is the difference between the actual position  $X$  and the target position  $X_0$

$$\delta X = X - X_0 \tag{4}$$

Taking the obtained error of the end as compensation value, then if we want to achieve the final actual position  $X_0$ , we should input the actual value  $X' = (X_0 - \delta X)$ . Taking the value  $(X_0 - \delta X)$  as the target location and using the obtained by inverse solution of kinematics of the branched chain length value as the driving instruction, we can drive assembly platform (see Fig. 5).

**Fig. 5** The diagram of error compensation



## 5 Simulation Result and Analysis

Here is a movement along the  $z$ -axis for example which tests the effect of error compensation.

### 5.1 Without Compensation

When the target position  $X_0$  is given, it can get the length of branched chains based on position inverse solution. And then the assembly platform position can be controlled using these length values. Error curves of every DOF using finite element method are obtained. Figure 6 is the output of error along the  $z$  direction and  $x$  direction when the movable plate goes in  $z$  direction.

As shown in Fig. 6, the error of  $x$  direction is small, while the error of  $z$  direction is big enough to affect the positioning precision of assembly platform. Using the same method, it is shown that the error A, B, C, and  $y$  direction is small. Therefore, it is reasonable that error compensation is made for the error of  $z$  direction, not the error of A, B, C,  $x$ , and  $y$  direction.

### 5.2 Using Compensation

When the assembly platform is moving along the  $z$ -axis, the following points shown in Table 2 are considered as the target position. According to the error source, it can get the output error value  $\delta X$  and driving position  $(X_0 - \delta X)$ . And then, it can get the length of each branched chain value according to the actual target position  $(X_0 - \delta X)$ . After inputting the values to control instruction of the assembly platform, it can realize the assembly platform position adjustment.

The error curves of  $x$  and  $z$  directions are shown in Fig. 7 after compensation in the same way.

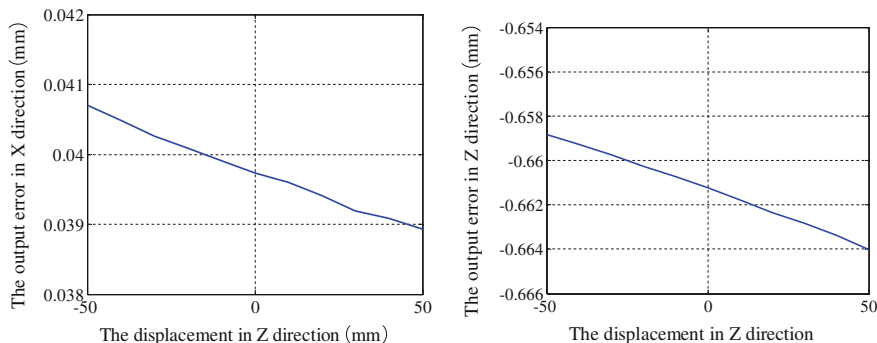


**Fig. 6** The output error in the  $z$  and  $x$  directions

**Table 2** Positioning values along z-axis

Target position $z$ (mm)	Error value $\delta z$ (mm)	Actual driving position ( $z_0 - \delta z$ ) (mm)
$z = -50$	-0.639305	-49.360695
$z = -40$	-0.639219	-39.360781
$z = -30$	-0.639167	-29.360833
$z = -20$	-0.639144	-19.360856
$z = -10$	-0.639147	-9.360853
$z = 0$	-0.639176	0.639176
$z = 10$	-0.639226	-10.639226
$z = 20$	-0.639296	-20.639296
$z = 30$	-0.639384	-30.639384
$z = 40$	-0.639489	-40.639489
$z = 50$	-0.639609	-50.639609

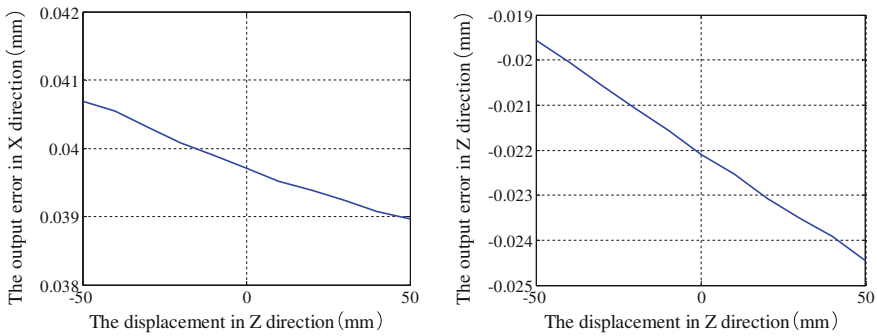


**Fig. 7** The error in the  $z$  and  $x$  directions after compensation

Comparing the error before compensation with the one after, it is found that the error of  $x$  direction remains unchanged, and the error of  $z$  direction is reduced to 0.020–0.024 from  $-0.66$ – $0.67$ . In conclusion, error of A, B, C,  $x$ , and  $y$  direction is small. This error compensation cannot affect the error of A, B, C,  $x$ , and  $y$  direction and reduce the error in  $z$  direction. Therefore, the compensation method is reasonable and effective.

## 6 Conclusion

In this paper, it analyzes deformation of the assembly platform on heavy-load condition. Then, it obtains the rules of structural deformation caused by heavy spacecraft and proposes the effective compensation measures. After the research and analysis, the following conclusions were obtained.



1. It can consider deformation errors of all parts in the assembly platform using advanced finite element analysis method.
2. It is proved by the theory of stiffness matrix that this finite element method can be used to analyze the deformation precision.
3. It is shown that this compensation method can improve positioning accuracy of the platform when the load is gravity, and the range of attitude adjustment is relatively small.

## References

1. Li Y, Song Y, Feng Z (2010) Overview of the study on the stiffness of parallel manipulators. *J Mach Des* 27(1):2–4
2. Zhu C, Cai G, Yang B (2006) Finite elements analysis of the stiffness of 3-TPT parallel kinematical machine based on ANSYS. *Manuf Technol Mach Tool* 8:48–51
3. Zhu C, Zhu L, Liu Y et al (2007) Effect of parallel mechanism of parallel machine tool on its static stiffness. *J Northeast Univ Nat Sci* 28(8):1171–1173
4. Gosselin CM (1990) Stiffness mapping for parallel manipulator. *IEEE Trans Robot Autom* 6(3):377–382
5. Huang TS, Blostein SD, Margerum EA (1986) Least-squares estimation of motion parameters from 3-D point correspondences. *IEEE Comput Vis Pattern Recognit* 5:24–26

# Research on CAD/CAM Integration Methods Based on the STL Model

Huiqun Zhou and Jianjun Wu

**Abstract** At present, data exchange between different CAD/CAM systems becomes an increasingly large issue for engineers and other technical personnel in enterprises. In this paper, in order to enable better integration of CAD/CAM systems applications, we put forward the CAD/CAM integration methods which are based on the STL model. The STL model is a generic interface for the current popular CAD/CAM systems; by means of analysis with the STL model, the integration methods for CAD/CAM have been accomplished, But also, the methods have been verified through examples that show that these methods are simple and practical.

**Keywords** STL model · CAD/CAM · Integration methods

## 1 Introduction

CAD/CAM integration refers to the organic combination of CAD/CAPP/CAM and other functions of the software, using a unified program to control and organize the extraction, transformation and sharing of the information function of the software, so as to achieve smooth flow of information and system coordination within the system operation. In general, a factory that applies only a kind of CAD/CAM software finds it difficult to meet the requirements; therefore data exchange between different software systems and modules has become an important problem. With the development of CAPP/CAE/CAM/CAD technology and the improvement of the degree of integration, data exchange between different systems is becoming more and more frequent, and the data transformation between different systems need to be solved urgently [1, 2].

---

H. Zhou (✉) · J. Wu  
The Key Laboratory of Contemporary Design and Integrated  
Manufacturing Technology, Northwestern Polytechnical University,  
Xi'an 710072, China  
e-mail: zhouhq@nwpu.edu.cn

In order to enable better integration of CAD/CAM systems applications, building a common channel is very important. The STL file is a physical interface protocol developed by the 3D SYSTEM Company in 1988 in the U.S.. In the rapid prototyping technology field, the STL file format has been widely used. The STL file to describe the 3D interpretation is unique. Most of the commonly-used CAD systems (such as that of Pro/E, Unigraphics, CATIA, SolidWorks, AutoCAD, I\_DEAS, CAXA, etc.) have a complex 3D solid model so that they can output to the STL model, and the STL model as the model of CAD data exchange has a strong versatility within the CAD/CAM system [1, 3].

This paper puts forward a kind of method for integrating different CAD systems and CAM systems for integrated applications. These methods use the STL model for the input and output and universal and simple data structures for CAD/CAM system. Through the introduction to the STL model, the introduction, analysis and consolidation, and feasibility has been proven.

## 2 STL Model and Its Error Correction

The format file of the STL model is a CAD data exchange file using a CAD model. It is widely used in the early stage between the CAD system and the rapid prototyping system data exchange. The STL file is obtained by the surface triangulation of the CAD solid or surface model, which is equivalent to the original CAD model, by using a polyhedral approximation of the space triangle. The file format is used to approximate the small-triangle-surface approximation of a 3D entity model, in which each triangle contains four data items. By the method of vectors, three vertices of the triangle-to-triangle model and external components, the normal vector by the entity's internal to the external, the three-point order, and the normal vector of the vertex must conform to the right-hand rule. The number of small triangles has a direct influence on the accuracy of the approximation. The larger the number of triangles, the higher is the accuracy; otherwise, vice versa. The STL file format documentation entails more, which is not repeated here.

When the CAD model is completed in a CAD/CAM system, the output and input of the STL file are required for other applications in different CAD/CAM systems. At present, almost all of the commercial CAD/CAM systems have an STL-file input and output data interface, and the operation and control are very convenient. In the STL file output, according to the complexity of the model and the required precision, the output accuracy of the STL file can be selected.

The correct STL data model is the key to the integration of CAD/CAM system. But in the STL file, most possess different degrees of error. Although the data structure of STL model is simple (i.e., the emissions data follows certain rules, the information on the solid surface is easy to read), the topology information is contained in the STL file and it is difficult to ensure the correctness of each adjacent triangle. After systematic analysis and induction, the common errors in the STL file are shown in Fig. 1 (cracks, voids, normal vector error, overlap, etc.) [4].

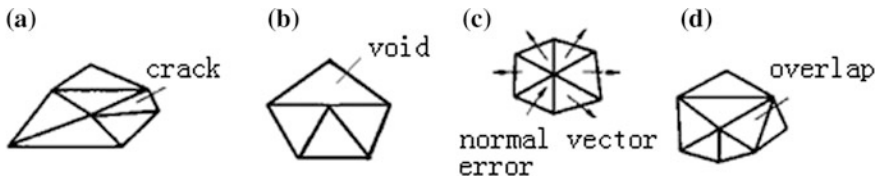


**Fig. 1** Common error graph of STL file. **a** Crack. **b** Void. **c** Normal vector error. **d** Overlap

The error correction and the integration of the process steps can be expressed as follows:

```

Procedure:
Begin
{
While do{
    Step1: Read STL file data;
    Step2 :{If (There is no common of several neighboring triangles )
            ((The STL file has cracks, heavy segment and then divided into several small triangle, fill the cracks) )
            Else
    Step3 :{ If (A vertex of a triangle on the edge of a neighboring triangle.)
            (The STL file is empty, the quadrilateral into two triangles, such that the vertices into two new vertex of a triangle.) }
            Else
    Step4 :{If (By judging the vector triangle according to the right-hand rule, if the error will be corrected)}
            Else
    Step5 :{If (A vertex of a triangle on the adjacent triangle overlap part, to remove a patch, that is, overlap and mesh deletion, also, re meshing) }
            Else
    Step6: ...}
        } End.
}
    
```

### 3 Based on the STL Model of the Integration Principle

The development trend of the machinery manufacturing industry is internationalization and globalization, but the data format used by different enterprises is usually different. If the data is used both in the design and manufacturing of different formats, it must be converted into the same kind of data exchange format for 3D model reconstruction or repair, and then manufactured. Although CAM can be completed by using the DXF or STEP file, after data is transformed, it is easy to lose and so on. So it cannot realize the seamless link of the converted data. On this basis, this paper proposes that, using the STL model file for the integration of a

CAD/CAM channel, the integration between different software systems can be realized.

Data conversion using STL file can be expressed as follows:

```

Procedure:
Begin {
While do {
  Step1: Call the 3D CAD system modeling (e.g. NX UG system) ;
  Step2: Storage CAD model map into STL model data format;
  Step3: Call other CAM systems (such as Pro/E system, must be different
from Step1) ;
  Step4: In the CAM system, a model of data format of STL model is pro-
posed.;
  Step5: Realization of the CAD model of NC machining and other CAM
functions.
} End.

```

## 4 NC Machining Based on STL Model

### 4.1 STL Models Section

In CAD/CAM system when conversion has been completed through the STL model, you can slice of STL model. The specific steps that can be expressed as follows:

```

Procedure:
Begin
{
While do {
  Step1: Determines the direction of STL model hierarchy (usually along
the Z axis);
  Step2: Find the intersection of stratification plane and the STL models;
  If {(Intersection points of the triangle vertices, Vertex coordinates direct-
ly record)
  Else
  If (The intersection on two sides of a triangle, record the coordinates of
the two vertices)
  Else (Stratification plane and one side of the triangle coincide, simulta-
neous planar and linear equations, that is, we can obtain the intersection points,
and then the intersection point coordinate in the record to the list of data);
  Step3: According to the coordinates of the point size of the proceeds will
be sorted by computer programming. }
}
} End.

```

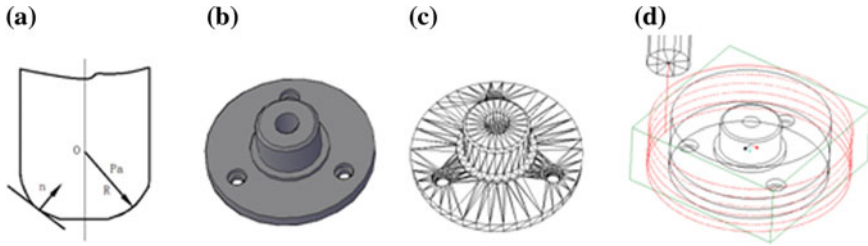


**Fig. 2** Calculation of the cutter location and the model of the numerical control machine. **a** Cutter drawing. **b** CAD model of part. **c** STL model of part. **d** Machine drawing

### 4.2 Calculation of Cutter-Contact Point and Position Point

In the NC machining process, the calculation of cutter location point is the core. And to calculate of the cutter location point, you must first calculate the cutter—contact points [5–8]. As shown in Fig. 2a, in the case of a ball—end cutter, from the cutting tool geometry can obtain the following equation:

$$P_a = P + R \times n \tag{1}$$

In the formula:  $P_a$  for cutter locations;  $P$  for the cutter—Contact Points;  $R$  is the radius of the cutter;  $n$  for the cutter—contact points of the Unit normal vector. After the contour curve of the STL model has been determined from Eq. (1), as can be seen, as long as you know the cutter—contact points, the cutter location points will be determined. Cutter—contact points must be along the contour curve of the STL model, so, as long as a given contour curve discretization step emerges from the points on the curve, the point is the cutter—contact point.

### 4.3 Method of NC Machining

To be implemented in the STL format files and data exchange between CAM, the STL format file needs to be a discrete process. From the foregoing it is evident that, to the extent that the original CAD model is an approximate representation of STL model, there exists a problem of accuracy loss in the model. After the conversion of different CAD/CAM systems in the process, especially in the machining of freeform surfaces, in order to ensure the machining accuracy of the grid, usually by dense triangular mesh subdivision, while also taking into account the line of intersection point of intersection of lines obtained in each triangle in the span is not the same.

In view of above analysis, based on the STL model of NC machining process, the steps can be expressed as follows:

```

Procedure:
Begin
{
While do {
    Step1: The CAD model into an STL model, and then slicing STL model;
    Step2: After slicing, the triangle of STL model and fractal dimension of in-
tersection layout handling after the connection;
    Step3: Of closed contour curve of a given step, reverse out of the points on
the curve, the point is the cutter - contact points;
    Step4: According to the geometry of the tool, first calculate cutter - contact
point, and then calculating the cutter location points。 }
} End.

```

## 5 Instances of the Implementing

Based on different CAD/CAM system, the paper completed a three—dimensional CAD model into an STL model of the entire process. Then, based on the NC machining of STL model, the integration of CAD/CAM application process has been realized.

Specific process can be expressed as follows:

```

Procedure:
Begin
{
While do{
    Step1: Call the AutoCAD software system;
    Step2: Complete CAD three - dimensional entity model;
    Step3: The CAD model into an STL Model Output;
    Step4: Call Pro/E software systems, input STL model;
    Step5: The model of NC programming。 }
}End.

```

Figure 2b is an image created with AutoCAD software system of CAD of three—dimensional solid models of parts. Figure 2c is the STL model created by the number of triangles described, shown in the CAXA system of the model for the CAD model into STL model. Figure 2d shows the outline of the NC machining of STL model data as sent to the Pro/E software system in the demonstration of the process graph. Examples show that, using the STL model integration interface file for CAD/CAM, the process is simple, practical and reliable. It is also suitable for different CAD systems and CAM systems producing many integrated applications.

## 6 Conclusion

The data exchange between different CAD/CAM systems is a problem that must be faced by the engineering and technical personnel of different enterprises and even within the same enterprise. Because the file format of STL model is clear, and it does not need the complex CAD system support, the model is easy to repair, and it has become the standard of data exchange between different CAD/CAM systems. With the expansion of the market of STL model, most mainstream CAM software can already read into the STL format, or even dedicated CAM software based on STL format file. On this basis, this paper presents a CAD/CAM integrated method based on the STL model. The STL model is a general interface of the current popular CAD/CAM system that, by analyzing the model and process integration and multi to multi schemes, can yield different CAD/CAM systems. Here, through an example, we verify the feasibility of this scheme. The result shows that the method is simple and practical. With the continuous development of the STL format, the defects of the STL model file will be completely solved, and it will become more and more adopted as a common interface for a CAD/CAM system.

## References

1. Zhu H, Fu J (2011) Data transformation from STL to parasolid. *Comput Integr Manuf Sys* 17 (1):117–124
2. Pang A, Joneja A, Lam DCC et al (2001) A CAD/CAM system for process planning and optimization in LOM (laminated object manufacturing). *IIE Trans* 33(4):345–355
3. Sun Y, Liu W, Wang Y (2002) Research on the algorithm of NC tool path calculation for triangular surface machining. *Chin J Mech Eng* 38(10):50–53 (in Chinese)
4. Nagy MS, Mátyási G (2003) Analysis of STL files. *Math Comput Model* 38:945–960
5. Zhao P, Sun H (2009) NC machining path planning on STL file. *Mach Des Manuf* 12(12):169–170 (in Chinese)
6. Qu X, Stucker B (2003) A 3D surface offset method for STL-format models. *Rapid Prototyp J* 9 (3):133–141
7. Zeng X, Liu J, Yan G (2002) Tool path generation based on STL data model. *J Eng Graph* 11 (1):8–14 (in Chinese)
8. Kim DS, Jun CS, Park SY (2005) Tool path generation for clean-up machining by a curve-based approach. *Comput Aided Des* 37(9):967–973



# Investigation on the Characteristics of DC Air Discharge at Low Pressure Based on Hydrodynamics and Chemistry Model

Xing-hua Liu, Xue-Feng Sun, Ri-chang Xian, Yu-Feng Chen  
and Peng Yu

**Abstract** Firstly, a presented model of hydrodynamics and chemistry which introduces an improved nonlocal collisionless electron heat flux and photoionization effect is used to simulate the low-pressure air discharge of DC. The plasma model is developed by COMSOL Multiphysics with plasma model and takes into account 12 species and 26 reactions which can accurately reflect the air discharge. Then, the characteristics and mechanism of air discharge under low pressure are analyzed. And this simulation model is validated by comparison between the experimental results and results in the current literature. The results show that  $N_2^+$  and  $O_2^+$  are the dominant positive ions;  $N_2$  ionization reaction is always higher than  $O_2$  ionization reaction; the cathode sheath has the greatest electron temperature due to the Joule heating in strong electric field; the main electron energy loss of volume in low-pressure air discharge is produced by inelastic collision.

**Keywords** Low pressure · Air discharge · Plasma · Electron temperature · Ionization reaction

---

X. Liu · X.-F. Sun  
State Grid Zibo Power Supply Company, Zibo 255000, China  
e-mail: 167274738@qq.com

X.-F. Sun  
e-mail: 30280241@qq.com

R. Xian  
Shandong University of Technology, Zibo 255000, China

Y.-F. Chen · P. Yu (✉)  
State Grid Shandong Electric Power Research Institute, Jinan 250002, China  
e-mail: benben2229@hotmail.com

Y.-F. Chen  
e-mail: fengxjt@sina.com

## 1 Introduction

DC glow discharge is widely used in a variety of many industry fields for its advantages, for example, modifying industry, power generation, display panel industry, and thin-film deposition. The detail characterization of the glow discharge is important for the optimization of practical engineering [1]. Scientist have been researched out to characterize the mechanism of air discharge in detail using numerical modeling. However, computational simulation modeling of air discharge requires plasma chemical reaction that is capable of representing all important finite-rate chemistry effects in the nonequilibrium air plasma. Owing to the complexity, rapid transient behavior, and randomness, the physical mechanism associated with the kinetics of air discharge processes is still not well understood [2]. In the research for numerical study of air discharge, the single theories and models are often used to simulate the microcosmic physical process of air discharge [3]. The method of this paper overcomes these disadvantages and is more suitable for DC air discharge at low pressure.

## 2 Computational Model

### 2.1 Governing Equations

The balance governing equation for the electron is [4]:

$$\frac{\partial n_e}{\partial t} + \nabla \cdot \vec{\Gamma}_e = R_e + S_{ph} \quad (1)$$

where  $n_e$  denotes the electron number density;  $R_e$  is the electron production rate in the chemical reactions included in the model;  $S_{ph}$  is the photoionization rate;  $\vec{\Gamma}_e$  is the electron density flux calculated by the Eq. (2):

$$\vec{\Gamma}_e = -(\mu_e \cdot \nabla \phi)m_e - D_e \nabla m_e, \quad (2)$$

where  $m_e$  is the electron mobility;  $D_e$  is the electron diffusion coefficient.

The complete electron energy conservation equation is given by the following equation [5]

$$\begin{aligned} & \frac{3}{2} \frac{\partial (k_B n_e T_e)}{\partial t} + \nabla \cdot \left( \frac{5}{2} k_B T_e \vec{\Gamma}_e \right) + \nabla q_e \\ & = \vec{j}_e \cdot \vec{E} - n_e \sum_k n_k \eta_k - 2k_B n_e \frac{m_e}{M_k} (T_e - T) \nu_{e,n} \end{aligned} \quad (3)$$

where  $T_e$  is the electron temperature;  $n_k$  is the  $k$  species particle number density;  $\eta_k$  is the rate coefficient for energy loss for collisions of electron with species  $k$ ;  $m_e$  is the mass of the electron; and  $M_k$  is the heavy species  $k$  mass.

To the heavy species (such as neutral species, positive ions, and negative ions), the multicomponent diffusion transport equations under the air discharge can be expressed as [6]:

$$\frac{\partial n_k}{\partial t} + (\vec{u} \cdot \nabla)n_k = \nabla \cdot \vec{j}_k + R_k + S_{\text{ph}(k=p,n)}, \quad (4)$$

where  $\vec{u}$  is the mass averaged fluid velocity vector;  $R_k$  is the species  $k$  change rate in the chemical reactions; and  $\vec{j}_k$  represents the diffusive flux vector.

The momentum equation of the all heavy species is the Eq. (5):

$$\frac{\partial m\vec{u}}{\partial t} + \nabla \cdot (m\vec{u}\vec{u}) = -\nabla p + \mu\nabla^2\vec{u} + \frac{\mu}{3}\nabla(\nabla\vec{u}) + \sum_k n_k\vec{F}_k, \quad (5)$$

where  $m$  is the dynamic viscosity and  $\vec{F}_k$  is the body force term action on species  $k$ .

The following equation is the Poisson's equation, and the calculated electric field of self-consistency can be obtained.

$$\nabla \cdot (\varepsilon_0\nabla\phi) = -e\left(\sum_i n_i - \sum_s n_s - n_e\right) \quad (6)$$

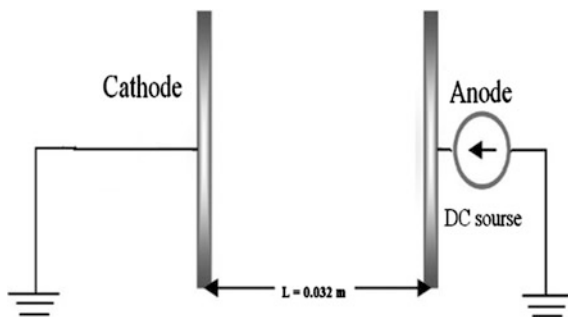
$$\vec{E} = -\nabla\phi, \quad (7)$$

where  $n_i$  is the density of the positive ion;  $n_n$  is the density of the negative ion; and  $\varepsilon_0$  is the vacuum permittivity.

## 2.2 Schematic of Modeling Geometry

Figure 1 shows a system model schematic of the parallel plate discharge. There are two electrodes that are separated from each other with a gap  $L = 0.032$  m: One electrode is grounded and the other electrode is driven with DC voltage  $V_0$ . The radius of two electrodes is 0.05 cm, and the gap between two electrodes is filled by air at low pressure. In the present work, the pressure in air discharge is fixed at 0.2 Torr or 0.6 Torr, and the gas temperature is assumed a constant value (300 K).

**Fig. 1** Schematic diagram for DC parallel plate for air discharge



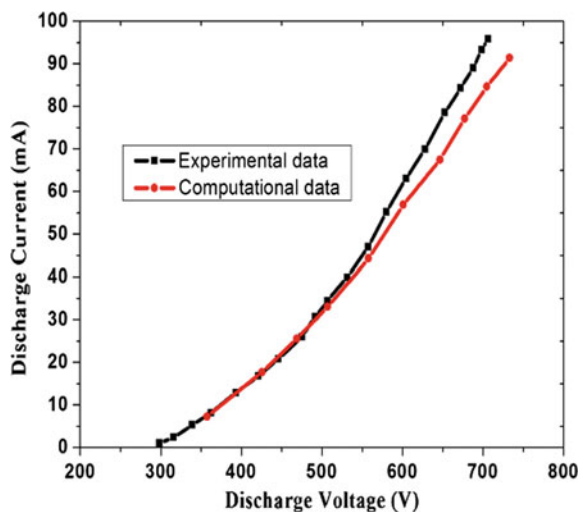
### 3 Results and Discussion

Figure 2 shows the comparison between computational and experimental discharge voltage–current (V-I) characteristics for DC air discharge with a 0.032-m inter-electrode gap.

Experimental data are chosen from reference. The computational data turn out to be right by contrasting the experimental data at low discharge voltage, and the measurement error is 2 % in the discharge. However, there is a slight discrepancy between computational and experimental data in higher discharge voltage region. A possible explanation for this discrepancy is the use of simple chemistry mechanism and the secondary electron emission coefficient which should be a variable at the cathode surface in fact.

The density of electron and positive ions along the axis of the air discharge are shown in Fig. 3.

**Fig. 2** The computational and experimental discharge current–voltage (I-V) characteristics



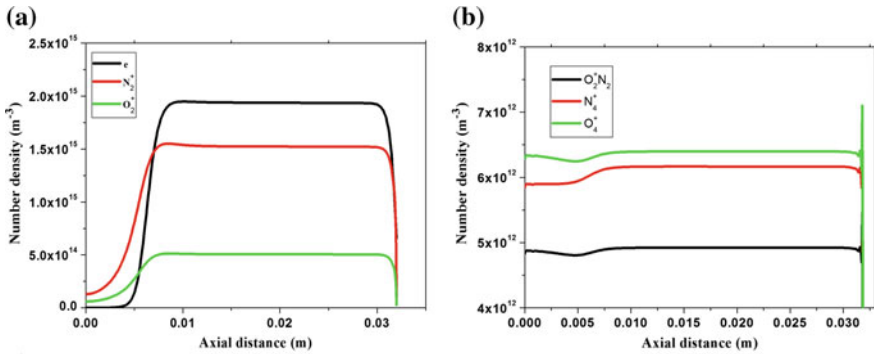
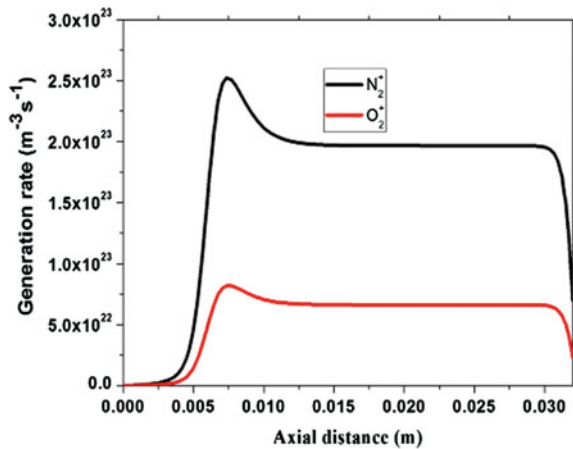


**Fig. 3** The charged species densities along the axial distance. Pressure  $P = 0.2$  Torr and applied voltage  $U = 600$  V. **a** Electron,  $N_2^+$  and  $O_2^+$  number density. **b**  $N_4^+$ ,  $O_4^+$  and  $O_2^+ N_2$  number density

**Fig. 4** The generation or destruction of  $N_2^+$  and  $O_2^+$

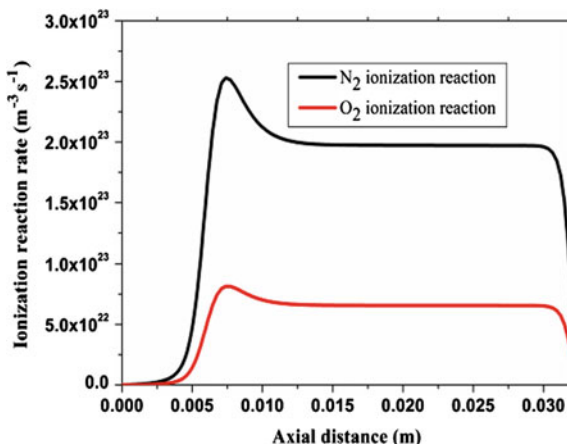


It can be concluded from Fig. 3a that the electron,  $N_2^+$  and  $O_2^+$  number density increase sharply to high value in cathode sheath and then kept almost constant value in the bulk plasma. The density profiles of  $N_4^+$ ,  $O_4^+$  and  $O_2^+ N_2$  are shown in Fig. 3b. Both these ions have lower density than the dominant ions  $N_2^+$  and  $O_2^+$  in the total plasma discharge process. The number density of  $O_2^+ N_2$  is about  $4.9 \times 10^{12} \text{ m}^{-3}$ , which is the minimum of positive ion, and it can be ignored contrasting with the other ionized species in the air discharge.

The contributions of the gas-phase reaction to the generation or destruction of  $N_2^+$  and  $O_2^+$  in the air discharge are shown in Fig. 4.

The generation rate of  $N_2^+$  is higher than the ionization rate of  $O_2^+$ . The important positive ion ( $N_2^+$  and  $O_2^+$ ) profiles are established by the combined effect of gas-phase plasma reactions, transport, and surface reactions in the air discharge.

**Fig. 5** The ionization reaction rate in the plasma model

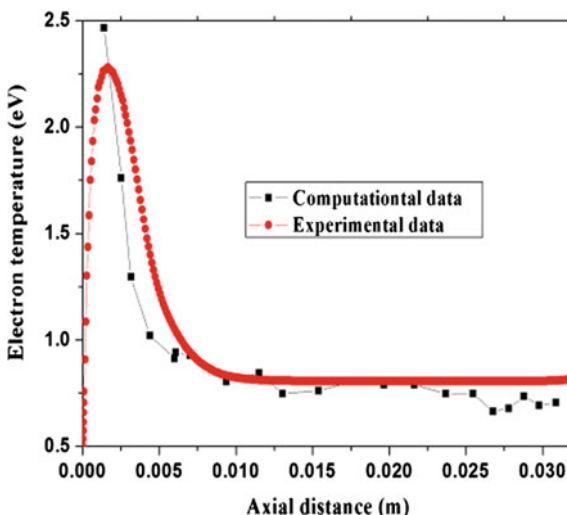


The spatial profile of the total ionization reaction rate is shown in Fig. 5.

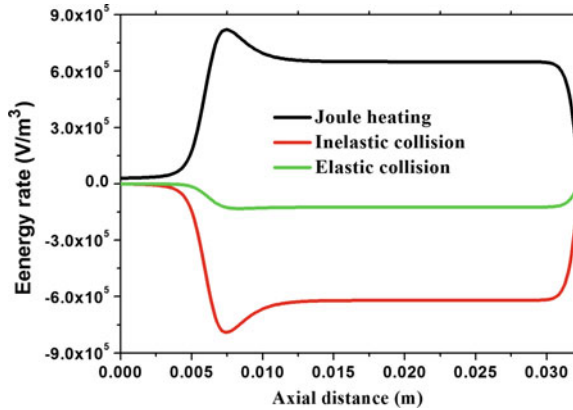
It is obvious that the maximum of ionization reaction rate occurs in the cathode sheath, because the electrons are strongly heated by high electric field and a large number of energetic electrons are generated. The  $\text{N}_2$  ionization reaction is always higher than  $\text{O}_2$  ionization reaction. Besides, the  $\text{N}_2^+$  is hard to generate neutral particles by reactions. This provides plenty of excited state nitrogen atoms ( $b^1\Pi$ ,  $b^1\Sigma_u^+$  and  $c_4^1\Sigma_u^+$ ). The excited state nitrogen atoms decay into neutral nitrogen molecules accompanied with radiation photons which are absorbed by oxygen molecules. Hence, the collision ionization intensified to the generation of photoionization. The photoionization in the air discharge under low pressure is rarely discussed in the current literatures.

Figure 6 shows the electron temperature distribution along the axis.

**Fig. 6** The computational and experimental electron temperature



**Fig. 7** The contribution of Joule heating, inelastic collision, and elastic collision to the electron energy



It can be seen that computational data turn out to be right by contrasting with experimental results. The peak electron temperature (2.28 eV) of computational results occurs in the cathode sheath ( $1.618 \times 10^{-3}$  m). The high electron temperature at the end of the cathode fall is because of Joule heating in high electric field. In addition, it could also be due to ionization reactions, which can lead to the production of energetic electrons in the cathode sheath. The major feature of electron temperature is approximately uniform in the bulk plasma. As electrons move toward the anode, the electron temperature decreases to much smaller value about 0.8 eV and keeps relative uniform electron energy in the bulk plasma. This is due to the energy loss of electron, which is caused by the electron collision with neutral species. The developed model is also validated by contrasting the computational with experimental electron temperature distribution.

It can be seen that in the air discharge, electron heating is caused by Joule heating which is mainly in the plasma interface region between the bulk plasma and cathode sheath in Fig. 7.

The main electron energy volumetric loss is caused by inelastic collision, and the contribution of elastic collision is small compared with inelastic collision, so the mechanism of electron energy under low-pressure air discharge is different to that of atmospheric pressure air discharge in which elastic collision cannot be ignored compared with inelastic collision.

## 4 Conclusions

The nonlocal collisionless electron heat flux and photoionization effect are introduced 12 species and 26 reactions which can accurately reflect the air discharge are took into account in the model. The plasma model is validated by contrasting with the experimental results in the current literature. The predicted discharge current–voltage characteristics and spatial profiles of electron temperature turn out to be

right in comparison with the experimental results in the literature. For low-pressure air discharge,  $N_2^+$  and  $O_2^+$  are the dominant positive ions, and  $N_2^+$  is much more than  $O_2^+$  about an order of magnitude.  $N_2$  ionization reaction is always higher than  $O_2$  ionization reaction. Electron heating is caused by Joule heating, and the main electron energy loss of volume in low-pressure air discharge is produced by inelastic collision, while inelastic collision can be ignored in atmosphere discharge. The air plasma kinetics behavior is suitable to predict by the presented computational model.

**Acknowledgements** This work is supported by the Major State Basic Research Development Program of China (973 Program) (No. 2011CB209401) and the scientific research fund of State Grid Shandong Electric Power Research Institute and the Foundation for Outstanding Young Scientist in Shandong Province.

## References

1. Nahomy J, Ferreira CM, Gordiets B et al (1995) Electron-driven processes in high-pressure plasmas. *J Phys D Appl Phys* 28:738
2. Cvelbar U, Pejovnik S, Mozetic M et al (2003) Increased surface roughness by oxygen plasma treatment of graphite/polymer composite. *Appl Surf Sci* 210:255–261
3. Belmonte T, Pintassilgo C, Czerwiec T et al (2005) Oxygen plasma surface interaction in treatments of polyolefins. *Surf Coat Technol* 200:26–30
4. Nagatsu M, Terashita F, Nonaka H et al (2005) Effects of oxygen radicals in low-pressure surface-wave plasma on sterilization. *Appl Phys Lett* 86:211502
5. Rossi F, Kylian O, Hasiwa M (2006) Decontamination of surfaces by low pressure plasma discharges. *Plasma Process Polym* 3:431–442
6. Niedre MJ, Yu CS, Patterson MS et al (2005) Singlet oxygen luminescence as an in vivo photodynamic therapy dose metric: validation in normal mouse skin with topical amino-levulinic acid. *Br J Cancer* 92:298–304



# Research on IOT Technology Applied to Intelligent Agriculture

Juntao Li, Weihua Gu and Hang Yuan

**Abstract** Internet of Things (IOT) technology has become one of the leading subjects of scientific research field because of its potential application. This paper briefly introduced the introduction of IOT technology and agriculture IOT technology. Agriculture development in China is transiting from traditional to modernization, and equipment with modern material conditions is urgently needed. In the first section, it describes the concept of IOT and agriculture of things, as well as some of the key technologies of agriculture networking applications, namely (a) agricultural sensor technology; (b) wireless transmission technology; (c) RFID technology; (d) agricultural product quality security technologies; (e) intelligent irrigation technology; and (f) precision seeding and spraying techniques. The second part introduces the development status of IOT technology in intelligent agriculture, and the use of resources in agriculture, agro-ecological monitoring of the environment, and agricultural production of fine management, application analysis and safety of agricultural traceability aspects. With the development and progress of science and technology, information technology in agriculture has become increasingly important, especially in recent years. With the development of new networking technologies, intelligent agriculture also shows a broad development prospect. The third part analyzes the intelligent microirrigation control technology. Followed by a discussion of the three aspects of IOT technology deficiencies in the existing practical applications, namely industry standards, information integration and business model aspects of the problem, and accordingly at the macro we give three suggestions. The last part gives the prospects of intelligent agriculture and its shift to wisdom of agriculture.

**Keywords** Internet of Things · Intelligent agriculture · Intelligent monitoring · Intelligent control · Microirrigation technology

---

J. Li (✉) · W. Gu · H. Yuan  
School of Beijing Wuzi University, Tongzhou 101149, China  
e-mail: ljletter@126.com

© Springer-Verlag Berlin Heidelberg 2016  
B. Huang and Y. Yao (eds.), *Proceedings of the 5th International Conference on Electrical Engineering and Automatic Control*, Lecture Notes in Electrical Engineering 367, DOI 10.1007/978-3-662-48768-6\_136

1217

## 1 Introduction

With the continuous development of times and information technology, networking technology is the second industry tide again. The easiest thing to understand Internet of Things (IOT) technology is the “substance and substance of interconnected Internet,” and any two objects can be connected via IOT technology, which combines sensor technology, embedded computer technology, distributed information processing technology, modern networking, and wireless communication technologies, through all kinds of microsensors integrated collaborative real-time monitoring and collecting information from various measured object, the information is sent wirelessly, and ad hoc multihop networks way transmitted to the user terminal, in order to achieve the physical, computer and human society connectivity world [1].

Agricultural IOT technology is used to combine variety of sensor organizations to form the sensor network, through which we can collect farmland sensor information and real-time analysis of the results transmitted to farmers to enable them to make the most profitable decisions [2].

## 2 Key Technology of Agriculture Things

### 2.1 IOT and Agricultural IOT

IOT is based on Internet, mobile communication, and other communication networks, through intelligent sensors, radio frequency identification, infrared sensors, global positioning systems, laser scanners, remote sensing, etc. Information sensing equipment and systems, in accordance with the agreed protocol for the needs of different applications, and all the physical objects can be individually addressable and interconnected to achieve a comprehensive perception, reliable transmission and intelligent processing, building a things and things Internet intelligent information Service System.

Agricultural IOT is the specific application of IOT technology in agricultural production, operation, management and services, using various types of sensors, RFID, visual perception collection terminals, and other equipment, extensively collecting field planting, horticulture, livestock and poultry, aquatic products' site information breeding, agricultural logistics, and other areas [3].

Currently, IOT applications are mainly in the following mature technologies:

- (a) Agricultural sensor technology. Agricultural products have been covered by many categories of sensors such as soil sensors, water sensors, meteorological sensors, heavy metal detection sensors, biosensors, gas sensors, and so on.

- (b) Radio transmission technology. ZigBee wireless sensor networks can achieve self-organizing wireless data transmission, which has been widely applied in large-scale farming.
- (c) RFID technology. It is widely used in animal identification, which can be performed on animals to achieve intelligent recognizing, positioning, tracking, monitoring, traceability, and management.
- (d) Technical quality safety of agricultural products. In the agricultural “production–circulation–sales” industrial chain, recording and monitoring the chain can realize the whole process of regulation.
- (e) Intelligent irrigation technology. Relying on satellite positioning network and “shallow wells underground cables + field + automatic irrigation system pipe” technology, it can collect irrigation water, electricity, irrigation, and time data to achieve automation of farmland irrigation and through a comprehensive analysis of information technology software to guide irrigation.
- (f) Precision seeding and spraying techniques. Relying on technology combined with GPS navigation technology, variable rate fertilization, and seeding technology, it can achieve uniform implementation of the planting, spraying, and improving the utilization of seeds, pesticides, and so on.

## ***2.2 IOT Technology in Intelligent Agriculture***

Intelligent agriculture refers to a high-tech artificial intelligence technology. The key technologies involved include detection, embedded, and communication technology. Intelligent farming system covers natural parameters that affect agricultural production in the acquisition to use computer technology for reasoning and parametric analyzing and ultimately guiding the management of the entire production chain of agricultural production through agricultural expert systems.

# **3 IOT Technology’s Development Status in Intelligent Agriculture and Its Application Analysis**

## ***3.1 Development Status***

Over the past decades, many foreign countries have developed some demonstrations, showing networking technology in agriculture, and application of this series is forming a good industrialization model, which promotes IOT technology into agricultural product circulation, resource use, and agricultural production.

### **3.2 *Its Application in Intelligent Agriculture***

(a) IOT technology in the utilization of agricultural resources

With the continuous development of networking technology, some developed countries have collected national land using information through satellite monitoring and then put the collected information to a series of analysis and ultimately achieve the overall planning and management of agriculture.

(b) IOT technology in agricultural ecological environment monitoring

Now, almost every country has attached great importance to security of agricultural protection. The USA has established a nationwide agricultural information platform. China has established the agricultural environment network monitoring system, implementing agricultural applications monitoring demonstrations, achieving the atmospheric sulfur, nitrogen dioxide, water temperature, pH, conductivity and dissolved oxygen in real-time monitoring.

(c) IOT technology in produce sophisticated management of agriculture

Through the combination of measures and information on agricultural production of high-tech applications, we can achieve precision agriculture production management.

(d) IOT technology in agricultural product safety traceability

Now, more and more people are concerned about food safety issues of agricultural products. Canada and Japan can trace back links, China has also developed to improve the safety of agricultural product traceability system for agricultural purposes, and we have succeeded in Shanghai, Beijing, Guangzhou, and Nanjing.

## **4 Technical Analysis of Intelligent Monitoring and Control of Microirrigation**

China's agricultural irrigation water consumption accounts for more than 70 % of the national economy of water, and farmland irrigation water inefficiency and wastewater problem is widespread. Therefore, the development of agricultural water-saving irrigation technology, especially intelligent microirrigation control technology, is very urgent [4]. Intelligent monitoring and control of microirrigation technology mainly include the following two aspects: first, access to information involved and second, in intelligent control, through which we can achieve intelligent irrigation according to microirrigation crop water demand [5].

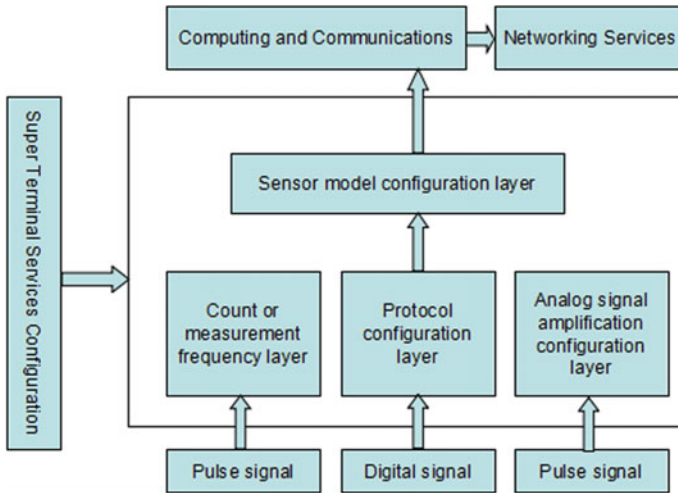


Fig. 1 Information collection node platform software architecture diagram

### 4.1 Access to Intelligent Information Technology

Sensor nodes configured information collection are mainly agricultural environment and soil information sensors. Sampling values can be calculated by the sensor sensing model to get the actual value. The transformation model can configure directly acquisition node, which can easily access the platform through the acquisition node configuration software. The main structure node platform software is shown in Fig. 1.

Access to data in the monitored region and the remote site can be divided into two ways. When performing the initial configuration and on-site maintenance tasks, you need on-site commissioning of the system, and researchers can directly query network data content through PDA [6].

### 4.2 Intelligent Control Technology

The main function of intelligent control technology are in environmental, fertilizer and water management and pest control. In summary, the agricultural production of intelligent control includes automatic irrigation, fertilizer control, automatic spraying to control greenhouse environment, and intelligent control. Several different control modes are from information to data processing and then to decision-making system, which issues commands to adjust the control command.

IOT backend control system considers PLC programmable controller as the core control mode, which mainly analogs signal output, the frequency of the signal

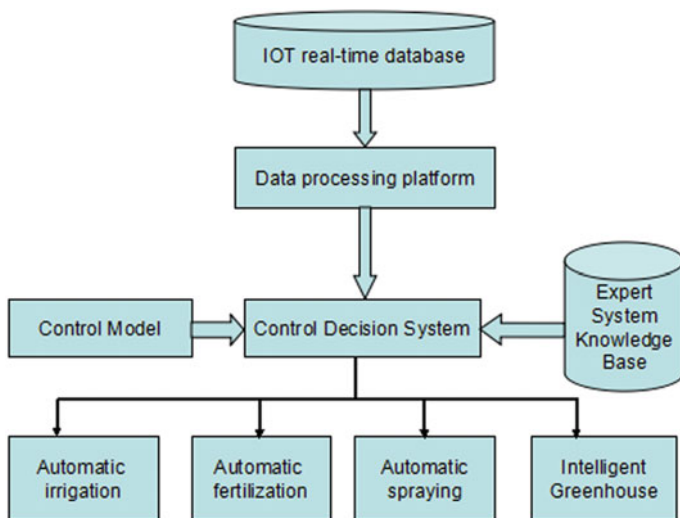


Fig. 2 Control system hardware architecture

output, PWM wave signal output and switch output to achieve agricultural electrification equipment control. Derived by the PLC program control, PLC control terminal has two, namely the control cabinet industrial touch, which can control running of the entire system. Further, the computer and the communication control cabinet may be wired communication or wireless communication. The choice of the communication means conditions by the actual application [7]. Usually, the frame mode control system is shown in Fig. 2.

Control system is based on real-time information collected to determine the comprehensive analysis of different models, which also can be introduced as control strategy expert system knowledge [8].

## 5 Inadequate and Recommendations of Existing Practical Application

Agriculture IOT has made some advanced experience in the perception of agricultural, data transmission, and intelligent processing technology, which also achieves some typical applications in monitoring and utilization of agricultural resources, ecological environment monitoring, product safety traceability, fine management of agricultural production, and agricultural cloud service field implements.

### **5.1 Problems of IOT Technology in Intelligent Agriculture**

First, the industry standards. Agriculture IOT's building needs to use all kinds of sensors to collect crop information, and then making the management platform for real-time data transmission by monitoring the farm environment, but in terms of information collection and transmission, platform interface and human-computer interaction interface lack uniform technical standards, then intelligent IOT technology promotion and application in agriculture are limited.

Second, information integration problems. During the growth of crops, it will collect information about a variety of crops, which will generate a lot of data and which must be stored, leading to a lot of disk space to be wasted. Therefore, we must reduce storage space by improving the storage algorithm, which is the only way to make IOT technology in intelligent agriculture popularity.

Third, the business model problem. Currently, our agricultural business model things include government-supported demonstration projects, networking company's demonstration projects, and state-owned large-scale agricultural projects. However, there are many disadvantages in these three methods such as high cost and insufficient chain members.

### **5.2 Recommendations**

In order to make IOT technology better used in intelligent agriculture, we give the following recommendations:

- (a) Ensure the transmission of information between various departments fluently;
- (b) Strengthen the administrative system and unify national standard industry equipment;
- (c) Build a more rational business model.

## **6 Summary**

Based on the analysis above, we should encourage agricultural scientists and IT personnel to exchanges ideas, especially those who not only understand planting but also understand IT to bring innovation to jointly promote the modernization of farming, which can improve agricultural production management and management information level, promoting agricultural production changes, achieving the goal of energy saving and environmental protection, and increasing production. Through intelligent analysis and management, farmers more clearly understand the current range of agricultural soils and other environmental information farmland and know which crops are suitable for cultivation in that current state. Meantime, we will see

the following scenario: Farmers do not toil in the fields under the hot weather, and they can directly manipulate on computer, such as a cell phone or some intelligent terminals, to realize watering, plowing, sowing, harvesting, and a series of farm labor and then easily finish the heavy farmwork. We should seize the opportunity to actively explore the development direction of things, and binding sites of modern agriculture, the development of sophisticated agriculture, IOT technology is more widely used in China's modern agriculture, which lays a solid foundation for the second and tertiary industries development. Overall, with the continued rapid development of computer, network, and microelectronic technology, agriculture IOT in information perceiving will be more intelligent, will be more interconnected in information transmission, also will become more flexible and wisdom in the information services, and be more rapid and reliable in terms of information processing.

## References

1. Cai B, Ma Y, Rong Q, Dayton W, Zhao Y, Ma B, Yuan C (2013) Intelligent application-oriented research in agriculture things. *J Mod Agric Sci Technol* 14:337–339
2. Guan J (2010) IOT technology in intelligent agriculture. *J Commun Manage Technol* 03:24–42
3. Peng Z (2014) Application of IOT technology in intelligent agriculture. *J Changchun Norm Univ* 02:59–60
4. Li J, Guo J, Zhu C, Nie P (2014) Application of intelligent monitoring and control of micro-irrigation technology in the cultivation of blueberries facility. *J Chin Agric Chem News* 35(2):250–253
5. Shen D (2012) Based on Wi-Fi greenhouses monitoring and control system. *J Chin Agric Mech* 1:162–165
6. Xie F, Qiao Y (2011) Prospects analysis of IOT technology in the field of biomass energy sources. *J Ecol Econ* 4:109–111
7. Dong Y, Zhu Y (2010) Development of Zhejiang agricultural information technology. *J Zhejiang Agric Sci* 5:689–695
8. Jiang C, Xu Z (2010) Remote monitoring of agricultural information system design and implementation. *J Agric Netw Inf* 11:40–43



# Effective FPGA-Based Enhancement of Quantitative Frequent Itemset Mining

Xiaoqi Gu, Yongxin Zhu, Meikang Qiu, Shengyan Zhou  
and Chaojun Wang

**Abstract** Frequent itemset mining (FIM) algorithms are widely used to discover common patterns in large-scale data sets. In conventional CPU-based systems, mining algorithms, which are usually data and memory intensive, often lead to critical power and latency issues growing even worse with a larger scale of data sets. Having identified the pipelining workflow behind the logic of frequent itemset mining, we propose a quantitative mining algorithm named Q-Bit-AssoRule and further design a pipelined FPGA-based implementation of Q-Bit-AssoRule algorithm to accelerate frequent itemset mining processing, achieving better performance, throughput, scalability as well as less hardware cost. Our evaluation result shows that our implementation outperforms other hardware approaches in terms of clock frequency and throughput.

**Keywords** Frequent itemset mining · Data mining · FPGA · Throughput

## 1 Introduction

Nowadays, the human society has been transformed into digitalized modalities represented by rich information in the form of big data. The rapidly increasing size of data requires efficient approaches to speed up data mining algorithms. Two possible accelerators, FPGAs and GPUs, can both achieve better performance than

---

X. Gu (✉) · Y. Zhu · S. Zhou · C. Wang  
School of Microelectronics, Shanghai Jiaotong University,  
Shanghai 200240, China  
e-mail: guxiaoqi@sjtu.edu.cn

M. Qiu  
Department of Computer Science, Pace University, 10038  
New York, NY, USA

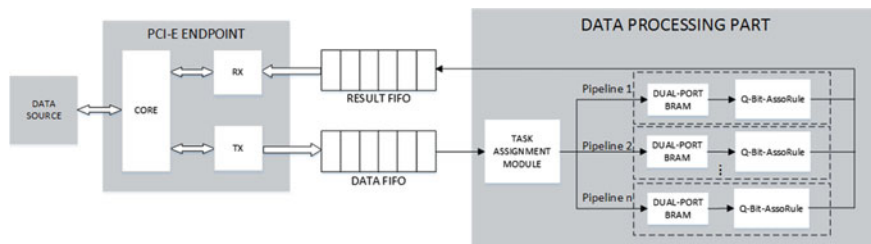


**Fig. 1** PCI-E-based streaming architecture

CPUs by invoking parallel computing resources. Considering the flexibility and low overhead provided by FPGAs, we use FPGAs to accelerate frequent itemset mining and make some improvement on FIM algorithm to make it more suitable for hardware implementation.

Some efforts into hardware-based accelerators for other FIM algorithms have been made in recent years. Systolic array architecture was employed in [1, 2] to implement Apriori algorithm [3] and in [4] to accelerate FP-growth [5]. But the repeatedly scan of database due to restriction of algorithms and low memory bandwidth within FPGAs become the bottleneck of these implementations. So we focus on improvement of algorithm and increase throughput of hardware design.

In this paper, we proposed a Q-Bit-AssoRule algorithm by applying Bit-AssoRule algorithm [6] to quantitative frequent itemset mining. We further implement a highly pipelined architecture including a set of parallel data processing units shown in Fig. 1, which achieves high clock frequency and throughput.

## 2 Q-Bit-AssoRule Algorithm

In FIM algorithms, a record in the database is called a transaction. Each transaction is composed of several items, named attributes. During data mining process, combinations of attributes which occurs commonly in the database are produced. This step is named as candidate generation. A candidate with  $k$  attributes is a  $k$ -candidate. The times the  $k$ -candidate occurs in database is called support count. Only when the support count is larger than predefined minimal support count, the  $k$ -candidate can be counted as a  $k$ -frequent item.

We proposed Quantitative Bit-AssoRule (Q-Bit-AssoRule) algorithm to extend Bit-AssoRule algorithm (a Boolean association rules mining algorithm) to quantitative association rules mining. In Boolean association rules mining, all the attributes are either 0 or 1 (0 represents this attribute does not exist in the transaction and 1 means the opposite). In quantitative association rules mining, an attribute can have more than two values to refine its level. Therefore, a large number of candidates will be produced under scenario of quantitative data mining. In Q-Bit-AssoRule, we

improve the condition of candidate joining to reduce the number of candidates. Bitset, a binary vector, is used to store each candidate's support count.

Q-Bit-AssoRule Algorithm
$L_1 = \{1\text{-frequent items}\}; j = \text{number of items in } L_1;$ For ( $k=2; L_{k-1} \neq \Phi; k++$ ) { For ( $i=1, i \leq j, i++$ ) { If (item number of $(L_{k-1} \cap L_{1,i}) \leq 1$ ) { // candidate joining $C_k = L_{k-1} \cup L_{1,i}$ // Generate new candidate Bitset of $C_k = (\text{Bitset of } L_{k-1}) \cap (\text{Bitset of } L_{1,i})$ // Count support } If (support count of $C_k \geq \text{minimal support count}$ ) $L_{k(\text{new})} = L_k \cup C_k$ // Add $C_k$ into $L_k$ } } Output = $\cup_k L_k$

### 3 Hardware Architecture

#### 3.1 PCI-E-Based Architecture

Traditional Apriori-like algorithms tend to download the whole database and candidate itemsets in the memory, which would cause a performance bottleneck. To avoid this, we divide the database into several parts and feed them into pipelines in FPGA. In our design, the data transmission interface between the data source (i.e., DDR or Internet) and FPGA accelerator is based on PCI-E, as shown in Fig. 1.

Data FIFO and result FIFO serve as buffers between PCI-E and pipelines. Task assignment module is designed to schedule data supply. When a pipeline finishes its work, Task assignment module will send a new pack of data to the dual-port BRAM of idle pipeline.

#### 3.2 Pipeline Implementation

The hardware architecture is shown in Fig. 2, consisting of a dual-port BRAM, a 1-frequent-item scheduler, a 1-candidate generator, a cluster of candidate generators (GEN cluster), and hash tables.

Each candidate has a bitset to store its support count. Each bit (0 or 1) corresponds to a transaction, indicating whether this candidate occurs in the transaction.

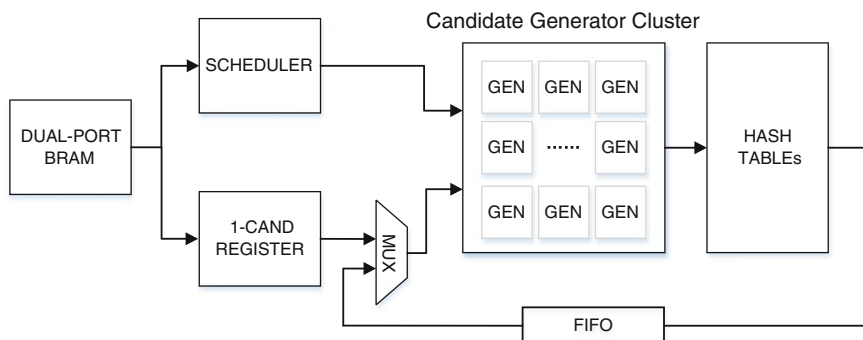


Fig. 2 Pipelined hardware architecture

To compute one candidate's support count, we just need to find number of '1's in its bitset. New candidate's bitset can be generated by doing AND operation to two jointed frequent items' bitsets. In our pipeline, data flows of bitsets and candidates are always synchronous.

The pipeline's working flow is as follows.

Firstly, digitalized transactions are transmitted to dual-port BRAM. 1-candidates along with their bitsets are produced in 1-CAND REGISTER. The 1-candidates whose support counts are equal or larger than minimal support count are marked as 1-frequent items and send to GEN cluster. Each GEN stores two 1-frequent items and their bitsets.

Secondly,  $(k + 1)$ -frequent items are generated in GEN cluster by joining 1-frequent items and  $k$ -frequent items.  $k$ -frequent items are chosen by the MUX. At the first round,  $k$ -frequent items are 1-frequent items coming from 1-CAND REGISTER. At later rounds,  $k$ -frequent items come from hash tables. The GEN units work dependently and generate new frequent items in parallel.

Thirdly, new frequent items are hashed to different hash tables to filter out the overlapped frequent items. The left frequent items flow into a FIFO and are fed to the next round of frequent items' generation and trimming until no more new frequent items generated.

### 3.3 Parallelization Method

We utilize multi-GEN units to generate frequent items in parallel and design a special hash mechanism to increase memory bandwidth and throughput. Figure 3 illustrates the frequent items' generation and hashing.

Suppose there are  $N$  1-candidates. They are allocated to  $M$  GEN units which are dependent from each other. We make  $M$  to be  $N/2$  for the following reason. Due to the inconsistent bandwidth between GEN clusters and hash tables, FIFOs made of

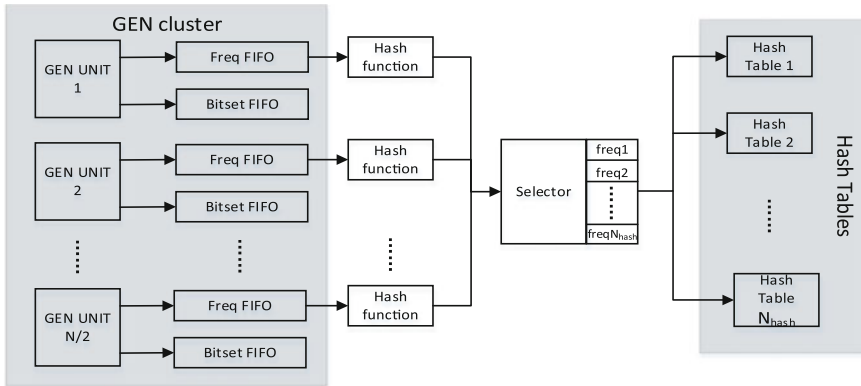


Fig. 3 Frequent items’ generation and hashing

dual-port RAMs are utilized to serve as buffers. If  $M$  is equal to  $N/2$ , one-GEN units can produce two frequent items per clock at most. A dual-port RAM guarantees these two frequent items can be written to FIFO simultaneously. By this way, the bandwidth of dual-port RAM can be taken full advantage of.

With  $N$  1-candidates, at most  $N$  new frequent items can be generated simultaneously,  $N/2$  of which are waiting to be hashed at one time. To avoid hash tables being the bottleneck, we divide the hash table into  $N_h$  parts. We also prepare  $N/2$  frequent items’ hash values in advance and pick out equal or less than  $N_h$  values that corresponds to different hash tables. As a result, frequent items can be sent to different hash tables in parallel. Throughput of hash tables increases to  $N_h$  per cycle.

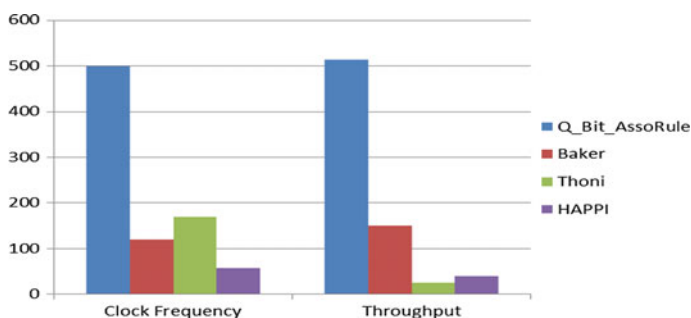
### 4 Experimental Results and Discussion

The highly pipelined hardware architecture is implemented in Verilog, simulated and synthesized in ISE 14.1 on target board Xilinx Virtex6 XC6VLX240T with speed of -1. The testing data were collected from the Cleveland Clinic Foundation (Cleveland database). The data set contains 303 transactions, each consists of 14 attributes. An attribute can be divided into 2 to 4 segments. Finally, candidates are represented with 35 bits while bitsets are represented as 64 bits. The clock rate of Q-Bit-AssoRule Frequent Itemset Mining pipeline is 489.7 MHz.

We utilized 4-lane-generation I PCI-E in DMA transmission mode of PCI-E x8 fabric. Bandwidth of each lane is 250 MB/s. Consequently, 1000 MB/s can be achieved for the total transmission bandwidth. To mining all the frequent itemsets in the testing data set, 2672 cycles are needed, not including the time of data transmission by PCI-E. The throughput of our design achieves 513 MB/s. According to the hardware utilization shown in Table 1, nearly 16 pipelines can be implemented on a FPGA board. So the bandwidth of PCI-E becomes the bottle

**Table 1** Resource utilization

	Registers	LUTs	LUT-FF	RAMs
PCI-E	1560	1895	0	8
Q-Bit-AssoRule	72	3154	71	75
Available	30,1440	15,0720	3155	1248
Utilization (%)	0.54	3.35	2.2	6.65

**Fig. 4** Comparison of other hardware in clock frequency and throughput

neck of the system. Fortunately, bandwidth of PCI-E can scale up to 16 lanes in PCI-E Generation III, namely 4000 MB/s in total. Throughput will also increase with expanding of PCI-E bandwidth.

As shown in Fig. 4, our design outperforms other hardware implementation of data mining algorithms in terms of clock frequency and throughput. We achieved a clock frequency of 489.7 MHz and throughput of 513 MB/s, much better than other Apriori-based hardware implementations, such as systolic array architecture proposed by Baker in [1], another similar design proposed by Thoni in [7], and HAPPI architecture in [4].

## 5 Conclusion

This paper proposed a quantitative frequent itemset mining algorithm Q-Bit-AssoRule based on Bit-AssoRule algorithm, which is suitable for hardware complementation. A pipelined FPGA-based hardware implementation was designed to accelerate the proposed data mining algorithm. We applied parallel processing methodology in the system to generate candidates and run them in hash tables to achieve high throughput. Dual-port FIFOs and multi-hash tables were utilized as data buffers to provide high memory bandwidth inside FPGA. Our hardware implementation outperformed previous hardware approaches in terms of clock rate and throughput.

**Acknowledgements** This work was supported in part by the National Science Foundation under Grants CNS-1457506, CNS-1359557, and CNS-1249223 (Prof. M. Qiu).

## References

1. Baker ZK et al (2005) Efficient hardware data mining with the Apriori algorithm on FPGAs. In: Proceedings of 13th annual IEEE symposium on FCCM
2. Sun S, Joseph Z (2011) Design and analysis of a reconfigurable platform for frequent pattern mining. *IEEE Trans Parallel Distrib Syst* 22:1497–1505
3. Agrawal R, Imielinski T, Swami A (1993) Mining association rules between sets of items in large databases. *J. ACM SIGMOD Record* 22(2):207–216
4. Ying Hsiang W, Jen Wei H, Ming Syan C (2008) Hardware-enhanced association rule mining with hashing and pipelining. *IEEE Trans Knowl Data Eng* 20:784–795
5. Jiawei H, Jian P, Yiwen Y (2000) Mining frequent patterns without candidate generation. *ACM SIGMOD Record* 29(2)
6. Lin TY et al (2003) A fast association rule algorithm based on bitmap and granular computing. *Fuzzy Syst (FUZZ'03)* 1:678–683
7. Thoni DW, Alfred S (2009) Novel strategies for hardware acceleration of frequent itemset mining with the apriori algorithm. In: Proceedings of IEEE field programmable logic and applications (FPL 2009), pp 489–492

# Image Classification Based on Deep Learning for Big Data of Power Grid

Jun Yin, Yongxin Zhu, Weiwei Shi, Yunru Qiu, Xingying Liu  
and Gehao Sheng

**Abstract** There are varieties of sensors and detection equipments in the power grid, generating large amount of data including pictures and videos captured by cameras and unmanned hovers. Automatic classifier is required to process massive number of images before accurate assessment of equipment status is made. As deep learning-based classifier has been used as a new effective tool in artificial intelligence domain recently, we construct an image classifier framework based on deep learning workflow on top of a deep learning engine CAFFE (convolutional architecture for fast feature embedding) to handle big data from power grid equipments. However, we identify a major drawback of CAFFE in our implementation that when the input training images stay in the same category in a continuous period, CAFFE's model is invalid regardless of the size of the training set. To bridge the gap, we introduce a preprocessing mechanism into deep learning-based classifier. This mechanism improves the adaptability of classifier to images of arbitrary size and sequence, and reduces the time to convergence of training the classifier. Experimental results show that our framework is able to classify images of different devices more accurately with much less training time.

---

J. Yin · Y. Zhu (✉) · W. Shi · X. Liu · G. Sheng  
School of Electronic Information and Electrical Engineering,  
Shanghai Jiao Tong University, Shanghai 200240, China  
e-mail: zhuyongxin@sjtu.edu.cn

J. Yin  
e-mail: yinjunideal@qq.com

W. Shi  
e-mail: iamweiweishi@gmail.com

X. Liu  
e-mail: michellezzz@sjtu.edu.cn

G. Sheng  
e-mail: shenghe@sjtu.edu.cn

Y. Qiu  
State Grid Weifang Power Supply Company, Weifang 261021  
Shandong, China  
e-mail: qyr0914@126.com



**Keywords** Big data · Classification · Convolution neural network · Deep learning

## 1 Introduction

As the widespread application of high-voltage transmission and transformation equipment, the protection of the power grid becomes increasingly important. To ensure the safety of transmission grid, a large number of sensors have been deployed in the power transmission system. But currently, the single-function sensor still cannot fully meet the demand of power grid security.

Existing evaluation systems usually use classification, regression, clustering, and other classic learning algorithms. These algorithms are mostly based on shallow neural network architecture. So they have limited ability of expression, given limited sample and calculation unit. For complex classification problems, their generalization capabilities are constrained. While deep learning (DL) algorithm can learn the essential feature of the data set from small amount of samples, it precedes other system for its multilayer network, which can achieve a distributed representation of input data and extract more essential characteristics of data.

In this paper, we propose a framework based on deep learning whose kernel is multilayer convolution neural network to classify images and other unstructured data from grid equipments. As DL usually requires intensive computation complexity, we will also explore acceleration with GPU (graphic processing unit), the impact on accuracy under different size of training set, the impact on the results under different learning speed, and comparison between shallow artificial neural networks and multilayer neural network based on CAFFE [1] platform.

## 2 Design and Implementation

Big data of grid contains roughly three categories: firstly, grid operation and equipment testing data; secondly, the data of power corporate marketing; and thirdly, the data of power enterprise management [2]. The traditional electricity production mainly produces structured data. In recent years, video, audio, and other unstructured data have been growing faster than structured data, and these unstructured data become major part of the big data of grid [3, 4].

### 2.1 Overall Design Based on CAFFE

Deep learning can process unstructured data. Combining statistical learning, support vector machine, relevance vector machine, association rule mining, and deep learning to deal with traditional data will play a complementary effect. In order to

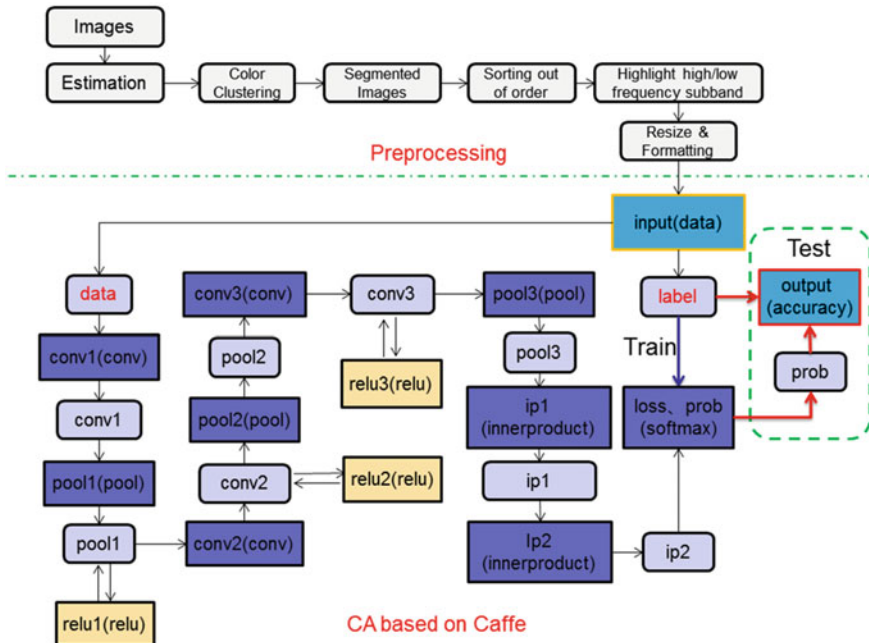


Fig. 1 Workflow and structure of CA

improve the computing speed and accuracy of image classification for large data of grid, we designed an improved structure based on Caffe. The workflow and convolutional architecture (CA) [1, 5] of this experiment are shown in Fig. 1.

The overall design can be divided into two parts: preprocessing and CA. Preprocess has six sections: estimation, color clustering, segmented images, sorting out of order, highlight high-/low-frequency subband, and resize and formatting. CA consists of an input layer, an output layer, and nine hidden layers. Hidden layers include convolution layer (conv), subsampling layer (pool), inner product layer, and softmax layer. The conv layer and innerproduct layer in hidden layer use Gaussian transform. Pool1 layer takes local maximum, whereas pool2 and pool3 layers use local averages. Relu layer is used for parameter calculation and adjustments. The output layer is used to compare the results of classification with the label and then calculates the recognition accuracy.

### 2.2 Implementation Details

In this experiment, 60,000 images are collected to form the data set from monitoring equipment in grid. These images fall in 10 categories, including transformers, towers, and switchgear. The input data of Caffe must be  $32 \times 32$  pixels. But images in our

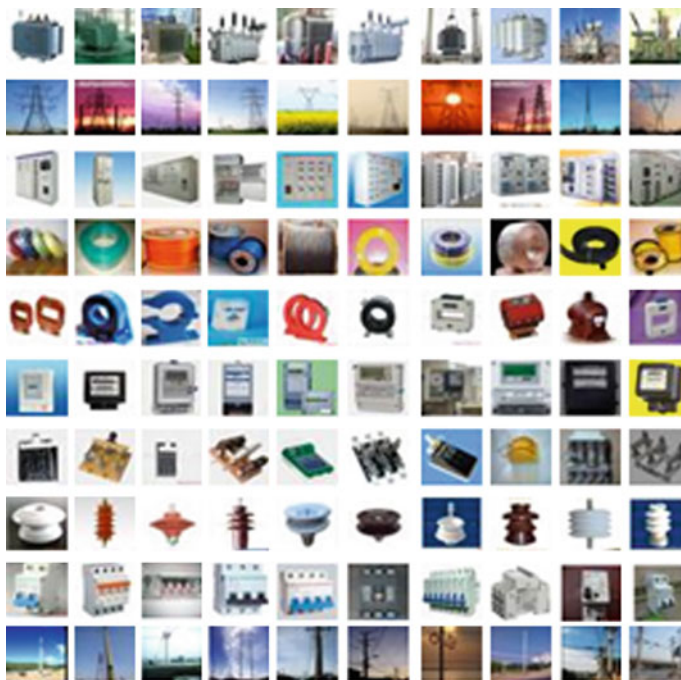


**Fig. 2** Images from each category

daily life usually do not fit CAFFE. So it is necessary to preprocess the images. For each category, 10 scaled images are selected randomly, as listed in Fig. 2.

After scaling, the images are transformed into appropriate data format. So they will be compatible with the format of input data of CAFFE. The customized format of data is shown in Fig. 3. Through a few tentative experiments, we found the best learning rate, and we also found that CAFFE has other deficiencies in the application. When the input training images are of the same category in a continuous period, the model is invalid regardless of the size of the training set.

Based on the above deficiencies of CAFFE, a preprocessing mechanism is designed. It allows the input images to be of arbitrary size and order. And the mechanism can change the format of the input data to fit CAFFE. The whole functional block diagram of the preprocessing mechanism is shown in Fig. 4.

As shown in Fig. 4, the mechanism first queues the images. Two buffers are applied to sort the data. The first one is used to store the latest 256 images need to be processed. Then, the controller will pick up appropriate data from the first buffer to form a sorted queue in the second buffer. The selection algorithm is to queue the images in ascending order of their category number (e.g., category 0, 1, 2, 3, 4, 5, 6, 7, 8, 9, 0, ...). If all of the 256 successive data in the first buffer do not belong to the category expected, then the controller will select an image in the next category. The steps mentioned above ensured that the data will not be of the same category in a

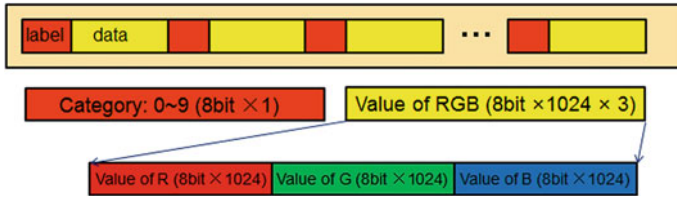


Fig. 3 Customized format of data

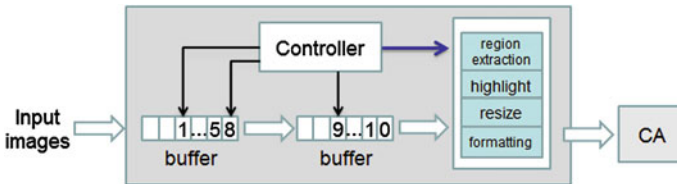


Fig. 4 Functional block diagram of the preprocessing mechanism

continuous period. At the end, the mechanism will do the following four steps to process the data sequentially: region extraction [6], highlight [7–9], resize, and formatting. The final products work as the input of CA.

### 3 Experimental Results and Discussion

The experimental platform of this paper is Intel i5 3470, 3.2 GHz, 8G memory, the operating system is Ubuntu12.04, and the graphics card is GTX650. In the process of experiment, one training set is composed of 50,000 pictures. And the training of all these images is regarded as one iteration.

#### 3.1 Comparison Between Shallow Network and Deep Learning

For comparison, traditional three-layer artificial neural network (ANN) is applied to train and analyze experimental data sets, and the experimental results of ANN and Deep Learning Networks (DLNs) are shown in Table 1.

Table 1 shows that the accuracy of ANN is only 45.14 % when the iteration number is 50. But as the iteration number reaches 5000, the accuracy converges to nearly 79 %. Besides, the convergence speed of traditional neural network is very slow. The accuracy is about only 70 % when the iteration number is almost 1000.

**Table 1** Comparison of image recognition accuracy between ANN and DLNs

Model	ANN					DLNs				
Iterations	50	500	1000	3000	5000	1	2	3	4	10
Accuracy (%)	45.14	65.31	69.84	75.4	78.34	68.17	82.61	89.09	91.81	97.95

But for the same data set, the accuracy of DLNs reaches 68.17 % when the iteration number is only 1. When the iteration number is 4, the accuracy converges to over 90 %. The accuracy of convergence increases by 24.1 % than the traditional neural network.

### 3.2 The Effect of Preprocessing Mechanism on the Performance of DLNs

As stated in Sect. 3, the input data of CAFFE should be in alternative sequence of category, and the size of it should be strictly  $32 \times 32$  pixels. Given the same training set, the experimental results of DLNs with and without preprocessing mechanism are shown in Fig. 5.

As shown in Fig. 5, DLNs with preprocessing mechanism can reach higher accuracy than traditional DLNs. The accuracy is 11.57 % higher on average. Besides, the mechanism also accelerates the convergence of accuracy. For DLNs with preprocessing mechanism, smaller training size is required to achieve the same accuracy.

### 3.3 The Influence of the Size of Training Set on the Performance of DLNs

For DLNs, we further analyze how the size of training set affects the accuracy of image classification. For the initial training set containing 50000 images, we trained

**Fig. 5** Comparison of accuracy between former and improved classifier

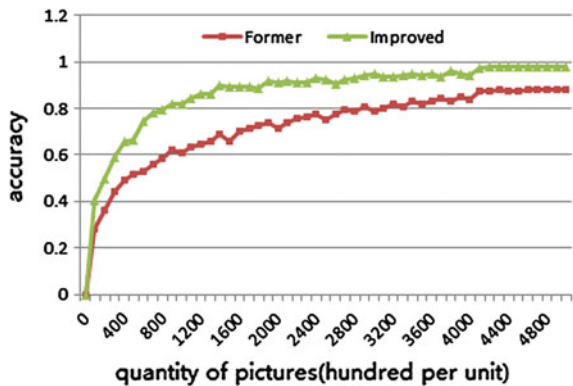


**Fig. 6** Relationship between initial size of training set and accuracy

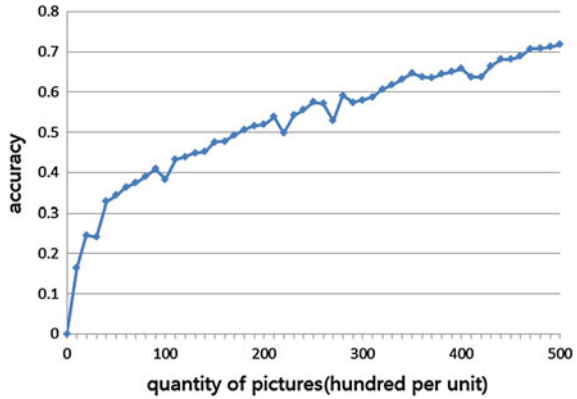
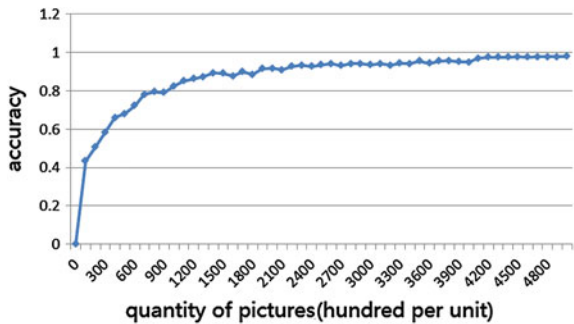


**Fig. 7** Relationship between iterative training set and accuracy



1000 images at a time, and recorded the accuracy of the current network. The relationship between the size of training set and accuracy is shown in Fig. 6.

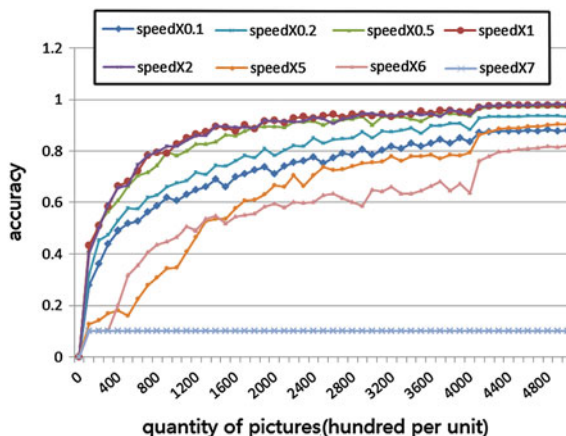
We find that the accuracy increases with the rising amount of training size. For further verification, we iterate the training set 10 times and train the DLNs with 10,000 images at a time. This experiment shows that the accuracy converges to approximately 98 % when the number of iterations is about 9 as shown in Fig. 7.

### 3.4 The Influence on Result of Different Learning Rates

This section studies the influence on training result using different learning rates. The benchmark is the learning rate whose measured result is best, and then, we adjust the learning rate for \*0.1, \*0.2, \*0.5, \*2, \*5, \*6, \*7, etc., and the corresponding convergence results are shown in Fig. 8.

It is obvious to see that the convergence speed slows down as the learning rate decreases, but it will eventually converge to a certain value. However, if the learning rate is too fast, the performance of the entire network will go bad. And

**Fig. 8** Relationship between iterative training set and accuracy under different learning rate



when the learning rate is 7 times of the benchmark or more, the accuracy rate will reduce to 10 %. That means, the network is completely out of work. Therefore, setting a suitable learning rate is very important.

### 3.5 *The Comparison Between Speed on GPU Mode and CPU Mode*

The experiments above were conducted in GPU mode. In this section, we analyze and compare the running time of GPU model and CPU model, giving the same training set and learning rate. The experimental result is shown that GPU requires less processing time than CPU when iteration time is the same. Its performance is 24.28 % higher than CPU as a whole. So the application of GPU model has more advantages in large data.

## 4 Conclusion

In this paper, we proposed an image classifier framework based on deep learning as an improvement of image classification for big data of power grid. To enhance the performance and to minimize the supervision in processing huge amount of data, a preprocessing mechanism was designed into our deep learning-based classifier framework. The mechanism improves the adaptability of classifier to images of arbitrary size and sequence and reduces the time to convergence of training the classifier. Apart from data preprocessing, the paper also identifies the relationship between learning rate, training size, mode, and training result. To improve the accuracy of image classification, appropriate learning rate and training size should

be carefully chosen. And for better training speed, GPU surpassed CPU by 24.28 % on average. In the future, we will speed up the implementation and application of the large data of grid, by developing image classification of high accuracy for images from electrical equipment based on the classifier of deep learning network.

**Acknowledgements** This work was supported in part by National High-tech R&D Program (863 Program) (SS2012AA050803, 2015AA050204) and the State Grid Corporation of China.

## References

1. Yangqing J et al (2013) An open source convolutional architecture for fast feature embedding. <http://caffe.berkeleyvision.org/>
2. Yaqi S, Guoliang Z, Yongli Z (2013) Present status and challenges of big data processing in smart grid. *Power Syst Technol* 37:927–935
3. Zhenyuan L, Baoju L, Zeyi W (2014) Research on influence of big data technology for the future development of the power grid. *Jilin Electr. Power* 42:10–13
4. Longchuan Y, Yaxi L, Binchen L, Ziyang Z (2013) Opportunity and challenge of big data for the power industry. *Electr Power IT* 11:1–4
5. Jia Y, Huang C, Darrell T (2012) Beyond spatial pyramids: receptive field learning for pooled image features. In: *IEEE conference on CVPR. IEEE 2012*, pp 3370–3377
6. Ji L, Pu X, Ye M et al (2011) Face extraction from video sequences by K-means clustering and fusion. In: *IEEE international conference on CSAE, vol 1. IEEE*, pp 358–361
7. Yue D, Yanjie W, Jingyu L et al (2012) Improvement of enhancement algorithm for aerial image. *Laser Infrared* 42:1080–1085
8. Cong Z, Zhiguo G (2011) Non-linear image sharpening approach based on noise estimation. *Comput Eng Appl* 47:154–156
9. Xuting T, Hongjie H, Fan C et al (2012) Pan-sharpening algorithm for remote sensing images based on local correlation. *ACTA PHOTONICA SINICA* 43:310003



# Whether the High-Voltage Transmission Lines Have Enough Load Capacity After Wildfire

Tianzheng Wang, Zhen Tang, Xinwei Wang, Jinzhao Yang,  
Xiaogang Wu, Kechao Zhao, Chong Zuo and Weiyi Chen

**Abstract** Wildfire which caused by a variety of reasons seriously affects the safe and stable operation of the high-voltage transmission lines, and the load capacity research of the high-voltage transmission lines after wildfire is particularly important. In the experiment, the average tensile force of three kinds of aluminum cable steel reinforced (ACSR), which are new, actually burned by wildfire and burned by simulated wildfire with firewood, respectively, is tested. The results show that the safety value of load capacity of the transmission lines is 15 kN. In the case where the horizontal span, height difference, and the maximum sag are known, the lowest point's horizontal tension of arc sag of the high-voltage transmission lines can be calculated. If it does not exceed 15 kN, even if the transmission lines subjected to wildfire, load capacity is greater than the tension of transmission lines. So it can usually operate safely. If the lowest point's horizontal tension exceeds 15 kN, in the process of design and installation of the high-voltage transmission lines, by properly increasing maximum arc sag of transmission lines, the tension of the lowest point of arc sag is not more than 15 kN.

**Keywords** Wildfire · The high-voltage transmission lines · The load capacity · Tension · Arc sag

## 1 Introduction

The high-voltage transmission lines, whose operation directly affects the whole power system, are an important part of power system. Therefore, it is particularly important to make accurate and detailed analysis on the high-voltage transmission lines. In order to ensure the safe and stable operation of the high-voltage trans-

---

T. Wang · Z. Tang · X. Wang  
State Grid Shanxi Electric Power Research Institute, Taiyuan 030001, China

J. Yang · X. Wu · K. Zhao · C. Zuo · W. Chen (✉)  
College of Mechanics, Taiyuan University of Technology, Taiyuan 030024, China  
e-mail: chenweiyi211@163.com

© Springer-Verlag Berlin Heidelberg 2016  
B. Huang and Y. Yao (eds.), *Proceedings of the 5th International Conference on Electrical Engineering and Automatic Control*, Lecture Notes in Electrical Engineering 367, DOI 10.1007/978-3-662-48768-6\_139

1243

mission lines, the domestic and foreign scholars have conducted a lot of research on mechanical properties of the high-voltage transmission lines at different conditions, including: Under the condition of different load and suspension mode, the formulas, which are often used in the process of design and installation, to calculate arc sag, stress, line length, and stress changes of the high-voltage transmission lines are deduced; by analyzing the unbalanced tension's damage of the high-voltage transmission lines, the mechanical model which is under the condition of unbalanced tension is established; by researching the high-voltage transmission lines' vibration characteristics of wind and rain, the theoretical model which is the coupling of rivulet motion and vibration on transmission line is established; by analyzing the dynamic tension of galloping process of transmission lines, the law of tension variation is derived; and using the method of harmonic synthesis simulates wind field numerically, transmission lines' analysis of response time-dependent of wind is derived by using the finite element software [1–5]. In the actual situation, China is a mountainous country, and the high-voltage transmission lines will inevitably pass through forest while trees and weeds could easily catch fire in the forest. In recent years, wildfire caused by various reasons often occurs. Wildfire will not only make the high-voltage transmission lines trip, but also make the tensile strength of transmission lines subjected to wildfire affected. If the tensile strength of transmission lines subjected to wildfire reduces too much, the security and stability of the high-voltage transmission lines will be seriously affected.

However, the research on the load capacity of the high-voltage transmission lines subjected to wildfire is not reported, in the public reported data. In view of this, through the combination of theoretical analysis and experimental method, according to the relationship among the tension of the lowest point of arc sag, maximum arc sag, and height difference, using the Matlab 12.0, under the condition of different horizontal span, height difference, and maximum arc sag, the lowest point's horizontal tension of arc sag of the high-voltage transmission lines is calculated. And combining with the obtained experimental data, the load capacity of the high-voltage transmission lines subjected to wildfire is further researched.

## 2 Mechanical Calculation of the High-Voltage Transmission Lines

Local transmission line is shown in Fig. 1. Universal type of catenary equation is as follows:

$$y = \frac{T_0}{\rho g} ch \frac{\rho g}{T_0} (x + C_1) + C_2 \quad (1)$$

For the case that suspension points on both ends of transmission lines are unequal height, usually taking the left side of the suspension point as the origin of cartesian coordinate system, which is shown in Fig. 2, the equations are as follows:

**Fig. 1** Local transmission line

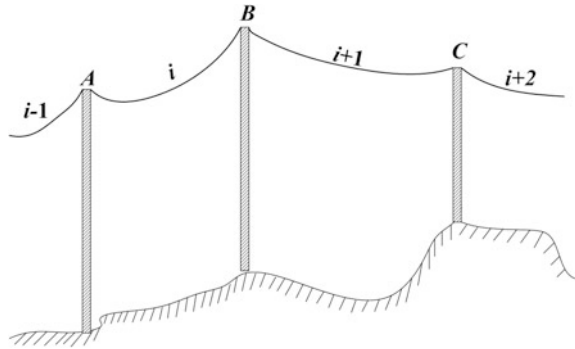
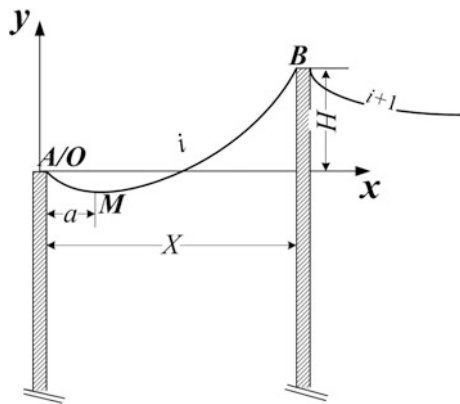


**Fig. 2** Established coordinate



$$y = \frac{T_0}{\rho g} \left[ ch \frac{\rho g}{T_0} (x - a) - ch \frac{\rho g a}{T_0} \right] \tag{2}$$

And

$$a = \frac{X}{2} - \frac{T_0}{\rho g} sh^{-1} \left( \frac{\rho g H}{2T_0 sh \frac{\rho g H}{2T_0}} \right) \tag{3}$$

where  $T_0$  is the lowest point's horizontal tension of arc sag of transmission lines, N/mm<sup>2</sup>;  $\rho$  is the density of transmission lines, kg/m;  $a$  is the abscissa of the lowest point of the arc sag;  $X$  is the horizontal span of two suspension points, m;  $H$  is the vertical height difference of two suspension points, m.

For the case that suspension points on both ends of transmission lines are equal height, just replacing above all equations with  $H = 0$ , the corresponding equations can be got.

Maximum arc sag  $f_m$  of the high-voltage transmission lines is as follows:

$$f_m = \frac{\rho g X^2}{8T_0 \cos \beta} \quad (4)$$

### 3 Analysis of Examples

The high-voltage transmission lines have 3 basic geometric parameters, which are horizontal span  $X$ , maximum arc sag  $f_m$ , and the height difference  $H$ , respectively. When these parameters are determined, the curve of the high-voltage transmission lines between two towers is determined exclusively. At the same time, the lowest point's horizontal tension of arc sag of the high-voltage transmission lines is also determined exclusively. For the actual transmission lines, horizontal span  $X$ , maximum arc sag  $f_m$ , and height difference  $H$  can be measured. Line density  $\rho$  and gravity acceleration  $g$  are constant. Therefore, the lowest point's horizontal tension  $T_0$  of arc sag of the high-voltage transmission lines can be calculated by Eq. (4).

In the case where horizontal spans are 500, 600, 700, 800, 900, and 1000 m, the lowest point's horizontal tension  $T_0$  of arc sag of the high-voltage transmission lines is calculated by using MATLAB 12.0. The calculation results are shown in Figs. 3, 4, 5, 6, 7, and 8.

From Figs. 3, 4, 5, 6, 7, and 8, in the case where horizontal span and maximum arc sag are constant, influence of the change of height difference on the tension of lowest point of arc sag can be ignored. In the case where horizontal span and height difference are constant, the tension of lowest point of arc sag will change obviously with the change of the maximum sag. And even if horizontal span is very large, for example, up to 1000 m, the tension of lowest point of arc sag is in the range from 20 to 25 kN when maximum sag is in the range from 70 to 80 m. This value is still not large. Therefore in the influence factors of height difference, maximum sag, and horizontal span, the most significant influence factor on the tension of lowest point

**Fig. 3** Changes of the lowest point's tension of arc sag, when horizontal span is 500 m

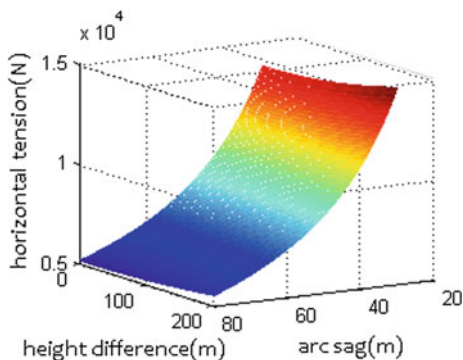


**Fig. 4** Changes of the lowest point's tension of arc sag, when horizontal span is 600 m

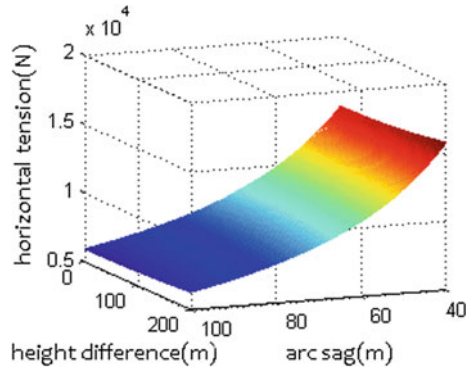


**Fig. 5** Changes of the lowest point's tension of arc sag, when horizontal span is 700 m

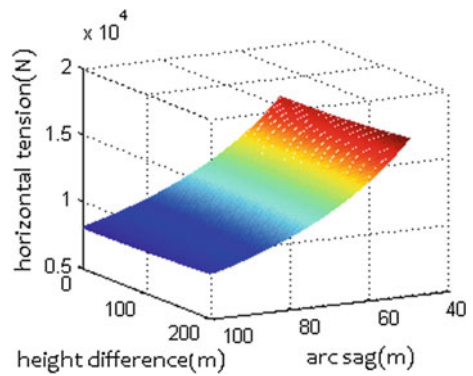
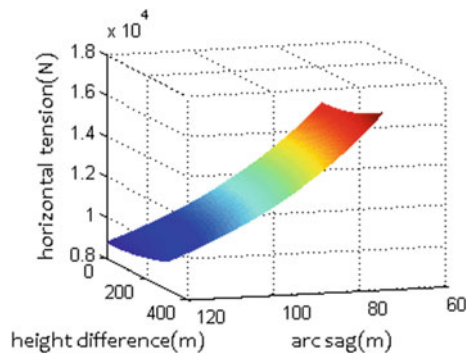


**Fig. 6** Changes of the lowest point's tension of arc sag, when horizontal span is 800 m



of arc sag is maximum sag. So even if the horizontal span is very large, the tension of lowest point of arc sag can always be reduced to expected value as long as maximum sag is increased properly.

**Fig. 7** Changes of the lowest point's tension of arc sag, when horizontal span is 900 m

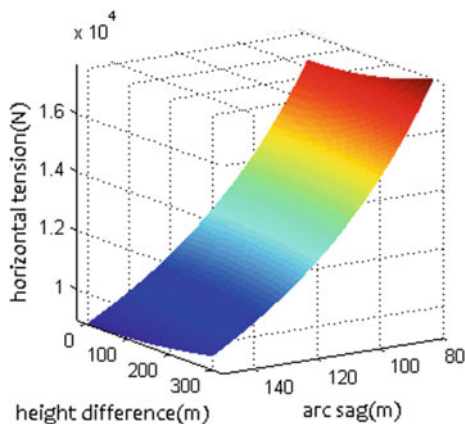
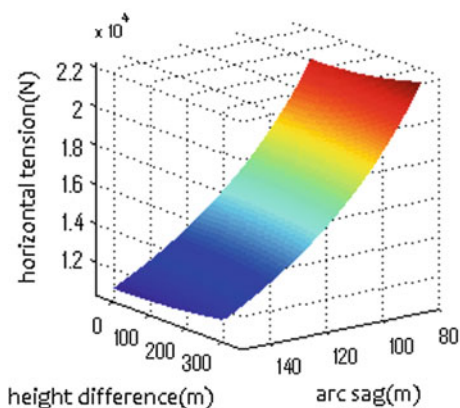


**Fig. 8** Changes of the lowest point's tension of arc sag, when horizontal span is 1000 m



## 4 Tensile Tests of ACSR

Taking JL/G1A-400/35 aluminum cable steel reinforced (ACSR) which is shown in Fig. 9 as experimental materials, and making the tensile test on ACSR by universal material testing machine which is shown in Fig. 10, tensile tests were conducted on three different cases of ACSR, respectively: new ACSR, ACSR actually burned by wildfire, and ACSR burned by simulated wildfire with firewood. The sample number of ACSR for untreated, burned by wildfire, and burned by simulated wildfire are 1, 1, and 3, respectively.

JL/G1A-400/35 ACSR consists of 3 layers of aluminum. From the outside to the inside, the quantities of each layer of aluminum wire are 22, 16, and 10, respectively. The quantity of steel core, which is located in the innermost layer, is 7. In the experiment, 5 samples of each layer were tested, and the test results were averaged.

The results are shown in Tables 1, 2, and 3.

**Fig. 9** JL/G 1A-400/35  
ACSR



**Fig. 10** Universal material testing machine



**Table 1** The average tensile force of new ACSR (N)

Wire	The first layer	The second layer	The third layer	Steel core
The average tensile strength	1718	1677	1554	7483

**Table 2** The average tensile force of ACSR actually burned by wildfire (N)

Wire	The first layer	The second layer	The third layer	Steel core
The average tensile strength	606	1411	1330	7459

**Table 3** The average tensile force of ACSR burned by simulated wildfire with firewood (N)

Wire	The first layer	The second layer	The third layer	Steel core
The first root	649	680	681	7239
The second root	652	656	660	6618
The third root	656	637	634	5547

## 5 Discussion

From Tables 1, 2, and 3, the average tensile force of ACSR actually burned by wildfire is higher than that of ACSR burned by simulated wildfire with firewood; the average tensile force of second and third layer of aluminum of ACSR actually burned by wildfire is higher than that of corresponding layer of aluminum of ACSR burned by simulated wildfire with firewood; the average tensile force of first layer of aluminum of ACSR actually burned by wildfire is approximately equal to that of corresponding layer of aluminum of ACSR burned by simulated wildfire with firewood. So it is safer to take the average tensile force of ACSR burned by simulated wildfire with firewood as calculation standard.

The minimum average tensile force of steel core burned by simulated wildfire with firewood is 5547 kN as shown in Table 3, which is lower than that of steel core actually burned by wildfire 7459 kN as shown in Table 2. So it is safer to take the average tensile force 5547 kN of steel core burned by simulated wildfire with firewood as the basis of experimental analysis.

JL/G1A-400/35 ACSR has 7 roots of steel cores. From above experimental data, the minimum tensile force of them is 38.8 kN. Considering the design safety factors of lowest point of arc sag shall not be less than 2.5 [6], even if without considering the load capacity of aluminum wire, ACSR actually burned by wildfire can withstand 15 kN.

In the process of the design and installation of the high-voltage transmission lines, by properly increasing of transmission lines' arc sag, the tension of the lowest point of arc sag is not more than 15 kN. Meanwhile, even if the transmission lines subjected to wildfire, the load capacity is greater than the tension of transmission lines. So it can usually operate safely.

## 6 Conclusion

The safe and stable operation of the high-voltage transmission lines is significant to guarantee the transmission capacity of power system. The results show that the safety value of load capacity of the transmission lines is 15 kN, which is derived from experiment. In the case where the horizontal span, height difference, and maximum sag are known, the lowest point's horizontal tension of arc sag of the high-voltage transmission lines can be calculated by Eq. (4). If it does not exceed



15 kN, even if the transmission lines subjected to wildfire, the load capacity is greater than the tension of transmission lines. So it can usually operate safely. If the lowest point's horizontal tension exceeds 15 kN, in the process of the design and installation of the high-voltage transmission lines, by properly increasing maximum arc sag of transmission lines, the tension of the lowest point of arc sag is not more than 15 kN.

## References

1. Shao T (2003) Mechanical calculation on overhead transmission line, 2nd edn. China Power Press, Beijing
2. Liu Q (2006) Analysis and calculation of transmission line unbalanced tensile force. *Electr Power Autom Equip* 26(1):93–95
3. Zhou C, Rui X (2013) Model of rain-induced vibration of transmission line and numerical analysis. *J Vib Shock* 32(6):173–175
4. Zhu K, Liu C, Ren X (2005) Analysis on dynamic tension of conductor under transmission line galloping. *Electr Power* 38(10):40–44
5. Lin X, Yan B, Liu Z, Chen Z (2009) Finite element simulation for windage yaw of 220 kV overhead transmission lines. *Chin J Appl Mech* 26(1):120–124
6. The China Power Enterprise Federation (editor in chief) (2010) Code for design of 110 kV ~ 750 kV overhead transmission line. China Planning Press, Beijing

# Design and Analysis of the Hydraulic System of the Small Slide Loader

Kailin Feng, Guanguo Ma and Yipeng Chen

**Abstract** The working theory of chain shotcrete machines was introduced. By analyzing the relationship between plungers' moving rules and beton throughput, as well as the relationship of the sending wind hole, we can acquire the best way and provide other designers the theoretical basis to design the chain shotcrete machines.

**Keywords** Slide loader · Hydraulic system · Elevating stent · AMESim

## 1 Introduction

Small loader is also called slide loader. It is a kind of mobile devices, wheeling with the different velocity of two sides. This kind of wheeling way can make the slide loader turn to a corner with a small radius, and its operating way is very smart. Based on these advantages [1], the slide loaders used in a limited situation such as coal mine tunnels to convey something are very convenient and can decrease the working intensity.

## 2 The Working Theory of Chain Beton Shotcrete Machines

This kind of slide loader can complete these works such as shoveling material, loading, conveying, elevating, and unloading, which decide the working device should conclude the shovel loader, tipper-hopper, and elevating stent. When the slide loader works, it goes forward and scoops up material [1–3]. Then, the hydraulic cylinder of shovel loader puts out, which puts the material into the tipper-hopper. And the loader turns back and goes to the aimed place. The hydraulic cylinder of the elevating stent puts out, and the tipper-hopper rises to the designated

---

K. Feng (✉) · G. Ma · Y. Chen

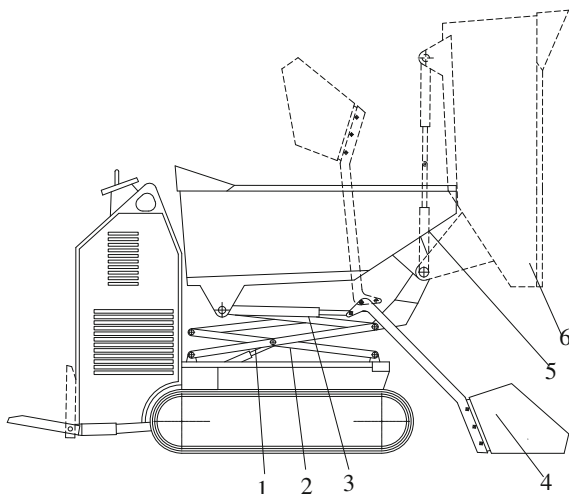
Shandong University of Science and Technology, Shandong 266590, China  
e-mail: qs\_shen@126.com

© Springer-Verlag Berlin Heidelberg 2016

B. Huang and Y. Yao (eds.), *Proceedings of the 5th International Conference on Electrical Engineering and Automatic Control*, Lecture Notes in Electrical Engineering 367, DOI 10.1007/978-3-662-48768-6\_140

1253

**Fig. 1** The slide loader working construction. 1 The hydraulic cylinder of the elevating stent, 2 elevating stent, 3 the hydraulic cylinder of shovel loader, 4 shovel loader, 5 the hydraulic cylinder of the tipper-hopper, and 6 tipper-hopper



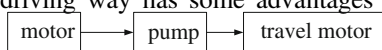
spot. The hydraulic cylinder of the tipper-hopper puts out, and the tipper-hopper overturns to put the material into the designated spot [4, 5]. Figure 1 shows the slide loader working construction.

Figure 1 shows the structure diagram of chain shotcrete machines. This kind of chain beton shotcrete machines use round link chain derived by the driving chain wheel pulling the plunger, which can convey beton to the place where the compressed air can blow the beton away.

### 3 The Design of the Hydraulic System of the Slide Loader

The slide loader uses the way of full hydraulic to convey power, which can be describe as follows:

The full hydraulic driving way has some advantages that other driving ways



cannot compete with, which can be described as follows:

1. Bigger torque can be exported, which can drive the big moving.
2. Continuously moving can be achieved, and the velocity can be changed with moving.
3. The install place is small, and the structure is compact.
4. The overload protection can be achieved.

This slide loader has a small whole structure. It can move smartly in the tunnel with the compact structure. In order to make the machine more compact, the hydraulic of the running gear was designed to be closed circuit.

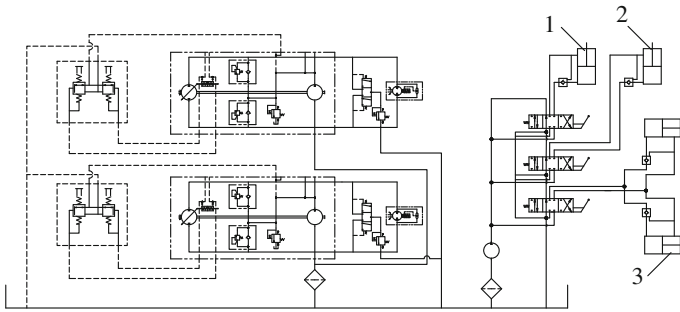


**Fig. 2** The principle of hydraulic system. 1 The hydraulic cylinder of the elevating stent, 2 the hydraulic cylinder of the tipper-hopper, and 3 the hydraulic cylinder of shovel loader

In order to make the two hydraulic motor work dependently in the running. The slide loader use two dependent closed-circuit pump. In the hydraulic system of the closed circuit, the rotate speed was under the control of the variable pump, which can change its flow rate with the change of its pump swashplate angle. We can use the pilot control handle to control the hydraulic cylinder that can change the pump swashplate angle. The hydraulic system can be shown as Fig. 2.

The working device of this slide loader includes the shovel loader, tipper-hopper, and elevating stent, whose driving device is hydraulic cylinder. When the system is not working, the working device may drop down, because of the leakage of the hydraulic cylinder, which is not allowed in the designing principle. We should avoid the condition appearing again. The system of the working device should have a pilot-operated check valve to avoid this situation. The hydraulic system is shown as Fig. 2.

## 4 The Simulated Analysis of the Hydraulic System of the Elevating Stent

### 4.1 The Force Analysis of the Hydraulic Cylinder of the Elevating Stent

In the working device, the hydraulic system of the elevating stent bears the biggest force. So if the hydraulic cylinder of the elevating stent meets the requirements, the other hydraulic cylinder will also meet the requirements (Fig. 3).

$$F_1 = \frac{G}{\cos \theta} \tag{1}$$



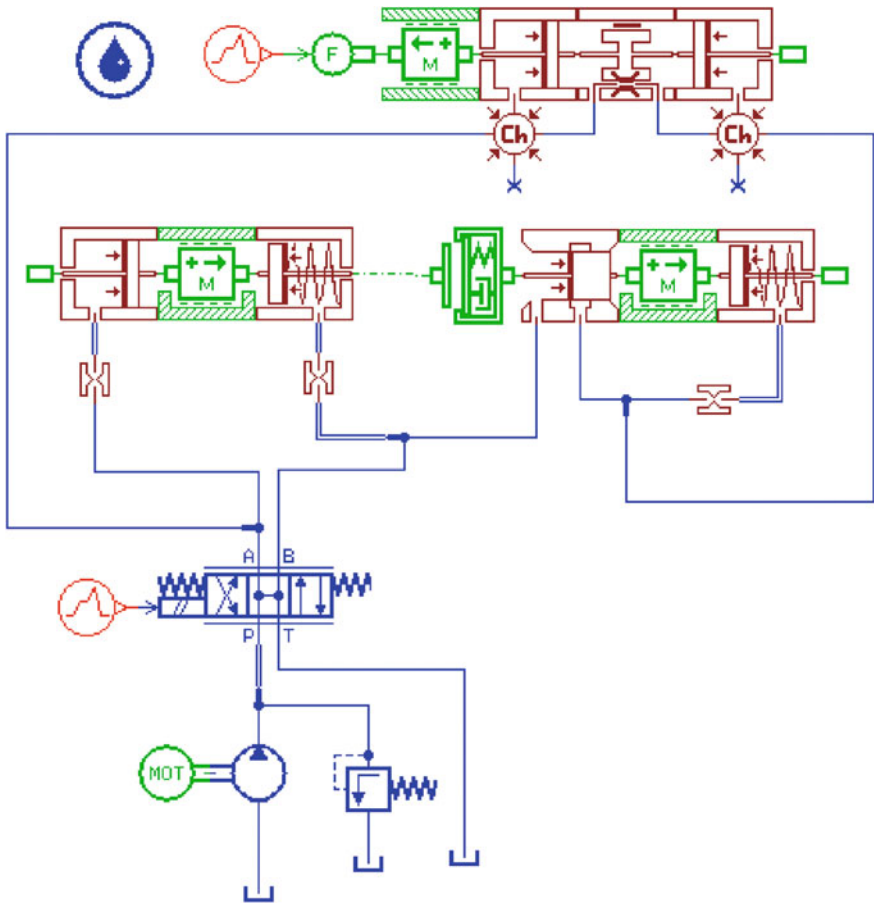


Fig. 5 The AMESim model of the hydraulic system of elevating stent

hydraulic cylinder. So we can search and verify the safety of the hydraulic system of the elevating stent.

The hydraulic system of the elevating stent can be established based on the AMESim, as in Fig. 5. Each pivotal element parameter is described as follows: The displacement of the dosing pump is 13 mL/r. The revolving velocity of the motor is 1500 r/min. The relief valve setting pressure is 16 MPa. The diameter of the plunger of the hydraulic cylinder is 100 mm. According to the equation, we can affirm the force that is applied to the hydraulic cylinder of the elevating stent.

## 5 Making up the AMESim Model

The stimulation time is set to 10 s. The calculation step time is set to 0.001 s. Fig. 6 shows the curve of the hydraulic control one-way valve pressure-displacement and the pressure-flow rate. Comparing the two curves, we can see that when the pressure of P1 is 0.18 MPa, the hydraulic control one-way valve opens. From the figure, we can see that when the pressure rises to 0.48 MPa, the two curves appear as the obvious transition, after which the slope would not change. All of these can say that when the pressure comes to 0.48 MPa, the hydraulic control one-way valve opens completely. The cracking pressure is less than 1 MPa, which fits the hydraulic system of the elevating stent demand.

When the elevating stent of the slide loader rises and stays at the high place, the hydraulic cylinder would bear a big force. If the hydraulic cylinder has no problem, the elevating stent will not drop down. According to the Formula 1, we can know that the force  $F_1$  is bigger with a bigger  $\theta$ . And the gravity is  $G = 2000$  N, so the  $F_1 = 7727$  N, with the biggest  $\theta = 75^\circ$ . In the AMESim model of the leg hydraulic cylinder in Fig. 5, when the inputting sign is zero, the valve element of reversing valve is at the middle place. The force applied to the piston rod of the hydraulic cylinder is  $F_1 = 7727$  N. Then, the AMESim model is run, and the pressure curve of the hydraulic cylinder of the elevating stent was putted out as in Fig. 7.

From Fig. 7, we can know that when the elevating stent was working, the pressure of the hydraulic cylinder big cavity can be stable at 8 MPa approximately,

**Fig. 6** The cracking pressure of the hydraulic control one-way valve.  
**a** Pressure-displacement.  
**b** Pressure-flow rate

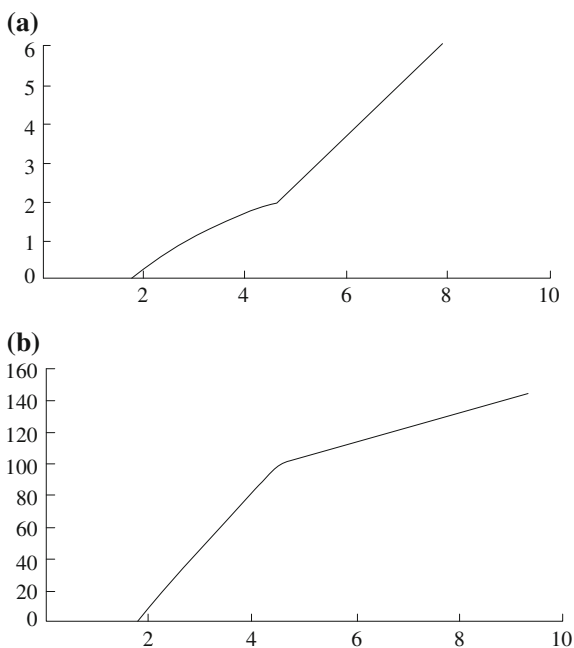
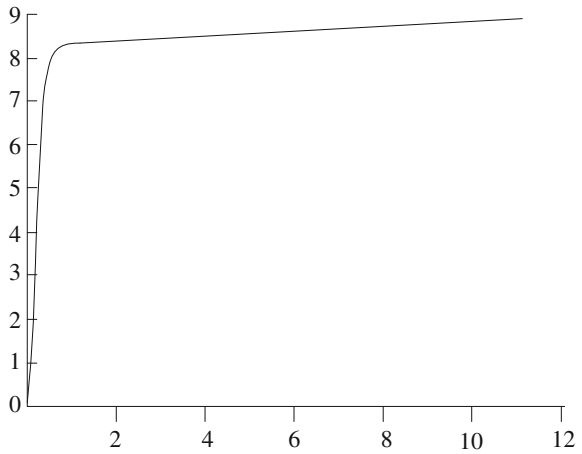


**Fig. 7** The pressure curve of the hydraulic cylinder of the elevating stent



which cannot exceed the design requirements of the hydraulic cylinder. So the elevating stent wouldn't happen Instability phenomenon.

## 6 Conclusions

Along with the development of the society, small slide loader gets a quicker development because of its advantage such as flexibility and accessibility. In this study, the structure of the slide loader was introduced. And the hydraulic system of the slide loader was designed, based on its structure. The advantage of the full hydraulic driving way was summarized. The hydraulic system of the elevating stent that bears the biggest force in the slide loader was analyzed using AMESim. The cracking pressure was analyzed, and the character of pressure maintenance was confirmed, which can ensure the working reliability. The AMESim is used to make simulation of the hydraulic system, which is convenient and smart. And the curve acquired from the simulation of the AMESim soft can react the system characteristic correctly, which can reduce the designing period, reduce the cost of product development, and provide useful parameter for designers. All of these can provide theoretical basis for further analysis and optimization of the system.

## References

1. Pingge Z, Hanjing H, Leilei G et al (2014) The fault research for hydraulic leg based on AMESim. *Chin Hydraulics Pneumatics* 11:88–90
2. Li W (2014) Analysis of FDD125/40 hydraulic operated check valve based on AMESim simulation. *Coal Mine Mach* 05:68–70



3. Zhou X, Jiang L, Gao J (2012) Simulation analysis for leakage of hydraulic cylinder based on AMESim. *Hydromechatronics Eng* 12:147–150
4. Wang H, Lu Z, Che X (2014) The design for the hydraulic system of small slide loaders using in the coal. *Coal Mine Mach* 06:114–115
5. Fu Y, Qi X (2006) *The modeling and simulation of AMESim system*. Beihang University Press, Beijing

# An Extended Kalman Filter Application on Moving Object Tracking

Yuan Niu and Lisheng Hu

**Abstract** In this paper, the problem of moving object tracking on 2D plane is addressed by combining uncertain information from measurement of the object to accurately estimate its trajectory. Due to the nonlinear motion model of the tracked moving object, the extended Kalman filter technique (EKF) is applied. In particular, the models of object motion and measurement including noise are established. After substituting those models to the equations of EKF, an optimal estimated trajectory can then be rendered that stays as close to the expected one. An example is given to perform the process of EKF algorithm. Simulation results with Monte Carlo simulation are shown to verify the validity of the EKF in solving the moving object tracking problem.

**Keywords** Extended Kalman filter · Moving object tracking · Nonlinear motion model · Monte Carlo simulation

## 1 Introduction

The object tracking problem is a critical issue in wide applications, such as radar surveillance in battlefield, anti-aircraft system, and the civil traffic control. The essence of that issue is estimating the positions and other relevant information of moving objects. Many filtering techniques have been proposed to obtain more reliable information through fusion of those obtained data that contains noise, i.e., White Gaussian Noise. The Kalman filter (KF) is the best possible estimator for a large class

---

Y. Niu (✉) · L. Hu  
Department of Automation, Shanghai Jiao Tong University,  
Shanghai 200240, China  
e-mail: ufo2kay@sjtu.edu.cn

Y. Niu · L. Hu  
Key Laboratory of System Control and Information Processing,  
Ministry of Education of China, Shanghai 200240, China

of systems with uncertainty [1]. It was first proposed in [2] and has been one of the most well-known tools for stochastic state estimation from noisy measurements.

However, for object tracking problem, motion of moving objects is often complex and nonlinear, which may invalidate the KF. Since then, other extensions of KF such as the extended Kalman filter (EKF) [3] or the unscented Kalman filter [4] are needed to solve data fusion of nonlinear system. The EKF is an adapted technique, namely multivariate Taylor series expansions, from calculus to linearize about a working point became the working solution. If the system model is not well known or is inaccurate, then Monte Carlo methods can be employed for estimation. In the case of well-defined transition models, the EKF has been considered standard in the theory of nonlinear state estimation, navigation systems, and GPS [5].

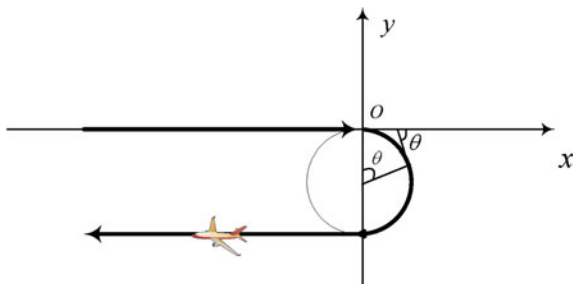
In this paper, we mainly use the EKF technique to consider a typical tracking problem for an aircraft moving on 2D plane. At first, basic equations of EKF are introduced. After that, we embedded the predicted object motion model and measurement equations in the form of EKF equations. Then, the recursive EKF algorithm can be applied to render an optimal estimated trajectory of the object.

## 2 Problem Formulation

This paper mainly discusses how EKF can be employed to solve object tracking problem. In this section, an object tracking task on 2D plane is formulated. Considering a flying vehicle in the air, we hope to estimate the position, velocity, and acceleration states of the vehicle, such that its trajectory can be better tracked by the radar, see Fig. 1.

To simplify the discussion, we assume that the motion of flying vehicle in Fig. 1 can be classified as three stages of motion, which are advancing, circular motion, and return, all with the same constant linear velocity.  $\theta \in (0, \pi)$  represents the orientation of the vehicle with respect to  $x$ -axis. The motion state of vehicle can be denoted by state vector as  $X = [r_x, r_y, \theta, v, a]^T$ , where  $r_x, r_y, \theta, v, a$  are the coordinates, orientation, linear velocity, and acceleration of the vehicle. According to the basic kinematic laws, we could obtain mutual relations among those state variables as follows ( $\omega$  denotes the angular velocity of the vehicle):

**Fig. 1** A flying vehicle levels off on 2D plane



$$\omega = a/v, \quad \theta = \omega t, \quad v_x = v \cos\theta, \quad v_y = -v \sin\theta \tag{1}$$

Furthermore, we can use the information at  $k - 1$  moment to predict new information at  $k$  moment without considering noise or disturbance, as follows ( $T$  is the sampling interval):

$$\begin{aligned} r_x(k) &= r_x(k - 1) + v_x T = r_x(k - 1) + v \cos \theta T, \quad r_y(k) = r_y(k - 1) + v_y T = r_x(k - 1) - v \sin \theta T \\ \theta(k) &= \theta(k - 1) + \omega T = \theta(k - 1) + \frac{a}{v} T, \quad v(k) = v(k - 1) + u_v(k), \quad a(k) = a(k - 1) + u_a(k) \end{aligned} \tag{2}$$

Until now, we have derived the state equations to predict vehicle’s state according to information at the last moment without noise and disturbance. The major task in this paper is to pick the optimal estimation of state vector  $X(k|k)$  from measurement and prediction with White Gaussian Noise, such that a desired tracking trajectory can be specified to formulate real path of the object as accurate as possible.

### 3 Basic Extended Kalman Filter

EKF is the most common method as a nonlinear filtering method. It uses a system’s dynamics model (e.g., physical laws of motion), known control inputs to that system, and multiple sequential measurements (such as from sensors) to form an estimate of the system’s varying quantities (its state) that is better than the estimate obtained by using any one measurement alone. Compared to simple KF algorithm, EKF focuses on single sampling points and conducts Taylor expansion at the estimated value in order to achieve linearization.

System model: First, we consider the general discrete control process system formulated by nonlinear stochastic difference equation and its observation equation as follows:

$$X(k + 1) = f(k, X(k)) + W(k), \quad Z(k) = h(k, X(k)) + V(k) \tag{3}$$

where  $X(k + 1)$  and  $Z(k)$  are the system state at  $k + 1$  moment and the measurement value at  $k$  moment, respectively.  $f(k, X(k))$  and  $h(k, X(k))$  are the nonlinear state transition matrix of the system and the nonlinear observation matrix, respectively.  $W(k)$  and  $V(k)$  represent the noise in motion process and measurement. They are assumed to be the White Gaussian Noise. Their corresponding covariances are  $Q$  and  $R$ . It is assumed that  $W(k): N(0, Q(k))$  and  $V(k): N(0, R(k))$  are independent process. The initial conditions of  $W(k)$  and  $V(k)$  are mutually independent.

Then, we conduct the first-order Taylor series expansion to the state transition matrix  $f(k, X(k))$  at  $X(k|k)$  in (3) and take the expectation, which yields the state prediction equation and the state prediction covariance equation as follows:

$$X(k+1|k) = f(k, X(k|k)), P(k+1|k) = F(k)P(k)F(k)^T + Q(k) \quad (4)$$

where

$$F(k) = \left. \frac{\partial f(k, X(k))}{\partial X(k)} \right|_{X(k)=x(k|k)} \quad (5)$$

is the Jacobian matrix of  $f$ . Likewise, we conduct the first-order Taylor series expansion to the nonlinear observation matrix  $h(k, X(k))$  at  $X(k+1|k)$  in (3) and take the expectation; then, we have observation prediction equation and the updated information covariance equation as follows:

$$\begin{aligned} Z(k+1|k) &= h(k+1, X(k+1|k)), \\ S(k+1) &= H(k+1)P(k+1|k)H(k+1)^T + R(k+1) \end{aligned} \quad (6)$$

where

$$H(k+1) = \left. \frac{\partial h(k+1, x(k+1))}{\partial X(k+1)} \right|_{X(k+1)=x(k+1|k)} \quad (7)$$

is the Jacobian matrix of  $h$ . It should be noted that in EKF there are two assumptions:

All the errors are zero-mean (unbiased).

The covariance of prediction error is equal to that obtained from the algorithm.

To that end, we have linearized the nonlinear system equations and obtained the approximate KF equations. In order to unify the notations, we denote the two matrices in (5) and (7) as  $A(k)$  and  $H(k)$ . The rest of the parts of the EKF are the same process as KF. Based on (4), we assume that  $X(k|k-1)$  is the predicted state based on the state at last moment.  $X(k-1|k-1)$  is the optimal state at  $k-1$  moment. With the information at last moment, new state can be updated. Next, with the new notation, we update the covariance  $P(k|k-1)$  that corresponds to  $X(k|k-1)$  as follows:

$$P(k|k-1) = A(k-1)P(k-1|k-1)A(k-1)^T + Q(k-1) \quad (8)$$

where  $P(k - 1|k - 1)$  is the corresponding covariance of state  $X(k - 1|k - 1)$ .  $Q(k - 1)$  is the covariance of system process. Equations (4) and (8) are the prediction processes. Now the predicted result is obtained, and measurement at  $k$  moment (present) can be collected. By integrating predicted and measured values, the optimal estimation of  $X(k|k)$  can be derived as follows:

$$\begin{aligned} X(k|k) &= X(k|k - 1) + Kg(k)(Z(k) - HX(k|k - 1)), \\ Kg(k) &= P(k|k - 1)H^T/S(k) \end{aligned} \tag{9}$$

where  $Kg(k)$  is the Kalman Gain(time variant) and  $S(k)$  is the updated information covariance equation from (6). Until now, we have obtained the optimal estimation of state  $X(k|k)$ . Moreover, in order to keep recursive calculation of EKF algorithm, we continue to update the covariance of state  $X(k|k)$  at  $k$  moment.

$$P(k|k) = (I - Kg(k)H)P(k|k - 1) \tag{10}$$

where  $I$  is the identity matrix. When  $k + 1$  moment arrives, value of  $P(k|k)$  is substituted to  $P(k - 1|k - 1)$  in (8). By doing so, the EKF algorithm could continue to calculate recursively. In this paper, we investigate the object tracking problem in the form of EKF Eqs. (4), (8)–(10) with updated matrices in (5) and (7).

### 3.1 Extended Kalman Filter Equations of Tracking Problem

In this part, we substitute corresponding information of tracking problem to specify system and measurement models in the form of those EKF equations and obtain the optimal estimation of state vector of the object. According to (3), we can rewrite the state Eq. (2) of object in a system form as:

$$X(k) = f(X(k - 1)) + u(k) \tag{11}$$

where  $u(k) = [0, 0, 0, u_v(k), u_a(k)]^T$  represents control input of the tracking system. It should be noted that the driving noise is included in  $u(k)$ . Then, consider Eq. (5), we can obtain the state transition matrix of tracking system (11) and the driving noise as follows:

$$A = \frac{\partial f}{\partial X} = \begin{bmatrix} 1, 0, -\frac{1}{2}v \sin \theta T, \cos \theta T, 0 \\ 0, 1, -\frac{1}{2}v \cos \theta T, -\sin \theta T, 0 \\ 0, 0, 1, -\frac{a}{v^2}T, T/v \\ 0, 0, 0, 1, 0 \\ 0, 0, 0, 0, 1 \end{bmatrix}, \quad Q = \begin{bmatrix} 0, 0, 0, 0, 0 \\ 0, 0, 0, 0, 0 \\ 0, 0, 0, \sigma_v^2, 0 \\ 0, 0, 0, 0, \sigma_a^2 \end{bmatrix} \tag{12}$$

It is assumed that  $u_v(k)$  and  $u_a(k)$  are irrelevant. Their respective variance are  $\sigma_v^2$  and  $\sigma_a^2$ . The observation vector is as follows. It should be noted that only positions of the object can be observed, which means that observation vector will not include orientation, velocity, and acceleration information.

$$Z(k) = \begin{bmatrix} r_x(k) \\ r_y(k) \end{bmatrix} + w(k) \quad (13)$$

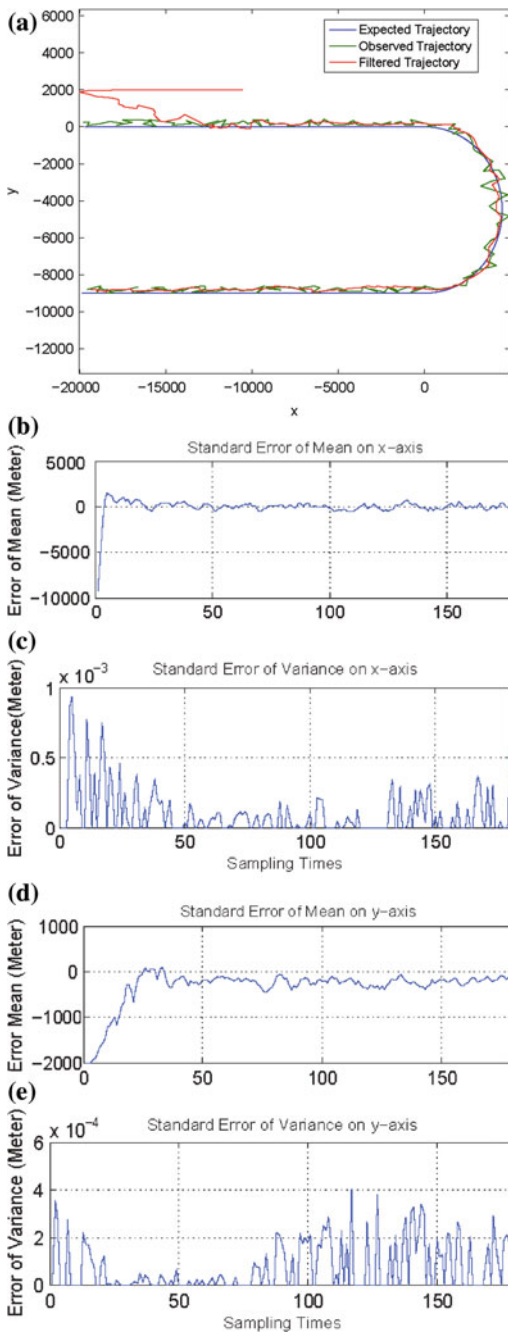
where  $w(k) = \begin{bmatrix} u_x(k) \\ u_y(k) \end{bmatrix}$ . Therefore, consider the equation in (7), the observation matrix  $H$  is  $H = \begin{bmatrix} 1, 0, 0, 0, 0 \\ 0, 1, 0, 0, 0 \end{bmatrix}$ . It is also assumed that  $u_x(k)$  and  $u_y(k)$  are irrelevant with respect to variance  $\sigma_x^2$  and  $\sigma_y^2$ . The observation noise matrix is  $R = \begin{bmatrix} \sigma_x^2, 0 \\ 0, \sigma_y^2 \end{bmatrix}$ . Combining the obtained equations above, we can derive the EKF equations of object tracking problem as follows:

$$\begin{aligned} \hat{X}(k|k-1) &= f(\hat{X}(k-1|k-1)), P(k|k-1) = AP(k-1|k-1)A^T + Q \\ \mathbf{K}g(k) &= P(k|k-1)H^T(R + HP(k|k-1)H^T)^{-1}, \hat{X}(k|k) \\ &= \hat{X}(k|k-1) + \mathbf{K}g(k)(X(k) - H\hat{X}(k|k-1)) \\ P(k|k) &= (I - \mathbf{K}g(k)H)P(k|k-1) \end{aligned} \quad (14)$$

## 4 Simulation

In this section, simulations are shown to verify the effectiveness of EKF method. The real and measured initial position of the vehicle are  $(-20000, 0)$  and  $(-10000, 2000)$ . The results of using EKF method with Monte Carlo running time  $M = 100$  are performed in Fig. 2. It is noted that the filtered trajectory is generated by recursively calculating EKF equations of object tracking problem in (14). The corresponding standard error of mean and variance on both axes is plotted in Fig. 2b–e. From these figures, it is shown that the filtered trajectory in Fig. 2a could well converge to the expected trajectory, even along the circular segments, which proves the good property of EKF method.

**Fig. 2** EKF application on moving object tracking problem. **a** The expected, observed, and filtered trajectories of the aircraft. **b** Standard error of mean on  $x$ -axis. **c** Standard error of variance on  $x$ -axis. **d** Standard error of mean on  $y$ -axis. **e** Standard error of variance on  $y$ -axis





## 5 Conclusions

This paper briefly introduces the framework of EKF and its application on object tracking problem. The motion system model of object and its observation model are explicitly established. By integrating the equations of object tracking problem into EKF forms, the optimal estimated trajectory is derived. Simulation results are provided to confirm the validity of EKF application on tracking problem addressed in this paper. Future works include finding derivative methods from EKF and other filtering techniques to deal with more complicated object motion model.

## References

1. Grewal M, Andrews A (1993) Kalman filtering: theory and practice. Prentice-Hall Inc, Englewood Cliffs
2. Kalman RE, Rudolph E (1960) A new approach to linear filtering and prediction problems. *Trans ASME-J Basic Eng* 82(1):35–45
3. Lefferts EJ, Markley FL, Shuster MD (1982) Kalman filtering for spacecraft attitude estimation. *J Guidance Control Dyn* 5(5):417–429
4. Wan EA, Van Der Merwe R (2000) The unscented Kalman filter for nonlinear estimation. In: *Adaptive systems for signal processing, communications, and control symposium, AS-SPCC*
5. Mohinder SG, Angus PA (2011) Kalman filtering: theory and practice using MATLAB. Wiley, Hoboken